frontiers | Research Topics

From cold seeps to hydrothermal vents: geology, chemistry, microbiology, and ecology in marine and coastal environments

Edited by
Glen T. Snyder, Stéphanie Dupré, Carolyn Ruppel, Marcelo Ketzer and Andrew R. Thurber

Published in
Frontiers in Earth Science
Frontiers in Marine Science



FRONTIERS EBOOK COPYRIGHT STATEMENT

The copyright in the text of individual articles in this ebook is the property of their respective authors or their respective institutions or funders. The copyright in graphics and images within each article may be subject to copyright of other parties. In both cases this is subject to a license granted to Frontiers.

The compilation of articles constituting this ebook is the property of Frontiers.

Each article within this ebook, and the ebook itself, are published under the most recent version of the Creative Commons CC-BY licence. The version current at the date of publication of this ebook is CC-BY 4.0. If the CC-BY licence is updated, the licence granted by Frontiers is automatically updated to the new version.

When exercising any right under the CC-BY licence, Frontiers must be attributed as the original publisher of the article or ebook, as applicable.

Authors have the responsibility of ensuring that any graphics or other materials which are the property of others may be included in the CC-BY licence, but this should be checked before relying on the CC-BY licence to reproduce those materials. Any copyright notices relating to those materials must be complied with.

Copyright and source acknowledgement notices may not be removed and must be displayed in any copy, derivative work or partial copy which includes the elements in question.

All copyright, and all rights therein, are protected by national and international copyright laws. The above represents a summary only. For further information please read Frontiers' Conditions for Website Use and Copyright Statement, and the applicable CC-BY licence.

ISSN 1664-8714
ISBN 978-2-8325-5566-8
DOI 10.3389/978-2-8325-5566-8

About Frontiers

Frontiers is more than just an open access publisher of scholarly articles: it is a pioneering approach to the world of academia, radically improving the way scholarly research is managed. The grand vision of Frontiers is a world where all people have an equal opportunity to seek, share and generate knowledge. Frontiers provides immediate and permanent online open access to all its publications, but this alone is not enough to realize our grand goals.

Frontiers journal series

The Frontiers journal series is a multi-tier and interdisciplinary set of open-access, online journals, promising a paradigm shift from the current review, selection and dissemination processes in academic publishing. All Frontiers journals are driven by researchers for researchers; therefore, they constitute a service to the scholarly community. At the same time, the *Frontiers journal series* operates on a revolutionary invention, the tiered publishing system, initially addressing specific communities of scholars, and gradually climbing up to broader public understanding, thus serving the interests of the lay society, too.

Dedication to quality

Each Frontiers article is a landmark of the highest quality, thanks to genuinely collaborative interactions between authors and review editors, who include some of the world's best academicians. Research must be certified by peers before entering a stream of knowledge that may eventually reach the public - and shape society; therefore, Frontiers only applies the most rigorous and unbiased reviews. Frontiers revolutionizes research publishing by freely delivering the most outstanding research, evaluated with no bias from both the academic and social point of view. By applying the most advanced information technologies, Frontiers is catapulting scholarly publishing into a new generation.

What are Frontiers Research Topics?

Frontiers Research Topics are very popular trademarks of the *Frontiers journals series*: they are collections of at least ten articles, all centered on a particular subject. With their unique mix of varied contributions from Original Research to Review Articles, Frontiers Research Topics unify the most influential researchers, the latest key findings and historical advances in a hot research area.

Find out more on how to host your own Frontiers Research Topic or contribute to one as an author by contacting the Frontiers editorial office: frontiersin.org/about/contact

From cold seeps to hydrothermal vents: geology, chemistry, microbiology, and ecology in marine and coastal environments

Topic editors

Glen T. Snyder — The University of Tokyo, Japan

Stéphanie Dupré — Centre de Bretagne, Institut Français de Recherche pour l'Exploitation de la Mer, France

Carolyn Ruppel — US Geological Survey (USGS), United States

Marcelo Ketzer — Linnaeus University, Sweden

Andrew R. Thurber — Oregon State University, United States

Citation

Snyder, G. T., Dupré, S., Ruppel, C., Ketzer, M., Thurber, A. R., eds. (2024). *From cold seeps to hydrothermal vents: geology, chemistry, microbiology, and ecology in marine and coastal environments*. Lausanne: Frontiers Media SA.

doi: 10.3389/978-2-8325-5566-8

Table of contents

06 Editorial: From cold seeps to hydrothermal vents: geology, chemistry, microbiology, and ecology in marine and coastal environments
Glen T. Snyder, Andrew R. Thurber, Stéphanie Dupré, Marcelo Ketzer and Carolyn D. Ruppel

11 A new species of the genus *Catillopecten* (Bivalvia: Pectinoidea: Propeamussiidae): morphology, mitochondrial genome, and phylogenetic relationship
Yi-Tao Lin, Yi-Xuan Li, Yanan Sun, Jun Tao and Jian-Wen Qiu

23 Microbial traces found in microdolomite associated with seep-related shallow gas hydrate
Fumito Shiraishi, Takayuki Akimoto, Naotaka Tomioka, Yoshio Takahashi, Ryo Matsumoto and Glen T. Snyder

32 Controlling factors on patterns of dissolved organic carbon and volatile fatty acids in a submarine mud volcano offshore southwestern Taiwan
Nai-Chen Chen, Tsanyao Frank Yang, Ya-Hsuan Liou, Huei-Ting Tina Lin, Wei-Li Hong, Saulwood Lin, Chih-Chieh Su, Li-Hung Lin and Pei-Ling Wang

47 Origins of sediments and fluids in submarine mud volcanoes off Tanegashima Island, northern Ryukyu Trench, Japan
Akira Ijiri, Ryoma Setoguchi, Yuki Mitsutome, Tomohiro Toki, Masafumi Murayama, Kyoko Hagino, Yohei Hamada, Takeyasu Yamagata, Hiroyuki Matsuzaki, Wataru Tanikawa, Osamu Tadai, Kazuya Kitada, Tatsuhiko Hoshino, Takuro Noguchi, Juichiro Ashi and Fumio Inagaki

67 Diving deeper into seep distribution along the Cascadia convergent margin, United States
Jane A. Rudebusch, Nancy G. Prouty, James E. Conrad, Janet T. Watt, Jared W. Kluesner, Jenna C. Hill, Nathaniel C. Miller, Sally J. Watson and Jess I. T. Hillman

83 Abundant off-axis hydrothermal activity in the 29–30 ridge segment of the Southwest Indian Ridge: evidence from ferromanganese crusts
Xianhui Yang, Chunhui Tao and Shili Liao

97 Assessing the activity of mud volcanism using boron isotope ratios in pore water from surface sediments of mud volcanoes off Tanegashima (SW Japan)
Yuki Mitsutome, Ko Agena, Tomohiro Toki, Ke-Han Song, Ryuichi Shinjo and Akira Ijiri

110 Methane-flow system within the Nyegga pockmark field, offshore mid-Norway
Stéphanie Dupré, Jean-Paul Foucher, Catherine Pierre, Carole Decker, Graham Westbrook, Stephan Ker, Karine Olu, Jean-Pierre Donval, Jean-Luc Charlou, Marie-Madeleine Blanc-Valleron and Hervé Nouzé

134 Integration of untargeted metabolomics and microbial community analyses to characterize distinct deep-sea methane seeps
Margaret A. Redick, Milo E. Cummings, George F. Neuhaus, Lila M. Ardor Bellucci, Andrew R. Thurber and Kerry L. McPhail

148 Microbial communities and mineral assemblages in sediments from various habitats at the Haima Cold Seep, South China Sea
Jianzhen Liang, Jing-Chun Feng, Jie Kong, Yongji Huang, Hui Zhang, Song Zhong, Li Tang and Si Zhang

163 Seascape ecology in the vicinity of a Blake Ridge cold seep
Kellie Johnson, Avery Taylor, Annika Socha, Ellie Barkyoumb, Koichi Nakamura, Carl L. Kaiser, Christopher R. German, Dana R. Yoerger and Cindy Lee Van Dover

183 Distribution of dissolved methane in seawater from the East China Sea to the Ryukyu forearc
Tomohiro Toki, Hideki Chibana, Teppei Shimabukuro and Yo Yamakawa

197 Recent and episodic activity of decoupled mud/fluid discharge at Sartori mud volcano in the Calabrian Arc, Mediterranean Sea
Mechthild Doll, Miriam Römer, Thomas Pape, Martin Kölling, Norbert Kaul, Christian dos Santos Ferreira and Gerhard Bohrmann

215 Identification of a large mud volcano field in the Hyuga-nada, northern end of the Ryukyu trench, offshore Japan
Miho Asada, Mikiya Yamashita, Rina Fukuchi, Toshiyuki Yokota, Tomohiro Toki, Akira Ijiri and Kiichiro Kawamura

230 Assessing biogeochemical controls on porewater dissolved inorganic carbon cycling in the gas hydrate-bearing sediments of the Makran accretionary wedge, Northeastern Arabian Sea off Pakistan
Yuanqing Chen, Sinan Xu, Weining Liu, Zhen Zhang, Tianbang Yang, Xiao Xiao, Xiguang Deng, Jiangtao Li, Huiqiang Yao and Zijun Wu

252 Hydrothermal activity fuels microbial sulfate reduction in deep and distal marine settings along the Arctic Mid Ocean Ridges
Desiree L. Roerdink, Francesca Vulcano, Jan-Kristoffer Landro, Karen E. Moltubakk, Hannah R. Babel, Steffen Leth Jørgensen, Tamara Baumberger, Ingeborg E. Økland, Eoghan P. Reeves, Ingunn H. Thorseth, Laila J. Reigstad, Harald Strauss and Ida H. Steen

270 Comparative omics analysis of a deep-sea barnacle species (Cirripedia, Scalpellomorpha) and shallow-water barnacle species provides insights into deep-sea adaptation
Ning Mao, Wentai Shao, Yuefeng Cai, Xue Kong, Nanjing Ji and Xin Shen

285 Corrigendum: Comparative omics analysis of a deep-sea barnacle species (Cirripedia, Scalpellomorpha) and shallow-water barnacle species provides insights into deep-sea adaptation
Ning Mao, Wentai Shao, Yuefeng Cai, Xue Kong, Nanjing Ji and Xin Shen

289 Commentary: Comparative omics analysis of a new deep-sea barnacle species (Cirripedia, Scalpellomorpha) and shallow-water barnacle species provides insights into deep-sea adaptation
Benny K. K. Chan, Hiromi Kayama Watanabe and Chong Chen

293 Exploring the pore fluid origin and methane-derived authigenic carbonate properties in response to changes in the methane flux at the southern Ulleung Basin, South Korea
Ji-Hoon Kim, Myong-Ho Park, Jong-Sik Ryu, Kwangchul Jang, Jiyoung Choi, Sanghee Park, Yungoo Song, Bo-Yeon Yi, Young Ji Joo, Tae-Hoon Kim and Jin Hur

311 Diversity, spatial distribution and evolution of inactive and weakly active hydrothermal deposits in the TAG hydrothermal field
Ewan-Loiz Pelleter, Mélanie Principaud, Anne-Sophie Alix, Audrey Boissier, Sandrine Cheron, Florian Besson, Vincent Altorffer, Charline Guérin, Arnaud Gaillot, Delphine Pierre, Mathieu Rospabé, Thomas Giunta, Léa Grenet, Cecile Cathalot, Marie-Anne Cambon and Yves Fouquet

336 Dispersion and fate of methane emissions from cold seeps on Hikurangi Margin, New Zealand
Cliff S. Law, Charine Collins, A. Marriner, Sarah J. Bury, Julie C. S. Brown and Graham Rickard

frontiers | Frontiers in Earth Science

TYPE Editorial
PUBLISHED 04 October 2024
DOI 10.3389/feart.2024.1496572

Check for updates

OPEN ACCESS

EDITED AND REVIEWED BY
Sabine Schmidt,
Centre National de la Recherche Scientifique (CNRS), France

*CORRESPONDENCE
Carolyn D. Ruppel,
cruppel@usgs.gov

RECEIVED 14 September 2024
ACCEPTED 20 September 2024
PUBLISHED 04 October 2024

CITATION
Snyder GT, Thurber AR, Dupré S, Ketzer M and Ruppel CD (2024) Editorial: From cold seeps to hydrothermal vents: geology, chemistry, microbiology, and ecology in marine and coastal environments.
Front. Earth Sci. 12:1496572.
doi: 10.3389/feart.2024.1496572

COPYRIGHT
© 2024 Snyder, Thurber, Dupré, Ketzer and Ruppel. This is an open-access article distributed under the terms of the Creative Commons Attribution License (CC BY). The use, distribution or reproduction in other forums is permitted, provided the original author(s) and the copyright owner(s) are credited and that the original publication in this journal is cited, in accordance with accepted academic practice. No use, distribution or reproduction is permitted which does not comply with these terms.

Editorial: From cold seeps to hydrothermal vents: geology, chemistry, microbiology, and ecology in marine and coastal environments

Glen T. Snyder[1,2], Andrew R. Thurber[3], Stéphanie Dupré[4], Marcelo Ketzer[5] and Carolyn D. Ruppel[6]*

[1]Atmosphere and Ocean Research Institute, The University of Tokyo, Kashiwa, Japan, [2]Faculty of Science, Gakushuin University, Toshima, Japan, [3]Department of Ecology, Evolution, and Marine Biology, University of California, Santa Barbara, CA, United States, [4]UMR GEO-OCEAN, Institut Français de Recherche pour l'Exploitation de la Mer, Plouzane, France, [5]Department of Biology and Environmental Science, Linnaeus University, Kalmar, Sweden, [6]U.S. Geological Survey, Woods Hole, MA, United States

KEYWORDS

seep, vent, mud volcanism, fluid flow, hydrate, seabed minerals

Editorial on the Research Topic
From cold seeps to hydrothermal vents: geology, chemistry, microbiology, and ecology in marine and coastal environments

1 Background

This Research Topic compiles contemporary studies on cold seeps, hydrothermal vents, mud volcanoes, and related seafloor features that are associated with focused fluid emissions and the transfer of carbon, other chemical species, and sometimes heat from the geosphere to the ocean. Because these features sometimes tap fluids and gas originating kilometers below the seafloor, they provide an important window into deep processes that are otherwise inaccessible to scientists. At the shallow portion of their journey, migrating fluids nearing the seafloor contribute to a range of unique biological, physical, and chemical processes within the sediments themselves and at the sediment-water interface.

Seafloor fluid emissions play a critical role in global biogeochemical cycles, ocean chemistry, and possibly even climate change. Seafloor leakage points often emit hydrocarbon gases (especially methane and CO_2) and are sometimes the loci for deposition of seafloor minerals that have economic value. A burgeoning area of research focuses on natural products generated at these features, seeking compounds with potential pharmaceutical or other applications.

Multidisciplinary studies have become routine for characterization of seafloor fluid emission sites, attesting to the inseparability of geologic, physical, chemical, and biological processes in these settings. It is increasingly common for researchers to combine in a single research cruise: subbottom imaging and seafloor mapping; porewater and water column geochemistry and gas sampling; sediment retrieval for lithologic, biostratigraphic, and solid phase analyses; and studies of benthic and subseafloor communities at the microbial to

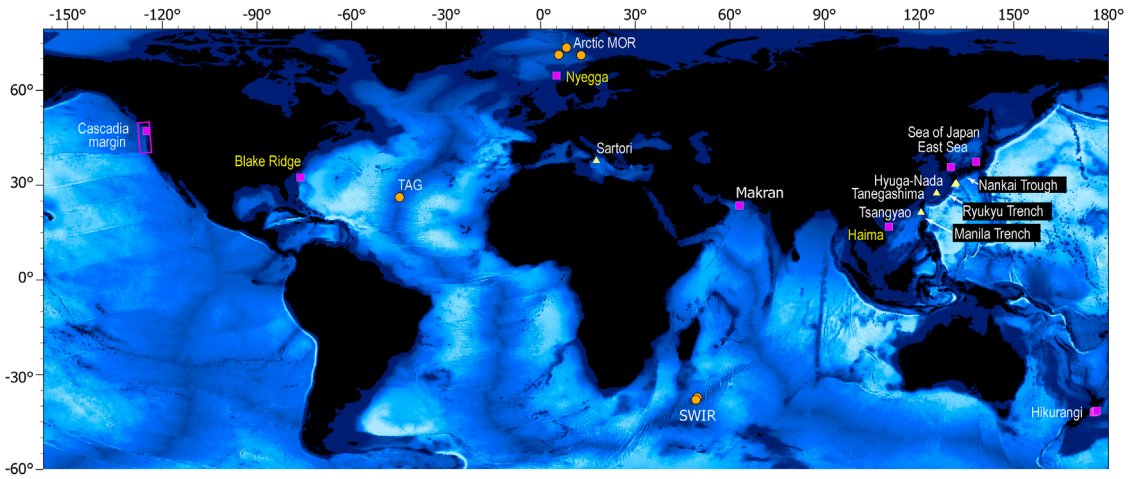

FIGURE 1
Geographic focus areas for studies included in the Research Topic. Purple squares and the box on the Cascadia margin mark cold seep sites, with yellow labels indicating those on passive margins (Blake Ridge, Nyegga, and Haima). Orange circles denote hydrothermal vent sites, and yellow triangles correspond to mud volcanoes. Seafloor fluid emission features have been recognized in all oceans, on most marine continental margins (active and passive), and near all types of plate boundaries. MOR denotes mid-ocean ridge; SWIR is the Southwest Indian Ridge; and TAG is the Trans-Atlantic Geotraverse hydrothermal area.

macrofaunal scales. This multidisciplinary approach has the advantage of ensuring the spatial and temporal coincidence of surveys and samples, an important factor at highly dynamic seafloor fluid emission sites. In addition, researchers often use remotely operated vehicles (ROVs), autonomous underwater vehicles (AUVs), or human-occupied vehicles (HOVs) to record video of the seafloor, compile photomosaics, collect targeted samples, and survey with high-resolution geophysical near-seafloor systems, providing a degree of detail about seafloor fluid emission sites that is unprecedented compared to most areas of the deep ocean. While rarer, long-term cabled observatories or shorter-term deployments of portable observatories are also used at some loci for seafloor fluid flux and are particularly helpful for capturing temporal variations at these dynamic features.

Here we summarize the Research Topic's contribution to multidisciplinary seafloor emission studies in the categories of cold seeps, mud volcanoes, and hydrothermal vents. Figure 1 shows the geographic distribution of the studies in this Research Topic and key features referred to in this Introduction.

2 Cold seeps

Cold seeps derive their name from seafloor fluid emissions at temperatures similar to those of the overlying seawater. Cold seeps are found in a variety of settings, and deep-sea cold seeps often originate in areas characterized by a range of processes, including deep-seated fluid overpressures or dewatering sediments, degradation of gas hydrate above salt diapirs, and suboxic or anoxic sediments in which microbial methanogenesis exceeds methane oxidation in the shallow seabed. Methane (mostly microbial) is usually the predominant gas emitted at cold seeps, but CO_2 and light thermogenic hydrocarbons (ethane, propane) may also be present. Anaerobic oxidation of methane (AOM) with accompanying sulphate reduction usually cannot keep pace with rapid methane flux directly at seeps, and AOM in the surrounding sediments contributes to the formation of methane derived authigenic carbonates (MDAC). Beneath the sulphate reduction zone that extends into the sediments from the seafloor in locations slightly removed from the point of emission, gas hydrates are common. Hydrate deposits in high flux seeps can sometimes be massive, in contrast to the low saturation pore-filling hydrates common in much of the deep ocean. On the seafloor, cold seeps can be associated with pockmarks, MDAC outcrops, hydrate mounds, barite chimneys, or other features.

The widespread adoption of shipborne technologies that can rapidly detect water column gas plumes associated with active cold seeps has led to the discovery of cold seep provinces in every ocean and on most continental margins over the past 15 years. The cold seep studies included in this Research Topic highlight both active (Hikurangi, Cascadia, and Makran) and passive (Nyegga, Blake Ridge, and South China Sea) margins and encompass papers ranging from multidisciplinary investigations of cold seep processes to focused studies on microbial and benthic community characteristics.

The deliberately multidisciplinary approach for investigation of seafloor fluid emissions is epitomized in the study by Dupré et al., who explore processes associated with active seepage in the Nyegga pockmark field on the Norwegian margin. The researchers supplement seismic imagery, seafloor mapping, and sedimentologic data with ROV surveys. Their work reveals strong heterogeneity in seepage patterns, seafloor morphology, and dissolved methane concentrations across the pockmark field and uses the distribution of chemosynthetic fauna and microbial mats as markers for the vigor of gas seepage. They also offer a conceptual model for the migration of methane gas through the seabed hydrate stability zone to reach the overlying ocean as bubbles emitted at a seafloor seep.

Another type of multidisciplinary approach is adopted by Rudebusch et al. who focus on the geologic factors controlling the spatial distribution of cold seeps across the accretionary prism of the Cascadia convergent margin offshore the U.S. Pacific Northwest. More than 3,000 gas flares having been recognized in this geologically complex setting, and the researchers combine water column and seafloor data and geologic maps in a statistical approach focused on identifying the geomorphological and structural controls on seep distribution. Although some past studies have attributed concentrated seepage on this margin to degradation of gas hydrate near its landward limit of stability (e.g., Johnson et al., 2019), the province-wide analysis shows that seeps are primarily associated with deformation features (faults, anticlines) in the outer arc high, as well as with canyons and slope failures on the upper continental slope.

As evidence has emerged that cold seeps are far more widespread than had been previously known, determining their role in the marine carbon cycle has become more important. Seeps not only transfer methane carbon from below the seafloor into the ocean, but also play a critical role in transporting aged dissolved organic carbon (DOC) to ocean waters (Pohlman et al., 2011). A study by Law et al. adds to research estimating regional methane fluxes from cold seeps using the Hikurangi Margin offshore New Zealand as the study area. Instead of scaling up from bubble studies or analyses of methane plumes at individual seeps, the researchers adopt an oceanography-based approach that combines water column methane concentration measurements and constraints on ocean currents in local and regional hydrodynamic models. Their results also show that water column oxidation of emitted methane is not expected to significantly change pH or local concentrations of dissolved CO_2.

While water column studies have significantly advanced understanding of the fluxes of gases and other chemical constituents across the sediment-water interface at cold seeps, the associated sediments and porewaters hold critical secrets about fluid migration, seabed biogeochemical cycling, and the formation of MDAC. In the Makran accretionary wedge seep province offshore Pakistan, Chen et al. study sulphate, dissolved inorganic carbon (DIC), and cation concentrations and δ^{13}C-DIC in sediment porewaters at seeps and background sites. DIC flux is up to four times greater at the hydrate-bearing seep sites than at background sites, and the dominance of AOM leads to MDAC formation at the seeps. Kim et al. supplement porewater geochemical analyses with stable carbon, oxygen, and hydrogen isotopic data and petrological analyses of MDAC in cold seeps from southern Ulleung Basin in the East Sea. They infer massive gas hydrate accumulations beneath the seeps and demonstrate the influence of seawater carbonate in MDAC formation above the sulphate-methane transition.

Investigations of the synergy between microbial processes and geologic characteristics continue to be at the forefront of interdisciplinary research on cold seeps and now extend beyond the well-known connection between MDAC and AOM. Liang et al. describe significant microbial heterogeneity among cold seeps in the Haima area of the South China Sea and uncover a striking interplay between sediment mineralogy and microbial community structure. In that study, the sediment composition appears to be influencing microbial communities. Shiraishi et al. focus on the opposite relationship, in which microbial surfaces affect microdolomite deposition. Using X-ray and electron microscopy of samples from a hydrate-bearing sediment core retrieved at a pockmark in the Umitaka Spur, Sea of Japan, they demonstrate clear differences between microdolomite formed inorganically *versus* in association with microbes at different depths within the hydrate deposits.

Instead of the biology-physics link, Redick et al. explore the link between microbes and chemical compounds, namely, natural products associated with microbes or other living organisms and potentially useful for medicinal, antiseptic, or other purposes. Their study couples metabolomic and microbial community structure analysis of sediments collected at seeps and background locations on the Cascadia margin. The investigation demonstrates that the degree of microbial diversity and the range of associated natural products at a seep are related not only to vigor of fluid activity at the site, but also the age of the seep.

Studies of seep macrofauna have long been a cornerstone of interdisciplinary studies linking fluid migration and benthic community structure. At a large scale, Johnson et al. choose the well-known Blake Ridge seeps as the focus area for a seascape approach focused on determining the distances over which seeps affect deep sea communities. They find that seeps influence benthic taxa to distances of tens of meters, underscoring the concept that seeps are critical oases of life in the deep ocean. Other macrofaunal studies in this Research Topic describe new organisms discvered at seeps. Lin et al. discovered a new species of the genus *Catillopecten*, a deep-sea glass scallop, in the Haima cold seep area. Their work included morphological, anatomical, and molecular analyses to characterize the new species and to estimate its time of divergence from a known genus.

3 Mud volcanoes

Mud volcanoes (e.g., Mazzini and Etiope, 2017) are a special category of cold seeps associated with seafloor constructional edifices that form by the fluidization and expulsion of fine-grained sediments. They commonly emit methane-rich gases, which are sometimes of thermogenic origin, and exist both onshore and offshore and on both active and passive margins. Some mud volcanoes are associated with fluids warmer than ambient seawater but still colder than hydrothermal vents. While mud volcanoes are observed in some hydrocarbon basins (e.g., Gulf of Mexico), many of these features have formed in the accretionary wedges and forearcs of convergent margins, likely due to dewatering of wedge sediments. With one exception, studies on mud volcanoes in this Research Topic all focus on western Pacific subduction zones.

Asada et al. describe the discovery of mud volcanoes in the tectonically-complex Hyuga-Nada area east of Japan. The Kyushu-Palau Ridge is subducting beneath the Amur plate in this area (Yamamoto et al., 2013), which is just north of the junction of the Ryukyu and Nankai troughs. Fourteen mud volcanoes have been mapped in the Kumano forearc basin to the north, and the identification of 27 mud volcanoes in the Hyuga-Nada area in this study substantially expands the geographic extent of these features on this margin. The authors use geophysical data to characterize the Hyuga-Nada mud volcanoes and describe multiple bottom simulating reflections in some locations. They postulate that the Hyuga-Nada mud volcano field extends southward to the

Tanegashima area of the Ryukyu trench forearc, forming a large and continuous zone of sediment fluidization.

The Sartori mud volcano is on the accretionary wedge of the Calabrian subduction zone on the northern margin of the Mediterranean Sea is in a similar position relative to the trench as the Hyuga-Nada area. Doll et al. use geophysical data and sediment, porewater, and gas samples to unravel spatio-temporal variations in mud volcanism at the Sartori site. Their results imply that mud volcanism has been largely quiescent since 10 ka, and they conclude that recent fluid migration and release are dominated by diffusive methane flux fed by mixed microbial and thermogenic sources.

Porewater geochemistry is a powerful tool for analyzing fluid dynamics and microbial processes at seeps, and the large footprint and high fluid flux at mud volcanoes make it possible to capture strong lateral gradients in geochemical signatures and to search for the influence of fluids derived from deep in the sedimentary section. Chen et al. measure dissolved organic carbon (DOC) and volatile fatty acid profiles in sediment cores from the Tsangyao Mud Volcano Group, which is set in an accretionary setting in the forearc of the Manila trench south of Taiwan. Numerical modeling indicates that *in situ* organic matter degradation controls DOC patterns in most locations, with fluid migration processes becoming more important in influencing DOC characteristics at loci of known active flows. The models also suggest the co-existence of sulphate reduction and methanogenesis in the sediments in this dynamic setting. Ijiri et al. focus on mud volcanoes in the Tanegashima area of the Ryukyu trench forearc and use primarily porewater chloride concentrations and isotopic data to demonstrate that fluids feeding the mud volcanoes originate deep in the sediments and are affected by clay mineral dehydration reactions. They show that the most active mud volcanoes are associated with the strongest signals for deep fluids and also highlight a component of thermogenic methane in the gas emissions. Working in the same area, Mitsutome et al. couple porewater salinity data with measurements of boron and lithium concentrations and boron isotopes. Porewaters that were fresher than seawater, but that also contained higher concentrations of boron and lithium, originate kilometers beneath the mud volcanoes, and upward advection rates are inferred to be as high as 14 cm/yr.

4 Hydrothermal vents

Hydrothermal vents emit fluids at temperatures significantly higher than ambient seawater and are found in areas with active submarine magmatism or volcanism, including mid-ocean ridges and associated off-axis sites. While fluids emitted at these vents may be influenced by deep magmatic processes, water-rock interactions are often the primary source of gas and fluid emissions. CO_2 is typically the most important component of emitted gases in these settings. Seafloor structures (e.g., minerals) surrounding hydrothermal vents result from the reaction between migrating fluids and cooler seawater, which leads to precipitation of minerals at the seafloor.

Hydrothermal vents are often emphasized as the loci for the leakage of hot fluids. However, a study by Pelleter et al. highlights the role of both high-temperature and later low-temperature flux in the formation of seafloor massive sulfide (SMS) mineral occurrences at hydrothermal vents. Working at the famous Trans-Atlantic Geotraverse (TAG) hydrothermal field (Scott et al., 1974) on the slow-spreading northern Mid-Atlantic Ridge, the researchers use observations from HOV dives, sampling, and mapping to study SMS, which are increasingly being scrutinized as potential sources for metals critical to manufacturing and industrial processes. The study highlights the role of diffuse, lower temperature fluid flow at SMS for which high temperature flow has ceased and concludes that the grades of some of the newly-discovered SMS at TAG are lower than comparable onshore volcanogenic massive sulfide deposits with respect to key metals.

Yang et al. also study mineral occurrences associated with hydrothermal vents, focusing on ferromanganese crusts near the ultra-slow-spreading Southwest Indian Ridge. They discover two new hydrothermal fields and describe mineralization processes in those and other off-axis hydrothermal areas. The study demonstrates a mixed hydrogenetic (from seawater) and hydrothermal origin for the ferromanganese crusts. These crusts contain lower concentrations of cobalt and rare earth elements than typical purely hydrogenetic crusts forming far from hydrothermal activity.

Hydrothermal vent fields at the rarely-visited Arctic Mid-Ocean Ridge (MOR) are the focus of a study that links hydrothermal and cold seep processes. While microbial sulphate reduction is a key process in near-seafloor sediments near many cold seeps, reactive organic carbon is rarely available to fuel widespread sulphate reduction in the deep sea, far from continental margins. Roerdink et al. show that sulphate reduction rates are substantially elevated near both low- and high-temperature hydrothermal vents at the remote Arctic MOR. The zones of vigorous sulphate reduction are associated with cold-seep-like flux indicators such as microbial mats and seep chemosynthetic communities.

Mao et al. and an associated commentary by Chan et al. focus on the identification and analysis of deep-sea barnacles associated with hydrothermal vent settings. Mao et al. compare a shallow water barnacle with a barnacle species (Cirripedia, Scalpellomorpha) that inhabits hydrothermal vents to discern the evolutionary adaptations to the vent species' genome and transcriptome. The data show that the hydrothermal vent taxa have undergone selection towards refined mitochondrial energy production. The marker gene and genomic approach caried out by Chan et al. refine the species identification of the vent species analyzed by Mao et al.

Toki et al. provide insights into all the types of seafloor fluid emissions sites covered in this Research Topic. They measure dissolved methane and seawater environmental parameters along a transect from the continental shelf of the East China Sea to the Ryukyu trench. Their results reveal clear water column signatures over known cold seeps, mud volcanoes, and hydrothermal vents. However, they also detect methane anomalies that are uncorrelated with known features, implying that new seafloor emission sites may await discovery.

5 Conclusion

The original research papers summarized here provide a broad overview of the current state of science on seafloor emissions sites, as well as an introduction to some novel techniques and approaches.

While the papers are not exhaustive in covering every component of geological, physical, chemical, and biological processes, they set the stage for future work on a wide variety of global seafloor fluid emission features.

Author contributions

GS: Writing–original draft, Writing–review and editing. AT: Writing–original draft, Writing–review and editing. SD: Writing–original draft, Writing–review and editing. MK: Writing–original draft, Writing–review and editing. CR: Visualization, Writing–original draft, Writing–review and editing.

Acknowledgments

We thank all authors, reviewers, and outside editors who contributed to the success of this Research Topic. K. Mizell (USGS) and B. Danforth (USGS) provided reviews that improved this manuscript. Any use of trade, firm, or product names is for descriptive purposes only and does not imply endorsement by the U.S. Government.

Conflict of interest

The authors declare that the research was conducted in the absence of any commercial or financial relationships that could be construed as a potential conflict of interest.

Publisher's note

All claims expressed in this article are solely those of the authors and do not necessarily represent those of their affiliated organizations, or those of the publisher, the editors and the reviewers. Any product that may be evaluated in this article, or claim that may be made by its manufacturer, is not guaranteed or endorsed by the publisher.

References

Johnson, H. P., Merle, S., Salmi, M., Embley, R., Sampaga, E., and Lee, M. (2019). Anomalous concentration of methane emissions at the continental shelf edge of the northern Cascadia margin. *J. Geophys. Res. Solid Earth* 124, 2829–2843. doi:10.1029/2018JB016453

Mazzini, A., and Etiope, G. (2017). Mud volcanism: an updated review. *Earth-Science Rev.* 168, 81–112. doi:10.1016/j.earscirev.2017.03.001

Pohlman, J. W., Bauer, J. E., Waite, W. F., Osburn, C. L., and Chapman, N. R. (2011). Methane hydrate-bearing seeps as a source of aged dissolved organic carbon to the oceans. *Nat. Geosci.* 4, 37–41. doi:10.1038/NGEO1016

Scott, R., Rona, P., McGregor, B., and Scott, M. R. (1974). The TAG hydrothermal field. *Nature* 251, 301–302. doi:10.1038/251301a0

Yamamoto, Y., Obana, K., Takahashi, T., Nakanishi, A., Kodaira, S., and Kaneda, Y. (2013). Imaging of the subducted Kyushu-Palau ridge in the Hyuga-nada region, western Nankai trough subduction zone. *Tectonophysics* 589:90–102. doi:10.1016/j.tecto.2012.12.028

frontiers | Frontiers in Marine Science

TYPE Original Research
PUBLISHED 27 April 2023
DOI 10.3389/fmars.2023.1168991

Check for updates

OPEN ACCESS

EDITED BY
Andrew R. Thurber,
Oregon State University, United States

REVIEWED BY
Gennady Kamenev,
Far Eastern Branch (RAS) (NSCMB FEB RAS), Russia
Helena Wiklund,
University of Gothenburg, Sweden

*CORRESPONDENCE
Jian-Wen Qiu
qiujw@hkbu.edu.hk

RECEIVED 18 February 2023
ACCEPTED 05 April 2023
PUBLISHED 27 April 2023

CITATION
Lin Y-T, Li Y-X, Sun Y, Tao J and Qiu J-W (2023) A new species of the genus *Catillopecten* (Bivalvia: Pectinoidea: Propeamussiidae): morphology, mitochondrial genome, and phylogenetic relationship. *Front. Mar. Sci.* 10:1168991. doi: 10.3389/fmars.2023.1168991

COPYRIGHT
© 2023 Lin, Li, Sun, Tao and Qiu. This is an open-access article distributed under the terms of the Creative Commons Attribution License (CC BY). The use, distribution or reproduction in other forums is permitted, provided the original author(s) and the copyright owner(s) are credited and that the original publication in this journal is cited, in accordance with accepted academic practice. No use, distribution or reproduction is permitted which does not comply with these terms.

A new species of the genus *Catillopecten* (Bivalvia: Pectinoidea: Propeamussiidae): morphology, mitochondrial genome, and phylogenetic relationship

Yi-Tao Lin[1,2], Yi-Xuan Li[1,2], Yanan Sun[3], Jun Tao[4] and Jian-Wen Qiu[1,2]*

[1]Department of Biology, Hong Kong Baptist University, Hong Kong, Hong Kong SAR, China, [2]Southern Marine Science and Engineering Guangdong Laboratory (Guangzhou), Guangzhou, China, [3]Laboratory of Marine Organism Taxonomy and Phylogeny, Qingdao Key Laboratory of Marine Biodiversity and Conservation, Institute of Oceanology, Chinese Academy of Sciences, Qingdao, China, [4]MLR Key Laboratory of Marine Mineral Resources, Guangzhou Marine Geological Survey, China Geological Survey, Guangzhou, China

Catillopecten is a small genus of deep-sea glass scallops, but its diversity is poorly known in many parts of the world ocean. We described *C. margaritatus* n. sp. (Pectinoidea: Propeamussiidae), and performed morphological analyses and DNA sequencing, and estimated the divergence time of scallops based on samples collected from Haima cold seep in the South China Sea. Morphologically, the new species can be distinguished from congeneric species by its large shell size, relatively small auricle length, absence of monocrystal aerials, presence of longitudinal radial ridges on the left valve, and the alternated rounded striae and distal and proximal growth lines of prisms on the right valve. Anatomically, this new species can be distinguished from *C. vulcani* by its anteriorly located auriculate gills, compared to the centrally located lamellar gills of the latter, and the different locations of the pericardium. Sequence comparison and phylogenetic analysis based on the *18S rRNA* fragments supported the placement of the new species in *Catillopecten*. We also report the mitogenome of *C. margaritatus* n. sp. as the only reported mitogenome of the family Propeamussiidae, which differs from those of other scallops substantially in gene order arrangement. Divergence time estimation revealed that Propeamussiidae and Pectinidae diverged in the early Carboniferous, while *Catillopecten* and *Parvamussium* diverged during the late Cretaceous to early Eocene. Finally, we presented a key to the species of *Catillopecten*.

KEYWORDS

Bivalvia, *Catillopecten*, cold seep, deep sea, scallop, Pectinoidea

Introduction

Scallops in the family Propeamussiidae Abbott, 1954, commonly called glass scallops due to their thin and semi-translucent shells, are inhabitants of the deep sea, with species recorded from 200 m to more than 5,000 m (Kamenev, 2018). The genus *Catillopecten* Iredale, 1939 (Propeamussiidae), including 11 species (MolluscaBase, 2022), is characterized by thin, inequilateral to subequilateral valves, unequal auricles, lack of internal ribs, and a deep byssal notch (Kamenev, 2018). Members of *Catillopecten* are widely distributed in the global deep oceans, including one species from the Atlantic, four species from the eastern Pacific Ocean, and six species from the western Pacific Ocean (Figure 1, Dall, 1898; Smith, 1885; Dautzenberg and Bavay, 1912; Knudsen, 1970; Bernard, 1978; Schein-Fatton, 1988; Dijkstra and Marshall, 2008; Kamenev, 2018). These species have been reported from a variety of substrates, including rocky bottoms of a hydrothermal vent (Beninger et al., 2003), and muddy bottoms of continental slopes to polymetallic nodule areas in abyssal plains (Table 1).

Previous taxonomic studies of *Catillopecten* heavily relied on shell morphology, such as shell proportion and auricle characters. By contrast, little attention was paid to the anatomic structures. In 1978, anatomic structures of *C. knudseni* Bernard, 1978 and *C. squamiformis* Bernard, 1978 were described without specimen images (Bernard, 1978). In *C. vulcani* Schein-Fatton, 1985, the internal structures were illustrated by a line drawing and briefly described (Beninger et al., 2003). Moreover, Le Pennec et al. (2002) described the spermatogenesis of *C. vulcani* and proposed that its acrosome features could be applied in studies of scallop evolution. Molecular data of *Catillopecten* are also limited, with only two *18S rRNA* sequences available, one from *C. vulcani* (Dufour et al., 2006), and the other from *Catillopecten* sp. (Wiklund et al., 2017), which may be a juvenile of *C. malyutinae* Kamenev, 2018 (Kamenev, 2019). These two sequences showed a high nucleotide similarity of 99.59% (Wiklund et al., 2017).

The Haima cold seep on the northwestern slope of the South China Sea (SCS) supports a large epibenthic fauna dominated by chemosynthetic bivalves and siboglinid tubeworms (Dong et al., 2021; Ke et al., 2022). In 2020, Ke et al. (2022) collected broken shells of a glass scallop from this area, and identified the specimen as a species of *Propeamussium* Gregorio, 1884. In 2022, we collected five specimens of propeamussiids from the same area, including three living individuals and two pairs of empty shells. Our preliminary analysis revealed that these glass scallop specimens all belong to a new species of *Catillopecten*. Therefore, this study aims to (i) describe the new species; (ii) assemble and annotate its mitochondrial genome; and (iii) determine its phylogenetic position. As the first report of propeamussiid species with detailed morphological and molecular information from the South China Sea, our study enhances our knowledge of the biodiversity of this large marginal sea of the western Pacific Ocean, and provides mitogenome and molecular data for a better understanding of the phylogenetic relationships and global biogeography of Propeamussiidae.

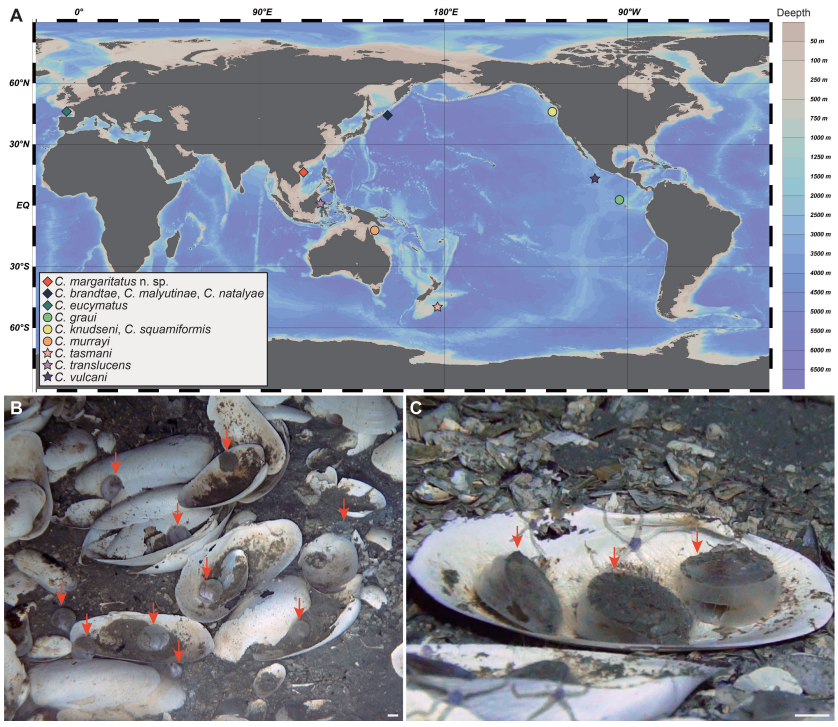

FIGURE 1
Worldwide geographical distribution of species in the genus *Catillopecten* and the typical habitat of the new species. **(A)** Locality of the species of *Catillopecten*, holotypes only. **(B, C)** Typical habitat of *C. margaritatus* n. sp. (indicated by red arrows), which were often found on the empty shells of *Archivessica marissinica*. Scale bar: **(B, C)** 10 mm.

TABLE 1 Comparison of shell characteristics (the largest specimen of each species) and distribution of *Catillopecten* species.

Species	Length (L)	Height (H)	Anterior end length (A)	Auricles length (AL)	Anterior auricle length (AAL)	H/L	A/L	AL/L	AAL/AL	Umbonal angle (UA)	Habitat	Depth (m)	Reference
C. margaritatus n. sp.	31.0	28.0	16.0	9.0	5.0	0.903	0.516	0.314	0.556	115°	Hydrocarbon seep	1,385–1,441	This study
C. brandtae	7.0	5.7	2.7	5.8	2.1	0.814	0.386	0.829	0.362	140°	Abyssal plain	4,860–5,423	Kamenev, 2018
C. eucymatus	12.0	10.0	5.2*	5.6	3.4*	0.833	0.433	0.467	0.607	110°	Abyssal plain	1,920–4,829	Schein-Fatton, 1988
C. graui	18.0	17.0	/	10.3	/	0.944	/	0.574	/	110°	Abyssal basin	3,270–3,670	Knudsen, 1970
C. knudseni	19.8	18.4	11.2*	9.0*	5.2*	0.929	0.566	0.455	0.578	110°	/	1,700–2,900	Bernard, 1978
C. malyutinae	8.2	7.1	4.5	4.2	2.4	0.866	0.549	0.512	0.571	110°	Abyssal plain	4,988–5,418	Kamenev, 2018
C. murrayi	15.5	14.5	8.1*	6.9*	3.8*	0.935	0.523	0.445	0.551	110°	Globigerina ooze	2,561	Smith, 1885
C. natalyae	6.0	5.4	2.6	4.9	2.2	0.900	0.433	0.817	0.449	120°	Abyssal plain	5,112–5,418	Kamenev, 2018
C. squamiformis	13.2	11.8	6.2	5.6	2.6	0.894	0.470	0.424	0.464	105°	Abyssal plain, basin, strait	2,901–5,020	Kamenev, 2018
C. tasmani	10.5*	10.0	5.5*	7.1*	3.6*	0.952	0.523	0.676	0.507	90°	Globigerina ooze	1,373–1,676	Dijkstra & Marshall, 2008
C. translucens	12.0	10.0	5.1*	6.0	3.4*	0.833	0.425	0.500	0.567	110°	Yellow mud strait	341–1,301	Dijkstra & Maestrati, 2008
C. vulcani	12.9	14.2	6.4*	4.4*	2.9*	1.101	0.496	0.341	0.659	100°	Hydrothermal Vent	2,530–2,620	Schein-Fatton, 1988
Catillopecten sp.	1.8	1.5	0.9*	1.2*	0.6*	0.833	0.500	0.667	0.500	110°*	Polymetallic nodule province	4,081	Wiklund et al., 2017

* Data measured from available figures; /: data unavailable.

10.3389/fmars.2023.1168991

Materials and methods

Sample collection

The specimens were captured using a scoop net from the Haima cold seep (16°54.04'N, 110°28.47'E), at 1,433–1,441 m water depth in September 2022, using the ROV *Pioneer* onboard R/V *Xiangyanghong 01* of The First Institute of Oceanography, Ministry of Natural Resources (Qingdao, China). The holotype was frozen with liquid nitrogen and stored at −80°C, while paratypes 1 and 2 were fixed in 4% paraformaldehyde, and paratypes 3 and 4 (empty shells) were kept at room temperature.

Morphological measurement and photography

Shell measurements were made according to Kamenev (2018). Shell length (L), height (H), anterior end length (A), auricles length (AL), anterior auricle length (AAL), and umbonal angle (UA) were measured using a vernier caliper. The shell size data of other species of *Catillopecten* were measured according to the scale or proportion when the specimen images were available. The ratios of these parameters to shell length (i.e., A/L, H/L, AL/L, and AAL/AL) were calculated. An EOS 5D Mark IV camera (Canon, Japan) was used for photography of the whole specimen. A digital Stereomicroscope SMZ1270 Imaging System (Nikon, Japan) was used to document the morphological details. The specimens used in this study were deposited in the Tropical Marine Biodiversity Collections of the South China Sea (TMBC), Chinese Academy of Sciences (Guangzhou, China).

DNA extraction, sequencing, and assembly

Genomic DNA was extracted from the adductor muscle of the holotype using the CTAB method (Stewart and Via, 1993). DNA quality was examined using agarose gel (1.0%) electrophoresis, and the quantity was determined using a NanoDrop ND-1000 spectrophotometer (Thermo Scientific, USA). DNA library was constructed with the NEBNext Ultra DNA Library Prep Kit for Illumina (NEB, United States) with an insert size of 350 bp. Genomic sequencing was conducted on an Illumina NovaSeq 6000 sequencer (Illumina, USA) in Novogene (Tianjin, China) to generate 150-bp paired-end reads. Raw Illumina reads were filtered using Trimmomatic v0.38 (Bolger et al., 2014) to remove adapter and low-quality reads with the following settings: LEADING = 15, TRAILING = 15, SLIDINGWINDOW = 4:20, MINLEN = 40. The clean reads were *de novo* assembled using SPAdes v3.14.1 (Bankevich et al., 2012) with *k*-mer sizes of 21, 33, 55, 77, 99, and 127. The nuclear gene *18S rRNA* was identified by conducting BLASTn using BLAST v2.11.0+ (Camacho et al., 2009) to search against the available corresponding sequences of Propeamussiidae species from NCBI (https://www.ncbi.nlm.nih.gov/), with an E-value of 1e-10. The mitogenome was assembled using NOVOPlasty v3.2 (Dierckxsens et al., 2016) under default settings with a *cox1* sequence of *Parvamussium carbaseum* Dijkstra, 1991 (AB084106) from NCBI (https://www.ncbi.nlm.nih.gov/) as the seed.

Mitogenome annotation and analyses

MITOS2 Web Server (Donath et al., 2019) was used to annotate the mitogenome under default settings. The annotated protein coding genes (PCGs) were manually examined and adjusted against the invertebrate genetic codes. The OGDRAW in the Geseq server (Greiner et al., 2019) was used to visualize the mitogenome arrangement. Phylogenetic analyses were conducted to determine the position of the new species in the tree of life of scallops, based on the mitogenome of the new species, as well as available mitogenomes of scallops from the order Pectinida, including *Amusium pleuronectes* Linnaeus, 1758 (MT419374), *Argopecten irradians* Lamarck, 1819 (DQ665851), *Argopecten purpuratus* Lamarck, 1819 (KF601246), *Chlamys farreri* Jones and Preston, 1904 (EU715252), *Crassadoma gigantea* Gray, 1825 (MH016739), *Mimachlamys crassicostata* Sowerby, 1842 (FJ415225), *Mimachlamys sanguinea* Linnaeus, 1758 (KF214684), *Mimachlamys varia* Linnaeus, 1758 (MZ520326), *Mizuhopecten yessoensis* Jay, 1857 (FJ595959), *Pecten albicans* Schröter, 1802 (KP900974), *Pecten maximus* Linnaeus, 1758 (KP900975), *Placopecten magellanicus* Gmelin, 1791 (DQ088274), and *Spondylus virgineus* Reeve, 1856 (MN019127), with *Ostrea edulis* Linnaeus, 1758 (NC_016180) as the outgroup. The PCGs and ribosome RNA sequences of these mitogenomes downloaded from NCBI were extracted. The analyses were conducted using PhyloSuite v1.2.2 (Zhang et al., 2020) with the help of several plug-in programs: MAFFT (Katoh and Standley, 2013) under the "auto" option was applied to align each gene fragment, with "Codon alignment mode" for PCGs and "Normal alignment mode" for rRNAs. Gblocks (Talavera and Castresana, 2007) was applied to remove ambiguously aligned fragments in batches, with missing genes or alignment gaps being filled with "-". Then, the fragments were concatenated and ModelFinder (Kalyaanamoorthy et al., 2017) was used to select the best-fit model based on the BIC criterion. Bayesian inference (BI) and maximum-likelihood (ML) analyses were conducted using MrBayes (Ronquist et al., 2012) and IQ-TREE (Nguyen et al., 2015), under the best-fit GTR+F+I+G4 model for 10 million generations and the GTR+R4+F model for 1,000 ultrafast bootstraps, respectively (Minh et al., 2013). Since the order of the PCGs and tRNAs may contain phylogenetic signal (Shen et al., 2009), we compared the arrangement orders of the mitochondrial genes among the species of Pectinida.

Phylogenetic analyses and divergence time estimation

Since only two *18S rRNA* sequences of *Catillopecten* were available in GenBank (https://www.ncbi.nlm.nih.gov/), we determined the sequence divergence between the new species and these two other *Catillopecten* sequences, as well as those of other

genera of Propeamussiidae based on this gene fragment. In addition, we also obtained 28 fragments of *18S rRNA* from the order Pectinida and four from Limidae (outgroup) from GenBank to determine the relationships between *Catillopecten* and other scallops (Table S1). Fragments with longer than 1,500 bp were kept and the longest sequence was selected when two or more sequences from the same species were available. The number of base substitutions per site among these sequences is calculated using MEGA7 (Kumar et al., 2016) under the Kimura 2-parameter model (Kimura, 1980). The rate variation among sites was modeled with a gamma distribution (shape parameter = 1), and all positions with less than 95% site coverage were eliminated. Phylogenetic analyses were similar to the phylogenetic tree construction of the mitogenome section except the BI and ML analyses were conducted under the best-fit K80+I+G model for 10 million generations and the K80+R2 model for 1,000 ultrafast bootstraps, respectively (Minh et al., 2013).

To estimate the divergence times, fossil ages were incorporated based on available data (Waller, 2006; and the Paleobiology Database, https://paleobiodb.org/). The ages of Pectinidae and Limidae were constrained approximately 251.3–247.2 MYA and 330.9–323.2 MYA, respectively (Smedley et al., 2019). BEAST v.2.6.6 (Bouckaert et al., 2019) was used to estimate the divergence times based on a concatenated dataset of mitochondrial PCGs, under the following settings: (i) HKY+G4 as the partition model; (ii) "strict clock" as the clock model with estimated clock rate; (iii) "calibrated Yule model" as the two prior and fossil calibration dates were set in the Pectinidae clade ("log normal" distribution, M parameter = 5.518, S parameter = 0.0033) and the Limidae clade ("log normal" distribution, M parameter = 5.792, S parameter = 0.0052); and (iv) running chain length as 10,000,000 MCMC generations with 1,000 sample frequencies. The default settings were adopted for other parameters. The convergence of the likelihood parameters in the log file was determined by Tracer v.1.7.2 (Rambaut et al., 2018) with the ESS over 200. The final tree file was generated using TreeAnnotator (Rambaut & Drummond, 2015) with 25% burn-in and plotted with FigTree v1.4.4 (Rambaut & Drummond, 2018).

Results

Systematics

Order: Pectinida, Gray, 1854

Superfamily: Pectinoidea Rafinesque, 1815

Family: Propeamussiidae, Abbott, 1954

Genus: *Catillopecten* Iredale, 1939

Synonym: *Bathypecten* Schein-Fatton, 1985

Type species: *Catillopecten murrayi* Smith, 1885

Diagnosis (adopted from Kamenev, 2018): Propeamussiidae with translucent shells, very thin, fragile and compressed, subequilateral to inequilateral. Valves smooth or undulated, sometimes with weak commarginal ribs and fine radial threads; left valve more convex. Auricles unequal; posterior auricles continuous or weakly separated from shell disc; anterior auricle of right valve distinct and sharply demarcated from shell disc. Internal ribs absent. Byssal notch rather deep; byssal fasciole narrow or absent.

Catillopecten margaritatus n. sp. http://zoobank.org/NomenclaturalActs/396CA196-5051-4A11-975F-D7A74C91568D

Type specimens

Holotype [TMBC (Tropical Marine Biodiversity Collections of the South China Sea), Chinese Academy of Sciences, Guangzhou, SCSMBC031006], paratypes 1–4 (TMBC, SCSMBC031007–SCSMBC031010), Haima cold seep in SCS, 16°54.04'N, 110°28.47'E, 1,433–1,441 m, organic sediment with empty shells of *Archivesica marissinica* Chen, Okutani, Liang & Qiu, 2018 (Figure 1), collected using the suction sampler of the ROV *Pioneer*, September 2022, ROV02, Dive 05.

Type locality

Haima cold seep, 1,407–1,441 m water depth, off southern Hainan Island, on the northwestern slope of the South China Sea (Figure 1).

Etymology

The species epithet "*margaritatus*" comes from "margarita" in Latin, which means pearl and refers to the pearlescent internal surface of the valves of this species.

Diagnosis

Catillopecten with a large shell up to 31 mm in length; internal shell silvery-white and pearlescent. Left valve surface slightly crumpled, with longitudinal radial ridges intersected with conspicuous, rounded, thin ribs. Right valve slightly convex with regular, rippled, and rounded commarginal striae alternated with distal and proximal growth lines of prisms. Auricles small and approximately equal in length. Left valve auricles approximate triangular, with intensive parallel ridges, connected with the rounded ribs of the disc. Right valve anterior auricle with rounded coarse commarginal ribs and ridges; posterior auricle with parallel, dense, indistinct striae and some distinct ridges.

Description

Shell (Figures 2, 3, Table 2) subcircular, external gray, internal silvery-white, iridescent, pearlescent, rayed, without internal ribs

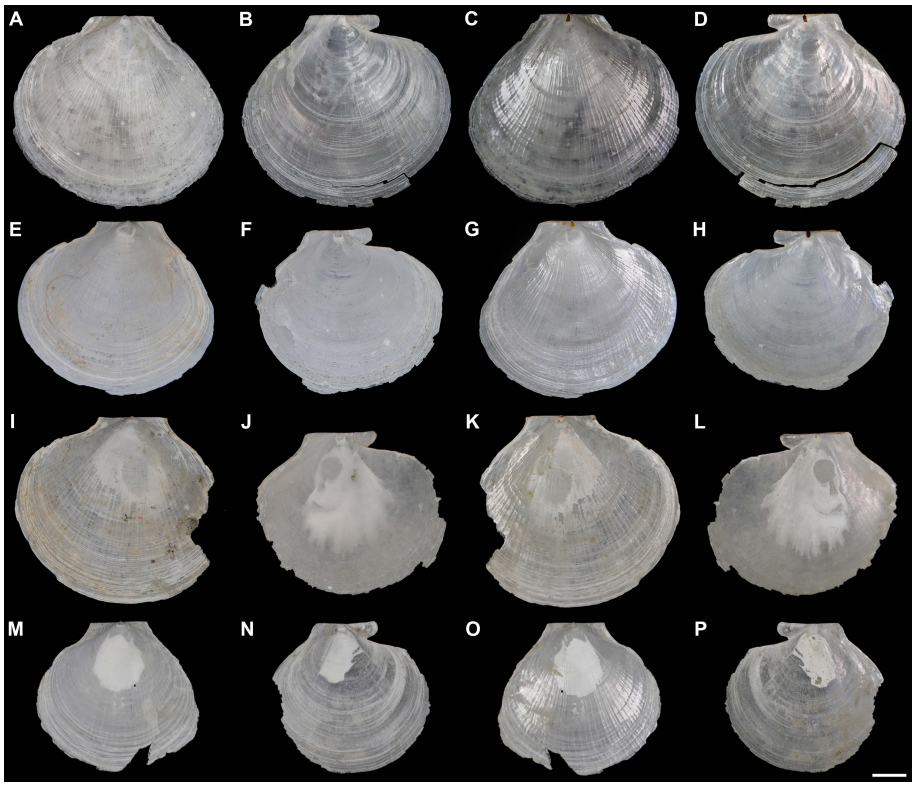

FIGURE 2
External and internal views of the left and right valves of *Catillopecten margaritatus* n. sp. specimens. **(A–D)** Holotype, TMBC, SCSMBC031006; **(E–H)** paratype 2, TMBC, SCSMBC031008; **(I–L)** paratype 3, TMBC, SCSMBC031009; **(M–P)** paratype 4, TMBC, SCSMBC031010. Scale bar: 5 mm.

(Figures 2C, D). Length up to 31.0 mm, slightly longer than height (H/L = 0.90–0.93) and approximate equilateral (A/L = 0.52–0.53). Shell anterodorsal and ventral margins gracefully curved, posterodorsal margin slightly curved and nearly straight. Auricles small (AL/L = 0.31–0.34), approximately equal in length (AAL/AL = 0.50–0.53). Hinge line straight (Figures 3A, B), subterminal umbones with an angle of 115°.

Left valve. Disc convex (Figure 2), surface slightly crumpled, with longitudinal radial ridges intersected with conspicuous, rounded, thin, ribs (Figures 3A, D); distinctly radial ridges and rounded ribs presented on the inner surface. Auricles approximate triangular, with compressed and slightly cambered surface; intensive parallel ridges clear, connected with the rounded ribs of the disc; anterior auricle disconnected with disc and with a shallow

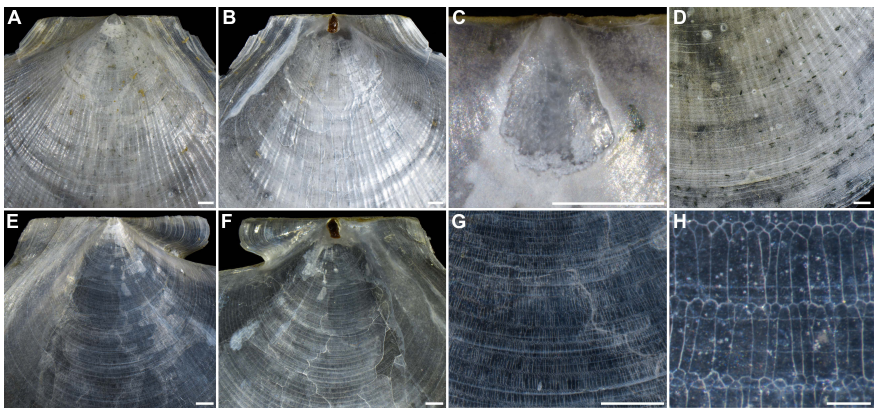

FIGURE 3
Morphological details of *Catillopecten margaritatus* n. sp. shells (holotype, TMBC, SCSMBC031006). **(A–D)** Left valve. **(A)** External view of auricles. **(B)** Internal view of auricles. **(C)** Umbo area of the left valve. **(D)** External surface commarginal undulations and fine radial threads. **(E–H)** Right valve. **(E)** External view of auricles. **(F)** Internal view of auricles. **(G)** Sculpture of the center. **(H)** Prismatic microstructure of the center. Scale bar: **(A–G)**, 1 mm; H, 0.1 mm.

10.3389/fmars.2023.1168991

TABLE 2 Shell measurements (mm) and ratios of *Catillopecten margaritatus* n. sp. specimens.

	Holotype	Paratype 1	Paratype 2	Paratype 3	Paratype 4
Depository	TMBC	TMBC	TMBC	TMBC	TMBC
Specimen number	SCSMBC031006	SCSMBC031007	SCSMBC031008	SCSMBC031009	SCSMBC031010
Length (L)	31.0	22.1	30.0	30.6	24.2
Height (H)	28.0	20.5	27.4	28.5	22.3
Anterior end length (A)	16.0	11.6	15.4	16.1	12.5
Auricles length (AL)	10.0	7.4	9.8	10.3	7.6
Anterior auricle length (AAL)	5.2	3.7	4.9	5.1	4.0
H/L	0.903	0.927	0.913	0.931	0.921
A/L	0.516	0.525	0.513	0.526	0.517
AL/L	0.323	0.335	0.327	0.337	0.314
AAL/AL	0.520	0.500	0.500	0.495	0.526

notch; posterior auricle continuous with shell edge (Figures 3A, B). Umbo clear, conical shape, convex, distinctively separated from shell disc (Figure 3C). Resilium distinct, teardrop-shaped and brownish black (Figure 3B).

Right valve. Disc slightly convex (Figure 2), thinner, more fragile and transparent than left valve. Regular, rippled, and rounded commarginal striae distinctly presented on the external and internal surfaces, intersected with longitudinal stripes of prisms (Figures 3E–G); prisms distinct, with alternating spherulitic and elongated layers, and clear distal and proximal growth lines, alternated with the rounded striae (Figures 3G, H). Auricles unequal; anterior auricle low-angle sector-shaped and inflated, with clear, rounded, coarse commarginal ribs and ridges, protruding with rounded anterior end, sharply demarcated from shell disc with a deep notch and gorge; posterior auricle triangular, with parallel, dense, indistinct striae and some distinct ridges, continuous connected to shell disc with slight turn (Figures 3E, F). Adductor muscle scar oval and clear (Figures 2D–L, 3F). Umbo very compressed and inconspicuous.

Anatomy (Figure 4). Mantle large, thin and transparent, with a row of long tentacles and velum at the margin. Unilaterally auriculate and large gills at anterior side, consisting of outer and inner demibranches. Rounded digested gland close to resilium, brown to dark color. Rectum extending from digested gland along the dorsal side of adductor muscle. Adductor muscle small, cylindrical, and robust. Foot small, covered by a pair of labial palps, connected to adductor muscle by foot contracted muscle. Gonad long scrotiform, surrounding adductor muscle on anterior side. Pericardium small, located between adductor muscle and gonad.

Remarks

Catillopecten is similar to *Propeamussium* and other genera of Propeamussiidae in having translucent shells. However, *Propeamussium* can be distinguished from *Catillopecten* by the almost equivalve and laterally compressed shell, weak byssal notch, and distinct internal ribs (Dijkstra, 2013). Based on the shell characteristics, our glass scallop specimens, as well as those empty shells described as *Propeamussium* sp. by Ke et al. (2022) all belong to *Catillopecten*.

Within *Catillopecten*, shell shape, shell and auricle proportion, monocrystal aerials and sculpture on shell surface, and byssal notch shape have been used to distinguish the species. Among the described species, *C. margaritatus* n. sp. most closely resembles *C. tasmani* Dijkstra and Marshall, 2008—a species reported from Bounty Trough, southern New Zealand at depths of 1,373 to 1,676 m—in shell shape, proportions, absence of monocrystal aerials, auricle features, deep and sharp byssal notch, and the prism structure of the right valve (Dijkstra and Marshall, 2008).

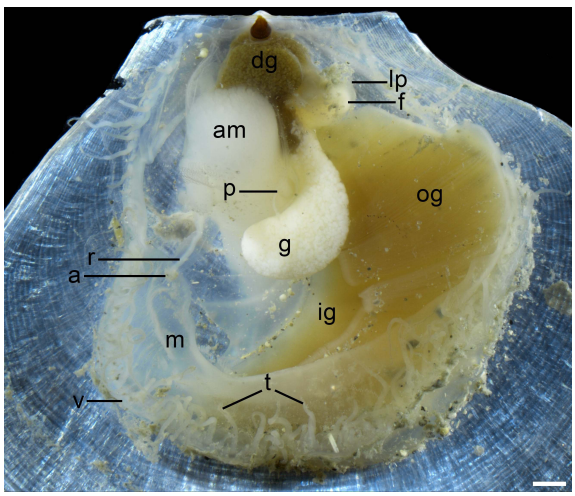

FIGURE 4
Anatomy features of *Catillopecten margaritatus* n. sp. of the paratype 1 (TMBC, SCSMBC031007) left valve. Abbreviations: a, anus; am, adductor muscle; dg, digestive gland; f, foot; g, gonad; ig, inner gill; lp, labial palp; m, mantle; og, outer gill; p, pericardium; r, rectum; t, tentacle; v, velum. Scale bar: 1 mm.

Nevertheless, *C. margaritatus* n. sp. can be easily distinguished from *C. tasmani* with its larger shell size (L: 22.1–31.0 mm *vs.* 10.5 mm), smaller auricle length (AL/L: 0.31-0.34 *vs.* 0.68), and the wide-angled umbones (UA: 115° *vs.* 90°). *Catillopecten margaritatus* n. sp. has relatively small auricles, which are about one-third of the total shell length, similar to those of *C. vulcani* (Schein-Fatton, 1985). Nevertheless, *C. vulcani* differs from the former with its small size and unique slim shell profile (H/L: 0.90–0.93 *vs.* 1.10). In addition, the shell surface of *C. margaritatus* n. sp. lacks monocrystal aerials, which differentiates it clearly from *C. brandtae* Kamenev, 2018, *C. malyutinae* Kamenev, 2018, *C. natalyae* Kamenev, 2018, and *Catillopecten* sp. (may be a synonym of *C. malyutinae*) (Wiklund et al., 2017; Kamenev, 2018; Kamenev, 2019; Checa et al., 2022). Significantly, in *C. margaritatus* n. sp., the presence of longitudinal radial ridges on the left valve and the alternated rounded striae and distal and proximal growth lines of prisms on the right valve, which are absent in all of its congeneric species, allow this new species to be distinguished from its congeneric species.

Although anatomical features have been used in the taxonomy of deep-sea bivalves (Xu et al., 2019), available data are too limited to judge whether they are useful for species delimitation in *Catillopecten* (Le Pennec et al., 2002; Beninger et al., 2003). Our comparison of the anatomical features with the drawing of Beninger et al. (2003) shows that *C. vulcani* has centrally located lamellar gills with a straight axis. By contrast, *C. margaritatus* n. sp. possesses a pair of large and unilaterally auriculate gills with a straight axis, located at the anterior side of the shell. Furthermore, the pericardium of *C. margaritatus* n. sp. is located between the adductor muscle and gonad, whereas the pericardium and heart of *C. vulcani* were speculated to be located at the dorsal side of the rectum (Beninger et al., 2003). Therefore, *C. margaritatus* n. sp. and *C. vulcani* can be distinguished by anatomical features. When anatomical data from other species become available, studies should be conducted to further examine their potential use in the taxonomy of these glass scallops.

Mitogenomic features, phylogenetic position, and divergence

Illumina sequencing generated 29.21 million paired-end reads. Our assembly produced a complete, circular mitogenome of *C. margaritatus* with a size of 17,979 bp, and an overall base composition of 40.24% for T, 10.01% for C, 27.78% for G, and 21.97% for A (Table S2). This is the first assembled mitogenome of the family Propeamussiidae. It contains 13 PCGs, namely, *cox1–3*, *nad1–6*, *nad4l*, *atp6*, *atp8*, and *cytb*; two rRNA genes; and 22 tRNA genes (Figure 5A, Table S3). There are three overlap regions between adjacent genes, including 1 bp between *trnN* and *trnS1*, 2 bp between *nad2* and *trnL*, and 23 bp between *rrnL* and *trnV*. All these genes are encoded in the same strand (Figure 5A), similar to other species of Pectinidae.

Phylogenetic analyses based on the *18S rRNA* fragment showed that the three *Catillopecten* sequences, including the one from *C. margaritatus*, formed a clade, which is sister to *Parvamussium undisonum* Dijkstra, 1995 (Figure 5B). Among the three *Catillopecten* species, *C. margaritatus* is more closely related to *C. vulcani*. Among the 1,835 bp aligned *18S rRNA* fragment, *C. margaritatus* only showed 7 bp (0.38%) difference from *C. vulcani*, with a K2P pairwise distance of 0.18% between the two species (Table S4), while *C. margaritatus* showed only 0.59% divergence from *Catillopecten* sp. and 1.25% from *P. undisonum* in *18S rRNA*, with genetic distances of 0.36% and 1.03%, respectively. Furthermore, the family Propeamussiidae appears polyphyletic, with *Cyclopecten* Verrill, 1897, currently accepted as a genus of Propeamussiidae, being placed in Pectinidae, consistent with previous studies (Combosch et al., 2017; Smedley et al., 2019). Phylogenetic analysis of 14 species of Pectinoidea based on mitogenomic PCGs showed that *Spondylus virgineus* is sister to a large clade of all other pectinoids, and within this clade, *C. margaritatus* is sister to a clade of all other 12 species (Figure 5C). Moreover, the *C. margaritatus* mitogenome differs substantially from those of Spondylidae and Pectinidae in the order of PCGs, rRNAs, and tRNAs (Figure 5C). Furthermore, even within Pectinidae, the gene order arrangements were very different among the species available for comparison.

The divergence times among Pectinoidea were estimated based on mitochondrial PCGs, using two fossil calibration points with horizontal bars representing the 95% highest posterior density (HPD) interval for each node (Figure 6). The results revealed the origin of the superfamily Pectinoidea in the Devonian (384.11–360.24 MYA, median value 371.42 MYA). Propeamussiidae is sister to Pectinidae and they diverged in the early Carboniferous (351.20–331.77 MYA, median value 341.03 MYA). *Catillopecten* and *Parvamussium* Sacco, 1897 diverged during the late Cretaceous to early Eocene (70.51–46.63 MYA, median value 57.68 MYA).

Discussion

Since most of the *Catillopecten* species lack gene sequences, and the only gene sequence available in two *Catillopecten* species was the *18S rRNA*, a conserved gene marker that is more appropriate for deep phylogenetic study than species delimitation (Zhan et al., 2019), it was not surprising that we only found 0.38%–0.59% divergences in *18S rRNA* among the three species of *Catillopecten* in this study. Nevertheless, the result of *C. margaritatus* and the other two species of *Catillopecten* forming a clade that is sister to *P. undisonum* supports that the new species belongs to *Catillopecten*. When sequences of more sensitive genetic markers, such as the mitochondrial cytochrome subunit I (*COI*) or *16S ribosomal RNA* sequences, from other *Catillopecten* species become available in the future, molecular delimitation should be conducted in future studies to determine the genetic distances between *C. margaritatus* and its congeneric species.

In this study, we presented the first mitogenome of Propeamussidae. Its length (17,979 bp) is similar to that of *Crassadoma gigantea* (18,495 bp), *Mimachlamys sanguinea* (17,383 bp), and *Pecten maximus* (17,252 bp), but much smaller than that of *Placopecten magellanicus* (32,115 bp) in Pectinidae and *Spondylus virgineus* (30,160 bp) in Spondylidae. Among the

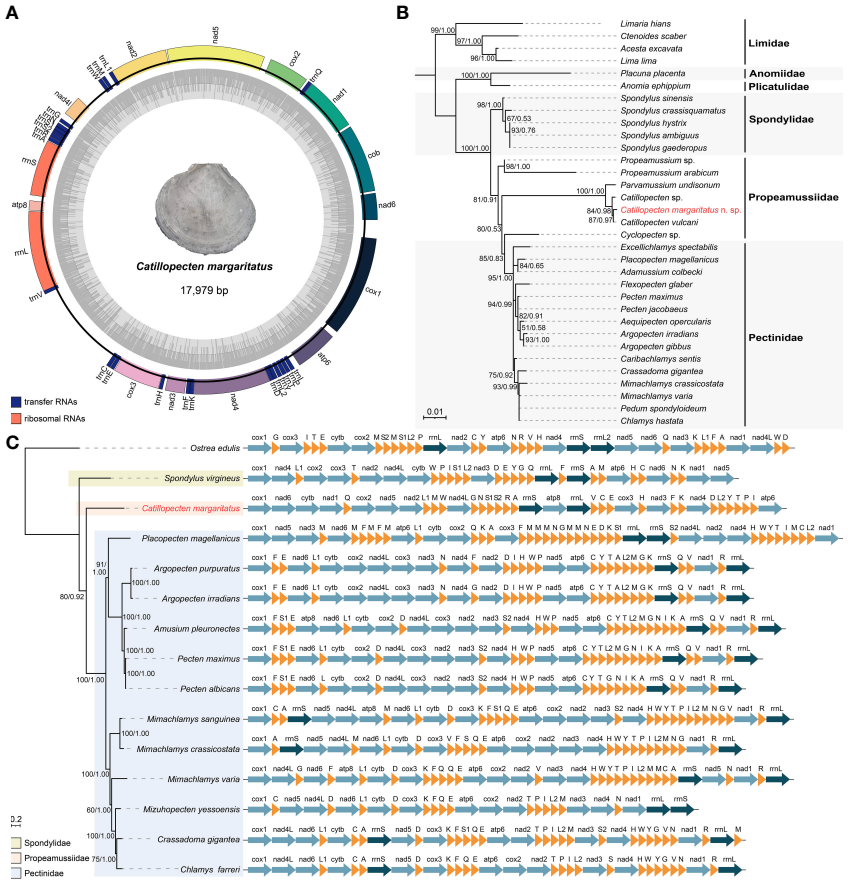

FIGURE 5
Mitogenome features of *Catillopecten margaritatus* n. sp. and its phylogenetic position. **(A)** Mitogenomic gene orders and relative lengths. **(B)** Phylogenetic tree of the order Pectinida based on *18S rRNA* fragments. The topology is based on BI analysis, with Limidae as the outgroup. The accession numbers are presented in Table S1. **(C)** Mitogenomic phylogenetic tree based on protein coding genes and rRNAs and the mitochondrial gene arrangements of the superfamily Pectinidea species. The topology is based on BI analysis, with *Ostrea edulis* as the outgroup. Posterior probabilities values (>0.50) from BI analysis and bootstraps values (>50) from the ML analysis are given at the nodes.

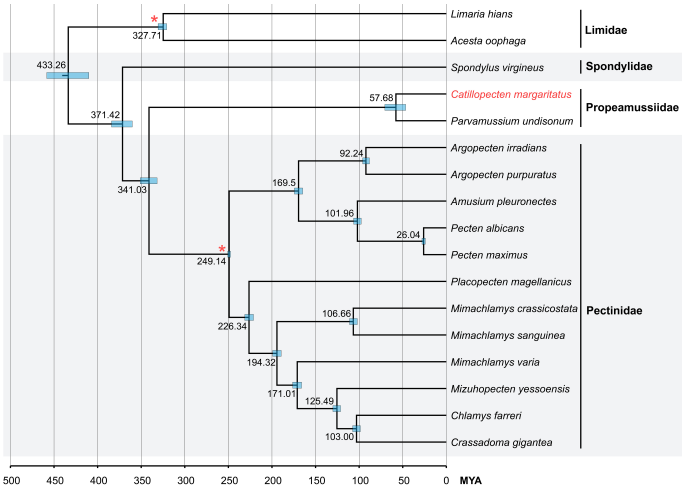

FIGURE 6
Divergence time estimation analysis of Pectinoidea based on concatenated mitochondrial PCG gene sequences. Bottom axis represents millions of years and the internal nodes calibrated by fossil records are represented by red asterisks. The 95% highest posterior density (HPD) is indicated as node blue bars and the Bayesian posterior probabilities of all nodes are 1.00.

sequenced mitogenomes of the three families of Pectinoidea, *C. margaritatus* presents the highest A+T bias with a proportion of 62.21%, while that of the others is from 55.39% to 58.77% (Table S2). Arrangements of PCGs may imply common ancestry (Shen et al., 2009), and such information may be useful to understand the transition from shallow-water to deep-sea habitats (Zhang et al., 2018). However, the substantially different orders of PCGs between the deep-sea *C. margaritatus* and other pectinoids and the bias in sequencing efforts (i.e., only one mitogenome each in Spondylidae and Propeamussiidae) make it difficult to associate these changes with the invasion from shallow water to the deep sea.

Catillopecten margaritatus is the first reported extant seep-dwelling species of this genus. These scallops usually stay on the empty shells of the vesicomyid clam *Archivesica marissinica* (Figures 1B, C), one of the dominant species in the Haima cold seep (Chen et al., 2018). In this seep area, bathymodioline mussel *Gigantidas haimaensis* Xu et al., 2019, and siboglinid tubeworms *Paraescarpia echinospica* Southward et al., 2002 (Sun et al., 2021) and *Sclerolinum annulatum* Xu et al., 2022 form huge colonies on the sea bed. Other low-density populations of bivalves were also reported in this area, including *Gigantidas platifrons* Hashimoto & Okutani, 1994, "*Bathymodiolus*" *aduloides* Hashimoto and Okutani, 1994, *Nypamodiolus samadiae* Lin et al., 2022, and other undetermined species of *Malletia* and *Acharax* (Xu et al., 2019; Guan et al., 2022; Ke et al., 2022). These siboglinid and bivalve species are endosymbiotic with chemosynthetic bacteria in their trophosome and gill epithelial cells, respectively, to provide energy and materials for the holobiont (Ip et al., 2021; Sun et al., 2021; Lin et al., 2023). These chemosymbioses allow vent and seep annelids and bivalves to flourish in the deep sea (Sen et al., 2018; Osman and Weinnig, 2021). Nevertheless, no deep-sea scallops have been reported to be symbiotic with chemosynthetic bacteria, including *C. vulcani*, which inhabits hydrothermal vent sites in the eastern Pacific Ocean (Schein-Fatton, 1985). This is reflected in the lack of morphological specialization of the flat and homorhabdic gill of *C. vulcani*, as well as the abundant particles on the gill indicating its suspension feeding trophic pattern (Beninger et al., 2003), although Le Pennec et al. (1988) observed a few bacteria in the gill filaments of this species. The gill of *C. margaritatus* is similar to that of *C. vulcani*, and therefore, we speculate that *C. margaritatus* also relies on filter-feeding for nutrition.

Key to species of *Catillopecten* Iredale, 1939:

1a. External shell surface with monocrystal aerials……2

1b. External shell surface without monocrystal aerials……4

2a. Shell rounded-triangular ……*C. malyutinae* Kamenev, 2018

2b. Shell D-shaped……3

3a. Shell with fine and closely located commarginal riblets……*C. natalyae* Kamenev, 2018

3b. Shell with irregular commarginal and radial undulations……*C. brandtae* Kamenev, 2018

4a. Shell height larger than length……*C. vulcani* Schein-Fatton, 1985

4b. Shell height slightly smaller than length……5

5a. Byssal notch shallow and rounded ……*C. knudseni* Bernard, 1978

5b. Byssal notch moderately deep or deep ……6

6a. Byssal notch sharp……7

6b. Byssal notch rounded……9

7a. Small auricles, length about one-third of shell length……*C. margaritatus*

7b. Large auricles, length more than half of shell length……8

8a. Right valve with obscure radial lines……*C. tasmani* Dijkstra and Marshall, 2008

8b. Right valve with sharp ribs and fine radial lines……*C. graui* Knudsen, 1970

9a. Auricles subequal in length……10

9b. Auricles unequal in length……11

10a. Dorsal shell margin straight……*C. squamiformis* Bernard, 1978

10b. Dorsal shell margin round……*C. eucymatus* Dall, 1898

11a. Anterior auricles longer than posterior auricles……*C. murrayi* Smith, 1885

11b. Posterior auricles slightly longer than anterior auricles……*C. translucens* Dautzenberg and Bavay, 1912

Conclusions and perspectives

We reported *Catillopecten margaritatus* as the first species of seep-inhabiting *Catillopecten* and described its morphological features of both shell and anatomy, mitogenome, and phylogenetic position. Morphologically, *C. margaritatus* can be easily distinguished from congeneric species with its largest shell size, smaller auricle length, and wide-angled umbones. Our anatomic description of the new species provides useful characteristics for the further taxonomic study of the genus *Catillopecten*. Our phylogenetic analyses confirm the placement of this new species in *Catillopecten*. As the only species of *Catillopecten* distributed within 10°N and 30°N in the western Pacific Ocean, our discovery of *C. margaritatus* enhances our understanding of seep fauna and fills a gap in the geographic distribution of *Catillopecten* in this region.

Data availability statement

The datasets presented in this study can be found in online repositories. Raw Illumina sequencing data were deposited in the National Centre for Biotechnology Information (NCBI) under the BioProject PRJNA934135. Sequence of the mitogenome and the 18S rRNA sequence were deposited in the GenBank with the accession number of OQ434059 and OQ427653, respectively.

Ethics statement

Ethical review and approval was not required for the study on animals in accordance with the local legislation and institutional requirements.

Author contributions

J-WQ conceived and designed this project. Y-TL, Y-XL, and JT collected and photographed the samples. Y-TL performed morphological examination and description. Y-TL, Y-XL and YS conducted DNA extraction and molecular analyses. Y-TL drafted the manuscript. All authors contributed to the article and approved the submitted version.

Funding

This study was supported by Southern Marine Science and Engineering Guangdong Laboratory (Guangzhou) (SMSEGL20SC02) and Research Grants Council of Hong Kong (12101021).

Acknowledgments

We thank the First Institute of Oceanography, MNR (Qingdao, China) for organizing the cruise, as well as the captains and crews of the *Xiangyanghong 01* for their supports.

Conflict of interest

The authors declare that the research was conducted in the absence of any commercial or financial relationships that could be construed as a potential conflict of interest.

Publisher's note

All claims expressed in this article are solely those of the authors and do not necessarily represent those of their affiliated organizations, or those of the publisher, the editors and the reviewers. Any product that may be evaluated in this article, or claim that may be made by its manufacturer, is not guaranteed or endorsed by the publisher.

Supplementary material

The Supplementary Material for this article can be found online at: https://www.frontiersin.org/articles/10.3389/fmars.2023.1168991/full#supplementary-material

References

Abbott, R. T. (1954). *American Seashells* (New Jersey: Princeton).

Bankevich, A., Nurk, S., Antipov, D., Gurevich, A. A., Dvorkin, M., Kulikov, A. S., et al. (2012). SPAdes: a new genome assembly algorithm and its applications to single-cell sequencing. *J. Comput. Biol.* 19 (5), 455–477. doi: 10.1089/cmb.2012.0021

Beninger, P. G., Dufour, S. C., Decottignies, P., and Le Pennec, M. (2003). Particle processing mechanisms in the archaic, peri-hydrothermal vent bivalve *Bathypecten vulcani*, inferred from cilia and mucocyte distributions on the gill. *Mar. Ecol. Prog. Ser.* 246, 183–195. doi: 10.3354/meps246183

Bernard, F. R. (1978). New bivalve molluscs, subclass pteriomorphia, from the northeastern pacific. *Venus* 37, 61–75. doi: 10.18941/venusjjm.37.2_61

Bolger, A. M., Lohse, M., and Usadel, B. (2014). Trimmomatic: a flexible trimmer for illumina sequence data. *Bioinformatics* 30 (15), 2114–2120. doi: 10.1093/bioinformatics/btu170

Bouckaert, R., Vaughan, T. G., Barido-Sottani, J., Duchêne, S., Fourment, M., Gavryushkina, A., et al. (2019). BEAST 2.5: an advanced software platform for Bayesian evolutionary analysis. *PloS Comput. Biol.* 15 (4), e1006650. doi: 10.1371/journal.pcbi.1006650

Camacho, C., Coulouris, G., Avagyan, V., Ma, N., Papadopoulos, J., Bealer, K., et al. (2009). BLAST+: architecture and applications. *BMC Bioinform.* 10 (421), 1–9. doi: 10.1186/1471-2105-10-421

Checa, A. G., Salas, C., Varela-Feria, F. M., Rodríguez-Navarro, A. B., Grenier, C., Kamenev, G. M., et al. (2022). Crystallographic control of the fabrication of an extremely sophisticated shell surface microornament in the glass scallop *Catillopecten*. *Sci. Rep.* 12 (1), 11510. doi: 10.1038/s41598-022-15796-1

Chen, C., Okutani, T., Liang, Q., and Qiu, J. W. (2018). A noteworthy new species of the family vesicomyidae from the south China Sea (Bivalvia: glossoidea). *Venus* 76 (1-4), 29–37. doi: 10.18941/venus.76.1-4_29

Combosch, D. J., Collins, T. M., Glover, E. A., Graf, D. L., Harper, E. M., Healy, J. M., et al. (2017). A family-level tree of life for bivalves based on a Sanger-sequencing approach. *Mol. Phylogenet. Evol.* 107, 191–208. doi: 10.1016/j.ympev.2016.11.003

Dall, W. H. (1898). Contributions to the tertiary fauna of Florida: with especial reference to the Miocene silex-beds of Tampa and the pliocene beds of the caloosahatchee river. *Wagner Free Inst. Sci.* 3 (4), 571–947. doi: 10.5962/bhl.title.29760

Dautzenberg, P., and Bavay, A. (1912). Les Lamellibranches de l'expédition du « siboga ». *Systématique I Pectinidés SibogaExpeditie* 53b, 1–41.

Dierckxsens, N., Mardulyn, P., and Smits, G. (2016). NOVOPlasty: *de novo* assembly of organelle genomes from whole genome data. *Nucleic Acids Res.* 45, e18. doi: 10.1093/nar/gkw955

Dijkstra, H. H. (1991). A contribution to the knowledge of the pectinacean Mollusca (Bivalvia: propeamussiidae, entoliidae, pectinidae) from the Indonesian archipelago. *Zool. Verh.* 271 (1), 1–54.

Dijkstra, H. H. (1995). Bathyal pectinoidea (Bivalvia: propeamussiidae, entoliidae, pectinidae) from new Caledonia and adjacent areas. *Mém. Mus. Natl. hist. nat. Sér. C Géol.* 167, 9–73.

Dijkstra, H. H. (2013). Pectinoidea (Bivalvia: propeamussiidae and pectinidae) from the panglao region, Philippine islands. *Vita. Malacologica* 10, 1–108.

Dijkstra, H. H., and Maestrati, P. (2008). *New species and new records of deep-water pectinoidea (Bivalvia: propeamussiidae, entoliidae and pectinidae) from the south pacific, in tropical deep-Sea benthos* Vol. 25. Eds. V. Héros, R. Cowie and P. Bouchet (Paris: Publications Scientifique du Muséum), 77–113.

Dijkstra, H. H., and Marshall, B. A. (2008). The recent pectinoidea of the new Zealand region (Mollusca: bivalvia: propeamussiidae, pectinidae and spondylidae. *Molluscan Res.* 28 (1), 1–88.

Donath, A., Jühling, F., Al-Arab, M., Bernhart, S. H., Reinhardt, F., Stadler, P. F., et al. (2019). Improved annotation of protein-coding genes boundaries in metazoan mitochondrial genomes. *Nucleic Acids Res.* 47 (20), 10543–10552. doi: 10.1093/nar/gkz833

Dong, D., Li, X., Yang, M., Gong, L., Li, Y., Sui, J., et al. (2021). Report of epibenthic macrofauna found from haima cold seeps and adjacent deep-sea habitats, south China Sea. *Mar. Life Sci. Technol.* 3, 1–12. doi: 10.1007/s42995-020-00073-9

Dufour, S. C., Steiner, G., and Beninger, P. G. (2006). Phylogenetic analysis of the peri-hydrothermal vent bivalve *Bathypecten vulcani* based on *18S rRNA*. *Malacologia* 48 (1-2), 35–42.

Gmelin, J. F. (1791). "Vermes," in *Caroli a linnaei, systema naturae per regna tria naturae*, vol. 1. (Lipsiae (Leipzig: Editio decima tertia, Aucta, Reformata), 3021–3910.

Gray, J. E. (1825). A list and description of some species of shells not taken notice of by lamarck. *Ann. Philos.* 9 (2), 134–140.

Gray, J. E. (1854). A revision of the arrangement of the families of bivalve shells (Conchifera). *Ann. Mag. Nat.* 13 (77), 408–418. doi: 10.1080/03745485709496364

Gregorio, A. (1884). Nota intorno ad alcune nuove conchiglie mioceniche di sicilia. *Nat. Sici.* 3, 119–120.

Greiner, S., Lehwark, P., and Bock, R. (2019). OrganellarGenomeDRAW (OGDRAW) version 1.3.1: expanded toolkit for the graphical visualization of organellar genomes. *Nucleic Acids Res.* 47, 59–64. doi: 10.1093/nar/gkz238

Guan, H., Feng, D., Birgel, D., Kiel, S., Peckmann, J., Li, S., et al. (2022). Lipid biomarker patterns reflect nutritional strategies of seep-dwelling bivalves from the south China Sea. *Front. Mar. Sci.* 9, 831286. doi: 10.3389/fmars.2022.831286

Hashimoto, J., and Okutani, T. (1994). Four new mytilid mussels associated with deepsea chemosynthetic communities around Japan. *Venus* 53 (2), 61–83. doi: 10.18941/venusjjm.53.2_61

Ip, J. C. H., Xu, T., Sun, J., Li, R., Chen, C., Lan, Y., et al. (2021). Host-endosymbiont genome integration in a deep-sea chemosymbiotic clam. *Mol. Biol. Evol.* 38 (2), 502–518. doi: 10.1093/molbev/msaa241

Iredale, T. (1939). Mollusca. part I, in British museum (Natural history) great barrier reef expedition 1928–29. *Sci. Rep.* 5, 209–425.

Jay, J. C. (1857). *Report on the shells collected by the Japan expedition together with a list of Japan shells* Vol. 2. Eds. M. C. Perry and F. L. Hawks (Washington: Tucker), 289–297.

Jones, K. H., and Preston, H. B. (1904). List of Mollusca collected during the commission of H.M.S. "Waterwitch" in the China seas 1900-1903, with descriptions of new species. *Proc. Malacol. Soc Lond.* 6, 138–154. doi: 10.1093/oxfordjournals.mollus.a066053

Kalyaanamoorthy, S., Minh, B. Q., Wong, T. K. F., von Haeseler, A., and Jermiin, L. S. (2017). ModelFinder: fast model selection for accurate phylogenetic estimates. *Nat. Methods* 14, 587–589. doi: 10.1038/nmeth.4285

Kamenev, G. M. (2018). Four new species of the family propeamussiidae (Mollusca: bivalvia) from the abyssal zone of the northwestern pacific, with notes on *Catillopecten squamiformis* (Bernard 1978). *Mar. Biodivers.* 48 (1), 647–676. doi: 10.1007/s12526-017-0821-1

Kamenev, G. M. (2019). Bivalve mollusks of the kuril-kamchatka trench, Northwest pacific ocean: species composition, distribution and taxonomic remarks. *Prog. Oceanogr.* 176, 102127. doi: 10.1016/j.pocean.2019.102127

Katoh, K., and Standley, D. M. (2013). MAFFT multiple sequence alignment software version 7: improvements in performance and usability. *Mol. Biol. Evol.* 30, 772–780. doi: 10.1093/molbev/mst010

Ke, Z., Li, R., Chen, Y., Chen, D., Chen, Z., and Tan, Y. (2022). A preliminary study of macrofaunal communities and their carbon and nitrogen stable isotopes in the haima cold seeps, south China Sea. *Deep Sea Res. Part I Oceanogr. Res. Pap.* 184, 103774. doi: 10.1016/j.dsr.2022.103774

Kimura, M. (1980). A simple method for estimating evolutionary rate of base substitutions through comparative studies of nucleotide sequences. *J. Mol. Evol.* 16, 111–120. doi: 10.1007/BF01731581

Knudsen, J. (1970). The systematics and biology of abyssal and hadal bivalvia. *Galathea. Rep.* 11, 1–241.

Kumar, S., Stecher, G., and Tamura, K. (2016). MEGA7: molecular evolutionary genetics analysis version 7.0 for bigger datasets. *Mol. Biol. Evol.* 33 (7), 1870–1874. doi: 10.1093/molbev/msw054

Lamarck, J. B. P. A. (1819). Histoire naturelle des animaux sans vertèbres. *Tome* 6 (1), 343.

Le Pennec, M., Herry, A., Lutz, R., and Fiala-Médioni, A. (1988). Premières observations ultrastructurales de la branchie d'un bivalve pectinidae hydrothermal profond. *Comptes. rendus. l'Académie. Des. Sci. Sér 3 Sci. Vie.* 307 (11), 627–633.

Le Pennec, G., Le Pennec, M., Beninger, P., and Dufour, S. (2002). Spermatogenesis in the archaic hydrothermal vent bivalve, *Bathypecten vulcani*, and comparison of spermatozoon ultrastructure with littoral pectinids. *Invertebr. Reprod. Dev.* 41 (1-3), 13–19. doi: 10.1080/07924259.2002.9652730

Lin, Y. T., Kiel, S., Xu, T., and Qiu, J. W. (2022). Phylogenetic placement, morphology and gill-associated bacteria of a new genus and species of deep-sea mussel (Mytilidae: bathymodiolinae) from the south China Sea. *Deep Sea Res. Part I Oceanogr. Res. Pap.* 190, 103894. doi: 10.1016/j.dsr.2022.103894

Lin, Y. T., Xu, T., Ip, J. C. H., Sun, Y., Fang, L., Luan, T., et al. (2023). Interactions among deep-sea mussels and their epibiotic and endosymbiotic chemoautotrophic bacteria: insights from multi-omics analysis. *Zool. Res.* 44 (1), 104–123. doi: 10.24272/j.issn.2095-8137.2022.279

Linnaeus, C. (1758). Systema naturæ per regna tria naturæ, secundum classes, ordines, genera, species, cum characteribus, differentiis, synonymis, locis. *Editio decima reformata. Salvius Holmiæ.* 1, 824. doi: 10.5962/bhl.title.542

Minh, B. Q., Nguyen, M. A. T., and von Haeseler, A. (2013). Ultrafast approximation for phylogenetic bootstrap. *Mol. Biol. Evol.* 30, 1188–1195. doi: 10.1093/molbev/mst024

MolluscaBase (2022). Available at: http://www.marinespecies.org/aphia.php?p=taxdetails&id=156983 (Accessed November 28, 2022).

Nguyen, L. T., Schmidt, H. A., von Haeseler, A., and Minh, B. Q. (2015). IQ-TREE: a fast and effective stochastic algorithm for estimating maximum-likelihood phylogenies. *Mol. Biol. Evol.* 32, 268–274. doi: 10.1093/molbev/msu300

Osman, E. O., and Weinnig, A. M. (2021). Microbiomes and obligate symbiosis of deep-sea animals. *Annu. Rev. Anim. Biosci.* 10, 151–176. doi: 10.1146/annurev-animal-081621-112021

Rafinesque, C. S. (1815). *Analyse de la nature, ou tableau de l'univers et des corps organisés* (Palerme: Aux dépens de l'auteur).

Rambaut, A., and Drummond, A. J. (2015) *TreeAnnotator v1.8.2. MCMC output analysis*. Available at: http://beast.bio.ed.ac.uk.

Rambaut, A., and Drummond, A. J. (2018). Available at: https://github.com/rambaut/figtree.

Rambaut, A., Drummond, A. J., Xie, D., Baele, G., and Suchard, M. A. (2018). Posterior summarization in Bayesian phylogenetics using tracer 1.7. *Syst. Biol.* 67 (5), 901–904. doi: 10.1093/sysbio/syy032

Reeve, L. A. (1856). "Monograph of the genus spondylus," in *Conchologia iconica, or, illustrations of the shells of molluscous animals* (London: L. Reeve & Co.).

Ronquist, F., Teslenko, M., van der Mark, P., Ayres, D. L., Darling, A., Höhna, S., et al. (2012). MrBayes 3.2: efficient Bayesian phylogenetic inference and model choice across a large model space. *Syst. Biol.* 61, 539–542. doi: 10.1093/sysbio/sys029

Sacco, F. (1897). *I Molluschi dei terreni terziarii del piemonte e della liguria. part 24 (Pectinidae)* Vol. 116 (Torino: Stamperia Reale).

Schein-Fatton, E. (1985). Découverte sur la ride du pacifique oriental à 13° n d'un pectinidae (Bivalvia, pteromorphia) d'affinités paléozoïques. *Comptes. rendus. l'Académie. Des. Sci. Sér 3 Sci. Vie.* 301 (10), 491–496.

Schein-Fatton, E. (1988). Un pectinacea (Bivalvia) tres primitif: *Bathypecten vulcani* du site hydrothermal de 13 degree n (Pacifique oriental). *Oceanol. Acta Special issue* 8, 83–98.

Schröter, J. S. (1802). Neue conchylienarten und abänderungen, anmerkungen, und berichtigungen nach dem linnéischen system der XII ausgabe. *Archiv für Zoologie und Zootomie.* 3 (1), 125–166.

Sen, A., Åström, E. K., Hong, W. L., Portnov, A., Waage, M., Serov, P., et al. (2018). Geophysical and geochemical controls on the megafaunal community of a high Arctic cold seep. *Biogeosciences* 15 (14), 4533–4559. doi: 10.5194/bg-15-4533-2018

Shen, X., Tian, M., Liu, Z., Cheng, H., Tan, J., Meng, X., et al. (2009). Complete mitochondrial genome of the sea cucumber *Apostichopus japonicus* (Echinodermata: holothuroidea): the first representative from the subclass aspidochirotacea with the echinoderm ground pattern. *Gene* 439 (1-2), 79–86. doi: 10.1016/j.gene.2009.03.008

Smedley, G. D., Audino, J. A., Grula, C., Porath-Krause, A., Pairett, A. N., Alejandrino, A., et al. (2019). Molecular phylogeny of the pectinoidea (Bivalvia) indicates propeamussiidae to be a non-monophyletic family with one clade sister to the scallops (Pectinidae). *Mol. Phylogenet. Evol.* 137, 293–299. doi: 10.1016/j.ympev.2019.05.006

Smith, E. A. (1885). *Report on the lamellibranchiata collected by H.M.S. challenger during the years 1873-76, in report on the scientific results of the voyage of H.M.S. challenger during the years 1873-1876* Vol. 13. Eds. C. W. Thomson and J. Murray (Edinburgh, Neill: Zoology), 1–341.

Southward, E. C., Schulze, A., and Tunnicliffe, V. (2002). Vestimentiferans (Pogonophora) in the pacific and Indian oceans: a new genus from lihir island (Papua new Guinea) and the Java trench, with the first report of *Arcovestia ivanovi* from the north Fiji basin. *J. Nat.* 36 (10), 1179–1197. doi: 10.1080/00222930110040402

Sowerby, G. B. (1842). Monograph of the genus pecten. *Thesaurus Conchyliorum.* 1, 45–82.

Stewart, C., and Via, L. E. (1993). A rapid CTAB DNA isolation technique useful forRAPD fingerprinting and other PCR applications. *Biotechniques* 14, 748–751

Sun, Y., Sun, J., Yang, Y., Lan, Y., Ip, J. C. H., Wong, W. C., et al. (2021). Genomic signatures supporting the symbiosis and formation of chitinous tube in the deep-sea tubeworm *Paraescarpia echinospica*. *Mol. Biol. Evol.* 38, 4116–4134. doi: 10.1093/molbev/msab203

Talavera, G., and Castresana, J. (2007). Improvement of phylogenies after removing divergent and ambiguously aligned blocks from protein sequence alignments. *Syst. Biol.* 56, 564–577. doi: 10.1080/10635150701472164

Verrill, A. E. (1897). A study of the family pectinidae, with a revision of their genera and subgenera. *Trans. Conn. Acad.* 10, 41–95.

Waller, T. R. (2006). Phylogeny of families in the pectinoidea (Mollusca: bivalvia): importance of the fossil record. *Zool. J. Linn. Soc* 148 (3), 313–342. doi: 10.1111/j.1096-3642.2006.00258.x

Wiklund, H., Taylor, J. D., Dahlgren, T. G., Todt, C., Ikebe, C., Rabone, M., et al. (2017). Abyssal fauna of the UK-1 polymetallic nodule exploration area, clarion-clipperton zone, central pacific ocean: Mollusca. *ZooKeys* 707), 1–46. doi: 10.3897/zookeys.707.13042

Xu, T., Feng, D., Tao, J., and Qiu, J. W. (2019). A new species of deep-sea mussel (Bivalvia: mytilidae: *Gigantidas*) from the south China Sea: morphology, phylogenetic position, and gill-associated microbes. *Deep Sea Res. Part I Oceanogr. Res. Pap.* 146, 79–90. doi: 10.1016/j.dsr.2019.03.001

Xu, T., Sun, Y., Wang, Z., Sen, A., Qian, P. Y., and Qiu, J. W. (2022). The morphology, mitogenome, phylogenetic position, and symbiotic bacteria of a new species of *Sclerolinum* (Annelida: siboglinidae) in the south China Sea. *Front. Mar. Sci.* 8, 793645. doi: 10.3389/fmars.2021.793645

Zhan, Z., Li, J., and Xu, K. (2019). Ciliate environmental diversity can be underestimated by the V4 region of SSU rDNA: insights from species delimitation and multilocus phylogeny of *Pseudokeronopsis* (Protist, ciliophora). *Microorganisms* 7 (11), 493. doi: 10.3390/microorganisms7110493

Zhang, D., Gao, F., Jakovlić, I., Zou, H., Zhang, J., Li, W. X., et al. (2020). PhyloSuite: an integrated and scalable desktop platform for streamlined molecular sequence data management and evolutionary phylogenetics studies. *Mol. Ecol. Resour.* 20 (1), 348–355. doi: 10.1111/1755-0998.13096

Zhang, Y., Sun, J., Rouse, G. W., Wiklund, H., Pleijel, F., Watanabe, H. K., et al. (2018). Phylogeny, evolution and mitochondrial gene order rearrangement in scale worms (Aphroditiformia, Annelida). *Mol. Phylogenet. Evol.* 125, 220–231. doi: 10.1016/j.ympev.2018.04.002

frontiers | Frontiers in Earth Science

TYPE Original Research
PUBLISHED 05 May 2023
DOI 10.3389/feart.2023.1188142

Check for updates

OPEN ACCESS

EDITED BY
Gilad Antler,
Ben-Gurion University of the Negev,
Israel

REVIEWED BY
Chin Yik Lin,
University of Malaya, Malaysia
Or M. Bialik,
University of Malta, Malta

*CORRESPONDENCE
Fumito Shiraishi,
fshirai@hiroshima-u.ac.jp

RECEIVED 17 March 2023
ACCEPTED 18 April 2023
PUBLISHED 05 May 2023

CITATION
Shiraishi F, Akimoto T, Tomioka N, Takahashi Y, Matsumoto R and Snyder GT (2023), Microbial traces found in microdolomite associated with seep-related shallow gas hydrate.
Front. Earth Sci. 11:1188142.
doi: 10.3389/feart.2023.1188142

COPYRIGHT
© 2023 Shiraishi, Akimoto, Tomioka, Takahashi, Matsumoto and Snyder. This is an open-access article distributed under the terms of the Creative Commons Attribution License (CC BY). The use, distribution or reproduction in other forums is permitted, provided the original author(s) and the copyright owner(s) are credited and that the original publication in this journal is cited, in accordance with accepted academic practice. No use, distribution or reproduction is permitted which does not comply with these terms.

Microbial traces found in microdolomite associated with seep-related shallow gas hydrate

Fumito Shiraishi[1]*, Takayuki Akimoto[1], Naotaka Tomioka[2], Yoshio Takahashi[3], Ryo Matsumoto[4] and Glen T. Snyder[5]

[1]Earth and Planetary Systems Science Program, Hiroshima University, Hiroshima, Japan, [2]Kochi Institute for Core Sample Research, X-star, JAMSTEC, Kochi, Japan, [3]Department of Earth and Planetary Science, The University of Tokyo, Tokyo, Japan, [4]Gas Hydrate Research Laboratory, Meiji University, Kawasaki, Kanagawa, Japan, [5]Atmosphere and Ocean Research Institute (AORI), The University of Tokyo, Kashiwa, Chiba, Japan

Recently, microdolomite grains with a diameter of about 30–150 μm were discovered within seep-related shallow gas hydrate in the eastern margin of the Japan Sea, and the preliminary assumption has been that their formation is mediated by microbially secreted extracellular polymeric substances (EPS). To verify this interpretation, the present study investigates the characteristics of minerals and organic matter inside the microdolomite grains. Observation by polarizing microscopy reveals that the microdolomite grains generally consist of combinations of distinct cores and external cements. The cores are mostly dark or cloudy and their abundance does not show clear depth dependence, while the external cements are generally isopachous in the shallow part and polygonal in the deeper portions. To further clarify the characteristics of these cores and external cements, thin-foil sections were prepared from two major types of microdolomite, one with a dark core and polygonal external cement, and one with a cloudy core and isopachous external cement. These thin-foil sections were then analyzed by scanning transmission X-ray microscopy (STXM) and transmission electron microscopy (TEM). In the dark core, fibriform pores of about 100 nm diameter were observed to be closely related with amorphous calcium carbonate (ACC) and carboxy groups, likely created by heterogeneous nucleation on microbial EPS surfaces. The polygonal external cement is composed of monocrystalline dolomite, representing slow crystal growth in the deeper part where hydrate formation is less active. On the other hand, the observed cloudy core and the isopachous external cement are, respectively, composed of scattered and accumulated rhombohedral dolomite crystals, presumably resulting from homogeneous nucleation in saline pockets of rapidly growing hydrate and subsequent crystal accumulation on the surface of spherical oil films.

KEYWORDS

ACC, dolomite, EPS, gas hydrate, Japan Sea, microbial carbonate, microhabitat

1 Introduction

The Joetsu Basin in the eastern margin of the Japan Sea hosts a number of areas with extensive shallow methane deposits and various related phenomena, including well-developed gas chimneys, active methane seeps and readily observed hydroacoustic plumes (Aoyama et al., 2004; Matsumoto et al., 2017). The seafloor in these areas hosts

pock marks and large depressions associated with methane hydrate collapse (Matsumoto et al., 2009) as well as authigenic carbonate crusts and nodules composed of aragonite and Mg-rich calcite (Hiruta et al., 2014; Zhang et al., 2019). Recently, a new type of authigenic mineral, microdolomite, with a diameter of about 30–150 μm was discovered from hydrate-bearing cores drilled in this area (Snyder et al., 2020a).

Dolomite [$CaMg(CO_3)_2$] is a carbonate mineral, of which the euhedral crystal is rhombic (e.g., Petrash et al., 2017). Dolostones composed mainly of dolomite are widespread in the geological record, while the occurrence of dolomite is limited in modern marine settings despite the general observation that the seawater is highly supersaturated for dolomite. This is mainly because the crystallization of dolomite under relatively low temperature/pressure conditions is inhibited by various factors, including strong hydration of Mg^{2+} and the presence of sulfate ion (e.g., James and Jones, 2016). Dolostones in the geological records are generally thought to have formed by weakening these inhibition factors particularly during diagenesis, and dolomite precipitated as cement or replaced primary $CaCO_3$ minerals (e.g., Tucker and Wright, 1990). On the other hand, sulfate-reducing bacteria has been reported to form dolomite primarily (Vasconcelos et al., 1995), which is accomplished by metabolic SO_4^{2-} removal and dolomite nucleation on the organic matrix (Warthmann et al., 2000).

The primary growth of microdolomite grains directly associated with microbial activity is thought to occur in a number of settings, such as shallow marine lagoon sediments in Brazil (Vasconcelos and McKenzie, 1997; Bahniuk et al., 2015) and Eocene and Quaternary petroleum seep sites in Kuwait (Gunatilaka, 1989). Like other dolomite-forming settings, the voids which develop inside of massive gas hydrate accumulations are also considered favorable sites for dolomite formation because the microenvironments in close contact with gas hydrate are also limited in SO_4^{2-} or sulfate-free due to anaerobic methane oxidation (AMO). In addition, water removal via rapid hydrate growth produces brine where hydration of Mg^{2+} is weakened. Snyder et al. (2020a) also suggested that oil-covered brine in the hydrates provides microhabitat for oil-metabolizing microorganisms and their secreted extracellular polymeric substances (EPS) supply suitable substrate for dolomite precipitation. One of the promising approaches to verify this interpretation is to detect carboxy groups and amorphous calcium carbonate (ACC) in the microdolomite. This is because the crystallization process of carbonate minerals on organic molecules is thought to proceed as follows: ACC nanoparticles are formed in the liquid phase, they accumulate on negatively charged organic matter such as EPS containing acidic groups (particularly carboxy groups characterized by a relatively low dissociation constant), and the crystalline phase nucleates from ACC precursors (Pouget et al., 2009). Carboxy groups may also facilitate dolomite precipitation by dehydration of Mg^{2+} (Roberts et al., 2013). Although ACC is less stable than crystalline phases, it is stabilized when it coexists with negatively charged organic matter (Addadi et al., 2003; Obst et al., 2009; Xu et al., 2018). Therefore, if microdolomite was formed by nucleation on negatively charged EPS, traces such as carboxy groups and ACC are expected to be remained inside.

These traces can be detected, for example, by analyzing a thin-foil sections with scanning transmission X-ray microscopy (STXM) and transmission electron microscopy (TEM). Actually, these methods were applied for investigating the calcification process of cyanobacteria, and revealed that the traces of ACC nanoparticles remained around EPS containing carboxy groups (Shiraishi et al., 2020). This study, therefore, aims to verify the involvement of microbial EPS in microdolomite formation by applying these methods. By doing so, this study will reveal the actual processes of primary dolomite formation by microorganisms and the characteristics of their products, which would provide essential information for interpreting dolostones in the geological past.

2 Materials and methods

The study site is the Umitaka Spur located in the Joetsu Basin, the eastern margin of the Japan Sea. Hydrocarbons in the region are presumably derived from gas and oil sourced from the organic-rich upper-Miocene Nanatani Formation located at several kilometers depth (Muramoto et al., 2007; Nyugen et al., 2016). The gas has subsequently migrated towards the surface forming gas chimney structures, shallow methane hydrate accumulations and active seeps (Hiruta et al., 2009; Matsumoto et al., 2009; 2017; Snyder et al., 2020b). In the course of exploration in this area, Snyder et al. (2020a) discovered microdolomite in oil-bearing hydrates and described the basic characteristics of these small mineral grains distributed within the hydrate matrix. The microdolomite grains often show dark internal cores, in which saline fluid and even the trace of microorganisms are occasionally hosted. In addition, microdolomite has positive $\delta^{13}C$ values (from +15.60 to +41.63‰ at Umitaka Spur), which is similar to the values of dissolved inorganic carbon in the interstitial water (from −4.9 to +41.4‰ at Umitaka Spur) while it is quite distinct from the values of hydrate (from −36.6 to −34.6‰ at Umitaka Spur) and methane derived authigenic carbonates (MDACS; from −46.8 to −5.6 at Umitaka Spur). Based on these results, Snyder et al. (2020a) interpreted that the rapid hydrate growth led to the exclusion of oily and saline pockets, in which the organotrophic microorganisms metabolize the oil and produce EPS to form spherulitic microdolomite. Among the microdolomite samples examined by Snyder et al. (2020a), this study focuses on a subset contained in a core drilled at the margin of large pock mark in the central western portion of Umitaka Spur (UTCW).

These microdolomite grains were collected by dissociating the hydrate, isolating the solid phase by centrifugation, washing twice with deionized water, rinsing with ethanol, and drying at 40 °C. Sample splits of those studied by Snyder et al. (2020a) were used for our current study as well as several not yet analyzed. The morphological features of the microdolomite grains observed in each sample were first observed using plane polarized light (PPL) with a polarizing microscope (Eclipse LV100POL, Nikon). From this observation, several types of microdolomite were recognized as described later, and samples containing two typical types were selected for further examinations (samples G122 and AMI01 collected respectively from 17.23 mbsf and 66.27 mbsf). These two samples were embedded in resin (LR White, London Resin) at 60°C for 24 h, and then conventional thin sections of about 50 μm thick were prepared. From these thin sections, thin-foil sections (~150–200 nm thick) were prepared using a focused ion

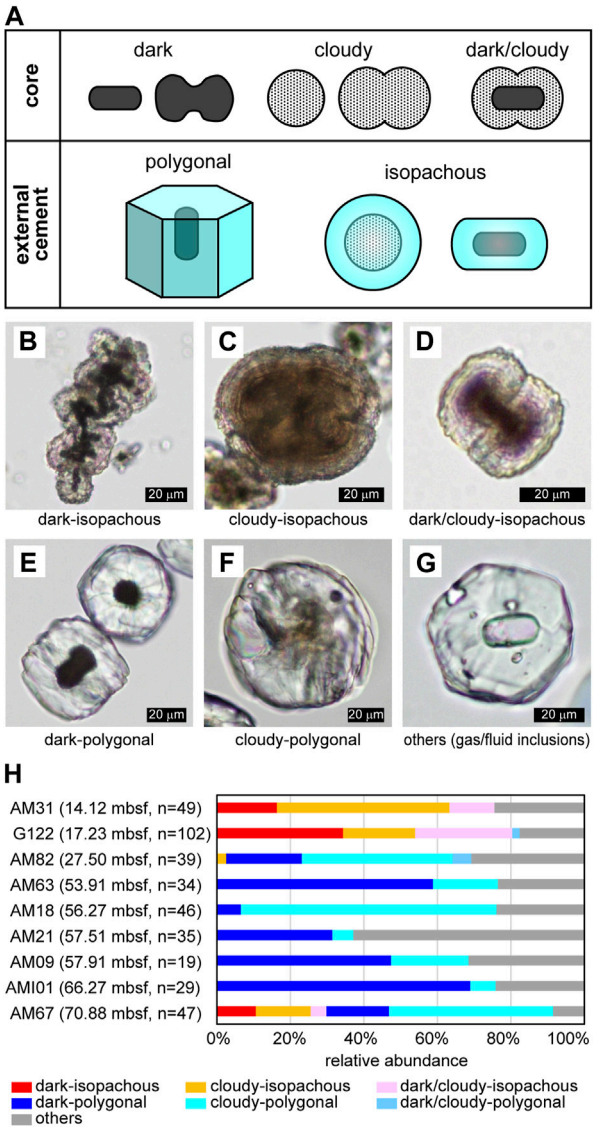

FIGURE 1
Morphological variations of microdolomite. **(A)** Summary of typical core and external cement types. **(B)**–**(G)** Typical combinations of core and external cement. PPL images. **(B)** Combination of dark core and isopachous external cement. Many bacilliform dark cores are observed. Sample G122. **(C)** Combination of cloudy core and isopachous external cement. It looks like conjoining of four spherical cores. Fine concentric laminae are sometimes recognized in the core and cement. Sample G122. **(D)** Combination of dark/cloudy core and isopachous external cement. The dark core is bacilliform, but the surrounding cloudy part is dumbbell-shaped. Fine laminae are recognizable in the external cement. Sample G122. **(E)** Combination of dark core and polygonal external cement. The grain on the upper right is a view of the hexagonal prism from above, and the faint streaks extending radially from the core are recognizable. On the other hand, the grain in the lower left is a view of hexagonal prism from the side, and the faint parallel to wedge-shaped streaks are recognizable. The elongating directions of the hexagonal prism and the bacilliform core are the same. Sample AM101. **(F)** Combination of cloudy core and polygonal external cement. The core is slightly dumbbell-shaped. Sample AM09. **(G)** An example of other types exhibiting polygonal external cement with some gas or fluid inclusions. Sample AM63. **(H)** Depth distribution of core-cement combinations. The sampling depth is also shown in parentheses.

beam (FIB) apparatus (SMI-4050, Hitachi) with a 30 keV Ga ion beam. Before ion milling, carbon was deposited on the sample surface for protection.

Thin-foil sections were observed using STXM and TEM mostly based on the methods of Shiraishi et al. (2020). Briefly, this study used STXM established at BL19A beamline of KEK-PF (Tsukuba, Japan). STXM is a type of X-ray microscopy using synchrotron radiation, which is capable of high-resolution mapping of the valency and chemical state of elements in the soft X-ray region. In this study, calcium L-edge and carbon K-edge NEXAFS (near edge X-ray absorption fine structure) spectra and images were obtained, and these spectra and images were analyzed using aXis 2000 software (Hitchcock, 2009). Whole images of thin-foil sections were acquired at several energy steps (345.0, 348.1, 348.5 and 352.6 eV for calcium; 280.0, 288.6, 290.3, and 301.5 eV for carbon), and their overviews were generated using the RGB composite method after subtracting the backgrounds (345.0 eV and 280.0 eV for calcium and carbon, respectively). Around the central part of microdolomite, image stacks were obtained and composition maps were generated using representative spectra with the singular value decomposition (SVD) method. Spectra of calcite, aragonite, and ACC reported by Shiraishi et al. (2017); Shiraishi et al. (2020) were used for references. In addition, reference spectra were acquired from dolomite, albumin (as a representative of protein), agarose (as a representative of saccharide without carboxy group), D-glucuronic acid (as a representative of saccharide with carboxy group), as well as artificial materials contained in the thin-foil sections, namely, LR White resin and carbon deposition. Thin-foil sections were further observed with TEM (JEM-ARM200F, JEOL) operated at an accelerating voltage of 200 kV. Apertures for obtaining selected-area electron diffraction (SAED) patterns were 0.25, 0.6, and 1.1 μm in diameter. In addition, high-angle annular dark field (HAADF) images were generated in scanning TEM (STEM) mode.

3 Results

3.1 Morphological variations of microdolomite

The morphology of microdolomite grains was described previously through the microscopic observation of external morphology and the degree to which microcrystalline spheroidal aggregates are conjoined, ranging from single grains to dumbbell, chain, and cauliflower-shapes (Snyder et al., 2020a). In this study we consider both the internal and external characteristics of the microdolomite grains and classify them according to the combinations of distinct cores and external cements. The internal cores of the microdolomite aggregates can be dark, or opaque, or they can be cloudy but still capable of transmitting light in microscopic section, or they can be a combination of cloudy and dark. The external, cemented portion of the microdolomites can be polygonal or isopachous (Figure 1A). Examples of these combinations include bacilliform black cores in PPL surrounded by isopachous external cement forming a chain aggregate

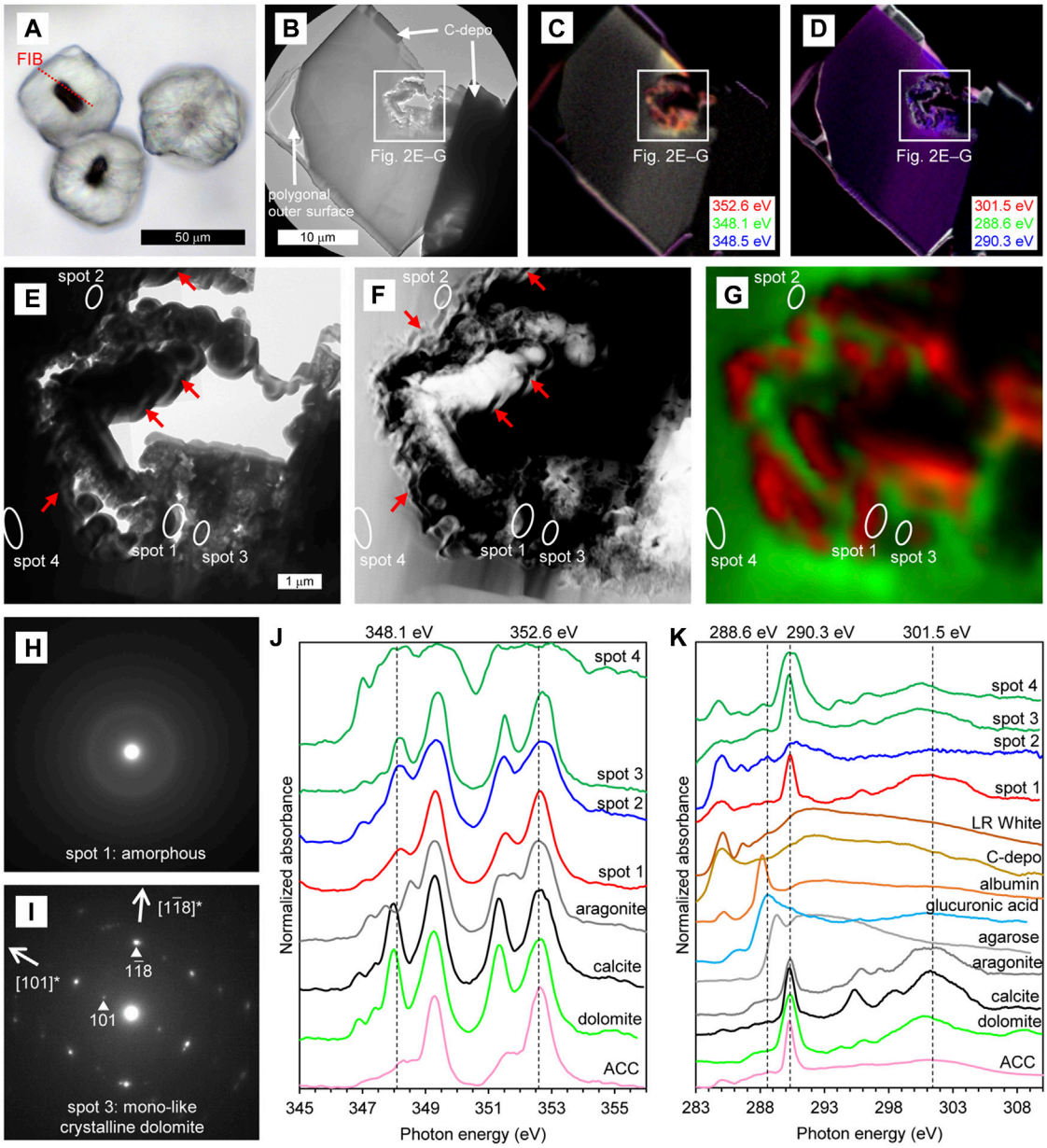

FIGURE 2
Characteristics of dark–polygonal type. **(A)** PPL image of the thin section. The red dashed line indicates the location of the thin-foil section prepared by FIB. **(B–D)** Overviews of the thin-foil section, showing BF-TEM image **(B)** and STXM-based compositional images for Ca **(C)** and C **(D)**. The upper margin of the thin-foil section is protective carbon deposition (C-depo). **(E–G)** Magnified region from **(B–D)**, showing a BF-TEM image **(E)**, HAADF-STEM image **(F)**, and STXM-based SVD mapping **(G)**. Spots for NEXAFS spectra and SAED patterns are indicated. Red arrows in **(E)** and **(F)** represent some examples of fibriform pores. **(H and I)** SAED patterns taken from spots 1 **(H)** and 3 **(I)**, showing the presence of amorphous phase and mono-like crystalline dolomite, respectively. **(J)** Ca NEXAFS spectra of four sample spots and reference materials. The spectrum of spot 1 is representative of the red areas in **(G)**. The spectra of spots 3 and 4 are representative of the green areas in **(G)**, exhibiting thin and thick parts of the dolomite, respectively. X-ray absorbance at spot 4 is saturated due to relatively thick sample section. **(K)** C NEXAFS spectra of four sample spots and reference materials. X-ray absorbance of spot 4 is also somewhat saturated due to relatively thick sample section.

(Figure 1B), cloudy-cores surrounded by isopachous cement (Figure 1C), dark/cloudy cores surrounded by isopachous cement forming a paired dumbbell structure (Figure 1D). In general, the isopachous cement is relatively transparent and conformably fringes the core morphology with a slight pinching in the case of dumbbell pairs. The microdolomites with polygonal surfaces all present transparent external cement and may have dark cores (Figure 1E) although others have cloudy cores (Figure 1F). Others have no apparent core (Figure 1G), yet may present either fluid or gas inclusions.

The relative abundance of each core and cement combination is shown for samples listed from shallow to deep (Figure 1H), along

with the number of grains counted for each sample. Isopachous cement was observed to be dominant at the depth above ~14–17 mbsf, while polygonal cement was found to be dominant in the deeper gas hydrates. On the other hand, the relative abundance of dark, dark/cloudy, and cloudy core types did not show a clear depth dependence.

In order to further characterize the cores and external cements, two distinct, yet fairly typical, microdolomite grains were selected for STXM and TEM observations: a dark-polygonal type (sample AMI01) recovered from gas hydrate at 66.27 mbsf and a cloudy-isopachous type (sample G122) recovered from relatively shallow gas hydrate at 17.23 mbsf.

3.2 Observation of thin-foil section: dark-polygonal type

For the dark-polygonal type, a thin-foil section was prepared so that the section included both the core and the external cemented portion (Figure 2A). However, since the core seemed to be weak when subjected to the Ga ion beam, FIB processing was stopped even though the section was relatively thick (approximately 200–300 nm). Bright-field (BF) TEM imagery shows that the obtained thin-foil section contains a cross-section of about 1/3 of the external cement in addition to the core, and that the core has cavities, while the external cement is rather structureless (Figure 2B). In the STXM-based compositional images for Ca (Figure 2C), the core is displayed in red because X-ray absorption at 348.1 eV is less significant than that at 352.6 eV, as is characteristic for ACC and aragonite (Figure 2J). On the other hand, the external cement is displayed in yellow because the absorptions both at 348.1 eV and 352.6 eV were significant (although the color was not prominent due to strong self-absorption by the relatively thick section), which is characteristic for dolomite and calcite (Figure 2J). In the STXM-based compositional images for C (Figure 2D), the external cement is displayed in purple because the absorptions both at 290.3 eV and 301.5 eV were significant. Absorptions at 290.3 eV and 301.5 eV (and also two peaks between ca. 294.0 eV and 298.5 eV) correspond, respectively, to π^* and σ^* carbonate resonances, and their relative intensities are sensitive to crystal orientation rather than to mineral species (Metzler et al., 2008; Brandes et al., 2010; Gilbert et al., 2011). Therefore, the uniform purple color in the external cement suggested that it was composed of single crystal of carbonate mineral at least across the observable range.

In a more detailed observation around the core, BF-TEM image shows that wavy/spiral fibriform pores of about 100 nm wide are observable near the boundary between the cavity and the mineral (e.g., arrows in Figure 2E). These fibriform pores are more clearly observed in the HAADF-STEM image (e.g., arrows in Figure 2F). STXM-based SVD mapping (Figure 2G) showed Ca NEXAFS spectra characteristic of ACC surrounding the fibriform pores (red areas including spot 1), and the spectra characteristic of dolomite and calcite in the surrounding area (green areas including spots 2–4). In the SAED patterns, the area showing the Ca NEXAFS spectrum characteristic of ACC was amorphous (spot 1, Figure 2H). On the other hand, in the area showing the spectra characteristic of dolomite and calcite, the SAED pattern is indicative of mono-like crystalline dolomite (i.e., dolomite with a slightly different crystal orientation; spot 3, Figure 2I). In the C NEXAFS spectra, a weak absorption peak at around 288.6 eV is recognizable, particularly near the fibriform pores (spot 2 in Figure 2K), was as is characteristic of carboxy groups exemplified by the spectrum of D-glucuronic acid (Benzerara et al., 2004; Mitsunobu et al., 2016; and references therein). Weak absorption peaks are also recognizable around 288.2 eV near the fibriform pores (spot 2 in Figure 2K) and surrounding dolomite (spots 3 and 4 in Figure 2K), which is characteristic of protein as exemplified by the spectrum of albumin. On the other hand, the peaks around 284.9 eV and 286.5 eV in the spectra of spots 1–4 also appeared in the resin and carbon deposition, suggesting that these peaks originated from artificial materials.

3.3 Observation of thin-foil section: cloudy-isopachous type

For the cloudy-isopachous type, the thin-foil section was also prepared so that the section included both the core and the externally cemented areas (Figure 3A). BF-TEM image shows that the obtained thin-foil section contains a cross-section of about 1/4 of the spherical core and the external cement, and that the scattered minerals in the core are divided by a dense mineral layer (Figure 3B). The external cement was also consisted of similar but thicker mineral layer. The STXM-based compositional images for Ca (Figure 3C) are largely displayed in light-yellow indicating significant absorptions at both 348.1 eV and 352.6 eV, was as is characteristic of dolomite and calcite (Figure 3J). On the other hand, the rim of the scattered minerals in the core is displayed as reddish, indicating a relatively weak absorption at 348.1 eV as described above. In the STXM-based compositional images for C (Figure 3D), the section is largely displayed in red due to relatively significant absorption at 301.5 eV, indicating that the crystal orientation is similar within the observable range. However, the lower left area of the thin-foil section and some of the scattered minerals in the core are displayed in purple due to significant absorption both at 290.3 eV and 301.5 eV, indicating their different crystal orientation.

In a more detailed observation around the core, BF-TEM (Figure 3E) and HAADF-STEM (Figure 3F) images shows that the minerals scattered in the core were generally rhombohedrons of about 0.1–2 μm in size, and that the dense mineral layer in the core and external cement are composed of aggregates of rhombohedral minerals. STXM-based SVD mapping (Figure 3G) shows Ca NEXAFS spectra characteristic of dolomite and calcite in most part of the core and external cement (green areas including spots 2 and 3). On the other hand, as with the overviewing compositional images for Ca, the rim of the scattered minerals in the core exhibits a spectrum with relatively weak absorption at 348.1 eV (red areas including spot 1), but this absorption peak is more significant if compared with the spectrum of ACC (Figure 3J). This is the crystal field peak, which is significant for crystals like dolomite, and is less significant for less-ordered crystals such as polycrystalline dolomite, and is insignificant for disordered ACC (Politi et al., 2008; Gong et al., 2012). In fact, the SAED pattern indicates that the area showing relatively weak absorption at 348.1 eV is polycrystalline dolomite (spot 1, Figure 3H). On the other hand, in the area showing Ca NEXAFS spectra characteristic of dolomite and calcite, the SAED pattern indicates monocrystalline dolomite (spot 2, Figure 3I). The C NEXAFS spectra does not show any significant peaks other than the resin, carbon deposition, and carbonate (Figure 3K).

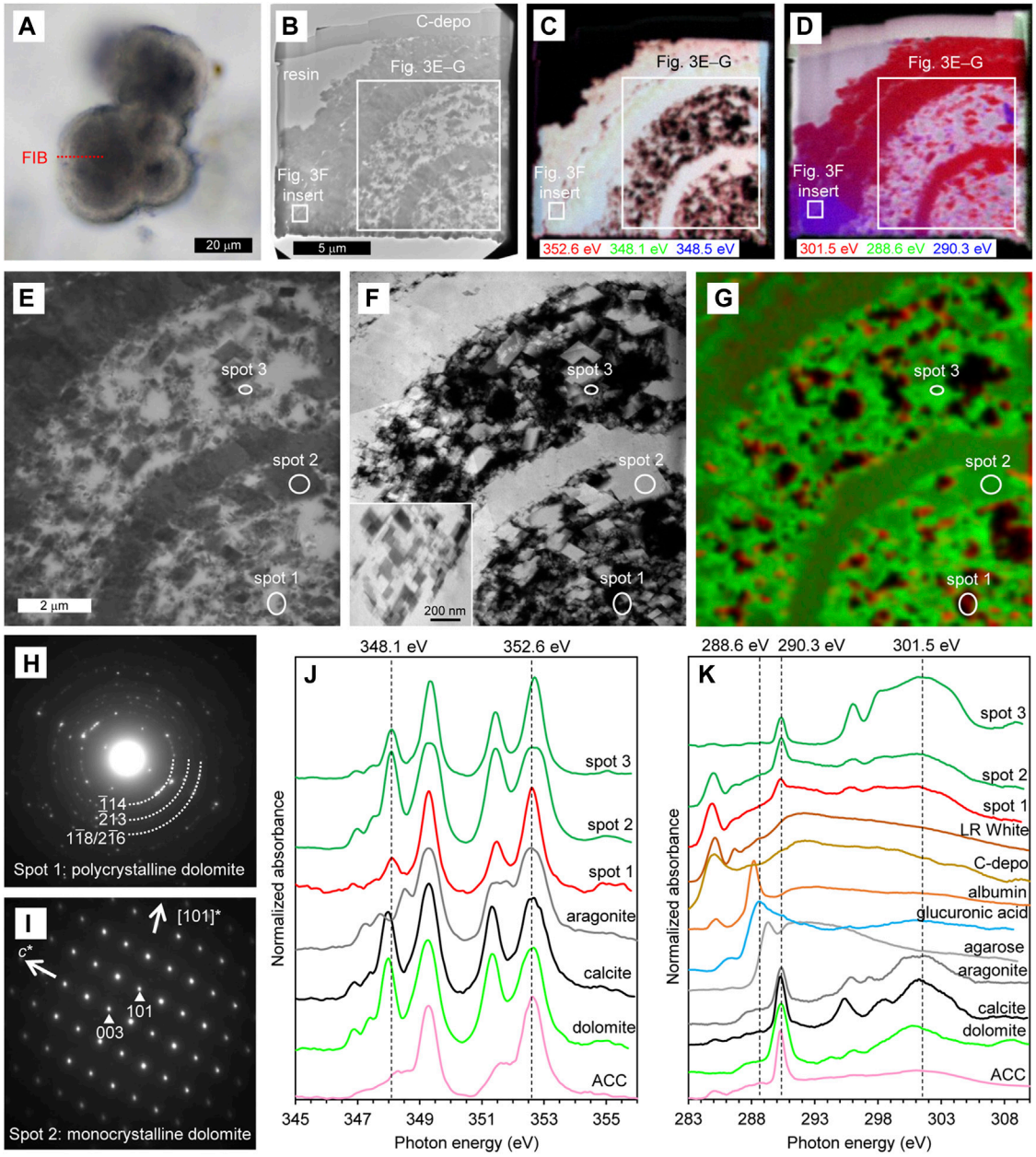

FIGURE 3
Characteristics of cloudy–isopachous type. **(A)** PPL image of the thin section. The red dashed line indicates the location of the thin-foil section prepared by FIB. **(B–D)** Overviews of the thin-foil section, showing BF-TEM image **(B)** and STXM-based compositional images for Ca **(C)** and C **(D)**. The upper margin of the thin-foil section is protective carbon deposition (C-depo). **(E–G)** Magnified region from **(B–D)**, showing a BF-TEM image **(E)**, HAADF-STEM image **(F)**, and STXM-based SVD mapping **(G)**. Spots for NEXAFS spectra and SAED patterns are indicated. An inserted image in F is a magnification of the external cement, as shown in **(B–D)**. **(H, I)** SAED patterns taken from spots 1 **(H)** and 2 **(I)**, showing the presence of polycrystalline and monocrystalline dolomite, respectively. **(J)** Ca NEXAFS spectra of three sample spots and reference materials. The spectrum of spot 1 is representative of the red areas in **(G)**. The spectra of spots 2 and 3 are representative of the green areas in **(G)**, exhibiting thick and thin parts of the dolomite, respectively. **(K)** C NEXAFS spectra of three sample spots and reference materials.

4 Discussion

The observations of this study reveal the typical characteristics of cores and external cements that constitute the microdolomite. In the dark-polygonal type, fibriform pores of about 100 nm in diameter are closely related with ACC and carboxy groups in the core areas, which are surrounded by a polygonal external cement composed of monocrystalline dolomite (Figure 2). While these pores were considerably smaller than typical prokaryotic cells (mostly 0.5–2.0 μm in diameter; e.g., Black, 2005), their size and morphology were similar to hydrogels of polysaccharides and EPS incorporated in carbonate minerals. For example, Li and Estroff (2007) reported that the fibriform pores of about 60–360 nm wide were formed in calcite if the fibers of agarose gel, a neutral

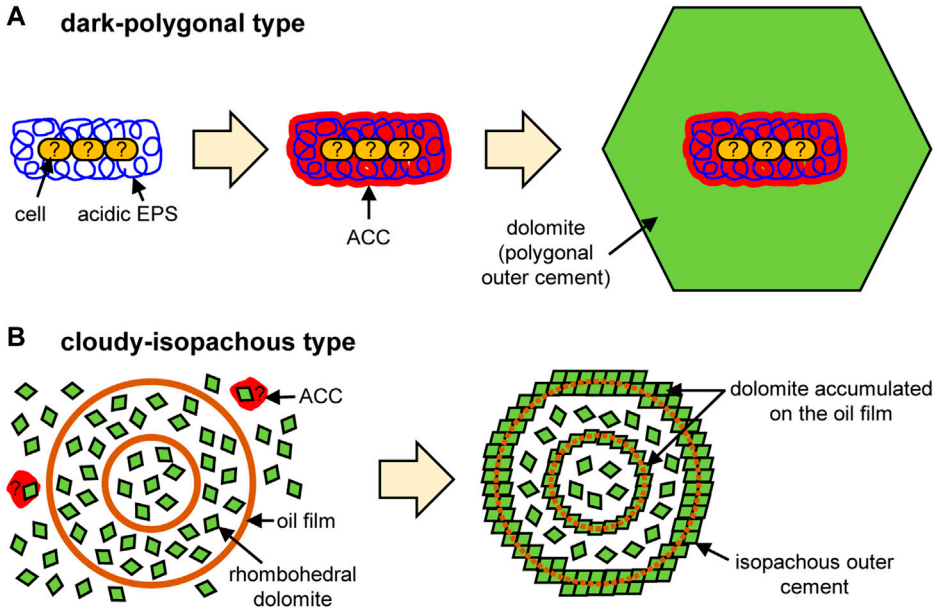

FIGURE 4
Conceptual models of microdolomite formation for **(A)** dark-polygonal type and **(B)** cloudy-isopachous type.

polysaccharide, were incorporated into the crystal. Yin et al. (2020) also reported similar results using both agarose and microbial acidic EPS. Therefore, it is likely that the fibriform pores in the dark core represent microbial EPS containing carboxy groups, which have induced heterogeneous nucleation (i.e., nucleation on the foreign surface; De Yoreo and Vekilov, 2003) of dolomite crystals via ACC precursors. The dark core of the examined microdolomite is bacilliform, but it is about 8 μm wide and 17 μm long, which is considerably larger than a single prokaryotic cell (Figure 2A). Alternative possibilities may be an assembly of multiple cells, or an aggregate of EPS separated from the cells. In the former case, it is possible that cells were degraded naturally by diagenesis or artificially during FIB processing, because there is no morphological evidence of cells in the thin-foil section despite the presence of protein around the core. Such EPS-producing microorganisms may be oil-metabolizing organotrophs such as Flavobacteria, as suggested by the previous study (Snyder et al., 2020a), and the dark color of the core may come from the coexisting oil. In any case, acidic EPS with or without cells would provide the necessary nucleation sites for dolomite, after which the crystal growth of dolomite can occur abiotically in the supersaturated saline pockets (Figure 4A).

The cloudy-isopachous type microdolomite does not present observable fibriform pores, ACC, or carboxy groups. Instead, the core consists mainly of scattered rhombohedral dolomite (Figure 3), which is capable of dispersing transmitted light to produce the observed cloudy appearance. Scattered rhombohedral dolomite also aggregates into spherical crusts to form core-dividing dense layers and isopachous external cement (Figure 3). Such scattered euhedral crystals suggest the occurrence of homogeneous nucleation (i.e., nucleation within the bulk solution; De Yoreo and Vekilov, 2003). Since homogeneous nucleation requires much higher supersaturation of solute than heterogeneous nucleation (Stumm and Morgan, 1996), it is conceivable that the rapid hydrate growth significantly concentrates the remaining water, in which hydration of Mg^{2+} has weakened and a conspicuous amount of rhombohedral dolomite has crystallized in this brine. Although ACC precursors may be involved in their nucleation, such traces would not be stabilized due to the lack of EPS containing carboxy groups (Addadi et al., 2003; Obst et al., 2009; Xu et al., 2018). On the other hand, in order for rhombohedral crystals to accumulate and form a hollow spherical crust (though rhombohedral crystals are scattered inside), a spherical template is required. A possible candidate is an oil-covered brine as suggested by the previous study (Snyder et al., 2020a). Although the traces of oil film were not detected in the course of this study, it is likely that the oil has been lost because ethanol was used for washing and resin embedding. If nanocrystals (e.g., the inserted image of Figure 3F) had accumulated on the surface of such a spherical template, a spherical crust would have been formed. In fact, it has become clear that crystallization by attachment of particles such as nanocrystals is a general phenomenon (De Yoreo et al., 2015). If the spherical oil film was double-layered, a concentric structure like the sample in this study would have been formed (Figure 4B).

In this study, the observations using polarizing microscopy have revealed that the microdolomite grains exhibit distinct cores and external cements. The high-resolution observations by TEM and STXM further reveal the formation processes of these unusual grains which are potentially ubiquitous in saline, sulfate-limited environments. We hope that these data will provide the essential information for understanding the origin of small dolomite grains found in the thin sections of geological samples. To our knowledge, there have been no similar studies carried out yet, but small dolomite grains have been reported from other areas. For example, Sadooni et al. (2010) described rounded and rhombic dolomite with a diameter of ~5 μm from sabkha in Abu Dhabi, and Perri et al. (2018) described

rhombic dolomite with a diameter of 1–20 μm from sabkha in Qatar. They are smaller in diameter and different in shape if compared to the microdolomite of this study. This suggests that they have different origins, which will be confirmed by applying approaches similar to those of this study to future investigations.

5 Conclusion

In order to understand the formation process of microdolomite grains found within gas hydrate at an active gas chimney site, this study investigated their internal structures using polarizing microscopy, TEM, and STXM. The results reveal that dark and cloudy cores, and polygonal and isopachous external cements which are intrinsically different. The dark cores reflect heterogeneous nucleation on microbial EPS inside the hydrate microhabitats (Figure 4A). On the other hand, the cloudy core and isopachous external cement reflects homogeneous nucleation in relatively shallow depth where hydrate grew rapidly and dolomite nanocrystals accumulated on the surface of spherical oil films (Figure 4B). The polygonal external cement would reflect slow crystal growth in the deeper part, where the hydrate formation was less active. Thus, this study further strengthens the view that microdolomite is the product of interactions between methane, oil, and possibly microorganisms that have migrated upward through the sediments. Saline seep environments, such as submarine gas chimneys which host massive methane hydrate, provide the necessary conditions for the development of microdolomite grains similar to those we have observed and it is likely that similar grains exist in both presently active seep environments and are also preserved in fossil seep sites. This study revealed the characteristics of only two core-cement combinations, and while it is necessary to continue research into other types, hopefully our approach will provide a template for future investigation.

Data availability statement

The original contributions presented in the study are included in the article/supplementary material, further inquiries can be directed to the corresponding author.

Author contributions

RM and GS collected samples, FS, TA, NT, and YT conducted microscopic analyses, and all authors discussed ideas and wrote the manuscript.

Funding

This research was supported by the Japan Society for the Promotion of Science (JSPS) Grants-in-Aid for Scientific Research Nos. 21K18658 and 21K03739.

Acknowledgments

We acknowledge Dr. Shohei Yamashita for supporting STXM analyses. Two reviewers gave valuable and helpful suggestions and comments. The Joetsu Basin samples used in this study were collected by Meiji University's Gas Hydrate Research Laboratory under the commission of AIST (National Institute of Advanced Industrial Science and Technology) from 2013–2015 as part of the methane hydrate research project funded by METI (Ministry of Economy, Trade and Industry), Japan.

Conflict of interest

The authors declare that the research was conducted in the absence of any commercial or financial relationships that could be construed as a potential conflict of interest.

Publisher's note

All claims expressed in this article are solely those of the authors and do not necessarily represent those of their affiliated organizations, or those of the publisher, the editors and the reviewers. Any product that may be evaluated in this article, or claim that may be made by its manufacturer, is not guaranteed or endorsed by the publisher.

References

Addadi, L., Raz, S., and Weiner, S. (2003). Taking advantage of disorder: Amorphous calcium carbonate and its roles in biomineralization. *Adv. Mat.* 15, 959–970. doi:10.1002/adma.200300381

Aoyama, C., Matsumoto, R., Okuda, Y., Ishida, Y., Hiruta, A., Sunamura, M., et al. (2004). Acoustical survey of methane plumes using the quantitative echo sounder in the eastern margin of the Sea of Japan, Oceans '04 MTS/IEEE Techno-Ocean '04 (IEEE Cat. No.04CH37600), Kobe. *Japan* 2, 1004–1009. doi:10.1109/OCEANS.2004.1405646

Bahniuk, A., McKenzie, J. A., Perri, E., Bontognali, T. R. R., Vögeli, N., Rezende, C. E., et al. (2015). Characterization of environmental conditions during microbial Mg-carbonate precipitation and early diagenetic dolomite crust formation: Brejo do Espinho, Rio de Janeiro, Brazil. *Geol. Soc. Lond. Spec. Publ.* 418, 243–259. doi:10.1144/sp418.11

Benzerara, K., Yoon, T. H., Tyliszczak, T., Constantz, B., Spormann, A. M., and Brown, G. E. (2004). Scanning transmission X-ray microscopy study of microbial calcification. *Geobiology* 2, 249–259. doi:10.1111/j.1472-4677.2004.00039.x

Black, J. G. (2005). *Microbiology: Principles and explorations*. Sixth ed. New York: Wiley & Sons.

Brandes, J. A., Wirick, S., and Jacobsen, C. (2010). Carbon K-edge spectra of carbonate minerals. *J. Synchrotron Radiat.* 17, 676–682. doi:10.1107/s0909049510020029

De Yoreo, J. J., and Vekilov, P. G. (2003). Principles of crystal nucleation and growth. *Rev. Mineral. Geochem.* 54, 57–93. doi:10.2113/0540057

De Yoreo, J. J., Gilbert, P. U. P. A., Sommerdijk, N. A. J. M., Penn, R. L., Whitelam, S., Joester, D., et al. (2015). Crystallization by particle attachment in synthetic, biogenic, and geologic environments. *Science* 349, 6760. doi:10.1126/science.aaa6760

Gilbert, P. U. P. A., Young, A., and Coppersmith, S. N. (2011). Measurement of c-axis angular orientation in calcite ($CaCO_3$) nanocrystals using x-ray absorption spectroscopy. *Proc. Natl. Acad. Sci. U. S. A.* 108, 11350–11355. doi:10.1073/pnas.1107917108

Gong, Y. U. T., Killian, C. E., Olson, I. C., Appathurai, N. P., Amasino, A. L., Martin, M. C., et al. (2012). Phase transitions in biogenic amorphous calcium carbonate. *Proc. Natl. Acad. Sci. U. S. A.* 109, 6088–6093. doi:10.1073/pnas.1118085109

Gunatilaka, A. (1989). Spheroidal dolomites – origin by hydrocarbon seepage? *Sedimentology* 36, 701–710. doi:10.1111/j.1365-3091.1989.tb02094.x

Hiruta, A., Snyder, G. T., Tomaru, H., and Matsumoto, R. (2009). Geochemical constraints for the formation and dissociation of gas hydrate in an area of high methane flux, eastern margin of the Japan Sea. *Earth Planet. Sci. Lett.* 279, 326–339. doi:10.1016/j.epsl.2009.01.015

Hiruta, A., Wang, L. C., Ishizaki, O., and Matsumoto, R. (2014). Last glacial emplacement of methane-derived authigenic carbonates in the Sea of Japan constrained by diatom assemblage, carbon-14, and carbonate content. *Mar. Pet. Geol.* 56, 51–62. doi:10.1016/j.marpetgeo.2014.04.005

Hitchcock, A. P. (2009). aXis2000 is written in interactive data language (IDL). Avaliable At: http://unicorn.mcmaster.ca/aXis2000.html.

James, N. P., and Jones, B. (2016). *Origin of carbonate sedimentary rocks*. Chichester: Wiley & Sons.

Li, H., and Estroff, L. A. (2007). Porous calcite single crystals grown from a hydrogel medium. *CrystEngComm* 9, 1153–1155. doi:10.1039/b709068d

Matsumoto, R., Okuda, Y., Hiruta, A., Tomaru, H., Takeuchi, E., Sanno, R., et al. (2009). Formation and collapse of gas hydrate deposits in high methane flux area of the Joetsu Basin, eastern margin of Japan sea. *J. Geogr.* 118, 43–71. doi:10.5026/jgeography.118.43

Matsumoto, R., Tanahashi, M., Kakuwa, Y., Snyder, G., Ohkawa, S., Tomaru, H., et al. (2017). Recovery of thick deposits of massive gas hydrates from gas chimney structures, eastern margin of Japan sea: Japan sea shallow gas hydrate project fire in the ice. Avaliable At: https://www.netl.doe.gov/sites/default/files/publication/MHNews-2017-Jan.pdf.

Metzler, R. A., Kim, W., Delak, K., Evans, J. S., Zhou, D., Beniash, E., et al. (2008). Probing the organic–mineral interface at the molecular level in model biominerals. *Langmuir* 24, 2680–2687. doi:10.1021/la7031237

Mitsunobu, S., Zhu, M., Takeichi, Y., Ohigashi, T., Suga, H., Jinno, M., et al. (2016). Direct detection of Fe(II) in extracellular polymeric substances (EPS) at the mineral-microbe interface in bacterial pyrite leaching. *Microbes Environ.* 31, 63–69. doi:10.1264/jsme2.me15137

Muramoto, K., Osawa, M., Kida, M., and Arisaka, H. (2007). A petroleum system in the deep water of the sado nanseioki area in the Japan sea based on the results of the MITI "sadooki nansei" seismic survey and the METI "sado nanseioki" wells. *J. Jpn. Assoc. Pet. Tech.* 72, 76–88. doi:10.3720/japt.72.76

Nguyen, B. T. T., Kido, M., Okawa, N., Fu, H., Kakizaki, S., and Imahori, S. (2016). Compaction of smectite-rich mudstone and its influence on pore pressure in the deepwater Joetsu Basin, Sea of Japan. *J. Mar. Pet. Geol.* 78, 848–869. doi:10.1016/j.marpetgeo.2016.07.011

Obst, M., Dynes, J. J., Lawrence, J. R., Swerhone, G. D. W., Benzerara, K., Karunakaran, C., et al. (2009). Precipitation of amorphous $CaCO_3$ (aragonite-like) by cyanobacteria: A STXM study of the influence of EPS on the nucleation process. *Geochim. Cosmochim. Acta* 73, 4180–4198. doi:10.1016/j.gca.2009.04.013

Perri, E., Tucker, M. E., Słowakiewicz, M., Whitaker, F., Bowen, L., and Perrotta, I. D. (2018). Carbonate and silicate biomineralization in a hypersaline microbial mat (Mesaieed sabkha, Qatar): Roles of bacteria, extracellular polymeric substances and viruses. *Sedimentology* 65, 1213–1245. doi:10.1111/sed.12419

Petrash, D. A., Bialik, O. M., Bontognali, T. R. R., Vasconcelos, C., Roberts, J. A., McKenzie, J. A., et al. (2017). Microbially catalyzed dolomite formation: From near-surface to burial. *Earth-Sci. Rev.* 171, 558–582. doi:10.1016/j.earscirev.2017.06.015

Politi, Y., Metzler, R. A., Abrecht, M., Gilbert, B., Wilt, F. H., Sagi, I., et al. (2008). Transformation mechanism of amorphous calcium carbonate into calcite in the sea urchin larval spicule. *Proc. Natl. Acad. Sci. U. S. A.* 105, 17362–17366. doi:10.1073/pnas.0806604105

Pouget, E. M., Bomans, P. H. H., Goos, J. A. C. M., Frederik, P. M., de With, G., and Sommerdijk, N. A. J. M. (2009). The initial stages of template-controlled $CaCO_3$ formation revealed by cryo-TEM. *Science* 323, 1455–1458. doi:10.1126/science.1169434

Roberts, J. A., Kenward, P. A., Fowle, D. A., Goldstein, R. H., González, L. A., and Moore, D. S. (2013). Surface chemistry allows for abiotic precipitation of dolomite at low temperature. *Proc. Natl. Acad. Sci. U. S. A.* 110, 14540–14545. doi:10.1073/pnas.1305403110

Sadooni, F. N., Howari, F., and El-Saiy, A. (2010). Microbial dolomites from carbonate-evaporite sediments of the coastal sabkha of Abu Dhabi and their exploration implications. *J. Pet. Geol.* 33, 289–298. doi:10.1111/j.1747-5457.2010.00480.x

Shiraishi, F., Hanzawa, Y., Okumura, T., Tomioka, N., Kodama, Y., Suga, H., et al. (2017). Cyanobacterial exopolymer properties differentiate microbial carbonate fabrics. *Sci. Rep.* 7, 11805. doi:10.1038/s41598-017-12303-9

Shiraishi, F., Omori, T., Tomioka, N., Motai, S., Suga, H., and Takahashi, Y. (2020). Characteristics of $CaCO_3$ nucleated around cyanobacteria: Implications for calcification process. *Geochim. Cosmochim. Acta* 285, 55–69. doi:10.1016/j.gca.2020.06.033

Snyder, G. T., Matsumoto, R., Suzuki, Y., Kouduka, M., Kakizaki, Y., Zhang, N., et al. (2020a). Evidence in the Japan Sea of microdolomite mineralization within gas hydrate microbiomes. *Sci. Rep.* 10, 1876. doi:10.1038/s41598-020-58723-y

Snyder, G. T., Sano, Y., Takahata, N., Matsumoto, R., Yoshihiro Kakizaki, Y., and Tomaru, H. (2020b). Magmatic fluids play a role in the development of active gas chimneys and massive gas hydrates in the Japan Sea. *Chem. Geol.* 535, 119462. doi:10.1016/j.chemgeo.2020.119462

Stumm, W., and Morgan, J. J. (1996). *Aquatic chemistry: Chemical equilibria and rates in natural waters*. New York: Wiley & Sons.

Tucker, M. E., and Wright, V. P. (1990). *Carbonate sedimentology*. Oxford: Blackwell.

Vasconcelos, C., and McKenzie, J. A. (1997). Microbial mediation of modern dolomite precipitation and diagenesis under anoxic conditions, Lagoa Vermelha, Rio de Janeiro, Brazil. *J. Sed. Res.* 67, 378–390. doi:10.1306/D4268577-2B26-11D7-8648000102C1865D

Vasconcelos, C., McKenzie, J. A., Bernasconi, S., Grujic, D., and Tien, A. J. (1995). Microbial mediation as a possible mechanism for natural dolomite formation at low temperatures. *Nature* 377, 220–222. doi:10.1038/377220a0

Warthmann, R., van Lith, Y., Vasconcelos, C., McKenzie, J. A., and Karpoff, A. M. (2000). Bacterially induced dolomite precipitation in anoxic culture experiments. *Geology* 28, 1091–1094. doi:10.1130/0091-7613(2000)028<1091:bidpia>2.3.co;2

Xu, Y., Tijssen, K. C. H., Bomans, P. H. H., Akiva, A., Friedrich, H., Kentgens, A. P. M., et al. (2018). Microscopic structure of the polymer-induced liquid precursor for calcium carbonate. *Nat. Commun.* 9, 2582. doi:10.1038/s41467-018-05006-w

Yin, X., Weitzel, F., Jiménez-López, C., Griesshaber, E., Fernández-Díaz, L., Rodríguez-Navarro, A., et al. (2020). Directing effect of bacterial extracellular polymeric substances (EPS) on calcite organization and EPS–carbonate composite aggregate formation. *Cryst. Growth Des.* 20, 1467–1484. doi:10.1021/acs.cgd.9b01113

Zhang, N., Lin, M., Snyder, G. T., Kakizaki, Y., Yamada, K., Yoshida, N., et al. (2019). Clumped isotope signatures of methane-derived authigenic carbonate presenting equilibrium values of their formation temperatures. *Earth Planet. Sci. Lett.* 512, 207–213. doi:10.1016/j.epsl.2019.02.005

frontiers | Frontiers in Earth Science

TYPE Original Research
PUBLISHED 25 July 2023
DOI 10.3389/feart.2023.1210088

Check for updates

OPEN ACCESS

EDITED BY
Glen T. Snyder,
The University of Tokyo, Japan

REVIEWED BY
Stephen A. Bowden,
University of Aberdeen, United Kingdom
Verena Heuer,
University of Bremen, Germany

*CORRESPONDENCE
Nai-Chen Chen,
nai-chen.chen@geo.su.se
Pei-Ling Wang,
plwang@ntu.edu.tw

†Deceased

RECEIVED 21 April 2023
ACCEPTED 12 July 2023
PUBLISHED 25 July 2023

CITATION
Chen N-C, Yang TF, Liou Y-H, Lin H-TT, Hong W-L, Lin S, Su C-C, Lin L-H and Wang P-L (2023), Controlling factors on patterns of dissolved organic carbon and volatile fatty acids in a submarine mud volcano offshore southwestern Taiwan. *Front. Earth Sci.* 11:1210088. doi: 10.3389/feart.2023.1210088

COPYRIGHT
© 2023 Chen, Yang, Liou, Lin, Hong, Lin, Su, Lin and Wang. This is an open-access article distributed under the terms of the Creative Commons Attribution License (CC BY). The use, distribution or reproduction in other forums is permitted, provided the original author(s) and the copyright owner(s) are credited and that the original publication in this journal is cited, in accordance with accepted academic practice. No use, distribution or reproduction is permitted which does not comply with these terms.

Controlling factors on patterns of dissolved organic carbon and volatile fatty acids in a submarine mud volcano offshore southwestern Taiwan

Nai-Chen Chen[1,2]*, Tsanyao Frank Yang[1†], Ya-Hsuan Liou[1,3], Huei-Ting Tina Lin[4], Wei-Li Hong[2], Saulwood Lin[4], Chih-Chieh Su[3,4], Li-Hung Lin[1,3] and Pei-Ling Wang[3,4]*

[1]Department of Geoscience, National Taiwan University, Taipei, Taiwan, [2]Department of Geological Sciences, Stockholm University, Stockholm, Sweden, [3]NTU Research Center for Future Earth, National Taiwan University, Taipei, Taiwan, [4]Institute of Oceanography, National Taiwan University, Taipei, Taiwan

Dissolved organic carbon (DOC) and volatile fatty acids (VFAs) play key roles in the carbon cycling of marine sediment. Both microbially or thermally activated cracking of organic matter often produces high quantities of DOC and VFAs. To uncover the distribution pattern of DOC and VFAs in sediments under both impacts, a submarine mud volcano (SMV), was chosen to denote a model system that could witness how microbial activities react under the mixing of seawater and deeply-sourced fluids in a subsurface environment. We examined the concentration profiles of DOC and several VFAs (lactate, formate, acetate, propionate, and butyrate) in pore water, covering both sulfate reduction and methanogenesis zones, and further numerically modeled six porewater species (DOC, bromide, calcium, magnesium, ammonium, and total alkalinity) to quantify their fluxes from depth as well as the rates of *in-situ* microbial processes. Apparently, bulk DOC concentrations fluctuated with depths, probably primarily controlled by *in situ* microbial processes. Lactate was detectable in some samples, while propionate and butyrate were under detection limit. Acetate and formate concentrations were consistently and uniformly low throughout all biogeochemical zones, with a slightly increasing trend with depth at the center of the SMV, suggesting active utilization and turnover by the terminal steps of organic matter mineralization. The numerical modeling suggests that most DOC patterns were primarily influenced by *in-situ* organic matter degradation, while the impact of upward migrating fluid become more significant at center sites. The calculation of the Gibbs energy of metabolic redox reactions reveals that acetoclastic sulfate reduction yields the highest energy throughout sediment columns and may co-exist with methanogenesis below sulfate reduction zone. In contrast, acetoclastic methanogenesis yields higher energy within sulfate reduction zone than below that region, suggesting it is thermodynamically feasible to co-occur with sulfate reduction in dynamic SMV environments.

KEYWORDS

dissolved organic carbon, volatile fatty acids, submarine mud volcano, deep fluid, numerical modeling, gibbs free energy

1 Introduction

Organic matter stored in marine sediments has been estimated to be up to 7.8×10^7 Gt C (Mackenzie et al., 2004), constituting the most important organic reservoir involved in the global carbon cycle (Hedges and Keil, 1995). Despite its sources from terrestrial detritus and marine primary producers, the burial of organic matter beneath the seafloor proceeds with a series of remineralization pathways accompanied by the production and consumption of dissolved organic carbon (DOC) (Arnosti, 2011; Fenchel et al., 2012; Komada et al., 2013). The estimated global budget of marine benthic DOC fluxes is comparable to global riverine DOC (Burdige et al., 1999), and this benthic export of DOC into the deep ocean would exert profound effects on the marine DOC budget, nutrient cycling and even the structure of food web (Pohlman et al., 2010; Haas et al., 2011; Eickenbusch et al., 2019).

The proximity to terrestrial and nutrient sources renders continental margins the locus of organic matter remineralization. Previous estimates suggest that about 60%–80% of total organic carbon (TOC) pool, including DOC and particulate organic carbon (POC), is converted to dissolved inorganic carbon (DIC) and high molecular-weight organic complex through microbial respiration and fermentation (Kandasamy and Nagender Nath, 2016). Such degradation processes cascade to the stepwise production of low-molecular-weight DOC (such as amino acids and monosaccharides) and further downstream short-chain organic acids and alcohols (such as volatile fatty acids (VFAs) and methanol) (Heuer et al., 2010; Komada et al., 2013; Burdige et al., 2016; Komada et al., 2016; Zhang et al., 2019). These energetic intermediate products are ideal electron donors for different terminal electron-accepting processes. Based on the concentration profiles and incubation experiments, acetate has been identified to serve as an important substrate for manganese and iron reduction (Burdige, 1993; Chuang et al., 2021), sulfate reduction (Glombitza et al., 2015), methanogenesis (Wellsbury et al., 1997; Parkes et al., 2007; Heuer et al., 2009; Ijiri et al., 2018), or denitrification (Thauer et al., 1989; Amend and Shock, 2001; Yoon et al., 2013) in shallow marine sediments. Furthermore, a fraction of VFAs (particularly acetate) could be directly assimilated into biomass (Morono et al., 2011; Na et al., 2015), contributing to the pool of particulate organic carbon. The rapid turnover often enables the limited accumulation of these intermediate, energetic substrates in most marine sediments (e.g., micromolar range of acetate in marine porewater; Finke et al., 2007; Sørensen et al., 1981; Valdemarsen and Kristensen, 2010). Therefore, although observations regarding the variation in the concentration of these molecules bear great implications for subseafloor microbial processes, their distribution pattern remains rarely explored.

In addition to the input from the water column, thermally or microbially activated cracking of organic matter in subseafloor also leads the production of high quantities of DOC from strata with relatively low TOC content (<1 wt%; e.g., Parkes et al., 2007). Typical examples include submarine mud volcanoes (SMVs) and seeps, which represent the seafloor expression of conduits tapping deep fluid reservoirs (Egeberg and Barth, 1998; Nuzzo et al., 2008; Hung et al., 2016; Eickenbusch et al., 2019). Few studies have demonstrated that the concentrations of specific DOC compounds could range up to millimolar ranges (e.g., Egeberg and Barth, 1998; Nuzzo et al., 2008; Pohlman et al., 2010; Heuer et al., 2020). Although such high concentrations are confined in a narrow depth range, the strong contrast from background seawater concentrations (few μM or less) could have sustained a high flux exported to the overlying seawater. Recent studies indicated that DOC benthic fluxes from sediments near cold seeps and mud volcanoes in offshore southwestern Taiwan (28–1,264 μmol m^{-2} d^{-1}) are several times higher than most DOC fluxes in coastal and continental margin sediments (Hung et al., 2016). If the estimates based on observations of near a few mud volcanoes are valid across the basin, the contribution of DOC from mud volcanoes and seeps would constitute a significant proportion of marine DOC pool and affect the biogeochemical network and ecosystem in benthic environments. As the DOC pool represents a mixture of various individual compounds, it remains unclear whether the fluxes of specific substrates are comparable with the bulk DOC pattern.

This study aims to better understand the distribution pattern of DOC and VFAs for sediments in a submarine mud volcano, TY1, offshore southwestern Taiwan. The TY1 mud volcano exports fluids and gases originating from a source depth estimated to be 4–6 km below the seafloor (kmbsf) to the seawater column (Chen et al., 2020); thus, it provides ideal materials to address how DOC associated with deep fluids is cycled through various microbial processes at shallow depths. To this aim, bulk DOC and various VFAs (acetate, formate, propionate, butyrate, and lactate) were specifically targeted and discussed together with other aqueous and gas geochemistry data obtained in a previous study (Chen et al., 2020). These results were further integrated into a reactive transport modeling to quantify how microbially dissimilative and assimilative metabolisms affect the patterns of bulk DOC.

2 Materials and methods

2.1 Geological settings and sampling sites

Offshore southwestern Taiwan is at the frontal area of the accretionary wedge generated during the subduction–collision between the Luzon Arc and the Eurasian passive continental margin (e.g., Teng, 1990). The boundary separating the passive from active margins is defined by the deformation front, a northward extension of the Manila trench. The active margin is further divided by the out-of-sequence thrust into the Upper and Lower Slope domains (e.g., Lin et al., 2009; Lin et al., 2014). Through the seismic reflection profiles and remotely operated vehicle (ROV) survey, a total of 13 submarine mud volcanoes (SMVs) have been identified in the Upper Slope domain of offshore southwestern Taiwan (Figure 1A; Chen et al., 2014a; Chen et al., 2014b). Two mud volcanoes fed by one mud diapir constitute the Tsangyao Mud Volcano Group (TYMV; re-named after MV12; Chen et al., 2017), the largest SMV offshore southwestern Taiwan. One of the mud volcanoes, TY1, has a conical structure and a wide flat top with a diameter of ~500 m at a water depth of ~370 m (Figures 1B, C; Chen et al., 2014a). Two major gas plumes, one at the west and the other at the south, were detected on the crest by a multibeam echo sounder. These gas plumes reached 367 m above the seafloor (Chen et al., 2014b). TY2 is not as active as TY1; although mud diapiric structure was found under its conical bathymetry in the seismic profile, no venting was detected (Wu, 2016). A previous study shows that three major lithologic units (mud breccia, moderate mud breccia, and massive units) were recovered in sediment cores collected from TY1 (Hiruta et al., 2017). 90% of the

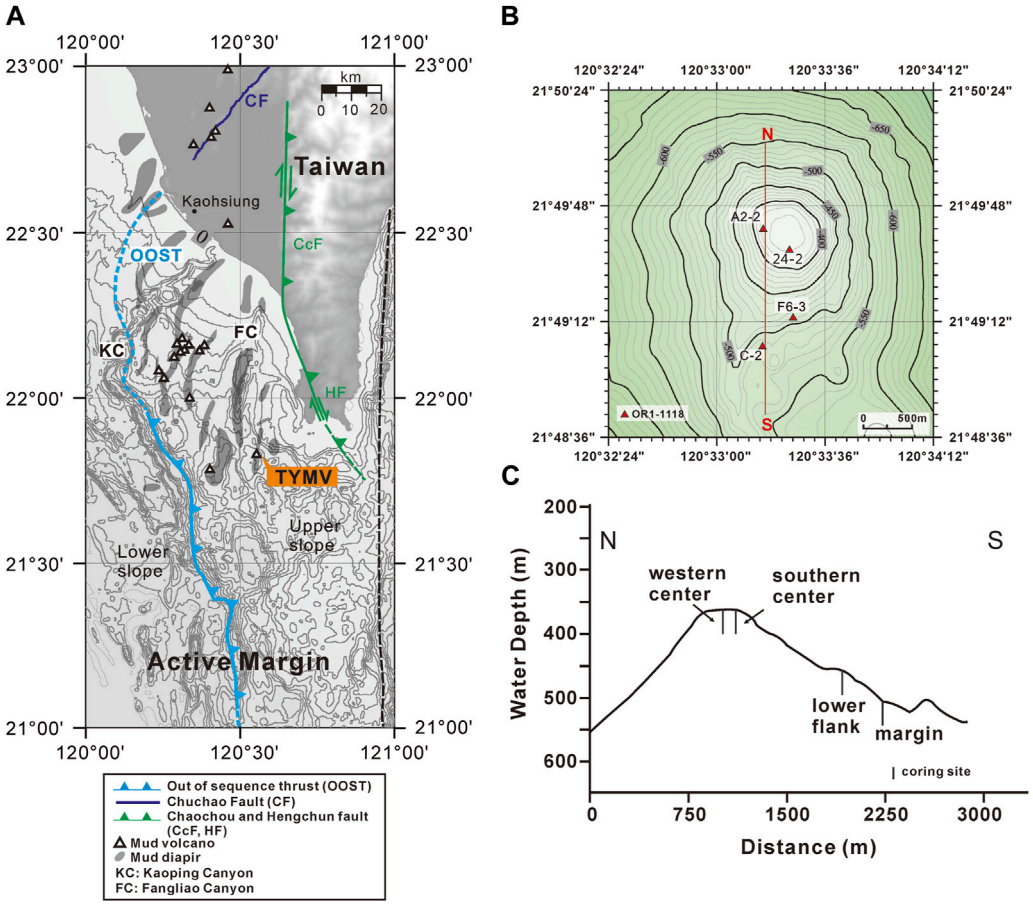

FIGURE 1
Coring sites and the tectonic structures in onshore and offshore south Taiwan. **(A)** Submarine mud volcanoes are distributed in the upper slope domain, active margin. The light blue line near the shelf edge is out of sequence thrust (OOST), while the dark blue line denotes the Chuchau fault (CF). The green line represents the Chaochou fault (CcF) and the Hengchun fault (HF). The tectonic structures are cited by Lin et al. (2009); Lin et al. (2014). The right boundary of the upper slope is defined by Lin et al. (2009). **(B, C)** "modified from Chen et al. (2020)" are views of coring sites on TY1 from above and cross-section, respectively. The map was created by the open-source GMT software (Wessel and Smith, 1998), using the NOAA public database (Amante and Eakins, 2009).

massive units is fine sand (63–212 μm), while moderate mud breccia, and mud breccia units are dominated by clay and silt. Chen et al. (2020) has shown that the deep fluid sourced from smectite dehydration has intruded in TY1, and these fluids mix with seawater percolating downward from the seabed, generating great salinity and other geochemical gradients in shallow sediments. The effect of fluid advection is swapped with the diffusive transport as the distance from the center increased (upward fluid velocity is also shown in Figure 2). The expedition on TY1 was conducted in offshore southwestern Taiwan by R/V Ocean Researcher I (Leg 1,118). Piston cores with lengths ranging from 260 to 450 cm were recovered along a transect from the center to the margin of the TY1 cone structure (Figure 1C). Sampling sites are listed in Table 1 and shown in Figures 1B, C.

2.2 Sampling and analytical methods

Pore fluid samples for aqueous geochemistry were obtained through centrifugation and subsequently collected through filtration using polypropylene rubber-free syringes and disposable 0.2-μm Supor membranes. At least 10 mL of the filtrate was split into five fractions first for the analyses of anion, cation, total alkalinity (Alk), water isotopes, and DOC as well as VFAs. Samples for DOC and VFA analyses were kept in pre-combusted 2-mL glass vials with Teflon-coated screw caps and stored at −20°C until analyses. Prior to sample collection, all glass vials were soaked in 10% HNO_3 for 3 days, rinsed with Milli-Q water, and then combusted at 550°C for 4 h. For cation samples, concentrated nitric acid (70%) was added at a volume ratio of 1:45 to preserve the valence state for elements sensitive to redox change. The data of some major ions, Alk, and water isotopes have been published by Chen et al. (2020).

The *ex-situ* pH was measured immediately on board while analyzing Alk (Supplementary Figure S1; Chen et al., 2020). Total dissolved manganese and iron concentrations were analyzed by an inductively coupled plasma optical emission spectrometry (ICP-OES). Bromide and ammonium were measured by an ion chromatography (IC, 882 Compact IC Plus; Chen et al., 2020; Hu et al., 2017). The concentrations of DOC were

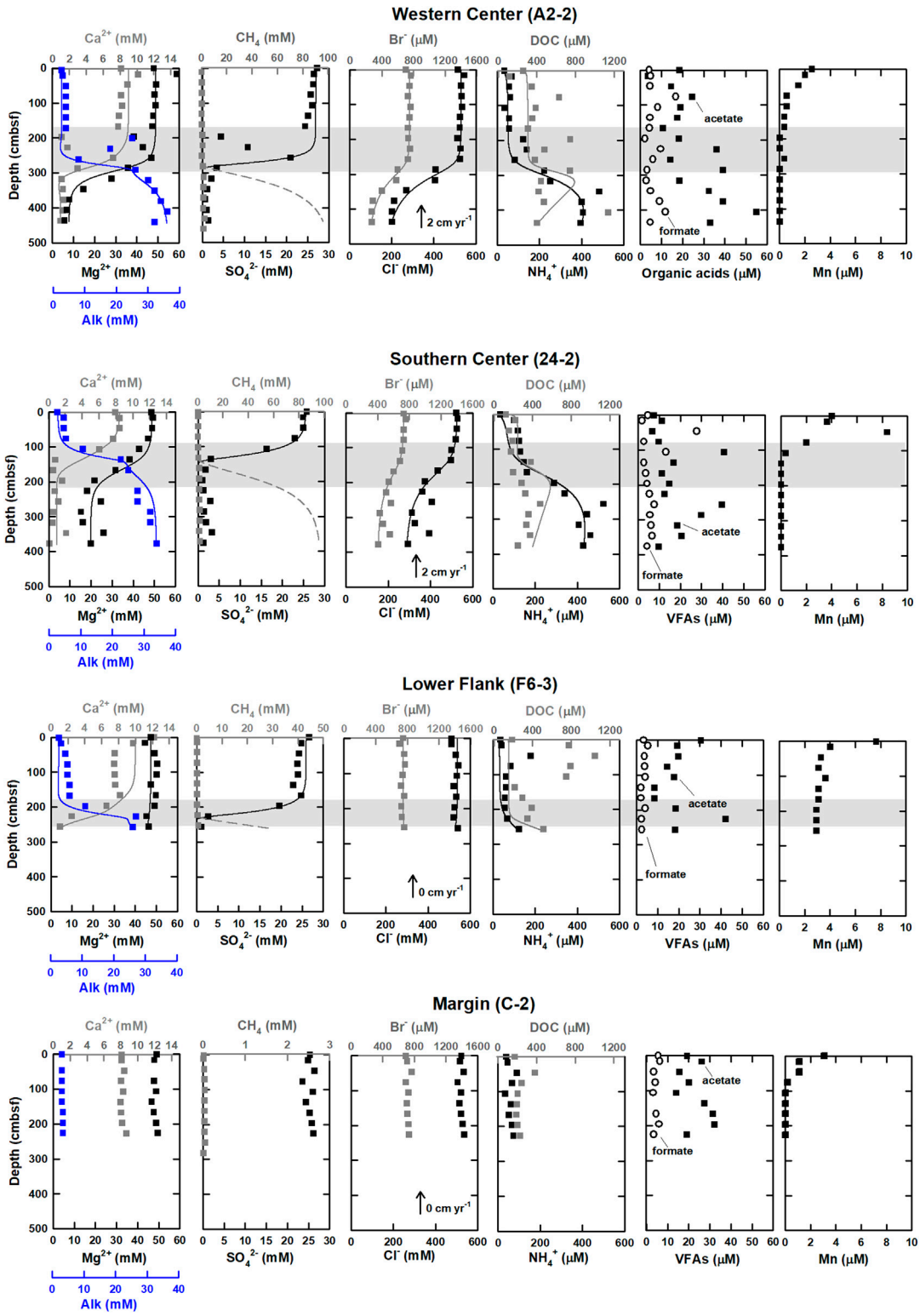

FIGURE 2
Geochemical profiles of western and southern center, lower flank, and margin sites at the submarine mud volcano, TY1. Shaded areas denote SMTZ. Measured data are shown by squares, while the solid and dashed lines represent the best fit between the model simulated profiles and measured data (after Chen et al., 2020). The data on methane, sulfate, chloride, Alk, calcium, and magnesium were cited from Chen et al. (2020).

determined by the Shimadzu-TOC-L carbon analyzer (Shimadzu Corp., Kyoto, Japan) equipped with a non-dispersive infrared detector and an auto-sampler. Samples were manually diluted by 10 to 30 folds, acidified with HCl, and purged using a helium stream prior to the injection into the analyzer. Five standards (5, 10, 15, 20, and 30 μM) were prepared from the Consensus Reference Material,

TABLE 1 Information on sites cored at a submarine mud volcano, TY1, during cruise OR1-1118.

Cruise	Site	Longitude	Latitude	Location
OR1-1118	A2-2	120° 33.48′	21° 49.63′	western center
	24-2	120° 33.28′	21° 49.66′	southern center
	F6-3	120° 33.34′	21° 49.24′	lower flank
	C-2	120° 33.27′	21° 49.07′	margin

TABLE 2 List of acronyms about reactions mentioned in the text.

Acronyms	Complete name
OSR	organoclastic sulfate reduction
ME	methanogenesis
AOM	anaerobic oxidation of methane
CP	carbonate precipitation
H_2-ME	hydrogenotrophic methanogenesis
Ac-ME	acetoclastic methanogenesis
Ac-SR	acetoclastic sulfate reduction
formate-SR	formate mediated sulfate reduction
Ac-CR	acetogenic CO_2 reduction

CRM (purchased from Hansell Lab, Miami, United States), with an uncertainty smaller than 5%. The analyses of VFAs were determined by an Agilent HPLC system, model 1,260 Infinity LC (Agilent Technologies, Santa Clara, CA, United States), equipped with a diode array detector (DAD). An ion exchange column (Agilent Hi-Plex H, 8 μm, 300 × 7.7 mm) coupled to a guard column (PL Hi-Plex H, 50 × 7.7 mm) was used to separate VFAs (targets including lactate, formate, acetate, propionate, and butyrate) at a flow rate of 0.6 mL min^{-1} of eluent 4.0 mM H_2SO_4 with a column temperature maintained at 65°C. Five standards (1, 5, 10, 25, and 50 μM) were prepared from 10 mM stocks of individual target compounds at a purity of ≥98%. Standard solutions (5 and 10 μM) were injected after every five analyses in order to monitor the drift of the retention time and signal intensity. The limit of detection (LOD) is calculated as LOD = 3.3σ/S (Borman and Elder, 2017). The σ is the standard deviation of the response derived from the calibration curve, and S is estimated from the slope of the calibration curve for the analyte. The LOD of each VFA was lower than 1.5 μM.

2.3 Numerical modeling

2.3.1 Modeling construction

To further quantify the impacts of deep fluids and heterotrophic processes on geochemical characteristics, a one-dimension reactive transport modeling, described in detail by Chen et al. (2020) and organic matter degradation simulations (Wallmann et al., 2006), was applied to generates the porewater concentration-depth profiles of Alk, calcium, magnesium, bromide, ammonium, and DOC. The simulation of VFAs is not included because VFAs are involved in many reactions but lack constraints. Since hydrogen sulfide was not measured, and thus, the modeling result of dissolved inorganic carbon (DIC = CO_2 + HCO_3^- + CO_3^{2-}) was assumed to be Alk. The model including transportation (molecular diffusion and fluid advection), bubble irrigation, and microbial reaction terms is as follows:

$$\varphi\frac{\partial C_i}{\partial t} = D_i\frac{\partial}{\partial x}\left(\frac{\varphi}{\theta^2}\cdot\frac{\partial C_i}{\partial x}\right) - \frac{\partial \varphi u C_i}{\partial x} + \varphi\cdot R_{irr} + \varphi\cdot\Sigma R_i \qquad (1)$$

where C_i is the concentration of dissolved species (i) in porewater, φ is porosity, u (m yr^{-1}) is upward fluid velocity, t (yr^{-1}) is time, x (m) is depth, D_i (m^2 yr^{-1}) is the diffusion coefficient at *in situ* temperatures (10.5°C; Boudreau, 1997; Wallmann et al., 2006), θ^2 (= 1 − ln(φ^2)) is the tortuosity used to correct the diffusion coefficients in porous media (Boudreau, 1997), R_{irr} is the term for bubble irrigation (Chuang et al., 2013), and ΣR_i defines the sum of reactions occurring in the simulated sediment column. Upward fluid velocities (u_0 with $u = \frac{u_0\cdot\varphi_0}{\varphi(x)}$) and bubble irrigation parameters ($R_{irr} = \alpha_0\cdot\frac{exp(\frac{L_{irr}-x}{\alpha_1})}{1+exp(\frac{L_{irr}-x}{\alpha_1})}\cdot(C_0 - C_i)$, where C_0 (mM) is the concentration of target solutes in the bottom water, L_{irr} (m) is the depth of the bubble irrigation layer, α_0 (yr^{-1}) is the intensity of bubble irrigation, and α_1 (m) is the parameter controlling how expeditiously this irrigation is weakened near the bottom of the irrigation zone) were obtained by fitting the model results to the observed chloride concentration profiles, which is considered to behave conservatively at the depth of sampling (Figure 2; Chen et al., 2020). R_i is a reaction term for porewater species i. Details are explained in next section.

2.3.2 Reactions

The mineralization reactions proceed with the POC degradation for the production of DOC through the following simple pathway:

$$POC \rightarrow DOC \rightarrow DIC \qquad (2)$$

where DOC plays as an intermediate product. Without constraints of carbon isotopes (e.g., Komada et al., 2013; Burdige et al., 2016), the kinetic rate law for DOC production (or POC degradation) depending on the concentration of dissolved metabolites is simplified and considered here (Wallmann et al., 2006):

$$R_{DOC} = K_G\cdot C_{org}\cdot rC\cdot\frac{K_C}{[DIC] + [CH_4] + K_C} \qquad (3)$$

where R_{DOC} is the rate of DOC production, which equals to POC degradation; K_G represents the kinetic constant of organic matter degradation (assumed to be 10^{-6} yr^{-1}; Hong et al., 2017; Middelburg, 1989; Vanneste et al., 2011); K_C denotes a Monod kinetic constant; rC is a parameter that converts carbon concentrations in unit of wt% C to mM (Burdige et al., 2016); C_{org} is the total organic carbon (TOC) content and assumed to be 0.45 wt%, considering that TOC varied between 0.3 and 0.5 wt% (Chen et al., 2020). Unlike regular marine sediments modeled by Wallmann et al. (2006), we assume the POC, originating from deep sediment columns, is relatively refractory in mud volcanoes; thus, K_G is set to be a constant instead of an age-dependent one.

POC degradation coexists with the release of bromide and ammonium and fuels downstream organoclastic sulfate reduction (OSR) as well as methanogenesis (ME) (see Table 2 for acronyms about all reactions). The reactions involved in the POC degradation (OSR and ME), anaerobic oxidation of methane (AOM), and carbonate precipitation (CP) are listed below:

OSR:

$$(CH_2O)(NH_3)_{\frac{N_s}{C_s}}(Br)_{r_{Br}} + \frac{1}{2}\cdot SO_4^{2-} + \frac{1}{C_s/N_s}H^+ \rightarrow \frac{1}{2}H_2S + HCO_3^- + \frac{1}{C_s/N_s}\cdot NH_4^+ + r_{Br}\cdot Br^- \quad (4)$$

ME:

$$(CH_2O)(NH_3)_{\frac{N_s}{C_s}}(Br)_{r_{Br}} + \frac{N_s}{4C_s}H_2O \rightarrow \left(\frac{N_s}{8C_s}+\frac{1}{2}\right)CO_2 + \left(\frac{3}{2}-\frac{N_s}{8C_s}\right)CH_4 + \frac{1}{C_s/N_s}\cdot NH_4^+ + r_{Br}\cdot Br^- \quad (5)$$

AOM:

$$CH_4 + SO_4^{2-} \rightarrow HCO_3^- + HS^- + H_2O \quad (6)$$

CP:

$$Mg^{2+} + Ca^{2+} + 2HCO_3^- \rightarrow CaMg(CO_3)_2 + 2H^+ \quad (7)$$

where C_s/N_s is the TOC/TN ratio in TY1 sediment (average = 5.58; Su et al., 2018); r_{Br} represents the Br/POC ratio in sediment offshore southwestern Taiwan (7.6 mg-Br/g-TOC; Kandasamy and Nagender Nath, 2018). More details of other rate laws and parameters can be found in Supplementary Material S1.

2.3.3 Numerical modeling scenarios

In order to observe the variation of *in-situ* processes and deep fluids (advection) under different modeling settings, three cases were considered. In case 1, all reactions were involved, but only diffusion was considered (without advection term). In case 2, diffusion and advection terms were considered (without reaction terms). In case 3, all reactions and transportation terms were considered. The influence of advection could be shown by comparing case 1 and case 3, while the impact of reactions could be revealed by comparing case 2 and case 3. Only cases 1 and 3 were considered at site F6-3 because there was no significant upward fluid flow (Chen et al., 2020). As there was no apparent geochemical variation at site C-2, no simulation was conducted.

2.4 Gibbs energy calculations

The Gibbs energy (ΔG) of the chemical reaction, governed by the concentration of reactants and products and the temperature and pressure, represents the energy obtained by microorganisms through a specific catabolic pathway. The Gibbs free energy for a suite of metabolic reactions involving acetate, formate, methane, and sulfate (Eqs 9–13) was calculated by using Eq. 8 considering that acetate and formate were focused as the representative electron donors because they are present throughout the sediment column and are two of the most common microbial fermentation products.

$$\Delta G_r = \Delta G_r^0 + RT\ln\frac{\Pi_i a_{(product)}^{\nu_i}}{\Pi_i a_{(reactant)}^{\nu_i}} \quad (8)$$

where R (0.008314 kJ mol^{-1} K^{-1}) is the universal gas constant, T (in K) is the temperature, a denotes the activities of the reaction participants (reactants and products), and ν_i is the stoichiometric coefficient of the ith reactant or product. Gibbs energy of hydrogentrophic and acetoclastic methanogenesis (Eqs 9, 10), sulfate reduction (Eqs 11, 12), and acetogenic CO_2 reduction (Eq. 13) were calculated:

Hydrogenotrophic methanogenesis (H_2-ME):

$$2H_2 + HCO_3^- + H^+ \rightarrow CH_4 + 3H_2O \quad (9)$$

Acetoclastic methanogenesis (Ac-ME):

$$CH_3COO^- + H_2O + H^+ \rightarrow CH_4 + HCO_3^- \quad (10)$$

Acetoclastic sulfate reduction (Ac-SR):

$$CH_3COO^- + SO_4^{2-} \rightarrow HS^- + 2HCO_3^- \quad (11)$$

formate mediated sulfate reduction (formate-SR):

$$4HCOO^- + SO_4^{2-} + H^+ \rightarrow HS^- + 4HCO_3^- \quad (12)$$

Acetogenic CO_2 reduction (Ac-CR):

$$2HCO_3^- + 4H_2 + H^+ \rightarrow CH_3COO^- + 4H_2O \quad (13)$$

The activities were computed by multiplying measured concentrations of the species by their activity coefficients. Activity coefficients were calculated from an extended version of the Debye-Hückel Extended equation at an ionic strength of 0.3–0.7 (Helgeson, 1969) and with chloride-derived salinity of 13–35 psu. Temperatures in sediments were calculated based on *in situ* bottom water temperature (10.5°C) and a temperature gradient of 0.39°C/m at TY1 (Wu, 2016). The *ex-situ* measured pH values ranged from 7.7 to 8.9 (Supplementary Figure S1). The density of porewater and the concentration of hydrogen were assumed to be 1.03 g/cm^3 and 2 nM, respectively. The numerical modeling results of methane concentrations were used for methanogenesis (Eqs 9, 10; Chen et al., 2020). As hydrogen sulfide was not measured, its concentration was assumed to be 1 nM and 1 mM in our calculations.

3 Results

3.1 Variation of solutes profiles across TY1 submarine mud volcano

Profiles of solute concentrations for the four sampling sites are shown in Figure 2. Bromide concentrations ranged from 0.2 to 0.8 mM and decreased with depth below SMTZ at center sites (A2-2 and 24-2), while they stayed constant at lower flank (F6-3) and margin (C-2) sites. Ammonium concentrations varied between 30 and 600 μM. Unlike the trend of bromide, ammonium concentrations increased with depths at sites A2-2 and 24-2. At sites F6-3 and C-2, ammonium concentrations were typically lower than 100 μM throughout the core except for values at 72 and 256 cmbsf. Manganese ion concentrations were lower than 10 μM and decreased with depth at all sites, while the total dissolved iron concentrations were almost below the detection limit and are not shown in the profiles.

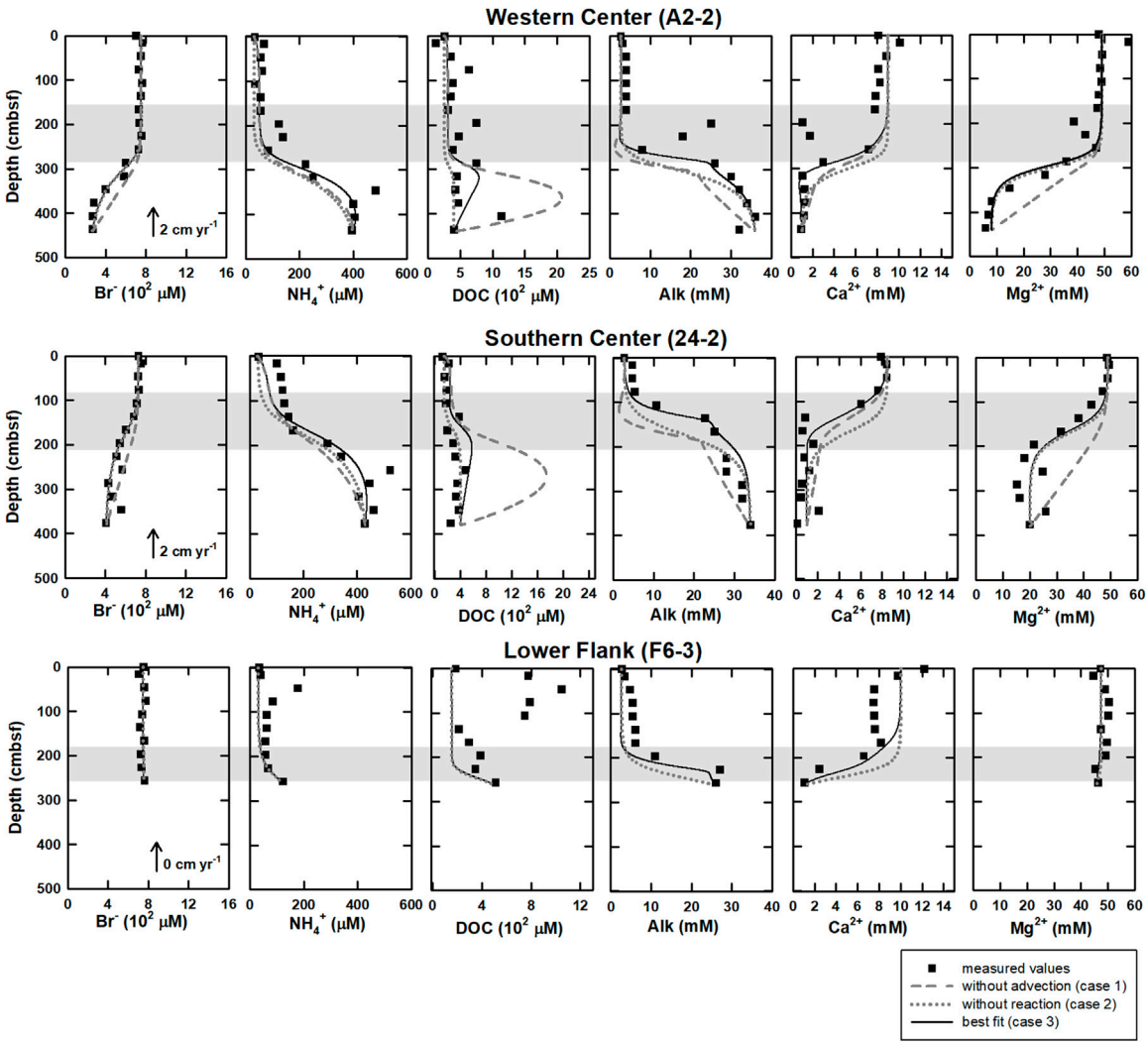

FIGURE 3
The modeling results under different scenarios of western and southern center as well as lower flank sites at the submarine mud volcano, TY1. The scenarios include 1) without advection (case 1, gray dashed lines), 2) without reactions (case 2, gray dotted lines), and 3) best fit (case 3, solid lines) of DOC, bromide, ammonium, calcium, magnesium, and Alk. At lower flank site (F6-3), because upward fluid velocity is 0 cm yr^{-1} (Chen et al., 2020), there are only case 1 and case 3. Closed circles are measured values, and shaded area denoted the SMTZ at each site.

DOC concentration ranged from 100 to 1,200 μM. At center sites (A2-2 and 24-2) with the mean value around 400 μM, and generally increased with depth, with some spiked values deviating from the increasing trend. In contrast, the lower flank (F6-3) and margin (C-2) sites were characterized by high concentrations at shallow depths and low concentrations at deeper depths. At the lower flank site (F6-3), the DOC concentration increased at above 130 cmbsf (up to 1,000 μM) and decreased to around 250 μM at the core bottom; at site C-2, the DOC concentration was almost constant (around 200 μM). Of all analyzed VFAs, formate and acetate appear to be the most abundant, with the ratios of acetate to DOC ranging from 2% to 8%, from 4% to 8%, from 2% to 4%, and from 4% to 17% at sites A2-2, 24-2, F6-3, and C-2, respectively (Figure 2; Supplementary Table S1). At center sites (A2-2 and 24-2), formate concentrations ranged from 3 to 30 μM and were higher than 13 μM at above 100 cmbsf and lower than 10 μM below that depth. However, formate concentrations were nearly constant (below 6 μM) at the lower flank and margin sites (F6-3 and C-2). Acetate concentrations were generally higher than formate and lactate and ranged from 3 to 55 μM. At site A2-2, acetate concentrations increased with depth. No noticeable trend except for two peaks at 100 and 250 cmbsf was observed at site 24-2. At site F6-3, acetate concentrations varied between 10 and 20 μM, with a peak value of 40 μM observed at 220 cmbsf. At site C-2, acetate concentrations were around 20 μM and increased to 30 μM at 130 to 200 cmbsf. Propionate and butyrate were below the detection limit for all samples, whereas lactate up to 10 μM was sporadically detected for a few samples (Supplementary Table S1).

3.2 Numerical modeling

The numerical modeling results of three cases are shown in Figure 3. For bromide, case 1 (without advection) could not fit

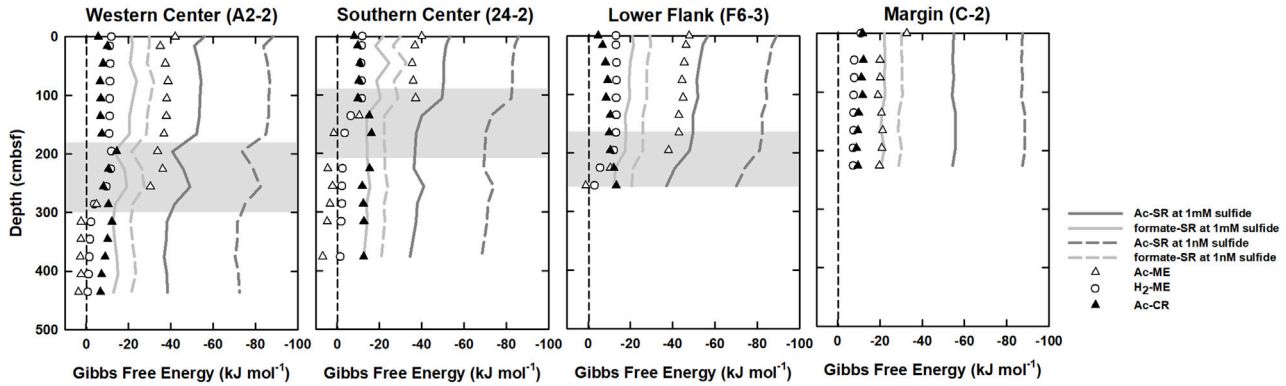

FIGURE 4
Gibbs free energies calculated for hydrogentrophic methanogenesis (H_2-ME; opened circles), acetoclastic methanogenesis (Ac-ME; opened triangles), acetoclastic sulfate reduction (Ac-SR; solid and dashed dark gray line), formate oxidized sulfate reduction (formate-SR; solid and dashed light gray line), and acetogenesis (Ac-CR; black filled triangles). Shaded areas denote SMTZ.

well with measured data, while case 2 (without reactions) and case 3 (transport and all reactions) could match. For ammonium at center sites, modeling results in all cases followed the trend of measured data, while the results of case 3 fit the best. For DOC at center sites, modeling results in all cases were lower than measured data above SMTZ at site A2-2 while they followed the trend of measured data at site 24-2. Below SMTZ, case 1 was much higher than measured data, while case 2 could fit well at site 24–2 but not site A2-2. Compared to case 1, both case 2 and case 3 were closer to measured data at center sites. For ammonium and DOC at site F6-3, all modeling results were lower than the data above SMTZ. For calcium, neither case 1 nor case 2 could fit measured data; although case 3 was closer to measured data than the other two cases, part of the data above 2.86 mbsf could not be fitted well. For magnesium, only case 1 could not match measured data. For Alk, the result of case 1 was much lower than measured data. Although results of case 2 could fit profiles of bottom and above SMTZ at center sites, the results were still lower than measured data at SMTZ. Only case 3 could fit the Alk profile better. To sum, by considering all reactions and transportations (case 3), the modeling results matched the observations for most ions and molecules.

3.3 Gibbs energies of formate and acetate in sulfate reduction, methanogenesis, and acetogenesis

Gibbs free energies calculated for five microbial processes—H_2-ME, Ac-ME, Ac-SR, formate-SR, and Ac-CR are shown in Figure 4. The energy yields of Ac-SR remained at constant above SMTZ at all sites but decreased below SMTZ. The highest yields (most negative ΔG values) of Ac-SR were obtained for samples above SMTZ (1.66–2.86 mbsf) with ΔG values around −50 and −90 kJ (mol acetate)$^{-1}$ under 1 mM and 1 nM of hydrogen sulfide, respectively. The lowest energy yields (less negative ΔG values) were found at below SMTZ and around −38 kJ and −70 kJ (mol acetate)$^{-1}$ under 1 mM and 1 nM of hydrogen sulfide, respectively. Similar to the energy yields trend of Ac-SR, the energy yields of formate oxidized sulfate reduction (formate-SR) were in the range of −15 and −30 kJ (mol formate)$^{-1}$ and were higher above SMTZ and slightly decreased as sulfate decreased.

The ΔG values of Ac-ME were around −5 to −50 kJ (mol CH_4)$^{-1}$ above the bottom SMTZ and increased rapidly to even positive values (around +3 (mol CH_4)$^{-1}$) below the SMTZ at all sites. Like Ac-ME, the ΔG values of H_2-ME were around −10 to −12 kJ (mol CH_4)$^{-1}$ above the SMTZ and increased to −1.0 kJ (mol CH_4)$^{-1}$ below the SMTZ at all sites. Below SMTZ, energy yields of methanogenesis decreased with depth due to higher DIC and methane concentrations beneath sulfate reduction zone. By contrast, the energy yields of Ac-CR were constantly low and around −10 kJ to −15 kJ (mol acetate)$^{-1}$. Its energy yield was similar to H_2-ME above SMTZ and higher than all methanogenesis below SMTZ.

4 Discussion

4.1 Impact of external fluid input and microbial degradation on DOC and VFAs patterns

The mud volcano represents the seafloor expression for fracture-channeled fluid flow from subseafloor and impacts the near seafloor sedimentary biogeochemistry. Chen et al. (2020) observed that chloride-depleted deep fluids rich in thermogenic methane originating from a depth of 3–5 kmbsf migrated upward at the crater center of the TY1 mud volcano. Furthermore, based on the evidence that water is more ^{18}O-enriched and ^{2}H- at western center site (A2-2), stronger deep fluid influence at western center site was inferred as compared to southern center site (24-2; Figure 2).

The fluctuations of the DOC and VFAs concentrations in the sediment porewater are generally influenced by the degrees of POC degradation and external fluid input. In this study, Pearson's correlation is used to address these two factors based on the fact that chloride serves as a conservative tracer to track fluid transport whereas bromide and ammonium are indirectly linked to POC degradation (Table 3). Similar to chloride, bromide concentrations

TABLE 3 Correlation with chloride, acetate, and DOC.

Site	Depth interval	Chloride	Bromide	Ammonia	Alk	DOC	Acetate	Formate
correlation with chloride								
A2-2	below SMTZ (2.3 mbsf)		1.00	− 0.92	− 0.87	− 0.30	− 0.74	− 0.53
24-2	below SMTZ (1.6 mbsf)		0.99	− 0.39	− 0.96	0.66	0.13	0.59
correlation with acetate								
A2-2	above SMTZ	− 0.29	− 0.09	0.51	0.47	0.57		0.53
	below SMTZ	− 0.74	− 0.73	0.63	0.70	0.80		0.66
24-2	above SMTZ	− 0.15	− 0.05	0.28	0.19	0.12		0.08
	below SMTZ	0.13	0.09	0.68	− 0.02	0.89		0.80
F6-3	at all depth	− 0.41	− 0.12	− 0.07	0.49	− 0.12		0.02
C-2	at all depth	− 0.17	− 0.30	− 0.04	0.61	− 0.47		0.68
correlation with DOC								
A2-2	above SMTZ	− 0.44	− 0.19	0.55	0.71		0.57	0.33
	below SMTZ	− 0.30	− 0.29	0.17	0.37		0.80	0.61
24-2	above SMTZ	− 0.18	− 0.24	0.52	0.64		0.12	− 0.38
	below SMTZ	0.66	0.59	0.69	− 0.69		0.92	0.94
F6-3	at all depth	0.35	0.19	0.61	− 0.23		− 0.12	0.61
C-2	at all depth	0.31	0.74	0.77	− 0.26		− 0.47	− 0.48

at depths shallower than SMTZ at site A2-2 were invariant. At and below SMTZ (2.3 mbsf), bromide was positively correlated with chloride at center sites (r is around +1.0). Although bromide has been considered to be released with the degradation of organic matter (e.g., Wallmann et al., 2006), the highly positive correlation with chloride suggests that bromide distribution is mainly controlled by a mixture of seawater and bromide-depleted deep fluid. In contrast, for sites F6-3 and C-2 distributed on the lower flank and margin of the TY1, respectively, bromide concentrations were invariant with depths, suggesting a limited impact of advective transport or biological activities. Same as bromide, ammonium and bicarbonate are also considered to be derived from the POC degradation, their concentration profiles suggest the *in-situ* POC degradation and the net accumulation of the reaction products (Figure 2), a pattern typically observed for marine sediments. However, over our studied regions, concentrations of ammonium and Alk generally increased with depth and were negatively correlated with chloride at different degrees, suggesting patterns are potentially influenced by deep fluids.

The correlation between chloride and DOC/VFAs also varied site by site while the DOC concentrations were positively correlated with the ammonium concentrations at most depth intervals and sites ($r > 0.5$; except for below SMTZ at site A2-2; Table 3), implying the potential influence of *in-situ* processes. Besides, the patterns of DOC and VFAs indeed varied considerably from site to site. At center sites (A2-2 and 24-2), DOC concentrations generally increased with depth with some spiked values deviating from the increasing trend. For comparison, the lower flank and margin sites (F6-3 and C-2) were generally characterized by high DOC concentrations at shallow depths and low concentrations at depth, suggesting DOC sourced from deep fluids is not significant.

Of all investigated VFAs, acetate and formate appear to be more abundant and prevalent in all cores. Although their concentrations ranged up to around 60 μM, they either fluctuated greatly or remained at a low level along depth. Acetate concentrations were positively correlated with ammonium and DOC at center sites while they were high in the low chloride zone (i.e., negatively correlated with chloride) below SMTZ at site A2-2, suggesting acetate sourced from deep fluid (probably from thermal degradation) and produced via microbial processes at subsurface at site A2-2 where the strongest advective flow was observed. No significant correlation between acetate and ammonium or DOC was observed for the lower flank sites ($|r| < 0.2$). Formate was correlated better with DOC than acetate. All these lines of evidence suggest that acetate and formate metabolisms were linked with organic degradation, and that formate is perhaps more labile than acetate and rapidly turned over between different metabolisms. Acetate and formate are both competitive substrates for terminal electron-accepting processes (e.g., Hoehler et al., 1998). Culture tests have shown that metal reduction, sulfate reduction, and methanogenesis compete for these two potential substrates and hydrogen gas for metabolic energy (e.g., Oremland and Polcin, 1982). Because they are primarily produced from the fermentation of complex organic matter, their abundances in natural environments are regulated at a certain low level to fulfill the efficient energy transfer between producing and consuming metabolisms (Orcutt et al., 2013; Glombitza et al., 2015; Beulig et al., 2018). Exceptions occur particularly for petroleum or natural gas reservoirs where acetate

TABLE 4 Microbial activity and DOC flux derived from reactive transport simulations. Depth-integrated consumption and production rates of DOC, bromide, and ammonium. The unit of rates and fluxes is mmol C m^{-2} yr^{-1}, but for rates and fluxes associated with ammonium and bromide, the units are mmol N m^{-2} yr^{-1} and mmol Br m^{-2} yr^{-1}, respectively.

	Site A2-2	Site 24-2	Site F6-3
Depth-integrated rate			
Above SMTZ			
DOC consumption			
OSR	29.4	12.0	0.9
ME	0.6	0.3	0.0
DOC production	67.1	24.6	1.9[a]
Ammonium production	12.0	4.4	0.1
Below SMTZ			
DOC consumption			
OSR	3.7	1.1	0.1
ME	6.7	3.7	0.1
DOC production	20.9	9.6	0.4
Ammonium production	3.8	1.7	0.3
Bromide production	0.7	0.3	0.0
Flux from depth			
DOC	4.3	4.7	−0.6[b]
Bromide	3.2	4.2	−0.1[b]
Ammonium	4.3	4.4	−0.9[b]
Benthic DOC flux	1.8	0.5	−0.0[b]

[a]The DOC, production rate could be under estimated because the simulation result could not fit the profile of DOC, at the interval of 10–100 cmbsf (Figure 3).
[b]The minus symbol indicates the downward direction.

and formate are produced by thermo-cracking, adding to those produced from biodegradation could amount up to a scale of mM (Egeberg and Barth, 1998). The scenario is complicated by the fact that acetate could be also produced by acetogenesis from hydrogen and a fraction of these two VFAs could be assimilated into cell biomass through acetyl-CoA or formate dehydrogenase (Jansen et al., 1984; Teece et al., 1999). The complex reaction network and the contribution of individual pathways or community members in SMV environments remain largely unraveled. Collectively, our correlation coefficients suggest that the VFAs and DOC in the porewater of our study sites were mostly related to the *in-situ* POC degradation and cycling, but their increase could be also contributed by the chloride-depleted deep fluid, which may carry thermal degradation VFAs and DOC, at the sites centered around TY1 mud volcano.

4.2 Numerical modeling evaluation

4.2.1 Quantifying microbial POC degradation rates and deep fluid inputs

The numerical modeling is constructed to quantify the effect of *in-situ* POC degradation and deep fluids on the pattern of bulk DOC. Our modeling results show that the model of case 3 can fit the measured data better than that of the other two cases (Figure 3). Further integration of rate over depth demonstrated that the whole depth-integrated rates of DOC accumulation were 17–47.6 mmol C m^{-2} yr^{-1} at center sites. This range is ten times higher than DOC flux from depth (4–5 mmol C m^{-2} yr^{-1}), suggesting that *in-situ* microbial processes dominated over fluid transport in DOC cycling and that the *in-situ* POC degradation is vital to supply DOC for terminal electron accepting processes. However, the DOC flux of deep fluids become relatively significant with depth. Its influence can be revealed by comparing the model results for the above and below the SMTZ (Table 4). The DOC accumulation rate below SMTZ (deducting the total DOC consumption of OSR and ME) is close to 10 mmol C m^{-2} yr^{-1} while DOC flux from depth is around 4 mmol C m^{-2} yr^{-1} at site A2-2, and those two are almost the same below SMTZ at site 24-2 (around 4.8 mmol C m^{-2} yr^{-1}), suggesting impact of deep fluids could not be ignored, especially below SMTZ. Additionally, the case 2 modeling derived profiles (without reactions) at center sites fit better to the DOC measured data when compared to case 1 (without advection; Figure 3), suggesting deep fluids that may carry thermally degraded DOC potentially controls the profiles. Although depth-integrated rates suggest lower impact of *in-situ* POC degradation at site F6-3 (Table 4), all of our modeling results could not fit DOC profile

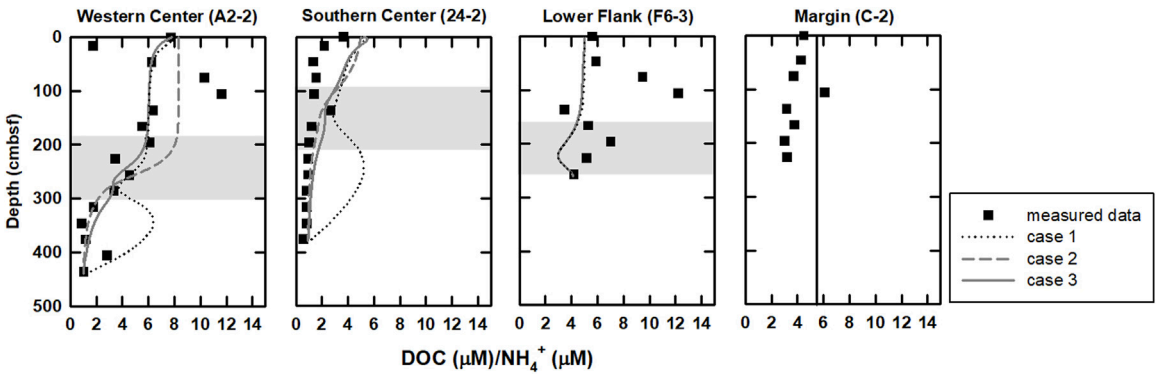

FIGURE 5
Profiles of DOC/NH_4^+ ratios for all sites. In general, this ratio is relatively high above the SMTZ and decreases below the SMTZ. DOC/NH_4^+ ratios derived from modeling results of case 3 (curved lines) are also plotted for comparison. Profiles are relatively invariant at site C-2 (Figure 2), indicating low microbial rates and potentially sharing DOC/NH_4^+ ratios similar to the source characteristics, and thus, C_s/N_s ratio in our study area is plotted for comparison (black solid line; Su et al., 2018). Shaded areas denote SMTZ.

well at site F6-3 and, therefore, underestimate the influence from *in-situ* processes (Figure 2). Similar to DOC, the patterns of ammonium are mainly controlled by *in-situ* processes, but the influence of deep fluids are obvious at center sites (Table 4). The ammonium production rate above SMTZ is higher than flux from depth, while its production below SMTZ is lower than deep flux, suggesting that deep fluids primarily control the ammonium patterns below SMTZ.

The small discrepancies between the modeled and measured DOC profiles could be further exploited to discuss the quality of organic matter in the sediment and the porewater at site F6-3. Because of low POC content (0.5 wt%; Su et al., 2018), a kinetic constant of POC degradation was assumed to be resemble that for recalcitrant POC (10^{-6} yr^{-1}; Middelburg, 1989), making it difficult to fit the real data above SMTZ well. In addition, profiles of modeled major ions are partly controlled by bubble irrigation above SMTZ (Chuang et al., 2013; see modeling construction in Supplementary Material S1), which may enhance the seawater dilution process. And thus, the deviation of the modeled DOC above SMTZ likely suggests a more labile POC/DOC pool with higher reactivity than we expected.

DOC/NH_4^+ ratios could provide additional insights of POC and DOC degradation. According to rate laws of POC degradation and ammonium production in Wallmann et al. (2006), the degradative products exempted from further exploitation postdating formation would share DOC/NH_4^+ ratios similar to the source characteristics (C_s/N_s). If DOC/NH_4^+ ratios are lower than C_s/N_s and without influence of deep fluids, then microbial consumption of DOC could be more obvious by considering abiotic or microbial ammonium consumption (Schrum et al., 2009; Alshameri et al., 2018). To examine additional DOC degradation, measured DOC/NH_4^+ ratios and those derived from modeling results based on three cases and C_s/N_s ratio are plotted for comparison (Figure 5). At the margin site C-2 (no external deep fluid input), the porewater DOC/NH_4^+ ratios were lower than the C_s/N_s ratio (value of 5.58), suggesting DOC consumption. Although the decline profile of manganese (by dropping only 3 μM) could indicate POC degradation at site C-2, the contribution of manganese reduction to POC degradation should be low for the invariant sulfate profile (Figure 2). Unlike site C-2, measured DOC/NH_4^+ ratios at site F6-3 (fluid velocity = 0 cm yr^{-1}) are higher than the C_s/N_s ratios and the DOC/NH_4^+ ratios derived from modeling results of case 3 (Figure 5), suggesting higher DOC accumulation or higher ammonium adsorption. The latter mechanism could be likely discarded considering that the modeling ratios are still insufficient to match the observed ones even assuming a much higher percentage of ammonium removal (20%) by adsorption than used in previous studies (e.g., Boatman and Murray, 1982; Wallmann et al., 2006). The DOC/NH_4^+ ratios derived from modeling at site 24-2 above the bottom of SMTZ also exceeded the observed ratios. Such a difference suggests an additional DOC degradation which was not considered in our modeling. However, DOC/NH_4^+ ratio may not be used alone to further infer additional POC/DOC degradation in areas where the influence of deep fluids is relatively pronounced and accounts for the production of both species. For example, the ratios of measured data and modeling results are similar at site A2-2 and the zone below SMTZ of site 24-2 where influence of deep fluid is significant (Figure 5; Table 4).

Bromide production could be attributed to POC degradation (Borowski, 2004; Wallmann et al., 2006; Wei et al., 2008); however, comparisons between cases 2 and 3 suggest that bromide is mainly controlled by advection (Figure 3). Although the molar Br/C ratio used in our model (Br/TOC=7.6 × 10^{-3}; Kandasamy et al., 2018) is not only the highest value in offshore southwestern Taiwan but also higher than the organic-rich area (Br/TOC=2–7 × 10^{-3}; Sea of Okhotsk; Wallmann et al., 2006), the depth-integrated bromide production rate (0.3–0.7 mmol m^{-2} yr^{-1}) is still lower than the bromide flux from depth (2.7–4.3 mmol m^{-2} yr^{-1}; Table 4), suggesting that bromide in porewater was primarily influenced by deep fluids, a pattern consistent with high correlations of bromide and chloride.

DIC could be either produced by POC degradation, AOM, or consumed by carbonate precipitation which is also influenced by the transport of divalent ions (Eqs 4–7). The modeling indicated that the deep DIC fluxes at center sites (ca. 350 C mmol m^{-2} yr^{-1}; Supplementary Table S2) are higher than the consumption rate of calcium and magnesium due to carbonate precipitation (5.0–9.0 C mmol m^{-2} yr^{-1}) and POC degradation (17–40 C mmol m^{-2} yr^{-1}) regardless of AOM production (700–850 C mmol m^{-2} yr^{-1}) at SMTZ

(Supplementary Table S2; Chen et al., 2020). The results suggest the dominance of fluid processes, such as advection and diffusion, over others in controlling the profiles of Alk, calcium and magnesium. Overall, the degradation of POC to produce metabolites and the advection of deep fluids explain most of the observations.

4.2.2 Benthic DOC flux at TY1

The venting of SMV transport not only thermogenic methane but also DOC into the ocean (Hung et al., 2016; Brogi et al., 2019; Chen et al., 2020; Amaral et al., 2021). Our simulations shows that the benthic DOC flux is in the range of 0.04–3.33 mmol C m^{-2} yr^{-1} (Table 4), which is much lower than that in the previous study (57–90 mmol C m^{-2} yr^{-1}; Hung et al., 2016). However, as we mentioned before, bubble irrigation is applied in our modeling construction, which could also act as a DOC sink because it dilutes sediment porewater DOC concentrations with low DOC seawater; namely, accumulated DOC has been transported to seawater through bubble irrigation. Under this scenario, the total accumulation of DOC in porewater transported to seawater is around 47.6 mmol C m^{-2} yr^{-1} (by deducting consumption of OSR and ME from DOC production; Table 4), which is close to the previous study.

4.3 Energy limitation

The depth-integrated total DOC production rate is in the range of 34–88 mmol m^{-2} yr^{-1} with approximate half of the flux attributed to the consumption mediated by OSR and ME. The simulation results indicate that OSR is dominated above SMTZ while ME is the major process consuming DOC below SMTZ at center sites (Table 4). Although OSR is limited below SMTZ, the simulation results still suggest that OSR may occur in this zone (Table 4). This interpretation could be supported by the calculation of Gibbs free energy at center sites (Figure 4), which shows the energy yields of Ac-SR (at 1 mM sulfide) are in the range of −35 to −40 kJ (mol acetate)$^{-1}$ below SMTZ. The energetic requirement of sulfate reduction was suggested to be between −33.1 and −42.8 kJ mol^{-1} in the culture experiments with *Desulfobacter hydrogenophilus* (DSM3380) consuming acetate and sulfate (Jin and Bethke, 2009). By using incubation experiments with ^{35}S-labeled sulfate, Glombitza et al. (2015) suggests that the minimum energy requirement of Ac-SR could be around −30 kJ (mol acetate)$^{-1}$ (or (mol sulfate) $^{-1}$). Based on assumptions of energy cost of ATP from ADP, Glombitza et al., 2019 suggest that −20 kJ (mol acetate)$^{-1}$ should be sufficient for sulfate reduction. While the co-existence of sulfate reducers and methanogens below SMTZ has been found in several areas (Leloup et al., 2007; Treude et al., 2014; Orsi et al., 2016; Chuang et al., 2021), and sulfate reducers are present below SMTZ in a terrestrial mud volcano (Cheng et al., 2012), we infer that Ac-SR might proceed at the energetic limit in the sediment below SMTZ at center sites.

The simulation results also suggest that ME may occur above SMTZ (Table 4). ΔG of Ac-ME at above SMTZ is in the range of −35 to −50 kJ (mol CH_4) $^{-1}$. This range is higher than that of H_2-ME and suggest that Ac-ME could co-exist with sulfate reduction. Co-occurrence of Ac-SR and Ac-ME has been observed at ODP site 1,226 (Wang et al., 2008). Their modeling derived reaction rates and thermodynamic calculations (ΔG) of Ac-SR and Ac-ME suggest that these processes can co-occur because both ΔG are exergonic throughout sediment core column and are close to the values in culturing experiments (Wang et al., 2008; Wang et al., 2010; Sela-Adler et al., 2017). Furthermore, Cheng et al. (2012) has shown the existence of Ac-ME above SMTZ from incubation results of mud volcano sediments. Although the potential energy limitation of H_2-ME was found to be at an even lower energy yield of −10 kJ (mol CH_4)$^{-1}$ (Hoehler et al., 2001), which is similar to what we derived at above SMTZ (ΔG = −10 to −12 kJ (mol CH_4) $^{-1}$; Figure 4), H_2-ME would be easily inhibited by sulfate-reducing bacteria because of competition for hydrogen (e.g., Abram and Nedwell, 1978), suggesting that H_2-ME is less likely to occur at above SMTZ. Our thermodynamic calculations show Ac-ME below SMTZ is endergonic (ΔG > 0 kJ) while H_2-ME is around −2 kJ (mol CH_4) $^{-1}$, which is more positive than the potential limit of ME. This could be because of high methane concentration below SMTZ (at center sites: 96 mM; at lower flank site: 40 mM; Chen et al., 2020), which could strongly shift the equilibrium towards the reactant side, making ME, especially Ac-ME, energetically unfavorable.

Previous studies have shown that the existence of Ac-CR in subsurface sediment by incubation and carbon isotopes approaches (Liu and Suflita, 1993; Heuer et al., 2009). In our study, Ac-CR is exergonic throughout sediment column and even higher than methanogenesis below SMTZ (Figure 4). Although the correlation between acetate and chloride is higher below SMTZ (Table 3), suggesting an obvious input from deep fluids, the depth-integrated rate of DOC production below SMTZ (after deducting consumption from OSR and ME) is comparable to the DOC flux from depth especially at center sites (Figure 2; Table 4), suggesting that higher acetate is resulted from both deep fluids and Ac-CR.

5 Conclusion

The *in-situ* processes and intrusion of deep fluids that may transport thermally activated cracking of VFAs and DOC around the mud volcano affect the geochemical conditions of the deep subsurface. Correlation between different controlling factors reveals that *in-situ* POC degradation is the main controlling mechanism for DOC, acetate, and formate patterns. At sites centered around the mud volcano, the effect of deep fluids on DOC and acetate concentrations becomes more significant, which is also the case for ammonium, bromine and Alk distributions. Numerical modeling for six key metabolic reactive parameters (DOC, bromide, calcium, magnesium, ammonium, and Alk) in the porewater further shows that these dissolved materials are controlled by deep fluids. Although the DOC and ammonium produced by *in-situ* POC degradation is dominant, the contribution from deep fluids becomes more significant with depth, especially below the SMTZ at center sites. The benthic DOC flux resulting from bubble irrigation and deep fluids is around 48 mmol C m^{-2} yr^{-1}, which was much greater than typical diffusional DOC flux into the deep ocean. Both the modeling results and the calculations of the Gibbs free energy of metabolic redox reactions suggest that acetoclastic sulfate reduction yields the highest energy and may co-exist with methanogenesis

below the SMTZ. Acetoclastic methanogenesis yields higher energy and can co-occur with sulfate reduction above the SMTZ; indeed, the observed elevations in acetate concentration could be a result of input from both deep fluids and acetogenesis. Our research quantified the impacts between microbial mediated reactions and the active transport by deep fluids, demonstrating how modeling and observations can work together to unravel an extremely dynamic subsurface environment.

Data availability statement

The original contributions presented in the study are included in the article/Supplementary Material, further inquiries can be directed to the corresponding authors.

Author contributions

N-CC, TY, P-LW, H-TL, and L-HL initiated the study and designed sampling and analyses. N-CC and SL collected samples. N-CC, P-LW, Y-HL, H-TL, and C-CS conducted analyses. N-CC, W-LH, P-LW, and L-HL conducted numerical modeling. N-CC, P-LW, L-HL, and H-TL wrote the paper. All authors contributed to the article and approved the submitted version.

Funding

This study is supported by the Taiwanese National Science and Technology Council, Ministry of Education as well as Stockholm University.

Acknowledgments

We would like to thank the captain and crew of the R/V Ocean Research Vessels I, and all assistants and students on board for their help in sample collections, especially Y-J. Chen, H-W. Chen, T-H. Yang, and Y-H. Chang. Y-J. Chen and H-W. Chen are specially acknowledged for invaluable technical and analytical support. We are also grateful to the suggestions for the structure and distribution of SMVs by Dr. S-C. Chen.

Conflict of interest

The authors declare that the research was conducted in the absence of any commercial or financial relationships that could be construed as a potential conflict of interest.

Publisher's note

All claims expressed in this article are solely those of the authors and do not necessarily represent those of their affiliated organizations, or those of the publisher, the editors and the reviewers. Any product that may be evaluated in this article, or claim that may be made by its manufacturer, is not guaranteed or endorsed by the publisher.

Supplementary material

The Supplementary Material for this article can be found online at: https://www.frontiersin.org/articles/10.3389/feart.2023.1210088/full#supplementary-material

References

Abram, J. W., and Nedwell, D. B. (1978). Inhibition of methanogenesis by sulphate reducing bacteria competing for transferred hydrogen. *Archives Microbiol.* 117, 89–92. doi:10.1007/bf00689356

Alshameri, A., He, H., Zhu, J., Xi, Y., Zhu, R., Ma, L., et al. (2018). Adsorption of ammonium by different natural clay minerals: Characterization, kinetics and adsorption isotherms. *Appl. Clay Sci.* 159, 83–93. doi:10.1016/j.clay.2017.11.007

Amante, C., and Eakins, B. W. (2009). *ETOPO1 arc-minute global relief model: Procedures, data sources and analysis.*

Amaral, V., Romera-Castillo, C., and Forja, J. (2021). Submarine mud volcanoes as a source of chromophoric dissolved organic matter to the deep waters of the Gulf of Cádiz. *Sci. Rep.* 11 (1), 3200–3212. doi:10.1038/s41598-021-82632-3

Amend, J. P., and Shock, E. L. (2001). Energetics of overall metabolic reactions of thermophilic and hyperthermophilic Archaea and Bacteria. *FEMS Microbiol. Rev.* 25 (2), 175–243. doi:10.1111/j.1574-6976.2001.tb00576.x

Arnosti, C. (2011). Microbial extracellular enzymes and the marine carbon cycle. *Annu. Rev. Mar. Sci.* 3, 401–425. doi:10.1146/annurev-marine-120709-142731

Beulig, F., Røy, H., Glombitza, C., and Jørgensen, B. (2018). Control on rate and pathway of anaerobic organic carbon degradation in the seabed. *Proc. Natl. Acad. Sci.* 115 (2), 367–372. doi:10.1073/pnas.1715789115

Boatman, C. D., and Murray, J. W. (1982). Modeling exchangeable NH4+ adsorption in marine sediments: Process and controls of adsorption 1, 2. *Limnol. Oceanogr.* 27 (1), 99–110. doi:10.4319/lo.1982.27.1.0099

Borman, P., and Elder, D. (2017). Q2(R1) validation of analytical procedures. *In ICH Quality Guidelines*, 127–166. doi:10.1002/9781118971147.ch5

Borowski, W. S. (2004). A review of methane and gas hydrates in the dynamic, stratified system of the Blake Ridge region, offshore southeastern North America. *Chem. Geol.* 205 (3-4), 311–346. doi:10.1016/j.chemgeo.2003.12.022

Boudreau, B. P. (1997). *Diagenetic Models and Their Implementation* 505, 132. Berlin: Springer

Brogi, S. R., Kim, J.-H., Ryu, J.-S., Jin, Y. K., Lee, Y. K., and Hur, J. (2019). Exploring sediment porewater dissolved organic matter (DOM) in a mud volcano: Clues of a thermogenic DOM source from fluorescence spectroscopy. *Mar. Chem.* 211, 15–24. doi:10.1016/j.marchem.2019.03.009

Burdige, D. J., Berelson, W. M., Coale, K. H., McManus, J., and Johnson, K. S. (1999). Fluxes of dissolved organic carbon from California continental margin sediments. *Geochimica Cosmochimica Acta* 63 (10), 1507–1515. doi:10.1016/s0016-7037(99)00066-6

Burdige, D. J., Komada, T., Magen, C., and Chanton, J. P. (2016). Carbon cycling in Santa Barbara Basin Sediments: A modeling study. *J. Mar. Res.* 74 (3), 133–159. doi:10.1357/002224016819594818

Burdige, D. J. (1993). The biogeochemistry of manganese and iron reduction in marine sediments. *Earth-Science Rev.* 35 (3), 249–284. doi:10.1016/0012-8252(93)90040-e

Chen, N.-C., Yang, T. F., Hong, W.-L., Yu, T.-L., Lin, I.-T., Wang, P.-L., et al. (2020). Discharge of deeply rooted fluids from submarine mud volcanism in the Taiwan accretionary prism. *Sci. Rep.* 10 (1), 381–392. doi:10.1038/s41598-019-57250-9

Chen, N. C., Yang, T. F., Hong, W. L., Chen, H. W., Chen, H. C., Hu, C. Y., et al. (2017). Production, consumption, and migration of methane in accretionary prism of southwestern Taiwan. *Geochem. Geophys. Geosystems* 18, 2970–2989. doi:10.1002/2017gc006798

Chen, S.-C., Hsu, S.-K., Wang, Y., Chung, S.-H., Chen, P.-C., Tsai, C.-H., et al. (2014a). Distribution and characters of the mud diapirs and mud volcanoes off southwest Taiwan. *J. Asian Earth Sci.* 92, 201–214. doi:10.1016/j.jseaes.2013.10.009

Chen, S.-C., Hsu, S. K., Wang, Y., Chung, S. H., Chen, P. C., Tsai, C. H., et al. (2014b). Distribution and characters of the mud diapirs and mud volcanoes off southwest Taiwan. *J. Asian Earth Sci.* 92, 201–214. doi:10.1016/j.jseaes.2013.10.009

Cheng, T.-W., Chang, Y.-H., Tang, S.-L., Tseng, C.-H., Chiang, P.-W., Chang, K.-T., et al. (2012). Metabolic stratification driven by surface and subsurface interactions in a terrestrial mud volcano. *ISME J.* 6 (12), 2280–2290. doi:10.1038/ismej.2012.61

Chuang, P.-C., Dale, A. W., Heuer, V. B., Hinrichs, K.-U., and Zabel, M. (2021). Coupling of dissolved organic carbon, sulfur and iron cycling in Black Sea sediments over the Holocene and the late Pleistocene: Insights from an empirical dynamic model. *Geochimica Cosmochimica Acta* 307, 302–318. doi:10.1016/j.gca.2021.04.032

Chuang, P. C., Dale, A. W., Wallmann, K., Haeckel, M., Yang, T. F., Chen, N. C., et al. (2013). Relating sulfate and methane dynamics to geology: Accretionary prism offshore SW Taiwan: Relating $SO_4$and CH_4Dynamics off SW Taiwan. *Geochem. Geophys. Geosystems* 14 (7), 2523–2545. doi:10.1002/ggge.20168

Egeberg, P. K., and Barth, T. (1998). Contribution of dissolved organic species to the carbon and energy budgets of hydrate bearing deep sea sediments (Ocean Drilling Program Site 997 Blake Ridge). *Chem. Geol.* 149 (1-2), 25–35. doi:10.1016/s0009-2541(98)00033-3

Eickenbusch, P., Takai, K., Sissman, O., Suzuki, S., Menzies, C., Sakai, S., et al. (2019). Origin of short-chain organic acids in serpentinite mud volcanoes of the mariana convergent margin. *Front. Microbiol.* 10, 1729. doi:10.3389/fmicb.2019.01729

Fenchel, T., Blackburn, H., Blackburn, T. H., and King, G. M. (2012). *Bacterial biogeochemistry: The ecophysiology of mineral cycling*. Academic Press.

Finke, N., Vandieken, V., and Jørgensen, B. B. (2007). Acetate, lactate, propionate, and isobutyrate as electron donors for iron and sulfate reduction in Arctic marine sediments, Svalbard. *Fems Microbiol. Ecol.* 59 (1), 10–22. doi:10.1111/j.1574-6941.2006.00214.x

Glombitza, C., Egger, M., Røy, H., and Jørgensen, B. B. (2019). Controls on volatile fatty acid concentrations in marine sediments (Baltic Sea). *Geochimica Cosmochimica Acta* 258, 226–241. doi:10.1016/j.gca.2019.05.038

Glombitza, C., Jaussi, M., Røy, H., Seidenkrantz, M.-S., Lomstein, B. A., and Jørgensen, B. B. (2015). Formate, acetate, and propionate as substrates for sulfate reduction in sub-arctic sediments of Southwest Greenland. *Front. Microbiol.* 6, 846. doi:10.3389/fmicb.2015.00846

Haas, A. F., Nelson, C. E., Kelly, L. W., Carlson, C. A., Rohwer, F., Leichter, J. J., et al. (2011). Effects of coral reef benthic primary producers on dissolved organic carbon and microbial activity. *PloS one* 6 (11), e27973. doi:10.1371/journal.pone.0027973

Hedges, J. I., and Keil, R. G. (1995). Sedimentary organic matter preservation: An assessment and speculative synthesis. *Mar. Chem.* 49(2–3), 81–115. doi:10.1016/0304-4203(95)00008-F

Helgeson, H. C. (1969). Thermodynamics of hydrothermal systems at elevated temperatures and pressures. *Am. J. Sci.* 267 (7), 729–804. doi:10.2475/ajs.267.7.729

Heuer, V. B., Inagaki, F., Morono, Y., Kubo, Y., Spivack, A. J., Viehweger, B., et al. (2020). Temperature limits to deep subseafloor life in the Nankai Trough subduction zone. *Science* 370 (6521), 1230–1234. doi:10.1126/science.abd7934

Heuer, V. B., Krueger, M., Elvert, M., and Hinrichs, K.-U. (2010). Experimental studies on the stable carbon isotope biogeochemistry of acetate in lake sediments. *Org. Geochem.* 41 (1), 22–30. doi:10.1016/j.orggeochem.2009.07.004

Heuer, V. B., Pohlman, J. W., Torres, M. E., Elvert, M., and Hinrichs, K. U. (2009). The stable carbon isotope biogeochemistry of acetate and other dissolved carbon species in deep subseafloor sediments at the northern Cascadia Margin. *Geochimica Cosmochimica Acta* 73 (11), 3323–3336. doi:10.1016/j.gca.2009.03.001

Hiruta, A., Yang, T. F., Lin, S., Su, C.-C., Chen, N.-C., Chen, Y.-J., et al. (2017). Activation of gas bubble emissions indicated by the upward decreasing Lead-210 activity at a submarine mud volcano (TY1) offshore southwestern Taiwan. *J. Asian Earth Sci.* 149, 160–171. doi:10.1016/j.jseaes.2017.08.007

Hoehler, T. M., Alperin, M. J., Albert, D. B., and Martens, C. S. (2001). Apparent minimum free energy requirements for methanogenic Archaea and sulfate-reducing bacteria in an anoxic marine sediment. *Fems Microbiol. Ecol.* 38 (1), 33–41. doi:10.1111/j.1574-6941.2001.tb00879.x

Hoehler, T. M., Alperin, M. J., Albert, D. B., and Martens, C. S. (1998). Thermodynamic control on hydrogen concentrations in anoxic sediments. *Geochimica Cosmochimica Acta* 62 (10), 1745–1756. doi:10.1016/s0016-7037(98)00106-9

Hong, W.-L., Torres, M. E., Carroll, J., Crémière, A., Panieri, G., Yao, H., et al. (2017). Seepage from an arctic shallow marine gas hydrate reservoir is insensitive to momentary ocean warming. *Nat. Commun.* 8, 15745. [Article]. doi:10.1038/ncomms15745

Hu, C.-Y., Yang, T. F., Burr, G. S., Chuang, P.-C., Chen, H.-W., Walia, M., et al. (2017). Biogeochemical cycles at the sulfate-methane transition zone (SMTZ) and geochemical characteristics of the pore fluids offshore southwestern Taiwan. *J. Asian Earth Sci.* 149, 172–183. doi:10.1016/j.jseaes.2017.07.002

Hung, C.-W., Huang, K.-H., Shih, Y.-Y., Lin, Y.-S., Chen, H.-H., Wang, C.-C., et al. (2016). Benthic fluxes of dissolved organic carbon from gas hydrate sediments in the northern South China Sea. *Sci. Rep.* 6, 29597. doi:10.1038/srep29597

Ijiri, A., Inagaki, F., Kubo, Y., Adhikari, R. R., Hattori, S., Hoshino, T., et al. (2018). Deep-biosphere methane production stimulated by geofluids in the Nankai accretionary complex. *Sci. Adv.* 4 (6), eaao4631. doi:10.1126/sciadv.aao4631

Jansen, K., Thauer, R. K., Widdel, F., and Fuchs, G. (1984). Carbon assimilation pathways in sulfate reducing bacteria. Formate, carbon dioxide, carbon monoxide, and acetate assimilation by Desulfovibrio baarsii. *Archives Microbiol.* 138, 257–262. doi:10.1007/bf00402132

Jin, Q., and Bethke, C. M. (2009). Cellular energy conservation and the rate of microbial sulfate reduction. *Geology* 37 (11), 1027–1030. doi:10.1130/g30185a.1

Kandasamy, S., Lin, B., Lou, J. Y., Kao, S. J., Chen, C. T. A., and Mayer, L. M. (2018). Estimation of marine versus terrigenous organic carbon in sediments off southwestern taiwan using the bromine to total organic carbon ratio as a proxy. *J. Geophys. Res. Biogeosciences* 123 (10), 3387–3402. doi:10.1029/2018jg004674

Kandasamy, S., and Nagender Nath, B. (2016). Perspectives on the terrestrial organic matter transport and burial along the land-deep sea continuum: Caveats in our understanding of biogeochemical processes and future needs. *Front. Mar. Sci.* 3 (259). doi:10.3389/fmars.2016.00259

Komada, T., Burdige, D. J., Crispo, S. M., Druffel, E. R., Griffin, S., Johnson, L., et al. (2013). Dissolved organic carbon dynamics in anaerobic sediments of the Santa Monica Basin. *Geochimica Cosmochimica Acta* 110, 253–273. doi:10.1016/j.gca.2013.02.017

Komada, T., Burdige, D. J., Li, H.-L., Magen, C., Chanton, J. P., and Cada, A. K. (2016). Organic matter cycling across the sulfate-methane transition zone of the Santa Barbara Basin, California Borderland. *Geochimica Cosmochimica Acta* 176, 259–278. doi:10.1016/j.gca.2015.12.022

Leloup, J., Loy, A., Knab, N. J., Borowski, C., Wagner, M., and Jørgensen, B. B. (2007). Diversity and abundance of sulfate-reducing microorganisms in the sulfate and methane zones of a marine sediment, Black Sea. *Environ. Microbiol.* 9(1), 131–142. doi:10.1111/j.1462-2920.2006.01122.x

Lin, A. T., Yao, B. C., Hsu, S. K., Liu, C. S., and Huang, C. Y. (2009). Tectonic features of the incipient arc-continent collision zone of Taiwan: Implications for seismicity. *Tectonophysics* 479 (1-2), 28–42. doi:10.1016/j.tecto.2008.11.004

Lin, C.-C., Lin, A. T.-S., Liu, C.-S., Horng, C.-S., Chen, G.-Y., and Wang, Y. (2014). Canyon-infilling and gas hydrate occurrences in the frontal fold of the offshore accretionary wedge off southern Taiwan. *Mar. Geophys. Res.* 35 (1), 21–35. doi:10.1007/s11001-013-9203-7

Liu, S., and Suflita, J. M. (1993). H_2 -CO_2 -dependent anaerobic O-demethylation activity in subsurface sediments and by an isolated bacterium. *Appl. Environ. Microbiol.* 59(5), 1325–1331. doi:10.1128/aem.59.5.1325-1331.1993

Mackenzie, F., Lerman, A., and Andersson, A. (2004). Past and present of sediment and carbon biogeochemical cycling models. *Biogeosciences Discuss.* 1 (1), 11–32. doi:10.5194/bg-1-11-2004

Middelburg, J. J. (1989). A simple rate model for organic matter decomposition in marine sediments. *Geochimica Cosmochimica Acta* 53 (7), 1577–1581. doi:10.1016/0016-7037(89)90239-1

Morono, Y., Terada, T., Nishizawa, M., Ito, M., Hillion, F., Takahata, N., et al. (2011). Carbon and nitrogen assimilation in deep subseafloor microbial cells. *Proc. Natl. Acad. Sci.* 108 (45), 18295–18300. doi:10.1073/pnas.1107763108

Na, H., Lever, M. A., Kjeldsen, K. U., Schulz, F., and Jørgensen, B. B. (2015). Uncultured D esulfobacteraceae and C renarchaeotal group C 3 incorporate 13 C-acetate in coastal marine sediment. *Environ. Microbiol. Rep.* 7 (4), 614–622. doi:10.1111/1758-2229.12296

Nuzzo, M., Hornibrook, E. R., Hensen, C., Parkes, R. J., Cragg, B. A., Rinna, J., et al. (2008). Shallow microbial recycling of deep-sourced carbon in Gulf of Cadiz mud volcanoes. *Geomicrobiol. J.* 25 (6), 283–295. doi:10.1080/01490450802258196

Orcutt, B. N., LaRowe, D. E., Biddle, J. F., Colwell, F. S., Glazer, B. T., Reese, B. K., et al. (2013). Microbial activity in the marine deep biosphere: Progress and prospects. *Front. Microbiol.* 4, 189. doi:10.3389/fmicb.2013.00189

Oremland, R. S., and Polcin, S. (1982). Methanogenesis and sulfate reduction: Competitive and noncompetitive substrates in estuarine sediments. *Appl. Environ. Microbiol.* 44 (6), 1270–1276. doi:10.1128/aem.44.6.1270-1276.1982

Orsi, W. D., Barker Jørgensen, B., and Biddle, J. F. (2016). Transcriptional analysis of sulfate reducing and chemolithoautotrophic sulfur oxidizing bacteria in the deep subseafloor. *Environ. Microbiol. Rep.* 8(4), 452–460. doi:10.1111/1758-2229.12387

Parkes, R. J., Wellsbury, P., Mather, I. D., Cobb, S. J., Cragg, B. A., Hornibrook, E. R. C., et al. (2007). Temperature activation of organic matter and minerals during burial has the potential to sustain the deep biosphere over geological timescales. *Org. Geochem.* 38(6), 845–852. doi:10.1016/j.orggeochem.2006.12.011

Pohlman, J. W., Bauer, J. E., Waite, W. F., Osburn, C. L., and Chapman, N. R. (2010). Methane hydrate-bearing seeps as a source of aged dissolved organic carbon to the oceans. *Nature* 4, 37–41. doi:10.1038/ngeo1016

Schrum, H. N., Spivack, A. J., Kastner, M., and D'Hondt, S. (2009). Sulfate-reducing ammonium oxidation: A thermodynamically feasible metabolic pathway in subseafloor sediment. *Geology* 37 (10), 939–942. doi:10.1130/g30238a.1

Sela-Adler, M., Ronen, Z., Herut, B., Antler, G., Vigderovich, H., Eckert, W., et al. (2017). Co-existence of methanogenesis and sulfate reduction with common substrates in sulfate-rich estuarine sediments. *Front. Microbiol.* 8, 766. doi:10.3389/fmicb.2017.00766

Sørensen, J., Christensen, D., and Jørgensen, B. B. (1981). Volatile fatty acids and hydrogen as substrates for sulfate-reducing bacteria in anaerobic marine sediment. *Appl. Environ. Microbiol.* 42 (1), 5–11. doi:10.1128/aem.42.1.5-11.1981

Su, C.-C., Hsu, S.-T., Hsu, H.-H., Lin, J.-Y., and Dong, J.-J. (2018). Sedimentological characteristics and seafloor failure offshore SW Taiwan. *Terr. Atmos. Ocean. Sci.* 29 (1), 65–76. doi:10.3319/tao.2017.06.21.01

Teece, M. A., Fogel, M. L., Dollhopf, M. E., and Nealson, K. H. (1999). Isotopic fractionation associated with biosynthesis of fatty acids by a marine bacterium under oxic and anoxic conditions. *Org. Geochem.* 30 (12), 1571–1579. doi:10.1016/s0146-6380(99)00108-4

Teng, L. S. (1990). Geotectonic evolution of late Cenozoic arc-continent collision in Taiwan. *Tectonophysics* 183 (1-4), 57–76. doi:10.1016/0040-1951(90)90188-e

Thauer, R., Zinkhan, D., and Spormann, A. (1989). Biochemistry of acetate catabolism in anaerobic chemotrophic bacteria. *Annu. Rev. Microbiol.* 43 (1), 43–67. doi:10.1146/annurev.mi.43.100189.000355

Treude, T., Krause, S., Maltby, J., Dale, A. W., Coffin, R., and Hamdan, L. J. (2014). Sulfate reduction and methane oxidation activity below the sulfate-methane transition zone in Alaskan Beaufort Sea continental margin sediments: Implications for deep sulfur cycling. *Geochimica Cosmochimica Acta* 144, 217–237. doi:10.1016/j.gca.2014.08.018

Valdemarsen, T., and Kristensen, E. (2010). Degradation of dissolved organic monomers and short-chain fatty acids in sandy marine sediment by fermentation and sulfate reduction. *Geochimica Cosmochimica Acta* 74 (5), 1593–1605. doi:10.1016/j.gca.2009.12.009

Vanneste, H., Kelly-Gerreyn, B. A., Connelly, D. P., James, R. H., Haeckel, M., Fisher, R. E., et al. (2011). Spatial variation in fluid flow and geochemical fluxes across the sediment–seawater interface at the Carlos Ribeiro mud volcano (Gulf of Cadiz). *Geochimica Cosmochimica Acta* 75 (4), 1124–1144. doi:10.1016/j.gca.2010.11.017

Wallmann, K., Aloisi, G., Haeckel, M., Obzhirov, A., Pavlova, G., and Tishchenko, P. (2006). Kinetics of organic matter degradation, microbial methane generation, and gas hydrate formation in anoxic marine sediments. *Geochimica Cosmochimica Acta* 70 (15), 3905–3927. doi:10.1016/j.gca.2006.06.003

Wang, G., Spivack, A. J., and D'Hondt, S. (2010). Gibbs energies of reaction and microbial mutualism in anaerobic deep subseafloor sediments of ODP Site 1226. *Geochimica Cosmochimica Acta* 74 (14), 3938–3947. doi:10.1016/j.gca.2010.03.034

Wang, G., Spivack, A. J., Rutherford, S., Manor, U., and D'Hondt, S. (2008). Quantification of co-occurring reaction rates in deep subseafloor sediments. *Geochimica Cosmochimica Acta*, 72(14), 3479–3488. doi:10.1016/j.gca.2008.04.024

Wei, W., Kastner, M., and Spivack, A. (2008). Reply to comment on: "Chlorine stable isotopes and halogen concentrations in convergent margins with implications for the Cl isotopes cycle in the ocean". *Earth Planet. Sci. Lett.* 274 (3-4), 535. doi:10.1016/j.epsl.2008.07.023

Wellsbury, P., Goodman, K., Barth, T., Cragg, B. A., Barnes, S. P., and Parkes, R. J. (1997). Deep marine biosphere fuelled by increasing organic matter availability during burial and heating. *Nature* 388 (6642), 573–576. doi:10.1038/41544

Wessel, P., and Smith, W. H. (1998). New, improved version of generic mapping tools released. *Eos, Trans. Am. Geophys. Union* 79 (47), 579. doi:10.1029/98eo00426

Wu, J. (2016). *New data processing algorithm for marine heat flow and thermal modeling for Tsan-Yao mud volcano offshore SW Taiwan*. Taipei: Institute of Oceanography College of Science, National Taiwan University.

Yoon, S., Sanford, R. A., and Löffler, F. E. (2013). Shewanella spp. use acetate as an electron donor for denitrification but not ferric iron or fumarate reduction. *Appl. Environ. Microbiol.* 79 (8), 2818–2822. doi:10.1128/aem.03872-12

Zhang, Y., Luo, M., Hu, Y., Wang, H., and Chen, D. (2019). *An areal assessment of subseafloor carbon cycling in cold seeps and hydrate-bearing areas in the northern south China Sea*. Geofluids.

frontiers | Frontiers in Earth Science

TYPE Original Research
PUBLISHED 28 July 2023
DOI 10.3389/feart.2023.1206810

Check for updates

OPEN ACCESS

EDITED BY
Carolyn Ruppel,
US Geological Survey (USGS),
United States

REVIEWED BY
Hitoshi Tomaru,
Chiba University, Japan
Akihiro Hachikubo,
Kitami Institute of Technology, Japan

*CORRESPONDENCE
Akira Ijiri,
ijiri@maritime.kobe-u.ac.jp

RECEIVED 16 April 2023
ACCEPTED 13 June 2023
PUBLISHED 28 July 2023

CITATION
Ijiri A, Setoguchi R, Mitsutome Y, Toki T, Murayama M, Hagino K, Hamada Y, Yamagata T, Matsuzaki H, Tanikawa W, Tadai O, Kitada K, Hoshino T, Noguchi T, Ashi J and Inagaki F (2023), Origins of sediments and fluids in submarine mud volcanoes off Tanegashima Island, northern Ryukyu Trench, Japan. *Front. Earth Sci.* 11:1206810. doi: 10.3389/feart.2023.1206810

COPYRIGHT
© 2023 Ijiri, Setoguchi, Mitsutome, Toki, Murayama, Hagino, Hamada, Yamagata, Matsuzaki, Tanikawa, Tadai, Kitada, Hoshino, Noguchi, Ashi and Inagaki. This is an open-access article distributed under the terms of the Creative Commons Attribution License (CC BY). The use, distribution or reproduction in other forums is permitted, provided the original author(s) and the copyright owner(s) are credited and that the original publication in this journal is cited, in accordance with accepted academic practice. No use, distribution or reproduction is permitted which does not comply with these terms.

Origins of sediments and fluids in submarine mud volcanoes off Tanegashima Island, northern Ryukyu Trench, Japan

Akira Ijiri[1,2]*, Ryoma Setoguchi[3], Yuki Mitsutome[4], Tomohiro Toki[5,6], Masafumi Murayama[7], Kyoko Hagino[8], Yohei Hamada[2], Takeyasu Yamagata[9], Hiroyuki Matsuzaki[9], Wataru Tanikawa[2], Osamu Tadai[10], Kazuya Kitada[11], Tatsuhiko Hoshino[2], Takuro Noguchi[7], Juichiro Ashi[12] and Fumio Inagaki[13,14]

[1]Graduate School of Maritime Sciences, Kobe University, Kobe, Japan, [2]Kochi Institute for Core Sample Research, Institute for Extra-Cutting-Edge Science and Technology Avant-Garde Research (X-Star), Japan Agency for Marine-Earth Science and Technology (JAMSTEC), Nankoku, Kochi, Japan, [3]Department of Agriculture and Marine Science, Graduate School of Integrated Arts and Sciences, Kochi University, Nankoku, Kochi, Japan, [4]Department of Chemistry Biology and Marine Science, Graduate School of Engineering and Science, University of the Ryukyus, Nishihara, Okinawa, Japan, [5]Department of Chemistry, Biology and Marine Science, Faculty of Science, University of the Ryukyus, Nishihara, Okinawa, Japan, [6]Research Institute for Humanity and Nature, Kita-ku, Kyoto, Japan, [7]Interdisciplinary Science Unit, Multidisciplinary Science Cluster, Research and Education Faculty, Kochi University, Nankoku, Kochi, Japan, [8]Marine Core Research Institute, Kochi University, Nankoku, Kochi, Japan, [9]The University Museum, The University of Tokyo, Bunkyo, Tokyo, Japan, [10]Marine Works Japan Ltd., Yokosuka, Japan, [11]Super-Cutting-Edge Grand and Advanced Research (SUGAR) Program, Institute for Extra-Cutting-Edge Science and Technology Avant-Garde Research (X-star), Japan Agency for Marine-Earth Science and Technology (JAMSTEC), Yokosuka, Japan, [12]Atmosphere and Ocean Research Institute, The University of Tokyo, Kashiwa, Chiba, Japan, [13]Institute for Marine-Earth Exploration and Engineering (MarE3), Japan Agency for Marine-Earth Science and Technology (JAMSTEC), Yokohama, Japan, [14]Department of Earth Sciences, Graduate School of Science, Tohoku University, Sendai, Japan

Mud volcanoes are topographic features through which over-pressurized sediments are intruded upward and erupted, transporting fluids and sediments from the deep subsurface to the surface/seafloor. To understand material and biogeochemical cycling through mud volcanoes, we investigated the origins of sediments and fluids erupted by four submarine mud volcanoes off Tanegashima Island, along the northern Ryukyu Trench: MV#1–3 and MV#14. We estimated the ages of the source sequences of the mud volcano sediments to be middle to late Miocene based on nannofossils and ^{10}Be ages. The sediments were characteristically enriched in illite. The similar mineral compositions and vitrinite reflectance values (0.42%–0.45%) of sediments erupted by the mud volcanoes strongly suggest that each is rooted in the same source sequence. Pore waters had Cl^- concentrations ~40% that of seawater and were proportionally enriched in ^{18}O and depleted in D, indicating the addition of freshwater from the dehydration of clay minerals. However, the smectite and illite contents (<40%) in the clay size fraction ruled out *in situ* smectite dewatering as the cause of the pore water Cl^- dilution. Thus, fluids derived from clay dewatering must have originated from deeper than the source sequence of the mud volcano sediments. Vertical Cl^- profiles indicate that the upward fluid advection rate and eruption frequency decrease from MV#3 to MV#2, MV#1, and MV#14 (MV#14 being dormant). At the active mud volcanoes, the C_1/C_2 ratios

(<100) and methane $\delta^{13}C$ values (−56‰ to −42‰) indicate that hydrocarbon gases are mostly derived from the thermal decomposition of organic matter in deep sediments where the *in situ* temperature exceeds 80°C. At the dormant MV#14, high C_1/C_2 ratios (700–4,000) and low methane $\delta^{13}C$ values (ca. −75‰) suggest the limited supply of thermogenic methane and the subsequent shallow methanogenesis. Because vitrinite reflectance values indicate that the source sediments are too immature to produce thermogenic hydrocarbons, the hydrocarbon gases, like the fluids derived from clay dewatering, were probably supplied from deeper than the source strata. The supply of deep fluids into the source sequence might be a universal phenomenon in subduction zones, and may play an important role in mud volcanism and associated biogeochemical cycling.

KEYWORDS

mud volcano, porewater, hydrocarbon gases, vitrinite, Ryukyu Trench

1 Introduction

Submarine mud volcanoes, which occur along the margins of convergent plate, are vertical intrusions of low-density, deformable sediments from the deep subsurface to the seafloor (Milkov, 2000; Kopf, 2002). Pore fluids in the sediments erupted by submarine mud volcanoes are characteristically diagenetically altered by clay-mineral dehydration and the presence of hydrocarbon gases derived from the thermocatalyte decomposition of sedimentary organic matter (e.g., Martin et al., 1996; Dahlmann and de Lange, 2003; Hensen et al., 2004). These characteristics suggest that mud volcano fluids originate from deep depths in which these chemical reactions typically occur (>60°C). Therefore, mud volcanoes are an important pathway by which deeply sourced materials (especially methane, a greenhouse gas) reach the hydrosphere and atmosphere (Milkov, 2000; Dimitrov, 2002; Kopf, 2002; Wallmann et al., 2006).

Recent studies have revealed the biogeochemical and microbiological characteristics of deeply sourced mud volcano sediments, as well as their ecological roles (e.g., Hoshino et al., 2017; Ijiri et al., 2018a). In the Kumano fore arc basin, Nankai Trough, the mud volcano's source layer is assumed to be located at the basin bottom where fluids in the accretionary prism are supplied via mega-splay faults, probably resulting high pore pressure. In this environment, water through clay dehydration, hydrogen, and other organic substrates are provided to the overlying fore arc sedimentary basin, coincidently stimulating *in situ* microbial activities such as hydrogenotrophic methanogenesis (Ijiri et al., 2018a). The observation indicates that the material and biogeochemical cycles through mud volcanoes are strongly related to the mechanism of the mud volcano eruption.

To understand biogeochemical cycling through mud volcanoes, it is therefore important to investigate the origins of both sediments and fluids. Excess fluid pressured is one of the key factors to explain the mud eruption (Tanikawa et al., 2010). When a fluid pressure is higher than estimated from the normal hydrostatic fluid gradient for a given depth, it is called overpressure (Duan and Flemings, 2000). The overpressure generated by the rapid sediment deposition and the lateral transfer of the pressure may cause slope failure and drive cold seeps on passive margins (Duan and Flemings, 2000). The eruption of mud volcanoes is also triggered by such overpressure. It has been debated whether the overpressure that causes the mud volcanic eruption is due to the sediments themselves, such as clay mineral dehydration in the sediments and fast sedimentation rates, or the supply of fluids to the source sequence of erupted sediments from deeper sedimentary layer (Kopf, 2002). The origin and composition of mud volcano fluids have been the subject of many studies (e.g., Martin et al., 1996; Dahlmann and de Lange, 2003; Hensen et al., 2004). However, fewer studies have included chemical and mineralogical analyses of mud volcano sediments (e.g., Schulz et al., 1997; Jurado-Rodriguez and Martinez-Ruiz, 1998; Ujiié, 2000; Alaoui Mhammedi et al., 2008; Ijiri et al., 2018b), despite the fact that the lithologies of erupted sediments are strongly related to the formation of mud volcanoes and their sediment sources.

In this study, we investigated the origins of sediments and fluids in four submarine mud volcanoes off Tanegashima Island, along the northern Ryukyu Trench, using sediment core samples retrieved from the mud volcano field. To investigate sediment origins, we determined the ages of the mud volcanoes' source sequences based on nannofossil observations and beryllium isotopic analysis. We estimated the mineral compositions of the bulk sediments and the clay size fraction by X-ray diffraction (XRD). To examine organic matter maturity and the temperatures experienced by mud volcano sediments, we analyzed vitrinite reflectance. Finally, to investigate the origins of fluids, we analyzed the chemical and isotopic compositions of pore water and hydrocarbon gases extracted from the mud volcanoes.

2 Geological setting and previous studies

Known submarine mud volcano fields around Japan include the Kumano fore arc basin of the Nankai Trough and the area off Tanegashima Island along the Ryukyu Trench, where the Philippine Sea Plate is being subducted beneath the Eurasian Plate (Ujiié, 2000; Nakayama et al., 2010; Pape et al., 2014; Menapace et al., 2017; Ijiri et al., 2018a; Ijiri et al., 2018b). The field off Tanegashima Island comprises more than 30 mud volcano-like mounds on the landward slope of the Ryukyu Trench (Figure 1A; Ujiié, 2000). The Ryukyu Trench is formed by the subduction of Phlippine Sea Plate to the Eurasian plate. The geological structure of deep subsurface in landward slope of the Ryukyu Trench is unclear (Ujiié, 2000). The sediments at Tanegashima Island

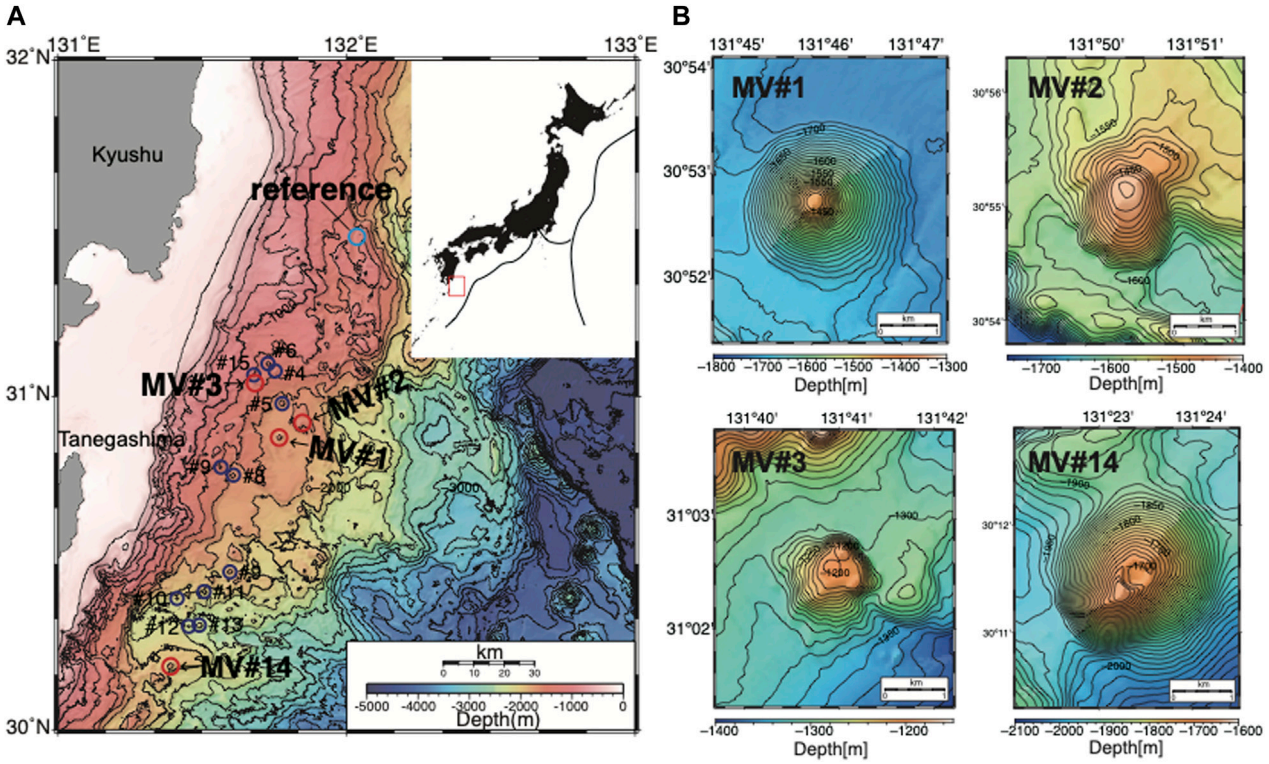

FIGURE 1
(A) The locations of mud volcanoes off Tanegashima Island, Japan, and **(B)** the detailed topography of mud volcanoes MV#1, MV#2, MV#3, and MV#14.

located close to the northern Ryukyu Trench, is composed of the Paleogene Kumage Group generally correlated with the Shimanto Belt of Southwest Japan (Hayasaka, 1988). The Shimanto Belt is an old accretionary prism divided into two major tectonostratigraphic units, the Northern Belt (Lower Shimanto Group) and the Southern Belt (Upper Shimanto Group). The former is characterized by uppermost Jurassic to Cretaceous strata, and the latter by Paleogene and lower Miocene rocks (Taira et al., 1982). Between 2012 and 2014, submarine topography surveys were conducted to clarify the spatial distribution of mud volcanoes off Tanegashima, and 15 mounds (numbered MV#1–15) were identified as potential mud volcanoes (Figure 1A) (Kitada et al., 2018). Single-channel seismic reflection data indicate that the mud volcanoes are located on the mud diapir structures, which have been identified by an acoustically transparent zone (Kitada et al., 2018). However, there is currently a lack of detailed seismic data to determine the presence of subducting structures in deeper subsurface of this area.

Ujiié (2000) investigated foraminifera and nannofossils in mud volcano sediments obtained from MV#2 and MV#13 during 1994 survey and reported the sediments to have various ages from late Eocene to Pleistocene. They interpreted the microfossils to have been incorporated from the strata surrounding mud diapirs during their intrusion. The chemical compositions of pore waters in sediments collected from MV#1 during 2002 survey indicate that water derived from the dehydration of clay minerals is supplied to near the surface (Nakayama et al., 2010).

Recent studies have revealed the biogeochemical and microbiological characteristics and ecological roles of mud volcano sediments at depth. At MV#1 and MV#14, sedimentary *Atribacteria* were found in methane plumes in the overlying water column (Hoshino et al., 2017). This observation suggests that submarine mud volcanism disperses microbes from the deep sedimentary biosphere into the overlying hydrosphere.

Recently, Mitsutome et al. (2023) investigated the helium isotopic and noble gas compositions of mud volcano sediments from MV#1–3 and #14 to estimate their depths of origin. They reported that approximately 90% of the He is of crustal origin, and the experienced temperature of heavy noble gases is consistent with the range of temperature conditions required for the dehydration of clay minerals.

3 Materials and methods

3.1 Visual survey and sediment core sampling

Details of the obtained sediment cores are summarized in Supplementary Table S1.

3.1.1 MV#1

MV#1 is in the northern area of the mud volcano field off Tanegashima Island (30° 52.7′N, 131° 46.0′E, 1,400 m water depth; Figures 1A, B); it is ~2.5 km in diameter and ~280 m height. During cruise NT15-15 of R/V *Natsushima* in 2015, we surveyed the summit

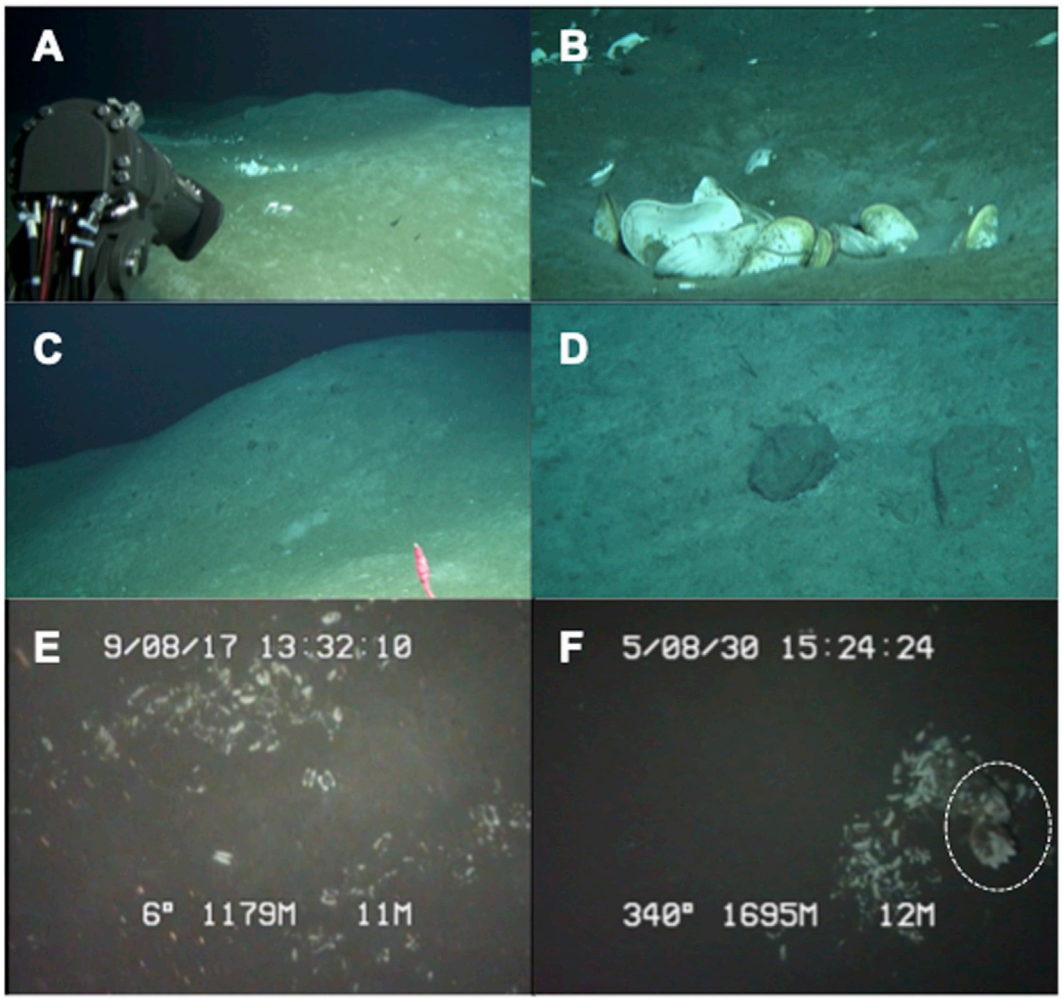

FIGURE 2
Photographs taken near the summits of MV#1, MV#3, and MV#14. **(A,B)** *Calyptogena* spp. and **(C,D)** consolidated mud clasts on the summit of MV#1. *Calyptogena* spp. were also observed on the summits of **(E)** MV#3 and **(F)** MV#14. In **(F)**, the dashed circle outlines a chimney-like white object.

of MV#1 during two dives (#1866 and #1867) of ROV *HYPER-DOLPHIN* (Figure 1B). We observed a small colony of *Calyptogena* (Figures 2A, B). Around the summit, we observed several consolidated sandy mudstone clasts (several to several tens of centimeters in size; Figures 2C, D) that were probably mixed with sediments fractured by diapiric mud intrusion. The presence of these clasts suggests that sediments around the summit comprise erupted mud and not hemipelagic sediments. During cruise KH-15-02 of R/V *Hakuho Maru* in 2015, two sediment cores were retrieved from MV#1 using a piston coring system: one was used for pore water analysis; the other for sediment analysis.

3.1.2 MV#2

MV#2 is near MV#1 (30° 55.1′N, 131° 50.6′E, 1,430 m water depth; Figures 1A, B); it is ~1.2–1.5 km in diameter and ~120–170 m height. At MV#2, two piston cores and two multiple cores were retrieved for pore water and sediment analyses during cruise KH-19-5 of R/V *Hakuho Maru* in 2019. Since only conventional piston coring was conducted, a visual survey for MV#2 could not be performed.

3.1.3 MV#3

MV#3 is in the northern area of the mud volcano field (31° 02.5′N, 131° 41.0′E, 1,200 m water depth; Figures 1A, B); it is ~1.5 km in diameter and ~100 m height, making it the smallest of the studied mud volcanoes. During cruise KH-19-5, two piston cores and two multiple cores were retrieved. One of the piston cores was retrieved using the Navigable Sampling System (NSS), which allows observation of the target seafloor area during piston coring via an underwater camera coupled to the piston coring system; the other piston core (for sediment analysis) was retrieved using the normal piston coring system. These camera observations revealed a *Calyptogena* colony near the summit coring site of MV#3 (Figure 2E), suggesting that this mud volcano was quite active.

3.1.4 MV#14

MV#14 is situated in the southern area of the mud volcano field (30° 11.5′N, 131° 23.5′E, 1,680 m water depth; Figures 1A, B); it is ~3 km in diameter and ~270 m height, making it the largest of the

studied mud volcanoes, and it has developed a summit caldera (Figure 1B). During cruise KH-15-2, one NSS piston core was retrieved; in the camera footage, we observed a *Calyptogena* colony on the eastern edge of the caldera (Figure 2F). Next to the colony, we observed a white, chimney-like object; it may have been a carbonate chimney, but the low resolution of the image precludes a precise interpretation (Figure 2F).

3.1.5 Reference site

A multiple core was retrieved from a reference site near the mud volcano field during cruise KS-21-18 of R/V *Shinsei-Maru* in 2021 (31° 29′N; 132° 02′E, 1,220 m water depth; Figure 1A).

3.2 Sediment samples

3.2.1 Sediment sampling

Piston core samples retrieved for sediment analyses [Length: 3.11–5.21 m, inner diameter: 75 cm (Supplementary Table S1)] were cut into 1-m-long sections and stored onboard at 4°C. Onshore laboratory, the sections were cut in half lengthwise and the sediments were subsampled from the cut surface after the scan for X-ray computed tomography. For the MV#14 core, sediments for pore water and microbial analyses were collected from the piston core onboard, and sediment analysis samples were later subsampled from the microbial analysis samples in onshore laboratory. For nannofossil observations and beryllium isotopic (^{10}Be) and mineral compositional analyses, sediments were subsampled from the muddy matrix representing the mud volcano sediments; we avoided mud breccias because they were probably incorporated during mud diapir intrusion (Ujiié, 2000).

3.2.2 X-ray computed tomography

To observe the internal structure of the core sample, we obtained X-ray computed tomography (X-ray CT) image using Aquilion PRIME/Focus (Canon Medical Systems Corporation, Japan). For the MV#3 core, the most sediments were collected for geochemical and microbial analyses onboard. Therefore, the residual sediments on the core-liner were scanned. For the MV#14 core, all sediments were sub-sampled on board, so we were unable to scan the core.

3.2.3 Calcareous nannofossil observation

To examine the origin of the source sequence of the mud volcano sediments, the age of the mud volcano sediments was estimated based on the calcareous nannofossils in the sediments. The samples were prepared as smear slides using standard techniques (Bown and Young, 1998), and then examined with a Nikon E600 polarizing light microscope at 1,500× magnification. Species identification and their occurrence age range of each species followed Backman et al. (2012) and Nannotax3 (https://www.mikrotax.org/Nannotax3/index.html). Semi-quantitative data were collected from the samples, which contained sufficient number of calcareous nannofossils, by identifying at least 200 upper photic zone specimens in a varying number of fields of view per sample. Lower photic zone species *Florisphaera profunda* was counted separately in the same fields of view when encountered. Upper photic-zone species were classified into six groups (*Emiliania huxleyi*, Pliocene–Pleistocene taxa except *E. huxleyi*, Miocene–Pleistocene taxa, Paleogene–Neogene taxa, Miocene taxa, and miscellaneous) based on their occurrence age range (Supplementary Table S2), and the relative abundance of each group was calculated (Supplementary Table S3).

3.2.4 Beryllium isotopic analysis

The age of the source sequence of the mud volcano sediments was also estimated using the beryllium isotope analysis. Meteoric ^{10}Be is formed in the atmosphere through cosmic ray interactions with oxygen and nitrogen nuclei, eventually reaching the ocean via precipitation and aerosols (e.g., Brown, 1987). In the ocean, it is incorporated into seafloor sediments through scavenging by biogenic opal, clay, carbonate, and organic materials (e.g., McHargue and Damon, 1991). It undergoes radioactive decay with a half-life of 1.36 million years, transforming into stable ^{10}B [Nishiizumi et al. (2007)]. Therefore, unless sediments are exposed at the surface after the deposition, their age can be can be estimated by the concentration of ^{10}Be in sediments (Amin et al., 1975).

The 0.3 g of sediment samples were decomposed at 110°C for 12 h in a tightly sealed vessel with 1 mL of HF, 6 mL of HNO_3, and 1 mL of $HClO_4$. After decomposition, 0.3 mg of Be carrier was added to the sample, which was then dried on a hotplate and converted to Cl manner by repeated drying with 2 mL of 35% HCl. To mask other interfering elements such as aluminum for the accelerator mass spectrometer (AMS) measurement, 25 mL of 21% EDTA solution with pH 6.0 was added to the sample, followed by the addition of 2 mL of acetylacetone to form the beryllium acetylacetonate complex. The Be complex was then extracted into 5 mL of CCl_4 using solvent extraction, and back-extracted into 10 mL of 1 M HCl. The extracted Be solution was purified using cation exchange with a 5 mL Dowex 50 W-X8 column (inner diameter 9 mm, length 10 mm, 1 column volume = 5 mL) with 1.0 M HCl. The Be fraction, eluted between 5 and 9 column volumes, was concentrated to 1 mL and transferred to a 15 mL polycarbonate spitch centrifuge tube. The purified Be solution was then precipitated as Be $(OH)_2$ by adding an ammonium solution. To remove ^{10}B, which causes isobaric interference in AMS measurement, the precipitation was washed three times with Milli-Q water (>18 MΩ), and re-precipitated using ultra-pure HCl and ammonium solution. After washing, the solution was dissolved in a few drops of ultra-pure HCl and transferred to a quartz tube for drying. The purified Be $(OH)_2$ was converted to BeO by igniting at temperatures above 800°C. The resulting BeO was mixed with Nb powder and pressed into an OFCu cathode with an inner diameter of 1 mm. The reactive ^{10}Be abundances were measured using a National Electrostatic Corporation (NEC) accelerator mass spectrometer (AMS) with a 4.8 MV terminal voltage at the Micro Analysis Laboratory, Tandem accelerator (MALT) of the University of Tokyo (U Tokyo), following the method described by Matsuzaki et al. (2020). Absolute values were obtained using the KNB5-2 standard (^{10}Be/^{9}Be = 8.56 × 10^{-12}; Nishiizumi et al., 2007) with a typical beam current of 4 micro A (^{9}Be^{16}O; Yokoyama et al., 2019). The ratios of ^{10}Be/^{9}Be in the samples ranged from (7–20) × 10^{-14}, while the carrier blank had a ratio of 1.4 × 10^{-14}.

3.2.5 Whole-rock and clay-fraction mineral compositions

To reveal the mineralogical characteristics of the mud volcano sediments, whole-rock and clay-fraction mineral compositions were determined by XRD using an X'Pert PRO MPD X-ray diffractometer system (Malvern Panalytical, Ltd., Malvern, United Kingdom) with CuKα radiation at 45 kV and 40 mA, 0.0083° divergence, anti-scattering slits, and a 0.15 mm receiving slit. The diffracted X-rays were counted for 10.2 s at steps of 0.0083° 2θ. For whole-rock and clay-fraction mineral compositions, we scanned 3°–75° 2θ and 3°–35° 2θ, respectively.

The whole rock mineral compositions were quantified based on relative peak intensities of XRD pattern and the Rock jock program (Eberl., 2003). The analysis procedure followed Tanikawa and Tadai (2018). Sediment samples were dried at 50°C, and then powdered using an agate mortar. Then, 1 g of powdered sample was mixed with 0.25 g of high-purity Al_2O_3 (AX-5HM, Hinomoto Kenmazai CO., Ltd., Tokyo, Japan), which is the internal standard for Rock jock analysis, using an agate mortar. The 0.1 g of the mixed sample was placed on a slide glass and subjected to XRD analysis.

For clay-fraction analyses, the clay size fraction (<2 μm) was separated from the bulk sediment samples by centrifugation. Clay suspensions were dropped onto glass slides and dried in an oven at 50°C to prepare oriented samples for XRD analysis. After a first round of XRD analysis, the samples were saturated with ethylene glycol vapor at 50°C for more than 5 h and reanalyzed. We also semiquantitatively estimated the proportion of major clay minerals in the clay size fraction using the method of Biscaye (1965). The proportions of illite and smectite crystallites in illite/smectite (I/S) mixed-layer clays were calculated using the angular separation (Δ° 2θ) between the composite illite-(001)/smectite-(002) reflection at 2θ ≈ 10.5° and the composite illite-(002)/smectite-(003) reflection at 2θ ≈ 16° (Moore and Reynolds, 1997).

The percentage of the clay size fraction in the bulk rock was determined by particle size analysis using a Mastersizer et al., 2020 (Malvern Panalytical, Ltd., Malvern, United Kingdom). The sediment samples were first washed through a 2-mm sieve with Milli-Q water, stirred in a dispersant (0.05% sodium hexametaphosphate solution) for 24 h, and then analyzed.

3.2.6 Vitrinite reflectance

The vitrinite reflection was analysed to examine the thermal maturity of organic matter. The vitrinite reflectance value (R_O) increases exponentially with temperature and records the highest temperature experienced by organic matter (Burnham and Sweeney, 1989). We collected samples of organic matter from MV#1, #2, #3, and #14. To collect enough samples for the vitrinite analysis, sediment samples were collected from three depths in each core, and the data was combined for each mud volcano. For each sample, coal fragments were separated and concentrated using heavy liquids (a sodium polytungstate solution with a specific gravity of 1.8). The separated grains were then mounted in resin and polished using 0.06-μm alumina powder. The measurements were conducted with a silicone-diode microphotometer using 546 nm non-polarized light, in line with the regulations of the International Organization for Standardization (ISO 7404-5), the American Society for Testing and Materials (ASTMD 2798-99), and the Japan Industrial Standard (JIS M 8816). A concentrated spot beam of 1.6-μm diameter was used to measure the reflectance. We measured mean random reflectance (R_m) following ASTMD 2798-05. A linear function between mean random reflectance and mean maximum reflectance has been reported in case of lower vitrinite reflectance (<3.0%: Chijiwa, 1990; <1.7%: ASTM Standard D2798-05). Therefore, the effect of anisotropy of vitrinite reflectance should be small when it was low. A total of >41 grains per each sample were measured in the immersion oil which has a refractive index of 1.516, where a sufficient number of polished grains were present on the sample surface. The equations for calculating the maximum temperature experienced by the sample using measured R_m values were defined by Sweeney and Burnham (1990).

3.3 Pore water samples and analyses

Pore water chemistry is crucial to examine the origin of fluids within the mud volcano sediments, as well as the biogeochemical processes occurring within these sediments. After piston core recovery, wet sediments were immediately sampled at 20- to 50-cm intervals and pore water samples were extracted onboard using a stainless-steel squeezer (Manheim and Sales, 1974). For sediment samples retrieved by a multiple corer, the porous tube of a Rhizon sampler (2.5-mm diameter, 0.15-μm mean pore size) was inserted and buried in the sediment to extract pore water.

In an onshore laboratory, Cl^- and SO_4^{2-} concentrations in the pore water samples were analyzed using an ion chromatograph (Dionex DX-500) with an isocratic carbonate/bicarbonate eluent coupled with suppressed conductivity detection and an IonPac AS12A carbonate eluent anion-exchange column (200 mm long, 4 mm inner diameter; Dionex, United States) equipped with a guard column (IonPac AG12A, 50 mm long, 4 mm inner diameter; Dionex, United States). Based on repeated measurements of the same samples, we estimate that our analytical precision was within 0.3% and 0.4% for Cl^- and SO_4^{2-}, respectively. The hydrogen and oxygen isotopic compositions (δD and $\delta^{18}O$, respectively) of pore water samples were analyzed by laser absorption spectroscopy (LWIA-24-EP, Los Gatos Research Inc., United States). Based on repeated analyses of our laboratory standard (Indian Ocean deep seawater), standard deviations were 0.3‰ and 0.1‰ for δD and $\delta^{18}O$, respectively. Pore water dissolved inorganic carbon (DIC) concentrations and carbon isotopic compositions ($\delta^{13}C$-DIC) were analyzed by isotope ratio monitoring gas chromatography/mass spectrometry using a Thermo Finnigan Delta Plus XP isotope-ratio mass spectrometer connected to a TRACE GC as described by Ijiri et al. (2012). Values of δD and $\delta^{18}O$ are reported relative to Vienna Standard Mean Ocean Water (VSMOW); $\delta^{13}C$ results are reported relative to the Vienna Peedee Belemnite (VPDB) standard.

3.4 Hydrocarbon gas analysis

To examine the origin of hydrocarbon gases, we analyzed chemical and isotopic compositions of the hydrocarbon gases. Sediment samples for methane and ethane concentration measurements were collected using tip-cut plastic syringes immediately after core recovery. Syringe ends were tightly capped with silicone-rubber stoppers. The sediment samples were

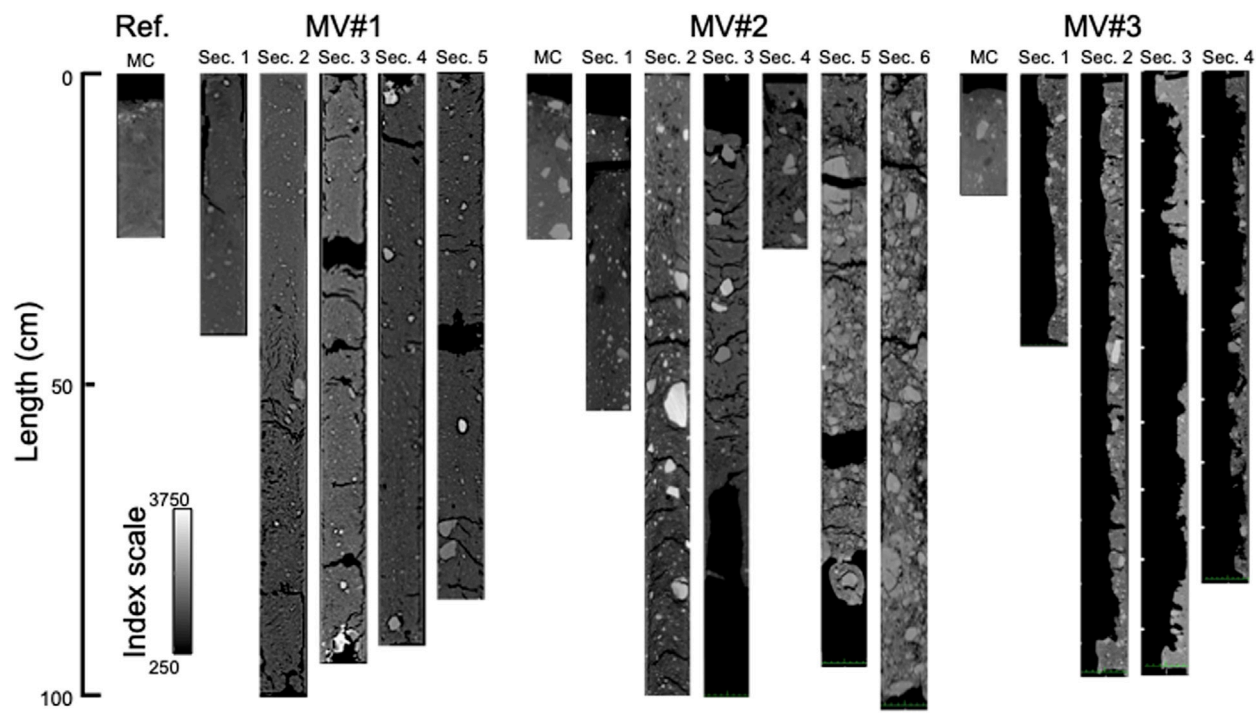

FIGURE 3
X-ray CT scans of the sediment cores obtained from MV#1–3 and the reference site. The gray scale is the index scale showing CT number.

transferred from the syringes into glass vials in a N_2-flushed glove bag, and the vials were capped with Teflon-coated rubber septa and aluminum seals, then frozen at 20°C and stored for subsequent geochemical analyses.

In an onshore laboratory, methane (CH_4) and ethane (C_2H_6) concentrations, stable carbon isotopic compositions ($\delta^{13}C$-CH_4), and stable hydrogen isotopic compositions (δD-CH_4) were determined by isotope ratio monitoring-gas chromatography and combustion mass spectrometry using a Thermo-Finnigan Delta Plus XP isotope-ratio mass spectrometer connected to a TRACE GC via a GC COMBUSTION III combustion furnace and via a High Temperature Conversion Interface, respectively, following the method of Tsunogai et al. (2002).

4 Results and discussion

4.1 Analyses of sediments

4.1.1 X-ray computed tomography images

X-ray computed tomography (CT) images of the cores from MV#1–3 showed that mud-supported breccias are included in the muddy sediments (X-ray intensity being proportional to density; Figure 3). The observed lack of sedimentary structure suggests that clasts of surrounding rocks were ripped away from their source strata and incorporated into the intruding mud diapir via hydraulic fracturing (Ujiié, 2000). Sediments from MV#2 in particular contain relatively hard, centimeter-scale clasts, especially at greater depths. However, these clasts in Section 5, Section 6 are loosely consolidated, so that they crumbled easily in hand. Note that MV#3 core was only imaged for less than half of its width due to scanning residual sediments after on-board sub-sampling. In contrast to the mud volcano sediments, the reference core did not contain any evidence of a mud breccia.

4.1.2 Sediment ages

All studied samples from the cores MV#1, MV#2, and MV#14 yielded sufficient number of calcareous nannofossils for sub-quantitative study. Samples from the core MV#3, however, varied in abundance of calcareous nannofossils. The samples from 47.5, 153.5, and 314.5 cm below seafloor (cmbsf) contained calcareous nannofossils abundantly, while the samples from 126.5 and from 263 cmbsf rarely yielded calcareous nannofossils (Supplementary Table S2).

The calcareous nannofossil assemblages of all studied samples contained long-ranged species such as the Eocene–Pleistocene species *Reticulofenestra minuta* and/or the Miocene–Pleistocene medium-sized *Reticulofenestra* species (*Reticulofenestra minuta*, *Reticulofenestra minuta/haquii, Reticulofenestra pseudoumbilicus* (5–7 μm), or *Reticulofenestra producta*) common-abundantly, as well as various Paleocene–modern species such as *Coccolithus pelagicus* in relatively low abundance. Twelve Miocene–specific species were recognized in low abundance in many samples, but the Paleocene–specific species were not recognized (Figure 4; Supplementary Table S2). These results suggest that the age of sediments of source sequence of mud volcanos is in the Miocene.

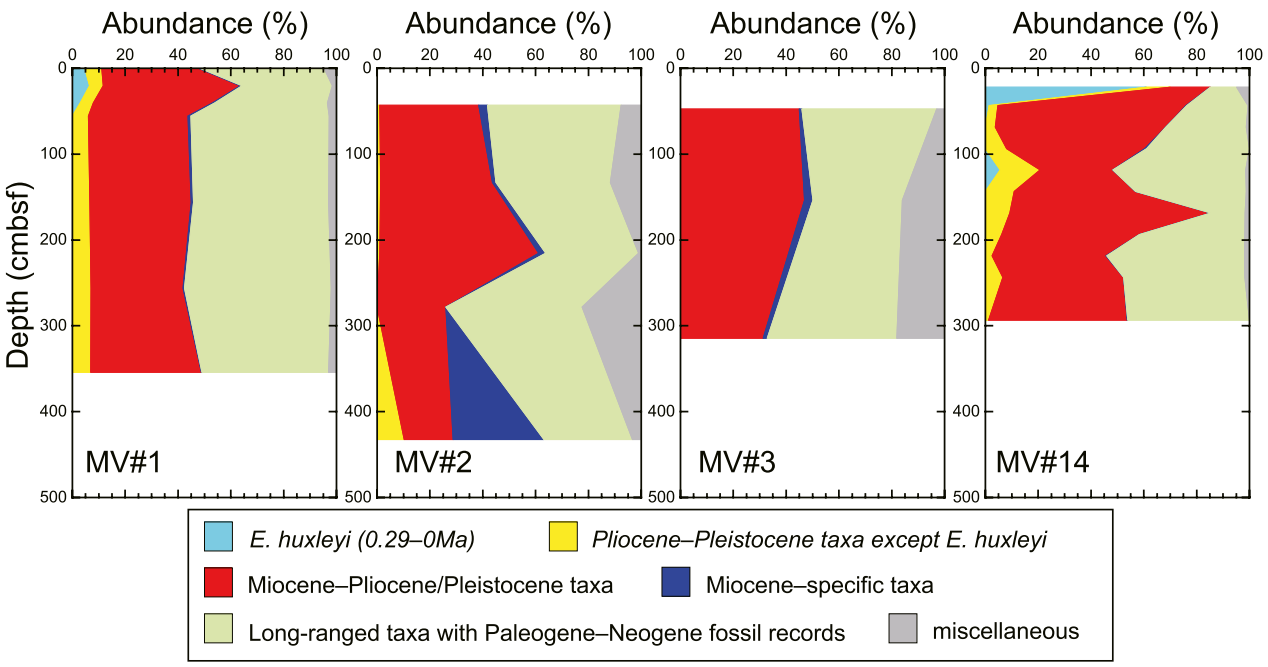

FIGURE 4
Relative abundances of calcareous nannofossils, grouped as *E. huxleyi*, *Gephyrocapsa* spp., early to late Miocene species, and other species.

Calcareous nannofossil assemblages from the uppermost sample (22 cmbsf) at MV#14 was dominated by *Emiliania huxleyi*, and lacked Miocene-specific species, suggesting that MV#14 is currently inactive and the uppermost sample (22 cmbsf) of the site was deposited after the end of mud–eruption activity in/before the *E. huxleyi* acme period (0.082 Ma–present, Raffi et al., 2006). Coexistence of *E. huxleyi* and Miocene–Pleistocene species in upper 40 cmbsf at MV#1 and around 120 cmbsf at MV#14 implies the incorporation of the Quaternary sediments by the movement of mud associated with the occasional mud eruption (Fesker et al., 2014). Ujiié (2000) reported that the Quaternary hemipelagic sediments, approximately 3.5 m thick, overlay the mud volcano sediments in MV#2, indicating that mud volcanism might have been inactive at the time of their 1994 survey. However, the absence of *E. huxleyi* in the surface sediments from MV#2 collected during 2019 survey suggests that mud eruptions may have occurred after 1994 or that the 1994 coring missed the location where mud was erupting.

The contents of ^{10}Be varied over a wide range across the four studied mud volcanoes (6–318 × 10^5 atoms g^{-1}; Figure 5A; Supplementary Table S4). At MV#1, ^{10}Be contents were relatively constant at ~115 × 10^5 atoms g^{-1} regardless of depth. At MV#3, ^{10}Be contents were ~25–50 × 10^5 atoms g^{-1}. At MV#14, ^{10}Be contents were 144–318 × 10^5 atoms g^{-1}, higher than those at the other mud volcanoes, and were greatest in the shallowest sample (22 cmbsf). At MV#2, we analyzed ^{10}Be contents in the mud breccia (>2 mm), mud matrix (2 μm–2 mm), and clay (<2 μm) fractions separately to test for any size-dependence of ^{10}Be contents (ages). Ujiié (2000) reported that the exotic fossils and clast shapes in the mud volcano sediments were torn off and taken into the mud diapir via hydraulic fracturing through an intrusive process. Therefore, we expected the ^{10}Be contents are different among the mud breccia, mud matrix, and clay. However, the ^{10}Be contents were not consistent across all particle sizes at each depth. Breccia, matrix, and clay ^{10}Be contents at 43 cmbsf were 22 × 10^5, 6 × 10^5, and 19 × 10^5 atoms g^{-1}, respectively (lowest content in the matrix, highest in the breccia); those at 216 cmbsf were 16 × 10^5, 34 × 10^5, and 30 × 10^5 atoms g^{-1}, respectively (lowest in the breccia, highest in the clay); and those at 433 cmbsf were 147 × 10^5, 272 × 10^5, and 261 × 10^5 atoms g^{-1}, respectively (lowest in the breccia and highest in the clay). More data would be required to investigate the ^{10}Be age differences depend on sediment type.

To calculate ^{10}Be ages, we used ^{10}Be data for surface sediments from two sites as initial concentrations: our reference site, off Tanegashima Island (4.4 × 10^8 atoms g^{-1}), and one in Sagami Bay, south of Honshu, central Japan (14.0 × 10^8 atoms g^{-1}), because of the wide variation in ^{10}Be contents in surface sediments ranging from 1.2 × 10^8 and 16.0 × 10^8 atoms g^{-1} (Bourles et al., 1989). The calculated ^{10}Be ages using the ^{10}Be content at the reference site ranged from 7 to 15 Ma, and those using the Sagami Bay data ranged from 5 to 13 Ma (Figure 5B). Although the estimated ages deviated by 2 Myr because of the difference in the assumed initial concentration, they are all middle to late Miocene.

This ^{10}Be age is consistent with the nannofossil assemblages which suggest that the age of the source sequence is the Miocene. Because the nannofossil observations indicate that the sediments comprise a mixture of sediments deposited at different ages, the ^{10}Be ages should be mixed values and the observed age variations are likely due to differences in the mixing ratio. Indeed, we obtained the youngest ^{10}Be age (7–5 Ma) for the highest ^{10}Be content observed at 22 cmbsf in MV#14, consistent with the dominance of *E. huxleyi* in

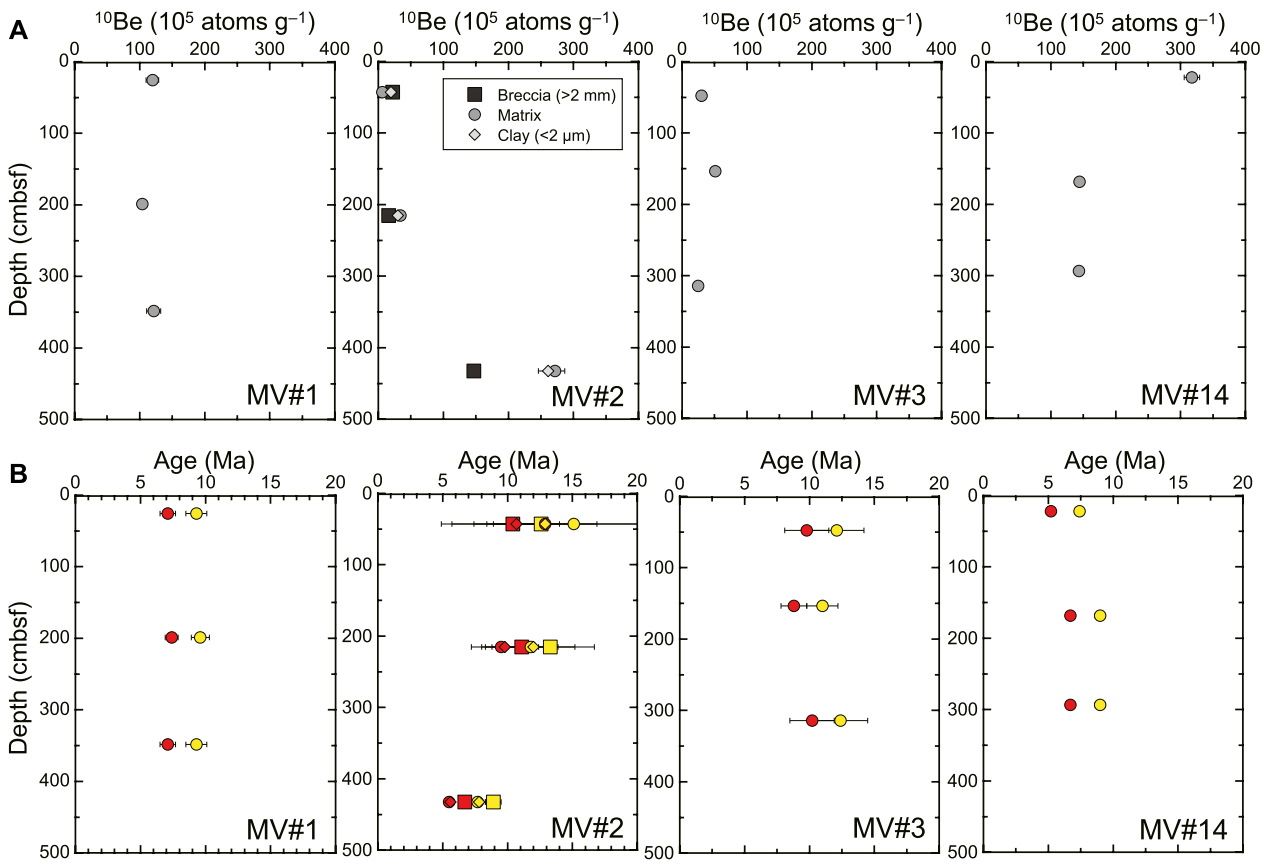

FIGURE 5
Vertical **(A)** ^{10}Be content and **(B)** estimated ^{10}Be age profiles at MV#1–3 and MV#14. In **(B)**, the red and yellow symbols represent the ages calculated using the initial concentrations of ^{10}Be assumed from the ^{10}Be concentrations in the surface sediments at the Sagami Bay and the reference site, respectively.

the nannofossil assemblage at that depth. Furthermore, the estimated ^{10}Be ages for MV#1 and MV#14 (<10 Ma) were younger than those for MV#2 and MV#3 (>10 Ma), consistent with the higher abundances of *Pliocene–Pleistocene taxa except E. huxleyi* at MV#1 and MV#14 than at MV#2 and MV#3 (Figure 4). Thus, we attribute the young ^{10}Be ages at MV#1 and MV#14 to increased mixing with younger sediments. We note that, at 432.5 cmbsf in MV#2, the ^{10}Be age was relatively young (8–6 Ma). However, *Minylitha convallis* (Zones NN9–NN11A; ~9.8–7.7 Ma) was abundant in the same sample (Supplementary Table S2), indicating good agreement between the ^{10}Be and nannofossil ages. Based on the nannofossil and ^{10}Be data, we conclude that each studied mud volcano has a middle to late Miocene source sequence. Note that depending on the proportion of younger sediments, there is a possibility that the sediments could attributed to the Early Miocene.

4.1.3 Whole-rock mineral compositions

The mud volcano sediments comprised 17–33 wt% quartz (avg. 26 wt%), 14–33 wt% illite (avg., 23 wt%), 12–19 wt% plagioclase (avg., 16 wt%), and other minerals (Figure 6A; Supplementary Table S5). Overall clay mineral contents were 32–52 wt% (illite, smectite, chlorite, and kaolinite; avg., 43 wt%), MV#1 sediments contained less pyroxene (<2 wt%) than other mud volcano sediments (3–7 wt%). MV#1 and MV#14 contained slightly more quartz (25–33 wt%) and slightly less clay minerals (32–47 wt%) than MV#2 and MV#3 (17–24 wt% quartz, 41–52 wt% clay minerals). The generally similar mineral contents of the sediments at each mud volcano (i.e., dominated by clay minerals, especially illite) implies that the mud volcanoes off Tanegashima Island are rooted in the same source sequence.

4.1.4 Mineral composition of the clay size fraction

Figure 7 shows X-ray diffractograms for ethylene-glycolated samples from MV#1–3, MV#14, and the reference site; those of the clay size fraction showed similar patterns. The X-ray diffractograms of the mud volcano sediments showed high peak intensities at $2\theta \approx 9^{\circ}$, which represents illite (001). A small peak at $2\theta \approx 5.5^{\circ}$, attributed to a mixture of discrete smectite and I/S mixed-layer clay, was hidden behind the chlorite (001) peak at $2\theta \approx 6^{\circ}$. The overlapping peaks of chlorite (002) and kaolinite (001) at $2\theta \approx 13.5^{\circ}$ were high. In the samples from deeper than 337 cmbsf in MV#2, the peak of discrete smectite and I/S mixed-layer clay was high. In that same sample, we could also identify the composite reflections of illite (001)/smectite (002) at $2\theta \approx 10^{\circ}$ and of illite (002)/smectite (003) at $2\theta \approx 16^{\circ}$. These observations indicate that illite dominates the mineralogy of the clay fraction, whereas smectite represents only a small proportion. Peak intensities in the X-ray diffractogram of the

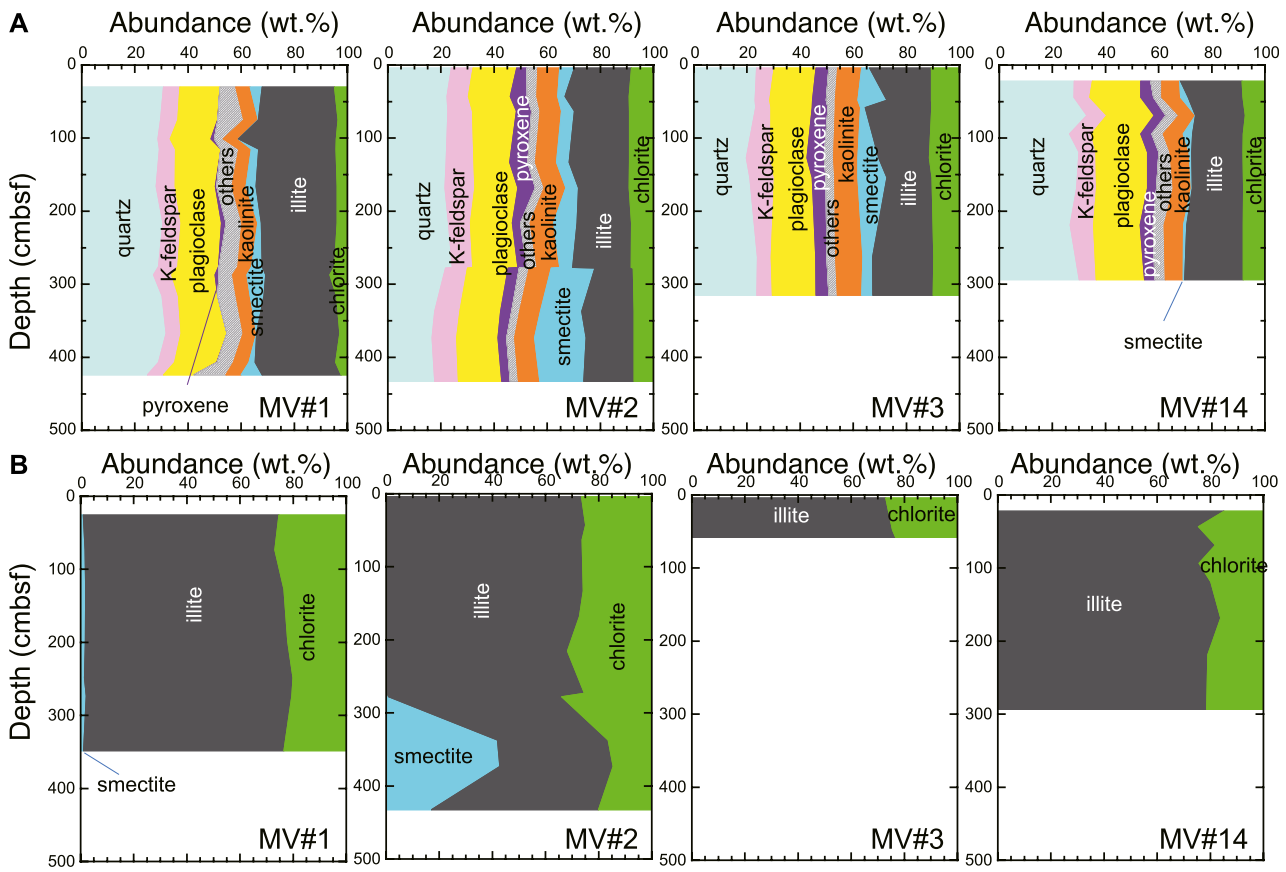

FIGURE 6
(A) Vertical profiles of whole-rock mineral compositions and **(B)** clay mineral compositions in the clay size fraction at MV#1–3 and MV#14.

reference site sample were much lower than those of the mud volcano sediments (Figure 7); in particular, the smectite peak at $2\theta \approx 5.5^{\circ}$ was subtle.

Particle size analysis showed that the clay size fraction (<2 μm) comprises 19%–28% of the mud volcano sediments and 4%–11% of the reference sediment (Supplementary Table S6).

The relative proportions of clay minerals in the clay size fraction, estimated following Biscaye (1965), are shown in Figure 6B and listed in Supplementary Table S6. Below 58 cmbsf at MV#3, the smectite peak could not be detected; therefore, we did not estimate relative clay mineral abundances at greater depths there. In most samples from MV#2 (<337 cmbsf), MV#3, and MV#14, the clay mineralogy of the clay fraction comprised <2% smectite, 65%–79% illite (avg., 74%), and 20%–34% chlorite + kaolinite (avg., 26%). At >337 cmbsf in MV#2, the smectite content increased to as high as 43%. Sediment at the reference site comprised ≲1% smectite, ~76% illite, and ~23% chlorite + kaolinite. In MV#3, the integrated peak areas for illite and chlorite + kaolinite peaks below 58 cmbsf are similar to those above 58 cmbsf (Figure 7; Supplementary Table S6). Therefore, it can be inferred that the abundance ratios of illite to chlorite + kaolinite below 58 cmbsf are similar to those above 58 cmbsf.

Overall, the clay fraction at each mud volcano was characterized by similar illite-dominated clay mineralogies. Alongside the similar whole-rock mineral compositions of sediments at each mud volcano, this finding further suggests that the mud volcanoes off Tanegashima Island are rooted in the same source sequence.

4.1.5 Vitrinite reflectance

Histograms of vitrinite reflectance at each mud volcano peaked at 0%–0.5%, with consistent median values at MV#1, MV#2, MV#3, and MV#14 of 0.42%, 0.43%, 0.44%, and 0.42%, respectively (Figure 8). Considering the thresholds for oil, wet gas, and dry gas production (0.5%–0.6%, >1.3%, and >1.7%, respectively; e.g., Tissot et al., 1987), these low reflectance values indicate that the organic matter transported to the surface at these mud volcanoes is too immature to produce oil or gas. The similar reflectance values and distributions at each mud volcano also indicate that the organic matter is derived from the same source sequence. Assuming the age of the sediment to be 15 Ma (i.e., our oldest ^{10}Be age), the experienced temperatures of organic matters for MV#1, MV#2, MV#3, and MV#14 were calculated to 81, 83, 85, and 81°C, respectively (Supplementary Table S7).

4.1.6 Constraints on the source sequence

The calcareous nannofossil assemblages, ^{10}Be ages, similar illite-dominated mineralogical compositions, and vitrinite reflectance values (~0.4%) of the sediments at the studied mud volcanoes

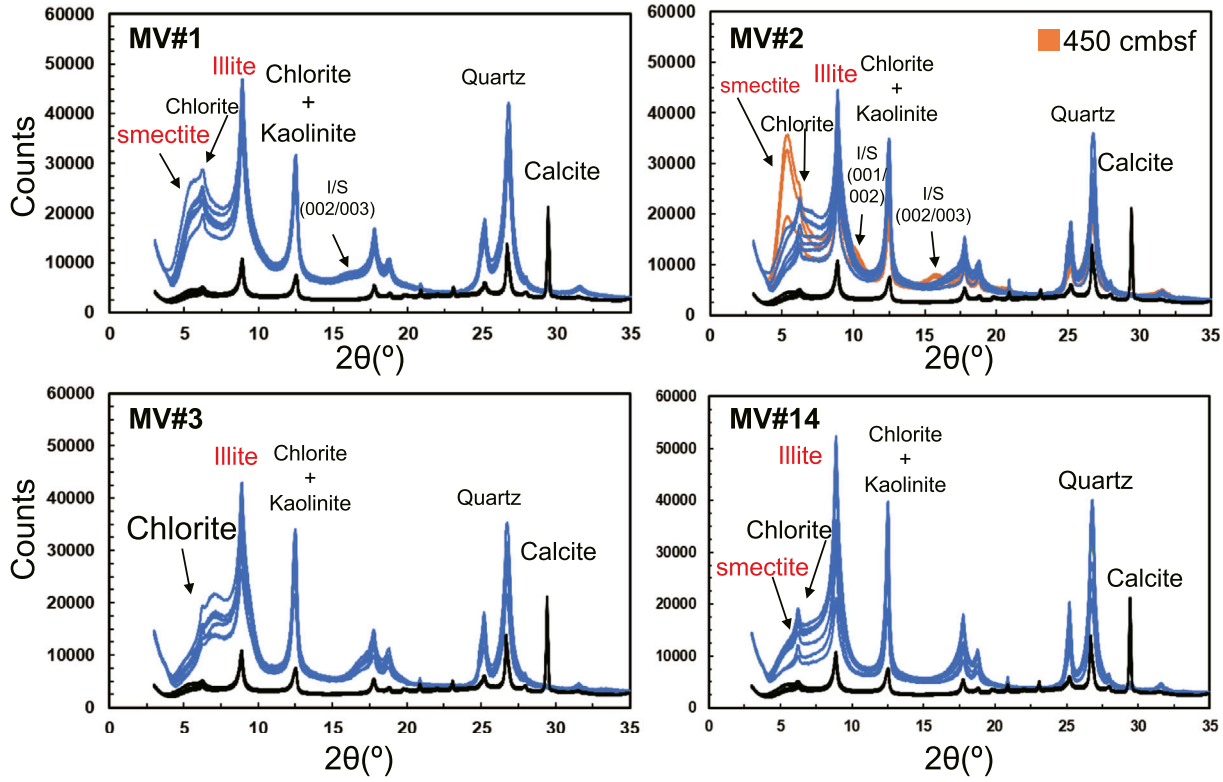

FIGURE 7
X-ray diffractograms of the clay size fraction in sediments from MV#1–3 and MV#14.

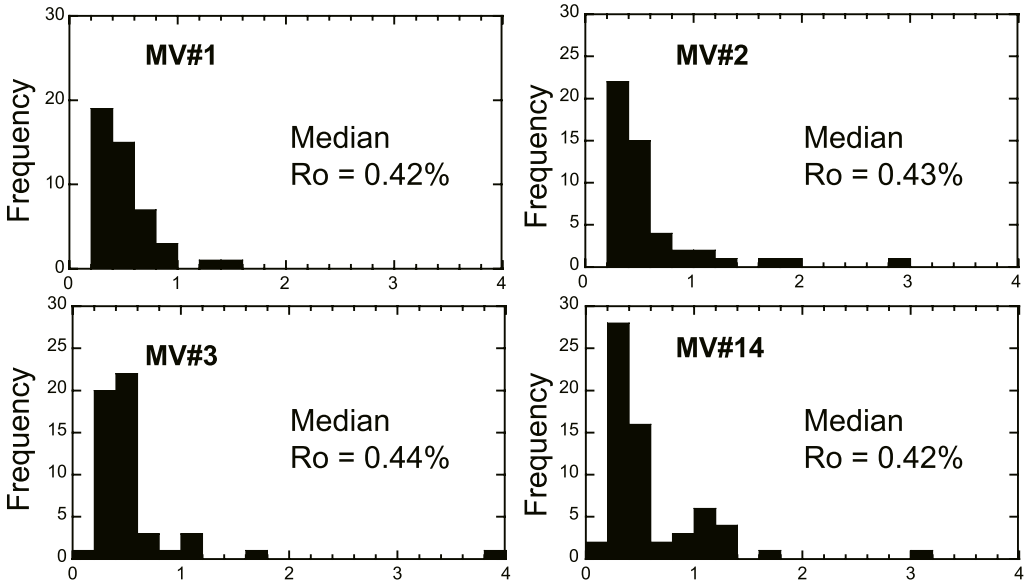

FIGURE 8
Vitrinite reflectance histograms in sediments from MV#1–3 and MV#14.

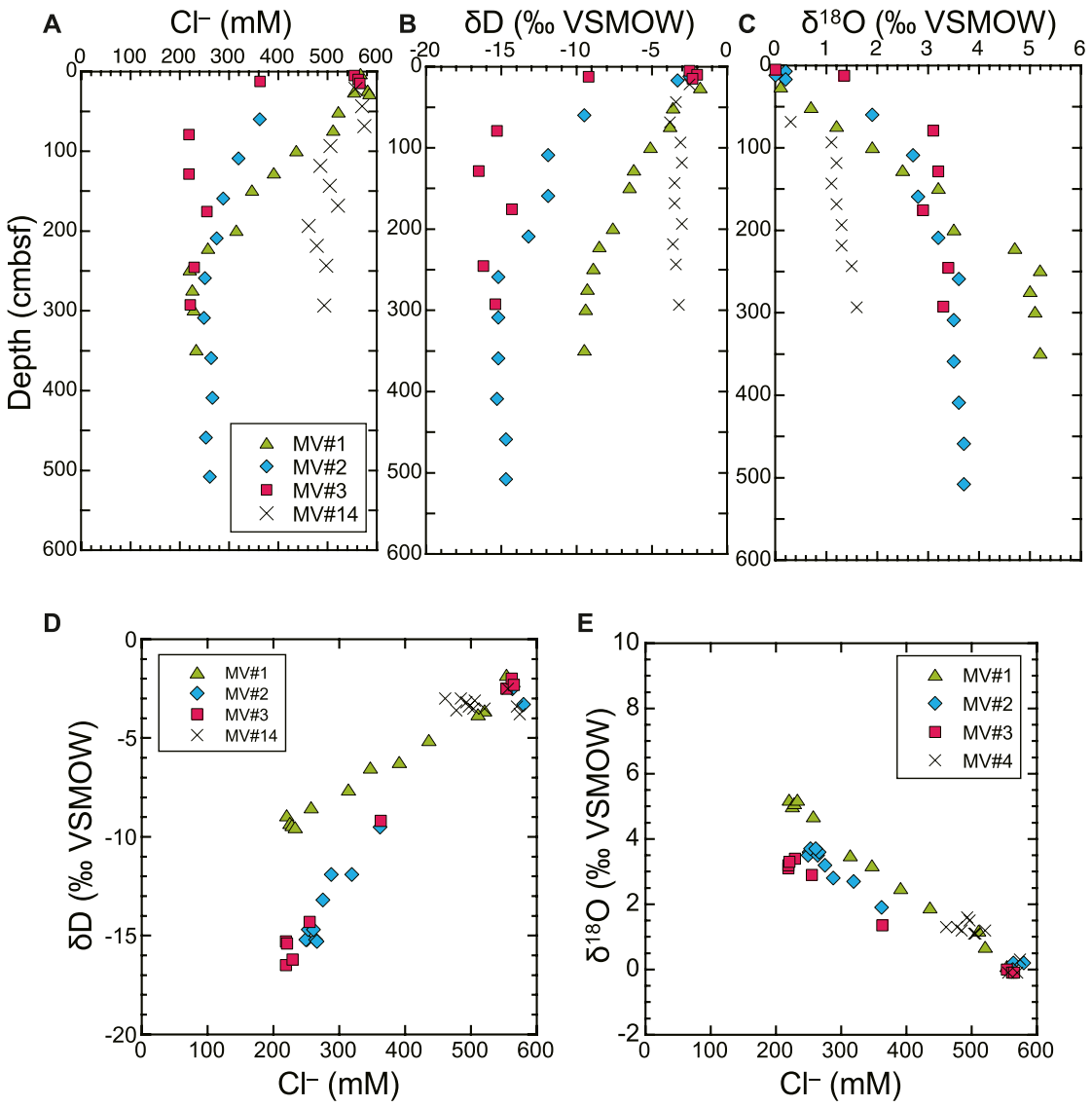

FIGURE 9
Vertical profiles of porewater **(A)** Cl^- concentrations and **(B,C)** δD and $\delta^{18}O$ values at MV#1–3 and MV#14. Plots of **(D)** Cl^- vs. δD and **(E)** Cl^- vs. $\delta^{18}O$.

strongly suggest that the mud volcano field off Tanegashima Island is rooted in the same Miocene source sequence containing immature organic matter. Although sediments at MV#1 and MV#14 are characterized by lower abundances of Miocene nannofossils, younger ^{10}Be ages, and lower clay mineral contents than MV#2 and MV#3, we attribute these differences to mixing with younger sediments.

Based on the analyzed sediment data, we can constrain the origin of the mud volcano sediments. The Upper Shimanto Group, characterized by Paleogene and lower Miocene rocks, is distributed along Tanegashima Island and the southern parts of Kyushu and Shikoku Islands (Taira et al., 1982). Thus, the group should also occur in the subseafloor in the mud volcano field off Tanegashima Island. If the age of the source sequence is early Miocene, i.e., older than our estimation, the source sediments might be accreted sediments of the Upper Shimanto Group. However, if the source sequence is middle to late Miocene as estimated here, the source sequence cannot be derived from the Shimanto Belt. Based on the experienced temperatures determined from the vitrinite reflectance values (81°C–85°C) and the local geothermal gradient of 25°C km^{-1} (Ohde et al., 2018), we estimate the depth of the source sequence to be 3.2–3.4 kmbsf.

The illite-rich sediments in the studied mud volcanoes off Tanegashima Island contrast with the smectite-rich sediments in mud volcanoes of the Kumano forearc basin (Ijiri et al., 2018b). The difference could be explained by the distribution of illite in the present surface sediments. Southeast of Kyushu Island, including our study area, illite contents are extremely high in the clay fraction of surface sediments (Aoki and Oinuma, 1988). The illite is detrital in origin, supplied to the East China Sea from mainland China by the Yangtze and Yellow Rivers (Nittrouer et al., 1984; Aoki and Oinuma, 1988) and transported from the East China Sea by the Kuroshio Current (Yin et al., 1987; Aoki and Oinuma, 1988). If the source sequence was deposited during

the Miocene, the East China Sea was not yet fully open during their deposition (e.g., Fu et al., 2022), and the illite in those sediments may have been transported directly from mainland China. Nonetheless, this variation in supply paths cannot explain the high clay mineral contents of the studied mud volcano sediments.

4.2 Porewaters and hydrocarbon gases

4.2.1 Porewater chemistry

Cl^- concentrations in pore waters at all studied mud volcanoes decreased from the seawater concentration (~560 mM) with increasing depth (Figure 9A; Supplementary Table S8). The Cl^- concentrations decreased asymptotically to ~230 mM by 250 cmbsf at MV#1, ~250 mM by 260 cmbsf at MV#2, and ~220 mM by 80 cmbsf at MV#3. In contrast, the Cl^- concentration only decreased to ~480 mM at the core bottom (294 cmbsf) at MV#14. The general asymptotic decrease of Cl^- concentrations with increasing depth at all studied mud volcanoes suggests the upward advection of low-Cl^- fluids.

Porewater δD and $\delta^{18}O$ profiles were consistent with the Cl^- profiles (Figures 9A–C; Supplementary Table S8). The δD values decreased asymptotically from ca. −2‰ near the seafloor to ca. −9‰ by 250 cmbsf at MV#1, ca. −15‰ by 260 cmbsf at MV#2, ca. −15‰ by 80 cmbsf at MV#3, and ca. −4‰ to −3‰ by 70 cmbsf at MV#14. The $\delta^{18}O$ values increased asymptotically from ~0‰ near the seafloor to ca. +5‰ by 250 cmbsf at MV#1, ca. +3.5‰ by 260 cmbsf at MV#2, ca. +3‰ by 80 cmbsf at MV#3, and +1.1‰ to +1.6‰ by 90 cmbsf at MV#14.

Plots of δD and $\delta^{18}O$ values against Cl^- concentrations reveal linear relationships at each mud volcano (Figures 9D, E), with the exception of δD vs. Cl^- at MV#14 ($R^2 = 0.01$). Enrichment in ^{18}O and depletion in D alongside depletion in Cl^- is attributed to the incorporation of freshwater due to clay-mineral dehydration, such as during the smectite-to-illite transformation that typically occurs at 60°C–160°C (Yeh, 1980; Kastner et al., 1991; You and Gieskes, 2001). Indeed, this process was previously reported at MV#1 by Nakayama et al. (2010).

Assuming that the porewater isotopic compositions result from simple mixing with freshwater [(Cl^-) = 0 mM], the $\delta^{18}O$ and δD values of the freshwater component can be estimated by extrapolating from [Cl^-] = 0 mM to the observed porewater data. We obtained extrapolated freshwater δD values at MV#1, #2, and #3 of −14‰ ± 1‰, −24‰ ± 2‰, and −25‰ ± 1‰, respectively (95% confidence interval); we did not extrapolate the δD value for MV#14 because δD was not correlated with Cl^-. We obtained extrapolated freshwater $\delta^{18}O$ values at MV#1, #2, #3, and #14 of +8.5‰ ± 0.3‰, +6.3‰ ± 0.4‰, +5.3‰ ± 0.4‰, and +8.0‰ ±3.0‰, respectively (95% confidence interval). The $\delta^{18}O$ values of the freshwater components are similar at MV#1 and MV#14 (+8.5‰ and +8.0‰, respectively) and at MV#2 and MV#3 (+6.3‰ and +5.3‰, respectively). These differences in the end member freshwater values may be due to differences in the $\delta^{18}O$ values of the source clays and/or variations in the temperature at which they dehydrated.

To constrain the reason for the different end member freshwater $\delta^{18}O$ values at each mud volcano, we calculated the formation temperature of the fluid following the method of Hensen et al. (2004). Using the estimated δD and $\delta^{18}O$ values of the freshwater component and previously reported clay–water equilibrium fractionation factors for δD (Yeh, 1980; Capuano, 1992) and $\delta^{18}O$ (Sheppard and Gilg, 1996), we estimated theoretical clay mineral δD and $\delta^{18}O$ values capable of producing the estimated δD and $\delta^{18}O$ values of the freshwater component at different temperatures (Figures 10A, B). Then, we compared previously reported H and O isotopic variations in marine clays (shaded ranges in Figure 10; Savin and Epstein, 1970; Suchecki and Land, 1983; Yeh, 1980) to the theoretical δD and $\delta^{18}O$ values calculated for clay minerals at different temperatures to constrain the fluid formation temperature (Figures 10A, B). The equilibrium fractionation curves for MV#1–3 and MV#14 intersect the $\delta^{18}O$ range of marine clays at 90, 70, 60, and 85°C, respectively, representing minimum values (Figure 10A). We could not estimate maximum values based on the $\delta^{18}O$ range because the high-temperature intersections were around 400°C, at which temperature clay-mineral dehydration should be complete. Nonetheless, we constrained the maximum formation temperature at MV#1,

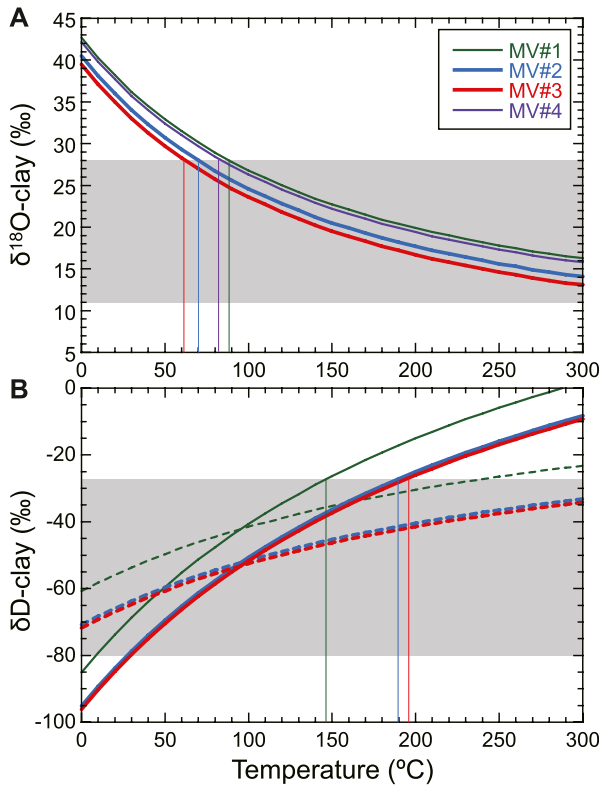

FIGURE 10
Calculation of theoretical temperatures of fluid formation assuming equilibrium fractionation between the pore fluid and clay minerals, after Hensen et al. (2004). **(A)** Theoretical $\delta^{18}O$ values of clays were calculated using fractionation factors from Sheppard and Gilg (1996) at different temperatures based on fluid endmembers for MV#1–3 and MV#14, and **(B)** theoretical δD values were calculated using fractionation factors from [Yeh (1980); dashed lines] and [Capuano (1992); solid lines]. The shaded areas indicate previously reported ranges of δD and $\delta^{18}O$ values for marine clays.

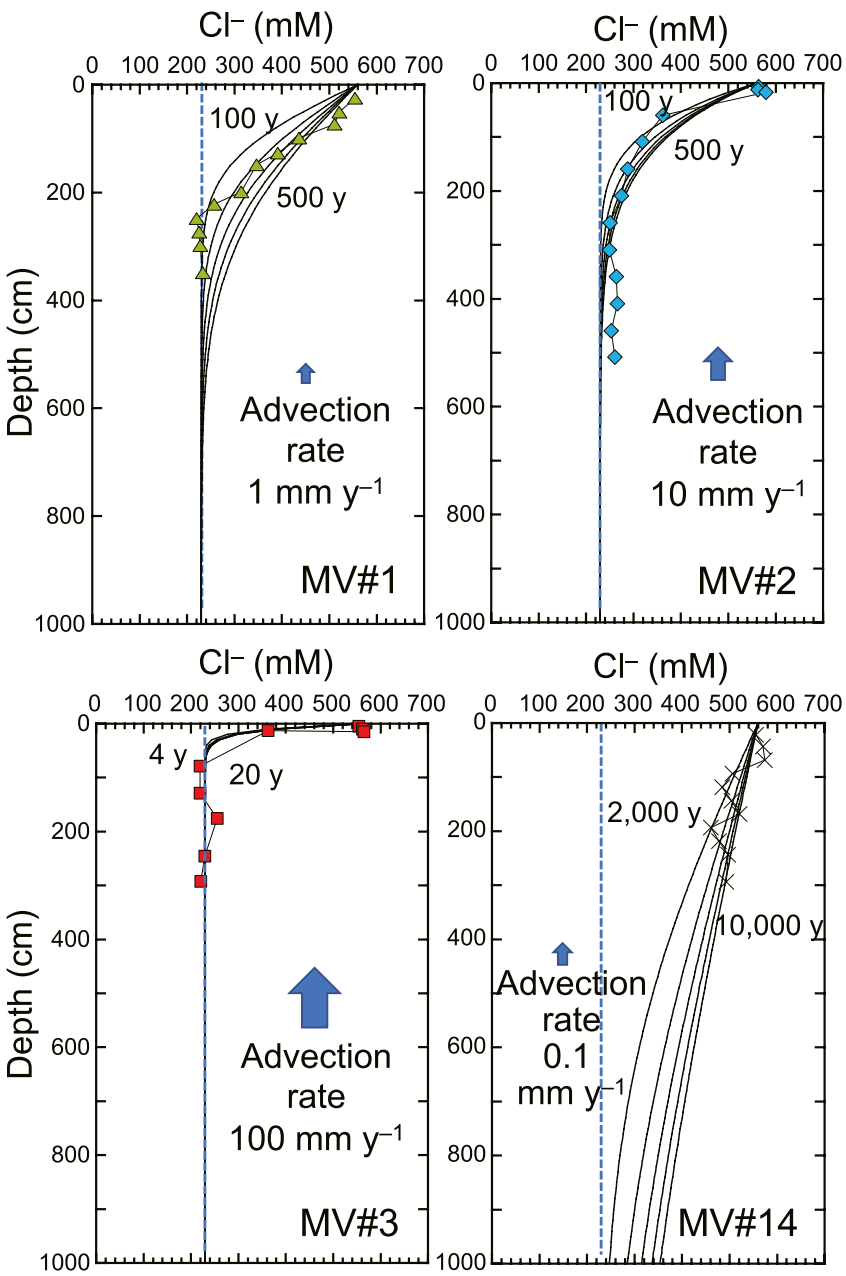

FIGURE 11
Modeled Cl^- profiles after a mud volcano eruption calculated using the one-dimensional unsteady advective diffusion model for MV#1–3 and MV#14. Dashed blue lines indicate the initial, constant Cl^- profiles just after a mud eruption.

#2, and #3 to 145, 185, and 190°C, respectively, using the δD fractionation factor of Capuano (1992) (Figure 10B). However, that fractionation factor gives low-temperature intersections below 60°C, at which temperature clay-mineral dehydration does not occur. Therefore, we estimate that the clay minerals dehydrated at 60°C–190°C, which is generally consistent with the smectite–illite transformation temperature (60°C–160°C; Yeh, 1980; Kastner et al., 1991) and estimated equilibrium temperatures of heavy noble gases at MV#1 and MV#14 (83°C–230°C; Mitsutome et al., 2023). Given the local geothermal gradient of 25°C km^{-1} (Ohde et al., 2018), we estimate that clay-mineral dehydration occurred at 2.4–7.6 kmbsf.

4.2.2 Quantitative evaluation of Cl^- profiles

To quantitatively evaluate the observed differences in the vertical Cl^- profiles, we modeled them down to 10,000 cmbsf in 10-cm increments by using the one-dimensional unsteady diffusion/advection tracer equation:

$$\frac{\partial C}{\partial t} = \frac{\partial\left(\phi D_{\mathrm{eff}} \frac{\partial C}{\partial z}\right)}{\phi \partial z} - \frac{\partial(\phi U C)}{\phi \partial z} \quad (1)$$

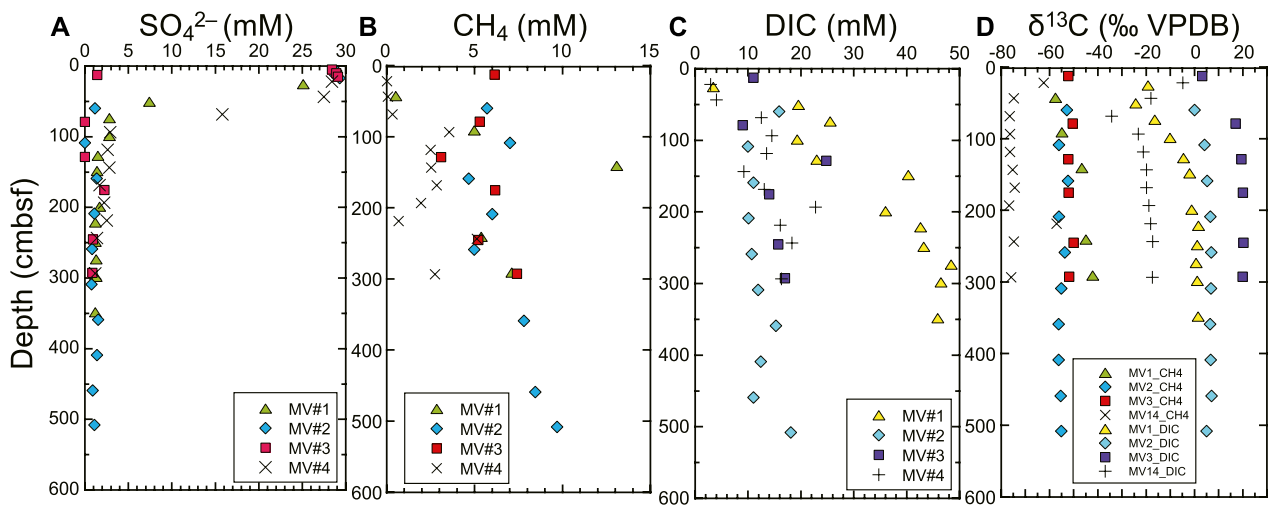

FIGURE 12
Vertical profiles of **(A)** SO_4^{2-}, **(B)** CH_4, and **(C)** DIC concentrations, and of **(D)** $\delta^{13}C$ values of methane and DIC in MV#1–3 and MV#14.

where C is the porewater Cl^- concentration, ϕ is porosity, D_{eff} is the effective diffusion coefficient of Cl^- in the sediment with respect to tortuosity, and U is the pore fluid velocity. We assumed $\phi = 0.5$, the average porosity of MV#1 sediments. We used the relationship (Van Loon and Mibus, 2015)

$$D_{eff} = D_0 \cdot \phi^{m_1} + B \cdot \phi^{m_2} \quad (2)$$

where $D_0 = 2 \times 10^{-9}$ m^2 s^{-1} is the diffusion coefficient of Cl^- in water and $m_1 = 2.4$, $m_2 = 1$, and $B = 10^{-11}$ are constants, to obtain $D_{eff} = 4.3 \times 10^{-10}$ m^2 s^{-1}. As the initial state of the Cl^- profile just after a mud eruption, we assumed the Cl^- concentration at the bottom of the MV#1 and MV#3 cores (~230 mM) to be the original value of the deep fluid, and that the Cl^- concentrations were constant from depth to the surface immediately after the eruption (dashed lines in Figure 11). Then, we estimated fluid advection rates and the time since the most recent mud eruption by comparing the numerically simulated and observed Cl^- profiles. We obtained respective advection rates and times since the most recent eruption of 10 mm y^{-1} and 100–500 years at MV#1, 1 mm y^{-1} and 100–200 years at MV#2, 100 mm y^{-1} and 4–20 years at MV#3, and 0.1 mm y^{-1} and 2,000–10,000 years at MV#4. At MV#3, the simulated Cl^- profiles change little from 4 to 20 years, indicating that the fast advection rate there mainly determines the vertical profile at steady state. In contrast, the slow advection rate and downward diffusion of seawater from the seafloor mainly determine the profile at MV#14. These results indicate that the relative levels of activity at each mud volcano are, in order of decreasing activity, MV#3, MV#2, MV#1, and MV#14, which is dormant. This result is consistent with our nannofossil observations and the conclusions of Mitsutome et al. (2023). The Cl^-profile in MV#1 sediment obtained during the 2002 survey (Nakayama et al., 2010) is similar to that obtained in this study during the 2015 survey, suggesting the activity of MV#1 has remained unchanged from 2002 to 2015.

4.2.3 Hydrocarbon gases, dissolved inorganic carbon, and sulfate

Porewater SO_4^{2-}, CH_4, and DIC concentrations and $\delta^{13}C$-CH_4 and $\delta^{13}C$-DIC values are shown in Figures 12A–D and reported in Supplementary Tables S8, S9. At MV#1, pore water contained <1 mM CH_4 at 40 cmbsf and >5 mM below 90 cmbsf. The $\delta^{13}C$-CH_4 values increased from −58‰ at 40 cmbsf to −42‰ at 290 cmbsf. Porewater SO_4^{2-} concentrations decreased from 25 mM at 25 cmbsf to 3 mM at 75 cmbsf and <2 mM below 125 cmbsf. Based on the CH_4 and SO_4^{2-} profiles, we interpret that the sulfate–methane transition zone (SMTZ), where most methane is consumed by microbial anoxic methane oxidation and microbial sulfate reduction) at MV#1 is at 70–90 cmbsf. DIC concentrations generally increased from 3 mM at 25 cmbsf to ~45 mM below 270 cmbsf, and $\delta^{13}C$-DIC values increased asymptotically from ca. −20‰ near the surface to +1‰–2‰ below 220 cmbsf.

At MV#2, CH_4 concentrations were 5–10 mM and $\delta^{13}C$-CH_4 values varied from −56‰ to −52‰, respectively, largely regardless of depth. SO_4^{2-} concentrations were ~28 mM near the seafloor and decreased to <1.5 mM below 60 cmbsf. The CH_4 and SO_4^{2-} profiles indicate that the SMTZ is within the upper 60 cmbsf. DIC concentrations varied within 10–18 mM and $\delta^{13}C$-DIC values increased asymptotically from 0‰ at 60 cmbsf to +7‰ below 210 cmbsf.

At MV#3, CH_4 concentrations were 3–7 mM and $\delta^{13}C$-CH_4 was stable at ca. −52‰ regardless of depth. SO_4^{2-} concentrations were 28 mM near the seafloor, 1 mM at 13 cmbsf in the piston core, and 0–2 mM at greater depths, placing the SMTZ near the seafloor. DIC concentrations generally increased from ~10 mM near the seafloor to 17 mM at the bottom of the core, except for an exceptionally high value of 25 mM at 130 cmbsf, and $\delta^{13}C$-DIC values increased asymptotically from +3‰ near the seafloor to ca. +20‰ below 130 cmbsf.

At MV#14, CH_4 concentrations were <1 mM in the upper 70 cmbsf and increased to 2–5 mM below 90 cmbsf (except for a

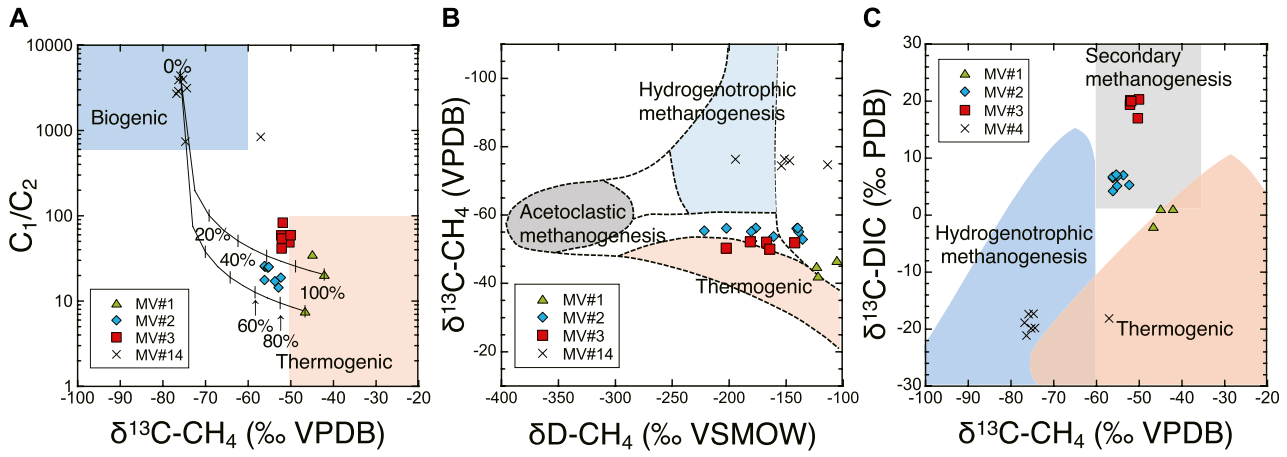

FIGURE 13
(A) C_1/C_2 ratios and $\delta^{13}C$-CH_4 values below SMTZ compared to methane sources (Bernard et al., 1976) at MV#1–3 and MV#14. Black solid lines represent the two most plausible two-end member mixing scenarios between biogenic and thermogenic hydrocarbons; percentage labels represent the contribution of thermogenic methane to the total methane content. **(B)** $\delta^{13}C$-CH_4 and δD-CH_4 values below SMTZ compared to methane sources (Whiticar, 1999). **(C)** $\delta^{13}C$-CH_4 and $\delta^{13}C$-DIC below SMTZ compared to methane sources (Milkov and Etiope, 2018). In MV#1 and MV#14, pore water sample and gas sample were collected different depths. Therefore, samples collected from similar depths were considered as the same sample, and plotted.

deviation to 0.7 mM at 219 cmbsf). $\delta^{13}C$-CH_4 values decreased from −63‰ at 22 cmbsf to ca −76‰ at greater depths (again, except for a deviation to −57‰ at 219 cmbsf). SO_4^{2-} concentrations decreased from 28 mM at 20 cmbsf to <3 mM below 95 cmbsf. The CH_4 and SO_4^{2-} profiles place the SMTZ at 70–90 cmbsf. DIC concentrations generally increased from 3 mM near the seafloor to ~18 mM at the bottom of the core. The $\delta^{13}C$-DIC values decreased from −5‰ near the seafloor to −34‰ at 94 cmbsf, then increased to −17‰ at the bottom of the core.

Based on the methane/ethane concentration ratios (C_1/C_2) and $\delta^{13}C$-CH_4 and δD-CH_4 values below the SMTZ, hydrocarbon gases at MV#1 are mostly derived from the thermal decomposition of organic matter in deep sediments (Figures 13A, B). At MV#14, these data indicate that most methane is of biogenic origin, i.e., produced by hydrogenotrophic methanogenesis. Based on the C_1/C_2 ratios and $\delta^{13}C$-CH_4 values at MV#1 and MV#14, we developed a two-end member mixing model between biogenic and thermogenic methane (Figure 13A). As the biogenic end member, we used the sample with the highest C_1/C_2 value (4,414) and the lowest $\delta^{13}C$-CH_4 value (−76‰) from MV#14. We used two different thermogenic end members: the lowest C_1/C_2 ratio (8; associated $\delta^{13}C$-CH_4 = −47‰) and the highest $\delta^{13}C$-CH_4 value (−42‰; associated C_1/C_2 = 20) from MV#1. This mixing scenario constrains the thermogenic contribution to 60%–80% of the methane at MV#2. In contrast, methane at MV#3 plots above the mixing line because of its high C_1/C_2. Below the SMTZ at MV#3, the $\delta^{13}C$-DIC values are high (ca. +20‰), and the isotope separation between $\delta^{13}C$-CH_4 and $\delta^{13}C$-DIC (expressed as the C isotopic separation factor $\varepsilon_C \approx \delta^{13}C_{DIC} - \delta^{13}C_{CH4}$) was >70‰ (Figure 13C). Despite the relatively ^{13}C-enriched CH_4 at MV#3, the large ε_C value indicates hydrogenotrophic methanogenesis (Whiticar, 1999). The addition of methane produced by hydrogenotrophic methanogenesis in a high-$\delta^{13}C$-DIC source sediment to thermogenic methane derived from greater depths was observed at a mud volcano in the Kumano forearc basin (Ijiri et al., 2018a). Such "secondary methanogenesis" may have occurred in the MV#3 mud reservoir (Milkov, 2011; Milkov and Etiope, 2018). As at MV#1–3, thermogenic methane should have been supplied to MV#14. However, because MV#14 is inactive, the present supply of thermogenic methane from deep sediments should be limited, and methanogenesis in shallower sediments likely overprinted the thermogenic signals at MV#14. Consequently, we assume that thermogenic methane was supplied to all studied mud volcanoes during their active periods, indicating that the supply of thermogenic hydrocarbon gases from a deep and hot sedimentary layer is characteristic of mud volcanism off Tanegashima Island. At IODP Site C0002 in the Kumano fore arc basin of the Nankai Trough, drilling to ~2 kmbsf reached temperatures of ~81°C–85°C, but the mixed thermogenic gas at that horizon was delivered from deeper and thus hotter sediments, indicating that no *in situ* thermogenic gas production occurs at that level (Hammerschmidt et al., 2014). Therefore, we infer that thermogenic gas production below the studied mud volcanoes does not occur below 80°C.

4.3 The difference between the depths of origin of sediments and fluids

We estimated the formation temperature for water derived from clay-mineral dehydration to be 60°C–190°C (2.4–7.6 kmbsf under the local geotherm). In contrast, the supply of thermogenic gases requires a hot temperature (>80°C), and vitrinite reflectance data and ^{10}Be ages indicate the source sediments experienced temperatures of 81°C–85°C (3.2–3.4 kmbsf under the local geotherm). The estimated temperature and depth of the source sequence are near the shallow limit for those of the fluid. However,

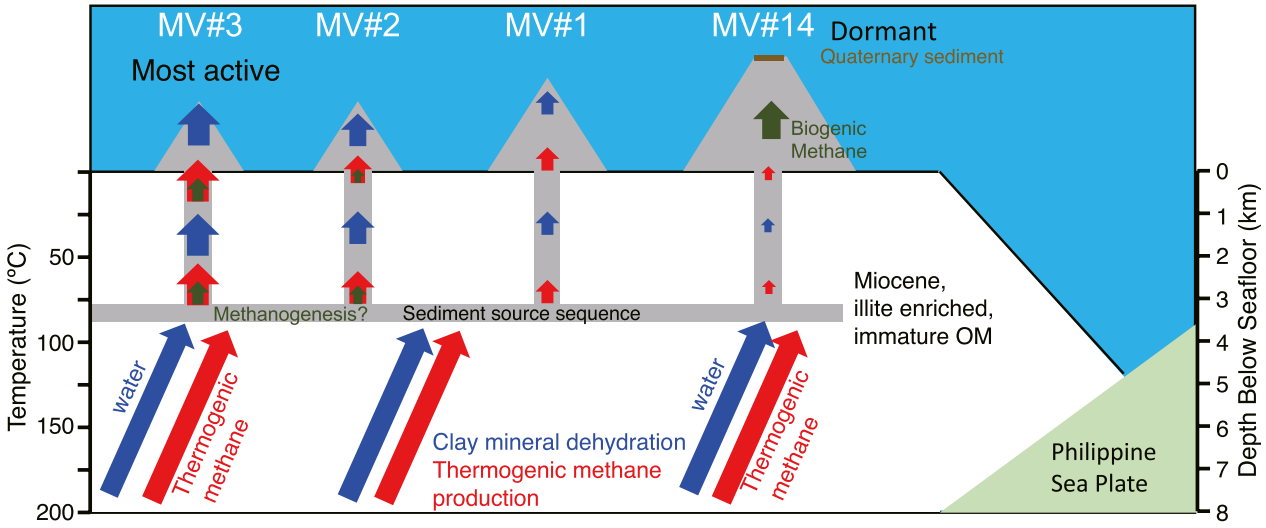

FIGURE 14
Schematic figure showing origins of sediments and fluids in MV#1–3 and MV#14.

the vitrinite reflectance values (0.42%–0.45%) indicate the source sediments to be too immature to produce thermogenic gases. Therefore, the thermogenic methane observed at the mud volcanoes off Tanegashima Island must have originated in a hotter and deeper sedimentary layer than the source sequence.

The smectite–illite transformation should also have occurred deeper than the source sequence because the smectite and illite contents in the mud volcano sediments are too small to produce the observed dilution of Cl^- in pore water by *in situ* clay diagenesis. The maximum observed porewater Cl^- depletion (~60%) in the mud volcano sediments requires the production of ~0.3 g of water per cubic centimeter of sediment at a porosity of 50% (the mean porosity measured at MV#1). Smectite in marine sediments has been found to bind 17.7–27 wt% water (Saffer and Tobin, 2011; Hüpers and Kopf, 2012), depending on environmental conditions. Assuming 20% smectite-bound water (Menapace et al., 2017), 1.5 g of smectite per cubic centimeter of sediment is required to produce 0.3 g of water per cubic centimeter of sediment. Given the mean bulk density (1.8 g cm^{-3}) and porosity (50%) of MV#1 sediments, such a smectic content exceeds the dry bulk density (1.3 g cm^{-3}). Even if all smectite was transformed to illite, the illite contents (<33 wt%) at the studied mud volcanoes are too small to produce so much water. Based on these results, we conclude that both the water and the thermogenic methane erupted by the mud volcanoes originated from greater depths than the source sequence (Figure 14).

Ijiri et al. (2018a); Ijiri et al. (2018b) reported the supply of abyssal fluids, such as water derived from clay-mineral dehydration and thermogenic gases, into the mud reservoir (i.e., the source sequence of the erupted mud) via a mega-splay fault in the accretionary prism at a mud volcano in the Kumano fore arc basin. Similarly, supply of fluids from deeper sedimentary layers to the mud reservoir was suggested in the mud volcanoes off Tanegashima Island by our study. Thus, fluids originating at greater depths than the source sediments might be typical of subduction-zone mud volcanoes. Indeed, the supply of abyssal fluids to clay mineral-rich sediments would promote mud intrusion and eruption by increasing pore water pressure. In addition, the supply of abyssal fluids has been demonstrated to stimulate microbial activity such as hydrogenotrophic methanogenesis in the mud volcano reservoir in the Kumano basin (Ijiri et al., 2018a). We also inferred such additional methanogenesis at MV#3, suggesting that fluid migration and subsequent mud volcanism in subduction zones broadly influences the deep subsurface biosphere.

5 Conclusion

We investigated the origins of sediments and fluids erupted by mud volcanoes off Tanegashima Island based on analyses of sediments and fluid obtained from four mud volcanoes, MV#1–3 and #14. Based on our results, we drew the following conclusions.

1) Using calcareous nannofossils and ^{10}Be ages, we constrained the age of the source sequence of the mud volcanoes off Tanegashima Island to the middle to late Miocene. At MV#14, Quaternary nannofossil species dominated in the surface sediment, indicating that MV#14 is dormant. The similar mineral compositions and vitrinite reflectance values of sediments erupted by the mud volcanoes strongly suggest that each is rooted in the same source sequence. Vitrinite reflectances (0.42%–0.44%) indicated that the sediments had experienced temperatures of 81°C–85°C, placing the source sequence at 3.2–3.4 kmbsf under the local geotherm.
2) Porewaters extracted from the mud volcano sediments contained ~40% the Cl^- concentration of seawater and had proportional enrichments in ^{18}O and depletions in D, indicating the addition of freshwater derived from clay-mineral dehydration. The estimated temperature, 60oC–190°C using the δD and $\delta^{18}O$

values of a freshwater end member and known equilibrium isotopic fractionation factors consistent with the optimal temperature range for the smectite–illite transformation. The smectite and illite contents (<40 wt%) in the clay size fraction rule out *in situ* smectite dewatering as the cause of the pore water Cl^- dilution. Thus, fluids derived from clay dewatering must have originated from greater depths than the source sediment.

3) We examined the relative level of activity at MV#1–3 and MV#14 based on pore water Cl^- concentration profiles and a one-dimensional unsteady advective diffusion model. In order of decreasing activity, they are MV#3, MV#2, and MV#1, whereas MV#14 is dormant (consistent with nannofossil observations).
4) At the active mud volcanoes MV#1–3, C_1/C_2 ratios (<100) and $\delta^{13}C$-CH_4 values (−57‰ to −42‰) indicate that hydrocarbon gases are mostly derived from the thermal decomposition of organic matter in deep sediments at >80°C. At MV#3, the C_1/C_2 ratios were relatively high (40–100) and the $\delta^{13}C$-DIC was high (ca. +20‰), corresponding to ε_C > 70‰, indicating the addition of biogenic methane produced by hydrogenotrophic methanogenesis to the thermogenic methane. At the inactive MV#14, C_1/C_2 ratios were in the range 700–4,000 and $\delta^{13}C$-CH_4 values were ca. −75‰, suggesting a limited supply of thermogenic methane and overprinting by subsequent shallow methanogenesis.
5) Combining these results, we concluded that that both the water and thermogenic methane in surface sediments of mud volcanoes off Tanegashima Island originate from deeper than the source sequence, as observed at mud volcanoes in the Kumano fore arc basin, Nankai Trough.

Data availability statement

The original contributions presented in the study are included in the article/Supplementary Material, further inquiries can be directed to the corresponding author.

Author contributions

AI proposed the topic, conceived and designed the study, and was responsible for the fluid analyses. RS conceived and designed the study, and conducted the entire sediments and hydrocarbon analyses. YM conducted the fluid analyses. TT was responsible for the fluid chemistry. MM was responsible for the sediment analyses. KH carried out nannofossil observation, and was responsible for nannofossil age determination. YH conducted numerical calculations for pore water diffusion-advection, and was responsible for vitrinite analysis. TY and HM conducted and were responsible for ^{10}Be analysis. WT and OT provided technical advice and were responsible for XRD analyses. KK conducted the topographic survey. TH and TN conducted sediment and fluid sampling on board. JA conducted and were responsible for the visual observation using NSS. FI proposed the topic. All authors contributed to the article and approved the submitted version.

Funding

This study was supported in part by JSPS Grant-in-Aid for Scientific Research (20H04315 and 22H05308 to AI).

Acknowledgments

We acknowledge the officers, crew, and scientific party of cruises KH-15-2, KH-19-5 of R/V *Hakuho Maru*, NT15-15 of R/V *Natsushima*, and KS-21-18 of R/V *Shinsei-Maru* for sample retrieval and technical support. The authors are grateful to A. Imajyo for technical assistance.

Conflict of interest

OT was employed by Marine Works Japan Ltd.

The remaining authors declare that the research was conducted in the absence of any commercial or financial relationships that could be construed as a potential conflict of interest.

Publisher's note

All claims expressed in this article are solely those of the authors and do not necessarily represent those of their affiliated organizations, or those of the publisher, the editors and the reviewers. Any product that may be evaluated in this article, or claim that may be made by its manufacturer, is not guaranteed or endorsed by the publisher.

Supplementary material

The Supplementary Material for this article can be found online at: https://www.frontiersin.org/articles/10.3389/feart.2023.1206810/full#supplementary-material

References

Alaoui Mhammedi, N., El Moumni, B., El Hmaidi, A., Raissouni, A., and El Arrim, A. (2008). Mineralogical and geochemical study of mud volcanoes in north Moroccan Atlantic margin. *Afr. J. Environ. Sci. Technol.* 2, 387–396. doi:10.5897/AJEST.9000077

Amin, B. S., Lal, D., and Somayajulu, B. L. K. (1975). Chronology of marine sediments using the ^{10}Be method: Intercomparison with other methods. *Geochim. Cosmochim. Acta* 39, 1187–1192. doi:10.1016/0016-7037(75)90060-5

Aoki, S., and Oinema, K. (1988). The distribution of clay minerals in surface sediments of the Okhotsk Sea to the South China Sea along the Asiatic continent. *Clay Sci.* 7, 73–82.

Backman, J., Raffi, I., Rio, D., Fornaciari, E., and Pälike, H. (2012). Biozonation and biochronology of Miocene through Pleistocene calcareous nannofossils from low and middle latitudes. *Newsletters Stratigr.* 45, 221–244. doi:10.1127/0078-0421/2012/0022

Bernard, B. B., Brooks, J. M., and andSackett, W. M. (1976). Natural gas seepage in the Gulf of Mexico. *Earth Planet. Sci. Lett.* 31, 48–54. doi:10.1016/0012-821x(76)90095-9

Biscaye, P. E. (1965). Mineralogy and sedimentation of recent deep-sea clay in the Atlantic Ocean and adjacent seas and oceans. *Geol. Soc. Am. Bull.* 76, 803–832. doi:10.1130/0016-7606(1965)76[803:masord]2.0.co;2

Bourles, D., Raisbeck, G. M., and Yiou, F. (1989). ^{10}Be and ^{9}Be in marine sediments and their potential for dating. *Geochem. Cosmochim. Acta* 53, 443–452. doi:10.1016/0016-7037(89)90395-5

Bown, P. R., and Young, J. R. (1998). "Techniques," in Calcareous nannofossil biostratigraphy: *London*. Editor P. R. Bown (Kluwer Academic Publishers), 16–28.

Brown, L. (1987). ^{10}Be: Recent applications in Earth sciences. *Philos. Trans. R. Soc. A* 323, 75–86. doi:10.1098/rsta.1987.0073

Burnham, A. K., and Sweeney, J. J. (1989). A chemical kinetic model of vitrinite maturation and reflectance. *Geochim. Cosmochim. Acta* 53, 2649–2657. doi:10.1016/0016-7037(89)90136-1

Capuano, R. M. (1992). The temperature dependence of hydrogen isotope fractionation between clay minerals and water: Evidence from a geopressured system. *Geochim. Cosmochim. Acta* 56, 2547–2554. doi:10.1016/0016-7037(92)90208-z

Dahlmann, A., and de Lange, G. J. (2003). Fluid-sediment interactions at eastern mediterranean mud volcanoes: A stable isotope study from ODP leg 160. *Earth Planet. Sci. Lett.* 212, 377–391. doi:10.1016/s0012-821x(03)00227-9

Dimitrov, L. I. (2002). Mud volcanoes - the most important pathway for degassing deeply buried sediments. *Earth-Sci. Rev.* 59, 49–76. doi:10.1016/s0012-8252(02)00069-7

Dugan, B., and Flemings, P. B. (2000). Overpressure and fluid flow in the New Jersey Continental Slope: Implications for slope failure and cold seeps. *Science* 289, 288–291. doi:10.1126/science.289.5477.288

Eberl, D. D. (2003). User guide to RockJock: A program for determining quantitative mineralogy from X-ray diffraction data. *U.S. Geol. Surv. Open File Rep.*03-78, 40. doi:10.3133/ofr200378

Feseker, T., Boetius, A., Wenzhöfer, F., Balandin, J., Olu, K., Yoerger, D. R., et al. (2014). Eruption of a deep-sea mud volcano triggers rapid sediment movement. *Nat. Commun.* 5, 5385. doi:10.1038/ncomms6385

Fu, X., Hu, L., Zhu, W., Huang, X., Feng, K., and Zhou, Z. (2022). Miocene provenance changes in taiwan caused by southward input of sediments from East China sea basin. *Front. Earth Sci.* 10, 849181. doi:10.3389/feart.2022.849181

Hammerschmidt, S. B., Wiersberg, T., Heuer, V. B., Wendt, J., Erzinger, J., and Kopf, A. (2014). Real-time drilling mud gas monitoring for qualitative evaluation of hydrocarbon gas composition during deep sea drilling in the Nankai Trough Kumano Basin. *Geochem. Trans.* 15, 15. doi:10.1186/s12932-014-0015-8

Hayasaka, S. (1988). Geology of tane-ga-shima. *Mod. Geol.* 12, 169–184.

Hensen, C., Wallman, K., Scmidt, M., Ranero, C. R., and Suess, E. (2004). Fluid expulsion related to mud extrusion off Costa Rica-A window to the subducting slab. *Geology* 32, 201–204. doi:10.1130/G20119.1

Hoshino, T., Toki, T., Ijiri, A., Morono, Y., Machiyama, H., Ashi, J., et al. (2017). Atribacteria from the subseafloor sedimentary biosphere disperse to the hydrosphere through submarine mud volcanoes. *Front. Microbiol.* 8, 1135. doi:10.3389/fmicb.2017.01135

Hüpers, A., and Kopf, A. J. (2012). Effect of smectite dehydration on pore water geochemistry in the shallow subduction zone: An experimental approach. *Geochem. Geophys. Geosyst.* 13, Q0AD26. doi:10.1029/2012GC004212

Ijiri, A., Harada, N., Hirota, A., Tsunogai, U., Ogawa, N. O., Itaki, T., et al. (2012). Biogeochemical processes involving acetate in sub-seafloor sediments from the Bering Sea shelf break. *Org. Geochem.* 48, 47–55. doi:10.1016/j.orggeochem.2012.04.004

Ijiri, A., Iijima, K., Tsunogai, U., Ashi, J., and Inagaki, F. (2018b). Clay mineral suites in submarine mud volcanoes in the Kumano forearc basin, Nankai Trough –Constraints on the origin of mud-volcano sediments. *Geosciences* 8, 220. doi:10.3390/geosciences8060220

Ijiri, A., Inagaki, F., Kubo, Y., Adhikari, R. R., Hattori, S., Hoshino, T., et al. (2018a). Deep-biosphere methane production stimulated by geofluids in the Nankai accretionary complex. *Sci. Adv.* 4, eaao4631. doi:10.1126/sciadv.aao4631

Jurado-Rodriguez, M. J., and Martinez-Ruiz, F. (1998). "Some clues about the Napoli and Milano mud volcanoes from an integrated log-core approach," in *Proceedings of the ocean drilling program scientific results*. Editors A. H. F. Robertson, K.-C. Emeis, C. Richter, and A. Camerlenghi (College Station, TX: Drilling Program), 160, 607–624.

Kastner, M., Elderfield, H., and Martin, J. B. (1991). Fluids in convergent margins: What do we know about their composition, origin, role in diagenesis and important for oceanic chemical fluxes? *Philos. Trans. R. Soc. Lond.* A335, 243–259. doi:10.1098/rsta.1991.0045

Kitada, K., Machiyama, H., Ijiri, A., Morita, S., and Inagaki, F. (2018). "Distribution and characteristics of mud volcanoes revealed by the single-channel seismic reflection survey and the near-bottom acoustic surveys using AUV off the Tanegashima Island, southwestern Japan," in *European geosciences union editor*. European geosciences union general assembly 2018 (Vienna, Austria: European Geosciences Union), 19605.

Kopf, A. J. (2002). Significance of mud volcanism. *Rev. Geophys.* 40, 2-1–2-52. doi:10.1029/2000rg000093

Manheim, F. T., and Sayles, F. L. (1974). "Composition and origin of interstitial waters of marine sediments, based on deep sea drill cores," in *The Sea, marine chemistry*. Editor E. D. Goldberg (New York, NY: Wiley-Interscience), 5, 527–568.

Martin, J. B., Kastner, M., Henry, P., LePichon, X., and Lallement, S. (1996). Chemical and isotopic evidence for sources of fluids in a mud volcano field seaward of the Barbados accretionary wedge. *J. Geophys. Res.-Solid* 101 (B9), 20325–20345. doi:10.1029/96jb00140

Matsuzaki, H., Miyake, Y., Nakashoji, K., Tokuyama, H., Tsuchiya, S. Y., Kusuno, H., et al. (2020). Current status of MALT AMS facility: A report of updated performance and recent achievement. *Nucl. Instrum. Methods Phys. Res. Sect. B Beam Interact. Mater. Atoms* 463, 55–63. doi:10.1016/j.nimb.2019.11.010

McHargue, L., and Damon, P. (1991). The global beryllium 10 cycle. *Rev. Geophys.* 29, 141–158. doi:10.1029/91rg00072

Menapace, W., Völker, D., Kaul, N., Tryon, M. D., and Kopf, A. J. (2017). The role of mud volcanism and deep-seated dewatering processes in the Nankai Trough accretionary prism and Kumano Basin, Japan. *Geochem. Geophys. Geosyst.* 18, 2486–2509. doi:10.1002/2016GC006763

Milkokv, A. V. (2011). Worldwide distribution and significance of secondary microbial methane formed during petroleum biodegradation in conventional reservoirs. *Org. Geochem.* 42, 184–207. doi:10.1016/j.orggeochem.2010.12.003

Milkov, A. V., and Etiope, G. (2018) Revised genetic diagrams for natural gases based on a global dataset of >20,000 samples. *Org. Geochem.* 125, 109–120. doi:10.1016/j.orggeochem.2018.09.002

Milkov, A. V. (2000). Worldwide distribution of submarine mud volcanoes and associated gas hydrates. *Mar. Geol.* 167, 29–42. doi:10.1016/s0025-3227(00)00022-0

Mitsutome, Y., Toki, T., Kagoshima, T., Sano, Y., Tomonaga, Y., and Ijiri, A. (2023). Estimation of the depth of origin of fluids using noble gases in the surface sediments of submarine mud volcanoes off Tanegashima Island. *Sci. Rep.* 13, 5051. doi:10.1038/s41598-023-31582-z

Moore, D. M., and Reynolds, R. C., Jr. (1997). *X-Ray diffraction and the identification and analysis of clay minerals*. 2nd edition. New York: Oxford University Press, 270–276.

Nakayama, N., Ashi, J., Tsunogai, U., Gamo, T., and Tanahashi, M. (2010). Sources of pore water in a Tanegashima mud volcano inferred from chemical and stable isotopic studies. *Geochem. Jour.* 44, 561–569. doi:10.2343/geochemj.1.0094

Nishiizumi, K., Imamura, M., Caffee, M. W., Southon, J. R., Finkel, R. C., and McAninch, J. (2007). Absolute calibration of ^{10}Be AMS standards. *Nucl. Instrum. Methods Phys. Res. Sect. B Beam Interact. Mater. Atoms* 258, 403–413. doi:10.1016/j.nimb.2007.01.297

Nittrouer, C. A., McKee, B. A., and DeMaster, D. J. (1984). Fine-scale stratigraphy in proximal and distal deposits of sediment dispersal systems in the East China Sea. *Mar. Geol.* 61, 13–24. doi:10.1016/0025-3227(84)90105-1

Ohde, A., Otsuka, H., Kioka, A., and Ashi, J. (2018). Distribution and depth of bottom simulating reflectors in the Nankai subduction margin. *Earth Planets Space* 70, 60. doi:10.1186/s40623-018-0833-5

Pape, T., Geprägs, P., Hammerschmidt, S., Wintersteller, P., Wei, J., Fleischmann, T., et al. (2014). Hydrocarbon seepage and its sources at mud volcanoes of the Kumano forearc basin, Nankai Trough subduction zone. *Geochem. Geophys. Geosyst.* 15, 2180–2194. doi:10.1002/2013GC005057

Raffi, I., Backman, J., Fornaciari, E., Palike, H., Rio, D., Lourens, L. J., et al. (2006). A review of calcareous nannofossil astrobiochronology encompassing the past 25 million years. *Quat. Sci. Rev.* 25, 3113–3137. doi:10.1016/j.quascirev.2006.07.007

Saffer, D. M., and Tobin, H. J. (2011). Hydrogeology and mechanics of subduction zone forearcs: Fluid flow and pore pressure. *Annu. Rev. Earth. Planet. Sci.* 39, 157–186. doi:10.1146/annurev-earth-040610-133408

Savin, S. M., and Epstein, S. (1970). The oxygen and hydrogen isotope geochemistry of clay minerals. *Geochim. Cosmochim. Acta* 34, 25–42. doi:10.1016/0016-7037(70)90149-3

Schulz, H. -M., Emeis, K.-C., and Volkmann, N. (1997). Organic carbon provenance and maturity in the mud breccia from the Napoli mud volcano: Indicators of origin and burial depth. *Earth Planet. Sc. Lett.* 147, 141–151. doi:10.1016/s0012-821x(97)00013-7

Sheppard, S. M. F., and Gilg, H. A. (1996). Stable isotope geochemistry of clay minerals. *Clay Min.* 31, 1–24. doi:10.1180/claymin.1996.031.1.01

Suchecki, R. K., and Land, L. S. (1983). Isotopic geochemistry of burial-metamorphosed volcanogenic sediments, great valley sequence, northern California. *Geochim. Cosmochim. Acta* 47, 1487–1499. doi:10.1016/0016-7037(83)90308-3

Sweeney, J. J., and Burnham, A. K. (1990). Evaluation of a simple model of vitrinite Reflectance based on chemical kinetics. *Am. Assoc. Pet. Geol. Bull.* 74, 1559–1570. doi:10.1306/0C9B251F-1710-11D7-8645000102C1865D

Taira, A., OkadaWhitaker, H. J. H. McD., and Smith, A. J. (1982). "The Shimanto belt of Japan: Cretaceous-Lower Miocene sedimentation in forearc basin to deep sea trench environments," in *Trench-forearc geology spec*. Editor J. K. Leggett (London: Publs geol. Soc. Lond.), 10, 5–26.

Tanikawa, W., Sakaguchi, M., Wibowo, H. T., Shimamoto, T., and Tadai, O. (2010). Fluid transport properties and estimation of overpressure at the Lusi mud volcano, East Java Basin. *Eng. Geol.* 116 (1–2), 73–85. doi:10.1016/j.enggeo.2010.07.008

Tanikawa, W., and Tadai, O. (2018). Data Report for quantitative analysis of mineral composition using powdered X-ray diffraction method and RockJock program. *JAMSTEC Rep. Res. Dev.* 27, 57–67. doi:10.5918/jamstecr.27.57

Tissot, B. P., Pelet, R., and Ungerer, P. H. (1987). Thermal history of sedimentary basins, maturation indices, and kinetics of oil and gas generation. *AAPG Bull.* 71 (12), 1445–1466. doi:10.1306/703C80E7-1707-11D7-8645000102C1865D

Tsunogai, U., Yoshida, N., and Gamo, T. (2002). Carbon isotopic evidence of methane oxidation through sulfate reduction in sediment beneath cold seep vents on the seafloor at Nankai Trough. *Mar. Geol.* 187, 145–160. doi:10.1016/S0025-3227(02)00263-3

Ujiié, Y. (2000). Mud diapirs observed in two piston cores from the landward slope of the northern Ryukyu Trench, northwestern Pacific Ocean. *Mar. Geol.* 163, 149–167. doi:10.1016/S0025-3227(99)00113-9

Van Loon, L. R., and Mibus, J. (2015). *A modified version of archie's law to estimate effective diffusion coefficients of radionuclides in argillaceous rocks and its application in safety analysis studies*. doi:10.1016/j.apgeochem.2015.04.002

Wallmann, K., Drews, M., Aloisi, G., and Bohrmann, G. (2006). Methane discharge into the Black Sea and the global ocean via fluid flow through submarine mud volcanoes. *Earth Planet. Sc. Lett.* 248, 545–560. doi:10.1016/j.epsl.2006.06.026

Whiticar, M. J. (1999). Carbon and hydrogen isotope systematics of bacterial formation and oxidation of methane. *Chem. Geol.* 161, 291–314. doi:10.1016/s0009-2541(99)00092-3

Yeh, H. W. (1980). Ratios and late-stage dehydration of shales during burial. *Geochim. Cosmochim. Acta* 44, 341–352. doi:10.1016/0016-7037(80)90142-8

Yin, J., Okada, H., and Labeyrie, L. (1987). Clay mineralogy of slope sediments around the Japanese Islands. *Geosci. Repts. Shizuoka Univ.* 13, 41–65.

Yokoyama, Y., Yamane, M., Nakamura, A., Miyairi, Y., Horiuchi, K., Aze, T., et al. (2019). *In-situ* and meteoric 10Be and 26Al measurements: Improved preparation and application at the university of Tokyo. *Nucl. Instrum. Methods Phys. Res. Sect. B Beam Interact. Mater. Atoms* 455, 260–264. doi:10.1016/j.nimb.2019.01.026

You, C.-F., and Gieskes, J. M. (2001). Hydrothermal alteration of hemi-pelagic sediments: Experimental evaluation of geochemical processes in shallow subduction zones. *Appl. Geochem* 16, 1055–1066. doi:10.1016/s0883-2927(01)00024-5

frontiers | Frontiers in Earth Science

TYPE Original Research
PUBLISHED 10 August 2023
DOI 10.3389/feart.2023.1205211

Check for updates

OPEN ACCESS

EDITED BY
Glen T. Snyder,
The University of Tokyo, Japan

REVIEWED BY
Renat Shakirov,
V.I. Il'ichev Pacific Oceanological Institute (RAS), Russia
Pawan Dewangan,
Council of Scientific and Industrial Research (CSIR), India

*CORRESPONDENCE
Nancy G. Prouty,
nprouty@usgs.gov

RECEIVED 13 April 2023
ACCEPTED 31 July 2023
PUBLISHED 10 August 2023

CITATION
Rudebusch JA, Prouty NG, Conrad JE, Watt JT, Kluesner JW, Hill JC, Miller NC, Watson SJ and Hillman JIT (2023), Diving deeper into seep distribution along the Cascadia convergent margin, United States. *Front. Earth Sci.* 11:1205211. doi: 10.3389/feart.2023.1205211

COPYRIGHT
© 2023 Rudebusch, Prouty, Conrad, Watt, Kluesner, Hill, Miller, Watson and Hillman. This is an open-access article distributed under the terms of the Creative Commons Attribution License (CC BY). The use, distribution or reproduction in other forums is permitted, provided the original author(s) and the copyright owner(s) are credited and that the original publication in this journal is cited, in accordance with accepted academic practice. No use, distribution or reproduction is permitted which does not comply with these terms.

Diving deeper into seep distribution along the Cascadia convergent margin, United States

Jane A. Rudebusch[1], Nancy G. Prouty[1]*, James E. Conrad[1], Janet T. Watt[1], Jared W. Kluesner[1], Jenna C. Hill[1], Nathaniel C. Miller[2], Sally J. Watson[3,4] and Jess I. T. Hillman[5]

[1]United States Geological Survey, Pacific Coastal and Marine Science Center, Santa Cruz, CA, United States, [2]United States Geological Survey, Woods Hole Coastal and Marine Science Center, Woods Hole, MA, United States, [3]National Institute of Water and Atmospheric Research (NIWA), Wellington, New Zealand, [4]Institute of Marine Science, University of Auckland, Auckland, New Zealand, [5]GNS Science, Lower Hutt, New Zealand

Previous margin-wide studies of methane seep distribution along the Cascadia Subduction Zone indicate peaks in seep density within the landward limit of the of gas hydrate stability zone (GHSZ; ≤500 m depth), suggesting a link between current ocean warming, acceleration of hydrate dissociated, and methane emissions. This inferred connection, however, may not account for regional geologic and/or structural complexities driving methane seepage. Expanding upon an existing seep database by adding new seep data, we conducted statistical and spatial analyses to determine margin-wide distribution trends and offer a tectonic framework for understanding the tendency toward non-normality and spatial clustering. We then highlight the role of local-scale drivers of seep formation in addition to the first-order tectonic framework, using systematic geologic/geomorphic characterization of seep emission sites in southern Cascadia and case studies using meta-attribute analysis of seismic reflection data. Seep distribution along the margin is non-random, but instead of clustering along the 500-m isobath, regions of high seep density occur in canyons and topographic highs. New findings from this study conclude that co-location of the outer arc high (OAH) and the landward limit of the GHSZ may explain high concentrations of seeps where deformation is the greatest and hydrates are unstable. Detailed analysis of the spatial relationships between seep sites and geologic-geomorphic features in southern Cascadia reveal a link between seeps and anticlines, with 52% of the seeps found in association with anticlines, 36% found at faults, 16% associated with canyons, and 11% at seafloor failure scarps. Given that a majority of anticlines are located along or seaward of the OAH in the actively deforming outer wedge, we suggest that the location of the OAH is a primary structural control on seep distribution. This scenario is supported by neural network analysis of multichannel seismic data revealing zones of probable fluid migration along vertical pipes, faults, and chimneys in the vicinity of active seep sites on anticlines. Determining linkages between seeps and submarine tectonic geomorphology is a crucial first step for understanding and forecasting the distribution of methane seepage, but also a necessity for evaluating causal relationships between ocean warming and gas hydrate stability.

KEYWORDS

methane plume, cold seep, hydrate, Cascadia, fluid-trapping, gas chimney

1 Introduction

Warming of ocean-bottom waters has been linked to hydrate dissociation at the landward limit of the gas hydrate stability zone (GHSZ) in the Southern Ocean (Ketzer et al., 2020) and Arctic Ocean (Westbrook et al., 2009; Berndt et al., 2014), and has been suggested as a mechanism to explain the high frequency of seep emissions along the 500-m isobath off the Oregon and Washington coasts (Hautala et al., 2014; Johnson et al., 2015). For example, Merle et al. (2021) reported a nearly bell-shaped normal distribution curve in the depth-frequency of over 1,300 emission sites along the Washington and northern/central Oregon margin that correlates with the landward limit of the GHSZ, suggesting a link between methane release and ocean warming. Emissions of hydrogen sulfide, methane, and other hydrocarbon-rich fluids into the sediment and water column are well documented and widespread along the Cascadia margin (e.g., Johnson et al., 2015; Riedel et al., 2018; Merle et al., 2021), with precipitates of slow growing methane-derived authigenic carbonates suggesting fluid seepage over thousands of years (Bohrmann et al., 1998; Suess et al., 1999; Teichert et al., 2003; Torres et al., 2009; Johnson et al., 2015; Paull et al., 2015). In addition, the occurrence of bottom simulating reflectors (BSRs), the boundary between hydrate-containing sediment overlying sediment that contains free gas (Trehu et al., 1995), over large areas suggests a high abundance of hydrates and trapped free gas below along the Cascadia margin accretionary complex (Tréhu et al., 2004; Torres et al., 2009). Gas hydrates are stable over moderate-pressure (P) conditions and a range of low temperatures (T) found close to the seafloor at deepwater continental slopes sites with sufficient methane saturation (Canfield et al., 2005; Collett, 2009). Changes to the P-T stability conditions, such as ocean warming, can drive the breakdown (e.g., dissociation) of hydrates (see review by Ruppel and Waite, 2020). However, these temporal processes are superimposed on long-lived geologic controls of fluid migration that define seep characteristics and help explain the driving mechanisms of fluid expulsion (Judd and Hovland, 2007; Suess, 2014). Therefore, a detailed geospatial analysis of seep distribution, including newly acquired data from southern Cascadia, is needed in order to determine if there is a link between current ocean warming and seep distribution along the Cascadia margin.

To address this knowledge gap and further explore geologic controls on focused seep distribution along the Cascadia margin, we examine new water-column data from U.S. Geological Survey (USGS) seafloor mapping activities on the National Oceanic and Atmospheric Administration (NOAA) Hydrographic Survey Vessels *Rainier* and *Fairweather* from 2018 to 2021, as well as from both active and relict (or dormant) seep indicators such as authigenic carbonates and microbial mats to supplement the existing seep composite database (Merle et al., 2021). To develop a tectonic framework of seep emissions based on geologic controls, along-margin variation in seep distribution is investigated in the context of morphotectonic regions and seismogenic behavior. In particular, we integrate new multibeam bathymetry, backscatter data, and seismic reflection profiles in southern Cascadia to

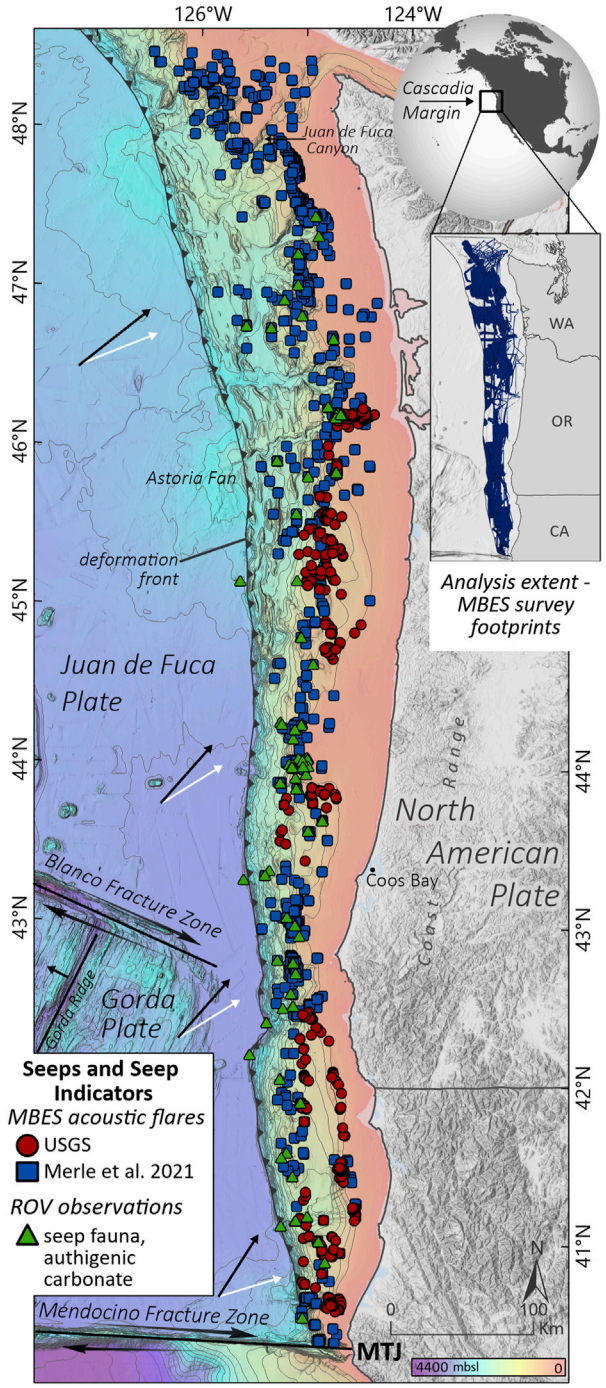

FIGURE 1
Regional overview map of the Cascadia convergent margin with the locations of seeps according to the data reference source. Inset shows the extents of the multibeam sonar surveys from which seep data were derived and that was used as a bounding polygon of the analysis extent. Topo-bathymetry is from Ryan et al. (2009). Black arrows indicate relative plate between the Juan de Fuca and Gorda plates and North America (DeMets et al., 2010); white arrows, relative plate motions between the Juan de Fuca and Gorda plates and Oregon Coast Range (Wells et al., 2002; McCaffrey et al., 2007). Isobaths (gray contour lines) are set at 200 m depth intervals from zero.

determine potential controls on focused fluid flow in an area with previously sparse coverage. With this updated composite dataset, we examine regional variation in the depth distribution of methane seeps along the Cascadia margin and test our hypothesis that seep distribution is fundamentally tied to first- and second-order geological phenomena that operate independently of gas hydrate dissociation in response to contemporary ocean warming.

1.1 Geologic setting

The Cascadia Subduction Zone (CSZ) is an active plate boundary where the Juan de Fuca, Gorda, and Explorer plates subduct beneath the North American plate. This convergent boundary extends over 1,300 km from the Nootka fracture zone offshore British Columbia (Canada) in the north (Audet et al., 2008) to the Mendocino triple junction offshore northern California (United States) in the south (Figure 1). A large accretionary wedge composed of both terrigenous and marine sediments has been accreted to the North America plate along the CSZ. This wedge contains a series of folded and thrusted ridges striking subparallel to the continental slope that form large anticlines (Cochrane and Lewis, 1984; Goldfinger et al., 1991). There is also significant along-strike geophysical and geologic heterogeneity that has been linked to different modes and rates of stress accumulation and release along the margin (see summary in Walton et al., 2021). Such variability could reflect differences in sediment and pore-fluid properties that ultimately influence fluid migration due to rapid compaction and dewatering rates (Tréhu et al., 2004; Han et al., 2017). For example, high glacial sediment flux during the Pleistocene significantly expanded the size of the outer wedge in northern Cascadia, between Juan de Fuca and Astoria Canyons (Silver, 1972; Barnard, 1973).

Broadly, the offshore accretionary wedge can be divided into two margin-parallel zones separated by the outer arc high (OAH), which is defined as a broad structural high that bounds the seaward edge of the shelf forearc basins (e.g., von Huene and Scholl, 1991; Clift and Vannucchi, 2004; McNeill and Henstock, 2014). While the OAH typically follows the shelf break along the 200-m isobath in Cascadia, deviations from the shelf break, both landward and seaward are observed, and may be linked to regional variations in the width of the outer wedge. Watt and Brothers (2020) identified four distinct morphotectonic regions based on careful examination of geophysical examination of seismic profiles to describe variable accretionary wedge width, shape, and structural vergence. These four regions include: (1) Vancouver Island, British Columbia, Canada (average width, linear wedge, seaward and mixed vergence); (2) Washington, United States (higher width, concave wedge, landward and mixed vergence); (3) northern and central Oregon, United States (average width, linear and convex wedge, mixed and seaward vergence); and (4) southern Oregon and northern California, United States (lower width, convex wedge, seaward and mixed vergence). Regional patterns and differences in the tectonic evolution of the outer accretionary wedge are also linked to Cascadia margin-wide heterogeneity in the distribution and character of the BSR (Tréhu and Phrampus, 2022). For example, BSRs were observed beneath anticlines where internal deformation of the wedge replenishes the supply of methane to the GHSZ at the crest of the anticlines by compacting sediments and providing pathways to the shallow subsurface (Tréhu and Phrampus, 2022). Therefore, tectonic factors influencing the occurrence and disruption of the BSR and associated fluid expulsion are also important in constraining the spatial distribution of cold seeps along the Cascadia margin.

2 Data and methods

2.1 Seafloor mapping and seep database

The seep database includes previously published data documenting over 2,850 active seep flares on the seafloor using ship-based multibeam echo-sounding (MBES) sonar (Johnson et al., 2015; Riedel et al., 2018; Merle et al., 2021), and 902 new seep flares identified during surveys by the NOAA Ships *Rainier* in 2018 (surveys H13117, H13118, H13119, H13137, and H13206) and *Fairweather* in 2019 and 2021 (surveys W00474, W00475, and H13549) (Conrad and Rudebusch, 2023; Supplementary Table S1). Bubble plumes associated with seeps were mapped in the MBES water column backscatter data using QPS FMMidwater software, using techniques and identification criteria similar to those described by Merle et al. (2021). The geologic setting of the bubble plume locations was determined from interpretation of the morphologic and bottom characteristics of the seafloor from multibeam bathymetry and backscatter data (https://www.ncei.noaa.gov/maps/bathymetry/) and from subbottom data derived from seismic reflection profiles (Balster-Gee et al., 2023a). In addition, evidence for both active and relict (or dormant) seep indicators including authigenic carbonates, vesicomyid clams, tubeworms, and microbial mats, were included from seafloor observations and collections made using remotely operated vehicles (ROVs) (Supplementary Table S1). The inclusion of seep evidence from ROVs proved useful for revealing additional seep locations that were not detected by traditional ship hull-mounted multibeam echosounders. Therefore, seep-distribution reported here is a presence-pseudoabsence dataset, not presence-absence. Diffuse seepage, where gas concentrations are not sufficient for gas phase emissions, was not included given the difficulty in identifying diffuse seepage acoustically. Following previously published methods of Johnson et al. (2015) for removing possible double-counted seeps due to overlapping surveys, we aggregated seeps found within 300 m of each other into single seep "emission site," yielding a dataset of 880 seep emission sites for a new composite database (Supplementary Table S1). To account for variance in surface area of the depth contour polygons and the effect of unequal survey effort across depth bins, we included only seeps detected via MBES so that we could normalize the number of seeps with the corresponding area mapped and determine seep density.

2.2 Statistical analysis

Survey footprints derived from the bathymetry of the corresponding MBES surveys used to acquire seep locations were loaded into a GIS and merged into a single polygon layer. This layer

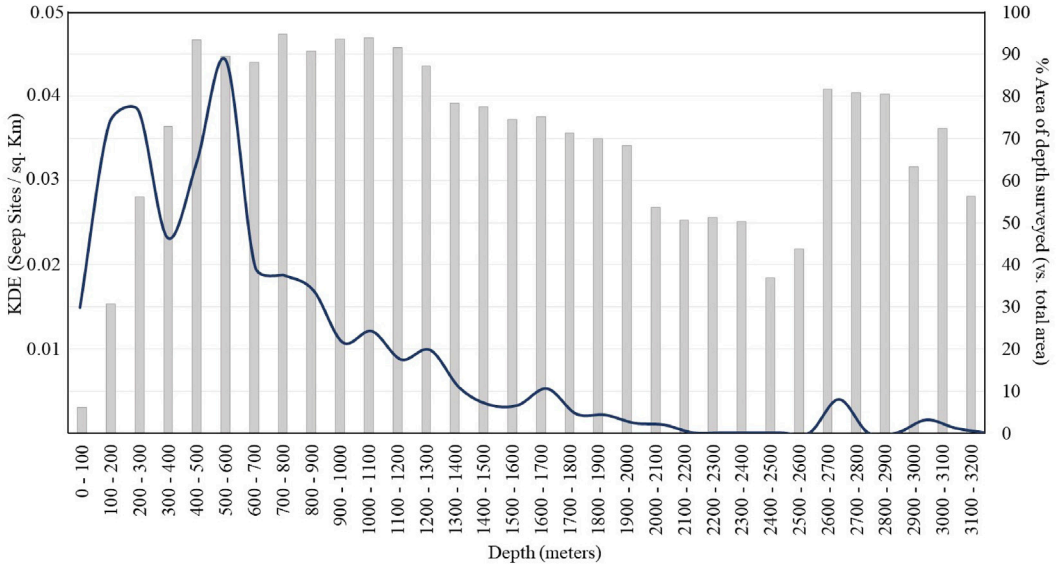

FIGURE 2
Kernel density estimation (KDE) of seeps (blue line) calculated as the number of emission sites per square kilometer of MBES-surveyed area in 100-m interval depth bins overlaid on the percentage of the seafloor mapped (gray bars) with MBES and co-located water-column data for each depth bin, as compared with the total area of the depth contour (area mapped/total area). Depths with values close to 100 signify near-complete survey coverage, whereas values close to 0 represent data deficiencies with regards to sparse MBES and water-column survey coverage.

was then used as a mask to extract a continuous 100-m resolution depth surface from a global multiresolution bathymetric elevation model (Ryan et al., 2009), representing the area mapped corresponding with the seep location data. Depth contour polygons were created from this layer at 100-m intervals and seep emission sites were spatially joined to their respective depth contour polygon. Seep density (per sq. kilometer) was calculated for each 100-m depth contour. A smoothed kernel density estimation curve was fitted to the data for the margin-wide (Figure 2), as well as at the regional scale (Figure 3), in order to investigate seep distribution per morphotectonic region. To test for normality in the seep depth distribution we used normal Q-Q plots and a Shapiro-Wilk test (Shapiro and Wilk, 1965; Wilk and Gnanadesikan, 1968). Patterns in seep distribution were further explored in order to identify significant seep clusters along the margin (Optimized Hot Spot Analysis tool in ArcGIS Pro 3.0, Esri). Optimized Hot Spot Analysis was used to spatially interrogate the dataset to optimally aggregate coincident features into hexbins based on the Global Moran's I statistic of spatial autocorrelation, and then calculate a Getis-Ord Gi* statistic for each hexbin to compare the aggregated counts of seeps within each hexbin against those of its nearest neighbors. Cluster predictions are determined by the aggregation of seeps within neighboring hexbins as compared to the null hypothesis of a random distribution. We used an analysis cell size of 10 km and a fixed distance band of 20 km, as determined by the initial steps run by the Optimized Hot Spot Analysis tool to identify the optimal scale of analysis. All aggregation hexbins had a minimum of 8 neighbors, and on average 16 nearest neighbors were used with a moving window analysis to determine statistical clusters. The resultant z-scores for each aggregation hexbin identified the intensity of the clustering, with larger positive z-scores (p-value<0.05) indicating more significant seep clusters. We included only the clustering for features significant at the 95%–99% confidence levels.

2.3 Geologic-geomorphic attribute

In order to determine potential controls on focused fluid flow in southern Cascadia, an area with previously sparse coverage, we systematically assigned a primary (and in some cases, secondary) geologic/geomorphic attribute to each seep emission site in region 4 of Watt and Brothers (2020) Seafloor expressions of fluid expulsion or other indicators of fluid flow, such as pockmarks or authigenic carbonates but otherwise lacking evidence of active seepage, were not included. Instead, we integrated new multibeam bathymetry, backscatter data, and seismic reflection profiles to identify attributes previously inferred to be associated with substrate fluid flow: anticline, fault, failure scarp, shelfbreak, channel, bedding outcrop, and canyon (e.g., Skarke et al., 2014; Crutchley et al., 2018; Riedel et al., 2018; Prouty et al., 2020). Locations of these attributes were determined from their geomorphic expression on the seafloor (Supplementary Figure S1) and supplemented with seismic reflection profiles where available. For example, bubble plume locations were combined with the multibeam bathymetry and backscatter data (https://www.ncei.noaa.gov/maps/bathymetry/) and seismic reflection profiles (Triezenberg et al., 2016) for visualization and interpretation of the local geologic/geomorphic setting within a 50-m buffer of the seep occurrences and logged using a geographic information system (GIS) (ArcMap 10, Esri). Information on anticline locations was derived from previously published neotectonic maps in southern Cascadia (Clarke and Carver, 1992; Goldfinger et al., 1992; Goldfinger et al., 1997) but is currently unavailable for northern Cascadia.

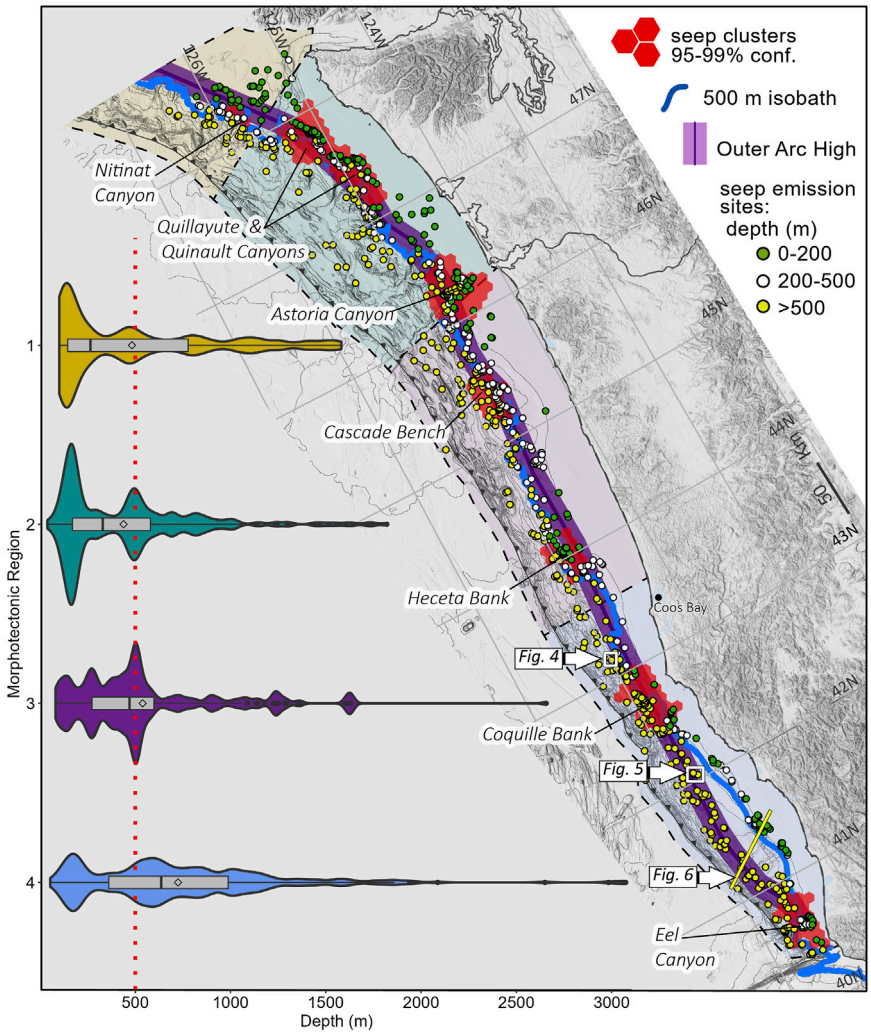

FIGURE 3
(right) Locations of the seven seep clusters (red) identified in Cascadia, and their spatial relationships with the landward limit of the gas hydrate stability zone (blue contour line), the outer arc high (purple shaded region) as defined in Watt and Brothers (2020) and significant associated submarine canyons or structural highs. Seep emission sites (circles) color coded by depth bin (0–200 green; 200–500 white; >500 yellow). Location for Figures 4, 5 and seismic line for Figure 6 (yellow line) are shown (left). Variability in seep depth distributions according to morphotectonic region (Watt and Brothers, 2020) as shown with violin plots inset with box plots. Violin plots show a kernel density estimation curve representing the probability of occurrence of seep emission sites at a given depth. Box-and-whisker plots display five-number summary statistics of seep depth, with both median (vertical line) and mean (diamond) depth values displayed inside the boxes. The landward limit of the gas hydrate stability zone for the Cascadia margin is indicated with the red dashed lines (500-m isobath).

In addition to examining seep distribution in the context of regional controls in southern Cascadia, margin-wide seep distribution was evaluated with respect to the landward limit of the GHSZ and the OAH. The OAH was designated as the location of broad structural high with a ±10-km buffer that runs along the seaward edge of the shelf forearc basins (Watt and Brothers, 2020). Joung et al. (2022) showed the landward limit of gas hydrate determined for the northern Cascadia margin based on bottom water temperatures recorded by CTD data. This type of analysis is hard to adapt for the whole margin due to lack of complete data coverage (C.D. Ruppel, USGS, written commun., 07/04/23) and we instead adopted the 500-m isobath as the nominal the landward limit of the GHSZ (Tréhu and Phrampus, 2022).

2.4 Seismic reflection data

Multichannel seismic reflection datasets were utilized to reveal subsurface structure and stratigraphy under mapped seeps where available (e.g., Triezenberg et al., 2016). Additional seismic surveys were collected in 2018 aboard the R/V *Coral Sea* using an 88-channel Geometrics GeoEel digital hydrophone streamer and Applied Acoustic Delta Sparker sound source (Balster-Gee et al., 2023a) and in 2019 onboard the R/V *Rachel Carson* and utilized a 72-channel Geometrics GeoEel streamer and the Delta Sparker sound source (Balster-Gee et al., 2023b). Both sparker datasets were processed following processing procedures laid out in Kluesner et al. (2019) and included SEGD to SEGY conversion, geometry

correction, UTM conversion, common mid-point (cmp) binning, FK filter, spike removal, bandpass filtering, velocity analysis, normal move-out correction, trim static corrections, cmp stacking, post-stack migration, gap deconvolution, water column mute, and automatic gain control. In addition to the workflow above, the 2019 sparker dataset included prestack deterministic deconvolution using shot-to-shot source signature information recorded during acquisition.

2.5 Chimney analysis

To optimize the detection of gas and fluid migration pathways in the vicinity of active seep sites with focused fluid flow (Heggland, 2005; Ligtenberg, 2005; Kluesner et al., 2013; Brothers et al., 2014; Connolly, 2015), a fully connected multi-layer perceptron neural-network approach was applied to 2-D high-resolution multichannel seismic (MCS) profiles at seep sites in region 4. Within the OpendTect software package, twenty-one attributes were used as input nodes into the supervised neural-network chimney calculation, and each node was weighted during the neural-network training (for details see Kluesner and Brothers (2016). The chimney meta-attribute results were projected onto seismic cross-sections using a gradational color scale with transparency that reveals only the highest (~80% and above) chimney probabilities, yielding a measurement of the probability between 0 (lowest) to 1 (highest) for presence of a chimney structure. Two types of features were identified, zones of probable fluid migration (e.g., vertical pipes, faults, and chimneys) and gassy sediments. The frequency-dependent reflectivity of gassy sediments due to scattering and absorption has been previously documented (e.g., Wood et al., 2008). The chimney meta-attribute analysis described above therefore represents a powerful method to discern subtle patterns of gas-related attenuation and their spatial relationships with the surrounding structure and stratigraphy in areas of focused fluid flow (Kluesner and Brothers, 2016; Prouty et al., 2020).

2.6 Methane-derived authigenic carbonates

Powdered carbonate samples for stable carbon ($\delta^{13}C$) and oxygen ($\delta^{18}O$) isotopic analysis were collected using a hand-held pneumatic drill to sample various components of authigenic carbonates collected along the Cascadia margin as a proxy for potential fluid sources. Isotopic composition was determined via ThemoScientific Kiel IV carbonate device interfaced to ThermoScientific MAT-253 dual-inlet isotope ratio mass spectrometer (IRMS) at the University of California, Santa Cruz, Stable Isotope Laboratory. Stable isotope values are reported in per mil (‰) relative to the international reference Pee Dee Belemnite (PDB). Analytical uncertainties (1σ) are 0.05‰ for $\delta^{13}C$ and 0.10‰ for $\delta^{18}O$. Mineralogy was determined by X-ray diffraction (XRD) using a Philips XRD with graphite monochromator at 40 kV and 45 mA as described in Prouty et al. (2016). Step scans were run from 5° to 65° 2θ with 0.02° steps, using CuKα radiation and a count time of 2 s per step following Hein et al. (2013). XRD digital scan data were analyzed using the Philips X'Pert High Score search-and-match function to identify minerals. The XRD 100 intensity peaks at 20 for calcite: 29.4, dolomite: 30.8, quartz: 26.6, and aragonite: 26.2 in order to determine major (>25%) carbonate phase. Results from new analysis were combined with previously published results from Cascadia (Torres et al., 2009).

TABLE 1 Number of seep emission sites and summary statistics of seep depth (m) including depth range, median depth, first and third interquartile, and interquartile range (IQR) per morphotectonic region as defined in Watt and Brothers (2020).

	Morphotectonic region			
	1 *n=77*	2 *n=275*	3 *n=250*	4 *n=278*
Minimum depth	101	39	81	54
1st Quartile	145	170	274	361
Median	264	329	470	636
3rd Quartile	777	579	598	989
Maximum depth	1,581	1,820	2,656	3,074
IQR	632	409	324	626

3 Results

3.1 Margin-wide and regional seep distribution

Margin-wide seep depth distribution is shown in Figure 2, based on results from the smoothed density estimation curve of seep sites per 100 m depth intervals overlaid on the relative percent-area surveyed of each depth contour (Table 1). The MBES survey coverages varies with depth and is lowest in the very shallow water on the continental shelf from 0 to 200 m, where the narrowing of the swath width makes collecting large surface areas exceedingly difficult for the typical MBES systems. In most other depth bins, however, coverage is between 60%–95%. The margin-wide seep depth distribution is left-skewed with bimodal peaks at 200–300 m and 500–600 m and long-tailed showing numerous observations of deep seeps up to 3,100 m. Non-normality of the distribution was confirmed using normal Q-Q plots, which show significant deviation of the sample points from the linear model especially in the lower and upper quantiles, and a Shapiro-Wilk test (W=0.5457, p-value<0.05; Supplementary Figure S2).

Given that margin-wide plots of seep depth distribution can mask along-margin variation in seep depth trends, we evaluated the depth distribution of the seep emission sites within four morphotectonic regions of the Cascadia margin (Watt and Brothers, 2020). The depth-distribution of each of the four morphotectonic regions shows considerable variation (Figure 3), especially compared to the margin-wide depth distribution (Figure 2). In addition to displaying the median and quartiles (i.e., inset box-and-whisker plots), the violin plots use a kernel density estimation to show the distribution shape of the data (i.e., position and relative amplitude) and probability of seep distribution along the depth range (Table 1). In regions 1 and 2,

10.3389/feart.2023.1205211

39%–42% of seeps are found on shallow continental shelf (0–200 m), with 23%–26% on the upper slope and landward limit of the GHSZ (200–500 m), and 35% found in deeper waters and within the GHSZ (>500 m) (Figure 3). In region 3, 42% are located on the upper slope up to the landward limit of GHSZ, characterized by an interquartile range of 300–600 m, but equally 42% are found within the GHSZ, and a smaller portion on the shelf (15%). In contrast, seeps in region 4 were found in deeper water, such that 68% of the seeps are within the GHSZ (interquartile range = 600–1,000 m), 15% on the upper slope and landward limit GHSZ, and the remaining 17% on the shelf. In summary, only the median seep depth in region 3 coincides with the depth range of the landward limit GHSZ. The probability of seeps occurring within the depth range of the landward limit GHSZ is only valid in region 3. In contrast, the median seep depth in regions 1 and 2 are shallower with respect to the landward limit of the GHSZ and deeper in region 4, suggesting a margin-wide seep distribution trend toward deeper water southward along the margin (Figure 3). Similar to the margin-wide analysis, seep depth-distribution displayed non-normality in each of the respective regions, as highlighted by the shape of the violin plots (i.e., multimodal data distribution), illustrating scatter rather than concentrated around the median (Figure 3). This nonuniform distribution is consistent with previous observations (Johnson et al., 2015; Riedel et al., 2018).

3.2 Cluster analysis

Testing for patterns in spatial distribution margin-wide revealed that seeps exhibit spatial clustering, as opposed to random or dispersed distributions. Along the margin seven distinct clusters (i.e., hot spots) of high-density seeps were identified (Figure 3). All of the major clusters, except the cluster at Heceta Bank, are in areas where the OAH and landward limit of the GHZS coincide (Figure 3), as discussed in more detail below. In region 1, a single cluster was identified from 200 to 900 m depth at the head of Nitinat Canyon. At this site the OAH and the landward limit of the GHSZ converge (Figure 3 and Supplementary Figure S4), in contrast to the majority of region 1 where the landward limit of the GHSZ has a seaward offset relative to the OAH (Supplementary Figure S3). Region 2 exhibited the highest incidence of clusters, where each of the three clusters occurred at the heads of major submarine canyons, Quinault and Quillayute, Grays, and Astoria Canyons, that incise the shelf at 200 m. However, seeps in Astoria Canyon extend into the canyon and occur at a range of depths along the canyon thalweg. In contrast to regions 1 and 2, region 3 is devoid of canyons and clusters in this region occur on local structural highs, at Cascade Bench and Heceta Bank. In addition, the highest probability (i.e., peak in kernel density estimation curve) of seeps occurring within the depth range of the landward limit GHSZ is only valid in region 3, as discussed in detail below. A cluster at Coquille Bank was identified in region 4 where the OAH and landward limit of the GHSZ converge. Notably, this cluster is located where an inferred backstop boundary fault (Watt and Brothers, 2020) intersects a unique seafloor seep characterized by gas bubbles containing mantle-derived helium suspected to be sourced from the subducting Gorda plate (Baumberger et al., 2018). In comparison, no cluster was detected directly offshore Coos Bay, despite convergence of the

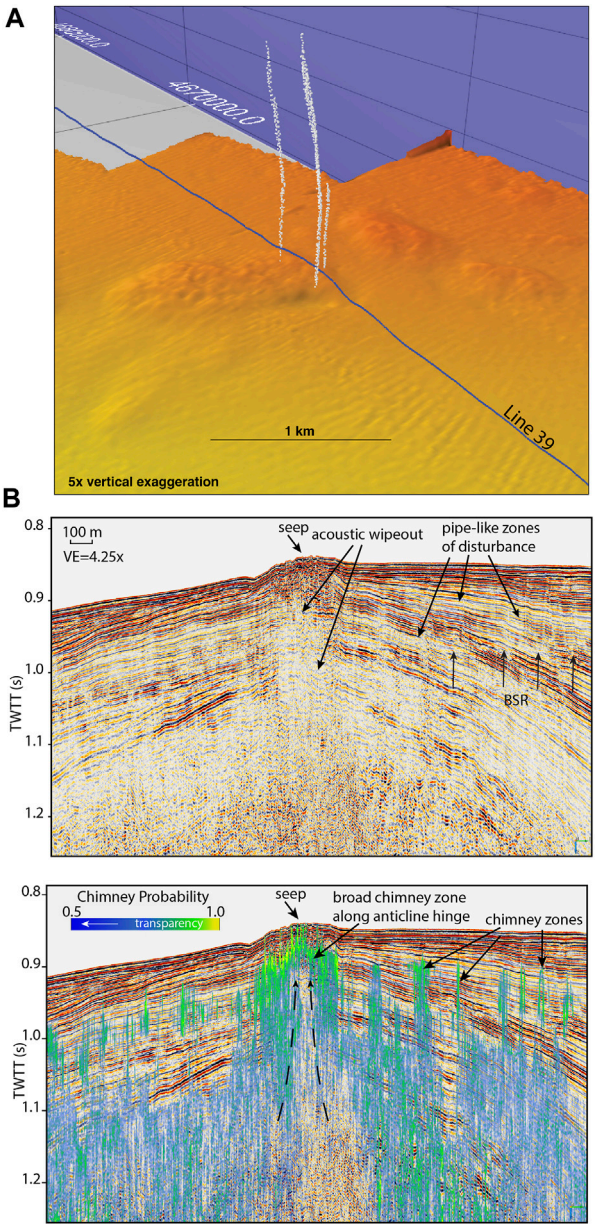

FIGURE 4
(A) Three-dimensional visualization of seep bubble plumes detected in water-column data from a 2018 NOAA Ship *Rainier* survey using QPS Fledermaus FMMidwater software. Location of multi-channel seismic reflection profile data used for subsurface investigation (Figure 4B) into seep expression is shown in relation to the seeps. Collocated color-shaded relief bathymetry shows uplifted and rough-textured seafloor underneath the seeps. **(B)** Two-dimensional multichannel seismic reflection profiles coincident to this seep site collected in 2018 on the R/V *Coral Sea*. Upper panel shows the uninterpreted profile, while the lower panel shows the application of the multilayer perceptron neural-network used to identify high-probability zones of fluid migration pathways and gas-filled sediments. Additional interpretations added with arrows and labels noting the locations of acoustic wipeout/chimneys, faults, bottom-simulating reflectors, and the seep location on the seafloor surface.

OAH and the landward limit of the GHSZ. However, pockmarks were observed in the bathymetry in this area, suggesting potential fluid seepage in the past. South of Rogue Canyon, the OAH deviates

10.3389/feart.2023.1205211

seaward to a depth range of 800 to 2,000 m, where seeps appear to be strongly associated with the OAH rather than the landward limit of the GHSZ (Figure 3). A second cluster was identified around the head of Eel Canyon at the southern terminus of the Cascadia margin and is also where the OAH rejoins with the landward limit of GHSZ.

3.3 Seep site geomorphology in southern Cascadia

The seep depth distribution in southern Cascadia is unique, as captured in the violin plot of region 4 (Figure 3), where most seeps (62%) occur within the GHSZ (>500 m deep), and in an area where there is a distinct seaward divergence of the OAH into deeper water (Supplementary Figure S3). Given the lack of overlap between the OAH and landward limit of the GHSZ in southern Cascadia, the deeper distribution of seeps was investigated in the context of site specific geologic-geomorphic controls. Seeps could have associations with multiple geologic-geomorphic attributes and were therefore assigned up to two primary attributes (Supplementary Table S2). Of the seven types of geologic-geomorphic attributes evaluated for facilitating fluid flow, more than half (52%) of the 278 seep emission sites in southern Cascadia occur on anticlines, with the majority of anticlines located within or seaward of the OAH (Figure 3). In comparison, 16% of seeps were associated with canyons, 14% with the shelfbreak, 11% with seafloor failure scarps, 7% in channels or gullies, and 7% at sites of bedding outcrop. While assigning site specific geologic attributes to all seeps on the Cascadia margin is outside the current scope of the study, we did find that 44% of the seep emission sites in region 3 were located on anticlines, suggesting the strong association of seeps on anticlines carries to morpho-tectonic regions other than region 4.

3.4 Fluid-flow pathways

To further investigate the link between the occurrence of seafloor seepage and underlying geologic structure in southern Cascadia, we combined high-resolution bathymetry, water-column, and two-dimensional MCS data at two seep flare sites in region 4 as representative examples of detection of gas reservoirs and fluid migration pathways. The first example is based on water-column data from 2018 NOAA Ship *Rainier* MBES survey, where three seep flares were detected at ~638 m depth, with fluid emissions reaching a height of 260 m above the seafloor (Figure 4A). Bathymetry from the associated MBES survey revealed an uplifted and rough seafloor character underneath the seep cluster and the high-intensity backscatter values accompanying these patches suggests the rough seafloor consists of authigenic carbonate precipitation. The seafloor morphology is mostly likely controlled by a broad anticlinal structure, as depicted in the MCS data (line 39 from the R/V *Coral Sea*). Within the anticline and beneath the active seep there is a zone of chaotic reflections and acoustic wipe-out located below the hinge line (Figure 4B). Chimney analysis reveals a broad high-probability zone below the seep field, indicating probable fluid-pathways (Figure 4B). Additional pipe-like zones of disturbance on both sides of the seep field are also highlighted as high-probability chimney zones. Fluids appear to be focused toward the hinge line where vertical pipes or faults provide a pathway to the seafloor, resulting in seafloor emissions.

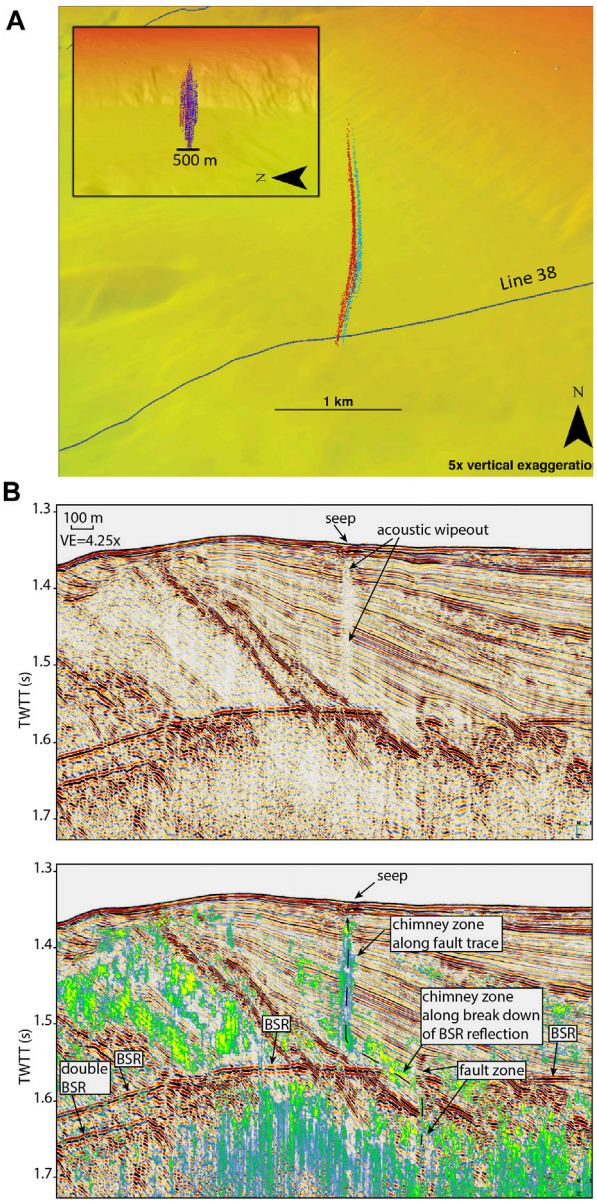

FIGURE 5
(A) Three-dimensional visualization of seep bubble plumes detected in water-column data from a 2017 E/V *Nautilus* survey using QPS Fledermaus FMMidwater software. Location of multi-channel seismic reflection profile data used for subsurface investigation (Figure 5B) into seep expression is shown in relation to the seeps. **(B)** Two-dimensional multichannel seismic reflection profiles coincident to this seep site collected in 2018 on the R/V *Rachel Carson*. Upper panel shows the uninterpreted profile, while the lower panel shows the application of the multilayer perceptron neural-network used to identify high-probability zones of fluid migration pathways and gas-filled sediments. The semi-transparent color overlay displays results from only the highest probability of occurrence results. Additional interpretations added with arrows and labels noting chimney areas, anticline hinge, and the seep location on the seafloor surface.

The second example is from a seep site identified from water-column data derived from a 2017 E/V *Nautilus* MBES survey at a

water depth of ~995 m depth and flare rising 430 m into the water column. By rotating the 3D perspective from north-south orientation to east-west, a long, thin "bubble curtain" with a horizontal extent of 500 m across is revealed (Figure 5A). Bathymetric shaded relief reveals uplifted and rough seafloor character underneath seep cluster. As depicted in the MCS data (line 38 from the R/V *Rachel Carson*), this seep site is above a normal fault on the flank of a broad anticlinal structure (Figure 5B). As described above, chimney analysis indicates the presence of probable fluid-pathways beneath a hydrate cap (BSR) and likely updip fluid migration through a chimney zone to the seafloor (Figure 5B). The seismic profile shows that at depth, disruption of the BSR coincides with the location of a deeper fault, as well as the presence of a relic ("double") BSR.

3.5 Authigenic carbonates

Authigenic carbonate $\delta^{13}C$ values range from −56.73‰ to 10.03‰ with an average value of −25.21‰ ± 15.39‰ (n=324), whereas $\delta^{18}O$ values range from −1.85‰–9.15‰ with an average value of −3.70‰ ± 1.67‰ (n=324) (Supplementary Table S3). Aragonite is the dominant carbonate phase of the authigenic carbonates and is the major component in 57% of the samples, with low and high-Mg calcite accounting for 29% and dolomite present at 13%. There is a $\delta^{13}C$ range of over 60‰ from samples collected along the margin, and $\delta^{13}C$ values correlate with both depth and latitude, with statistically significant ($p<0.01$) Pearson-Product Correlation Coefficient ($p<0.01$) of −0.49 and −0.48, respectively. In contrast, no correlation was found between authigenic carbonate $\delta^{18}O$ values with either depth or latitude. Based on the aragonite-temperature equation of Grossman and Ku (1986) and seawater $\delta^{18}O$ value of 0.08‰ SMOW (Bohrmann et al., 1998), the average $\delta^{18}O$-derived temperature is 5.0°C ± 3.7°C, overlapping with CTD bottom water temperatures at a depth range between 150 and 1,600 m (Baker and Prouty, 2022; Prouty and Baker, 2022).

4 Discussion

4.1 Margin-wide seep depth distribution and cluster analysis

The identification of new seep sites in central and southern Cascadia in this study extends our understanding of seep depth distribution along a subducting margin. The margin-wide depth distribution presented here is consistent with other findings that seep density peaks around 500-m depth (Merle et al., 2021), but the non-normality contradicts the assumption of symmetrical probability distribution around ~500 m. Instead of exhibiting symmetrical probability distribution around ~500 m, the margin-wide depth distribution is left-skewed with a long-tail highlighting numerous observations of deep seeps up to 3,100 m. On a regional basis, the probability of seeps occurring within the depth range of the landward limit GHSZ is only valid in region 3 (Figure 3). While the seep distribution is non-random, the clustering described above is not restricted to the 500-m isobath but rather at distinct clusters with unique geologic and geomorphic characteristics. Whereas Merle et al. (2021) normalized seeps to percent area mapped for only a subset of eight multibeam surveys, we normalized seep occurrence to area mapped using all the co-located footprints from 30 multibeam surveys. Between 200–1,500 m depth, MBES mapping coverage was consistently high (80%–95%), such that our results and interpretation were not significantly hindered by data gaps in survey coverage at different depth bins. Increasing multibeam data acquisition in the 0–200 m water depth range would further refine our estimation of seep density in shallow waters along the margin. The opportunistic discovery of seeps and seep-indicators (i.e., chemosynthetic biota) using ROVs at sites where MBES did not detect seeps is a reminder that, in addition to the temporal ephemerality of seeps releasing detectable gas bubbles, an absence of seeps recorded in MBES surveyed area does not indicate a true absence of seeps.

In regions 1 and 2, the majority of seeps are on the shallow continental shelf (<200 m), with the seep clusters at the heads of canyons in northern Cascadia (Figure 3). Given that the canyons incise the shelf at (or less than) 200 m, it is not surprising that seeps in regions 1 and 2 have the highest probability of occurring at depths less than 200, consistent with previous observations (Johnson et al., 2019). Seep clusters are located at the heads of major submarine canyons except in Astoria Canyon, where seeps span a depth range from 109 to 300 m at the canyon head to 480–1,026 m in the canyon. As suggested by Merle et al. (2021), the large seep distribution in Astoria is likely linked to a combination of factors, with Astoria Canyon deeply incising into the shelf, resulting in steep canyon walls, facilitating massive sidewall and channel levee failures and exposing bedding planes on the mid to lower slope (Hill et al., 2022), thus promoting seepage pathways within the permeable sediment layers. In addition to a high occurrence of seep clusters in canyons in region 2, this region is also characterized by landward migration of the OAH, most likely in response to active extensional faulting. As a result, the OAH overlaps with the landward limit of the GHSZ (Figure 3), which most likely further facilitates focused fluid in these clusters.

Seep depth distribution in the south is progressively deeper but also signifies the only region (region 3) devoid of canyons and where the probability of seeps occurring within the depth range of the landward limit GHSZ is valid (Figure 3). The predominant cluster in region 3 is at Cascade Bench, a topographic high situated between Cascade Head and Tillamook Bay at depth of 400–600 m and inferred to be a paleo–shelf edge formed during the Pleistocene lowstand (McNeill et al., 2000). A second cluster was identified at Heceta Bank, a structural high along the outer shelf caused by subducting seamounts (Tréhu et al., 2012). Within this region, the OAH is co-located with the landward limit of the GHSZ except at Heceta Bank, suggesting some discrepancy of cluster behavior on structural highs with regards to convergence of the OAH and landward limit of the GHSZ.

The overlap between the OAH and the landward limit of the GHSZ may help explain the occurrence of the two clusters in region 4, one at Rogue Canyon and Coquille Bank, a north-south trending double plunging, asymmetrical anticline (Kulm and Bales, 1969), and the other around the head of Eel Canyon. Both sites are places where the OAH and landward limit of the GHSZ converge, along with the presence of submarine canyon heads (the importance of

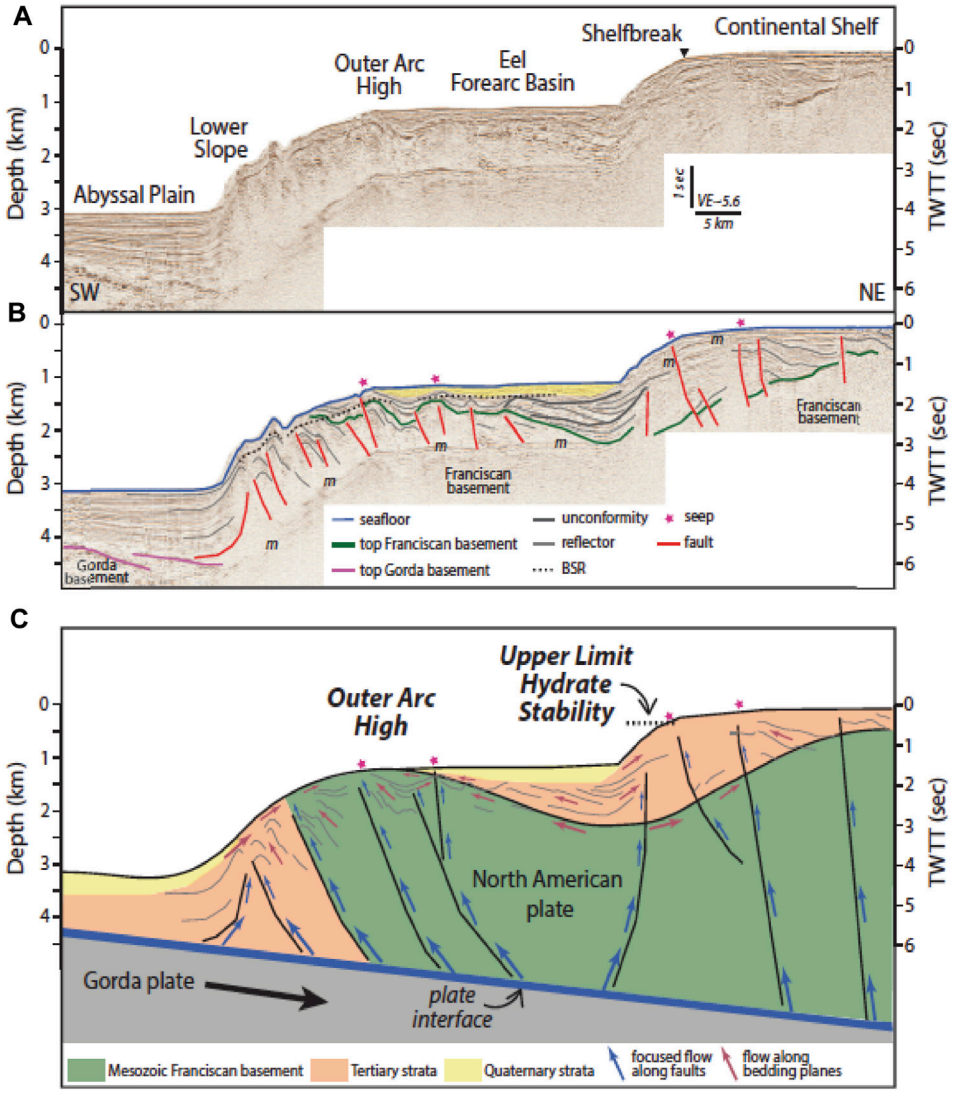

FIGURE 6
Cross-sections of the southern Cascadia margin in Region 4 (location shown in Figure 3), showing the subsurface structure of the outer arc high (OAH) in **(A)** uninterpreted, **(B)** interpreted migrated industry seismic profile, Line W675NC-524 (Triezenberg et al., 2016). The OAH in this region forms a broad structural high (10s of km wide) comprised of numerous imbricated thrust faults and associated folds. The OAH bounds the seaward edge of the forearc basin. The seafloor multiple is indicated by "m". **(C)** shows a conceptual model depicting the OAH as a first-order anticlinal trap that focuses fluid flow along individual faults and bedding planes. Note that within this region the outer arc high and upper limit of hydrate stability are spatially distinct features that each play an important role in focusing fluid seepage at the seafloor. Depth of Franciscan basement is estimated based on nearby interpretations from Gulick et al. (2002).

which was discussed above). Seafloor fluid emission at Coquille Bank may also be further facilitated by a backstop fault formed from the subducting Gorda Plate (Watt and Brothers, 2020) with access to mantle-derived fluids (Baumberger et al., 2018), and associated with a mafic ridge buried beneath the sediments of the accretionary complex from about 43° to 45°N (Fleming and Tréhu, 1999). In the rest of region 4, the OAH and the landward limit of the GHSZ are separated from each other by an average of 23 ± 6.1 km as the OAH deviates seaward around the Eel River Basin. As noted in this study, many seeps occurred in the deep water in association with the OAH, and prolific seep activity was also observed proximal to the channel heads of Trinidad Canyon where a north-south trending fault cuts across the channel heads and the shelfbreak (Balster-Gee et al., 2023a), but there was a dearth of seeps in the basin between. We posit that the lack of seeps here may be due to high sedimentation rates in the Eel River Basin that cause deposition of mud and silt to drape over the Basin and Trinidad Canyon (Nittrouer, 1999; Sommerfield and Nittrouer, 1999), which may limit sufficient porefluid methane saturation. Whereas gas hydrates tend to concentrate in coarser-grained sandy/silty turbidite sediments (Torres et al., 2008), high sedimentation rate of fine-grained sediment may preclude sufficient porefluid methane saturation. This scenario is consistent with observations by Tréhu and Phrampus (2022) to explain the absence of BSR and extension of the seaward edge of the Eel River Basin well to the west of the theoretical landward edge of the GHSZ. Therefore, we suggest that

the lack of overlap between the OAH and the landward limit of the GHSZ and sedimentation history precludes development of seep cluster anywhere else in region 4.

The discussion above provides an interpretive framework for understanding and potentially predicting seep clusters along a subducting margin and helps address the unresolved origin of seeps at 500 m by identifying processes and characteristics that facilitate focused fluid independently of gas hydrate dissociation in response to contemporary ocean warming. While canyons and structural highs are critical geomorphic features facilitating seep occurrence, overlap between the OAH and the landward limit of the GHSZ may be required for statistically significant clustering of seep emissions. In Cascadia, there is co-occurrence of the OAH (and shelf break) with the downdip end of seismic ruptures and interseismic coupling (McNeill et al., 2000; Booth-Rea et al., 2008; Malatesta et al., 2021). Therefore, there may be links between seep distribution and seismogenic patterns given the release and drainage of fluids from clay dehydration in the transition between locked and seismogenic zone (Saffer and Tobin, 2011). Low permeability and porosity of marine sediment could lead to significant overpressure in these environments and trapping of fluids (Sahling et al., 2008; Saffer and Tobin, 2011). In other words, there is upward/updip fluid migration from zones of peak dehydration and/or elevated pore pressure toward that OAH along permeable stratigraphic layers and fault conduits. The OAH acts as a first-order anticlinal trap that focuses fluid flow along individual faults and bedding plane (Figure 6), as supported by sub-surface data showing where widespread folds channel fluids and gases toward the anticlinal crests, as seen in the structurally controlled seeps offshore Costa Rica (Kluesner et al., 2013). This may not apply to seeps away from the deformation front since dehydration may occur at a shallow depth and near the deformation front (Hyndman and Wang, 1993; Hyndman, 2007), given the high temperatures of the very young hot subducting plate (e.g., Hyndman, 2007). In contrast, near Hydrate Ridge, Torres et al. (2004) and Teichert et al. (2005) found an increase in deep freshening eastward (i.e., relative to the toe), whereas accretion at the westernmost sites is too recent for the sediments to have undergone significant illitization. While differentiating fluids from dehydration relative to hydrate dissociation requires analysis of porefluids, the co-location of the seep clusters with the OAH and inferred downdip end of interseismic coupling in Cascadia is intriguing and warrants further investigation.

4.2 Fluid source

As a proxy for the composition of fluids, the authigenic carbonate isotope values suggest a range of sources, including thermogenic decomposition of organic matter and biogenic mediation from microbial activity (Claypool et al., 1985). The average authigenic carbonate $\delta^{13}C$ values (−53.53‰ ± 1.95‰) at the Astoria deep sites (>800 m) are depleted relative to carbonate $\delta^{13}C$ values at the shallow site (500 m; −28.51‰ ± 2.26‰), yielding a difference of 25‰, similar in magnitude between gas samples at the shallow *versus* deeper Astoria sites (Baumberger et al., 2018). As described in Baumberger et al. (2018), anerobic oxidation of methane (AOM), as well as incorporation of dissolved inorganic carbon (DIC) and co-existing CO_2 and its associated shift in isotope composition, can produce heavy $\delta^{13}C$ values that mimic a thermogenic origin (Pohlman et al., 2009). Given gas isotopic and hydrocarbon composition indicative microbial methane at Astoria (Baumberger et al., 2018), the heavier carbonate $\delta^{13}C$ values at the shallow site are in line with ^{13}C-enrichment by AOM.

In contrast, at Coquille the presence of only thermogenic methane (Collier and Lilley, 2005; Baumberger et al., 2018) provides an opportunity to calibrate the range in carbonate $\delta^{13}C$ values (−26.50 to −17.76‰) in the absence of mixing with microbial sources. Taken together, data from Coquille and Astoria can be used as endmember values for estimating contribution from microbial and thermogenic methane sources to carbonate $\delta^{13}C$ values at other sites where both sources are identified, such as at Heceta Bank (Baumberger et al. (2018). For example, carbonate $\delta^{13}C$ values greater than the range reported at Coquille can be explained by oxidation of methane and DIC incorporation, whereas carbonate $\delta^{13}C$ values less than this range reflect mixing with microbial methane. Assuming endmember microbial and thermogenic $\delta^{13}C$ values from Baumberger et al. (2018), mixing with a microbial methane at Heceta Bank could contribute to a depletion of 15‰, equivalent to a contribution of less than 10% from microbial methane.

The inverse correlation between $\delta^{13}C$ values and depth supports earlier views that seeps from within the gas hydrate stability zone are of microbial origin and seeps from the upper slope and the shelf have a thermogenic source (e.g., Collier and Lilley, 2005; Heeschen et al., 2005; Baumberger et al., 2018). However, the discussion above also demonstrates how processes impacting fluid chemistry, such as mixing and AOM, can impact the fluid isotopic composition (Pohlman et al., 2009) and ultimately alter the archived fluid-source signature in the authigenic carbonates. In addition, gas hydrate dissociation can provide a potential source of ^{18}O-enriched fluids, which releases hydrate water and contributes to enrichment by up to 3.5‰ (Maekawa, 2004). Samples with ^{18}O-enriched carbonate values yield unrealistically cold temperatures (<2°C) relative to CTD bottom water data (Baker and Prouty, 2022; Prouty and Baker, 2022), indicating influence from ^{18}O-enriched fluid source. Margin-wide carbonate $\delta^{18}O$ values and mineralogy, however, support shallow precipitation of aragonite driven by AOM and in isotopic equilibrium with seawater.

4.3 Anticlines as trappings for focused fluid flow

While the occurrence of seep clusters and the justification for their distribution may help explain the spatial distribution of seeps along the Cascadia margin, it does not explain the range or probability of seep depth distribution across the four regions. Instead, the site-specific investigation of region 4 reveals quantitative links between seafloor geomorphology/geology and seep occurrence. As reported above, over half of the seeps in region 4 occur on anticlines. This characteristic of region 4 helps to explain the probability depth distribution of seeps within the GHSZ. As shown in Figure 3 the OAH diverges seaward, representing a unique feature of southern Cascadia not observed elsewhere along the margin. According to Tréhu and Phrampus

(2022), this region is also marked by the greatest distance between the landward-most BSR pick and 500 m contour (Supplementary Figure S4). Given that the OAH is an actively deforming portion of the margin, younger anticlines are formed from west to east (i.e., seaward or within the OAH) by uplift and horizonal compression as the deformation front steps seaward (Carson et al., 1974; McNeill et al., 1999; McCrory et al., 2002). In this region, the BSR is also tens of km seaward of the landward limit of the GHSZ where accretion of trench sediments forms a thick accretionary wedge (Tréhu and Phrampus, 2022). This spatial pattern highlights the potential role of the OAH on not only seep distribution but hydrate formation, where accretionary wedge tectonics and seafloor morphology serve as structural controls on fluid reservoirs, trapping, and transport. The 2-D conceptual model shown in Figure 6 demonstrates fluid flow paths and seafloor seepage features that are dependent on folds and fault patterns. Whereas convergence rates are similar along the Cascadia margin, the structural style and width of the actively deforming outer wedge varies along-strike, with a narrower wedge in the south relative to wider wedge in the north (Watt and Brothers, 2020). As a result, the narrower wedge forms a steeper accretionary prism with closely spaced faults/anticlines that stack on top of one another (i.e., imbricate faulting). In contrast, the wide wedge in northern Cascadia forms widely spaced anticlines. Region 3 is also characterized by a relatively high occurrence of seeps on anticlines characterized by mixed or dual vergence (Watt and Brothers, 2020), resulting in more-symmetrical fold structures and steeper seafloor gradients along the fold limbs evident in seismic data (Booth-Rea et al., 2008; Phrampus et al., 2017).

The occurrence of seeps on anticlines follows the conceptual models of focused fluid flow and gas migration along the crest of an anticline described by Paull et al. (2008), such as observed offshore north Panama (Reed et al., 1990), Costa Rica (Kluesner et al., 2013), and along the Queen Charlotte Fault (Prouty et al., 2020), where folding, thrust faulting, and sedimentation along a deformation front may facilitate fluid flow and seafloor venting. This relationship has been previously noted on the Cascadia margin, where the development of anticlinal ridges controls the location of seepage and are strongly correlated with vertical fluid migration paths (Carson et al., 1991; Carson et al., 1994; Johnson et al., 2003). Similarly, Tréhu et al. (1999) speculated positive feedback between gas hydrate formation and anticlines. Merle et al. (2021) also noted that deeper seeps (>525 m) were coincident with major compressional anticlinal (and diapiric ridges) within the accretionary prism. The efficiency of anticlines to trap and focus fluid flow is clearly seen in the MSC data and chimney analysis (Figures 4, 5), where broad high-probability zones of fluid migration and areas of chaotic reflections and acoustic wipe-out are located below the anticline hinge line. At depth, disruption of the BSR coincides with the location of a deeper fault, which is likely channeling fluids and causing breakdown of the hydrate cap. Upon intersecting the first fault up-dip, the gas/fluid presumably migrates upward along a path of least resistance to the seafloor. The seismic profile also shows the presence of a relic ("double") BSR (Figure 5), possibly caused by episodes of uplift leading to shoaling/reestablishment of the BSR due to changing thermal conditions. This analysis also illustrates how faults disrupt the BSR (and presumably hydrate stability) and provide a pathway for fluids and gas to reach the seafloor, resulting in seafloor emissions. Hydraulic fracturing can also serve as a gas conduit. For example, along the southern Hikurangi margin in Aotearoa/New Zealand, anticlines act as a focusing mechanism for the fluids, where there is sufficient upward pressure to overcome the lithostatic load of the overburden and blow-out, or fracture, leading to a vertical pathway to the seafloor (Crutchley et al., 2021).

4.4 Tectonic framework for seep distribution

Taken together, this quantitative approach has identified characteristics/features as well as processes along the margin that facilitate seep emissions that operate independently of gas hydrate dissociation in response to contemporary ocean warming. In doing so, this study provides an expanded interpretive framework for understanding the controls and influencing factors on the depth and spatial distribution of seeps along the Cascadia margin and is consistent with stable gas hydrate occurrences even under future scenarios of warming bottom waters (Ruppel, 2011; Ruppel and Kessler, 2017). This interpretive framework may also be applied to other subduction margins that are dominated by accretion, such as the southern Hikurangi margin offshore Aotearoa/New Zealand (Barnes et al., 2010), where high fluid pressures play an important role in maintaining thrust wedges (Saffer and Bekins, 2002). For example, the majority of seeps on the southern Hikurangi margin were detected on crests of thrust-faulted anticlinal ridges at 700–1,200 m and where a network of near-surface faults and chimneys facilitates fluid expulsion and a breakdown in BSR (Mountjoy et al., 2009a; Barnes et al., 2010; Law et al., 2010; Crutchley et al., 2018; Watson et al., 2020). While seeps along the Hikurangi margin are consistently located above the deforming backstop, seep distribution based on MBES water column backscatter data is not uniform, and similar to the Cascadia margin, no evidence was found to suggest clustering of seeps near the landward limit of the GHSZ (650 m; Supplementary Figure S5). Instead, seeps in the north are concentrated near the shelf break within the Tuaheni Landslide Complex, where a combination of factors have contributed to slope instability, including earthquake ground shaking and gas release (Mountjoy et al., 2009b; Mountjoy et al., 2014; Gross et al., 2018; Carey et al., 2022; Crutchley et al., 2022). In comparison, seeps in the south occupy deeper water depths and are found to cluster along the crests of parallel ridges (Supplementary Figure S6), where gas is trapped beneath large sedimentary folds/anticlines formed by deep-seated thrust faults, and focused fluid flow is facilitated by both faults and hydraulic fractures (Crutchley et al., 2021).

This comparison highlights the role of regional geologic structures influencing clusters of focused fluid flow, as well as detailing margin-wide variability in seep distribution along both margins. For example, the largest depth range of seeps is located in the relatively narrow southern end of both margins where there is a transition from subduction to strike-slip deformation (Barnes et al., 2010; Watt and Brothers, 2020). At this transition, strike-slip faults that trend across the slope (Gulick et al., 2002) may provide additional near-vertical pathways for fluid flow across a range of water depths. The importance of the geometry of geologic structures to influence spatial location and character of seeps has been

previously documented (Kulm et al., 1986; Le Pichon et al., 1992). However, results from our study, which demonstrate the importance of both geometry of geologic structures and the role of the margin-wide morphotectonics, may expand previous models of the distribution of fluid expulsion along subduction zones.

5 Conclusion

By applying a spatial and statistical analysis to an expanded seep database, coupled with multibeam bathymetry and chimney meta-attribute analysis of seismic reflection profiles, we show that gas hydrate stability is one of many other controls, primarily morphologic and tectonic, on seep distribution in Cascadia. Seep distribution along the margin is non-random, but instead of clustering along the 500-m isobath, seep clusters are dominated by the presence of canyons and topographical highs. New findings from this study suggest that co-location of the outer arc high (OAH) and landward limit of the gas hydrate stability zone (GHSZ) may be a prerequisite for seep cluster development in Cascadia, where a broad area of deformation overlaps a zone where hydrates are particularly vulnerable to dissociation, such as in areas with focused uplift and in headward-eroding canyons. The wide range in seep depth distribution, and in particular the trend toward deeper depths in southern Cascadia can also be linked to the location of the OAH where the development of thrust-faulted anticlines along the seaward edge of the Eel River forearc basin plays a crucial role in facilitating focused fluid flow and seep emissions despite being within the GHSZ. Refining models of fluid expulsion is critical, given the importance of fluid flow on plate boundary seismogenesis, global carbon budgets, and supporting sensitive seafloor ecosystems.

Data availability statement

The datasets presented in this study can be found in online repositories. The names of the repository/repositories and accession number(s) can be found in the article/Supplementary Material.

Author contributions

JR compiled and prepared datasets used, performed all spatial and statistical analyses, created publication figures and tables, and assisted with manuscript preparation. NP conceived the study, analyzed carbonate geochemistry, and wrote the paper with input from all authors. JC identified seep locations from MBES water column data and helped determine geologic attributes of seep areas. JWK helped collect and process the MCS data, conducted the neural-network chimney analysis, and provided interpretation of the results. JW and JCH provided input on the tectonic setting and regional geology. JW also helped determine geological attributes of seep sites in region 4. SW and JIH contributed seeps database for the Hikurangi margin and assisted with manuscript preparation, focusing on the comparison to the Hikurangi margin. NM helped collect and process the MCS data. All authors contributed to the article and approved the submitted version.

Funding

The U.S. Geological Survey Coastal and Marine Geohazards Resource Program funded this study with additional support from the USGS Environments Program through the Outer Continental Shelf study and Bureau of Ocean and Energy Management (BOEM) Interagency Agreement.

Acknowledgments

We thank C. Ruppel (USGS), D. Brothers (USGS), P. Dartnell (USGS) and J. Beeson (NOAA) for helpful discussions, C. Paull and L. Lemon (Monterey Bay Aquarium Research Institute) for sharing ROV video annotation logs of chemosynthetic biota, T. Baumberger (Oregon State University) and S. Merle (Oregon State University) for sharing archived authigenic carbonate samples, and S. Pit (UCSC), S. Stremmler (UCSC), C. Carney, and A. Gartman (USGS) for sample preparation and geochemical analysis. Input from reviewers improved the manuscript. Any use of trade, firm, or product names is for descriptive purposes only and does not imply endorsement by the U.S. Government.

Conflict of interest

The authors declare that the research was conducted in the absence of any commercial or financial relationships that could be construed as a potential conflict of interest.

Publisher's note

All claims expressed in this article are solely those of the authors and do not necessarily represent those of their affiliated organizations, or those of the publisher, the editors and the reviewers. Any product that may be evaluated in this article, or claim that may be made by its manufacturer, is not guaranteed or endorsed by the publisher.

Supplementary material

The Supplementary Material for this article can be found online at: https://www.frontiersin.org/articles/10.3389/feart.2023.1205211/full#supplementary-material

References

Audet, P., Bostock, M. G., Mercier, J. P., and Cassidy, J. F. (2008). Morphology of the Explorer–Juan de Fuca slab edge in northern Cascadia: Imaging plate capture at a ridge-trench-transform triple junction. *Geology* 36, 895–898. doi:10.1130/g25356a.1

Baker, M. C., and Prouty, N. G. (2022). *Conductivity temperature depth) data collected october-november 2019 offshore of California and Oregon*. U.S. Geological Survey Data Release. doi:10.5066/P9F7K9F2

Balster-Gee, A. F., Kluesner, J. W., Watt, J. T., Hill, J. C., Brothers, D. S., Michalak, M. J., et al. (2023a). *Multichannel sparker and chirp seismic reflection data collected during USGS field activity 2018-658-FA between cape blanco and cape Mendocino in october of 2018: U.S.* Geological Survey data release. doi:10.5066/P9MYL7WJ

Balster-Gee, A. F., Miller, N. C., Watt, J. T., Roland, E., Kluesner, J. K., Heller, S. J., et al. (2023b). *High-resolution multichannel sparker seismic-reflection and chirp subbottom data acquired along the Cascadia margin during USGS field activity 2019-024-FA:* U.S. Geological Survey Data Release. doi:10.5066/P96ZBXK8

Barnard, W. D. (1973). *Late Cenozoic sedimentation on the Washington continental slope*. University of Washington.

Barnes, P. M., Lamarche, G., Bialas, J., Henrys, S., Pecher, I., Netzeband, G. L., et al. (2010). Tectonic and geological framework for gas hydrates and cold seeps on the Hikurangi subduction margin, New Zealand. *Mar. Geol.* 272, 26–48. doi:10.1016/j.margeo.2009.03.012

Baumberger, T., Embley, R. W., Merle, S. G., Lilley, M. D., Raineault, N. A., and Lupton, J. E. (2018). Mantle-derived helium and multiple methane sources in gas bubbles of cold seeps along the Cascadia continental margin. *Geochem. Geophys. Geosystems* 19, 4476–4486. doi:10.1029/2018GC007859

Berndt, C., Feseker, T., Treude, T., Krastel, S., Liebetrau, V., Niemann, H., et al. (2014). Temporal constraints on hydrate-controlled methane seepage off Svalbard. *Science* 343, 284–287. doi:10.1126/science.1246298

Bohrmann, G., Greinert, J., Suess, E., and Torres, M. (1998). Authigenic carbonates from the Cascadia subduction zone and their relation to gas hydrate stability. *Geology* 26, 647–650. doi:10.1130/0091-7613(1998)026<0647:acftcs>2.3.co;2

Booth-Rea, G., Klaeschen, D., Grevemeyer, I., and Reston, T. (2008). Heterogeneous deformation in the Cascadia convergent margin and its relation to thermal gradient (Washington, NW USA). *Tectonics* 27. doi:10.1029/2007TC002209

Brothers, D. S., Ruppel, C., Kluesner, J. W., Ten Brink, U. S., Chaytor, J. D., Hill, J. C., et al. (2014). Seabed fluid expulsion along the upper slope and outer shelf of the U.S. Atlantic continental margin. *Geophys. Res. Lett.* 41, 96–101. doi:10.1002/2013GL058048

Canfield, D. E., Kristensen, E., and Thamdrup, B. (2005). Aquatic geomicrobiology. *Adv. Mar. Biol.* 48, 1–599. doi:10.1016/s0065-2881(05)48017-7

Carey, J. M., Mountjoy, J. J., Crutchley, G. J., Petley, D. N., Holden, C. F., Kaneko, Y., et al. (2022). Episodic movement of a submarine landslide complex driven by dynamic loading during earthquakes. *Geomorphology* 408, 108247. doi:10.1016/j.geomorph.2022.108247

Carson, B., Holmes Mark, L., Umstattd, K., Strasser Jeffrey, C., Johnson, H. P., Tarney, J., et al. (1991). Fluid expulsion from the Cascadia accretionary prism: Evidence from porosity distribution, direct measurements, and GLORIA imagery. *Philosophical Trans. R. Soc. Lond. Ser. A Phys. Eng. Sci.* 335, 331–340. doi:10.1098/rsta.1991.0049

Carson, B., Seke, E., Paskevich, V., and Holmes, M. L. (1994). Fluid expulsion sites on the Cascadia accretionary prism: Mapping diagenetic deposits with processed GLORIA imagery. *J. Geophys. Res. Solid Earth* 99, 11959–11969. doi:10.1029/94JB00120

Carson, B., Yuan, J., Myers, P. B., Jr, and Barnard, W. D. (1974). Initial deep-sea sediment deformation at the base of the Washington continental slope: A response to subduction. *Geology* 2, 561–564. doi:10.1130/0091-7613(1974)2<561:idsdat>2.0.co;2

Clarke, J. S. H., and Carver, G. A. (1992). Late Holocene tectonics and paleoseismicity, southern Cascadia subduction zone. *Science* 255, 188–192. doi:10.1126/science.255.5041.188

Claypool, G. E., Threlkeld, C. N., Mankiewicz, P. N., Arthur, M. A., and Anderson, T. F. (1985). *Isotopic composition of interstitial fluids and origin of methane in slope sediment of the Middle America Trench, Deep Sea Drilling Project Leg 84. Initial reports DSDP, Leg 84*. Balboa to Manzanillo, 683–691.

Clift, P., and Vannucchi, P. (2004). Controls on tectonic accretion versus erosion in subduction zones: Implications for the origin and recycling of the continental crust. *Rev. Geophys.* 42. doi:10.1029/2003RG000127

Cochrane, G. R., and Lewis, B. T. (1984). Comparison of structures in underthrusting and overthrusting lower slope sediments of the Was hington-Oregon convergent margin [abs. *EOS Am. Geophys. Union Trans.* 65, 1089.

Collett, T. S. (2009). Natural gas hydrates: A review, in natural gas hydrates. Energy resource potential and associated geologic hazards. *AAPG Mem.* 89, 146–219. doi:10.1306/13201101M891602

Collier, R. W., and Lilley, M. D. (2005). Composition of shelf methane seeps on the Cascadia continental margin. *Geophys. Res. Lett.* 32, L06609. doi:10.1029/2004GL022050

Connolly, D. L. (2015). Visualization of vertical hydrocarbon migration in seismic data: Case studies from the Dutch North Sea. *Interpretation* 3, SX21–SX27. doi:10.1190/INT-2015-0007.1

Conrad, J. E., and Rudebusch, J. A. (2023). *Methane seeps derived from water-column acoustic backscatter data collected along Cascadia margin offshore Oregon and Northern California, 2018-2021*. U.S. Geological Survey Data Release. doi:10.5066/P9TW2X7Y

Crutchley, G. J., Elger, J., Kuhlmann, J., Mountjoy, J. J., Orpin, A., Georgiopoulou, A., et al. (2022). Investigating the basal shear zone of the submarine Tuaheni landslide complex, New Zealand: A core-log-seismic integration study. *J. Geophys. Res. Solid Earth* 127, e2021JB021997. doi:10.1029/2021JB021997

Crutchley, G. J., Kroeger, K. F., Pecher, I. A., and Gorman, A. R. (2018). How tectonic folding influences gas hydrate formation: New Zealand's Hikurangi subduction margin. *Geology* 47, 39–42. doi:10.1130/G45151.1

Crutchley, G. J., Mountjoy, J. J., Hillman, J. I. T., Turco, F., Watson, S., Flemings, P. B., et al. (2021). Upward-doming zones of gas hydrate and free gas at the bases of gas chimneys, New Zealand's Hikurangi margin. *J. Geophys. Res. Solid Earth* 126, e2020JB021489. doi:10.1029/2020JB021489

DeMets, C., Gordon, R. G., and Argus, D. F. (2010). Geologically current plate motions. *Geophys. J. Int.* 181, 1–80. doi:10.1111/j.1365-246X.2009.04491.x

Fleming, S. W., and Tréhu, A. M. (1999). Crustal structure beneath the central Oregon convergent margin from potential-field modeling: Evidence for a buried basement ridge in local contact with a seaward dipping backstop. *J. Geophys. Res. Solid Earth* 104, 20431–20447. doi:10.1029/1999jb900159

Goldfinger, C., Kulm, L. D., Yeats, R. S., Appelgate, B., Mackay, M. E., and Moore, G. F. (1992). Transverse structural trends along the Oregon convergent margin: Implications for Cascadia earthquake potential and crustal rotations. *Geology* 20, 141–144. doi:10.1130/0091-7613(1992)020<0141:tstato>2.3.co;2

Goldfinger, C., Kulm, L. D., Yeats, R. S., Appelgate, T. B., Jr, Mackay, M. E., and Cochrane, G. R. (1991). *Active strike-slip faulting and folding of the Cascadia plate boundary and forearc in central and northern Oregon*. U. S. Geological Survey Open-File Report. doi:10.3133/ofr91441S

Goldfinger, C., Kulm, L. D., Yeats, R. S., Mcneill, L., and Hummon, C. (1997). Oblique strike-slip faulting of the central Cascadia submarine forearc. *J. Geophys. Res. Solid Earth* 102, 8217–8243. doi:10.1029/96jb02655

Gross, F., Mountjoy, J. J., Crutchley, G. J., Böttner, C., Koch, S., Bialas, J., et al. (2018). Free gas distribution and basal shear zone development in a subaqueous landslide – insight from 3D seismic imaging of the Tuaheni Landslide Complex, New Zealand. *Earth Planet. Sci. Lett.* 502, 231–243. doi:10.1016/j.epsl.2018.09.002

Grossman, E., and Ku, T. L. (1986). Oxygen and carbon isotope fractionation in biogenic aragonite: Temperature effects. *Isot. Geosci.* 59, 59–74. doi:10.1016/0168-9622(86)90057-6

Gulick, S. P. S., Meltzer, A. S., and Clarke, S. H., Jr. (2002). Effect of the northward-migrating Mendocino triple junction on the Eel River forearc basin, California: Stratigraphic development. *GSA Bull.* 114, 178–191doi. doi:10.1130/0016-7606(2002)114<0178:EOTNMM>2.0.CO;2

Han, S., Bangs, N. L., Carbotte, S. M., Saffer, D. M., and Gibson, J. C. (2017). Links between sediment consolidation and Cascadia megathrust slip behaviour. *Nat. Geosci.* 10, 954–959. doi:10.1038/s41561-017-0007-2

Hautala, S. L., Solomon, E. A., Johnson, H. P., Harris, R. N., and Miller, U. K. (2014). Dissociation of Cascadia margin gas hydrates in response to contemporary ocean warming. *Geophys. Res. Lett.* 41, 8486–8494. doi:10.1002/2014GL061606

Heeschen, K. U., Collier, R. W., De Angelis, M. A., Suess, E., Rehder, G., Linke, P., et al. (2005). Methane sources, distributions, and fluxes from cold vent sites at Hydrate Ridge, Cascadia Margin. *Glob. Biogeochem. Cycles* 19. doi:10.1029/2004GB002266

Heggland, R. (2005). "Using gas chimneys in seal integrity analysis: A discussion based on case histories," in *Evaluating Fault and cap rock seals*. Editors P. Boult and J. Kaldi (American Association of Petroleum Geologists).

Hein, J. R., Mizell, K., and Barnard, P. L. (2013). Sand sources and transport pathways for the San Francisco Bay coastal system, based on X-ray diffraction mineralogy. *Mar. Geol.* 345, 154–169. doi:10.1016/j.margeo.2013.04.003

Hill, J. C., Watt, J. T., and Brothers, D. S. (2022). Mass wasting along the Cascadia subduction zone: Implications for abyssal turbidite sources and the earthquake record. *Earth Planet. Sci. Lett.* 597, 117797. doi:10.1016/j.epsl.2022.117797

Hyndman, R. D. (2007). "2. The seismogenic zone of subduction thrust faults: What we know and don't know," in *The seismogenic zone of subduction thrust faults*. Editors H. D. Timothy and M. Casey (New York Chichester, West Sussex: Columbia University Press), 15–40.

Hyndman, R. D., and Wang, K. (1993). Thermal constraints on the zone of major thrust earthquake failure: The Cascadia Subduction Zone. *J. Geophys. Res. Solid Earth* 98, 2039–2060. doi:10.1029/92JB02279

Johnson, H. P., Merle, S., Salmi, M., Embley, R., Sampaga, E., and Lee, M. (2019). Anomalous concentration of methane emissions at the continental shelf edge of the northern Cascadia margin. *J. Geophys. Res. Solid Earth* 124, 2829–2843. doi:10.1029/2018JB016453

Johnson, H. P., Miller, U. K., Salmi, M. S., and Solomon, E. A. (2015). Analysis of bubble plume distributions to evaluate methane hydrate decomposition on the

continental slope. *Geochem. Geophys. Geosystems* 16, 3825–3839. doi:10.1002/2015GC005955

Johnson, J. E., Goldfinger, C., and Suess, E. (2003). Geophysical constraints on the surface distribution of authigenic carbonates across the Hydrate Ridge region, Cascadia margin. *Mar. Geol.* 202, 79–120. doi:10.1016/S0025-3227(03)00268-8

Joung, D., Ruppel, C., Southon, J., Weber, T. S., and Kessler, J. D. (2022). Negligible atmospheric release of methane from decomposing hydrates in mid-latitude oceans. *Nat. Geosci.* 15, 885–891doi. doi:10.1038/s41561-022-01044-8

Judd, A., and Hovland, M. (2007). *Seabed fluid flow: The impact on geology, biology and the marine environment*. Cambridge University Press.

Ketzer, M., Praeg, D., Rodrigues, L. F., Augustin, A., Pivel, M. a. G., Rahmati-Abkenar, M., et al. (2020). Gas hydrate dissociation linked to contemporary ocean warming in the southern hemisphere. *Nat. Commun.* 11, 3788. doi:10.1038/s41467-020-17289-z

Kluesner, J., Brothers, D., Hart, P., Miller, N., and Hatcher, G. (2019). Practical approaches to maximizing the resolution of sparker seismic reflection data. *Mar. Geophys. Res.* 40, 279–301. doi:10.1007/s11001-018-9367-2

Kluesner, J. W., and Brothers, D. S. (2016). Seismic attribute detection of faults and fluid pathways within an active strike-slip shear zone: New insights from high-resolution 3D P-Cable™ seismic data along the Hosgri Fault, offshore California. *Interpretation* 4, SB131–SB148. doi:10.1190/INT-2015-0143.1

Kluesner, J. W., Silver, E. A., Bangs, N. L., Mcintosh, K. D., Gibson, J., Orange, D., et al. (2013). High density of structurally controlled, shallow to deep water fluid seep indicators imaged offshore Costa Rica. *Geochem. Geophys. Geosystems* 14, 519–539. doi:10.1002/ggge.20058

Kulm, L. D., and Bales, W. E. (1969). Shallow structure and sedimentation of upper continental slope off southern and central Oregon: A preliminary investigation. *AAPG Bull.* 53, 472. doi:10.1306/5d25c68f-16c1-11d7-8645000102c1865d

Kulm, L. D., Suess, E., Moore, J. C., Carson, B., Lewis, B. T., Ritger, S. D., et al. (1986). Oregon subduction zone: Venting, fauna, and carbonates. *Science* 231, 561–566. doi:10.1126/science.231.4738.561

Law, C. S., Nodder, S. D., Mountjoy, J. J., Marriner, A., Orpin, A., Pilditch, C. A., et al. (2010). Geological, hydrodynamic and biogeochemical variability of a New Zealand deep-water methane cold seep during an integrated three-year time-series study. *Mar. Geol.* 272, 189–208. doi:10.1016/j.margeo.2009.06.018

Le Pichon, X., Kobayashi, K., and Crew, K.-N. S. (1992). Fluid venting activity within the eastern nankai trough accretionary wedge: A summary of the 1989 kaiko-nankai results. *Earth Planet. Sci. Lett.* 109, 303–318. doi:10.1016/0012-821x(92)90094-c

Ligtenberg, J. H. (2005). Detection of fluid migration pathways in seismic data: Implications for fault seal analysis. *Basin Res.* 17, 141–153. doi:10.1111/j.1365-2117.2005.00258.x

Maekawa, T. (2004). Experimental study on isotopic fractiona-tion in water during gas hydrate formation. *Geochem. J.* 38, 129–138. doi:10.2343/geochemj.38.129

Malatesta, L. C., Bruhat, L., Finnegan, N. J., and Olive, J.-a. L. (2021). Co-Location of the downdip end of seismic coupling and the continental shelf break. *J. Geophys. Res. Solid Earth* 126, e2020JB019589. doi:10.1029/2020JB019589

McCaffrey, R., Qamar, A. I., King, R. W., Wells, R., Khazaradze, G., Williams, C. A., et al. (2007). Fault locking, block rotation and crustal deformation in the Pacific Northwest. *Geophys. J. Int.* 169, 1315–1340. doi:10.1111/j.1365-246X.2007.03371.x

Mccrory, P. A., Foster, D. S., Danforth, W. W., and Hamer, M. R. (2002). "Crustal deformation at the leading edge of the Oregon coast range block, offshore Washington (Columbia river to hoh river)," in *Professional paper*. 0 ed. Version 1.

Mcneill, L. C., Goldfinger, C., Kulm, L. D., and Yeats, R. S. (2000). Tectonics of the Neogene Cascadia forearc basin: Investigations of a deformed late Miocene unconformity. *GSA Bull.* 112, 1209–1224. doi:10.1130/0016-7606(2000)112<1209:totncf>2.0.co;2

Mcneill, L. C., Goldfinger, C., Yeats, R. S., and Kulm, L. D. (1999). The effects of upper plate deformation on records of prehistoric Cascadia subduction zone earthquakes. *Geol. Soc. Lond. Spec. Publ.* 146, 321–342. doi:10.1144/gsl.sp.1999.146.01.19

Mcneill, L. C., and Henstock, T. J. (2014). Forearc structure and morphology along the Sumatra-Andaman subduction zone. *Tectonics* 33, 112–134. doi:10.1002/2012TC003264

Merle, S. G., Embley, R. W., Johnson, H. P., Lau, T.-K., Phrampus, B. J., Raineault, N. A., et al. (2021). Distribution of methane plumes on Cascadia margin and implications for the landward limit of methane hydrate stability. *Front. Earth Sci.* 9. doi:10.3389/feart.2021.531714

Mountjoy, J. J., Barnes, P. M., and Pettinga, J. R. (2009a). Morphostructure and evolution of submarine canyons across an active margin: Cook Strait sector of the Hikurangi Margin, New Zealand. *Mar. Geol.* 260, 45–68. doi:10.1016/j.margeo.2009.01.006

Mountjoy, J. J., Mckean, J., Barnes, P. M., and Pettinga, J. R. (2009b). Terrestrial-style slow-moving earthflow kinematics in a submarine landslide complex. *Mar. Geol.* 267, 114–127. doi:10.1016/j.margeo.2009.09.007

Mountjoy, J. J., Pecher, I., Henrys, S., Crutchley, G., Barnes, P. M., and Plaza-Faverola, A. (2014). Shallow methane hydrate system controls ongoing, downslope sediment transport in a low-velocity active submarine landslide complex, Hikurangi Margin, New Zealand. *Geochem. Geophys. Geosystems* 15, 4137–4156. doi:10.1002/2014GC005379

Nittrouer, C. A. (1999). Strataform: Overview of its design and synthesis of its results. *Mar. Geol.* 154, 3–12. doi:10.1016/S0025-3227(98)00128-5

Paull, C. K., Caress, D. W., Thomas, H., Lundsten, E., Anderson, K., Gwiazda, R., et al. (2015). Seafloor geomorphic manifestations of gas venting and shallow subbottom gas hydrate occurrences. *Geosphere* 11, 491–513. doi:10.1130/ges01012.1

Paull, C. K., Normark, W. R., Ussler, W., Iii, Caress, D. W., and Keaten, R. (2008). Association among active seafloor deformation, mound formation, and gas hydrate growth and accumulation within the seafloor of the Santa Monica Basin, offshore California. *Mar. Geol.* 250, 258–275. doi:10.1016/j.margeo.2008.01.011

Phrampus, B. J., Harris, R. N., and Tréhu, A. M. (2017). Heat flow bounds over the C ascadia margin derived from bottom simulating reflectors and implications for thermal models of subduction. *Geochem. Geophys. Geosystems* 18, 3309–3326. doi:10.1002/2017gc007077

Pohlman, J. W., Kaneko, M., Heuer, V. B., Coffin, R. B., and Whiticar, M. (2009). Methane sources and production in the northern Cascadia margin gas hydrate system. *Earth Planet. Sci. Lett.* 287, 504–512. doi:10.1016/j.epsl.2009.08.037

Prouty, N. G., and Baker, M. C. (2022). *CTD profiles and discrete water-column measurements collected off California and Oregon during NOAA cruise SH-18-12 (USGS field activity 2018-663-FA) from October to November 2018 U.S*. Geological Survey Data Release. doi:10.5066/P99MJ096

Prouty, N. G., Brothers, D. S., Kluesner, J. W., Barrie, J. V., Andrews, B. D., Lauer, R. M., et al. (2020). Focused fluid flow and methane venting along the Queen Charlotte fault, offshore Alaska (USA) and British Columbia (Canada). *Geosphere* 16, 1336–1357. doi:10.1130/ges02269.1

Prouty, N. G. (2023). *Geochemistry of authigenic carbonates from Cascadia margin*. U.S. Geological Survey data release. doi:10.5066/P9J10NH5

Prouty, N. G., Sahy, D., Ruppel, C. D., Roark, E. B., Condon, D., Brooke, S., et al. (2016). Insights into methane dynamics from analysis of authigenic carbonates and chemosynthetic mussels at newly-discovered Atlantic Margin seeps. *Earth Planet. Sci. Lett.* 449, 332–344. doi:10.1016/j.epsl.2016.05.023

Reed, D. L., Silver, E. A., Tagudin, J. E., Shipley, T. H., and Vrolijk, P. (1990). Relations between mud volcanoes, thrust deformation, slope sedimentation, and gas hydrate, offshore north Panama. *Mar. Petroleum Geol.* 7, 44–54. doi:10.1016/0264-8172(90)90055-L

Riedel, M., Scherwath, M., Römer, M., Veloso, M., Heesemann, M., and Spence, G. D. (2018). Distributed natural gas venting offshore along the Cascadia margin. *Nat. Commun.* 9, 3264. doi:10.1038/s41467-018-05736-x

Ruppel, C. D., and Kessler, J. D. (2017). The interaction of climate change and methane hydrates. *Rev. Geophys.* 55, 126–168. doi:10.1002/2016RG000534

Ruppel, C. D. (2011). Methane hydrates and contemporary climate change. *Nat. Eduction Knowl.* 2, 12.

Ruppel, C. D., and Waite, W. F. (2020). Timescales and processes of methane hydrate formation and breakdown, with application to geologic systems. *J. Geophys. Res. Solid Earth* 125, e2018JB016459. doi:10.1029/2018JB016459

Ryan, W. B. F., Carbotte, S. M., Coplan, J. O., O'hara, S., Melkonian, A., Arko, R., et al. (2009). Global multi-resolution topography synthesis. *Geochem. Geophys. Geosystems* 10. doi:10.1029/2008gc002332

Saffer, D. M., and Bekins, B. A. (2002). Hydrologic controls on the morphology and mechanics of accretionary wedges. *Geology* 30, 271–274. doi:10.1130/0091-7613(2002)030<0271:hcotma>2.0.co;2

Saffer, D. M., and Tobin, H. J. (2011). Hydrogeology and mechanics of subduction zone forearcs: Fluid flow and pore pressure. *Annu. Rev. Earth Planet. Sci.* 39, 157–186. doi:10.1146/annurev-earth-040610-133408

Sahling, H., Masson, D. G., Ranero, C. R., Hühnerbach, V., Weinrebe, W., Klaucke, I., et al. (2008). Fluid seepage at the continental margin offshore Costa Rica and southern Nicaragua. *Geochem. Geophys. Geosystems* 9. doi:10.1029/2008GC001978

Shapiro, S. S., and Wilk, M. B. (1965). An analysis of variance test for normality (complete samples). *Biometrika* 52 (3–4), 591–611. doi:10.1093/biomet/52.3-4.591

Silver, E. A. (1972). Pleistocene tectonic accretion of the continental slope off Washington. *Mar. Geol.* 13, 239–249doi. doi:10.1016/0025-3227(72)90053-9

Skarke, A., Ruppel, C., Kodis, M., Brothers, D., and Lobecker, E. (2014). Widespread methane leakage from the sea floor on the northern US Atlantic margin. *Nat. Geosci.* 7, 657–661. doi:10.1038/ngeo2232

Sommerfield, C. K., and Nittrouer, C. A. (1999). Modern accumulation rates and a sediment budget for the Eel shelf: A flood-dominated depositional environment. *Mar. Geol.* 154, 227–241. doi:10.1016/S0025-3227(98)00115-7

Suess, E. (2014). Marine cold seeps and their manifestations: Geological control, biogeochemical criteria and environmental conditions. *Int. J. Earth Sci.* 103, 1889–1916. doi:10.1007/s00531-014-1010-0

Suess, E., Torres, M. E., Bohrmann, G., Collier, R. W., Greinert, J., Linke, P., et al. (1999). Gas hydrate destabilization: Enhanced dewatering, benthic material turnover and large methane plumes at the Cascadia convergent margin. *Earth Planet. Sci. Lett.* 170, 1–15. doi:10.1016/S0012-821X(99)00092-8

Teichert, B. M. A., Eisenhauer, A., Bohrmann, G., Haase-Schramm, A., Bock, B., and Linke, P. (2003). U/Th systematics and ages of authigenic carbonates from Hydrate

Ridge, Cascadia margin: Recorders of fluid flow variations. *Geochimica Cosmochimica Acta* 67, 3845–3857. doi:10.1016/S0016-7037(03)00128-5

Teichert, B. M. A., Torres, M. E., Bohrmann, G., and Eisenhauer, A. (2005). Fluid sources, fluid pathways and diagenetic reactions across an accretionary prism revealed by Sr and B geochemistry. *Earth Planet. Sci. Lett.* 239, 106–121. doi:10.1016/j.epsl.2005.08.002

Torres, M. E., Embley, R. W., Merle, S. G., Tréhu, A. M., Collier, R. W., Suess, E., et al. (2009). Methane sources feeding cold seeps on the shelf and upper continental slope off central Oregon, USA. *Geochem. Geophys. Geosystems* 10. doi:10.1029/2009GC002518

Torres, M. E., Teichert, B. M. A., Tréhu, A. M., Borowski, W., and Tomaru, H. (2004). Relationship of pore water freshening to accretionary processes in the Cascadia margin: Fluid sources and gas hydrate abundance. *Geophys. Res. Lett.* 31. doi:10.1029/2004GL021219

Torres, M. E., Tréhu, A. M., Cespedes, N., Kastner, M., Wortmann, U. G., Kim, J. H., et al. (2008). Methane hydrate formation in turbidite sediments of northern Cascadia, IODP Expedition 311. *Earth Planet. Sci. Lett.* 271, 170–180. doi:10.1016/j.epsl.2008.03.061

Tréhu, A. M., Blakely, R. J., and Williams, M. C. (2012). Subducted seamounts and recent earthquakes beneath the central Cascadia forearc. *Geology* 40, 103–106. doi:10.1130/g32460.1

Trehu, A. M., Lin, G., Maxwell, E., and Goldfinger, C. (1995). A seismic reflection profile across the Cascadia subduction zone offshore central Oregon: New constraints on methane distribution and crustal structure. *J. Geophys. Res. Solid Earth* 100, 15101–15116. doi:10.1029/95jb00240

Tréhu, A. M., Long, P. E., Torres, M. E., Bohrmann, G., Rack, F. R., Collett, T. S., et al. (2004). Three-dimensional distribution of gas hydrate beneath southern Hydrate Ridge: Constraints from ODP leg 204. *Earth Planet. Sci. Lett.* 222, 845–862. doi:10.1016/j.epsl.2004.03.035

Tréhu, A. M., and Phrampus, B. J. (2022). "Accretionary wedge tectonics and gas hydrate distribution in the Cascadia forearc," in *World atlas of submarine gas hydrates in continental margins*. Editors J. Mienert, C. Berndt, A. M. Tréhu, A. Camerlenghi, and C.-S. Liu (Cham: Springer International Publishing), 121–130.

Tréhu, A. M., Torres, M. E., Moore, G. F., Suess, E., and Bohrmann, G. (1999). Temporal and spatial evolution of a gas hydrate–bearing accretionary ridge on the Oregon continental margin. *Geology* 27, 939–942. doi:10.1130/0091-7613(1999)027<0939:taseoa>2.3.co;2

Triezenberg, P. J., Hart, P. E., and Childs, J. R. (2016). *National archive of marine seismic surveys (namss): A United States geological survey data website of marine seismic reflection data within the us exclusive economic zone (eez)*. U.S. Geological Survey Data Release. doi:10.5066/F7930R7P

Von Huene, R., and Scholl, D. W. (1991). Observations at convergent margins concerning sediment subduction, subduction erosion, and the growth of continental crust. *Rev. Geophys.* 29, 279–316. doi:10.1029/91RG00969

Walton, M. a. L., Staisch, L. M., Dura, T., Pearl, J. K., Sherrod, B., Gomberg, J., et al. (2021). Toward an integrative geological and geophysical view of Cascadia subduction zone earthquakes. *Annu. Rev. Earth Planet. Sci.* 49, 367–398. doi:10.1146/annurev-earth-071620-065605

Watson, S. J., Mountjoy, J. J., Barnes, P. M., Crutchley, G. J., Lamarche, G., Higgs, B., et al. (2020). Focused fluid seepage related to variations in accretionary wedge structure, Hikurangi margin, New Zealand. *Geology* 48, 56–61. doi:10.1130/G46666.1

Watt, J. T., and Brothers, D. S. (2020). Systematic characterization of morphotectonic variability along the Cascadia convergent margin: Implications for shallow megathrust behavior and tsunami hazards. *Geosphere* 17, 95–117. doi:10.1130/ges02178.1

Wells, R. E., Blakely, R. J., and Weaver, C. S. (2002). "Cascadia microplate models and within-slab earthquake," in *The Cascadia subduction zone and related subduction systems: U.S. Geological survey open-file report 02-328 and geological survey of Canada open-file 4350.* Editors S. Kirby, K. Wang, and S. Dunlop, 17–23. doi:10.3133/ofr02328

Westbrook, G. K., Thatcher, K. E., Rohling, E. J., Piotrowski, A. M., Pälike, H., Osborne, A. H., et al. (2009). Escape of methane gas from the seabed along the West Spitsbergen continental margin. *Geophys. Res. Lett.* 36. doi:10.1029/2009GL039191

Wilk, M. B., and Gnanadesikan, R. (1968). Probability plotting methods for the analysis of data. *Biometrika* 55 (1), 1–17. doi:10.2307/2334448

Wood, W. T., Hart, P. E., Hutchinson, D. R., Dutta, N., Snyder, F., Coffin, R. B., et al. (2008). Gas and gas hydrate distribution around seafloor seeps in Mississippi Canyon, Northern Gulf of Mexico, using multi-resolution seismic imagery. *Mar. Petroleum Geol.* 25, 952–959. doi:10.1016/j.marpetgeo.2008.01.015

frontiers | Frontiers in Earth Science

TYPE Original Research
PUBLISHED 28 August 2023
DOI 10.3389/feart.2023.1176458

Check for updates

OPEN ACCESS

EDITED BY
Andrew R. Thurber,
Oregon State University, United States

REVIEWED BY
Entao Liu,
China University of Geosciences Wuhan, China
Pavlos Megalovasilis,
University of Patras, Greece

*CORRESPONDENCE
Chunhui Tao,
taochunhui@sio.org.cn

RECEIVED 28 February 2023
ACCEPTED 14 August 2023
PUBLISHED 28 August 2023

CITATION
Yang X, Tao C and Liao S (2023), Abundant off-axis hydrothermal activity in the 29–30 ridge segment of the Southwest Indian Ridge: evidence from ferromanganese crusts.
Front. Earth Sci. 11:1176458.
doi: 10.3389/feart.2023.1176458

COPYRIGHT
© 2023 Yang, Tao and Liao. This is an open-access article distributed under the terms of the Creative Commons Attribution License (CC BY). The use, distribution or reproduction in other forums is permitted, provided the original author(s) and the copyright owner(s) are credited and that the original publication in this journal is cited, in accordance with accepted academic practice. No use, distribution or reproduction is permitted which does not comply with these terms.

Abundant off-axis hydrothermal activity in the 29–30 ridge segment of the Southwest Indian Ridge: evidence from ferromanganese crusts

Xianhui Yang[1,2], Chunhui Tao[1,2]* and Shili Liao[1,2]

[1]School of Oceanography, Shanghai Jiao Tong University, Shanghai, China, [2]Key Laboratory of Submarine Geosciences, Second Institute of Oceanography, Ministry of Natural Resources, Hangzhou, Zhejiang, China

In the ultra-slow spreading mid-ocean ridge, seafloor hydrothermal ventings mostly occur in the off-axis region. The plume of hydrothermal venting provides Fe, Mn and other metal materials for the growth of ferromanganese crust in the surrounding seamounts, showing unique geochemical characteristics that are different from that of hydrogenetic crust. Based on five samples of ferromanganese crusts, major, trace and rare earth element analysis was carried out to identify their material sources. Combined with the investigation data of water column and seafloor camera photos by deep towed hydrothermal detection system, the potential of hydrothermal activity in the 29–30 ridge segment of the Southwest Indian ridge was evaluated. The results showed that the ferromanganese crust in the study area had significantly higher Fe/Mn value (average 1.9), relatively higher Si and Al contents, and significantly higher Ca/P value (average 9.3),without significant phosphorylation. ferromanganese crust in the study area have significantly lower Co and Ni contents (about 1600 mg/kg on average), and relatively lower Sr, Ba, Pb, Cu, Zr and Mo contents (between 100-1000 mg/kg on average). The contents of W, Th and Te are also relatively low (average content between 10–50 mg/kg); The total rare earth element content of the crust in the study area is relatively low (about 928 mg/kg on average), and the light rare earth is relatively enriched. The standardized rare earth curve of the shale shows a left-leaning pattern as a whole, showing the enrichment of heavy rare earth relative to the shale. The Co content and rare earth element content of the ferromanganese crusts in this area are significantly lower than those of hydrogenetic crusts. The discrimination diagrams of ternary and bivariate material sources reveal that they have mixed hydrothermal and hydrogenetic origins. The three crust samples of S1, S2, and S5 are located within 2 km of the known hydrothermal fields, indicating a correlation between ferromanganese crust and the location of hydrothermal activity. There is no known hydrothermal field near the S3 and S4 stations. Altered rocks and water column turbidity anomalies were found near S3 station, and large areas of altered rocks and suspected hydrothermal biological remains were also found near S4 station, indicating that hydrothermal activity may exist in both areas. In addition to the two new hydrothermal fields identified in this article, the spatial frequency of hydrothermal activity in the study area reaches 15 sites/100 km, which is significantly higher than other well investigated oceanic ridges. Out of the eight hydrothermal fields in the study area, seven are located in the off axis region,

mainly because the hydrothermal activity in this area is controlled by high angle and large offset normal faults and one-way detachment faults. This also indicates that the off-axis region of the Southwest Indian Ridge has high potential for hydrothermal activity.

KEYWORDS

Southwest Indian Ridge, ultra-slow spreading, off-axis, hydrothermal activity, ferromanganese crust, tectonic-controlled

1 Introduction

Seafloor polymetallic sulfide deposits are layered or stratabound sulfide deposits formed at or near the seafloor hydrothermal vents (Hannington et al., 2005). The deposits are formed at the hydrothermal vent by high-temperature, metal-rich and sulfur-rich fluid mixed with cold seawater and precipitated sulfide minerals (Hannington et al., 2011). Since the first discovery of seafloor hydrothermal vents, it has been known that seafloor hydrothermal ventings may occur in all mid-ocean ridges and ocean basins (Beaulieu et al., 2015). The discovery of seafloor hydrothermal fields is mainly concentrated in the slow-fast spreading ridges, such as the East Pacific Rise, the Central Indian Ridge, the Mid-Atlantic Ridge, etc. (Baker et al., 2016), but relatively few hydrothermal fields were found in ultra-slow spreading ridges, such as the Southwest Indian Ridge. In the slow-ultra slow-spreading ridge, "too many" high-temperature hydrothermal venting fields have been found, which may be because tectonic activity plays a greater role in the hydrothermal circulation than the magma supply (Beaulieu et al., 2015; German et al., 2016). It has been found that half of the high-temperature hydrothermal venting of the North Mid-Atlantic Ridge is controlled by tectonic activities (Escartín et al., 2008; Fouquet et al., 2010). In the slow-ultra slow-spreading ridge, the tectonically controlled seafloor hydrothermal activity often deviates from the ridge axis by 0–10 km. They have stable hydrothermal circulation fluid channels and stable heat sources and can maintain long-term hydrothermal activity for tens to hundreds of thousands of years (Tivey et al., 2003; Tao et al., 2020; Wu et al., 2021). This type of hydrothermal system will play an important role in both the formation of large-scale polymetallic sulfide deposits and the stable and long-term input of a large number of trace elements into the ocean.

The seafloor hydrothermal activity survey was initially started by the on-site observation of manned or unmanned submersibles on the seabed (Baker et al., 2016). The scope of the survey is very small, and there are few hydrothermal activity areas found. The plume of seafloor hydrothermal venting has unique physical, chemical and optical characteristics that are different from the surrounding seawater: such as temperature, salinity, turbidity, oxidation-reduction potential, methane and other abnormal parameters (Baker, 2017). Near-bottom detection of hydrothermal plumes is the most widely used technical method to investigate seafloor hydrothermal activities at present (German et al., 2016). In the database of seafloor hydrothermal fields published by Inter Ridge, about 80% of them were discovered by hydrothermal plume detection (Beaulieu and Szafrański, 2020). However, all hydrothermal activities will eventually stop. For inactive seafloor hydrothermal fields, there is no signal of hydrothermal plume, which is difficult to find. In the database, only 54 are identified as inactive. These inactive hydrothermal areas have undergone a complete hydrothermal circulation, and the accumulated polymetallic sulfide deposits are larger in scale and can avoid the risk of damaging the ecosystem near the active hydrothermal vents, which is conducive to marine mining and has attracted more attention (Jamieson and Gartman, 2020).

Ferromanganese crusts are commonly found on seamounts or ridges in ocean basins, which are precipitated by hydroxyl iron oxide and manganese oxide in seawater, and are rich in Fe, Mn, Co, Cu, Ni, rare earth elements (REE) and other metal elements (Hein and Koschinsky, 2014). In the vicinity of ocean ridges or hot spots, seafloor hydrothermal ventings provide rich Fe and Mn for the formation of ferromanganese crusts. Due to the high growth rate of crusts, the contents of metal elements such as Co, Cu, Ni and REE are depleted, showing unique geochemical characteristics (Kuhn et al., 1998; Josso et al., 2017). Fe-Mn crusts farther away from the hydrothermal field are more likely to be of hydrogenetic origin (such as increased Co and REE content) (Manheim and Lane-Bostwick, 1988; Surya et al., 2020). Therefore, through the investigation and sampling of ferromanganese crusts in the area to be investigated, geochemical research can indicate whether there is hydrothermal activity in the area.

Based on the geochemical analysis of five ferromanganese crust samples collected from the 29–30 ridge segment of the Southwest Indian Ridge, combined with the survey data of the hydrothermal activity in the region, this paper reveals its relationship with the hydrothermal activity in the vicinity.

2 Geological setting

The Southwest Indian Ridge is the boundary between the Antarctic plate and the Indian Ocean plate, with a total length of about 7,700 km, accounting for about 10% of the total length of the mid-ocean ridge (Dick et al., 2003). The full spreading rate of SWIR is about 14–16 mm/yr, belonging to the ultra-slow spreading ridge (Dick et al., 2003). The Andrew Bain transform fault divides SWIR (0–70°E) into two sections, with the western section (0–30°E) having an overall NEE trend and the eastern section (30–70°E) an overall NE trend (DeMets et al., 1990). Our study area is located in the middle of the eastern section of the Southwest Indian Ridge, between the Indomed and Gallieni transform faults. The thickness of the oceanic crust varies greatly. Basalt is mainly exposed on the seabed, and deep

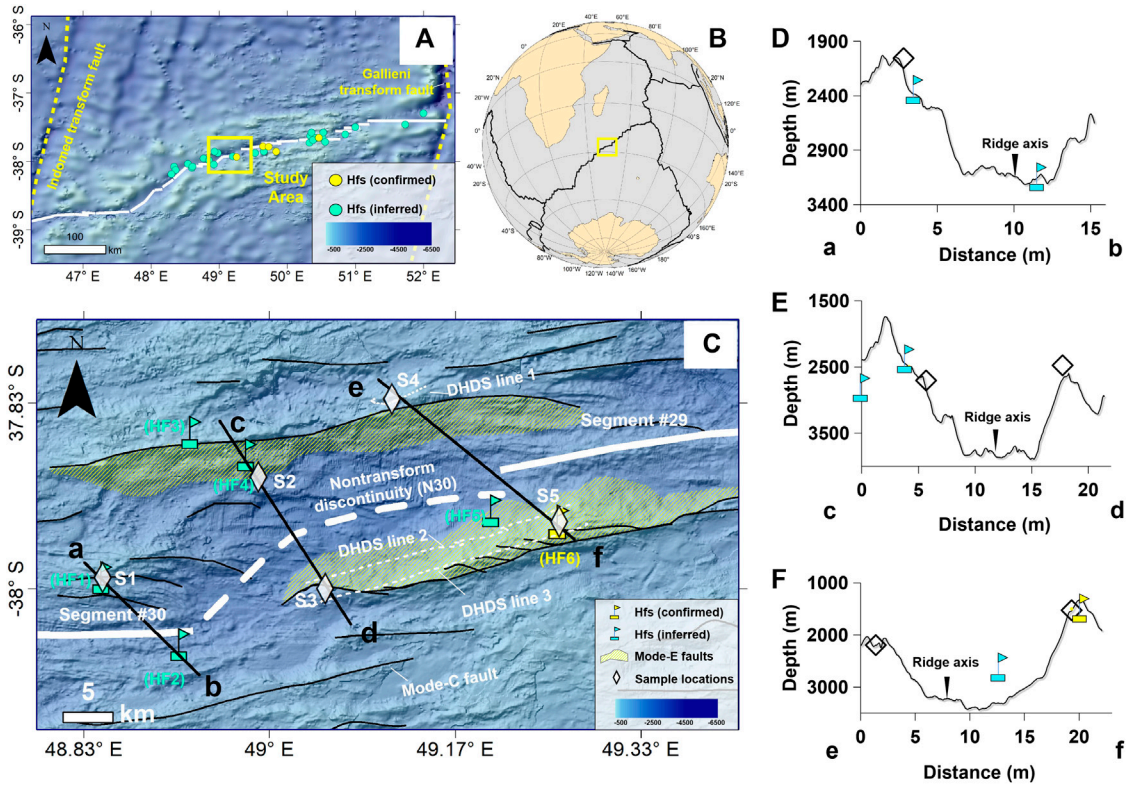

FIGURE 1
Sampling station and geological background. **(A–C)** Topographic map and sampling location of the study area; **(D)** a-b topographic profile; **(E)** c-d topographic profile; **(F)** e-f topographic profile. The white solid line represents the ridge axis, and the white thick dotted line represents the non-transformed discontinuities (NTDs). The white thin dotted line represents the deep-towed survey line. Ridge segmentation and NTDs delimitation are from refs (Cannat et al., 1999; Li et al., 2020). The location information of the seafloor hydrothermal field (HF1-HF6) is from refs (Li et al., 2020; Yue, 2020; Zhang et al., 2022).

TABLE 1 Sampling station information.

Station	Latitude (°S)	Longitude (°E)	Depth (m)	Substrate rock	Crust thickness (mm)
S1	37.99	48.85	2,054	Basalt	5–6
S2	37.90	48.99	2,706	Serpentinite	5–10
S3	38.00	49.05	2,477	Basalt	5–6
S4	37.83	49.11	2,196	Basalt	5–10
S5	37.94	49.26	1,527	Basalt	5–7

oceanic crust and mantle materials are exposed in some areas (Zhou and Dick, 2013). There are 10 central volcanic ridges (AVR) in this region, numbered 25–34 from east to west (Cannat et al., 1999; Li et al., 2020). AVR is offset by nine non-transform discontinuities (NTDs) from 0 to 35 km. The study area is located between 29 and 30 AVR, two AVRs are divided by an NTD, and there is a mode-E type fault on both sides of the ridge axis, with a length of more than 25 km (Liu et al., 2020) (Figure 1). Among them, there are many studies on the mode-E fault located on the south side of the ridge axis. The main part of the fault is oceanic basalt, and the ultramafic rock is exposed at the bottom of the fault, which is in the early stage of detachment fault development.

3 Materials and methods

Five ferromanganese crusts used in this paper were collected by the Chinese "Da Yang Yi Hao" ship in the 29–30 segment of the Southwest Indian Ridge using a television grab during the 2014–2019 marine survey. The sampling location is located on the rift wall 5–7 km away from the ridge axis, and the sampling

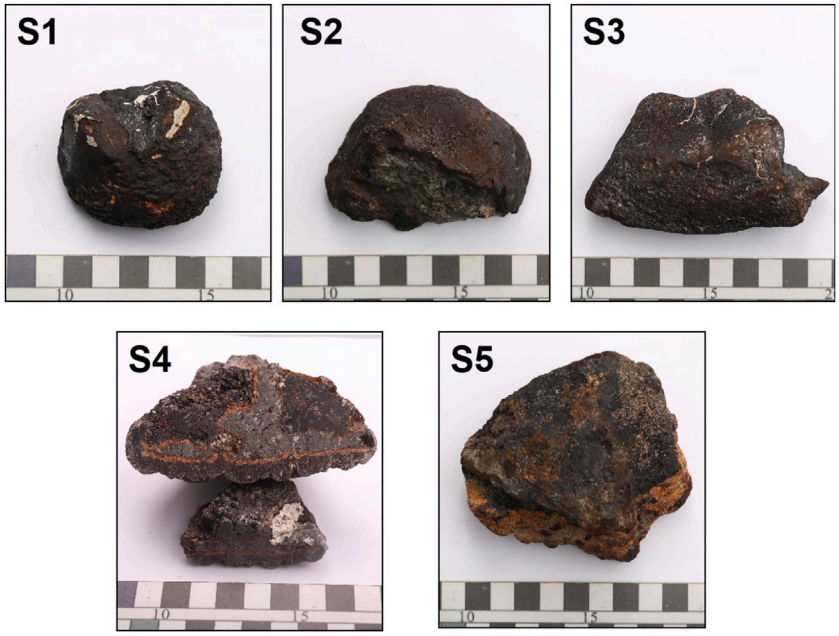

FIGURE 2
Photos of ferromanganese crust samples.

depth ranges from 1,500 to 2,700 m (Figure 1). The sample sampling station information is shown in Table 1.

After cleaning and drying the sample, take a photo of the original sample (Figure 2) and describe the sample. Cut the sample into thin slices using a cutting machine, and perform optical microscopy observation and photography, as shown in Figure 3. The size of the hand specimen to which the ferromanganese crust belongs ranges from 4 to 10 cm, and the thickness of the crust ranges from 5 to 10 mm (Figure 2). The crusts are all black brown in colour, with micro papillary surface morphology. The microscopic observation of ferromanganese crusts in the study area mainly presents parallel layered structures, without obvious sedimentary discontinuities, indicating that the formation environment and material transport of these samples are relatively stable (Figure 3).

After the ferromanganese is peeled off from the original rock, it is cleaned by an ultrasonic cleaning machine with deionized water and ground in an agate mortar to 200 mesh (74 μm). The geochemical analysis of ferromanganese crust samples was carried out in the ALS Laboratory in Guangzhou. The major elements were analyzed by X-ray fluorescence (PANalytical PW2424). Before analysis, each sample is fully mixed with a flux containing Lithium nitrate and heated at 1,000°C for about 1 h. After melting, each sample is transferred to a platinum mould to form a flat glass plate. Three standard samples (GBW07105, NCSDC47009, and SARM-4) were used to monitor the accuracy of data during analysis. The precision of the analysis was better than that of ±5%. Analyze trace elements in Agilent 7700x ICP-MS. Weigh approximately 250 mg of each sample and digest it with $HClO_4$, HNO_3, and HF. Evaporate the solution until dry, discharge the residue, dissolve with dilute HCl, and analyze the dissolved sample. In the spectrum, the results were adjusted based on inter-element interference. The reference samples GBM908-10 and MRGeo08 are used as internal standards for data quality control, the precision of the analysis was better than that of ±10%.

The deep towed hydrothermal detection system (DHDS) was used to investigate the hydrothermal activity of the 29–30 ridge segment of the Southwest Indian Ridge during the 2014–2015 sea survey by the Chinese “Da Yang Yi Hao” ship. The DHDS system includes two cameras that can be used to photograph the seabed and a series of hydrothermal plume detectors (redox potential sensors, turbidity sensors, etc.); among them, the camera was placed on the towed body near the seabed (3–5 m from the bottom), and the hydrothermal plume detectors were placed on the cable of the towed body. Four groups were placed at 50, 100, 150, and 200 m from the bottom, respectively. The deployment test line of DHDS is shown in Figure 1.

4 Results

4.1 Major element

The composition of the bulk chemical major elements of the five ferromanganese crust samples in the study area is shown in Table 2. Among them, the content of Fe and Mn is the highest, and the element content is mostly greater than 10%. Among them, the Fe content ranged from 19.54% to 24.12%, with an average of 22.16%; the Mn content ranges from 6.14% to 15.44%, with an average of 11.58%. The Fe content of crust samples in the study area is significantly higher than that of hydrogenetic ferromanganese crusts in the Northwest Pacific and Indian Ocean, and also

10.3389/feart.2023.1176458

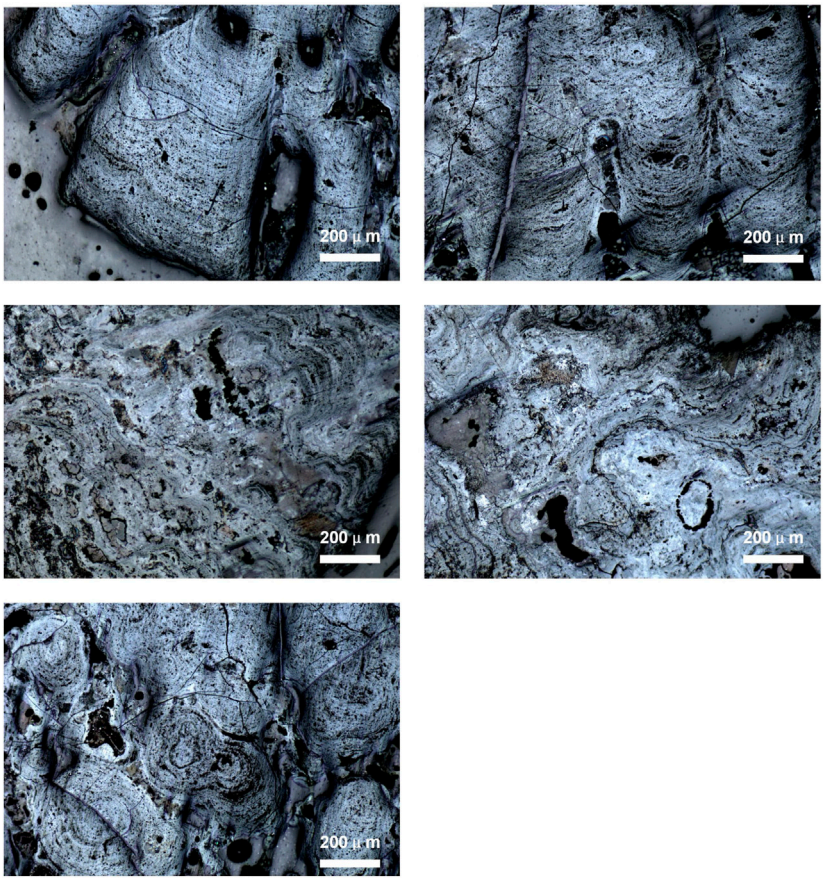

FIGURE 3
Microstructure of ferromanganese crust.

TABLE 2 Major element composition.

Element	Unit	Detection limit	S1	S2	S3	S4	S5	Mean
Fe	wt %	0.01	21.11	19.54	22.42	23.63	24.12	22.16
Mn	wt %	0.01	15.44	12.78	9.96	13.60	6.14	11.58
Si	wt %	0.05	6.55	10.16	8.49	6.16	11.21	8.51
Ca	wt %	0.01	5.98	2.68	4.85	3.49	4.06	4.21
Al	wt %	0.01	3.54	2.70	2.37	1.76	2.29	2.53
Mg	wt %	0.01	3.13	2.17	1.36	1.15	1.82	1.93
Na	wt %	0.01	0.95	1.93	1.79	1.37	1.05	1.42
Ti	wt %	0.01	0.91	0.61	0.61	0.70	0.31	0.63
K	wt %	0.01	0.44	0.49	0.50	0.54	0.72	0.54
P	wt %	0.01	0.46	0.35	0.48	0.52	0.45	0.45
Fe/Mn			1.37	1.54	2.27	1.72	4.00	1.91
Ca/P			13.00	7.66	10.10	6.71	9.02	9.30

higher than that of global ferromanganese nodules (Figure 4). The Mn content is lower than that of hydrogenetic crusts in the Northwest Pacific and Indian Ocean, and also lower than that of global ferromanganese nodules. The Fe/Mn ratio of ferromanganese crusts in the study area is 1.37–4.00, with an average of 1.91, which is significantly higher than that of northwest Pacific crusts (0.68) and

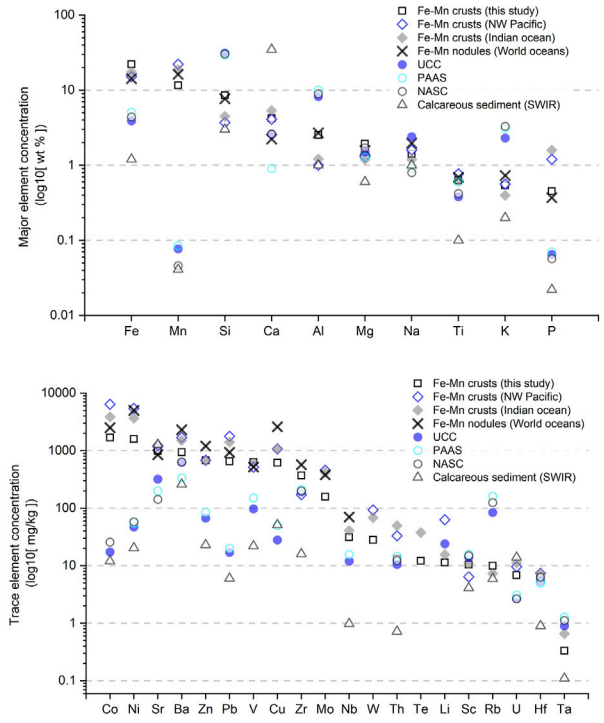

FIGURE 4
Comparison of the bulk chemical major and trace element content of samples in the study area with other samples. The data of Fe-Mn crusts (NW Pacific) are from ref Jamieson and Gartman (2020). The data of Fe-Mn crusts (Indian ocean) are from ref Hein et al. (2016). The Fe-Mn nodules (world ocean) data are from ref Mukhopadhyay et al. (2008). The data of UCC, PAAS and NASC are from ref Ray and Paul (2021). The data of calcareous sediment (SWIR) are from ref Dasong et al. (2016).

Indian Ocean crusts (1.13), and also higher than that of global ferromanganese nodules (0.88) (Figure 4).

The secondary elements are Si, Ca, Al, Mg, and Na, and the element content is mostly between 1% and 10%, with an average content of 8.51%, 4.21%, 2.53%, 1.93%, and 1.42%, respectively (Table 2). Among them, the Si content of the crusts in the study area is significantly higher than that of the hydrogenetic crusts in the Northwest Pacific and Indian Ocean, which is comparable to the global ferromanganese nodules. The Ca content of the crusts in the study area is comparable to that of the Northwest Pacific crusts, slightly lower than that of the Indian Ocean crusts, and significantly higher than that of the global ferromanganese nodules. The Al content of crusts in the study area is significantly higher than that of crusts in the Northwest Pacific and Indian Ocean, which is comparable to that of global ferromanganese nodules. The Mg and Na contents of the crusts in the study area are comparable to those of the Northwest Pacific and Indian Ocean crusts, as well as global ferromanganese nodules. The average contents of Ti, K and P elements in the crust of the study area are lower than 1%, which are 0.63%, 0.54%, and 0.45%, respectively (Table 2).

Among them, the Ti and K contents of the crusts in the study area are equivalent to those of the crusts in the northwest Pacific Ocean and the Indian Ocean, as well as global ferromanganese nodule; The P content of the crusts in the study area is significantly lower than that of the crusts in the Northwest Pacific Ocean and the Indian Ocean and is equivalent to the global ferromanganese nodule. The average Ca/P value of the crusts in the study area is 9.30, which is much higher than that of fluorocarbon Apatite (less than 2), and also significantly higher than that of the crusts in the northwest Pacific Ocean and the Indian Ocean (about 3.4), indicating that there is no obvious phosphorylation of the crusts in the study area (Beaulieu et al., 2015; Surya et al., 2020).

4.2 Trace element

The composition of the bulk chemical trace element of the five ferromanganese crusts in the study area is shown in Table 3. The average content of Co and Ni in ferromanganese crusts in the study area is more than 1,000 mg/kg, and the average content is about 1,600 mg/kg, which is far lower than that in the northwest Pacific, Indian Ocean and global ferromanganese nodule (Figure 4). The average content of Sr, Ba, Zn, Pb, V, Cu, Zr, and Mo in the ferromanganese crusts in the study area ranges from 100 to 1,000 mg/kg. Except for Zn and V, the content of other elements is significantly lower than the hydrogenetic crusts of the Northwest Pacific and Indian Ocean. The Zn content in the crusts of the study area is equivalent to that of the hydrogenetic crusts of the Northwest Pacific Ocean and the Indian Ocean, but significantly lower than that of the global ferromanganese nodule. The V content of crusts in the study area is comparable to that of hydrogenetic crusts in the Northwest Pacific and Indian Ocean, as well as global ferromanganese nodules. The content of Sr in the study area is slightly higher than that of global ferromanganese nodules, and the content of Ba, Pb, Cu, Zr and Mo is significantly lower than that of global ferromanganese nodule. It is worth noting that the Cu element content of S5 is significantly higher, reaching 1.43 wt%, which is 15–31 times the content of the other four samples. Moreover, the Zn content of S5 is significantly higher, approximately twice that of the other four samples. The average content of Nb, W, Th, Te, Li, and Sc in the ferromanganese crusts in the study area ranges from 10 to 50 mg/kg, while the average content of Rb, U, and Hf ranges from 1 to 10 mg/kg. The content of Ta is below 1 mg/kg, with an average of 0.33 mg/kg; Among them, except for the significantly lower content of W, Th, and Te compared to hydrogenetic crusts in the Northwest Pacific and Indian Ocean, the content of other elements is equivalent to that in hydrogenetic crusts in the Northwest Pacific and Indian Ocean.

4.3 Rare earth elements and yttrium

The composition of bulk chemical rare earth elements and yttrium (REY) of the five ferromanganese crusts in the study area is shown in Table 4. The total REE content ranges from 3,208 to 1,415 mg/kg, with an average content of 928 mg/kg, which is lower than that of hydrogenetic ferromanganese crusts (Figure 5). Among them, the total REE content of S5 is very low, which is 320 mg/kg, 2.5–4 times lower than the other four samples. The contents of light rare earth (LREE) and heavy rare earth (HREE) are 285–1,274 mg/kg and 35–140 mg/kg, respectively. LREE/HREE

TABLE 3 Trace element composition.

Element	Unit	Detection limit	S1	S2	S3	S4	S5	Mean
Co	mg/kg	0.1	1,835	1,605	879	1,945	2,210	1,695
Ni	mg/kg	0.2	2,390	2,620	1,015	1,475	515	1,603
Sr	mg/kg	0.2	1,060	923	1,190	1,195	567	987
Ba	mg/kg	0.5	1,040	1,195	990	860	621	941
Zn	mg/kg	2	633	560	449	506	1,250	680
Pb	mg/kg	0.5	754	702	540	1,050	207	651
V	mg/kg	5	672	573	590	744	586	633
Cu	mg/kg	0.2	447	930	599	492	14,300	617[a]
Zr	mg/kg	2	386	395	387	484	201	371
Mo	mg/kg	0.05	238	165.5	76.3	242	69.3	158.0
Nb	mg/kg	0.1	34.0	31.1	32.8	47.6	11.5	31.4
W	mg/kg	1	45	21	14	51	10	28.2
Th	mg/kg	0.01	14.8	10.2	15.1	21.2	4.7	13.2
Te	mg/kg	0.05	13.4	11.5	10.3	18.7	7.2	12.2
Li	mg/kg	0.2	23.2	15.2	5.6	6.2	6.6	11.4
Sc	mg/kg	0.1	10.4	11.8	10.2	10.3	9.8	10.5
Rb	mg/kg	0.1	7.2	8.8	8.0	9.6	16.2	10.0
U	mg/kg	0.05	8.3	5.8	5.7	9.7	4.9	6.9
Hf	mg/kg	0.1	6.0	7.1	7.2	8.7	3.6	6.5
Ta	mg/kg	0.05	0.35	0.33	0.31	0.53	0.14	0.33

[a]Due to the extremely high Cu content of S5 compared to the other four samples, which is not representative, only the average Cu content of S1–S4 is taken for comparison with samples from other regions.

values range from 8.14 to 11.18, with an average of 8.90, which shows light rare earth enrichment. δCe value is 1.50–2.53, with an average of 1.94, indicating that the crust growth environment is partial oxidation. From the normalized distribution curve of rare earth elements of Post-Archean Australian Shales (PAAS) (Figure 5), it can be seen that the five ferromanganese crusts in the study area have a similar distribution trend with hydrogenetic ferromanganese crusts, Ce and Eu elements show obvious positive anomalies and Y elements show obvious negative anomalies except S5. The rare earth curve shows a left-dipping type as a whole, with La_{SN}/Yb_{SN} values ranging from 0.58 to 0.91 and an average of 0.78, showing the enrichment of heavy rare earth relative to shale.

5 Discussion

5.1 Identification of the material source

Fe-(Co + Ni + Cu) × The 10-Mn ternary discriminant diagram is often used to distinguish the material sources of ocean ferromanganese deposits, which are mainly divided into three types of hydrogenetic, hydrothermal and diagenetic genesis (Bau et al., 2014). The ferromanganese crusts of S1-S4 in the study area are in the hydrogenetic origin region of the ternary diagram but are closer to the hydrothermal origin region compared to the hydrogenetic ferromanganese crusts, similar to the ferromanganese crusts affected by the hydrothermal activity (Figure 6A). Among them, the Cu content of S5 is very high, causing a significant deviation from the hydrogenetic region of the ternary diagram. Recently, Josso et al. (2017) used Fe, Mn, Cu, Ni elements, high field strength elements Zr, and rare earth elements Ce, Y to distinguish the material sources of ferromanganese deposits, avoiding the problem of traditional ternary diagrams that are difficult to distinguish between types of hydrogenetic and diagenetic origins. The S1–S4 is in the mixed region of hydrothermal and hydrogenetic genesis, indicating the possible influence of hydrothermal activity (Figure 6B). S5 is close to the diagenetic region due to its high Cu content.

Different types of oceanic ferromanganese deposits have different REY distributions. Bau et al. (2014) distinguished different oceanic ferromanganese deposits using Nd content, Ce and Y anomalies (Figures 7A, B). Among them, hydrothermal deposits have low Nd content, negative Ce anomalies, and positive Y anomalies; Hydrogenetic crusts exhibit high Nd content, positive Ce anomalies, and negative Y anomalies (Bau et al., 2014). In the ferromanganese crusts in the study area,

10.3389/feart.2023.1176458

TABLE 4 Composition of rare earth elements and yttrium.

Element	Unit	Detection limit	S1	S2	S3	S4	S5	Mean	Hydrogenetic Fe-Mn crusts[a]
Y	mg/kg	0.1	140	72	106	158	48	104	175
La	mg/kg	0.1	184	111	170	221	45	146	209
Ce	mg/kg	0.1	572	501	480	775	182	502	700
Pr	mg/kg	0.02	37.8	20.4	35.1	45.3	9.2	29.6	34
Nd	mg/kg	0.1	160	90	152	187	39	125	147
Sm	mg/kg	0.03	31.9	17.5	30.0	36.8	8.1	24.8	28
Eu	mg/kg	0.02	8.3	4.4	7.3	9.5	2.3	6.4	7.5
Gd	mg/kg	0.05	35.8	19.9	32.6	41.5	9.5	27.9	35
Tb	mg/kg	0.01	5.5	3.1	5.0	6.3	1.5	4.2	5.6
Dy	mg/kg	0.05	32.9	18.3	29.9	38.4	9.4	25.8	35.9
Ho	mg/kg	0.01	6.8	3.7	5.7	7.8	2.0	5.2	8.1
Er	mg/kg	0.03	19.0	10.3	15.8	21.8	5.8	14.5	25.1
Tm	mg/kg	0.01	2.6	1.4	2.1	3.0	0.8	2.0	3.6
Yb	mg/kg	0.03	16.2	8.6	12.6	18.7	5.3	12.3	24.4
Lu	mg/kg	0.01	2.6	1.3	1.9	2.9	0.9	1.9	3.8
∑REE	mg/kg		1,115	811	979	1,415	320	928	1,267
LREE	mg/kg		993	744	874	1,274	285	834	1,125
HREE	mg/kg		121	67	106	140	35	94	142
LREE/HREE			8.19	11.18	8.28	9.08	8.14	8.90	7.90
δCe			1.65	2.53	1.50	1.86	2.14	1.94	2.07
La_{SN}/Yb_{SN}			0.77	0.86	0.91	0.80	0.58	0.78	0.58

Note: δ Ce = $2Ce_{SN}/(La_{SN} + Pr_{SN})$, Ce_{SN}, La_{SN}, and Pr_{SN} are the normalized values of Post-Archean Australian Shales. Shale data from ref Pourmand et al. (2012).
[a]The data is the average from the literature (Bau et al., 1996).

S3 exhibits weak Ce negative anomalies, while S1, S4, and S5 exhibit weak Ce positive anomalies, between typical hydrogenetic crusts and hydrothermal ferromanganese oxides, indicating that they may be affected by hydrothermal activity (Figure 7A). The Ce positive anomaly of S2 is slightly higher than that of the other four samples, but it is also significantly lower than typical hydrogenetic crusts, and the Nd content is also significantly lower than that of hydrogenetic crusts, indicating that it may be affected by hydrothermal activity (Figure 7A). All five crusts in the study area exhibit weak Y negative anomalies, Ce weak positive or weak negative anomalies, and are in the transition zone between hydrogenetic crusts and hydrothermal ferromanganese oxides, indicating the possible influence of hydrothermal activity (Figure 7B). The Co and REE elements in ferromanganese crusts mainly come from seawater, which is often enriched in hydrogenetic crusts and depleted in hydrothermal crusts (reference). In addition, there are significant differences in Mn/Fe values among ferromanganese deposits of different origins. Hydrothermal ferromanganese deposits often exhibit significant differentiation between Fe and Mn, with high Fe and low Mn being common, indicating low Mn/Fe values (Manheim and Lane-Bostwick, 1988). The Co and REE content of crusts in the study area is between the hydrogenetic crusts and the hydrothermal ferromanganese deposits, with the characteristics of hydrogenetic and hydrothermal mixing (Figures 7C, D). The Mn/Fe value of the crust in the study area is slightly lower than that of typical hydrogenetic crusts, indicating possible hydrothermal activity effects (Figure 7C).

5.2 Indication of off-axis hydrothermal activity

Previous investigations have shown that there is one confirmed Yuhuang-1 hydrothermal field (Figure 1, HF6) and five inferred hydrothermal fields (Figure 1, HF1-HF5) in the study area (Li et al., 2020; Yue, 2020; Zhang et al., 2022). Among them, three are inferred active hydrothermal fields (HF2: S30 hydrothermal field, HF3: Yuhuang-3 hydrothermal field, HF5: Yuhuang-2 hydrothermal field), and there are also water turbidity anomalies and ORP anomalies (Li et al., 2020). There are also two inferred inactive hydrothermal fields (HF1: Baidi hydrothermal field and HF4: Chunxi hydrothermal field). Alteration rocks and hydrothermal products (opals) related to hydrothermal activity were found, but no turbidity anomaly of the water column was found (Tao et al., 2012). Except that the HF2 hydrothermal anomaly field is located near the ocean ridge axis (<3 km), the other hydrothermal fields or

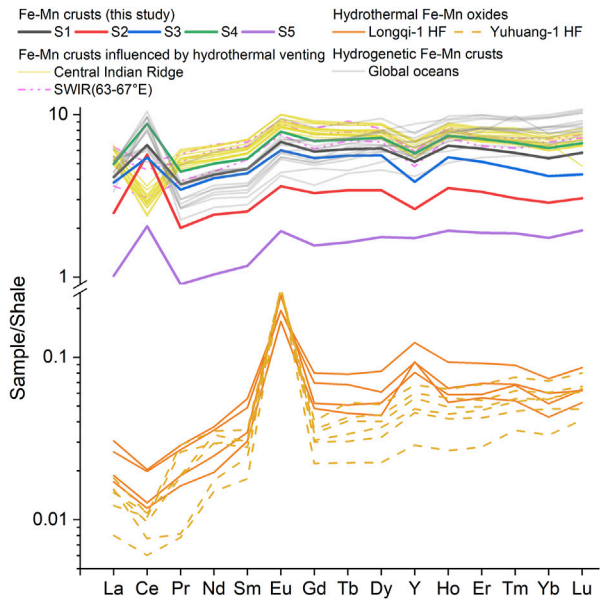

FIGURE 5
Range of shale-normalized rare-earth element (REE) and Y. Shales data of Post-Archean Australian comes from ref Pourmand et al. (2012). The data of hydrothermal Fe-Mn oxides are from refs Ye (2010) and Hu et al. (2022). The data of hydrogenetic ferromanganese crusts are from ref Bau et al. (2014). Data on Fe-Mn crusts influenced by hydrothermal venting come from refs Kuhn et al. (1998) and Surya et al. (2020).

hydrothermal anomaly fields are located in the off-axis area (5–10 km) on both sides of the ocean ridge axis.

The previous investigation showed that the diffusion range of the hydrothermal plume in the Southwest Indian Ridge was not more than 10 km, and most of them were less than 5 km (Yue et al., 2019; Chen et al., 2021). After being more than 10 km away from the hydrothermal activity field, many parameters for tracing the hydrothermal plume decrease to lower levels, close to the background seawater (Yue et al., 2019; Chen et al., 2021). In addition, the geochemical analysis of the surface sediments around the hydrothermal field also shows that the chemical anomaly of the sediments affected by the hydrothermal substances has significantly decreased to the level close to the background sediments after being more than 10 km away from the hydrothermal activity field (Liao et al., 2018; Liao et al., 2019).

Among the ferromanganese crusts sampled in the study area, S1 was taken from the vicinity of the Baidi hydrothermal field (~2 km), S2 was taken from the vicinity of the Chunxi hydrothermal field (~2 km), S5 was taken from the confirmed Yuhuang-1 hydrothermal field. To sum up, the content of Cu and Zn in S5 is significantly higher, especially the very high content of Cu, which may be related to the abundant supply of Cu and Zn in the hydrothermal field. In addition, the REE content of S5 is significantly lower than that of aqueous crusts and the other four crusts, which is also similar to that of hydrothermal products. In addition to S5 affected by hydrothermal activity, the other four crust samples may also be affected by hydrothermal activity to a certain

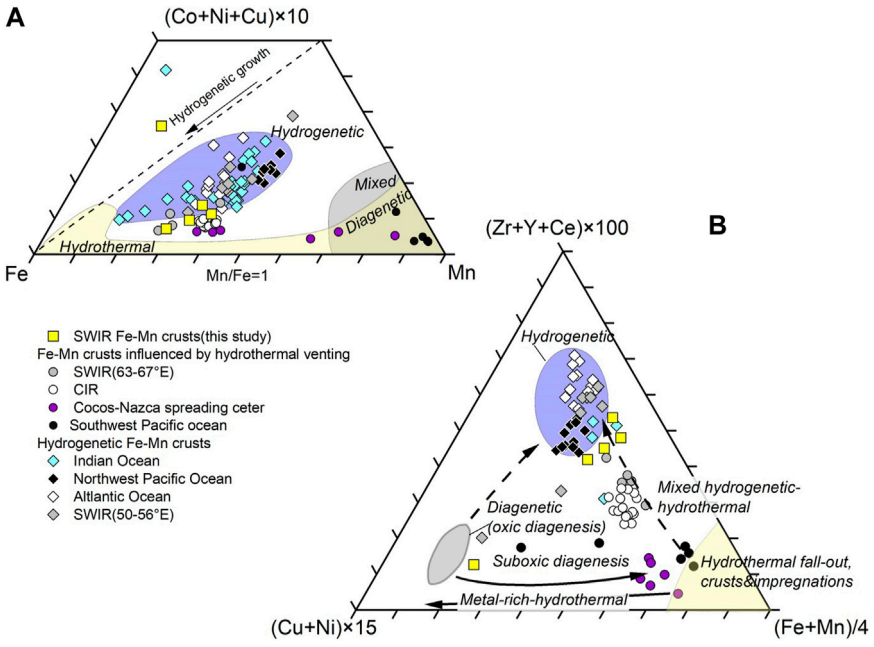

FIGURE 6
Ternary discriminant diagram of ferromanganese crust. **(A)** Fe-(Co + Ni + Cu) × 10-Mn ternary discriminant diagram, modified from ref Bonatti et al. (1972); **(B)** 15 × (Cu + Ni)-(Zr + Y + Ce) × 100-(Fe + Mn)/4, modified from ref Josso et al. (2017). Data on hydrogenetic ferromanganese crusts from refs Yu et al. (2013), Bau et al. (2014), and Yu et al. (2021); Data of Fe-Mn crusts influenced by hydrothermal venting are from refs Kuhn et al. (1998), Surya et al. (2020), Staszak et al. (2022), and Zawadzki et al. (2022).

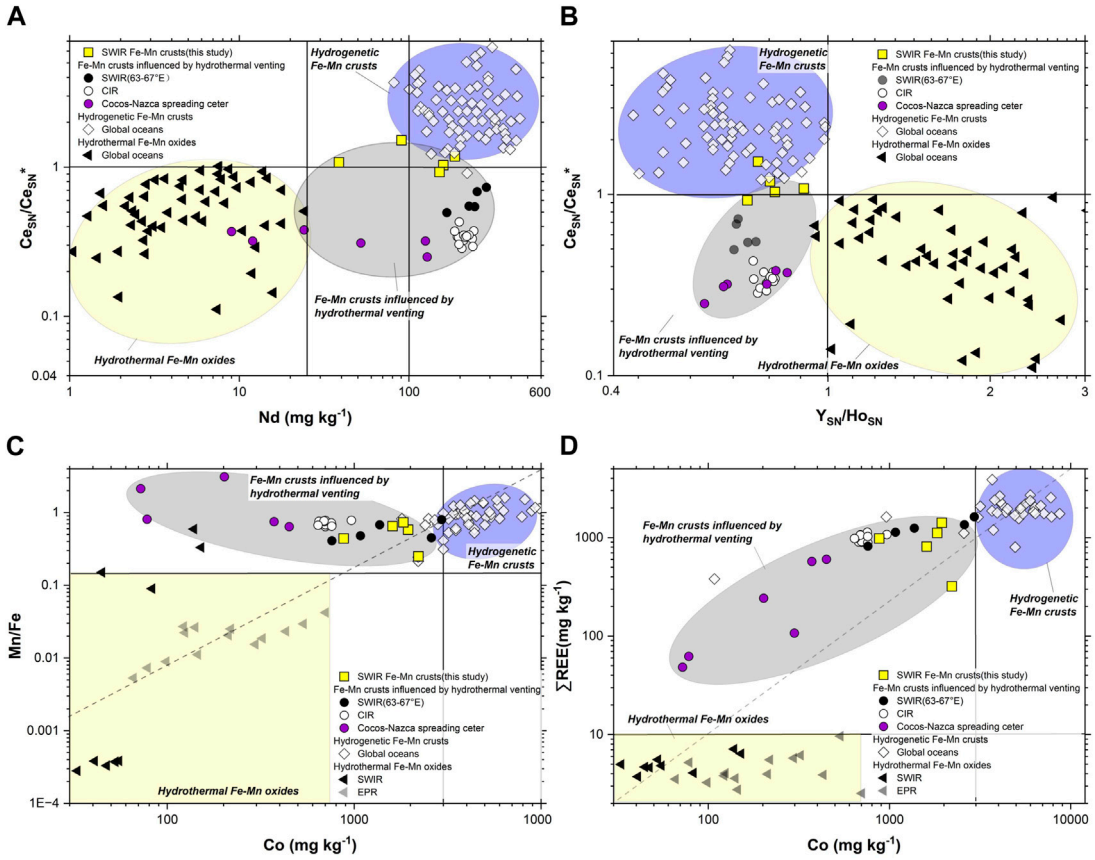

FIGURE 7
Bivariate discriminant diagram of ferromanganese crust. **(A)** Ce_{SN}/Ce_{SN}* ratio vs. Nd content; **(B)** Ce_{SN}/Ce_{SN}* ratio vs Y_{SN}/Ho_{SN} ratio; **(C)** Mn/Fe ratio vs Co content; **(D)** Total REE content vs Co content. The data of hydrogenetic ferromanganese crusts are from Bau et al. (2014); The data of Fe-Mn crusts influenced by hydrothermal venting are from refs (Kuhn et al., 1998; Surya et al., 2020; Zawadzki et al., 2022); The data of hydrothermal Fe-Mn oxides are from refs (Zhigang et al., 2007; Ye, 2010; Bau et al., 2014; Hu et al., 2022).



FIGURE 8
Photographs of altered rocks near the S3 station.

extent, thus showing characteristics different from common hydrogenetic crusts (Figures 6, 7). S3 and S4 are more than 10 km away from the known hydrothermal field or hydrothermal anomaly field, which exceeds the diffusion range of the hydrothermal plume in this region. The influence of hydrothermal activity on these two ferromanganese crusts may come from the undiscovered hydrothermal field.

On DHDS survey line 2, adjacent to the S3 station area, a large area of yellowish-brown breccia covered by thin sediment layers was observed in seabed photography (Figure 8), suspected to have been

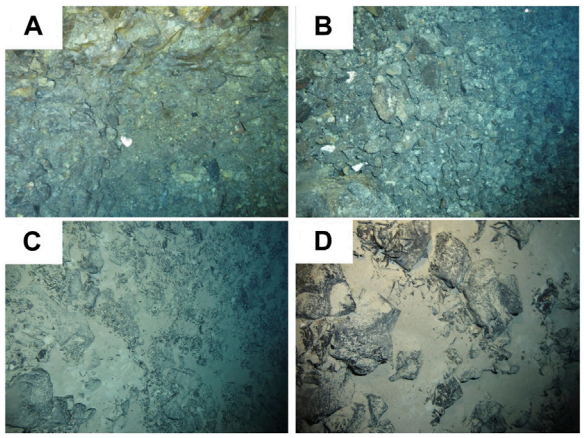

FIGURE 9
Photographs of seabed near S4 station. **(A,B)** Altered rocks; **(C,D)** Suspected hydrothermal biological remains.

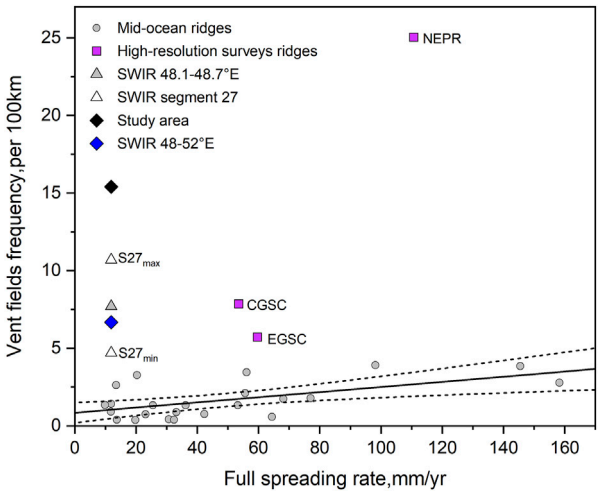

FIGURE 10
The relationship between the spatial frequency of hydrothermal activity and the spreading rate of the oceanic spreading ridge. The grey circle data is from ref Beaulieu et al. (2015), representing the well-surveyed area; The purple square data comes from ref Baker et al. (2016), representing the area of detailed optical and ORP survey. CGSC is the Galapagos spreading centre, EGSC is the east side of Galapagos spreading centre, and NEPR is 9–10°N of the East Pacific Rise; The black diamond is the data of the study area; The grey triangle data is from ref Chen et al. (2021), which represents the area between SWIR 30 and 31 ridge segments of the detailed optical and ORP survey; The white triangle data is from ref Yue et al. (2019), representing the SWIR 27 ridge segment of the detailed optical and ORP survey; The blue diamond is a synthesis of the research results of this paper and the publicly reported data of the hydrothermal fields in the SWIR 48–52°E area. The black line represents the linear regression fitting line of the well-surveyed ridges, and the black dotted line represents the ±95% confidence interval.

modified by surrounding hydrothermal fluids. The hydrothermal plume sensor deployed on the survey line did not record any water column anomalies. On DHDS Line 3, adjacent to S3 station, the hydrothermal plume sensor deployed recorded a significant sudden increase in water turbidity and a sudden decrease in oxidation Reduction potential near 2,200 m water depth (Li et al., 2015); In summary, there is a high possibility of an unknown hydrothermal field near the S3 station, and we have temporarily named it the 49.05°E hydrothermal field.

On the DHDS survey line 1, a large area of yellowish-brown rock was observed in the seabed camera near the S4 station (Figure 9), which is different from the mid-ocean ridge basement rock dominated by grey-black oceanic basalt and is suspected to be modified by the surrounding high-temperature hydrothermal fluid (Tao et al., 2012; Chen et al., 2021). The hydrothermal plume sensor did not record the water chemistry and water turbidity anomalies, indicating that the hydrothermal activity in this area may be inactive. In addition, the seabed camera also observed a large area of dead shell remnants (Figure 9), suspected to be mussels living near the hydrothermal field (Tao et al., 2012). This also further proves that there is seafloor hydrothermal activity in this area, which has ceased. In summary, there is a high possibility that there is an unknown hydrothermal field near the S4 station. We temporarily named it the 49.11°E hydrothermal field.

Together with the two off-axis hydrothermal fields identified in this paper, a total of eight hydrothermal fields were found in the 29–30 ridge segment of the Southwest Indian Ridge, of which only one was near the ridge axis and the remaining seven were located in the off-axis 5–10 km region (Figure 1), showing high off-axis hydrothermal activity abundance. In the region with a total length of about 52 km, the spatial frequency of hydrothermal activity (Fs) is 15.4 sites/100 km. It is significantly higher than the well-investigated ocean ridge and 14 times higher than the linear fit prediction (Fs: 1.1 sites/100 km) (Figure 10). Compared to other detailed hydrothermal activity surveys on the Southwest Indian Ridge, the Fs of the study area is at a high level. Among them, the Fs of the study area is twice as high as that of the adjacent SWIR 48.1–48.7°E region located on its western side, which is 44% higher than the highest prediction of the SWIR 27 segment on the east side of the study area. The study area also had a higher Fs than other well-investigated spreading centres, one time higher than the Galapagos spreading centre, but significantly lower than the North East Pacific Rise. This means that the off-axis hydrothermal activity of the Southwest Indian Ridge is still underestimated compared to past understanding.

5.3 Factors controlling the distribution of hydrothermal activity

The seafloor hydrothermal circulation is ultimately driven by heat sources, and magmatic activity can provide sufficient heat sources for hydrothermal activity. The variability of magma supply is the main controlling factor affecting the distribution pattern of hydrothermal activity on the mid-ocean ridge, and hydrothermal activity increases linearly with the increase of magma supply (Beaulieu et al., 2015; Baker, 2017). Due to the influence of segmentation and local magma supply characteristics, there are differences in the amount of magma and the proportion of tectonic activity between different ridge segments in the Southwest Indian Ocean. This in turn leads to the diversity of

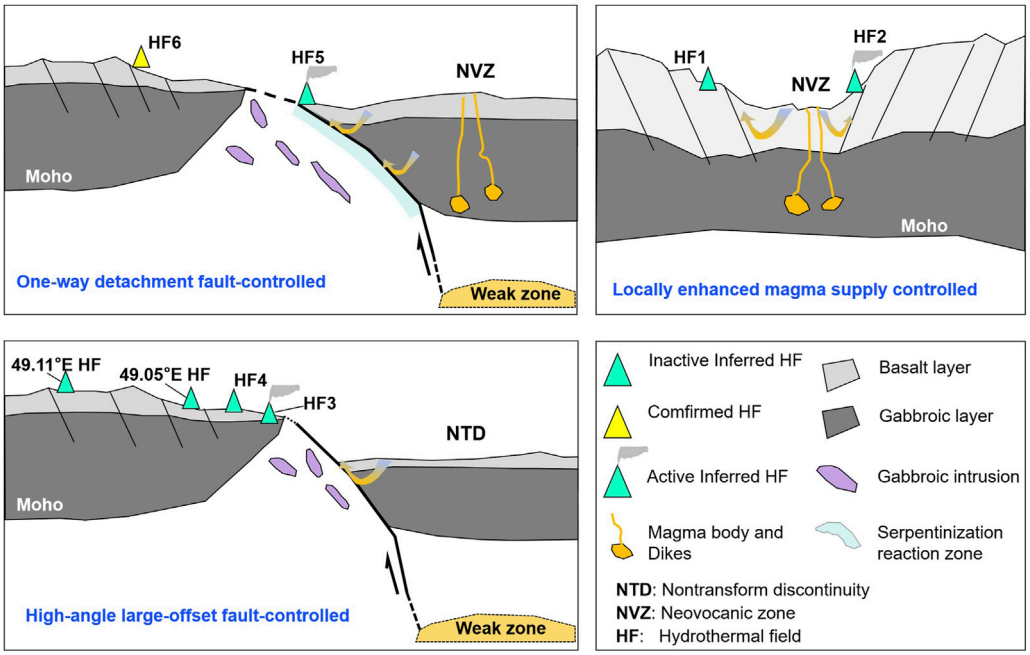

FIGURE 11
Hydrothermal circulation system model in the study area [Modified from Tao et al. (2023)].

heat sources and channels in the hydrothermal circulation system, ultimately resulting in a rich diversity of hydrothermal activities (Tao et al., 2020; Wu et al., 2021; Zhou et al., 2022; Tao et al., 2023). Tao et al. (2023) divided the hydrothermal circulation of the Southwest Indian Ridge into four types: localized strong magmatic supply-controlled type, high angle large offset fault controlled type, one-way detachment fault controlled type, and flip-flop detachment fault controlled type. In this study area, the Baidi hydrothermal field (HF1) is classified as a localized strong magmatic supply-controlled type, the Yuhuang-1 hydrothermal field (HF6) is classified as a one-way detachment fault-controlled type, and the Chunxi hydrothermal field (HF4) is classified as high angle large offset fault controlled type (Tao et al., 2023).

According to the above classification method of Hydrothermal circulation, other hydrothermal fields in this study area are classified as follows, and the model of the hydrothermal circulation system in this study area is summarized in Figure 11. Yuhuang-2 hydrothermal field (HF5) and Yuhuang-1 hydrothermal field are located on the Yuhuang detachment fault (Chen et al., 2023), both controlled by detachment faults and should be classified as one-way detachment fault controlled Hydrothermal circulation. Yuhuang-3 hydrothermal field (HF3), 49.05° E hydrothermal field and 49.11° E hydrothermal field are all located on Mode-E fault (also can be expressed as high angle and large offset normal fault), similar to Chunxi hydrothermal field, and should be classified as high angle large offset fault controlled Hydrothermal circulation; Among them, the Yuhuang-3 hydrothermal field, Chunxi hydrothermal field, and 49.11°E hydrothermal field are all located on the same Mode-E fault on the north side of Nontransform discontinuity (N30), while the 49.05° E hydrothermal field is located on the Mode-E fault on the south side of N30. The heat source of one-way detachment fault-controlled Hydrothermal circulation is similar to that of high angle large offset fault-controlled Hydrothermal circulation. It is a local high-temperature Gabbro intrusion or deep high-temperature mantle, and the hydrothermal circulation channels are respectively deep detachment faults and high angle and large offset faults (Tao et al., 2023).

The S30 hydrothermal field (HF2) is similar to the Baidi hydrothermal field, both located near the neovolcanic ridge of the #30 segment, and should be classified as a localized strong magmatic supply-controlled type; Among them, the Baidi hydrothermal field is located on the north side of #30 segment, and the S30 hydrothermal field is located on the south side of this ridge segment. In this kind of localized strong magmatic supply-controlled Hydrothermal circulation, the magma intruded from the axis becomes the heat source of the hydrothermal circulation system, and the axial fault provides a channel for fluid migration (Tao et al., 2023).

6 Conclusion

In this paper, the abundant off-axis hydrothermal activity of the 29–30 ridge of the Southwest Indian Ocean Ridge was studied. By analyzing the chemical composition and REE composition of ferromanganese crusts, the influence of hydrothermal activities on the origin and evolution of ferromanganese crusts and the controlling factors of the distribution of hydrothermal activities were discussed. The main conclusions are as follows:

1. The crust samples in the study area have low Co and rare earth element contents, and the material source discrimination diagram reveals that they have a mixed hydrogenetic and hydrothermal origin;
2. Identify two unknown seafloor hydrothermal fields, one of which is an inactive hydrothermal field, and obtain evidence from

seabed camera images. Based on the geochemical survey of ferromanganese crusts, it can be an effective means of investigating inactive seafloor hydrothermal activity;

3. The spatial frequency of hydrothermal activity in the study area reaches 15 sites/100 km, which is significantly higher than other well-investigated oceanic ridges, indicating that the Southwest Indian Ridge still has high potential for hydrothermal activity investigation;
4. The control factors of hydrothermal activity in the study area are diverse, including localized strong magmatic supply-controlled type, high angle large offset fault controlled type, one-way detachment fault controlled type.

Data availability statement

The original contributions presented in the study are included in the article/supplementary material, further inquiries can be directed to the corresponding author.

Author contributions

CT led the project and finished the interpretation. XY prepared the original manuscript, analyses and geochemistry interpretation. SL participated in the interpretation of the results. All authors contributed to the article and approved the submitted version.

Funding

This research was funded by the National Natural Science Foundation of China (42127807 and 42006074), the Key R&D Program of Zhejiang Province (2021C03016), and the China Ocean Mineral Resources R&D Association Project (DY135-S1-1-02, 08).

Acknowledgments

We would like to thank the captains and crews who contributed to the success of this project.

Conflict of interest

The authors declare that the research was conducted in the absence of any commercial or financial relationships that could be construed as a potential conflict of interest.

Publisher's note

All claims expressed in this article are solely those of the authors and do not necessarily represent those of their affiliated organizations, or those of the publisher, the editors and the reviewers. Any product that may be evaluated in this article, or claim that may be made by its manufacturer, is not guaranteed or endorsed by the publisher.

References

Baker, E. (2017). Exploring the ocean for hydrothermal venting: new techniques, new discoveries, new insights. *Ore Geol. Rev.* 86, 55–69. doi:10.1016/j.oregeorev.2017.02.006

Baker, E. T., Resing, J. A., Haymon, R. M., Tunnicliffe, V., Lavelle, J. W., Martinez, F., et al. (2016). How many vent fields? New estimates of vent field populations on ocean ridges from precise mapping of hydrothermal discharge locations. *Earth Planet. Sci. Lett.* 449, 186–196. doi:10.1016/j.epsl.2016.05.031

Bau, M., Koschinsky, A., Dulski, P., and Hein, J. R. (1996). Comparison of the partitioning behaviours of yttrium, rare earth elements, and titanium between hydrogenetic marine ferromanganese crusts and seawater. *Geochimica Cosmochimica Acta* 60 (10), 1709–1725. doi:10.1016/0016-7037(96)00063-4

Bau, M., Schmidt, K., Koschinsky, A., Hein, J., Kuhn, T., and Usui, A. (2014). Discriminating between different genetic types of marine ferro-manganese crusts and nodules based on rare earth elements and yttrium. *Chem. Geol.* 381, 1–9. doi:10.1016/j.chemgeo.2014.05.004

Beaulieu, S. E., Baker, E. T., and German, C. R. (2015). Where are the undiscovered hydrothermal vents on oceanic spreading ridges? *Deep Sea Res. Part II* 121, 202–212. doi:10.1016/j.dsr2.2015.05.001

Beaulieu, S. E., and Szafrański, K. M. (2020). *InterRidge global database of active submarine hydrothermal vent fields.* United States: PANGAEA. doi:10.1594/PANGAEA.917894

Bonatti, E., Kraemer, T., and Rydell, H. (1972). Classification and genesis of submarine iron-manganese deposits. in *Ferromanganese deposits on the ocean floor* (Berlin, Germany: Springer), 149–166.

Cannat, M., Rommevaux-Jestin, C., Sauter, D., Deplus, C., and Mendel, V. (1999). Formation of the axial relief at the very slow spreading Southwest Indian Ridge (49° to 69°E). *J. Geophys. Res.* 104 (10), 22825–22843. doi:10.1029/1999JB900195

Chen, D., Tao, C., Wang, Y., Chen, S., Liang, J., Liao, S., et al. (2021). Seafloor hydrothermal activity around a large non-transform discontinuity along ultraslow-spreading southwest Indian ridge (48.1–48.7° E). *J. Mar. Sci. Eng.* 9 (8), 825. doi:10.3390/jmse9080825

Chen, J., Zhang, T., Li, H., Tao, C., Cannat, M., and Sauter, D. (2023). Evolution of enhanced magmatism at the ultraslow spreading Southwest Indian Ridge between 46°E and 53.5°E. *Tectonophysics* 860, 229903. doi:10.1016/j.tecto.2023.229903

Dasong, H., Xiaoyu, Z., Guoyin, Z., Chunhui, T., and Huaiming, L. (2016). Geochemical characteristics of sediments in southwest Indian ridge48.6°-51.7°E. *Geol. Sci. Technol. Inf.* 35 (1), 8.

DeMets, C., Gordon, R. G., Argus, D. F., and Stein, S. (1990). Current plate motions. *Geophys. J. Int.* 101 (2), 425–478. doi:10.1111/j.1365-246X.1990.tb06579.x

Dick, H. J. B., Lin, J., and Schouten, H. (2003). An ultraslow-spreading class of ocean ridge. *Nature* 426 (6965), 405–412. doi:10.1038/nature02128

Escartín, J., Smith, D. K., Cann, J., Schouten, H., Langmuir, C. H., and Escrig, S. (2008). Central role of detachment faults in accretion of slow-spreading oceanic lithosphere. *Nature* 455 (7214), 790–794. doi:10.1038/nature07333

Fouquet, Y., Cambon, P., Etoubleau, J., Charlou, J. L., OndréAs, H., Barriga, F. J. A. S., et al. (2010). "Geodiversity of hydrothermal processes along the Mid-Atlantic Ridge and ultramafic-hosted mineralization: a new type of oceanic Cu-Zn-Co-Au volcanogenic massive sulfide deposit," in *Diversity of hydrothermal systems on slow spreading ocean ridges* (Berlin, Germany: Springer), 321–367.

German, C. R., Petersen, S., and Hannington, M. D. (2016). Hydrothermal exploration of mid-ocean ridges: where might the largest sulfide deposits be forming? *Chem. Geol.* 420, 114–126. doi:10.1016/j.chemgeo.2015.11.006

Hannington, M. D., De Ronde, C. E. J., Petersen, S., Hedenquist, J. W., Thompson, J. F. H., Goldfarb, R. J., et al. (2005). "Sea-floor tectonics and submarine hydrothermal systems," in *One hundredth anniversary volume* (United States: Society of Economic Geologists).

Hannington, M., Jamieson, J., Monecke, T., Petersen, S., and Beaulieu, S. (2011). The abundance of seafloor massive sulfide deposits. *Geology* 39 (12), 1155–1158. doi:10.1130/G32468.1

Hein, J. R., Conrad, T., Mizell, K., Banakar, V. K., Frey, F. A., and Sager, W. W. (2016). Controls on ferromanganese crust composition and reconnaissance resource potential, Ninetyeast Ridge, Indian Ocean. *Deep Sea Res. Part I* 110, 1–19. doi:10.1016/j.dsr.2015.11.006

Hein, J. R., and Koschinsky, A. (2014). "Deep-Ocean ferromanganese crusts and nodules," in *Treatise on geochemistry* Editors H. D. Holland and K. K. Turekian Second Edition (Oxford: Elsevier), 273–291.

Hu, S., Tao, C., Liao, S., Zhu, C., and Qiu, Z. (2022). Transformation of minerals and mobility of heavy metals during oxidative weathering of seafloor massive sulfide and their environmental significance. *Sci. Total Environ.* 819, 153091. doi:10.1016/j.scitotenv.2022.153091

Jamieson, J., and Gartman, A. (2020). Defining active, inactive, and extinct seafloor massive sulfide deposits. *Mar. Policy* 117, 103926. doi:10.1016/j.marpol.2020.103926

Josso, P., Pelleter, E., Pourret, O., Fouquet, Y., Etoubleau, J., Cheron, S., et al. (2017). A new discrimination scheme for oceanic ferromanganese deposits using high field strength and rare earth elements. *Ore Geol. Rev.* 87, 3–15. doi:10.1016/j.oregeorev.2016.09.003

Kuhn, T., Bau, M., Blum, N., and Halbach, P. (1998). Origin of negative Ce anomalies in mixed hydrothermal–hydrogenetic Fe–Mn crusts from the Central Indian Ridge. *Earth Planet. Sci. Lett.* 163 (1), 207–220. doi:10.1016/S0012-821X(98)00188-5

Li, H., Lei, J., Zhang, K., and Sun, Y. (2015). *China Ocean Mineral Resources R&D association 34th cruise leg 2 cruise report*. Beijing: China Ocean Mineral Resources R&D Association.

Li, H., Tao, C., Yue, X., Baker, E. T., Deng, X., Zhou, J., et al. (2020). Enhanced hydrothermal activity on an ultraslow-spreading supersegment with a seismically detected melting anomaly. *Mar. Geol.* 430, 106335. doi:10.1016/j.margeo.2020.106335

Liao, S., Tao, C., Dias, A. A., Su, X., Yang, Z., Ni, J., et al. (2019). Surface sediment composition and distribution of hydrothermal derived elements at the Duanqiao-1 hydrothermal field, Southwest Indian Ridge. *Mar. Geol.* 416, 105975. doi:10.1016/j.margeo.2019.105975

Liao, S., Tao, C., Li, H., Zhang, G., Liang, J., Yang, W., et al. (2018). Surface sediment geochemistry and hydrothermal activity indicators in the Dragon Horn area on the Southwest Indian Ridge. *Mar. Geol.* 398, 22–34. doi:10.1016/j.margeo.2017.12.005

Liu, C., Li, J., Tao, C., Fan, Q., Song, J., Luo, Y., et al. (2020). Variations in faulting style of the Southwest Indian ridge (46°–53.5°E): implications for crustal accretion process at ultraslow-spreading ridges. *Tectonophysics* 790, 228552. doi:10.1016/j.tecto.2020.228552

Manheim, F. T., and Lane-Bostwick, C. M. (1988). Cobalt in ferromanganese crusts as a monitor of hydrothermal discharge on the Pacific sea floor. *Nature* 335 (6185), 59–62. doi:10.1038/335059a0

Mukhopadhyay, R., Ghosh, A. K., and Iyer, S. D. (2008). "Ferromanganese deposits," in *Handbook of exploration and environmental geochemistry* (Netherlands: Elsevier Science BV), 155–224.

Pourmand, A., Dauphas, N., and Ireland, T. J. (2012). A novel extraction chromatography and MC-ICP-MS technique for rapid analysis of REE, Sc and Y: revising CI-chondrite and post-archean Australian shale (PAAS) abundances. *Chem. Geol.* 291, 38–54. doi:10.1016/j.chemgeo.2011.08.011

Ray, E., and Paul, D. (2021). Major and trace element characteristics of the average Indian post-archean shale: implications for provenance, weathering, and depositional environment. *ACS Earth Space Chem.* 5 (5), 1114–1129. doi:10.1021/acsearthspacechem.1c00030

Staszak, P., Collot, J., Josso, P., Pelleter, E., Etienne, S., Patriat, M., et al. (2022). Origin and composition of ferromanganese deposits of New Caledonia exclusive economic zone. *Minerals* 12, 255. doi:10.3390/min12020255

Surya, P., Ray, D., Kurian, J. P., M., S., K.a., K. R., et al. (2020). Anomalous phase association of REE in ferromanganese crusts from Indian mid-oceanic ridges: evidence for large scale dispersion of hydrothermal iron. *Chem. Geol.* 549, 119679. doi:10.1016/j.chemgeo.2020.119679

Tao, C., Guo, Z., Liang, J., Ding, T., Yang, W., Liao, S., et al. (2023). Sulfide metallogenic model for the ultraslow-spreading Southwest Indian Ridge. *Sci. China Earth Sci.* 66 (6), 1212–1230. doi:10.1007/s11430-023-1108-7

Tao, C., Lin, J., Guo, S., Chen, Y. J., Wu, G., Han, X., et al. (2012). First active hydrothermal vents on an ultraslow-spreading center: southwest Indian ridge. *Geology* 40 (1), 47–50. doi:10.1130/g32389.1

Tao, C., Seyfried, W. E., Jr., Lowell, R. P., Liu, Y., Liang, J., Guo, Z., et al. (2020). Deep high-temperature hydrothermal circulation in a detachment faulting system on the ultra-slow spreading ridge. *Nat. Commun.* 11 (1), 1300. doi:10.1038/s41467-020-15062-w

Tivey, M. A., Schouten, H., and Kleinrock, M. C. (2003). A near-bottom magnetic survey of the Mid-Atlantic Ridgeridge axis at 26°N: implications for the tectonic evolution of the TAG segment. *J. Geophys. Res.* 108 (5). doi:10.1029/2002JB001967

Wu, T., Tivey, M. A., Tao, C., Zhang, J., Zhou, F., and Liu, Y. (2021). An intermittent detachment faulting system with a large sulfide deposit revealed by multi-scale magnetic surveys. *Nat. Commun.* 12 (1), 5642. doi:10.1038/s41467-021-25880-1

Ye, J. (2010). *Mineralization of polymetallic sulfides on ultra-slow spreading southwest indian ridge at 49.6°E(Chineses)*. doctor of philosophy doctor (China: Graduate university of Chinese academy of sciences).

Yu, J., Tao, C., Liao, S., Dias, A. A., Liang, J., Yang, W., et al. (2021). Resource estimation of the sulfide-rich deposits of the Yuhuang-1 hydrothermal field on the ultraslow-spreading Southwest Indian Ridge. *Ore Geol. Rev.* 134, 104169. doi:10.1016/j.oregeorev.2021.104169

Yu, Z., Fan, D., Zhang, A., Sun, X., and Yang, Z. (2013). Mineralogy and geochemistry of cobalt-rich crusts from the Southwest Indian Ridge. *Mar. Geol. Quat. Geol.* 33 (6), 10.

Yue, X., Li, H., Ren, J., Tao, C., Zhou, J., Wang, Y., et al. (2019). Seafloor hydrothermal activity along mid-ocean ridge with strong melt supply: study from segment 27, southwest Indian ridge. *Sci. Rep.* 9 (1), 9874. doi:10.1038/s41598-019-46299-1

Yue, X. (2020). *Seafloor hydrothermal activity along the mid-ocean ridge with high melt supply: study from segment 27, Southwest Indian Ridge(Chineses)*. doctor (China: China University of Geosciences).

Zawadzki, D., Maciąg, Ł., Blasco, I., González, F. J., Wernette, B., Marino, E., et al. (2022). Geochemistry and mineralogy of ferromanganese crusts from the western cocos-nazca spreading centre, pacific. *Minerals* 12 (5), 538. doi:10.3390/min12050538

Zhang, L., Tao, C., Su, X., Lv, S., Zhou, J., Deng, X., et al. (2022). Characteristics of rare earth elements in the surface sediments of southwest Indian ridge: implication of grain size for the identification of hydrothermal activity. *Geo-Marine Lett.* 42 (1), 7. doi:10.1007/s00367-022-00729-8

Zhigang, Z., Xiaoyuan, W., Guoliang, Z., Xuebo, Y., Daigeng, C., and Xiaomei, W. (2007). Formation of Fe-oxyhydroxylation near 13 ° N of the East pacific Rise: mineral and geochemical evidence. *Chin. Sci. earth Sci.* 37 (10), 1349–1357.

Zhou, F., Dyment, J., Tao, C., and Wu, T. (2022). Magmatism at oceanic core complexes on the ultraslow southwest Indian ridge: insights from near-seafloor magnetics. *Geology* 50 (6), 726–730. doi:10.1130/G49771.1

Zhou, H., and Dick, H. J. B. (2013). Thin crust as evidence for depleted mantle supporting the Marion Rise. *Nature* 494 (7436), 195–200. doi:10.1038/nature11842

frontiers | Frontiers in Marine Science

TYPE Original Research
PUBLISHED 29 September 2023
DOI 10.3389/fmars.2023.1229797

Check for updates

OPEN ACCESS

EDITED BY
Marcelo Ketzer,
Linnaeus University, Sweden

REVIEWED BY
Chen-Feng You,
National Cheng Kung University, Taiwan
Orlando Vaselli,
University of Florence, Italy

*CORRESPONDENCE
Tomohiro Toki
toki@sci.u-ryukyu.ac.jp

RECEIVED 27 May 2023
ACCEPTED 18 September 2023
PUBLISHED 29 September 2023

CITATION
Mitsutome Y, Agena K, Toki T, Song K-H, Shinjo R and Ijiri A (2023) Assessing the activity of mud volcanism using boron isotope ratios in pore water from surface sediments of mud volcanoes off Tanegashima (SW Japan).
Front. Mar. Sci. 10:1229797.
doi: 10.3389/fmars.2023.1229797

COPYRIGHT
© 2023 Mitsutome, Agena, Toki, Song, Shinjo and Ijiri. This is an open-access article distributed under the terms of the Creative Commons Attribution License (CC BY). The use, distribution or reproduction in other forums is permitted, provided the original author(s) and the copyright owner(s) are credited and that the original publication in this journal is cited, in accordance with accepted academic practice. No use, distribution or reproduction is permitted which does not comply with these terms.

Assessing the activity of mud volcanism using boron isotope ratios in pore water from surface sediments of mud volcanoes off Tanegashima (SW Japan)

Yuki Mitsutome[1], Ko Agena[2], Tomohiro Toki[2,3]*, Ke-Han Song[4], Ryuichi Shinjo[3,5] and Akira Ijiri[6,7]

[1]Department of Chemistry Biology and Marine Science, Graduate School of Engineering and Science, University of the Ryukyus, Nishihara, Japan, [2]Department of Chemistry, Biology and Marine Science, Faculty of Science, University of the Ryukyus, Nishihara, Japan, [3]Research Institute for Humanity and Nature (RIHN), Kyoto, Japan, [4]Graduate School of Science and Engineering, University of the Ryukyus, Nishihara, Japan, [5]Department of Physics and Earth Sciences, Faculty of Science, University of the Ryukyus, Nishihara, Japan, [6]Graduate School of Maritime Sciences, Kobe University, Kobe, Japan, [7]Kochi Institute for Core Sample Research, Institute for Extra-Cutting-Edge Science and Technology Avant-Garde Research (X-Star), Japan Agency for Marine-Earth Science and Technology (JAMSTEC), Nankoku, Kochi, Japan

Mud volcanoes can cause various geohazards, so it is very important to know their activity level and their distribution. Surface sediments were collected from four submarine mud volcanoes (MVs) off Tanegashima (SW Japan), namely, MV1, MV2, MV3, and MV14. We extracted pore water from the surface sediments and investigated its chemical and isotopic compositions. The sodium (Na) and chloride (Cl^-) concentrations decreased and the boron (B) and lithium (Li) concentrations increased with increasing depth, suggesting that some fluids with lower Na and Cl^- concentrations and higher B and Li concentrations than seawater were supplied upward from the deep sub-seafloor. The fluid advection velocities estimated from the pore-water profiles differed for each MV, and those of MV3 were the fastest (14 cm/yr) in this study. The estimated equilibrium temperature with clay minerals using Na and Li concentrations were 93-134°C, corresponding to the temperature of environments around 3.7 to 5.3 km below the seafloor. This indicates that these components originated from these depths and that the origin depth did not reach the plate boundary in this area. The B isotope ratio in the pore water was extremely high up to +57 ‰, suggesting that it was strongly affected by adsorption onto the surface of the sediments. A higher B isotope ratio (+57 ‰) was detected in MV3, which was considered to be more active, indicating that more B was adsorbed onto clay minerals supplied from deeper depths.

KEYWORDS

mud volcano, Tanegashima, pore water, boron isotope, activity

1 Introduction

Mud volcanoes (MVs) are structures formed by the eruption of mud breccia from below the surface to the surface owing to increased pressure and buoyancy (Mazzini and Etiope, 2017). The number of MVs on land is probably approximately 10^3 (Etiope and Milkov, 2004); conversely, that on the seafloor was estimated to be 10^3-10^5 as the sedimentation rate is high (Milkov, 2000). The ejected materials comprise gas, mainly CH_4 and CO_2, mud, rock fragments, and water (Kopf, 2002), which are thought to be related to natural gases, petroleum, and/or gas hydrates (Etiope et al., 2009; Tinivella and Giustiniani, 2012). Some studies have indicated that earthquakes trigger MV activities (e.g., Tsunogai et al., 2012), but not all earthquakes are associated with MVs (Manga et al., 2009; Tingay et al., 2018; Wang and Manga, 2021). To investigate causal relationships, it is essential to monitor MV activity. On land, detailed topographical changes can be monitored using satellites (Kopanina and Shvidskaya, 2021). However, seafloor monitoring is difficult. Feseker et al. (2014) installed a submarine observation station at the Håkon Mosby MV off the coast of Norway, monitored it for 431 days, recorded four major events, and observed a rapid sediment uplift of 1 m (Feseker et al., 2014). Topographical changes on the seafloor can cause submarine landslides, which can lead to accidents involving the disconnection of communication cables (Carter et al., 2012; Carter et al., 2014; Gavey et al., 2017). Therefore, understanding the activities and distribution of submarine MVs and identifying the factors that determine the effects of earthquakes and subducting seamounts on MVs are vital (Kioka, 2020).

The indexes of the activity of submarine MVs can be estimated from the CH_4 flux directly in surface water (Tsunogai et al., 2012), sedimentary activity analysis using microfossil age (biostratigraphy) and ^{14}C age (Ujiié, 2000), and determination of the depth of origin using various geothermometers (Hensen et al., 2004; Nishio et al., 2015; Lalk et al., 2022; Mitsutome et al., 2023). The greater the depth of origin, the greater was the amount of energy that migrated through the material, suggesting the existence of large-scale mud volcanic activity. Hensen et al. (2004) estimated the temperature at which water reaches equilibrium with clay from water isotope ratios. Nishio et al. (2015) estimated the temperature at which lithium equilibrates with clay using lithium isotope ratios. Lalk et al. (2022) used clamp isotopes of methane to estimate the temperature of methane formation. Mitsutome et al. (2023) used the solubilities of Ar, Kr, and Xe to estimate the depths at which those heavy noble gases were present immediately before. Boron isotope ratio also has the potential to be used as a geothermometer (Palmer, 1991; James et al., 1999; Williams et al., 2001; You and Gieskes, 2001).

Boron (B) has two isotopes with mass numbers of 10 and 11. The B isotope ratio, which is the abundance ratio, indicates that B in fluids released at equilibrium from silicates undergoes smaller isotope fractionation at higher temperatures (Deyhle and Kopf, 2005). In contrast, MVs represent the progression of clay mineral alteration (Kopf and Deyhle, 2002). Deyhle and Kopf (2005) investigated B isotope fractionation in fluid and solid phases in nature and found that the B isotope ratio in the fluid was influenced by multiple factors, such as the weight ratio of the fluid to solid phases in the reaction field, B isotope ratio in the solid phase, reaction temperature, and pH in the reaction field. Chao et al. (2011) investigated the B isotope ratios in the pore water of MVs in Taiwan and found that after high-temperature release from the solid phase at depth, B re-adsorption during the ascent of the fluid resulted in an extremely high B isotope ratio. However, they did not specify on its usefulness as a geothermometer (Chao et al., 2011).

In this study, to verify the method of evaluating the activity of each MV using the B isotope ratio, we did the following. First, we collected pore water from the surface sediments of the MVs off Tanegashima Island and investigated their chemical and isotopic compositions. Next, we estimated the advection velocity using the vertical distribution of the chloride (Cl^-) concentration. Subsequently, we estimated the depth of origin from the equilibrium temperature with clay minerals using sodium (Na) and lithium (Li) concentrations. Finally, we discussed the relationship between the origin temperature and isotopic fractionation of the B isotope ratios in the pore water and sediments.

2 Geological setting

Tanegashima is located in southwest Japan (Figure 1A) in the plate convergence zone where the Philippine Sea plate subducts below the Eurasian plate at a rate of 4.6 cm per year (Seno and Maruyama, 1984). The plate boundary off Tanegashima is at the northern end of the Ryukyu Trench, which is roughly classified as an erosion type, and the Nankai Trough, which extends eastward from the Ryukyu Trench into the accretion type (Clift and Vannucchi, 2004). A wedge of approximately 8 km was observed in the forearc region of the plate boundary off Tanegashima (Ujiié, 2000). The basement around Tanegashima comprises the Eocene Kumage Group, corresponding to the Shimanto Belt and exhibiting thrust faults and folds associated with subduction (Okada and Whitaker, 1979). Although the Kumage Group is not always distributed under the seafloor in the MV area, a layer of the same age as the Kumage Group was distributed below because Eocene foraminifera were obtained from the surface layer of the MV (Ujiié, 2000). The side-scan sonar survey conducted in 1990 covered an area with a width and depth of 20-30 km and 1,200-3,500 m, respectively, from the northern tip of the Ryukyu Trench slope to the southern tip of the central Ryukyu Trench slope. More than 30 mud diapirs were found on the northern trench slope (Ujiié, 2000). Currently, the presence of MV1–MV15 off Tanegashima have been confirmed (Figure 1B). Additionally, Nakayama et al. (2010), who investigated the pore water in MV1, suggested that water originating from the dehydration of clay minerals was supplied from the deep subseafloor (Nakayama et al., 2010). Furthermore, water masses containing high concentrations of methane (CH_4) and characteristic microbial plumes in the surface sediments were observed several tens of meters above the summits of MV1 and MV14, indicating that these MVs were still active (Hoshino et al., 2017). Moreover, Mitsutome et al. (2023) investigated the noble gases in the surface sediments of MV1 and MV14, and used their solubility at 80 to 230°C to estimate that their depth of origin was 3-9 km below the seafloor (Mitsutome et al., 2023).

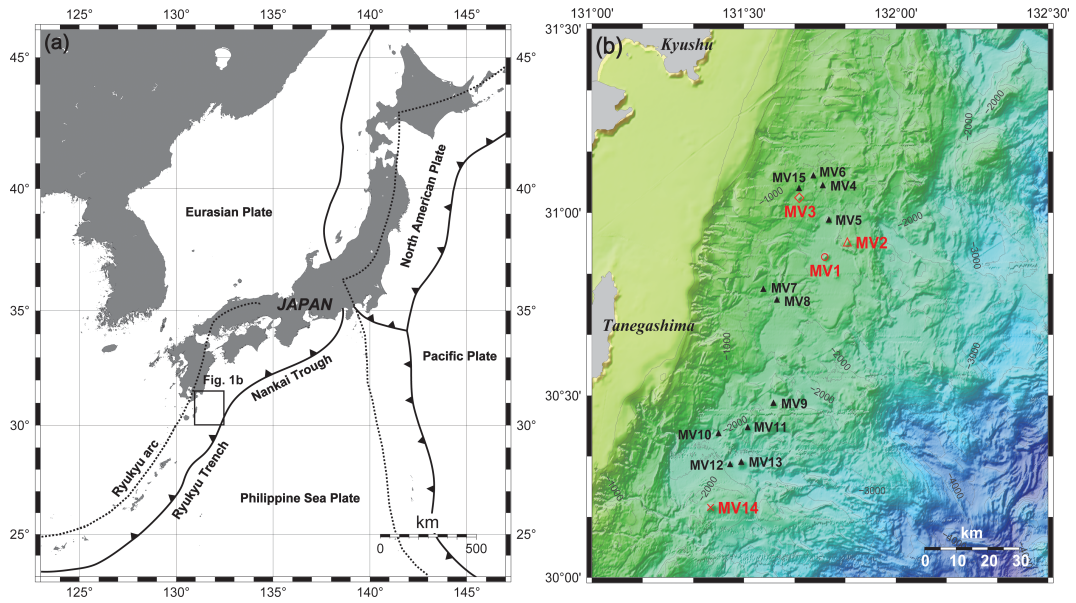

FIGURE 1
(A) Plate tectonics around Japan. The area surrounded by the square indicates the range of **(B)**. The red triangle marks represent the numbered MVs, namely, MV1 to MV15. Contour lines are present at intervals of 200 m.

3 Sampling and analytical method

Pore water was extracted from the surface sediments collected during the KH-15-2 cruise from August 19 to September 1, 2015, and the KH-19-5 cruise from August 9 to August 18, 2019 (Table 1). For surface sediment sampling, we used the Navigable Sampling System (NSS; Ashi and Tokuyama, 2005) with a piston corer (length: 4-6 m) and a multiple corer (length: 60 cm) mounted on the R/V *Hakuho-Maru*, and randomly selected the following MVs: MV1, MV2, MV3, and MV14 (Supplementary Figures 1A–D). The lengths of the surface deposits obtained ranged from 3.11 to 5.21 m where piston corers were used and from 0.2 to 0.27 m where multiple corers were used (Table 1). The lithofacies of all the MVs mainly comprise 2-3-cmΦ breccia with a maximum size of approximately 5 cmΦ and are covered by semi-pelagic sediments. Mud was sub-sampled from the sediment on board at approximately 25-cm intervals for samples by a piston corer (Type PC in Table 2) and 5-cm intervals for samples by a multiple corer (Type MC in Table 2).

In the case of sediments collected by the piston corer, the mud in contact with the inner tube was removed because it may have been contaminated with seawater. The collected mud was placed in a squeezer set with a mesh and filter paper (Advantec; Filter paper No. 1), and pressure was applied with a hydraulic press to extract pore water into a 50-mL syringe (Manheim, 1966). The pore water extracted into the syringe was passed through a disc filter (Advantec; disposable syringe filter unit, 0.45 µm) and divided to analyze the: 1) anion concentration, ammonium ion concentration (NH_4^+), pH, and alkalinity; and 2) cation concentration. It was placed in a high-density polyethylene narrow mouth bottle (Nalgene; HDPE Bottle) and stored in a refrigerator at 4 °C. After pore water extraction, the residual sediments were frozen and transported to a land-based laboratory. In the case of sediments taken with the multiple corer, pore water was extracted with a Rhizon sampler (Seeberg-Elverfeldt et al., 2005; Dickens et al., 2007), distributed, stored, and brought back to the land-based laboratory in the same manner as pore water extracted from sediments taken with a piston corer.

TABLE 1 The location and date of collection of the samples used in this study, and the length of the collected sediments.

Site	Date	Lat.	Long.	Depth	Core length
		N	E	m	m
MV1	August 23, 2015	30°52.71'	131°46.01'	1,415	3.66
MV2	August 16, 2019	30°55.104'	131°50.4085'	1,443	5.21
		30°55.1158'	131°50.3944'	1,366	0.27
MV3	August 17, 2019	31°02.5552'	131°40.9319'	1,168	3.44
		31°02.5373'	131°40.9536'	1,136	0.2
MV14	August 30, 2015	30°11.46'	131°23.58'	1,693	3.11

TABLE 2 Chemical composition analysis results of pore water samples collected in this study.

Site	Type	Section	Depth	pH	Cl^-	Na	Mg	SO_4^{2-}	K	Ca	B	NH_4^+	Li	Si	Sr	Ba	Alkalinity	HCO_3^-	$\delta^{11}B$	2S.E.
	PC/MC		cmbsf		mM	mM	mM	mM	mM	mM	mM	μM	μM	μM	μM	μM	meq./L	mmol/L	‰	‰
MV1	PC3	3	26	N.A.	554	450	52.4	25.1	11.9	8.40	0.61	N.A.	42	N.A.	90	1	N.A.	N.A.	+32.8	0.06
			51	N.A.	521	430	40.3	7.4	9.6	4.55	1.06	N.A.	99	N.A.	107	1	N.A.	N.A.	+31.2	0.06
		4	74	N.A.	511	458	33.8	2.8	8.3	2.95	1.32	N.A.	153	N.A.	98	7	N.A.	N.A.	+31.1	0.07
			99	N.A.	436	409	24.6	2.8	6.6	2.01	1.76	N.A.	226	N.A.	115	42	N.A.	N.A.	+32.6	0.05
			127	N.A.	391	386	16.4	1.5	4.5	1.23	1.96	N.A.	298	N.A.	107	51	N.A.	N.A.	+33.1	0.05
			149	N.A.	347	366	11.2	1.4	4.0	1.05	2.23	N.A.	331	N.A.	101	42	N.A.	N.A.	+32.8	0.04
		5	199	N.A.	314	342	6.8	1.7	3.0	0.74	2.03	N.A.	342	N.A.	99	29	N.A.	N.A.	+32.2	0.06
			222	N.A.	257	306	1.1	1.2	1.1	0.30	2.46	N.A.	381	N.A.	94	29	N.A.	N.A.	+32.4	0.03
			249	N.A.	220	270	0.6	1.2	0.6	0.20	2.62	N.A.	383	N.A.	75	24	N.A.	N.A.	+31.7	0.04
		6	274	N.A.	225	276	0.7	1.3	0.9	0.26	2.90	N.A.	399	N.A.	84	27	N.A.	N.A.	+33.0	0.04
			299	N.A.	228	281	0.6	1.3	0.8	0.25	2.98	N.A.	399	N.A.	82	26	N.A.	N.A.	+32.6	0.06
			349	N.A.	233	288	0.7	1.2	0.9	0.26	3.12	N.A.	437	N.A.	88	28	N.A.	N.A.	+32.3	0.04
MV2	MC1	1	7	8.15	564	474	52.8	28.9	10.9	9.75	0.53	0.0	29	352	87	N.D.	2.8	1.8	+39.2	0.07
			12	7.89	563	470	52.8	28.7	10.3	9.64	0.53	7.2	40	340	89	N.D.	3.1	2.5	+39.0	0.07
			17	N.A.	580	474	52.8	29.3	11.1	9.58	0.55	5.0	84	290	89	N.D.	3.2	2.9	+39.7	0.07
	PC1	2	60	8.32	362	354	5.9	1.1	1.0	1.31	1.03	708	437	120	132	38	23.8	20.1	+46.0	0.08
			109	8.25	319	324	0.3	N.D	2.1	1.15	1.26	764	487	131	123	99	25.9	22.4	+47.5	0.06
		3	159	8.34	288	302	N.D.	1.4	1.8	0.72	1.15	732	483	107	99	67	22.6	18.9	+46.7	0.06
			209	8.35	275	287	N.D.	1.1	1.6	0.77	1.23	682	495	110	94	68	24.9	20.8	+47.8	0.07
		4	259	8.55	251	269	N.D.	0.8	1.6	0.45	1.02	658	476	88	74	68	24.1	18.3	+47.4	0.08
			309	8.50	249	267	N.D.	0.8	1.5	0.41	1.08	714	474	94	75	63	24.3	18.9	+47.1	0.07
		5	359	8.50	264	281	N.D.	1.5	2.2	0.52	1.15	623	481	95	81	48	25.1	19.5	+47.9	0.08
			409	8.60	266	286	N.D.	1.4	1.6	0.48	1.12	592	488	104	83	51	23.9	17.7	+47.8	0.09
		6	459	8.12	253	274	N.D.	0.9	1.5	0.35	1.20	570	487	93	77	68	17.7	15.9	+48.0	0.08
			508	8.55	261	274	N.D.	1.1	1.6	0.27	1.21	583	487	102	85	63	23.4	17.7	+46.7	0.08
MV3	MC2		5	7.86	554	467	52.9	28.4	10.1	9.74	0.47	N.D.	22	361	87	N.D.	2.7	2.6	+38.9	0.08

(Continued)

10.3389/fmars.2023.1229797

TABLE 2 Continued

Site	Type	Section	Depth	pH	Cl^-	Na	Mg	SO_4^{2-}	K	Ca	B	NH_4^+	Li	Si	Sr	Ba	Alkalinity	HCO_3^-	$\delta^{11}B$	2S.E.
	PC/MC		cmbsf		mM	mM	mM	mM	mM	mM	mM	µM	µM	µM	µM	µM	meq./L	mmol/L	‰	‰
			10	7.79	562	469	53.2	28.9	10.0	9.84	0.48	N.D.	32	299	88	N.D.	2.7	2.6	+39.1	0.09
			15	7.73	565	469	52.9	29.1	10.9	9.79	0.48	N.D.	24	258	88	N.D.	2.8	2.7	+38.8	0.10
			20	N.A.	N.A.	460	51.6	N.A.	10.1	9.53	0.52	22.8	30	251	88	N.D.	4.7	N.A.	N.A.	N.A.
	PC3	1	13	7.28	363	358	10.5	1.4	4.7	2.61	0.47	390	417	154	192	58	22.9	22.6	+55.1	0.08
		2	79	7.63	219	241	N.D.	N.D.	1.5	0.92	0.44	563	487	95	118	168	23.6	22.7	+57.2	0.10
			129	7.80	219	242	N.D.	N.D.	1.4	0.94	0.40	535	478	84	116	164	23.4	22.1	+56.0	0.08
		3	176	8.29	255	273	N.D.	2.2	1.6	1.65	0.56	638	469	113	139	90	20.8	17.7	+55.4	0.08
		4	246	8.17	229	250	N.D.	0.9	1.4	0.96	0.71	590	463	107	112	128	22.6	19.9	+54.0	0.10
			293	7.83	221	247	N.D.	0.9	2.2	1.04	0.86	551	455	124	110	126	25.5	24.0	+53.2	0.10
MV14	PC6	4	22	N.A.	556	452	55.4	28.4	12.7	9.86	0.55	N.A.	30	N.A.	83	1	N.A.	N.A.	+36.5	0.08
			44	N.A.	570	462	56.0	27.5	12.8	9.65	0.59	N.A.	29	N.A.	74	1	N.A.	N.A.	+37.2	0.07
			69	N.A.	574	466	49.8	15.8	12.4	5.73	0.86	N.A.	34	N.A.	81	1	N.A.	N.A.	+39.4	0.06
			94	N.A.	506	426	33.3	2.9	10.7	3.17	1.70	N.A.	44	N.A.	74	7	N.A.	N.A.	+40.8	0.04
		5	119	N.A.	485	405	30.9	2.6	10.3	2.85	1.64	N.A.	41	N.A.	66	12	N.A.	N.A.	+40.5	0.05
			144	N.A.	504	423	31.3	2.8	11.1	2.58	1.51	N.A.	45	N.A.	71	9	N.A.	N.A.	+40.2	0.05
			169	N.A.	521	463	31.5	1.7	12.4	2.36	1.32	N.A.	43	N.A.	70	19	N.A.	N.A.	+40.7	0.05
			194	N.A.	461	387	28.5	2.2	9.8	2.53	1.40	N.A.	37	N.A.	64	9	N.A.	N.A.	+40.6	0.05
		6	219	N.A.	478	406	29.8	2.5	10.4	2.59	1.31	N.A.	41	N.A.	66	7	N.A.	N.A.	+40.6	0.05
			244	N.A.	497	422	29.2	1.4	10.9	2.50	1.44	N.A.	41	N.A.	73	56	N.A.	N.A.	+40.7	0.05
			294	N.A.	493	419	29.2	1.2	10.6	2.53	1.76	N.A.	47	N.A.	83	31	N.A.	N.A.	+40.9	0.06

M, mol/kg.
PC, Piston corer.
MC, Multiple corer.
N.A, Not analysed.
N.D, Not detected.

10.3389/fmars.2023.1229797

The pore water samples were analyzed by ion chromatography for anions, inductively coupled plasma-atomic emission spectroscopy (ICP-AES) for cations, titration with hydrochloric acid for alkalinity, and the phenol blue colorimetric method for ammonium ions. The accuracies were less than 0.2, 3, 5, and 1%, respectively. The HCO_3^- concentration was calculated from the pH and alkalinity, assuming equilibrium for carbonic acid. The dissociation constants used in the calculation were $K_1 = 10^{-5.847}$, $K_2 = 10^{-8.966}$, and $K_w = 10^{-13.127}$, and the water temperature was 2°C.

B in the pore water was separated using a 5-cm^3 PFA conical vial by the micro-sublimation method (Wang et al., 2010) and final solution was adjusted to 50 ppb B concentration in 0.3 N nitrate matrix. Measurements were conducted using a multicollector inductively coupled plasma mass spectrometer (MC-ICP-MS; Neptune Plus) manufactured by Thermo Fisher Scientific, and standard samples of NBS SRM 951 ($^{11}B/^{10}B = 4.0056 \pm 0.5$) were used. The accuracy of analysis was +39.39 ± 0.33‰ for five measurements of standard seawater NASS-5. Analytical errors (2 S.E.) for individual data are presented in Table 2.

A portion of the sediment sample was dried at 60°C immediately before use, and a portion of the dried sample was ground to a powder using a mortar and pestle. Approximately 0.6 g of the powdered sample was weighed out and place into a vinyl chloride ring (Rigaku; PVC ring for powder samples, RS100-10) on the WC die pellet (Rigaku; WC die pellet, RS2550). Then WC die pellet was placed on top and pressurized at 50 MPa for 5 min using an electric pump (RIKEN; SMP-3012SK) and a press (RIKEN; CDM-10M). The pellets were stored in a desiccator until further analysis. The mortar, pestle, PVC ring, spatula, and WC die pellets were washed with acetone before and after use. The B concentration and isotope ratio analyses were conducted using MC-ICP-MS (the same machine as described above), with the laser ablation system (ESI NWR-Femto, United States). Data processing was conducted using IOLITE ver. 3.7 software (e.g., Woodhead et al., 2005; Hellstrom et al., 2008; Paton et al., 2011). GSD, supplied by the U.S. Geological Survey, was used as the standard material, and all B isotope ratios were denoted by δ as the deviation (‰) from the international standard material NIST SRM951 (Table 3). Additionally, for the analysis, a laser was applied to three different locations on the same sample to calculate the average; the standard deviations (2 S.D.) were calculated and are presented with each data point (Table 3).

4 Results

Table 2 summarizes the chemical and isotopic compositions of the pore water and Table 3 presents the B concentrations and isotopic ratios of the sediments. Figure 2 shows the vertical distributions of Cl^-, Na, Li, magnesium (Mg), calcium (Ca), and B concentrations and isotope ratios ($\delta^{11}B$) in the pore water, and B concentrations and isotope ratios in the sediments. The concentrations of Cl^-, Na, Mg, and Ca in all the MVs were similar to those in the seawater immediately below the seafloor and decreased with depth (Figures 2A–E). The B and Li concentrations increased with depth just below the seafloor (Figures 2C, I). At MV14, the change in the concentration was not large; however, at MV3, it was remarkable. The magnitude of the change in concentration was greatest at MV3, followed by MV2, MV1, and MV14, which gradually decreased (Figure 2).

The B concentration in the sediment was almost 100 ppm, and the concentration seemed to increase with depth (Figure 2H). There was almost no difference in concentration between the mud volcanoes; however, the concentrations of MV14 (84 ± 14 ppm) and MV3 (101 ± 34 ppm) were slightly lower. The isotope ratio tended to increase with depth; however, it slightly varied between mountains (Figure 2I). The comparison between each MV showed that MV2 had the highest $\delta^{11}B$ value (+4.5 ± 2.0‰), and MV1 (–2.9 ± 2.7‰) and MV14 (–2.8 ± 1.6‰) had low $\delta^{11}B$ values (Table 3). Our data (B concentration: 84–160 ppm, B isotope ratio: –2.9 to +4.5 ‰; Table 3) are similar to those (B = 80 to 160 ppm; $\delta^{11}B$ = –6.6 to +4.8‰) of Ishikawa and Nakamura (1993).

5 Discussion

5.1 Estimation of advection velocity using Cl^- concentration

Figure 3A shows the depth distribution of Cl^- concentration in each MV. Cl^- is chemically extremely stable, hardly produces precipitates, and hardly participates during microorganism metabolism. Nevertheless, the Cl^- concentration in the pore water tended to decrease with depth for all the MVs (Figure 3A). The Cl^- concentration at the seafloor surface, which is considered to be the seawater itself, is distributed in a convex downward arc toward the depth below the seafloor (Figure 3A). If the water were circulating, as in the hydrothermal circulation, the distribution of Cl^- concentration would be uniform regardless of depth, but this is not the case. This is because fluid with lower Cl^- concentrations than seawater is distributed in the deep subseafloor, and this fluid rises above. The shape of the vertical distribution of the Cl^- concentration differs for each MV. It gradually decreased to 349 cm below the seafloor (cmbsf) and showed a relatively constant value from there up to 349 cmbsf. However, MV2 and MV3 showed relatively low Cl^- values, even just below the seafloor. There was a clear difference in the distribution of concentrations with depth for each volcanic edifice (Figure 3A), which can be explained by the difference in the advection velocity of the fluid. Therefore, the advective diffusion equation (Eq. 1) was used for quantitative analysis.

$$\phi \cdot \frac{\partial [C]}{\partial t} = \partial \left(\frac{\phi \cdot D_{sed} \cdot \frac{\partial [C]}{\partial x}}{\partial x} \right) - \phi \cdot v \cdot \frac{\partial [C]}{\partial x} + \phi \cdot R \qquad \text{(Eq. 1)}$$

The above equation represents the temporal change in the concentration of a chemical in the pore water at any depth in terms of diffusion, advection, and reaction (Hensen et al., 2007). t is the time (y), x is the distance from the seafloor (cm), and [C] is the Cl^- concentration (mM). D_{sed} is the diffusion coefficient of Cl^- in

TABLE 3 List of boron concentrations and isotope ratios of sediment samples collected in this study.

Site	Type	Section	Depth	B	2S.D.	Average	1σ	$\delta^{11}B$	2S.D.	Average	1σ
	PC/MC		cmbsf	ppm	ppm	ppm	ppm	‰	‰	‰	‰
MV1	PC3	3	26	135	8	160	32	-4.8	0.8	-2.9	2.7
		5	199	149	14			+0.1	0.7		
		6	349	197	3			-4.1	1.5		
MV2	PC1	2	109	132	8	138	8	+1.6	0.7	+4.5	2.0
		3	209	152	7			+4.7	0.1		
		4	309	134	6			+7.4	0.8		
		5	409	137	5			+4.5	0.4		
		6	508	135	22			+4.5	0.7		
MV3	PC3	1	13	82	15	101	34	+0.3	1.2	+2.2	1.7
		2	129	71	4			+1.7	0.7		
		3	176	149	5			+4.3	1.1		
		4	293	103	13			+2.5	0.5		
MV14	PC6	4	22	83	5	84	14	-5.0	0.4	-2.8	1.6
		4	69	64	1			-2.6	1.0		
		5	194	92	4			-2.6	0.5		
		6	294	96	3			-1.1	0.4		

PC, Piston corer.
MC, Multiple corer.

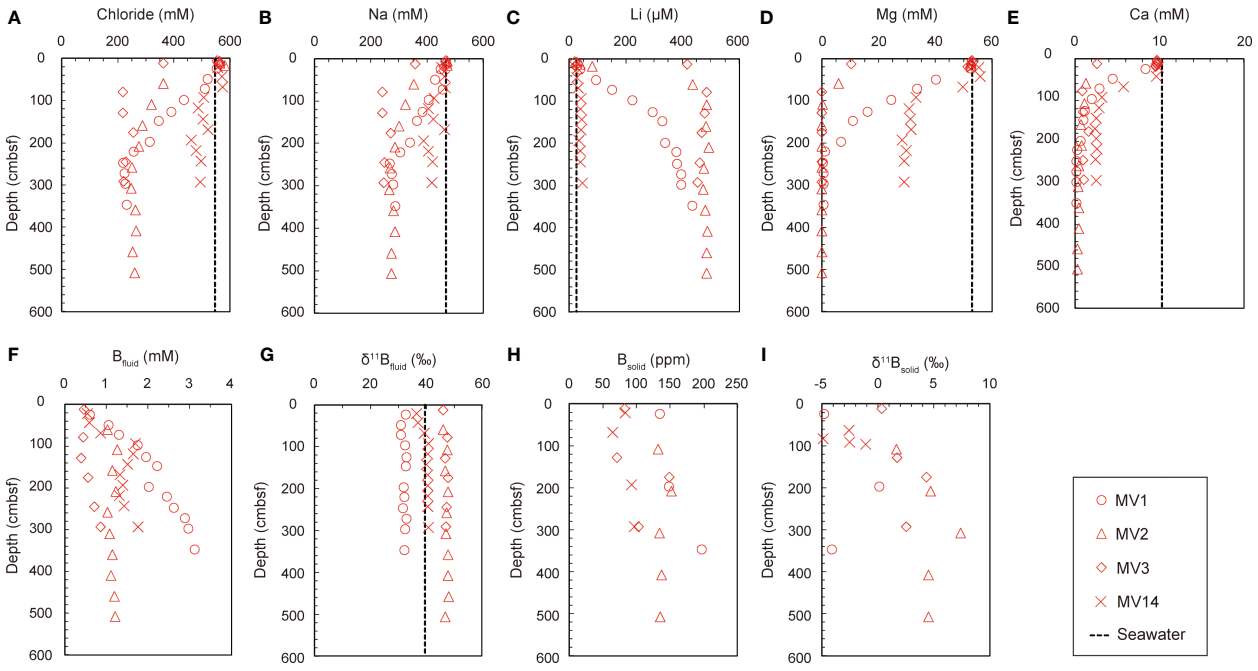

FIGURE 2
(A–G) The distribution of dissolved components in the pore water with depth. Concentration of **(A)** Cl^-, **(B)** Na, **(C)** Li, **(D)** Mg, **(E)** Ca, and **(F)** B; **(G)** B isotope ratio. **(H, I)** Solid phase information, showing the vertical distribution of the **(H)** B content in the sediment and the **(I)** B isotope ratio of the sediment with depth.

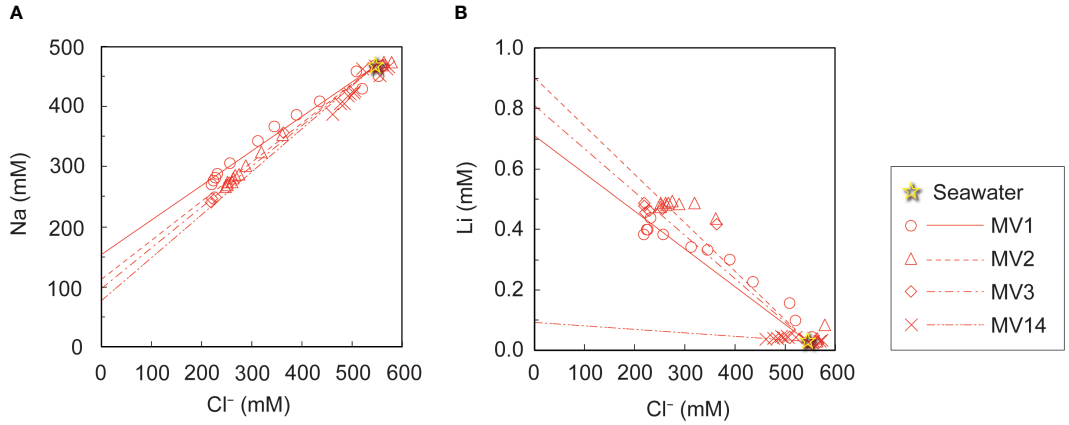

FIGURE 3
Relationship of **(A)** Na and **(B)** Li concentrations with the Cl^- concentration in pore water. Approximate straight lines are drawn for each MV for comparison with seawater values.

the sediment ($cm^2\ yr^{-1}$); ϕ is the porosity; v is the downward fluid velocity (cm yr−1); and R is the reaction rate. Notably, R = 0 because Cl^- does not participate to the reaction. We also assumed that the change in porosity with depth was negligible. Assuming a steady state, the left sides of Eq. 1 can be expressed as zero, and the following special solution (Eq. 2) can be derived.

$$C(x) = C_\infty - (C_\infty - C_0) \cdot \exp\left(\frac{v}{D_{sed}} x\right) \qquad \text{(Eq. 2)}$$

where C_∞ is the converging concentration; C_0 is the initial concentration; D_{sed} is the diffusion coefficient of Cl^- in the sediment ($cm^2\ yr^{-1}$); and v is the velocity of the fluid (cm yr^{-1}), wherein the downward direction is positive. x is the distance (cm) from the seafloor. The average diffusion rates were determined by fitting the data to each graph. The estimated advection velocities are listed in Table 4. As the downward direction is positive, the outflow rate is negative. Although sedimentation should be treated as a downward advection phenomenon, Ujiié (2000) estimates that the average sedimentation rate on the slope of the North Ryukyu Trench is 10 −13 cm over 1,000 years. This value is equivalent to 0.01 cm yr^{-1} for the downward advection velocity; thus, it is negligible in this case (Table 4). The advection velocities of each MV were different, and the results were in the order of MV3 > MV2 > MV1 > MV14 in the upward direction.

TABLE 4 Convergence values of advective velocity and chloride ion concentration derived by applying the advection-diffusion model assuming a steady state to the vertical distribution of chloride ions.

Site	C∞	Advection rate
	mM	cm/yr
MV1	191	-2
MV2	259	-3
MV3	229	-14
MV14	466	-1

5.2 Estimation of equilibrium temperature with clay minerals using Na and Li concentrations

In general, fluids with low Cl^- concentration on the seafloor are thought to include dissolution water occurring during gas hydrate recovery, inflow of groundwater, and water originating from dehydration reactions of clay minerals (Kastner et al., 1991). In the submarine MVs off Tanegashima, studies have found that water originating from the dehydration of clay minerals is supplied to the seafloor surface based on $\delta^{18}O$ and δD data of pore water in the seafloor surface layer (Nakayama et al., 2010). The dehydration reaction of clay minerals is known to occur at 60–150°C, suggesting that the fluid is derived from a high-temperature environment. To estimate the original temperature, geothermometers were applied to the Na and Li concentrations in the pore water of each MV (Fouillac and Michard, 1981). Figures 3A, B show the relationship between the Na and Cl^- concentrations in the pore water, and the Li concentration against the Cl^- concentration, respectively. To determine the concentrations of the freshwater components mixed with seawater, we recorded the y-intercept values when a straight line was drawn through the data and seawater values for each MV. The resulting end-members are summarized in Table 5 as Na^* and Li^*, respectively. The following equation (Eq. 3) was applied to the obtained end-members to obtain the equilibrium temperature t (°C) when Na and Li were considered to be in equilibrium with the clay minerals.

$$t(^\circ C) = \left[\frac{1000}{log\left(\frac{Na^*}{Li^*}\right) + 0.38}\right] - 273 \qquad \text{(Eq. 3)}$$

Fouillac and Michard (1981) proposed a total of two different equations for Cl^- concentrations higher and lower than 300 mM, respectively. As we consider a freshwater source when the Cl^- concentration is 0, we use this equation, which is expressed under the condition of a Cl^- concentration of< 300 mM, from the two equations given by Fouillac and Michard (1981). According to the obtained temperatures, the equilibrium temperature estimated from

10.3389/fmars.2023.1229797

TABLE 5 Assuming that there is a source with a chloride concentration of 0 mM, the estimated Na and Li end-member concentrations, the equilibrium temperatures with clay minerals estimated from their ratio, and the depth at which Na and Li have reached equilibrium with clay minerals, estimated from their temperatures.

Site	Na*			Li*			*t*			Depth		
	mM			mM			°C			km		
							Min.		Max.	Min.		Max.
MV1	155	±	2	0.709	±	0.003	93	–	96	3.7	–	3.8
MV2	113	±	2	0.903	±	0.004	129	–	132	5.2	–	5.3
MV3	99	±	2	0.808	±	0.004	130	–	134	5.2	–	5.3
MV14	78	±	14	0.093	±	0.002	23	–	39	0.9	–	1.6

the Tanegashima MV varied from approximately 23 to 134°C, with the highest temperature being observed at MV3, followed by MV2 and MV1, and the lowest temperature at MV14 (Table 5). The temperature estimated for MV14 was below the reaction temperature range for the dehydration of clay minerals, and the actual Li concentration was almost the same as that of seawater. It is possible that the fluid derived from clay mineral dehydration was not supplied in the first place. The other temperatures (93–134°C; Table 5) fit very well with the range of reaction temperatures originating from the dehydration of clay minerals. Thus, we suggest that MV1 to MV3 are undoubtedly supported by fluids originating from the dehydration of clay minerals. On the other hand, MV14 may not be supplied by fluids derived from dehydration of clay minerals.

When calculated with the reported geothermal gradient of 25°C/km in this region (Ohde et al., 2018), MV3 has the deepest source depth of ~5 km and that of MV14 the shallowest of only around 1–2 km (Table 5). In any case, the plate boundary, which is supposed to be around 18 km, has not been reached (Nishizawa et al., 2017). This is consistent with the results of Mitsutome et al. (2023), who used the concentration of noble gases in the surface sediments of mud volcanoes in this area and showed that the depth of origin of noble gases in the surface sediments of mud volcanoes off Tanegashima is about 3 to 9 km.

5.3 Isotope fractionation of B isotope ratio between the solid and liquid phases

The vertical distribution of B concentration in the pore water suggests that fluid with a higher B concentration than seawater was supplied from the deep subseafloor (Figure 2F). The B isotope ratios in the pore water showed different values for each MV, suggesting that B was supplied from different sources for each MV (Figure 2G). Here, given that we are collecting pore water from the seafloor, if boron in pore water can be explained by the mixing of fluids of multiple origins, it would be reasonable to consider seawater as a candidate as one of the origins (Figure 2F). The isotope ratio of the source was obtained by recording the *y*-intercept of the isotope ratio of the element against the reciprocal of its concentration (Keeling, 1958). However, in the case of pore water of the deep seafloor, if gas hydrates are present in the sediment and dissolve to release fresh water during recovery, the B concentration will also decrease accordingly. Therefore, this effect was offset by considering the concentration ratio of Cl^- and B (Cl^-/B ratio) (Figure 4). Furthermore, a straight line was drawn through the background seawater to obtain the *y*-intercept of each MV (Figure 4). The obtained *y*-intercept values are listed in Table 6. Both values differed from the B isotope ratio of seawater (+39.5‰; Spivack and Edmond, 1987), and showed different values for each MV (Table 6). MV3 showed much higher values, followed by MV2 and MV14 with similar values, and MV1 had the lowest value (Table 6). Moreover, the isotope ratio of B in the sediment cannot be determined for end-members; thus, the difference from the average value for each MV (Table 3), namely, the isotope fractionation of B between the solid and liquid phases ($\Delta_{solid\text{-}fluid}$), was determined (Table 6). According to the results, the isotope fractionation values of MV3 were the largest, whereas those of MV2 and MV14 were almost the same (Table 6).

To verify the potential of the B isotope ratio as a geothermometer, the horizontal axis represents the equilibrium temperature of the clay minerals obtained from the Na and Li concentrations determined in this study (Table 5). A graph was created with 1000/T (K^{-1}) and $\Delta_{solid\text{-}fluid}$ (Table 6) on the vertical axis (Figure 5). The geothermometer trend (black dashed line in Figure 5) proposed by Williams et al. (2001), and the trend of B isotope fractionation (brown dashed line in Figure 5), which indicates the degree of alteration of clay minerals observed in global MVs reported by Kopf and Deyhle (2002), are shown in Figure 5. According to this graph, the B isotope fractionation trend obtained in this study is different from any other trends and corresponds to the observations of normal pore water levels (blue area in Figure 5; Brumsack et al., 1992; You et al., 1995; Deyhle et al., 2004). The only deviation in this area was the value observed at MV3, which was plotted on the lower side of the trend (Figure 5). This was because the B isotope ratio was extremely high in the pore water at MV3 (Figure 4; Table 6).

5.4 Origin of B in the pore water from MVs off Tanegashima

The reported B isotope ratios that were higher than those in seawater are limited to specific environments (Palmer and Swihart, 1996; Kopf and Deyhle, 2002; Marschall, 2018). This phenomenon is usually observed in brines formed by the evaporation of seawater: +59‰ in Australian lakes (Vengosh et al., 1991a) and +56‰ in the Dead Sea (Vengosh et al., 1991b). Laboratory experiments have confirmed this trend: when seawater evaporates, the B isotope ratio

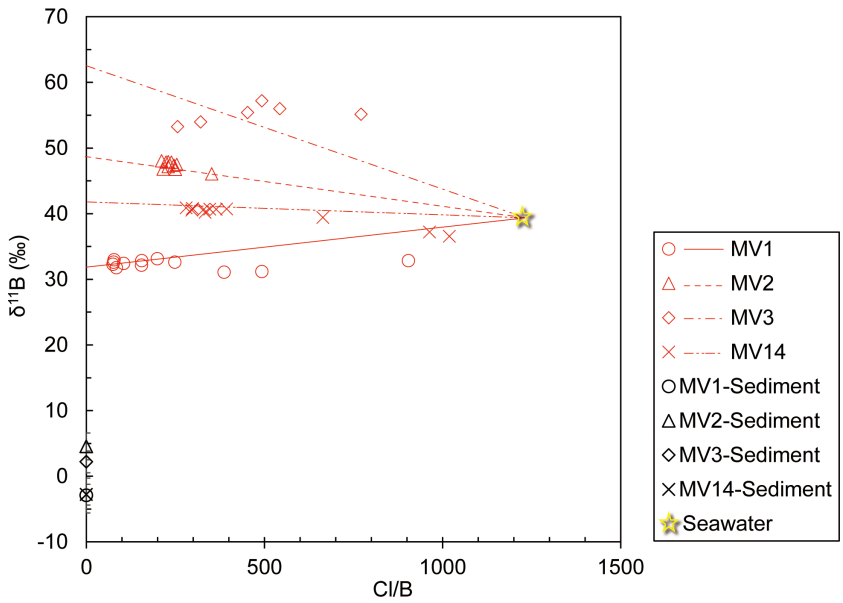

FIGURE 4
Relationship between the B isotope ratio and the ratio of Cl^- to B concentrations in pore water and the B isotope ratio in sediments of each MV.

in the deposited salt ranges from +10 to +30‰, and that in the residual brine ranges from +40 to +70‰ (Vengosh et al., 1992). In this solution, the adsorption of B is considered to have occurred, and ^{10}B is more likely to be adsorbed (Spivack et al., 1987). Another fluid with an extremely high B isotope ratio is pore water in the deep subseafloor (Marschall, 2018). At depths of 600 m below the seafloor in Hole 808, which was drilled at the tip of the Nankai Trough accretionary prism off Muroto during the ODP Leg 131, a B isotope ratio of approximately +50‰ was observed in the pore water (You et al., 1993). Additionally, a B isotope ratio of +45.9‰ was observed 874 m below the seafloor in Hole 1150, which was drilled in the forearc of the Japan Trench during ODP Leg 186 (Deyhle and Kopf, 2002). Both values are thought to be the result of advanced re-adsorption, and remarkably high values have been found in the pore water of MVs (Kopf and Deyhle, 2002). B isotope ratios in pore water reaching +65‰ were found in an MV in Taiwan (Gieskes et al., 1992), and Chao et al. (2011) also found a B isotope ratio reaching +55.8‰ in an MV in Taiwan. Considering the results of these studies, the extremely high B isotope ratio observed in this study appears to be the result of strong adsorption. Such a high B isotope ratio is considered to be one of the characteristics of B in the surface sediments of MVs (Kopf and Deyhle, 2002). The surface layers of MVs contain buried sediments and authigenic minerals that would normally be distributed deep below the seafloor (Sokol et al., 2018); B in pore water in the surface sediments of MVs exhibits extremely high B isotope ratios, suggesting that it is subject to very strong adsorption (Kopf and Deyhle, 2002). Therefore, we propose the hypothesis that these MV-specific solid phases may have the ability to strongly adsorb B in pore water.

TABLE 6 End members of boron isotope ratios in pore water and the mean values of boron isotope ratios in sediments, and their differences (isotopic fractionation).

Site	$\delta^{11}B_{fluid}$*			$\Delta_{solid-fluid}$		
	‰			‰		
MV1	+32.01	±	0.02	-34.9	±	2.7
MV2	+49.28	±	0.04	-44.7	±	2.0
MV3	+62.17	±	0.07	-60.0	±	1.7
MV14	+41.81	±	0.03	-44.6	±	1.6

5.5 Evaluation of MV activity using various indexes

In this study, we compared each MV using the chemical and isotopic compositions of the pore water collected from the surface sediment of the MV off Tanegashima. The estimation of advection velocity using the vertical distribution of the Cl^- concentration indicates that the upward advection velocity of MV3 is an order of magnitude higher and MV3 may be the most active MV (Table 4). Estimation of the origin depth using the Na/Li concentration ratio suggests that Na and Li are supplied from clay minerals at the deepest parts of MV3 and MV2 (Table 5), indicating that compared with other MVs, these MVs were formed by the supply of a large amount of energy to migrate materials from deeper regions. This indicates relatively extensive activity. Based on these results, we suggested that MV3 is currently the most active MV. The B isotope ratio in the pore water of MV3, which was the most active, showed the highest value (Table 6). This trend is the opposite of that reported by Chao et al. (2011). MVs in Taiwan show a high B isotope ratio, although the tendency is not clear; however, the slower fluid velocity is strongly affected by re-adsorption (Chao et al., 2011). However, the results of this study are consistent with those of Kopf and Deyhle (2002), who indicated that the larger the isotopic fractionation of the B isotope ratio, the greater is the supply of B from deeper layers. The B isotope ratio in the pore water

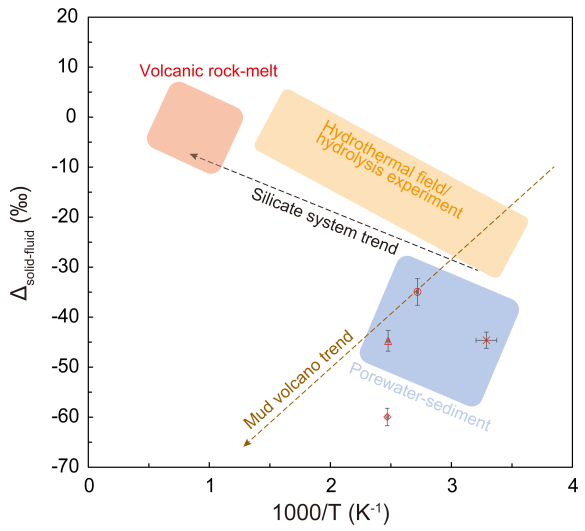

FIGURE 5
Relationship between the equilibrium temperature with clay minerals estimated from the Na and Li concentrations and the isotope fractionation of B isotope ratios in the sediment and pore water.

observed at the surface of the MV shows a stronger degree of adsorption in the more active MV, indicating that the clay minerals were absorbed from the deeper part. This suggests that when the MVs start to be active the B isotope ratio in the surface pore water of the MVs increases. In future studies, the number of observational cases need to be increased to thoroughly verify these regularities.

6 Conclusion

We investigated the chemical composition of pore water in sediments collected from the MVs off Tanegashima and discussed the origin depth, advection velocity, and MV activity. The advection velocity was estimated from the Cl^- concentrations, and it was found to be different for each MV. The equilibrium temperature with clay minerals was estimated from Na and Li concentrations in the fresh water source, and we found that it differed for each MV, ranging from 93 to 134°C for MV1 to MV3. The Li concentration in the pore water of MV14 is almost the same as that of seawater, and we presumed that water originating from the dehydration of clay minerals is not supplied. Considering a geothermal gradient of 25°C/km, this indicates that the origin depth is approximately 3.7 to 5.5 km, suggesting that the depth corresponds to the upper crust under the seafloor. Additionally, the B isotope ratio in pore water was very high, suggesting that adsorption had a strong effect. As MV3, which is considered the most active, showed the most adsorption, we assumed that the clay minerals that migrated from deeper depths may have a stronger adsorption capacity. The trend between the isotopic fractionation of B isotope ratios in the solid and liquid phases and the equilibrium temperature with clay minerals estimated from the Na/Li ratios in the pore water is different from the usual trend between the isotopic fractionation of silicate and water and the equilibrium temperature, which is unique to mud volcanoes. Rather than functioning as a geothermometer, the pore water of an active mud volcano may be used as an indicator of extremely high B isotope ratios.

Data availability statement

The original contributions presented in the study are included in the article/Supplementary Material. Further inquiries can be directed to the corresponding author.

Author contributions

AI, TT, and RS: Conception or design of the study. YM, KA, TT, K-HS, RS, and AI: Data collection. TT: Analysis and interpretation of data. YM, KA, TT, and RS: Writing the paper. YM, KA, TT, K-HS, RS, and AI: Approval of final draft. All authors contributed to the article and approved the submitted version.

Funding

This research was supported by JSPS KAKENHI JP (18H03733 and 20H04315), NIHU Research Projects "Interdisciplinary and Integrated Studies on Local Cultures: Aiming for the Emergence of Novel Communities" and the RIHN LINKAGE Project (No.14200145).

Acknowledgments

We express our gratitude to the captain of the R/V *Hakuho-Maru*, all crew members, and the NSS operations staff for their help in collecting the samples. We would like to express our gratitude for the opportunity to conduct this research. Finally, we thank Professors Orlando Vaselli and Chen-Feng You for their valuable comments on the manuscript. I would also like to thank Professor Marcelo Ketzer for his free editing work in his busy schedule.

Conflict of interest

The authors declare that the research was conducted in the absence of any commercial or financial relationships that could be construed as a potential conflict of interest.

Publisher's note

All claims expressed in this article are solely those of the authors and do not necessarily represent those of their affiliated organizations, or those of the publisher, the editors and the reviewers. Any product that may be evaluated in this article, or claim that may be made by its manufacturer, is not guaranteed or endorsed by the publisher.

Supplementary material

The Supplementary Material for this article can be found online at: https://www.frontiersin.org/articles/10.3389/fmars.2023.1229797/full#supplementary-material

SUPPLEMENTARY FIGURE 1
Bathymetric maps of **(A)** MV1, **(B)** MV2, **(C)** MV3, and **(D)** MV14.

References

Ashi, J., and Tokuyama, H. (2005). Navigable sampling system -NSS- (in Japanese). *Techno marine: Bull. Soc. Naval Architects Japan* 127, 29–33. doi: 10.14856/technom.883.0_29

Brumsack, H. J., Zuleger, E., Gohn, E., and Murray, R. W. (1992). Stable and radiogenic isotopes in pore waters from Leg 127, Japan Sea. *Proc. Ocean Drilling Program Sci. Results* 127, 635–650. doi: 10.2973/odp.proc.sr.127128.165.1992

Carter, L., Gavey, R., Talling, P. J., and Liu, J. T. (2014). Insights into submarine geohazards from breaks in subsea telecommunication cables. *Oceanography* 27, 58–67. doi: 10.5670/oceanog.2014.40

Carter, L., Milliman, J. D., Talling, P. J., Gavey, R., and Wynn, R. B. (2012). Near-synchronous and delayed initiation of long run-out submarine sediment flows from a record-breaking river flood, offshore Taiwan. *Geophysical Res. Lett.* 39. doi: 10.1029/2012GL051172

Chao, H., You, C., Wang, B., Chung, C., and Huang, K. (2011). Boron isotopic composition of mud volcano fluids: Implications for fluid migration in shallow subduction zones. *Earth Planetary Sci. Lett.* 305, 32–44. doi: 10.1016/j.epsl.2011.02.033

Clift, P., and Vannucchi, P. (2004). Controls on tectonic accretion versus erosion in subduction zones: Implications for the origin and recycling of the continental crust. *Rev. Geophysics* 42. doi: 10.1029/2003RG000127

Deyhle, A., and Kopf, A. (2002). Strong B enrichment and anomalous δ^{11}B in pore fluids from the Japan Trench forearc. *Mar. Geology* 183, 1–15. doi: 10.1016/S0025-3227(02)00186-X

Deyhle, A., and Kopf, A. J. (2005). The use and usefulness of boron isotopes in natural silicate–water systems. *Phys. Chem. Earth Parts A/B/C* 30, 1038–1046. doi: 10.1016/j.pce.2005.04.003

Deyhle, A., Kopf, A., Frape, S., and Hesse, R. (2004). Evidence for fluid flow in the Japan Trench forearc using isotope geochemistry (Cl Sr. B): Results from ODP Site 1150. *Island Arc* 13, 258–270. doi: 10.1111/j.1440-1738.2003.00424.x

Dickens, G. R., Koelling, M., Smith, D. C., and Schnieders, L. (2007). Rhizon sampling of pore waters on scientific drilling expeditions: An example from the IODP Expedition 302, Arctic Coring Expedition (ACEX). *Sci. Drilling* 4, 22–25. doi: 10.5194/sd-4-22-2007

Etiope, G., Feyzullayev, A., Milkov, A. V., Waseda, A., Mizobe, K., and Sun, C. H. (2009). Evidence of subsurface anaerobic biodegradation of hydrocarbons and potential secondary methanogenesis in terrestrial mud volcanoes. *Mar. Petroleum Geology* 26, 1692–1703. doi: 10.1016/j.marpetgeo.2008.12.002

Etiope, G., and Milkov, A. V. (2004). A new estimate of global methane flux from onshore and shallow submarine mud volcanoes to the atmosphere. *Environ. Geology* 46, 997–1002. doi: 10.1007/s00254-004-1085-1

Feseker, T., Boetius, A., Wenzhöfer, F., Blandin, J., Olu, K., Yoerger, D. R., et al. (2014). Eruption of a deep-sea mud volcano triggers rapid sediment movement. *Nat. Commun.* 5, 5385. doi: 10.1038/ncomms6385

Fouillac, C., and Michard, G. (1981). Sodium/lithium ratio in water applied to geothermometry of geothermal reservoirs. *Geothermics* 10, 55–70. doi: 10.1016/0375-6505(81)90025-0

Gavey, R., Carter, L., Liu, J. T., Talling, P. J., Hsu, R., Pope, E., et al. (2017). Frequent sediment density flows during 2006 to 2015, triggered by competing seismic and weather events: Observations from subsea cable breaks off southern Taiwan. *Mar. Geology* 384, 147–158. doi: 10.1016/j.margeo.2016.06.001

Gieskes, J. M., Chen-Feng, Y., Typhoon, L., Tzen-Fu, Y., and Hsin-Wei, C. (1992). Hydro-geochemistry of mud volcanoes in Taiwan. *Acta Geologica Taiwanica Sci. Rep. Natl. Taiwan Univ.* 30, 79–88.

Hellstrom, J., Paton, C., Woodhead, J., and Hergt, J. (2008). Iolite: software for spatially resolved LA-(quad and MC) ICPMS analysis. *Mineralogical Assoc. Canada short course Ser.* 40, 343–348.

Hensen, C., Nuzzo, M., Hornibrook, E., Pinheiro, L., Bock, B., Magalhães, V., et al. (2007). Sources of mud volcano fluids in the Gulf of Cadiz - indications for hydrothermal imprint. *Geochimica Cosmochimica Acta* 71, 1232–1248. doi: 10.1016/j.gca.2006.11.022

Hensen, C., Wallmann, K., Schmidt, M., Ranero, C. R., and Suess, E. (2004). Fluid expulsion related to mud extrusion off Costa Rica—A window to the subducting slab. *Geology* 32, 201–204. doi: 10.1130/G20119.1

Hoshino, T., Toki, T., Ijiri, A., Morono, Y., Machiyama, H., Ashi, J., et al. (2017). *Atribacteria* from the subseafloor sedimentary biosphere disperse to the hydrosphere through submarine mud volcanoes. *Front. Microbiol.* 8. doi: 10.3389/fmicb.2017.01135

Ishikawa, T., and Nakamura, E. (1993). Boron isotope systematics of marine sediments. *Earth and Planetary Science Letters* 117, 567–580. doi: 10.1016/0012-821X(93)90103-G

James, R. H., Rudnicki, M. D., and Palmer, M. R. (1999). The alkali element and boron geochemistry of the Escanaba Trough sediment-hosted hydrothermal system. *Earth Planetary Sci. Lett.* 171, 157–169. doi: 10.1016/S0012-821X(99)00140-5

Kastner, M., Elderfield, H., and Martin, J. B. (1991). Fluids in Convergent Margins: What do We Know about their Composition, Origin, Role in Diagenesis and Importance for Oceanic Chemical Fluxes? *Philos. Trans. R. Soc. London. Ser. A: Phys. Eng. Sci.* 335, 243–259. doi: 10.1098/rsta.1991.0045

Keeling, C. D. (1958). The concentration and isotopic abundances of atmospheric carbon dioxide in rural areas. *Geochimica Cosmochimica Acta* 13, 322–334. doi: 10.1016/0016-7037(58)90033-4

Kioka, A. (2020). Geological occurrence and morphological feature of submarine mud volcanoes: A brief review (in Japanese with English abstract). *J. Geological Soc. Japan* 126, 17–28. doi: 10.5575/geosoc.2019.0004

Kopanina, A. V., and Shvidskaya, K. A. (2021). Possibility of using satellite-based monitoring for large-scale mapping and research of dynamics of mud volcanic landscapes. *IOP Conf. Series: Earth Environ. Sci.* 946, 012040. doi: 10.1088/1755-1315/946/1/012040

Kopf, A. J. (2002). Significance of mud volcanism. *Rev. Geophysics* 40, 1005. doi: 10.1029/2000RG000093

Kopf, A., and Deyhle, A. (2002). Back to the roots: boron geochemistry of mud volcanoes and its implications for mobilization depth and global B cycling. *Chem. Geology* 192, 195–210. doi: 10.1016/S0009-2541(02)00221-8

Lalk, E., Pape, T., Gruen, D. S., Kaul, N., Karolewski, J. S., Bohrmann, G., et al. (2022). Clumped methane isotopologue-based temperature estimates for sources of methane in marine gas hydrates and associated vent gases. *Geochimica Cosmochimica Acta* 327, 276–297. doi: 10.1016/j.gca.2022.04.013

Manga, M., Brumm, M., and Rudolph, M. L. (2009). Earthquake triggering of mud volcanoes. *Mar. Petroleum Geology* 26, 1785–1798. doi: 10.1016/j.marpetgeo.2009.01.019

Manheim, F. T. (1966). A hydraulic squeezer for obtaining interstitial water from consolidated and unconsolidated sediments. *Geological Survey Prof. Paper (United States)* 550, 256–261.

Marschall, H. R. (2018). "Boron isotopes in the ocean floor realm and the mantle," in *Boron isotopes: The fifth element*. Eds. H. Marschall and G. Foster (Cham: Springer international publishing), 189–215.

Mazzini, A., and Etiope, G. (2017). Mud volcanism: An updated review. *Earth-Science Rev.* 168, 81–112. doi: 10.1016/j.earscirev.2017.03.001

Milkov, A. V. (2000). Worldwide distribution of submarine mud volcanoes and associated gas hydrates. *Mar. Geology* 167, 29–42. doi: 10.1016/S0025-3227(00)00022-0

Mitsutome, Y., Toki, T., Kagoshima, T., Sano, Y., Tomonaga, Y., and Ijiri, A. (2023). Estimation of the depth of origin of fluids using noble gases in the surface sediments of submarine mud volcanoes off Tanegashima Island. *Sci. Rep.* 13, 5051. doi: 10.1038/s41598-023-31582-z

Nakayama, N., Ashi, J., Tsunogai, U., Gamo, T., and Tanahashi, M. (2010). Sources of pore water in a Tanegashima mud volcano inferred from chemical and stable isotopic studies. *Geochemical J.* 44, 561–569. doi: 10.2343/geochemj.1.0094

Nishio, Y., Ijiri, A., Toki, T., Morono, Y., Tanimizu, M., Nagaishi, K., et al. (2015). Origins of lithium in submarine mud volcano fluid in the Nankai accretionary wedge. *Earth Planetary Sci. Lett.* 414, 144–155. doi: 10.1016/j.epsl.2015.01.018

Nishizawa, A., Kaneda, K., Oikawa, M., Horiuchi, D., Fujioka, Y., and Okada, C. (2017). Variations in seismic velocity distribution along the Ryukyu (Nansei-Shoto) Trench subduction zone at the northwestern end of the Philippine Sea plate. *Earth Planets Space* 69, 86. doi: 10.1186/s40623-017-0674-7

Ohde, A., Otsuka, H., Kioka, A., and Ashi, J. (2018). Distribution and depth of bottom-simulating reflectors in the Nankai subduction margin. *Earth Planets Space* 60, 70. doi: 10.1186/s40623-018-0833-5

Okada, H., and Whitaker, J. H. M. (1979). Sand volcanoes of the Palaeogene Kumage Group, Tanegashima, southwest Japan (In Japanese with English abstract). *J. Geological Soc. Japan* 85, 187–196. doi: 10.5575/geosoc.85.187

Palmer, M. R. (1991). Boron isotope systematics of hydrothermal fluids and tourmalines: A synthesis. *Chem. Geology: Isotope Geosci. section* 94, 111–121. doi: 10.1016/0168-9622(91)90004-G

Palmer, M. R., and Swihart, G. H. (1996). Boron isotope geochemistry: an overview. *Rev. Mineralogy Geochemistry* 33, 709–744. doi: 10.1515/9781501509223-015

Paton, C., Hellstrom, J., Paul, B., Woodhead, J., and Hergt, J. (2011). Iolite: Freeware for the visualisation and processing of mass spectrometric data. *J. Analytical Atomic Spectrometry* 26, 2508–2518. doi: 10.1039/c1ja10172b

Seeberg-Elverfeldt, J., Schlüter, M., Feseker, T., and Koelling, M. (2005). Rhizon sampling of pore waters near the sediment/water interface of aquatic systems. *Limnology oceanography Methods* 3, 361–371. doi: 10.4319/lom.2005.3.361

Seno, T., and Maruyama, S. (1984). Paleogeographic reconstruction and origin of the Philippine Sea. *Tectonophysics* 102, 53–84. doi: 10.1016/0040-1951(84)90008-8

Sokol, E., Kokh, S., Kozmenko, O., Novikova, S., Khvorov, P., Nigmatulina, E., et al. (2018). Mineralogy and geochemistry of mud volcanic ejecta: A new look at old issues (A case study from the bulganak field, northern black sea). *Minerals* 8, 344. doi: 10.3390/min8080344

Spivack, A. J., and Edmond, J. M. (1987). Boron isotope exchange between seawater and the oceanic crust. *Geochimica Cosmochimica Acta* 51, 1033–1043. doi: 10.1016/0016-7037(87)90198-0

Spivack, A. J., Palmer, M. R., and Edmond, J. M. (1987). The sedimentary cycle of the boron isotopes. *Geochimica Cosmochimica Acta* 51, 1939–1949. doi: 10.1016/0016-7037(87)90183-9

Tingay, M., Manga, M., Rudolph, M. L., and Davies, R. (2018). An alternative review of facts, coincidences and past and future studies of the Lusi eruption. *Mar. Petroleum Geology* 95, 345–361. doi: 10.1016/j.marpetgeo.2017.12.031

Tinivella, U., and Giustiniani, M. (2012). "An overview of mud volcanoes associated to gas hydrate system," in *Updates in volcanology—New advances in understanding volcanic systems*. Ed. N. Karoly (Rijeka: Intech Open Science 225–267).

Tsunogai, U., Maegawa, K., Sato, S., Komatsu, D. D., Nakagawa, F., Toki, T., et al. (2012). Coseimic massive methane release from a submarine mud volcano. *Earth Planetary Sci. Lett.* 341–344, 79–85. doi: 10.1016/j.epsl.2012.06.004

Ujiié, Y. (2000). Mud diapirs observed in two piston cores from the landward slope of the northern Ryukyu Trench, northwestern Pacific Ocean. *Mar. Geology* 163, 149–167. doi: 10.1016/S0025-3227(99)00113-9

Vengosh, A., Chivas, A. R., Mcculloch, M. T., Starinsky, A., and Kolodny, Y. (1991a). Boron isotope geochemistry of Australian salt lakes. *Geochimica Cosmochimica Acta* 55, 2591–2606. doi: 10.1016/0016-7037(91)90375-F

Vengosh, A., Starinsky, A., Kolodny, Y., and Chivas, A. R. (1991b). Boron isotope geochemistry as a tracer for the evolution of brines and associated hot springs from the Dead Sea, Israel. *Geochimica Cosmochimica Acta* 55, 1689–1695. doi: 10.1016/0016-7037(91)90139-V

Vengosh, A., Starinsky, A., Kolodny, Y., Chivas, A. R., and Raab, M. (1992). Boron isotope variations during fractional evaporation of sea water: New constraints on the marine vs. nonmarine debate. *Geology* 20, 799–802. doi: 10.1130/0091-7613(1992)020<0799:BIVDFE>2.3.CO;2

Wang, C.-Y., and Manga, M. (2021). "Mud volcanoes," in *Water and earthquakes* (Cham:Springer Nature), 323–342. doi: 10.1007/978-3-030-64308-9_12

Wang, B.-S., You, C.-F., Huang, K.-F., Wu, S.-F., Aggarwal, S. K., Chung, C.-H., et al. (2010). Direct separation of boron from Na- and Ca-rich matrices by sublimation for stable isotope measurement by MC-ICP-MS. *Talanta* 82, 1378–1384. doi: 10.1016/j.talanta.2010.07.010

Williams, L. B., Hervig, R. L., Holloway, J. R., and Hutcheon, I. (2001). Boron isotope geochemistry during diagenesis. Part I. Experimental determination of fractionation during illitization of smectite. *Geochimica Cosmochimica Acta* 65, 1769–1782. doi: 10.1016/S0016-7037(01)00557-9

Woodhead, J., Swearer, S., Hergt, J., and Maas, R. (2005). *In situ* Sr-isotope analysis of carbonates by LA-MC-ICP-MS: interference corrections, high spatial resolution and an example from otolith studies. *J. Analytical Atomic Spectrometry* 20, 22–27. doi: 10.1039/b412730g

You, C.-F., Chan, L. H., Spivack, A. J., and Gieskes, J. M. (1995). Lithium, boron, and their isotopes in sediments and pore waters of Ocean Drilling Program Site 808, Nankai Trough: Implications for fluid expulsion in accretionary prisms. *Geology* 23, 37–40. doi: 10.1130/0091-7613(1995)023<0037:LBATII>2.3.CO;2

You, C. F., and Gieskes, J. M. (2001). Hydrothermal alteration of hemi-pelagic sediments: experimental evaluation of geochemical processes in shallow subduction zones. *Appl. Geochemistry* 16, 1055–1066. doi: 10.1016/S0883-2927(01)00024-5

You, C. F., Spivack, A. J., Smith, J. H., and Gieskes, J. M. (1993). Mobilization of boron in convergent margins: Implications for the boron geochemical cycle. *Geology* 21, 207–210. doi: 10.1130/0091-7613(1993)021<0207:MOBICM>2.3.CO;2

frontiers | Frontiers in Earth Science

TYPE Original Research
PUBLISHED 18 October 2023
DOI 10.3389/feart.2023.1250619

Check for updates

OPEN ACCESS

EDITED BY
Marzia Rovere,
Institute of Marine Sciences, Italy

REVIEWED BY
Giuliana Panieri,
UiT The Arctic University of Norway, Norway
Klaus Wallmann,
GEOMAR Helmholtz Center for Ocean Research Kiel, Germany

*CORRESPONDENCE
Stéphanie Dupré,
stephanie.dupre@ifremer.fr

RECEIVED 30 June 2023
ACCEPTED 06 October 2023
PUBLISHED 18 October 2023

CITATION
Dupré S, Foucher J-P, Pierre C, Decker C, Westbrook G, Ker S, Olu K, Donval J-P, Charlou J-L, Blanc-Valleron M-M and Nouzé H (2023), Methane-flow system within the Nyegga pockmark field, offshore mid-Norway.
Front. Earth Sci. 11:1250619.
doi: 10.3389/feart.2023.1250619

COPYRIGHT
© 2023 Dupré, Foucher, Pierre, Decker, Westbrook, Ker, Olu, Donval, Charlou, Blanc-Valleron and Nouzé. This is an open-access article distributed under the terms of the Creative Commons Attribution License (CC BY). The use, distribution or reproduction in other forums is permitted, provided the original author(s) and the copyright owner(s) are credited and that the original publication in this journal is cited, in accordance with accepted academic practice. No use, distribution or reproduction is permitted which does not comply with these terms.

Methane-flow system within the Nyegga pockmark field, offshore mid-Norway

Stéphanie Dupré[1]*, Jean-Paul Foucher[1], Catherine Pierre[2], Carole Decker[3], Graham Westbrook[4], Stephan Ker[1], Karine Olu[3], Jean-Pierre Donval[1], Jean-Luc Charlou[1], Marie-Madeleine Blanc-Valleron[5] and Hervé Nouzé[1]

[1]UMR GEO-OCEAN, IFREMER, Plouzané, France, [2]UMR LOCEAN, Sorbonne Université, Paris, France, [3]UMR BEEP, IFREMER, Plouzané, France, [4]School of Geography, Earth & Environmental Sciences, University of Birmingham, Birmingham, United Kingdom, [5]UMR-CR2P, CNRS-MNHN, Paris, France

We investigated fluid seepage within the Nyegga pockmark field (600–900 m water depths) off mid-Norway from Remotely Operated Vehicle dives at the so-called CNE sites (CNE01 to CNE17). The seafloor morphology of some of these features corresponds to pockmarks and adjacent ridges, with the latter being the focus of present seepage activity. These structures are underlain by chimneys above a gas-charged zone with, in some cases, a substantial body of hydrate-invaded sediment (down to 1.3 s in two-way travel time at CNE03). Present-day methane-rich fluid seepage through the seabed is indicated by chemosynthetic fauna, in particular Siboglinidae polychaetes (*Oligobrachia haakonmobiensis webbi* and *Sclerolinum contortum*), microbial mats and associated Rissoidae gastropod (*Alvania* sp.) grazers, and confirmed by measured *in situ* bottom-water methane anomalies, up to 2,130 nL/L. No free-gas bubble emissions were observed or acoustically identified. The presence of authigenic carbonates reveals past seepage with very low $\delta^{13}C$ values (down to −58‰) indicating that the major source of carbon was methane carried by the venting fluids. The ages of major periods of methane venting are provided by vesicomyid bivalve shells (*Isorropodon nyeggaensis*) present in two sedimentary layers, 14,930 and 15,500 ^{14}C yr BP (ca. 17,238 and 17,952 cal yr BP), respectively, corresponding to the time of Melt Water Pulse IA. The seafloor morphology and pattern of seepage -chemosynthetic fauna and microbial mat distribution and dissolved methane concentration-are remarkably heterogeneous. Pore-water chemistry profiles in a gravity core taken only 40 m from major seepage sites indicate no seepage and anaerobic methane oxidation at a sub-bottom depth of about 2 m. Present-day seepage from the studied pockmark-chimney fluid-flow system charged with gas hydrate is dominated by the advection of methane solution in pore water. Some of this methane could result from the dissolution of hydrate in the chimney, most of which would have formed during an earlier period (post-LGM times) of history of the chimney, when it was venting free gas. However, the presence of free gas beneath this chimney is probably why the water entering the chimney is already saturated with methane and the process of hydrate formation in the chimney continues today.

KEYWORDS

Norwegian margin, gas chimneys, pockmarks, seeps, authigenic carbonates, chemosynthesis-based communities, gas hydrate, dissolved methane

1 Introduction

Pockmarks are commonly interpreted as sites of hydrodynamic removal of sediment caused by focused fluid discharge through the seabed (Judd and Hovland, 2007). Mainly associated with light hydrocarbon gases, pockmarks, since their first discovery off Nova Scotia (King and MacLean, 1970) have been identified and studied worldwide at numerous continental margins, in particular offshore Norway (Vogt et al., 1999b). Marine fluid-flow systems are relevant for geohazards with i) triggering of sedimentary instabilities in relation or not with gas hydrate dissociation (Bünz et al., 2003), ii) their relationships with earthquakes (Field and Jennings, 1987) and iii) possible massive methane release into the ocean and the atmosphere (Borges et al., 2016). Cold seeps are also hotspots for biology with the establishment of chemosynthetic organisms and microbial communities and the potential to provide specific habitats (Sibuet and Olu, 1998; Vanreusel et al., 2009).

The studied area is located on the continental slope off mid-Norway within the Nyegga pockmark field and lies at water depths of 600–800 m, ~20–30 km from the northern Storegga slide scar (Figure 1). This area comprises pockmark features above gas chimneys labelled CNE01 to CNE17 (CNE standing for

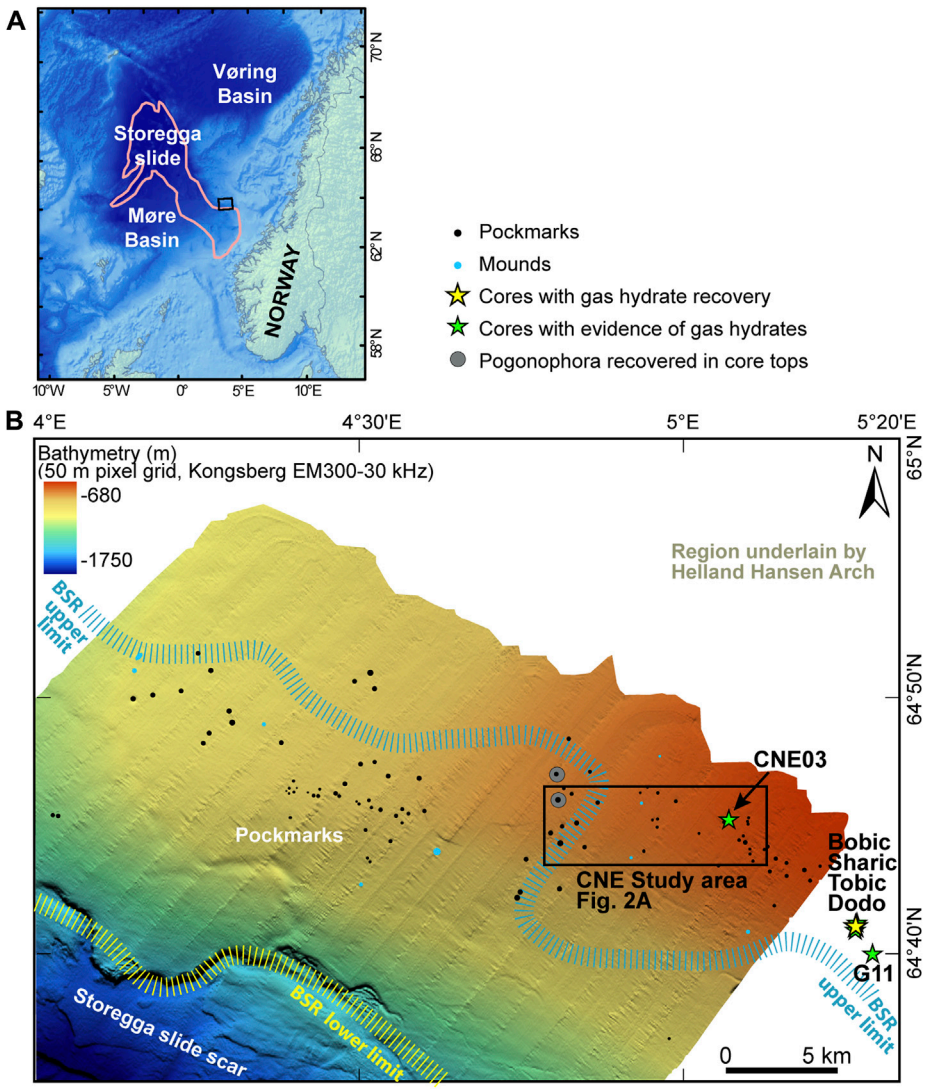

FIGURE 1
(A) General location map of the study area within the Nyegga area on the mid-Norwegian continental margin (Norwegian Sea) with contour of the Storegga Slide from Bünz and Mienert (2004). Black rectangle stands for the frame of Figure 1B. **(B)** Shaded regional bathymetry map of part of the Nyegga slope (Hydratech data) with areas of seabed occupied by the largest pockmarks, shown in black, and mounds, shown in blue. The pockmarks were identified from this regional multibeam bathymetry and associated chirp profiler records, with some of them previously identified from seismic reflection sections by Bünz et al. (2003). The upper and lower limits of the area of the slope underlain, at least partly, by gas-hydrate-related Bottom-Simulating Reflectors (BSRs) are indicated by blue and yellow barred lines, respectively. The yellow and green stars stand for locations of gravity cores (mainly TTR16 data) with gas hydrate recovery (Sharic pockmark) and evidence of the presence of gas hydrates in the sediment (CNE03, G11, Bobic and Tobic pockmarks), respectively (Ivanov et al., 2007; Akhmetzhanov et al., 2008; Ivanov et al., 2010; Attias et al., 2020). The green star in the study area is the CNE03 location of cores that evidenced gas hydrates (AT634G, Ivanov et al., 2010; Core CNE03; Attias et al., 2020). Pogonophora were recovered in the core tops of AT634G (CNE03), AT117G and AT118G (displayed as grey dots) from TTR16 and TTR8 cruises, respectively (Ivanov et al., 2010).

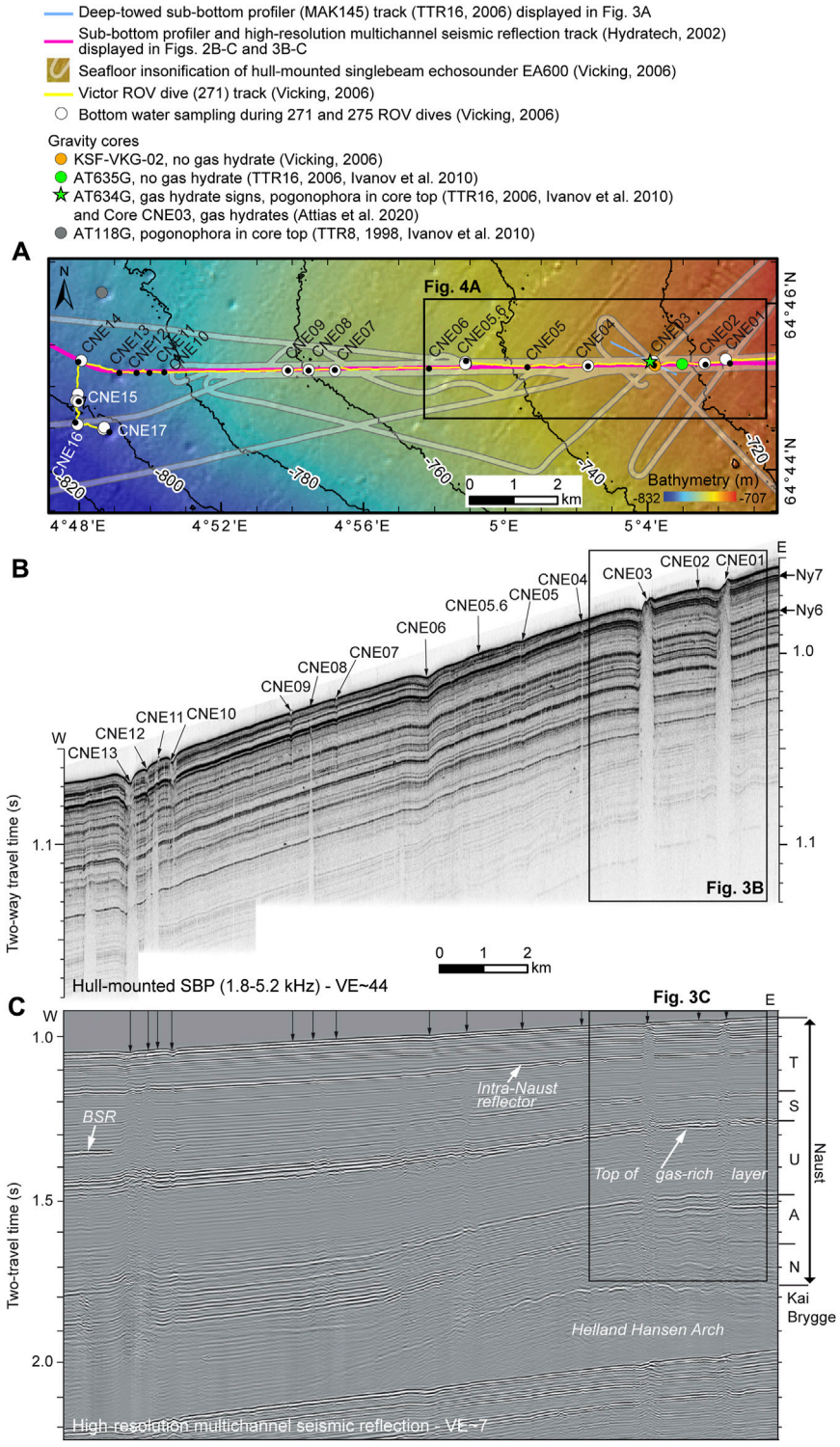

FIGURE 2
(A) Bathymetric zoom of the Nyegga study corridor displayed in Figure 1B with location of the unpublished hull-mounted sub-bottom profiler and 120-channel high-resolution reflection seismic records (Hydratech data) shown in Figures 2B,C, respectively. Seafloor imprint of the Kongsberg EA600 single-beam echosounder (Vicking data) insonification is reported. All subfigures have the same horizontal scale. Identified pockmarks and their underlying chimneys (CNE01 to CNE17) are shown along the Victor ROV track during Vicking dive 271. **(B)** Record from a hull-mounted 1.8–5.2 kHz sub-bottom profiler acquired along the track shown in Figure 2A. Arrows indicate the positions of pockmarks investigated with Victor ROV. Acoustic responses of the wider 'chimneys' and narrower 'conduits' beneath the pockmarks are typically zones of low amplitude and coherence, with deformation of strata in the flanks of chimneys. The interval between horizons Ny6 and Ny7, with ages of 15,800 ^{14}C ky BP and 15,000 ^{14}C ky BP (ca. 18,314 and 17,366 cal yr BP), respectively, was one of rapid sedimentation (Reiche et al., 2011). **(C)** Stacked and migrated seismic line from 120-channel high-resolution seismic survey along the track shown in Figure 2A. Positions of pockmarks are indicated by arrows at the seabed. The top of the layer, which from its low seismic velocity, appears to contain gas, is marked, as a local
(*Continued*)

FIGURE 2 (Continued)
occurrence of a hydrate-related bottom-simulating reflector. Near the time axis on the right, is the seismo-stratigraphy for the Naust and Kai formations, after Rise et al. (2006) and following, in part, the interpretations of Hustoft et al. (2007) and Plaza-Faverola et al. (2012). The Intra-Naust reflector is dated at 130 ky (Solheim et al., 2005).

ChimNEy) from east to west (Figure 2A). The CNE sites were identified previous to this study at the seafloor and in depth using conventional bathymetric mapping and seismics, respectively. These data that we can qualify as 'vintage' were acquired during the Hydratech marine expedition (Nouzé et al., 2002; Nouzé et al., 2004) with a few of the unpublished seismic lines presented here. Although the Nyegga pockmark field has been investigated for many years (e.g., Mienert et al., 1998; Vogt et al., 1999a; Vogt et al., 1999c; Berndt et al., 2003; Bünz et al., 2003; Bünz and Mienert, 2004) resulting in significant geophysical acquisition and to a less extent geological sampling, near-bottom investigation including biological studies is limited to a few sites (e.g., G11, see location in Figure 1B; Hovland et al., 2005; Hovland and Svensen, 2006) and there has been no multidisciplinary investigation to date for the CNE area.

Evidence of fluid escape in the past has been demonstrated at several Nyegga pockmarks by observations of authigenic carbonates, chemosynthetic fauna and hydrate (Hovland et al., 2005; Mazzini et al., 2006; Ivanov et al., 2007; Paull et al., 2008; Ivanov et al., 2010; Attias et al., 2020). However, clear evidence of current seepage has only been found at the G11 pockmark (Hovland et al., 2005; Hovland and Svensen, 2006; Vanreusel et al., 2009; Decker et al., 2012; Decker and Olu, 2012), although the presence of living Siboglinidae (pogonophora) in the tops of cores indicates possible seepage at three pockmarks, CNE03 and coring sites AT117G and AT118G located l.6 and 3.6 km north of CNE14, respectively (Figures 1B, 2A) (Ivanov et al., 2010).

For the first time, multi-frequency seismics, seafloor cartography (multi-frequency bathymetry and seafloor backscatter), near-bottom *in situ* observations and sampling using a Remotely Operated Vehicle (ROV) and acoustic records of the water column were combined in the CNE area. Most of these data are unpublished. The geophysical data were mainly acquired during the Hydratech (Nouzé et al., 2002; Nouzé et al., 2004) and Vicking (Nouzé et al., 2007) expeditions with however a few additional data acquired during the TTR16 expedition (Akhmetzhanov et al., 2008). The near-bottom investigation was conducted during the Vicking cruise with the Ifremer Victor ROV, and included biological and geological observations and sampling of the seabed. This data is reported here with additional information on gravity coring. This paper includes results on the seismic signatures of gas and hydrate-bearing sediments, seafloor acoustic signatures of seep-related areas and reports evidence for current and past seepage activity including methane concentration measurements, fauna description and distribution and geochemical analysis of methane-derived authigenic carbonates. Finally, we discuss the formation of methane-derived authigenic carbonates and consolidated sediment outcrops and present-day *versus* past seepage activity. The relationship between fluid seepage activity at the seabed and the occurrence of gas hydrate at depth is presented through a conceptual model illustrating the present-day status of the methane-fluid flow system at the CNE pockmark field area.

2 Geological setting of the Nyegga area

The Nyegga area is located on the continental slope off mid-Norway (Figure 1). It forms the southern margin of the Vøring Plateau and borders the north of the Storegga Slide. It lies above the Helland-Hansen Arch, an anticline formed during Tertiary compressive deformation in the North Atlantic (Rise et al., 2006) (Figure 1B). The sedimentary stratigraphy above the Helland-Hansen Arch consists of a Miocene-Oligocene basal unit (Kai and Brygge formations), up to 2 km thick at the westward toe of the arch, overlain by an up to 1-km-thick Plio-Pleistocene sequence (Naust formation) (Figure 2C). The Plio-Pleistocene sequence shows alternations of hemipelagic mud and glacigenic deposits (e.g., Hjelstuen et al., 2010).

Hydrate-related Bottom Simulating Reflectors (BSR) commonly occur in the region with a fluid-flow system composed of free gas and gas hydrates (Mienert et al., 1998; Bünz et al., 2003; Bünz and Mienert, 2004; Westbrook et al., 2008). The Nyegga area on the continental slope off mid-Norway is an area known for its particularly dense distribution of pockmarks (Hjelstuen et al., 2010), ranging from small circular depressions with diameters <5 m (the unit-pockmarks as named by Hovland et al., 2010) to large complex structures with diameters of several hundreds of meters showing up to 10-m-high carbonate ridges inside their depressions (Hovland et al., 2005). A large number of Nyegga pockmarks are underlain by seismically defined chimney-like features, often referred to as « gas chimneys » or « pipes » (Bünz et al., 2003). These pockmarks and the underlying chimneys form complex fluid-escape systems (Hustoft et al., 2007; Paull et al., 2008; Hjelstuen et al., 2010), that may host gas hydrate in the subsurface sediment as suggested at several pockmarks and confirmed at CNE03 (Attias et al., 2020) and Sharic (Ivanov et al., 2007) from core data, seismic (Plaza-Faverola et al., 2010) and electromagnetic results (Attias et al., 2016) (Figure 1B). The presence of gas hydrate in the study area was also inferred at a shallow depth from gravity coring (AT634G) at the CNE03 site during the TTR16 expedition of the R/V (Research Vessel) Professor Logachev (Ivanov et al., 2007; Akhmetzhanov et al., 2008) (Figures 1B, 2A). The CNE03 site was also investigated with a high-resolution 3D seismic-tomography experiment showing that P-wave velocity inside the chimney was up to 300 m/s higher than in the surrounding strata within the methane-hydrate stability zone (Plaza-Faverola et al., 2010) (Figure 3C). This zone of anomalously high velocity is about 200 m wide near the seabed, and increases to about 500 m wide near its base, at a depth of 250 m below the seafloor. It is likely that the higher seismic velocity in this zone is produced by the presence of gas hydrate with a concentration of up to 14% of total volume rather than by the presence of carbonates (Plaza-Faverola et al., 2010).

Some of the chimneys can be traced downwards, several hundreds of meters below the seabed through the entire Plio-Pleistocene sedimentary unit to the polygonal faults of the

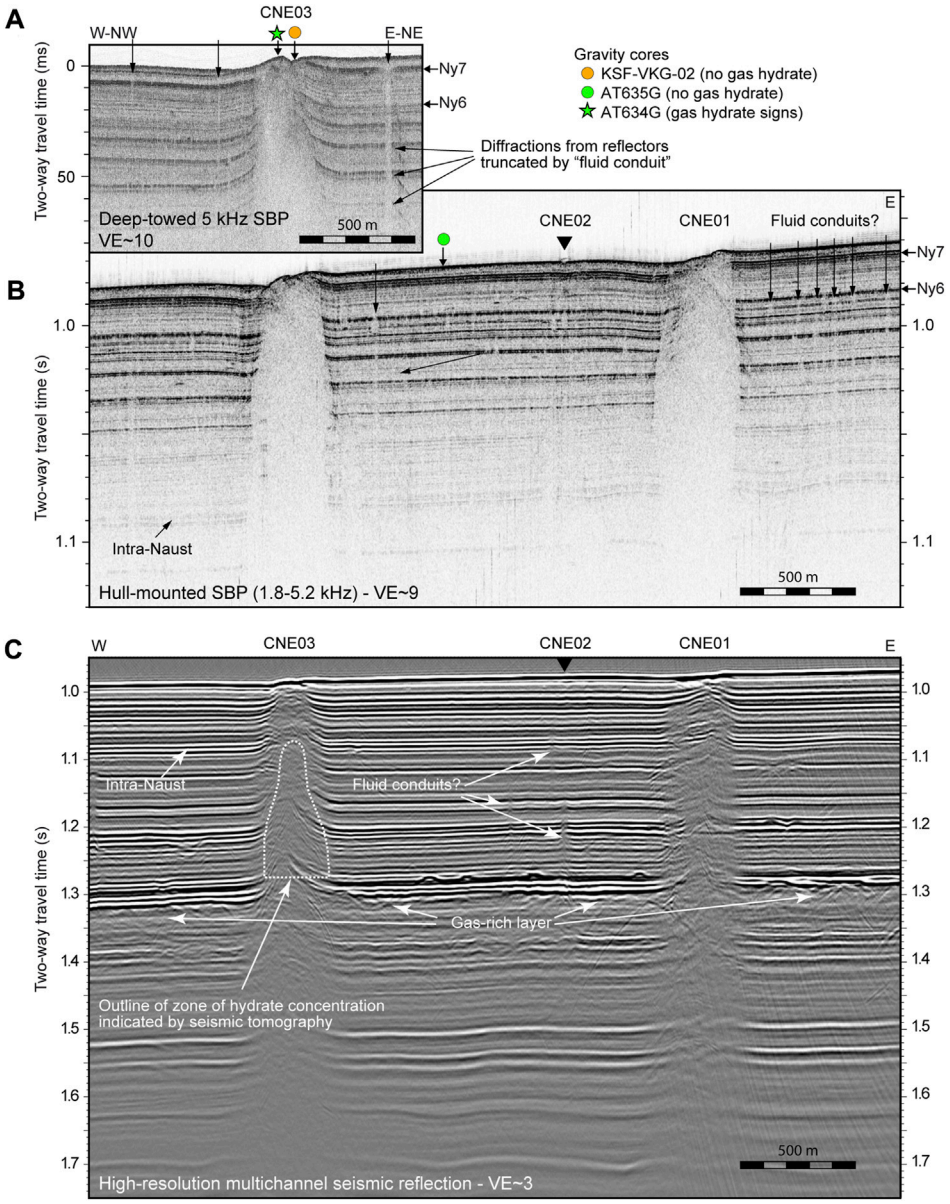

FIGURE 3
Three seismic sections (see locations in Figure 2) with the same horizontal scale across the CNE01, CNE02 and CNE03 pockmarks, with Figures 3B,C zooms of Figures 2B,C, respectively. **(A)** a MAK-1M deep-towed 5 kHz Sub-Bottom Profiler (SBP) line. This profile was acquired during the TTR16 expedition (Akhmetzhanov et al., 2008) and was published in Ivanov et al. (2007) and Ivanov et al. (2010), **(B)** a hull-mounted 1.8–5.2 kHz sub-bottom profiler line. This profile was acquired during the Hydratech expedition (Nouzé et al., 2002) and the presented section was published in Foucher et al. (2009), and **(C)** a 120-channel high-resolution stacked and migrated seismic line. This unpublished profile was acquired during the Hydratech expedition (Nouzé et al., 2002). Star and circles stand for the locations of gravity cores mentioned in the text (see legend in Figure 2A). Sections from the deep-towed and hull-mounted sub-bottom profiler show narrow zones of low amplitude and low coherence, marked by arrows, which are interpreted as narrow conduits conveying pore fluid to the seabed. Scattering from truncated beds at the margins of some of these zones demonstrates that solely by bodies of high acoustic impedance at their tops cause them. Large chimneys beneath CNE01 and CNE03 are represented by zones of scattering, low amplitude and low coherence in the high-frequency records **(A and B)**, but the lower-frequency mini-GI gun records **(C)** show more of the upward bending of the strata towards the centers of chimneys, where the strata are locally more deformed and, in the case of CNE03, faulted (upthrown to the southeast). The outline of the body of gas hydrate identified beneath CNE03 by Plaza-Faverola et al. (2010) is shown in this high-resolution seismic section **(C)**.

underlying Miocene-Pliocene sequence and appear to relay fluid migration from deep sources to the seafloor (Berndt et al., 2003; Gay and Berndt, 2007; Hustoft et al., 2007; Plaza-Faverola et al., 2012). It has been demonstrated from high-resolution 3D seismic data that some of the chimneys with a surface expression at the seabed have been reactivated once or twice over the past 200 ky, whereas others formed since the last glacial maximum (Plaza-Faverola et al., 2011). Reiche et al. (2011) correlate periods of fluid expulsion with periods of rapid sedimentation that occurred at 18,200 ^{14}C yr BP (ca. 21,079 cal yr BP), 17,500 ^{14}C yr BP (ca. 20,200 cal yr BP) and

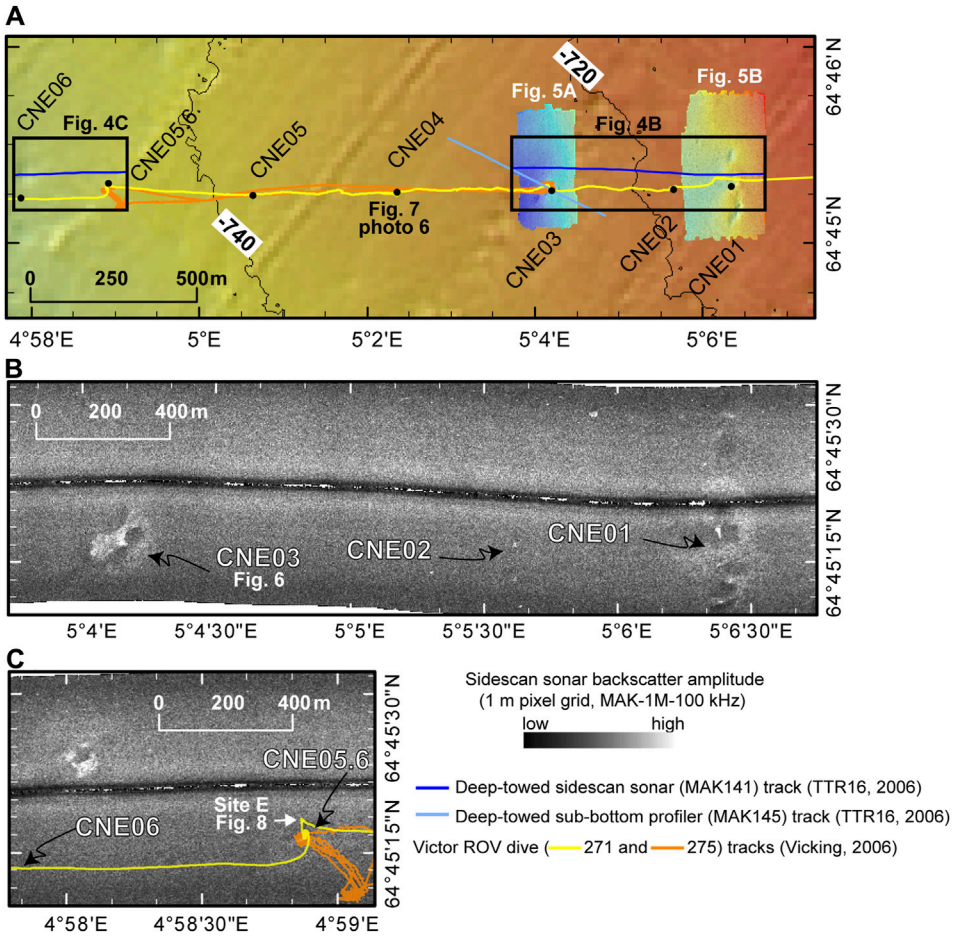

FIGURE 4
(A) Zoom on the regional bathymetry map of the Nyegga study corridor (Figure 2A) limited to the eastern part and comprising the CNE03 and CNE05.6 sites, two main geological structures investigated during the Vicking cruise with Victor ROV for high-resolution seafloor mapping (Figures 5, 6) and/or near-bottom observation and sampling (Figures 7–10). **(B)** and **(C)** Deep-towed MAK-1M side-scan sonar records displayed at the same scale along the study corridor (see location in **(A)**) and showing the highest backscatter amplitudes for structures CNE01, CNE03 and CNE06.

16,900 ^{14}C yr BP (ca. 19,502 cal yr BP) and between 15,800 ^{14}C yr BP (ca. 18,314 cal yr BP) and 15,000 ^{14}C yr BP (ca. 17,366 cal yr BP) and they speculate that the triggering of the Storegga Slide at 7,250 ^{14}C yr BP (ca. 7,525 cal yr BP) (Bondevik et al., 1997; Haflidason et al., 2005) led to fluid expulsion through tension cracks created by this event (represented at the seabed by linear furrows). Recent studies led to revisit the multi-phase history of the Storegga Slide with the identification of an older so-called Nyegga Slide initiated 20,000 years BP at the end of the Last Glacial Maximum (LGM) (Karstens et al., 2023).

3 Materials and methods

High-resolution 2D 120-channel seismic reflection (acquired with two mini-GI guns) and hull-mounted sub-bottom profiler (1.8–5.2 kHz) surveys were conducted during the Hydratech expedition onboard the R/V Le Suroît in 2002 (Nouzé et al., 2002; Nouzé et al., 2004). Three unpublished processed lines crossing the studied Nyegga area (Figure 2A) are shown in Figure 2B, Figure 2C and Figure 3C, including stacked and migrated sections for the multichannel seismics. The high-resolution seismic data have a vertical resolution of 3.5 m and a horizontal resolution of 150 m at the surveyed water depths. The Vicking cruise conducted in 2006 mainly focused on near-seafloor investigations on a seafloor corridor (frame in Figure 1B; Figure 2A) encompassing several pockmarks and their underlying chimneys identified from this Hydratech seismic dataset.

A multibeam survey was conducted onboard the R/V Le Suroît (Hydratech, 2002) with a ship-borne echosounder operated at 30 kHz (Kongsberg EM300), providing a 50-m-pixel bathymetric grid (Nouzé et al., 2002; Nouzé et al., 2004) (Figure 1B; Figure 2A; Figure 4A). High-resolution seabed mapping surveys were carried out during the Vicking cruise (2006) with deployment of the Victor ROV (Nouzé et al., 2007). The ROV was equipped with a Reson 7,125 multibeam echosounder operated at a frequency of 400 kHz. The ROV travelled 20 m above the seafloor at 0.4–0.5 m/s speed with a total swath of 70 m and a line spacing set to 40 m (Figure 5B). Two surveys extended over seafloor areas of ~1,300 m by 700 m at CNE01 and ~1,000 m by 500 m at CNE03, and were primarily intended to cover the seabed above the chimneys and immediately

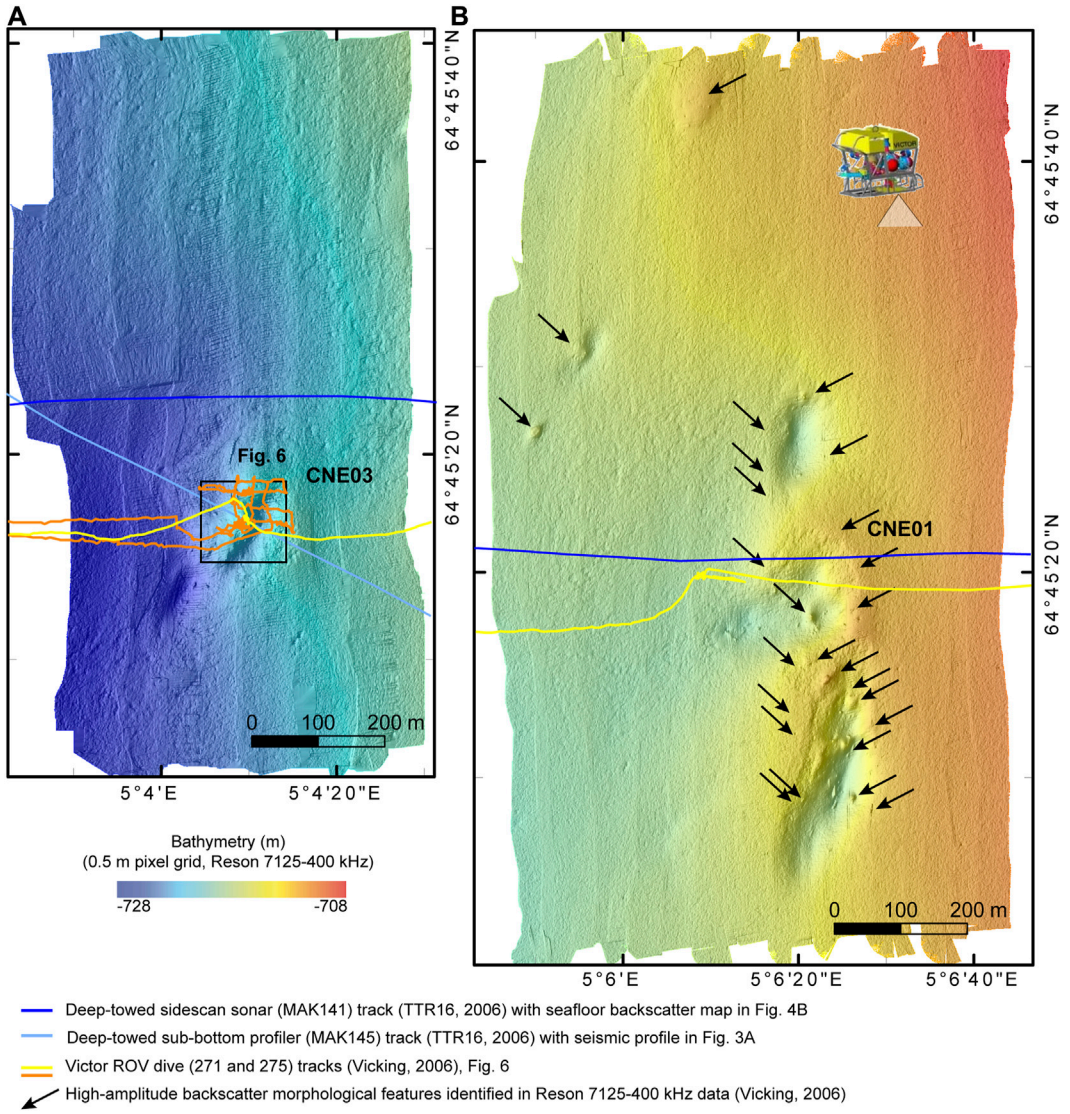

FIGURE 5
Shaded high-resolution bathymetry maps (0.5 m pixel grids) of **(A)** CNE03 and **(B)** CNE01 pockmark areas from data acquired with a Reson 7,125 multibeam echosounder operated at 400 kHz and mounted on the Victor ROV (Vicking, 2006) with tracks of the geophysical data presented in Figures 3, 4 and Victor ROV tracks of dives 271 and 275.

adjacent areas (Figure 4A). Detailed seabed maps, gridded with a 0.5-m and 0.1-m-cell-size for bathymetry and seafloor backscatter, respectively, were created using CARAIBES software (©Ifremer) (Figures 5, 6). In addition, unpublished seafloor side-scan-sonar backscatter maps at CNE01, CNE02 and CNE05.6 are presented (Figures 4B,C). These data were acquired during the TTR16 expedition (2006) onboard the R/V Professor Logatchev (Akhmetzhanov et al., 2008) with the MAK-1M system towed at a speed of 1.5-2 knots and operated at a frequency of 100 kHz. With a survey altitude of 50 m, the total swath range of the side-scan sonar data reaches 700 m and the seafloor mosaics can be gridded with a 1-m cell size.

A water column single-beam survey was performed during the Vicking expedition using the hull-mounted echosounder of the R/V Pourquoi pas ? (Kongsberg EA600, 38 kHz, 9.6° beam width) to detect gas bubbles escaping from the seafloor (Foucher et al., 2010). At the water depth range of the Nyegga studied area (700–830 m), the footprint of the insonified seafloor is 130 m (Figure 2A).

Geological and biological observations were carried out during two dives of the Victor ROV 6000 in the study area. Dive 271 was a 21-km-long exploratory survey designed to cross pre-identified chimneys along the corridor (Figure 2A). One of the primary objectives of dive 271 was to provide an overview of the current fluid seepage activity at all crossed chimneys, prior to more extensive investigations at the most active sites during dive 275 (Figure 4A; Figure 5A; Figure 6B). In addition to video surveying (Figure 7; Figure 8; Figure 9), the Victor ROV sampled sediment by means of a 0.6-m-long push corer; bottom water with a gas-tight water multi-sampler (Figure 2A; Supplementary Table S1) (Ifremer PEP sampler mounted on the ROV, Olu-Le Roy et al., 2007); and fauna and consolidated rock samples (carbonates, Figure 10) were sampled by means of various suckers and grabs. ROV video records were

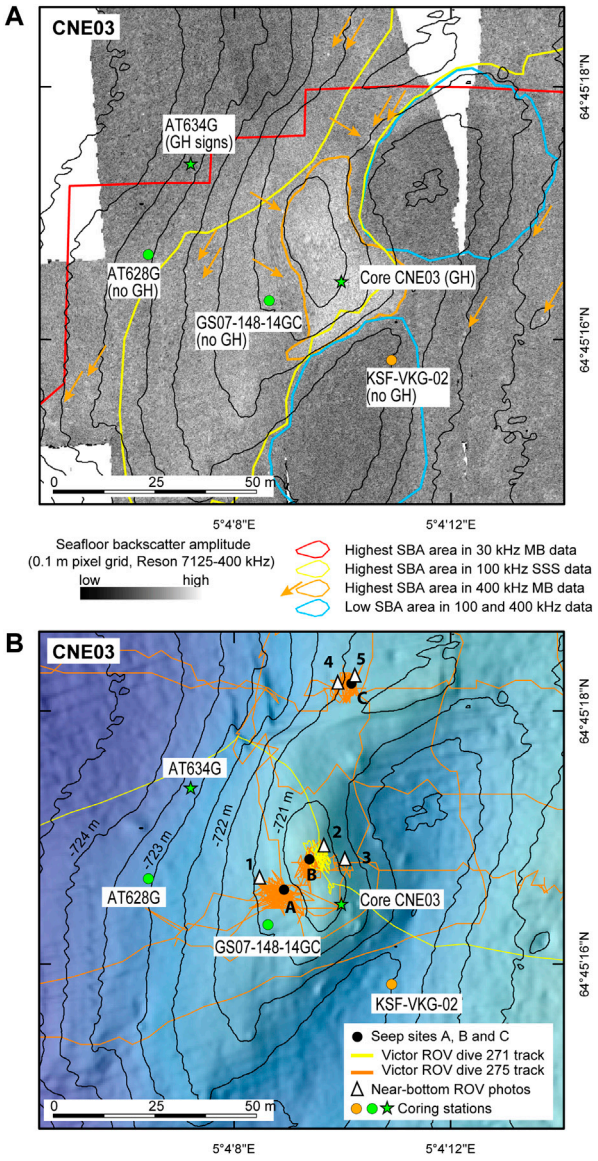

FIGURE 6
High-resolution **(A)** seafloor backscatter of the central ridge where seepage occurs and surroundings of CNE03 area (see location in Figure 5A). Three distinct contours of the highest Seafloor Backscatter Areas (SBA) based on ship-borne and ROV-mounted MultiBeam (MB) and Side-Scan Sonar (SSS) data are shown. Orange arrows point to small-scale seafloor features of high-amplitude backscatter in high-frequency data (400 kHz). East of the ridge, blue contours delineate two main low SBA areas identified in both 100 and 400 kHz data. **(B)** Shaded bathymetry map of the same area with 0.5-m-interval isobaths. These seafloor data were acquired with a Reson 7,125 multibeam echosounder operated at 400 kHz and mounted on the Victor ROV (Vicking, 2006). Seepage sites are labelled A, B and C. Locations of Victor ROV photographs (1–5) shown in Figure 7 and gravity cores (AT634G, AT628G, KSF-VKG-02, GS07-148-14GC and Core CNE03) are reported.

processed using ADELIE software (©Ifremer), an extension tool for ArcGIS, which allows post-processing of ROV data and georeferencing annotations of faunal counts along dive tracks. Details of the faunal sampling strategy, processing and analysis can be found in Decker et al. (2012) and Decker and Olu (2012).

Bulk mineralogy of carbonate crusts and concretions was obtained by X-ray diffraction combined with estimations of the % weight of total carbonate content to estimate the relative proportions of major mineral components. Scanning Electron Microscope (SEM) observations were performed on selected samples to characterize the morphologies and compositions of crystals as well as the structural relationships between mineral phases (Figure 11). Oxygen and carbon isotopic compositions were measured on bulk carbonate (Figure 12) treated with 100% phosphoric acid at 25°C to obtain CO_2. The isotopic compositions are expressed in the conventional δ notation defined as δ = [(Rs/Rr) – 1] x 1,000, where R = $^{18}O/^{16}O$ or $^{13}C/^{12}C$ respectively in the sample s and in the reference r. The reference for $\delta^{18}O$ and $\delta^{13}C$ is the V-PDB (Craig, 1957). The isotopic compositions of carbonates were measured on a dual-inlet isotopic ratio mass spectrometer (DI-IRMS Isogas-Sira 9). The analytical precision 2σ was 0.01‰ and the reproducibility was 0.1‰ for both $\delta^{18}O$ and $\delta^{13}C$. Sample location, water depth and the method of collection (at the seabed or in core) are indicated in Supplementary Table S2. In addition, Accelerator Mass Spectrometry (AMS) radiocarbon dating was conducted on selected Vesicomyid shells (Figure 13) at the LMC14 laboratory (CEA Saclay). Prior to analysis, the material was cleaned by sand abrasion followed by leaching for 15' in 0.01N nitric acid. The calibration of radiocarbon dates of these shells was based on the Calib8.1.0 tool (revision of Stuiver and Reimer, 1993) using the Marine20 calibration curve (Heaton et al., 2020). Calibrated radiocarbon ages from cited works were recalculated using the same procedure for coherence (cal yr BP with 2σ ranges). All calibrated ages of the post-LGM period are maximum possible ages, considering neither the effect of local reservoir (for foraminifers and shells, Heaton et al., 2023) nor the difference in water masses between the atmosphere-water interface and the sea bottom (for shells).

In addition to seabed ROV investigations, a gravity core was taken while on the R/V Pourquoi pas ? at one location on CNE03 (KSF-VKG-02 coring station, N 64°45.263, E 05°4.1806, depth: 729 m, Figure 2A; Figure 3A; Figure 6). Penetration of the corer was approximately 5 m, with recovery of a 2.6-m-long sediment core. The core was split and described onboard (Figure 13). Three thermometers attached to outriggers on the lance measured sediment temperatures at 1.33, 3.12 and 4.62 m below the seafloor (Figure 14). Chemical analysis of pore water was performed every 20–30 cm along the recovered core by ionic chromatography using a Dionex ICS-2000 instrument (Figure 14). The estimated accuracy on the pore-water chemistry measurements is within ±3% of the mole fraction. Methane concentration was determined by headspace gas chromatography (Donval et al., 2008) with an accuracy of ±5%.

4 Results

4.1 Stratigraphy, structure and evidence of free gas and gas hydrate from seismic data

Nearly all the chimneys of the investigated part of the Nyegga area (Figure 2A) exhibit upwarping of strata towards their centers, which are seismically incoherent (Figure 2B; Figure 2C; Figure 3).

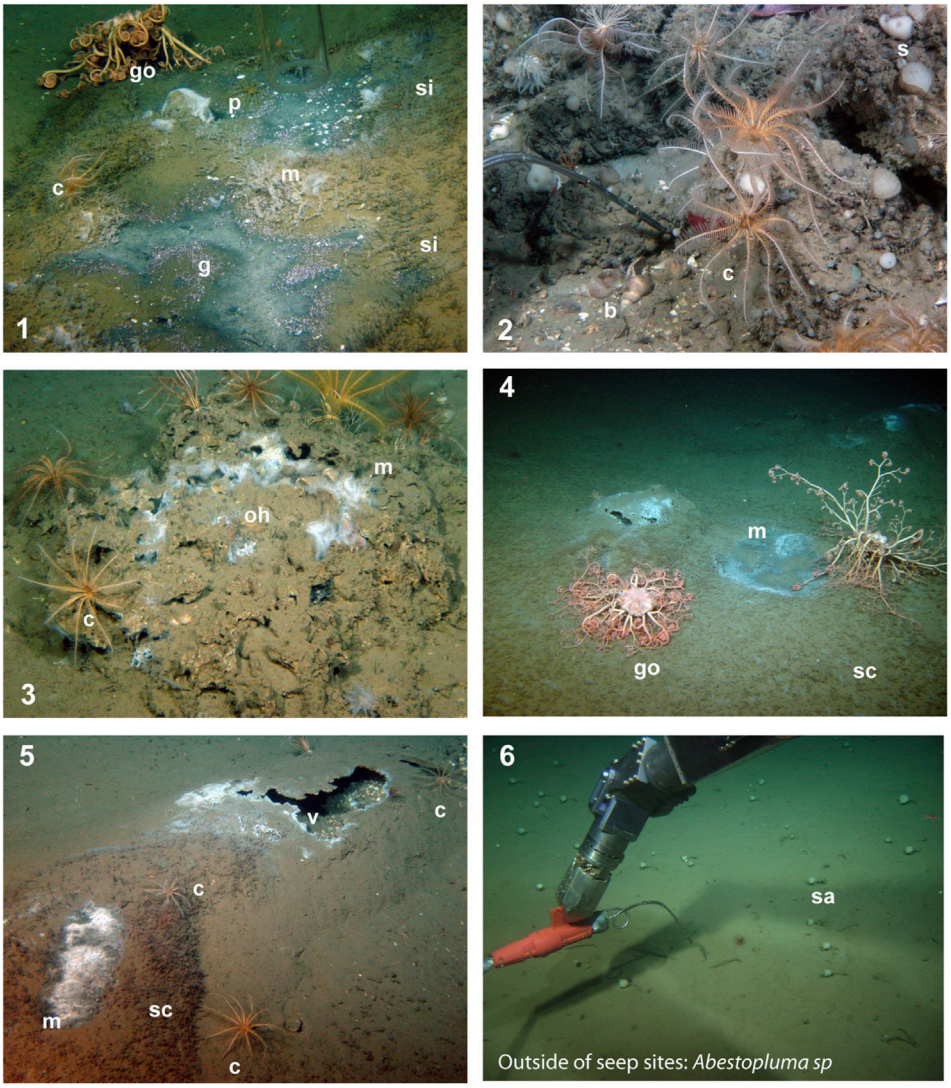

FIGURE 7
Near-bottom seafloor images taken by the Victor ROV (Vicking, 2006) during dives 271 and 275 at CNE03 site (1–5, see locations in Figure 6B) and surroundings (6, CNE4, see location in Figures 2A, 4A). The image 5 corresponds to the area where near-bottom water (275-PEP15) was sampled, following the break of the carbonate crust, with an elevated methane concentration of 9,664 nL/L (Supplementary Table S1). Symbol letters on the photographs: c: comatulids, g: Rissoidae gastropods *Alvania* sp., b: Buccinidae shells, go: ophiurids *Gorgonocephalus* sp., m: white microbial filaments, s: sponges (Porifera), sa: sponges *Abestopluma* sp., si: siboglinids *Sclerolinum contortum* -sc-(brown curly tubes) and *Oligobrachia haakonmosbiensis webbi* -oh- (black straight tubes), p: pycnogonids, v: Vesicomyidae bivalves.

The cause of this upwarping is twofold. In the shallowest part of the section, including the seabed, upwarping is caused by deformation of the strata, typically above the Ny7 horizon, one of the seven seismic boundaries Ny that subdivide the Upper Naust unit (corresponding to the T unit in Figure 2C). The 5 kHz profiler section across the CNE03 pockmark (Figure 3A) shows that the eastern side of the chimney has been upfaulted. However, the displacement of this fault diminishes to zero to both the north and south of the pockmark, and it appears that the faulting was associated with the emplacement of the chimney. Deeper in the section, velocity pull-up, caused by the presence of material with high-seismic velocity (Figure 3C), inferred to be hydrates (Plaza-Faverola et al., 2010), in the centers of the chimneys, contributes to the apparent upward bending shown by seismic sections that have not been correctly depth converted. Seismic data with large offset between source and receiver show that at depths greater than 250 mbsf, the strata beneath CNE03 are not upwarped and do not show a large degree of incoherence (Plaza-Faverola et al., 2010).

It is probable that depth extent of many of the chimneys, shown by single-channel and short-offset multichannel seismic sections, is not as great as it appears: the deeper part of the seismic images of the chimneys is represented by so-called seismic transparency, which is, in fact, a seismic shadow caused by reflection and scattering of the seismic energy in the upper parts of the chimneys, and is not caused by the presence of gas-bearing sediments. With wide-offset seismic data, the rays imaging the deeper parts of the chimneys do not pass through the upper parts of the chimneys and so are not subject to the same loss of energy caused by scattering and absorption in the

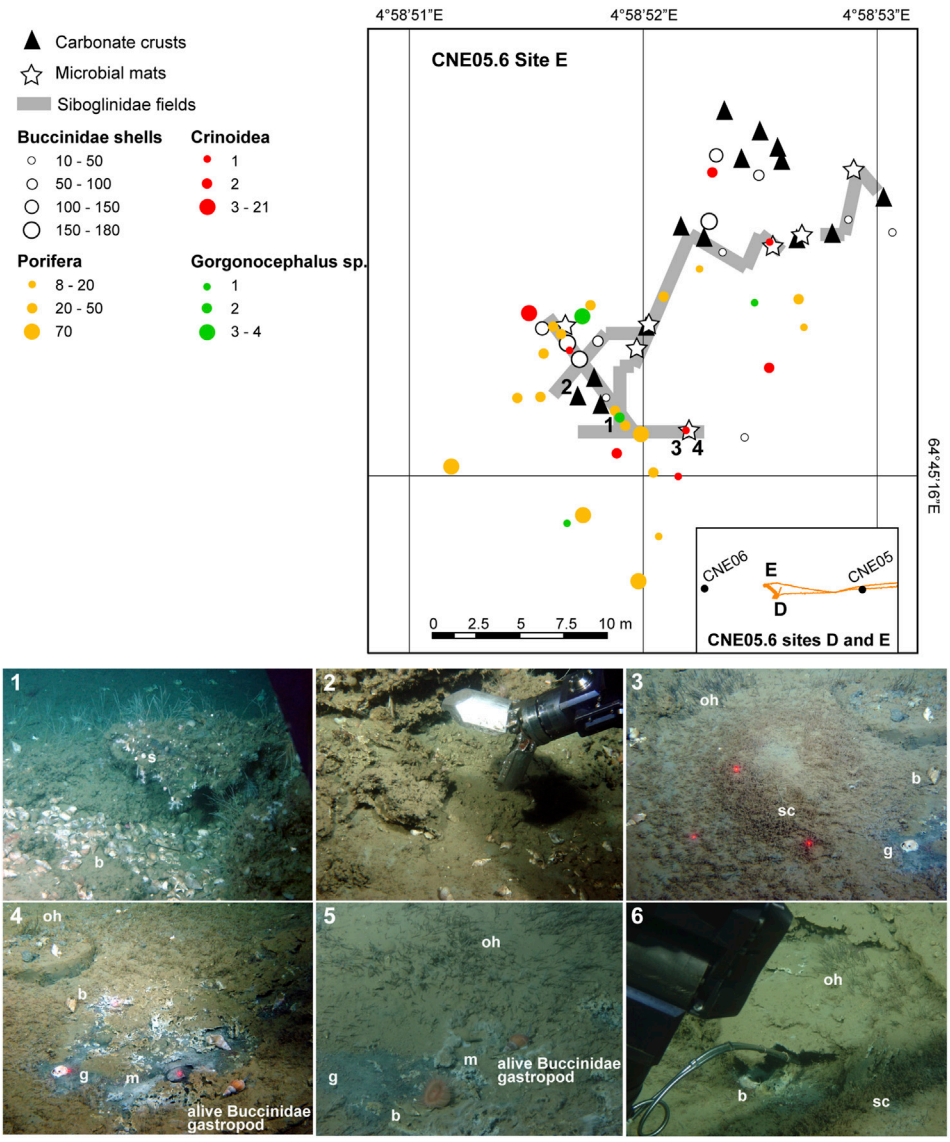

FIGURE 8
Benthic and chemosynthetic macrofauna and microbial mat distributions at CNE05.6-E site based on near-bottom observations performed during the Victor ROV dive 275 (Vicking, 2006) with corresponding images from dives 275 (1–4) and 271 (5–6). The images 5 and 6 correspond to the areas where near-bottom water (271-PEP7 and 271-PEP8, respectively) was sampled and elevated *in situ* methane concentrations were measured (2,130 and 853 nL/L, respectively) Supplementary Table S1. See the meaning of the letters in the caption of Figure 7.

heterogeneous upper parts of the chimneys. However, it is clear that strata around the chimney deep beneath CNE12 and CNE13 are deformed where they lie outside the zone obscured by seismic scattering in the upper part of the chimney (e.g., at 1.7 s TWT in Figure 2C).

The strong negative polarity reflector at the top of the U unit of the Naust formation (about 1.3 s TWT at CNE01, CNE02 and CNE03, Figure 3C) locally marks the presence beneath it of a layer with seismic velocity lower than that of the layer above by about 100 m/s from the chimney center (Plaza-Faverola et al., 2010). The velocity reduction is very likely caused by the presence of a small amount of free gas. The bottom-simulating seismic reflector that follows the base of the methane-hydrate stability zone and marks the transition from sediment containing hydrate, above, to sediment containing free gas, below, is not observed in most of the study area. The BSR, which is seismically visible further downslope, only occurs in units with sufficiently high permeability to be invaded by gas and so it is discontinuous and stratigraphically controlled (e.g., Bouriak et al., 2003; Bünz et al., 2003; Westbrook et al., 2008). The limits of the BSR observed on seismic sections in this part of the Nyegga slope are shown in Figure 1B. In the westernmost part of the study area, the BSR locally occurs at 1.36 s TWT (Figure 2C).

In addition to the large chimneys with widths of a few hundred meters, there are many other smaller conduits of fluid flow, some of which lie beneath pockmarks CNE02, CNE04, CNE05, CNE07, CNE08, CNE09, CNE10 and CNE12 (Figure 2B). The deep-towed 5 kHz profiler and the hull-mounted sub-bottom profiler acoustically imaged these conduits. Examples of these narrow,

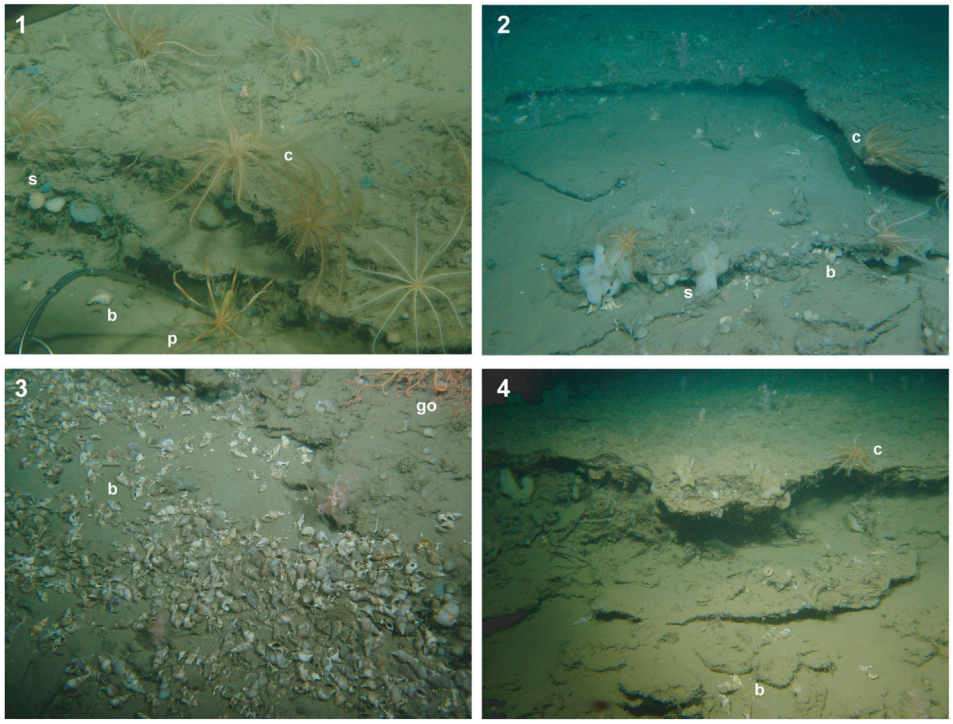

FIGURE 9
Near-bottom seafloor images (1–2 m across) of tabular outcrops of consolidated sediment observed along the study corridor (Victor ROV dives, Vicking 2006; Figure 2A), near CNE02 (photo 1), at CNE05.6 Site E (photo 2), at CNE07 (photo 3), and near CNE14 (photo 4). See the meaning of the letters in the caption of Figure 7. The outcrops comprise distinct horizontal hard layers each a few cm thick. Buccinidae shells have accumulated at the base of the outcrops (photo 3). Supplementary Table S2 for correspondence with analyzed carbonate samples.

near-vertical features are shown in Figures 3A, B as narrow zones of very low amplitude and low coherence. This could be caused by the acoustic shadows of shallow features with high acoustic impedance, such as deposits of carbonate, but the diffractions from the edges of reflectors that are cut by the conduits show that some, at least, penetrate to more than 50 mbsf (Figure 3A). The absence of strong reflections from the tops of many of these zones also makes it more likely that they are zones of changed properties in the sediments rather than acoustic shadows. There are a large number of these conduits, of which about half of those investigated by the ROV during the Vicking expedition show evidence of active or past fluid flow, in the form of carbonate crusts, microbial mats and localized colonies of fauna (near-bottom photos, Figures 7–9). Judging from their frequent occurrence on the seismic records, there are at least ten times as many of these smaller conduits as chimneys.

4.2 Seabed observations from sonars and dives

4.2.1 Pockmark morphology and seafloor backscatter signature

The morphology of pockmarks remains hardly detectable on regional bathymetric maps except for the largest structures (Figures 1B, 2A) but is well-displayed on the high-resolution maps that were produced for the two sites CNE01 and CNE03 from ROV-mounted multibeam echosounder data (Figures 5, 6B). At a regional scale, the bathymetry at CNE01 and CNE03 is dominated by a marked deepening of the seabed westwards (topographic gradient of ca. 10 m per 500 m). Superimposed on this gradient, the high-resolution bathymetric maps show that both CNE01 and CNE03 display in their central parts NNE-SSW trending elongated depressions fringed by small-relief ridges (Figures 5, 6B). CNE03 displays a single, central depression, whereas CNE01 has a greater spatial expression and displays a more complex depression-ridge system.

CNE01 and CNE03 are clearly identified on the high-resolution seafloor backscatter maps, both from the multibeam (Figures 5B, 6A) and side-scan MAK-1M line (Figure 4B) (Akhmetzhanov et al., 2008). Ridges are displayed as high-amplitude seafloor-backscatter features that may relate to the occurrence of more consolidated surface sediments on ridges with respect to the surrounding seafloor or the occurrence of carbonate crusts, which was demonstrated locally by dive observations (Figure 7, photos 1–3). The relief amplitude across the two pockmarks CNE01 and CNE03, from depressions to ridges, is <5 m. The highest-frequency backscatter data provide information on the subsurface, which can be easily correlated to near-bottom ROV observations, while the lowest-frequency data provide information on subsurface volume insonified by a higher penetration signal. Interestingly, the spatial extent of the high-backscatter seafloor at CNE03 increases with signal penetration (corresponding to 400, 100 and 30 kHz signal, Figure 6A). This observation could be related to a more widespread seepage-related activity in the past compared to present-day activity,

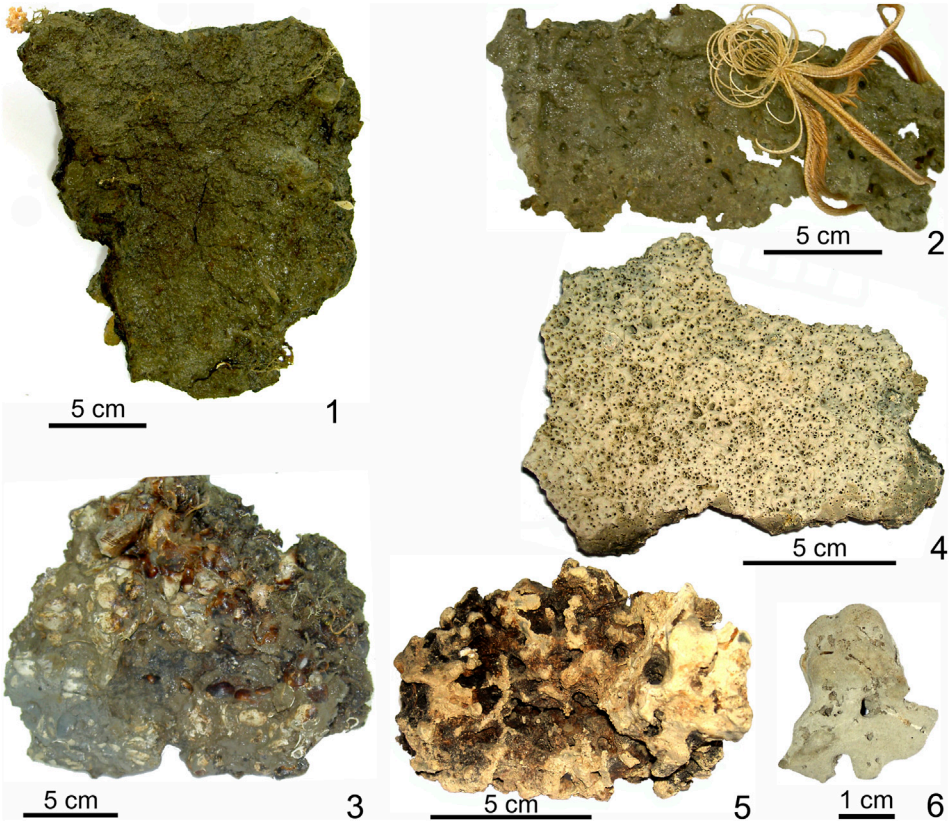

FIGURE 10
Lithofacies of some selected diagenetic crusts from the Nyegga gas chimneys collected by Victor ROV (Vicking, 2006). (1) sample 271-CC1 at CNE02. (2) sample 271-CC3 at CNE05.6 with a crinoid. (3) sample 275-CC2 and (4) sample 275-CC3 at CNE03. (5) sample 275-CC1 and (6) sample 275-CL6 at CNE05.6. Supplementary Table S2 for detailed information.

which is restricted to ridge summits and its uppermost flanks. Depressions are shown as low-amplitude seafloor-backscatter features (Figures 5B, 6A) presumably related to their soft hemipelagic sediment infilling. This is consistent with the uppermost 87-cm-thick homogeneous marl layer recovered from core KSF-VKG-02 (Figure 13).

At other chimney sites of the study area, high-resolution bathymetric data were not collected, but ROV-based water depths along the track indicate the presence of pockmarks up to a few hundreds of meters wide and a few meters deep (e.g., ~5–6 m at CNE02, CNE10 and CNE13). CNE05.6 may be similar in morphology to CNE03, with a ridge adjacent to a depression with a depth difference of ~3 m.

4.2.2 Methane seeping sites and chemosynthetic fauna (CNE03 and CNE05.6)

Potential gas bubbles escaping from the seafloor were neither identified in the single-beam records, nor observed during ROV dives. Instead, methane seepage is inferred from near-bottom biological observations and water-sample measurements conducted during these dives. *In-situ* near-bottom methane enrichments ranges from 105 to 2,130 nL/L (see details in Supplementary Table S1 with cross-references to near-bottom photos of the sampling areas). The investigated Nyegga area appears to be characterized by focused fluid flow that transports dissolved methane from bottom sediments into the water column rather than through free gas escapes. No pingoes were observed at the seafloor along the ROV tracks from CNE01 to CNE17 sites as described at the Nyegga G11 site (located 14 km south-east of CNE03, Figure 1B) and suspected to be hydrate-related pingoes (Hovland and Svensen, 2006). The G11 site was surveyed during ROV dive 272. There was no evidence of gas hydrates in the subsurface. Only small meter-scale domes recovered by dense pogonophorans (Vanreusel et al., 2009) were observed with uppermost soft muddy sediments (Supplementary Figure S1). Similar pingo structures were reported at Tobic and Sharic sites (located 12 km south-east of CNE03, Figure 1B) by Ivanov et al. (2010).

CNE03. Seeps were found at three distinct sites (A, B, C) on the summit of the ridge and at the uppermost flanks at CNE03 (Figures 6, 7). Seepage site A measures a few square meters (based on the lateral extent on the seabed of the Siboglinidae fields) and displays two dark-grey spots, each approximately 0.5 m across, both located within a bush of densely distributed Siboglinidae polychaetes (Figure 7, photo 1). A push core taken from one spot recovered dark-grey reduced sediment overlain by whitish bacterial filaments. The biological habitat zonation at site A is of the type described by Decker et al. (2012) as for other pockmarks of the Nyegga area. It is characterized by an inner area of dark-grey sediment surrounded by a rim of small (a few mm in size) reddish Rissoidae gastropods

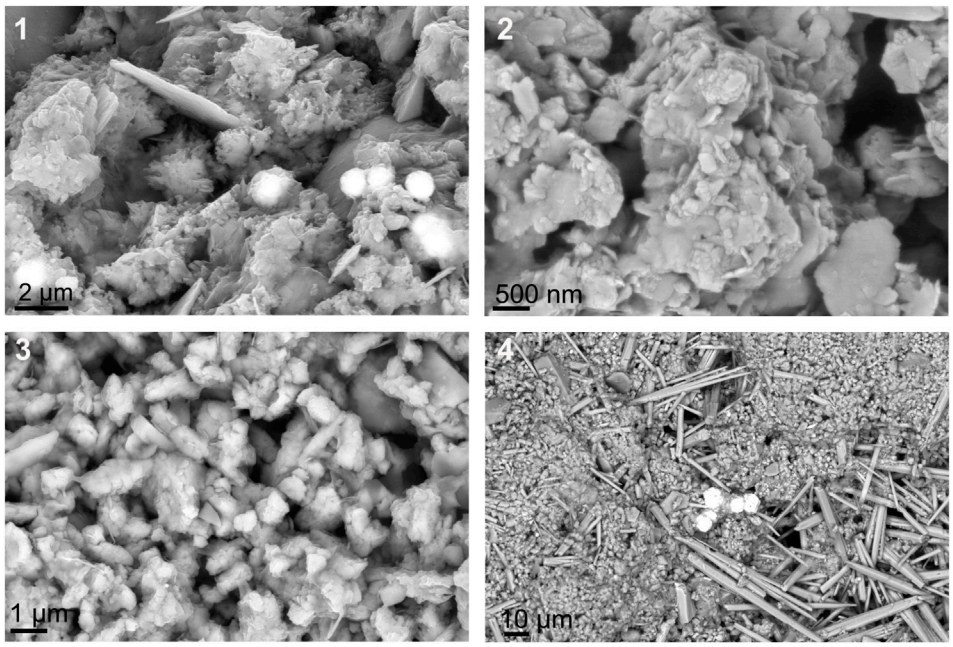

FIGURE 11
SEM photographs of selected methane-related carbonates collected by Victor ROV and recovered from gravity coring (Vicking, 2006). (1) Sample 271-CL6 (CNE05.6): aggregates of Mg-calcite crystals; framboids of pyrite are clearly distinct by their high backscatter intensity. Scale bar = 2 µm; (2) Sample 275-CC3 (CNE03): aggregates of platy euhedral crystals of Mg-calcite. Scale bar = 1 µm; (3) Sample 275-CC3 (CNE03): aggregates of very fine-grained Mg-calcite crystals. Scale bar = 500 nm; (4) Sample collected in the gravity core KSF-VKG-02–130 cm (site CNE03, see location in Figure 2A; Figure 3A; Figure 6) (Figure 13): association of Mg-calcite aggregates, acicular aragonite and framboids of pyrite. Scale bar = 10 µm. Supplementary Table S2 for detailed information.

(*Alvania* sp.), microbial filaments, Capitellidae polychaetes and outer fields of Siboglinidae polychaetes (*Oligobrachia haakonmobiensis*, i. e., *webbi* and *Sclerolinum contortum*) (Meunier et al., 2010). This specific zonation of chemosynthetic communities has previously been identified at the Håkon Mosby mud volcano (Gebruk et al., 2003; Jerosch et al., 2007) where it is associated with drastic changes in the macrofauna (Decker et al., 2012) and interpreted to reflect a decreasing strength of methane seepage away from the seep center (de Beer et al., 2006). Seepage site B is distinctly characterized by the occurrence of several small-sized (<1 m) carbonate build-ups (Figure 7, photos 2 and 3) scattered over the seabed. The carbonate rocks that form them are highly porous. Abundant Buccinidae gastropod shells (*Buccinum* sp., A. Warén, pers. com.) are tightly intermixed with the carbonate matrix and lie on the sediment at the base of the build-ups at CNE03 and also at other CNE sites (e.g., CNE07, photo 3 in Figure 9). A few Vesicomyidae bivalves (empty shells, photo 5 in Figure 7) were also sampled and were described as a new species, *Isorropodon nyeggaensis* (Krylova et al., 2011) recovered from core samples taken at the G11 Nyegga pockmark (see location in Figure 1B) (Ivanov et al., 2010). Small holes pierce the carbonate surface with rims of white bacterial filamentous material (Figure 7, photo 3). Seepage site C shows seeps with a quite distinct type of carbonate structure, herein named soufflé-type seeps after their puffed shape. At a soufflé-type seep, a thin carbonate crust has developed above a seep but is currently separated from the sediment underneath by 10–20 cm of seawater trapped between the sediment and the carbonate crust (Figure 7; photos 4 and 5). Several soufflé-type seeps, 2–3 m long, were observed along the ROV track at site C. Significant methane anomalies of 9,664 nL/L compared to a background value of about 26 nL/L were measured in the seawater 5 cm above the sediment inside a soufflé after the crust was broken apart (Figure 7, photo 5). Abundant Siboglinidae polychaetes protruding dark-grey sediment were observed. This methane concentration is by far the highest concentration measured during the two ROV dives (Supplementary Table S1) and is possibly due to the accumulation of dissolved methane trapped within the puffed carbonate crust.

CNE05.6. Site CNE05.6 was named after its location between pre-identified chimney sites CNE05 and CNE06 (Figures 2, 4). Two main seeping sites were discovered, located ~200 m apart, one in a depression (E) and the other on a possible adjacent ridge (D) (Figure 8). At seepage site E (Figure 8), carbonate constructions range from thick crusts and chaotic blocks (<1 m) observed in the western part of the site (Figure 8, photos 1 and 2) to thin crust pavements (a few cm thick) mostly observed in its eastern part (Figure 8, photos 3 and 4). A small elongated mound (<10 m long, 1–2 m high) in this eastern part appears to concentrate the seepage activity identified during the ROV inspection by the presence of several spots of dark-grey sediment, up to 0.3 m across for the largest ones, with many showing whitish bacterial rims (Figure 8, photos 3 and 4). Curled brown and longer black Siboglinidae species, *Sclerolinum contortum* and *Oligobrachia haakonmosbiensis webbi* (Smirnov, 2000) respectively, colonize the mound (Meunier et al., 2010). The biological zonation at CNE05.6 (Figure 8, photo 4) is similar to that observed at CNE03 (Figure 7, photo 1). A water

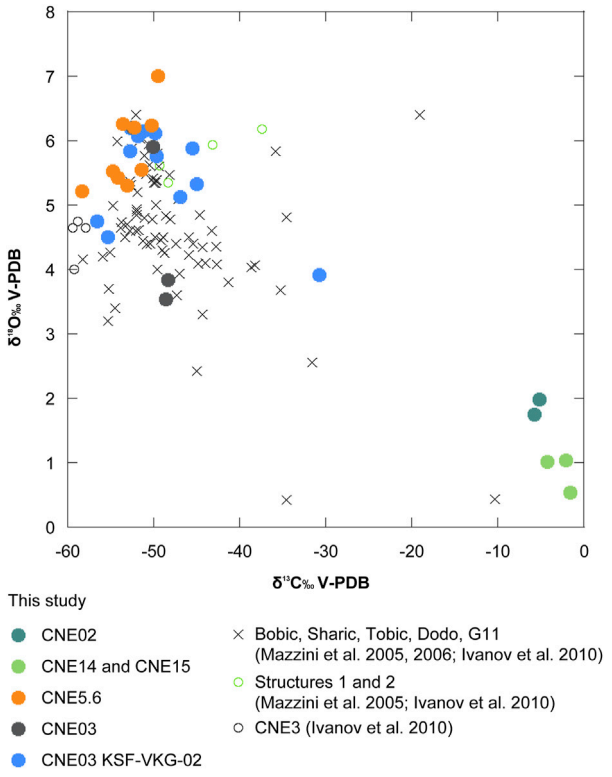

FIGURE 12
Oxygen and carbon isotopic compositions of carbonate crusts and concretions and consolidated sediment sampled at the Nyegga chimneys CNE02, CNE03, CNE05.6, CNE14 and CNE15 (see location in Figure 2A). See Supplementary Table S2 for detailed information. Published isotopic compositions of authigenic carbonate crusts are also reported for 85 samples collected at the following Nyegga pockmark sites: Bobic, Sharic, Tobic, Dodo, G11, CNE03 (see location in Figure 1B) and 'Structures 1 and 2' close to CNE14 (for corresponding core locations see grey dots in Figures 1B, 2A) (Mazzini et al., 2005; Mazzini et al., 2006; Ivanov et al., 2010).

sample taken 10 cm above a dark-grey spot (photo 5 in Figure 8) and a second sample taken in a niche of gastropods and bacterial mats under the crust (photo 6 in Figure 8), determined significant methane anomalies of 2,130 nL/L and 853 nL/L, respectively, relative to a background value of about 26 nL/L (Supplementary Table S1). These measured values indicate current active methane seepage. Empty shells of Buccinidae gastropods were observed at several locations in CNE05.6, locally with a distribution of up to ~50 shells/m^2 (Figure 8, photo 1) and with a few living ones (photos 4 and 5 in Figure 8). Vesicomyid shells (*Isorropodon nyeggaensis* n. sp.) were sampled near the seeps.

4.2.3 Outcrops of consolidated sediment crusts and carbonates and benthic background fauna

Consolidated sediment outcrops were observed at locations in close proximity to pre-identified chimney sites (CNE02, 03, 07, 09, 10), but also between pre-identified chimney sites such as at CNE05.6 (site E) and at several locations in the western part of the study corridor between CNE10 and CNE17 (see location of the CNE site in Figure 2). They form large tabular platforms that extend laterally over distances of up to 20 m, rise up to 1.0 m above the seabed, and terminate at sharp edges cutting through distinct sub-horizontal layers (Figure 9). Morphologies of these outcrops make them look quite distinct from the chaotic-shaped authigenic massive carbonates observed at seeping sites of CNE03 and CNE05.6 as reported above (Figures 7, 8). Authigenic carbonates also occur as cm to tens of cm thick crusts and as cm-size concretions dispersed within the sediments.

The sedimentary matrix of recovered consolidated sediment mostly consists of silty sand and silty clay (Supplementary Table S2; Figure 10). At CNE02, CNE14 and CNE15, it is mostly cemented by iron and manganese oxides and has a very low carbonate content (3–4.5 weight %); the carbonate mineralogy consists of mixtures of calcite, dolomite and possibly siderite. Differently, the grey carbonate crusts and concretions from CNE01, CNE03 and CNE05.6 contain more than 56 weight percent of total carbonate, except for one crust cementing bivalve shells (271-CC2) with about 23 weight percent of total carbonate. Their carbonate mineralogy mostly consists of aragonite, calcite (from stoichiometry to Mg-calcite with up to 16-mol percent $MgCO_3$) and dolomite that is more abundant in the buried concretions than in the sub-surface crusts.

The microfacies of the authigenic carbonates display various crystal habits; acicular and prismatic crystals of aragonite form palisadic cements and geodes within cavities and pores (Figure 11). Calcite may occur as very small aggregates (100–200 nm), euhedral platy crystals or fine-grained (micron sized) aggregates of subhedral crystals. Framboids of pyrite frequently occur in association with the carbonate.

The oxygen and carbon isotopic compositions of the carbonate fraction of the consolidated sediment (indurated sediment), carbonate crusts and concretions are distributed into two distinct groups (Figure 12; Supplementary Table S2). The dark-brown crusts of CNE02, CNE14 and CNE15 are characterized by slightly positive $\delta^{18}O$ values (+0.53 to +1.98‰ V-PDB) and moderately low $\delta^{13}C$ values (−5.72 to −1.57‰ V-PDB) of carbonate. Differently, the carbonate crusts and concretions from CNE03 and CNE05.6 exhibit highly positive $\delta^{18}O$ values (+3.53 to +7.00‰ V-PDB) and very low $\delta^{13}C$ values (−58.34 to −30.71‰ V-PDB).

Both seabed authigenic carbonate crusts at seepage sites and outcrops of consolidated sediment are colonized by typical background fauna, dominated by suspension feeders (e.g., alcyonarians, hydrozoans, sponges) (Figures 7–9). One demosponge (*Crellomima imparidens*), two calcareous sponges (*Sycettusa* n. sp. and *Sycon abyssale*) and several encrusting sponges (*Hymedesmia basispinosa, H. grandis* and *H. truncata*; A. Plotktin, pers. com.) were sampled, as well as comatulids identified as *Poliometra proxila* (M. Elaume, pers. com.). We observed stalked Chaldorhizidae sponges (*Abestopluma furcata* and *Abestopluma lycopodium,* A. Plotkin, pers. com.) in abundance (up to 10 ind./m^2), and stalked pennatulacean (*Umbellula* sp.) with more than 1-m-tall stems (N. Améziane, pers. com.), along the whole ROV transect, in soft sediment and on hard ground. Very large ophiurids (*Gorgonocephalus* sp.), up to several tens of centimeters in size, were found on crusts as well as on sediment near the seepage sites (e.g., photos 1 and 4 in Figure 7). Nevertheless, stable isotope analyses did not reveal any nutritional link with a chemosynthesis-based production (Decker and Olu, 2012). Large pycnogonids (e.g., photos 1 in Figures 7, 9), rare asteroids and rays were also observed.

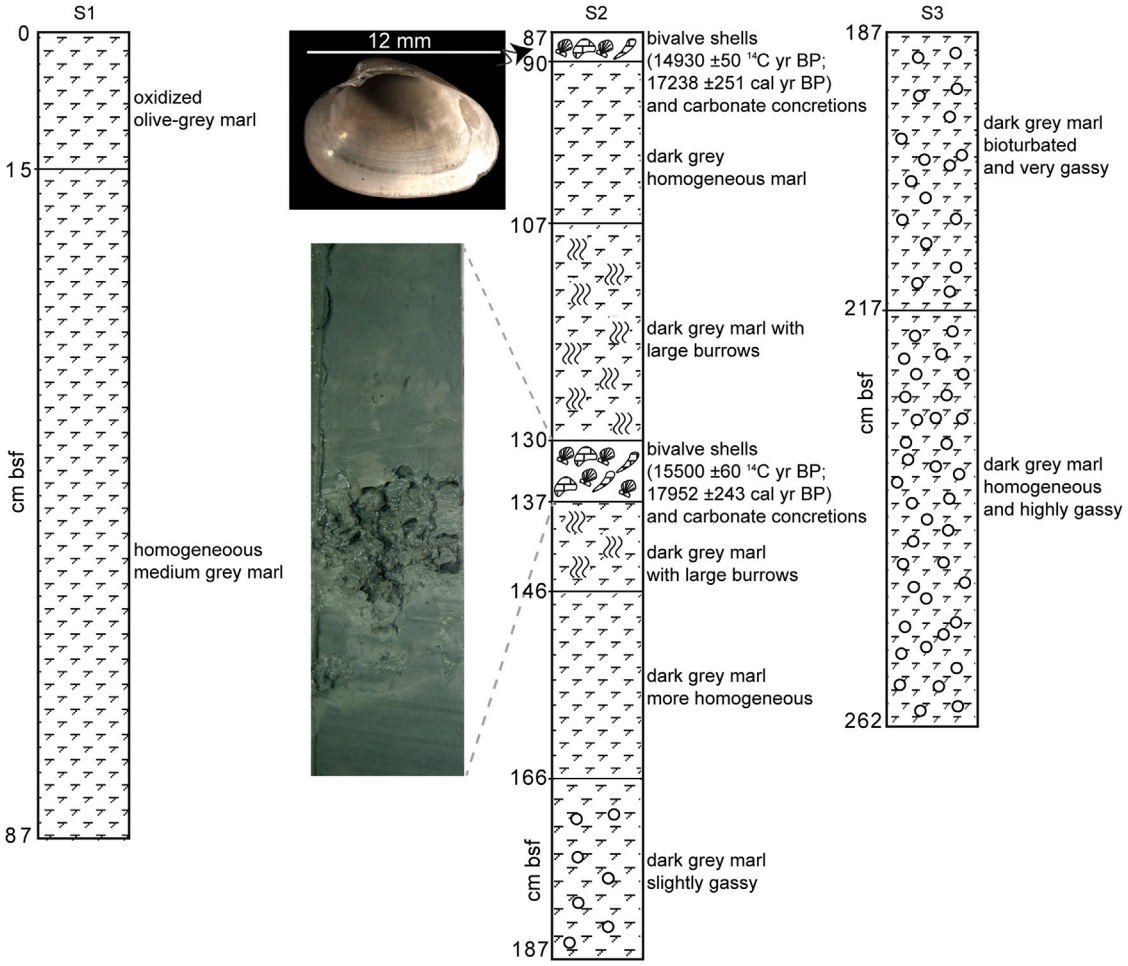

FIGURE 13
Visual lithological description of the 2.62-m-long core KSF-VKG-02 (https://doi.org/10.58006/bfbgx-87535) taken at CNE03 site (see location in Figure 2A; Figure 3A; Figure 6) which contains H_2S-rich sediment. The top of the core is characterized by relatively homogeneous marl in comparison with underlying sediments (S1). The second section (S2) exhibits dark grey marl with intercalations of two beds of bivalve shells at 0.87–0.90 and 1.30–1.37 mbsf. Photographs of the 1.30–1.37-mbsf interval showing carbonate concretions and bivalves (bottom) and a shell recovered from the 0.87–0.90-mbsf interval, sampled at 0.92 mbsf and identified as *Isorropodon nyeggaensis* (Krylova et al., 2011) (top). From 1.87 mbsf to the bottom of the core (2.62 mbsf), sediment is increasingly disturbed by gas (S3). (S = section; mbsf = meters below seafloor).

4.3 Subsurface information at surrounding seepage sites (CNE03)

Core description and dating. Core KSF-VKG-02 is located within a depression with no geophysical indication of seep activity and 40 m from the seeping sites discovered at the summit of a ridge and its uppermost flank (Figure 6). The upper 15 cm sedimentary layer consists of oxidized olive-grey marl (Figure 13). This marl layer is underlain by homogeneous medium grey marl down to 87 cm where a 3-cm-thick layer contains abundant bivalve shells of the Vesicomyidae family. The underlying sediments are dark grey marls with alternating homogeneous and intensively burrowed layers; in the 130–137 cm interval, there is another layer with abundant vesicomyids shells associated with cm-sized medium-grey carbonate concretions. Below around 170 cm, the sediment becomes increasingly gassy with a strong H_2S smell indicative of active sulfate reduction. Like those sampled at the seabed in the seep areas, the vesicomyids shells found in the two layers of the core were identified as the same species of *Isorropodon nyeggaensis* (Krylova et al., 2011) (Figure 13). Their small size (from 8.0 to 18.2 mm) is in the range of those sampled at the other Nyegga pockmarks, namely, G11 and Tobic (Figure 1B) (12.7–18.3 mm) (Krylova et al., 2011). Radiocarbon dating by AMS of the bivalve shells gives ages of 14,930 ±50 ^{14}C yr BP and 15,500 ±60 ^{14}C yr BP (17,238± 251 and 17,952 ± 243 cal yr BP) for the two layers at 87/92 cm and 130/133.5 cm, respectively. The δ^{13}C values of the carbonate of the bivalve shells (−1.7 and −1.9‰) indicate that there was no contribution of methane during the biomineralization process.

Pore water chemistry. The chloride profile exhibits little variation in concentration, apart from a slight deviation to higher concentration at a sub-bottom depth of about 1 m, with no curvature suggestive of fluid advection (Figure 14). The sulfate profile exhibits a concentration decrease from an average sea bottom value of about 27 mM to zero at about 2 m. Calcium and

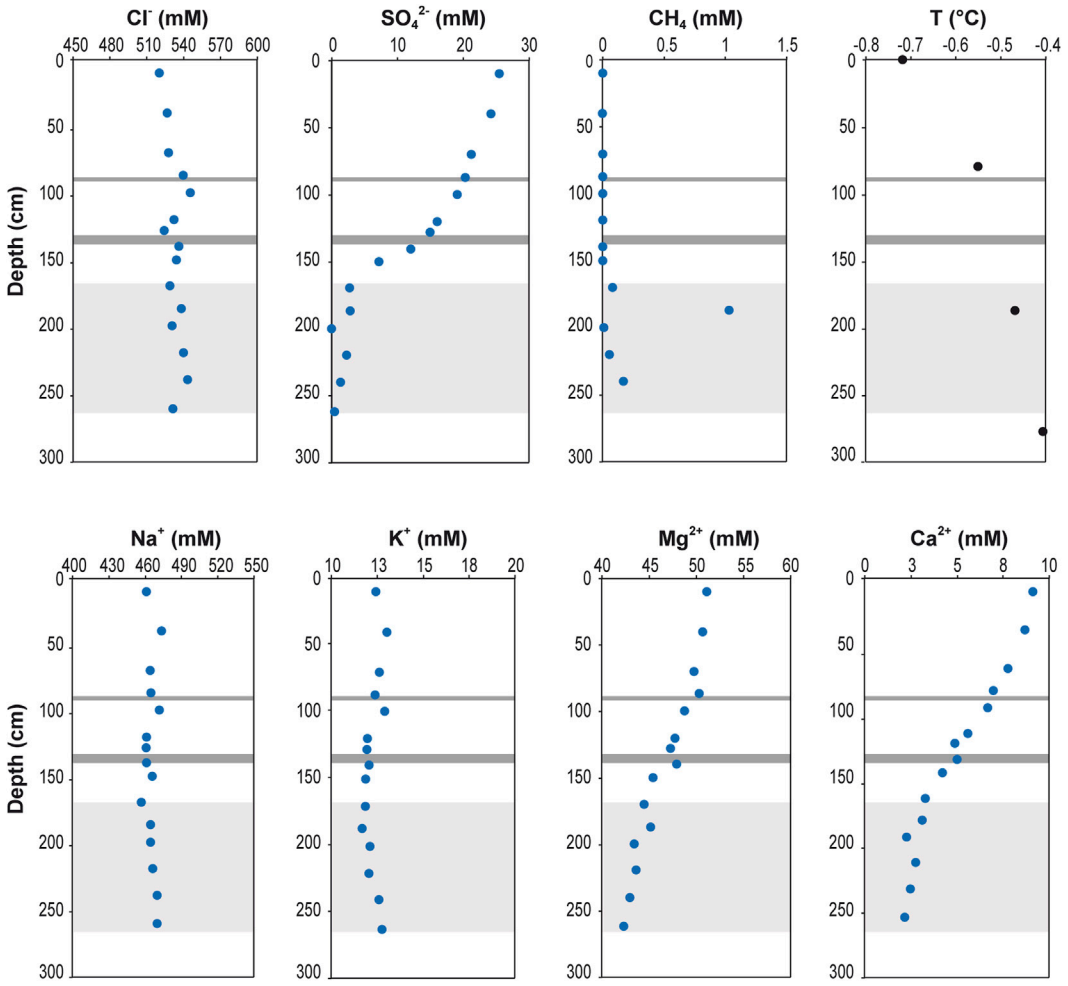

FIGURE 14
Pore-water geochemical profiles from laboratory measurements on core KSF-VKG-02 (https://doi.org/10.58006/bfbgx-87535) at CNE03 site (see location in Figure 2A; Figure 3A; Figure 6). Also shown is the temperature profile from *in situ* temperature data measured at 1.33, 3.12 and 4.62 mbsf. The dark grey intervals correspond to the levels containing bivalve shells and methane-derived authigenic carbonates (Figure 13). The light grey interval corresponds to gassy sediment.

magnesium profiles display similarities to the sulfate profile. The methane and sulfate profiles suggest an Anaerobic Oxidation of Methane (AOM) zone at a sub-bottom depth of about 2 m (with a peak of methane concentration slightly exceeding 1 mM), an intermediate value between the 5 m depth measured by Paull et al. (2008) as the background value of the sulfate methane transition outside Nyegga pockmarks and a close to zero value (seabed) at seeping sites.

Thermal measurements. Three thermal probes attached to the pipe of the corer at KSF-VKG-02 measured a temperature gradient of 0.044 C/m between estimated penetration depths of 1.33 m and 4.62 m (Figure 14). The bottom seawater temperature extrapolated from this gradient is −0.608°C whereas the measured one was −0.719°C, which suggests possible bottom seawater temperature fluctuations at the coring site and an associated occurrence of thermal transients in the upper sediment that may induce uncertainty in the interpretation of the measured temperature gradient of 0.044 C/m as representative of the thermal regime at depth.

5 Discussion

5.1 Methane-derived authigenic carbonate and consolidated sediment crust formation

The crusts from chimneys CNE02, CNE03, CNE05.6, CNE14 and CNE15 (Supplementary Table S2; Figure 12) display marked differences in mineralogy and isotopic values of the carbonate fraction. There are two groups of crusts that have clearly precipitated in different environmental conditions: 1) Crusts with a mainly diagenetically formed carbonate fraction and (2) crusts with a carbonate fraction predominantly formed by foraminifers and coccoliths.

In crusts from CNE03 and CNE05.6, the carbonate fraction is mostly diagenetic with mixtures of aragonite, Mg-calcite and dolomite. For the present-day bottom water conditions at these sites (t = −0.8°C; $\delta^{18}O$ = +0.14‰ V-SMOW; unpublished data C. Pierre), the equilibrium $\delta^{18}O$ values of carbonates would be +3.56‰ for calcite, +4.52 for Mg-calcite, +4.96‰ for aragonite and +7.30‰

for dolomite, using the equations of Tarutani et al. (1969), Fritz and Smith (1970), Grossman and Ku (1986) and Kim and O'Neil (1997). The $\delta^{18}O$ values of the diagenetic carbonates from Nyegga chimneys (+3.53 to +7.00‰ V-PDB) are consistent with the range of these equilibrium values, indicating that they were precipitated at conditions similar to those of present-day bottom water. The $\delta^{18}O$ enrichment in authigenic carbonates could also be partly attributed to the seepage of ^{18}O-rich water issued from the decomposition of massive gas hydrate accumulation at depth in the gas chimneys (Ussler and Paull, 1995). The very low $\delta^{13}C$ values of the carbonates (down to −58‰) clearly indicate that the major source of carbon was methane issued from the venting fluids, and converted to HCO_3^- during microbial anaerobic oxidation; AOM coupled with sulfate reduction is evidenced by the close association of carbonate and pyrite. Similar ranges of very low $\delta^{13}C$ values (down to −59‰) were measured by Mazzini et al. (2005), Mazzini et al. (2006) and Ivanov et al. (2010) on 85 crusts from Nyegga pockmark areas including four samples collected at CNE03 and four others collected a few kilometers from CNE14 (Ivanov et al., 2010) (Figure 12). Only two samples have higher $\delta^{13}C$ values of −19 and −10‰. The $\delta^{13}C$ values of methane analyzed from cores taken at Nyegga pockmarks and the dry composition of gas indicate a biogenic origin, with, for example, at CNE03 the $\delta^{13}C$ values of methane ranging from −82‰ to −68‰ (Ivanov et al., 2010). Although thermogenic sources may be present in depth, there is no geochemical evidence so far of a thermogenic methane contribution in the subsurface of the studied Nyegga pockmarks (Ivanov et al., 2010). During AOM, the lighter ^{12}C isotope is preferentially incorporated into the produced CO_2 with a fractionation factor of 1.0088 ± 0.0013 (Whiticar and Faber, 1986; Alperin et al., 1988; Whiticar, 1999), giving an average $\delta^{13}C$ value of −88‰ for the CO_2 issued from AOM at CNE03; considering an enrichment factor of −14.86‰ between CO_2 and calcite (Bottinga, 1969) at seafloor temperature (t = −0.8°C), the average $\delta^{13}C$ value of "pure" methane-derived carbonate would be −73‰. The $\delta^{13}C$ values measured in the diagenetic carbonates from the Nyegga chimneys (from −58‰ to −31‰) are thus much higher (by 15‰ and 42‰ respectively) than this calculated value. The relative ^{13}C enrichment in carbonate could indicate a mixing of methane-derived bicarbonate with another ^{13}C-rich DIC source, possibly bottom seawater ($\delta^{13}C$ = +1.1‰; Kroopnick, 1980). Consequently, mass balance calculation ($\delta^{13}C$ authigenic carbonate = [-73 * f] + [3.1 * (1-f)] where f corresponds to the fraction of pure methane-derived carbonate and (1-f) corresponds to the fraction of carbonate derived from seawater DIC using an enrichment factor of 2‰ between carbonate and DIC) gives an estimation between 67% and 80% for the contribution of oxidized methane to authigenic carbonate formation. This estimation appears unrealistic because the DIC concentration (~2 mM) of seawater is less than 10% compared to the high DIC concentrations (>20 mM) produced by AOM (Paull et al., 2008). A more probable source of ^{13}C-rich DIC could be provided by high fluxes of fluids with high alkalinities issued from the methanogenic zone (Chatterjee et al., 2011). Alternatively, the carbon isotopic shift could be explained by the reservoir effect during AOM when residual CH_4 becomes progressively enriched in ^{13}C due to microbial CH_4 consumption (Whiticar, 1999); the residual fraction f of CH_4 calculated using the Rayleigh distillation equation ($\delta - \delta_0 = \varepsilon \ln f$, where $\varepsilon CH_4\text{-}CO_2 \sim 9$) would be between 19% and 6%. These estimations are reasonable considering that large fractions of oxidized methane are trapped as authigenic carbonate precipitating within the sediment whereas the remaining methane may escape through the seafloor toward the water column. Similar high methane turnover rates (93%) were estimated in the siboglinid tubeworm habitat at Håkon Mosby mud volcano (Felden et al., 2010).

In the crusts sampled at CNE02, CNE14 and CNE15, the carbonate fraction corresponds to planktonic foraminifers and coccoliths mixed with minor amounts of diagenetic carbonates (dolomite and possibly siderite). The $\delta^{13}C$ values ranging from −5.72 to −1.57‰ indicate that there was no contribution of carbon from methane oxidation during the formation of these crusts that may thus be considered as hard grounds probably formed when bottom waters were poorly ventilated, a situation prevailing during glacial times (Keigwin and Boyle, 2008). These carbonates, which differ significantly from authigenic carbonates associated with methane release in their mineral and isotopic signature and formation, deserve further investigation (mapping, sampling and analyses).

5.2 Present-day *versus* past seepage activity

Present-day seepage activity. Our observations point to present-day seepage activity through the seabed in two areas of the Nyegga study corridor (Figure 2), CNE03 (Figure 7) and CNE05.6 (Figure 8). However, we do not exclude present-day seepage activity elsewhere and particularly at the CNE01 site which presents similar acoustic sediment and seafloor signatures to CNE03 and CNE05.6. Unfortunately, the ROV was unable to operate effectively due to a positioning problem encountered at the beginning of dive 271 (Figure 2A). Consequently, most of the targeted areas at CNE01 were uninvestigated, including the southern ridge and adjacent depressions where several morphostructures resemble those of authigenic carbonates (Figure 5B).

At both CNE03 and CNE05.6 sites, several areas of reduced dark grey sediment surrounded by chemosynthetic fauna covering a few square meters, and *in situ* methane anomalies in the bottom seawater (up to 2,130 nL/L), attest to present-day upward advection through the seabed of pore water containing dissolved methane. Although direct measurements of the flow rates were not obtained, it was noted that biological zonation at the active sites presents similarities to seepage sites along the Norwegian margin, such as the Håkon Mosby mud volcano in the Barents Sea (Decker et al., 2012; Decker and Olu, 2012), where oxygen and sulfide fluxes were calculated based on microprofile measurements indicating pore water seepage rates of up to a few meters per year (de Beer et al., 2006). The presence of filamentous bacteria and siboglinid tubeworms, both depending on sulphide availability, suggests that this compound is produced at CNE03 and CNE05.6 in the subsurface sediments, from anaerobic methane oxidation, with a gradient from the central area of reduced sediments and microbial mats, to the external zones colonized by the siboglinids, as described for the other sites of the Norwegian margin.

Spatial heterogeneity. The pore-water chloride profile located only 40 m from the seepage sites, shows no evidence of upward

advective flow (Figure 14). The methane and sulfate profiles suggest an AOM zone at a sub-bottom depth of about 2 m, an intermediate value between the 5 m depth measured by Paull et al. (2008) as the background value of the sulfate methane transition outside Nyegga pockmarks and a close to zero value (seabed) at active sites. Subseafloor fluid flow is heterogeneously distributed within such a pockmark site, which is more than 200 m wide (Figure 5A). Similarly, fluid indicators in the subsurface sediments at CNE03 vary drastically from one core to another, although they are only a few tens of meters apart (Figures 2A, 6). Maximum pore water methane concentration varies in a 50-m distance from 1 mM (this study) to 6.7 mM (Ivanov et al., 2010); these values are lower than the peak of methane measured at Tobic pockmark reaching 12.0 mM (Ivanov et al., 2010). Thus, the uppermost sediment at one location with gas hydrates and abundant living Siboglinidae (pogonophora) contrasts with some others that present no signs of present or past seep-related activity (this study; Ivanov et al., 2010; Attias et al., 2020).

Past seepage activity. The area occupied at CNE03 by the identified seeping sites is probably less than 1% of the total area explored with the ROV during the Vicking cruise. From hydrological modeling of sedimentation and compaction in the Nyegga region for the period of the past 2.6 Ma, Hustoft et al. (2009) suggest that Nyegga chimneys and pockmarks could have formed in association with a post-LGM peak of fluid expulsion caused by rapid sedimentary loading in the period. The period 15,800–15,000 ^{14}C yr BP (ca. 18,314–17,366 cal yr BP) was one of rapid glacio-marine sedimentation of about 30 m/ky (Reiche et al., 2011) and correlates with a period of fluid expulsion at CNE03 indicated by two beds of vesicomyids dated at 15,500 ±60 and 14,930 ±50 ^{14}C yr BP (ca. 17,952 and 17,238 cal yr BP), respectively (Figure 13). Similar beds of vesicomyids were also recovered at other locations at CNE03 (core GS07-148-14GC, Chen et al., 2012; Karstens et al., 2018; core CNE03; Attias et al., 2020; Figure 6). Two distinctive chemosynthetic shell beds are centered around depth intervals of 1.05–1.11 and 1.48–1.62 mbs (Chen et al., 2012). Radiocarbon dating of these shells provides evidence for two main methane seepage episodes, between 15,500 and 13,900 ^{14}C yr BP (ca. 17,952 and 15,951 cal yr BP), respectively (Chen et al., 2012). The ages of vesicomyids recovered at CNE03 are also consistent with the AMS ^{14}C dating of planktonic foraminifers, 15,295 ±45 ^{14}C yr BP (17,692 ±278 cal yr BP), recovered just above a similar bed of vesicomyids (although initially mistakenly described as Bathymodiolus shells) and carbonate concretions found deeper in the sediments (6.95–7.05 mbsf) in a core taken at the CNE13 site at 807 m water depth and 12 km from the KSF-VKG-02. Numerical modeling of gas hydrate dynamics at the Nyegga pockmark field emphasizes the role of increased sediment accumulation as the main driver of gas hydrate dissociation with a peak at 17,800 years BP (Karstens et al., 2018). Moreover, in the Nyegga area, the occurrence of fluid expulsion towards the seafloor between 200 and 130 ky was inferred from seismic data and identification of paleo-BSRs (Plaza-Faverola et al., 2012). These fluid expulsion events and the associated paleo-chimneys could have provided weakness zones for the formation of chimneys since the last glacial maximum.

The Norwegian margin from the North Sea, the Norwegian Sea to the Barents Sea hosts numerous pockmark fields in connection with seismically identified gas chimneys. Some of them are inactive with no evidence of present-day seepage (e.g., Barents Sea, Nickel et al., 2012; giant pockmark field in the northern North Sea; Mazzini et al., 2017) while some others are still active (e.g., Loppa High in South-West Barents Sea, Chand et al., 2012; Central North Sea; Chand et al., 2017). The onset of methane seepage for the Barents Sea pockmarks is dated to 17,000 years BP based on U/Th dating of methane-derived authigenic carbonates, that coincides there with the deglaciation-induced pressure release and thinning of the hydrate stability zone (Crémière et al., 2016). The methane originates from gas hydrate dissociation triggered by pressure changes on the continental shelf due to collapse and retreat of the Scandinavian Ice Sheet (SIS) (Chand et al., 2012). Karstens and Berndt (2015) suggested the same possible triggering mechanism for high overpressure resulting in hydrofracturing at chimneys of the Southern Viking Graben (North Sea). The extent of the ice cover during the last glacial period does not include the Nyegga area (Hughes et al., 2016); SIS-related overpressure cannot be the driven force for the formation of the Nyegga chimneys.

5.3 Relationship between hydrate occurrences at depth and methane seepage through the seabed

Based on geophysical, geochemical and biological data, we propose a conceptual model for the functioning and evolution of the CNE Nyegga chimneys, through four main successive stages (A to D in Figure 15). This model is well constrained by the CNE03 dataset which is the most complete, with in particular the present-day state, illustrated by stage 2 in Figure 15B. Based on available data at CNE01-CNE17 sites, we suggest that the different investigated CNE chimneys underwent similar evolution with slight differences in their present-day state. While some chimneys present moderate to low seepage activity (e.g., CNE03, Figure 15B), others are characterized by a lower level of seepage at the seafloor (as illustrated in Figure 15C).

Stage 1. Gas hydrate formation and free-gas venting during the post-LGM period. This initial stage was certainly the most active, with plumes of free gas emitted to the seabed (Figure 15A). The rate of methane flow to the chimney was at its highest and it is probable that most of the hydrate in the chimney was formed during this stage. This initial stage with gas bubbles escaping into the water column is clearly over as no emission of free gas has been observed there or elsewhere in the Nyegga region. The past seepage activity at the Nyegga studied area is evidenced by i) the presence at depth of empty bivalve shells of the Vesicomyidae family (*Isorropodon nyeggaensis* n. sp.) dated to 15,500 ±60 and 14,930 ±50 ^{14}C yr BP (ca. 17,952 and 17,238 cal yr BP) (Figure 13); similar beds of vesicomyids were recovered at CNE03 (Chen et al., 2012; Karstens et al., 2018; Attias et al., 2020) and CNE13 (Paull et al., 2008) with some of these shells dated, giving analogue radiocarbon ages; and ii) the presence of widespread methane-derived authigenic carbonates buried in subsurface sediments inferred from multi-frequency seafloor backscatter data; their extent increases with depth. Seismic tomography showed that there is a body of higher-than-normal

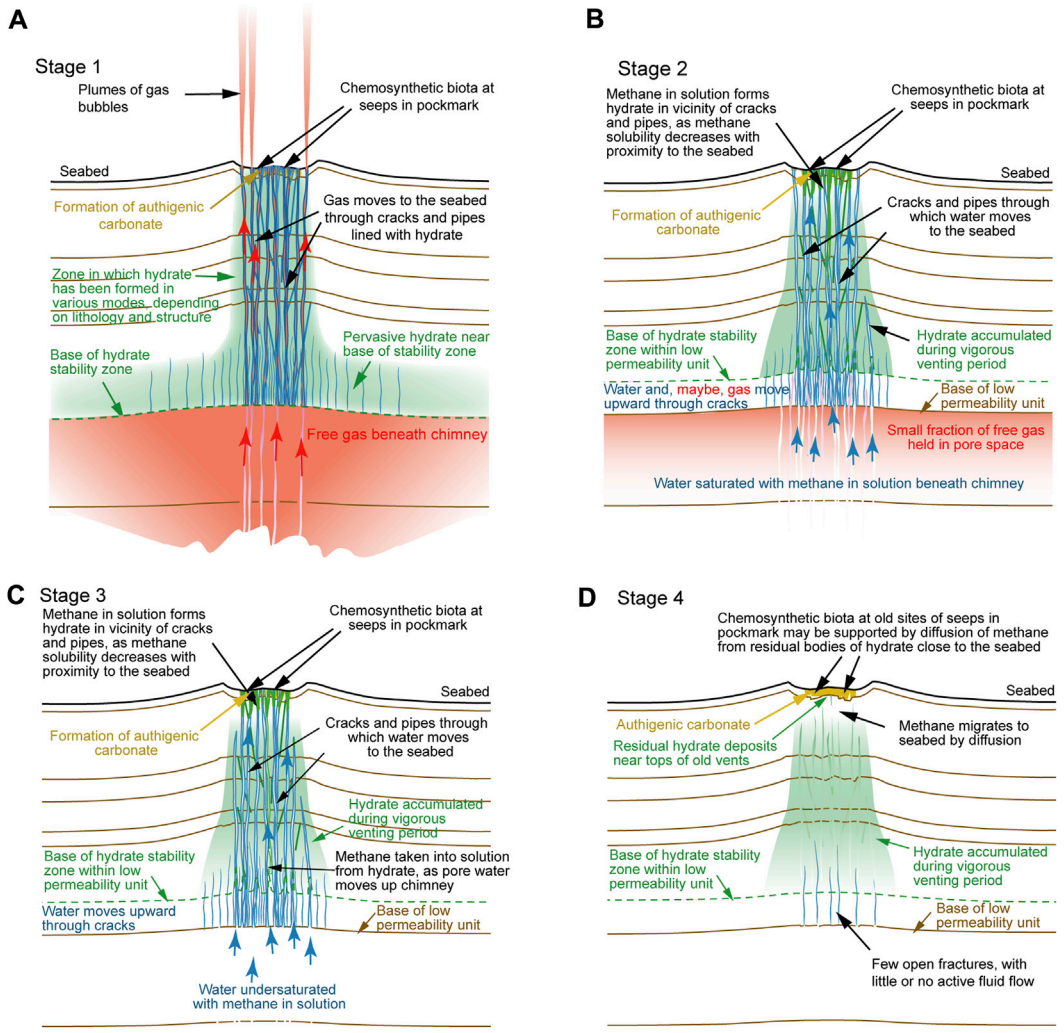

FIGURE 15
Diagrams representing four main evolutive stages of activity of methane transport through a chimney containing hydrate, adapted and supplemented from Foucher et al. (2009). Pink-red represents free gas, blue represents pore water and green represents gas hydrate. **(A)** Stage 1. Gas hydrate formation and free-gas venting during the post-LGM period. **(B)** Stage 2. Decrease in hydrate formation and moderate to low seepage activity (present-day CNE03). **(C)** Stage 3. Gas hydrate dissolution and low to very low level of seepage activity. **(D)** Stage 4. Methane diffusion and cessation of seepage.

seismic velocity in the chimney beneath CNE03 (Plaza-Faverola et al., 2010) (Figure 3C). The likely cause is the presence of hydrate within the sediment, primarily occupying cracks in the low-permeability sediment, with a maximum concentration of about a quarter of the rock volume. Hence, most of this hydrate could have formed when the chimney was venting free gas, earlier in its history. The possibility that some of the hydrate was formed from methane in solution in advecting pore water cannot be overlooked. However, it is more likely that invasion of the Gas Hydrate Stability Zone (GHSZ) by free gas was the primary mechanism initiating the formation of hydrate, as illustrated in Figure 15A. Indeed, this view is supported by the seismic indications of free gas beneath the chimney at present and the higher rate of formation of hydrate from free gas (Waite et al., 2009). Thus, the gas may have followed cracks opened by overpressured gas and held transiently dry by the effect of hydrate formation on the walls of the cracks in sediment of already very low intrinsic permeability. Gas may also have migrated through the developing chimney by the process proposed by Liu and Flemings (2007). Following initial invasion of the base of the chimney through fractures opened by overpressured gas, gas continues to migrate upward, progressively creating hydrate. Indeed, the increase in pore water salinity caused by the formation of hydrate (dissolved ions are not taken into the hydrate structure) means that, locally, the system can reach the limit of hydrate stability.

Stage 2. Decrease in hydrate formation and moderate to low seepage activity (present-day CNE03). When the rate of free-gas supply to the chimney greatly diminishes or ceases, the flow of methane-rich pore water throughout the chimney can be sustained if the ascending pore water remains saturated in methane by passing through the zone containing free gas (Plaza-Faverola et al., 2010). If very small amounts of free gas enter the GHSZ, they are likely to be consumed in the formation of hydrates, without any free gas reaching the seabed. The hydrate in the chimney maintains the

concentration of methane in ascending pore water at saturation level, and hydrate will continue to form within the shallower parts of the chimney, because methane solubility decreases towards the seabed (Figure 15B). Stage 2 corresponds to the current situation of CNE03 site with i) the presence of gas beneath the base of the GHSZ evidenced in the vicinity of the chimney, presented here and in previous seismic studies (Plaza-Faverola et al., 2010; Plaza-Faverola et al., 2012); and ii) the absence of gas bubbles emitted into the water column (acoustic insonification in Figure 2A). This view is consistent with results from marine electromagnetic and seismic studies conducted at CNE03 (Attias et al., 2016). Strong resistivity anomalies in the shallow part are attributed to the presence of gas hydrates and authigenic carbonates. The authors conclude that above the base of the GHSZ, gas hydrates mainly occupy the pore space of sediments whereas the free gas extends laterally below the base of GHSZ. The evidence of fluid flow from the seabed at CNE03 and CNE05.6 also supports the case where the situation is dominated by the advection of methane dissolved in pore water (Supplementary Table S1). Part of this methane could arise from the dissolution of hydrates in the chimney. At CNE03, there is evidence of hydrates a few meters beneath the seabed (Ivanov et al., 2007; Ivanov et al., 2010). The relatively shallow depth of the Sulfate Methane Transition Zone (SMTZ) of 2 m in core KFS-VKG-02, compared with about 5 m depth in the areas outside pockmarks (Paull et al., 2008), could be due to heterogeneous fluid flow related to the activity of the pockmark area or a consequence of a local occurrence of shallow hydrate. The sulfate profile in core AT634G (Ivanov et al., 2010) shows some scatter between 150 and 250 cm depth. This may be because the core intercepts non-vertical migration paths of water with methane in solution, which locally expels sulfate-rich water and reacts with it to remove sulfate by AOM. Alternatively, this could reflect the presence of gas hydrates at different stratigraphic levels or repeated gas seepage events (Ivanov et al., 2010). At present, methane continues to sustain chemosynthetic communities at the seafloor, e.g., Siboglinidae polychaetes (*Oligobrachia haakonmobiensis*, i. e., *webbi* and *Sclerolinum contortum*) as well as microbial mats (Figure 7), and possibly the precipitation of methane-derived authigenic carbonates in the near-seabed sediment.

Stage 3. Gas hydrate dissolution and low to very low level of seepage activity. When free gas is absent from the base of the chimney, pore water entering the chimney is likely to be undersaturated in methane. A high concentration of methane in pore water near the seabed can however be maintained for a long period of time (thousands of years). Dissolution of hydrate at the base of the chimney would bring the methane in solution in pore water to saturation level, which would lead to the creation of hydrate closer to the seabed, where the solubility of methane is lower (Figure 15C). This process will maintain methane in solution near the seabed at saturation until all the hydrate has dissolved, with the concentration profile near the seabed being controlled by the rate of fluid advection competing against molecular diffusion to the seabed and processes, such as anaerobic oxidation of methane, that consume methane (Foucher et al., 2009). In the Nyegga area, depending on the migration path of ascending pore fluids relative to sedimentary units containing free gas, the situation could be represented by Stage 3 (Figure 15C) where the water migrating beneath the GHSZ is undersaturated in methane, but flow through the chimney containing hydrate brings it to saturation.

Stage 4. Methane diffusion and cessation of seepage. If fluid flow into the base of the chimney ceases, hydrate in the chimney will gradually be diminished by the diffusion of methane to the seabed (Figure 15D). Pore water surrounding hydrate will remain saturated in methane until the hydrate has dissolved. Depending on the amount of hydrate present, this could take thousands to tens of thousands of years (Foucher et al., 2009). The concentration of methane in solution near the seabed, in this case, will depend on the quantity of hydrate in the proximity of the seabed, its depth beneath the seabed when inflow at the base of the chimney ceased and on the time elapsed since. The top of hydrate within the top meter or so would recede downward quite quickly, taking a few hundred years for a layer with an average concentration of about 10% of total volume to deepen from 1 m to 2 m (Foucher et al., 2009). The concentration of methane in pore water near the seabed is rapidly reduced by the combined effects of diffusion and oxidation. Isolated pipes and veins lose hydrate more rapidly as is most likely the case of many inactive Nyegga spots.

6 Summary and conclusion

ROV dive observations identified several seeping sites at the CNE03 and at a nearby 4-km-distanced location named CNE05.6. Morphology at the seabed, imaged by high-resolution bathymetry, reveals not only depressions, corresponding to pockmarks, but also adjacent ridges whose summits and uppermost flanks are the locations of present-day seepage activity. The seafloor morphology of pockmark features located above hydrate-bearing chimneys is known to be chaotic and more complex than free-gas related pockmarks (Riboulot et al., 2016). At seeps of CNE03 and CNE05.6, there is a clear zonation of the biological chemosynthetic habitat, from an inner area of dark-grey reduced sediment, bacterial mats and Rissoidae gastropods to outer fields of Siboglinidae. This change in macrofauna at the active Nyegga seeps is interpreted to reflect a decreasing strength of fluid flow away from the seep center, similarly to other seeps of the Norwegian margin (Gebruk et al., 2003; de Beer et al., 2006; Jerosch et al., 2007; Decker et al., 2012). All the sites of high-seepage activity are restricted to a few square meters of the seabed. No free-gas bubble emissions were observed at any of the sites, but *in situ* methane anomalies were detected in the water column within a few tens of centimeters of the seabed with a highest concentration of 2,130 nL/L. The pattern of seepage is heterogeneous. For example, at CNE03, sulfate and chloride profiles in the pore water of core KSF-VKG-02 show that there is no upward fluid advection within 40 m of the most active seepage area. Besides the direct influence of seeps on chemosynthetic fauna, there is an indirect impact on the benthic background fauna. Methane-derived authigenic crusts and consolidated sediment layers both provide a hard substrate habitat for very rich benthic fauna, including sponges, comatulids and ophiurids.

Two beds with carbonate concretions and vesicomyids dated at 15,500 ±60 and 14,930 ±50 ^{14}C yr BP (17,952 ±243 and 17,238 ±251 cal yr BP) in the KSF-VKG-02 core taken at CNE03 most likely mark past events of intense seepage, as observed in three other cores from the CNE area (Paull et al.,

2008; Chen et al., 2012; Karstens et al., 2018; Attias et al., 2020). These periods coincide with episodes of rapid sedimentation that induced fluid circulation and the formation of the Nyegga pockmark field (Hustoft et al., 2009; Reiche et al., 2011) and triggered widespread gas hydrate dissociation (Karstens et al., 2018). The recent identification of the Nyegga Slide and the triggering of its associated slope failure, 20,000 years BP (Karstens et al., 2023), rule out the view that the Nyegga pockmark field predates the giant Storegga Slide event (e.g., Hustoft et al., 2009), and emphasize the probable close spatio-temporal link between fluid seepage and sedimentary destabilization in the region. The very low $\delta^{13}C$ values in the carbonates (down to −58‰) clearly indicate that the major source of carbon was methane issued from the venting fluids and converted to HCO_3^- during microbial anaerobic oxidation. Our observations are consistent with a history of seepage showing a peak of activity and perhaps the formation or reactivation of chimneys in immediate post-LGM times, as suggested by hydrological modeling (Hustoft et al., 2010) and gas hydrate dissociation simulation (Karstens et al., 2018). It is probable that during this period free gas was emitted from the seabed and also formed hydrate in the chimneys beneath the pockmarks. Our preferred model for the present-day situation is one in which there is minimal input or no input of free gas at the base of the chimney. Seepage is dominated by advection of methane in solution in pore water that enters the base of the chimney saturated in methane, because it migrates through layers that contain free gas. Even if the water entering the base of the chimney was not methane-saturated, it would become saturated with methane derived from dissolution of hydrate in the chimney, provided that the migration paths pass through the hydrate-bearing parts of the chimney.

Attention has justifiably tended to focus on large pockmarks, such as CNE03, both in this and other investigations of seepage in the Nyegga area, but total seepage through the far more numerous smaller pockmarks and other seabed features that host seeps might be of similar importance. CNE05.6 exhibits a similar level of present-day activity to CNE03, although it has far less prominent seabed relief and acoustic backscatter than CNE03 (Figure 4). Because it is offset from the seismic line, its underlying chimney is not imaged on the very-high resolution seismic section (Figure 2B), but can be seen on the high-resolution seismic section below the Intra-Naust reflector (Figure 2C). The even smaller conduits, which are imaged by the very-high resolution seismic sections, commonly terminate at features on the seabed, which although are possibly inactive at present, must have been active at some time in the post-LGM period. These smaller structures have the potential to contribute as much as or more than the present-day fluid outflow from the seabed above the chimneys. Further investigation of flow evidence is required to establish the relative importance of the two groups of seeping features.

We conclude that the Nyegga pockmark area investigated during this study (CNE01-CNE17) is an area of modest seepage activity at present, but seepage is possibly not weaker, on average, than the areas to the south-east (e.g., Sharic and G11 sites, Figure 1B) which have been previously suggested to be more active at present than the CNE area (Ivanov et al., 2010). More extensive investigations are required to establish the general distribution of seepage in these areas, and document the apparently high degree of heterogeneity of seepage at pockmarks. From the experience of ROV dives on the pockmarks investigated during this study, it is evident that intense observation and sampling is needed to characterize seepage activity, and that the results from two or three cores or restricted visual seabed inspection from a single pockmark area could give a false impression of the feature being either highly active or inactive. Near-bottom observations, at least, confirms that there is activity, but cannot quantify it. Core sampling could lead to a feature being wrongly classified as inactive. Consequently, we contend that the present level of investigation of seepage activity in the Nyegga region is far too low to be able to draw conclusions on general trends in activity across the region. We suggest that any area underlain by gas below the base of the GHSZ is likely to present some methane seepage.

Data availability statement

The datasets presented in this study can be found in online repositories. The names of the repository/repositories and accession number(s) can be found in the article/Supplementary Material.

Ethics statement

Ethical approval was not required for the study involving animals in accordance with the local legislation and institutional requirements because There was no such procedure at that time.

Author contributions

J-PF conceived this study. J-PF, GW, CP, CD, KO and SD wrote the manuscript and produced the figures. HN was the chief scientist of the Hydratech (2002) and Vicking (2006) cruises. J-PF, CP, KO, J-PD and J-LC participated in the Vicking cruise. SD conducted seafloor and water column data analysis and interpretation, compiled the data and contributed to illustration work of all figures. HN, GW and SK were in charge of seismic data processing and interpretation. CP and M-MB were involved in geochemical analyses of carbonate and sediment and subsequent interpretation. CD and KO were in charge of the biological studies and related analyses. J-PD and J-LC conducted the bottom water sample analyses for methane concentration measurements and were involved in pore-water chemical analyses. All authors contributed to the article and approved the submitted version.

Funding

The MAK-1M side-scan sonar and profiler data were acquired during Leg 3 of Training Through Research Cruise 16 (2006) of the Professor Logachev, funded by the HERMES EU Integrated Project and STATOIL (co-chiefs M. Ivanov and GK. GW). The VICKING cruise was also supported by the HERMES project, funded by the European Commission's Framework Six Programme, under the priority Sustainable Development, Global Change and Ecosystems, EC Contract No. GOCE-CT-2005-511234.

Acknowledgments

We thank the crews and scientific party of the HYDRATECH 2002 (https://doi.org/10.17600/2020060) and VICKING 2006 cruises (https://doi.org/10.17600/6030090) that took place onboard R/V Le Suroît and Pourquoi pas ? with the Ifremer ROV Victor, respectively. We are especially grateful to Ann Andersen, Marie-Claire Fabri and Philippe Noël. We are indebted to Alexander Plotkin for Porifera determination, Anders Warèn for Gastropoda, Elena Krylova for Bivalvia, Marc Elaume for Comatulidae and Pennatulacea and Ann Andersen for Polychaeta Siboglinidae. We thank Catherine Satra and Jean-Pierre Mazé for their valuable help in producing some of the figures, Patrick Briand for laboratory photographs and Livio Ruffine for earlier discussion of the manuscript. We thank also Omar Boudouma for his helpful assistance during SEM sessions. The AMS ^{14}C measurements were realized at the UMS 2572 LMC14 (CEA-CNRS-IRD-IRSN-MCC) of Saclay by Jean Pascal Dumoulin and Christophe Moreau that we acknowledge warmly. We thank Samuel Toucanne and Guillaume Soulet for their guidance in radiocarbon age calibration. We are also grateful to Carine Chaduteau for her participation in gas analyses. We greatly thank Alison Chalm for language corrections.

Conflict of interest

The authors declare that the research was conducted in the absence of any commercial or financial relationships that could be construed as a potential conflict of interest.

Publisher's note

All claims expressed in this article are solely those of the authors and do not necessarily represent those of their affiliated organizations, or those of the publisher, the editors and the reviewers. Any product that may be evaluated in this article, or claim that may be made by its manufacturer, is not guaranteed or endorsed by the publisher.

Supplementary material

The Supplementary Material for this article can be found online at: https://www.frontiersin.org/articles/10.3389/feart.2023.1250619/full#supplementary-material

References

Akhmetzhanov, A. M., Kenyon, N. M., Ivanov, M., Westbrook, G. K., and Mazzini, A. (2008). *Preliminary results of investigations during the TTR-16 cruise of R/V professor Logachev. UNESCO-IOC Technical Series* 76.

Alperin, M., Reeburg, W., and Whiticar, M. J. (1988). Carbon and hydrogen isotope fractionation resulting from anaerobic methane oxidation. *Glob. Biogeochem. Cycles* 2 (3), 279–288. doi:10.1029/gb002i003p00279

Attias, E., Amalokwu, K., Watts, M., Falcon-Suarez, I. H., North, L., Hu, G. W., et al. (2020). Gas hydrate quantification at a pockmark offshore Norway from joint effective medium modelling of resistivity and seismic velocity. *Mar. Petroleum Geol.* 113, 104151. doi:10.1016/j.marpetgeo.2019.104151

Attias, E., Weitemeyer, K., Minshull, T. A., Best, A. I., Sinha, M., Jegen-Kulcsar, M., et al. (2016). Controlled-source electromagnetic and seismic delineation of subseafloor fluid flow structures in a gas hydrate province, offshore Norway. *Geophys. J. Int.* 206 (2), 1093–1110. doi:10.1093/gji/ggw188

Berndt, C., Bünz, S., and Mienert, J. (2003). Polygonal fault systems on the mid-Norwegian margin: a long-term source for fluid flow. *Geol. Soc. Lond. Spec. Publ.* 216 (1), 283–290. doi:10.1144/gsl.sp.2003.216.01.18

Bondevik, S., Svendsen, J. I., Johnsen, G., Mangerud, J., and Kaland, P. E. (1997). The Storegga tsunami along the Norwegian coast, its age and run up. *Boreas* 26 (1), 29–53. doi:10.1111/j.1502-3885.1997.tb00649.x

Borges, A. V., Champenois, W., Gypens, N., Delille, B., and Harlay, J. (2016). Massive marine methane emissions from near-shore shallow coastal areas. *Sci. Rep.* 6, 27908. doi:10.1038/srep27908

Bottinga, Y. (1969). Calculated fractionation factors for carbon and hydrogen isotope exchange in the system calcite-carbon dioxide-graphite-methane-hydrogen-water vapor. *Geochimica Cosmochimica Acta* 33 (1), 49–64. doi:10.1016/0016-7037(69)90092-1

Bouriak, S., Volkonskaia, A., and Galaktionov, V. (2003). Split' strata-bounded gas hydrate BSR below deposits of the Storegga Slide and at the southern edge of the Voring Plateau. *Mar. Geol.* 195 (1-4), 301–318. doi:10.1016/s0025-3227(02)00694-1

Bünz, S., and Mienert, J. (2004). Acoustic imaging of gas hydrate and free gas at the Storegga Slide. *J. Geophys. Res. Solid Earth* 109 (B4), B04102. doi:10.1029/2003jb002863

Bünz, S., Mienert, J., and Berndt, C. (2003). Geological controls on the Storegga gas-hydrate system of the mid-Norwegian continental margin. *Earth Planet. Sci. Lett.* 209 (3–4), 291–307. doi:10.1016/s0012-821x(03)00097-9

Chand, S., Crémière, A., Lepland, A., Thorsnes, T., Brunstad, H., and Stoddart, D. (2017). Long-term fluid expulsion revealed by carbonate crusts and pockmarks connected to subsurface gas anomalies and palaeo-channels in the central North Sea. *Geo-Marine Lett.* 37 (3), 215–227. doi:10.1007/s00367-016-0487-x

Chand, S., Thorsnes, T., Rise, L., Brunstad, H., Stoddart, D., Bøe, R., et al. (2012). Multiple episodes of fluid flow in the SW Barents Sea (Loppa High) evidenced by gas flares, pockmarks and gas hydrate accumulation. *Earth Planet. Sci. Lett.* 331-332, 305–314. doi:10.1016/j.epsl.2012.03.021

Chatterjee, S., Dickens, G. R., Bhatnagar, G., Chapman, W. G., Dugan, B., Snyder, G. T., et al. (2011). Pore water sulfate, alkalinity, and carbon isotope profiles in shallow sediment above marine gas hydrate systems: a numerical modeling perspective. *J. Geophys. Res. Solid Earth* 116 (B9), B09103. doi:10.1029/2011JB008290

Chen, Y., Bian, Y., Haflidason, H., and Matsumoto, R. (2012). Present and past methane seepage in pockmark CN 03, Nyegga, Offshore Mid-Norway. *In. Proc. 7th International Conference on Gas Hydrates (ICGH 2011)* (Edinburgh, Scotland, UK), 1–10.

Craig, H. (1957). Isotopic standards for carbon and oxygen and correction factors for mass-spectrometric analysis of carbon dioxide. *Geochimica Cosmochimica Acta* 12 (1–2), 133–149. doi:10.1016/0016-7037(57)90024-8

Crémière, A., Lepland, A., Chand, S., Sahy, D., Condon, D. J., Noble, S. R., et al. (2016). Timescales of methane seepage on the Norwegian margin following collapse of the Scandinavian Ice Sheet. *Nat. Commun.* 7, 11509. doi:10.1038/ncomms11509

de Beer, D., Sauter, E., Niemann, H., Kaul, N., Foucher, J.-P., Witte, U., et al. (2006). *In situ* fluxes and zonation of microbial activity in surface sediments of the Håkon Mosby Mud Volcano. *Limnol. Oceanogr.* 51 (3), 1315–1331. doi:10.4319/lo.2006.51.3.1315

Decker, C., Morineaux, M., Van Gaever, S., Caprais, J. C., Lichtschlag, A., Gauthier, O., et al. (2012). Habitat heterogeneity influences cold-seep macrofaunal communities within and among seeps along the Norwegian margin. Part 1: macrofaunal community structure. *Mar. Ecol.* 33 (2), 205–230. doi:10.1111/j.1439-0485.2011.00503.x

Decker, C., and Olu, K. (2012). Habitat heterogeneity influences cold-seep macrofaunal communities within and among seeps along the Norwegian margin. Part 2: contribution of chemosynthesis and nutritional patterns. *Mar. Ecol.* 33 (2), 231–245. doi:10.1111/j.1439-0485.2011.00486.x

Donval, J. P., Charlou, J. L., and Lucas, L. (2008). Analysis of light hydrocarbons in marine sediments by headspace technique: optimization using design of experiments. *Chemom. Intelligent Laboratory Syst.* 94 (2), 89–94. doi:10.1016/j.chemolab.2008.06.010

Felden, J., Wenhhöfer, F., Feseker, T., and Boetius, A. (2010). Transport and consumption of oxygen and methane in different habitats of the Håkon Mosby Mud Volcano (HMMV). *Limnol. Oceanogr.* 55 (6), 2366–2380. doi:10.4319/lo.2010.55.6.2366

Field, M. E., and Jennings, A. E. (1987). Seafloor gas seeps triggered by a northern California earthquake. *Mar. Geol.* 77 (1–2), 39–51. doi:10.1016/0025-3227(87)90082-x

Foucher, J.-P., Westbrook, G. K., Boetius, A., Ceramicola, S., Dupré, S., Mascle, J., et al. (2009). Structure and drivers of hydrocarbon seep ecosystems in the European seas: an

overview from HERMES results. *Oceanography* 22 (1), 92–109. doi:10.5670/oceanog.2009.11

Foucher, J. P., Dupré, S., Scalabrin, C., Feseker, T., Harmegnies, F., and Nouzé, H. (2010). Changes in seabed morphology, mud temperature and free gas venting at the Håkon Mosby Mud Volcano, offshore Northern Norway, over the time period 2003-2006. *Geo-Marine Lett.* 30, 157–167. doi:10.1007/s00367-010-0193-z

Fritz, P., and Smith, D. G. W. (1970). The isotopic composition of secondary dolomites. *Geochimica Cosmochimica Acta* 34 (11), 1161–1173. doi:10.1016/0016-7037(70)90056-6

Gay, A., and Berndt, C. (2007). Cessation/reactivation of polygonal faulting and effects on fluid flow in the Vøring Basin, Norwegian Margin. *J. Geol. Soc. Lond.* 164, 129–141. doi:10.1144/0016-76492005-178

Gebruk, A. V., Krylova, E. M., Lein, A. Y., Vinogradov, G. M., Anderson, E., Pimenov, N. V., et al. (2003). Methane seep community of the Håkon Mosby mud volcano (the Norwegian Sea): composition and trophic aspects. *Sarsia* 88 (6), 394–403. doi:10.1080/00364820310003190

Grossman, E. L., and Ku, T.-L. (1986). Oxygen and carbon isotope fractionation in biogenic aragonite: temperature effects. *Chem. Geol. Isot. Geosci. Sect.* 59 (0), 59–74. doi:10.1016/0168-9622(86)90057-6

Haflidason, H., Lien, R., Sejrup, H. P., Forsberg, C. F., and Bryn, P. (2005). The dating and morphometry of the Storegga Slide. *Mar. Petroleum Geol.* 22 (1), 123–136. doi:10.1016/j.marpetgeo.2004.10.008

Heaton, T. J., Butzin, M., Bard, E., Bronk Ramsey, C., Hughen, K. A., Köhler, P., et al. (2023). Marine radiocarbon calibraiton in polar regions: a simple approximate approach using Marine20. *Radiocarbon*, 1–28. doi:10.1017/RDC.2023.42

Heaton, T. J., Köhler, P., Butzin, M., Bard, E., Reimer, R. W., Austin, W. E. N., et al. (2020). Marine20—the marine radiocarbon age calibration curve (0–55,000 cal BP). *Radiocarbon* 62 (4), 779–820. doi:10.1017/RDC.2020.68

Hjelstuen, B., Haflidason, H., Sejrup, H., and Nygård, A. (2010). Sedimentary and structural control on pockmark development—evidence from the Nyegga pockmark field, NW European margin. *Geo-Marine Lett.* 30 (3), 221–230. doi:10.1007/s00367-009-0172-4

Hovland, M., Heggland, R., De Vries, M. H., and Tjelta, T. I. (2010). Unit-pockmarks and their potential significance for predicting fluid flow. *Mar. Petroleum Geol.* 27 (6), 1190–1199. doi:10.1016/j.marpetgeo.2010.02.005

Hovland, M., Svensen, H., Forsberg, C. F., Johansen, H., Fichler, C., Fosså, J. H., et al. (2005). Complex pockmarks with carbonate-ridges off mid-Norway: products of sediment degassing. *Mar. Geol.* 218 (1–4), 191–206. doi:10.1016/j.margeo.2005.04.005

Hovland, M., and Svensen, H. (2006). Submarine pingoes: indicators of shallow gas hydrates in a pockmark at Nyegga, Norwegian Sea. *Mar. Geol.* 228 (1), 15–23. doi:10.1016/j.margeo.2005.12.005

Hughes, A. L. C., Gyllencreutz, R., Lohne, Ø. S., Mangerud, J., and Svendsen, J. I. (2016). The last Eurasian ice sheets – a chronological database and time-slice reconstruction, DATED-1. *Boreas* 45 (1), 1–45. doi:10.1111/bor.12142

Hustoft, S., Bünz, S., and Mienert, J. (2010). Three-dimensional seismic analysis of the morphology and spatial distribution of chimneys beneath the Nyegga pockmark field, offshore mid-Norway. *Basin Res.* 22 (4), 465–480. doi:10.1111/j.1365-2117.2010.00486.x

Hustoft, S., Dugan, B., and Mienert, J. (2009). Effects of rapid sedimentation on developing the Nyegga pockmark field: constraints from hydrological modeling and 3-D seismic data, offshore mid-Norway. *Geochem. Geophys. Geosystems* 10. doi:10.1029/2009gc002409

Hustoft, S., Mienert, J., Bünz, S., and Nouzé, H. (2007). High-resolution 3D-seismic data indicate focussed fluid migration pathways above polygonal fault systems of the mid-Norwegian margin. *Mar. Geol.* 245 (1–4), 89–106. doi:10.1016/j.margeo.2007.07.004

Ivanov, M. K., Blinova, V., Kozlova, E., Westbrook, G. K., Mazzini, A., Minshull, T. A., et al. (2007). First sampling of gas hydrate from the Vøring Plateau. *Eos, Trans. Am. Geophys. Union* 88 (19), 209–212. doi:10.1029/2007EO190001

Ivanov, M., Mazzini, A., Blinova, V., Kozlova, E., Laberg, J.-S., Matveeva, T., et al. (2010). Seep mounds on the southern Vøring Plateau (offshore Norway). *Mar. Petroleum Geol.* 27 (6), 1235–1261. doi:10.1016/j.marpetgeo.2009.11.009

Jerosch, K., Schlüter, M., Foucher, J.-P., Allais, A.-G., Klages, M., and Edy, C. (2007). Spatial distribution of mud flows, chemoautotrophic communities, and biogeochemical habitats at Håkon Mosby Mud Volcano. *Mar. Geol.* 243 (1-4), 1–17. doi:10.1016/j.margeo.2007.03.010

Judd, A. G., and Hovland, M. (2007). *Seabed fluid flow. The impact on geology, biology and the marine environment*. Cambridge: Cambridge University Press.

Karstens, J., and Berndt, C. (2015). Seismic chimneys in the Southern Viking Graben – implications for palaeo fluid migration and overpressure evolution. *Earth Planet. Sci. Lett.* 412 (0), 88–100. doi:10.1016/j.epsl.2014.12.017

Karstens, J., Haflidason, H., Becker, L. W. M., Berndt, C., Rüpke, L., Planke, S., et al. (2018). Glacigenic sedimentation pulses triggered post-glacial gas hydrate dissociation. *Nat. Commun.* 9 (1), 635. doi:10.1038/s41467-018-03043-z

Karstens, J., Haflidason, H., Berndt, C., and Crutchley, G. J. (2023). Revised Storegga Slide reconstruction reveals two major submarine landslides 12,000 years apart. *Commun. Earth Environ.* 4 (1), 55. doi:10.1038/s43247-023-00710-y

Keigwin, L. D., and Boyle, E. A. (2008). Did North Atlantic overturning halt 17,000 years ago? *Paleoceanography* 23 (1), PA1101. doi:10.1029/2007pa001500

Kim, S.-T., and O'Neil, J. R. (1997). Equilibrium and nonequilibrium oxygen isotope effects in synthetic carbonates. *Geochimica Cosmochimica Acta* 61 (16), 3461–3475. doi:10.1016/S0016-7037(97)00169-5

King, L. H., and MacLean, B. (1970). Pockmarks on the scotian shelf. *Geol. Soc. Am. Bull.* 81 (10), 3141–3148. doi:10.1130/0016-7606(1970)81[3141:POTSS]2.0.CO;2

Kroopnick, P. (1980). The distribution of 13C in the atlantic ocean. *Earth Planet. Sci. Lett.* 49 (2), 469–484. doi:10.1016/0012-821X(80)90088-6

Krylova, E. M., Gebruk, A. V., Portnova, D. A., Todt, C., and Haflidason, H. (2011). New species of the genus Isorropodon (Bivalvia: vesicomyidae: pliocardiinae) from cold methane seeps at Nyegga (Norwegian sea, voring plateau, storrega slide). *J. Mar. Biol. Assoc. U. K.* 91 (5), 1135–1144. doi:10.1017/s002531541100004x

Liu, X., and Flemings, P. B. (2007). Dynamic multiphase flow model of hydrate formation in marine sediments. *J. Geophys. Res. Solid Earth* 112 (B3), B03101. doi:10.1029/2005jb004227

Mazzini, A., Aloisi, G., Akhmanov, G. G., Parnell, J., Cronin, B. T., and Murphy, P. (2005). Integrated petrographic and geochemical record of hydrocarbon seepage on the Vøring Plateau. *J. Geol. Soc.* 162 (5), 815–827. doi:10.1144/0016-764904-133

Mazzini, A., Svensen, H. H., Forsberg, C. F., Linge, H., Lauritzen, S.-E., Haflidason, H., et al. (2017). A climatic trigger for the giant Troll pockmark field in the northern North Sea. *Earth Planet. Sci. Lett.* 464, 24–34. doi:10.1016/j.epsl.2017.02.014

Mazzini, A., Svensen, H., Hovland, M., and Planke, S. (2006). Comparison and implications from strikingly different authigenic carbonates in a Nyegga complex pockmark, G11, Norwegian Sea. *Mar. Geol.* 231 (1–4), 89–102. doi:10.1016/j.margeo.2006.05.012

Meunier, C., Andersen, A. C., Bruneaux, M., Le Guen, D., Terrier, P., Leize-Wagner, E., et al. (2010). Structural characterization of hemoglobins from Monilifera and Frenulata tubeworms (Siboglinids): first discovery of giant hexagonal-bilayer hemoglobin in the former "Pogonophora" group. *Comp. Biochem. Physiology Part A Mol. Integr. Physiology* 155 (1), 41–48. doi:10.1016/j.cbpa.2009.09.010

Mienert, J., Posewang, J., and Baumann, M. (1998). Gas hydrates along the northeastern Atlantic margin: possible hydrate-bound margin instabilities and possible release of methane. *Geol. Soc. Lond. Special Publ.* 137, 275–291. doi:10.1144/gsl.Sp.1998.137.01.22

Nickel, J. C., di Primio, R., Mangelsdorf, K., Stoddart, D., and Kallmeyer, J. (2012). Characterization of microbial activity in pockmark fields of the SW-Barents Sea. *Mar. Geol.* 332-334, 152–162. doi:10.1016/j.margeo.2012.02.002

Nouzé, H., Contrucci, I., Foucher, J.-P., Marsset, B., Thomas, Y., Thereau, E., et al. (2004). Premiers résultats d'une étude géophysique sur le flanc nord des glissements de Storegga (Norvège). *Comptes Rendus Geosci.* 336 (13), 1181–1189. doi:10.1016/j.crte.2004.06.005

Nouzé, H., Contrucci, I., Foucher, J.-P., Thomas, T., Marsset, B., Normand, A., et al. (2002). Cruise report HYDRATECH 2002. High resolution 2D et 3D seismic survey in the Storegga area. Available at: https://w3.ifremer.fr/archimer/doc/00433/54446/55810.pdf. 75.

Nouzé, H., Fabri, M.-C., and l'équipe scientifique embarquée (2007). Vicking cruise report. Cold seeps on the Norwegian margin. Associated Ecosystem. R/V Pourquoi Pas ? May 19th-June 18th, 2006. Alesund-Alesund. Available at: https://w3.ifremer.fr/archimer/doc/00433/54465/55840.pdf. 191.

Olu-Le Roy, K., Caprais, J. C., Fifis, A., Fabri, M. C., Galéron, J., Budzinsky, H., et al. (2007). Cold-seep assemblages on a giant pockmark off West Africa: spatial patterns and environmental control. *Mar. Ecol.* 28 (1), 115–130. doi:10.1111/j.1439-0485.2006.00145.x

Paull, C. K., Ussler, W., Holbrook, W. S., Hill, T. M., Keaten, R., Mienert, J., et al. (2008). Origin of pockmarks and chimney structures on the flanks of the Storegga Slide, offshore Norway. *Geo-Marine Lett.* 28 (1), 43–51. doi:10.1007/s00367-007-0088-9

Plaza-Faverola, A., Bünz, S., and Mienert, J. (2011). Repeated fluid expulsion through sub-seabed chimneys offshore Norway in response to glacial cycles. *Earth Planet. Sci. Lett.* 305 (3–4), 297–308. doi:10.1016/j.epsl.2011.03.001

Plaza-Faverola, A., Bünz, S., and Mienert, J. (2012). The free gas zone beneath gas hydrate bearing sediments and its link to fluid flow: 3-D seismic imaging offshore mid-Norway. *Mar. Geol.* 291–294 (0), 211–226. doi:10.1016/j.margeo.2011.07.002

Plaza-Faverola, A., Westbrook, G. K., Ker, S., Exley, R. J. K., Gailler, A., Minshull, T. A., et al. (2010). Evidence from three-dimensional seismic tomography for a substantial accumulation of gas hydrate in a fluid-escape chimney in the Nyegga pockmark field, offshore Norway. *J. Geophys. Res.* 115 (B8), B08104. doi:10.1029/2009jb007078

Reiche, S., Hjelstuen, B. O., and Haflidason, H. (2011). High-resolution seismic stratigraphy, sedimentary processes and the origin of seabed cracks and pockmarks at Nyegga, mid-Norwegian margin. *Mar. Geol.* 284 (1-4), 28–39. doi:10.1016/j.margeo.2011.03.006

Riboulot, V., Sultan, N., Imbert, P., and Ker, S. (2016). Initiation of gas-hydrate pockmark in deep-water Nigeria: geo-mechanical analysis and modelling. *Earth Planet. Sci. Lett.* 434, 252–263. doi:10.1016/j.epsl.2015.11.047

Rise, L., Ottesen, D., Longva, O., Solheim, A., Andersen, E. S., and Ayers, S. (2006). The Sklinnadjupet slide and its relation to the Elsterian glaciation on the mid-Norwegian margin. *Mar. Petroleum Geol.* 23 (5), 569–583. doi:10.1016/j.marpetgeo.2006.05.005

Sibuet, M., and Olu, K. (1998). Biogeography, biodiversity and fluid dependence of deep-sea cold-seep communities at active and passive margins. *Deep Sea Res. Part II Top. Stud. Oceanogr.* 45 (1-3), 517–567. doi:10.1016/S0967-0645(97)00074-X

Smirnov, R. V. (2000). Two new species of Pogonophora from the arctic mud volcano off northwestern Norway. *Sarsia* 85 (2), 141–150. doi:10.1080/00364827.2000.10414563

Solheim, A., Berg, K., Forsberg, C. F., and Bryn, P. (2005). The Storegga Slide complex: repetitive large scale sliding with similar cause and development. *Mar. Petroleum Geol.* 22 (1–2), 97–107. doi:10.1016/j.marpetgeo.2004.10.013

Stuiver, M., and Reimer, P. J. (1993). Extended 14C data base and revised CALIB 3.0 14C age calibration program. *Radiocarbon* 35 (1), 215–230. doi:10.1017/S0033822200013904

Tarutani, T., Clayton, R. N., and Mayeda, T. K. (1969). The effect of polymorphism and magnesium substitution on oxygen isotope fractionation between calcium carbonate and water. *Geochimica Cosmochimica Acta* 33 (8), 987–996. doi:10.1016/0016-7037(69)90108-2

Ussler, W., and Paull, C. K. (1995). Effects of ion exclusion and isotopic fractionation on pore water geochemistry during gas hydrate formation and decomposition. *Geo-Marine Lett.* 15 (1), 37–44. doi:10.1007/BF01204496

Vanreusel, A., Andersen, A. C., Boetius, A., Connelly, D., Cunha, M. R., Decker, C., et al. (2009). Biodiversity of cold seep ecosystems along the European Margins. *Oceanography* 22 (1), 110–127. doi:10.5670/oceanog.2009.12

Vogt, P. R., Crane, K., Sundvor, E., Hjelstuen, B. O., Gardner, J., Bowles, F., et al. (1999a). Ground-truthing 11- to 12-kHz side-scan sonar imagery in the Norwegian–Greenland Sea: part II: probable diapirs on the Bear Island fan slide valley margins and the Voring Plateau. *Geo-Marine Lett.* 19, 111–130. doi:10.1007/s003670050099

Vogt, P. R., Gardner, J., Crane, K., Sundvor, E., Bowles, F., and Cherkashev, G. (1999c). Ground-truthing 11- to 12-kHz side-scan sonar imagery in the Norwegia–Greenland Sea: part I: pockmarks on the Vestnesa Ridge and Storegga slide margin. *Geo-Marine Lett.* 19 (1), 97–110. doi:10.1007/s003670050098

Vogt, P. R., Gardner, J., and Crane, K. (1999b). The Norwegian–Barents–Svalbard (NBS) continental margin: introducing a natural laboratory of mass wasting, hydrates, and ascent of sediment, pore water, and methane. *Geo-Marine Lett.* 19 (1), 2–21. doi:10.1007/s003670050088

Waite, W. F., Santamarina, J. C., Cortes, D. D., Dugan, B., Espinoza, D. N., Germaine, J., et al. (2009). Physical properties of hydrate-bearing sediments. *Rev. Geophys.* 47 (4). doi:10.1029/2008RG000279

Westbrook, G. K., Chand, S., Rossi, G., Long, C., Bünz, S., Camerlenghi, A., et al. (2008). Estimation of gas hydrate concentration from multi-component seismic data at sites on the continental margins of NW Svalbard and the Storegga region of Norway. *Mar. Petroleum Geol.* 25 (8), 744–758. doi:10.1016/j.marpetgeo.2008.02.003

Whiticar, M. J. (1999). Carbon and hydrogen isotope systematics of bacterial formation and oxidation of methane. *Chem. Geol.* 161 (1–3), 291–314. doi:10.1016/S0009-2541(99)00092-3

Whiticar, M. J., and Faber, E. (1986). Methane oxidation in sediment and water column environments—isotope evidence. *Org. Geochem.* 10 (4–6), 759–768. doi:10.1016/S0146-6380(86)80013-4

frontiers | Frontiers in Marine Science

TYPE Original Research
PUBLISHED 20 October 2023
DOI 10.3389/fmars.2023.1197338

Check for updates

OPEN ACCESS

EDITED BY
Mark Alexander Lever,
The University of Texas at Austin,
United States

REVIEWED BY
Maria Pachiadaki,
Woods Hole Oceanographic Institution,
United States
Lauren M. Seyler,
Stockton University, United States

*CORRESPONDENCE
Kerry L. McPhail
kerry.mcphail@oregonstate.edu
Andrew R. Thurber
andrew.thurber@oregonstate.edu

RECEIVED 30 March 2023
ACCEPTED 03 October 2023
PUBLISHED 20 October 2023

CITATION
Redick MA, Cummings ME, Neuhaus GF, Ardor Bellucci LM, Thurber AR and McPhail KL (2023) Integration of untargeted metabolomics and microbial community analyses to characterize distinct deep-sea methane seeps. *Front. Mar. Sci.* 10:1197338. doi: 10.3389/fmars.2023.1197338

COPYRIGHT
© 2023 Redick, Cummings, Neuhaus, Ardor Bellucci, Thurber and McPhail. This is an open-access article distributed under the terms of the Creative Commons Attribution License (CC BY). The use, distribution or reproduction in other forums is permitted, provided the original author(s) and the copyright owner(s) are credited and that the original publication in this journal is cited, in accordance with accepted academic practice. No use, distribution or reproduction is permitted which does not comply with these terms.

Integration of untargeted metabolomics and microbial community analyses to characterize distinct deep-sea methane seeps

Margaret A. Redick[1], Milo E. Cummings[2], George F. Neuhaus[1], Lila M. Ardor Bellucci[3], Andrew R. Thurber[2,3]* and Kerry L. McPhail[1]*

[1]Department of Pharmaceutical Sciences, College of Pharmacy, Oregon State University, Corvallis, OR, United States, [2]Department of Microbiology, College of Science, Oregon State University, Corvallis, OR, United States, [3]College of Earth, Ocean, and Atmospheric Sciences, Oregon State University, Corvallis, OR, United States

Deep-sea methane seeps host highly diverse microbial communities whose biological diversity is distinct from other marine habitats. Coupled with microbial community analysis, untargeted metabolomics of environmental samples using high resolution tandem mass spectrometry provides unprecedented access to the unique specialized metabolisms of these chemosynthetic microorganisms. In addition, the diverse microbial natural products are of broad interest due to their potential applications for human and environmental health and well-being. In this exploratory study, sediment cores were collected from two methane seeps (-1000 m water depth) with very different gross geomorphologies, as well as a non-seep control site. Cores were subjected to parallel metabolomic and microbial community analyses to assess the feasibility of representative metabolite detection and identify congruent patterns between metabolites and microbes. Metabolomes generated using high resolution liquid chromatography tandem mass spectrometry were annotated with predicted structure classifications of the majority of mass features using SIRIUS and CANOPUS. The microbiome was characterized by analysis of 16S rRNA genes and analyzed both at the whole community level, as well as the small subgroup of Actinobacteria, which are known to produce societally useful compounds. Overall, the younger Dagorlad seep possessed a greater abundance of metabolites while there was more variation in abundance, number, and distribution of metabolites between samples at the older Emyn Muil seep. Lipid and lipid-like molecules displayed the greatest variation between sites and accounted for a larger proportion of metabolites found at the older seep. Overall, significant differences in composition of the microbial community mirrored the patterns of metabolite diversity within the samples; both varied greatly as a function of distance from methane seep, indicating a deterministic role of seepage. Interdisciplinary research to understand microbial and metabolic

diversity is essential for understanding the processes and role of ubiquitous methane seeps in global systems and here we increase understanding of these systems by visualizing some of the chemical diversity that seeps add to marine systems.

KEYWORDS

methane seep, deep-sea, untargeted metabolomics, microbial community, tandem mass spectrometry, environmental analysis

1 Introduction

Methane seeps are areas where methane leaks from vast subseafloor reservoirs, fueling dense communities of organisms. Methane seep communities, including endemic microorganisms and animals, either harness the chemical energy being released from the seafloor directly or through symbiosis, or make use of the habitat (both physical and chemical) created by seep biological processes. Alongside endemic species, methane seeps host organisms that are found throughout the margin, including species that are harvested commercially (Grupe et al., 2015; Seabrook et al., 2019). The seeps themselves are a mosaic of different habitats with varying biogeochemistry and fauna (Boetius and Suess, 2004; Bernardino et al., 2012) in which communities change over time. Over the geologic time scales that methane seepage can occur, the metabolic activity of microbial communities results in carbonate precipitation that can pave vast areas of the seafloor (Cordes et al., 2009; Bowden et al., 2013). The resulting hard substrate, termed authigenic carbonate, provides for attachment and growth of anemones, sponges, and corals at mature methane seep sites in the otherwise expansive soft sediment of the deep ocean. Methane seeps enhance biological diversity of the ocean margin by producing substrate, hosting divergent biological processes and biogeochemistry, and contributing significantly to primary production in the deep ocean. Here we add to this foundational knowledge by revealing chemical diversity, which has implications for future societal use.

Methane seeps comprise a diversity of habitats in close proximity, creating a unique opportunity for natural products (NPs) discovery. The high biological diversity of seeps is illustrated in a recent study focused on the habitat along the Oregon and Washington margins in which more than 72,000 different amplicon sequence variants (ASVs) were documented from six seep and non-seep collection sites, plus a control site (Cummings et al., 2023). At the three methane seep sites sampled, 11,631 different amplicon sequence variants (ASVs) were present only in the on-seep core samples. While on-seep cores had relatively low Chao1 diversity values, with a mean of 452 ± 204 for Emyn Muil and Dagorlad seeps, the 5m off-seep cores had local peaks in diversity with values of 861 ± 162. Even in earlier studies where ASVs with 97% similarity are combined into Operational Taxonomic Units (OTUs), more than 30,000 distinct OTUs have been measured at methane seep habitats (Seabrook et al., 2018).

Oxygen, sulfide (toxic to most animals), and redox gradients typify seep habitats, and the microbial communities reflect this diverse environment through an abundance of metabolic pathways, including aerobic methane oxidation, anaerobic oxidation of methane, sulfate reduction, sulfide oxidation, manganese and iron reduction, and nitrogen fixation (Levin, 2005; Reeburgh, 2007; Knittel and Boetius, 2009; Dekas et al., 2014). Sediment communities, including those at seeps, use or must exist in the presence of metabolites produced by co-occurring taxa as defense chemicals, transient chemical signals, and/or in a multitude of possible undefined ecological roles (Dekas et al., 2016; Patin et al., 2017).

Knowledge of the diverse metabolic strategies at methane seeps resulting in a diversity of pathways involved in cellular energy production and compound biosynthesis is far from comprehensive. Most studies investigating environmental microbiomes have focused on phylogenetic identity and abundance of microbial community members, without metabolomic analyses or testing for biological activity or potential ecological roles. Technological advances in high resolution mass spectrometry and associated data analysis tools have facilitated and been driven further by targeted and untargeted metabolomics coupled to microbial community analysis in microbiome studies (Bauermeister et al., 2022), with applications in human health (Aleti et al., 2022; Zhang et al., 2023) and agriculture (Rothman et al., 2019; Sun et al., 2022; Nie et al., 2023). With continued development of computational methods to annotate structurally complex specialized metabolites in complex mixtures (Morehouse et al., 2023), these integrated approaches are increasingly applicable to detection and structural annotation of microbial specialized metabolites in environmental microbiome samples (Shaffer et al., 2022), although structural annotations in untargeted mass spectrometry experiments are putative assignments of structural class or planar molecular structure that require follow-up for valid molecular structure characterization.

Limited material from environmental sampling poses a challenge for traditional NP isolations of new compounds for structure elucidation and biological activity testing. However, untargeted metabolomics analyses of environmental samples using high resolution liquid chromatography tandem mass spectrometry ($LCMS^2$) may require only nanograms of chemical extract from milligrams of collected sample. This approach provides data for comparative analyses when working with limited materials. Importantly, the identities of metabolites detected via untargeted

analyses remain largely unknown, with an estimated 10% average annotation rate possible using LCMS spectral databases and computational prediction tools (de Jonge et al., 2022).

Untargeted LCMS^2 surveys coupled with computational tools permit generation of hypotheses from exploratory data to direct further investigation and prioritization of organisms or metabolites for targeted analyses. Open access tools such as GNPS, SIRIUS, and CANOPUS enable predictions of metabolite structure or structure class based on tandem mass spectrometry (MS^2) fragmentation patterns. GNPS is a web-based mass spectrometry platform for sharing and comparative networking of MS^2 data (Wang et al., 2016). The downloadable software framework SIRIUS (Dührkop et al., 2021) incorporates CSI : FingerID and CANOPUS for prediction of molecular formulas and structure classifications using MS^1 isotope and MS^2 fragmentation patterns (Djoumbou Feunang et al., 2016; Kim et al., 2021). Here we present the results of a coupled metabolome-microbiome approach using untargeted high-resolution LCMS^2 analysis and bacterial 16S rRNA amplicon sequencing of environmental samples to assess metabolite detection and explore the chemical and biological relationships between two methane seep habitats that differ significantly in their gross morphology (Figure 1). The 16S rRNA sequence data used for our comparative analyses of the Emyn Muil and Dagorlad methane seeps comprise a subset of the larger ASV dataset reported by Cummings et al. (2023).

The Dagorlad seep site is an expansive microbial mat, likely indicative of a recent onset of seepage, and the Emyn Muil seep site is a large carbonate outcrop consistent with seepage that has been ongoing for hundreds to thousands of years. These two sites potentially represent the opposite ends of seep succession. By comparison with nearby off-seep habitats, as well as a deep-sea non-seep control site, we address the overarching question of whether different seep microbiomes can be distinguished by untargeted metabolomics of environmental samples. We also present a correlation analysis of the subset of putative peptides with actinobacterial 16S rRNA sequence since Actinobacteria are well-known to produce biologically active peptides (Zhao et al., 2018). Our results thus may provide preliminary insight on the potential for discovery of new biotechnological or biopharmaceutical compounds from deep-sea methane seeps. Our long term goal is to better understand the role of seeps in marine biological diversity and future pharmaceutical and biotechnological research.

2 Methods

2.1 Sample collection

Sediment cores were collected from two methane seeps along the Cascadia Margin using the *ROV* Hercules on *E/V* Nautilus cruise NA121, in partnership with the Ocean Exploration Trust. Here we focused on one core collected directly at the seep and one core collected 5 m away from areas of active seepage at each of two contrasting seep sites (Figure 1). These areas of active seepage had the highest microbial diversity present in the region (Cummings et al., 2023). An additional core from the Slope Base site of the Ocean Observatories Initiative (OOI) Regional Cabled Array was collected at a water depth of 2,900 m by *ROV* JASON during routine maintenance of the site (44.5152°N, -125.3898°W). The OOI site located 300 km south of the other sampling sites was included to compare a deeper non-seep site in the same geographical region. Sediment push cores were extruded shipboard and sectioned into 1 cm-thick sections ranging from 0 (surface) to 10 cm deep in the core, with the exterior discarded to prevent sediment smearing from impacting the measured microbial community and metabolome. Core sections were

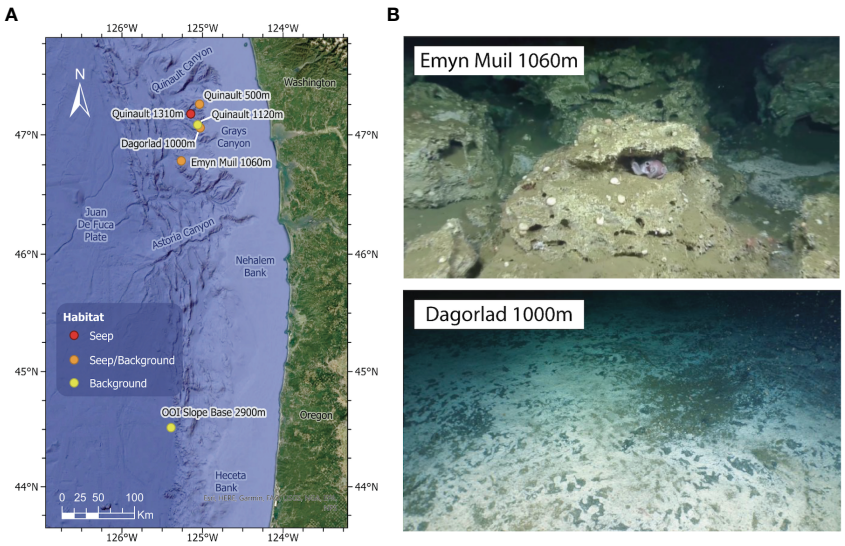

FIGURE 1
(A) Map indicating the locations of the three sampling sites (older seep Emyn Muil, younger seep Dagorlad, OOI Slope Base control). The two seeps are approximately 50 miles off the Washington coast on the Juan de Fuca Plate. **(B)** Images of the two methane seep sites sampled: upper is the older seep, Emyn Muil (1,060 m), characterized by carbonate deposits; lower is the younger seep, Dagorlad (1,000 m), characterized by soft sediments and extensive microbial mats. This figure is reproduced in part with permission from Cummings et al. (2023, https://doi.org/10.7717/peerj.15119/fig-1).

subdivided for metabolite and 16S rRNA analysis and frozen at -80°C until analysis. Samples for metabolite profiling were only handled with metal core slicing devices and were stored frozen in glass vials.

2.2 Microbial community analysis

Microbial analysis of sediment samples was performed as described in Seabrook et al. (2018). In brief, DNA was extracted from ~ 0.5 g frozen sediment using the QIAgen PowerSoil kit according to the kit protocol. The V4 region of the 16S rRNA gene was amplified and sequenced following the Earth Microbiome protocol, including the updated primers (Parada et al., 2016). Sequencing was carried out at the Oregon State University Center for Quantitative Life Sciences on the Illumina MiSeq platform, with 250-bp paired-end reads. Bioinformatics of the 16S rRNA analysis was carried out as part of a larger study using a Qiime2 pipeline as described in Cummings et al. (2023). The actinobacterial taxa from the resulting ASV table were selected for separate analyses.

2.3 Chemical extraction and LCMS^2

Each sediment core subsection (48 in total) was lyophilized, resuspended in HPLC grade methanol (15 mL), sonicated (30 min) and left to extract overnight at room temperature. The solvent supernatants were then filtered using 0.2 µM PTFE syringe filters, dried *in vacuo*, and the resulting 48 extracts were weighed. High-resolution LCMS^2 profiling of all samples was performed using an Agilent 1260 Infinity II LC system with detection by an Agilent 6545 TOF mass spectrometer. For this analysis, the sample extracts were reconstituted at 10 mg/mL in LCMS grade methanol of which 5 µL were injected. A reversed phase C18 porous core column (Kinetex C18, 50 x 2.1 mm, 2.6 µm particle size, 100 Å pore size, Phenomenex, Torrance, USA) was used for chromatographic separation. A binary gradient system with mobile phase consisting of H_2O (solvent A) and acetonitrile (ACN, solvent B), and flow rate of 0.4 mL/min was used. After injection, the samples were eluted with a linear gradient from 0-5.5 min at 15% B, 5.5-15 min 15-80% B, 15-20 min 100% B. Initially the first 5.5 minutes were sent to waste but as no peaks were seen until after 8 minutes, 7.5 min of eluent was sent to waste to divert salt from the mass spectrometer for subsequent runs. Data dependent acquisition (DDA) of MS^2 spectra was performed in positive mode.

2.4 Chemoinformatic analysis of metabolomic data

For LCMS^2 data analysis, raw data (Agilent .d format) were converted to .mzML files using MSconvert (ProteoWizard); data pre-processing to extract MS^1 and MS^2 features was performed using MZmine3 (Pluskal et al., 2010). The parameters used in MZmine3 are listed in Supplementary Table S1. Mass spectrometric data are available via MassIVE (MassIVE ID MSV000090543) (MassIVE, n.d.). The MZmine3 peak list was exported as an .mgf file and uploaded to SIRIUS 5 GUI (Dührkop et al., 2019). SIRIUS (Dührkop et al., 2019), CSI : FingerID (Dührkop et al., 2015), and CANOPUS (Djoumbou Feunang et al., 2016; Dührkop et al., 2021; Kim et al., 2021) analyses were performed using the parameters in Supplementary Table S2. The MZmine3 generated feature list and quantification table were also analyzed using the GNPS platform (Wang et al., 2016). Peak areas of LCMS (MS1) features were summed by CANOPUS-assigned NPClassifier pathways to generate a pie chart for each core, representing the distribution of features across major structure classes (Figure 2). The fatty acid and terpenoid pathways were combined to form "Lipids and Lipid-like molecules". Peak areas of LCMS (MS^1) features were summed by CANOPUS-assigned NPClassifier pathways and stacked bar plots (Figure 3) showing the proportions of each pathway by core/depth were generated using the R package ggplot2 (Torondel et al., 2016; Wickham et al., 2019; R Core Team, 2022).

2.5 Statistical analyses of microbial and metabolomic data

Comparative analyses were performed on the microbial ASV, actinobacterial ASV, and LCMS ion feature peak area datasets using multivariate analysis in PRIMER v7 (Clarke and Gorley, 2015). Data were Log(X+1) transformed and Bray-Curtis similarity was used to construct a resemblance matrix. Significant patterns in the resulting data were identified via similarity profile (SIMPROF) analysis, which is also available in R package. SIMPROF identifies significant differences within datasets without *a priori* groupings and without an arbitrary cutoff of overall similarity. We used a significance level for SIMPROF groupings of 5%. We generated SIMPROF groupings for each MS^2, total bacterial community, and actinobacteria only. We also visualized these data using non-metric multidimensional scaling (NMDS). Data were processed to visualize significant Spearman's correlations between LCMS features and microbial ASVs in heatmaps using the R (R Core Team, 2022) script provided in the supplemental data repository and performed previously (Neuhaus et al., 2022). In brief, the MS ion feature list was filtered to generate a list containing only the subset of features annotated as potentially peptide by CANOPUS in either ontology. Correlation analysis with the family level microbial data was then performed separately for this peptidic metabolite subset in which features (microbial family or MS feature) observed in less than 10% of samples were removed prior to correlation. Microbial amplicon sequencing data were transformed to proportions by dividing the counts in each sample by the sample's total sequencing depth. The dataset was mean centered and scaled before Spearman's correlations were calculated (R package "Hmisc") between each pair (microbe~metabolite) of features. P values were adjusted according to the Benjamini-Hochberg procedure to control the false discovery rate. Adjusted p values < 0.05 were considered significant.

3 Results

High resolution LCMS^2 and 16S rRNA amplicon sequence data were curated for each of ten core sections from four sediment cores (40 samples in total). One core was collected on-seep and one core

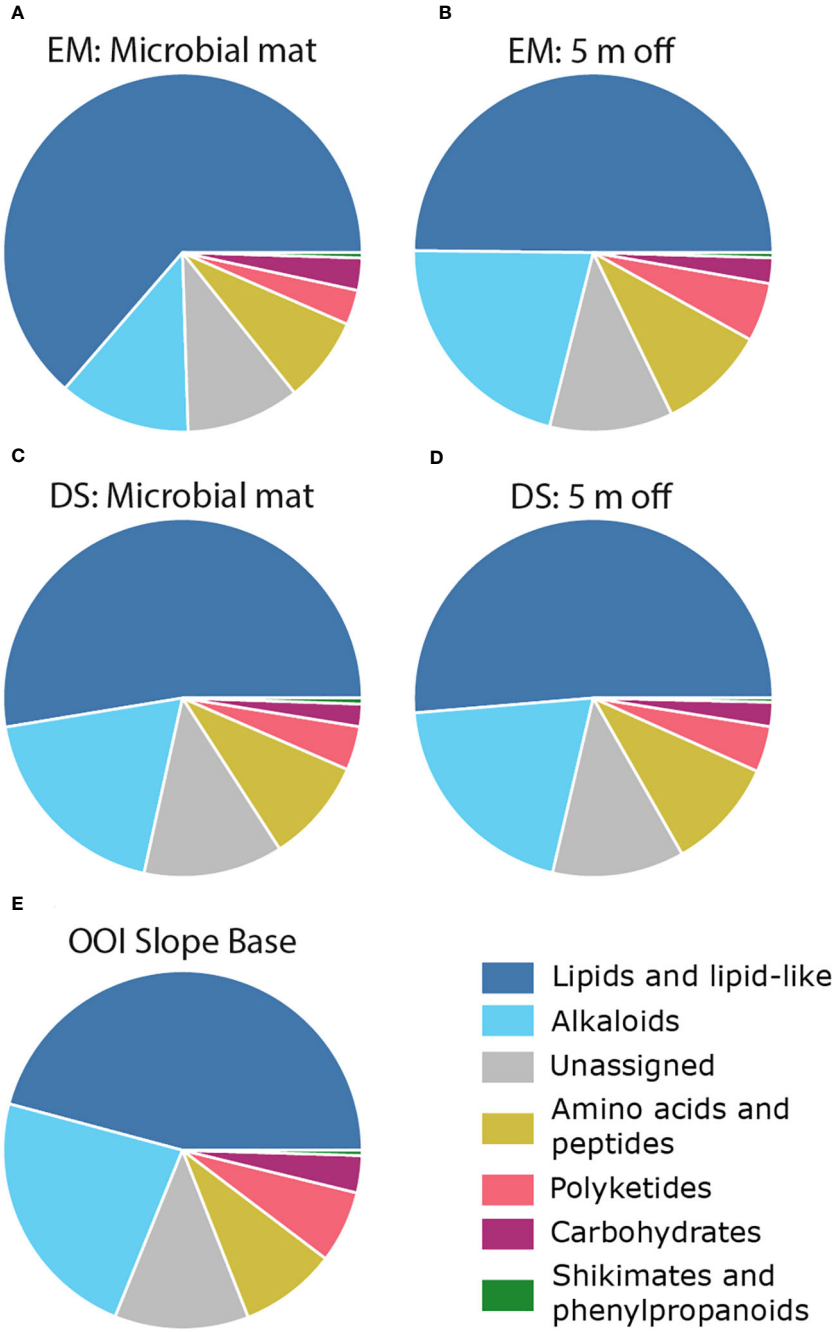

FIGURE 2
Pie charts of all MS features assigned to structural classes based on NPClassifier Pathways designated by CANOPUS. Terpenoids and fatty acids have been combined to form the class of "lipids and lipid-like" compounds. The plots display proportions based on MS^1 peak areas summed by sample collection site. **(A)** Emyn Muil (EM) on-seep microbial mat. **(B)** Emyn Muil (EM) 5 m off-seep. **(C)** Dagorlad Seep (DS) microbial mat. **(D)** Dagorlad Seep (DS) 5 m off-seep **(E)** Non-seep control site, OOI slope base 2900 m.

was collected 5 m off-seep from each of two seep sites with distinct geomorphologies (Figure 1) and variable geochemistry (Cummings et al., 2023). Paired data were similarly obtained for depth sections of a non-seep OOI core as a background control (8 samples in total). Throughout this manuscript we use the term "older" for the carbonate-dominated Emyn Muil seep and "younger" for the soft-sediment Dagorlad seep as it provides context for the results, however, we do not know the time of onset of seepage at the sites sampled. At both sites, soft sediment habitats were sampled, although the sediment cores collected from the Emyn Muil seep were next to an expansive carbonate outcrop indicative of persistent seepage in the region for hundreds to thousands of years.

3.1 Microbial community

A total of 1,423,130 sequences belonging to 17,217 microbial ASVs were detected from the four methane seep sediment cores

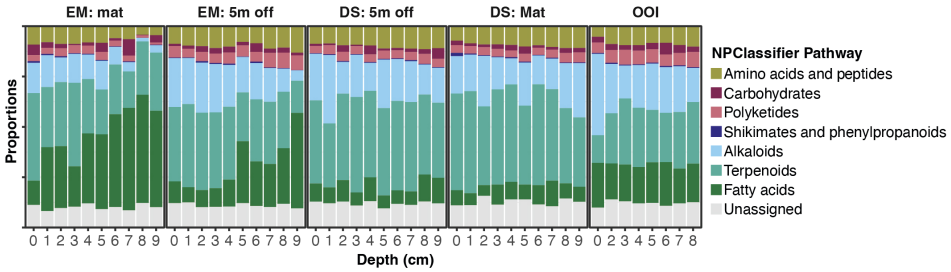

FIGURE 3
Stacked bar graphs displaying proportions of MS features assigned to structural classes based on NPClassifier Pathways designated by CANOPUS for core sections from each of the 5 different cores. EM: Mat is Emyn Muil on-seep mat core; EM: 5 m off is Emyn Muil 5 m off-seep core; DS: Mat is Dagorlad Seep on-seep mat core; DS: 5 m off is Dagorlad Seep 5 m off-seep core; OOI: non-seep is the OOI slope base core.

selected. The ASVs comprised 686 families in total. Actinobacterial sequences were a minor component of the total ASVs present. Overall, 2,046 sequences were identified within the Actinobacteria, representing 142 distinct ASVs. The Actinobacteria ASVs represented 27 families in total, although two families accounted for 85% of all ASVs, with half (54%) of those belonging to WCHB1-81 and the others falling outside of currently identifiable families.

3.2 Untargeted metabolomics

Processing of LCMS^2 raw data with MZMine3 resulted in a total of 1,304 mass features, which were assigned to 119 out of the 672 NPClassifier (Kim et al., 2021) structural classes across all seven NP biosynthetic pathways using CANOPUS (Dührkop et al., 2021). The metabolite profiles for cores from both methane seep sites (Figures 2A–D) exhibited a higher proportion of lipids and lipid-like molecules than the non-methane seep OOI site (Figure 2E). The chemistry of the microbial mat at the older seep with hard carbonate substrate clearly comprised the highest proportion of lipids and lipid-like molecules of all the sites (Figure 2A). The distribution of metabolites among NPClassifier pathways was most similar between the 5 m off-seep cores from each site (Figures 2B, D). While the relative proportion of features assigned to each structure class did not change markedly for non-lipid metabolites, the specific metabolites within each class varied significantly between sites.

Stacked bar plots of MS^1 feature peak areas summed by their NPClassifier assignments display the proportions of each biosynthetic class by depth in each core (Figure 3). The plots for both cores from Emyn Muil displayed the highest overall proportion and greatest variation in fatty acids and terpenoids, with the proportion of fatty acids generally increasing with depth in core. The on-seep microbial mat had a remarkably high proportion of fatty acids, and a concomitantly lower proportion of alkaloids and amino acids/peptides, especially with increasing depth in the core. In contrast, the Dagorlad cores displayed the lowest abundance of fatty acids with proportionally more terpenoids, and a relatively uniform distribution of metabolite biosynthetic classes between the on-seep microbial mat and 5 m off-seep cores. These data are summarized in Figure 4, in which MS feature counts, summed peak areas and NPClassifier classes are summarized in parallel for each core by depth. The older Emyn Muil seep displayed greater variability in the abundance (peak areas, Figure 4A) and number (counts, Figure 4B) of LCMS features, with deeper core sections containing fewer and less abundance of features than shallower sections. In contrast, the number and abundance of LCMS features in both the control OOI slope base and the younger Dagorlad seep samples were less variable across depths. The number of distinct metabolite structural classes annotated for each sample using the NPClassifier ontology in CANOPUS was also determined and revealed consistent trends with depth (Figure 4C). Comparison of the shallower samples at the two seep sites revealed similar numbers and abundance of LCMS features (Figures 4A, B), with fewer structural classes assigned within the deeper samples from the older Emyn Muil seep (Figure 4C).

3.3 Integrated analysis of microbial and metabolite data

Separate NMDS plots of total microbial ASV and MS^1 data for all core samples exhibited corresponding patterns of variation. The subset of actinobacterial ASV abundances was also analyzed separately from the rest of the microbial ASV data because of the known capacity of Actinobacteria for specialized metabolism, resulting in structurally diverse compounds with antibiotic and other biological activities (Zhao et al., 2018).

Greatest variability in both metabolites (Figure 5A) and microbes (Figure 5B) was evident around the older carbonate Emyn Muil seep compared to the relatively clustered samples of the younger soft sediment Dagorlad seep, and the distinct microbial community and chemistry of the non-seep OOI slope base. We note that each point represents both a core location and depth within that core, making statistical analysis using *a priori* groupings (i.e. PERMANOVA) inappropriate to apply. Hence our application of exploratory significance testing using similarity profile (SIMPROF) analysis. The SIMPROF method examines whether the similarities observed in the data are smaller and/or larger than those expected by chance (null hypothesis testing). The MS^1 data showed more

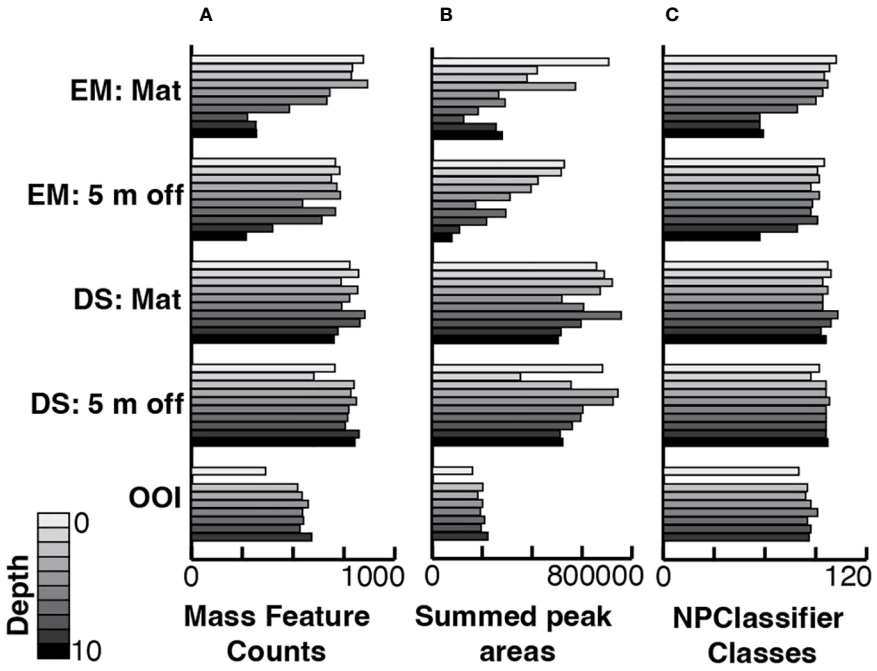

FIGURE 4
Bar graphs displaying per sample, stacked by core and sample depth in core, **(A)** the number of mass features, **(B)** the sum of all LCMS peak areas from the feature list generated in MzMine3, and **(C)** the number of distinct NPClassifier classes in each sample. EM: Mat is Emyn Muil on-seep mat core; EM: 5 m off is Emyn Muil 5 m off-seep core; DS: Mat is Dagorlad Seep on-seep mat core; DS: 5 m off is Dagorlad Seep 5 m off-seep core; OOI: non-seep is the OOI slope base core.

variability in both feature counts (on-seep mat: 602.9 ± 233.6; 5 m off-seep: 613.5 ± 160.2) and abundances (on-seep mat: 3.48E5 ± 1.78E5; 5 m off-seep: 3.05 ± 1.61E5) at the older Emyn Muil seep, with deeper sections yielding lower feature counts and abundances than shallower ones (Figure 4). The LCMS data for the two Dagorlad seep cores varied less, in both feature counts (on-seep mat: 777.3 ± 51.8; 5 m off-seep: 762.5 ± 65.6) and abundances (on-seep mat: 6.24E5 ± 9.02E4; 5 m off-seep 5.85E5 ± 1.15E5). This is further reflected in the greater spread in core section LCMS data for the two Emyn Muil cores compared to the Dagorlad cores (Figure 5A). Additionally, the LCMS data formed less distinct clusters (Figure 5A) compared to the corresponding microbial ASV data (Figure 5B) of the sediment cores, reflecting the shared chemistry of metabolisms between different microbial taxa. In both the ASV and LCMS data plots, the OOI slope base core samples clustered separately from the on-seep and 5 m off-seep samples (Figures 5A, B).

The 5 m off-seep cores possessed greater ASV richness than their corresponding on-seep microbial mat cores. The Emyn Muil sediment core from 5 m off-seep had greater microbial ASV richness (6,948 ASVs) than the on-seep microbial mat core from the same site (4,427 ASVs). The Dagorlad seep cores had less ASV richness than the corresponding cores at the Emyn Muil seep but again, greater richness was seen in the 5 m off-seep core (5,802 ASVs) than the on-seep mat (1,338 ASVs). Sediment samples were generally clustered by core using microbial ASV data (Figure 5B). However, the samples from the younger Dagorlad seep cores clustered more tightly than those from the older Emyn Muil seep, where deeper depths were less clustered than shallower depths (Figure 5B). The NMDS plot of core samples based on the actinobacterial ASVs (Figure 5C) displayed the least separation between the cores, likely due to the low overall counts of Actinobacteria. Nevertheless, it is noteworthy that actinobacterial ASV richness appeared to be less diverse for the on-seep microbial mat cores (EM:28, DS:12) than for the 5 m off-seep cores (EM:78, DS:35).

Clustering by similarity using the SIMPROF routine is a method of exploratory data analysis that detects patterns using null hypothesis testing. In summary, a Bray-Curtis similarity matrix for the data is compared, using the pi statistic, to a mean permuted similarity profile generated from iterative random shuffling of the raw data. This SIMPROF method was performed on microbial ASV abundance data, the actinobacterial ASV subset, and LCMS peak area (abundance) data for the sediment samples. Sediment core schematics, representing the spatial distribution of SIMPROF groupings for the three datasets by depth of core section sample, are presented in Figure 6, together with a template core on which section depths are labeled (Figure 6A). In general, for Emyn Muil and Dagorlad seep sites, changes in metabolites with depth, indicated by bold line boundaries between different colored sections, are consistent with changes in microorganisms with depth (Figures 6C–F). In contrast, the metabolite and microbial datasets for the non-seep OOI control site do not correlate well in terms of variation with depth, and there are overall fewer changes/boundaries (Figure 6B). In numerous instances for the two seep sites, as indicated by circled letters, SIMPROF groupings match between the LCMS and total microbial ASV datasets. These

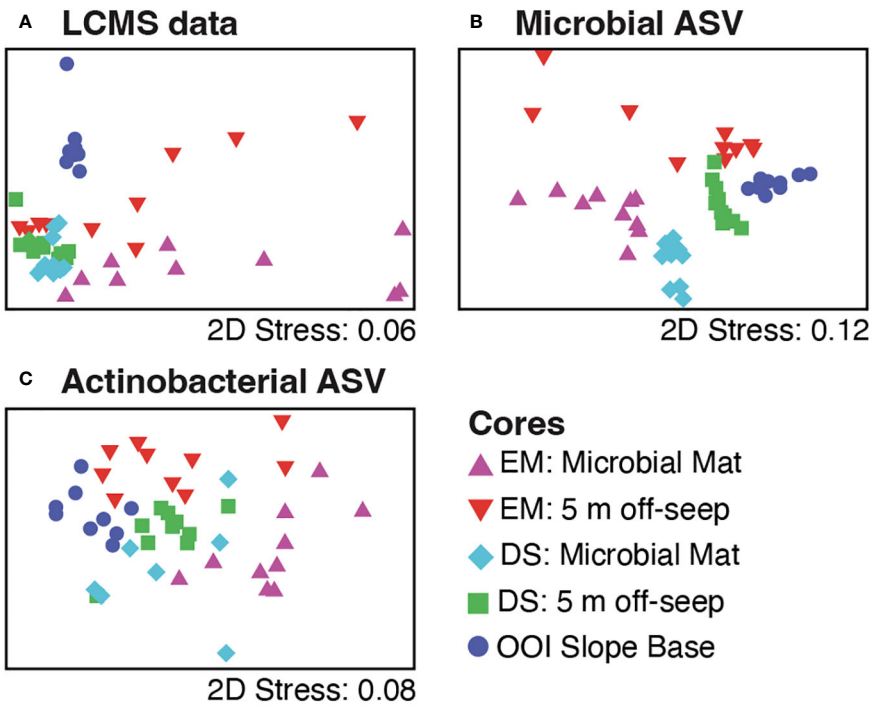

FIGURE 5
Non-metric multidimensional scaling (nMDS) plots of the data for 10 core sections from five different cores, including on-seep mat (Emyn Muil, EM, purple; Dagorlad Seep, DS, cyan), 5 m off-seep (EM, red; DS, green), and non-seep OOI control (dark blue) using **(A)** LCMS data, **(B)** all microbial (16S rRNA) ASV data, and **(C)** actinobacterial ASV data only.

correlations imply the presence of distinct microbial populations with correspondingly distinct chemistry in these core sections. There is less correlation in the change with depth of LCMS versus actinobacterial ASV data alone, which may again reflect the relatively low overall counts of actinobacterial ASVs. Somewhat correlated changes in depth between actinobacteria and LCMS datasets are apparent for the 5 m off-seep sites, for example, between 4-7 cm core section depth in the Emyn Muil samples and variously throughout the Dagorlad samples.

Significant positive and negative microbe~metabolite Spearman's correlations occurred between microbial ASVs assigned at the family level and LCMS features annotated as putative peptides in either ontology (Supplementary Figure S1). The Log(X+1) normalized abundances of each of these features, separated by sample core depth for each site, is presented in Figure 7. Many individual LCMS features in this peptide dataset were simultaneously categorized in other NPClassifier pathways by CANOPUS, as anticipated for metabolites substituted with various functional groups, or with low probability peptide annotations. The 407 mass ion features annotated as "peptide" ranged from *m/z* 361.2448 to 1239.9522. While the overall proportion of peptides did not change much between cores (Figure 4), at the feature level there are differences in the pattern of these metabolites present in the different cores. Peptidic metabolites significantly correlated to microbes were predominant in the upper two-thirds of the older Emyn Muil on-seep microbial mat core with relatively few correlated metabolites distributed throughout all core sections (Figure 7). By comparison, the Emyn Muil 5 m off-seep core possessed a greater proportion of significantly correlated peptidic metabolites distributed from the surface to deeper in the core. The Dagorlad on-seep microbial mat and 5 m off-seep core profiles were comparable to each other and contained a majority of significantly correlated peptidic metabolites throughout the core, as was also found in the non-seep OOI core (Figure 7). The corresponding abundance of significantly correlated peptide metabolites plotted on the right-hand y axis indicates a decrease in peptide abundance with core section depth for the two Emyn Muil carbonate seep cores, but not for the soft sediment Dagorlad seep cores. This is in agreement with the trend across all metabolites (Figure 2). Notably, positive correlations were observed between actinobacterial families and putative cyclic peptides (Table 1). The complete dataset of correlations between features annotated as peptidic and microbial families can be found in the Supplemental Material (Supplementary Table S3, Supplementary Figure S1).

4 Discussion

Our coupled metabolomics and bacterial community survey revealed distinct chemistry at methane seep sites compared to non-seep sites at the level of microbial family and metabolite structure class. The microbial family level was chosen for our analyses to facilitate data handling and visualization, and for consistency with our previous report (Cummings et al., 2023). Furthermore,

variations in specific molecular analogues within a series of biosynthetically related molecules (molecular family) may occur at the microbial genus, species or strain level, however, presence or absence of biosynthetic genes encoding a biologically important molecular family is most often noted at the microbial genus or higher taxonomic level (Donia et al., 2014). Chemical diversity changed across sites and core depth in relation to the changes in microbial diversity (Figures 5, 6). While the proportions of structure superclasses did not vary markedly across sites (Figures 2, 3), individual features and subclasses of compounds varied considerably between samples (e.g., for peptides, Figure 7).

We previously reported relative abundance of the 13 most abundant microbial families in the on-seep microbial mat and 5 m off-seep cores from Dagorlad and Emyn Muil seeps (Cummings et al., 2023). Notably, the microbial mat core from older Emyn Muil comprises a relatively large portion of anaerobic methanotrophic archaea (ANME), specifically ANME-1, not represented in the younger Dagorlad microbial mat. The Dagorlad microbial mat instead comprises a relatively high abundance of sulfur-reducing bacteria (SRB) in the families Desulfobulbaceae and Desulfobacteraceae, with ANME-2 present. The partitioning of ANME-1 and ANME-2 in this way has been reported to be driven by methane supply (Niu et al., 2023) and suggests that the older Emyn Muil seep may experience higher methane seepage than Dagorlad seep. However, in the absence of flux data, there are a variety of possible interpretations, such as is proposed in Cummings et al., 2023. Further, nitrogen-fixing ANME-2 and SRB have been deemed responsible for the majority of new nitrogen production previously (Dekas et al., 2014). Thus other limiting nutrients or processes, besides methane seepage, may impact the community compositions observed here.

The relatively high abundance of lipids and lipid-like molecules at both methane seep sites versus the non-seep OOI control site (Figures 2, 3) may be attributed to methane seep-specialized bacteria, which are known to produce large quantities of methanotroph-specific monounsaturated fatty acids (Guan et al,

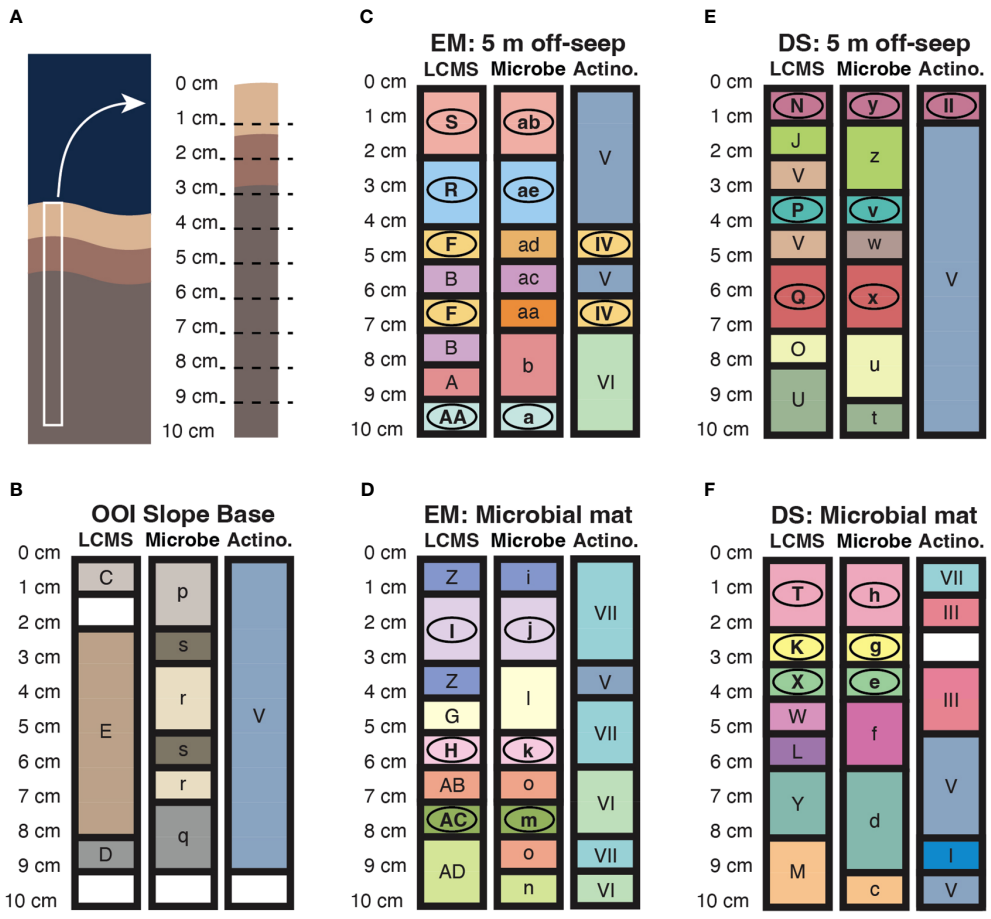

FIGURE 6
Core schematics representing the spatial distribution of similarity groupings according to SIMPROF analysis of LCMS features (LCMS), microbial 16S ASVs (Microbe), and actinobacterial 16S ASVs (Actino). Conserved color and label of core section within LCMS, Microbe or Actino datasets indicates that those sections belong to the same SIMPROF grouping. Circled letters indicate groupings that match across at least two datasets. **(A)** Diagrammatic representation of a sediment core *in situ*, in benthic substrate, alongside a representative core with depth graduations corresponding to sectioning of the core during sample processing. **(B–F)** Data for the non-seep OOI Slope Base, and off-seep and on-seep microbial mat for the younger Dagorlad (DS) and older Emyn Muil (EM) seeps, as labeled.

2022; Cordova-Gonzalez et al., 2020) and terpenoid compounds including carotenoids, steroids, polyprenols, and hopanoids (Salvador-Castell et al., 2019; Grivard et al., 2022). The unknown reason for the highest proportion of lipids and lipid-like molecules at the older carbonate substrate seep (Figure 2A) is presumably associated with the specific microbial community (and geochemistry) at the older carbonate substrate seep. These observations present opportunities for future hypothesis-driven research, potentially using targeted lipid analysis. These chemosynthetic habitats add to the chemical diversity of the ocean, and our exploratory work here demonstrates that even comparable habitats (soft sediment microbial mats, fueled by methane) have divergent metabolites (Figure 4), demonstrating that different chemosynthetic habitats add to the overall chemical diversity present in marine systems.

As very few MS ion features had spectral library or *in silico* predicted annotations in GNPS, we relied on CANOPUS to provide structural information for LCMS features that could be used to compare sediment cores from different sites. CANOPUS annotations are predictions that require further analysis and additional data for confirmation and comprehensive structure elucidation. CANOPUS predictions are also less accurate for molecules with masses greater than 850 Da, and SIRIUS does not currently support formula prediction or structural class prediction from doubly charged ion features. The semantic ontologies (NPClassifier and ClassyFire) used for computational assignment of structural class or 'pathway' may offer several alternatives since many chemical compounds comprise multiple substructures which fall into separate structural categories. Hence, assignment of a reasonably complex compound to only one structural class or another is subjective and requires manual assignment. Thus, metabolites are considered only at the level of biosynthetic class in this study.

Marine sediment samples posed challenges for LCMS analysis that may have resulted in an underestimation of the NPs present. Salt comprised a large portion of the mass-limited extracts obtained and potentially contributed to ion suppression, reducing the sensitivity of the mass detector (Metwally et al., 2015). To prevent large quantities of salt from entering the mass spectrometer, the LC column eluent was directed to waste for the first several minutes, meaning that more polar metabolites were likely lost to waste. The proportions of metabolites belonging to the various pathways are also likely skewed by electrospray ionization (ESI) technique and (positive or negative) mode used, as well as parameters set in the mass detection method, which affect metabolite ionizability. For example, carbohydrates may be underrepresented because many glycans do not give strong signals in positive mode due to lack of basic sites for protonation (Grabarics et al., 2022). Additionally, there is a large amount of elemental sulfur in deep-sea sediments around methane seeps, and organic polysulfide compounds may require chemical ionization (CI) or Fast Atom Bombardment (FAB) for mass detection, as is the case for lissoclinotoxins (Davis et al., 2003) and lissoclibadins (Nakazawa et al., 2007). As a result, while we have used a powerful technique coupled with multiple computational pathways, we are likely underestimating the chemical diversity present in methane seep habitats.

The correlations between LCMS features and particular bacterial families determined here will direct future investigation. The heatmap of peptidic feature correlations to microbial families (Supplementary Figure S1) emphasizes the chemical and biological complexity of methane seep sediment communities, illustrating that any one LCMS feature may have multiple positive and negative correlations with diverse microbial families and *vice versa*. The heatmap is organized by similarity of patterns in correlations, so that MS ion features with

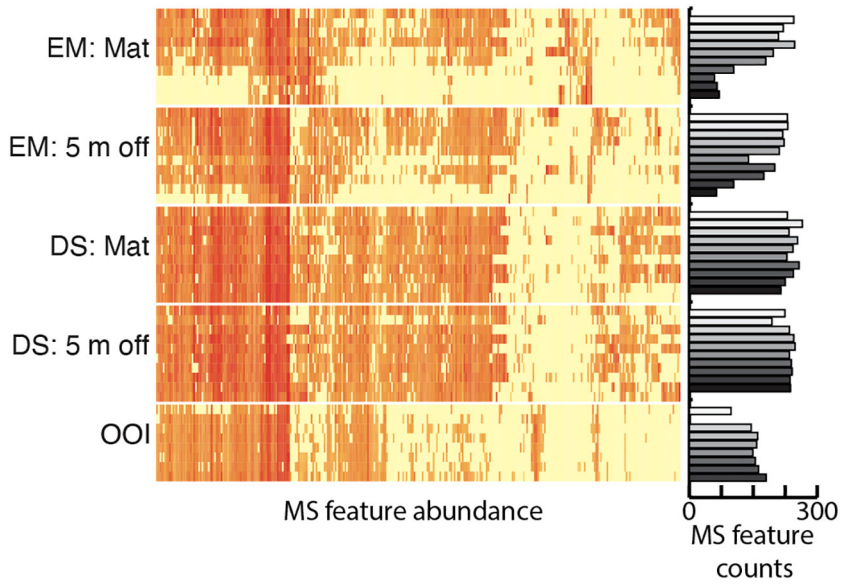

FIGURE 7
Heatmap of MS ion feature abundance representing distribution by core of putative peptidic metabolites with significant positive or negative correlations to families of microbial ASVs. Bar graph representing total numbers of features annotated as putative peptides by depth and core. For both heatmap and bar graphs, rows are stacked by depth within cores.

similar patterns of correlation across microbial families are clustered together. Thus, in the upper portion of the heatmap, there are obvious groupings of microbial families (in rows) that display consistent positive and negative correlations with groupings of metabolites, which may form the basis of hypotheses for future investigation.

While it is not possible to confidently assign producing organisms or functional roles to (structurally unassigned) metabolites based on Spearman's correlations (Carr et al., 2019), the co-occurrence of known biologically active classes of metabolites with bacterial families known to produce those metabolites demonstrates relevance and rationale for natural products biomedical and biotechnological research. Our data reveal that several bacterial families belonging to orders that have previously yielded structurally diverse bioactive NPs are positively correlated with LCMS features of the same structural classes as the known bioactive NPs. For example, positive correlations were seen between actinobacterial ASVs and several LCMS features annotated as cyclic peptides (Table 1). Actinobacteria are well-known to produce biologically active cyclic peptides (Zhao et al., 2018). Additionally, other bacterial families within Cellvibrionales (Han et al., 2013), Campylobacterales (Rischer et al., 2018) and Rhodobacterales (Ióca et al., 2021) also have significant positive correlations with putative peptidic features (correlation data in Supplementary Table S3), and members of these orders are known producers of bioactive nonribosomal peptides. Rhodobacteraceae are reported to produce peptide-derived alkaloids (Dickschat et al., 2005a; Dickschat et al., 2005b; Nicacio et al., 2017) and several LCMS features in our methane seep cores that were annotated as both alkaloid and peptide positively correlated with Rhodobacteraceae. The exploratory analysis undertaken here leverages significant bioinformatic and analytical advancement and provides a foundation for future work to realize the NP potential as well as the functional role of specialized metabolites in marine systems. In order to bridge the gap between specialized metabolite discovery by LCMS feature annotation and identification of biologically active metabolites relevant to human health, the adoption of computational methods is essential. Emerging tools such as NPAnalyst (Lee et al., 2022) or Pearson correlation pipelines (Nothias et al., 2018) permit mapping of biological activity observed for complex mixtures to individual components therein. The ability to discern structural and substructural motifs known to be associated with specific bioactivities further enables more targeted testing of limited sample quantities. In addition, tools such as GNPS may allow identification of other sources of the same or related metabolites of interest, facilitating access to larger quantities for more extensive biological testing and structure elucidation. The deep sea, beyond depths accessible by SCUBA, is only beginning to be included in the search for new NPs, with 75% of the new metabolites discovered found to be biologically active, and almost half having some anti-cancer potential (Skropeta and Wei, 2014). The challenges of accessing, isolating, and characterizing new organic molecules requires ongoing technological innovations and interdisciplinary collaborative research, which is well justified given the tremendous contributions to date of small organic compounds in chemical and biological research, and to global health (Cheng et al., 2014; Newman and Cragg, 2020; Carroll et al, 2022). Here we present a snapshot of the potential for NP discovery in methane fueled habitats, where we found different metabolite profiles at two sites at the same water depth in relatively close proximity. Seep biodiversity is known to vary latitudinally across the Cascadia Margin (Seabrook et al., 2018) and there is high microbial heterogeneity at <1 m spatial scale (Boetius and Suess, 2004; Cummings et al., 2023). In addition, seeps change over time, as do the biological communities that inhabit them (Cordes

TABLE 1 Correlations between families within Actinobacteriota and mass features annotated as cyclic peptides by CANOPUS.

Microbial Families within Phylum Actinobacteriota			Corr. Coeff.	Adj. p value	Feature ID	m/z	NPC Class	NPC Class Prob.
Class	Order	Family						
Unassigned	Unassigned	Unassigned	0.4781	0.018	260	420.250666	Cyclic peptides	0.888
Acidimicrobiia	Microtrichales	Ilumatobacteraceae	0.5155	0.009	259	655.395939	Cyclic peptides	0.226
Coriobacteriia	CG2-30-50-142	CG2-30-50-142	0.5934	0.001	260	420.250666	Cyclic peptides	0.888
RBG-16-55-12	RBG-16-55-12	RBG-16-55-12	0.7564	4.40E-6	260	420.250666	Cyclic peptides	0.888
Thermoleophilia	Solirubrobacterales	67-14	0.5335	0.006	260	420.250666	Cyclic peptides	0.888
Thermoleophilia	Solirubrobacterales	67-14	0.4311	0.041	1109	693.551802	Cyclic peptides	0.990
WCHB1-81	WCHB1-81	WCHB1-81	0.5703	0.003	260	420.250666	Cyclic peptides	0.888
WCHB1-81	WCHB1-81	WCHB1-81	0.4553	0.027	1112	725.577524	Cyclic peptides	0.987

et al., 2005; Bowden et al., 2013; Thurber et al., 2020). If we presume our two seep sites are at the opposite ends of seep succession, temporal patterns also contribute to the diversity of metabolites present in these habitats. Continued and increased characterization of habitats at the interface of metabolome and microbiome science has astounding potential, especially considering the more than 3,500 seeps that are present but 99% unexplored on the Cascadia Margin (Merle et al., 2021), where this research was carried out. Characterizing the role of habitat heterogeneity on deep-sea ecosystem services, such as NP discovery, will allow informed management of deep-sea habitats with an eye towards future potential balancing immediate gains.

Data availability statement

The original contributions presented in the study are publicly available. These data can be found here: For the LCMS data, MassIVE ID MSV000090543, https://massive.ucsd.edu/ProteoSAFe/dataset.jsp?task=0de7900cc26b433fbf18049d0bdf622b; 16S sequence data, https://www.ncbi.nlm.nih.gov/bioproject/?term=PRJNA718843.

Author contributions

AT, KM contributed to conceptualization of the study and funding acquisition; all authors contributed to the investigation; MR and MC led formal analysis and data visualization with contributions by all authors; MR, KM and AT contributed to writing – original draft. All authors contributed to the article and approved the submitted version.

Funding

This research was funded by NOAA Ocean Exploration Grant NA19OAR0110301, and by the National Institutes of Health via NCCIH T32 AT010131 (support of MR), NIGMS 1R01GM132649 (KM), and National Science Foundation grants 2046800 and 1933165 (AT).

Acknowledgments

We thank Prof. Benjamin Philmus for assistance with LCMS data acquisition.

Conflict of interest

The authors declare that the research was conducted in the absence of any commercial or financial relationships that could be construed as a potential conflict of interest.

Publisher's note

All claims expressed in this article are solely those of the authors and do not necessarily represent those of their affiliated organizations, or those of the publisher, the editors and the reviewers. Any product that may be evaluated in this article, or claim that may be made by its manufacturer, is not guaranteed or endorsed by the publisher.

Supplementary material

The Supplementary Material for this article can be found online at: https://www.frontiersin.org/articles/10.3389/fmars.2023.1197338/full#supplementary-material

SUPPLEMENTARY FIGURE S1
Heatmap of significant positive (red) and negative (blue) correlations between putative peptidic LCMS features and families of microbial ASVs.

SUPPLEMENTARY TABLE S3
Dataset of correlations between all features annotated as peptidic and microbial families.

References

Aleti, G., Kohn, J. N., Troyer, E. A., Weldon, K., Huang, S., Tripathi, A., et al. (2022). Salivary bacterial signatures in depression-obesity comorbidity are associated with neurotransmitters and neuroactive dipeptides. *BMC Microbiol.* 22, 75. doi: 10.1186/s12866-022-02483-4

Bauermeister, A., Mannochio-Russo, H., Costa-Lotufo, L. V., Jarmusch, A. K., and Dorrestein, P. C. (2022). Mass spectrometry-based metabolomics in microbiome investigations. *Nat. Rev. Microbiol.* 20, 143–160. doi: 10.1038/s41579-021-00621-9

Bernardino, A. F., Levin, L. A., Thurber, A. R., and Smith, C. R. (2012). Comparative composition, diversity and trophic ecology of sediment macrofauna at vents, seeps and organic falls. *PloS One* 7, e33515. doi: 10.1371/journal.pone.0033515

Boetius, A., and Suess, E. (2004). Hydrate Ridge: A natural laboratory for the study of microbial life fueled by methane from near-surface gas hydrates. *Chem. Geol.* 205, 291–310. doi: 10.1016/j.chemgeo.2003.12.034

Bowden, D. A., Rowden, A. A., Thurber, A. R., Baco, A. R., Levin, L. A., and Smith, C. R. (2013). Cold seep epifaunal communities on the Hikurangi margin, New Zealand: composition, succession, and vulnerability to human activities. *PloS One* 8, e76869. doi: 10.1371/journal.pone.0076869

Carroll, A. R., Copp, B. R., Davis, R. A., Keyzers, R. A., and Prinsep, M. R. (2022). Marine natural products. *Nat. Prod. Rep.* 39, 1122–1171. doi: 10.1039/d1np00076d

Clarke and Gorley, (2015). *Getting started with PRIMER v7* (Plymouth: PRIMER-E: Plymouth). Available at: http://updates.primer-e.com/primer7/manuals/Getting_started_with_PRIMER_7.pdf.

Carr, A., Diener, C., Baliga, N. S., and Gibbons, S. M. (2019). Use and abuse of correlation analyses in microbial ecology. *ISME J.* 13, 2647–2655. doi: 10.1038/s41396-019-0459-z

Cheng, G., Hao, H., Xie, S., Wang, X., Dai, M., Huang, L., et al. (2014). Antibiotic alternatives: the substitution of antibiotics in animal husbandry? *Front. Microbiol.* 5. doi: 10.3389/fmicb.2014.00217

Cordes, E. E., Hourdez, S., Predmore, B. L., Redding, M. L., and Fisher, C. R. (2005). Succession of hydrocarbon seep communities associated with the long-lived foundation species Lamellibrachia luymesi. *Mar. Ecol. Prog. Ser.* 305, 17–29. doi: 10.3354/meps305017

Cordova-Gonzalez, A., Birgel, D., Kappler, A., and Peckmann, J. (2020). Carbon stable isotope patterns of cyclic terpenoids: A comparison of cultured alkaliphilic

aerobic methanotrophic bacteria and methane-seep environments. *Org. Geochem.* 139, 103940. doi: 10.1016/j.orggeochem.2019.103940

Cordes, E. E., Bergquist, D. C., and Fisher, C. R. (2009). Macro-ecology of Gulf of Mexico cold seeps. *Ann. Rev. Mar. Sci.* 1, 143–168. doi: 10.1146/annurev.marine.010908.163912

Cummings, S., Ardor Bellucci, L. M., Seabrook, S., Raineault, N. A., McPhail, K. L., and Thurber, A. R. (2023). Variations and gradients between methane seep and off-seep microbial communities in a submarine canyon system in the Northeast Pacific. *PeerJ* 11, e15119. doi: 10.7717/peerj.15119

Davis, R. A., Sandoval, I. T., Concepcion, G. P., Moreira da Rocha, R., and Ireland, C. M. (2003). Lissoclinotoxins E and F, novel cytotoxic alkaloids from a Philippine didemnid ascidian. *Tetrahedron* 59, 2855–2859. doi: 10.1016/S0040-4020(03)00335-1

de Jonge, N. F., Mildau, K., Meijer, D., Louwen, J. J.R., Bueschl, C., Huber, F., et al. (2022). Good practices and recommendations for using and benchmarking computational metabolomics metabolite annotation tools. *Metabolomics* 18 (12), 103. doi: 10.1007/s11306-022-01963-y

Dekas, A. E., Chadwick, G. L., Bowles, M. W., Joye, S. B., and Orphan, V. J. (2014). Spatial distribution of nitrogen fixation in methane seep sediment and the role of the ANME archaea. *Environ. Microbiol.* 16, 3012–3029. doi: 10.1111/1462-2920.12247

Dekas, A. E., Connon, S. A., Chadwick, G. L., Trembath-Reichert, E., and Orphan, V. J. (2016). Activity and interactions of methane seep microorganisms assessed by parallel transcription and FISH-NanoSIMS analyses. *ISME J.* 10, 678–692. doi: 10.1038/ismej.2015.145

Dickschat, J. S., Reichenbach, H., Wagner-Döbler, I., and Schulz, S. (2005a). Novel pyrazines from the MyxobacteriumChondromyces crocatusand marine bacteria. *Eur. J. Org. Chem.* 2005, 4141–4153. doi: 10.1002/ejoc.200500280

Dickschat, J. S., Wagner-Döbler, I., and Schulz, S. (2005b). The chafer pheromone buibuilactone and ant pyrazines are also produced by marine bacteria. *J. Chem. Ecol.* 31, 925–947. doi: 10.1007/s10886-005-3553-9

Djoumbou Feunang, Y., Eisner, R., Knox, C., Chepelev, L., Hastings, J., Owen, G., et al. (2016). ClassyFire: automated chemical classification with a comprehensive, computable taxonomy. *J. Cheminform.* 8, 61. doi: 10.1186/s13321-016-0174-y

Donia, M. S., Cimermancic, P., Schulze, C. J., Brown, L. C.W., Martin, J., Mitreva, M., et al. (2014). A systematic analysis of biosynthetic gene clusters in the human microbiome reveals a common family of antibiotics. *Cell* 158 (6), 1402–1145. doi: 10.1016/j.cell.2014.08.032

Dührkop, K., Fleischauer, M., Ludwig, M., Aksenov, A. A., Melnik, A. V., Meusel, M., et al. (2019). SIRIUS 4: a rapid tool for turning tandem mass spectra into metabolite structure information. *Nat. Methods* 16, 299–302. doi: 10.1038/s41592-019-0344-8

Dührkop, K., Nothias, L.-F., Fleischauer, M., Reher, R., Ludwig, M., Hoffmann, M. A., et al. (2021). Systematic classification of unknown metabolites using high-resolution fragmentation mass spectra. *Nat. Biotechnol.* 39, 462–471. doi: 10.1038/s41587-020-0740-8

Dührkop, K., Shen, H., Meusel, M., Rousu, J., and Böcker, S. (2015). Searching molecular structure databases with tandem mass spectra using CSI:FingerID. *Proc. Natl. Acad. Sci. U. S. A.* 112, 12580–12585. doi: 10.1073/pnas.1509788112

Grabarics, M., Lettow, M., Kirschbaum, C., Greis, K., Manz, C., and Pagel, K. (2022). Mass spectrometry-based techniques to elucidate the sugar code. *Chem. Rev.* 122, 7840–7908. doi: 10.1021/acs.chemrev.1c00380

Grivard, A., Goubet, I., Filho, L. M. d. S., Thiéry, V., Chevalier, S., de Oliveira-Junior, R. G., et al. (2022). Archaea carotenoids: natural pigments with unexplored innovative potential. *Mar. Drugs* 20, 524. doi: 10.3390/md20080524

Grupe, B. M., Krach, M. L., Pasulka, A. L., Maloney, J. M., Levin, L. A., and Frieder, C. A. (2015). Methane seep ecosystem functions and services from a recently discovered southern California seep. *Mar. Ecol.* 36, 91–108. doi: 10.1111/maec.12243

Guan, H., Feng, D., Birgel, D., Kiel, S., Peckmann, J., Li, S., et al. (2022). Lipid biomarker patterns reflect nutritional strategies of seep-dwelling bivalves from the South China Sea. *Front. Mar. Sci.* 9. doi: 10.3389/fmars.2022.831286

Han, A. W., Sandy, M., Fishman, B., Trindade-Silva, A. E., Soares, C. A. G., Distel, D. L., et al. (2013). Turnerbactin, a novel triscatecholate siderophore from the shipworm endosymbiont Teredinibacter turnerae T7901. *PloS One* 8, e76151. doi: 10.1371/journal.pone.0076151

Ióca, L. P., Dai, Y., Kunakom, S., Diaz-Espinosa, J., Krunic, A., Crnkovic, C. M., et al. (2021). A family of nonribosomal peptides modulate collective behavior in pseudovibrio bacteria isolated from marine sponges*. *Angew. Chem. Int. Ed. Engl.* 60, 15891–15898. doi: 10.1021/acs.jnatprod.1c00399

Kim, H. W., Wang, M., Leber, C. A., Nothias, L.-F., Reher, R., Kang, K. B., et al. (2021). NPClassifier: A deep neural network-based structural classification tool for natural products. *J. Nat. Prod.* 84, 2795–2807. doi: 10.1021/acs.jnatprod.1c00399

Knittel, K., and Boetius, A. (2009). Anaerobic oxidation of methane: progress with an unknown process. *Annu. Rev. Microbiol.* 63, 311–334. doi: 10.1146/annurev.micro.61.080706.093130

Lee, S., van Santen, J. A., Farzaneh, N., Liu, D. Y., Pye, C. R., Baumeister, T. U. H., et al. (2022). NP analyst: an open online platform for compound activity mapping. *ACS Cent. Sci.* 8, 223–234. doi: 10.1021/acscentsci.1c01108

Levin, L. A. (2005). "Ecology of cold seep sediments: interactions of fauna with flow, chemistry and microbes," in *Oceanography and Marine Biology* (Boca Raton, FL: CRC Press), 11–56. doi: 10.1201/9781420037449-3

MassIVE (n.d). Available at: https://massive.ucsd.edu/ProteoSAFe/static/massive.jsp (Accessed March 7, 2023).

Merle, S. G., Embley, R. W., Johnson, H. P., Lau, T.-K., Phrampus, B. J., Raineault, N. A., et al. (2021). Distribution of methane plumes on cascadia margin and implications for the landward limit of methane hydrate stability. *Front. Earth Sci. Chin.* 9. doi: 10.3389/feart.2021.531714

Metwally, H., McAllister, R. G., and Konermann, L. (2015). Exploring the mechanism of salt-induced signal suppression in protein electrospray mass spectrometry using experiments and molecular dynamics simulations. *Anal. Chem.* 87, 2434–2442. doi: 10.1021/ac5044016

Morehouse, N. J., Clark, T. N., McMann, E. J., van Santen, J. A., Haeckl, F. P. J., Gray, C. A., et al. (2023). Annotation of natural product compound families using molecular networking topology and structural similarity fingerprinting. *Nat. Commun.* 14, 308. doi: 10.1038/s41467-022-35734-z

Nakazawa, T., Xu, J., Nishikawa, T., Oda, T., Fujita, A., Ukai, K., et al. (2007). Lissoclibadins 4-7, polysulfur aromatic alkaloids from the Indonesian ascidian Lissoclinum cf. badium. *J. Nat. Prod.* 70, 439–442. doi: 10.1021/np060593c

Neuhaus, G., Aron, A., Isemonger, E., Petras, D., Waterworth, S., Gentry, E., et al. (2022). Metabolomics spatial survey of modern stromatolites from South Africa and characterization of ibhayipeptolides. Cambridge: Cambridge Open Engage. *ChemRxiv*. doi: 10.26434/chemrxiv-2022-1vr86

Newman, D. J., and Cragg, G. M. (2020). Natural products as sources of new drugs over the nearly four decades from 01/1981 to 09/2019. *J. Nat. Prod.* 83, 770–803. doi: 10.1021/acs.jnatprod.9b01285

Nicacio, K. J., Ióca, L. P., Fróes, A. M., Leomil, L., Appolinario, L. R., Thompson, C. C., et al. (2017). Cultures of the marine bacterium pseudovibrio denitrificans ab134 produce bromotyrosine-derived alkaloids previously only isolated from marine sponges. *J. Nat. Prod.* 80, 235–240. doi: 10.1021/acs.jnatprod.6b00838

Nie, Z., Xu, X., Shao, N., He, J., Li, P., Xu, P., et al. (2023). Integrative analysis of microbiome and metabolome reveals the linkage between gut microbiota and carp growth. *Environ. Res.* 220, 115133. doi: 10.1016/j.envres.2022.115133

Niu, M., Deng, L., Su, L., Ruff, S.E., Yang, N., Luo, M., et al. (2023). Methane supply drives prokaryotic community assembly and networks at cold seeps of the South China Sea. *Mol. Ecol.* 32 (3), 660–795. doi: 10.1111/mec.16786

Nothias, L.-F., Nothias-Esposito, M., da Silva, R., Wang, M., Protsyuk, I., Zhang, Z., et al. (2018). Bioactivity-based molecular networking for the discovery of drug leads in natural product bioassay-guided fractionation. *J. Nat. Prod.* 81, 758–767. doi: 10.1021/acs.jnatprod.7b00737

Parada, A. E., Needham, D. M., and Fuhrman, J. A. (2016). Every base matters: assessing small subunit rRNA primers for marine microbiomes with mock communities, time series and global field samples. *Environ. Microbiol.* 18, 1403–1414. doi: 10.1111/1462-2920.13023

Patin, N. V., Schorn, M., Aguinaldo, K., Lincecum, T., Moore, B. S., and Jensen, P. R. (2017). Effects of actinomycete secondary metabolites on sediment microbial communities. *Appl. Environ. Microbiol.* 83, e02676-16. doi: 10.1128/AEM.02676-16

Pluskal, T., Castillo, S., Villar-Briones, A., and Oresic, M. (2010). MZmine 2: modular framework for processing, visualizing, and analyzing mass spectrometry-based molecular profile data. *BMC Bioinf.* 11, 395. doi: 10.1186/1471-2105-11-395

R Core Team (2022) *R: A Language and Environment for Statistical Computing*. Available at: https://www.R-project.org/.

Reeburgh, W. S. (2007). Oceanic methane biogeochemistry. *Chem. Rev.* 107, 486–513. doi: 10.1021/cr050362v

Rischer, M., Raguž, L., Guo, H., Keiff, F., Diekert, G., Goris, T., et al. (2018). Biosynthesis, synthesis, and activities of barnesin A, a NRPS-PKS hybrid produced by an anaerobic epsilonproteobacterium. *ACS Chem. Biol.* 13, 1990–1995. doi: 10.1021/acschembio.8b00445

Rothman, J. A., Leger, L., Kirkwood, J. S., and McFrederick, Q. S. (2019). Cadmium and selenate exposure affects the honey bee microbiome and metabolome, and bee-associated bacteria show potential for bioaccumulation. *Appl. Environ. Microbiol.* 85, e01411-19. doi: 10.1128/AEM.01411-19

Salvador-Castell, M., Tourte, M., and Oger, P. M. (2019). In search for the membrane regulators of archaea. *Int. J. Mol. Sci.* 20, 4434. doi: 10.3390/ijms20184434

Seabrook, S., Cabrera De Leo, F., and Thurber, A. (2019). Flipping for Food: The use of a methane seep by Tanner Crabs (Chionoecetes tanneri). *Front. Mar. Sci.* 6. doi: 10.3389/fmars.2019.00043

Seabrook, S., De Leo, C., Baumberger, T., Raineault, N., and Thurber, A. R. (2018). Heterogeneity of methane seep biomes in the Northeast Pacific. *Deep Sea Res. Part 2 Top. Stud. Oceanogr.* 150, 195–209. doi: 10.1016/j.dsr2.2017.10.016

Shaffer, J. P., Nothias, L.-F., Thompson, L. R., Sanders, J. G., Salido, R. A., Couvillion, S. P., et al. (2022). Standardized multi-omics of Earth's microbiomes reveals microbial and metabolite diversity. *Nat. Microbiol.* 7, 2128–2150. doi: 10.1038/s41564-022-01266-x

Skropeta, D., and Wei, L. (2014). Recent advances in deep-sea natural products. *Nat. Prod. Rep.* 31, 999–1025. doi: 10.1039/c3np70118b

Sun, L., Wang, Y., Ma, D., Wang, L., Zhang, X., Ding, Y., et al. (2022). Differential responses of the rhizosphere microbiome structure and soil metabolites in tea (Camellia sinensis) upon application of cow manure. *BMC Microbiol.* 22, 55. doi: 10.1186/s12866-022-02470-9

Thurber, A. R., Seabrook, S., and Welsh, R. M. (2020). Riddles in the cold: Antarctic endemism and microbial succession impact methane cycling in the Southern Ocean. *Proc. Biol. Sci.* 287, 20201134. doi: 10.1098/rspb.2020.1134

Torondel, B., Ensink, J. H.J., Gundogdu, O., Ijaz, U. Z., Parkhill, J., Abdelahi, F., et al. (2016). Assessment of the influence of intrinsic environmental and geographical factors on the bacterial ecology of pit latrines. *Microbial Biotechnol.* 9 (2), 209–223. doi: 10.1111/1751-7915.12334

Wang, M., Carver, J. J., Phelan, V. V., Sanchez, L. M., Garg, N., Peng, Y., et al. (2016). Sharing and community curation of mass spectrometry data with Global Natural Products Social Molecular Networking. *Nat. Biotechnol.* 34, 828–837. doi: 10.1038/nbt.3597

Wickham, H., Averick, M., Bryan, J., Chang, W., McGowan, L. D., François, R., et al. (2019). Welcome to the tidyverse. *J. Open Source Softw.* 4, 1686. doi: 10.21105/joss.01686.Wilson

Zhang, S.-L., Cheng, L.-S., Zhang, Z.-Y., Sun, H.-T., and Li, J.-J. (2023). Untangling determinants of gut microbiota and tumor immunologic status through a multi-omics approach in colorectal cancer. *Pharmacol. Res.* 188, 106633. doi: 10.1016/j.phrs.2022.106633

Zhao, P., Xue, Y., Gao, W., Li, J., Zu, X., Fu, D., et al. (2018). Actinobacteria-Derived peptide antibiotics since 2000. *Peptides* 103, 48–59. doi: 10.1016/j.peptides.2018.03.011

frontiers | Frontiers in Marine Science

TYPE Original Research
PUBLISHED 25 October 2023
DOI 10.3389/fmars.2023.1254450

Check for updates

OPEN ACCESS

EDITED BY
Andrew R. Thurber,
Oregon State University, United States

REVIEWED BY
Weichao Wu,
Shanghai Ocean University, China
Amy Renee Smith,
Bard College at Simon's Rock,
United States

*CORRESPONDENCE
Jing-Chun Feng
fengjc@gdut.edu.cn

RECEIVED 10 July 2023
ACCEPTED 12 October 2023
PUBLISHED 25 October 2023

CITATION
Liang J, Feng J-C, Kong J, Huang Y, Zhang H, Zhong S, Tang L and Zhang S (2023) Microbial communities and mineral assemblages in sediments from various habitats at the Haima Cold Seep, South China Sea. *Front. Mar. Sci.* 10:1254450. doi: 10.3389/fmars.2023.1254450

COPYRIGHT
© 2023 Liang, Feng, Kong, Huang, Zhang, Zhong, Tang and Zhang. This is an open-access article distributed under the terms of the Creative Commons Attribution License (CC BY). The use, distribution or reproduction in other forums is permitted, provided the original author(s) and the copyright owner(s) are credited and that the original publication in this journal is cited, in accordance with accepted academic practice. No use, distribution or reproduction is permitted which does not comply with these terms.

Microbial communities and mineral assemblages in sediments from various habitats at the Haima Cold Seep, South China Sea

Jianzhen Liang[1], Jing-Chun Feng[1,2]*, Jie Kong[2], Yongji Huang[2,3], Hui Zhang[1], Song Zhong[1], Li Tang[1] and Si Zhang[2,3]

[1]School of Ecology, Environmental, and Resources, Guangdong University of Technology, Guangzhou, China, [2]Southern Marine Science and Engineering Guangdong Laboratory (Guangzhou), Guangzhou, China, [3]South China Sea Institute of Oceanology, Chinese Academy of Sciences, Guangzhou, China

Cold seeps create diverse habitats in the deep sea and play an important role in the global carbon cycling. Anaerobic oxidation of methane (AOM) and biogenic mineralization are essential carbon pathways of methane and carbon transformation in cold seeps, however, the effects of habitat heterogeneity on the processes are still poorly understood. In this study, we investigated the microbial communities and mineral assemblages at distinct habitats in the Haima cold seep and their relationships with environmental factors. These habitats were classified as methane seep site (MS), seep-free faunal habitat (FH), and control site (CS). Bacterial communities were significantly different among the three habitats. *ANME-3* archaea, *Sulfurovum* bacteria, and mineralization-associated microbes (e.g., Campylobacterales) were detected in high relative abundances at ROV2. Mineralogical analysis revealed abundant calcite minerals at the seep site, indicating that authigenic carbonate minerals were formed at highly active seep. Multivariate statistical analysis demonstrated that the concentrations of SO_4^{2-}, Ca^{2+}, and Mg^{2+} were significantly correlated with the presence of calcite minerals and bacterial communities. These results suggested that AOM-accompanied authigenic carbonate formation is an important factor influencing the mineral assemblages in seep habitats. This finding improves our understanding of marine microbial carbon cycling.

KEYWORDS

microbial community, mineral assemblage, cold seep, habitat, anaerobic oxidation of methane

1 Introduction

Cold seeps are highly productive ecosystems that host thriving biomes and play an important role in global biogeochemical cycling (Offre et al., 2013; Dan et al., 2023). Seep ecosystems are typically characterized by the upward flow from deep sediments of cold fluids rich in methane and hydrogen sulfide. These fluids support diverse chemosynthetic microbial communities (Chen et al., 2022b; Feng et al., 2022a). A diverse array of seep habitats are created by different geochemical processes occurring at different locations within the cold seep area. These processes include the cycling of methane, sulfate, metal elements, and nutrients (Zhuang et al., 2019; Cao et al., 2021). Unique habitats associated with cold seeps include methane bubble seeps (Xin et al., 2022), faunal habitats (Xu et al., 2020), and carbonate rocks (Caesar et al., 2019). Although it has been shown that different types of habitats may be dominated by distinct microorganisms that provide unique ecological functions (Bowles et al., 2016), detailed knowledge of the microbiology and mineralogy of various habitats in the cold seep area remains less understood.

In seep habitats, chemosynthetic microorganisms use methane and sulfate-bearing fluids to produce metabolites and energy to support various faunal communities (Chen et al., 2022b) such as tubeworms (Lee et al., 2021), mussels (Sun et al., 2022), and clams (Ling et al., 2020). The distribution of seep faunal communities is influenced by variations in the dominant chemoautotrophic microbial taxa in seep habitats (Thomas et al., 2018). Microbial communities are controlled by environmental factors in seep habitats such as nutrient supply, and thus their metabolic activity is influenced by habitat heterogeneity (Xin et al., 2022). Sulfate-dependent anaerobic oxidation of methane (SR-AOM) induced by methanotrophic archaea (ANME) and sulfate-reducing bacteria (SRB) is a deep-sea methane sink that consumes a large fraction of methane in seafloor sediments (Niemann et al., 2006; Feng et al., 2022b). Moreover, the SR-AOM process leads to an increase in alkalinity and dissolved inorganic carbon, thereby promoting the precipitation of authigenic carbonates (Liu et al., 2020). Authigenic carbonate minerals are often indicative of methane seepage activity and constitute the most common mineral matrix in seep habitats (Pierre et al., 2017). Thus, habitat heterogeneity in cold seep areas may drive changes in microbial community structure and affect the formation of authigenic minerals.

The Haima Seep is a cold seep system recently discovered in the South China Sea (SCS), which is located in the western Qiongdong Southeast Basin. This seep system is active and at the early and middle development stage (Feng et al., 2023). Submersible surveys have revealed that the Haima seep consisted of multiple unique habitats containing faunal communities and carbonate mounds (Xu et al., 2020). Seepage bubbles, carbonate rocks, and mussel beds have been found in seep habitats, which have various habitat characteristics and distinct microbial communities. In recent years, comparative studies of different habitats in the Haima seep have revealed that the microbial composition differs significantly between habitats in active seeps and non-seep sites (Chen et al., 2022b). Methane content is a key environmental factor driving microbial community variation in these habitats (Li et al., 2021). It has been reported that cold-seep carbonates provide a record of the seepage properties, including changes in fluid source, depositional environment, and seep activity (Guan et al., 2018). A biogeochemical study has indicated that the carbonate phase in the surface sediment from Haima is predominantly high-Mg calcite, suggesting high methane fluxes, and significant AOM activity in the area (Liu et al., 2020). The carbonate minerals at Haima are mainly aragonite, calcite, and lesser amounts of dolomite, which vary greatly in mineral composition (Chen et al., 2022a). These studies have revealed the role of geochemical factors of cold seeps in driving changes in microbial communities and mineral composition. Investigating the effects of habitat heterogeneity on microbial communities and mineral composition is important for detailed assessment of carbon cycling in cold seeps.

To determine how habitat heterogeneity within a seep area shapes microbial communities and mineral characteristics, we compared the microbial communities, environmental factors, and mineral assemblages in sediments from habitats distinguished by distinct landscapes in the Haima cold seep. Sediment samples were collected from the MS, FH, and CS. Bacterial and archaeal communities were studied using 16S rRNA gene amplicon sequencing. Mineral compositions and environmental factors in the habitats were quantified using mineralogical and geochemical analyses. The goal of this study was to better understand: (i) whether intergroup differences exist among sampling sites with various habitats in the cold seep zone, (ii) correlations among microbial community structure, mineral assemblages, and environmental factors, and (iii) the signature microbes in cold seep habitats and carbonate minerals, particularly with respect to whether species associated with methane oxidation and carbonate precipitation inhabit this ecosystem.

2 Materials and methods

2.1 Study area and collection of sediment samples

Sampling was conducted during an expedition in September 2020 at the Haima cold seep area, which is located on the northern SCS continental slope (Feng et al., 2022c) (Figure 1A). Surface sediment samples (0–30 cm) in the area were collected from the seafloor to the ship by using a box corer. For subsequent experimental analyses, sediment samples were collected only in the surface 0–5 cm of the box and then immediately frozen for preservation. The sampling sites in the cold seep area were visually classified based on the presence or absence of methane bubbles in the habitats observed through the diving ROV *Haima*. Three sampling sites were selected based on distinct landscapes: a site with continuous methane bubbles and some live mussels (MS); a site without methane bubbles and with fauna such as live mussels, live conches, dead clams, and live king crabs (FH); and a site with only normal sediments and outside the active seepage (CS) (Figure 1B). Two samples (ROV1 and ROV2; water depths: 1,420

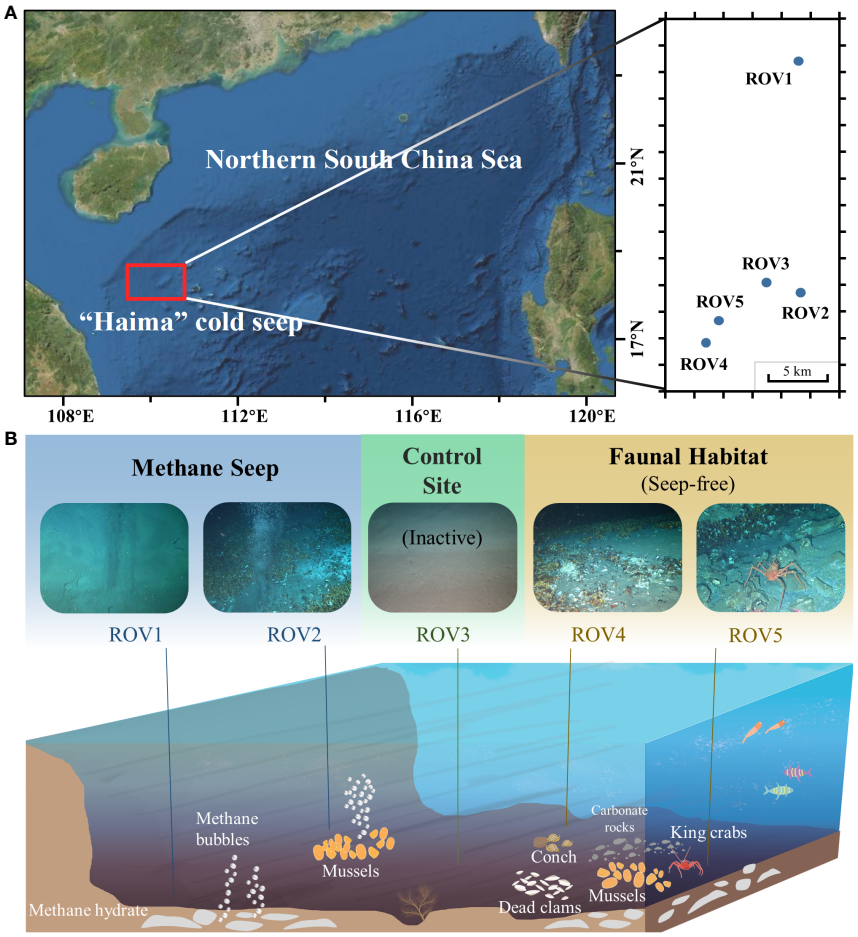

FIGURE 1
Sampling locations **(A)** and habitat features **(B)** at the MS site (ROV 1 and ROV 2), the CS site (ROV 3), and the FH site (ROV 4 and ROV 5) in the Haima cold seep area.

m and 1,384 m) were collected at the MS site, two samples (ROV4 and ROV5; water depth: 1,348 m and 1,347 m) were collected at the FH site, and one sample (ROV3; water depth: 1,378 m) was collected at the CS site. The three sampling sites of MS, CS, and FH were 1–5 km apart. Stations ROV1 and ROV2 were approximately 10 km apart at two different sites of methane seepage. In the *in-situ* observations, ROV1 had no characteristic species and low-rate methane bubbles, while ROV2 had significant mussels and methane bubbles. Based on the theory of the developmental stages of cold seeps (Feng et al., 2023), Stations ROV1 and ROV2 were in the early and early-mid stages of cold seep development, respectively. ROV5 was in the mid-late stage of non-seepage and was evidenced by live and dead mussels and some exposed hydrates. The hydrates in the ROV5 sediment were also observed in the collected samples.

2.2 Geochemical and mineralogical analyses

Salinity, temperature, and dissolved oxygen of bottom seawater were recorded by a conductivity–temperature–depth (CTD) sampler (SBE 911, Sea-Bird Electronics Co. Ltd., Bellevue, Washington, USA). Total organic carbon (TOC) and inorganic carbon (IC) in the sediments were quantified using a TOC analyzer (Shimadzu TOC-L, Kyoto, Japan) that employed catalytic combustion at 900°C (following the manufacturer's instruction). After extraction of pore waters from sediments, the samples were filtered through a 0.22 μm membrane to remove sediment and then were diluted according to the detection limit of the analyzing instrument. The anions (NO_3^- and SO_4^{2-}) were detected using ion chromatography (Thermo Fisher AQ-1200, Waltham, MA, USA) operating at 30°C (Feng et al., 2023). An AS11-HC column was used at a flow rate of 1 mL/min. The ADRS600 suppressor current was set at 120 mA, and the sample test was conducted according to the manufacturer's instructions. For quantification of the metal elements, an inductively coupled plasma-optical emission spectrometer (ICP-OES, Thermo Fisher iCAP 7000 SERIES, Waltham, MA, USA) was used to detect the concentrations of Calcium (Ca), Magnesium (Mg), Natrium (Na), and Strontium (Sr) (Feng et al., 2023). Analysis procedures followed the manufacturer's instructions.

After removing organic matter and carbonate with 10% H_2O_2 and 10% HCl (v/v), respectively, grain-size composition was

analyzed using a Laser Particle Size Analyzer (Mastersizer 3000, Malvern, UK), (Feng et al., 2022c). A 0.05 mol/l sodium metaphosphate solution was added to the samples to prevent the aggregation of fine particles before the analysis. For mineral analysis, the crystalline phases of the five sediment samples were analyzed using X-ray diffraction (XRD, D/Max-rA, Rigaku, Japan). All samples were air-dried, ground to homogenize them and run as packaged powders. The samples were scanned by XRD with Cu Kα radiation at 40 kV/45 mA over a range of 5–70° 2θ (where θ is the scan angle) (Wei et al., 2020). The results were identified using the International Center for Diffraction Data 2014. The relative quantification of phases was given in weight percent. The morphological features and element components of the samples were then characterized using scanning/transmission electron microscopy (S/TEM, Thermo Fisher Talos F200S, Waltham, MA, USA) coupled with energy dispersive spectroscopy (EDS) (Marlow et al., 2021).

2.3 DNA extraction, PCR, and 16S rRNA gene sequencing

The microbial community compositions in the Haima area were explored using an Illumina high-throughput sequencing approach (Kong et al., 2023). The total genomic deoxyribonucleic acid (DNA) of the microbes was extracted from 0.5 g sediment following the Zhou method (Zhou et al., 1996). Sediments were freeze-thawed in a high-salt extraction buffer containing hexadecyltrimethylammonium bromide (CTAB) and 1.5 M NaCl. Samples were then treated with sodium dodecyl sulfate (SDS) and proteinase K, and extracted with chloroform-isoamyl alcohol. The purity and quality of extracted DNAs were evaluated using a NanoDrop ND-2000 spectrophotometer (Thermo Fisher, Waltham, MA, USA) and agarose gel electrophoresis. The DNA concentrations were measured using a Qubit 3.0 Fluorometer (Life Technologies, CA, USA).

Polymerase chain reaction (PCR) amplification of the 16S rRNA gene of the V3-V4 region was performed using the primers bacteria (341F: 5′-CCTACGGGNGGCWGCAG-3′/806R: 5′-GACTACHVGGGTATCTAATCC-3′) and archaea (Arc349F: 5′-GYGCASCAGKCGMGAAW-3′/Arc806R: 5′- GGACTACVS GGGTATCTAAT-3′) (Takahashi et al., 2014). Sample-specific16-bp barcodes were incorporated into the primers for multiplex sequencing. The PCR components contained 5 μL of KAPA HiFi Buffer (5×), 0.75 μL of KAPA HiFi Hot Start DNA Polymerase (1U/μL), 0.75 μL (10 mM) of dNTPs, 0.75 μL (10 μM) of each Forward and Reverse primer, 2 μL of DNA Template, and 15 μL of ddH2O. Thermal cycling consisted of initial denaturation at 95°C for 5 s, followed by 25 cycles consisting of denaturation at 95°C for 30 s, annealing at 57°C for 30 s, and extension at 72°C for 60 s, with a final extension of 5 min at 72°C. PCR amplicons were purified with Agencourt AMPure Beads (Beckman Coulter, Indianapolis, IN) and quantified using the PicoGreen dsDNA Assay Kit (Invitrogen, Carlsbad, CA, USA). After the individual quantification step, PCR products were pooled in equal amounts. The pooled sample was then used to generate a library using SMRTbell Template Prep Kit 1.0-SPv3, and sequencing was conducted using an Illumina Miseq PE300 Sequencer system (Illumina Inc., San Diego, CA, USA).

2.4 Quality control, sequence assembly, and taxonomy assignment

Sequencing data were processed and analyzed using the software VSEARCH v2.7.0 and QIIME v1.9.1. The adapter and low-quality base pairs (bp) were identified and trimmed from the ends of the raw paired-end reads using Trim Galore v0.4.5, and then the short reads (< 100 bp) were removed. The paired-end reads were merged using VSEARCH, the sequences with low quality (total expected errors > 1) and shorter than 300 bp were discarded. The operational taxonomic units (OTUs) were clustered at 97% identity using the command cluster_fast (Rognes et al., 2016). Then, OTU-based chimera was detected using the command uchime_ref based on the Silva132 Database (Yilmaz et al., 2013). The taxonomy assignments for the representative sequence of the OTUs was conducted by BLAST against the Silva132 Database, using assign_taxonomy.py in QIIME (Caporaso et al., 2010). Taxonomy files and OTUs were further generated and the OTUs with less than 0.001% of total sequences in all samples were discarded. Before downstream analysis, 64,400 sequencing reads were obtained from the 5 samples after a flattening process. All raw data has been submitted to the NCBI Sequence Read Archive (accession code PRJNA973956).

2.5 Statistical analysis

All statistical analyses were performed using R software (version 4.1.1) with various packages. Alpha diversity indices (Shannon diversity, Simpson diversity, Chao1 richness, ACE richness) were used to assess the diversity of microbial communities, which were calculated using the "vegan" package (version 2.6-4) (Willis, 2019). Sparse curves were constructed using the "rarecurve" function ("vegan" package). Mantel's test ("LinkET" package, version 0.0.6.1) and Pearson's correlation analysis were performed to identify the subset of environmental variables that statistically explained the largest proportion of taxonomic unit variation (Legendre et al., 2015). Redundancy analysis (RDA, "vegan" package) was used to find environmental factors that could potentially explain community variances (Forester et al., 2018).

To visualize the analysis results, charts of geochemical parameters and mineral composition were plotted by Origin (version 2021). Microbial community compositions at the phylum level were illustrated as stacked bar charts by R ("ggplot2" package, version 3.4). The taxonomic abundance heatmap and Venn diagram were completed using the online tool Wekemo Bioincloud (https://www.bioincloud.tech). Chord diagrams were constructed using the online tool "circus" (http://circos.ca).

3 Results

3.1 Sampling sites and geochemical parameters

The three sampling sites (MS, CS, and FH) had distinct landscapes and habitats (Figure 1B). The MS site (stations ROV1 and ROV2) was an active seep with continuous methane bubbles. Live mussels and tubeworms were observed at this site. The FH site (stations ROV4 and ROV5) was a non-active seep without bubbles. Carbonate rocks, dead clams, and live king crabs were observed there. As the control, the CS site (station ROV3) was outside the active seep and had no characteristic faunal or rock.

Fundamental geochemical parameters, including TOC, IC, nitrate, sulfate, Mg, Ca, Sr, and median pore diameter, varied among the five sampling locations. Other parameters, including salinity, temperature, and dissolved oxygen, were relatively constant among these sites (Supplementary Table 1). The highest amounts of TOC and IC were found at the MS site. Peaks of 2.94% and 2.33% were observed for TOC and IC at ROV2 (Figure 2A). At the CS site, low values of 1.68% TOC and 1.57% IC were observed at ROV3. Notably, concentrations of sulfate and the metal elements Mg and Ca were highest at ROV2 (Figure 2B). Mg/Ca and Sr/Ca ratios were determined to identify the mineral type due to geochemical precipitation processes at these sites. The Mg/Ca ratios of all five sites were high, indicating that high-Mg calcite may be the dominant mineralogical composition of carbonate rocks at the Haima seep (Figure 2C). A maximum median pore diameter of 9.42 μm was observed at ROV2 (Figure 2C). The ROV2 site also had high organic matter and mineral content, which may be supporting numerous microorganisms and high chemosynthetic activity.

3.2 Microbial community structure and alpha diversity

The DNA of the microorganisms in the sampling sediment was extracted and sequenced. The average sequences of archaea and bacteria in samples from the five sites were 35,168 and 29,232 respectively. Rarefaction curves based on the archaeal and bacterial OTUs were plotted (Supplementary Figure 1). All of the curves reached an asymptote for the libraries of archaea and bacteria. Therefore, the sequencing data are sufficient to detect the presence of microbes and provide reliable results.

There was a difference in microbial community structure between the sites with and without methane-bubble seep. Site MS community was dominated by bacteria, accounting for 52–80% of the total sequences (Supplementary Figure 2). In contrast, archaea were more abundant at the FH site, contributing to 80–85% of the total populations. With respect to the archaeal community composition, Thaumarchaeota was the most abundant phylum in this area, especially at the sites of ROV1, ROV3, and ROV4 (Figure 3A). Notably, Euryarchaeota was the most abundant phylum ROV2 and ROV5. In terms of bacterial community composition, site ROV2 had a richer and more diverse set of taxa than the other sites (Figure 3B). *Proteobacteria* was the most abundant phylum at all sites except for ROV5 site, where Chloroflexi was the most abundant phylum. The relative

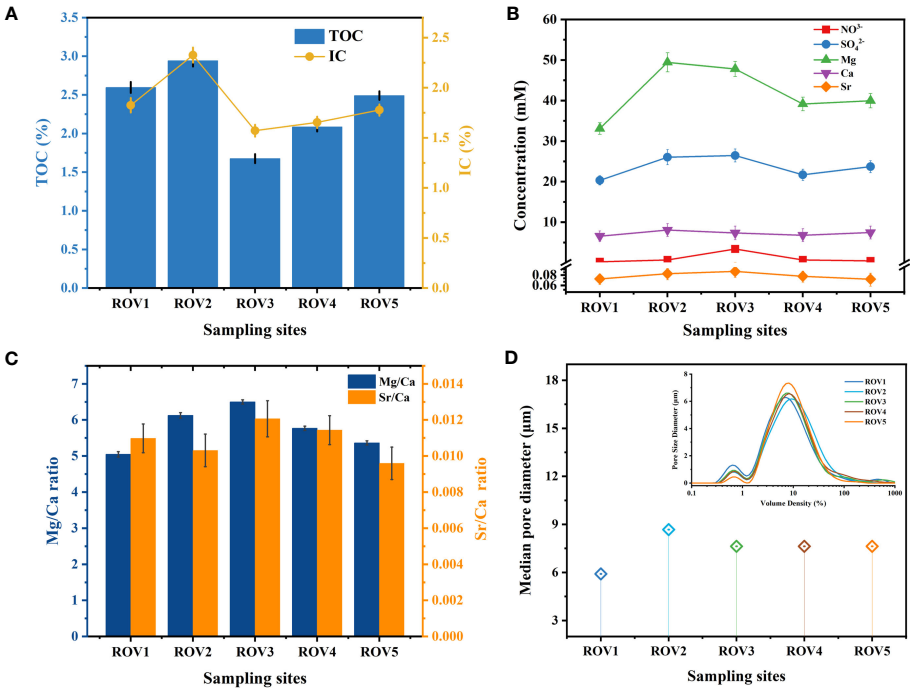

FIGURE 2
Fundamental geochemical parameters of sediments from the five sampling locations: organic content **(A)**, concentrations of the anions and metal elements **(B)**, Mg/Ca and Sr/Ca ratio **(C)**, and median pore diameter **(D)**.

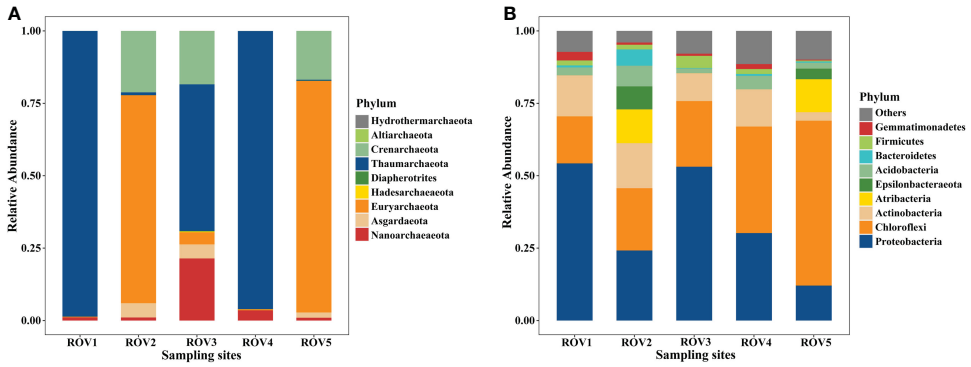

FIGURE 3
Relative abundance of phylum-level archaea **(A)** and bacteria **(B)** among the five sites.

abundance of archaeal and bacterial phyla varied among all five sites. The variability of community composition was visualized by Principal coordinate analysis (PCoA). The results showed that the distribution patterns of archaeal and bacterial genera at the MS and FH sites were similar, but the pattern at the CS site differed from other sites (Supplementary Figure 7). As shown in the genus heatmap (Figure 4), the distribution of top 25 abundant genera of bacteria was different between the MS site and FH site, but that of archaea was relatively similar between the two sites. Corresponding abundance relationships between all sites and the communities, including archaea and bacteria, were visualized using Circos analysis (Supplementary Figure 4). The relationships showed that site ROV2 had the least abundant archaeal genera and the most abundant bacterial genera. Notably, the genera associated with the SR-AOM process, such as *ANME-3*, *SEEP-SRB1*, and *SEEP-SRB4*, were found mainly distributed in site ROV2.

The fact that distinct habitats hosted quite different microbial communities (Figure 4) but shared many OTUs (Figure 5) means that compositional differences were generally a function of differential OTU relative abundance. The MS site exhibited approximately 40% lower archaeal OTU richness and 40% higher bacterial OTU richness than the other sites (Supplementary Figure 3). The analysis of OTU overlap among these sites revealed that microbial communities within the Haima seep area demonstrated clear differentiation according to habitat heterogeneity (Figure 5). The results indicated that microbial community shared only 88 (~9%) archaeal OTUs and 371 (~15%) bacterial OTUs across the habitats. The MS site had relatively less unique archaeal OTUs and more unique bacterial OTUs in comparison to the FH site. In terms of specific sites, the distribution of unique OTUs at each site is similar to the habitat to which it belongs. Therefore, both archaeal and bacterial communities were generally divided by habitat type, with significant differences among the distinct habitats of MS, FH, and CS sites within the Haima seep area.

We also explored the alpha diversity of archaeal and bacterial communities at sites with distinct habitats. Chao1 and ACE indices reveal community richness and estimate the number of OTUs in the samples (Kemp and Aller, 2004). The Chao1 and ACE indices of the MS site were different from those of both the CS and FH sites (Supplementary Figure 3). Archaeal richness was the lowest at site MS and the highest at site FH, whereas the bacterial richness was the highest at site MS and lowest at site FH. Shannon and Simpson indices are used to describe community diversity (Chao et al., 2014). The Shannon and Simpson indices of the CS site were different from those of both the MS and FH sites (Supplementary Figure 3). Community diversity was low when the Shannon index was small and the Simpson index was large. As a result, the bacterial diversity at the CS site and the archaeal diversities at the MS and FH sites were low.

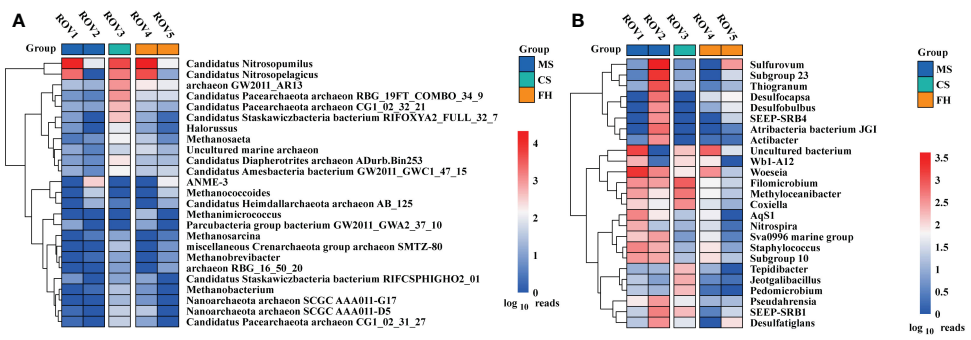

FIGURE 4
Heatmaps based on the 25 most abundant genera of archaea **(A)** and bacteria **(B)** at the five sites.

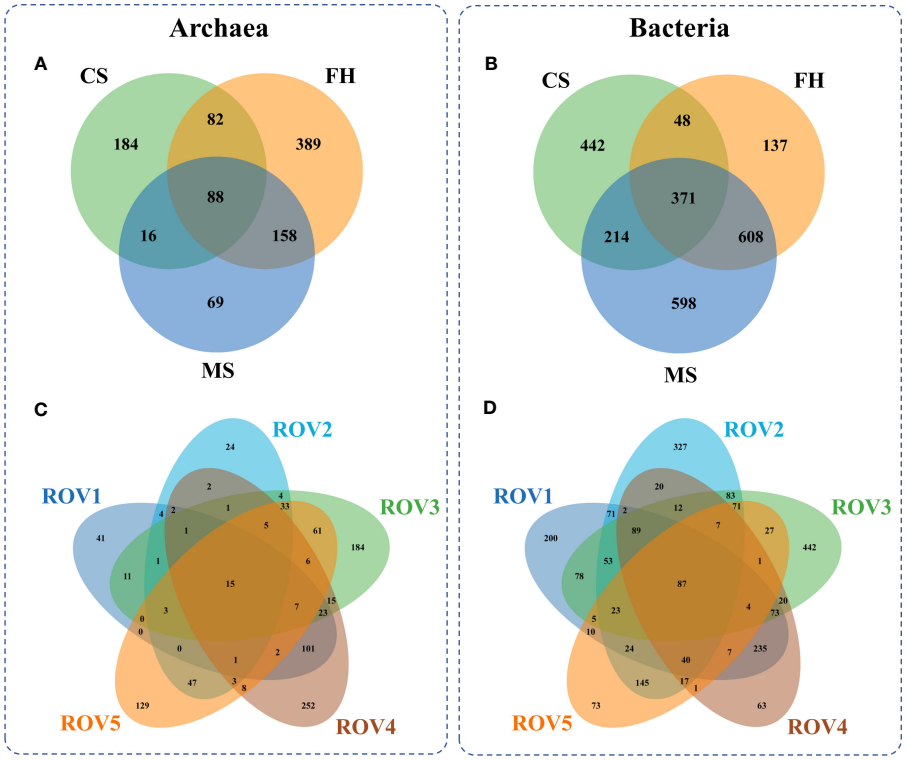

FIGURE 5
Archaeal OTU overlap among various habitats **(A)** and sampling sites **(C)**, and bacterial OTU overlap among the habitats **(B)** and the sites **(D)**.

3.3 Correlations among microbial community structure, mineral assemblages, and environmental factors

To explore the key environmental variables and mineral assemblages that may have shaped microbial community composition, correlations between the microbial diversity and the variables were evaluated using RDA analysis and a permutation test based on the relative abundance at the genus level. Quantification of major environmental and mineral parameters, including TOC, IC, NO_3^-, SO_4^{2-}, Ca, Mg, Na, Sr, D50, Illite, Clinochlore, Quartz, Albite, Calcite, and Halite, was used for RDA analysis. The permutation test indicated that TOC made a statistically significant ($p < 0.05$) contribution to explaining the variance in archaeal communities (Figure 6A). Comparatively, Ca, SO_4^{2-}, Mg, and calcite were suggested as the most significant ($p < 0.01$) environmental factors in the bacterial communities (Figure 6B). Notably, site ROV2 was most relevant to the key variables of TOC, IC, Ca, and calcite, indicating that this site may have a strong correlation with the process of carbonate precipitation. In addition, characteristic genera

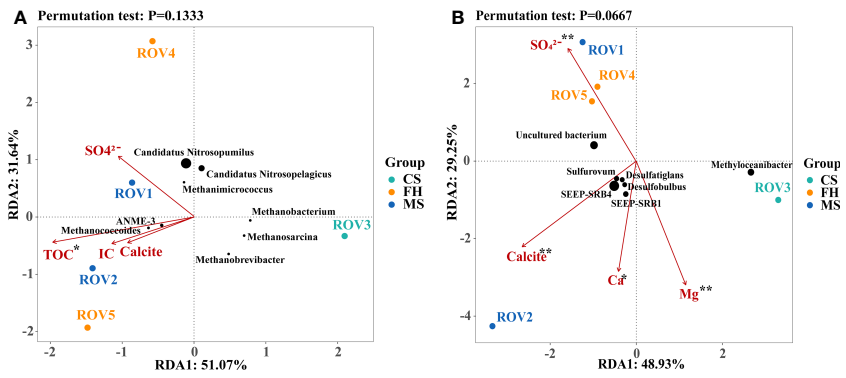

FIGURE 6
Redundancy analysis (RDA) correlation of the environmental and mineral variables to archaeal **(A)** and bacterial **(B)** communities. The green, yellow, and blue dots in the figure represent the sites CS, FH, and MS, respectively. The black points indicate the characteristic genera, and their sizes represent the genera abundance. The pink arrows indicated individual environmental and mineral parameters. Significance levels (marked by asterisks) were based on the permutation test. **$p < 0.01$; *$p < 0.05$.

such as *ANME-3*, *SEEP-SRB1*, and *SEEP-SRB4* showed a strong correlation with the key variables of carbonate precipitation.

Environmental drivers at the habitats in the Haima seep were identified based on our dataset to validate the independence of the microbial communities at different habitats. Differences in bacterial and archaeal community composition were correlated with differences in environmental factors as shown in Figure 7. The results showed that SO_4^{2-}, Mg, and calcite were the strongest correlates (<0.01) with bacterial community composition in the habitats. In addition, IC, Ca, and calcite were found to be significantly correlated (<0.05) with bacterial community composition. Thus, the environmental drivers of microbial communities in the habitats in the Haima area are mainly SO_4^{2-}, Ca, Mg, and Calcite, all of which are associated with mineralization processes.

3.4 Mineral assemblages in cold seep habitats

Minerals from sediment at the five Haima area sampling sites showed a relatively similar composition (Figure 8). The minerals in the sediments included illite, clinochlore, quartz, albite, calcite, and halite (Figure 8A). The results indicate that most of the sediments in Haima seep were dominated by siliciclastic minerals such as quartz and illite. Quartz content varied between 19% and 38%, and illite content ranged from 16% to 31% (Figure 8B). Sample ROV2 was dominated by calcite (48%), which was the major microcrystalline carbonate phase. Due to the ROV2 site was in a methane-seep habitat and had abundant genera associated with the SR-AOM process (Figure 4), the mineralization of authigenic carbonate at this site may relate to the methane-seep process. The calcite content varied between 2% and 12% at the other sites. In the FH site, Sample ROV5 had a relatively high amount (~12%) of authigenic carbonate.

Minerals with distinct morphologies from different habitats of the Haima area were observed using SEM (Figure 9). The mineral samples were observed to be mostly clastic mineral forms 10 μm in size. High levels of terrestrial clasts were found in the sites of ROV1, ROV3, and ROV4 (Figures 9A, C, D). The mineral phases at these sites were dominated by illite and quartz, while authigenic calcite was rarely present (Figure 8B). By contrast, authigenic calcite had a relatively high distribution at site ROV2 (Figure 9B) and was locally present at site ROV5 (Figure 9E). This phenomenon was related to the relatively high content of Ca and organic carbon at sites ROV2 and ROV5 and the abundance of methane cycle taxa (Figures 2, 3). Interestingly, some calcite showed axial growth morphology (Figures 9B, E), suggesting that it may have formed from authigenic carbonates. In addition, carbonates were present in different mineral forms. Carbonate minerals at site ROV2 exhibited not only strip morphology but also flake and block morphology (Supplementary Figure 5).

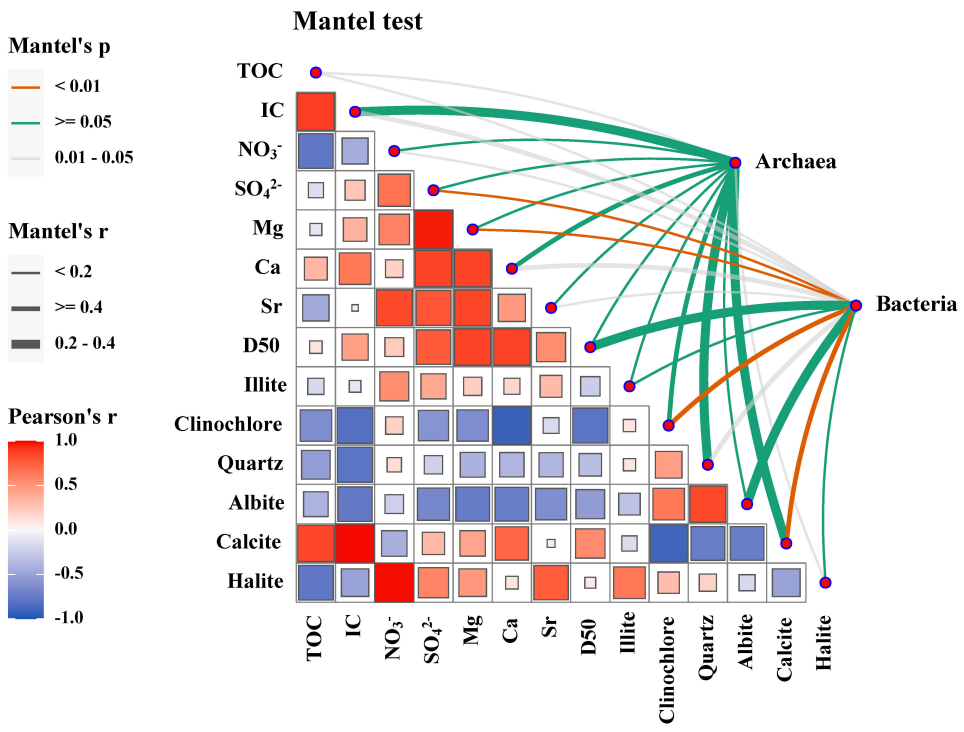

FIGURE 7
Environmental drivers of the microbial community compositions. Pairwise comparisons of environmental and mineral variables are shown, with a color gradient indicating Spearman's correlation coefficients. The community composition of genera was related to each variable by partial Mantel tests. Edge width corresponds to the Mantel's r statistic for the corresponding distance correlations, and edge color denotes the statistical significance based on the permutation test.

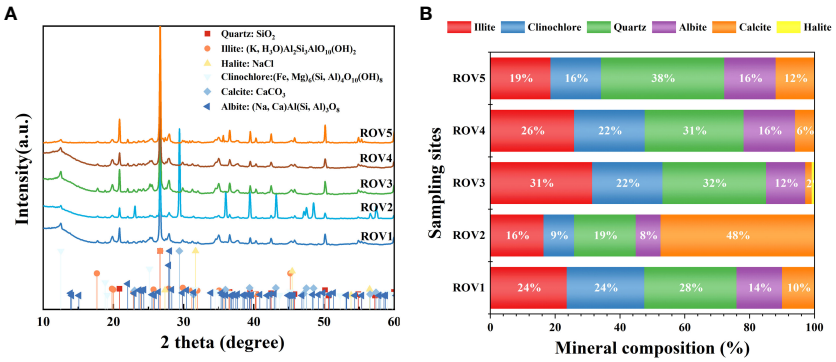

FIGURE 8
XRD patterns **(A)** of minerals in cold-seep habitats. Mineral composition **(B)** of the sediment sample was characterized by illite, clinochlore, quartz, albite, calcite, and halite.

3.5 Indicator microbes associated with SR-AOM and mineralization in different habitats

Calcite-dominated minerals were identified at site ROV2 (Figure 8B). They were mainly authigenic carbonates resulting from biological mineralization (Li et al., 2018a). SR-AOM is considered an organic matter mineralization process (Han et al., 2013). The distribution of indicator microbes associated with this process at each sample site was evaluated (Figure 10). The results indicate that the taxa associated with SR-AOM processes were found in relatively low relative abundance (<10%) at sites ROV1, ROV3, and ROV4, while significant enrichment of *ANME-3*, *Methanococoides*, *Sulfurovum*, *Desulfocapsa*, and *SEEP-SRB2* was identified at sites ROV2 and ROV5. The dominant genus *ANME-3*, which induces the AOM process, had a relative abundance in

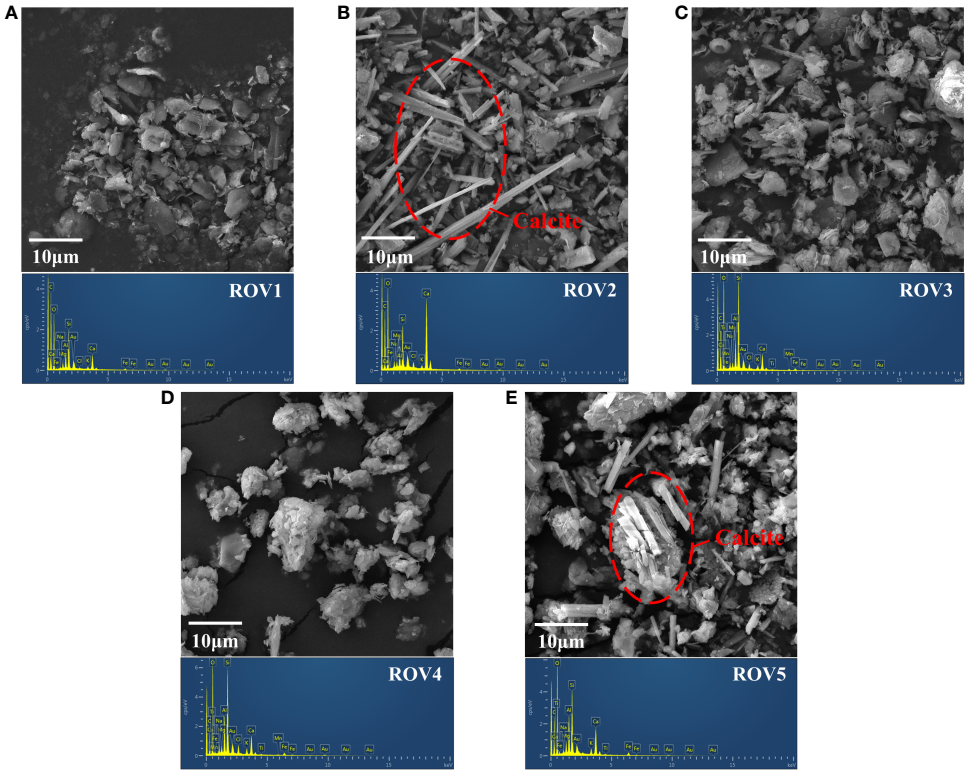

FIGURE 9
Multiple morphologies of minerals in various habitats at the Haima seep. The SEM images of minerals at the sites ROV1 **(A)**, ROV2 **(B)**, ROV3 **(C)**, ROV4 **(D)**, and ROV5 **(E)**. Calcite is marked by a red arrow.

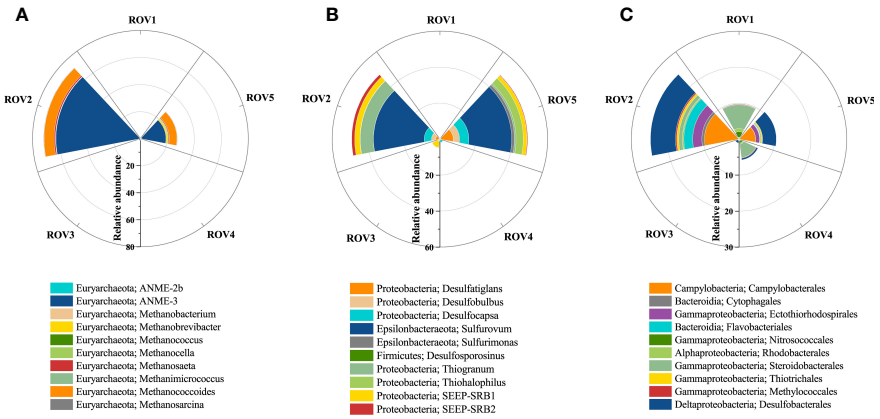

FIGURE 10
Signature microbes associated with the processes of SR-AOM and mineralization. Relative abundance of AOM-related genera **(A)**, SR-related genera **(B)**, and mineralization-related microbes at order level **(C)** in the seep area.

archaea of 62.3% in ROV2 and 18.1% in ROV5 (Figure 10A). The genus *Sulfurovum*, which induces the SR process, had a relative abundance in bacteria of 28.3% at ROV2 and 23.8% at ROV5 (Figure 10B). These organisms were likely supported by the high organic carbon content and sulfate concentration in the seep areas (Figure 2). Euryarchaeota *ANME-3* and Epsilonbacteraeota *Sulfurovum* were found to be characteristic of microorganisms in seep sediments of the Haima area (Niu et al., 2017). Our data corroborate this finding.

Taxa related to authigenic carbonates, such as Campylobacterales, Desulfobacterales, and Ectothiorhodospirales, were found to be present in the Haima area (Figure 10C). The taxa composition was similar to carbonate-host microbes that are considered early successional communities of carbonate biofilms (Case et al., 2015; Leprich et al., 2021). The abundance of those taxa was relatively high at sites ROV2 and ROV5 and was significantly different from that at other sites. Therefore, minerals with high carbonate content were associated with the enriched indicator microbes. Correlations of mineral and environmental factors with the abundance of indicator microbes were analyzed (Supplementary Figure 6). The results show that the abundance of Desulfobacterales was strongly correlated ($p < 0.001$) with Ca concentration variation, and the abundance of Campylobacterales, Thiotrichales, and Ectothiorhodospirales was significantly correlated with calcite content ($p < 0.05$). In addition, the abundance of genera such as *ANME-3*, *Methanococoides*, and *SEEP-SRB2* was significantly correlated ($p < 0.05$) with changes in Ca concentration and calcite content (Supplementary Figures 6A, B), suggesting that the SR-AOM process was strongly associated with the process of carbonate formation.

4 Discussion

We conducted this comprehensive study of the variability in microbial communities, environmental factors, and mineral assemblages among different habitats to explore how microbial communities and mineral assemblages were shaped by the distinct habitats in the Haima seep area. Surface sediments were collected from different habitats including methane seep sites, seep-free faunal habitats, and a seep-free control site in the Haima area. Different microbial communities and mineral compositions revealed environmental controls on the relative importance of the biogeochemical processes. Environmental factors were likely to influence microbial community structure and thus authigenic mineral formation. These observations invoke questions about the linkage between environmental factors, microbial communities, and mineral assemblages in the sediments of Haima.

4.1 Geochemical characteristics of different habitats in the Haima seep

Characteristics of sediment from the Haima area revealed that environmental factors varied among habitats. The amount of organic matter and metal ions was higher in the seep habitat compared with other habitats. Organic carbon and metal elements in subsurface sediments were possibly sourced from deep fluids associated with methane seepage (Pierre et al., 2017). The TOC and IC were highest at site ROV2 (Figure 2A), indicating that microbially induced carbon cycling was active at this site (Dan et al., 2023). The high content of TOC indicated methane seepages, abundant microorganisms, and organic metabolites (Valentine et al., 2005). High IC suggests the presence of organic matter mineralization at the site (Núñez-Useche et al., 2018). Intense AOM promotes the combination of oversaturated HCO_3^- with metal ions and leads to the precipitation of carbonate minerals (Baker and Burns, 1985). TOC and IC were higher at the Haima sampling sites than at other cold seep areas in the SCS (Li et al., 2018b; Zhuang et al., 2019; Zhang et al., 2022b). TOC and IC can indicate the geochemical processes of methane seepage activity, as explained in recent studies on the long history of cold seep evolution in the Haima (Zhang et al., 2022a; Dan et al., 2023).

Sulfate acts as an important electron acceptor for the AOM process, and variations in its concentration affect the efficiency of

SR-AOM (Boetius et al., 2000). The levels of sulfate at the sampling sites were consistent with Haima seep sediments from previous studies (Zhuang et al., 2019; Liu et al., 2020; Huang et al., 2023). At ROV2 and ROV5, the sulfate concentrations in the sediments were relatively high (Figure 2B), implying a potentially high geochemical reactivity, especially SR-AOM (Li et al., 2020). Sulfate concentration was controlled by the upper water column, and the difference in its distribution affected the reaction efficiency of AOM (Orcutt et al., 2005). Since authigenic carbonate was one of the products of the AOM process, its content can be indirectly affected by sulfate (Li et al., 2018a). In addition, the relatively large grain size of sediments at ROV2 indicated the presence of numerous large-grained minerals (Figure 2D). The minerals were mostly authigenic carbonates (Figure 8B), which usually precipitate at seep sites due to the AOM reaction and gradually form carbonate rocks (Caesar et al., 2019).

To evaluate the potential of biological mineralization in the study area, we investigated the substances associated with authigenic carbonates. Variations in Ca^{2+}, Mg^{2+}, and Sr^{2+} concentrations can be used to identify the mineral phases of carbonate precipitation (Nöthen and Kasten, 2011; Liu et al., 2020). In this study, the metal elements Mg and Ca were at high levels at ROV2 (Figure 2B). The Mg/Ca ratio was also relatively high (Figure 2C). The results indicate that authigenic carbonate precipitation may have occurred in the sediments. The mineral composition of carbonates in cold seeps can be used to indicate seepage intensity (Roberts et al., 2010; Nöthen and Kasten, 2011). Carbonates were the most abundant minerals at site ROV2 (Figure 8), suggesting a high-activity methane seepage at this location. XRD analysis results of carbonate minerals are consistent with findings in other reports that calcite is one of the authigenic carbonate minerals formed in the cold seep system (Naehr et al., 2007; Liu et al., 2020). Calcite has been proven to preferentially precipitate in sediments with low sulfate concentrations due to the inhibition of calcite precipitation by sulfate ions (Nöthen and Kasten, 2011; Hu et al., 2015). In this study, the sulfate concentrations at the sampling sites were at high levels (>20 mM, Figure 2B), which may be an important reason for the generally low calcite content in the area (except at site ROV2). In addition, the Sr/Ca of aragonite is higher than that of seawater, and thus the precipitation of aragonite will lead to lower Sr/Ca in pore water (Nöthen and Kasten, 2011). The Sr/Ca ratio at ROV2 was low (Figure 2C), so it was inferred that a very small amount of aragonite precipitation may be present at this site. Therefore, we suggest that environmental factors such as Mg, Ca, and SO_4^{2-} concentrations were important factors influencing the formation of authigenic carbonate minerals.

4.2 Microbial community similarity and variability among different habitats

Similarities and variability of archaeal and bacterial communities were found in different habitats of the seep area. Dominant archaeal groups, such as Thaumarchaeota and Euryarchaeota, were consistently detected at all five sites (Figure 3A). These archaea are widespread in marine seep sediments (Cui et al., 2019; Jing et al., 2020; Xin et al., 2022), and they largely constrain the ecological roles in local habitats. Thaumarchaeota, an aerobic archaeal phylum capable of ammonium oxidation, can be involved in various biogeochemical processes, including but not limited to nitrification and carbon fixation (Offre et al., 2013). Some of its members are chemoorganotrophs with multiple functions such as aerobic mineralization of organic matter (Adam et al., 2017). The archaea at ROV2 had the lowest abundance compared with other sites (Supplementary Figure 2), and were simple in composition, with the dominant phylum being Euryarchaeota (relative abundance >70%, Figure 3A). The taxa of Euryarchaeota, such as methanogens and methanotrophs, are mostly associated with methane cycling processes consisting of methane production and the anaerobic oxidation of methane (Jing et al., 2020; Fischer et al., 2021). A previous study has indicated that methane oxidation and methane production occur simultaneously in seep sediments although the AOM process dominates at the site (Orcutt et al., 2005). In this study, enriched *Methanococcoides* and *ANME-3* were detected simultaneously at the seep site (Figure 10A). Thus, our results support the notion that methane-seep habitats have high relative proportions of methane-cycling communities.

For bacterial communities in our study, Proteobacteria and Chloroflexi were dominant at the sampling sites (Figure 3B). Phylum Chloroflexi is widely distributed and diverse in the marine environment, but poorly characterized (Zhang et al., 2012). Chloroflexi generally dominates pelagic or organic-rich seafloor sediments (Inagaki et al., 2003). The large number of benthic fauna found at ROV4 and ROV5 supports this finding (Figure 1B). Proteobacteria are found in high relative abundance and phylogenetic diversity in various marine habitats (Cui et al., 2019; Xin et al., 2022). Heterotrophic Proteobacteria are deeply involved in the sulfur cycle through the sulfate reduction mediated by *SEEP-SRB1* and the sulfur oxidation mediated by *Sulfurovum*. SR-related genera associated with particular ANME partners contribute to carbon cycling through the SR-AOM process (Chen et al., 2022b).

In this study, the diversity and relative abundance of archaea were low at the MS site, while bacteria were high (Supplementary Figure 3). The abundance of unique archaeal OTUs was lowest in the methane-seep habitat compared with the other habitats (Figure 5). Comparatively, the abundance of unique bacterial OTUs was highest in the methane-seep habitat compared with the other habitats. This spatial distribution is consistent with other studies (Niu et al., 2017; Xin et al., 2022) and is caused by the heterogeneity of the geochemistry of different habitats. The MS site and the seep-free FH site shared more archaea and bacteria OTUs than any other two habitats, indicating an overall similarity between them (Figure 5; Supplementary Figure 7). Methane-seep habitat and faunal habitat belong to different developmental stages of cold seeps (Feng et al., 2023). The microbial communities in the faunal habitat are largely sourced from the cold seep vent, and they are symbiotic with seep fauna such as mussels and clams (Chen et al., 2022b). The fauna is supplied with metabolic material and energy by the chemoautotrophic microbes. In both habitats, although ROV2

and ROV5 sites showed similarities, whereas ROV2 had more AOM- and SR-related genera and produced more authigenic carbonates compared to ROV5 (Figures 8, 10). Thus, the SR-AOM process differs in reactivity across distinct habitats within a cold seep area. Further, habitat heterogeneity contributes to differences in methane oxidation efficiency, thereby influencing carbon cycling in cold seeps.

Community distribution in cold seep areas is closely related to the location of the seepage. The microbial taxa associated with SR-AOM reflect different levels of activity at different sites (Zhuang et al., 2019). In this study, ANME was detected at ROV2 (Figure 4A), indicating high methane oxidation activity at this site. *ANME-2* was the most widespread and abundant clade, yet only a small amount of *ANME-2b* (<5%) was detected at the Haima seep site (Figure 10A). In contrast to previous investigations, *ANME-3* is detected as the dominant clade of the methane-metabolizing genus (relative abundance >60%, Figure 10A). *ANME-3* was generally found in mud volcanoes and some seep sediments (Niemann et al., 2006). Thus, it was reasonable for *ANME-3* to be present in seep sediment at our sampling sites. On the other hand, sulfate-cycling bacteria were highly diverse and varied widely between sites. They were dominated by *Sulfurovum* at ROV2 and ROV5, while relatively high abundances of *SEEP-SRB1*, *SEEP-SRB2*, and *SEEP-SRB4* were also present (Figure 10B). This is consistent with a previous report that *Sulfurovum* is abundant in the surface sediments of a cold seep (Li et al., 2021). *Sulfurovum*, the sulfur-oxidizing member of Epsilonbacteraeota, uses CO_2 produced by ANME as a carbon source and is able to oxidize sulfide produced by SRB to sulfate (Liu et al., 2016). *Sulfurovum* is involved in carbon fixation and sulfur oxidation in marine ecosystems. Through the sulfur oxidation, sulfur bioavailability is further enhanced to support the metabolism of SRB, thereby facilitating the SR-AOM process. Thus, functionally diverse sulfur-cycling bacteria coupled with methane oxidation support carbon cycling in cold seep habitats.

4.3 Linkage between environmental factors, microbial community, and mineral assemblage

The effect of habitat heterogeneity on community diversity and mineral assemblage was evident. We found that the diversity of microbial communities in habitats was affected by environmental factors. The variables with statistical differences between habitats were SO_4^{2-}, Ca, Mg, and TOC (Figures 6, 7). SO_4^{2-} has been proven to be the most important factor in the structure of the microbial bacterial community in the sediment environment (Orcutt et al., 2005; Zhuang et al., 2019). Sulfate is abundant at the seep and SR is the main terminal electron-accepting process. The availability of the electron acceptor SO_4^{2-} may drive the distribution of methane oxidizers (Li et al., 2020). In addition, the distribution of the archaeal community may be influenced by high organic carbon in the habitat. The high organic carbon represented abundant organic matter or methane, indicating that both methanogens and methanotrophs may be present in this habitat (Jing et al., 2020; Fischer et al., 2021). Therefore, different environmental conditions are selected for different types of methane metabolizing communities.

Authigenic carbonate precipitation induced by AOM is an important sink in marine carbon cycling (Marlow et al., 2014; Marlow et al., 2021). Our results showed that the IC content and the concentrations of alkaline earth elements (Mg, Ca, and Sr) were relatively high at ROV2 (Figure 2), indicating that authigenic carbonate precipitation occurred in the sediments (Figure 9). Different carbonate mineralogy was inferred through the relationship between Sr/Ca and Mg/Ca ratios in the pore water (Nöthen and Kasten, 2011; Liu et al., 2020). The high Mg/Ca ratios (>5) in pore water indicated the occurrence of possible primary high-Mg calcite (Bayon et al., 2007). The precipitation of high-Mg calcite may indicate a relatively low-activity seep environment (Hu et al., 2015). *ANME-3* found in association with the *Desulfobulbus* has been determined to oxidize seafloor methane and deliver reductants to their synthetic partner (Niemann et al., 2006). AOM produces two units of alkalinity per one unit of dissolved inorganic carbon, increasing the alkalinity of the pore water and promoting the precipitation of authigenic carbonate minerals (Aloisi et al., 2002).

The formation of carbonate minerals not only occurs through biological mineralization of organic matter but also is facilitated by the secretion of extracellular macromolecules by specific microbes (Wei et al., 2021). In this study, strong correlations with carbonate were found for Campylobacterales and Desulfobacterales (Supplementary Figure 6). These taxa are considered early successional communities of carbonate biofilms (Case et al., 2015; Leprich et al., 2021; Marlow et al., 2021). Campylobacterales attach to mineral surfaces and dominate the formation of biofilm communities. Desulfobacterales, as heterotrophic bacteria, are believed to have a potential role in the production of the extracellular matrix. The amounts of exopolymeric substances can affect the morphology and mineralogy of the carbonate minerals (Braissant et al., 2007). Interactions between elemental Ca and exopolymeric substances are the main processes by which the extracellular matrix controls the precipitation of carbonate minerals.

In general, the environmental characteristics of the habitat and the benthic microorganisms collectively influenced the mineral assemblages. Environmental drivers such as SO_4^{2-}, Ca, and Mg shaped the microbial communities in seep habitats. The SR-AOM and mineralization processes induced by microbes were affected by the seepage activity in the habitat. Microbial metabolism altered the environmental factors, leading to changes in the precipitation conditions of certain minerals. Thus, the formation of authigenic carbonate minerals resulted in variations of mineral assemblages in different habitats.

5 Conclusion

We conducted a comprehensive biogeochemical and mineralogical study to investigate microbial community structure, mineral assemblages, and their relationship with environmental variations in different habitats in the Haima seep, SCS. Archaeal and bacterial composition and abundance were significantly different in the three habitats (MS, FH, and CS). By contrast, the archaeal composition in sites ROV2 and ROV5 was similar. The most abundant SR-AOM and mineralization process-related taxa

occurred at site ROV2, indicating the highest seepage activity and most active mineralization at that location. A high amount of calcite minerals was found at the seep, suggesting that the high activity of SR-AOM was accompanied by the formation of authigenic carbonate minerals. Significant correlations between bacterial communities, calcite, and environmental factors such as SO_4^{2-}, Ca, and Mg revealed that the formation of authigenic carbonate was an important process influencing the mineral assemblages in seep habitats. Our study illustrated the geochemical, microbiological, and mineralogical characteristics of cold seep habitats in the Haima area and improved our understanding of microbe-induced carbon cycling and the formation of authigenic carbonate.

Data availability statement

The datasets presented in this study can be found in the online repository. The names of the repository and accession number can be found below: NCBI Sequence Read Archive (accession code PRJNA973956).

Author contributions

JL: Formal Analysis, Methodology, Writing – original draft, Writing – review & editing. JF: Conceptualization, Funding acquisition, Supervision, Writing – review & editing. JK: Data curation, Writing – review & editing. YH: Data curation, Writing – review & editing. HZ: Methodology, Writing – review & editing. SongZ: Methodology, Writing – review & editing. LT: Software, Visualization, Writing – review & editing. SiZ: Supervision, Writing – review & editing.

Funding

The author(s) declare financial support was received for the research, authorship, and/or publication of this article. We acknowledge the financial support for this research that was received from the National Key Research and Development Program (2021YFF0502300), the National Natural Science Foundation of China (42325603, 41890850, 42022046, and 42227803), Guangdong Natural Resources Foundation (GDNRC [2022]45), PI project of Southern Marine Science and Engineering Guangdong Laboratory (Guangzhou) (GML20190609, GML2022009, GML20230921), and Guangdong Provincial Key Laboratory Project (2019B121203011).

Acknowledgments

We are grateful to the crew of the RV Haiyang-6 and ROV Haima team for their assistance in collecting the samples.

Conflict of interest

The authors declare that the research was conducted in the absence of any commercial or financial relationships that could be construed as a potential conflict of interest.

Publisher's note

All claims expressed in this article are solely those of the authors and do not necessarily represent those of their affiliated organizations, or those of the publisher, the editors and the reviewers. Any product that may be evaluated in this article, or claim that may be made by its manufacturer, is not guaranteed or endorsed by the publisher.

Supplementary material

The Supplementary Material for this article can be found online at: https://www.frontiersin.org/articles/10.3389/fmars.2023.1254450/full#supplementary-material

References

Adam, P. S., Borrel, G., Brochier-Armanet, C., and Gribaldo, S. (2017). The growing tree of Archaea: new perspectives on their diversity, evolution and ecology. *ISME J.* 11 (11), 2407–2425. doi: 10.1038/ismej.2017.122

Aloisi, G., Bouloubassi, I., Heijs, S. K., Pancost, R. D., Pierre, C., Sinninghe Damsté, J. S., et al. (2002). CH4-consuming microorganisms and the formation of carbonate crusts at cold seeps. *Earth Planetary Sci. Lett.* 203 (1), 195–203. doi: 10.1016/S0012-821X(02)00878-6

Baker, P. A., and Burns, S. J. (1985). Occurrence and formation of dolomite in organic-rich continental margin sediments. *Bulletin Am. Assoc. Petroleum Geologists* 69 (11), 1917–1930. doi: 10.1306/94885570-1704-11D7-8645000102C1865D

Bayon, G., Pierre, C., Etoubleau, J., Voisset, M., Cauquil, E., Marsset, T., et al. (2007). Sr/Ca and Mg/Ca ratios in Niger Delta sediments: Implications for authigenic carbonate genesis in cold seep environments. *Mar. Geology* 241 (1), 93–109. doi: 10.1016/j.margeo.2007.03.007

Boetius, A., Ravenschlag, K., Schubert, C. J., Rickert, D., Widdel, F., Gieseke, A., et al. (2000). A marine microbial consortium apparently mediating anaerobic oxidation of methane. *Nature* 407 (6804), 623–626. doi: 10.1038/35036572

Bowles, M., Hunter, K. S., Samarkin, V., and Joye, S. (2016). Patterns and variability in geochemical signatures and microbial activity within and between diverse cold seep habitats along the lower continental slope, Northern Gulf of Mexico. *Deep-Sea Res. Part Ii-Topical Stud. Oceanography* 129, 31–40. doi: 10.1016/j.dsr2.2016.02.011

Braissant, O., Decho, A. W., Dupraz, C., Glunk, C., Przekop, K. M., and Visscher, P. T. (2007). Exopolymeric substances of sulfate-reducing bacteria: Interactions with calcium at alkaline pH and implication for formation of carbonate minerals. *Geobiology* 5 (4), 401–411. doi: 10.1111/j.1472-4669.2007.00117.x

Caesar, K. H., Kyle, J. R., Lyons, T. W., Tripati, A., and Loyd, S. J. (2019). Carbonate formation in salt dome cap rocks by microbial anaerobic oxidation of methane. *Nat. Commun.* 10 (1), 808. doi: 10.1038/s41467-019-08687-z

Cao, L., Lian, C., Zhang, X., Zhang, H., Wang, H., Zhou, L., et al. (2021). *In situ* detection of the fine scale heterogeneity of active cold seep environment of the Formosa Ridge, the South China Sea. *J. Mar. Syst.* 218, 103530. doi: 10.1016/j.jmarsys.2021.103530

Caporaso, J. G., Kuczynski, J., Stombaugh, J., Bittinger, K., Bushman, F. D., Costello, E. K., et al. (2010). QIIME allows analysis of high-throughput community sequencing data. *Nat. Methods* 7 (5), 335–336. doi: 10.1038/nmeth.f.303

Case, D. H., Pasulka, A. L., Marlow, J. J., Grupe, B. M., Levin, L. A., and Orphan, V. J. (2015). Methane seep carbonates host distinct, diverse, and dynamic microbial assemblages. *mBio* 6 (6), e01348–e01315. doi: 10.1128/mBio.01348-15

Chao, A., Gotelli, N. J., Hsieh, T. C., Sander, E. L., Ma, K. H., Colwell, R. K., et al. (2014). Rarefaction and extrapolation with Hill numbers: a framework for sampling and estimation in species diversity studies. *Ecol. Monogr.* 84 (1), 45–67. doi: 10.1890/13-0133.1

Chen, C., Zhong, L., Wan, Z., Cheng, C., Zhou, W., and Xu, X. (2022a). Geochemical characteristics of cold-seep carbonates in Shenhu area, South China Sea. *J. Oceanology Limnology* 40 (3), 969–985. doi: 10.1007/s00343-021-1112-z

Chen, Y., Lyu, Y., Zhang, J., Li, Q., Lyu, L., Zhou, Y., et al. (2022b). Riddles of lost city: chemotrophic prokaryotes drives carbon, sulfur, and nitrogen cycling at an extinct cold seep, South China sea. *Microbiol. Spectr.* 0 (0), e03338–e03322. doi: 10.1128/spectrum.03338-22

Cui, H., Su, X., Chen, F., Holland, M., Yang, S., Liang, J., et al. (2019). Microbial diversity of two cold seep systems in gas hydrate-bearing sediments in the South China Sea. *Mar. Environ. Res.* 144, 230–239. doi: 10.1016/j.marenvres.2019.01.009

Dan, X., Liu, S., Feng, X., Lin, L., Tang, R., Yang, C., et al. (2023). Geochemical record of methane seepage in carbon cycling and possible correlation with climate events in the Qiongdongnan basin, South China Sea. *Mar. Petroleum Geology* 149, 106061. doi: 10.1016/j.marpetgeo.2022.106061

Feng, J.-C., Li, C.-R., Tang, L., Wu, X.-N., Wang, Y., Yang, Z., et al. (2023). Tracing the century-long evolution of microplastics deposition in a cold seep. *Advanced Sci.* 10, 2206120. doi: 10.1002/advs.202206120

Feng, J.-C., Liang, J., Cai, Y., Zhang, S., Xue, J., and Yang, Z. (2022a). Deep-sea organisms research oriented by deep-sea technologies development. *Sci. Bull.* 67 (17), 1802–1816. doi: 10.1016/j.scib.2022.07.016

Feng, J.-C., Yan, J., Wang, Y., Yang, Z., Zhang, S., Liang, S., et al. (2022b). Methane mitigation: Learning from the natural marine environment. *Innovation* 3 (5), 100297. doi: 10.1016/j.xinn.2022.100297

Feng, J.-C., Yang, Z., Zhou, W., Feng, X., Wei, F., Li, B., et al. (2022c). Interactions of microplastics and methane seepage in the deep-sea environment. *Engineering*. 8(9). doi: 10.1016/j.eng.2022.08.009

Fischer, P. Q., Sánchez-Andrea, I., Stams, A. J. M., Villanueva, L., and Sousa, D. Z. (2021). Anaerobic microbial methanol conversion in marine sediments. *Environ. Microbiol.* 23 (3), 1348–1362. doi: 10.1111/1462-2920.15434

Forester, B. R., Lasky, J. R., Wagner, H. H., and Urban, D. L. (2018). Comparing methods for detecting multilocus adaptation with multivariate genotype-environment associations. *Mol. Ecol.* 27 (9), 2215–2233. doi: 10.1111/mec.14584

Guan, H., Birgel, D., Peckmann, J., Liang, Q., Feng, D., Yang, S., et al. (2018). Lipid biomarker patterns of authigenic carbonates reveal fluid composition and seepage intensity at Haima cold seeps, South China Sea. *J. Asian Earth Sci.* 168, 163–172. doi: 10.1016/j.jseaes.2018.04.035

Han, X. Q., Yang, K. H., and Huang, Y. Y. (2013). Origin and nature of cold seep in northeastern Dongsha area, South China Sea: Evidence from chimney-like seep carbonates. *Chin. Sci. Bull.* 58 (30), 3689–3697. doi: 10.1007/s11434-013-5819-x

Hu, Y., Feng, D., Liang, Q., Xia, Z., Chen, L., and Chen, D. (2015). Impact of anaerobic oxidation of methane on the geochemical cycle of redox-sensitive elements at cold-seep sites of the northern South China Sea. *Deep Sea Res. Part II: Topical Stud. Oceanography* 122, 84–94. doi: 10.1016/j.dsr2.2015.06.012

Huang, Y., Feng, J.-C., Kong, J., Sun, L., Zhang, M., Huang, Y., et al. (2023). Community assemblages and species coexistence of prokaryotes controlled by local environmental heterogeneity in a cold seep water column. *Sci. Total Environ.* 868, 161725. doi: 10.1016/j.scitotenv.2023.161725

Inagaki, F., Suzuki, M., Takai, K., Oida, H., Sakamoto, T., Aoki, K., et al. (2003). Microbial communities associated with geological horizons in coastal subseafloor sediments from the sea of Okhotsk. *Appl. Environ. Microbiol.* 69 (12), 7224–7235. doi: 10.1128/AEM.69.12.7224-7235.2003

Jing, H., Wang, R., Jiang, Q., Zhang, Y., and Peng, X. (2020). Anaerobic methane oxidation coupled to denitrification is an important potential methane sink in deep-sea cold seeps. *Sci. Total Environ.* 748, 142459. doi: 10.1016/j.scitotenv.2020.142459

Kemp, P. F., and Aller, J. Y. (2004). Estimating prokaryotic diversity: When are 16S rDNA libraries large enough? *Limnology Oceanography-Methods* 2, 114–125. doi: 10.4319/lom.2004.2.114

Kong, J., Feng, J., Sun, L., and Zhang, S. (2023). Evaluating the reproducibility of amplicon sequencing data derived from deep-sea cold seep sediment-associated microbiota. *Microbiol. Spectr.* 11 (3), e04048–e04022. doi: 10.1128/spectrum.04048-22

Lee, D.-H., Kim, J.-H., Lee, Y. M., Kim, J.-H., Jin, Y. K., Paull, C., et al. (2021). Geochemical and microbial signatures of siboglinid tubeworm habitats at an active mud volcano in the Canadian Beaufort Sea. *Front. Mar. Sci.* 8. doi: 10.3389/fmars.2021.656171

Legendre, P., Fortin, M.-J., and Borcard, D. (2015). Should the Mantel test be used in spatial analysis? *Methods Ecol. Evol.* 6 (11), 1239–1247. doi: 10.1111/2041-210x.12425

Leprich, D. J., Flood, B. E., Schroedl, P. R., Ricci, E., Marlow, J. J., Girguis, P. R., et al. (2021). Sulfur bacteria promote dissolution of authigenic carbonates at marine methane seeps. *ISME J.* 15 (7), 2043–2056. doi: 10.1038/s41396-021-00903-3

Li, X., Dai, Z., Di, P., Feng, J., Tao, J., Chen, D., et al. (2021). Distinct bottom-water bacterial communities at methane seeps with various seepage intensities in Haima, South China Sea. *Front. Mar. Sci.* 8. doi: 10.3389/fmars.2021.753952

Li, J. W., Peng, X. T., Bai, S. J., Chen, Z. Y., and Van Nostrand, J. D. (2018a). Biogeochemical processes controlling authigenic carbonate formation within the sediment column from the Okinawa Trough. *Geochimica Et Cosmochimica Acta* 222, 363–382. doi: 10.1016/j.gca.2017.10.029

Li, N., Yang, X., Peng, J., Zhou, Q., and Chen, D. (2018b). Paleo-cold seep activity in the southern South China Sea: Evidence from the geochemical and geophysical records of sediments. *J. Asian Earth Sci.* 168, 106–111. doi: 10.1016/j.jseaes.2017.10.022

Li, H., Yang, Q., and Zhou, H. (2020). Niche differentiation of sulfate- and iron-dependent anaerobic methane oxidation and methylotrophic methanogenesis in deep sea methane seeps. *Front. Microbiol.* 11. doi: 10.3389/fmicb.2020.01409

Ling, J., Guan, H., Liu, L., Tao, J., Li, J., Dong, J., et al. (2020). The diversity, composition, and putative functions of gill-associated bacteria of bathymodiolin mussel and vesicomyid clam from haima cold seep, South China Sea. *Microorganisms* 8 (11), 1699. doi: 10.3390/microorganisms8111699

Liu, C., Han, K., Lee, D.-J., and Wang, Q. (2016). Simultaneous biological removal of phenol, sulfide, and nitrate using expanded granular sludge bed reactor. *Appl. Microbiol. Biotechnol.* 100 (9), 4211–4217. doi: 10.1007/s00253-016-7293-2

Liu, W., Wu, Z., Xu, S., Wei, J., Peng, X., Li, J., et al. (2020). Pore-water dissolved inorganic carbon sources and cycling in the shallow sediments of the Haima cold seeps, South China Sea. *J. Asian Earth Sci.* 201, 104495. doi: 10.1016/j.jseaes.2020.104495

Marlow, J. J., Hoer, D., Jungbluth, S. P., Reynard, L. M., Gartman, A., Chavez, M. S., et al. (2021). Carbonate-hosted microbial communities are prolific and pervasive methane oxidizers at geologically diverse marine methane seep sites. *Proc. Natl. Acad. Sci.* 118 (25), e2006857118. doi: 10.1073/pnas.2006857118

Marlow, J. J., Steele, J. A., Ziebis, W., Thurber, A. R., Levin, L. A., and Orphan, V. J. (2014). Carbonate-hosted methanotrophy represents an unrecognized methane sink in the deep sea. *Nat. Commun.* 5 (1), 5094. doi: 10.1038/ncomms6094

Naehr, T. H., Eichhubl, P., Orphan, V. J., Hovland, M., Paull, C. K., Ussler, W., et al. (2007). Authigenic carbonate formation at hydrocarbon seeps in continental margin sediments: A comparative study. *Deep Sea Res. Part II: Topical Stud. Oceanography* 54 (11), 1268–1291. doi: 10.1016/j.dsr2.2007.04.010

Niemann, H., Lösekann, T., de Beer, D., Elvert, M., Nadalig, T., Knittel, K., et al. (2006). Novel microbial communities of the Haakon Mosby mud volcano and their role as a methane sink. *Nature* 443 (7113), 854–858. doi: 10.1038/nature05227

Niu, M., Fan, X., Zhuang, G., Liang, Q., and Wang, F. (2017). Methane-metabolizing microbial communities in sediments of the Haima cold seep area, northwest slope of the South China Sea. *FEMS Microbiol. Ecol.* 93 (9). doi: 10.1093/femsec/fix101

Nöthen, K., and Kasten, S. (2011). Reconstructing changes in seep activity by means of pore water and solid phase Sr/Ca and Mg/Ca ratios in pockmark sediments of the Northern Congo Fan. *Mar. Geology* 287 (1), 1–13. doi: 10.1016/j.margeo.2011.06.008

Núñez-Useche, F., Canet, C., Liebetrau, V., Puig, T. P., Ponciano, A. C., Alfonso, P., et al. (2018). Redox conditions and authigenic mineralization related to cold seeps in central Guaymas Basin, Gulf of California. *Mar. Petroleum Geology* 95, 1–15. doi: 10.1016/j.marpetgeo.2018.04.010

Offre, P., Spang, A., and Schleper, C. (2013). Archaea in biogeochemical cycles. *Annu. Rev. Microbiol.* 67 (1), 437–457. doi: 10.1146/annurev-micro-092412-155614

Orcutt, B., Boetius, A., Elvert, M., Samarkin, V., and Joye, S. B. (2005). Molecular biogeochemistry of sulfate reduction, methanogenesis and the anaerobic oxidation of methane at Gulf of Mexico cold seeps. *Geochimica Cosmochimica Acta* 69 (17), 4267–4281. doi: 10.1016/j.gca.2005.04.012

Pierre, C., Demange, J., Blanc-Valleron, M.-M., and Dupré, S. (2017). Authigenic carbonate mounds from active methane seeps on the southern Aquitaine Shelf (Bay of Biscay, France): Evidence for anaerobic oxidation of biogenic methane and submarine groundwater discharge during formation. *Continental Shelf Res.* 133, 13–25. doi: 10.1016/j.csr.2016.12.003

Roberts, H. H., Feng, D., and Joye, S. B. (2010). Cold-seep carbonates of the middle and lower continental slope, northern Gulf of Mexico. *Deep Sea Res. Part II: Topical Stud. Oceanography* 57 (21), 2040–2054. doi: 10.1016/j.dsr2.2010.09.003

Rognes, T., Flouri, T., Nichols, B., Quince, C., and Mahe, F. (2016). VSEARCH: a versatile open source tool for metagenomics. *Peerj* 4, e2584. doi: 10.7717/peerj.2584

Sun, Y., Wang, M., Zhong, Z., Chen, H., Wang, H., Zhou, L., et al. (2022). Adaption to hydrogen sulfide-rich environments: Strategies for active detoxification in deep-sea symbiotic mussels, Gigantidas platifrons. *Sci. Total Environ.* 804, 150054. doi: 10.1016/j.scitotenv.2021.150054

Takahashi, S., Tomita, J., Nishioka, K., Hisada, T., and Nishijima, M. (2014). Development of a prokaryotic universal primer for simultaneous analysis of bacteria and archaea using next-generation sequencing. *PloS One* 9 (8), e105592. doi: 10.1371/journal.pone.0105592

Thomas, T. R. A., Das, A., and Adikesavan, L. P. (2018). A review on the phylogeography of potentially chemoautotrophic bacteria from major vent and seep fauna and their contribution to primary production. *Geomicrobiology J.* 35 (7), 612–634. doi: 10.1080/01490451.2018.1440035

Valentine, D. L., Kastner, M., Wardlaw, G. D., Wang, X., Purdy, A., and Bartlett, D. H. (2005). Biogeochemical investigations of marine methane seeps, Hydrate Ridge,

Oregon. *J. Geophysical Research: Biogeosciences* 110 (G2), G02005. doi: 10.1029/2005JG000025

Wei, J., Wu, T., Zhang, W., Deng, Y., Xie, R., Feng, J., et al. (2020). Deeply buried authigenic carbonates in the qiongdongnan basin, South China Sea: implications for ancient cold seep activities. *Minerals* 10 (12), 1135. doi: 10.3390/min10121135

Wei, Z., Xu, T., Shang, S., Tian, H., Cao, Y., Wang, J., et al. (2021). Laboratory experimental study on the formation of authigenic carbonates induced by microbes in marine sediments. *J. Mar. Sci. Eng.* 9 (5), 479. doi: 10.3390/jmse9050479

Willis, A. D. (2019). Rarefaction, alpha diversity, and statistics. *Front. Microbiol.* 10. doi: 10.3389/fmicb.2019.02407

Xin, Y., Wu, N., Sun, Z., Wang, H., Chen, Y., Xu, C., et al. (2022). Methane seepage intensity distinguish microbial communities in sediments at the Mid-Okinawa Trough. *Sci. Total Environ.* 851, 158213. doi: 10.1016/j.scitotenv.2022.158213

Xu, H., Du, M., Li, J., Zhang, H., Chen, W., Wei, J., et al. (2020). Spatial distribution of seepages and associated biological communities within Haima cold seep field, South China Sea. *J. Sea Res.* 165, 101957. doi: 10.1016/j.seares.2020.101957

Yilmaz, P., Parfrey, L. W., Yarza, P., Gerken, J., Pruesse, E., Quast, C., et al. (2013). The SILVA and "All-species Living Tree Project (LTP)" taxonomic frameworks. *Nucleic Acids Res.* 42 (D1), D643–D648. doi: 10.1093/nar/gkt1209

Zhang, Y., Su, X., Chen, F., Wang, Y., Jiao, L., Dong, H., et al. (2012). Microbial diversity in cold seep sediments from the northern South China Sea. *Geosci. Front.* 3 (3), 301–316. doi: 10.1016/j.gsf.2011.11.014

Zhang, Q., Wu, D., Jin, G., Mao, S., Liu, J., Yang, C., et al. (2022a). Novel use of unique minerals to reveal an intensified methane seep during the last glacial period in the South China Sea. *Mar. Geology* 452, 106901. doi: 10.1016/j.margeo.2022.106901

Zhang, Q., Wu, D., Jin, G., Xu, X., Yang, C., and Liu, L. (2022b). Methane seep in the Shenhu area of the South China sea using geochemical and mineralogical features. *Mar. Petroleum Geology* 144, 105829. doi: 10.1016/j.marpetgeo.2022.105829

Zhou, J., Bruns, M. A., and Tiedje, J. M. (1996). DNA recovery from soils of diverse composition. *Appl. Environ. Microbiol.* 62 (2), 316–322. doi: 10.1128/aem.62.2.316-322.1996

Zhuang, G.-C., Xu, L., Liang, Q., Fan, X., Xia, Z., Joye, S. B., et al. (2019). Biogeochemistry, microbial activity, and diversity in surface and subsurface deep-sea sediments of South China Sea. *Limnology Oceanography* 64 (5), 2252–2270. doi: 10.1002/lno.11182

frontiers | Frontiers in Marine Science

TYPE Original Research
PUBLISHED 06 November 2023
DOI 10.3389/fmars.2023.1198226

Check for updates

OPEN ACCESS

EDITED BY
Andrew R. Thurber,
Oregon State University, United States

REVIEWED BY
Michael Vecchione,
National Oceanic and Atmospheric Administration (NOAA), United States
Jill R. Bourque,
U.S. Geological Survey, United States
Amanda Demopoulos,
Wetland and Aquatic Research Center, United States
Mauricio Shimabukuro,
Universidade Federal do Rio Grande, Brazil

*CORRESPONDENCE
Kellie Johnson
kellie.a.johnson@alumni.duke.edu

†PRESENT ADDRESSES
Koichi Nakamura,
Earth and Evolution Sciences, Graduate School of Science and Technology, University of Tsukuba, Tsukuba, Japan
Carl L. Kaiser,
56 Hillcrest Dr, Falmouth, Massachusetts, MA, United States

RECEIVED 31 March 2023
ACCEPTED 25 September 2023
PUBLISHED 06 November 2023

CITATION
Johnson K, Taylor A, Socha A, Barkyoumb E, Nakamura K, Kaiser CL, German CR, Yoerger DR and Van Dover CL (2023) Seascape ecology in the vicinity of a Blake Ridge cold seep. *Front. Mar. Sci.* 10:1198226. doi: 10.3389/fmars.2023.1198226

COPYRIGHT
© 2023 Johnson, Taylor, Socha, Barkyoumb, Nakamura, Kaiser, German, Yoerger and Van Dover. This is an open-access article distributed under the terms of the Creative Commons Attribution License (CC BY). The use, distribution or reproduction in other forums is permitted, provided the original author(s) and the copyright owner(s) are credited and that the original publication in this journal is cited, in accordance with accepted academic practice. No use, distribution or reproduction is permitted which does not comply with these terms.

Seascape ecology in the vicinity of a Blake Ridge cold seep

Kellie Johnson[1*], Avery Taylor[1], Annika Socha[1], Ellie Barkyoumb[1], Koichi Nakamura[2†], Carl L. Kaiser[3†], Christopher R. German[4], Dana R. Yoerger[3] and Cindy Lee Van Dover[1]

[1]Division of Marine Science and Conservation, Nicholas School of the Environment, Duke University, Beaufort, North Carolina, NC, United States, [2]The Research Institute of Geology and Geoinformation, National Institute of Advanced Industrial Science and Technology, Tsukuba, Japan, [3]Applied Ocean Physics and Engineering, Woods Hole Oceanographic Institution, Woods Hole, Massachusetts, MA, United States, [4]Geology and Geophysics, Woods Hole Oceanographic Institution, Woods Hole, Massachusetts, MA, United States

Systematic surveys of the distribution of epibenthic megafaunal species relative to one another and to environmental variables in the deep sea can lead to inferences and testable hypotheses regarding factors that influence their distributions. Here we use a seascape approach to provide insight into the character and spatial extent of the influence of a chemosynthetic seep on the distribution of epibenthic megafauna and the nature of transition zones (ecotones). Faunal distributions were determined from georeferenced images of the seabed collected during a systematic survey (~ 400 m x 400 m) by the Autonomous Underwater Vehicle *Sentry* in the vicinity of a newly discovered methane bubble plume on the Blake Ridge Diapir. The survey area was found to include both seep and non-seep habitats. The sphere of influence of seep productivity on the surrounding benthic megafaunal assemblage was limited—on the order of 10's of meters—based on ecotone analysis. Small but detectable redox anomalies in the water column (5 m above bottom) in the study area occurred on a similar horizontal scale. Distributions of background megafaunal taxa were non-random for many morphotypes and included both positive and negative associations between morphotypes and the seep habitat. Subtle variations in depth (<6 m) correlated with distributions of seep-associated vesicomyid clams, which occupy shallow depressions in the seabed. The seep habitat itself, comprising a patchy mosaic of megafaunal sub-communities (e.g., clam bed, mussel bed, background soft-sediment bathyal taxa) and transition zones, was at least as diverse as the surrounding non-seep habitat and contributes seep endemic morphotypes to regional biodiversity. While seep productivity may support prey fields for deep-diving beaked whales, any relationship between the seeps and whale feeding areas remains intriguing speculation. Like many other regions of the deep sea, Blake Ridge South has accumulated marine litter, including litter likely originating from scientific endeavors. The suite of observations and analyses deployed here underscore the importance of seep habitats in enriching regional biodiversity, provide a glimpse of the non-random complexity of species distributions from a seascape

perspective, and establish ecological baselines against which future studies may measure natural and anthropogenic changes in the seascape.

KEYWORDS

Blake Ridge seep, cooccurrence, network analysis, ecotone, species distributions, sphere of influence, seascape ecology, marine litter

1 Introduction

Study of the seascape ecology of deep-sea ecosystems can provide insight into complex spatial relationships between environmental variables and community structure, as well as inform environmental management of the seabed (Pittman et al., 2021; Swanborn et al., 2022). Similar to landscape ecology, seascape ecological approaches focus on pattern-oriented assessment, with an emphasis on composition, configuration, spatial transitions, and context, and on linking spatial patterns with biodiversity and ecological processes (Swanborn et al., 2022). Advances in the acquisition of systematically collected, georeferenced images and environmental data by remotely operated and autonomous underwater vehicles (Huvenne et al., 2018), enable new assessments of seascape ecology (Pittman, 2017) in the deep sea (Wagner et al., 2013; Price et al., 2019; Sen et al., 2019; Goffredi et al., 2020; Piechaud and Howell, 2022; Swanborn et al., 2022).

Several recent examples of seascape approaches in the deep sea address the "sphere of influence" of chemosynthetic ecosystems (Levin et al., 2016). Such examples include mapping of feather-duster (serpulid) polychaetes hosting methanotrophic symbionts adjacent to seep-endemic taxa (tubeworms, mussels) at the Jaco Scar seep site off the west coast of Costa Rica (Goffredi et al., 2020) and evidence for an ecotone surrounding the Jaco Scar seep and 4 other nearby seeps (Ashford et al., 2021a). Observations of ecotones associated with deep-sea chemosynthetic ecosystems date back to initial descriptions of hydrothermal-vent ecosystems on the Galapagos Spreading Center, where vent-endemic tubeworms, mussels, clams, and associated macroinvertebrates occupied zones in the hydrothermal heart of vent fields, surrounded by peripheral fields of anemones and serpulid worms (Hessler and Smithey, 1982). Increased abundances of predators (Van Dover et al., 1987; MacAvoy et al., 2008) and of infauna (Demopoulos et al., 2018) have also been reported in ecotones associated with chemosynthetic ecosystems. In addition to serving as prey fields for predators, benthic ecotones at deep-sea seeps and vents implicate local export of chemosynthetic energy as particulate organic material or advection of dissolved methane and microbial primary production (Hessler and Smithey, 1982; Goffredi et al., 2020). This larger sphere of influence of chemosynthetic ecosystems is hypothesized to be important in generating ecosystem services (Levin et al., 2016), though for most chemosynthetic systems there is a paucity of detail regarding the nature and extent of these ecotones and the services they provide.

Occupation of seep environments by heterotrophic species from the surrounding benthos does take place, but only a few background species are involved (Carney, 1994). Georeferenced species occurrences can be used to assess the distribution of benthic species across an ecotone, allowing taxa to be characterized in terms of positive (spatially aggregated), negative (spatially segregated) and random associations (Royan et al., 2016; Astarloa et al., 2019; Calatayud et al., 2020) relative to the seep habitat.

Spatial organization data alone does not confirm cause and effect, and spatial associations may be poor proxies for biotic interactions or habitat preferences in the absence of additional information (Blanchet et al., 2020). But spatial organization of species can lead to inferences and testable hypotheses regarding factors that influence their distributions and ecosystem functions that may be reflected in those distributions (Lessard-Pilon et al., 2010; Ashford et al., 2021a). Associations and interactions between and among taxa and environmental variables (e.g., resource use or avoidance) can improve our understanding of factors resulting in non-random species distributions in space and time (Tumolo et al., 2020).

Here we use a seascape approach to i) define the boundary of a seep habitat in an ~400 m x 400 m study area and the location of redox (Eh) anomalies relative to the seep habitat, ii) describe and compare seep and non-seep megafaunal epibenthic community structure, including alpha and beta diversity, rank abundance, and ordination by habitat and within the context of subtle variations in depth, iii) identify positive, negative, and random distributions of taxa relative to the seep boundary, co-occurrences, associations, and networks of benthic morphotypes, and iv) explore evidence for ecotones between seep and non-seep habitats. We also describe the spatial distribution and abundance of purported feeding scars of beaked whales (*Ziphius cavirostris*; Marsh et al., 2018) and marine litter. Insights gained from this work may inform future environmental management of the Blake Ridge seep system, especially if methane reserves in the region prove to be a target for exploitation (Sahu et al., 2020).

1.1 Blake Ridge study site

Methane seepage and chemosynthetic activity at the Blake Ridge Diapir was first discovered during site surveys by the Ocean Drilling Program (ODP; Site 996, 2155 m) in 1995 (Paull et al., 1996). Evidence for a methane seep included gas (bubble)

plumes extending up to 320 m above bottom, sediments consisting of 20-40% authigenic carbonate, high concentrations of porewater methane (1000–3400 µM) and sulfide (1300 µM), and a serendipitous collection of bathymodiolin mussels at the sediment-water interface of a sediment core. Deep Submergence Vehicle (DSV) *Alvin* dives in 2001 enabled extensive *in situ* visualization of the geological setting, including gas hydrate formation under a carbonate overhang, and of a chemosynthetic community dominated by dense beds of *Bathymodiolus heckerae* mussels and *Vesicomya* cf. *venusta* clams, at ODP Site 996D (Van Dover et al., 2003). Bacterial mats, preliminarily identified as belonging to the genus *Arcobacter* (Robinson et al., 2004) were also observed. Live clam beds were found in sediment with a wide range of porewater sulfide concentrations [0.1 to 6.4 mmol/L at 10 cm depth; (Heyl et al., 2007)]. At the pore-water interface of live clam beds, sulfide concentrations were low (<1 mmol/L) compared to the higher concentrations found at shell beds with only dead clams [3.3 to 12.1 mmol/L (Heyl et al., 2007)].

Multiple subsurface conduits evident in chirp echosounder 1.5 to 11.5 kHz profiles suggested the presence of a seep complex (Hornbach et al., 2007) at the Blake Ridge Diapir. Three additional seep communities within 200 m of one another and of ODP hole 996 seep site were subsequently discovered using the Autonomous Underwater Vehicle (AUV) *Sentry* in 2012 (Brothers et al., 2013). High-resolution maps detailed the relationship of seep-associated bivalves and authigenic carbonates at the Main Blake Ridge seep site (Wagner et al., 2013). This present study is the first to describe benthic communities of the Blake Ridge South (BR South) seep and adjacent habitat in detail.

2 Materials and methods

2.1 Data collection

The Blake Ridge Diapir (Figure 1) was mapped by the AUV *Sentry* operated by the Woods Hole Oceanographic Institution and deployed from the NOAA Ship *Okeanos Explorer* (EX1205 Leg 1; CLVD, Chief Scientist) from 11 to 23 July 2012. During this technologically innovative expedition, mission programming, engineering troubleshooting, data processing, and watch standing for *Sentry* were undertaken from shore using a satellite link (Kaiser et al., 2012; Van Dover et al., 2012). *Sentry* collected high-resolution multibeam (Reson 7125 echosounder, 400 kHz) bathymetric data ~20 m above bottom at Blake Ridge (Figure 1B). Photo transects (~7-s intervals; 12-bit, 1024 x 1024 pixels, down-looking digital color camera) were conducted at an average speed of 0.7 m s^{-1} and ~5 m above bottom. Bathymetry and image data were digitally transferred to shore daily to support *Sentry* mission programming.

Redox potentials indicative of reducing conditions—a useful exploratory tool for chemosynthetic ecosystems (Henry et al., 2002; Baker et al., 2005; Connelly et al., 2012)—were assessed using an Eh sensor on *Sentry*. Eh is a measurement of electrical potential indicative of oxidation/reduction potential, and was measured as raw values of platinum electrode voltage against an Ag–AgCl reference electrode in a saturated KCl solution (Nakamura et al., 2000). When the Pt electrode encounters reduced fluids, the Eh value drops rapidly, followed by a logarithmic recovery curve. The sawtooth pattern in the Eh record (Supplementary Figure 1) results from states of disequilibrium experienced by the electrode as the AUV platform moves through the ocean and encounters seawater with differing redox poise. Each rapid drop in Eh voltage is presumed to be related to the moment at which the vehicle encounters fresh sulfide-rich waters at any location as it progresses along a given survey line, resulting in HS^- ions reacting at the surface of the Pt electrode. In this context, the recovery curve represents a reverse process during which sulfide deposited on the surface of Pt electrode undergoes oxidation and removal through interaction with well-oxygenated ambient seawater. As such, the recovery curve part of the Eh record has no direct spatial relationship to seafloor fluid flow in the same way as the initial drops in Eh voltage. As an exploration tool, therefore, the negative value of the first derivatives of Eh (i.e., dEh/dt mV s^{-1}) provides a practical approach to identifying locations of rapid Eh drops near the seabed, even though dEh/dt has no direct physical-chemical meaning. An 8-second moving average of dEh/dt was used to avoid analog-digital conversion noise with sufficient spatial resolution. *Sentry 148* metadata for the survey area [date, time, depth, latitude, longitude, Eh (mV)] may be found in Supplementary Data 1.

Co-located sensor data collected by *Sentry* (temperature, salinity) at 5 meters above the bottom varied by fractions of a unit (<0.01C;<0.01 psu) across the survey (very low signal to noise ratio) and were not of ecological interest. While there was a data stream from the dissolved oxygen optode, the sensor was uncalibrated and the signal decayed during the dive by a value equivalent to the variance in the data. Further analysis of the dissolved oxygen data was thus deemed unwarranted.

For this study, only photos from *Sentry 148* were analyzed, i.e., from the Blake Ridge South (BR South) seep (Figure 1B, C). A photo atlas (Supplementary Figure 2) was generated to document 46 morphotypes (Supplementary Table 1). Substratum type (soft sediment, carbonate, live mussels, mussel shells, and clams) was noted for each photo. Organisms that were observed but could not be reliably counted due, for example, to their small size or their obscurity among other organisms or background, were not retained in the final data set. Precautions were taken to ensure that the same individual in overlapping photos (either sequentially or between adjacent lines) were not counted twice. We could not estimate the error associated with counting mobile taxa (fish, octopus) more than once, but, based on observation of mobile individuals that did not change their location from one photo to the next, double- (or more) counting was deemed unlikely, except possibly for the halosaurid and synaphobranchid fishes. We also could not distinguish between patches of live and dead clams.

2.1.1 Large-scale mapping

Photo analyses were undertaken at the scale of the entire BR South survey area [~400 m x 400 m (or ~16 hectares, or ~ 22.5 football pitches)] to map the boundaries of the seep habitat, operationally defined here as the polygon encompassing dense

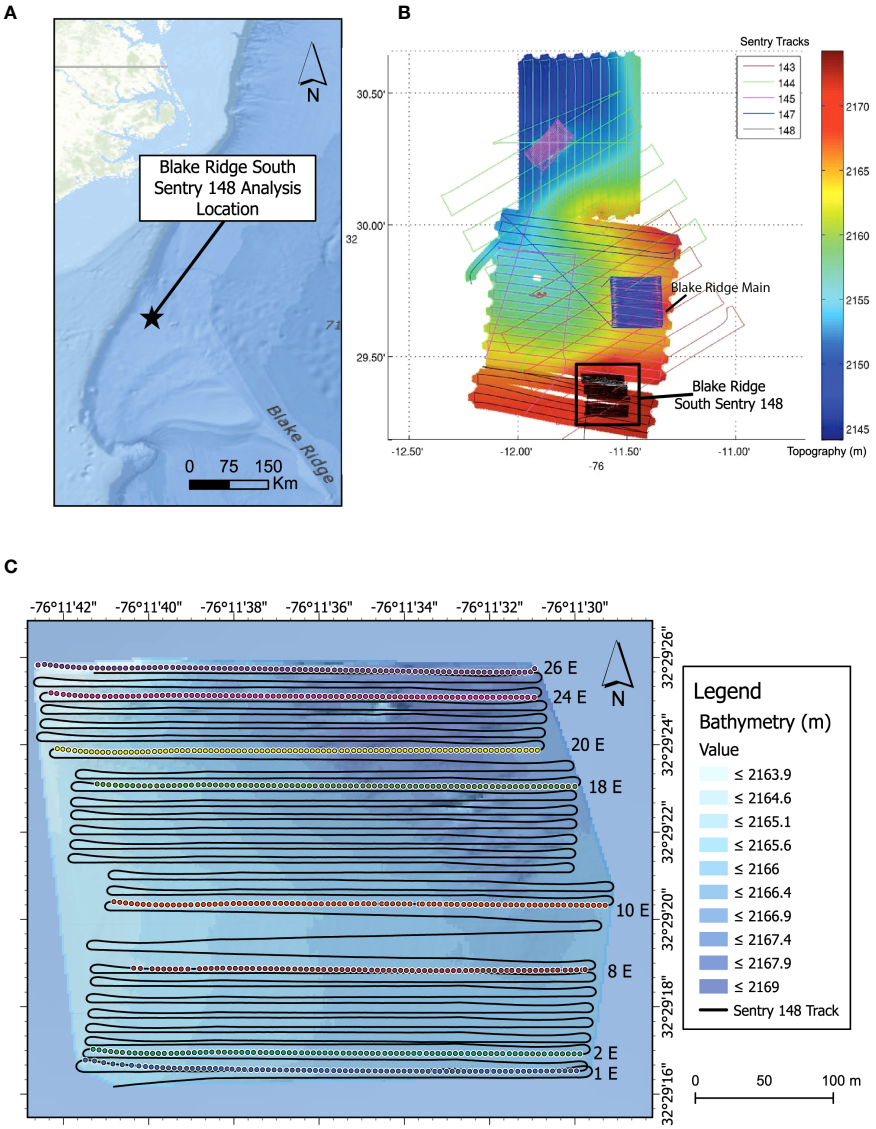

FIGURE 1
Blake Ridge Study Site. **(A)** Location relative to the continental margin off the Carolinas (USA). **(B)** Blake Ridge bathymetry with and all photo transects from the expedition. Colors and numbers indicate different Sentry dives. The black box highlights the location of the Blake Ridge South seep and the photo transects of Sentry 148. White areas: no high-resolution bathymetric data. **(C)** Bathymetric detail of the Blake Ridge South seep site and location of the eight eastward transect lines used for detailed photo analysis. Colored dots: image locations.

live mussels (Bathymodiolus heckerae) and dense clams (Vesicomya cf. venusta)]. Other seep indicators that are obligately restricted to seep environments—authigenic carbonates and bacterial mats on soft sediments—were nested within the mussel and clam bed areas and thus their distribution was not needed to define the seep boundary. Localized fields of short, thready, unsampled tubeworms emergent from soft sediment, tentatively identified as siboglinids based on their morphology and their restricted distribution in the seep habitat, were also assumed to be seep indicators. Distributions of 11 large, reliably, and readily detected invertebrate and fish morphotypes (Supplementary Data 2; Supplementary Figure 3) were mapped for all transect lines (Figure 1C) to visualize their distributions relative to the seep habitat. Observations of sediment 'gouges' tentatively attributed to feeding activities of beaked whales (Ziphius cavirostris; Auster and Watling, 2010) and of marine litter observed during this large-scale mapping effort were also compiled as elements of the Blake Ridge South seascape (Supplementary Data 2).

2.1.2 High-resolution mapping

More detailed photo analyses were undertaken for 8 east-heading transects (lines 1E, 2E, 8E, 10E, 18E, 20E, 24E, 26E; Figure 1C) with overlapping photos. Lines 1E and 2E were south of the seep habitat polygon; all other lines included both seep and non-seep habitats. Photos collected during AUV turns at the end of

each transect were excluded from the analysis. The taxon-abundance matrix for 46 morphotypes, together with associated metadata (Supplementary Data 3), was used to analyze differences in community structure in seep and non-seep habitats, to test for significant positive, negative, and random relationships using cooccurrence and associations using PCA and network analysis tools, and to test for the existence of ecotone (transitional) assemblages between seep and non-seep habitats.

2.2 Taxonomic identifications

The vertical, downward-looking angle of the camera, the relatively low image quality, together with the low contrast and small size of some taxa relative to the seabed made it challenging to identify organisms in *Sentry* photographs to species or sometimes even higher order taxonomic levels. Most taxa were classified using morphotype descriptors. A few of the seep-associated taxa had been sampled on previous expeditions to the Blake Ridge seep area (Van Dover et al., 2003), which allowed us to assign them to taxonomic groups with some confidence. Some provisional identifications of echinoderms were made by D Pawson, octopus by M Vechionne (both of the Smithsonian Museum of Natural History), and fish by S Ross (University of North Carolina, Wilmington). Additional provisional identifications especially at higher taxonomic levels, was assisted by members of the Deep-Ocean Stewardship Initiative (DOSI) in response to a request published in the DOSI weekly newsletter. Despite generous taxonomic assistance, identifications were challenging; the authors accept responsibility for all errors.

2.3 GIS visualization

All GIS maps were generated using ArcGIS Pro software (Esri). *Sentry 148* track lines were plotted using AUV-operator-processed navigation data. Vehicle depth and Eh anomalies (8-second moving- average dEh/dt) were interpolated using the Kriging tool to generate continuous surfaces. Distributions of morphotypes were georeferenced by matching timestamps in the photo filename with corresponding navigation timestamps and map coordinates (Supplementary Data 1).

2.4 Statistical analyses

2.4.1 Biodiversity and community structure

Biodiversity and community structure analyses were performed in R (R Core Team, 2020) using the vegan package (Oksanen et al., 2018) except where noted, and ggplot2 (Wickham, 2016) or native R plot scripts. Species richness was calculated on a per-photo basis and randomized accumulation curves for morphotypes (presence-absence matrices) at seep and non-seep habitats within the seascape were generated for high-resolution transect data using the exact method (Lomolino model), with cumulative number of photos as the measure of sampling effort. Morphotypes reported simply as categorical values, i.e., present or absent (mussels, clams, tubeworms, bacterial mat) were included in the total number of morphotypes present in a habitat but were excluded wherever abundance data was used in an analysis.

2.4.2 Morphotype abundance models

Relative Abundance Distributions (RADs) are useful for empirical description and comparison of the distribution of commonness and rarity in a system and convey more information than non-parametric diversity indices such as Shannon's index of diversity (Matthews and Whittaker, 2015). The best-fit model (null, niche preemption, lognormal, Zipf, or Mandelbrot) for RADs in high-resolution seep and non-seep habitats was determined by the lowest Akaike Information Criterion (AIC) using the *radfit* function in the vegan package (Oksanen et al., 2018).

2.4.3 Abundance-based analysis of community structure

Non-metric multidimensional scaling (NMDS) ordination was used to generate two-dimensional plots of assemblages based on morphotype composition and abundance (i.e., exclusive of clams, mussels, tubeworms, bacteria mat). Average abundances of a given morphotype per photo within a given habitat (seep, non-seep) were calculated to generate a standardized morphotype-abundance matrix indexed by transect line number and habitat. A Bray-Curtis dissimilarity matrix was then calculated using the *metaMDS* function in the vegan package. Analysis of similarities (*anosim*) was used to test for significant differences (R statistic, $\alpha < 0.05$) between seep and non-seep community composition. Differentially abundant morphotypes across habitats ("indicators") were assessed using the package indicspecies and the function *multipatt* (De Cáceres, 2020). In NMDS plots, proximity of any two points conveys the degree of similarity between these data points in the original, high-dimensional space.

2.4.4 Morphotype distributions and environmental variables

Principal Component Analysis (PCA) was performed in R using the vegan package to explore associations among morphotypes, habitat, and depth. Individual photos were treated as sample sites, each with an associated depth and habitat type (seep or non-seep). The morphotype-abundance matrix was transformed to presence/absence data to include both numerical and categorical (presence or absence of clam, mussel, bacterial mat, authigenic carbonate) data. PCA was also performed on Hellinger-transformed abundance data, a transformation that gives low weight to rare species (Legendre and Gallagher, 2001). In contrast to the NMDS analysis, where the relationship between community composition of seep and non-seep habitats and line-by-line variation was explored, the PCA analysis used the "species" scaling method (scale = 2) to focus on relationships among morphotypes. Acute angles between morphotype loadings indicate positive correlations, obtuse angles (>90 degrees) indicate negative correlations. Depth data was overlaid on PCA plots as vectors using the function *envfit*

in vegan, which calculates the multiple regression of environmental variables with ordination axes.

2.4.5 Co-Occurrence analysis

Pairwise probabilistic co-occurrence matrices for morphotypes were generated using the cooccur package in R (Griffith et al., 2016). Clams, mussels, tubeworms, bacterial mat, and authigenic carbonates were aggregated into a single measure labeled "Seep Indicators". Individual photos were used as "samples". Presence-absence data was filtered using the threshold filter (n=5) in cooccur to eliminate morphotypes with insufficient occurrence data. In addition to "Seep Indicators", 28 morphotypes (including the seaweed *Sargassum*) were included in the analysis. Morphotype presence-absence data for each of the 8 transect lines were concatenated to generate the data frame used in cooccur.

2.4.6 Network analysis

Network analysis was performed in R using the asnipe package (Farine, 2013). Morphotypes observed<10 times in the entire data set were removed from the matrix to reduce network noise; abundances were transformed to presence-absence records. Twenty-eight morphotypes were included in the final network analysis, including clams, mussels, and bacterial mat. Association indices that model the probability that two individuals were observed together given that one had been seen (a.k.a. the Simple Ratio Index; ranges from 0 for pairs never observed together, to 1 for pairs always observed together) were calculated for all morphotype pairs to yield an association matrix. The association matrix was visualized as a network, where thicker edge weights correspond to stronger association indices between nodes (morphotypes). To identify sub-communities of morphotypes within the larger network, the *fastgreedy* community detection function (igraph; Csardi and Nepusz, 2006) was employed (Clauset et al., 2004). Nodes representing each morphotype were colored according to sub-community assignment by *fastgreedy* and were also visualized as a dendrogram using *dendPlot* withn igraph.

2.4.7 Ecotone analysis

The existence, location, and extent of ecotones along each high-resolution photo transect were explored using Split-Moving-Window (SMW) analyses. This approach is commonly deployed to detect the extent and location of dissimilarities in ordered data series in terrestrial ecosystems (Panis and Verheyen, 1995). Here, SMW was used to calculate rates of change of morphotype assemblages along phototransects to detect locations of greatest change (breakpoints) and obtain information about the extent of the transition (ecotone). The SMW subroutine of the segRDA package in R (Vieira et al., 2019) detected discontinuities in Bray-Curtis matrices generated from abundance data; categorical data (clams, mussels, tubeworms, bacterial mat) were not included. SMW delivers dissimilarity profiles of mean Zscores (standardized dissimilarity values) plotted against window midpoint locations along each transect. Based on significance tests for SMW peaks in vegetation studies, Zscores > 1.85 were considered significant (Erdős et al., 2014; Vieira et al., 2019;. Breakpoints were identified as the sample position of the maximum dissimilarity in a sequence of significant Zscores; when there was no sequence of significant Zscores, no breakpoint was identified. To determine the optimal window sizes for SMW analysis of each transect, dissimilarity profiles for each transect were generated with even-numbered window sizes of 4 to 30 photos [maximum number of photos in each line ranged from 76 to 88 (Table 1)]. Window sizes that identified an outlier breakpoint undetected by any other window size were eliminated. The remaining window sizes were then used in a pooled analysis that averaged the results to yield a single dissimilarity profile per transect. For transects where no breakpoints were detected for any window size, results are displayed using the two median window sizes (14 and 18).

2.4.8 Graphical enhancement

Adobe Illustrator (2020) was used to enhance readability of graphical outputs.

TABLE 1 High-resolution faunal mapping: Sampling effort (number of photos, transect distance, estimated area), morphotype richness, and percent photos seep indicators for each high-resolution line.

Line Number	Number of Photos	Transect Distance (m)	Estimated Areal Coverage (m^2)	% Photos with Seep Indicators
1E	81	300	1380	0
2E	83	300	1380	0
8E	76	270	1242	18
10E	83	300	1380	22
18E	82	290	1334	44
20E	85	290	1334	41
24E	84	300	1380	67
26E	88	300	1280	44
TOTAL	662	2350	10810	

Distance was calculated from transect start-end coordinates. Photo area (average): 4.6 m width x 3.5 m length. Morphotype richness includes seep indicator taxa (mussel, clam, tubeworm, bacterial mat).

3 Results

3.1 Large-scale mapping

3.1.1 Seep polygons and eh anomalies

Seep polygons were determined from analysis of 4808 images, representing 26 eastward and 27 westward straight-line transects and a seafloor area of ~400 m x 400 m. Subtle depth variations (~6 m; depth range: 2163 to 2169 m) were detected, with highest relief associated with mussel beds on authigenic carbonates, as reported by Wagner et al. (2013) at the Blake Ridge "Main" seep site. The BR South seep polygon (defined here by the presence of "Seep Indicators": mussels, clams, tubeworms, bacterial mats, authigenic carbonate) was located along the northern border and eastern portions of the photo transect area (Figure 2). Vesicomyid clams have a semi-infaunal habit in soft sediment and thus were absent wherever dense mussels and/or authigenic carbonates covered the seabed. Eh values ranged from 184.7 to 191.7 mV. Steepest drops in dEh/dt at Blake Ridge South (i.e., the most negative values of dEh/dt) were detected along the eastern edge of the study area, especially just east of dense clam beds in the southern part of the seep polygon (Figure 2).

3.1.2 Distribution of selected megafauna in the BR South seascape

Eleven readily identified megafaunal taxa (Supplementary Figures 3, 4) differed in their distributions relative to the seep polygon (Figure 3). Octopus [possibly *Graneledone verrucosa* and/or *Muusoctopus johnsonianus;* (Pratt et al., 2021)], squat lobsters, nematocarcinid shrimp, and blue hake (*Antimora* sp.) were more common in the seep habitat than in the non-seep habitat. *Benthodytes* sp. sea cucumbers, *Hygrosoma* sp. urchins, brisingid seastars, red ophiuroids, and *Synaphobranchus* sp. cutthroat eels were more common outside the seep area. Statistical analyses of

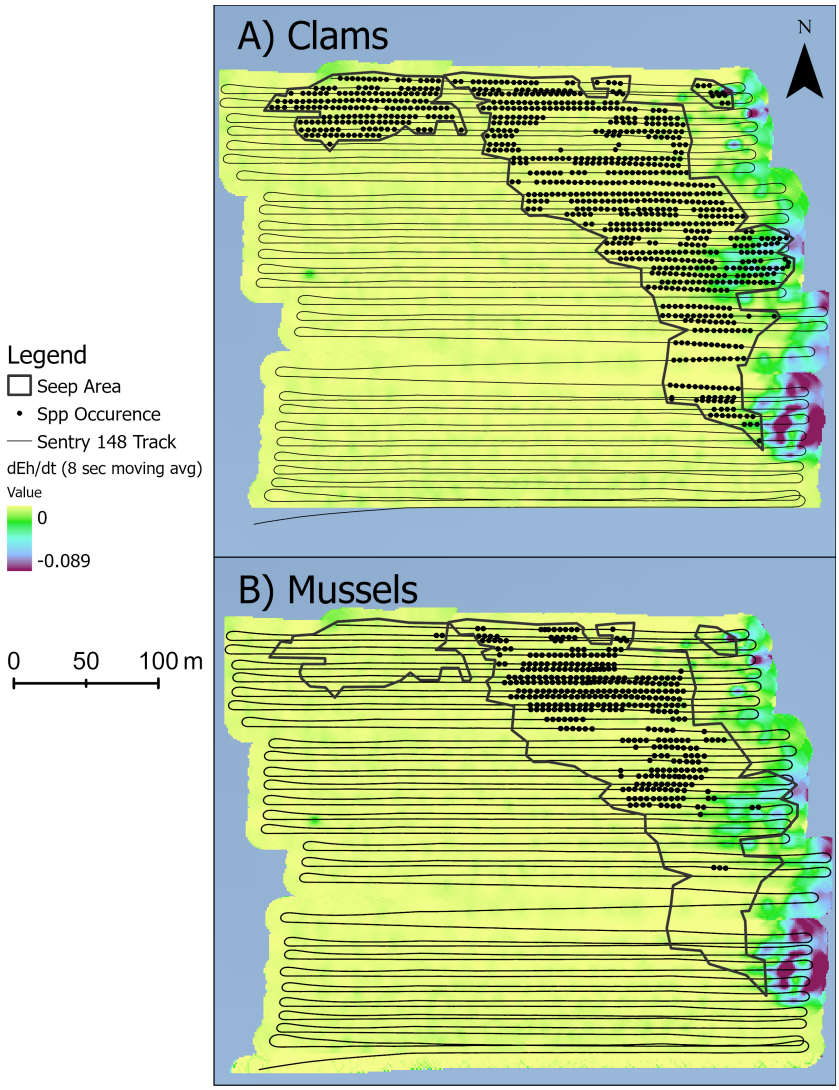

FIGURE 2
Seep indicators (circles) and the seep habitat (black polygons). Each circle represents one photo with either **(A)** dense clams or **(B)** dense mussels. Color ramp is 8-second moving averages of dEh/dt (mV s^{-1}).

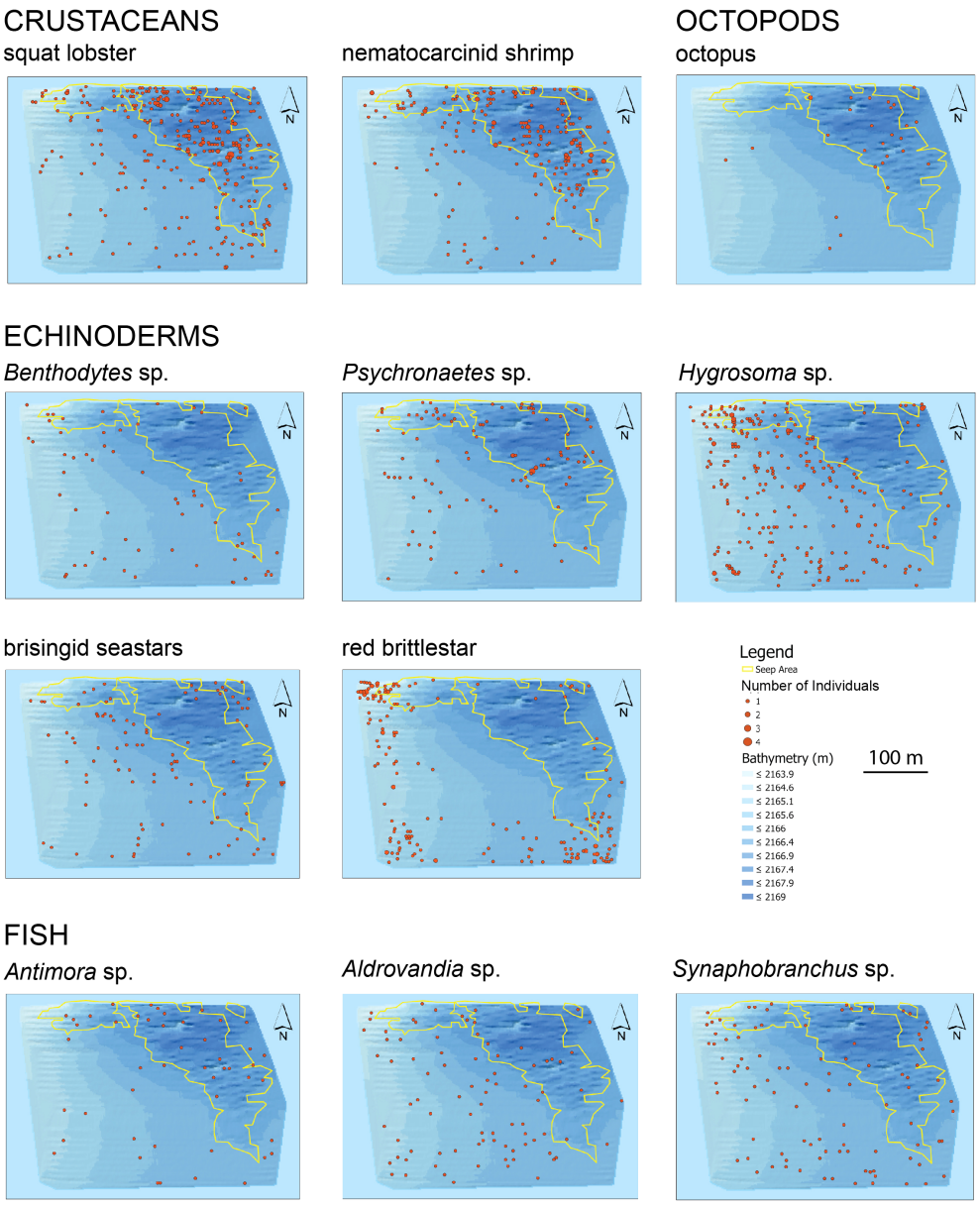

FIGURE 3
Distribution and abundance of eleven megafaunal taxa in the BR South area. Yellow polygons outline the seep habitat. Each point represents an individual photo. Scale is the same for all maps.

associations between these taxa and seep indicators are detailed below for the high-resolution mapping effort.

3.1.3 Putative whale-feeding gouges in the BR South seascape

Disturbed sediment with a central linear depression, narrower at one end and approximately 1 m in length were observed in 45 photos (Supplementary Figure 5) and interpreted as possible feeding gouges from beaked whales (*Ziphius cavirostris*). All feeding gouges were observed outside the seep polygon (Supplementary Figure 6), except the gouge in photo 1197 (Supplementary Figure 5A), which was in soft sediment among scattered clams. The age of the gouges was impossible to determine; two of the putative feeding gouges appeared to be relatively "fresh" (photos 1021, 1197; Supplementary Figure 5A), but most appeared to be older, with accumulations of sediment and other material in the depressions.

3.1.4 Marine litter in the BR South seascape

Within the study area, 17 discrete items of litter were observed (Supplementary Figure 7), equivalent to ~2 pieces of litter per hectare (2 per 0.1 km^2). The litter was dominated by glass bottles (n = 7), with 1 coke can, 1 drink carton, 1 piece of corrugated cardboard, 2 spools, 1 rectangular tray (~1 m x 0.5 m), a rectangular piece of metal, and 4 unidentified objects (possibly 3 metallic, 1 wooden).

3.2 High-resolution mapping

3.2.1 Overview of sampling effort

In the eight *Sentry 148* transect lines heading eastward selected for detailed analysis, the number of photos per line ranged from 76 to 88. These overlapping photos covered distances ranging from ~270 to 300 m and areas of 1242 m^2 to 1380 m^2 (Table 1). Seep indicators (clams, mussels, bacteria, tubeworms, authigenic carbonates) were absent in the southernmost pair of lines (Lines 1E, 2E, Figure 1C). On the more northerly lines, the percent of photos with seep indicators ranged from 18% to 67% (Table 1).

3.2.2 Biodiversity and community structure

Xenophyophore protists (Syringammina sp.) were the most abundant morphotype (2,008 individuals), accounting for 57% of total morphotype abundance (excluding non-enumerated mussels, clams, tubeworms, bacterial mat) in the BR South seascape. Abundance maxima of xenophyophores on each transect line were associated with seep indicators (Figure 4). Syringammina sp. was not observed on Lines 1E and 2E, where seep indicators were absent.

Per-photo morphotype richness was significantly lower (t-test, $p < 0.001$) in non-seep habitats ($\bar{x}_{non\text{-}seep} = 1.97$) than seep habitats ($\bar{x}_{seep} = 4.2$), though there were similar ranges in non-seep (0 to 6

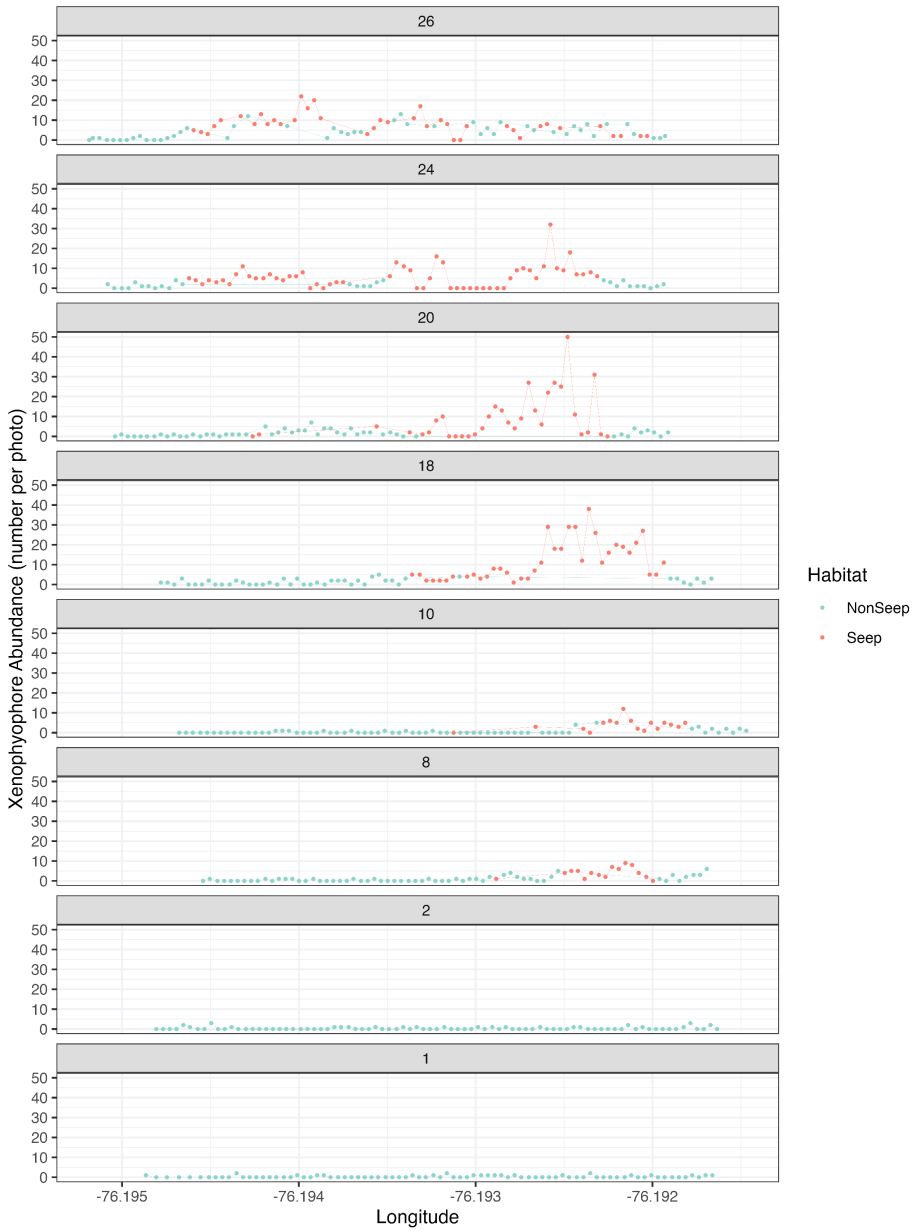

FIGURE 4
Xenophyophore (*Syringammina* sp.) abundance in seep and non-seep habitats. Each graph represents one of the 8 high-resolution eastward transects (see Figure 1C) within the BR South study area.

morphotypes photo) and seep habitats (1 to 8 morphotypes per photo).

Morphotype richness was the same in seep and non-seep habitats (36 morphotypes), despite nearly twice the sampling effort in the non-seep habitat. The steeper slope of the seep habitat accumulation curve, the lack of overlap between confidence intervals of seep and non-seep accumulation curves, and the greater number of morphotypes for a given number of photos in the seep habitat suggest that seep habitat diversity may be higher than non-seep habitat diversity (Figure 5A). Neither curve approached an asymptote, indicating the potential for additional effort to yield additional morphotypes in each habitat.

In addition to endemic taxa that are obligate inhabitants of seep (or seep-like) environments (mussels, clams, tubeworms, bacterial mat), differences in the relative abundances of other higher-level taxa at seep and non-seep habitats were evident (Figure 5B). As noted above, seep habitat supported relatively more xenophyophoran protists than non-seep habitats. Non-seep

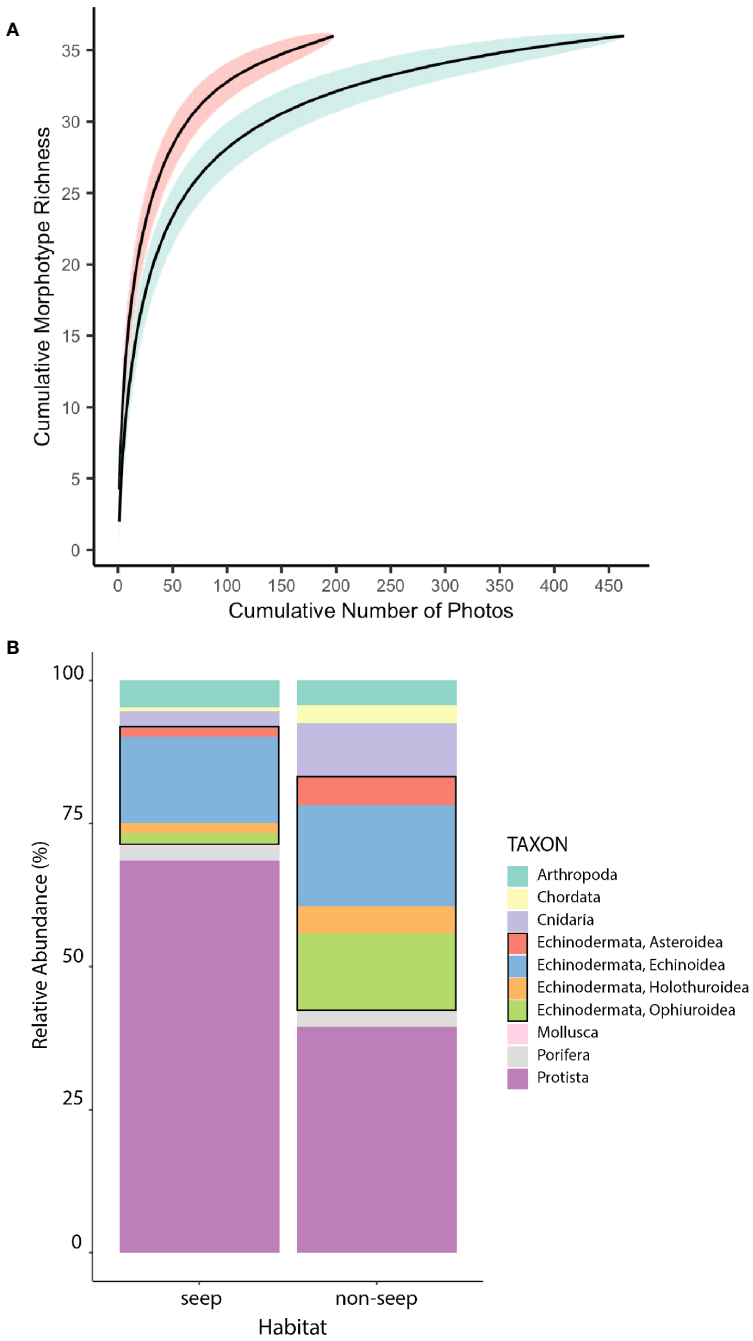

FIGURE 5
Diversity overview by habitat. **(A)** Morphotype accumulation curves for seep (red) and non-seep (green) habitats. Shaded areas represent 95% confidence intervals. **(B)** Relative abundance of higher-level taxa at seep and non-seep habitats. Black rectangles highlight Echinodermata. Excludes mussels, clams, tubeworms, and bacterial mat at seeps, which were not enumerated.

habitats supported greater relative abundances of Echinodermata (especially Holothuroidea, Ophiuroidea and Asteroidea) and Cnidaria than seep habitats.

The total number of eukaryotic morphotypes observed in the BR South seascape (gamma diversity) was 46. Of these morphotypes, 28 were common to both seep and non-seep habitats. The change in morphotype richness between seep and non-seep habitats (absolute Beta diversity) was 16, with 8 morphotypes only found in the seep habitat and 8 morphotypes only found in the non-seep habitat (Table 2).

3.2.3 Morphotype relative-abundance distributions (RADs)

Best-fit models for RADs differed for the seep (Zipf model) and non-seep (lognormal model) habitats (Figure 6). As expected for Relative Abundance Distributions, both habitats were dominated by a few morphotypes, but the seep habitat had a greater abundance of rare morphotypes than expected from a lognormal distribution.

3.2.4 Community structure and morphotype distributions, associations, networks

The NMDS analysis for Blake Ridge South seep and non-seep habitats indicated that the community compositions of these habitats were distinct (Figure 7). The seep community located along lines 18E, 20E, and 24E grouped together—these lines included patches of both clams and mussels. Four morphotypes were non-endemic taxa closely associated with the seep habitat: xenophyophores (*Syringammina* sp.), nematocarcinid shrimp, spatangoid urchins (*Sarsiaster griegii*), and squat lobsters. Two morphotypes were indicator taxa for non-seep habitats: cutthroat eels (*Synaphobranchus* sp.) and the solitary hydroid.

Only 11.4% of the variance in the morphotype occurrence could be explained by principal component axes 1 and 2 for presence-absence data (Figure 8A), suggesting that the data set is inherently complex and cannot be captured by just a few principal components. For abundance data (Figure 8B), even less of the variation in community structure (7.72%) was explained by PC1 and PC2. The depth vector was significantly related to the first two ordination axes ($p = 0.001$, $a = 0.05$) in both PCA plots. Photos from non-seep seabed clustered more closely than photos with seep indicators, underscoring greater variation in faunal adjacencies within the seep habitat that is in part attributable to the presence of sub-communities in the seep habitat, as highlighted in the network analysis below (Figure 9A).

TABLE 2 Morphotypes unique to either seep or non-seep habitats in high-resolution photo transects.

Seep Habitat	Non-Seep Habitat
Bacterial mat	Burrowing anemone
Venus-flytrap anemone	Sunflower anemone
Tubeworms (frenulates)?	Plump white seastar
Octopus	Frilly seastar
Bathymodiolus heckerae	*Benthodytes* shiny
Vesicomya cf. *venusta*	*Neoraja carolinensis*
sea spider	*Hydrolagus affinus*
Lycodes sp.	Large eelfish

For PCA using presence-absence data, clam- and mussel-associated assemblages were evident, as was the association of clams with greater depth. For PCA with quantitative data, abundances of xenophyophores (*Syringammina* sp.), spatangoid urchins (*Sarsiaster griegii*), squat lobsters, and nematocarcinid shrimp were associated with increasing depth and clams. Background bathyal megafauna contributing most to the variance of the principal components tended to be negatively associated with seep morphotypes or, as in the case of the "large eel" and the halosaur *Aldrovandia* sp., were randomly associated with seep morphotypes and closely associated with one another. There were also positive associations between background morphotypes, notably between several echinoderms [red saleniid urchins (*Bathysalenia goesiana*) and red brittle stars for the presence-absence data; goniasterid seastars (*Mediaster* sp.), *Bathysalenia goesiana*, and persiculidan sea cucumbers (*Oloughlinius* sp.) for the abundance data set, among others)] and the hydroid.

Cooccurrence analysis (Figure 10; Supplementary Table 2) of 662 "samples" (photos) from the 8 high-resolution transect lines identified 19 positive and 30 negative significant associations among 42 morphotypes, where one of these "morphotypes" represented the aggregate of seep indicators (mussels, clams, bacterial mat, tubeworms, and/or authigenic carbonates). There were ten positive associations with seep indicators: xenophyophores (*Syringammina* sp.), holothurians (*Psychronaetes* sp.), spatangoid urchins (*Sarsiaster griegii*), squat lobsters, nematocarcinid shrimp, sponges, *Sargassum*, the benthopectinid seastar *Cheiraster blakei*, the octopus, and the Venus Fly-Trap anemone. Four negative associations with seep indicators were identified: the white and red brittle stars, the red saleniid urchins (*Bathysalenia goesiana*), and the solitary hydroid. Network analysis revealed numerous spatial associations among morphotypes. All 28 morphotypes had some degree of connectivity (Figure 9A), i.e., they cooccurred with one other morphotype in at least one image. The highest association index value (0.72) was between live mussels and mussel shells – they were often observed in the same photo. Relatively high associations (0.21 to 0.42) were detected for a few other morphotype pairs, all primarily or exclusively restricted to the seep habitat (Table 3). Three sub-communities—referred to here as clam-associated, mussel-associated, and background bathyal communities—were identified by the "fastgreedy" community detection function (Figure 9). In this analysis, the background bathyal sub-community was most diverse, with 15 morphotypes, of which 10 were echinoderms.

3.2.5 Ecotone analysis

Dissimilarity profiles derived from Split Moving Window analysis of transects 1E and 2E, where no seep indicators were present, showed no evidence of significant dissimilarities in morphotype composition, i.e., no ecotones (Figures 11A, B). In contrast, dissimilarity profiles of other transects had one (8E, 10E,

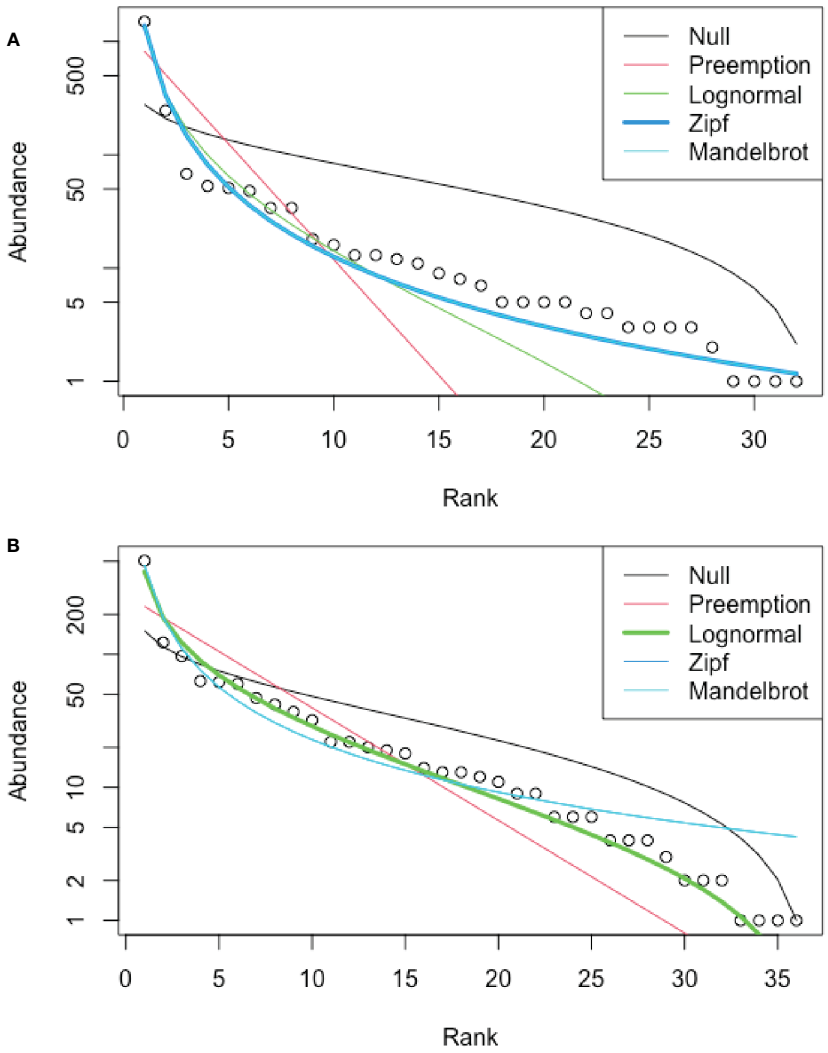

FIGURE 6
Rank Abundance Distributions (RAD), Blake Ridge South. **(A)** Seep habitat; best fit: Zipf model. **(B)** Non-seep habitat; best fit: lognormal. Excludes mussels, clams, tubeworms, and bacterial mat at seeps, for which abundances were not determined.

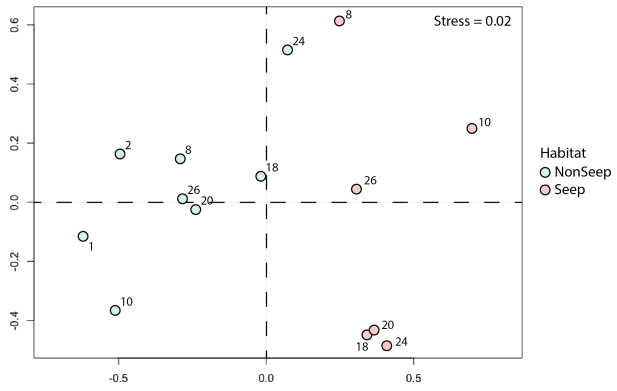

FIGURE 7
NMDS plot (Bray-Curtis) of seep and non-seep habitats. Numbers: Line numbers for high-resolution transect lines (see Figure 1C). Abundance standardized as 'per photo' from high-resolution transects. Global R: 0.722 (p =0.001).

18E, 26E); two (20E); or three (24E) breakpoints, indicative of transitional (ecotone) assemblages (Figures 11C–H; Supplementary Table 3). Collections of significant dissimilarities with breakpoints extended from 5 to 15 "sample positions" (i.e., photos) or ~15 to 50 m.

4 Discussion

4.1 Watercolumn variables

Negative dEh/dt anomalies 5 m above bottom were small but consistent with the anomalous redox potential of seep effluents relative to background environments (Henry et al., 2002; Joye, 2020). Eh anomalies at Blake Ridge South were concentrated in the eastern region of the study area, beyond the boundary of the seep habitat defined by seep indicator taxa. Given that only a single water-column anomaly (bubble plume) was detected in the region

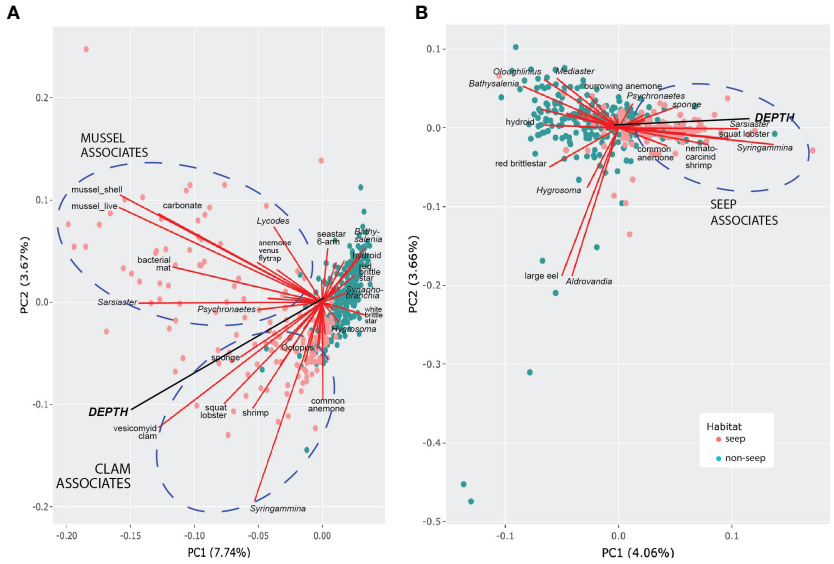

FIGURE 8
Morphotype-depth PCA biplots. **(A)** Presence-absence data. **(B)** Hellinger-transformed abundance data (excludes mussels, shells, clams, bacterial mat, carbonate). Circles represent photos ("sites") coded by habitat type. Morphotypes contributing most to PC1 and PC2 are labeled. Ellipses highlight morphotypes within seep habitats that are positively associated and contributed to most of the variance.

of BR South during shipboard multibeam surveys undertaken on the same expedition (Brothers et al., 2013), a parsimonious interpretation is that the Eh anomalies reported here likely reflect the intersection of *Sentry*'s Eh sensor 5 m above bottom with a diluted, advected Eh signal in a boundary layer that is moving eastward from the seep and above a down-sloping seafloor. We expect that environmental variables such as boundary layer and porewater sulfide chemistry may exert a strong influence on species' distributions in seep and non-seep habitats (Heyl et al., 2007), but these variables were not possible to detect with the remote sensors used in this study.

4.2 Biodiversity and community structure

For a given sampling effort, seep habitats at Blake Ridge South supported greater species richness than adjacent non-seep habitats. This finding supports emerging views of seeps as facilitators of species aggregation (Sen et al., 2019), though other reports document seeps as environments with low diversity (Sibuet and Olu-LeRoy, 2003; Fisher et al., 2007). Biomass at BR South seeps was dominated by endemic taxa hosting chemoautotrophic endosymbionts (bathymodiolin mussels, vesicomyid clams), as is well documented for many other seeps in the deep sea (Stewart et al., 2005; Cavanaugh et al., 2013).

Large-scale mapping provides robust visual evidence that certain background epibenthic megafauna are negatively associated with the seep habitat (i.e., *Benthodytes* sp., *Hygrosoma* sp., brisingid seastar, red brittlestar, *Aldrovandia* sp., *Synaphobranchus* sp.) while others are positively associated with seeps (i.e., squat lobsters, nematocarcinid shrimp, octopus). Although sulfide toxicity may limit survival of some non-seep-endemic species in areas of active seepage (Levin, 2005; Riesch et al., 2015), a variety of adaptations and mechanisms likely evolved to reduce the toxic effect in some taxa, allowing them to thrive as consumers of other taxa in productive seep habitats (Bagarinao, 1992; Chou et al., 2023).

Faunal differences between seep and adjacent non-seep habitats are evident in NMDS analyses, consistent with observations at seeps throughout the global ocean (e.g., Levin, 2005; Dubilier et al., 2008; Wang et al., 2022). The lognormal relative abundance distribution (RAD) has been proposed as an accurate model for undisturbed communities (Matthews and Whittaker, 2015) and was the best fit to community data for the non-seep habitat at Blake Ridge South. The Zipf distribution has been posited as the outcome of lumping together species belonging to two different ecological communities in microbial studies (Shoemaker et al., 2017). A Zipf distribution model for the Blake Ridge South seep habitat likely reflects the mingling of non-seep taxa with seep taxa. This is consistent with the presence of soft-sediment environments interspersed among the mussels, clams, tubeworms, bacterial mat, and authigenic carbonates, i.e., the seep habitat itself is a mosaic of seep and non-seep patches. In addition, as mentioned above, some non-seep-endemic taxa apparently thrive in close association with seep-endemic taxa.

4.2.1 Morphotype distributions and associations

Only a small percentage (<12%) of the overall variation in morphotype occurrence and distribution can be explained by the first two principal components. Even so, there was a significant

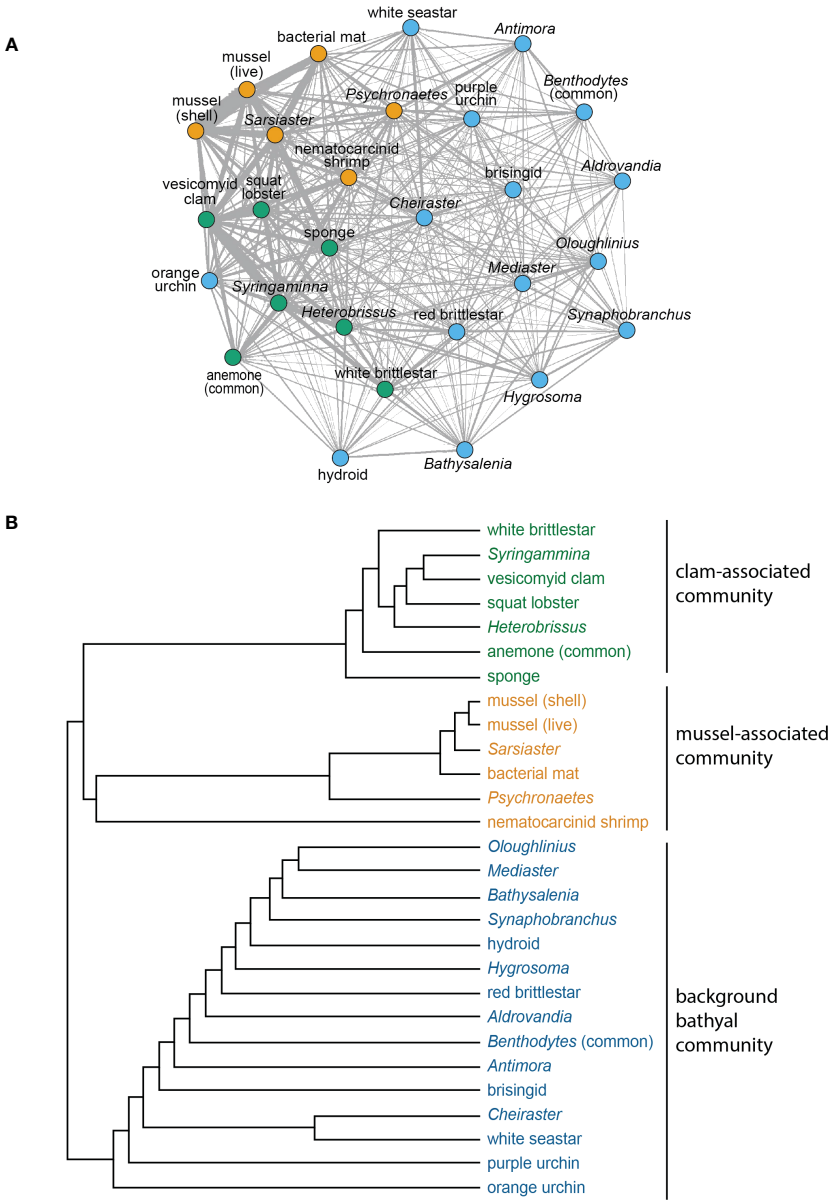

FIGURE 9
(A) Network analysis for morphotypes with 10 or more occurrences in the high-resolution phototransects. Sub-communities grouped by node color. Edge thicknesses corresponds to the association index values for morphospecies pairs. **(B)** Dendrogram illustrating similarity relationships in **(A)**, based on agglomerative hierarchical clustering.

association between increased depth and clam beds, despite the narrow range of depths encountered (~6 m). This relationship between clam distribution and local lows on a soft-sediment seabed may reflect hydrogeological processes, including methane escape and sediment instabilities (Rogers, 2015). This relationship was not consistently observed at the Blake Ridge "Main" seep site (Wagner et al., 2013).

Network analysis revealed associations among morphotypes that confirm and expand upon previously described associations among megafaunal morphotypes of seep and non-seep habitats in general (Levin, 2005) and at Blake Ridge in particular (Van Dover et al., 2003; Wagner et al., 2013). Two sub-communities were identified in the seep habitat: one associated with mussel-engineered hard, complex substratum associated with microbially generated authigenic carbonates, the other with clams living in soft sediments. Megafauna associated with mussel or clam beds typically have a trophic relationship with hydrocarbon seepage and primary production by chemoautotrophic microbes (Van Dover et al., 2003; MacAvoy et al., 2005; Sen et al., 2019; Lin et al., 2020; Turner et al., 2020).

Several seep-endemic/non-seep-endemic morphotype pairs had high association. For example, the abundant xenophyophore *Syringammina* sp. had a high association index with the seep-endemic clam *Vesicomya* cf. *venusta* and soft sediments.

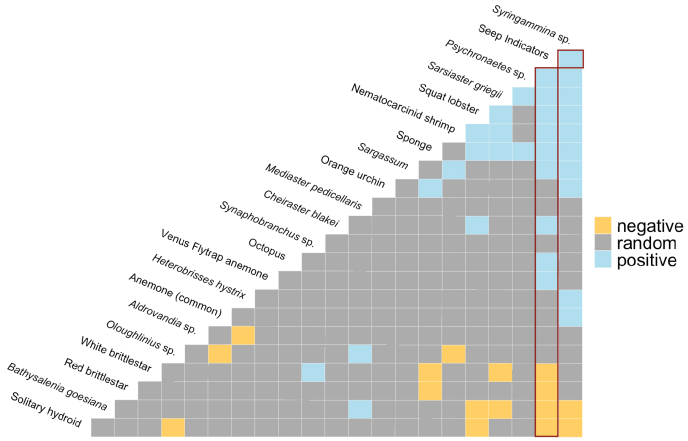

FIGURE 10
Co-occurrence patterns within individual photos. Positive (blue), negative (yellow), and random (grey) pairwise associations. "Seep Indicators" = clams, mussels, tubeworms, bacterial mat, and/or authigenic carbonates. Red rectangles highlight associations with Seep Indicators. The most negative pairwise associations are on the left-hand side, the most positive pairwise associations are on the right-hand side of the matrix.

Syringammina sp. subsists at least partially on microbes (Laureillard et al., 2004), but, since they do not have a high association with bacterial mats (also on soft sediments), mat microbes are unlikely to be important contributors to *Syringammina* nutrition. The spatangoid urchin *Sarsiaster griegii* had relatively high association indices with mussels, bacterial mat, and clams. While *S. griegii* was observed in photos with mussels, it did not occur on the mussels but on soft sediment adjacent to them. We infer that both *Syringammina* sp. and *S. griegii* are sulfide-tolerant taxa that aggregate in microbially enriched soft-sediment of the seep environment and that *S. griegii* may consume the bacterial mat through which it leaves distinctive trails (Supplementary Figure 2, photo 4699). The nemaotcarcinid shrimp was assigned to the mussel community in the network analysis here, but the stable isotopic composition of shrimp from the Blake Ridge Main seep suggests that shrimp in Blake Ridge seep habitats may rely mostly on organic carbon derived from sulfide oxidation (Van Dover et al., 2003). The shrimp may use the habitat complexity of mussel beds as refugia from predation.

TABLE 3 Rank order of highly associated morphotype pairs (association index > 0.2) in photos, based on network analysis.

Morphotype Pair		Association Index
Bathymodiolus heckerae live	*Bathymodiolus heckerae* shell	0.72
Vesicomya cf. *venusta*	*Syringammina* sp.	0.42
Bathymodiolus heckerae live	*Sarsiaster griegii*	0.35
Bacterial mat	*Sarsiaster griegii*	0.28
Vesicomya cf. *venusta*	*Sarsiaster griegii*	0.25
Vesicomya cf. *venusta*	Squat lobster	0.25
Syringammina sp.	*Heterobrisses hystrix*	0.21

To our knowledge, the Blake Ridge South morphotype network is the first of its kind to be created with megafauna occurrence data from a chemosynthetic ecosystem in the deep sea. Insights gained from this effort highlight the information potential of network analysis in the deep sea, as noted elsewhere (Mitchell et al., 2020). Robust biotic networks for threatened deep-sea habitats can inform spatial planning of conservation areas (Jones et al., 2020) and function as important components of Environmental Impact Assessments (Durden et al., 2018).

4.3 Ecotone analysis

Ecologists have often treated habitats in the vicinity of seeps in a binary fashion: being either seep or non-seep (Levin et al., 2016). Ecotone analysis of the Blake Ridge South high-resolution mapping effort revealed multiple transition zones associated with seep habitats. That is, there is a patchwork of seep, non-seep, and ecotone habitats within the seep polygon, as has been reported at seeps elsewhere (e.g., Lessard-Pilon et al., 2010; Åström et al., 2020). Community transitions occur between these habitat patches as well as between the seep community and the background bathyal benthic assemblage. The horizontal extent of ecotone features detected through spatial distributions of epibenthic morphotypes at Blake Ridge South was on the order of 10's of meters. Elsewhere, measures of the sphere of influence of deep-sea seeps range from 200 m across a "chemotone" (Ashford et al., 2021b) to as much as ~2 km based on carbon isotopic signals of seep carbon in squat lobster tissues (MacAvoy et al., 2008).

This Blake Ridge South study addresses community transitions in one dimension (horizontally west to east) but the sphere of influence of the seep environment on microbial, invertebrate, and fish community assemblages transitions in vertical dimensions as well (Levin et al., 2016; Sisma-Ventura et al., 2022). Multi-dimensional ecotone analyses would provide greater insight into the seascape ecology associated with seep habitats.

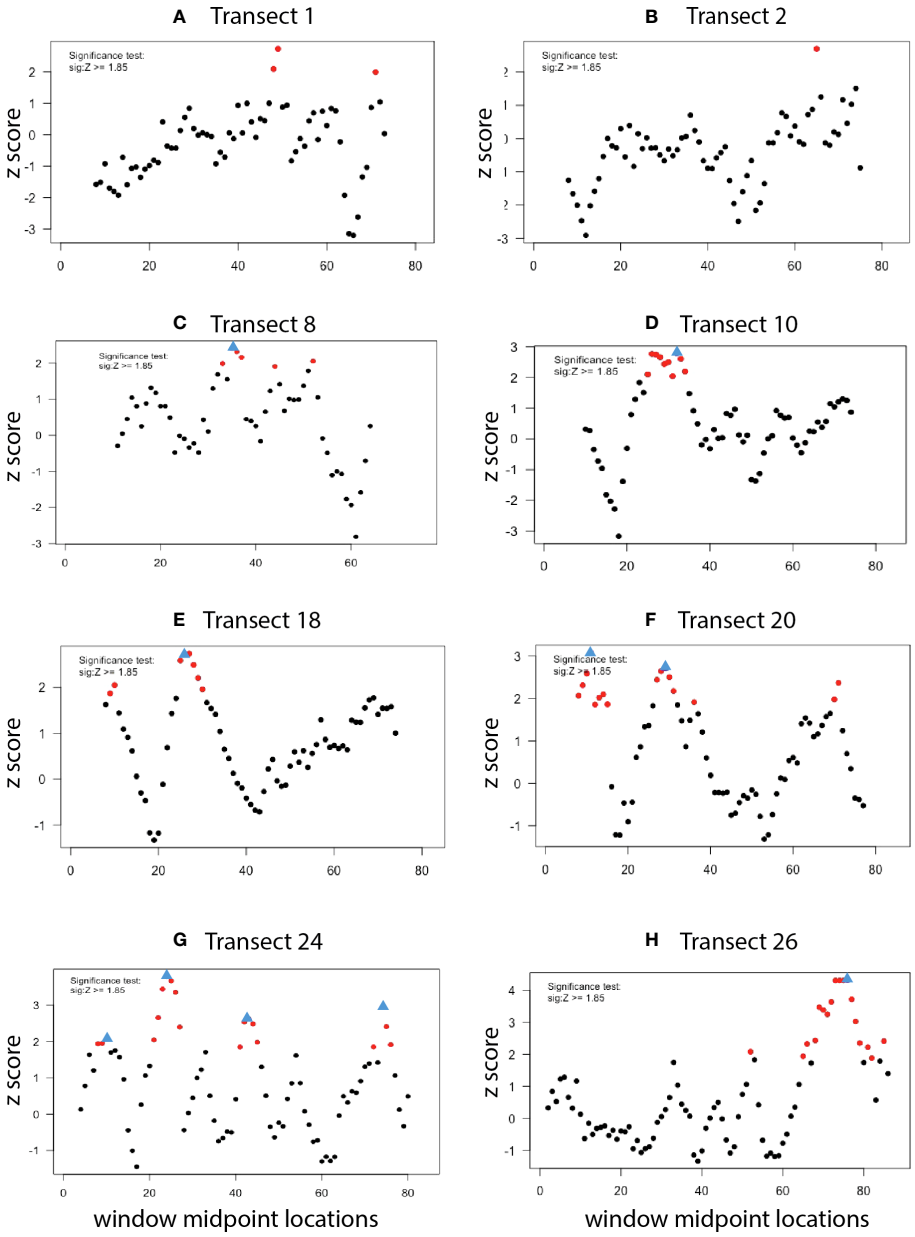

FIGURE 11
Ecotone analysis (dissimilarity profiles) for high-resolution transects. Red circles: Points of significant dissimilarity (Z score > 1.85). Blue triangles: Ecotone "breakpoints" associated with a collection of significant dissimilarities. Window sizes: **(A–C)**, **(F–H)**: 16, 18; **(D, E)**: 20, 22, 24, 26, 28.

4.4 Blake Ridge seeps as a whale foraging area?

Ziphius beaked whales are cosmopolitan species (MacLeod et al., 2006) that dive to depths greater than 1000 m and up to 2500 m to forage on cephalopods and fishes along the continental margin of the western North Atlantic (Shearer et al., 2019), but little is known about their prey fields at depth (Auster and Watling, 2010). These whales are suction feeders (Woodside et al., 2006), but knowledge of their diet is largely from gut contents of dead animals (West et al., 2017). Forty-five discrete depressions in the sediment within the ~16 hectare study area at BR South resemble those interpreted elsewhere as feeding gouges of beaked whales in the vicinity of chemosynthetic ecosystems in the Mediterranean (Woodside et al., 2006). If this interpretation is valid, then densities of near-bottom cephalopods and fishes observed during the *Sentry 148* survey may provide insight into prey fields that attract foraging whales (Auster and Watling, 2010).

At the Blake Ridge South study area, blue hake (*Antimora* sp.; family Moridae), halosaurid fish, and synaphobranchid fish dominated the potential prey field in areas where gouges were observed. Of these families, only Moridae were reported as a prey item in the stomach of a beaked whale from South African waters (West et al., 2017). Although benthic invertebrates at seeps were postulated as a potential food resource for beaked whales (Woodside et al., 2006), the presence of only a single gouge on

soft sediments of the Blake Ridge South seep habitat polygon provides little support for this hypothesis. Instead, enhanced primary and secondary production within the seep site and secondary production exported from the seep site may attract and aggregate marauding fish predators and scavengers to the seep ecotone, which in turn serve as prey for beaked whales. Without direct observations of beaked whales making foraging dives on the Blake Ridge, any relationship between the seeps and whales remains intriguing speculation.

4.5 Marine litter at Blake Ridge South

The density of litter in the BR South seascape (~2 items h^{-1}) is within the range of values reported on seabed features elsewhere in the Atlantic and the Indian Ocean [0.6 to 12.2 items ha^{-1} (Woodall et al., 2015)], though the density of litter reported from hydrothermal-vent ecosystems of the Aeolian volcanic arc off Italy was much higher [~57 items h^{-1} (Consoli et al., 2021)]. In contrast to litter observed by Woodall et al. (2015) and Consoli et al. (2021) in areas of relatively high fishing activity, no obvious fishing gear was observed at BR South. Instead, much of the litter resembled galley items routinely carried on any vessel (bottle, can, carton); it also included what looks like Expendable BathyThermograph (XBT) spools (scientific gear). This litter is consistent with the site having been occupied by numerous scientific research vessels since the 1990s, including the 2012 *Sentry* expedition reported here.

4.6 Potential for automated image analysis and environmental impact studies

Autonomous underwater vehicles capture thousands of overlapping images during systematic surveys. Frame-by-frame detailing of morphotype abundances in a study area as undertaken here was a time-consuming, albeit rewarding, effort. A subset of 11 large, distinctive, and common megafaunal taxa could, however, be rapidly and reliably counted and used to visually characterize positive and negative associations of these taxa at a relatively large scale and with relative ease and accuracy. Quantitative assessment of this subset of taxa could readily be undertaken using automated image analysis (Schoening et al., 2012; Piechaud et al., 2019; Piechaud and Howell, 2022), use of artificial intelligence design, and collaborative studies (Bell et al., 2022). Most other taxa in this study, however, were enumerated using a team approach, with multiple pairs of eyes analyzing each photo in the "high-resolution" study [i.e., a fraction (13%) of the total number of photos in the *Sentry 148* survey]. With improved camera resolution, some of these taxa may be amenable to enumeration through automated image analysis. Cryptic species may remain under-reported in both manually annotated and automated analyses; rare species will be a particular challenge for automated systems, since training sets may be inadequate for machine learning (Durden et al., 2021). Additionally, infauna of all sizes are missed by such photographic surveys. For baseline and subsequent monitoring to assess environmental impacts of human activities on the seafloor, a practical approach may be to identify a set of indicator taxa that contribute to important ecological functions and that are amenable to automated analysis. Such an approach would be a complement to, not a substitute for, more detailed analyses of ecosystem structure and function prior to and at intervals during the activity.

5 Conclusions

Lack of an aerial view or landscape vista makes it challenging to understand distributions of species in a deep seascape. From frame-by-frame analysis of photo surveys such as those undertaken here, an observer can begin to detect transitions and associations. The resulting large matrix of data—a 662 photo x 46 taxa matrix for the high-resolution analysis undertaken here—benefits from exploration and visualization using multivariate tools. Visual analysis of megafaunal distributions from AUV imaging transects provides quantitative data for seascape perspectives on deep-sea ecology, but it is time-consuming and will benefit immensely from continued development of automated image analysis.

Multiple multivariate analyses used in landscape ecology (e.g., principal component, cooccurrence, network, ecotone analyses) yielded insights into the seascape ecology of the Blake Ridge South. Distributions of background epibenthic megafauna were non-random for many morphotypes, with positive and negative associations between morphotypes and the seep habitat. Distinct benthic megafaunal assemblages were associated with clams, mussels, transition zones, and background habitats. Four morphotypes were non-endemic indicator taxa for the seep habitat: *Syringammina* sp., nematocarcinid shrimp, *Sarsiaster griegii*, and squat lobsters; two morphotypes were indicator taxa for non-seep habitats: *Synaphobranchus* sp. and the solitary hydroid. Further multivariate analyses suggested that binary characterization of Blake Ridge South as comprising seep and non-seep habitats is useful, but simplistic.

The seep area is itself a patchy mosaic of habitats, and transition zones occur within the seep area as well as between seep and non-seep environments. Factors underlying positive associations of background fauna with seep habitats are sometimes easy to infer, as in the case of the octopus, which feed on bivalves; spatangoid urchins, which feed on enriched organic material in sediments; and squat lobsters, which benefit from enhanced secondary productivity and from habitat complexity (escape from predation) associated with mussel beds. Negative associations between morphotypes and seep habitats are more difficult to understand or predict; sulfide toxicity remains the prevalent but untested hypothesis for this pattern of morphotype distribution. The sphere of influence of seep productivity appears to be relatively limited, 10's of meters, for epibenthic megafauna. Like many other regions of the deep sea, Blake Ridge South has accumulated marine litter, including litter likely originating from scientific endeavors. The suite of analyses deployed here establish ecological baselines against which future studies may measure natural (and anthropogenic) changes in the BR South seascape through time.

Data availability statement

The original contributions presented in the study are included in the article/Supplementary Material. Further inquiries can be directed to the corresponding author.

Author contributions

Field campaign: CG, CK, DY. Eh sensor and analyses: KN. Shore-based analyses: CVD, with contributions from KJ, AT, AS. Analysis, visualization, and interpretation of data: All authors. Drafting of manuscript: KJ, AT, CG, KN, CVD. All authors contributed to the article and approved the submitted version.

Funding

Field work was supported by a National Science Foundation award (BioOce-1031050) and the NOAA Office of Ocean Exploration and Research to CVD. KJ and AT received research funding from the Rachel Carson Scholars Program (Duke University).

Acknowledgments

We thank the 2012 on-shore and at-sea cruise participants and support teams, with special thanks to L Brothers (USGS), J Wagner (Duke), Z McKelvey (Duke), M Shimizu (Duke). We are also grateful to colleagues who assisted with identifications: S Ross (University of North Carolina Wilmington; fish); D Pawson (Smithsonian National Museum of Natural History; echinoderms); C Seid (Scripps Institute of Oceanography; echinoderms); S Auscavitch (Temple University; echinoderms and cnidarians) as well as along with R Centurion (University of Washington), A Hosie (Western Australian Museum), G Oliver (National Museum of Wales), and members of the DOSI community for their participation in the morphospecies identification survey. E Rodríguez (American Museum of Natural History) and J Durden (UK National Oceanography Centre) also provided taxonomic support. We also thank M. Vecchione and three reviewers for insight and thoughtful suggestions that improved the manuscript.

Conflict of interest

The authors declare that the research was conducted in the absence of ay commercial or financial relationships that could be construed as potential conflict of interest.

The handling editor AT declared a past co-authorship with the author CG.

Publisher's note

All claims expressed in this article are solely those of the authors and do not necessarily represent those of their affiliated organizations, or those of the publisher, the editors and the reviewers. Any product that may be evaluated in this article, or claim that may be made by its manufacturer, is not guaranteed or endorsed by the publisher.

Supplementary material

The Supplementary Material for this article can be found online at: https://www.frontiersin.org/articles/10.3389/fmars.2023.1198226/full#supplementary-material

References

Ashford, O. S., Guan, S., Capone, D., Rigney, K., Rowley, K., Cordes, E. E., et al. (2021a). Relationships between biodiversity and ecosystem functioning proxies strengthen when approaching chemosynthetic deep-sea methane seeps. *Proc. R. Soc B Biol. Sci.* 288, 4–6. doi: 10.1098/rspb.2021.0950

Ashford, O. S., Guan, S., Capone, D., Rigney, K., Rowley, K., Orphan, V., et al. (2021b). A chemosynthetic ecotone—"chemotone"—in the sediments surrounding deep-sea methane seeps. *Limnol. Oceanogr.* 66, 1687–1702. doi: 10.1002/lno.11713

Astarloa, A., Louzao, M., Boyra, G., Martinez, U., Rubio, A., Irigoien, X., et al. (2019). Identifying main interactions in marine predator-prey networks of the Bay of Biscay. *ICES J. Mar. Sci.* 76, 2247–2259. doi: 10.1093/icesjms/fsz140

Åström, E. K. L., Sen, A., Carroll, M. L., and Carroll, J. L. (2020). Cold seeps in a warming arctic: insights for benthic ecology. *Front. Mar. Sci.* 7. doi: 10.3389/fmars.2020.00244

Auster, P. J., and Watling, L. (2010). Beaked whale foraging areas inferred by gouges in the seafloor. *Mar. Mammal Sci.* 26, 226–233. doi: 10.1111/j.1748-7692.2009.00325.x

Bagarinao, T. (1992). Sulfide as an environmental factor and toxicant: Tolerance and adaptations in aquatic organisms. *Aquat. Toxicol.* 24, 21–62. doi: 10.1016/0166-445X(92)90015-F

Baker, E. T., Massoth, G. J., Nakamura, K. I., Embley, R. W., De Ronde, C. E. J., and Arculus, R. J. (2005). Hydrothermal activity on near-arc sections of back-arc ridges: Results from the Mariana Trough and Lau Basin. *Geochemistry Geophys. Geosystems* 6. doi: 10.1029/2005GC000948

Bell, K. L. C., Chow, J. S., Hope, A., Quinzin, M. C., Cantner, K. A., Amon, D. J., et al. (2022). Low-cost, deep-sea imaging and analysis tools for deep-sea exploration: A collaborative design study. *Front. Mar. Sci.* 9. doi: 10.3389/fmars.2022.873700

Blanchet, F. G., Cazelles, K., and Gravel, D. (2020). Co-occurrence is not evidence of ecological interactions. *Ecol. Lett.* 23, 1050–1063. doi: 10.1111/ele.13525

Brothers, L. L., Van Dover, C. L., German, C. R., Kaiser, C. L., Yoerger, D. R., Ruppel, C. D., et al. (2013). Evidence for extensive methane venting on the southeastern U.S. Atlantic margin. *Geology* 41, 807–810. doi: 10.1130/G34217.1

Calatayud, J., Andivia, E., Escudero, A., Melián, C. J., Bernardo-Madrid, R., Stoffel, M., et al. (2020). Positive associations among rare species and their persistence in ecological assemblages. *Nat. Ecol. Evol.* 4, 40–45. doi: 10.1038/s41559-019-1053-5

Carney, R. S. (1994). Consideration of the oasis analogy for chemosynthetic communities at Gulf of Mexico hydrocarbon vents. *Geo-Marine Lett.* 14, 149–159. doi: 10.1007/BF01203726

Cavanaugh, C., McKiness, Z., Newton, I., and Stewart, F. (2013). "Marine chemosynthetic symbioses," in *The prokaryotes: prokaryotic biology and symbiotic associations*. Eds. E. Rosenberg, E. F. DeLong, F. Thompson, S. Lory and E. Stackebrandt (New York: Springer), 1–607. doi: 10.1007/978-3-642-30194-0

Chou, P. H., Hu, M. Y., Guh, Y. J., Wu, G. C., Yang, S. H., Tandon, K., et al. (2023). Cellular mechanisms underlying extraordinary sulfide tolerance in a crustacean holobiont from hydrothermal vents. *Proc. R. Soc B Biol. Sci.* 290, 20221973. doi: 10.1098/rspb.2022.1973

Clauset, A., Newman, M. E. J., and Moore, C. (2004). Finding community structure in very large networks. *Phys. Rev. E - Stat. Physics Plasmas Fluids Relat. Interdiscip. Top.* 70, 6. doi: 10.1103/PhysRevE.70.066111

Connelly, D. P., Copley, J. T., Murton, B. J., Stansfield, K., Tyler, P. A., German, C. R., et al. (2012). Hydrothermal vent fields and chemosynthetic biota on the world's deepest seafloor spreading centre. *Nat. Commun.* 3, 620. doi: 10.1038/ncomms1636

Consoli, P., Esposito, V., Battaglia, P., Perzia, P., Scotti, G., D'Alessandro, M., et al. (2021). Marine litter pollution associated with hydrothermal sites in the AEOLIAN archipelago (western Mediterranean Sea). *Sci. Total Environ.* 773, 108947. doi: 10.1016/j.scitotenv.2021.144968

Csardi, G., and Nepusz, T. (2006). The igraph software package for complex network research. *InterJournal Complex Systems.* 1695, 1–9.

De Cáceres, M. (2020) *How to use the indicspecies package (ver. 1.7.8)*. Available at: https://cran.r-project.org/web/packages/indicspecies/vignettes/indicspeciesTutorial.pdf.

Demopoulos, A. W. J., Bourque, J. R., Durkin, A., and Cordes, E. E. (2018). The influence of seep habitats on sediment macrofaunal biodiversity and functional traits. *Deep. Res. Part I Oceanogr. Res. Pap.* 142, 77–93. doi: 10.1016/j.dsr.2018.10.004

Dubilier, N., Bergin, C., and Lott, C. (2008). Symbiotic diversity in marine animals: The art of harnessing chemosynthesis. *Nat. Rev. Microbiol.* 6, 725–740. doi: 10.1038/nrmicro1992

Durden, J. M., Hosking, B., Bett, B. J., Cline, D., and Ruhl, H. A. (2021). Automated classification of fauna in seabed photographs: The impact of training and validation dataset size, with considerations for the class imbalance. *Prog. Oceanogr.* 196, 102612. doi: 10.1016/j.pocean.2021.102612

Durden, J. M., Lallier, L. E., Murphy, K., Jaeckel, A., Gjerde, K., and Jones, D. O. B. (2018). Environmental Impact Assessment process for deep-sea mining in 'the Area.'. *Mar. Policy* 87, 194–202. doi: 10.1016/j.marpol.2017.10.013

Erdős, L., Zalatnai, M., Bátori, Z., and Körmöczi, L. (2014). Transitions between community complexes: a case study analysing gradients through mountain ridges in south Hungary. *Acta Botanica Croatica.* 73 (1), 63–77. doi: 10.2478/botcro-2013-0009

Farine, D. R. (2013). Animal social network inference and permutations for ecologists in R using asnipe. *Methods Ecol Evol.* 4 (12), 1187–1194. doi: 10.1111/2041-210X.12121

Fisher, C., Roberts, H., Cordes, E., and Bernard, B. (2007). Cold Seeps and associated communities of the Gulf of Mexico. *Oceanography* 20, 118–129. doi: 10.5670/oceanog.2007.12

Goffredi, S. K., Tilic, E., Mullin, S. W., Dawson, K. S., Keller, A., Lee, R. W., et al. (2020). Methanotrophic bacterial symbionts fuel dense populations of deep-sea feather duster worms (Sabellida, Annelida) and extend the spatial influence of methane seepage. *Sci. Adv.* 6, 1–12. doi: 10.1126/sciadv.aay8562

Griffith, D. M., Veech, J. A., and Marsh, C. J. (2016). Cooccur: Probabilistic species co-occurrence analysis in R. *J. Stat. Software* 69, 1–17. doi: 10.18637/jss.v069.c02

Henry, P., Lallemant, S., Nakamura, K. I., Tsunogai, U., Mazzotti, S., and Kobayashi, K. (2002). Surface expression of fluid venting at the toe of the Nankai wedge and implications for flow paths. *Mar. Geol.* 187, 119–143. doi: 10.1016/S0025-3227(02)00262-1

Hessler, R., and Smithey, W. (1982). "The distribution and community structure of megafauna at the Galapagos Rift hydrothermal vents," in *Hydrothermal processes at seafloor spreading centers* (Boston: Springer), 735–770.

Heyl, T., Gilhooly, W., Chambers, R., Gilchrist, G., Macko, S., Ruppel, C., et al. (2007). Characteristics of vesicomyid clams and their environment at the Blake Ridge cold seep, South Carolina, USA. *Mar. Ecol. Prog. Ser.* 339, 169–184. doi: 10.3354/meps339169

Hornbach, M. J., Ruppel, C., and Van Dover, C. L. (2007). Three-dimensional structure of fluid conduits sustaining an active deep marine cold seep. *Geophys. Res. Lett.* 34, L05601. doi: 10.1029/2006GL028859

Huvenne, V. A. I., Robert, K., Marsh, L., Lo Iacono, C., Le Bas, T., and Wynn, R. B. (2018). "ROVs and AUVs," in *Submarine geomorphology* (Cham: Springer), 93–108. doi: 10.1007/978-3-319-57852-1

Jones, D. O. B., Ardron, J. A., Colaço, A., and Durden, J. M. (2020). Environmental considerations for impact and preservation reference zones for deep-sea polymetallic nodule mining. *Mar. Policy* 118, 103312. doi: 10.1016/j.marpol.2018.10.025

Joye, S. B. (2020). The geology and biogeochemistry of hydrocarbon seeps. *Annu. Rev. Earth Planet. Sci.* 48, 205–231. doi: 10.1146/annurev-earth-063016-020052

Kaiser, C., Kinsey, J., Pinner, W., Yoerger, D., German, C., and Van Dover, C. (2012). "Satellite based remote management and operation of a 6000m AUV," in *2012 Oceans*. (IEEE), 1–7. doi: 10.1109/OCEANS.2012.6404900

Laureillard, J., Méjanelle, L., and Sibuet, M. (2004). Use of lipids to study the trophic ecology of deep-sea xenophyophores. *Marine Ecology Progress Series* 270, 129–140. doi: 10.3354/meps270129

Legendre, P., and Gallagher, E. D. (2001). Ecologically meaningful transformations for ordination of species data. *Oecologia* 129, 271–280. doi: 10.1007/s004420100716

Lessard-Pilon, S., Porter, M. D., Cordes, E. E., MacDonald, I., and Fisher, C. R. (2010). Community composition and temporal change at deep Gulf of Mexico cold seeps. *Deep. Res. Part II Top. Stud. Oceanogr.* 57, 1891–1903. doi: 10.1016/j.dsr2.2010.05.012

Levin, L. A. (2005). Ecology of cold seep sediments: Interactions of fauna with flow, chemistry and microbes. *Oceanogr. Mar. Biol. Annu. Rev.* 43, 1–46. doi: 10.1201/9781420037449.ch1

Levin, L. A., Baco, A. R., Bowden, D. A., Colaco, A., Cordes, E. E., Cunha, M. R., et al. (2016). Hydrothermal vents and methane seeps: Rethinking the sphere of influence. *Front. Mar. Sci.* 3. doi: 10.3389/fmars.2016.00072

Lin, Z. Y., Chen, H. W., and Lin, H. J. (2020). Deep-Sea Research Part I Trophic model of a deep-sea ecosystem with methane seeps in the South China Sea. *Deep. Res. Part I* 159, 103251. doi: 10.1016/j.dsr.2020.103251

MacAvoy, S. E., Fisher, C. R., Carney, R. S., and Macko, S. A. (2005). Nutritional associations among fauna at hydrocarbon seep communities in the Gulf of Mexico. *Mar. Ecol. Prog. Ser.* 292, 51–60. doi: 10.3354/meps292051

MacAvoy, S. E., Morgan, E., Carney, R. S., and Macko, S. A. (2008). Chemoautotrophic production incorporated by heterotrophs in Gulf of Mexico hydrocarbon seeps: An examination of mobile benthic predators and seep residents. *J. Shellfish Res.* 27, 153–161. doi: 10.2983/0730-8000(2008)27[153:CPIBHI]2.0.CO;2

MacLeod, C. D., Perrin, W. F., Pitman, R., Barlow, J., Balance, L. D., Amico, A. N., et al (2006). Known and inferred distributions of beaked whale species (Cetacea: Ziphiidae). *J. Cetacean Res. Manag.* 7, 271–286.

Marsh, L., Huvenne, V. A. I., and Jones, O. B. (2018). Geomorphological evidence of large vertebrates interacting with the seafloor at abyssal depths in a region designated for deep-sea mining. *R. Soc Open Sci.* 5, 180286. doi: 10.6084/m9.figshare.c.4191131

Matthews, T. J., and Whittaker, R. J. (2015). On the species abundance distribution in applied ecology and biodiversity management. *J. Appl. Ecol.* 52, 443–454. doi: 10.1111/1365-2664.12380

Mitchell, E. G., Durden, J. M., and Ruhl, H. A. (2020). First network analysis of interspecific associations of abyssal benthic megafauna reveals potential vulnerability of abyssal hill community. *Prog. Oceanogr.* 187, 102401. doi: 10.1016/j.pocean.2020.102401

Nakamura, K., Veirs, S., Sarason, C. P., McDuff, R. E., Stahr, F., Yoerger, D. R., et al. (2000). Electrochemical signals in rising buoyant plumes and tidally oscillating plumes at the main Endeavour vent field, Juan de Fuca Ridge. *EOS Trans. Am. Geophys. Union* 81, 48.

Oksanen, J., Blanchet, F. G., Kindt, R., Legendre, P., Minchin, P. R., O'Hara, R. B., et al. (2018) *Vegan: Community Ecology Package R package version 20-7*. Available at: http://cran.r-project.org/package=vegan.

Panis, L. I., and Verheyen, R. F. (1995). On the use of split moving window analysis for boundary detection in ordered dataseries from benthic communities. *Netherlands J. Aquat. Ecol.* 29, 49–53. doi: 10.1007/BF02061788

Paull, C., Matsumoto, R., and Wallace, P. (1996). Initial Reports–Gas hydrate sampling on the Blake Ridge and Carolina Rise. *Proc. Ocean Drill. Progr.* 164, 623.

Piechaud, N., and Howell, K. L. (2022). Fast and accurate mapping of fine scale abundance of a VME in the deep sea with computer vision. *Ecol. Inform.* 71, 101786. doi: 10.1016/j.ecoinf.2022.101786

Piechaud, N., Hunt, C., Culverhouse, P. F., Foster, N. L., and Howell, K. L. (2019). Automated identification of benthic epifauna with computer vision. *Mar. Ecol. Prog. Ser.* 615, 15–30. doi: 10.3354/meps12925

Pittman, S. (2017). *Seascape ecology* (New Jersey: John Wiley & Sons).

Pittman, S., Yates, K., Bouchet, P., Alvarez-Berastegui, D., Andréfouët, S., Bell, S., et al. (2021). Seascape ecology: Identifying research priorities for an emerging ocean sustainability science. *Mar. Ecol. Prog. Ser.* 663, 1–29. doi: 10.3354/meps13661

Pratt, A., France, S. C., and Vecchione, M. (2021). Survey of bathyal incirrate octopods in the western North Atlantic. *Mar. Biodivers.* 51, 49. doi: 10.1007/s12526-021-01191-y

Price, D. M., Robert, K., Callaway, A., Lo Iacono, C., Hall, R. A., and Huvenne, V. A. I. (2019). Using 3D photogrammetry from ROV video to quantify cold-water coral reef structural complexity and investigate its influence on biodiversity and community assemblage. *Coral Reefs.* 38, 1007–1021. doi: 10.1007/s00338-019-01827-3

R Core Team (2020) *R: A language and environment for statistical computing. R A Lang. Environ. Stat. Comput.* Available at: http://www.r-project.org/.

Riesch, R., Tobler, M., and Plath, M. (2015). "Hydrogen sulfide-toxic habitats," in *Extremophile fishes: ecology, evolution, and physiology of teleosts in extreme environments*. (Cham: Springer), 137–159. doi: 10.1007/978-3-319-13362-1_7

Robinson, C. A., Bernhard, J. M., Levin, L. A., Mendoza, G. F., and Blanks, J. K. (2004). Surficial hydrocarbon seep infauna from the Blake Ridge (Atlantic Ocean 2150m) and the Gulf of Mexico (690-2240 m). *Mar. Ecol.* 25, 313–336. doi: 10.1111/j.1439-0485.2004.00034.x

Rogers, R. (2015). *Offshore gas hydrates: Origins, development, and production* (Waltham MA: Gulf Professional Publishing).

Royan, A., Reynolds, S. J., Hannah, D. M., Prudhomme, C., Noble, D. G., and Sadler, J. P. (2016). Shared environmental responses drive co-occurrence patterns in river bird communities. *Ecography (Cop.).* 39, 733–742. doi: 10.1111/ecog.01703

Sahu, C., Kumar, R., and Sangwai, J. S. (2020). Comprehensive review on exploration and drilling techniques for natural gas hydrate reservoirs. *Energy Fuels* 34, 11813–11839. doi: 10.1021/acs.energyfuels.0c02202

Schoening, T., Bergmann, M., Ontrup, J., Taylor, J., Dannheim, J., Gutt, J., et al. (2012). Semi-automated image analysis for the assessment of megafaunal densities at the Artic deep-sea observatory HAUSGARTEN. *PloS One* 7, 1–14. doi: 10.1371/journal.pone.0038179

Sen, A., Chitkara, C., Hong, W.-L., Lepland, A., Cochrane, S., di Primio, R., et al. (2019). Image based quantitative comparisons indicate heightened megabenthos diversity and abundance at a site of weak hydrocarbon seepage in the southwestern Barents Sea. *PeerJ* 7, e7398. doi: 10.7717/peerj.7398

Shearer, J. M., Quick, N. J., Cioffi, W. R., Baird, R. W., Webster, D. L., Foley, H. J., et al. (2019). Diving behaviour of Cuvier's beaked whales (Ziphius cavirostris) off Cape Hatteras, North Carolina. *R. Soc Open Sci.* 6, 181728. doi: 10.1098/rsos.181728

Shoemaker, W. R., Locey, K. J., and Lennon, J. T. (2017). A macroecological theory of microbial biodiversity. *Nat. Ecol. Evol.* 1, 1–6. doi: 10.1038/s41559-017-0107

Sibuet, M., and Olu-LeRoy, K. (2003). "Cold seep communities on continental cargins: Structure and quantitative distribution relative to geological and fluid venting patterns," in *Ocean margin systems*. Eds. G. Wefer, D. Billett, D. Hebbeln, B. B. Jørgensen, M. Schlüter and T. C. E. Van Weering (Berlin, Heidelberg: Springer Berlin Heidelberg), 235–251. doi: 10.1007/978-3-662-05127-6_15

Sisma-Ventura, G., Bialik, O. M., Makovsky, Y., Rahav, E., Ozer, T., Kanari, M., et al. (2022). Cold seeps alter the near-bottom biogeochemistry in the ultraoligotrophic Southeastern Mediterranean Sea. *Deep. Res. Part I Oceanogr. Res. Pap.* 183, 103744. doi: 10.1016/j.dsr.2022.103744

Stewart, F. J., Newton, I. L. G., and Cavanaugh, C. M. (2005). Chemosynthetic endosymbioses: adaptations to oxic-anoxic interfaces. *Trends Microbiol.* 13, 439–448. doi: 10.1016/j.tim.2005.07.007

Swanborn, D. J. B., Huvenne, V. A. I., Pittman, S. J., and Woodall, L. C. (2022). Bringing seascape ecology to the deep seabed: A review and framework for its application. *Limnol. Oceanogr.* 67, 66–88. doi: 10.1002/lno.11976

Tumolo, B. B., Calle, L., Anderson, H. E., Briggs, M. A., Carlson, S., MacDonald, M. J., et al. (2020). Toward spatio-temporal delineation of positive interactions in ecology. *Ecol. Evol.* 10, 9026–9036. doi: 10.1002/ece3.6616

Turner, P. J., Ball, B., Diana, Z., Fariñas-Bermejo, A., Grace, I., Mcveigh, D., et al. (2020). Methane seeps on the US atlantic margin and their potential importance to populations of the commercially valuable deep-sea red crab, chaceon quinquedens. *Front. Mar. Sci.* 7:75. doi: 10.3389/fmars.2020.00075

Van Dover, C. L., Aharon, P., Bernhard, J. M., Caylor, E., Doerries, M., Flickinger, W., et al. (2003). Blake Ridge methane seeps: Characterization of a soft-sediment, chemosynthetically based ecosystem. *Deep. Res. Part I Oceanogr. Res. Pap.* 50, 281–300. doi: 10.1016/S0967-0637(02)00162-0

Van Dover, C., Franks, P., and Ballard, R. (1987). Prediction of hydrothermal vent locations from distributions of brachyuran crabs. *Limnol. Oceanogr.* 32, 1006–1010. doi: 10.4319/lo.1987.32.4.1006

Van Dover, C., German, C., Yoerger, D., Kaiser, C., and Brothers, L. (2012). "Telepresence field research experience for undergraduate and graduate students: An R/V Okeanos Explorer/AUV Sentry success story," in *AGU fall meeting abstracts, OS51D-1909*. (Washington DC: American Geophysical Union),

Vieira, D. C., Brustolin, M. C., Ferreira, F. C., and Fonseca, G. (2019). segRDA: An R package for performing piecewise redundancy analysis. *Methods Ecol. Evol.* 10, 2189–2194. doi: 10.1111/2041-210X.13300

Wagner, J., McEntee, M., Brothers, L., German, C., Kaiser, C., Yoerger, D., et al. (2013). Cold-seep habitat mapping: High-resolution spatial characterization of the Blake Ridge Diapir seep field. *Deep Sea Res. Part II Top. Stud. Oceanogr.* 92, 183–188. doi: 10.1016/j.dsr2.2013.02.008

Wang, X., Guan, H., Qiu, J.-W., Xu, T., Peckmann, J., Chen, D., et al. (2022). Macroecology of cold seeps in the South China Sea. *Geosystems Geoenvironment* 1, 100081. doi: 10.1016/j.geogeo.2022.100081

West, K. L., Walker, W. A., Baird, R. W., Mead, J. G., and Collins, P. W. (2017). Diet of Cuvier's beaked whales *Ziphius cavirostris* from the North Pacific and a comparison with their diet world-wide. *Mar. Ecol. Prog. Ser.* 574, 227–242. doi: 10.3354/meps12214

Wickham, H. (2016). *ggplot2: elegant graphics for data analysis* (New York: Springer-Verlag). Available at: https://ggplot2.tidyverse.org.

Woodall, L. C., Robinson, L. F., Rogers, A. D., Narayanaswamy, B. E., and Paterson, G. L. J. (2015). Deep-sea litter: a comparison of seamounts, banks and a ridge in the Atlantic and Indian Oceans reveals both environmental and anthropogenic factors impact accumulation and composition. *Front. Mar. Sci.* 2. doi: 10.3389/fmars.2015.00003

Woodside, J. M., David, L., Frantzis, A., and Hooker, S. K. (2006). Gouge marks on deep-sea mud volcanoes in the eastern Mediterranean: Caused by Cuvier's beaked whales? *Deep Sea Res. Part I Oceanogr. Res. Pap.* 53, 1762–1771. doi: 10.1016/j.dsr.2006.08.011

frontiers | Frontiers in Earth Science

TYPE Original Research
PUBLISHED 09 November 2023
DOI 10.3389/feart.2023.1174504

Check for updates

OPEN ACCESS

EDITED BY
Marcelo Ketzer,
Linnaeus University, Sweden

REVIEWED BY
Shinsuke Aoki,
Kagawa University, Japan
Nadezhda Syrbu,
V.I. Il'ichev Pacific Oceanological Institute (RAS), Russia
Saulwood Lin,
National Taiwan University, Taiwan

*CORRESPONDENCE
Tomohiro Toki,
toki@sci.u-ryukyu.ac.jp

RECEIVED 26 February 2023
ACCEPTED 26 October 2023
PUBLISHED 09 November 2023

CITATION
Toki T, Chibana H, Shimabukuro T and Yamakawa Y (2023), Distribution of dissolved methane in seawater from the East China Sea to the Ryukyu forearc. *Front. Earth Sci.* 11:1174504. doi: 10.3389/feart.2023.1174504

COPYRIGHT
© 2023 Toki, Chibana, Shimabukuro and Yamakawa. This is an open-access article distributed under the terms of the Creative Commons Attribution License (CC BY). The use, distribution or reproduction in other forums is permitted, provided the original author(s) and the copyright owner(s) are credited and that the original publication in this journal is cited, in accordance with accepted academic practice. No use, distribution or reproduction is permitted which does not comply with these terms.

Distribution of dissolved methane in seawater from the East China Sea to the Ryukyu forearc

Tomohiro Toki[1,2]*, Hideki Chibana[1], Teppei Shimabukuro[1] and Yo Yamakawa[1]

[1]Department of Chemistry, Biology and Marine Science, Faculty of Science, University of the Ryukyus, Nishihara, Okinawa, Japan, [2]Research Institute for Humanity and Nature, Kyoto, Japan

Methane is a greenhouse gas, and the East China Sea acts as a source of emissions to the atmosphere. On the other hand, the distribution of methane concentration in the Ryukyu Arc shelf and forearc region has not been clarified. Therefore, we investigated the continental slope and continental shelf areas from the Okinawa Trough to the landward side and the island shelf and forearc areas to the seaward side of the East China Sea. The methane concentration in the Kuroshio Current region was very low, and the methane concentration in the seawater just above the seafloor in the area directly above the hydrothermal systems was exceptionally high. In addition, methane concentration in seawater just above the seafloor where cold seeps and mud volcanoes are known is higher than the background, and higher methane concentrations were found in continental slope area and the island shelf area. The results suggest the existence of previously unreported methane sources such as cold seeps and mud volcanoes in the continental slope region and the island shelf region.

KEYWORDS

East China Sea, seawater, water column, methane, concentration, distribution, Ryukyu forearc

1 Introduction

Methane is a greenhouse gas that is estimated to be 80 times more potent than carbon dioxide over the next 20 years, making it extremely important to quantify the material cycle of the gas in the Earth's surface layer (Shukla et al., 2022). Continental shelves play extremely important roles as sources of the methane that is released into the atmosphere (Bange et al., 1994; Holmes et al., 2000; Bange, 2006). The methane that is stored in the stratified seawater of the East China Sea during summer is released into the atmosphere by the mixed layer that develops during winter (Tsurushima et al., 1996). Topographic features and gas chimneys that are presumed to be associated with mud volcanoes have been observed on the continental shelf and in the Okinawa Trough (Yin et al., 2003; Xing et al., 2016), together with cold seep sites on the continental slope (Xu et al., 2021), chemosynthetic organisms in the northern part of the Okinawa Trough (Kuhara et al., 2014; Xu et al., 2021), and exposed carbonate sites on the seafloor surface that suggest former cold-seep activity (Sun et al., 2015; Peng et al., 2017; Cao et al., 2020), all of which were potential sources of methane. Methane concentration anomalies and acoustic anomalies that suggest the presence of gas flares have been observed immediately above these sites, indicating that the cold-seep activity is ongoing (Zhang et al., 2020). These cold seep activities are considered related to the dissociation of methane hydrate (Sun et al., 2015; Cao et al., 2020), and are

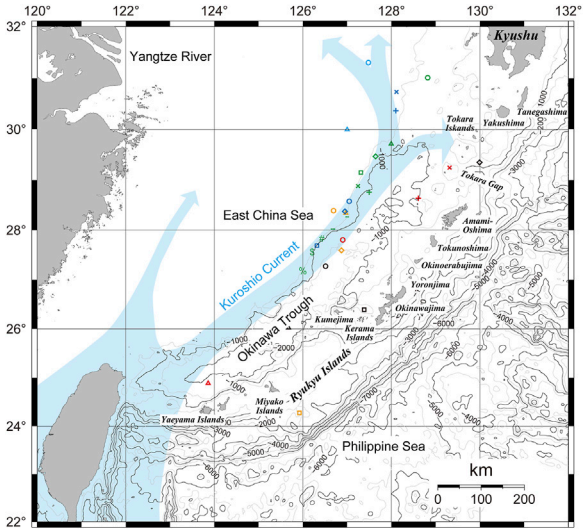

FIGURE 1
Location of sampling points and bathymetric map of the surrounding seas. Sampling points are indicated using the symbols shown in Table 1. Revisited sites are denoted using open symbols. Thin contour lines denote distances of 500 m and thick lines 1,000 m, and water depth is labeled every 1,000 m. The blue square and diamond indicate high methane concentrations in pore water found by the Chinese group (Li et al., 2015). Blue × and + indicate locations where the Chinese group found carbonate (×: Sun et al., 2015; +: Sun et al., 2019).

thought to have been one cause of the slope failure (blue × in Figure 1) and contributed to global warming that occurred after the last glacial period (Cao et al., 2020). Methane is rarely found in oxidizing seawater, and is abundant in methane-seeping phenomena on the seafloor, such as cold seeps, hydrothermal systems, and mud volcanoes, and river water of continental origin (Sun et al., 2018). For this reason, many studies have been conducted to discuss the supply source of methane to seawater by combining the T-S diagram, which combines water temperature and salinity, with the concentration distribution of methane (e.g., Zhang et al., 2020). In accordance with them, in this study, we investigated the concentration distribution of methane from the continental shelf of the East China Sea to the forearc region of the Ryukyu arc, and combined it with the T-S diagram to discuss the supply source of methane to seawater.

2 Methods

2.1 Sampling points

Seawater samples were collected aboard the Nagasaki Maru vessel during end of May to the beginning of June in 2010–2015 (Table 1; Figure 1). We took 303 samples (Figure 1). Sampling was conducted over the continental shelf, continental slope, the Okinawa Trough, island shelf, and forearc slope, which were classified in accordance with distance from the continent. The sites were selected such that each area had as many "featureless seafloor" combinations and singular geological points as possible. Henceforth in this paper, we refer to "featureless seafloor" as seafloor with no reported submarine hydrothermal systems, mud volcanoes, cold seeps, pockmarks, etc. The symbols used are summarized in Table 1, and the same symbols are used in all figures. The continental shelf is denoted yellow, continental slope is green, and sites further offshore are black. Mud volcanoes are indicated in brown, cold seeps in blue, and submarine hydrothermal systems in red. In the five revisited sites (Site No. 2015-3, 2012-1, 2015-5, 2012-7, and 2012-8), data from the first visit are indicated by open symbols, and data from the second by solid symbols. Only the open symbols are utilized on the map (Figure 1). Continental slope data were collected from a large number of points located in the same study area; therefore, this feature was divided into north and south with a boundary lying at approximately 28°30′N.

2.2 Seawater sampling

Niskin samplers were used to collect seawater, and CTD sensors utilized to simultaneously measure water temperature, pressure, and salinity. Once at the designated location, the water sampler was lowered to the area just above the seafloor, and seawater was sampled at the designated depth using the water sampler with a 12-hanger. Sampling was conducted according to depth, and a bucket was used to obtain surface samples. Seawater samples were divided into two vials and 500 µL of saturated mercury solution immediately added to inhibit the microbial activity. Samples were then capped with a butyl rubber stopper and aluminum cap and stored around 4 °C in a refrigerator to prevent rupture before transfer to a laboratory refrigerator for analysis.

2.3 Analytical procedures

Dissolved gases were extracted from 100 mL samples of seawater and measured using a gas chromatograph equipped with an FID (GC-2014; Shimadzu, Supplementary Figure S1). The samples (100 mL) were transferred to a purge bottle using helium gas and helium bubbling initiated until almost all dissolved gas reached the gas-phase. Initial water vapor removal was performed by passing gas through a cold trap that was cooled at −120 to −80°C using liquid nitrogen and ethanol, after which gas was filtered through silica gel at room temperature for further water vapor removal. The six-way valve was used to allow carrier gas to flow out of the gas chromatograph, and all trapped gas was vaporized with boiling water. The degassed sample was then placed in the gas chromatograph, separated by a Porapak Q column, and carried into the FID detector, where all gases were burned and ionized to measure the concentration of hydrocarbons. The standard gas was introduced upstream of a bottle filled with ultrapure water, after ensuring that the blank containing 10 ppm methane was completely lowered at a measured pressure. Gas extracted using a similar method was analyzed by FID to determine the sensitivity for methane. Analysis was performed until the accuracy reached less than 8%. The same seawater sample was measured daily to ensure that the concentrations were within the error limit of 8% before the sample was measured. Sample weights were calculated by weighing

TABLE 1 Location and description of seawater sampling by a Niskin sampler.

Location	Area	Site no.	Year	Month	Symbol	Longtitude	Latitude	Depth (m)	Remarks
Continental shelf		2011-6	2011	May	○	127°28.899′E	31°18.042′N	127	
		2011-5	2011	May	△	127°00.020′E	29°59.945′N	105	
		2012-3	2012	May	○	126°41.336′E	28°22.234′N	186	Mud volcano Yin et al. (2003)
Continental slope	Northern area	2011-7	2011	May	○	128°49.805′E	31°00.336′N	679	
		2015-1	2015	June	△	127°59.916′E	29°43.132′N	726	
		2015-2	2015	June	◇	127°38.223′E	29°27.710′N	821	
		2011-4	2011	May	□	127°20.055′E	29°08.207′N	601	
		2015-3	2015	June	■	127°19.910′E	29°08.175′N	595	Revisit to Site 2011-4
		2015-4	2015	June	×	127°15.16′E	28°51.70′N	778	
		2011-3	2011	May	+	127°30.092′E	28°44.832′N	1,027	
		2012-1	2012	June	⊞	127°30.250′E	28°44.996′N	1,025	Revisit to Site 2011-3
		2012-2	2012	May	○	127°02.830′E	28°33.655′N	648	Cold seep Kuhara et al. (2014)
		2015-5	2015	May	●	127°02.944′E	28°33.811′N	655	Revisit to Site 2012-2
	Southern area	2015-6	2015	May	-	127°00.149′E	28°13.636′N	864	
		2015-7	2015	May	−	126°40.30′E	28°00.544′N	710	
		2015-8	2015	May	#	126°25.576′E	27°48.572′N	1,024	
		2015-9	2015	May	$	126°12.513′E	27°33.070′N	970	
		2015-10	2015	May	%	125°59.65′E	27°10.32′N	1,024	
		2012-4	2012	May	△	126°58.176′E	28°19.612′N	431	Pockmark Yin et al. (2003)
Backarc area		2011-1	2011	May	○	126°30.185′E	27°14.869′N	1,554	Control site 1
		2012-7	2012	May	●	126°30.507′E	27°15.182′N	1,563	Revisit to Site 2011-1
		2010-1	2010	May	△	125°40.132′E	26°00.202′N	1,889	
		2012-5	2012	May	◇	126°52.314′E	27°34.298′N	1,478	Mud volcano Ning et al. (2009)
		2012-6	2012	May	○	126°54.021′E	27°47.318′N	1,835	Iheya North Knoll Monma et al. (1996)
		2010-2	2010	May	△	123°50.992′E	24°51.661′N	1,596	Hatoma Knoll Watanabe et al. (1999)

(Continued on following page)

TABLE 1 (*Continued*) **Location and description of seawater sampling by a Niskin sampler.**

Location	Area	Site no.	Year	Month	Symbol	Longtitude	Latitude	Depth (m)	Remarks
Island shelf		2011-8	2011	May	◇	129°59.865′E	29°20.105′N	1,134	
		2011-2	2011	May	□	127°23.007′E	26°22.095′N	748	
		2012-8	2012	May	■	127°23.053′E	26°22.174′N	746	Revisit to Site 2011-2
Forearc slope		2010-3	2010	May	□	125°55.135′E	24°15.067′N	1,385	Potential mud volcano

each tare and subtracting the average weights of the empty bottle, butyl rubber stopper, and aluminum cap. The concentration of each sample (M) was then calculated as the concentration of methane per kilogram of seawater (mol/kg).

3 Results

3.1 T-S diagram

The salinity and temperature data obtained from the CTD were used to produce a T-S diagram with salinity on the horizontal axis and temperature on the vertical axis (Figure 2). Kuroshio Surface Seawater (KSW), Kuroshio Sub-surface Seawater (KSSW), Kuroshio Intermediate Seawater (KIW), and Shelf mixed seawater (SMW) are identified in all water masses (Zhang et al., 2008). Graphs were divided into different sea areas and "geological singularities" (Figure 2). Henceforth in this paper, submarine hydrothermal systems, mud volcanoes, cold seeps, and pockmarks are referred to as geologic singularities. Figures 2A–C shows the salinity and temperature data describing seawater collected from the featureless seafloor of the continental shelf (Site No. 2011–6, 2011–5, and 2012–3). Among them, Figure 2C is the CTD data acquired over the mud volcanic landform reported by Yin et al. (2003). Figures 2D–M shows the northern part of the continental slope, Figures 2L, M shows the cold seep site reported at the southern end of the northern continental slope (Kuhara et al., 2014), and Figures 2N–S shows the T-S data acquired from the southern part of the continental slope, and Figure 2S shows data collected over the pockmarks reported by Yin et al. (2003). Figures 2T–Y shows the T-S data from above the Okinawa Trough, Figure 2W shows data acquired from above the mud volcanoes (Ning et al., 2009) reported in the Okinawa Trough, and Figures 2X, Y shows the T-S data obtained from the area above the submarine hydrothermal system corresponding to the geological singularity in the Okinawa Trough. Figures 2Z–ab shows the data acquired from the area above the island shelf, and Figure 2ac illustrates the data acquired from the forearc region.

The T-S data obtained from the top of the featureless seafloor of the Okinawa Trough are considered representative of the Kuroshio Current (Figures 2T–V), and the inverse S-shaped curve from the KSW to the KIW via the KSSW is typical of that obtained using T-S data for water masses in the Kuroshio Current (Figures 2T–V). Data from water masses above the continental shelf are mostly outside these regions and curves, and are interpreted to be continental shelf mixed water (SMW) (Figures 2A–C). The surface water above the continental shelf is cooler and less saline than that of the KSW (Figures 2A–C). Ultimately, continental river water is considered to be the end member; however, because it is river water, its salinity is lower than that of seawater, and its water temperature is also lower than that of warmer currents such as the Kuroshio Current. The influence of the SMW is clearly visible in the water masses above the continental shelf (Figures 2A–C, but it is also visible in some of the water masses in the continental slope region, especially the northern waters (Figures 2D–I). Similarly, the influence of the SMW is visible in the water masses above the cold-seep site classified as the northern sea area, especially in 2012 (Figure 2L). The fact that this is not as evident in the 2015 data (Figure 2M) suggests differences in water mass between 2012 and 2015. However, the SMW influence was relatively small in the data from 2015-6, 2015-7, 2015-8, 2015-9, and 2015-10 at sites south of 28°30′N and above the pockmark (site 2012-4), which are classified as the southern area (Figures 2N–S). The data obtained from the seafloor hydrothermal system on the island shelf and in the forearc slope region are plotted within the KSW, KSSW, and KIW (Figures 2T–ab). Only data from the slope area of the forearc deviated slightly from the KIW region, possibly because it was not a Kuroshio Current region in the first place (Figure 2ac). In any case, the T-S diagram generally shows the strong influence of continental shelf mixed waters on the continental shelf and in the northern part of the continental slope area, but not in other areas, and geological features such as submarine hydrothermal or mud volcanoes do not seem to influence the T-S diagram (Figure 2). The T-S is thus considered to be controlled mainly by factors such as ocean area, distance from the continent, and the influence of the meandering Kuroshio Current or continental rivers at shallower than about 100 m.

3.2 Vertical distribution of methane concentration

The distribution of methane concentrations was divided in the same manner as the CTD data (Figure 3). Classification was categorized into continental shelf (Figures 3A–C), northern continental slope (Figures 3D–K), the cold seep located at the southern end of the northern continental slope (Figures 3L, M), southern continental slope (Figures 3N–S), Okinawa Trough (Figures 3T–W), submarine hydrothermal system located in the Okinawa Trough (Figures 3X, Y), island shelf (Figures 3Z–ab), and mud volcano-like features in the forearc slope area (Figure 3ac).

10.3389/feart.2023.1174504

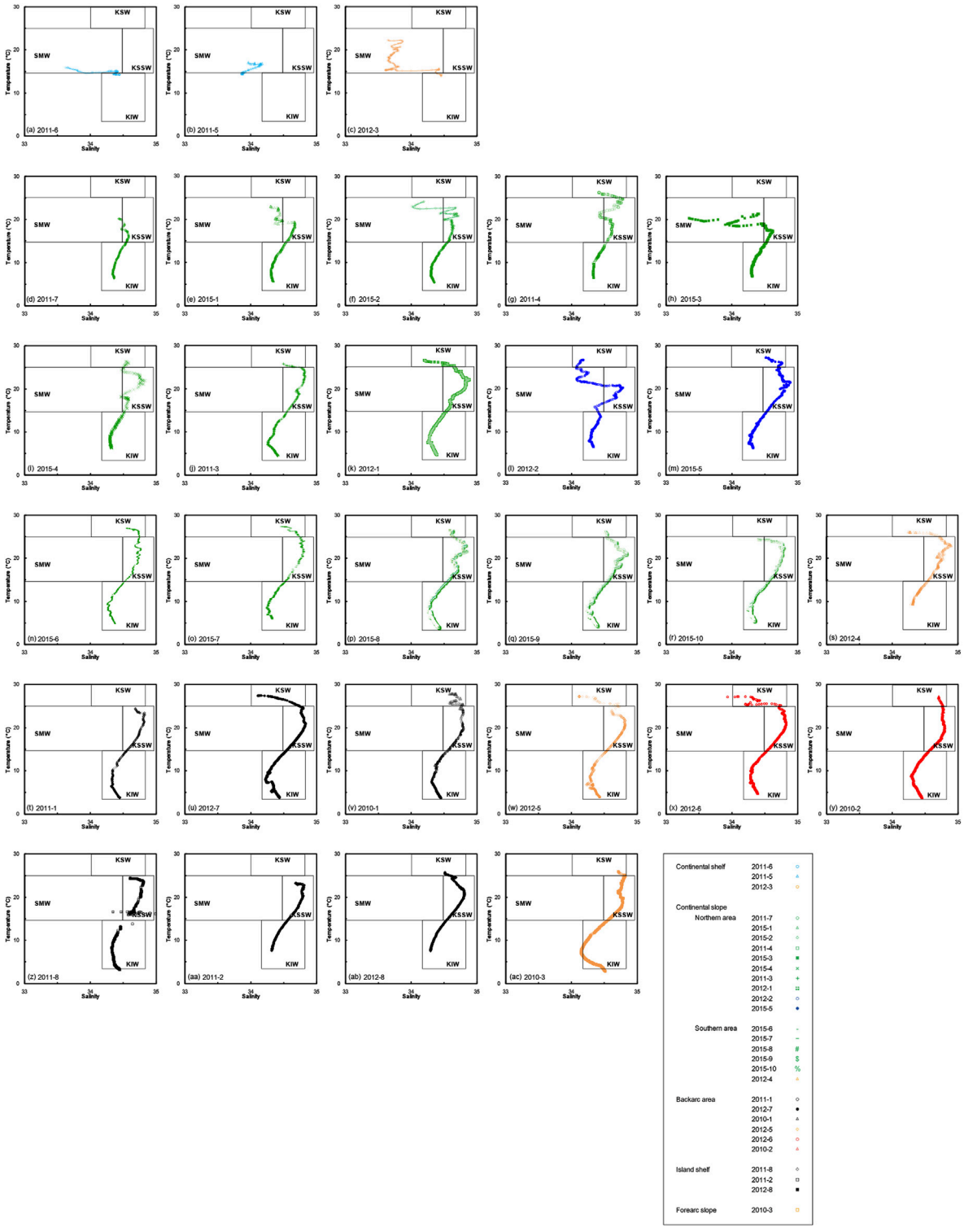

FIGURE 2
T-S diagram for sampling stations in the study. KSW, Kuroshio Surface Water; KSSW, Kuroshio Subsurface Water; KIW: Kuroshio Intermediate Water; SMW, the Shelf Mixed Water in the ECS. Water masses are classified according to Zhang et al. (2008). Light blue symbols indicate samples collected from the continental shelf **(A,B)**, green indicates samples collected above the continental slope **(D–K)**, **(N–R)**, and black denotes samples collected from other areas **(T–V)**, **(Z–ab)**. Samples collected directly above mud volcanoes are in orange **(C, S, W, and ac)**, samples collected just above the cold seep site are in blue **(L,M)**, and samples collected just above the hydrothermal system are in red **(X,Y)**. The high number of sampling points on the continental slope area led to division of this feature into northern **(D–K)** and southern **(N–R)** regions with the boundary at around 28°30′N latitude.

10.3389/feart.2023.1174504



FIGURE 3
Vertical distribution of methane concentrations in seawater obtained in this study. Symbols and groupings are the same as in Figure 2. Shading indicates background levels in seawater certified with reference to data from site 2017-7 **(U)** (see Section 3.2).

Classification is based on submarine morphology such as continental shelf, continental slope, back-arc basin (Okinawa Trough), forearc uplift zone (island shelf), and forearc trench side slope, which changes significantly with distance from the continent, and by the presence of as geological features such as submarine hydrothermal systems, cold seeps, and mud volcanoes (both reported and potential). Each site is plotted on a different graph. The colors and shapes of the symbols used are listed in Table 1.

First, we examine the distribution of methane concentrations in seawater collected from the area over Okinawa Trough (Figures

3T–V). This area could have ocean water without continental influence as the distribution of methane, because it is part of the Kuroshio Current region. According to these data, the methane concentrations in the seawater were one to two nM up to 400 m below the surface and 0–1 nM at greater depths (Figure 3U). These methane concentration distributions are shown as shaded areas in all graphs in Figure 3, as they correspond to the background of this area.

The distribution of methane concentrations in seawater collected over the continental shelf reveals slightly higher methane concentrations (Figures 3A, B), albeit with small differences, even on a featureless seafloor. On the other hand, the methane concentration in the seawater sampled above a mud volcano (Yin et al., 2003) on the continental shelf (Figure 3C) indicated that the methane concentration was within the same range as the background in the surface layer and increased rapidly below 100 m depth, with a maximum concentration observed at 120 m, below which it dropped. However, a particularly large peak of 10–12 nM was observed at approximately 150 m, and the methane concentration decreased to almost background levels immediately above the seafloor (Figure 3C).

Next, we examined the distribution of methane concentrations in seawater collected from the continental slope region (Figures 3D–S). According to these results, methane concentrations appear to be somewhat scattered in the southern region (Figures 3N–S) but are mostly within the range of background methane concentrations (note that the other graphs have different concentration ranges), including seawater above the pockmarked topography on the continental slope reported by Yin et al. (2003) (Figure 3S). In addition, the distribution of methane concentrations in the seawater just above the cold-seep site, where sampling was conducted twice (Figures 3L, M), shows much higher methane concentrations (~4 nM) over the surface 100–200 m (Figure 3L) than the background (shaded area in Figure 3L). The methane concentration decreases at 300 m, increases at 400 m, decreases again at 500 m, and increases just above the seafloor. However, in the seawater sampled during the return visit in 2015 (Figure 3M), the methane concentration anomaly observed at around 200 m was not observed, with only the increase just above the seafloor observed. In comparison, methane concentrations in the northern part of the continental slope were generally high (Figures 3D–K) and were significantly higher than the background at approximately 100–200 m below the surface at most sites. Methane concentrations reaching far above background levels were observed at depths below 400 m at several of the sites, with relatively large concentrations observed just above the seafloor at Site No. 2012-1 (Figure 3K). This site was also visited in 2011, the year before the concentration anomaly was observed (Figure 3I), and although the methane concentration at that time was not as high, a peak was observed in the seawater at 800 m (approximately 200 m above the seafloor), similar to 2012 (Figure 3I).

The methane concentrations in seawater sampled above the submarine hydrothermal systems were exceptionally high (Figures 3X, Y). High concentrations of >10 nM were obtained from seawater above known mud volcanoes on the continental shelf (Figure 3C) and in methane-rich seawater on the continental slope (Figure 3G). In contrast, methane concentrations in seawater collected above the seafloor hydrothermal system at the Iheya North Knoll (Figure 3X) exceeded 30 nM, although methane concentrations of only slightly above 10 nM were obtained above the Hatoma Knoll (Figure 3Y).

Site No. 2011-2, an island shelf area (Figure 3aa), was revisited in 2012 (Figure 3ab) and methane above background levels was detected in the samples taken during the second visit in 2012. The concentration distribution of methane in the seawater collected during the first visit in 2011 (Figure 3aa) was similar in shape to that in 2012; however, the absolute value of concentration was approximately 30% lower. Methane concentrations in seawater up to 200 m below the surface remained at background levels in 2011 (Figure 3Z) but were slightly higher than the background in the water mass at 300–500 m. Site No. 2011-8 (Figure 3Z) is located on the same island shelf; however, it is much farther north than the other island shelf sites and is situated in the Tokara Gap, which connects the Okinawa Trough to the Philippine Sea (Figure 1). The methane concentration distribution at Site No. 2011-8 (Figure 3Z) shows background levels in the surface layer with mild methane concentration anomalies in water masses below 400 m in depth.

Finally, the distribution of methane concentrations in the seawater sampled over the volcano-like mud terrain in the forearc region showed methane concentrations at background levels (Figure 3ac).

4 Discussion

4.1 Background concentration distribution of methane in seawater

Let us define the normal distribution of methane in seawater. In the surface layer of the ocean, the concentration is approximately 1–2 nM, which decreases to an extremely low concentration of 0–1 nM at depths below 400 m (Figure 3U). This suggests that methane reaches a solubility equilibrium with the atmosphere in the surface layer and is oxidized by microorganisms in the water column at depths below 400 m, resulting in the low concentrations observed. Methane is also produced by the decomposition of organic matter in the sediments, from which it can seep, resulting in high methane concentrations both in the sediments and in the seawater just above the seafloor (Sun et al., 2018). In some locations, the methane concentrations in the seawater immediately above the seafloor are particularly high because of disturbance to the seafloor surface, such as that observed in shallow waters under the action of strong currents or in areas with discharging fluids such as hydrothermal or cold-seep fluids (Zhang et al., 2020). Even at these locations, methane in the seawater is degraded by methane-oxidizing microorganisms away from the seafloor, and methane concentrations in the mid-water drop to very low concentrations of 0–1 nM (Watanabe et al., 1995).

4.2 The Yangtze River as a source of methane

The distribution of methane in seawater above the continental shelf is characterized by 1) low salinity and high methane concentration, mainly in the ocean surface layer at the mouth of

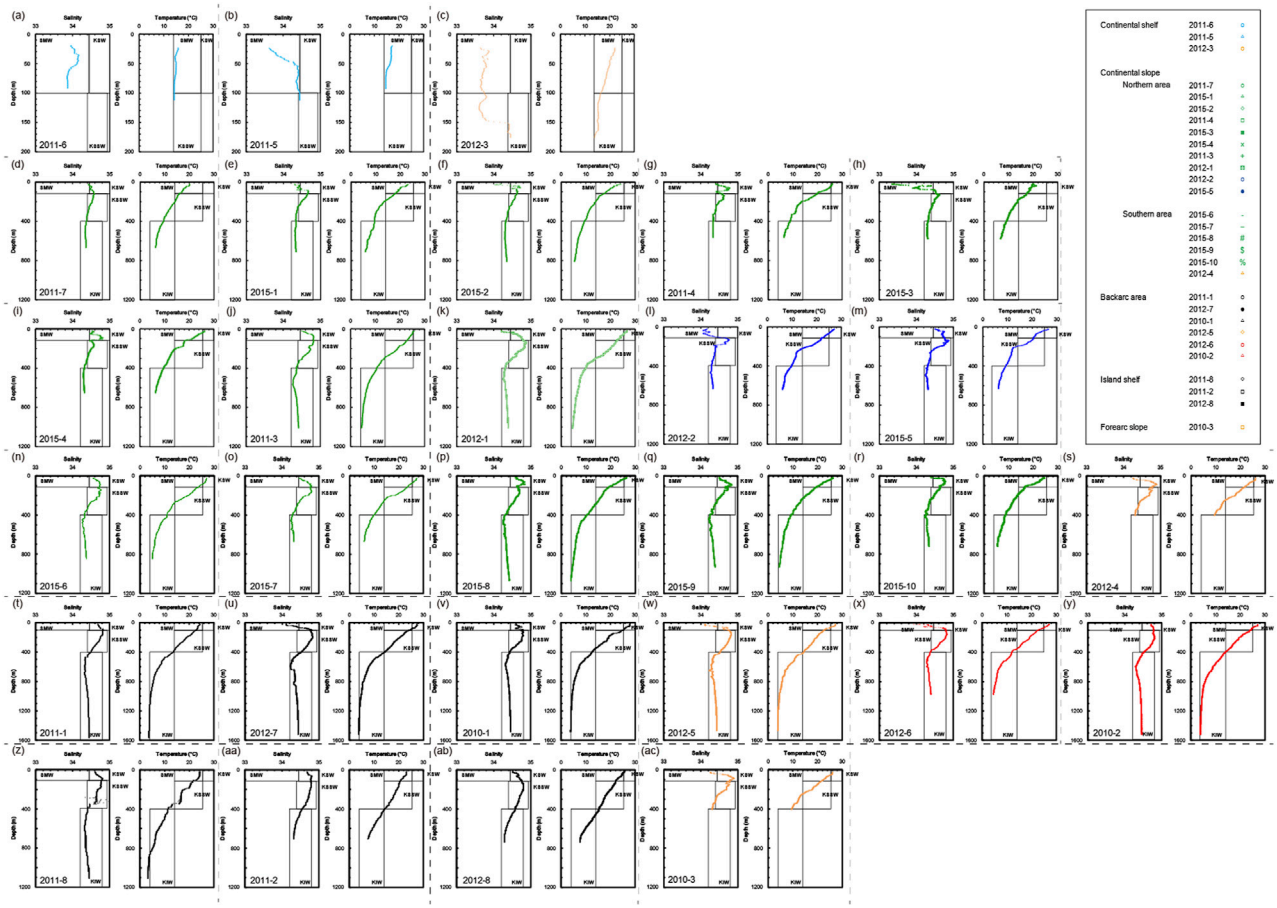

FIGURE 4
Vertical profiles of salinity and water temperature at the grouped stations. Symbols and groupings are the same as in Figure 2. The areas of each water mass are indicated by squares using water temperature and salinity data from Zhang et al. (2008).

the Yangtze River, and 2) high methane concentrations just above the seafloor due to the release of methane from the sediments (Sun et al., 2018). In this study, the effects of SMW mixing with low-salinity water of riverine origin were observed on the continental shelf (Figures 2A, B) and continental slope areas (Figures 2D–M). To verify whether these influences also affect the methane concentrations in ocean water, we plotted the distributions of salinity and temperature with depth (Figure 4). As before, the graphs were divided into the continental shelf (Figures 4A–C), northern part of the continental slope (Figures 4D–K), cold seep site located in the northern part of the continental slope (Figures 4L, M), southern part of the continental slope (Figures 4N–S), Okinawa Trough (Figures 4T–W), submarine hydrothermal system in the Okinawa Trough (Figures 4X, Y), and the island shelf area (Figures 4z–ab). The colors and shapes of the symbols used are the same as those listed in Table 1. The water temperature and salinity characteristics for each water mass shown in Figure 2 are boxed in accordance with depth, with water depths shallower than 100 m considered KSW, water between 100 and 400 m denoted KSSW, and water masses deeper than 400 m characteristic of KIW (Zhang et al., 2008). No distribution of the water masses was observed outside the KIW at any of the sites, and no middle water other than that of Kuroshio origin was found. In contrast, water masses with lower salinity (≤34–34.45 psu) and temperatures (≤25 C) than KSW are distributed in water at depths shallower than 100 m (Figures 4A–M).

The water sampled on the continental shelf, which is only approximately 100 m deep, shows lower salinity and temperature than the KSW (Figures 4A, B), suggesting that it is influenced by water of riverine origin (SMW in Figures 4A, B). The methane concentrations on the continental shelf show modest anomalies (~two to three nM) that are only slightly higher than the background (~1–1.5 nM; Figures 3A, B). This suggests that SMW is characterized by a methane concentration anomaly of only a few nM.

Seawater was also sampled just above the mud volcanoes on the continental shelf (Figure 3C), where the salinity is uniformly low (<34.5 psu) from the surface to a depth of approximately 150 m (Figure 4C), suggesting that low-salinity water of riverine origin may be influential in this area. Salinity was observed to increase sharply from ~33.7–33.8 psu to ~34.4 psu and water temperature decrease slightly around 15°C with depth in this location (Figure 4C), indicating that the KSSW can affect depths below 150 m (Figure 4C). In contrast, the methane concentration increases sharply at a depth of approximately 100 m, decreases at around 130 m, and reaches a maximum between 140 and 160 m (Figure 3C). Continental water originally contains a large amount of methane

TABLE 2 Maximum concentrations of methane in seawater immediately above the hydrothermal system in the Iheya North and Hatoma Knoll obtained in this study and reported end-membered concentrations of methane in hydrothermal fluid. In addition, similar datasets reported for the Okinawa Trough and representative similar datasets for other areas are also presented for comparison.

		Endmembered CH_4	Plume CH_4	References
		mM	nM	
Iheya North Knoll		3.7	30	Kawagucci et al. (2011); This study
Hatoma Knoll		21	10	Toki et al. (2016); This study
Izena Hole	JADE	0	650	Kawagucci et al. (2013); Ishibashi et al. (2014)
	HAKUREI	6.8	650	*ditto*
Yonaguni IV Knoll		13.5	1030	Konno et al. (2006); Gamo et al. (2010)
Kairei Field		0.082	52	Gamo et al. (2001)
TOTO Caldera		0.026	10	Gamo et al. (2004)

(Zhang et al., 2020), but continental water near the Kuroshio Current region, which is about 400 km away from the continent, does not seem to contain so much methane. Instead, our data suggest an origin from mud volcanoes (Figure 3C).

4.3 Marine sediments as a source of methane

While SMW effects are visible at depths shallower than 100 m from the continental shelf to the continental slope (Figures 4A–M), methane concentrations reaching 10 nM (Figures 3C, G) or 4 nM (Figure 3L) have been detected at 100–200 m. As we have mentioned, methane concentrations in seawater without anomalies decrease with depth (Figure 3U), however even on the seafloor without anomalies, methane concentrations in sediments are so much higher than in seawater that methane concentrations can increase in seawater just above the seafloor due to gas diffusion and bubble release (Reeburgh, 2007; Weber et al., 2019). On continental shelves, methane concentrations of >10 nM have been reported just above the seafloor in previous studies (Zhang et al., 2020), which likely result from methane reaching the water via sedimentary particles drifting through the seawater (Sun et al., 2018). Based on these observations, we can say that methane that was abundantly distributed in sediments disturbed by bottom currents can spread into seawater, resulting in higher methane concentrations in seawater just above seafloor. It is quite possible that methane-rich seawater just above the seafloor on the continental shelf at depths of 100–200 m formed in such a way migrates horizontally, leading to the observed methane concentration anomalies that exceed 10 nM in the water masses around 100–200 m on the continental slope.

4.4 Hydrothermal systems as a source of methane

Several different methane distributions were identified in seawater immediately above hydrothermal vents (Figures 3X, Y). Seawater sampled directly above the seafloor hydrothermal system

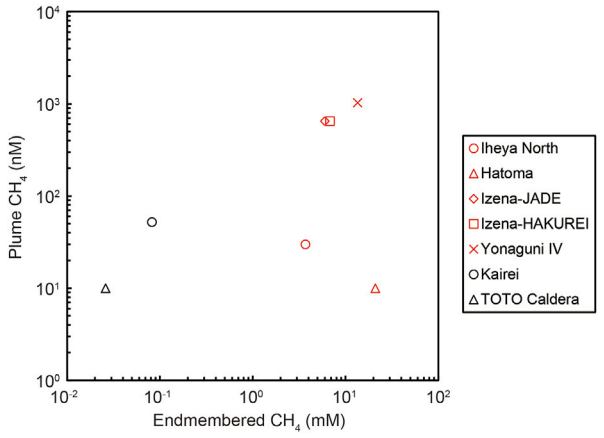

FIGURE 5
Comparison of the highest methane concentration in seawater above the hydrothermal system to the concentration of methane in the hydrothermal fluid.

shows an unparalleled methane concentration distribution (Figure 3X) that covers a range of several tens of nM, whereas a range of only a few nM with a maximum of 10 nM was observed in other areas (Figure 3Y). The submarine hydrothermal systems found at several locations in the Okinawa Trough exhibit high methane concentrations (Kawagucci, 2015). This feature is thought to be due to the geological background of the Okinawa Trough, which is classified as a sediment-covered back-arc system, from which methane from organic matter in the sediment is released when submarine hydrothermal fluids circulating through the sediment are expelled (Kawagucci, 2015). Table 2 summarizes the methane concentrations in the seafloor hydrothermal fluids of the Okinawa Trough reported to date. The maximum methane concentrations in the seawater immediately above the hydrothermally active zone are also summarized (Table 2), and for comparison, the maximum concentrations of methane detected in seawater immediately above a seafloor hydrothermal system without sediment are summarized (Table 2). A methane concentration of 3.7 mM was observed at the Iheya North Knoll,

which is marked with a red open circle (Kawagucci et al., 2011), whereas 21 mM was reported at the Hatoma Knoll, which is marked with a red open triangle (Toki et al., 2016). Two submarine hydrothermal activity zones JADE and HAKUREI, have been identified in the Izena Hole, where methane concentrations of 4.9–7.1 mM and 6.8 mM have been observed, respectively (Ishibashi et al., 2014). In addition, a value of 13.5 mM was reported for Yonaguni Knoll IV (Konno et al., 2006). By comparison, methane concentrations in the hydrothermal fluid of 82 μM were reported in a submarine hydrothermal system without sediment cover in the Kairei field at the Rodriguez Triple Junction in the Central Indian Ridge (Gamo et al., 2001) and concentrations of 2 μM were observed in the TOTO caldera at the southern end of the Mariana arc (Gamo et al., 2004). Using the Mg concentrations listed in Gamo et al. (2004), assuming that pure hydrothermal fluid contains no Mg and that all Mg is derived from seawater (Von Damm, 1995) and correcting for seawater dilution, we estimate that approximately 26 μM of hydrothermal fluids are vented from the TOTO caldera around the southern end of the Mariana arc (Gamo et al., 2004). The methane concentrations detected in the seawater immediately above the features described have been reported at ~10–1,030 nM (Table 2; Gamo et al., 2001; Gamo et al., 2004; Gamo et al., 2010; Kawagucci et al., 2010). The datasets describing these areas are shown in Figure 5.

Thus, there was an overwhelming difference in the concentration of methane in the hydrothermal fluids from the sediment-covered Okinawa Trough and that of other hydrothermal systems without sediment cover. However, regarding the methane concentrations obtained previously, little difference was observed in the methane concentrations of seawater obtained in this study (Figure 5). Furthermore, the methane concentrations in the seafloor hydrothermal fluid reported at Hatoma Knoll and Yonaguni Knoll IV were one order of magnitude higher than those at Iheya North Knoll and the Izena Hole. However, the concentration of methane in the seawater was overwhelmingly high just above Yonaguni Knoll IV and lowest at Hatoma Knoll (Figure 5). These results indicate that it is relatively difficult to quantitatively determine the methane concentration in a seafloor hydrothermal system as compared to seawater. For example, even if a Niskin water sampler is used directly above the point of a reported seafloor hydrothermal system, the proximity of the sampler to the seabed cannot be accurately determined, and the results obtained by a surface ship survey are limited by sampler sweep and the distance at which samples are obtained in the horizontal direction. Nevertheless, the methane concentrations in seawater sampled by the Niskin water sampler directly above various geological features such as the submarine hydrothermal system were found to be orders of magnitude higher those observed in seawater from other locations (Figure 3), indicating that the submarine hydrothermal system is an exceptional source of methane to the water column.

At the very least, we can be certain that there is a source of methane where water masses with methane concentrations higher than background are found. Conversely, no active sources are assumed in areas where the methane concentration is similar to background levels. If a sampler is lowered at a location where there should be a source of methane as a result of latitude and longitude but no water mass higher methane concentrations are observed, it is possible that the sampler has been swept away or that the source of methane is currently inactive. For example, anomalous methane concentrations can be detected several tens of kilometers downstream of a bottom flow stream, but not upstream, of water masses with methane concentrations higher than the background, even at a distance of only a few kilometers (Zhang et al., 2020). Indeed, it is common for no methane concentration anomalies to be detected in the seawater near undiscovered hydrothermal systems (Gamo et al., 2001; Yamanaka et al., 2015).

4.5 Mud volcanoes as a source of methane

Figure 3W shows the distribution of methane concentrations directly above a mud volcano (Ning et al., 2009), in an area where the water reaches a depth of *ca.* 1,500 m. A concentration anomaly can be observed just above the seafloor, albeit small (~1.5 nM), with background levels of methane at other depths (Figure 3W). The site marked with a brown open square (Figure 3ac) selected from the bathymetry map as a mud volcano-shaped site was associated with methane concentrations slightly above background levels approximately 100 m above the seafloor (1,200 m depth). This indicates that this site, which is located in the southern part of the Ryukyu Forearc, where no mud volcanoes have been reported, may be close to a slightly active methane venting area (Figure 1). Considering the normal places for magma formation (near an island arc, back-arc, mid-ocean ridge, or hot spot), the source of methane venting into the fore-arc would be either mud volcanoes or cold seeps.

4.6 Cold seeps as a source of methane

Seawater samples were collected over 2 years in the area directly above the cold seep site (Figure 3L: 2012, Figure 3M: 2015). In both years, very mild methane concentration anomalies (~2 nM) were found just above the seafloor surface, and once the methane concentration dropped to background levels, methane concentrations (~2.5 nM in 2015 and ~1.5 nM in 2012) were still detected in water masses a few hundred meters above the seafloor surface (Figures 3L, M). We cannot confirm whether this is an indication of methane migration via bubbles or discharge at different heights, except through direct observation of the seafloor. However, the methane concentration anomaly at around 100–200 m (~4 nM), which was observed only in 2012 at this site, may have been due to bottom currents on the continental shelf, as discussed in Section 4.3. Because this methane concentration anomaly was not observed in 2015, it can be assumed that such currents yearly, depending on the conditions just above the seafloor surface. These methane concentration anomalies (Figures 3L, M) are mild as compared to the methane concentration anomalies observed above the submarine hydrothermal systems (Figures 3X, Y) or highly active mud volcanoes (Figure 3C). This may be partly due to the relatively mild material fluxes of mainly reducing substances such as methane, hydrogen sulfide, and ammonia associated with cold-seep events as compared to mud volcanoes and submarine hydrothermal systems (Levin et al., 2016). Nevertheless, the results of this study indicate that methane can also be used to detect cold-seep activity.

4.7 Unidentified methane sources in the continental slope area

The data for water masses collected from the continental slope area are shown in green; however, because of the large number of sites, those in the north (Figures 3D–K) were plotted separately from those in the south (Figures 3N–R). Sites with relatively high methane concentrations are located farther north. The sites located to the south had relatively lower methane concentrations in comparison (<~1–3 nM); however, the overall concentrations appear more scattered than those in the background (Figures 3N–R). It is possible that the continental slope is supplying methane laterally at various depths with some phenomenon that will be discussed later (Figures 3N–R). However, this is likely not a significant source. Such a supply was observed at relatively systematic depths at the northern site, with three positive sites at 100 m (~4 nM), a large peak at approximately 150 m (~10 nM), another at 600 m (~7 nM), three at 800 m (~3 nM or ~9 nM), and one at 1,000 m (~8 nM; Figures 3D–K). The methane concentration anomalies observed at 100–200 m may indicate diffusion of methane from seafloor sediments, as discussed previously. However, the source at 1,000 m may be located on the seafloor surface, whereas the methane concentration anomalies observed around 600 m or 800 m may indicate methane on the continental slope. In the case of a submarine hydrothermal system, magma can be assumed present in the Okinawa Trough; however, the existence of magma on the continental slope area is unthinkable. As for other sources of methane supply from the seafloor, methane emissions caused by the decomposition of organic matter, such as mud volcanoes and cold seeps (Kopf, 2002), may occur even in continental slope areas. It is thought that a source of methane is present 600–1,000 m below the seafloor at around 29°N, as indicated by the green open triangles, open diamonds, and green plus marks in Figure 1.

Of these, at Site No. 2012-1 (white plus mark in green solid square; Figure 3K), seawater was also sampled in 2011 (green plus mark), at that time a small methane concentration anomaly (~2 nM) was detected at 800 m (Figure 3I). Near this site, a Chinese group recently found a cold seep (Xu et al., 2021), and bubbles emanating from the seafloor have been suggested by acoustic imagery (Chen et al., 2022). Although the detailed location has not been specified, bacterial mats and *Calyptogena* colonies have been found on the seafloor at a depth of about 900–1,000 m near 127°30′E, 29°N, and water masses with methane concentrations exceeding 20 nM have been detected in the seawater directly above the area (Zhang et al., 2020). In this study, only a maximum of approximately 8 nM was detected (Figure 3K). However, it seems certain that there was a source of methane on the seafloor in the continental slope area. Further clarification of the distribution of methane sources is required through extended seafloor observation.

4.8 Unidentified methane sources in the shelf area

Sites that are described by black open and solid squares were sampled in 2011 and 2012 by selecting an empty area on the island shelf and considering it a reference. Anomalous methane concentrations (~1.5–2.5 nM) were detected from 200 m to 600 m in 2011 (Figure 3aa), whereas anomalous methane concentrations (~1.5 nM) were detected from the surface to approximately 600 m in 2012 (Figure 3ab). This site is located on the Ryukyu Islands across the Okinawa Trough in mainland China. The Kuroshio Current flows into the sea just above the Okinawa Trough (Figure 1), and the distribution of methane in this current is at background levels (Figure 3U). The influence of continental shelf-mixed water was also observed just above the continental shelf in the yellow open circle and open triangle areas in the T-S diagram, where slightly higher methane concentrations were detected (Figures 3A, B); however, these effects are expected to be reset in the Kuroshio watershed. This suggests that the island shelf itself is the source of the methane concentration anomalies observed in the middle layers of these island shelf areas (Figures 3aa, ab). Because of the influence of domestic wastewater, rivers, and coral reefs, it is possible that groundwater that previously seeped into the subsurface may be upwelling from the coastal seafloor (Umezawa et al., 2002). Submarine groundwater discharge has been observed along the world's coasts, and it has been reported that as groundwater passes through sediments, it entrains and discharges reducing substances such as methane, hydrogen sulfide, and ammonia, which are rarely distributed in seawater (Lecher et al., 2016; Purkamo et al., 2022; Brankovits et al., 2017; Lecher, 2017; Lecher and Mackey, 2018; Sadat-Noori et al., 2018). Such an inflow of land water, such as groundwater or river water, could be observed using anomalies in the T-S diagram. However, such salinity and temperature anomalies were not visible in the T-S diagrams (Figures 2aa, ab) and the T-S profiles (Figures 4aa, ab). Therefore, groundwater and river water from the island cannot explain the anomalous methane concentrations in the middle layer that was observed at these sites. This area is not completely enclosed, but is surrounded by the Kerama Islands, Okinawajima, and Kumejima (Figure 1), and only the north, which is considered shallow water at a depth of approximately 750 m, can be considered open (Figure 1). No volcanic or hydrothermal activity was observed in the surrounding area, and the methane distribution did not seem to indicate a source on the seafloor (Figures 3aa, ab). Instead, the methane accumulates annually in this area, with concentration peaking at approximately 300–400 m, and despite the concentration differences, it appears to have peaked at the same depth in 2011 (Figure 3aa). One possible explanation is that methane seeps from the seafloor of the nearby island shelf at this depth, forming the peak. Around southern Okinawajima, an organic-rich formation called the Shimajiri Group is known to contain natural gas (Toki, 2013). The origin of methane is thought to be the Nago Formation, which is equivalent to the lower Shimanto Formation but is exposed in the Kerama Islands as the Kerama Formation (Chinen et al., 2004; Miyagi et al., 2013). In addition, faults that are associated with the marine terraces that were actively formed during the Pleistocene have been inferred along steep cliffs near the isobath at a depth of 500 m (Izumi et al., 2016), which may form pathways along which methane from beneath the seafloor can traverse. Methane accumulates in summer and is released into the atmosphere during the development of the mixed layer in winter and reset (Tsurushima et al., 1996). Its distribution varies from year to year. However, further studies are required to confirm this hypothesis.

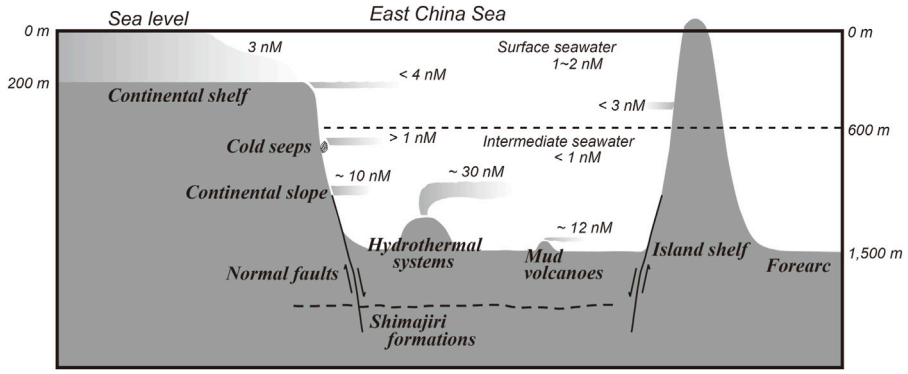

FIGURE 6
Schematic representation of representative methane sources in the East China Sea obtained in this study.

The site (black open diamond) at which the East China Sea and the Philippine Sea are connected, denoted the Tokara Gap, is located between Amami Oshima and Yakushima and has a water depth of nearly 1,100 m (Figure 1). Anomalous methane concentrations (~one to two nM) were also observed in the mid-oceanic layer at depths of 200–800 m at this site (Figure 3Z). Similar to the site denoted by the black open square, the influence of continental China is unlikely here (Figure 1). Furthermore, no influence of land-sourced water from the island is visible in the T-S diagram (Figure 2Z) and the T-S profile (Figure 4Z). However, plumes with methane concentrations of 200 nM and of 6 μM have been observed at depths of 140 m and 300–350 m, respectively, at the Tokara Islands located immediately to the west (Wen et al., 2016). The supply of these high methane concentrations can be effective, depending on the distance and direction. However, the effect is not quantifiable as the methane peak at 300 m may have been affected by high concentrations of methane spread over a distance. Because anomalous concentrations were observed to a depth of approximately 800 m, it is possible that other unknown submarine hydrothermal activities are present on the seafloor slope between the Tokara Islands and the Tokara Gap.

4.9 Overview of the sources of methane in the East China Sea

Vertical sampling of seawater was conducted intermittently over the East China Sea in early June from 2011 to 2015. The combination of temperature and salinity indicates that different water masses are distributed in each geographical area, such as the Kuroshio, continental slope, and continental shelf regions, which can be explained by water masses mixing with continental shelf mixed water, which comprises pure seawater and river water from the continent. On the other hand, an additional feature observed in the methane concentration indicates the presence of a geological singularity (Figure 6). Mild anomalies in the methane concentration were observed in the water masses around the continental shelf area, suggesting the influence of water with high organic matter and methane content derived from the diffusion of methane from seafloor sediments. Seawater sampled just above the mud volcano also showed larger methane concentrations, which probably depend on the activity level and distance to which the water sampler was swept from the volcano. The identification of the world's first methane concentration anomaly indicating the presence of a mud volcano that is not associated with the southern Ryukyu Islands created a stir for future research on new mud volcanoes.

Anomalous methane concentrations were observed directly above the submarine hydrothermal system at levels not observed in other areas, indicating the high potential of this area as a source of methane. Anomalous methane concentrations were also observed directly above the cold-seep site, but not the submarine hydrothermal system. During the 2 years over which samples were taken from the cold seep site, high methane concentrations observed just above the seafloor on both occasions indicate that the cold seep was definitely discharging methane. In addition, anomalous methane concentrations were often observed at 100–200 m in the vertical profiles collected from continental slope areas, including a cold-seep site, suggesting that diffusion from submarine sediments on the continental shelf was probably the source of the methane. The vertical profiles of seawater sampled from the continental slope appear to show greater methane concentration scatter than other areas of the ocean as compared to the background. This suggests that methane is supplied from continental slopes at various depths, and may be the cause of the variation in concentration. This is particularly true for the continental slope around 29°N, where methane concentrations are high, suggesting that the continental slope itself may provide other sources of methane such as cold seeps and mud volcanoes, which are not related to igneous activity. In addition, slight anomalies in the methane concentrations were detected mid-level in the shelf area of the Ryukyu Islands. Because methane seeps from the surrounding seafloor may occur, it is necessary to search for seafloor phenomena such as cold seeps, mud volcanoes, or submarine hydrothermal activity that could be sources of methane in the continental slope area, southern Ryukyu forearc, and the Ryukyu Islands shelf area.

5 Conclusion

Our study of methane distribution in seawater around the Ryukyu Arc reveals the following. Terrestrial water from continental China is a relatively mild source of methane to seawater (<4 nM), while more methane appears to be supplied by mud volcanoes (~12 nM). In addition, submarine hydrothermal systems are a uniquely large source of methane (~30 nM). The continental slope appears to be a source of methane mainly north of 29°N (~10 nM). High concentrations (<3 nM) of methane water masses have also been detected on the island shelf and in forearc region, and it appears that there are still undiscovered sources of methane on the island shelf and in forearc region.

Data availability statement

The original contributions presented in the study are included in the article/Supplementary Material, further inquiries can be directed to the corresponding author.

Author contributions

TT took on all the roles. Others assisted with sampling, performed analysis, and analyzed data.

Funding

This work was supported by the "Okinawa Research Core for Highly Innovative Discipline Science (ORCHIDS)" project at the Faculty of Science, University of the Ryukyus during 2017–2021, JSPS KAKENHI Grant Numbers 18H03733, 20H04315, and 23K11391, the Research Institute of Science and Technology for Society (RISTEX), Solution-Driven Co-creative R&D Program for SDGs (SOLVE for SDGs) the "Development of watershed governance based on participation and consensus for sustainable water resource use on subtropical islands" (funding agency: Japan Science and Technology Agency; JST) during 2019–2023, and the Research Institute for Humanity and Nature (RIHN: a constituent member of NIHU) Project "Adaptive Governance of Multiple Resources based on Land-Sea Linkages of the Water Cycle: Application to Coral Reef Island Systems (LINKAGE; No. 14200145)".

Acknowledgments

This paper was developed as part of the graduation works produced by HC, TS, and YY; our heartfelt gratitude goes to every professor and staff member at the University of Ryukyus who were associated with examining this work. We are also grateful to the Captain and crew of the T/V Nagasaki for sampling the seawater. We would like to thank Editage (www.editage.com) for English language editing. We would like to express our deep gratitude to Professor MK, who edited the paper patiently from the poor first draft, and to the three reviewers (Professor SA, NS, and Professor SL).

Conflict of interest

The authors declare that the research was conducted in the absence of any commercial or financial relationships that could be construed as a potential conflict of interest.

Publisher's note

All claims expressed in this article are solely those of the authors and do not necessarily represent those of their affiliated organizations, or those of the publisher, the editors and the reviewers. Any product that may be evaluated in this article, or claim that may be made by its manufacturer, is not guaranteed or endorsed by the publisher.

Supplementary material

The Supplementary Material for this article can be found online at: https://www.frontiersin.org/articles/10.3389/feart.2023.1174504/full#supplementary-material

References

Bange, H. W. (2006). Nitrous oxide and methane in European coastal waters. *Estuar. Coast. Shelf Sci.* 70, 361–374. doi:10.1016/j.ecss.2006.05.042

Bange, H. W., Bartell, U. H., Rapsomanikis, S., and Andreae, M. O. (1994). Methane in the Baltic and North Seas and a reassessment of the marine emissions of methane. *Glob. Biogeochem. Cycles.* 8, 465–480. doi:10.1029/94GB02181

Brankovits, D., Pohlman, J. W., Niemann, H., Leigh, M. B., Leewis, M. C., Becker, K. W., et al. (2017). Methane- and dissolved organic carbon-fueled microbial loop supports a tropical subterranean estuary ecosystem. *Nat. Commun.* 8, 1835. doi:10.1038/s41467-017-01776-x

Cao, H., Sun, Z., Wu, N., Liu, W., Liu, C., Jiang, Z., et al. (2020). Mineralogical and geochemical records of seafloor cold seepage history in the northern Okinawa Trough, East China Sea. *Deep Sea Res. I.* 155, 103165. doi:10.1016/j.dsr.2019.103165

Chen, Y., Xu, C., Wu, N., Sun, Z., Liu, C., Zhen, Y., et al. (2022). Diversity of anaerobic methane oxidizers in the cold seep sediments of the Okinawa Trough. *Front. Microbiol.* 13, 819187. doi:10.3389/fmicb.2022.819187

Chinen, M., Shinjo, R., and Kato, Y. (2004). Occurrence and geochemistry of *in-situ* greenstones from the Shimanto belt in the Ryukyu islands. *Ganseki Kobutsu Kagaku Mineral. Petrol. Sci.* 33, 208–220. doi:10.2465/gkk.33.208

Gamo, T., Chiba, H., Yamanaka, T., Okudaira, T., Hashimoto, J., Tsuchida, S., et al. (2001). Chemical characteristics of newly discovered black smoker fluids and associated hydrothermal plumes at the Rodriguez Triple Junction, Central Indian Ridge. *Earth Planet. Sci. Lett.* 193, 371–379. doi:10.1016/S0012-821X(01)00511-8

Gamo, T., Masuda, H., Yamanaka, T., Okamura, K., Ishibashi, J., Nakayama, E., et al. (2004). Discovery of a new hydrothermal venting site in the southernmost Mariana Arc: Al-rich hydrothermal plumes and white smoker activity associated with biogenic methane. *Geochem J.* 38, 527–534. doi:10.2343/geochemj.38.527

Gamo, T., Tsunogai, U., Ichibayashi, S., Chiba, H., Obata, H., Oomori, T., et al. (2010). Microbial carbon isotope fractionation to produce extraordinarily heavy methane in aging hydrothermal plumes over the southwestern Okinawa Trough. *Geochem. J.* 44, 477–487. doi:10.2343/geochemj.1.0097

Holmes, M. E., Sansone, F. J., Rust, T. M., and Popp, B. N. (2000). Methane production, consumption, and air-sea exchange in the open ocean: an Evaluation based on carbon isotopic ratios. *Glob. Biogeochem. Cycles.* 14, 1–10. doi:10.1029/1999GB001209

Ishibashi, J., Noguchi, T., Toki, T., Miyabe, S., Yamagami, S., Onishi, Y., et al. (2014). Diversity of fluid geochemistry affected by processes during fluid upwelling in active

hydrothermal fields in the Izena Hole, the middle Okinawa Trough back-arc basin. *Geochem. J.* 48, 357–369. doi:10.2343/geochemj.2.0311

Izumi, N., Nishizawa, A., Horiuchi, D., Kido, Y., Goto, H., and Nakata, T. (2016). 3D bathymetric image of Nansei-shoto Trench and its vicinity (in Japanese with English abstract). *Rep. Hydrogr. Oceanogr. Res.*, 133–149.

Kawagucci, S. (2015). "Fluid geochemistry of high-temperature hydrothermal fields in the Okinawa Trough: how and where TAIGA of methane is generated," in *Subseafloor biosphere linked to global hydrothermal systems; TAIGA concept*. Editors K. Okino, J. Ishibashi, and M. Sunamura (Tokyo Heidelberg New York Dordrecht London: Springer), 387–403.

Kawagucci, S., Chiba, H., Ishibashi, J., Yamanaka, T., Toki, T., Muramatsu, Y., et al. (2011). Hydrothermal fluid geochemistry at the Iheya North field in the mid-Okinawa Trough: implication for origin of methane in subseafloor fluid circulation systems. *Geochem. J.* 45, 109–124. doi:10.2343/geochemj.1.0105

Kawagucci, S., Shirai, K., Lan, T. F., Takahata, N., Tsunogai, U., Sano, Y., et al. (2010). Gas geochemical characteristics of hydrothermal plumes at the HAKUREI and JADE vent sites, the Izena Cauldron, Okinawa Trough. *Geochem. J.* 44, 507–518. doi:10.2343/geochemj.1.0100

Kawagucci, S., Ueno, Y., Takai, K., Toki, T., Ito, M., Inoue, K., et al. (2013). Geochemical origin of hydrothermal fluid methane in sediment-associated fields and its relevance to the geographical distribution of whole hydrothermal circulation. *Chem. Geol.* 339, 213–225. doi:10.1016/j.chemgeo.2012.05.003

Konno, U., Tsunogai, U., Nakagawa, F., Nakaseama, M., Ishibashi, J., Nunoura, T., et al. (2006). Liquid CO_2 venting on seafloor: Yonaguni IV Knoll hydrothermal system, Okinawa Trough. *Geophys. Res. Lett.* 33, L16607. doi:10.1029/2006GL026115

Kopf, A. J. (2002). Significance of mud volcanism. *Rev. Geophys.* 40, 1005. doi:10.1029/2000rg000093

Kuhara, T., Kano, Y., Yoshikoshi, K., and Hashimoto, J. (2014). Shell morphology, anatomy and gill histology of the deep-sea bivalve *Elliptio lucina ingens* and molecular phylogenetic reconstruction of the chemosynthetic family Lucinidae. *Venus J. Malacol. Soc. Jpn.* 72, 13–27. doi:10.18941/venus.72.1-4_13

Lecher, A. L. (2017). Groundwater discharge in the Arctic: a review of studies and implications for biogeochemistry. *Hydrology* 4, 41. doi:10.3390/hydrology4030041

Lecher, A. L., Kessler, J., Sparrow, K., Garcia-Tigreros Kodovska, F., Dimova, N., Murray, J., et al. (2016). Methane transport through submarine groundwater discharge to the North Pacific and Arctic Ocean at two Alaskan sites. *Limnol. Oceanogr.* 61, S344–S355. doi:10.1002/lno.10118

Lecher, A. L., and Mackey, K. R. M. (2018). Synthesizing the effects of submarine groundwater discharge on marine biota. *Hydrology* 5, 60. doi:10.3390/hydrology5040060

Levin, L. A., Baco, A. R., Bowden, D. A., Colaco, A., Cordes, E. E., Cunha, M. R., et al. (2016). Hydrothermal vents and methane seeps: rethinking the sphere of influence. *Front. Mar. Sci.* 3. doi:10.3389/fmars.2016.00072

Li, Q., Cai, F., Liang, J., Shao, H., Dong, G., Wang, F., et al. (2015). Geochemical constraints on the methane seep activity in western slope of the middle Okinawa Trough, the East China Sea. *Sci. China Earth Sci.* 58, 986–995. doi:10.1007/s11430-014-5034-x

Miyagi, N., Baba, S., and Shinjo, R. (2013). Whole-rock chemical composition of the pre-Neogene basement rocks and detritus garnet composition in the Okinawa-jima and neighbor islands. *Jour. Geol. Soc. Jpn.* 119, 665–678. doi:10.5575/geosoc.2013.0045

Monma, H., Iwase, R., Mitsuzawa, K., Kaiho, Y., Fujiwara, Y., Amitani, Y., et al. (1996). Deep tow survey in Nanseishoto Region (K95-07-NSS) (In Japanese with English abstract). *JAMSTEC Journal of Deep Sea Research* 12, 195–210.

Ning, X., Shiguo, W., Buqing, S., Bing, L., Liangqing, X., Xiujuan, W., et al. (2009). Gas hydrate associated with mud diapirs in southern Okinawa Trough. *Mar. Petrol. Geol.* 26, 1413–1418. doi:10.1016/j.marpetgeo.2008.10.001

Peng, X., Guo, Z., Chen, S., Sun, Z., Xu, H., Ta, K., et al. (2017). Formation of carbonate pipes in the northern Okinawa Trough linked to strong sulfate exhaustion and iron supply. *Geochim. Cosmochim. Acta.* 205, 1–13. doi:10.1016/j.gca.2017.02.010

Purkamo, L., Von Ahn, C. M. E., Jilbert, T., Muniruzzaman, M., Bange, H. W., Jenner, A.-K., et al. (2022). Impact of submarine groundwater discharge on biogeochemistry and microbial communities in pockmarks. *Geochim. Cosmochim. Acta.* 334, 14–44. doi:10.1016/j.gca.2022.06.040

Reeburgh, W. S. (2007). Oceanic methane biogeochemistry. *Chem. Rev.* 107, 486–513. doi:10.1021/cr050362v

Sadat-Noori, M., Tait, D. R., Maher, D. T., Holloway, C., and Santos, I. R. (2018). Greenhouse gases and submarine groundwater discharge in a Sydney Harbour embayment (Australia). *Estuar. Coast. Shelf Sci.* 207, 499–509. doi:10.1016/j.ecss.2017.05.020

Shukla, R., Slade, A., Khourdajie, A., Van Diemen, R., Mccollum, D., Pathak, M., et al. (2022). in *Mitigation of climate change. Contribution of working group III to the sixth assessment report of the intergovernmental panel on climate change*. Editor P. R. Shuka (New York, NY: Cambridge, UK). IPCC (2022). Clim. Change.

Sun, M.-S., Zhang, G.-L., Ma, X., Cao, X.-P., Mao, X.-Y., Li, J., et al. (2018). Dissolved methane in the East China Sea: distribution, seasonal variation and emission. *Mar. Chem.* 202, 12–26. doi:10.1016/j.marchem.2018.03.001

Sun, Z., Wei, H., Zhang, X., Shang, L., Yin, X., Sun, Y., et al. (2015). A unique Fe-rich carbonate chimney associated with cold seeps in the northern Okinawa Trough, East China Sea. *Deep Sea Res. I.* 95, 37–53. doi:10.1016/j.dsr.2014.10.005

Sun, Z., Wu, N., Cao, H., Xu, C., Liu, L., Yin, X., et al. (2019). Hydrothermal metal supplies enhance the benthic methane filter in oceans: an example from the Okinawa Trough. *Chem. Geol.* 525, 190–209. doi:10.1016/j.chemgeo.2019.07.025

Toki, T. (2013). Distribution of crustal fluid mainly composed by methane around the Ryukyu Islands and its relationship with geological settings (in Japanese with English abstract). *Chikyukagaku (Geochem.)* 47, 53–69. doi:10.14934/chikyukagaku.47.53

Toki, T., Itoh, M., Iwata, D., Ohshima, S., Shinjo, R., Ishibashi, J., et al. (2016). Geochemical characteristics of hydrothermal fluids at hatoma Knoll in the southern Okinawa Trough. *Geochem. J.* 50, 493–525. doi:10.2343/geochemj.2.0449

Tsurushima, N., Watanabe, S., and Tsunogai, S. (1996). Methane in the East China sea water. *J. Oceanogr.* 52, 221–233. doi:10.1007/BF02235671

Umezawa, Y., Miyajima, T., Kayanne, H., and Koike, I. (2002). Significance of groundwater nitrogen discharge into coral reefs at Ishigaki Island, southwest of Japan. *Coral Reefs* 21, 346–356. doi:10.1007/s00338-002-0254-5

Von Damm, K. L. (1995). "Controls on the chemistry and temporal variability of seafloor hydrothermal fluids," in *Seafloor hydrothermal systems: physical, chemical, biological, andgeological interactions*. Editors S. E. Humphris, R. A. Zierenberg, L. S. Mullineaux, and R. E. Thomson (Washington DC: American Geophysical Union), 222–247.

Watanabe, S., Higashitani, N., Tsurushima, N., and Tsunogai, S. (1995). Methane in the western north pacific. *J. Oceanogr.* 51, 39–60. doi:10.1007/BF02235935

Weber, T., Wiseman, N. A., and Kock, A. (2019). Global ocean methane emissions dominated by shallow coastal waters. *Nat. Commun.* 10, 4584. doi:10.1038/s41467-019-12541-7

Wen, H. Y., Sano, Y., Takahata, N., Tomonaga, Y., Ishida, A., Tanaka, K., et al. (2016). Helium and methane sources and fluxes of shallow submarine hydrothermal plumes near the Tokara Islands, Southern Japan. *South. Jpn. Sci. Rep.* 6, 34126. doi:10.1038/srep34126

Xing, J., Jiang, X., and Li, D. (2016). Seismic study of the mud diapir structures in the Okinawa Trough. *Geol. J.* 51, 203–208. doi:10.1002/gj.2824

Xu, C., Wu, N., Sun, Z., Zhang, X., Geng, W., Cao, H., et al. (2021). Assessing methane cycling in the seep sediments of the mid-Okinawa Trough: insights from pore-water geochemistry and numerical modeling. *Ore Geol. Rev.* 129, 103909. doi:10.1016/j.oregeorev.2020.103909

Yamanaka, T., Nagashio, H., Nishio, R., Kondo, K., Noguchi, T., Okamura, K., et al. (2015). "The Tarama Knoll: geochemical and biological profiles of hydrothermal activity," in *Subseafloor biosphere linked to global hydrothermal systems; TAIGA concept*. Editors K. Okino, J. Ishibashi, and M. Sunamura (Tokyo Heidelberg New York Dordrecht London: Springer), 497–504.

Yin, P., Berné, S., Vagner, P., Loubrieu, B., and Liu, Z. (2003). Mud volcanoes at the shelf margin of the East China Sea. *Mar. Geol.* 194, 135–149. doi:10.1016/S0025-3227(02)00678-3

Zhang, G., Zhang, J., Ren, J., Li, J., and Liu, S. (2008). Distributions and sea-to-air fluxes of methane and nitrous oxide in the north East China Sea in summer. *Mar. Chem.* 110, 42–55. doi:10.1016/j.marchem.2008.02.005

Zhang, X., Sun, Z., Wang, L., Zhang, X., Zhai, B., Xu, C., et al. (2020). Distribution and discharge of dissolved methane in the middle Okinawa Trough, East China sea. *Front. Earth Sci.* 8. doi:10.3389/feart.2020.00333

frontiers | Frontiers in Earth Science

TYPE Original Research
PUBLISHED 21 November 2023
DOI 10.3389/feart.2023.1181380

Check for updates

OPEN ACCESS

EDITED BY
Stéphanie Dupré,
Institut Français de Recherche pour l'Exploitation de la Mer, France

REVIEWED BY
Grigorii Georgievich Akhmanov,
Lomonosov Moscow State University, Russia
Charles Geoffrey Wheat,
University of Alaska Fairbanks, United States

*CORRESPONDENCE
Mechthild Doll,
mdoll@marum.de

RECEIVED 07 March 2023
ACCEPTED 19 October 2023
PUBLISHED 21 November 2023

CITATION
Doll M, Römer M, Pape T, Kölling M, Kaul N, dos Santos Ferreira C and Bohrmann G (2023), Recent and episodic activity of decoupled mud/fluid discharge at Sartori mud volcano in the Calabrian Arc, Mediterranean Sea.
Front. Earth Sci. 11:1181380.
doi: 10.3389/feart.2023.1181380

COPYRIGHT
© 2023 Doll, Römer, Pape, Kölling, Kaul, dos Santos Ferreira and Bohrmann. This is an open-access article distributed under the terms of the Creative Commons Attribution License (CC BY). The use, distribution or reproduction in other forums is permitted, provided the original author(s) and the copyright owner(s) are credited and that the original publication in this journal is cited, in accordance with accepted academic practice. No use, distribution or reproduction is permitted which does not comply with these terms.

Recent and episodic activity of decoupled mud/fluid discharge at Sartori mud volcano in the Calabrian Arc, Mediterranean Sea

Mechthild Doll[1]*, Miriam Römer[1], Thomas Pape[1], Martin Kölling[1], Norbert Kaul[2], Christian dos Santos Ferreira[1] and Gerhard Bohrmann[1]

[1]MARUM - Center for Marine Environmental Sciences and Faculty of Geosciences, University of Bremen, Bremen, Germany, [2]Faculty of Geosciences, University of Bremen, Bremen, Germany

Mud volcanoes (MVs) are surface structures typically created by episodic discharge of fluids and solids, often associated to onshore and offshore accretionary prisms on convergent plate boundaries. Detailed investigations of ongoing activity and its associated morphological changes, as well as a better understanding of the temporal evolution of these highly dynamic systems, may improve the estimations of material fluxes from MVs drastically. Until today, approximately 70 individual MVs were discovered in the northern Ionian Sea in the Calabrian Arc (Central Mediterranean Sea), but only a few have been analyzed and described in detail. In this study, new evidence for recent recurring eruptive activity of the ~45 m-high and 1 km-wide Sartori MV situated in the clastic wedge of the Calabrian Arc is presented. High-resolution seafloor mapping as well as sediment temperature, geochemical, and sedimentological data received from two research cruises in 2016 and 2020 are used. Bathymetric and seafloor backscatter data (1 m scale) indicate the presence of two active eruption centers at the flat-topped Sartori MV. Elevated sediment temperature gradients at both eruption centers show that currently heat is transferred to the surface sediments. Pore water analyses indicate that fluids rising below the eruption centers are CH_4-rich, Cl^--poor, and SO_4^{2-}-free. Stable C and H isotopic compositions of methane suggest that it originates from a mix of primary microbial, secondary microbial, and/or thermogenic sources. A relatively shallow position of the sulfate–methane interface at both eruption centers also indicates the presence of upward fluid migration in recent times. Pore water modeling suggests that seawater has penetrated the surface sediments to a greater extent within the last few years. In contrast, centimeter-thick layers of hemipelagic sediments overlying mud breccia in sediment cores taken from both eruption centers show that no solid material has been ejected in recent times. Sediment core analyses combined with high-resolution seafloor mapping show an absence of rim-passing mudflows over the past ~10 ka. It is concluded that Sartori MV is an episodically active MV from which fluids with a comparatively low flux were released into the bottom water in recent times.

KEYWORDS

mud volcano, Calabrian Arc, AUV mapping, fluid flux, sediment temperatures, pore water chemistry, methane, stable isotopes of methane

1 Introduction

Mud volcanoes (MVs) are geological structures that occur in onshore and offshore settings but are most abundant in geologically active regions (Higgins and Saunders, 1974; Milkov, 2000; Kopf, 2002; Mazzini and Etiope, 2017). The majority of MVs are distributed in compressional tectonic settings, such as accretionary prisms (Dimitrov, 2002; Kopf, 2002). MVs are fed by one or more feeder channels rooting deep within their source rock (Etiope and Milkov, 2004; Somoza et al., 2012; Menapace et al., 2017b) and are driven by the upward migration of overpressured fluids, ending in the extrusion of solids (mud breccia), liquids, and gases (Revil, 2002; Planke et al., 2003; Etiope, 2015; Mazzini and Etiope, 2017). Mud breccia contain fine-grained mud and clasts of different sizes from strata the material crossed on its way up through the sub-surface (Milkov, 2000; Revil, 2002). The morpho-structural shapes of MVs consist of a broad variety, including crater-like structures, (collapsed) mud cones, and flat-topped edifices (Kopf, 2002; Paull et al., 2015; Mazzini and Etiope, 2017). It has been proposed to divide the activity cycle of a MV into four phases: *eruption* (episodic overpressured material in the feeder channel with the formation of the MV edifice and the eruption of high volumes of mud breccia), *depletion* (upward fluid migration and the ejection of small volumes of mud breccia), *quiescence* (MV subsidence, caldera build-up, accumulation of pore pressure, and ejection of small volumes of mud breccia), and *reactivation* (resuming of the active phase; Mazzini and Etiope, 2017; Menapace et al., 2017a). Ongoing MV activity is often associated with seafloor discharge of bubble-forming gas originating from overpressured or naturally escaping pore fluids, which are hydroacoustically detectable as flares in the water column (Greinert et al., 2006; Sauter et al., 2006; Sahling et al., 2009; Römer et al., 2014). Further evidence of MV activity comes from temperature and pore water concentration anomalies (Bohrmann et al., 2003; Castellini et al., 2006; Mastalerz et al., 2007; Feseker et al., 2009; Pape et al., 2010; Feseker et al., 2014; Pape et al., 2014), which are, in contrast to gas bubble escape in the water column, also identifiable after the eruptive phase of a MV. When pore water compositions show a significant depth gradient, any transient deviation from stationary conditions may be used to estimate the timing of sediment-disturbing events (Niewöhner et al., 1998; Hensen et al., 2007; Strasser et al., 2013; Pape et al., 2020b).

Marine sediments typically show pore water of dissolved sulfate concentrations to be linearly decreasing with depth until they reach the sulfate–methane interface (SMI), where most of the seawater-derived SO_4^{2-} is consumed by the microbially mediated anaerobic oxidation of methane (AOM; Claypool and Kaplan, 1974; Boetius et al., 2000). Below the SMI, methanogenesis is the main metabolism and pore waters are characterized by increasing methane concentrations with depth (Castellini et al., 2006). The depth of the SMI is controlled by the flux of organic matter, the intensity of sulfate consumption, and the strength of upward migrating CH_4 from buried methane reservoirs in the sediment column (Dickens, 2001; Bhatnagar et al., 2008; Pape et al., 2020b). In advection-dominated regimes (such as MVs), the SMI is situated close to the seafloor when CH_4 and other light hydrocarbons migrate rapidly through the channel to the seafloor, driving hydrocarbon oxidation in the shallow seabed (Borowski et al., 1999; Suess et al., 1999). To prove transient SO_4^{2-} concentration profiles and track the fluid evolution over time, pore water chloride (Cl^-) concentrations can be used (Castellini et al., 2006).

More than 500 submarine MVs are known from the Mediterranean Sea so far (Mascle et al., 2014; Miramontes et al., 2023), and the regions of MV activity are influenced by the African–European subduction zone (Dimitrov, 2002; Kopf, 2002). From the northern Ionian Sea, which hosts Sartori MV investigated here, approximately 70 individual MVs were discovered until today (Ceramicola et al., 2014b; Cuffaro et al., 2019). Except from detailed analyses of the active twin-cone Venere MV (Loher et al., 2018a; b, c) and the dormant flat-topped Bortoluzzi MV (Cuffaro et al., 2019), both located in the forearc basins, studies about the Calabrian Arc MVs mainly concentrated on their general distribution and morphologies (Praeg et al., 2009; Panieri et al., 2013; Ceramicola et al., 2014b). In the area of Sartori MV, two sediment cores consisting of chaotic deposits and pebbly mudstones were recovered in 1981 (Morlotti et al., 1982) and referred to MV activity by Sartori (2003), confirmed by Panieri et al. (2013). In 2014, the ~45 m-high and ~1 km-wide Sartori MV was first described and named by Ceramicola et al. (2014b).

In this study, new data from Sartori MV that was investigated in detail during two research cruises in May 2016 and October–December 2020 (POS499 with *R/V POSEIDON* and SO278 with *R/V SONNE*) are reported. It includes high-resolution seafloor mapping, investigations of *in-situ* sediment temperatures, geochemical pore water analyses, and sedimentological observations. These data are used to define the timing and extent of mass and pore water egress and the utility of these sampling techniques for constraining active processes in mud volcano settings.

2 Geological setting

The Calabrian Arc subduction complex in the central Mediterranean Sea is the Calabrian Accretionary Prism (CAP; Figure 1). It is formed as a result of the progressive northwest-oriented subduction of the African Plate below the Eurasian Plate, accompanied by slab-rollback and formation of back-arc basins during the past 30 Ma (Malinverno and Ryan, 1986; Wortel and Spakman, 2000; Faccenna et al., 2011). The African–Eurasian convergence in this area is relatively slow, with rates of less than 5 mm/yr (Serpelloni et al., 2007; Palano et al., 2012). The Calabrian subduction zone is assumed to present an area where remnants of the Mesozoic oceanic crust of the Neo-Tethys Ocean are involved in subduction until today (Spakman, 1986; Rosenbaum et al., 2002; Granot, 2016). The CAP consists of up to 10 km of scraped-off sediments which accumulated and formed the overall accretionary complex spanning over 300 km from onshore Calabria to the Ionian Abyssal Plain, where it intersects with the Mediterranean Ridge (Figure 1; Rossi and Sartori, 1981; Minelli and Faccenna, 2010). It is bounded by the Malta escarpment to the southwest and the Apulia escarpment to the northeast. These are the two major structural discontinuities in this area (Cernobori et al., 1996; Gallais et al., 2012). The morphology and structure of the CAP may be divided into three main parts: 1) the post-Messinian external evaporitic wedge, 2) the pre-Messinian internal clastic wedge in which Sartori

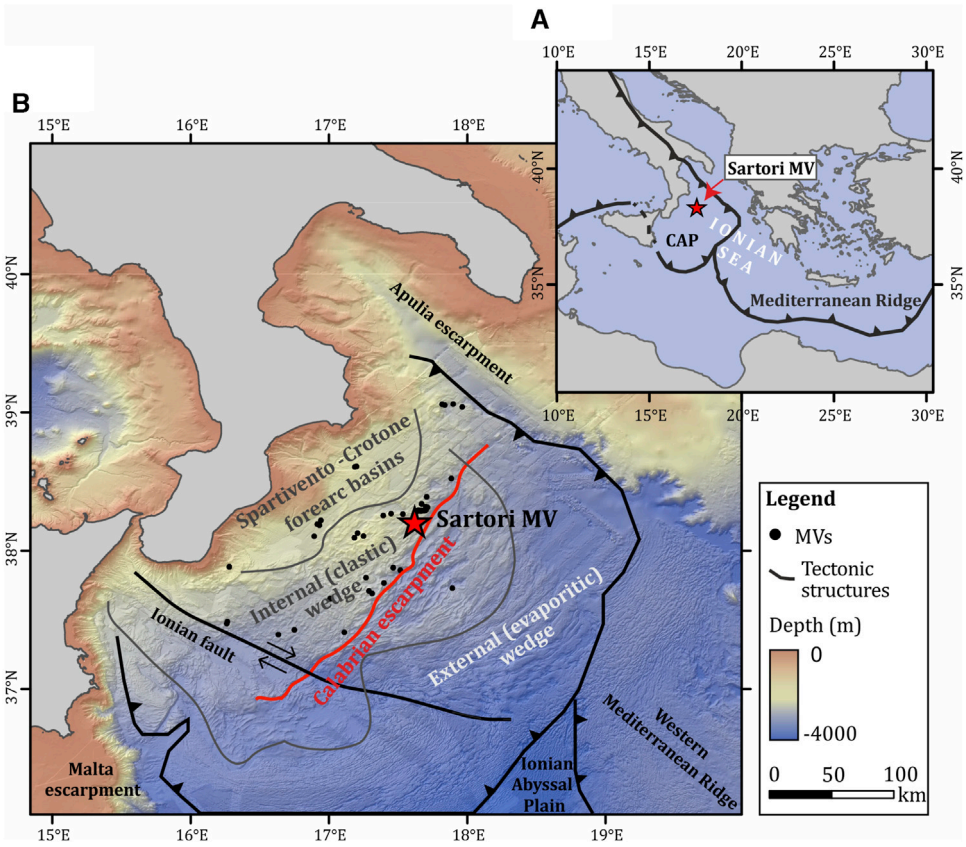

FIGURE 1
(A) Overview map showing the location of Sartori MV (red star) in the northern Calabrian Accretionary Prism (CAP) within the northern-central Ionian Sea. Plate boundaries and the African–Eurasian subduction zone are shown in black (according to Gutscher et al. (2017)). **(B)** Bathymetric map of the CAP (https://emodnet.ec.europa.eu/en/bathymetry). Sartori MV (red star) is situated within the internal clastic wedge of the CAP, west of the Calabrian escarpment (red line, Ceramicola et al., 2014b). Black dots represent other MVs in this region which are expected, inferred, and partially approved (Ceramicola et al., 2014b; Loher et al., 2018a). Plate boundaries and the African–Eurasian subduction zone are shown in black (according to Gutscher et al., 2017).

MV studied herein is located, and 3) the Spartivento–Crotone forearc basins (Figure 1; Polonia et al., 2011; Ceramicola et al., 2014a; Gutscher et al., 2017). The pre-Messinian internal wedge mainly hosts clastic sediments affected by thrusts forming basins and ridges of several hundred meters in relief. The Calabrian Escarpment, which reaches up to 750 m above the seafloor, marks the transition from an inner plateau to an outer, more rugged area (Cernobori et al., 1996; Praeg et al., 2009; Polonia et al., 2011; Gutscher et al., 2017). In contrast, the post-Messinian external wedge hosts evaporites originating from the Messinian salinity crises (Hsü et al., 1977; Roveri et al., 2014). Complex geodynamic processes, strike–slip faulting, and internal deformation of the external and internal wedges are the responses of the steady and ongoing subduction (Gutscher et al., 2019). Low-velocity anomalies of seismic waves are coincident spatially with compressional structures and tectonic thrusting, resulting in mud volcanism associated with fluid and mud expulsion at the surface (Prada et al., 2020). The offshore Spartivento–Crotone forearc basins with accreted Mesozoic–Cenozoic units at their basements are filled with sediments of the Miocene age (i.e., Messinian evaporites) up to Plio-Pleistocene units (Capozzi et al., 2012; Zecchin et al., 2015).

3 Materials and methods

3.1 Hydroacoustic seafloor and water column investigations

Swath bathymetry data were obtained during cruise SO278 in 2020 (Bohrmann et al., 2022) using a Kongsberg EM122 (12 kHz) ship-borne hydroacoustic system. The multibeam data included the water column backscatter information, which has been analyzed for anomalies resulting from gas bubble emissions using the QPS Fledermaus midwater tool. During cruise POS499 (Bohrmann et al., 2016), high-resolution swath bathymetry and seafloor backscatter data were collected with a Kongsberg EM 2040 (400 kHz) system mounted on the autonomous underwater vehicle (AUV) MARUM-SEAL 5000. The altitude of the AUV was ~80 m above seafloor. Post-processing of bathymetric and backscatter data was carried out using the open-source software MB-System (Caress and Chayes, 1996). While the resulting ship-based bathymetric grid has a resolution of 25 m, the AUV-based bathymetry data were gridded at 1 m lateral and decimeter-scale vertical resolution. The AUV-borne grids were tied to the ship-borne bathymetry by setting anchor points at prominent

10.3389/feart.2023.1181380

TABLE 1 Specifics of GC and MUC cores collected during cruises POS499 (2016) and SO278 (2020) relevant in this study and geochemical analyses performed for gas and pore water samples.

Cruise name	GeoB No.	Tool No.	Latitude [N]	Longitude [E]	Water depth [m]	Core length [cm]	TOC	Alkalinity	Cl^-	SO_4^{2-}	CH_4	$\delta^{13}C\text{-}CH_4$	$\delta^2H\text{-}CH_4$	$\delta^2H\text{-}H_2O$
POS499	21363–1	GC21	38°12.343′	17°36.956′	1,857	300			x	x	x			
SO278	24302–2	GC01	38°12.321′	17°37.113′	1,856	205	x	x	x	x	x	x	x	x
SO278	24365–1	MUC23	38°12.320′	17°37.109′	1,856	38		x	x	x	x			
SO278	24370–1	GC33	38°12.362′	17°36.749′	1,887	324	x	x	x	x	x	x		
SO278	24376–1	MUC30	38°12.386′	17°36.999′	1,858	34		x	x	x	x			
SO278	24376–2	GC38	38°12.388′	17°37.001′	1,858	254	x	x	x	x	x	x	x	x

morphological features which shifted the AUV grids both vertically and laterally to its final position with an uncertainty of ~30 m.

3.2 Sediment sampling, core description, and line scanning

Cores of near-surface sediment from Sartori MV were collected during cruises POS499 and SO278 with a gravity corer (GC) equipped with a 5.75 m-long core barrel (Table 1). For retrieval of sediment cores with almost undisturbed sediment surfaces, a multicorer (MUC) equipped with six tubes (≤50 cm core length) was used.

Individual coring positions were chosen by investigating bathymetric and seafloor backscatter data, focusing on sampling sites as close as possible to the mud extrusion sites (Figure 2). For accurate positioning, the Posidonia underwater navigation system (IXSEA) with a transducer mounted on the cable 50 m above both coring devices was used. Gravity core GC21 was taken in a flexible plastic foil liner, which allowed for rapid access to the sediment. The core was used for core description and pore water sampling. Gravity cores GC01, GC33, and GC38 were taken in rigid plastic liners for transportation and long-term storage in the MARUM core repository. The uppermost (~5 cm) of very fluidized material of GC01 is not preserved within the core liner and, therefore, not further analyzed. To capture sedimentary structure patterns, such cores were longitudinally split immediatedly after recovery on board during cruise SO278, and the archive halves were photographed at a 500-dpi resolution using the smartCIS1600 line scanner of the MARUM GeoB Core Repository. To investigate the presence of mud breccia and analyze changes in the lithology, macroscopic core descriptions were generated for all cores. These can be found, merged with the line scans, in the Supplementary Material.

3.3 Preparation of headspace gas and pore water samples

For vertical profiling of *ex-situ* concentrations of dissolved methane and the determination of methane stable C and H isotopic composition, headspace gas samples were prepared from both MUC cores and gravity cores, following a modified method based on Kvenvolden and McDonald (1986), as described in Pape et al. (2014). Approximately 3 mL of bulk sediment was collected from the cores with cut-off plastic syringes and transferred into 22-mL glass vials prefilled with 5 mL of a 1 M NaOH solution. The vials were crimp-capped with a butyl rubber stopper and stored upside-down until analysis. The sampling interval for pore water CH_4 measurements was 2 cm in MUC tubes and generally 25 cm in GCs (min. 21 cm to max 50 cm depending on the core characteristics).

Pore water concentrations were used for i) assessment of the modern SMI depth and ii) for modeling the evolution of pore water concentration profiles. Pore water was extracted *ex situ* from selected sediment depths of four gravity cores (GC01, GC21, GC33, and GC38) and two MUC cores (MUC23 and MUC30). Pore water samples were collected from whole round sediment cores using disposable syringes and rhizon samplers (Seeberg-Elverfeldt et al., 2005; Dickens et al., 2007). Rhizons automatically filter samples at <0.15 µm. Unused rhizons have

10.3389/feart.2023.1181380

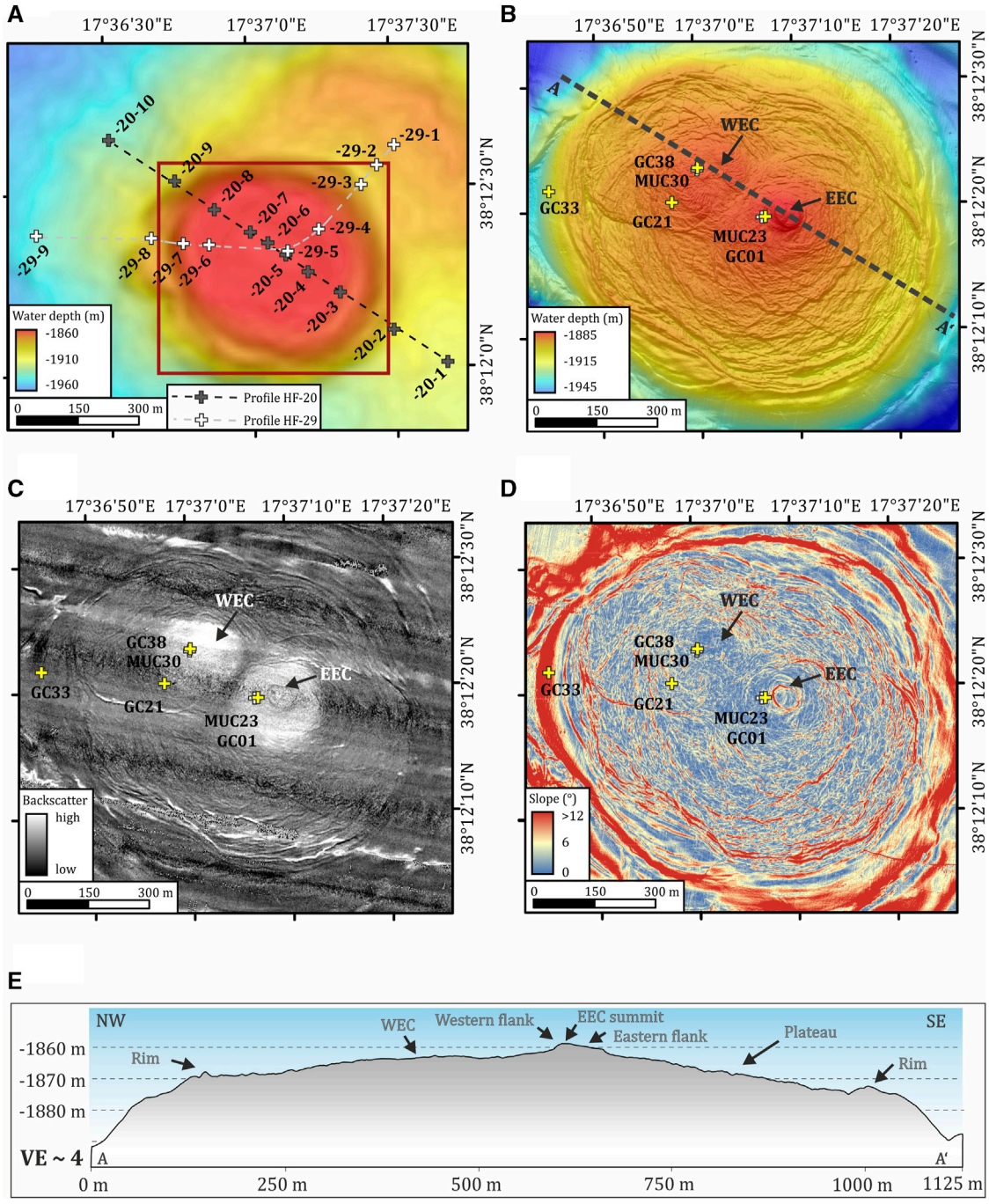

FIGURE 2
(A) Ship-borne bathymetry acquired during cruise SO278 showing the flat-topped Sartori MV at a resolution of 25 m and the positioning of the heat flow probe sites. **(B)** High-resolution (1 m) AUV-borne bathymetry of the entire edifice of Sartori MV visualizing small-scale seafloor features. Positions of GC and MUC coring sites are also shown. EEC, eastern eruption center; WEC, western eruption center. **(C)** High-resolution backscatter map showing central high seafloor backscatter areas and GC and MUC sites. **(D)** Slope data as well as GC and MUC locations. **(E)** NW–SE-oriented profile across the MV showing major morphological elements (WEC, EEC, plateau, and rim).

been soaked in DI water prior to use; to rinse the dead volume (approximately 120 µL) and potential production-related contaminants, the initial volume of the pore water sample has been discarded. The sampling interval for pore water measurements of SO_4^{2-} and Cl^- at MUC cores was every 5 cm, starting from 2 cm (MUC30) and 3 cm (MUC23) core depth. A sampling interval of 10 cm was used for pore water measurements of SO_4^{2-} and Cl^- in GC cores ranging from a core depth of 5 cm (GC21; GC33; and GC38) or 10 cm (GC01) sediment depth. For concentration analysis of anions Cl^- and SO_4^{2-} at the MARUM sediment geochemistry lab, untreated pore water samples of filtered and unacidified aliquots were extracted and stored at 4°C until analysis.

3.4 Gas and pore water analyses and modeling of pore water concentration profiles

Concentrations of dissolved methane in headspace gas samples were either determined onshore (POS499) or on board (SO278) using an Agilent Technologies three-channel 7890B gas chromatograph (Pape et al., 2010). Methane and C_2–C_6 hydrocarbons were separated and quantified with a capillary column connected to a flame ionization detector. Calibrations and performance checks of the analytical system were conducted regularly using commercial pure gas standards and gas mixtures, which yielded a precision better than 1.5%. Reported concentrations are not corrected for sediment porosity and Bunsen coefficient.

Stable carbon and hydrogen isotope ratios ($^{13}C/^{12}C$ and $^{2}H/^{1}H$) of methane were determined for selected headspace gas samples prepared from gravity cores at MARUM as described in Pape et al. (2020a) and Pape et al. (2020b). A Trace GC Ultra-GC IsoLink connected to a MAT 253 isotope ratio mass spectrometer (IRMS) via a ConFlo IV interface (all components Thermo Fisher Scientific Inc.) was used. Methane was separated by gas chromatography and either combusted (1,030°C) or pyrolyzed (1,440°C) to generate CO_2 or H_2, respectively. CO_2 or H_2 was then transferred to the IRMS for analysis of $^{13}C/^{12}C$ or $^{2}H/^{1}H$. Reported isotope ratios are arithmetic means of duplicate measurements at least in the δ-notation (in ‰) relative to Vienna PeeDee Belemnite (VPDB) for carbon and Vienna Standard Mean Ocean Water (VSMOW) for hydrogen. Reproducibility was checked daily using commercial methane standards (Isometric Instruments, Canada; Air Liquide GmbH, Germany). The standard deviations of triplicate measurements ($\delta^{13}C$-CH_4) were <0.5‰.

Concentrations of Cl^- and SO_4^{2-} in pore water samples were analyzed by ion chromatography (IC) using a Metrohm 882 Compact Ion Chromatograph with an 858 Professional Sample Processor. Standardization was performed against multi-element solutions prepared from commercial single-element standard solutions (National Institute of Standards and Technology Certified Reference Material® NIST CRM). Moreover, IAPSO Standard Seawater from Osil® was used as an external reference material. The precision was 1-σ: < ± 1.0% for Cl^- and 1-σ: < ± 2.0% for SO_4^{2-}.

Depth correction by +10 cm was successfully applied at GC01 only (see Supplementary Material). The alignment is found to be most sensitive by comparing the pore water alkalinity profile (Supplementary Figure S1). The corrected depth of GC01 is used for depth estimation of the SMI and for modeling the pore water concentration profiles of GC01.

Modeling of pore water concentration profiles was performed to mimic the diffusive response to the last disturbance in pore water concentration gradients that may be used to estimate the time that has elapsed since the last MV activity. It is a diffusion-only model in which the initial conditions are prescribed, and the boundary conditions are fixed at the seafloor and at the base of the pore water profile. The method is described in detail in Schulz and Schulz (2005). For modeling, Cl^- and SO_4^{2-} depth-corrected concentrations of GC01 and depth-uncorrected data of GC21 and GC38 were used.

3.5 *In-situ* sediment temperature measurements

At site GC21 of cruise POS499, five miniaturized temperature data loggers (MTLs; ANTARES Datensysteme GmbH, Germany) attached to the gravity corer were used for measuring *in-situ* sediment temperatures at an interval of 0.5–1 m (Pfender and Villinger, 2002). An additional logger was mounted on top of the weight to measure bottom water temperature as reference. The gravity corer was left in the seabed for ~10 min. The accuracy of the MTLs is ~0.1°C, while the resolution is more than ±0.002 K. During cruise SO278, two *in-situ* temperature gradient profiles, including 20 individual temperature probe sites, were measured with a conventional 6 m-long giant heat flow probe from the GEOMAR Helmholtz Center for Ocean Research Kiel, Germany. The temperature probe is constructed following the classical "violin bow" design (Bullard, 1954) and described in detail in Hyndman et al. (1979) and Villinger et al. (2010). In total, 22 single thermistors were distributed in an interval of 0.25 m in an oil-filled sensor tube, resulting in an active length of 5.25 m. The resolution of the thermistors is better than 0.002 K over a temperature range from −2 to 60°C. The sensor tube contains a heating wire for heat pulse generation for *in-situ* thermal conductivity measurements. The sampling interval of temperature readings was set to 1 Hz. A calibrated PT-100 seawater temperature sensor allowed calibrating all thermistors with reference to the seawater. At each site, the heat flow probe was left in the sediment for ~10 min after penetration to allow the thermistors to adjust to ambient temperatures at each depth. The *in-situ* sediment temperature in its equilibrium state was calculated afterward by extrapolation from the time series of each individual thermistor. Usually, 21 thermistors were found to work properly.

All temperature data are analyzed and processed after deployment using the program MHFRed, according to Villinger and Davis (1987). A penetration-depth control and tilt correction are included in this program (Villinger and Davis, 1987).

4 Results

4.1 Seafloor morphology

The ship-based multibeam bathymetry of the region around Sartori MV (Figure 2) shows that the MV is a nearly circular, flat-topped topographic structure. The MV has a diameter of ~1 km and a height of ~45 m, relative to the surrounding seafloor. In general, the surface of the central area is characterized by a relatively rough and chaotic morphology and is downward sloping from its geometric center toward the outer rim with steep flanks (Figures 2D, E). The high-resolution bathymetry shows two mud eruption centers located approximately 225 m apart from each other in the inner part of the MV to the east and west of the geometrical center of the MV (Figures 2B, E). In the following text, these eruption centers are called the western eruption center (WEC; situated at ~1,863 m water depth) and the eastern eruption center (EEC; situated at ~1,853 m water depth).

The EEC is a positive surface feature with a summit (peak) that rises about 3 m above the surrounding area and has a diameter of ~50 m. It

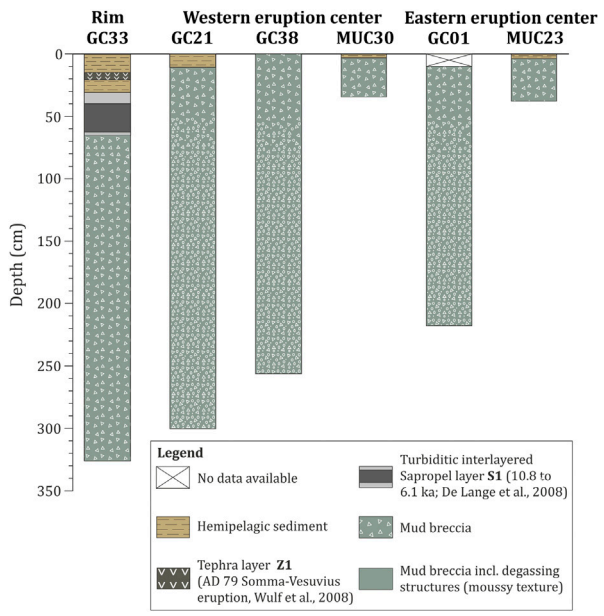

FIGURE 3
Schematic representation of sediment compositions in individual GC and MUC cores from Sartori MV collected during cruises POS499 (2016) and SO278 (2020). Mud breccia recovered from the eastern and western eruption centers is fluidized in the upper part and shows a moussy texture in the deeper parts of the cores. The hemipelagic sediment consists of foraminifera-bearing silty clay. For GC01, depth-corrected data are used. Detailed core descriptions can be found in Supplementary Material.

has a smooth and plain surface, which is in contrast to the rough surface structure of the rest of the plateau (Figure 2B). The profile of the EEC (Figure 2E) shows a steeper flank in the west and a flatter side in the east of the summit. The WEC shows a morphologic depression in its inner part, which is bordered by a rim-like frame (Figures 2B, D). Both eruption centers are also identifiable in the AUV-derived seafloor backscatter map which shows pronounced and high backscatter signatures at these sites (Figure 2C). The backscatter amplitudes at the EEC and WEC are significantly higher than those of a relatively low backscatter on the remaining plateau of Sartori MV. The high-resolution bathymetry allows to distinguish numerous topographic ridges and depressions forming concentric mud rings (*cf.* Dupré et al., 2008) propagating radially and sub-circular as elongated surface features from the two eruption centers to the outer areas of the plateau (Figures 2B, D). The plateau of the MV is surrounded by a pronounced and sub-circular rim, forming its outer edge (Figure 2D).

Emissions of bubble-forming gas migrating from the seafloor to the water column were not observed during research cruises POS499 and SO278.

4.2 Sediment characteristics

The two MUC cores (MUC23 and MUC30) taken from the EEC and WEC, respectively, consist of unconsolidated mud breccia overlain by a hemipelagic sediment cover of 4 cm (MUC23) and 3 cm (MUC30), respectively (Figure 3). The mud breccia contains mud clasts of up to 6 cm in size and is characterized by a strong smell characteristic of H_2S. The hemipelagic sediment is composed of brownish foraminifera-bearing silty clay with blackish grains of <1 mm in size (see core description in Supplementary Material).

The mud breccia of gravity core GC21 from the southwestern edge of the WEC is overlain by a ~11 cm hemipelagic sediment dominated by foraminifera-bearing silty clay. As the hemipelagic sediment cover is strongly fluidized, the thickness might be overestimated. The underlying greenish-gray mud breccia revealed abundant mud breccia clasts of sandstones and carbonates with calcite veins. The mud breccia shows degassing structures (moussy texture) at core depths >50 cm (Figure 3; see core description in Supplementary Material). The two gravity cores recovered close to the EEC and WEC (GC01 ~50 m southwest of the EEC; GC38 ~40 m of the WEC) show greenish-gray mud breccia and abundant friable mud breccia clasts in sizes of a few millimeter up to 9 cm throughout the core. Degassing structures (moussy texture) are present below an approximate depth of 50 cm of GC01 and ~55 cm of GC38. No boundaries indicating individual mud breccia sequences are found (Figure 3; see core description in Supplementary Material). A hemipelagic sediment coverage is virtually absent in GC01 and GC38 due to an overpenetration of the gravity corer at both sites. Gravity core GC33 from the western rim of the MV consists of a greenish-gray mud breccia that is overlain by a ~66 cm-thick hemipelagic sediment package of foraminifera-bearing silty clay. The hemipelagic sediment may be divided into three groups. The 30 cm-thick, light olive-brown clay layer is interrupted by a ~5 cm interval of silty fine sand with blackish particles, which is graded to its top. This layer of silty fine sand is referred to as the tephra layer Z1 of the Somma–Vesuvius eruption AD 79 (Wulf et al., 2008; Zanchetta et al., 2011). Underneath, a pronounced and turbiditic interlayered (Polonia et al., 2015), organic-rich, dark greenish-gray clay layer of ~40 cm thickness is present, which is referred to as sapropel S1, with its age dated back to 10.8 ka to 6.1 ka (De Lange et al., 2008; Polonia et al., 2015). In contrast to cores GC01, GC21, and GC38, no degassing structures are observed within the mud breccia of GC33. Instead, the uppermost ~159 cm of the mud breccia layer comprises only a few clasts, whereas the clast size and clast content increase to larger fragments up to 5 cm in the lower ~100 cm of the mud breccia layer (Figure 3; see core description in Supplementary Material).

4.3 Pore water composition and methane stable isotopes

Vertical concentration profiles of pore water Cl^- of GC21, GC38 (WEC), and GC01 (EEC) show a general decrease with depth (Figure 9, Supplementary Material). Cl^- concentrations of GC21 scatter within the upper 50 cm, with the concentrations ranging between ~493 and 624 mmol/L. Below 50 cm, Cl^- concentrations decrease constantly, reaching ~206 mmol/L at the maximum sampling depth of 275 cm (Supplementary Figure S2). In GC38, the Cl^- concentration is nearly constant within the upper 50 cm, ranging between 612 mmol/L and 627 mmol/L. The concentrations decrease from 50 cm to the maximum sampling depth (245 cm), from ~617 mmol/L to ~204 mmol/L. In GC01, the Cl^- concentrations in the upper sediment layer show a continuous decrease, with a changing magnitude at a depth of

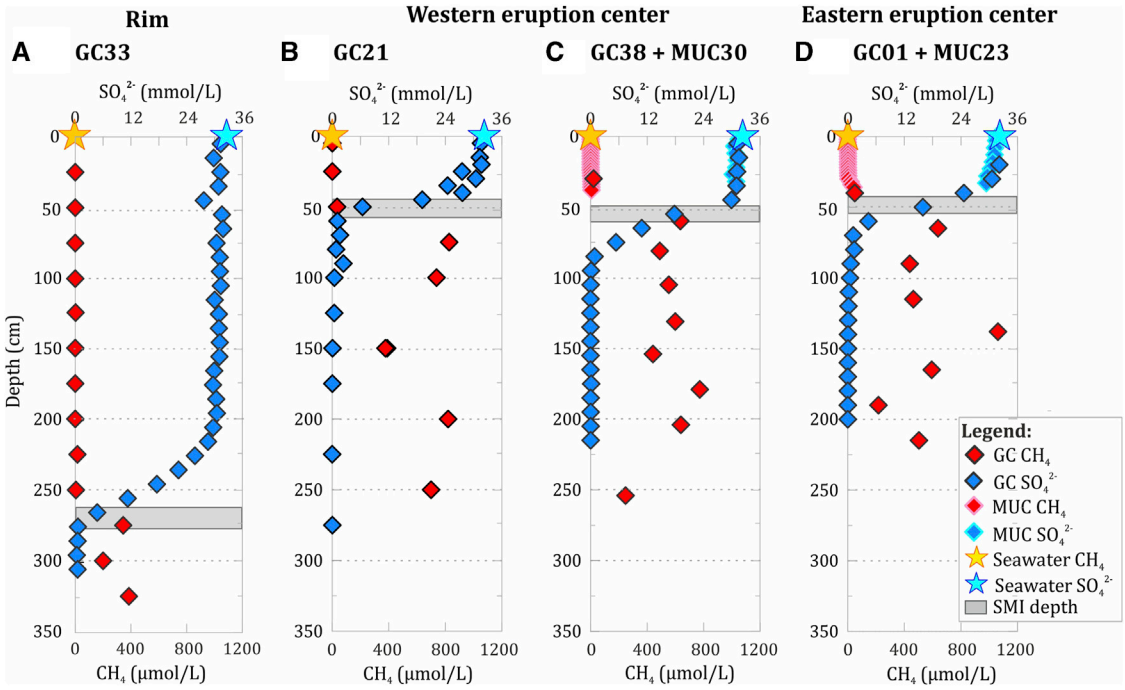

FIGURE 4
Concentrations of pore water sulfate and methane (*ex situ* concentration) at **(A)** the western rim, **(B, C)** the western eruption center, and **(D)** the eastern eruption center of Sartori MV. Seawater concentrations (stars) are plotted as the reference. Core GC21 was collected in 2016 (cruise POS499), and cores GC01, GC33, and GC38 were recovered in 2020 (cruise SO278).

approximately 70 cm, from approximately ~633 mmol/L at the top to ~213 mmol/L at the lowermost sampling depth (190 cm). In GC33, the Cl^- concentrations are stable between 0 cm and 265 cm sediment depth but slightly decrease from ~600 mmol/L to ~462 mmol/L at a sampling depth between 265 cm and 315 cm.

Pore water SO_4^{2-} concentrations of GC21 are slightly scattering between ~31 mmol/L and ~24 mmol/L in a sediment depth from 0 cm to 40 cm (Supplementary Figure S3). In a sediment depth between 40 cm and 60 cm, SO_4^{2-} concentrations decrease to 0 mmol/L and are stable until reaching the maximum sampling depth of 275 cm. In GC38, the SO_4^{2-} concentrations of ~30 mmol/L are stable in the upper 45 cm sediment depth and decrease between 45 cm and 85 cm until reaching 0 mmol/L and are stable until reaching the maximum sampling depth. Pore water SO_4^{2-} concentrations of GC01 decrease from 0 cm to 70 cm sediment depth to concentrations from ~32 mmol/L to 0 mmol/L and are stable downcore until reaching the maximum sampling depth. In GC33, the SO_4^{2-} concentrations are stable at ~30 mmol/L from 0 cm to 195 cm sediment depth and decrease between 195 mmol/L and 275 mmol/L until reaching 0 mmol/L. The SO_4^{2-} concentrations are stable downcore until reaching its maximum sampling depth of 315 cm.

Vertical concentration profiles of pore water SO_4^{2-} and CH_4 show that the current SMI at both eruption centers of Sartori MV is positioned at a relatively shallow depth [WEC—GC21: ~45–75 cm (Figure 4B), GC38: ~50–70 cm (Figure 4C); EEC—GC01: ~40–60 cm (Figure 4D)]. At the western rim site (Figure 4A), the SMI is positioned significantly deeper (GC33: ~250–270 cm). Due to differences in the depth correction (see method section), the position of the SMI at GC01 and GC38 is in approximately the same sediment depth, but depth differences should be mentioned. It is suggested that the SMI of GC38 occurs deeper in the sediment, as indicated by the uncorrected depth data.

The highest *ex situ* CH_4 concentration (~1.06 mmol/L) is present in GC01 from the EEC at a depth of 128 cm below the seafloor (Figure 4). In GC38 and GC21 recovered from the WEC, maximum CH_4 concentrations are slightly lower, between ~0.77 mmol/L and ~0.83 mmol/L, respectively. GC33 taken from the western rim site shows comparably low CH_4 concentrations (maximum 0.38 mmol/L). CH_4 concentrations in the two gravity cores [GeoB21366-1, 21367–1; maximum core length 4.89 m; data available on the PANGAEA database; Bohrmann et al. (2016)] taken approximately 0.5–1.0 km west of Sartori MV are lower than 0.003 mmol/L. This demonstrates that mud volcanic activity leads to considerable methane enrichments in near-surface deposits, presumably within the entire MV.

$\delta^{13}C$-CH_4 values in headspace samples from GC01 (EEC), GC33 (western rim), and GC38 (WEC) ranged between ~−56 and −63‰ with an irregular and insignificant negative trend with depth (Figure 5). The only two outliers from the general trend are samples from GC01 at ~0.5 m and from GC33 at ~2.7 m, which are depleted in ^{13}C by ~12‰ and ~5‰, respectively, compared to the adjacent samples. These samples are positioned close to the SMI (see Figure 4D) and may have been affected by microbial isotope fractionation in the course of AOM. δ^2H-CH_4 values in headspace samples ~from GC01 (EEC) and GC38 (WEC) show a steep decrease from ~−140‰ to ~−190‰ in the uppermost layer (meter) of sediment. Below that depth, δ^2H-CH_4 values only slightly decrease with depth, and the most negative δ^2H-CH_4

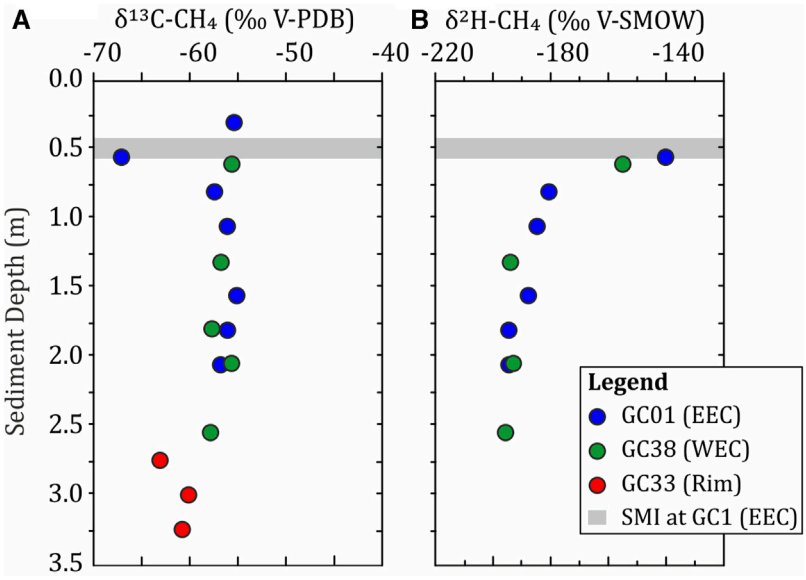

FIGURE 5
(A) Stable carbon and **(B)** hydrogen isotopic composition of methane in headspace gas samples prepared from gravity cores collected from the western rim (GC33), the western eruption center (GC38; WEC), and the eastern eruption center (GC01; EEC). The depth of the SMI at the eastern eruption center is shown as the horizontal gray bar.

value of ~198‰ is determined for the deepest sample from GC38 at ~2.6 m.

4.4 Temperature distribution in near surface sediments

Temperature gradients from the central area of Sartori MV vary between −15.4 mK/m and 447.2 mK/m (Figures 6A, B). High gradients were restricted to the central area of the MV. Maximum gradients were measured at sites close to the WEC (139.9 mK/m at HF-20-7; Figure 6A) and EEC (367.8 mK/m at HF-20-5 and 447.2 mK/m at HF-29-5; Figures 6A, B). Gradients from the EEC (HF-29-5) were about three times higher than those from the WEC (HF-20-7). Both eruption centers are characterized by generally higher absolute temperatures near the sediment surface and steeper temperature gradients compared to its surrounding sites. The maximum temperature difference is measured at site HF-29-5 and varies from 14.7°C at the seafloor up to 17.4°C at a sediment depth of 5.7 m below the seafloor (Supplementary Figure S4). The temperature gradient of temperature probe site HF-20-6 is about five times smaller compared to that of both temperature probe sites at the EEC (HF-20-5 and HF-29-5; Figures 6A, B). At a distance of ~100 m from the EEC, vertical temperature gradients decrease from 447.2 mK/m (HF-29-5) to 66.5 mK/m (HF-20-4) and 89.5 mK/m (HF-20-6). This is a difference from the measured temperature gradient of 357.7 mK/m at a distance of less than 100 m (Figures 6A, B). The linear temperature gradient at site GC21 at the southwestern edge of the WEC is moderate with 44.8 mK/m (Figure 6B). Linear temperature gradients in the nearby areas surrounding the MV ranged between 6.6 mK/m and 10.7 mK/m (Figures 6A, B). Negative temperature gradients (−15.4 mK/m to −1.9 mK/m), which are mainly caused by relatively low sediment temperatures below ~3 m depth, were measured at six sites (HF-20-3, HF-20-8, HF-29-4, HF-29-6, HF-29-7, and HF-29-9) on the plateau and in the surrounding area of Sartori MV (Supplementary Table S1). All measurement sites of negative temperature gradients are distant to the WEC and EEC (Figures 6A, B).

5 Discussion

5.1 Seafloor topography and episodic MV activity

The flat-topped Sartori MV (Figures 2E, 7) with its steep rim flanks and relatively smooth elevation in its central part can be categorized as a plateau-like MV, according to Mazzini and Etiope (2017). The generally smooth morphology is attributed to intermittent eruption events of highly viscous mud breccia stacking in the most central part of the MV. Ring-like structures are present at the flat top, and the mud builds up a slightly positive morphology (Figure 7A). However, gradually collapsing mud cones, which are typical for plateau-like MVs, prevent the development of significant elevations in the central part (Mazzini and Etiope, 2017). Plateau-like MVs in the Mediterranean Sea that have similar dimensions to the Sartori MV include Isis MV, Amon MV (Dupré et al., 2008; Feseker et al., 2009), and Giza MV that are all located in the Nile deep-sea fan (Feseker et al., 2010).

Bathymetric and seafloor backscatter mapping show a non-damaged and non-disturbed rim of the MV. The most recently erupted mud breccia, which show the thinnest hemipelagic sediment coverage, is deposited near the central part of the EEC and WEC, respectively (see GC01 and GC33). It is

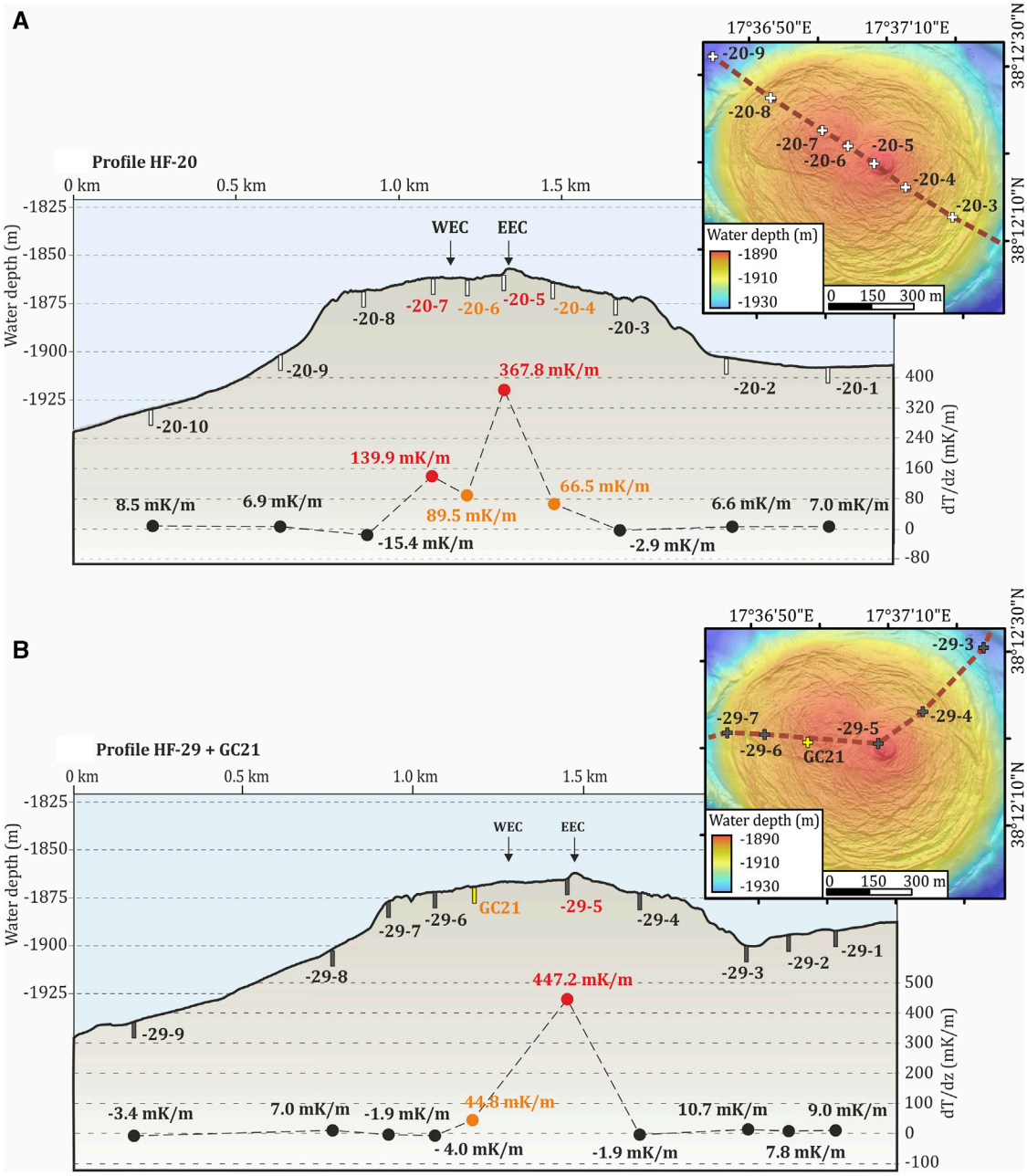

FIGURE 6
Temperature gradient profiles HF-20 **(A)** and HF-29 **(B)** from cruise SO278 (2020) and the position of GC21, equipped with MTLs, from cruise POS499 (2016). AUV-derived high-resolution map shows the positioning of temperature sites for the central part of Sartori MV. Positions of all temperature measurement sites including those being located outside the MV are shown in Figure 2A. *In-situ* temperatures at the central part of Sartori MV are higher compared to background temperatures of the surrounding area.

assumed that the featureless surface of the cone-like summit (peak) of the EEC (Figure 7B) consists of the freshest, and therefore youngest, material erupted by Sartori MV. From this mud cone, the most recent erupted material would downflow to the east, creating a flat, sloping (~2.5°) eastern flank of the EEC peak (Figure 7B). The western flank of the EEC is much steeper (~8.2°), giving rise to the assumption of a constant mud build-up with no layers of downflowing mudflows at the western flank. The morphological profile of the WEC (Figure 7C) indicates a depression in its most central part, which might result from a mud cone collapse, creating a rugged and slightly depressed topography.

The more or less concentric ridges and depressions on the plateau are interpreted as mud rings attributed to the irregular supply of mud breccia from the eruption centers and its lateral transport toward the MV rim (Figure 7A). Such mud rings show superposition and intercalation, pointing to several consecutive eruption events. It is assumed that episodical activity and,

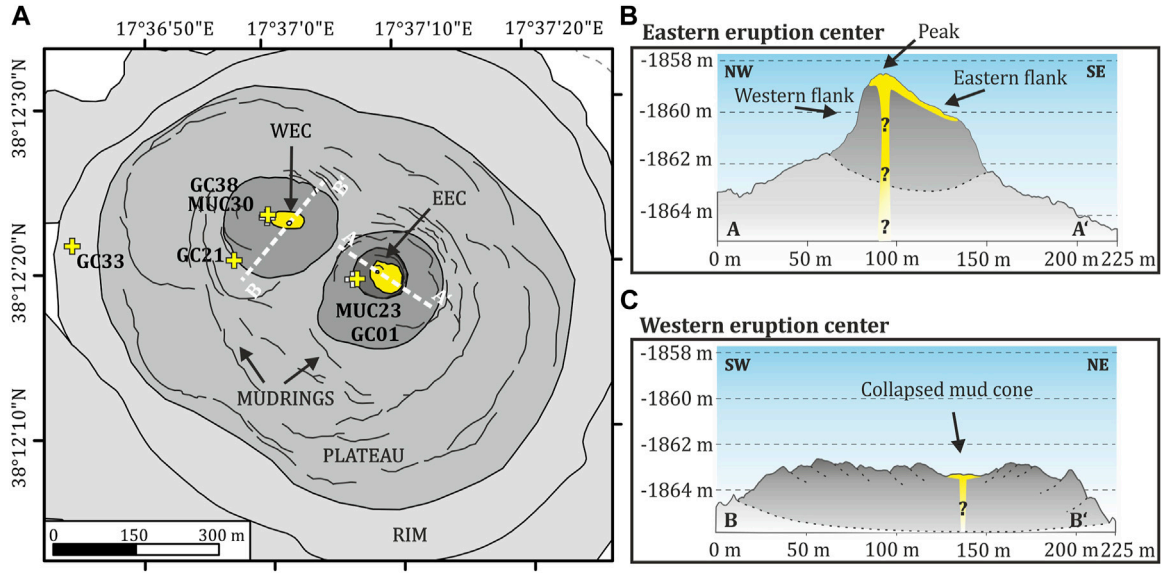

FIGURE 7
(A) Schematic drawing of prominent morphological features of Sartori MV showing positions of the eastern and western eruption centers, mud rings, the plateau, and the rim of the MV. GC and MUC positions are shown for orientation. High backscatter patches of both eruption centers (shaded in dark gray) and the most prominent mud rings derived from slope data are illustrated. Youngest and top-most material is colored in yellow. **(B)** NW–SE-oriented profile crossing the EEC showing a pronounced peak within its youngest part. The most recent erupted mud breccia was flowing down the peak to the SE. **(C)** SW–NE-oriented profile crossing the WEC illustrating the central morphologic depression assumed to result from a mud cone collapse.

therefore, upward migration of fluids and solids within the central parts of the eruption centers push mud breccia within the conduit vertically and mud breccia that has already been expelled (mud rings) to the sides. Sediment (mud) displacement was also reported for, e.g., Håkon Mosby MV on the Barents Sea slope, from which a lateral displacement of 0.4 m per year, triggered by episodical recurring mud eruption events within the central part, is measured (Feseker et al., 2014).

5.2 Sedimentological aspects indicating sub-recent mud eruption

Generally, the dating of hemipelagic sediment above mud breccia provides information on the dynamics, rates, and ages of mud extrusion events and its related fluid flow (Lykousis et al., 2009). Moreover, knowledge of the local sedimentation rate is necessary to constrain the timing of the extrusive activity of Sartori MV. At the investigated sites close to the eruption centers, the moussy mud breccia is covered by hemipelagic sediment of ~40 mm (MUC23; EEC) and ~30 mm (MUC30; WEC) in thickness. The sedimentation rate of the Calabrian Arc is estimated to range between 0.04 and 0.26 mm/yr (Kastens, 1984; Polonia et al., 2013a; Ceramicola et al., 2014b; Loher et al., 2018a). At Sartori MV, a sedimentation rate of 0.077 mm/yr is estimated (Morlotti et al., 1982; Ceramicola et al., 2014b). Specific time markers, such as sapropel- (Mercone et al., 2000; Mercone et al., 2001; De Lange et al., 2008) or tephra layers (Keller et al., 1978; Narcisi and Vezzoli, 1999; Wulf et al., 2008), may help delimit the relative age dating in more detail. The pronounced and coarse-grained postglacial tephra layer Z1 of the Somma–Vesuvius eruption in AD 79 (Wulf et al., 2008; Zanchetta et al., 2011) can be found at shallow sediment depth all over the central Mediterranean Sea (Keller et al., 1978). Underneath, the dark and anoxic sapropel S1 layer, which was deposited 10.8 ka to 6.1 ka ago (De Lange et al., 2008; Polonia et al., 2015), is present in sediment cores all over the Mediterranean Sea (Capotondi et al., 2011). By combining the information, it is suggested that the ~30 mm (MUC30; WEC) and 40 mm (MUC23; EEC) thick hemipelagic sediment layers cover a time span of ~390 years and ~520 years, respectively. However, the GC and MUC cores were not taken from the most central part of the eruption centers (Figures 2, 7), which presumably hosts the youngest mud breccia extruded at the MV (Figure 7B). The high-resolution bathymetry shows that the preferred mudflow direction was progressing downslope from the peak of the EEC to the SE rather than flowing to the southwestern direction where the sediment cores are taken (Figures 7A, B). Mudflows in the SE of the EEC are most likely younger than the mud breccia recovered with GC01 and MUC23 ~50 m SW of the peak of the EEC. Therefore, it is assumed that the recovered sediment cores do not contain the youngest mud breccia ejected at Sartori MV.

The presence of sapropel S1 (10.8–6.1 ka) in GC33 clearly points to an estimated age of maximum 10.8 ka for the underlying mud breccia. Whether the mud breccia deposition ended immediatedly before or during the anoxic phase is beyond the scope of this study. Therefore, an age estimation of ~10 ka is made for the latest mud breccia deposition at the western rim of Sartori MV. By combining sediment core information with the high-resolution bathymetry of the non-damaged rim, it is assumed that no substantial mudflows were transported beyond the rim of Sartori MV during the past ~10 ka.

5.3 Temperature anomalies as an indication of recent MV activity

In-situ sediment temperatures show laterally considerable changes. With decreasing distance to both eruption centers of Sartori MV, the gradients increase first gradually and then rapidly towards the center, resulting in a distinct peak of 447.2 mK/m close to the EEC. The highest temperature gradient is observed at the EEC, but its intensity is much lower compared to that determined at other active MV summits in the eastern Mediterranean Sea. For instance, a maximum temperature gradient of 15.5 mK/m was reported from the mud extrusion site of Venere MV in the Calabrian Arc (Loher et al., 2018c). In addition, Feseker et al. (2010) reported temperature gradients of 25,890 mK/m at the active summit site of North Alex MV in the Nile deep-sea fan delta. Nevertheless, a locally restricted anomaly of the temperature gradient on top of Sartori MV is distinguishable from background data (Figure 6; Supplementary Table S1). Compiled background temperature gradients of the study area published in the Global Heat Flow Database are generally low, varying between 0 mK/m and 20 mK/m (Fuchs et al., 2021).

The considerable difference in temperature gradients close to the WEC and EEC suggests that heat transport from below is spatially restricted to areas that are believed to be characterized by most recent mud eruptions as well. Gravity core site GC21 and heat flow sites HF-20-5; HF-20-7, and HF-29-5 missed the most central and, therefore, most active areas of the MV by ~46 m west of the WEC (HF-20-7), 32 m southwest (HF-20-5), and 18 m west of the EEC (HF-29-5), respectively. Therefore, comparably higher temperature gradients are expected for the summit of the EEC and most central area of the WEC. However, the temperatures are considerably elevated, pointing to the recent activity of the MV. Both eruption centers show elevated temperatures and temperature gradients. We interpret that the EEC was more active in recent times compared to the WEC because it has revealed higher absolute temperatures and also higher temperature gradients with depth.

At some sites, negative temperature gradients, ranging from −15.4 mK/m (HF-20-8) to −1.9 mK/m (HF-29-4, HF-29-7), were measured. In comparison to measured positive temperature gradients, the scatter of negative temperature gradients is relatively small (Supplementary Figure S4). An explanation of negative temperature gradients could be the transient effect of gas hydrate dissociation. Frictional heat generated as the heat flow probe penetrates the seafloor can lead to dissociation of gas hydrates in an endothermic process. *In-situ* temperature excursions attributed to hydrate decomposition were previously proposed for sites in the Kumano Forearc Basin in Japan (Kinoshita et al., 2015). As Sartori MV is located within the gas hydrate stability zone (GHSZ) close to the phase boundary for sI hydrate (see Section 5.4), hydrate dissociation caused by sediment temperature increase due to frictional heat is possible (Supplementary Figure S5). However, neither intact gas hydrate specimen nor significant anomalies in pore water chloride concentrations, which are indicative of the presence of hydrates, were found in the max. 3.24 m-long gravity cores. Determining if negative temperature gradients are related to the effect of gas hydrate dissociation needs further and more detailed analyses; however this investigation is beyond the scope of this study.

5.4 Flux and sources of methane in the uppermost sediments

Seafloor emission of bubble-forming gas was not observed during the investigations in 2016 and 2020, and it was also not reported from previous studies of Sartori MV (Morlotti et al., 1982; Ceramicola et al., 2014b; Bohrmann et al., 2016; Bohrmann et al., 2022). However, relatively shallow depths of the SMI and substantial CH_4 enrichments below it at the four coring stations surveyed within the MV demonstrate activity in the recent past. The shallowest SMI and highest *ex situ* CH_4 concentration (~1.1 mmol/L, GC01) below suggest that the EEC was the area of most intense and/or recent fluid upward migration. This assumption is supported by the highest sediment temperature gradient being detected at the EEC (see Section 5.3).

Both gravity cores recovered in the WEC area (GC21 and GC38) showed maximum CH_4 concentrations in the same range (~0.8 mmol/L). However, since the cores were obtained with a time interval of almost 4.5 years (spring 2016 and fall 2020) and a spatial distance of ~100 m from each other, it is unclear whether the similar concentrations originate from one or more fluid ascent pulses.

Calculations of the phase boundary of sI gas hydrate using the HWHyd software by Masoudi and Tohidi (2005) show that Sartori MV (P ~19 MPa, S ~15 PSU, T ~16.5°C) is basically within the GHSZ (Supplementary Figure S5). However, since the *in-situ* CH_4 solubility (141.4 mmol/kg; Tishchenko et al., 2005; Kossel et al., 2013) is more than two orders of magnitude above the measured maximum *ex situ* CH_4 concentrations, the presence of gas hydrates in the sediment sampled is unlikely. Moreover, stable pore water profiles of Cl^- concentrations do not show any indication for gas hydrate dissociation. This is in contrast to the sites of the previously described negative temperature anomalies, which might be related to the instant dissociation of gas hydrates within the disturbed sediment by the measurement itself.

In general, maximum CH_4 concentrations at each site correlate positively with temperature gradients (Figures 4, 6A, B). However, the maximum concentration at the western rim station (GC33, ~0.4 mmol/L, Figure 2B) is significantly elevated relative to background values [<0.003 mmol/L, gravity cores GeoB21366-1, 21367-1, Bohrmann et al. (2016)], whereas the temperature gradient at nearby temperature probe sites HF-29-7 and HF-29-8 (Figure 2A) is not. Hence, the data suggest that the methane signal persists longer than the temperature signal after an eruption, which is consistent with thermal conductivity being significantly faster than the diffusion of solutes. In addition, lateral methane propagation might be more effective than temperature propagation.

Very similar stable C and H isotopic compositions of methane in the deepest samples of gravity cores GC01 and GC38 suggest that fluids migrating toward the EEC and WEC are fueled from the same reservoir. These samples are positioned lowest below the SMI and should be least affected by microbial alteration of the AOM. Therefore, their isotopic composition should mostly reflect the isotopic composition of the source(s). In Figure 8A, the fields representative of methane generation pathways based on methane stable C and H isotopic compositions are shown. The deepest samples from GC01 and GC38 plot close to the field representative of methane originating from secondary microbial

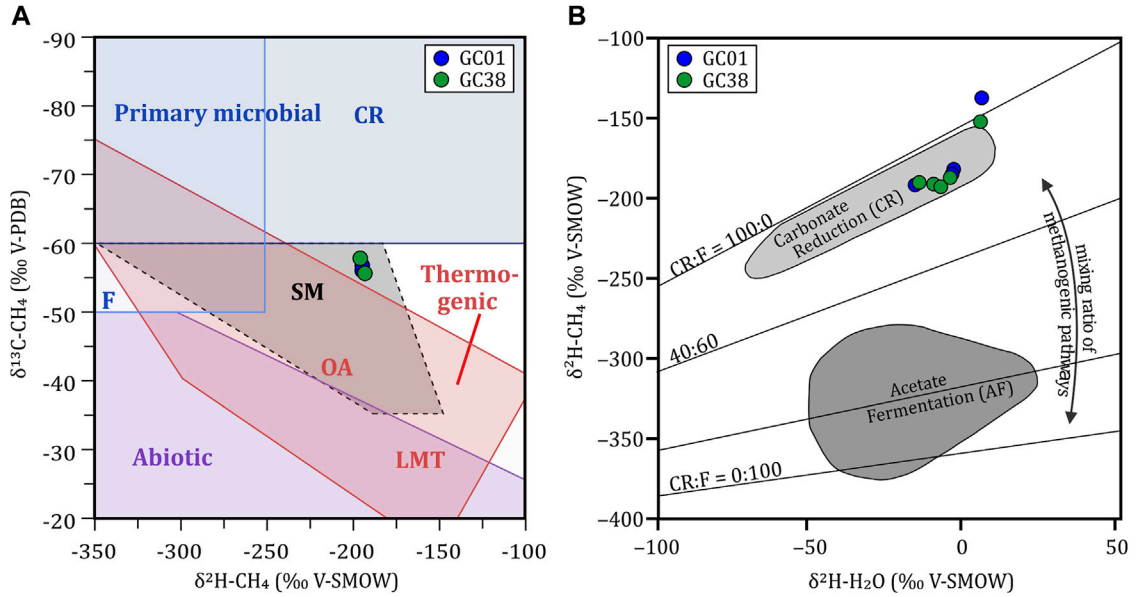

FIGURE 8
(A) Generic diagram based on stable C and H isotopic compositions of methane showing the major methane production pathways at Sartori MV (modified after Milkov and Etiope (2018)). Deepest samples from GC01 (EEC) and GC38 (WEC) plot close to the field assigned for secondary microbial methane, in between the fields representative for primary microbial and thermogenic methane. Given the known depths of MV roots and geometries of internal structures from other submarine MVs (Somoza et al., 2012), the admixture of methane from several sources resulting in measured stable C and H isotope values is likely. **(B)** Diagram showing δ^2H-CH_4–δ^2H-H_2O relationships diagnostic for the two microbial methane generation pathways, carbonate reduction (CR) and acetate fermentation (AF; Whiticar, 1999). All samples from GC01 and GC38 plot within or close to the field assigned for the carbonate reduction pathway.

sources, which are based on methanogenic petroleum biodegradation (Milkov and Etiope, 2018). The presence of secondary microbial methane has also been proposed for submarine and terrestrial MVs in other regions (Stadnitskaia et al., 2008; Etiope et al., 2009; Gilbert et al., 2022). For Sartori MV, stable C isotope signatures of CO_2, which would provide better information on the presence of secondary microbial methane (Milkov and Etiope, 2018), are not available. However, relatively low contents of organic carbon (TOC; ~0.3%; Supplementary Table S2) in the three gravity cores investigated suggest that petroleum degradation is not the main source of methane.

Alternatively, methane stable C and H isotopic compositions may also reflect the mixture of methane from primary microbial and thermogenic sources to some extent. MVs are typically deeply rooting structures in which fluids are mobilized from several kilometers of depth (Mazzini and Etiope, 2017). In addition, fluids and solids are homogenized during their passage toward the seafloor (Lalk et al., 2022). Therefore, it is plausible to assume that the methane isotopic compositions determined in this study do not reflect a single source but result from the mixture of methane from several sources.

Consequently, methane collected from near-surface sediments at Sartori MV most likely originates from a mix of primary microbial, secondary microbial, and/or thermogenic sources. Figure 8B shows H isotope relationships of methane and pore water typical for the microbial methane generation pathways, including carbonate reduction (CR) of microbial bacteria and acetate fermentation (AF). However, the CR pathway is believed to dominate in marine settings, while the AF pathways appear to predominantly occur in freshwater systems (Whiticar, 1999). Because samples from GC01 and GC38 plot within or close to the field indicative for the CR pathway, it is proposed that low-salinity water potentially released in the course of clay mineral alteration (e.g., Dählmann and De Lange, 2003; Mazzini and Etiope, 2017) does not promote significant methane production via the AF pathway at Sartori MV.

5.5 Diffusive fluid discharge as an indicator of recent MV activity

Pore water Cl^- and SO_4^{2-} concentration profiles show the intrusion of seawater into the uppermost 0.5–1 m of the sediment (Figure 9). A transient diffusive effect of this initial disturbance was calculated to reach the measured concentration distribution for both Cl^- and SO_4^{2-}, as described in detail in Schulz and Schulz (2005), using depth-dependent data for regional porosities and temperatures. In all three sites, an initial situation with no SO_4^{2-} in the lower layer and an upper event layer with seawater SO_4^{2-} concentration has been assumed. In order to match the SO_4^{2-} concentration distribution measured, sulfate reduction rates were fine-tuned individually. For Cl^- profiles, an initial situation with seawater chlorinity of 600 mmol/L with a linear decrease to a low chlorinity of approximately 200 mmol/L, most probably due to freshwater input from depth and to a much lesser extent to dilution with crystal water from disintegrating gas

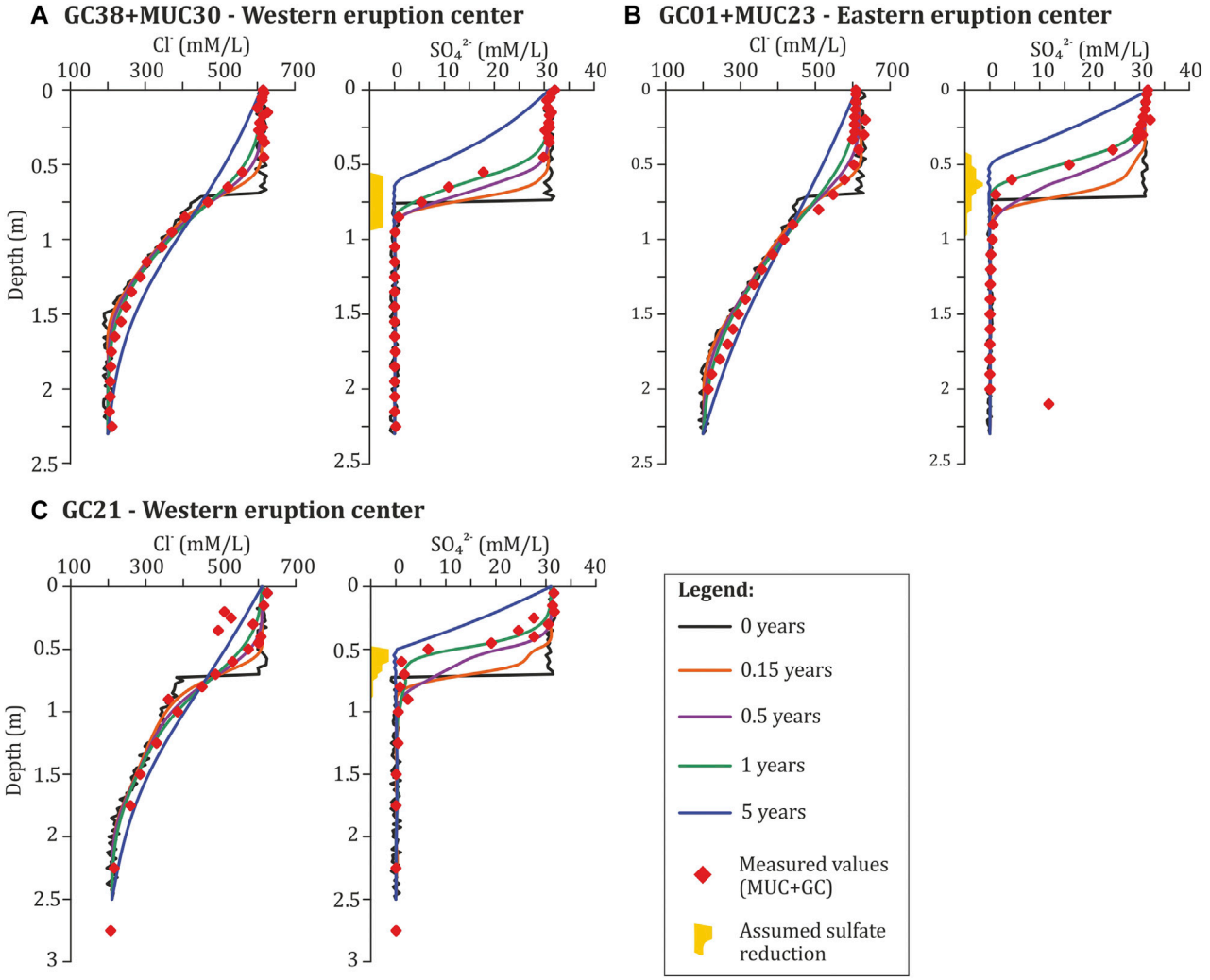

FIGURE 9
Measured and modeled pore water concentration profiles of chloride and sulfate in GC and MUC cores (red squares) taken from **(A)** the WEC in 2020, **(B)** the EEC in 2020, and **(C)** the WEC in 2016. The black lines indicate the start conditions assumed to model the measured transient pore water profiles using *in-situ* temperatures and porosities. The best fit to the pore water data is reached after approximately 1 year of diffusive readjustment (green line). The yellow fields indicate the location and the relative intensity of sulfate reduction assumed to match the measured data.

hydrates, was assumed. The steep decrease in pore water chlorinity in the uppermost sediment layers is attributed to diffusive seawater infiltration into the mud, as previously reported in other MV systems (Henry et al., 1996; Feseker et al., 2009; Paull et al., 2015; Loher et al., 2018c). Modeling was optimized to match the measured Cl^- and SO_4^{2-} profiles with the modeled time, which has passed from the initial start until measurement, while maintaining the same physical boundary conditions. That modeling curvature, which fits best with measured Cl^- and SO_4^{2-} concentrations, is expected to be the most accurate modeling result for this prescribed scenario.

The actual transient stage found in the pore water Cl^- and SO_4^{2-} profiles is reached after 1 year or less in all three sites (green and purple lines in Figure 9). The measured steep gradients could be diffusively significantly smoothed within another 4 years (see blue line in Figure 9). On a larger scale, such pore water profiles are typical for slumps overlying background sediments at the slope of continental margins (Niewöhner et al., 1998; Strasser et al., 2013). In this study, the modeling of pore water diffusion might also indicate a very recent and abrupt onset of fluid migration within the conduit of the MV. The pore water data might indicate either a MV activity-related exchange or an intensive mixing with seawater concentrations within the uppermost 0.5–1 m of all three gravity cores (GC21, GC38, and GC01) close to the two eruption centers. The data lead to steep transient pore water profiles in both Cl^- and SO_4^{2-}. Those pore water profiles are created by either a sudden but relatively slow exchange of pore fluid with seawater fluid concentrations due to a low MV activity only or due to a sudden but very active phase of the MV accompanied by the discharge of fluids and solids. The analyzed sediment cores do not show any indication of the extrusion of solids in the past ~390 years to ~520 years. In contrast, from pore water analyses, a very recent fluid migration event accompanied by elevated

temperatures at the EEW and WEC, is observed. Therefore, it is assumed that a sudden but relatively slow pore fluid exchange with seawater fluid concentration, created due to the low activity of Sartori MV, is responsible for the measured data in 2016 and 2020. The new findings clearly show a decoupling of these processes at Sartori MV. A low activity, responsible for pore fluid and heat anomalies at the EEC and WEC, is episodically ongoing very recently. In contrast, high-active phases, accompanied by degassing to the water column, very high CH_4 concentrations, and strong temperature anomalies, as well as the extrusion of high viscous solids, occur episodically in time scales of hundreds of years.

6 Conclusion

Sartori MV in the Calabrian Arc is a flat-topped mud volcano that was virtually dormant in terms of focused gas emission and mud ejection during two research campaigns in 2016 and 2020. High-resolution bathymetry, in combination with seafloor backscatter data, revealed the presence of two eruption centers (WEC and EEC) close to the geometric center of the MV. The EEC shows a peak-like summit, whereas a slight depression was found in the area of the WEC. Fluid migration and the exchange of pore fluid with seawater fluid concentrations within the uppermost sediment layers, in combination with elevated temperatures at both eruption centers, support the assumption of a low activity of the MV in 2016 and 2020. These low active phases were not accompanied by the eruption of solids. Sediment cores from the central part of the MV show a hemipelagic sediment coverage ranging from 30 mm (MUC30) to 40 mm (MUC23), allowing to estimate the age of the youngest mud breccia deposits at the coring position to ~0.39 and ~0.52 ka ago, respectively. Potentially, these materials did not reach gravity and MUC core positions located ~50 m SW to the most central part of the EEC (GC01) and ~132 m SW (GC21) and ~44 m W (GC38) to the most central part of the WEC. This might explain the moderate temperature gradients measured at those sites. Higher *in-situ* sediment temperatures and even less (or missing) hemipelagic sediment coverage are assumed for the most central parts of both eruption centers. We suggest that the low activity of Sartori MV, responsible for diffusive fluid migration, is decoupled from the extrusion of solids (mud breccia), and only pore fluid exchange was occurring in recent times. This could explain the gap between pore water modeling results, pointing to a very recent fluid flux, and sedimentological observations, pointing to only sub-recent material extrusion at the eruption centers. It is proposed that only high active phases of the MV are responsible for the extrusion of solids and that low active phases, responsible for changes in fluid and heat flux, may occur more often. In contrast to those low active phases, stronger activity of the MV is accompanied by very high temperature excursions and very high CH_4 concentrations (also identifiable in the water column as gas bubbling) and the formation of new and relocated mud rings. However, these phases of low activity could be categorized to the *depletion* phase of a MV, whereas high active phases are typical for categorized *eruption* phases of a MV.

The SMI depth is shallower close to the EEC compared to the WEC. CH_4 concentrations in 2020 are higher compared to those in 2016, and they are clearly elevated close to both eruption centers. The highest CH_4 concentration was detected at the EEC. Moreover, it is assumed that the EEC (higher CH_4 concentrations, flatter SMI, temperature anomaly, and peak-like structure with downflowing mudflow) was active in recent times compared to the WEC. In addition, we assume that relatively small volumes of high-viscous mud breccia have been erupted and deposited in the recent past. The material was not overflowing older mud rings from older eruption events and also not the rim of the MV edifice. The high-resolution bathymetry of the rim shows its non-damaged and undisturbed appearance. Analyses of sediment core GC33 and the presence of sapropel S1 allow us to conclude that no mudflow has overflown the western rim of the MV edifice for the past ~10 ka.

Data availability statement

The datasets presented in this study can be found in online repositories. The names of the repository/repositories and accession number(s) can be found in the article/Supplementary Material.

Author contributions

MD, MR, and GB conceived this study. MD wrote the draft version of the manuscript, created the illustrations presented here, and analyzed and interpreted the data. MR did the original mapping of AUV-based bathymetry, created the original illustration of AUV-based bathymetry, and supported with proof-reading and editing. TP did geochemical data analyses and interpretation, created original geochemical illustrations, and supported with the writing of geochemical sections, proof-reading, and editing. MK did the pore water modeling, created the original illustration, and provided support with proof-reading and editing. NK participated in the joint expedition SO278 for *in-situ* sediment temperature data acquisition and the processing of temperature data, proof-reading, and editing. CdSF helped MD with processing the AUV-based bathymetry, did the processing of ship-based bathymetry and navigation adjustment of the data, and supported with proof-reading and editing. GB provided support with proof-reading and editing, funding acquisition, resources, and supervision. All authors contributed to the article and approved the submitted version.

Funding

This study received support by grant no. BO 1049/22-1 from the Deutsche Forschungsgemeinschaft (DFG). The ship-time of expedition POS499 was funded by the DFG through the MARUM cluster of excellence EXC 309: "The Ocean in the Earth System" (grant/award no. 49926684) as an incentive fund proposal grant. Expedition SO278 was supported by the DFG through the MARUM cluster of excellence EXC 2077: "The Ocean Floor—Earth's Uncharted Interface" (grant/award

no. 390741603) and through funds related to the GPF review procedure (GPF 20-1_054, Sartori MV plus).

Acknowledgments

The authors are grateful to the masters and crews of cruises *R/V POSEIDON* POS499 and *R/V SONNE* SO278. The team of the AUV MARUM-SEAL 5000 is very much appreciated for their efforts during POS499. The authors are grateful for the help and contributions of Michael Riedel. The authors appreciated the work by Paul Wintersteller and his help during the acoustic acquisition and planning on board POS499. Markus Loher, Janice Malnati, Silvana Pape, Antonia Witzleb, and all cruise participants from POS499 and SO278 are deeply thanked for their support and laboratory work on pore water and isotope data. Vera Bender as well as the GeoB Core Repository at the MARUM - Center for Marine Environmental Sciences, University of Bremen, Germany, are thanked for providing the sediment material used in this study. The authors are thankful for the constructive comments by Stephanie Dupré and the two reviewers who helped improve the manuscript.

Conflict of interest

The authors declare that the research was conducted in the absence of any commercial or financial relationships that could be construed as a potential conflict of interest.

Publisher's note

All claims expressed in this article are solely those of the authors and do not necessarily represent those of their affiliated organizations, or those of the publisher, the editors, and the reviewers. Any product that may be evaluated in this article, or claim that may be made by its manufacturer, is not guaranteed or endorsed by the publisher.

Supplementary material

The Supplementary Material for this article can be found online at: https://www.frontiersin.org/articles/10.3389/feart.2023.1181380/full#supplementary-material

References

Bhatnagar, G., Chapman, W. G., Dickens, G. R., Dugan, B., and Hirasaki, G. J. (2008). Sulfate-methane transition as a proxy for average methane hydrate saturation in marine sediments. *Geophys. Res. Lett.* 35 (3), L03611. doi:10.1029/2007gl032500

Boetius, A., Ravenschlag, K., Schubert, C. J., Rickert, D., Widdel, F., Gieseke, A., et al. (2000). A marine microbial consortium apparently mediating anaerobic oxidation of methane. *Nature* 407 (6804), 623–626. doi:10.1038/35036572

Bohrmann, G., Ahrlich, F., Antoniou, D., Behrendt, N., Innocentini, S., Coulibaly, O., et al. (2022). *Fluid-rock interaction at the backstop to the Mediterranean Ridge accretionary complex south of crete: R/V SONNE cruise report SO278 Emden (Germany), 12.10.2020—Emden (Germany), 01.12.2020. FRINGE*. Berichte: MARUM–Zentrum für Marine Umweltwissenschaften, Fachbereich Geowissenschaften, Universität Bremen. 326, 208. Bremen, 2021. doi:10.26092/elib/1776

Bohrmann, G., Bachmann, K., Buchheister, S., Candoni, O., Ceramicola, S., Loher, M., et al. (2016). *Report and preliminary results of R/V POSEIDON cruise POS499*. Calabrian Mud Volcanoes, Catania (Italy)–Catania (Italy) 04 May–22 May, 2016. Berichte: MARUM–Zentrum für Marine Umweltwissenschaften, Fachbereich Geowissenschaften, Universität Bremen 311, 76. Bremen, 2016. Available at: http://nbn-resolving.de/urn:nbn:de:gbv:46-00105556-16

Bohrmann, G., Ivanov, M., Foucher, J.-P., Spiess, V., Bialas, J., Greinert, J., et al. (2003). Mud volcanoes and gas hydrates in the Black Sea: new data from Dvurechenskii and Odessa mud volcanoes. *Geo-Marine Lett.* 23, 239–249. doi:10.1007/s00367-003-0157-7

Borowski, W. S., Paull, C. K., and Ussler, W., III (1999). Global and local variations of interstitial sulfate gradients in deep-water, continental margin sediments: sensitivity to underlying methane and gas hydrates. *Mar. Geol.* 159 (1-4), 131–154. doi:10.1016/s0025-3227(99)00004-3

Bullard, E. C. (1954). The flow of heat through the floor of the Atlantic Ocean. *Proc. R. Soc. Lond. Ser. A. Math. Phys. Sci.* 222 (1150), 408–429. doi:10.1098/rspa.1954.0085

Capotondi, L., Vigliotti, L., Bergami, C., and Sangiorgi, F. (2011). The dark side of the mediterranean geological record: the sapropel layers and a case study from the Ionian Sea. *Marine Research at CNR. Dipartimento Terra e Ambiente—CNR ed.* Roma: CNR, 658–669.

Capozzi, R., Artoni, A., Torelli, L., Lorenzini, S., Oppo, D., Mussoni, P., et al. (2012). Neogene to Quaternary tectonics and mud diapirism in the Gulf of Squillace (Crotone-Spartivento Basin, Calabrian Arc, Italy). *Mar. Petroleum Geol.* 35 (1), 219–234. doi:10.1016/j.marpetgeo.2012.01.007

Caress, D. W., and Chayes, D. N. (1996). Improved processing of Hydrosweep DS multibeam data on the R/V *Maurice Ewing*. *Mar. Geophys. Res.* 18 (6), 631–650. doi:10.1007/bf00313878

Castellini, D. G., Dickens, G. R., Snyder, G. T., and Ruppel, C. D. (2006). Barium cycling in shallow sediment above active mud volcanoes in the Gulf of Mexico. *Chem. Geol.* 226 (1-2), 1–30. doi:10.1016/j.chemgeo.2005.08.008

Ceramicola, S., Praeg, D., Coste, M., Forlin, E., Cova, A., Colizza, E., et al. (2014a). "Submarine mass-movements along the slopes of the active Ionian continental margins and their consequences for marine geohazards (Mediterranean Sea)," in *Submarine mass movements and their consequences advances in natural and technological Hazards research*. Editors S. Krastel, J-H. Behrmann, D. Völker, M. Stipp, C. Berndt, R. Urgeles, et al. (Springer, Cham) 37, 295–306. doi:10.1007/978-3-319-00972-8_26

Ceramicola, S., Praeg, D., Cova, A., Accettella, D., and Zecchin, M. (2014b). Seafloor distribution and last glacial to postglacial activity of mud volcanoes on the Calabrian accretionary prism, Ionian Sea. *Geo-Marine Lett.* 34 (2), 111–129. doi:10.1007/s00367-013-0354-y

Cernobori, L., Hirn, A., McBride, J., Nicolich, R., Petronio, L., and Romanelli, M. (1996). Crustal image of the Ionian basin and its Calabrian margins. *Tectonophysics* 264 (1-4), 175–189. doi:10.1016/s0040-1951(96)00125-4

Claypool, G. E., and Kaplan, I. R. (1974). "The origin and distribution of methane in marine sediments," in *Natural gases in marine sediments marine science*. Editor I. R. Kaplan (Boston, MA: Springer) 3. doi:10.1007/978-1-4684-2757-8_8

Cuffaro, M., Billi, A., Bigi, S., Bosman, A., Caruso, C. G., Conti, A., et al. (2019). The Bortoluzzi Mud Volcano (Ionian Sea, Italy) and its potential for tracking the seismic cycle of active faults. *Solid Earth.* 10 (3), 741–763. doi:10.5194/se-10-741-2019

Dählmann, A., and De Lange, G. (2003). Fluid–sediment interactions at Eastern Mediterranean mud volcanoes: a stable isotope study from ODP Leg 160. *Earth Planet. Sci. Lett.* 212 (3-4), 377–391. doi:10.1016/S0012-821X(03)00227-9

De Lange, G. J., Thomson, J., Reitz, A., Slomp, C. P., Speranza Principato, M., Erba, E., et al. (2008). Synchronous basin-wide formation and redox-controlled preservation of a Mediterranean sapropel. *Nat. Geosci.* 1 (9), 606–610. doi:10.1038/ngeo283

Dickens, G. R. (2001). Sulfate profiles and barium fronts in sediment on the Blake Ridge: present and past methane fluxes through a large gas hydrate reservoir. *Geochimica Cosmochimica Acta* 65 (4), 529–543. doi:10.1016/s0016-7037(00)00556-1

Dickens, G. R., Koelling, M., Smith, D. C., and Schnieders, L. (2007). Rhizon sampling of pore waters on scientific drilling expeditions: an example from the IODP Expedition 302, Arctic Coring Expedition (ACEX). *Sci. Drill.* 4, 22–25. doi:10.5194/sd-4-22-2007

Dimitrov, L. I. (2002). Mud volcanoes—the most important pathway for degassing deeply buried sediments. *Earth-Science Rev.* 59 (1-4), 49–76. doi:10.1016/s0012-8252(02)00069-7

Dupré, S., Buffet, G., Mascle, J., Foucher, J.-P., Gauger, S., Boetius, A., et al. (2008). High-resolution mapping of large gas emitting mud volcanoes on the Egyptian continental margin (Nile Deep Sea Fan) by AUV surveys. *Mar. Geophys. Res.* 29 (4), 275–290. doi:10.1007/s11001-009-9063-3

Etiope, G. (2015). *Natural gas seepage. The Earth's hydrocarbon degassing*. Springer International Publishing Switzerland. doi:10.1007/978-3-319-14601-0

Etiope, G., Feyzullayev, A., Milkov, A., Waseda, A., Mizobe, K., and Sun, C. (2009). Evidence of subsurface anaerobic biodegradation of hydrocarbons and potential secondary methanogenesis in terrestrial mud volcanoes. *Mar. Petroleum Geol.* 26 (9), 1692–1703. doi:10.1016/j.marpetgeo.2008.12.002

Etiope, G., and Milkov, A. V. (2004). A new estimate of global methane flux from onshore and shallow submarine mud volcanoes to the atmosphere. *Environ. Geol.* 46 (8), 997–1002. doi:10.1007/s00254-004-1085-1

Faccenna, C., Molin, P., Orecchio, B., Olivetti, V., Bellier, O., Funiciello, F., et al. (2011). Topography of the Calabria subduction zone (southern Italy): clues for the origin of Mt. Etna. *Tectonics* 30 (1), TC1003. doi:10.1029/2010tc002694

Feseker, T., Boetius, A., Wenzhöfer, F., Blandin, J., Olu, K., Yoerger, D. R., et al. (2014). Eruption of a deep-sea mud volcano triggers rapid sediment movement. *Nat. Commun.* 5 (1), 5385–5388. doi:10.1038/ncomms6385

Feseker, T., Brown, K. R., Blanchet, C., Scholz, F., Nuzzo, M., Reitz, A., et al. (2010). Active mud volcanoes on the upper slope of the western Nile deep-sea fan—first results from the P362/2 cruise of R/V Poseidon. *Geo-Marine Lett.* 30 (3), 169–186. doi:10.1007/s00367-010-0192-0

Feseker, T., Dählmann, A., Foucher, J.-P., and Harmegnies, F. (2009). *In-situ* sediment temperature measurements and geochemical porewater data suggest highly dynamic fluid flow at Isis mud volcano, eastern Mediterranean Sea. *Mar. Geol.* 261 (1-4), 128–137. doi:10.1016/j.margeo.2008.09.003

Fuchs, S., Norden, B., Artemieva, I., Chiozzi, P., Dedecek, P., Demezhko, D., et al. (2021). *The global heat flow database: release 2021*. GFZ Data Services. doi:10.5880/fidgeo.2021.014

Gallais, F., Gutscher, M.-A., Klaeschen, D., and Graindorge, D. (2012). Two-stage growth of the Calabrian accretionary wedge in the Ionian Sea (Central Mediterranean): constraints from depth-migrated multichannel seismic data. *Mar. Geol.* 326, 28–45. doi:10.1016/j.margeo.2012.08.006

Gilbert, A., Nakagawa, M., Taguchi, K., Zhang, N., Nishida, A., and Yoshida, N. (2022). Hydrocarbon cycling in the Tokamachi Mud Volcano (Japan): insights from isotopologue and metataxonomic analyses. *Microorganisms* 10 (7), 1417. doi:10.3390/microorganisms10071417

Granot, R. (2016). Palaeozoic oceanic crust preserved beneath the eastern Mediterranean. *Nat. Geosci.* 9 (9), 701–705. doi:10.1038/ngeo2784

Greinert, J., Artemov, Y., Egorov, V., De Batist, M., and McGinnis, D. (2006). 1300-m-high rising bubbles from mud volcanoes at 2080 m in the Black Sea: hydroacoustic characteristics and temporal variability. *Earth Planet. Sci. Lett.* 244 (1-2), 1–15. doi:10.1016/j.epsl.2006.02.011

Gutscher, M.-A., Dellong, D., Dominguez, S., Malavieille, J., Graindorge, D., and Klingelhoefer, F. (2019). "Strike-slip faulting in the calabrian accretionary wedge: using analog modeling to test the kinematic boundary conditions of geodynamic models," in *Transform plate boundaries and fracture zones*. Editor J. C. Duarte (Elsevier), 321–337. doi:10.1016/B978-0-12-812064-4.00013-X

Gutscher, M.-A., Kopp, H., Krastel, S., Bohrmann, G., Garlan, T., Zaragosi, S., et al. (2017). Active tectonics of the Calabrian subduction revealed by new multi-beam bathymetric data and high-resolution seismic profiles in the Ionian Sea (Central Mediterranean). *Earth Planet. Sci. Lett.* 461, 61–72. doi:10.1016/j.epsl.2016.12.020

Henry, P., Le Pichon, X., Lallemant, S., Lance, S., Martin, J. B., Foucher, J. P., et al. (1996). Fluid flow in and around a mud volcano field seaward of the Barbados accretionary wedge: results from Manon cruise. *J. Geophys. Res. Solid Earth* 101 (B9), 20297–20323. doi:10.1029/96jb00953

Hensen, C., Nuzzo, M., Hornibrook, E., Pinheiro, L. M., Bock, B., Magalhães, V. H., et al. (2007). Sources of mud volcano fluids in the Gulf of Cadiz—indications for hydrothermal imprint. *Geochimica Cosmochimica Acta* 71 (5), 1232–1248. doi:10.1016/j.gca.2006.11.022

Higgins, G., and Saunders, J. (1974). Mud volcanoes-their nature and origin. *Verhandl Naturforsch Gesellschaft in Basel* 84, 101–152. Basel.

Hsü, K. J., Montadert, L., Bernoulli, D., Cita, M. B., Erickson, A., Garrison, R. E., et al. (1977). History of the Mediterranean salinity crisis. *Nature* 267 (5610), 399–403. doi:10.1038/267399a0

Hyndman, R., Davis, E., and Wright, J. (1979). The measurement of marine geothermal heat flow by a multipenetration probe with digital acoustic telemetry and insitu thermal conductivity. *Mar. Geophys. Res.* 4 (2), 181–205. doi:10.1007/bf00286404

Kastens, K. A. (1984). Earthquakes as a triggering mechanism for debris flows and turbidites on the Calabrian Ridge. *Mar. Geol.* 55 (1-2), 13–33. doi:10.1016/0025-3227(84)90130-0

Keller, J., Ryan, W., Ninkovich, D., and Altherr, R. (1978). Explosive volcanic activity in the Mediterranean over the past 200,000 yr as recorded in deep-sea sediments. *Geol. Soc. Am. Bull.* 89 (4), 591–604. doi:10.1130/0016-7606(1978)89<591:evaitm>2.0.co;2

Kinoshita, M., Fukase, H., Goto, S., and Toki, T. (2015). *In situ* thermal excursions detected in the Nankai Trough forearc slope sediment at IODP NanTroSEIZE Site C0008. *Earth, Planets Space* 67 (1), 16–19. doi:10.1186/s40623-014-0171-1

Kopf, A. J. (2002). Significance of mud volcanism. *Rev. Geophys.* 40 (2), 2–52. doi:10.1029/2000RG000093

Kossel, E., Bigalke, N., Piñero, E., and Haeckel, M. (2013). *The SUGAR Toolbox-A library of numerical algorithms and data for modelling of gas hydrate systems and marine environments*. GEOMAR Report 8 (N. Ser.). GEOMAR Helmholtz Centre for Ocean Research Kiel. doi:10.3289/GEOMAR_REP_NS_8_2013

Kvenvolden, K. A., and McDonald, T. J. (1986). Organic Geochemistry on the JOIDES Resolution: an assay. *Ocean Drilling Program, Technical Note 6, 1–147*. College Station, Texas: Texas A&M University.

Lalk, E., Pape, T., Gruen, D. S., Kaul, N., Karolewski, J. S., Bohrmann, G., et al. (2022). Clumped methane isotopologue-based temperature estimates for sources of methane in marine gas hydrates and associated vent gases. *Geochimica Cosmochimica Acta* 327, 276–297. doi:10.1016/j.gca.2022.04.013

Loher, M., Ceramicola, S., Wintersteller, P., Meinecke, G., Sahling, H., and Bohrmann, G. (2018a). Mud volcanism in a canyon: morphodynamic evolution of the active Venere mud volcano and its interplay with Squillace Canyon, Central Mediterranean. *Geochem. Geophys. Geosystems* 19 (2), 356–378. doi:10.1002/2017gc007166

Loher, M., Marcon, Y., Pape, T., Römer, M., Wintersteller, P., dos Santos Ferreira, C., et al. (2018b). Seafloor sealing, doming, and collapse associated with gas seeps and authigenic carbonate structures at Venere mud volcano, Central Mediterranean. *Deep Sea Res. Part I: Oceanogr. Res. Pap.* 137, 76–96. doi:10.1016/j.dsr.2018.04.006

Loher, M., Pape, T., Marcon, Y., Römer, M., Wintersteller, P., Praeg, D., et al. (2018c). Mud extrusion and ring-fault gas seepage - upward branching fluid discharge at a deep-sea mud volcano. *Sci. Rep.* 8 (1), 6275. doi:10.1038/s41598-018-24689-1

Lykousis, V., Alexandri, S., Woodside, J., De Lange, G., Dählmann, A., Perissoratis, C., et al. (2009). Mud volcanoes and gas hydrates in the Anaximander mountains (Eastern Mediterranean Sea). *Mar. Petroleum Geol.* 26 (6), 854–872. doi:10.1016/j.marpetgeo.2008.05.002

Malinverno, A., and Ryan, W. B. (1986). Extension in the Tyrrhenian Sea and shortening in the Apennines as result of arc migration driven by sinking of the lithosphere. *Tectonics* 5 (2), 227–245. doi:10.1029/tc005i002p00227

Mascle, J., Mary, F., Praeg, D., Brosolo, L., Camera, L., Ceramicola, S., et al. (2014). Distribution and geological control of mud volcanoes and other fluid/free gas seepage features in the Mediterranean Sea and nearby Gulf of Cadiz. *Geo-Marine Lett.* 34 (2), 89–110. doi:10.1007/s00367-014-0356-4

Masoudi, R., and Tohidi, B. (2005). Estimating the hydrate stability zone in the presence of salts and/or organic inhibitors using water partial pressure. *J. Petroleum Sci. Eng.* 46 (1), 23–36. doi:10.1016/j.petrol.2004.10.002

Mastalerz, V., de Lange, G. J., Dählmann, A., and Feseker, T. (2007). Active venting at the Isis mud volcano, offshore Egypt: origin and migration of hydrocarbons. *Chem. Geol.* 246 (1-2), 87–106. doi:10.1016/j.chemgeo.2007.09.005

Mazzini, A., and Etiope, G. (2017). Mud volcanism: an updated review. *Earth-Science Rev.* 168, 81–112. doi:10.1016/j.earscirev.2017.03.001

Menapace, W., Kopf, A., Zabel, M., and de Beer, D. (2017a). "3. Mud volcanoes as dynamic sedimentary phenomena that host marine ecosystems," in *Life at vents and seeps*. Editor K. Jens (Berlin, Boston: De Gruyter), 53–84. doi:10.1515/9783110493672-003

Menapace, W., Völker, D., Kaul, N., Tryon, M. D., and Kopf, A. J. (2017b). The role of mud volcanism and deep-seated dewatering processes in the Nankai Trough accretionary prism and Kumano Basin, Japan. *Geochem. Geophys. Geosystems* 18 (7), 2486–2509. doi:10.1002/2016GC006763

Mercone, D., Thomson, J., Abu-Zied, R., Croudace, I., and Rohling, E. (2001). High-resolution geochemical and micropalaeontological profiling of the most recent eastern Mediterranean sapropel. *Mar. Geol.* 177 (1-2), 25–44. doi:10.1016/s0025-3227(01)00122-0

Mercone, D., Thomson, J., Croudace, I., Siani, G., Paterne, M., and Troelstra, S. (2000). Duration of S1, the most recent sapropel in the eastern Mediterranean Sea, as indicated by accelerator mass spectrometry radiocarbon and geochemical evidence. *Paleoceanography* 15 (3), 336–347. doi:10.1029/1999pa000397

Milkov, A. (2000). Worldwide distribution of submarine mud volcanoes and associated gas hydrates. *Mar. Geol.* 167 (1-2), 29–42. doi:10.1016/s0025-3227(00)00022-0

Milkov, A. V., and Etiope, G. (2018). Revised genetic diagrams for natural gases based on a global dataset of >20,000 samples. *Org. Geochem.* 125, 109–120. doi:10.1016/j.orggeochem.2018.09.002

Minelli, L., and Faccenna, C. (2010). Evolution of the Calabrian accretionary wedge (central Mediterranean). *Tectonics* 29 (4). doi:10.1029/2009tc002562

Miramontes, E., Pellegrini, C., Casalbore, D., and Dupré, S. (2023). "Active geological processes in the Mediterranean Sea," in *Oceanography of the Mediterranean Sea*. Editors Schroeder, K., and Chiggiato, J. (Elsevier), 453–499. doi:10.1016/B978-0-12-823692-5.00010-8

Morlotti, E., Sartori, R., Torelli, L., Barbieri, F., and Raffi, I. (1982). Chaotic deposits from the external Calabrian Arc (Ionian Sea). *Mem. della Soc. Geol. Ital.* 24, 261–275.

Narcisi, B., and Vezzoli, L. (1999). Quaternary stratigraphy of distal tephra layers in the Mediterranean—an overview. *Glob. Planet. Change* 21 (1-3), 31–50. doi:10.1016/s0921-8181(99)00006-5

Niewöhner, C., Hensen, C., Kasten, S., Zabel, M., and Schulz, H. (1998). Deep sulfate reduction completely mediated by anaerobic methane oxidation in sediments of the upwelling area off Namibia. *Geochimica Cosmochimica Acta* 62 (3), 455–464. doi:10.1016/s0016-7037(98)00055-6

Palano, M., Ferranti, L., Monaco, C., Mattia, M., Aloisi, M., Bruno, V., et al. (2012). GPS velocity and strain fields in Sicily and southern Calabria, Italy: updated geodetic constraints on tectonic block interaction in the central Mediterranean. *J. Geophys. Res. Solid Earth* 117 (B7). doi:10.1029/2012jb009254

Panieri, G., Polonia, A., Lucchi, R., Zironi, S., Capotondi, L., Negri, A., et al. (2013). Mud volcanoes along the inner deformation front of the Calabrian Arc accretionary wedge (Ionian Sea). *Mar. Geol.* 336, 84–98. doi:10.1016/j.margeo.2012.11.003

Pape, T., Geprägs, P., Hammerschmidt, S., Wintersteller, P., Wei, J., Fleischmann, T., et al. (2014). Hydrocarbon seepage and its sources at mud volcanoes of the Kumano forearc basin, Nankai Trough subduction zone. *Geochem. Geophys. Geosystems* 15 (6), 2180–2194. doi:10.1002/2013gc005057

Pape, T., Haeckel, M., Riedel, M., Kölling, M., Schmidt, M., Wallmann, K., et al. (2020a). Formation pathways of light hydrocarbons in deep sediments of the Danube deep-sea fan, Western Black Sea. *Mar. Petroleum Geol.* 122, 104627. doi:10.1016/j.marpetgeo.2020.104627

Pape, T., Kasten, S., Zabel, M., Bahr, A., Abegg, F., Hohnberg, H.-J., et al. (2010). Gas hydrates in shallow deposits of the Amsterdam mud volcano, Anaximander Mountains, Northeastern Mediterranean Sea. *Geo-Marine Lett.* 30 (3), 187–206. doi:10.1007/s00367-010-0197-8

Pape, T., Ruffine, L., Hong, W. L., Sultan, N., Riboulot, V., Peters, C. A., et al. (2020b). Shallow gas hydrate accumulations at a Nigerian deepwater pockmark—quantities and dynamics. *J. Geophys. Res. Solid Earth* 125 (9), e2019JB018283. doi:10.1029/2019jb018283

Paull, C. K., Dallimore, S., Caress, D., Gwiazda, R., Melling, H., Riedel, M., et al. (2015). Active mud volcanoes on the continental slope of the Canadian Beaufort Sea. *Geochem. Geophys. Geosystems* 16 (9), 3160–3181. doi:10.1002/2015gc005928

Pfender, M., and Villinger, H. (2002). Miniaturized data loggers for deep sea sediment temperature gradient measurements. *Mar. Geol.* 186 (3-4), 557–570. doi:10.1016/s0025-3227(02)00213-x

Planke, S., Svensen, H., Hovland, M., Banks, D., and Jamtveit, B. (2003). Mud and fluid migration in active mud volcanoes in Azerbaijan. *Geo-Marine Lett.* 23 (3), 258–268. doi:10.1007/s00367-003-0152-z

Polonia, A., Bonatti, E., Camerlenghi, A., Lucchi, R. G., Panieri, G., and Gasperini, L. (2013a). Mediterranean megaturbidite triggered by the AD 365 Crete earthquake and tsunami. *Sci. Rep.* 3 (1), 1285. doi:10.1038/srep01285

Polonia, A., Romano, S., Çağatay, M., Capotondi, L., Gasparotto, G., Gasperini, L., et al. (2015). Are repetitive slumpings during sapropel S1 related to paleo-earthquakes? *Mar. Geol.* 361, 41–52. doi:10.1016/j.margeo.2015.01.001

Polonia, A., Torelli, L., Mussoni, P., Gasperini, L., Artoni, A., and Klaeschen, D. (2011). The Calabrian Arc subduction complex in the Ionian Sea: regional architecture, active deformation, and seismic hazard. *Tectonics* 30 (5), TC5018. doi:10.1029/2010tc002821

Prada, M., Ranero, C. R., Sallarès, V., Grevemeyer, I., de Franco, R., Gervasi, A., et al. (2020). The structure of Mediterranean arcs: new insights from the Calabrian Arc subduction system. *Earth Planet. Sci. Lett.* 548, 116480. doi:10.1016/j.epsl.2020.116480

Praeg, D., Ceramicola, S., Barbieri, R., Unnithan, V., and Wardell, N. (2009). Tectonically-driven mud volcanism since the late Pliocene on the Calabrian accretionary prism, central Mediterranean Sea. *Mar. Petroleum Geol.* 26 (9), 1849–1865. doi:10.1016/j.marpetgeo.2009.03.008

Revil, A. (2002). Genesis of mud volcanoes in sedimentary basins: a solitary wave-based mechanism. *Geophys. Res. Lett.* 29 (12). doi:10.1029/2001gl014465

Römer, M., Sahling, H., Pape, T., dos Santos Ferreira, C., Wenzhöfer, F., Boetius, A., et al. (2014). Methane fluxes and carbonate deposits at a cold seep area of the Central Nile Deep Sea Fan, Eastern Mediterranean Sea. *Mar. Geol.* 347, 27–42. doi:10.1016/j.margeo.2013.10.011

Rosenbaum, G., Lister, G. S., and Duboz, C. (2002). Reconstruction of the tectonic evolution of the western Mediterranean since the Oligocene. *J. Virtual Explor.* 8, 107–130. doi:10.3809/jvirtex.2002.00053

Rossi, S., and Sartori, R. (1981). A seismic reflection study of the external Calabrian Arc in the northern Ionian Sea (eastern Mediterranean). *Mar. Geophys. Res.* 4 (4), 403–426. doi:10.1007/bf00286036

Roveri, M., Flecker, R., Krijgsman, W., Lofi, J., Lugli, S., Manzi, V., et al. (2014). The Messinian Salinity Crisis: past and future of a great challenge for marine sciences. *Mar. Geol.* 352, 25–58. doi:10.1016/j.margeo.2014.02.002

Sahling, H., Bohrmann, G., Artemov, Y. G., Bahr, A., Brüning, M., Klapp, S. A., et al. (2009). Vodyanitskii mud volcano, Sorokin trough, Black Sea: geological characterization and quantification of gas bubble streams. *Mar. Petroleum Geol.* 26 (9), 1799–1811. doi:10.1016/j.marpetgeo.2009.01.010

Sartori, R. (2003). The Tyrrhenian back-arc basin and subduction of the Ionian lithosphere. *Episodes* 26 (3), 217–221. doi:10.18814/epiiugs/2003/v26i3/011

Sauter, E. J., Muyakshin, S. I., Charlou, J.-L., Schlüter, M., Boetius, A., Jerosch, K., et al. (2006). Methane discharge from a deep-sea submarine mud volcano into the upper water column by gas hydrate-coated methane bubbles. *Earth Planet. Sci. Lett.* 243 (3-4), 354–365. doi:10.1016/j.epsl.2006.01.041

Schulz, H. N., and Schulz, H. D. (2005). Large sulfur bacteria and the formation of phosphorite. *Science* 307 (5708), 416–418. doi:10.1126/science.1103096

Seeberg-Elverfeldt, J., Schlüter, M., Feseker, T., and Kölling, M. (2005). Rhizon sampling of porewaters near the sediment-water interface of aquatic systems. *Limnol. Oceanogr. Methods* 3 (8), 361–371. doi:10.4319/lom.2005.3.361

Serpelloni, E., Vannucci, G., Pondrelli, S., Argnani, A., Casula, G., Anzidei, M., et al. (2007). Kinematics of the Western Africa-Eurasia plate boundary from focal mechanisms and GPS data. *Geophys. J. Int.* 169 (3), 1180–1200. doi:10.1111/j.1365-246x.2007.03367.x

Somoza, L., Medialdea, T., León, R., Ercilla, G., Vázquez, J. T., Hernández-Molina, J., et al. (2012). Structure of mud volcano systems and pockmarks in the region of the Ceuta Contourite Depositional System (Western Alborán Sea). *Mar. Geol.* 332, 4–26. doi:10.1016/j.margeo.2012.06.002

Spakman, W. (1986). Subduction beneath Eurasia in connection with the Mesozoic Tethys. *Neth. J. Geosciences/Geologie en Mijnbouw* 65, 145–153.

Stadnitskaia, A., Ivanov, M. K., Poludetkina, E. N., Kreulen, R., and van Weering, T. C. (2008). Sources of hydrocarbon gases in mud volcanoes from the Sorokin Trough, NE Black Sea, based on molecular and carbon isotopic compositions. *Mar. Petroleum Geol.* 25 (10), 1040–1057. doi:10.1016/j.marpetgeo.2007.08.001

Strasser, M., Kölling, M., dos Santos Ferreira, C., Fink, H. G., Fujiwara, T., Henkel, S., et al. (2013). A slump in the trench: tracking the impact of the 2011 Tohoku-Oki earthquake. *Geology* 41 (8), 935–938. doi:10.1130/g34477.1

Suess, E., Torres, M., Bohrmann, G., Collier, R., Greinert, J., Linke, P., et al. (1999). Gas hydrate destabilization: enhanced dewatering, benthic material turnover and large methane plumes at the Cascadia convergent margin. *Earth Planet. Sci. Lett.* 170 (1-2), 1–15. doi:10.1016/s0012-821x(99)00092-8

Tishchenko, P., Hensen, C., Wallmann, K., and Wong, C. S. (2005). Calculation of the stability and solubility of methane hydrate in seawater. *Chem. Geol.* 219 (1-4), 37–52. doi:10.1016/j.chemgeo.2005.02.008

Villinger, H., and Davis, E. E. (1987). A new reduction algorithm for marine heat flow measurements. *J. Geophys. Res. Solid Earth* 92 (B12), 12846–12856. doi:10.1029/jb092ib12p12846

Villinger, H. W., Tréhu, A. M., Grevemeyer, I., Andreassen, K., Mienert, J., Bryn, P., et al. (2010). "Seafloor marine heat flux measurements and estimation of heat flux from seismic observations of bottom simulating reflectors," in *Geophysical characterization of gas hydrates*. Editors Riedel, M., Willoughby, E. C., and Chopra, S. (Society of Exploration Geophysicists), 279–300. doi:10.1190/1.9781560802197.ch18

Whiticar, M. J. (1999). Carbon and hydrogen isotope systematics of bacterial formation and oxidation of methane. *Chem. Geol.* 161 (1-3), 291–314. doi:10.1016/S0009-2541(99)00092-3

Wortel, M., and Spakman, W. (2000). Subduction and slab detachment in the Mediterranean-Carpathian region. *Science* 290 (5498), 1910–1917. doi:10.1126/science.290.5498.1910

Wulf, S., Kraml, M., and Keller, J. (2008). Towards a detailed distal tephrostratigraphy in the Central Mediterranean: the last 20,000 yrs record of Lago Grande di Monticchio. *J. Volcanol. Geotherm. Res.* 177 (1), 118–132. doi:10.1016/j.jvolgeores.2007.10.009

Zanchetta, G., Sulpizio, R., Roberts, N., Cioni, R., Eastwood, W. J., Siani, G., et al. (2011). Tephrostratigraphy, chronology and climatic events of the Mediterranean basin during the Holocene: an overview. *Holocene* 21 (1), 33–52. doi:10.1177/0959683610377531

Zecchin, M., Praeg, D., Ceramicola, S., and Muto, F. (2015). Onshore to offshore correlation of regional unconformities in the Plio-Pleistocene sedimentary successions of the Calabrian Arc (central Mediterranean). *Earth-Science Rev.* 142, 60–78. doi:10.1016/j.earscirev.2015.01.006

frontiers | Frontiers in Earth Science

TYPE Original Research
PUBLISHED 30 November 2023
DOI 10.3389/feart.2023.1232302

Check for updates

OPEN ACCESS

EDITED BY
Stéphanie Dupré,
Institut Français de Recherche pour l'Exploitation de la Mer, France

REVIEWED BY
Luis Somoza,
Instituto Geológico y Minero de España (IGME), Spain
Juan I. Soto,
The University of Texas at Austin, United States

*CORRESPONDENCE
Miho Asada,
asada.miho@aist.go.jp

RECEIVED 31 May 2023
ACCEPTED 11 October 2023
PUBLISHED 30 November 2023

CITATION
Asada M, Yamashita M, Fukuchi R, Yokota T, Toki T, Ijiri A and Kawamura K (2023), Identification of a large mud volcano field in the Hyuga-nada, northern end of the Ryukyu trench, offshore Japan.
Front. Earth Sci. 11:1232302.
doi: 10.3389/feart.2023.1232302

COPYRIGHT
© 2023 Asada, Yamashita, Fukuchi, Yokota, Toki, Ijiri and Kawamura. This is an open-access article distributed under the terms of the Creative Commons Attribution License (CC BY). The use, distribution or reproduction in other forums is permitted, provided the original author(s) and the copyright owner(s) are credited and that the original publication in this journal is cited, in accordance with accepted academic practice. No use, distribution or reproduction is permitted which does not comply with these terms.

Identification of a large mud volcano field in the Hyuga-nada, northern end of the Ryukyu trench, offshore Japan

Miho Asada[1]*, Mikiya Yamashita[1], Rina Fukuchi[2], Toshiyuki Yokota[1], Tomohiro Toki[3,4], Akira Ijiri[5,6] and Kiichiro Kawamura[7]

[1]Geological Survey of Japan, National Institute of Advanced Industrial Science and Technology (AIST), Ibaraki, Japan, [2]Graduate School of Education, Naruto University of Education, Tokushima, Japan, [3]Department of Chemistry, Biology and Marine Science, Faculty of Science, University of the Ryukyus, Okinawa, Japan, [4]Research Institute for Humanity and Nature, Kyoto, Japan, [5]Graduate School of Maritime Sciences, Kobe University, Kobe, Japan, [6]Kochi Institute for Core Sample Research, Institute for Extra-cutting-edge Science and Technology Avant-garde Research (X-Star), Japan Agency for Marine-Earth Science and Technology (JAMSTEC), Kochi, Japan, [7]Graduate School of Science and Technology for Innovation, Yamaguchi University, Yamaguchi, Japan

We identified 27 new mud volcanoes, including potential ones, in a part of the Hyuga-nada area, southwest offshore Japan, at the northern end of the Ryukyu Trench, based on subseafloor geological structures using geophysical investigations. These mud volcanoes exhibited high density and breadth and were likely connected to other mud volcano fields in the south. Acoustic investigations indicated subseafloor structures. Multiple acoustically transparent bodies were interpreted as a region containing gas. They were likely to appear along faults and below the bottom of valleys and sometimes reached the seafloor, expressing mud volcanoes onto the seafloor. They also indicated the wide distribution of subseafloor free-gas throughout the area. These acoustic investigations suggested that a swarm of mud volcanoes exists over the Hyuga-nada area, heterogeneously distributed along a series of plate convergent margins, the Nankai Trough, and the northern part of the Ryukyu Trench.

KEYWORDS

mud volcano, Hyuga-nada, Kumano Basin, three-dimensional reflection seismic survey, sub-bottom profiler, subseafloor structure

1 Introduction

Mud volcanoes are a surface expression of moving sediment and fluid from the Earth's depths to the surface. Mud volcanoes can only be certified when mud diapirs reach the surface and change the topography (Milkov, 2000; Dimitrov, 2002; Kopf, 2002). Mud volcanoes have been used as subsurface oil and natural gas reservoir indicators because they were initially observed in oilfields (Bates and Jackson, 1987). Despite the name "volcano" being reminiscent of a hot and mountain-like structure, the definition of the mud volcano does not include high temperature any specific landform because they are formed by sediment and the shape is determined by the viscosity of the extrudes which varies with the water content (Shih, 1967; Brown, 1990; Hamada et al., 2009). Mud volcanoes have been reported worldwide from sediment basins, along convergent margins, delta systems of large rivers with high sedimentation rates, inland seas, lakes, and geothermal fields (Milkov, 2000;

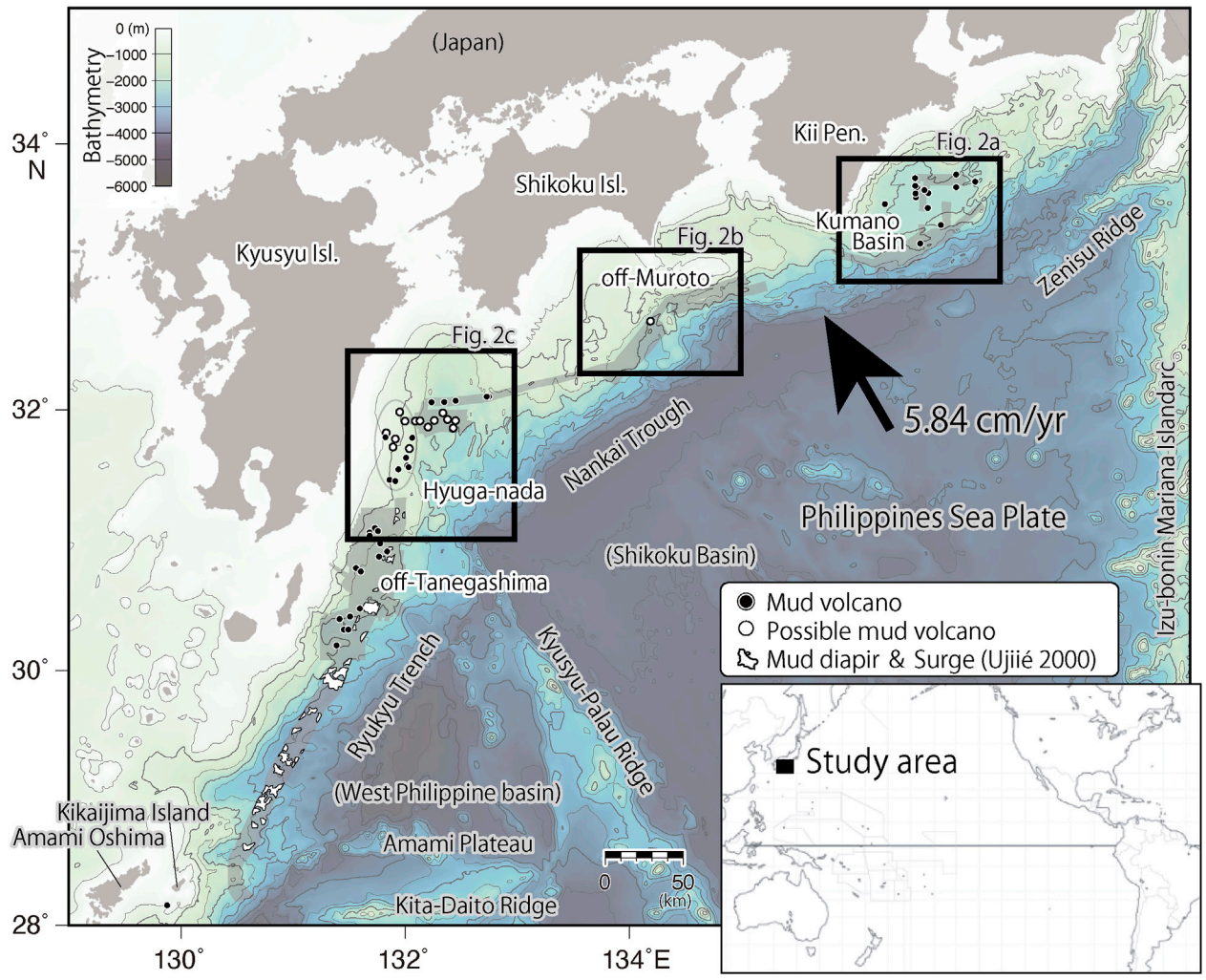

FIGURE 1
Bathymetry map of the study area. Circles: mud volcanoes (white) and potential mud volcanoes (black) in the Kumano Basin (Kopf et al., 2013; Pape et al., 2014; Asada et al., 2021), off-Muroto (this study), Hyuga-nada (this study), mud volcanoes in off-Tanegashima (Inagaki et al., 2018). Polygon: mud diapir and surge off Tanegashima to off-Amami Oshima (Ujiié, 2000), and mud volcano off-Kikaijima (Sato and Itaki, 2015); black arrow: direction of the Pacific Plate convergence relative to the Eurasian Plate (DeMets et al., 2010). The isobath contour interval is 100 m. The black boxes on the map indicate the location of Figures 2A–C.

Dimitrov, 2002; Kopf, 2002; 2016; Mazzini and Etiope, 2017). Thus, mud volcanoes are considered to be constructed under a compressional stress field. To make mud and fluid move upward from depths to the surface, gravitational instability and/or buoyancy sources such as heat and gas are required as driving forces (Milkov, 2000; Dimitrov, 2002; Kopf, 2002; 2016; Mazzini and Etiope, 2017). In particular, gas is necessary for buoyancy during the formation of mud diapirs that reach the Earth's surface (Brown, 1990). Over 98% of land mud volcanoes discharge methane gas (Milkov, 2005). Deformation and decreasing strength of rocks under the compressional stress field can be a driving or triggering force for mud volcanism (Soto et al., 2021a; b). Seismic activities that occur nearby can also trigger mud volcanisms (Manga et al., 2009; Wang and Manga, 2021).

Because mud volcanoes transport mud and fluids from the depths to the surface, heat and elements discharged from mud volcanoes sometimes harm living organisms (as observed for the Lusi mud volcano, Sidoarjo, Indonesia) and may result in pollution. Mud volcanoes can sometimes trigger tsunamis if located offshore and have explosive characteristics, resulting in large slump-generating waves. Thus, mud volcanoes are considered a potential submarine geohazard, and this is a reason why attention should be paid to them (URL1). Moreover, mud volcanoes can discharge fluid and living organisms from the subseafloor (e.g., Hoshino et al., 2017); they can affect the submarine environment and be a stepstone for the propagation and distribution of chemosynthetic ecosystems. These are the reasons why we want to determine an accurate distribution of offshore mud volcanoes.

Japan, located along a convergent plate margin, has large and a few small mud volcano fields in offshore areas and on land, respectively. Previous studies of offshore mud volcanoes in Japan have mainly focused on the Kumano Basin, a forearc basin in the Nankai Trough (Figure 1). Within the Kumano Basin, a swarm of 14 mud volcanoes, comprising a large mud volcano field, has been reported (Kuramoto et al., 2001; Pape et al., 2014; Asada et al., 2021)

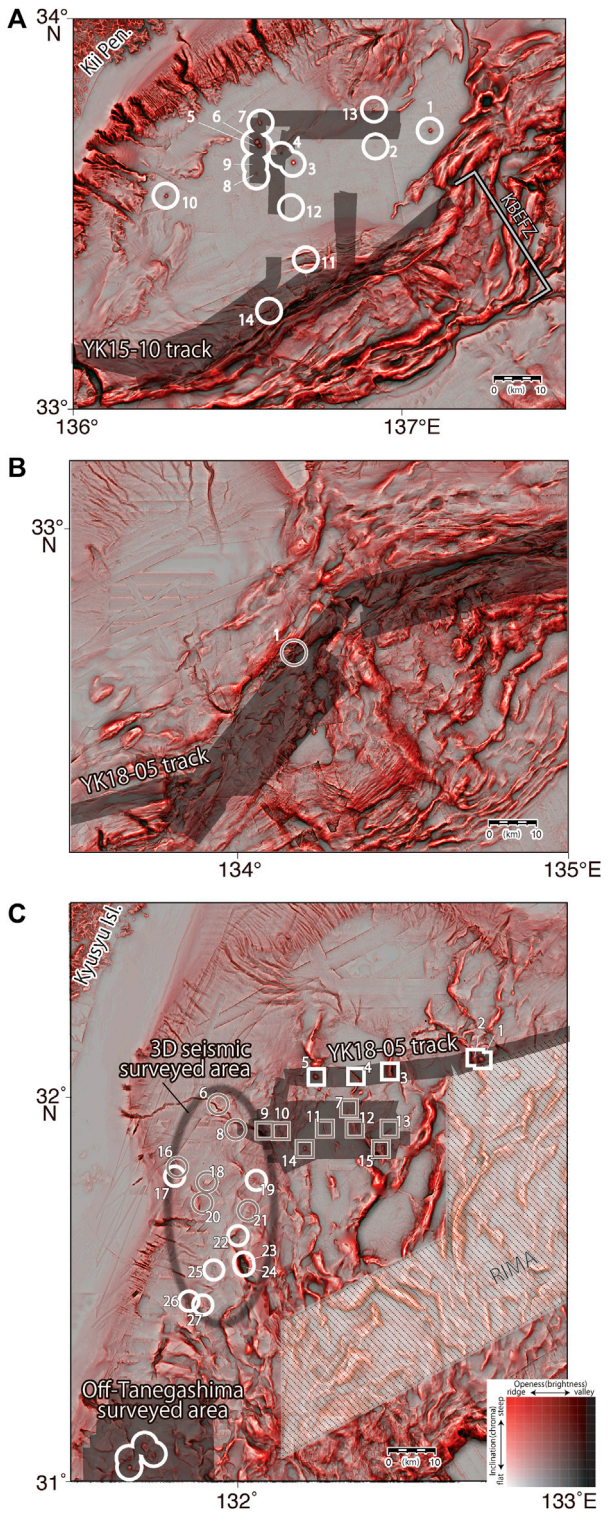

FIGURE 2
Location of mud volcanoes on Red Relief Image Maps. Gray-colored narrow belts indicate areas in which acoustic mapping has been performed during two cruises (YK15-10 and YK18-05). **(A)** Kumano Basin. Circles and numbers indicate known mud volcanoes (Kopf et al., 2013; Pape et al., 2014, 1a). KBEFZ: Kumano Basin Edge Fault Zone (Martin et al., 2010). **(B)** off-Muroto. Circle: a potential mud volcano. **(C)** Hyuga-nada. The 13 open boxes indicate the location of the newly identified mud volcanoes including potential ones, confirmed using an SBP, and the 14 open circles indicate mud

(*Continued*)

FIGURE 2 (Continued)
volcanoes identified using seismic profiles, respectively. White symbol: mud volcano with distinguished high backscatter intensity (square) or with subseafloor feature (circle); gray symbols: potential mud volcano with unclear features. Number: a newly certified number in this study. RIMA: restricted area because it is used by the U.S. Navy for training purposes.

(Figure 2). Geochemical (Tsunogai et al., 2012; Toki et al., 2013; Pape et al., 2014; Nishio et al., 2015; Menapace et al., 2017; Ijiri et al., 2018a; b; Lalk et al., 2022), geophysical (Martin et al., 2010; Strasser et al., 2011; Tsuji et al., 2014; Moore et al., 2015), and other investigations have been conducted in the area. Bottom simulating reflectors (BSRs), seismic reflections nearly parallel to the seafloor, are significant indicators of subseafloor free-gas distribution and have been reported through the Kumano Basin.

Our research target area, the Hyuga-nada (Figure 1), is another offshore and scientifically underrepresented location positioned at the intersection of two trenches, the Nankai Trough and the Ryukyu Trench, in the eastern offshore region of Kyushu Island. Mud volcanoes in the Hyuga-nada were first identified around the 2000s during the installation of submarine cables by a telecommunication company; however, to date, academic investigations have yet to be performed.

We report 27 newly identified mud volcanoes in the Hyuga-nada area, including mud volcano candidates. We defined new mud volcanoes based on whether their conduit reached the seafloor on subseafloor profiles obtained from three-dimensional (3D) seismic surveys or sub-bottom profilers (SBP). Moreover, bathymetric expressions and backscatter intensity on the seafloor in the surrounding area where the conduit reached the seafloor sometimes helped recognize new mud volcanoes. Furthermore, we propose that the huge mud volcano field (a swarm of multiple mud volcanoes) encompassing the Hyuga-nada and areas further south, which are off Tanegashima, and the region toward Kikai-jima Island (Ujiié, 2000; Nakayama et al., 2010; Inagaki et al., 2018) are established along the Ryukyu Trench (Figure 1). The series of mud volcano fields may be the largest mud volcano field in offshore areas of Japan.

2 Geological setting

2.1 Mud volcano

Mud volcano fields can be found worldwide in Azerbaijan (both on land and offshore oilfields) (Planke et al., 2003; Yusifov and Rabinowitz, 2004), Cadiz Bay (offshore sedimentary field; e.g., Somoza et al., 2003; Van Rensbergen et al., 2005), southwest Taiwan (both on land and offshore sedimentary fields; Shih, 1967; Chuang et al., 2010; Sun et al., 2010; Doo et al., 2015), northeast New Zealand (both on land and offshore sedimentary fields; Ridd, 1970; Leighton et al., 2022), Barbados (offshore sedimentary field; Brown and Westbrook, 1987; Lance et al., 1998; Summer and Westbrook, 2001), and in the Kumano Basin in Japan (offshore sedimentary fields) for instance. The mud volcano is sometimes used in geothermal fields (e.g., Yellowstone in the US, LUSI in Indonesia, and Rotorua in New Zealand). However, this phenomenon is rather confusing because mud volcanoes are not

formed from magmatic rocks like many other volcanoes in the region but from buoyant sediments owing to gases and heat. Mud volcanoes frequently appear along existing geological structures such as faults and fissures (Bonini, 2012; Soto et al., 2021a; Soto et al., 2021b) and anticline (Shih, 1967; Hamada et al., 2009). Nevertheless, not all faults, fissures, and ridges accompany mud volcanoes. Knowledge of the characteristics of seismic signals (Soto et al., 2021a; Soto et al., 2021b; Hudec and Soto, 2021), which visualize conduits below the mud volcanoes, is essential to understanding the depths; however, knowledge on the origin of conduits remains limited. Several studies have discussed planar distribution and original depths of conduits by comparing sediments with geological data (Miyakawa et al., 2013). The planar distribution of mud volcanoes can be easily investigated on land, but it is difficult offshore because they sometimes display tiny geophysical features. Geophysical investigations have indicated the presence of conduits just below mud volcanoes, which can be evidence of sediment movement from the depths toward and reaching the surface (Van Rensbergen et al., 2005; Deville et al., 2006; Feyzullayev, 2012; Asada et al., 2021; Soto et al., 2021a; Soto et al., 2021b; Hudec and Soto, 2021; Kirkham and Cartwright, 2022). We sometimes need to use several methods to verify mud volcanoes.

2.2 Geology along southwest Japan from the Kumano Basin to Hyuga-nada

The Philippine Sea Plate subducts beneath southwest Japan, along the eastern edge of the Eurasian Plate at the Nankai Trough and the Ryukyu Trench (Figure 1). The Nankai Trough is notorious for large earthquakes triggered by the subducting Philippine Sea Plate, which subducts at a rate of approximately 5.84 cm/yr (DeMets et al., 2010). The Kumano forearc basin is located along the eastern part of the Nankai Trough (Figure 2A) and is a sedimentary basin with a thickness of > ~1 km overlying the accretionary complex (Moore et al., 2015; Ramirez et al., 2015). The bathymetry within the basin undergoes a minimal change across tens of kilometers across the area. The basin's south-eastern (oceanward) edge, known as the Kumano Basin Edge Fault Zone, is characterized by its steep geometry (Martin et al., 2010). The distribution and geochemical characteristics of mud volcanoes in the Kumano Basin have been reported in previous studies based on results from the scientific drilling vessel Chikyu (Japan Agency for Marine-Earth Science and Technology) (Nishio et al., 2015; Ijiri et al., 2018a; b).

The fluid discharged from several mud volcanoes in the Kumano Basin is mostly methane gas of biogenic and thermogenic origins. The depth from which this methane gas originated is approximately 1 km below the seafloor (near the bottom of the sedimentary basin of the Kumano Basin) for biogenic gas, and several kilometers below the seafloor (within the accretionary prism) for thermogenic gas, respectively (Pape et al., 2014; Ijiri et al., 2018b; Wiersberg et al., 2018). Additionally, fluid originating from the depth of the mantle wedge, possibly deeper than approximately 30 km below the seafloor, is included within the discharged fluid from mud volcanoes in the Kumano Basin (Nishio et al., 2015). Sediments discharged from mud volcanoes are considered to have originated at depths of a few kilometers below the seafloor (near the basement rocks of the sedimentary basin; Ijiri et al., 2018a), suggesting that the depths from which fluids and sediment are sourced are not necessarily the same.

The ancient accretionary complex, named the Shimanto Belt, formed between the Cretaceous and Paleogene periods is exposed onshore of southwestern Japan parallel to the trench axis in the Nankai Trough (e.g., Taira et al., 1992; Moore and Saffer, 2001; Kawabata et al., 2007). Industrial operation of gas fields is performed along the eastern coast of Kyusyu Island, which is adjacent to the western onshore area of the Hyuga-nada, based on the accretionary complex. Gas products from onshore gas fields indicate that the gas has a mixed origin and is both biogenic and thermogenic and is released upon mining from 150 to 1700 m below the surface (Kato et al., 2011). The original stratigraphy and reservoir of the onshore gas fields consist of late Miocene sediments (Kato et al., 2011) belonging to the accretionary complex and continue to dip steeply oceanward (Okamura, 2008). The narrow shelf along Kyusyu Island is tens of kilometers wide. There is a forearc basin named the Miyazaki-oki Basin with a rough bathymetry, which is unlike that of the Kumano Basin. Deformation structures, such as faults and folds, can be recognized on the offshore geological map and seismic profiles (Okamura, 2008).

3 Data acquisition

3.1 3D seismic reflection data

Subseafloor geological structures were obtained from 3D seismic reflection surveys conducted between 2009 and 2013 by domestic oil and natural gas explorations in the eastern offshore area of Kyushu Island. Since disclosing specifics of the exploration is forbidden, we cannot provide more details; however, seismic profiles showed high-quality subseafloor structures to depths of ~3500~4000 ms in two-way travel time below the seafloor, which sufficiently supports the purpose of this research. The dominant frequency of the seismic waves at the seafloor was ~35 Hz, corresponding to a wavelength of –40 m when the sound wave velocity was 1,500 m/s (Figure 3). The frequency within 10 dB from the peak frequency was in the range between ~ 15 and 60 Hz, with a corresponding vertical resolution of ~ 4–25 m ($\lambda/4$). The bin size of the profiles ranged from approximately ten to several tens of meters the inline and crossline, and each bin contained 10 or more reflection points. The acquired seismic data were processed with a series of data processing steps centered on 3D pre-stack time migration.

3.2 Acoustic mapping through the YK15-10 and YK18-05 cruises

An acoustic investigation using a shipboard SBP for shallow subseafloor structures (EdgeTech, 3300-HM, 2–16 kHz, for shallow subseafloor structures) and a shipboard multi-beam echo sounder for mapping (Kongsberg, EM122, 12 kHz, for bathymetry and backscatter intensity) was conducted during research cruises in 2015 (YK15-10, URL2) and 2018 (YK18-05, URL3) along southwest offshore Japan, over the areas connecting the Kumano Basin and Hyuga-nada areas (Figure 1). Bathymetry data and backscatter intensity were obtained along the same survey lines as the sub-bottom profiles. The sub-bottom

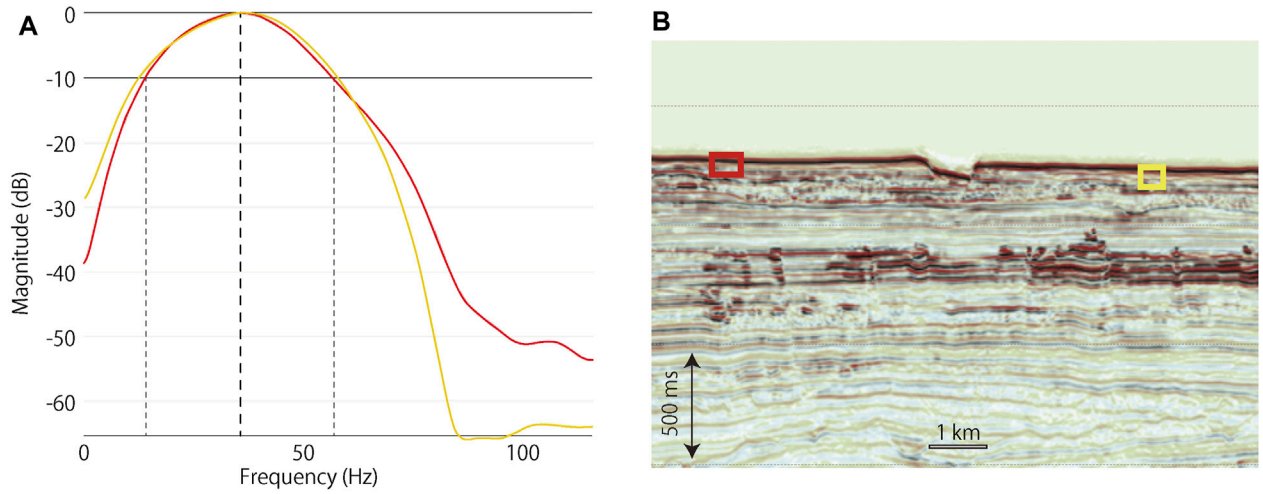

FIGURE 3
Results from the frequency analysis. **(A)** Frequency spectrum distribution of reflected waves on the seafloor. Red and yellow lines show the results of the frequency analysis performed at the location of the boxes in the same color in **(B)**. **(B)** Seismic profile. Frequency spectrum analysis was performed at the position of each box, indicating a simple and flat seafloor. The color of the box corresponds to the colored line in **(A)**.

profiles displayed shallow subseafloor structures down to ~ 60 ms of two-way travel time below the seafloor. The SBP transmits a single conical acoustic signal per ping, thus it only detects the structure just below the survey lines (Figure 4).

3.3 Bathymetric visualization

The compiled bathymetry data (Yamashita et al., 2017) were used to observe surface expressions in the area in which the acoustically transparent body touched the seafloor in the Hyuga-nada or the locations of known mud volcanoes in the Kumano Basin reported by previous studies (Kuramoto et al., 2001; Pape et al., 2014; Asada et al., 2021). Figures 2, 5 display bathymetry maps using a 3D presentation technique called the Red Relief Image Map (RRIM) (Chiba et al., 2007; 2008). RRIM is an elaborate illumination-independent 3D visualization method that uses high-density and high-resolution digital elevation model (DEM) data to extract the slope, concavities, and convexities from a given zenith (Chiba et al., 2007; 2008). In RRIM, a change in the slope angle is represented by a red-to-white color variation and concavities and convexities by grayscales, which enhances the characteristics of bathymetric features such as small-scale deformations. The source of the bathymetric data for our target area was compiled from acoustic mapping data provided by Yamashita et al. (2017), which does not include backscatter intensity.

4 Interpretations of acoustic investigations

4.1 Methods for recognizing mud volcanoes in the Hyuga-nada

We identified conduits that appeared transparent with few reflected waves ("acoustically transparent body") in the sub-bottom and 3D seismic profiles to identify subseafloor moving sediment. The acoustically transparent body is mostly a vertical structure which sometimes cuts through the stratigraphy from the depths toward the surface. If there are no sediment layers on top of the acoustically transparent body, we inferred that the location of the point of the acoustically transparent body reaching the seafloor is a point of extrusion, and the bathymetric feature at the point is a surface expression of it, a mud volcano. At the same time, if the top of the acoustically transparent body is covered by sediment layers, it should not be a mud volcano and might be a mud diapir and/or a part of a compressional ridge. The identification of "Christmas-tree structures" (a typical subseafloor structure below mud volcanoes, which refers to the penetration of a lateral part of the acoustically transparent body into the surrounding stratigraphy) contributed to the identification of the subseafloor structure forming the mud volcano.

The bathymetric feature with high backscatter intensity suggests fluid discharge from the seafloor. The higher backscatter intensity on the seafloor indicates harder materials such as outcrops and/or animals with hard shells. This is because hard materials generate larger jumps in acoustic impedance than the surrounding sediment (Asada and Yokota, 2021). Chemosynthetic shelled animal communities often inhabit fluids discharged from the seafloor. Methane-derived authigenic carbonates (MDACs; Hovland et al., 1987; Buckman et al., 2020; Aloisi et al., 2002) are also generated in such areas due to the reaction between seawater and methane gas, and they contribute to generating higher backscatter intensity of acoustic signals (Ceramicola et al., 2018). Consequently, the detection of high backscatter intensities has been used historically for the exploration of mud volcanoes (e.g., Van Rensbergen et al., 2005; Blondel, 2009; Ceramicola et al., 2018; Asada et al., 2021). Circular patterns of high backscatter intensities support the identification of locations in which fluid is discharged from a point source. Bathymetry is often useful in identifying mud volcanoes, however, due to the resolution limits of

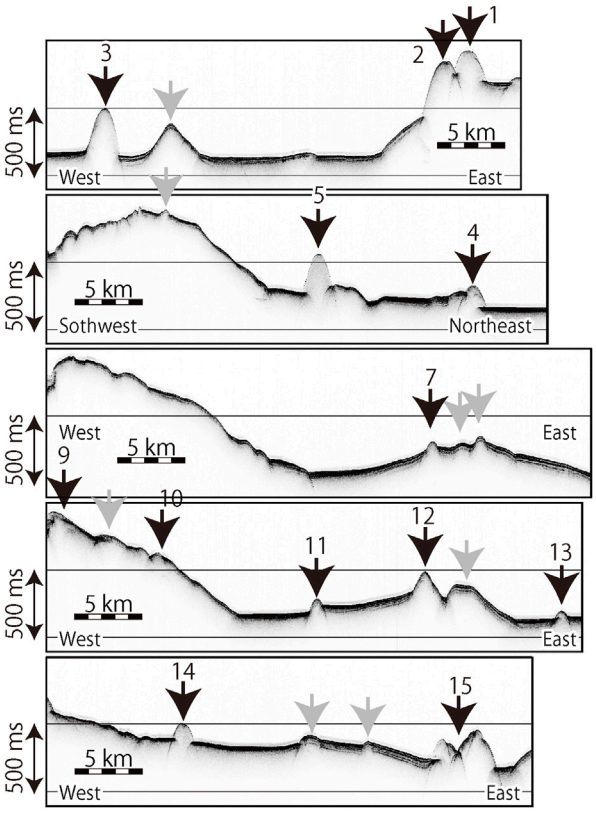

FIGURE 4
Subseafloor structures obtained by the SBP, in the Hyuga-nada area, for HyMV1–5, 7, and 9–15. Darker colors indicate a higher amplitude. Black arrow: mud volcano; gray arrow: anticline. Vertical exaggeration is ~2.0. The horizontal lines (on both left and right panels) are spaced 500 ms in two-way time.

geophysical surveys, its accuracy is not always sufficient to indicate bathymetric changes in the seafloor.

4.2 Mud volcanoes in the Kumano Basin

Based on previous studies, we have summarized the bathymetric characteristics of mud volcanoes in the Kumano Basin (Kopf et al., 2013; Pape et al., 2014; Asada et al., 2021; Table 1). A total of 14 mud volcanoes have been reported in the Kumano Basin, and they have been numbered based on the order of their discovery (Figure 2A). They are distributed on the relatively flat basin floor and mostly classified as the "pancake type" with a mean surface gentle slope angle of <10° (Kioka and Ashi, 2015).

Depths (Pape et al., 2014) at the top of a small hill. The small and remarkably steep KMV14 shows a local inclination exceeding 30°, indicating high ejecta viscosity. Asada et al. (2021) suggested that KMV14 may have fault gouges because it is located in the Kumano Basin Edge Fault Zone (Martin et al., 2010).

A remarkably high backscatter intensity was observed near the mud volcano KMV14, where gas discharge had been reported (Menapace et al., 2017; Asada et al., 2021; Asada and Yokota, 2021). The high backscatter intensity of KMV5, a known active mud volcano discharging fluids (Nishio et al., 2015; Ijiri et al., 2018a; b), displays a circular pattern (Figure 5, KMV5 and 6), indicating an area influenced by fluid discharged from a point source.

4.3 Mud volcanoes off Muroto, the area connecting the Kumano Basin and Hyuga-nada

Acoustic mapping with sub-bottom profiles connecting the Kumano Basin and Hyuga-nada areas was obtained during the YK18-05 cruise (Figure 1). The survey line was designed along a constant depth of ~2,000 m, roughly the same depth as that of the mud volcanoes in the Kumano Basin, to maintain a stable acoustic signal output power level. This survey enables us to compare the observed backscatter intensities between different areas. Only one potential mud volcano was identified along the connecting area, marked by a notably high backscatter intensity and an isolated hill slightly off-nadir of SBP (Figure 2B). The high backscatter intensity shows a characteristic three-way branching resembling the tip of a chicken foot (Figure 5, MuMV1). The isolated hill is located at the heel of the chicken foot, and the high backscatter intensity distributes flow downward to increase water depth. The hill is located along the fault zone in the off-Muroto area. Because MuMV1 was slightly off-nadir, the shallow subseafloor structures could not be obtained, so we designated the isolated hill as a "potential" mud volcano.

4.4 Mud volcanoes in the Hyuga-nada

We identified 27 mud volcanoes including potential ones in the Hyuga-nada, based on a subseafloor acoustically transparent body reaching the seafloor (Figures 4, 5, HyMV1–27). HyMV1–5, 17, 19, and 22–27 have distinctive subsurface features; thus, we propose that they are mud volcanoes (Figure 2C, white open symbols). At the same time, subseafloor features below HyMV6–16, 18, 20, and 21 were weak and required more verification using other methods such as the dating of sampling materials; nevertheless, they are new potential mud volcanoes (Figure 2C, gray open symbols). These mud volcanoes show a dense distribution within the surveyed area. Several other bathymetric features were detected outside the seismically studied area and off the survey line of SBP, suggesting the presence of other mud volcanoes in the area. Most mud volcanoes in the Hyuga-nada were identified on slopes; therefore, it is difficult to define their exact diameter and inclination.

Sub-bottom profiles display acoustically transparent bodies cutting through the sediment layers at shallow depths. In this study, if the stratigraphy was not cut by acoustically transparent bodies or a shallow sedimentary layer was found on top of these bodies, thus not reaching the seafloor at present, they were not considered mud volcanoes (gray arrows in Figure 4). A circular to semi-circular high backscatter intensity pattern was recognized around HyMV5, 9, and 15 (Figure 5). Partially high backscatter intensities reflect a patchy distribution of relatively harder materials on the seafloor and/or shallow subseafloor, suggesting the existence of hard rocks and/or shelled animals due to fluid discharge from the seafloor. Although the bathymetric expression was distinct at HyMV1, 10, and 14, the backscatter intensity is relatively low. This

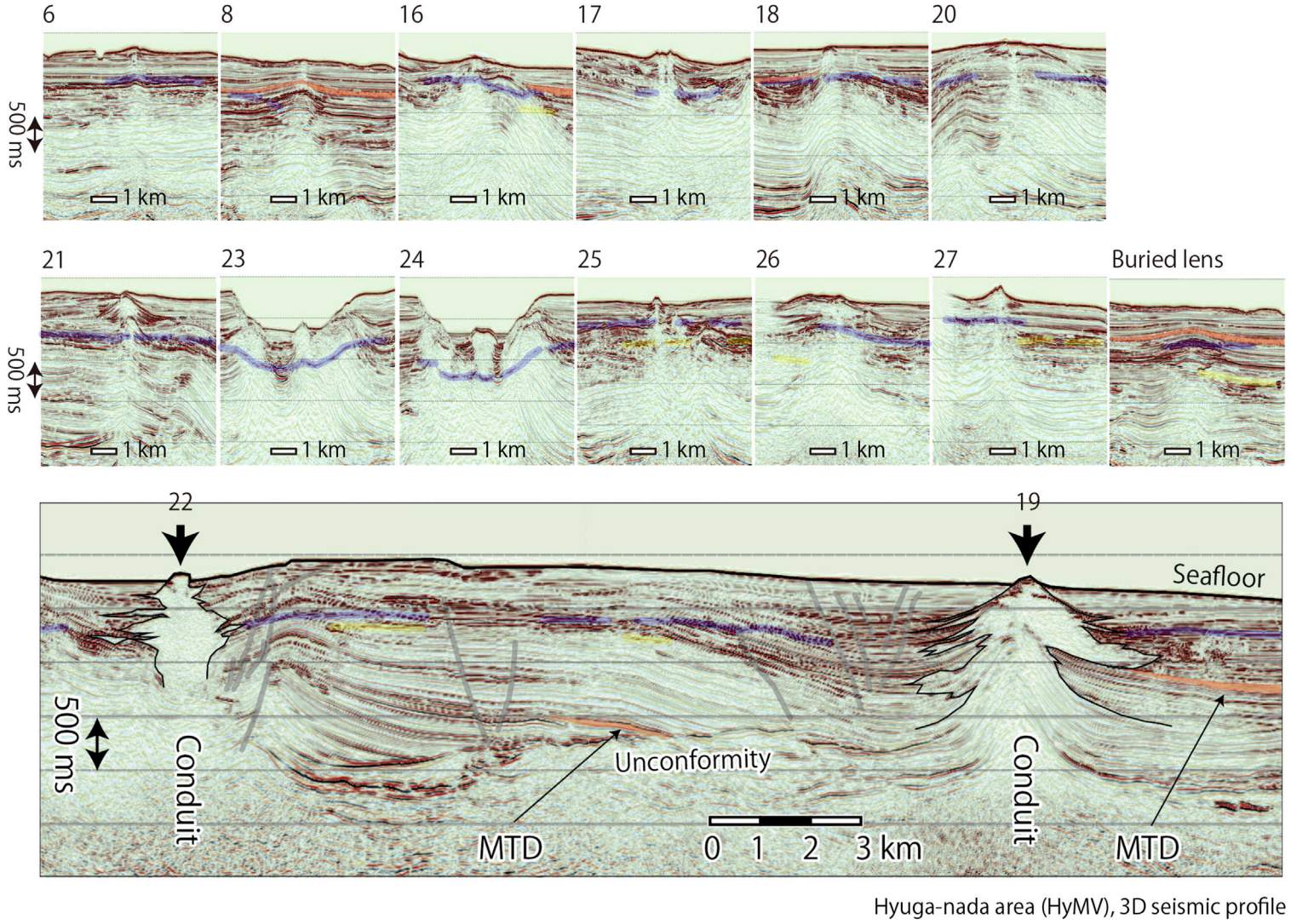

FIGURE 5
Subseafloor structures obtained by the seismic reflection survey in the Hyuga-nada area, for HyMV6, 8, and 16–27. The horizontal lines (on both left and right panels) are spaced 500 ms in two-way time. Bold lines indicate BSRs (blue: shallowest BSR, yellow: second BSR). Orange area indicates layer or block with internal chaotic facies. Vertical exaggeration is ~4.0.

10.3389/feart.2023.1232302

TABLE 1 Center location, depth, and remarks regarding the bathymetric features of mud volcanoes, including potential ones, in the Kumano Basin, off-Muroto, and Hyuga-nada areas based on the bathymetry map drawn by the RRIM shown in Figure 6. If no bathymetric feature was found in the bathymetry map, only the location of the point at which the acoustic transparent body reaches the seafloor (determined by the profiles shown in Figures 4, 5) is shown in the table. The basis of the location is shown in the remarks, 1: Pape et al. (2014); 2: Asada et al. (2021); 3: this study, positions from the sub-bottom profile; and 4: this study, positions from the 3D reflection seismic profile.

Area	Name	Longitude	Latitude	Top depth	Max. depth	Max. Local inclination	Max. Diameter	Basis of the location and characteristics of mud volcanoes
The Kumano Basin	KMA1	137.0875	33.7139	1846	1984	14	1,140	1
	2	136.9208	33.6750	1999	2014	5	900	1
	3	136.6708	33.6333	1951	2066	8	1,010	1
	4	136.6339	33.6561	1981	2064	24	520	1
	5	136.5669	33.6767	1902	2060	19	1,140	1
	6	136.5597	33.6847	1923	2055	15	1,690	1
	7	136.5681	33.7333	1936	2015	14	1,280	1
	8	136.5572	33.6042	2031	2065	10	710	1
	9	136.5589	33.6319	2048	2060	3	1,010	1
	10	136.2822	33.5478	1825	1953	18	860	1
	11	136.7078	33.3881	2009	2050	30	300	1
	12	136.6675	33.5236	2061	2062	2	210	1, subtle high
	13	136.9153	33.7683	1879	1960	15	560	1, keyhole-shape high
	14	136.5972	33.2522	1923	1956	30	420	2, peninsula
Off-Muroto	MuMV1	134.1689	32.6778	1994	2030	12	490	3
The Hyuga-nada	HyMV1	132.7417	32.0983	1,346	1,585	29	1,580	3
	2	132.7225	32.1019	1,363	1780	31	1,580	3, irregular shape along fault scarp
	3	132.4667	32.0764	1,623	1880	15	1,690	3, ridge along fault scarp
	4	132.3708	32.0417	1742	1900	20	1,060	3, L-shaped ridge
	5	132.2439	32.0528	1,605	1820	27	1,300	3
	6	131.9486	31.9819	890	930	7	900	4, nearly round shape along the valley
	7	132.3439	31.9583	1763	1850	11	810	3, irregular-shaped ridge
	8	131.9917	31.9083	1,130	Unable to define outline of mud volcano			4, part of the valley floor
	9	132.0833	31.9125	1,443	1,560	18	880	3
	10	132.1389	31.9150	1,622	1,675	10	550	3
	11	132.2717	31.9167	1883	1945	10	700	3
	12	132.3592	31.9250	1729	1860	8	1,620	3
	13	132.4556	31.9022	1883	1985	19	1,030	3
	14	132.2114	31.8669	1824	1910	12	960	3
	15	132.4389	31.8625	1828	1980	12	1,200	3, X-shaped ridge
	16	131.8231	31.8283	609	640	6	650	4
	17	131.8156	31.7967	568	Unable to define outline of mud volcano			4, small peninsula
	18	131.9086	31.7800	855	Unable to define outline of mud volcano			4
	19	132.0569	31.7867	1,270	1,324	9	510	4
	20	131.8906	31.7172	870	Unable to define outline of mud volcano			4, part of slope
	21	132.0356	31.7083	1,197	Unable to define outline of mud volcano			4, small peninsula
	22	132.0069	31.6417	1,285	1,305	5	380	4
	23	132.0236	31.5744	1,574	1,615	8	580	4, in a depression like a bean pod
	24	132.0283	31.5628	1,595	1,635	5	790	4, in a depression like a bean pod
	25	131.9272	31.5542	1,141	Unable to define outline of mud volcano			4, small peninsula
	26	131.8558	31.4722	869	Unable to define outline of mud volcano			4, round shape on scarp
	27	131.8919	31.4586	1,043	1,135	10	2000	4

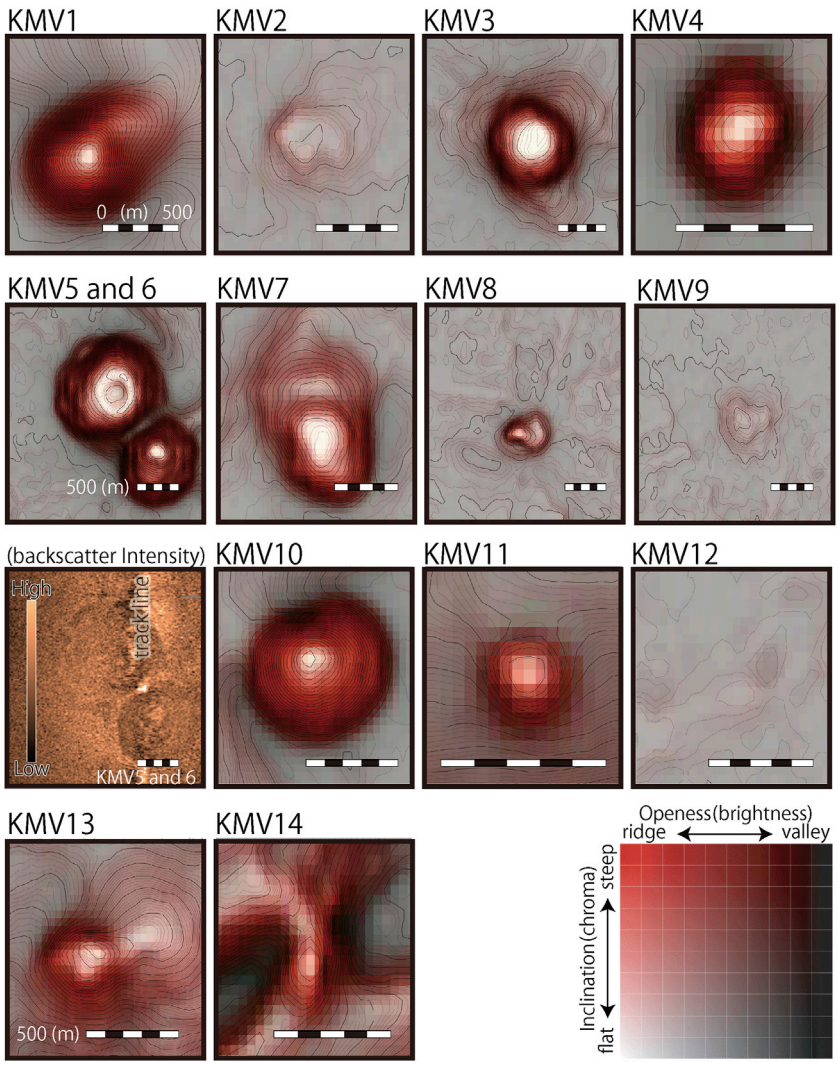

FIGURE 6
(Continued).

suggests that HyMV1, 10, and 14 are mostly covered by sediment similar to that covering the surrounding seafloor, which indicates ceased fluid discharge. HyMV2–4, 7, and 11–13 stand on acoustically transparent bodies; however, their bathymetric expression and the backscatter intensity were not distinct, thus they were categorized as potential mud volcanoes.

Seismic profiles provide the fine structure of the deeper subseafloor (Figure 5). The shallower part of the profile shows a horizontally traceable stratigraphy. The attenuation of seismic waves weakens the intensity of reflection waves in areas deeper than 1,000 ms below the seafloor. The lateral continuity of the stratigraphy is more prominent landward, and deformation increases oceanward. A layer and/or a block with chaotic facies inside bounded by a well-continuous upper and lower stratigraphy are interpreted as a result of mass transport which occurred during the geological timescales. The blocks are especially interpreted as a part of mass transport deposits (MTDs), whose internal geometry and configuration can be used to reconstruct the kinematics of the sediment (Moore et al., 2015; Lackey et al., 2018; Figure 5). Some MTDs had a duplex structure within their internal facies, which is interpreted as deformation due to the horizontal shortening of stratigraphy. Unlike MTDs, the lenticular bodies show mostly transparent interiors and lack duplex structures inside (Figure 5, HyMV20 and buried lens). Lenses are occasionally situated at the upper end of the acoustically transparent body and reach the seafloor. Acoustically transparent bodies were likely to appear along a ridge of gentle anticlines (HyMV8, 16, 18–21, 25, 26), places at which the stratigraphy changes depth, likely due to being faulted (HyMV17, 22, 27), and below the bottom of a valley (HyMV23, 24). Sometimes the acoustically transparent body included a weak stratigraphy dragged upward.

BSRs were widely distributed throughout the area (Figure 5). They occurred sub-parallel to the seafloor, with a high-amplitude and reverse polarity of seismic waves from the seafloor (Figure 5, blue line). BSRs became continuous and clearer oceanward. In places, two and three BSRs were identified (Figure 5, yellow line).

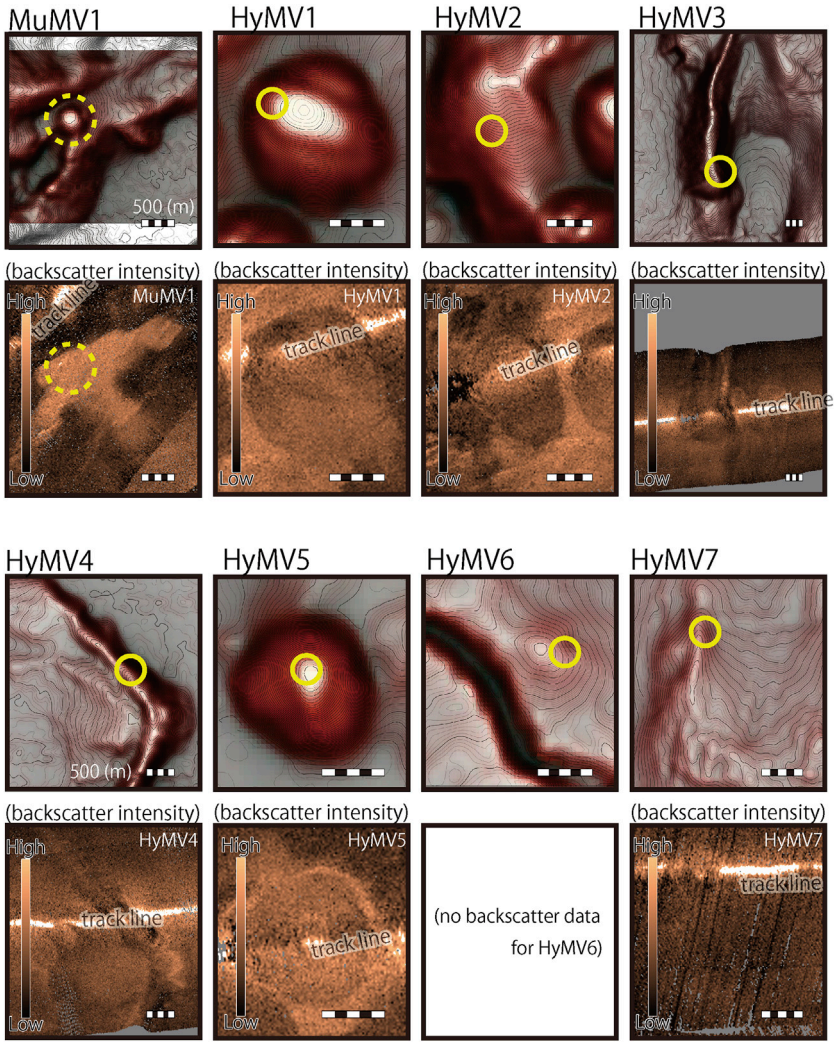

FIGURE 6
(Continued).

In this case, the shallowest BSR shows relatively good lateral continuity, and the second and third ones tend to be discontinuous and weak. Most mud volcanoes were accompanied by BSRs in and around the underlying acoustically transparent bodies.

Acoustically transparent bodies reaching the seafloor could be especially clear below HyMV17, 19, and 22–27, which had bathymetric expressions on the seafloor. Seismic profiles showed a Christmas-tree structure at the side of the acoustically transparent bodies, especially below HyMV19–22 (Figure 5). The acoustically transparent bodies below HyMV6, 8, 16, 18, and 25–27 were relatively weak and narrow. The acoustically transparent bodies become less distinct at greater depths, and their bottom could not be identified. The magnified bathymetry map around the location at which subseafloor structures reached the seafloor (Figure 6) shows various bathymetric expressions such as hills or ridges with various backscatter intensities. Some of them (HyMV8, for example) lacked distinct bathymetric features.

5 Discussion

5.1 A large mud volcano field in the Hyuga-nada

The Hyuga-nada is located ~100 km eastward from the onshore industrial gas field on Kyusyu Island. As the source stratigraphy of the gas field is inclined oceanward (Okamura, 2008), the gas field is expected to extend to the Hyuga-nada. The 3D reflection seismic profiles showed that BSRs were widely distributed over the surveyed area and became more pronounced oceanward; thus, gas-bearing fluids are also expected to spread over the area of interest. The mud volcanoes identified in the Hyuga-nada displayed a variety of bathymetric features: mounds and ridges with various sizes and inclinations. Furthermore, some of these topographical features could not be detected within the observation accuracy. Additional mounds outside the observed area suggest the

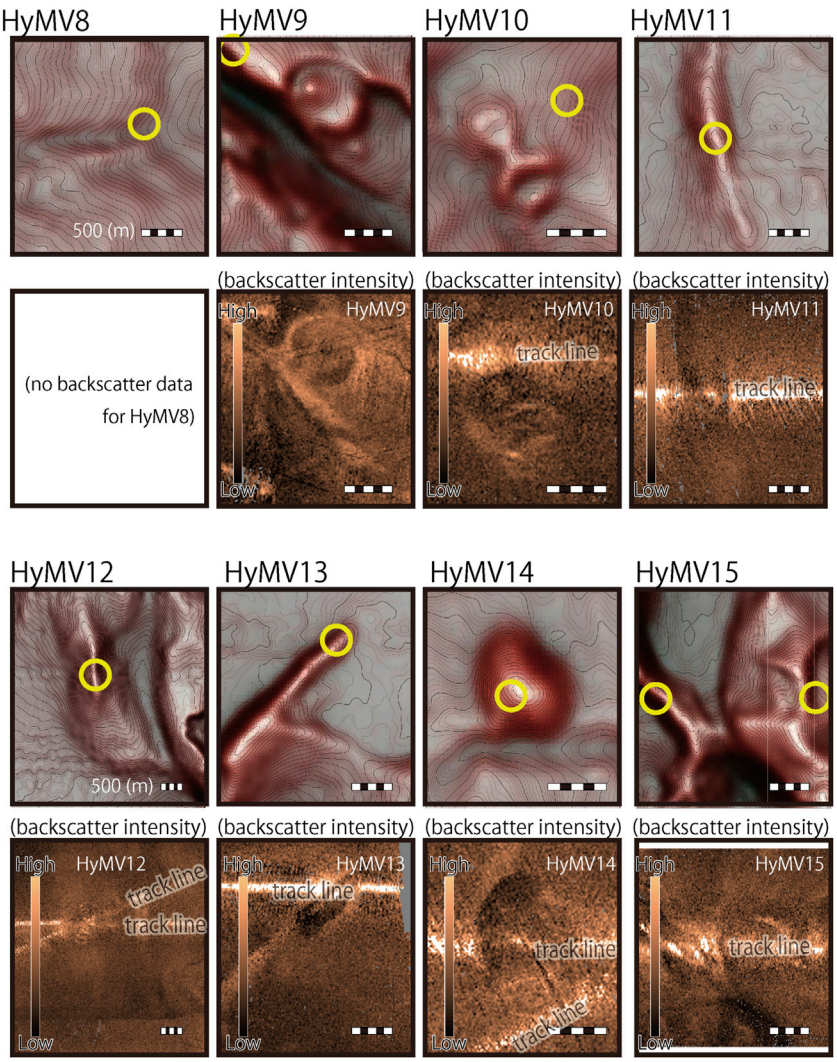

FIGURE 6
(Continued).

presence of more mud volcanoes in the target area. Including potential ones, we suspect the number, density, and area of mud volcanoes covering the Hyuga-nada to be extensive, possibly much larger than those covering the Kumano Basin. Moreover, the mud volcano field in the Hyuga-nada may extend toward southern areas. Ujiié (2000) reported a wide-ranging distribution of "mud diapir and surge" along the landward slope of the Ryukyu Trench, extending off-Tanegashima and southward (Figure 1). Other scientific research cruises conducted in the off-Tanegashima region, which lies on the southern side of the Hyuga-nada, reported that a group of mud volcanoes had been discovered in that area (Hoshino et al., 2017; Inagaki et al., 2018). Itaki et al. (2015, 2017) and Sato and Itaki (2015) reported at least one mud volcano and 11 similar bathymetric features off-Kikai-jima area (Figure 1) based on the results of acoustic mapping and sediment sampling. The huge area from the Hyuga-nada to off-Kikai-jima may contain a large mud volcano field.

5.2 Characteristics of mud-volcano conduits based on seismic profiles

Acoustically transparent bodies nearly correspond to "mobile shales" (Soto et al., 2021a; b; Hudec and Soto, 2021), nearly vertical conduits below mud volcanoes that cut the stratigraphy. Soto et al. (2021a) mentioned that shales become mobile owing to increasing overpressure and shear and then reduce the rock strength. They reviewed physical properties indicated by seismic characteristics and reported that sediment had decreased porosity, phase change of clay minerals, and smectite to illite transformation with increasing depth and temperature. Gas, another main component of discharged elements by mud volcanoes worldwide, is generated thermogenically at greater depths (and then migrate upward) and biologically at shallower depth; thus, changes in gas saturation within sediments affect acoustic impedance and can be detected in seismic signals (Soto et al., 2021a). The seismic profiles shown in Figures 3, 5 that reach down to a depth of several hundred meters (~a few kilometers deep

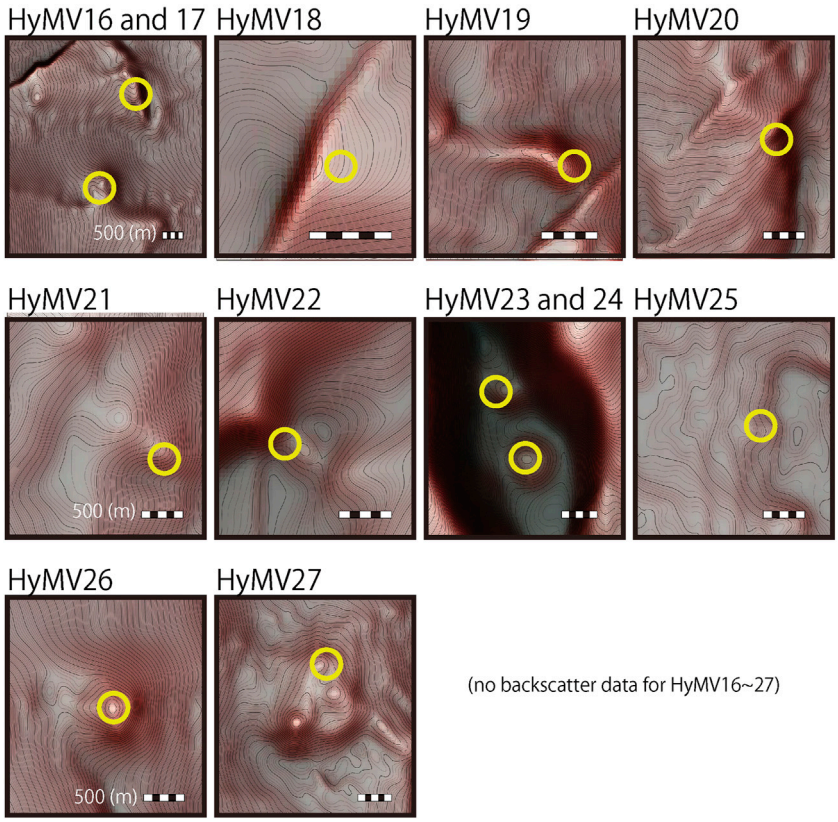

FIGURE 6
(Continued). Closeup bathymetric maps of mud volcanoes and their candidates, shown as isobath contour lines (1-m depth intervals) on Red Relief Image Maps (Yamashita et al., 2017). KMV1–KMV14: mud volcano in the Kumano Basin. The backscatter intensity obtained by the YK15-10 cruise (URL2) is shown below KMV5 and 6. MuMV1: a potential mud volcano in the off-Muroto area (yellow dotted circle). The backscatter intensity obtained by the YK18-05 cruise is shown below MuMV1. HyMV1–27: mud volcano in the Hyuga-nada area. The backscatter intensity obtained by the YK18-05 cruise (URL3) is shown below HyMV1–5, 7, and 9–15. Circles on HyMV1–27 show the location of the mud volcano, which are indicated by points where acoustic transparent bodies reach the seafloor (Figure 4). The center location and morphological features in Table 1 are based on this map of bathymetrically recognized features. Continuing from Figure 6, HyMV1–8, HyMV6, and 8 are in the area of seismic observation; thus, there is no backscatter strength image. Continuing from Figure 5, HyMV9–15. Continuing from Figure 5, HyMV16–27 are in the area of seismic observation; thus, there is no backscatter strength image.

below the seafloor) may indicate such a change in physical properties, although we cannot confirm this suggestion without having *in-situ* and geophysical data at depth.

Acoustically transparent bodies represent a part of the transparent interior of seismic or sub-bottom profiles from which weak signals are returned and where nearly no stratigraphy exists inside. As discussed by Brown (1990), all conduits reaching the seafloor require buoyancy containing gas. In addition, as discussed by Domenico (1976), the transparent acoustic nature suggests that the gas within the body absorb seismic waves. Acoustically transparent bodies can also occur in other scenarios, such as in the absence of any structure (no density-velocity contrast) within the body or reflection of all seismic energy at the top. The former is quite likely when a conduit lacks the inner layered structure. Even in that case, it is natural to assume that the gas is not necessarily contained in the entire acoustically transparent body but only in a part of the conduit. In contrast, the reflection of all energy at the top of acoustically transparent bodies in this study was unlikely, as there were no remarkable high-amplitude parts at the top of these bodies. Therefore, it is reasonable for us to assume that a gas field exists in the background of our target area, and the condition is an important setting for forming mud volcano fields. The existence of multiple BSRs in this field (Figure 5) implies a continuous gas supply, thus supporting this idea.

5.3 Heterogeneous distribution of mud volcano field along offshore southwest Japan

The acoustic investigations connecting the Kumano basin and Hyuga-nada did not reveal the existence of any other dense mud volcano field within the area covered by our acoustic investigation (Figure 2B). Only one potential mud volcano was found in the off-Muroto area, which is located in a fault zone. It is an isolated hill with a high backscatter intensity and a steep surface slope angle. Although we could not clearly identify the isolated hill as a mud volcano because we did not have data on the subseafloor structure nor samplings, the distinctive bathymetric expression implies that the hill consists of a highly viscous sediment captured fault gouge along the fault zone,

similar to KMV14 in the KBEFZ (Asada et al., 2021). The distinctive high backscatter intensity over the hill suggests that large amounts of fluid are discharged at present and may cultivate shelled animals and carbonate rocks. Thus, we expect the isolated hill to be a mud volcano. However, no other similar features that could be considered mud volcanoes were found nearby.

No swarm of mud volcanoes in the off-Muroto area indicates a heterogeneous distribution of mud volcano fields (with a blank area from the Kumano basin to Hyuga-nada) under a series of convergent plate margins. We expect that the subseafloor environment of the off-Muroto area differs from the Kumano and Hyuga-nada areas, which may explain the heterogeneity in the mud volcano fields. The Kumano Basin and the potentially vast area extending from the Hyuga-nada toward the south are in a similar tectonic setting: subducting seamounts are present, i.e., Paleo-zenisu and related seamounts are subducting under the Kumano Basin, and the Kyusyu-Palau Ridge and related ridges and plateaus are subducting under the Hyuga-nada and regions further south (Figure 1). Subducting volcanic and sedimentary rocks are widely encountered in other mud volcano fields worldwide; for example, the Gagua ridge near the southwest part of Taiwan, the northern part of Hikurangi part of New Zealand, and the oceanic plate (does not accompany thick hemipelagic sediment) below Barbados and the Bay of Cadiz, on a regional scale. The subduction of seamounts results in a higher number of volcanic rocks that are a source of clay minerals, which are the main component of mud volcanoes in the Kumano Basin (Menapace et al., 2017; Ijiri et al., 2018a), rather than pelagic sediments (Kameda et al., 2011; 2017). Further, the formation of local stress fields owing to the bumpy surface of subducting seamounts may contribute to the formation of mud volcanoes. In other words, clay minerals may be needed to form swarms of mud volcanoes. Moreover, subseafloor temperature, the chemical environment, and loading conditions at depth may characterize the subseafloor environment. In other words, satisfying compressional stress fields and relatively large amounts of gas discharge along convergent plate margins are insufficient for forming the swarm of mud volcanoes, and other subseafloor conditions are required. Such characteristic subseafloor environments may contribute to other geological phenomena, such as crustal deformation and/or slip. The heterogeneous distributions of mud volcanoes may thus be used as indicators of deep and local subseafloor geological conditions, which may be difficult to visualize using geophysical surveys or sediment core samplings.

6 Conclusion

Faults, folds, lenses, MTDs, BSRs, and other geological subseafloor structures were located across the target area. The deformation of stratigraphy increased, and BSRs became clearer oceanward. We identified new mud volcanoes, including potential ones, in the Hyuga-nada by analyzing subseafloor structures indicated by seismic and sub-bottom profiles. In the Hyuga-nada, abundant mud volcanoes show a dense distribution and are considered extensive in the area toward the south, connected to the off-Tanegashima and off-Kikai-jima areas. However, mud volcanoes may be scarce in the connecting area between the Kumano Basin and the Hyuga-nada, suggesting heterogeneous distribution of the mud volcano fields along the series of convergent margins, the Nankai Trough and the northern part of the Ryukyu Trench, off the southwest coast of Japan.

Data availability statement

The datasets presented in this study can be found in online repositories. The names of the repository/repositories and accession number(s) can be found below: YK15-10 cruise data: https://doi.org/10.17596/0001663 (URL2) and YK18-05 cruises data: https://doi.org/10.17596/0002693 (URL3), respectively.

Author contributions

MA and TY contributed to the conception and design of this study. MA designed this work, organized the wo research cruises (YK15-10 and YK18-05), and contributed to acoustic data processing. RF contributed to the description of the onshore geological setting and discussion. TY was responsible for the process of obtaining permission to publish the 3D seismic data and drawings. TT and AI contributed to the discussions of the off-Tanegashima mud volcano field. KK contributed to the discussion and provided general information on mud volcano studies. All authors contributed to the article and approved the submitted version.

Funding

This study was supported by the Japan Society of the Promotion of Science KAKEN from fiscal years 2016–2018 ending on 31 March 2019.

Acknowledgments

We are grateful to the two reviewers and editor for their constructive comments. This study was in a part based on data from the off-Miyazaki area's domestic oil and natural gas survey, led by the Ministry of Economy, Trade, and Industry (METI), Japan. The Generic Mapping Tools software was used to generate bathymetric maps (Wessel and Smith, 1998).

Conflict of interest

The authors declare that the research was conducted in the absence of any commercial or financial relationships that could be construed as a potential conflict of interest.

Publisher's note

All claims expressed in this article are solely those of the authors and do not necessarily represent those of their affiliated organizations, or those of the publisher, the editors and the reviewers. Any product that may be evaluated in this article, or claim that may be made by its manufacturer, is not guaranteed or endorsed by the publisher.

References

Aloisi, G., Bouloubassi, I., Heijs, S. K., Pancost, R. D., Pierre, C., Sinninghe Damste, J. S., et al. (2002). CH_4-consuming microorganisms and the formation of carbonate crusts at cold seeps. *Earth Planet. Sci. Lett.* 203, 195–203. doi:10.1016/S0012-821X(02)00878-6

Asada, M., Moore, G. F., Kawamura, K., and Noguchi, T. (2021). Mud volcano possibly linked to seismogenic faults in the Kumano Basin, Nankai Trough, Japan. *Mar. Geophys. Res.* 42, 4. doi:10.1007/s11001-020-09425-7

Asada, M., and Yokota, T. (2021). A case study on the penetration difference of acoustic signals into sediment due to frequency based on backscatter strength distribution obtained along the Kumano Basin Edge Fault Zone. *Proc. 14th SEGJ Int. Symp.*, AS-01. doi:10.1190/segj2021-001.1

Bates, R. L., and Jackson, J. A. (1987). *Glossary of Geology*. 3rd edition. American Geological Institute, 788.

Blondel, P. (2009). "7. Continental margins," in *The Handbook od SIDESCAN SONAR*. Editor P. Blondel (Springer), 147–183.

Bonini, M. (2012). Mud volcanoes: indicators of stress orientation and tectonic controls. *Earth-Sci. Rev.* 115, 121–152. doi:10.1016/j.earscirev.2012.09.002

Brown, K. M. (1990). The nature and hydrogeologic significance of mud diapirs and diatremes for accretionary systems. *J. Geophys. Res. B Solid Earth* 95, 8969–8982. doi:10.1029/jb095ib06p08969

Brown, K. M., and Westbrook, G. K. (1987). The tectonic fabric of the Barbados Ridge accretionary complex. *Mar. Petrol. Geol.* 4, 71–81. doi:10.1016/0264-8172(87)90022-5

Buckman, J., Donnelly, T., Jiang, Z., Lewis, H., and Ruffell, A. (2020). Methane derived authigenic carbonate (MDAC) aragonite cemented quaternary hardground from a methane cold seep, Rathlin Basin, Northern Ireland: $\delta^{13}C$ and $\delta^{18}O$ isotopes, environment, porosity and permeability. *Geoscence* 10, 255. doi:10.3390/geosciences10070255

Ceramicola, S., Dupre, S., Somoza, L., and Woodside, J. (2018). "Cold seep systems," in *Submarine geomorphology*. Editors A. Micallef, S. Krastel, and A. Savini (Springer Nature), 367–387. doi:10.1007/978-3-319-57852-1_19

Chiba, T., Kaneda, S., and Suzuki, Y. (2008). Red relief image map: new visualization method for three dimensional data. *ISPRS Ann. Photogramm. Remote Sens. Spat. Inf. Sci.* 37, 1071–1076.

Chiba, T., Suzuki, Y., and Hiramatsu, T. (2007). Digital terrain representation methods and red relief image map, a new visualization approach. *J. Jpn. Cartogr. Assoc. "Map"*. 45 (1), 27–36. doi:10.11212/jjca1963.45.27

Chuang, P.-C., Yang, T. F., Hong, W.-L., Lin, S., Sun, C.-H., Lin, A. T.-S., et al. (2010). Estimation of methane flux offshore SW Taiwan and the influence of tectonics on gas hydrate accumulation. *Geofluids* 10, 497–510. doi:10.1111/j.1468-8123.2010.00313.x

DeMets, C., Gordon, R. G., and Argus, D. F. (2010). Geologically current plate motions. *Geophys. J. Int.* 181, 1–80. doi:10.1111/j.1365-246x.2009.04491.x

Deville, E., Guerlais, S. H., Callec, Y., Griboulard, R., Huyghe, P., Lallemant, S., et al. (2006). Liquefied vs stratified sediment mobilization processes: insight from the South of the Barbados accretionary prism. *Tectonophysics* 428, 33–47. doi:10.1016/j.tecto.2006.08.011

Dimitrov, L. I. (2002). Mud volcanoes—the most important pathway for degassing deeply buried sediments-The most important pathway for degassing deeply buried sediments. *Earth Sci. Rev.* 59, 49–76. doi:10.1016/s0012-8252(02)00069-7

Domenico, S. N. (1976). Effect of brine-gas mixture on velocity in an unconsolidated sand reservoir. *Geophysics* 41, 882–894. doi:10.1190/1.1440670

Doo, W. B., Hsu, S. K., Lo, C.-L., Chen, S. C., Tsai, C. H., Lin, J. Y., et al. (2015). Gravity anomalies of the active mud diapirs off southwest Taiwan. *Geophys. J. Int.* 203, 2089–2098. doi:10.1093/gji/ggv430

Feyzullayev, A. A. (2012). Mud volcanoes in the South Caspian basin: nature and estimated depth of its products. *Nat. Sci.* 04, 445–453. doi:10.4236/ns.2012.47060

Hamada, Y., Tanaka, K., and Miyata, Y. (2009). Geologic structure and geochemistry of Taiwanese mud volcanoes. *J. Geogr.* 118, 408–423. (in Japanese with English abstract). doi:10.5026/jgeography.118.408

Hoshino, T., Toki, T., Ijiri, A., Morono, Y., Machiyama, H., Ashi, J., et al. (2017). Atribacteria from the subseafloor sedimentary biosphere disperse to the hydrosphere through submarine mud volcanoes. *Fron. Microbiol.* 8, 1135. doi:10.3389/fmicb.2017.01135

Hovland, M., Talbot, M. R., Qvale, H., Olaussen, S., and Aasberg, L. (1987). Methane-related carbonate cements in pockmarks of the North Sea. *J. Sed. Petrol.* 57, 881–892. doi:10.1306/212F8C92-2B24-11D7-8648000102C1865D

Hudec, M. R., and Soto, J. I. (2021). Piercement mechanisms for mobile shales. *Basin Res.* 33, 2862–2882. doi:10.1111/bre.12586

Ijiri, A., Iijima, K., Tsunogai, U., Ashi, J., and Inagaki, F. (2018a). Clay mineral suites in submarine mud volcanoes in the Kumano forearc basin, Nankai Trough: constraints on the origin of mud volcano sediments. *Geosci* 8, 220. doi:10.3390/geosciences8060220

Ijiri, A., Inagaki, F., Kubo, Y., Adhikari, R. R., Hattori, S., Hoshino, T., et al. (2018b). Deep-biosphere methane production stimulated by geofluids in the Nankai accretionary complex. *Sci. Adv.* 4, eaao4631–15. doi:10.1126/sciadv.aao4631

Inagaki, F., Ijiri, A., Kitada, K., and Machiyama, H. (2018). Interactions between biogenic gas and microbial activity in the subseafloor– Frontiers in scientific ocean drilling. *J. Jpn. Assoc. Petrol. Technol.* 83, 130–137. (in Japanese with English abstract). doi:10.3720/japt.83.130

Itaki, T., Sato, T., Inoue, T., Amano, A., and Tanaka, Y. (2015). "Characteristics of bottom sediments collected from the submarine caldera off south of the Kikai-jima Island," in Annual Meet. Geol. Soc. Japan (northern Ryukyu Arc. *Abstract* 158.

Itaki, T., Sato, T., Inoue, T., Amano, A., and Tanaka, Y. (2017). *Mud volcano distributed around the kikai-jima Island, northern Ryukyu arc*. JpGU-AGU Joint Meet. *Abstract,* SGL-34–05.

Kameda, J., Inoue, S., Tanikawa, W., Yamaguchi, A., Hamada, Y., Hashimoto, Y., et al. (2017). Alteration and dehydration of subducting oceanic crust within subduction zones: implications for décollement step-down and plate-boundary seismogenesis. *Earth Planets. Space* 69, 52. doi:10.1186/s40623-017-0635-1

Kameda, J., Yamaguchi, A., Saito, S., Sakuma, H., Kawamura, K., and Kimura, G. (2011). A new source of water in seismogenic subduction zones. *Geophys. Res. Lett.* 38. doi:10.1029/2011gl048883

Kato, S., Waseda, M., and Iwano, H. (2011). Geochemistry of natural gas and formation water from water-dissolved gas fields in Miyazaki Prefecture. *J. Jpn. Assoc. Petrol. Technol.* 76, 244–253. doi:10.3720/japt.76.244

Kawabata, K., Tanaka, H., and Kimura, G. (2007). Mass transfer and pressure solution in deformed shale of accretionary complex: examples from the Shimanto Belt, southwestern Japan. *J. Struct. Geol.* 29, 697–711. doi:10.1016/j.jsg.2006.11.009

Kioka, A., and Ashi, J. (2015). Episodic massive mud eruptions from submarine mud volcanoes examined through topographical signatures. *Geophys. Res. Lett.* 42, 8406–8414. doi:10.1002/2015gl065713

Kirkham, C., and Cartwright, J. (2022). Mud volcanoes and dissolution structures as kinematic markers during salt tectonic deformation. *Basin Res.* 34, 99–120. doi:10.1111/bre.12612

Kopf, A., Asshoff, K., Belke-Brea, M., Bergenthal, M., Bohrmann, G., Bräunig, A., et al. (2013). Report and preliminary results of RV Sonne cruise SO222: MEMO–MeBo drilling and *in situ* long-term monitoring in the Nankai Trough accretionary complex, Japan. *Berichte MARUM—*Zentrum für Mar. Umweltwiss. Fachbereich Geowiss. Univ. Brem. 297, 123.

Kopf, A. J. (2002). Significance of mud volcanism. *Rev. Geophys.* 40, 2–1. doi:10.1029/2000RG000093

Kopf, A. J. (2016). "Mud volcano," in *Encyclopedia mar. Geosci*. Editors J. Harff, M. Meschede, S. Petersen, and J. Thiede (Springer), 527–536.

Kuramoto, S., Ashi, J., Greinert, J., Gulick, S., Ishimura, T., Morita, S., et al. (2001). Surface observation of subduction related mud volcanoes and large thrust sheets in the Nankai subduction margin; Report on YK00-10 and YK01-04 cruises. *JAMSTEC Deep Sea Res.* 19, 131–139.

Lackey, J., Moore, G., and Strasser, M. (2018). Three-dimensional mapping and kinematic characterization of mass transport deposits along the outer Kumano Basin and Nankai accretionary wedge, southwest Japan. *Prog. Earth Planet Sci.* 5, 65. doi:10.1186/s40645-018-0223-4

Lalk, E., Pape, T., Gruen, D. S., Kaul, N., Karolewski, J. S., Bohrmann, G., et al. (2022). Clumped methane isotopologue-based temperature estimates for sources of methane in marine gas hydrates and associated vent gases. *Geochim. Cosmo. Acta.* 327, 276–297. doi:10.1016/j.gca.2022.04.013

Lance, S., Henry, P., Le Pichon, X., Lallemant, S., Chamley, H., Rostek, F., et al. (1998). Submersible study of mud volcanoes seaward of the Barbados accretionary wedge: sedimentology, structure and rheology. *Mar. Geol.* 145, 255–292. doi:10.1016/s0025-3227(97)00117-5

Leighton, A., Brook, M. S., Cave, M., Rowe, M. C., Stanley, A., and Tunnicliffe, J. F. (2022). Engineering geomorphological reconnaissance of the December 2018 Waimata Valley mud volcano eruption, Gisborne, New Zealand. *Quat. J. Eng. Geol. Hydrogeol.* 55. doi:10.1144/qjegh2021-149

Manga, M., Brumm, M., and Rudolph, M. L. (2009). Earthquake triggering of mud volcanoes. *Mar. Petrol. Geol.* 26, 1785–1798. doi:10.1016/j.marpetgeo.2009.01.019

Martin, K. M., Gulick, S. P. S., Bangs, N. B. L., Moore, G. F., Ashi, J., Park, J. O., et al. (2010). Possible strain partitioning structure between the Kumano forearc basin and the slope of the Nankai Trough accretionary prism. *Geochem. Geophys. Geosyst.* 11 (5), 68. doi:10.1029/2009G

Mazzini, A., and Etiope, G. (2017). Mud volcanism: an updated review. *Earth. Sci. Rev.* 168, 81–112. doi:10.1016/j.earscirev.2017.03.001

Menapace, W., Völker, D., Kaul, N., Tryon, M. D., and Kopf, A. J. (2017). The role of mud volcanism and deep-seated dewatering processes in the Nankai Trough accretionary prism and Kumano Basin, Japan. *Geochem. Geophys. Geosyst.* 18, 2486–2509. doi:10.1002/2016GC006763

Milkov, A. V. (2000). Worldwide distribution of submarine mud volcanoes and associated gas hydrates. *Mar. Geol.* 167, 29–42. doi:10.1016/s0025-3227(00)00022-0

Milkov, A. V. (2005). "Global distribution of mud volcanoes and their significance in petroleum exploration as a source of methane in the atmosphere and hydrosphere and as a geohazard," in *Mud volcanoes, geodynamics and seismicity, NATO sci. Ser*. Editors G. Martinelli and B. Panahi (Springer), 29–34.

Miyakawa, K., Tokiwa, T., and Murakami, H. (2013). The origin of muddy sand sediments associated with mud volcanism in the Horonobe area of northern Hokkaido, Japan. *Geochem. Geophys. Geosyst.* 14, 4980–4988. doi:10.1002/2013GC004924

Moore, G. F., Boston, B. B., Strasser, M., Underwood, M. B., and Ratliff, R. A. (2015). Evolution of tectono-sedimentary systems in the Kumano Basin, Nankai Trough forearc. *Mar. Petrol. Geol.* 67, 604–616. doi:10.1016/j.marpetgeo.2015.05.032

Moore, J. C., and Saffer, D. (2001). Updip limit of the seismogenic zone beneath the accretionary prism of southwest Japan: an effect of diagenetic to low-grade metamorphic processes and increasing effective stress. *Geology* 29, 183–186. doi:10.1130/0091-7613(2001)029<0183:ulotsz>2.0.co;2

Nakayama, N., Ashi, J., Tsunogai, U., Gamo, T., and Tanahashi, M. (2010). Sources of pore water in a Tanegashima mud volcano inferred from chemical and stable isotopic studies. *Geochem. J.* 44, 561–569. doi:10.2343/geochemj.1.0094

Nishio, Y., Ijiri, A., Toki, T., Morono, Y., Tanimizu, M., Nagaishi, K., et al. (2015). Origins of lithium in submarine mud volcano fluid in the Nankai accretionary wedge. *Earth Planet. Sci. Lett.* 414, 144–155. doi:10.1016/j.epsl.2015.01.018

Okamura, N. (2008). *Geological map of Hyuga nada,* mari. Geol. Map series, *64*. Geological Survey of Japan.

Pape, T., Geprägs, P., Hammerschmidt, S., Wintersteller, P., Wei, J., Fleischmann, T., et al. (2014). Hydrocarbon seepage and its sources at mud volcanoes of the Kumano forearc basin, Nankai Trough subduction zone. *Geochem. Geophys. Geosys.* 15, 2180–2194. doi:10.1002/2013gc005057

Planke, S., Svensen, H., Holand, M., Banks, D. A., and Jamtveit, B. (2003). Mud and fluid migration in active mud volcanoes in Azerbaijan. *Geo-Mar Lett.* 23, 258–268. doi:10.1007/s00367-003-0152-z

Ramirez, S. G., Gulick, S. P. S., and Hayman, N. W. (2015). Early sedimentation and deformation in the Kumano forearc basin linked with Nankai accretionary prism evolution, southwest Japan. *Geochem. Geophys. Geosys.* 16, 1616–1633. doi:10.1002/2014gc005643

Ridd, M. F. (1970). Mud volcano in New Zealand. *Am. Assoc. Petrol. Geol. Bull.* 54, 601–616.

Sato, T., and Itaki, T. (2015). Bathymetry of GH14 cruise area (Amami-Oshima island-kikai-jima Island), marine geological and geophysical studies around okinawa islands -around of amami-oshima, tokuno-shima and okinoerabu-jima islands-, preliminary reports on research in fiscal year 2014. *GSJ Interim Rep.* 67, 5–14.

Shih, T. T. (1967). A survey of the active mud volcanoes in Taiwan and a study of their types and the character of the mud. *Petrol. Geol. Taiwan* 5, 259–311.

Somoza, L., Díaz-del-Río, V., León, R., Ivanóv, M., Fernández-Puga, M. C., Gardner, J. M., et al. (2003). Seabed morphology and hydrocarbon seepage in the Gulf of Cádiz mud volcano area: acoustic imagery, multibeam and ultra-high resolution seismic data. *Mar. Geol.* 195 (1-4), 153–176. doi:10.1016/s0025-3227(02)00686-2

Soto, J. I., Heidari, M., and Hudec, M. R. (2021b). Proposal for a mechanical model of mobile shales. *Sci. Rep.* 11, 23785. doi:10.1038/s41598-021-02868-x

Soto, J. I., Hudec, M. R., Mondel, N. H., and Heidari, M. (2021a). Shale transformations and physical properties—implications for seismic expression of mobile shales. *Earth-Sci. Rev.* 220, 103746. doi:10.1016/j.earscirev.2021.103746

Strasser, M., Moore, G. F., Kimura, G., Kopf, A. J., Underwood, M. B., Guo, J., et al. (2011). Slumping and mass transport deposition in the Nankai fore arc: evidence from IODP drilling and 3-D reflection seismic data. *Geochem. Geophys. Geosyts* 12, Q0AD13. doi:10.1029/2010gc003431

Sumner, R. H., and Westbrook, G. K. (2001). Mud diapirism in front of the Barbados accretionary wedge: the influence of fracture zones and North America–South America plate motions. *Mar. Petrol. Geol.* 18, 591–613. doi:10.1016/s0264-8172(01)00010-1

Sun, C. H., Chang, S. C., Kuo, C. L., Wu, J. C., Shao, P. H., and Oung, J. N. (2010). Origins of Taiwan's mud volcanoes: evidence from geochemistry. *J. Asian Earth Sci.* 37, 105–116. doi:10.1016/j.jseaes.2009.02.007

Taira, A., Hill, I., Firth, J., Berner, U., Brückmann, W., Byrne, T., et al. (1992). Sediment deformation and hydrogeology of the Nankai Trough accretionary prism: synthesis of shipboard results of ODP Leg 131. *Earth Planet. Sci. Lett.* 109, 431–450. doi:10.1016/0012-821x(92)90104-4

Toki, T., Higa, R., Tanahara, A., Ijiri, A., Tsunogai, U., and Ashi, J. (2013). Origin of pore water in Kumano mud volcanoes (in Japanese with English abstract). *Chikyukagaku* 47, 221–236. doi:10.14934/chikyukagaku.47.221

Tsuji, T., Kamei, R., and Pratt, R. G. (2014). Pore pressure distribution of a mega-splay fault system in the Nankai Trough subduction zone: insight into up-dip extent of the seismogenic zone. *Earth Planet. Sci. Lett.* 396, 165–178. doi:10.1016/j.epsl.2014.04.011

Tsunogai, U., Maegawa, K., Sato, S., Komatsu, D. D., Nakagawa, F., Toki, T., et al. (2012). Coseimic massive methane release from a submarine mud volcano. *Earth Planet. Sci. Lett.* 341–344, 79–85. doi:10.1016/j.epsl.2012.06.004

Ujiié, Y. (2000). Mud diapirs observed in two piston cores from the landward slope of the northern Ryukyu Trench, northwestern Pacific Ocean. *Mar. Geol.* 163, 149–167. doi:10.1016/s0025-3227(99)00113-9

[URL1] International Union of International Geosciences (2023). Task group on submarine geohazards (IUGS-TGSG.com). (visited on March 15, 2023) Available at: https://www.kiso.co.jp/sssgr/about/TGSG/entry-962.html.

[URL2] YOKOSUKA YK15-10 Cruise Data (2023). [URL2] YOKOSUKA YK15-10 cruise data. *JAMSTEC*. doi:10.17596/0001663

[URL3] R/V Yokosuka Cruise Report YK18-05 (2023). [URL3] R/V yokosuka cruise report YK18-05. *JAMSTEC*. doi:10.17596/0002693

Van Rensbergen, P., Depreiter, D., Pannemans, B., and Henriet, J.-P. (2005). Seafloor expression of sediment extrusion and intrusion at the El Arraiche mud volcano field, Gulf of Cadiz. *J. Geophys. Res. Earth Surf.* 110, F02010. doi:10.1029/2004jf000165

Wang, C.-Y., and Manga, M. (2021). "Mud volcanoes," in *Water and earthquakes*. Editors C.-Y. Wang and M. Manga (Springer Nature), 323–342. doi:10.1007/978-3-030-64308-9_12

Wessel, P., and Smith, W. H. F. (1998). New, improved version of generic mapping tools released. Eos Trans. *AGU* 79, 579. doi:10.1029/98eo00426

Wiersberg, T., Hammerschmidt, S. B., Fuchida, S., Kopf, A., and Erzinger, J. (2018). Mantle-derived fluids in the Nankai Trough Kumano forearc basin. *Prog. Earth Planet. Sci.* 5, 79. doi:10.1186/s40645-018-0235-0

Yamashita, M., Miura, S., Moore, G. F., Nakanishi, A., Kodaira, S., and Kaneda, Y. (2017). Bathymetric imaging of protothrust zone along the Nankai Trough. *Isl. Arc* 27. doi:10.1111/iar.12233

Yusifov, M., and Rabinowitz, P. D. (2004). Classification of mud volcanoes in the south caspian basin, offshore Azerbaijan. *Mar. Petrol. Geol.* 21, 965–975. doi:10.1016/j.marpetgeo.2004.06.002

frontiers | Frontiers in Marine Science

TYPE Original Research
PUBLISHED 08 January 2024
DOI 10.3389/fmars.2023.1181921

Check for updates

OPEN ACCESS

EDITED BY
Glen T. Snyder,
The University of Tokyo, Japan

REVIEWED BY
Dong Feng,
Shanghai Ocean University, China
Firoz Badesab,
Council of Scientific and Industrial Research (CSIR), India

*CORRESPONDENCE
Huiqiang Yao
hqyao@163.com
Zijun Wu
wuzj@tongji.edu.cn

RECEIVED 08 March 2023
ACCEPTED 13 December 2023
PUBLISHED 08 January 2024

CITATION
Chen Y, Xu S, Liu W, Zhang Z, Yang T, Xiao X, Deng X, Li J, Yao H and Wu Z (2024) Assessing biogeochemical controls on porewater dissolved inorganic carbon cycling in the gas hydrate-bearing sediments of the Makran accretionary wedge, Northeastern Arabian Sea off Pakistan.
Front. Mar. Sci. 10:1181921.
doi: 10.3389/fmars.2023.1181921

COPYRIGHT
© 2024 Chen, Xu, Liu, Zhang, Yang, Xiao, Deng, Li, Yao and Wu. This is an open-access article distributed under the terms of the Creative Commons Attribution License (CC BY). The use, distribution or reproduction in other forums is permitted, provided the original author(s) and the copyright owner(s) are credited and that the original publication in this journal is cited, in accordance with accepted academic practice. No use, distribution or reproduction is permitted which does not comply with these terms.

Assessing biogeochemical controls on porewater dissolved inorganic carbon cycling in the gas hydrate-bearing sediments of the Makran accretionary wedge, Northeastern Arabian Sea off Pakistan

Yuanqing Chen[1], Sinan Xu[1], Weining Liu[1], Zhen Zhang[2], Tianbang Yang[2], Xiao Xiao[2], Xiguang Deng[2], Jiangtao Li[1], Huiqiang Yao[2]* and Zijun Wu[1]*

[1]State Key Laboratory of Marine Geology, Tongji University, Shanghai, China, [2]Key Laboratory of Marine Mineral Resources, Ministry of Natural Resources, Guangzhou Marine Geological Survey, China Geological Survey, Guangzhou, China

Quantitatively assessing the porewater dissolved inorganic carbon (DIC) cycling in methane-enriched marine sediments is crucial to understanding the contributions of different carbon sources to the global marine carbon pool. In this study, Makran accretionary wedge was divided into Zone 1 (high methane flux area) and Zone 2 (background area). Porewater geochemical compositions (Cl^-, SO_4^{2-}, NH_4^+, Mg^{2+}, Ca^{2+}, Ba^{2+}, DIC and $\delta^{13}C$-DIC) and a reaction-transport model were used to determine the DIC source and calculate the DIC flux through carbonate precipitation and releasing into overlying seawater in sediments. Zone 1 is characterized by the shallower depth of sulfate-methane transition (SMT), where most of porewater sulfate was consumed by anaerobic oxidation of methane (AOM). In contrast, a relatively low flux of methane diffusion in Zone 2 results in a deeper SMT depth and shallow sulfate is predominantly consumed by organoclastic sulfate reduction (OSR). Based on the porewater geochemical profiles and $\delta^{13}C$ mass balance, the proportions of porewater DIC originating from methane were calculated as 51% in Zone 1 and nearly 0% in Zone 2. An increase of porewater DIC concentration leads to authigenic carbonate precipitation. Solid total inorganic carbon (TIC), X-ray diffractometry (XRD) and scanning electron microscopy (SEM) analysis display that carbonate content increases with depth and aragonite appears at or below the depths of SMT. Meanwhile, the flux of DIC released from sediments calculated by the reaction-transport model is 51.3 ~ 90.4 mmol/m^2·yr in Zone 1, which is

significantly higher than that in Zone 2 (22.4 mmol/m^2·yr). This study demonstrates that AOM serves as the dominant biogeochemical process regulating the porewater DIC cycle, which has an important impact on the authigenic carbonate burial and the seawater carbonate chemistry.

KEYWORDS

Makran accretionary wedge, anaerobic oxidation of methane (AOM), sulfate reduction, dissolved inorganic carbon (DIC), authigenic carbonate precipitation

1 Introduction

Methane (CH_4) seepage refers to methane-rich fluid leakage from the seabed, which is widely observed in active and passive continental margin slopes. The fluids show apparent spatial-temporal variations (Haas et al., 2010; Feng et al., 2016; Feng et al., 2020; Liu et al., 2020b; Wei et al., 2021), and often be accompanied by gas hydrate accumulations in areas of gas hydrate stability and where methane concentrations reach saturation (Milkov, 2004; Coffin et al., 2014; Mau et al., 2017; Feng et al., 2018; Zhang et al., 2021a). Under the driving force of geological structure, pressure or temperature changes, the gas hydrate can dissociate and increase the intensity of gas seeps, thereby significantly affecting benthic biogeochemical processes that control the highly spatially heterogeneous seafloor ecosystems (Suess, 2014; Liu et al., 2020a; Liao et al., 2022).

Although the CH_4 carbon estimates of hydrate-bound gas in global marine sediments are thought to be highly uncertain, the current estimate is widely believed to range from 1000 to 2500 Gt (Kvenvolden, 1988; Lerche, 2000; Milkov, 2004; Kretschmer et al., 2015). This buried organic carbon reservoir greatly exceeds many other reservoirs such as marine dissolved materials (980 Gt), terrestrial biota (830 Gt), the atmosphere (3.6 Gt) and marine biota (3 Gt) in the global carbon cycle (Kvenvolden, 1988). The dissociation of gas hydrates will result in the consequent liberation of various carbonaceous compounds such as CH_4, CO_2, and HCO_3^- (Suess et al., 1999; Phrampus and Hornbach, 2012). Previous studies have shown that more than 90% of the CH_4 is consumed through anaerobic oxidation of methane (AOM) in marine sediments (e.g., Boetius et al., 2000; Haese et al., 2003; Chen et al., 2021; Wei et al., 2021; Li et al., 2023), which effectively prevents the diffusion of dissolved CH_4 into overlying seawater or even the atmosphere. The AOM is mainly coupled to the sulfate reduction and occurs at a distinct zone which is known as the sulfate-methane transition (SMT) in the sediments (Equation 1) (Reeburgh, 1976; Borowski et al., 1996; D'Hondt et al., 2002; Snyder et al., 2007).

$$CH_4 + SO_4^{2-} \rightarrow HCO_3^- + HS^- + H_2O \quad (1)$$

The upward flux of methane is theoretically nearly equal to the downward diffusive sulfate flux within the SMT due to the stoichiometric ratio of 1:1 between SO_4^{2-} and CH_4 in the AOM (Niewöhner et al., 1998; Knittel and Boetius, 2009; Akam et al., 2020). However, the calculated downward diffusive sulfate flux often exceeds that of the upward flux of methane (e.g., Wu et al., 2016; Akam et al., 2020; Zha et al., 2022). A compilation by Egger et al. (2018) from 740 sites covering a wide range of oceanic conditions observed the global mean net flux ratio between SO_4^{2-} and CH_4 of 1.4:1. This observed flux imbalance can be attributed to the organoclastic sulfate reduction (OSR) through the oxidation of buried organic matter (Berner, 1980; Jørgensen et al., 2019; Chen et al., 2020; Zha et al., 2022), and the reaction is represented in very simple form as Equation 2:

$$2CH_2O + SO_4^{2-} \rightarrow H_2S + 2HCO_3^- \quad (2)$$

Both the microbially-mediated AOM and OSR can generate dissolved inorganic carbon (DIC) and increase porewater alkalinity (Equations 1, 2), thus leading to the promotion of authigenic carbonate precipitation (Equation 3) (Chatterjee et al., 2011; Smith and Coffin, 2014; Chen et al., 2023).

$$Ca^{2+} + 2HCO_3^- \rightarrow CaCO_3 + H_2O + CO_2 \quad (3)$$

It should be pointed out that other alkaline earth elements such as Mg, Sr, Ba, and Fe can substitute for Ca in varying amounts during the process of carbonate precipitation (Equation 3). In addition to being removed by carbonate precipitation, a portion of the porewater DIC will migrate toward the seafloor and finally enter the overlying seawater (e.g., Smith and Coffin, 2014; Graves et al., 2015; Feng et al., 2020). Therefore, quantitative assessment of the porewater DIC cycle in marine sediments is crucial for better understanding the global authigenic carbonate burial and seawater carbonate chemistry.

The DIC concentration and its isotopic composition (δ^{13}C-DIC) in porewater serve as sensitive indicators of the alteration of carbon species in marine sediments (Chen et al., 2010; Feng et al., 2020; Zha et al., 2022). Previous studies of DIC concentration and its δ^{13}C-DIC have quantitatively tracked various sources, sinks, and transformation terms using the end-member isotopic compositions of various carbon pools (e.g., Aller and Blair, 2004; Formolo et al., 2004; Winde et al., 2014; Wu et al., 2016). Due to the high spatial and temporal heterogeneity of methane turnover above the gas

hydrate stability zone (GHSZ), it is necessary to conduct geochemical investigations of the dissolved species found in the porewater of closely associated marine sediments. These resulting geochemical data will help constrain the cycling and fate of DIC related to diagenetic processes in marine sediments with similar continental margin environments, and thus contribute to ascertaining global carbon flux in these settings.

Methane seepage and obvious gas emissions widely occur on the continental slope of the Makran accretionary wedge off Pakistan (von Rad et al., 2000; Delisle and Berner, 2002; Fischer et al., 2012; Wei et al., 2021). Existing works have mainly focused on the use of geophysical methods to identify the distribution and reserves of methane hydrate in this area (von Rad et al., 2000; Römer et al., 2012; Wei et al., 2021; Wu et al., 2021). The conversion of methane carbon to DIC by geochemical processes in the Makran accretionary wedge was rarely reported and in particular, the quantitative assessment of the DIC cycle was not involved. In 2018, China Geological Survey carried out a China - Pakistan joint marine scientific cruise on the Makran continental margin offshore Pakistan (Figure 1A). The hydroacoustic evidence for Bottom Simulating Reflections (BSRs) indicates significant methane-hydrate burial in the study area (e.g., Wei et al., 2021; Wu et al., 2021; Zhang et al., 2021b). In this study, we collected six sediment gravity cores and analyzed the porewater geochemical composition (e.g., Cl^-, SO_4^{2-}, NH_4^+, Ca^{2+}, Mg^{2+}, Ba^{2+}, DIC and δ^{13}C-DIC), total organic carbon (TOC) and carbonate phase

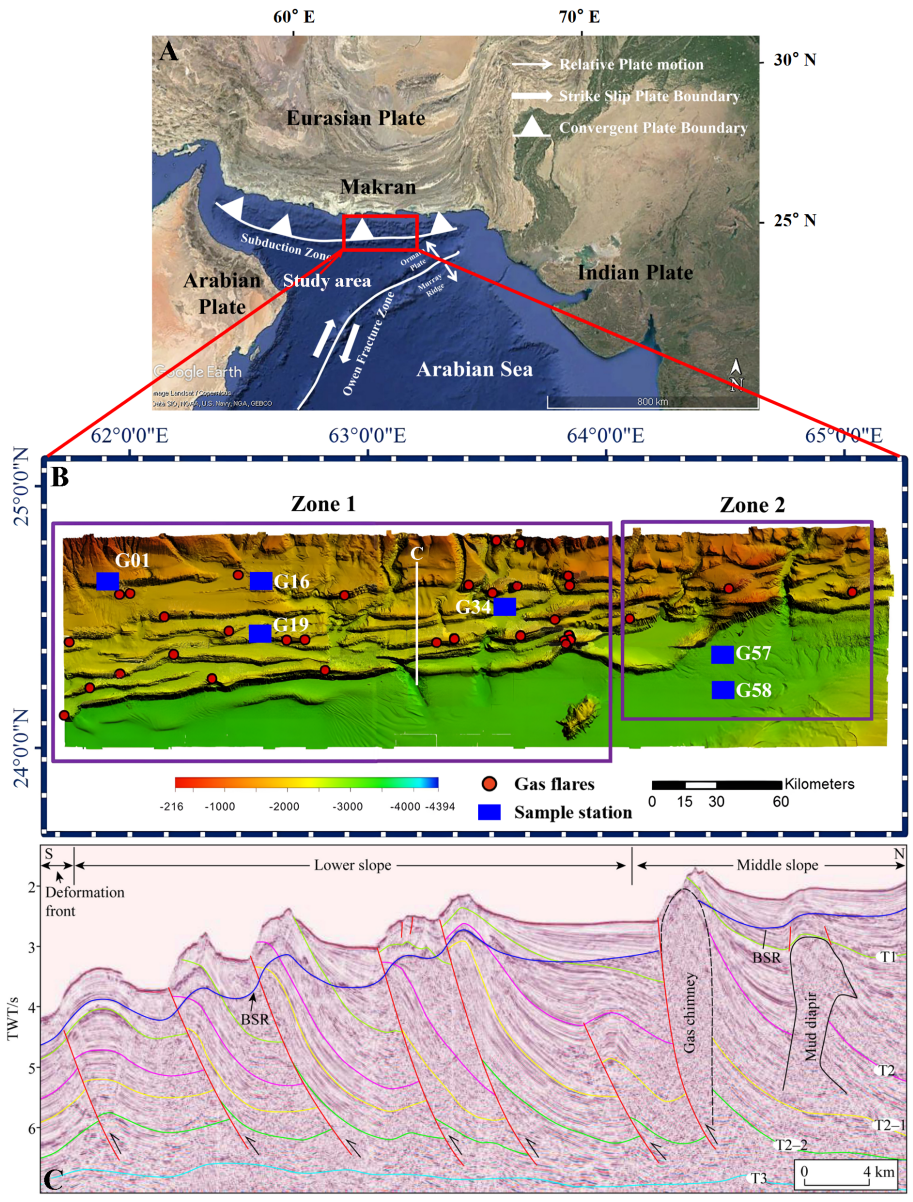

FIGURE 1
The maps of the study area and sampling sites. **(A)** Study area and its related tectonic setting; **(B)** Sampling sites and bottom topography of the investigated area. The stations with gas flares are referred to Wei et al. (2021). White line is the track line of the seismic profiles panel **(C)**; **(C)** Multi-channel seismic data shows the occurring of bottom simulating with reversed polarity (BSR) in the study area (Zhang et al., 2020).

compositions. Our aims are to determine the source of DIC, the relative contributions of different geochemical processes (AOM vs. OSR) to the porewater DIC pool, and quantitatively assess the fate of DIC in the study area using the reaction-transport model.

2 Study location and methodology

2.1 Study area

The study area is located in the Makran accretionary wedge of the northern Indian Ocean, which has a complex thrust structure and the lowest subduction angle worldwide (about 3°) (Kopp et al., 2000; Wu et al., 2021) (Figure 1A). Shallow gas accumulates and moves along normal faults in abundant anticlinal hinges created by the highest subducted sediments, resulting in seepage to the seafloor (Römer et al., 2012; Himmler et al., 2015; Liao et al., 2022). Seismic data revealed widespread distributions of BSRs in the slope area across the Makran continental margin (Figure 1C), indicating the widespread occurrence of gas hydrates in this area (e.g., Grando and McClay, 2007; Zhang et al., 2020; Liao et al., 2022). Various types of faults, mud diapirs, gas chimneys, and associated diapiric structures provide conduits for methane seepage in the Makran (von Rad et al., 2000; Schlüter et al., 2002; Khan et al., 2020; Wei et al., 2021; Wu et al., 2021; Liao et al., 2022). Methane seepage has been discovered ubiquitously (Römer et al., 2012), accompanied by cold seep ecosystems (Fischer et al., 2012) and authigenic carbonates (Himmler et al., 2015).

2.2 Sample collection

From December 2018 to February 2019, a systematic multi-beam sonar survey for gas emissions was conducted with the R/V "Haiyangdizhi 10" during a scientific diving expedition of the Makran accretionary wedge off Pakistan (Wu et al., 2021). Based on active flare density and methane seepage intensity, six sediment gravity cores with lengths ranging from 355 to 835 cm were recovered in two zones: Zone 1 (sites G01, G16, G19, and G34) has a high methane flux and a water depth of 500-2500 m; Zone 2 is the background area near Zone 1, with a water depth greater than 3000 m. In terms of geological structure, Zone 1 is heavily transected by imbricate faults and accretionary structures, while the forearc area is largely intact in deeper Zone 2 (Figure 1B).

After being retrieved, the core was promptly transported to the onboard laboratory for the purpose of collecting methane and extracting porewater. Sediment samples for methane analysis (3 ml) were taken using a 10 ml cut syringe and immediately transferred into 10 ml headspace vials, which contained 3 ml of 1 mol/l NaOH solution. The vials were subsequently capped with a rubber septum and sealed with a crimper, stored at low temperatures for the determination of sediment CH_4 concentration. Porewater samples were collected at 60 cm intervals using Rhizon samplers according to the procedure presented by Liu et al. (2020a). The porewater samples were then immediately chemically treated and preserved for a variety of analysis purposes. The solid phase was divided into sub-samples at 10 cm intervals and stored at −20 °C for further analysis.

About 2 ml of porewater subsamples for cations (Ca^{2+} and Mg^{2+}) and anions (SO_4^{2-} and Cl^-) analysis was acidified with 20 µl 65% HNO_3 (suprapure, Merck) to prevent precipitation and sulfur oxidation. Samples for porewater NH_4^+ analysis were preserved in a 2 ml PE tube and frozen. Subsamples for measurements of DIC concentration and its isotopic composition were stored in 3 ml Labco anaerobic flasks without a headspace and kept at 4 °C in the research vessel's cold room. Once on land, these samples were immediately placed in a refrigerated case and shipped to the onshore laboratories for further analysis within 4 weeks.

2.3 Analytical methods

2.3.1 Chemical and isotopic analysis of porewater

Dissolved Ca^{2+}, Mg^{2+} and Ba^{2+} concentrations were diluted at 1:30 with 18-MΩ water and measured with inductively coupled plasma atomic emission spectroscopy (ICP-AES; IRIS Advantage, Thermo Jarrell Ash). Scandium (0.5 mg/L) was added to both standards and samples for correcting signal drift during instrument operation. Porewater samples were diluted with 2% subboiled HNO_3 along with reference materials (CASS-4) from the National Research Council of Canada (NRCC). The accuracy and precision were better than ± 5%.

Porewater samples for SO_4^{2-} and Cl^- concentrations were diluted at 1:250 using 18-MΩ water and measured using a Dionex DX-600 ion chromatograph equipped with a 4 mm AS-9HC column. Reagents from the National Research Center for Certified Reference Materials (Beijing, China) were used as standards. Measurement of duplicate samples indicates the analytical error is less than 2%.

The samples for ammonium (NH_4^+-N) concentration were diluted at 1:5 and determined using flow injection spectrophotometry in wavelength 543 nm, as described by Hall and Aller (1992). NH_4^+-N standard solution was prepared using the NH_4^+-N reference material (BWZ6768-2016). All standard solutions were appropriately diluted to generate a series of standard concentrations. Duplicate analysis after every 10 samples was performed to validate the porewater analysis procedure, and the reproducibility is better than ± 5%.

The CH_4 concentration was measured using the method of Jørgensen et al. (2001). The vial containing the sediment sample was shaken thoroughly to allow the porewater methane between the aqueous and gaseous phases to equilibrate. A 0.2-ml headspace gas sample was injected into a gas chromatograph (Agilent 6820). For porewater dissolved CH_4 concentration, the calculated CH_4 concentration per sediment volume is corrected by assuming a constant sediment porosity of 0.75. The two duplicate samples were measured with a precision of ± 3.0%.

The DIC concentration and its δ^{13}C-DIC were analyzed with the 0.3 ml porewater samples according to the methods described by Liu et al. (2020a). The sealed porewater samples were acidified in precleaned extainers with 0.2 ml of 2 mol/l H_3PO_4, and the resulting CO_2 was purged from the samples. The DIC concentration and the

carbon isotopic composition of the CO_2 were measured using a Thermo Finnigan MAT 253 isotope ratio mass spectrometer coupled with a Thermo Finnigan Gasbench II. The DIC concentration was measured with a precision of ± 2%. The carbon isotopic ratios are reported in the standard δ notation concerning the Vienna PeeDee Belemnite (VPDB) standard and with both precision and accuracy of better than ± 0.15% (1σ).

2.3.2 Solid sediment analysis

Sediment total organic carbon (TOC) and its stable isotopic values (δ^{13}C-TOC) were analyzed in duplicate, using an elemental analyzer (Vario EL III, Germany) connected to a continuous flow system (Isoprime 100), after removal of carbonate with HCl. The average standard deviations of the measurements were ± 0.2% for TOC and ± 0.2‰ for δ^{13}C-TOC. Weight percentages of total carbon (TC) were determined in duplicate (without acidification) by combustion (at 1000°C) on the elemental analyzer, and total inorganic carbon (TIC) was determined by difference: TIC = TC − TOC.

The X-ray diffraction (XRD) was performed to characterize the mineralogy of the powders of interest. Selected samples (55 cm, 415 cm, and 475 cm at site G16; 55 cm, 415 cm, and 535 cm at site G34; 55 cm, 355 cm and 775 cm at site G58) of 1.5 g were micronized under ethanol with a McCrone micronizing mill and then oven-dried at 60°C. After drying, the micronized samples were thoroughly mixed in an agate mortar and pestle to ensure homogeneity, followed by analyses using an X'pert Pro X-ray powder diffractometer (PANalytical, Netherlands) with Cu Kα radiation at 40 kV and 40 mA. The measurements were carried out in the range of diffraction angles 2θ from 4° to 80° with a scanning step of 0.033° and rotation of the sample at a speed of 15 rpm. Qualitative and quantitative analyses of minerals were performed using the software Profex (version 5.0.2) (Doebelin and Kleeberg, 2015).

Scanning electron microscopy (SEM) (Tescan Mira 3) with energy-dispersive X-ray microanalysis (EDX) (Oxford Ultim Max 40) was used to determine the morphology and elemental composition of the sites G16 and G34 samples because of their high level of carbonate content based on the XRD analysis (Supplementary Table S1). The freeze-dried subsamples were fixed onto aluminum stubs with two-way adherent tabs and allowed to dry overnight. Subsequently, the samples were sputter-coated with gold for 30 s. The SEM was operated at 2 kV with a working distance of 10 mm to facilitate optimum image collection while minimizing charging and sample damage. For EDX analysis, an accelerating voltage of 20 kV was used to generate sufficient X-ray counts.

3 Results

3.1 The depth profiles of porewater geochemistry

Figure 2 shows the depth profiles of the Cl^-, SO_4^{2-}, CH_4 and NH_4^+ concentrations in the porewater of Zone 1 and Zone 2. Porewater Cl^- concentration at all sampling sites remains almost constant and close to that in seawater. The SO_4^{2-} concentration decreases almost linearly with depth in Zone 1, and complete depletion occurs at around the depth of 400 cmbsf (centimeters below sea floor) ~ 500 cmbsf (SMT depth). By contrast, complete depletion of SO_4^{2-} concentration appears at around 1800 cmbsf at site G57 and 1100 cmbsf at site G58 in Zone 2. A noticeable increase

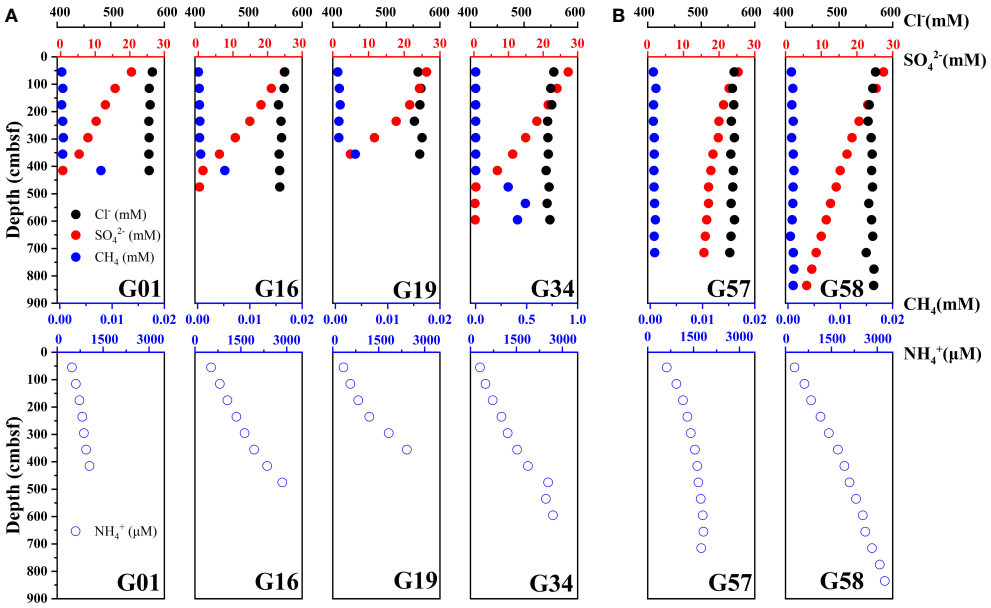

FIGURE 2
Down-depth profiles of porewater SO_4^{2-}, Cl^-, CH_4 and NH_4^+ in the sediments of the sites **(A)** G01, G16, G19, and G34 (Zone 1), and **(B)** G57, G58 (Zone 2).

in CH_4 concentration was observed around the SMT of the sites G01, G16, G19 and G34 in Zone 1, but CH_4 concentration is close to 0 and no change with depth at sites in Zone 2. The concentration of NH_4^+ ranges from 209.50 μM to 3243.00 μM, and an obvious negative correlation between the NH_4^+ and SO_4^{2-} in depth profiles occurs at all sites.

Depth profiles of the porewater Ca^{2+}, Mg^{2+} and Ba^{2+} are shown in Figure 3. The porewater Ca^{2+} concentrations at sites in Zone 1 and Zone 2 vary from 1.38 – 7.96 mM and 4.40 – 8.50 mM, respectively. The porewater Mg^{2+} concentrations are in the range of 37.76 – 55.91 mM and 50.64 – 56.33 mM at sites in Zone 1 and Zone 2. The concentrations of Ca^{2+} and Mg^{2+} decrease with depth in Zone 1, and their decreasing trends are more pronounced than those in Zone 2. The porewater Ba^{2+} concentrations at the sites of Zone 1 vary from 0.33 to 4.76 μM, and display a noticeable increasing trend below the depth of complete depletion of porewater sulfate. At the sites of Zone 2, however, the Ba^{2+} concentrations remain almost constant in the depth profiles, with a range of 0.35 to 0.54 μM.

The porewater DIC concentration increases with the depth, and the δ^{13}C-DIC values are negatively correlated with DIC concentration at all sites in Zone 1 (Figure 4A). The porewater DIC concentrations at sites G01, G16, G19 and G34 vary from 11.85 – 24.29 mM, 5.47 – 18.26 mM, 4.24 – 15.45 mM and 3.79 – 18.87 mM, and the δ^{13}C-DIC values range from −29.57 to −15.82 ‰, −35.04 to −15.70 ‰, −39.60 to −12.20 ‰ and −27.39 to −11.27 ‰, respectively. The most negative δ^{13}C-DIC occurs at the depth of maximum sulfate depletion. For site G58 in Zone 2 (Figure 4B), δ^{13}C-DIC values decrease almost linearly from −8.48‰ at the top to a minimum of −15.52‰ at the bottom. For site G57 in Zone 2 (Figure 4B), which has a much deeper SMT, the change in δ^{13}C-DIC values is much more gradual since the site of AOM contributions to DIC is located deeper.

3.2 The depth profiles of sediment TOC, TIC and δ^{13}C-TOC

Figure 5 displays the depth profiles of sediment TOC, TIC and δ^{13}C-TOC. At the sites of Zone 1, the TOC shows a decreasing trend as depth increases, varying from 2.02% to 0.28%, while the TIC contents are in the range of 2.03% – 4.21% and exhibit a small increase trend with depth. In contrast, the TOC and TIC at site G58 in Zone 2 show small fluctuations in the depth profile, with ranges of 0.59% – 1.32% for TOC and 2.15% – 2.69% for TIC, respectively. At all sites, there is no clear trend of the δ^{13}C-TOC variation in the depth profile, and their values range from −24.14‰ to −20.59‰.

3.3 Morphology and mineralogy of the carbonate phase

Based on the vertical distribution of porewater geochemical profiles (Figures 2, 3), we selected the sediment samples from three different depths of Zone 1 (sites G16 and G34) and Zone 2 (site G58) for XRD analysis, and the results are shown in Figure 6 and Supplementary Table S1. Quantitative analyses of minerals were performed using the default structure repositories in the software Profex (version 5.0.2). Overall, the carbonates at sites G16, G34 and G58 are composed of calcite, aragonite, and dolomite. The percentage of each carbonate mineral within the bulk sediment and the relative abundance of each carbonate type in total

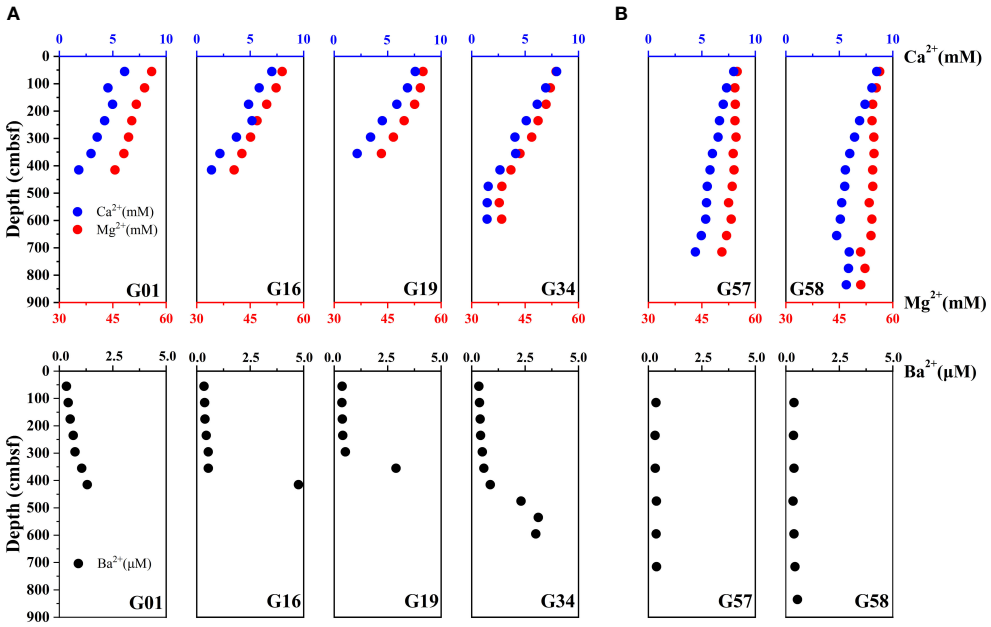

FIGURE 3
Down-depth profiles of porewater Ca^{2+}, Mg^{2+} and Ba^{2+}. **(A)** G01, G16, G19, and G34 (Zone 1), and **(B)** G57, G58 (Zone 2).

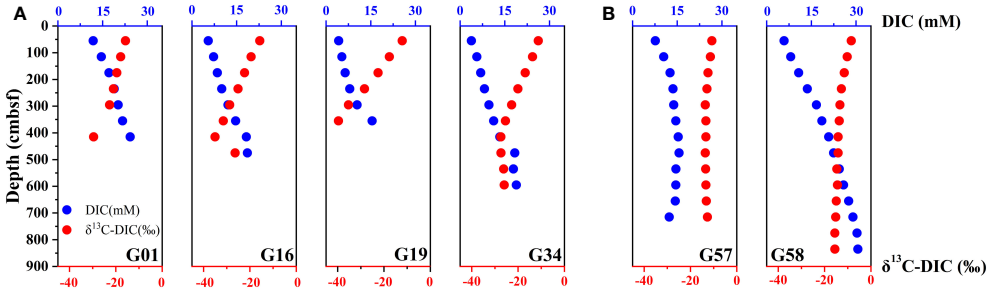

FIGURE 4
Down-depth profiles of porewater DIC and δ^{13}C-DIC in the sampling sites **(A)** G01, G16, G19, and G34 (Zone 1), **(B)** G57, G58 (Zone 2).

carbonates are listed in Supplementary Table S2. By comparison, the ratio of calcite/∑carbonate is the highest in all selected samples (66.48% ~ 85.18% at site G16; 51.56% ~ 81.69% at site G34; 75.59% ~ 82.68% at site G58). Aragonite is almost undetectable in the shallow sediments (55 cmbsf depth) of sites G16 and G34 (aragonite/∑carbonate = 0), and not detected at all selected depths of site G58. The ratio of aragonite/∑carbonate decreases from 20.61% at 415 cmbsf depth to 6.94% at 475 cmbsf depth of site G16, and it increases dramatically from 4.50% at 415 cmbsf depth to 35.26% at 535 cmbsf depth of the site G34. However, the difference in the ratio of dolomite/∑carbonate is very small in all selected samples (12.91% ~ 14.82% at site G16; 13.18% ~ 18.64% at site G34; 17.32% ~ 24.41% at site G58).

In addition to XRD analysis, the SEM images and EDS signals can also be utilized to identify the various carbonate phases. In this study, most of the carbonate concretions were observed in the deep layer of sites G16 and G34 (Figure 7; Supplementary Table S3). The mineral morphology at the 415 cmbsf depth of site G16 is analogous to that at the 535 cmbsf depth of site G34. Both samples contain aragonite and calcite, where aragonite occurs in the habit of acicular $CaCO_3$ with roughly strip-shaped bodies ranging from 1 to 3 μm in diameter (Figures 7B, G), and calcite appears in a massive form (Figures 7C,

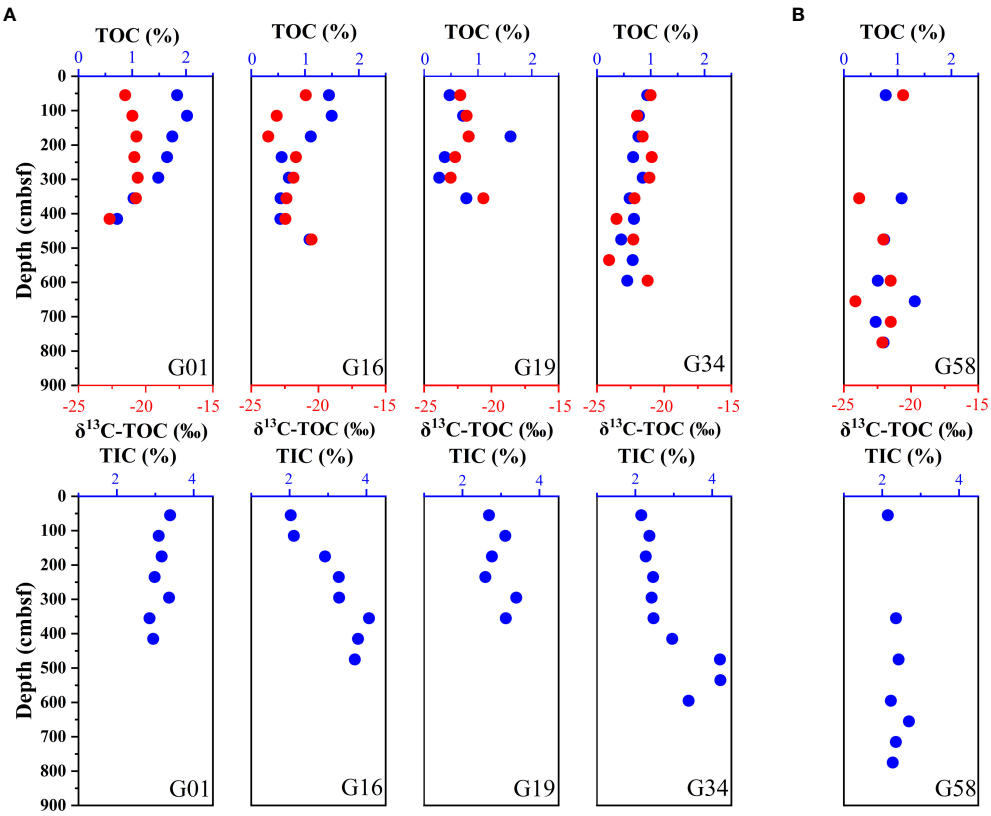

FIGURE 5
Down-depth profiles of sediment TOC, δ^{13}C-TOC and TIC. **(A)** G01, G16, G19, and G34 (Zone 1), **(B)** G58 (Zone 2).

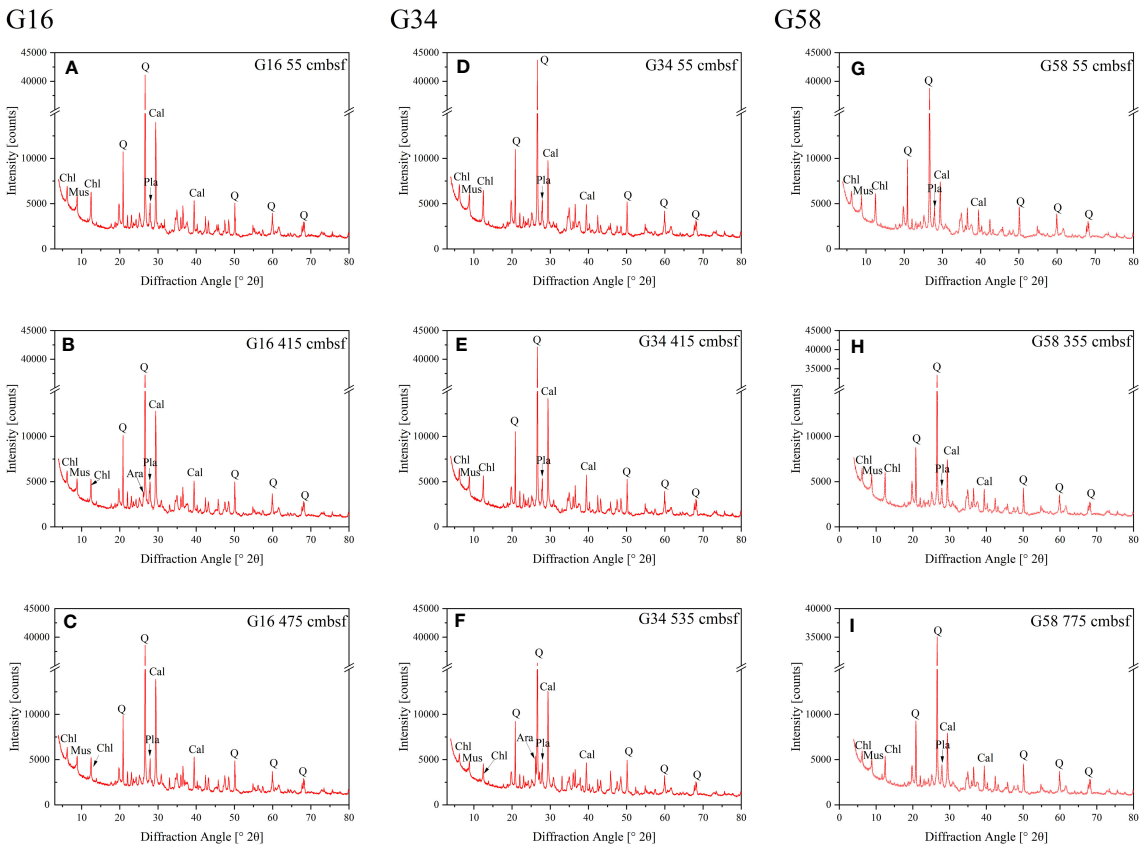

FIGURE 6
The XRD spectra of the selected sediment samples from three different depths of Zone 1 (G16 and G34) and Zone 2 (G58). **(A)** G16 55 cmbsf; **(B)** G16 415 cmbsf; **(C)** G16 475 cmbsf; **(D)** G34 55 cmbsf; **(E)** G34 415 cmbsf; **(F)** G34 535 cmbsf; **(G)** G58 55 cmbsf; **(H)** G58 355 cmbsf and **(I)** G58 775 cmbsf. Only minerals with a content greater than 5% are shown in the figures (Q, quartz; Cal, calcite; Mus, muscovite; Chl, chlorite; Pla, Plagioclase; Ara, aragonite).

H). At the other depths of the sites G16 and G34, no strip-shaped aragonite but only calcite was found (Figures 7A, D–F).

4 Modeling results of porewater geochemical profiles

The porewater geochemical profiles of sulfate, methane, calcium, magnesium, and DIC concentration were simulated by a reaction-transport model (RTM) under steady state (e.g., Berner, 1980; Chatterjee et al., 2011; Meister et al., 2019; Xu et al., 2023). The RTM was written using MATLAB R2023a and its code is provided in the Supplementary Material.

The instantaneous reaction rate equation (Equation 4) is as follows:

$$\frac{\partial(\varphi \cdot C)}{\partial t} = \frac{\partial\left(\varphi \cdot \frac{D_s(x)}{\tau^2} \cdot \frac{\partial C}{\partial x}\right)}{\partial x} - \frac{\partial(\varphi \cdot \omega \cdot C)}{\partial x} + \varphi \cdot \sum R(x,t) \quad (4)$$

where C is the concentrations, t is time, ω is the sedimentation rate, φ is the porosity of the marine sediment, Ds is the effective diffusion constant and is corrected by advection and tortuosity (τ^2) as $\tau^2 = 1\text{-}2\cdot\ln\varphi$ (Boudreau, 1997). The specific values of simulation parameters are shown in Table 1, and part of the relevant data in the table refers to previous studies in this area (Luff et al., 2000; Hu et al., 2018).

The time of simulation is related to the sedimentation rate and porosity. Here we used an exponential function to describe porosity:

$$\varphi(x) = \varphi_0 \cdot e^{\lambda x} \quad (5)$$

where the value of porosity (φ_0) of sediment at the sediment-water interface (SWI) is set to 0.8, λ (-0.01) is the attenuation coefficient and x is the depth. The burial time can be calculated as (Meister et al., 2019):

$$t(x) = \int_0^x \omega^{-1} dx = \frac{\left[x - \frac{\varphi_0}{\lambda} \cdot (e^{\lambda x} - 1)\right]}{\omega \cdot (1 - \varphi_0)} \quad (6)$$

Sources and sinks of methane, sulfate, and DIC are stoichiometrically coupled to rates of organic matter (OM) degradation via the simplified reactions for sulfate reduction (SR) and methanogenesis (ME).

For OM degradation, the reactive continuum model (RCM) was applied (Boudreau and Ruddick B., 1991):

$$R_G(t) = -v \cdot (a + t)^{-1} \cdot G(t) \quad (7)$$

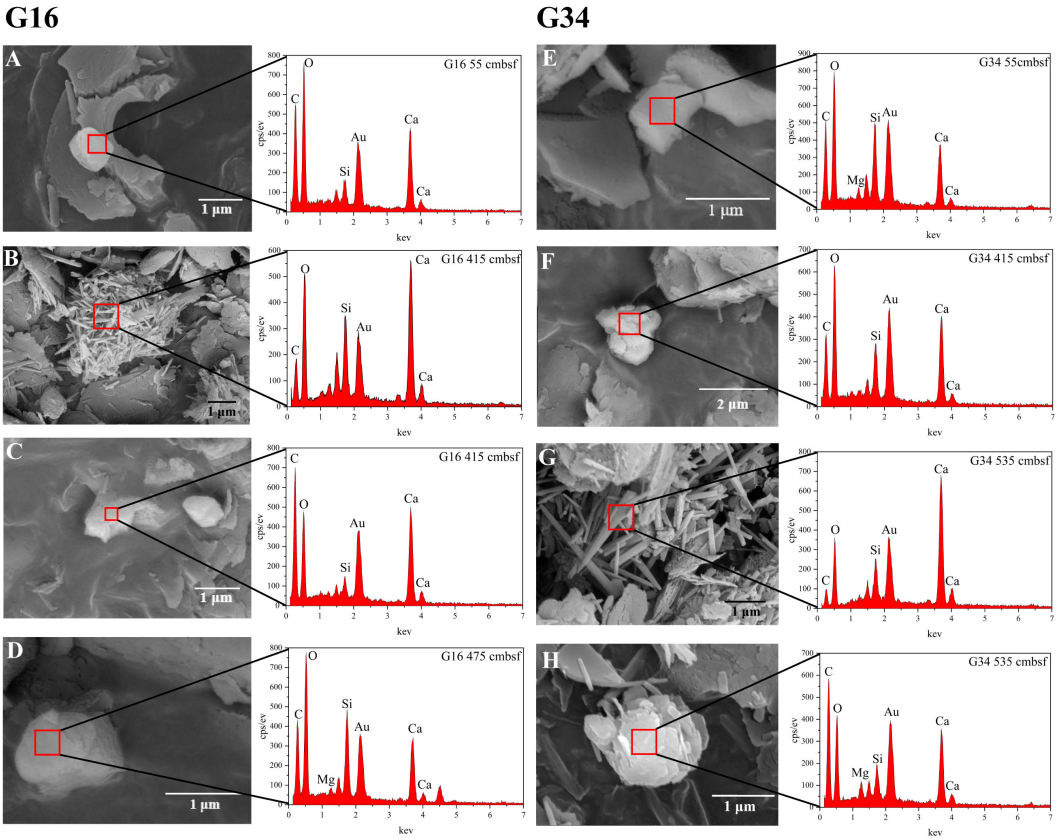

FIGURE 7
SEM images and EDS signals for sites G16 and G34. **(A)** Massive calcite at a depth of 55 cmbsf of site G16, **(B)** small loosely packed aragonite needle cluster with mainly long needles (1 ~ 3 μm) at a depth of 415 cmbsf of site G16, **(C)** the presence of calcite at a depth of 415 cmbsf of site G16, **(D)** calcite at a depth of 475 cmbsf of site G16, **(E)** massive calcite at a depth of 55 cmbsf of site G34, **(F)** a notable presence of calcite at a depth of 415 cmbsf of site G34, **(G)** the aragonite at a depth of 535 cmbsf of site G34, which is closely resembled that at a depth of 415 cmbsf of site G16, **(H)** calcite at a depth of 535 cmbsf of site G34.

where the parameter a describes the average lifetime of OM, v defines the shape of the distribution, t is burial time calculated by Equation 6 and G represents the content of OM.

Based on the OM degradation rate, the SR and ME rates can be written as follows:

$$R_{SR} = \frac{1}{2} \cdot f_S \cdot R_{OM} \tag{8}$$

$$R_{ME} = \frac{1}{2} \cdot (1 - f_S) \cdot R_{OM} \tag{9}$$

where fs is an error residual function (Chuang et al., 2019; Xu et al., 2023), as:

$$f_S = 0.5 \cdot erfc\left(\frac{C_S - C_S^*}{b}\right) \tag{10}$$

where C_s is the sulfate concentration, $C_S{}^*$ is the threshold sulfate concentration for methanogenesis (~ 1 mM), and b (~ 0.001) is a parameter controlling the steepness of f_S. When OM is degradated by OSR, fs = 1; and when OM is degradated by methanogenesis, fs = 0.

The ratio of DIC production from sulfate consumption via AOM is 1:1, and the rate of AOM can be described as:

$$R_{AOM} = k_{AOM} \cdot C_M \cdot C_S \tag{11}$$

where C_M is methane concentration, C_S is sulfate concentration and k_{AOM} is the first order rate constant for AOM.

The precipitation of carbonate is the sink of calcium and DIC (Equation 3), and its rate was calculated as Equation 12 (Luff et al., 2001):

$$R_{CA} = k_{Ca} \cdot \left(\frac{C_{calcium} \cdot C_{carbonate}}{K_{SP}^*} - 1\right) \tag{12}$$

where $C_{calcium}$ and $C_{carbonate}$ represent the contents of calcium ions and carbonate, K^*_{SP} is the stoichiometric solubility constant of solid carbonate, k_{Ca} is the first-order kinetic rate constant for carbonate precipitation. The precipitation rate of magnesium (Mg^{2+}) in porewater is correlated with the precipitation rate of Ca^{2+} (Fantle and DePaolo, 2006; Fantle and DePaolo, 2007; Zhang and DePaolo, 2020), which can be written as following:

$$R_{Mg} = K_{Mg} \cdot \frac{C_{Mg}}{C_{Ca}} \cdot R_{cal} \tag{13}$$

TABLE 1 Model parameters and boundary conditions for the sediment cores in the study area.

Parameter	G01	G16	G19	G34	G57	G58	Source
Seafloor temperature (T, °C)	5.2	4.3	3.7	3.4	1.9	1.8	a
Salinity (S)	36.9	36.3	35.8	35.6	35.9	36.3	b
Pressure (P, MPa)	10.5	13.5	15.4	16.5	21.5	21.8	c
Density (ρ, kg/m^3)	2.6×10^3	2.6×10^3	2.6×10^3	2.6×10^3	2.6×10^3	2.6×10^3	c
Sedimentation rate (ω, cm/a)	4.2×10^{-3}	3.8×10^{-3}	3.4×10^{-3}	3.5×10^{-3}	2.9×10^{-3}	2.8×10^{-3}	d
Molecular diffusion coefficient of Sulfate (m^2/a)	1.8×10^{-2}	1.8×10^{-2}	1.8×10^{-2}	1.8×10^{-2}	1.8×10^{-2}	1.8×10^{-2}	e
Molecular diffusion coefficient of Methane (m^2/a)	2.9×10^{-2}	2.9×10^{-2}	2.9×10^{-2}	2.9×10^{-2}	2.9×10^{-2}	2.9×10^{-2}	e
Molecular diffusion coefficient of DIC (m^2/a)	1.9×10^{-2}	1.9×10^{-2}	1.9×10^{-2}	1.9×10^{-2}	1.9×10^{-2}	1.9×10^{-2}	e
Molecular diffusion coefficient of Ca (m^2/a)	1.3×10^{-2}	1.3×10^{-2}	1.3×10^{-2}	1.3×10^{-2}	1.3×10^{-2}	1.3×10^{-2}	e
Molecular diffusion coefficient of Mg (m^2/a)	1.2×10^{-2}	1.2×10^{-2}	1.2×10^{-2}	1.2×10^{-2}	1.2×10^{-2}	1.2×10^{-2}	e
Upper boundary condition for sulfate (mM)	25	28	29	32	28	30	b
Upper boundary condition for methane	∂ C/∂ X = 0	∂ C/∂ X = 0	∂ C/∂ X = 0	∂ C/∂ X = 0	∂ C/∂ X = 0	∂ C/∂ X = 0	b
Upper boundary condition for DIC (mM)	9.1	2.1	2.1	2.1	5	3.5	b
Upper boundary condition for Ca (mM)	7	8	8.5	9.5	8	9.2	b
Upper boundary condition for Mg (mM)	58	56	56.5	56	56	56	b
Upper boundary condition for ^{13}DIC	-10	-5	-5	-7	-10	-5	b
Lower boundary condition for sulfate (mM)	∂ C/∂ X = 0	∂ C/∂ X = 0	∂ C/∂ X = 0	∂ C/∂ X = 0	∂ C/∂ X = 0	∂ C/∂ X = 0	b
Lower boundary condition for methane (mM)	8	8	10	10	/	/	b
Lower boundary condition for DIC	∂ C/∂ X = 0	∂ C/∂ X = 0	∂ C/∂ X = 0	∂ C/∂ X = 0	∂ C/∂ X = 0	∂ C/∂ X = 0	b
Lower boundary condition for Ca	∂ C/∂ X = 0	∂ C/∂ X = 0	∂ C/∂ X = 0	∂ C/∂ X = 0	∂ C/∂ X = 0	∂ C/∂ X = 0	b
Lower boundary condition for Mg	∂ C/∂ X = 0	∂ C/∂ X = 0	∂ C/∂ X = 0	∂ C/∂ X = 0	∂ C/∂ X = 0	∂ C/∂ X = 0	b
Upper boundary condition for ^{13}DIC	∂ C/∂ X = 0	∂ C/∂ X = 0	∂ C/∂ X = 0	∂ C/∂ X = 0	∂ C/∂ X = 0	∂ C/∂ X = 0	b

[a]Wu et al., 2021; [b]this study; [c]Bohrmann and cruise participants, 2008; [d]Boudreau, 1997; Luff et al., 2000.
The upper boundary of SO_4^{2-}, Ca^{2+}, δ^{13}C-DIC of the model was based on the porewater data of the shallowest sample, and DIC was derived from the modern seawater dataset (Meister et al., 2019). The lower boundary of SO_4^{2-}, Ca^{2+}, DIC, δ^{13}C-DIC, and the upper boundary of methane were designed as the Neumann boundary (the gradients of their concentrations were assumed to be zero) (Dale et al., 2019). The production and consumption of each dissolved species are based on reaction equations (Equations 1–3), and their rates were described as (Equations 7–16).

where C_{Mg} and C_{Ca} are the porewater concentrations of Mg^{2+} and Ca^{2+}, and k_{Mg} is the first-order kinetic rate constant for magnesium precipitation.

The absolute concentrations of [^{13}DIC] and [^{12}DIC] were computed by separate reaction-transport (Equation 14) for each isotope ($R = R_{12} + R_{13}$). Minor carbon isotope fractionation occurs during OSR, AOM and carbonate precipitation (Meister et al., 2013; Chuang et al., 2019; Meister et al., 2019). Hence, the sources and sinks are assumed proportional to the isotopic composition of the source pool, and the rate of CH_4 can be calculated as follows:

$$\frac{R_{13-AOM}}{R_{12-AOM}} = \alpha_{AOM} \cdot R_{CH_4} \tag{14}$$

Methanogenesis can occur via two main pathways: the autotrophic pathway using CO_2 and H_2 and the acetoclastic pathway using acetate. However, independent of the pathway, the sources of methane and DIC are in isotopic proportion with the OM by the fractionation factor α and 2-α, respectively (Meister et al., 2019).

$$\frac{R_{13}(CH_4)}{R_{12}(CH_4)} = \alpha_{ME} \cdot R_G \tag{15}$$

$$\frac{R_{13}(DIC)}{R_{12}(DIC)} = (2 - \alpha_{ME}) \cdot R_G \tag{16}$$

The concentration profiles of diverse species and R_{AOM} from Zone 1 and Zone 2 were simulated in this study. The modeling results are almost consistent with the measured concentrations of SO_4^{2-}, Ca^{2+}, and Mg^{2+} in Zone 1 and Zone 2 (Supplementary Table S4; Figure 8). By contrast, DIC concentration and δ^{13}C-DIC have a poor match with the simulated curve (Figure 8) and the possible explanation is that DIC samples undergo degassing during collection and storage, which will cause $CaCO_3$ to precipitate

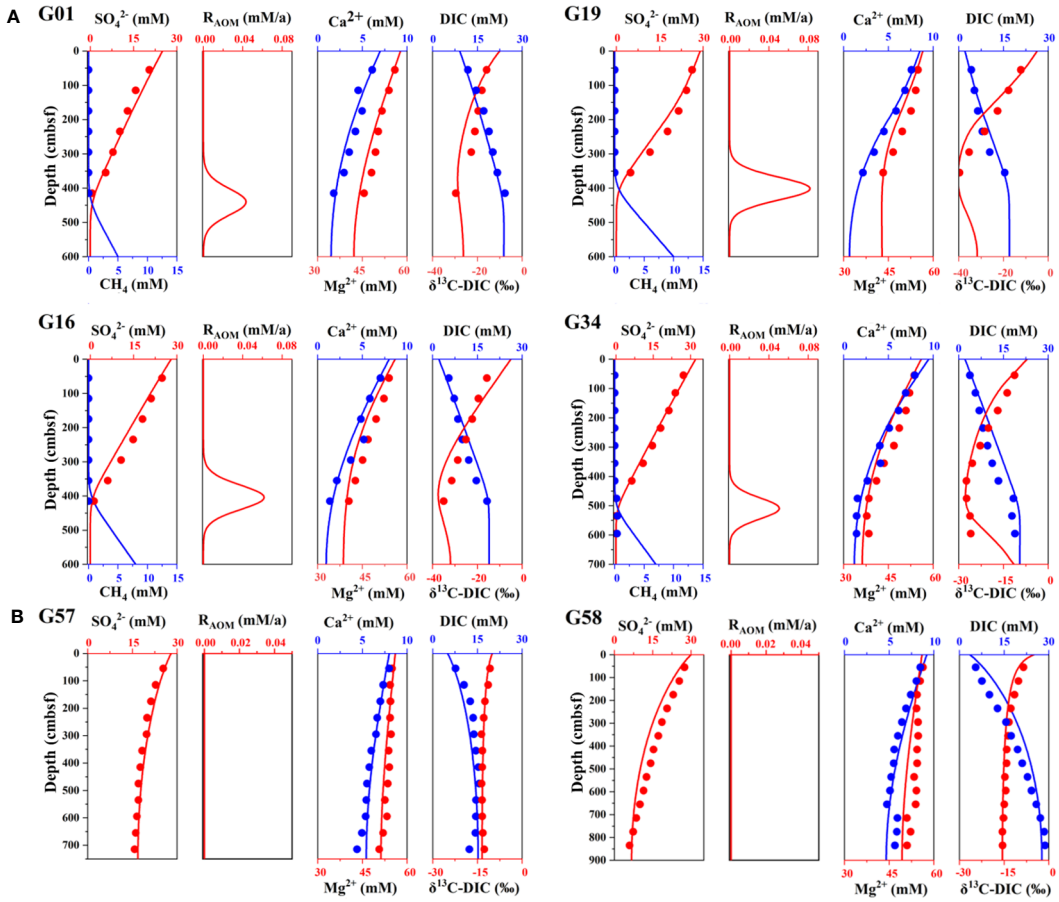

FIGURE 8
Measured (dots) and simulated (curves) depth profiles of the study sites **(A)** G01, G16, G19, and G34 (Zone 1) and **(B)** G57 and G58 (Zone 2). Down-depth profiles of SO_4^{2-}, CH_4, R_{AOM}, Ca^{2+}, Mg^{2+}, DIC and δ^{13}C-DIC. (The depth range of each site in the figure is different).

from the solution and lead to changes in physiochemical conditions (Miller et al., 2017).

Considering the uncertainty in methane sampling, the simulation of methane profiles is not only based on methane concentration profiles but also the porewater profiles of SO_4^{2-} and δ^{13}C-DIC. As shown in Figure 8, the methane concentration at sites G01, G16, G19, and G34 in Zone 1 increases significantly at the bottom of sediments, while there is no methane occurring within the depth profiles of the sites G57 and G58 in Zone 2. In addition, the R_{AOM} of Zone 2 is zero and the decreasing trend of Ca^{2+} and Mg^{2+} is not as obvious as that of Zone 1. Based on the calculation of the reaction-transport model, site G19 has the highest value of R_{AOM} with 71.55 mmol/m^2·yr. Furthermore, the rates of authigenic carbonate precipitation are simulated as 7.54 mmol/m^2·yr at site G01, 8.12 mmol/m^2·yr at site G16, 7.20 mmol/m^2·yr at site G19, and 10.11 mmol/m^2·yr at site G34, respectively. In contrast, the rates of authigenic carbonate precipitation in Zone 2 are much lower than those in Zone 1. According to the OM degradation rate and calculation by the reaction-transport model (Equation 9), the methanogenesis rates at sites G01, G16, G19 and G34 are 1.70 mmol/m^2·yr, 2.30 mmol/m^2·yr, 1.40 mmol/m^2·yr and 0.92 mmol/m^2·yr, respectively, however, the rates at sites G57 and G58 are nearly 0 (Supplementary Table S5).

5 Discussion

5.1 The relationship of the fluxes of DIC and SO_4^{2-} with SMT depth

The SMT, an important biogeochemical zone characterized by the simultaneous consumption of sulfate and methane (AOM, Equation 1), is commonly observed in methane-rich marine sediments at relatively shallow depths below the seafloor (1 ~ 30 mbsf) (Malinverno and Pohlman, 2011). Within or near the SMT zone, the depletion of sulfate can lead to the dissolution of barite, thereby causing an increase in the concentration of porewater Ba^{2+} (Aloisi et al., 2004; Riedinger et al., 2006; Snyder et al., 2007). In this study, we also observed an increasing trend of Ba^{2+} concentration at or below the depth of SMT, but its concentration was relatively low, which may be mainly due to the lower content of barite minerals in the sediments (Supplementary Table S1). Here, we define the depth of SO_4^{2-} becomes near depleted (1 mM) as the SMT depth, which can be derived using the least square method by fitting the SO_4^{2-} depth profiles of all sampling sites (Borowski et al., 1999; Arndt et al., 2013; Chuang et al., 2016; Feng et al., 2018). When the sediment core sampling does not cross the SMT, the depth of the SMT can be achieved by extrapolating the SO_4^{2-} concentration

gradient to a depth where porewater SO_4^{2-} concentrations are near depleted (Smith and Coffin, 2014).

It should be noted that a shallow SMT often occurs a few centimeters below the seafloor with significant advection of upward fluids, such as seeps and vents, because the advecting fluids typically have a higher concentration of CH_4 than surrounding sediment, and advection often involves multiphase fluid flow (free gas and liquid) that may be episodic (Luff and Wallmann, 2003; Miller et al., 2017). However, the depths of SMT at our sampling sites are greater than 4 m and the porewater SO_4^{2-} concentrations exhibit a linear decrease in depth profiles, thereby suggesting that the impact of advection of upward fluids is not significant in this study area. Assuming under steady-state conditions, the diffusion rates of diverse species such as SO_4^{2-}, Ca^{2+}, Mg^{2+} and DIC, can be calculated from the linear fit to the species concentration (Supplementary Table S4) gradient according to Fick's first law (Equation 17) (e.g., Berner, 1978; Coffin et al., 2015):

$$J = -\varphi \cdot Ds \cdot \frac{dc}{dx} \quad (17)$$

where J is the diffusive flux (mmol/m^2 yr); φ is the porosity; Ds is the diffusion coefficient (m^2/s) which is related to temperature; c is the concentration of diverse species in pore water (mM), and x is the depth (mbsf). The bottom water temperatures at the study sites are shown in Table 1, and porosity is obtained by a functional relationship with depth (Equation 5). In this study, we set that the downward flux (SO_4^{2-}) is negative (into the sediments) corresponding to an upward flux (positive) for DIC out of the sediments. Due to the core sampling not crossing the SMT, it is difficult to estimate the flux of DIC upward from below the SMT. Nonetheless, our calculation results of the reaction-transport model show that the methanogenesis rate is much lower than the rates of AOM and OSR, indicating the flux of DIC from below SMT is much smaller than that from above SMT (Equation 9; Supplementary Table S5). Thus, the DIC_{net} flux is approximated as DIC diffusion upward through the sediments above the SMT (J_{DIC}) and the loss of DIC by authigenic carbonate precipitation (Table 2), where the loss flux of DIC can be estimated using the porewater concentration profiles of Ca^{2+} and Mg^{2+} (Equation 18) (Smith and Coffin, 2014):

$$J_{DIC_{net}} = J_{DIC} + J_{Mg^{2+}} + J_{Ca^{2+}} \quad (18)$$

The fluxes of SO_4^{2-} and DIC_{net} in Zone 2 are significantly lower than those in Zone 1, and the larger fluxes of SO_4^{2-} and DIC_{net} correspond to the shallower SMT depth (Table 2). We combined the data from this study with the published data (Figure 9), and found that the DIC_{net} and SO_4^{2-} fluxes of all comparing sites have an exponential relationship with SMT depths ($y = 273.63x^{-1.17}$ and $y = -267.89x^{-1.37}$, Figure 9), which is very consistent with the report by Miller et al. (2017). The explanation for this correlation potentially lies in the fact that the fluxes of DIC and SO_4^{2-} to the SMT depth are mainly controlled by the reactivity and content of sediment OM in depth profiles (Egger et al., 2018; Xu et al., 2023). The diffusion flux of SO_4^{2-} is approximately equal to that of CH_4 within the SMT (Equation 1), so the depth of the SMT can provide a relatively qualitative prediction of upward CH_4 flux in the sediments.

5.2 Sulfate consumption pathways (OSR vs. AOM)

The depth profiles of porewater δ^{13}C-DIC exhibit the obvious characteristic pattern reflecting the occurrence of AOM. Especially, the minimum values of δ^{13}C-DIC (−27.40 ‰ to −39.60 ‰, Figure 4) at the depth of sulfate depletion are significantly more negative than that of the δ^{13}C of sedimentary OM found in this region (~ −21.0 ‰, von Rad et al., 1996). If only the degradation of organic carbon occurs within this depth range, then the δ^{13}C-DIC value should lie between that of seawater (0 ‰ PDB) and that of organic carbon (~−21.0 ‰). Thus, the isotopic signature of DIC of this study indicates the additional source of light carbon in Zone 1 (Figure 4). The most likely source is AOM, which produces δ^{13}C-DIC that is isotopically lighter than that predicted from the simple mixing of the carbon derived from the OM degradation and seawater. Besides this, the

TABLE 2 SMT depth, sulfate diffusion rates (J_{SO4}^{2-}), Ca^{2+} diffusion rates (J_{Ca}^{2+}), Mg^{2+} diffusion rates (J_{Mg}^{2+}) and DIC diffusion rates (J_{DIC}) at all sampling sites of methane-hydrate area in Makran continental margin.

Sample station	Water depth (m)	Core length (cm)	SMT depth (m)	J_{SO4}^{2-} (mmol/m^2·yr)	J_{Ca}^{2+} (mmol/m^2·yr)	J_{Mg}^{2+} (mmol/m^2·yr)	J_{DIC} (mmol/m^2·yr)	J_{DICnet} (mmol/m^2·yr)
Zone 1								
G01	844	415	4.12	−78.00	11.53	23.03	52.44	87.00
G16	1441	415	4.35	−92.68	14.34	32.23	45.64	92.21
G19	2214	355	4.32	−101.38	17.02	32.58	37.72	87.32
G34	2046	595	5.36	−77.82	12.76	28.92	37.61	79.30
Zone 2								
G57	3047	715	17.81	−16.63	3.88	4.20	22.83	30.92
G58	3102	835	10.23	−34.10	4.99	3.99	42.85	51.83

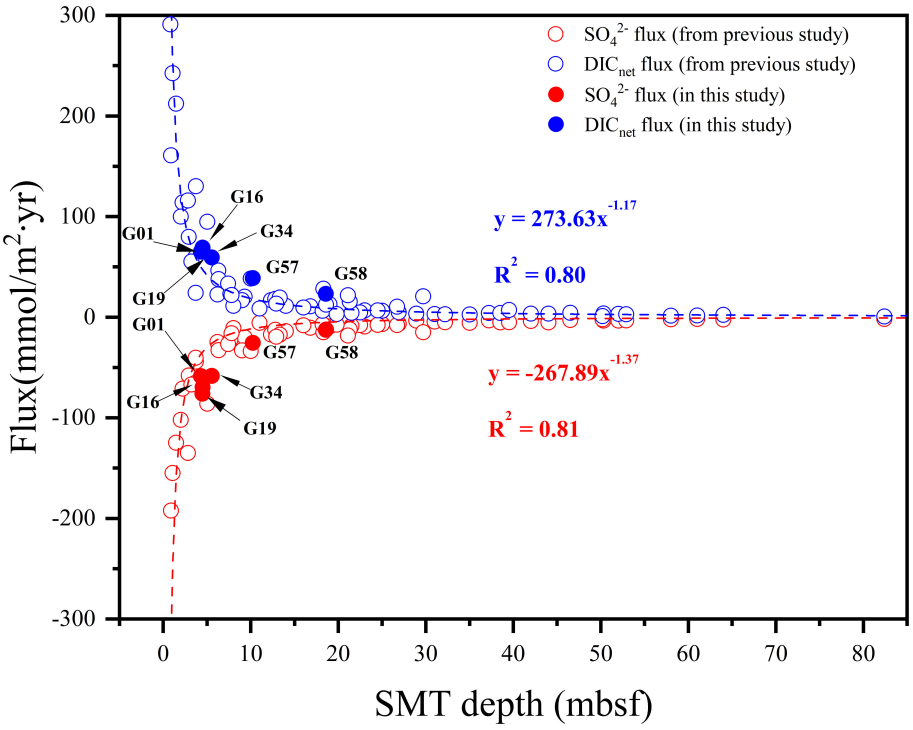

FIGURE 9
The exponential relationship of SO_4^{2-} and DIC_{net} flux with SMT depth. The data are soured from the Makran accretionary wedge (Zhang et al., 2021b), Beaufort Sea (Coffin et al., 2013; Miller et al., 2017), East Siberian Slope (Miller et al., 2017), New Jersey Continental Slope (Berg, 2008), Blake Ridge (Paull et al., 1996; Keigwin et al., 1998; Berg, 2008), Gulf of Mexico (Kastner et al., 2008), Amazon Fan (Flood et al., 1995; Burns, 1998; Berg, 2008), Western Africa (Wefer et al., 1998; Berg, 2008), Oman (Berg, 2008), Bering Sea (Keigwin et al., 1998; Takahashi et al., 2011), Cascadia (Claypool et al., 2006; Dickens and Snyder, 2009), Umitaka Spur (Snyder et al., 2007), Japan Sea (D'Hondt et al., 2002), California Margin (Berg, 2008), Nankai Trough (Moore et al., 2001; Berg, 2008), Costa Rica Margin (Kimura et al., 1997; Berg, 2008), New Zealand (Hamdan et al., 2011; Coffin et al., 2014) and Antarctic (Geprägs et al., 2016), where the flux calculation results are cited from Miller et al. (2017).

decomposition of OM through bacterial sulfate reduction (OSR) can generate DIC and NH_4^+ and enter the surrounding porewater in the methane-bearing sediments (e.g., Luo et al., 2013; Zha et al., 2022), so NH_4^+ is an effective indicator of the extent of OM degradation because NH_4^+ is mainly produced via anaerobic bacterial decomposition of nitrogen-bearing organic compounds (Wehrmann et al., 2011; Mazumdar et al., 2014). It should be mentioned that the distribution of porewater NH_4^+ is influenced by many other factors. The first is the dilution of freshwater released by methane-hydrate decomposition. However, no significant fluctuations in Cl^- concentration were observed in the depth profiles, indicating that porewater NH_4^+ concentration is not affected by this effect. Secondly, methanogenesis in the sediments can also increase porewater NH_4^+ concentration (Mazumdar et al., 2014), but our results from the species concentration profiles and reaction-transport modeling confirm that the effect of deep methanogenesis is very limited (Supplementary Table S5). In addition, the temperature can affect ion diffusion and microbial-mediated OM decomposition, leading to changes in porewater NH_4^+ concentration in depth profiles (Sivan et al., 2007; Zhang et al., 2021b), but the temperature variation is very small due to a relatively short sediment core (< 8.5 m) in our sampling sites. Thus, the influence of temperature on NH_4^+ concentration can be ignored.

As shown in Figures 10A and B, the cross-plots of SO_4^{2-} vs. NH_4^+ display a significant negative relationship, indicating the OSR process is accompanied by OM decomposition and NH_4^+ release in the study area. By comparison, the slope of SO_4^{2-}–$NH4^+$ at site G01 (k = −0.033) is larger than those at all other sites (Figure 10), and the possible reason is due to the adsorption of NH_4^+ by clay minerals in the sediment at this site (Lukawska-Matuszewska and Kielczewska, 2016). Avinash et al. (2016) showed that the Arabian Sea sediments contain abundant illite with a large capacity for potassium-ammonium cation exchange, which originates from the fluvial or aeolian transport (wind-blown dust from the adjacent deserts). Therefore, we speculate that site G01 is more likely to receive abundant clay minerals like illite to absorb more NH_4^+ than other sites because it is located in a shallower water depth (844 m, Tabel 2). Although the OSR process occurs, our calculated flux of NH_4^+ (3.35 ~ 17.78 mmol/m^2·yr) is much smaller than that of SO_4^{2-} (77.82 ~ 101.38 mmol/m^2·yr), indicating that OSR does not play a dominant role in porewater sulfate reduction.

Distinguishing the relative contributions of OSR and AOM to sulfate consumption is crucial to accessing methane flux into the SMT and the associated biogeochemical processes occurring in marine sediments (Malinverno and Pohlman, 2011; Luo et al., 2013). In the reaction of AOM, the molecule ratio of the sulfate consumption vs. DIC generation is 1:1 on the basis of the chemical reaction formula (Equation 1), while in the OSR process, the consumption of one molecule of sulfate produces two molecules of DIC (Equation 2).

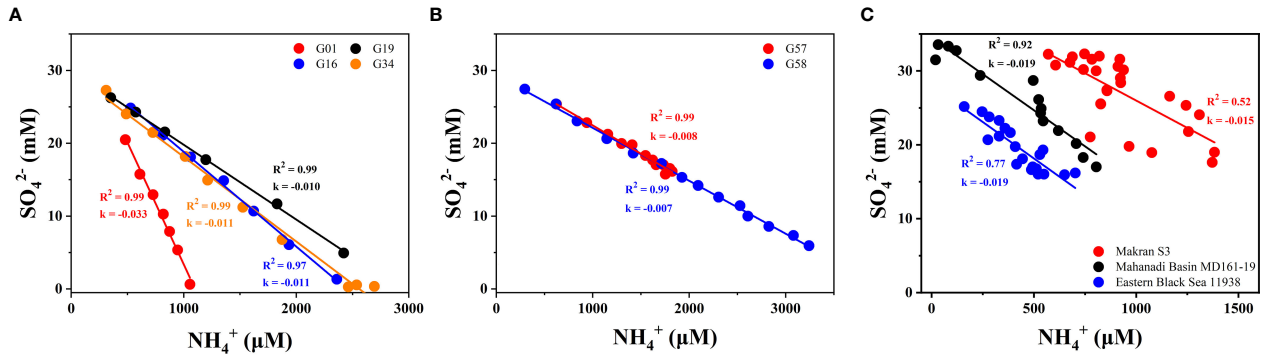

FIGURE 10
Cross-plot of porewater sulfate versus ammonium at the study sites. **(A)** sites G01, G16, G19, and G34 (Zone 1); **(B)** sites G57 and G58 (Zone 2); **(C)** different seepage sites in previous studies. The k represents the slope of SO_4^{2-} - NH_4^+. The correlation coefficients are labeled close to the fitting lines, together with corresponding annotations. Data for Eastern Black Sea 11938 is cited from Reitz et al. (2011); Mahanadi Basin MD161-19 from Mazumdar et al. (2014); and Makran S3 from Zhang et al. (2021b).

Therefore, the scatter plot of the flux of SO_4^{2-} vs. DIC_{net} can be used to estimate the relative contribution fractions of AOM and OSR to total porewater SO_4^{2-} consumption (Smith and Coffin, 2014).

As shown in Figure 11, dots of Zone 1 (G01, G16, G19 and G34) in the methane-hydrate area fall near the AOM line, indicating the AOM reaction is the major process for sulfate reduction (Akam et al., 2020; Zhang et al., 2021b). In comparison, dots of G57 and G58 of Zone 2 in the background area are closer to the OSR line, thus proving that OSR is the dominant process for sulfate consumption. This is further supported by simulation results from the reaction-transport model, as the rates of AOM in Zone 1 are higher than those in Zone 2 (Figure 8; Supplementary Table S5).

5.3 Sources of porewater DIC

Porewater DIC mainly originates from AOM, OSR and the seawater that trapped during sediment accumulation (e.g., Borowski et al., 2000; Chatterjee et al., 2011; Feng et al., 2018; Meister et al., 2019; Akam et al., 2020). In some cases, the

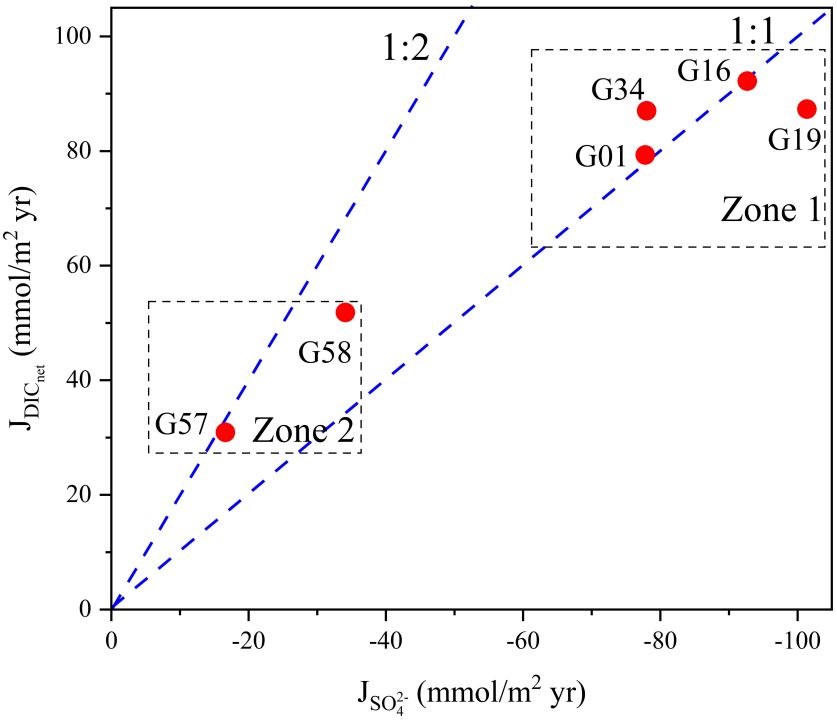

FIGURE 11
Scatter plot of flux of porewater SO_4^{2-} vs. DIC_{net} for the sites in Zone 1 and Zone 2 (Table 2). The 1:2 line indicates the molar stoichiometry of SO_4^{2-} consumption to DIC production for OSR (Equation 2), and the 1:1 line indicates the molar stoichiometry of SO_4^{2-} consumption to DIC production for AOM (Equation 1).

incorporation of DIC from deep sediments may affect the δ^{13}C-DIC within the SMT (e.g., Chatterjee et al., 2011; Hu et al., 2022; Zha et al., 2022), but based on the modeling results of methane turnovers, the calculating depth-integrated AOM rates at sites G01, G16, G19 and G34 are about 25 to 51 times of the *in situ* methanogenesis rates (Supplementary Table S6). Therefore, *in situ* methanogenesis constitutes a minor proportion of the total DIC, whose effect on deep DIC production can thus be ignored in this study.

Here, an isotope mass balance model (Equation 19) was used to distinguish the source of porewater DIC in the closed systems (Borowski et al., 2000; Chen et al., 2010; Zhang et al., 2021b):

$$\delta^{13}C_{\mathrm{DIC-added}} = (X_{OM}) \star (\delta^{13}C_{OM}) + (X_{AOM}) \star (\delta^{13}C_{AOM}) + (X_{SW}) \star (\delta^{13}C_{SW}) \quad (19)$$

where X is the proportion of DIC from different sources, and δ^{13}C is the carbon isotope composition. The subscripts *AOM*, *SW* and *OM* refer to DIC derived from the sources listed above and the value of *Xsw* is obtained through dividing the DIC concentration of the overlying seawater by the DIC value within the SMT (Borowski et al., 2000). In this study, the average value of δ^{13}C-TOC for each core sediment is taken as the $\delta^{13}C_{OM}$. The δ^{13}C value of CH_4 (−68.5 ‰) is followed as reported by Römer et al. (2012). The $\delta^{13}C_{\mathrm{DIC\text{-}added}}$ is defined as the isotopic value of the DIC being added to the initial porewater since the burial, which can be obtained from the slope of the linear regression graph of DIC vs. δ^{13}C-DIC*DIC (Ussler and Paull, 2008; Chen et al., 2010; Zhang et al., 2021b).

The $\delta^{13}C_{\mathrm{DIC\text{-}added}}$ at sites G57 (−16.7 ‰) and G58 (−17.2 ‰) are more positive than $\delta^{13}C_{OM}$ (Figure 12B), indicating that the porewater DIC in Zone 2 is less affected by AOM. In Zone 1, however, the relative contributions of the AOM process to total porewater DIC are 60% at site G01, 52% at site G16, 68% at site G19, and 25% at site G34 (Table 3). By comparison, the δ^{13}C-DIC$_{\mathrm{added}}$ value at site G34 (−31.6 ‰) is similar to that at site S3 in Makran from Zhang et al. (2021b) (−33.1 ‰) indicating that the two adjacent sites have the same DIC source (Figure 12A; Table 3). The difference in the percentage of porewater DIC sources at different sites is likely related to the flux of the upward diffusion of CH_4 in the methane-hydrate area (Chuang et al., 2013; Wei et al., 2019; Feng et al., 2020).

5.4 Removal of DIC by authigenic carbonate precipitation

The formation of authigenic carbonate is an important pathway to remove porewater DIC, particularly in continental shelf regions (e.g., Sun and Turchyn, 2014; Bradbury and Turchyn, 2019; Wang et al., 2019; Ruban et al., 2020; Loyd and Smirnoff, 2022). In this study, porewater Ca^{2+} and Mg^{2+} concentrations decrease with depth, suggesting the authigenic carbonate precipitation at sites in the study area (Ritger et al., 1987; Aloisi et al., 2002; Snyder et al., 2007; Nöthen and Kasten, 2011). Numerical simulation by the reaction-transport model shows that the rate of authigenic carbonate precipitation is 10 mmol/m^2·yr at site G34, slightly higher than that at sites G01 (8 mmol/m^2·yr), G16 (8 mmol/m^2·yr), and G19 (7 mmol/m^2·yr). The rates of authigenic carbonate precipitation at the sites in Zone 1 (average 8.25 mmol/m^2·yr) are much higher than the global average (~5 mmol/m^2·yr, Sun and Turchyn, 2014), emphasizing the significance of the methane hydrate area in the formation and burial of authigenic carbonate in global marine sediments. Compared with Zone 1, the rate of authigenic carbonates at sites G57 and G58 in the background area (Zone 2) is much lower (average 4 mmol/m^2·yr).

The XRD analysis shows the mineral species of authigenic carbonate precipitation at sites G16, G34 and G58, which are

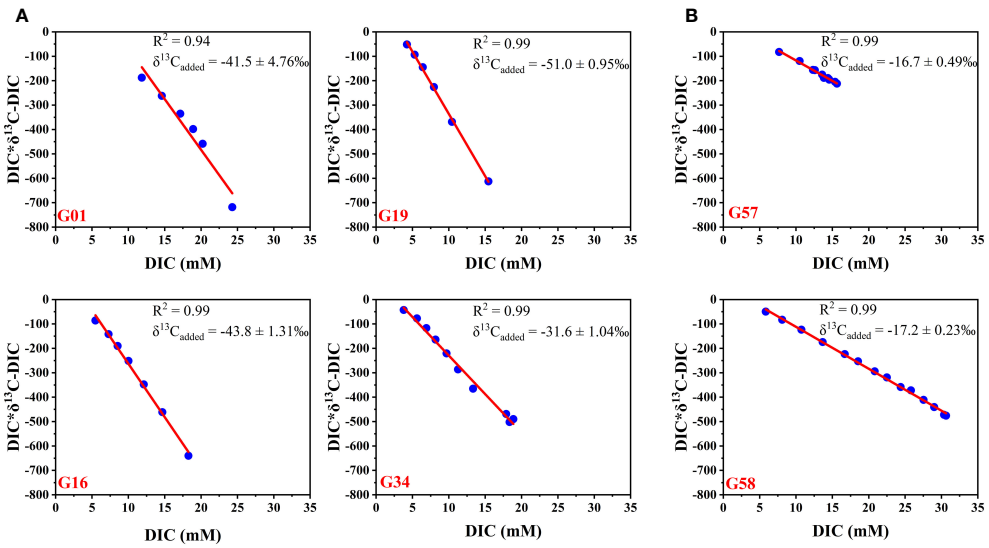

FIGURE 12
Linear regression diagrams of DIC vs δ^{13}C-DIC*DIC at different sampling sites. **(A)** sites G01, G16, G19, and G34 (Zone 1); **(B)** sites G57 and G58 (Zone 2).

TABLE 3 The proportions of the various sources of DIC at different sampling sites.

Sample station	$\delta^{13}C_{DIC\text{-}added}$ (‰)	$\delta^{13}C_{OM}$ (‰)	X_{OM} (%)	$\delta^{13}C_{SW}$ (‰)	X_{SW} (%)	$\delta^{13}C_{AOM}$ (‰)	X_{AOM} (%)
Zone 1							
G01	−41.5	−21.2	2	0	38	−68.5	60
G16	−43.8	−22.1	36	0	12	−68.5	52
G19	−51.0	−22.0	20	0	12	−68.5	68
G34	−31.6	−22.0	65	0	10	−68.5	25
Zone 2							
G57	−16.7	−22.2	ND	0	ND	−68.5	0
G58	−17.2	−22.2	ND	0	ND	−68.5	0
Makran							
S3	−33.1	−21.0	63	0	7	−68.5	30

ND means not determined. The data of site S3 is cited from Zhang et al. (2021b). The values of $\delta^{13}C_{SW}$ were estimated to be 0 ‰V-PDB refer to Zhang et al. (2021b).

mainly composed of calcite, aragonite, and dolomite (Figure 6; Supplementary Table S1). The molar fraction of $MgCO_3$ in calcite can be obtained by lattice parameters of calcite (Titschack et al., 2011; Dos Santos et al., 2017; Fahad and Saeed, 2018). Based on the XRD/Rietveld analysis, we found that the molar fraction of $MgCO_3$ in calcite is less than 10% at all sites in our study, indicating the absence of high-Mg calcite (Supplementary Table S6). In Zone 1, authigenic carbonate phases exhibit notable variations at different depths (Supplementary Table S1; Figure 6) of sites G16 and G34. At the surface sediments (55 cmbsf depth), calcite is the main component of carbonate phases, and aragonite is almost undetectable. However, the highest aragonite content occurs around the SMT with a depth of 415 cmbsf at site G16 (5.27%) and 535 cmbsf at site G34 (12.09%) (Supplementary Table S1), resulting in the highest ratio of aragonite/∑carbonate and the lowest ratio of calcite/∑carbonate appear at the SMT depth (Supplementary Table S2; Supplementary Figure S1). Many factors, such as sulfate inhibition and the presence of extracellular polymeric substances (EPS), can affect the formation of carbonate mineral phases (e.g., Formolo et al., 2004; Himmler et al., 2015; Li et al., 2018; Wang et al., 2019). Based on the results of porewater DIC and XRD analysis, however, we speculate that the solubility of carbonate minerals may play a significant role in the aragonite precipitation. According to carbonate solubility, calcite (K'= 7.98×10^{-7} at 5°C in 34.5‰ seawater) precipitation takes priority over aragonite (K'= 11.4×10^{-7} at 5°C in 34.5‰ seawater) (Berner, 1976). Therefore, at surface depth with relatively low DIC concentrations, calcite precipitates first. With the increase of DIC generated by the microbial-mediated AOM occurring around SMT depth (Chafetz et al., 1991; Peckmann et al., 2001; Liu et al., 2016), aragonite starts to precipitate, leading to the highest ratio of aragonite/∑carbonate around the SMT depth compared to other depths. Nevertheless, this ratio remains lower than that of calcite/∑carbonate at all depths. By contrast, aragonite does not appear while calcite is the dominant carbonate phase in Zone 2 (site G58) (Supplementary Tables S1, S2), which is similar to the distribution of carbonate phases in surface sediments of Zone 1, as it is less affected by AOM (Liu et al., 2016; Li et al., 2018; Wei et al., 2020). Although dolomite is one of the carbonate phases in the study area, its content is relatively low (Zone 1: 2.73% ~ 4.47% at site G16; 2.47% ~ 4.52% at site G34; Zone 2: 2.52% ~ 3.10% at site G58) (Supplementary Table S1). Currently, the formation mechanism of dolomite is very complex and remains elusive (Cai et al., 2021). Microbially-mediated dolomite precipitation could possibly occur in modern reductive saline and anoxic environments (Warren, 2000; Cai et al., 2021), such as lagoons and gas hydrate areas (e.g., Casado et al., 2014; Li et al., 2018). Therefore, we infer that it is possible in the past that the accumulation of gas hydrates resulted in saline, sulfate-free porewaters which could host the small amounts of dolomite that we observed in this study.

5.5 Release of DIC to the overlying seawater

Theoretically, DIC that is not precipitated into authigenic carbonates can enter the upper sediment and eventually the overlying seawater through advection or diffusion (Chatterjee et al., 2011; Rassmann et al., 2018; Akam et al., 2020; Zhao et al., 2020). Based on extensive seafloor observations and geochemical analysis, methane hydrate systems contribute considerable proportions of the local carbon budget to the overlying seawater by emitting a large amount of DIC (Aharon et al., 1992; Suess et al., 1999; Garcia-Tigreros and Kessler, 2018; Feng et al., 2020). DIC released from marine sediments has an important influence on the carbonate equilibrium system in seawater (Chen, 2002; Krumins et al., 2013; Akam et al., 2020; Feng et al., 2020). Previous studies have shown that global DIC flux released from sediments to overlying seawater averages 6.5 Tmol/yr (3.2 ~ 9.2 Tmol/yr), of which 98% is released from continental margin sediments with the depth of SMT less than 13 m, equivalent to approximately 20% of the global river DIC (~ 33 Tmol/yr) flowing into the ocean (Meybeck, 1993; Amiotte Suchet et al., 2003; Treude et al., 2005; Aufdenkampe et al., 2011; Egger et al., 2018; Akam et al., 2020).

TABLE 4 The calculated DIC fluxes of the Makran continental margin by simulation using the reaction-transport model.

Sample station	DIC_{OSR} (mmol/m^2·yr)	DIC_{AOM} (mmol/m^2·yr)	DIC_{total} (mmol/m^2·yr)	$DIC_{carbonate}$ (mmol/m^2·yr)	DIC_{burial} (mmol/m^2·yr)	DIC_{out} (mmol/m^2·yr)
Zone 1						
G01	27	43	70	8	1	61
G16	21	57	78	8	0.7	69.3
G19	27	71	98	7	0.6	90.4
G34	15	47	62	10	0.7	51.3
Zone 2						
G57	27	0	27	4	0.4	22.6
G58	27	0	27	4	0.8	22.2

In this study, we use the reaction-transport model to quantitatively assess the DIC fluxes released from the sediments into the overlying seawater of the Makran continental margin (Table 4). In this calculation, DIC_{OSR}, DIC_{AOM} and $DIC_{carbonate}$ are simulated by the rate of OM decomposition, the rate of AOM within SMT, and the depth profile of Ca^{2+} concentration, respectively. As described previously, the situ methanogenesis via shallow OM decomposition is very low (Supplementary Table S5), so the contribution of DIC generated through this process is not considered. The flux of DIC_{burial} is constrained by the sedimentation rate and DIC concentration (Zha et al., 2022), thus it can be estimated by the reaction-transport model (Table 4). Furthermore, the DIC released from sediment to overlying seawater can be defined as Equation 20 (Wallmann et al., 2008; Dickens and Snyder, 2009; Chatterjee et al., 2011; Solomon et al., 2014; Akam et al., 2020):

$$DIC_{out} = DIC_{OSR} + DIC_{AOM} - DIC_{carbonate} - DIC_{burial} \quad (20)$$

Based on the Equation 20, we find that DIC_{out} differs greatly between the site G19 (90.4 mmol/m^2·yr) and G34 (51.3 mmol/m^2·yr), although both sites are located in the methane-hydrate area (Figure 1). In addition, we compared the DIC_{out} values in Zone 1 (68 ± 14 mmol/m^2·yr) and Zone 2 (22.4 mmol/m^2·yr), and this difference is likely caused by the different DIC cycling patterns between the two Zones (Table 4; Figure 13). As shown in Table 4 and Figure 13, the DIC fluxes produced by AOM in Zone 1 is 55 ± 11 mmol/m^2·yr, which is significantly higher than that in Zone 2 (DIC_{AOM} = 0). Although the rate of authigenic carbonate formation is also relatively high in Zone 1, the process of carbonate precipitation is insufficient to prevent the release of large amounts of DIC from the sediment into the overlying seawater. By comparison, the fluxes of DIC released from sediments range from 51.3 to 90.4 mmol/m^2·yr in Zone 1, which is higher than those of other methane-hydrate areas, such as the Gulf of Mexico (9 ~ 33 mmol/m^2·yr, Smith and Coffin, 2014), Dongsha area of the southern South China Sea (13.1 ~ 26.1 mmol/m^2·yr, Chen et al., 2017), Shenhu area of the southern South China Sea (10.1 ~ 31.7 mmol/m^2·yr, Wu et al., 2013), and Beikang Basin (32.3 ~ 50.1 mmol/m^2·yr, Feng et al., 2018).

This upward DIC flux across the seafloor accounts for an average of 88% of the total DIC in Zone 1. Importantly, the process of AOM contributed a large proportion of DIC_{out} at sites G01, G16, G19, and G34 in Zone 1 (Table 4) due to the upward flux of CH_4. High rates of AOM can lead to an increase in DIC_{out} flux and total alkalinity (TA) in the overlying seawater (Akam et al., 2020; Zha et al., 2022), which is beneficial to reduce ocean acidification and increases the CO_2 absorption capacity of seawater (Chen, 2002; Krumins et al., 2013; Akam et al., 2020; Feng et al., 2020). In future, more related work on carbon cycling in methane-bearing sediments should be conducted to quantitatively assess the DIC and TA released from global marine

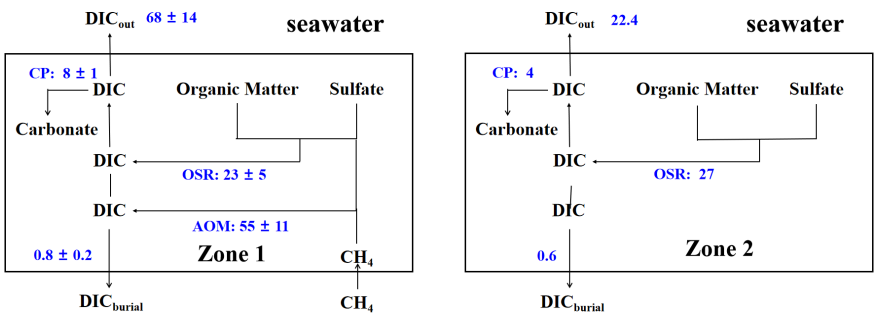

FIGURE 13
Two simplified schematics of the DIC release to the overlying seawater in Zone 1 and Zone 2. CP is the abbreviation for carbonate precipitation. The numbers represent the average flux and depth-integrated rates of DIC production and consumption in mmol/m^2·yr of DIC.

sediments to the overlying seawater and their impact on carbonate equilibrium in marine systems.

6 Conclusion

Based on the active density of flares at the Makran continental margin, we divided the study area into Zone 1 (an active accretionary environment with high methane flux) and Zone 2 (a farther offshore background area). The differences in geological structures and sampling locations between the two zones have a potential impact on the porewater geochemistry and DIC flux. Our results show that Zone 1 has the larger CH_4 flux with the shallower SMT depth, and a noticeable increase in porewater Ba^{2+} concentration was observed within or near the SMT zone. The flux of SO_4^{2-} vs. DIC_{net} was used to determine the pathway of sulfate consumption at each site, revealing that almost all porewater SO_4^{2-} at sites G57 and G58 in Zone 2 is consumed by OSR, the AOM reaction, however, is the main process of sulfate consumption affected by methane diffusion at sites in Zone 1. The relative contributions of AOM to the porewater DIC calculated by the isotope mass balance model are 60% (G01) and 52% (G16), 68% (G19), and 25% (G34) in Zone 1, respectively. The TIC, XRD and SEM analyses show that the total carbonate content increases with depth, and the carbonate phases are composed of calcite, aragonite, and dolomite. By comparison, calcite is the main carbonate phase while the dolomite content is relatively low. Due to high concentration of DIC induced by AOM, aragonite appears at or below the depth of SMT. The reaction-transport model results and calculation reveal that the flux of DIC released from sediments is 51.3 to 90.4 mmol/m^2·yr in Zone 1, which is significantly higher than that in Zone 2 (22.4 mmol/m^2·yr). Overall, this study highlights that the methane-related carbon pools are highly heterogeneous in the methane-hydrate area, and the contribution of AOM is essential to the authigenic carbonate burial and the bottom seawater chemistry.

Data availability statement

The raw data supporting the conclusions of this article will be made available by the authors, without undue reservation.

Author contributions

YC: Investigation, Formal analysis, Writing - Original Draft. SX: Formal analysis. WL: Investigation. JL: Resources, Investigation. ZZ: Investigation. TY: Investigation. XX: Investigation. XD: Investigation. HY: Resources, Investigation, Conceptualization, Methodology. ZW: Conceptualization, Methodology, Writing - Review & Editing. All authors contributed to the article and approved the submitted version.

Funding

The author(s) declare financial support was received for the research, authorship, and/or publication of this article. This study was funded by the Development Program of China (No. 2022YFC2805400) and National Natural Science Foundation of China (No. 41976057, 42276059).

Acknowledgments

We thank reviewers and Editor Glen T. Snyder for their constructive comments and suggestions, which greatly helped us improve our manuscript. We also thank Dr. Zhe Zhou (Tongji University) for constructive comments on manuscript writing.

Conflict of interest

The authors declare that the research was conducted in the absence of any commercial or financial relationships that could be construed as a potential conflict of interest.

Publisher's note

All claims expressed in this article are solely those of the authors and do not necessarily represent those of their affiliated organizations, or those of the publisher, the editors and the reviewers. Any product that may be evaluated in this article, or claim that may be made by its manufacturer, is not guaranteed or endorsed by the publisher.

Supplementary material

The Supplementary Material for this article can be found online at: https://www.frontiersin.org/articles/10.3389/fmars.2023.1181921/full#supplementary-material

References

Aharon, P., Graber, E. R., and Roberts, H. H. (1992). Dissolved carbon and $\delta^{13}C$ anomalies in the water column caused by hydrocarbon seeps on the northwestern Gulf of Mexico slope. *Geo-Marine Lett.* 12, 33–40. doi: 10.1007/BF02092106

Akam, S. A., Coffin, R. B., Abdulla, H. A. N., and Lyons, T. W. (2020). Dissolved inorganic carbon pump in methane-charged shallow marine sediments: state of the art and new model perspectives. *Front. Mar. Sci.* 7. doi: 10.3389/fmars.2020.00206

Aller, R. C., and Blair, N. E. (2004). Early diagenetic remineralization of sedimentary organic C in the Gulf of Papua deltaic complex (Papua New Guinea): Net loss of terrestrial C and diagenetic fractionation of C isotopes. *Geochim. Cosmochim. Acta* 68, 1815–1825. doi: 10.1016/j.gca.2003.10.028

Aloisi, G., Bouloubassi, I., Heijs, S., Pancost, R. D., Pierre, C., Sinninghe Damsteé, J. S., et al. (2002). CH4-consuming microorganisms and the formation of carbonate crusts at cold seeps. *Earth Planet. Sci. Lett.* 203, 195–203. doi: 10.1016/S0012-821X(02)00878-6

Aloisi, G., Wallmann, K., Bollwerk, S. M., Derkachev, A., Bohrmann, G., and Suess, E. (2004). The effect of dissolved barium on biogeochemical processes at cold seeps. *Geochim. Cosmochim. Acta* 68 (8), 1735–1748. doi: 10.1016/j.gca.2003.10.010

Amiotte Suchet, P., Probst, J.-L., and Ludwig, W. (2003). Worldwide distribution of continental rock lithology: Implications for the atmospheric/soil CO_2 uptake by continental weathering and alkalinity river transport to the oceans. *Global Biogeochem. Cycles* 17 (2), 1038. doi: 10.1029/2002gb001891

Arndt, S., Jørgensen, B. B., LaRowe, D. E., Middelburg, J., Pancost, R., and Regnier, P. (2013). Quantifying the degradation of organic matter in marine sediments: a review and synthesis. *Earth-sci. Rev.* 123, 53–86. doi: 10.1016/j.earscirev.2013.02.008

Aufdenkampe, A. K., Mayorga, E., Raymond, P. A., Melack, J. M., Doney, S. C., Alin, S. R., et al. (2011). Riverine coupling of biogeochemical cycles between land, oceans, and atmosphere. *Front. Ecol. Environ.* 9, 53–60. doi: 10.1890/100014

Avinash, K., Kurian, P. J., Warrier, A. K., Shankar, R., Vineesh, T. C., and Ravindra, R. (2016). Sedimentary sources and processes in the eastern Arabian Sea: Insights from environmental magnetism, geochemistry and clay mineralogy. *Geosci. Front.* 7, 253–264. doi: 10.1016/j.gsf.2015.05.001

Berg, R. D. (2008). *Diffusional methane fluxes within continental margin sediments and depositional constraints on formation factor estimates*, (University of California, San Diego).

Berner, R. A. (1976). The solubility of calcite and aragonite in seawater at atmospheric pressure and 34.5‰ salinity. *Am. J. Sci.* 276 (6), 713–730. doi: 10.2475/ajs.276.6.713

Berner, R. A. (1978). Sulfate reduction and the rate of deposition of marine sediments. *Earth Planet. Sci. Lett.* 37 (3), 492–498. doi: 10.1016/0012-821x(78)90209-1

Berner, R. A. (1980). *Early Diagenesis: A Theoretical Approach (No.1).* (Princeton University Press). doi: 10.1515/9780691209401

Boetius, A., Ravenschlag, K., Schubert, C. J., Rickert, D., Widdel, F., Gleeske, A., et al. (2000). A marine microbial consortium apparently mediating AOM. *Nature* 407, 623–626. doi: 10.1038/35036572

Borowski, W. S., Hoehler, T. M., Alperin, M. J., Rodriguez, N. M., and Paull, C. K. (2000). Significance of anaerobic methane oxidation in methane-rich sediments overlying the Blake Ridge gas hydrates. *Proc. Ocean Drill. Progr. Sci. Results* 164, 87–99. doi: 10.2973/odp.proc.sr.164.214.2000

Borowski, W. S., Paull, C. K., and Ussler, W. (1996). Marine pore-water sulfate profiles indicate *in situ* methane flux from underlying gas hydrate. *Geology* 24, 655–658. doi: 10.1130/0091-7613(1996)024<0655:MPWSPI>2.3.CO;2

Borowski, W. S., Paull, C. K., and Ussler, W. (1999). Global and local variations of interstitial sulfate gradients in deep-water, continental margin sediments: Sensitivity to underlying methane and gas hydrates. *Mar. Geol.* 159, 131–154. doi: 10.1016/S0025-3227(99)00004-3

Boudreau, B. P. (1997). *Diagenetic models and their implementation (Vol. 505)* (Berlin: Springer).

Boudreau, B. P., and Ruddick B., R. (1991). On a reactive continuum representation of organic matter diagenesis. *Am. J. Sci.* 291, 507–538. doi: 10.2475/ajs.291.5.507

Bradbury, H. J., and Turchyn, A. V. (2019). Reevaluating the carbon sink due to sedimentary carbonate formation in modern marine sediments. *Earth Planet. Sci. Lett.* 519, 40–49. doi: 10.1016/j.epsl.2019.04.044

Burns, S. J. (1998). Carbon isotopic evidence for coupled sulfate reduction-methane oxidation in Amazon Fan sediments. *Geochim. Cosmochim. Acta* 62, 797–804. doi: 10.1016/S0016-7037(98)00035-0

Cai, W. K., Liu, J. H., Zhou, C. H., Keeling, J., and Glasmacher, U. A. (2021). Structure, genesis and resources efficiency of dolomite: New insights and remaining enigmas. *Chem. Geol.* 573, 120191. doi: 10.1016/j.chemgeo.2021.120191

Casado, A. I., Alonso-Zarza, A. M., and La Iglesia, Á. (2014). Morphology and origin of dolomite in paleosols and lacustrine sequences. Examples from the Miocene of the Madrid Basin. *Sediment. Geol.* 312, 50–62. doi: 10.1016/j.sedgeo.2014.07.005

Chafetz, H., Rush, P. F., and Utech, N. M. (1991). Microenvironmental controls on mineralogy and habit of $CaCO_3$ precipitates: an example from an active travertine system. *Sedimentology* 38, 107–126. doi: 10.1111/j.1365-3091.1991.tb01857.x

Chatterjee, S., Dickens, G. R., Bhatnagar, G., Chapman, W. G., Dugan, B., Snyder, G. T., et al. (2011). Pore water sulfate, alkalinity, and carbon isotope profiles in shallow sediment above marine gas hydrate systems: A numerical modeling perspective. *J. Geophys. Res. Solid Earth* 116, 1–25. doi: 10.1029/2011JB008290

Chen, C. T. A. (2002). Shelf-vs. dissolution-generated alkalinity above the chemical lysocline. *Deep. Res. Part II Top. Stud. Oceanogr.* 49 (24-25), 5365–5375. doi: 10.1016/S0967-0645(02)00196-0

Chen, Y., Shen, L., Huang, T., Chu, Z., and Xie, Z. (2020). Transformation of sulfur species in lake sediments at Ardley Island and Fildes Peninsula, King George Island, Antarctic Peninsula. *Sci. Total Environ.* 703, 135591. doi: 10.1016/j.scitotenv.2019.135591

Chen, T., Sun, X., Lin, Z., Lu, Y., Fang, Y., Wu, Z., et al. (2021). Deciphering the geochemical link between seep carbonates and enclosed pyrite: A case study from the northern South China sea. *Mar. Pet. Geol.* 128, 105020. doi: 10.1016/j.marpetgeo.2021.105020

Chen, Y., Ussler, W., Haflidason, H., Lepland, A., Rise, L., Hovland, M., et al. (2010). Sources of methane inferred from pore-water $\delta^{13}C$ of dissolved inorganic carbon in Pockmark G11, offshore Mid-Norway. *Chem. Geol.* 275, 127–138. doi: 10.1016/j.chemgeo.2010.04.013

Chen, N. C., Yang, T. F., Hong, W. L., Chen, H. W., Chen, H. C., Hu, C. Y., et al. (2017). Production, consumption, and migration of methane in accretionary prism of southwestern Taiwan. *Geochem. Geophys. Geosy.* 18, 2970–2989. doi: 10.1002/2017GC006798

Chen, N., Yang, T. F., Liou, Y., Lin, H. T., Hong, W., Lin, S., et al. (2023). Controlling factors on patterns of dissolved organic carbon and volatile fatty acids in a submarine mud volcano offshore southwestern Taiwan. *Front. Earth Sci.* 11. doi: 10.3389/feart.2023.1210088

Chuang, P. C., Dale, A. W., Wallmann, K., Haeckel, M., Yang, T. F., Chen, N. C., et al. (2013). Relating sulfate and methane dynamics to geology: Accretionary prism offshore SW Taiwan. *Geochem. Geophys. Geosy.* 14, 2523–2545. doi: 10.1002/ggge.20168

Chuang, P. C., Yang, T. F., Wallmann, K., Matsumoto, R., Hu, C. Y., Chen, H. W., et al. (2019). Carbon isotope exchange during anaerobic oxidation of methane (AOM) in sediments of the northeastern South China Sea. *Geochim. Cosmochim. Acta* 246, 138–155. doi: 10.1016/j.gca.2018.11.003

Chuang, P. C., Young, M. B., Dale, A. W., Miller, L. G., Herrera-Silveira, J. A., and Paytan, A. (2016). Methane and sulfate dynamics in sediments from mangrove-dominated tropical coastal lagoons, Yucatan, Mexico. *Biogeosciences* 13, 2981–3001. doi: 10.5194/bg-13-2981-2016

Claypool, G. E., Milkov, A. V., Lee, Y. J., Torres, M. E., Borowski, W. S., and Tomaru, H. (2006). "Microbial Methane Generation and Gas Transport in Shallow Sediments of an Accretionary Complex, Southern Hydrate Ridge (ODP Leg 204), Offshore Oregon USA," in *Proceedings of the ODP, Scientific Results*. Eds. A. M. Trehu, G. Bohrmann, M. E. Torres and F. S. Colwell (College Station, Texas: Ocean Drilling Program).

Coffin, R. B., Hamdan, L. J., Smith, J. P., Rose, P. S., Plummer, R. E., Yoza, B., et al. (2014). Contribution of vertical methane flux to shallow sediment carbon pools across Porangahau Ridge, New Zealand. *Energies* 7, 5332–5356. doi: 10.3390/en7085332

Coffin, R. B., Osburn, C. L., Plummer, R. E., Smith, J. P., Rose, P. S., and Grabowski, K. S. (2015). Deep sediment-sourced methane contribution to shallow sediment organic carbon: Atwater Valley, Texas-Louisiana Shelf, Gulf of Mexico. *Energies* 8, 1561–1583. doi: 10.3390/en8031561

Coffin, R. B., Smith, J. P., Plummer, R. E., Yoza, B., Larsen, R. K., Millholland, L. C., et al. (2013). Spatial variation in shallow sediment methane sources and cycling on the Alaskan Beaufort Sea Shelf/Slope. *Mar. Pet. Geol.* 45, 186–197. doi: 10.1016/j.marpetgeo.2013.05.002

D'Hondt, S., Rutherford, S., and Spivack, A. J. (2002). Metabolic activity of subsurface life in deep-sea sediments. *Science* 295 (5562), 2067–2070. doi: 10.1126/science.1064878

Dale, A. W., Flury, S., Fossing, H., Regnier, P., Røy, H., Scholze, C., et al. (2019). Kinetics of organic carbon mineralization and methane formation in marine sediments (Aarhus Bay, Denmark). *Geochim. Cosmochim. Acta* 252, 159–178. doi: 10.1016/j.gca.2019.02.033

Delisle, G., and Berner, U. (2002). Gas hydrates acting as cap rock to fluid discharge in the Makran accretionary prism? *Geol. Soc Spec. Publ.* 195, 137–146. doi: 10.1144/GSL.SP.2002.195.01.09

Dickens, G. R., and Snyder, G. T. (2009). Interpreting upward methane flux from marine pore water profiles. *Fire Ice* 9 (1), 7–10. Available at: https://netl.doe.gov/sites/default/files/publication/MHNewsWinter09.pdf.

Doebelin, N., and Kleeberg, R. (2015). Profex: A graphical user interface for the Rietveld refinement program BGMN. *J. Appl. Crystallogr.* 48, 1573–1580. doi: 10.1107/S1600576715014685

Dos Santos, H. N., Neumann, R., and Ávila, C. A. (2017). Mineral quantification with simultaneous refinement of Ca-Mg carbonates non-stoichiometry by X-Ray diffraction, rietveld method. *Minerals* 7, 164. doi: 10.3390/min7090164

Egger, M., Riedinger, N., Mogollón, J. M., and Jørgensen, B. B. (2018). Global diffusive fluxes of methane in marine sediments. *Nat. Geosci.* 11, 421–425. doi: 10.1038/s41561-018-0122-8

Fahad, M., and Saeed, S. (2018). Determination and estimation of magnesium content in the single phase magnesium-calcite [Ca(1–x)Mg_xCO_3(s)] using electron probe micro-analysis (EPMA) and X-ray diffraction (XRD). *Geosci. J.* 22, 303–312. doi: 10.1007/s12303-017-0059-8

Fantle, M. S., and DePaolo, D. J. (2006). S.R.X.X.X isotopes and pore fluid chemistry in carbonate sediment of the Ontong Java Plateau: Calcite recrystallization rates and evidence for a rapid rise in seawater Mg over the last 10 million years. *Geochim. Cosmochi. Acta* 70, 3883–3904. doi: 10.1016/j.gca.2006.06.009

Fantle, M. S., and DePaolo, D. J. (2007). Ca isotopes in carbonate sediment and pore fluid from ODP Site 807A: The Ca^{2+} (aq)–calcite equilibrium fractionation factor and calcite recrystallization rates in Pleistocene sediments. *Geochim. Cosmochi. Acta* 71, 2524–2546. doi: 10.1016/j.gca.2007.03.006

Feng, J., Li, N., Luo, M., Liang, J., Yang, S., Wang, H., et al. (2020). A quantitative assessment of methane-derived carbon cycling at the cold seeps in the northwestern south China sea. *Minerals* 10, 1–23. doi: 10.3390/min10030256

Feng, D., Peng, Y., Bao, H., Peckmann, J., Roberts, H. H., and Chen, D. (2016). A carbonate-based proxy for sulfate-driven anaerobic oxidation of methane. *Geology* 44, 999–1002. doi: 10.1130/G38233.1

Feng, J., Yang, S., Liang, J., Fang, Y., He, Y., Luo, M., et al. (2018). Methane seepage inferred from the porewater geochemistry of shallow sediments in the Beikang Basin of the southern South China Sea. *J. Asian Earth Sci.* 168, 77–86. doi: 10.1016/j.jseaes.2018.02.005

Fischer, D., Sahling, H., Nöthen, K., Bohrmann, G., Zabel, M., and Kasten, S. (2012). Interaction between hydrocarbon seepage, chemosynthetic communities, and bottom water redox at cold seeps of the Makran accretionary prism: Insights from habitat-specific pore water sampling and modeling. *Biogeosciences* 9, 2013–2031. doi: 10.5194/bg-9-2013-2012

Flood, R. D., Piper, D. J. W., Klaus, A.Scientific Research Party. (1995). *Proceedings of the Ocean Drilling Program, Initial Reports*. (College Station, TX: Ocean Drilling Program), 155.

Formolo, M. J., Lyons, T. W., Zhang, C., Kelley, C., Sassen, R., Horita, J., et al. (2004). Quantifying carbon sources in the formation of authigenic carbonates at gas hydrate sites in the Gulf of Mexico. *Chem. Geol.* 205, 253–264. doi: 10.1016/j.chemgeo.2003.12.021

Garcia-Tigreros, F., and Kessler, J. D. (2018). Limited acute influence of aerobic methane oxidation on ocean carbon dioxide and pH in hudson canyon, northern U.S. Atlantic margin. *J. Geophys. Res. Biogeosciences* 123, 2135–2144. doi: 10.1029/2018JG004384

Geprägs, P., Torres, M. E., Mau, S., Kasten, S., Römer, M., and Bohrmann, G. (2016). Carbon cycling fed by methane seepage at the shallow Cumberland Bay, South Georgia, sub-Antarctic. *Geochem. Geophys. Geosy.* 17, 1401–1418. doi: 10.1002/2016GC006276

Grando, G., and McClay, K. (2007). Morphotectonics domains and structural styles in the Makran accretionary prism, offshore Iran. *Sediment. Geol.* 196, 157–179. doi: 10.1016/j.sedgeo.2006.05.030

Graves, C. A., Steinle, L., Rehder, G., Niemann, H., Connelly, D. P., Lowry, D., et al. (2015). Fluxes and fate of dissolved methane released at the seafloor at the landward limit of the gas hydrate stability zone offshore western Svalbard. *J. Geophys. Res-Oceans* 120 (9), 6185–6201. doi: 10.1016/S0016-7037(03)00127-3

Haas, A., Peckmann, J., Elvert, M., Sahling, H., and Bohrmann, G. (2010). Patterns of carbonate authigenesis at the Kouilou pockmarks on the Congo deep-sea fan. *Mar. Geol.* 268, 129–136. doi: 10.1016/j.margeo.2009.10.027

Haese, R. R., Meile, C., Van Cappellen, P., and De Lange, G. J. (2003). Carbon geochemistry of cold seeps: Methane fluxes and transformation in sediments from Kazan mud volcano, eastern Mediterranean Sea. *Earth Planet. Sci. Lett.* 212, 361–375. doi: 10.1016/S0012-821X(03)00226-7

Hall, P. O. J., and Aller, R. C. (1992). Rapid, small-volume, flow injection analysis for ΣCO_2, and NH_4^+ in marine and freshwaters. *Limnol. Oceanogr.* 37, 1113–1119. doi: 10.4319/lo.1992.37.5.1113

Hamdan, L. J., Gillevet, P. M., Pohlman, J. W., Sikaroodi, M., Greinert, J., and Coffin, R. B. (2011). Diversity and biogeochemical structuring of bacterial communities across the Porangahau ridge accretionary prism, New Zealand. *FEMS Microbiol. Ecol.* 77, 518–532. doi: 10.1111/j.1574-6941.2011.01133.x

Himmler, T., Birgel, D., Bayon, G., Pape, T., Ge, L., Bohrmann, G., et al. (2015). Formation of seep carbonates along the Makran convergent margin, northern Arabian Sea and a molecular and isotopic approach to constrain the carbon isotopic composition of parent methane. *Chem. Geol.* 415, 102–117. doi: 10.1016/j.chemgeo.2015.09.016

Hu, Y., Luo, M., Chen, L., Liang, Q., Feng, D., Tao, J., et al. (2018). Methane source linked to gas hydrate system at hydrate drilling areas of the South China Sea: Porewater geochemistry and numerical model constraints. *J. Asian Earth Sci.* 168, 87–95. doi: 10.1016/j.jseaes.2018.04.028

Hu, Y., Zhang, X., Feng, D., Peckmann, J., Feng, J., Wang, H., et al. (2022). Enhanced sulfate consumption fueled by deep-sourced methane in a hydrate-bearing area. *Sci. Bull.* 67, 122–124. doi: 10.1016/j.scib.2021.09.006

Jørgensen, B. B., Beulig, F., Egger, M., Petro, C., Scholze, C., and Røy, H. (2019). Organoclastic sulfate reduction in the sulfate-methane transition of marine sediments. *Geochim. Cosmochim. Acta* 254, 231–245. doi: 10.1016/j.gca.2019.03.016

Jørgensen, B. B., Weber, A., and Zopfi, J. (2001). Sulphate reduction and anaerobic oxidation in Black Sea sediments. *Deep. Res. I* 48, 2097–2120. doi: 10.1016/s0967-0637(01)00007-3

Kastner, M., Claypool, G., and Robertson, G. (2008). Geochemical constraints on the origin of the pore fluids and gas hydrate distribution at Atwater Valley and Keathley Canyon, northern Gulf of Mexico. *Mar. Pet. Geol.* 25, 860–872. doi: 10.1016/j.marpetgeo.2008.01.022

Keigwin, L. D., Rio, D., Acton, G. D., and Shipboard Scientific Party. (1998). *Proceedings of the Ocean Drilling Program, Initial Reports*. (College Station, TX: Ocean Drilling Program), 172.

Khan, M. J., Ali, M., Xu, M., and Khan, M. (2020). Seismicity analysis of selected faults in Makran Southern Pakistan. *Acta Geophys.* 68, 965–978. doi: 10.1007/s11600-020-00447-8

Kimura, G., Silver, E. A., Blum, P., and Shipboard Scientific Party. (1997). *Proceedings of the Ocean Drilling Program, Initial Reports*, vol. 170.

Knittel, K., and Boetius, A. (2009). Anaerobic oxidation of methane: Progress with an unknown process. *Annu. Rev. Microbiol.* 63, 311–334. doi: 10.1146/annurev.micro.61.080706.093130

Kopp, C., Fruehn, J., Flueh, E. R., Reichert, C., Kukowski, N., Bialas, J., et al. (2000). Structure of the makran subduction zone from wide-angle and reflection seismic data. *Tectonophysics* 329, 171–191. doi: 10.1016/S0040-1951(00)00195-5

Kretschmer, K., Biastoch, A., Rüpke, L., and Burwicz, E. (2015). Modeling the fate of methane hydrates under global warming. *Global Biogeochem. Cycles* 29, 610–625. doi: 10.1002/2014GB005011

Krumins, V., Gehlen, M., Arndt, S., Van Cappellen, P., and Regnier, P. (2013). Dissolved inorganic carbon and alkalinity fluxes from coastal marine sediments: Model estimates for different shelf environments and sensitivity to global change. *Biogeosciences* 10, 371–398. doi: 10.5194/bg-10-371-2013

Kvenvolden, K. A. (1988). Methane hydrate - A major reservoir of carbon in the shallow geosphere? *Chem. Geol.* 71, 41–51. doi: 10.1016/0009-2541(88)90104-0

Lerche, I. (2000). Estimates of worldwide gas hydrate resources. *Energy Explor. Exploit.* 18, 329–337. doi: 10.1260/0144598001492157

Li, N., Jin, M., Peckmann, J., Chen, D., and Feng, D. (2023). Quantification of the sources of sedimentary organic carbon at methane seeps: A case study from the South China Sea. *Chem. Geol.* 627, 121463. doi: 10.1016/j.chemgeo.2023.121463

Li, J., Peng, X., Bai, S., Chen, Z., and Van Nostrand, J. D. (2018). Biogeochemical processes controlling authigenic carbonate formation within the sediment column from the Okinawa Trough. *Geochim. Cosmochim. Acta* 222, 363–382. doi: 10.1016/j.gca.2017.10.029

Liao, J., Liu, X., Zhao, Q., Gong, J., Yin, W., Li, S., et al. (2022). Characteristics of high saturation hydrate reservoirs in the low-angle subduction area of the makran accretionary prism. *Front. Earth Sci.* 10. doi: 10.3389/feart.2022.861162

Liu, S., Feng, X., Feng, Z., Xiao, X., and Feng, L. (2020b). Geochemical evidence of methane seepage in the sediments of the Qiongdongnan Basin, South China Sea. *Chem. Geol.* 543, 119588. doi: 10.1016/j.chemgeo.2020.119588

Liu, W., Wu, Z., Xu, S., Wei, J., Peng, X., Li, J., et al. (2020a). Pore-water dissolved inorganic carbon sources and cycling in the shallow sediments of the Haima cold seeps, South China Sea. *J. Asian Earth Sci.* 201, 104495. doi: 10.1016/j.jseaes.2020.104495

Liu, X., Xu, T., Tian, H., Wei, M., Jin, G., and Liu, N. (2016). Numerical modeling study of mineralization induced by methane cold seep at the sea bottom. *Mar. Pet. Geol.* 75, 14–28. doi: 10.1016/j.marpetgeo.2016.04.010

Loyd, S. J., and Smirnoff, M. N. (2022). Progressive formation of authigenic carbonate with depth in siliciclastic marine sediments including substantial formation in sediments experiencing methanogenesis. *Chem. Geol.* 594, 120775. doi: 10.1016/j.chemgeo.2022.120775

Luff, R., Haeckel, M., and Wallmann, K. (2001). Robust and fast FORTRAN and MATLAB® libraries to calculate pH distributions in marine systems. *Comput. Geosci-UK* 27, 157–169. doi: 10.1016/S0098-3004(00)00097-2

Luff, R., and Wallmann, K. (2003). Fluid flow, methane fluxes, carbonate precipitation and biogeochemical turnover in gas hydrate-bearing sediments at Hydrate Ridge, Cascadia Margin: Numerical modeling and mass balances. *Geochim. Cosmochim. Acta* 67, 3403–3421. doi: 10.1016/S0016-7037(03)00127-3

Luff, R., Wallmann, K., Grandel, S., and Schlüter, M. (2000). Numerical modeling of benthic processes in the deep Arabian Sea. *Deep. Res. Part II Top. Stud. Oceanogr.* 47, 3039–3072. doi: 10.1016/S0967-0645(00)00058-8

Lukawska-Matuszewska, K., and Kielczewska, J. (2016). Effects of near-bottom water oxygen concentration on biogeochemical cycling of C, N and S in sediments of the Gulf of Gdansk (southern Baltic). *Cont. Shelf Res.* 117, 30–42. doi: 10.1016/j.csr.2016.02.001

Luo, M., Chen, L., Wang, S., Yan, W., Wang, H., and Chen, D. (2013). Pockmark activity inferred from pore water geochemistry in shallow sediments of the pockmark field in southwestern Xisha Uplift, northwestern South China Sea. *Mar. Pet. Geol.* 48, 247–259. doi: 10.1016/j.marpetgeo.2013.08.018

Malinverno, A., and Pohlman, J. W. (2011). Modeling sulfate reduction in methane hydrate-bearing continental margin sediments: Does a sulfate-methane transition require anaerobic oxidation of methane? *Geochem. Geophy. Geosy.* 12, Q07006. doi: 10.1029/2011GC003501

Mau, S., Römer, M., Torres, M. E., Bussmann, I., Pape, T., Damm, E., et al. (2017). Widespread methane seepage along the continental margin off Svalbard-from Bjørnøya to Kongsfjorden. *Sci. Rep.* 7, 1–13. doi: 10.1038/srep42997

Mazumdar, A., Peketi, A., Joao, H. M., Dewangan, P., and Ramprasad, T. (2014). Pore-water chemistry of sediment cores off Mahanadi Basin, Bay of Bengal: Possible link to deep seated methane hydrate deposit. *Mar. Pet. Geol.* 49, 162–175. doi: 10.1016/j.marpetgeo.2013.10.011

Meister, P., Liu, B., Ferdelman, T. G., Jørgensen, B. B., and Khalili, A. (2013). Control of sulphate and methane distributions in marine sediments by organic matter reactivity. *Geochim. Cosmochi. Acta* 104, 183–193. doi: 10.1016/j.gca.2012.11.011

Meister, P., Liu, B., Khalili, A., Böttcher, M. E., and Jørgensen, B. B. (2019). Factors controlling the carbon isotope composition of dissolved inorganic carbon and methane in marine porewater: An evaluation by reaction-transport modelling. *J. Mar. Syst.* 200, 103227. doi: 10.1016/j.jmarsys.2019.103227

Meybeck, M. (1993). Riverine transport of atmospheric carbon: sources, global typology and budget. *Water Air Soil pollut.* 70, 443–463. doi: 10.1007/BF01105015

Milkov, A. V. (2004). Global estimates of hydrate-bound gas in marine sediments: How much is really out there? *Earth-Science Rev.* 66, 183–197. doi: 10.1016/j.earscirev.2003.11.002

Miller, C. M., Dickens, G. R., Jakobsson, M., Johansson, C., Koshurnikov, A., O'Regan, M., et al. (2017). Pore water geochemistry along continental slopes north of the East Siberian Sea: Inference of low methane concentrations. *Biogeosciences* 14, 2929–2953. doi: 10.5194/bg-14-2929-2017

Moore, G. F., Taira, A., Klaus, A., and Shipboard Scientific Party. (2001). *Proceedings of the Ocean Drilling Program, Initial Reports*. Volume 190.

Niewöhner, C., Hensen, C., Kasten, S., Zabel, M., and Schulz, H. D. (1998). Deep sulfate reduction completely mediated by anaerobic methane oxidation in sediments of the upwelling area off Namibia. *Geochim. Cosmochim. Acta* 62, 455–464. doi: 10.1016/S0016-7037(98)00055-6

Nöthen, K., and Kasten, S. (2011). Reconstructing changes in seep activity by means of pore water and solid phase Sr/Ca and Mg/Ca ratios in pockmark sediments of the Northern Congo Fan. *Mar. Geol.* 287, 1–13. doi: 10.1016/j.margeo.2011.06.008

Paull, C. K., Matsumoto, R., Wallace, P. J., and Shipboard Scientific Party. (1996). *Proceedings of the IODP, Initial Reports*. (College Station, TX, USA), Volume 164.

Peckmann, J., Reimer, A., Luth, U., Luth, C., Hansen, B. T., Heinicke, C., et al. (2001). Methane-derived carbonates and authigenic pyrite from the northwestern Black Sea. *Mar. Geol.* 177, 129–150. doi: 10.1016/S0025-3227(01)00128-1

Phrampus, B. J., and Hornbach, M. J. (2012). Recent changes to the Gulf Stream causing widespread gas hydrate destabilization. *Nature* 490, 527–530. doi: 10.1038/nature11528

Rassmann, J., Lansard, B., Gazeau, F., Guidi-Guilvard, L., Pozzato, L., Alliouane, S., et al. (2018). Impact of ocean acidification on the biogeochemistry and meiofaunal assemblage of carbonate-rich sediments: Results from core incubations (Bay of Villefranche, NW Mediterranean Sea). *Mar. Chem.* 203, 102–119. doi: 10.1016/j.marchem.2018.05.006

Reeburgh, W. S. (1976). Methane consumption in Cariaco Trench waters and sediments. *Earth Planet. Sci. Lett.* 28, 337–344. doi: 10.1016/0012-821X(76)90195-3

Reitz, A., Pape, T., Haeckel, M., Schmidt, M., Berner, U., Scholz, F., et al. (2011). Sources of fluids and gases expelled at cold seeps offshore Georgia, eastern Black Sea. *Geochim. Cosmochim. Acta* 75, 3250–3268. doi: 10.1016/j.gca.2011.03.018

Riedinger, N., Kasten, S., Gröger, J., Franke, C., and Pfeifer, K. (2006). Active and buried authigenic barite fronts in sediments from the Eastern Cape Basin. *Earth Planet. Sci. Lett.* 241, 876–887. doi: 10.1016/j.epsl.2005.10.032

Ritger, S., Carson, B., and Suess, E. (1987). Methane-derived authigenic carbonates formed by subduction-induced pore-water expulsion along the oregon/washington margin. *Bull. Geol. Soc Am.* 98, 147–156. doi: 10.1130/0016-7606(1987)98<147:MACFBS>2.0.CO;2

Römer, M., Sahling, H., Pape, T., Bohrmann, G., and Spieß, V. (2012). Quantification of gas bubble emissions from submarine hydrocarbon seeps at the Makran continental margin (offshore Pakistan). *J. Geophys. Res-Oceans* 117, C10015. doi: 10.1029/2011JC007424

Ruban, A., Rudmin, M., Dudarev, O., and Mazurov, A. (2020). The formation of authigenic carbonates at a methane seep site in the northern part of the laptev sea. *Minerals* 10, 1–14. doi: 10.3390/min10110948

Schlüter, H. U., Prexl, A., Gaedicke, C., Roeser, H., Reichert, C., Meyer, H., et al. (2002). The Makran accretionary wedge: Sediment thicknesses and ages and the origin of mud volcanoes. *Mar. Geol.* 185, 219–232. doi: 10.1016/S0025-3227(02)00192-5

Sivan, O., Schrag, D. P., and Murray, R. W. (2007). Rates of methanogenesis and methanotrophy in deep-sea sediments. *Geobiology* 5, 141–151. doi: 10.1111/j.1472-4669.2007.00098.x

Smith, J. P., and Coffin, R. B. (2014). Methane flux and authigenic carbonate in shallow sediments overlying methane hydrate bearing strata in Alaminos Canyon, Gulf of Mexico. *Energies* 7, 6118–6141. doi: 10.3390/en7096118

Snyder, G. T., Hiruta, A., Matsumoto, R., Dickens, G. R., Tomaru, H., Takeuchi, R., et al. (2007). Pore water profiles and authigenic mineralization in shallow marine sediments above the methane-charged system on Umitaka Spur, Japan Sea. *Deep. Res. Part II Top. Stud. Oceanogr.* 54, 1216–1239. doi: 10.1016/j.dsr2.2007.04.001

Solomon, E. A., Spivack, A. J., Kastner, M., Torres, M. E., and Robertson, G. (2014). Gas hydrate distribution and carbon sequestration through coupled microbial methanogenesis and silicate weathering in the Krishna-Godavari Basin, offshore India. *Mar. Pet. Geol.* 58, 233–253. doi: 10.1016/j.marpetgeo.2014.08.020

Suess, E. (2014). Marine cold seeps and their manifestations: geological control, biogeochemical criteria and environmental conditions. *Int. J. Earth Sci.* 103, 1889–1916. doi: 10.1007/s00531-014-1010-0

Suess, E., Torres, M. E., Bohrmann, G., Collier, R. W., Greinert, J., Linke, P., et al. (1999). Gas hydrate destabilization: Enhanced dewatering, benthic material turnover and large methane plumes at the Cascadia convergent margin. *Earth Planet. Sci. Lett.* 170, 1–15. doi: 10.1016/S0012-821X(99)00092-8

Sun, X., and Turchyn, A. V. (2014). Significant contribution of authigenic carbonate to marine carbon burial. *Nat. Geosci.* 7, 201–204. doi: 10.1038/ngeo2070

Takahashi, K., Ravelo, A. C., Alvarez Zarikian, C. A. and the Expedition 323 Scientists. (2011). *Proceedings of the Integrated Ocean Drilling Program*, Volume 323.

Titschack, J., Goetz-Neunhoeffer, F., and Neubauer, J. (2011). Magnesium quantifcation in calcites [(Ca, Mg)CO_3] by rietveld-based XRD analysis: Revisiting a well-established method. *Am. Mineral.* 96, 1028–1038. doi: 10.2138/am.2011.3665

Treude, T., Niggemann, J., Kallmeyer, J., Wintersteller, P., Schubert, C. J., Boetius, A., et al. (2005). Anaerobic oxidation of methane and sulfate reduction along the Chilean continental margin. *Geochim. Cosmochim. Acta* 69, 2767–2779. doi: 10.1016/j.gca.2005.01.002

Ussler, W., and Paull, C. K. (2008). Rates of anaerobic oxidation of methane and authigenic carbonate mineralization in methane-rich deep-sea sediments inferred from models and geochemical profiles. *Earth Planet. Sci. Lett.* 266, 271–287. doi: 10.1016/j.epsl.2007.10.056

von Rad, U., Berner, U., Delisle, G., Doose-Rolinski, H., Fechner, N., Linke, P., et al. (2000). Gas and fluid venting at the Makran accretionary wedge off Pakistan. *Geo-Marine Lett.* 20, 10–19. doi: 10.1007/s003670000033

von Rad, U., Rösch, H., Berner, U., Geyh, M., Marchig, V., and Schulz, H. (1996). Authigenic carbonates derived from oxidized methane vented from the Makran accretionary prism off Pakistan. *Mar. Geol.* 136, 55–77. doi: 10.1016/S0025-3227(96)00017-5

Wallmann, K., Aloisi, G., Haeckel, M., Tishchenko, P., Pavlova, G., Greinert, J., et al. (2008). Silicate weathering in anoxic marine sediments. *Geochim. Cosmochim. Acta* 72, 2895–2918. doi: 10.1016/j.gca.2008.03.026

Wang, M., Li, Q., Cai, F., Liang, J., Yan, G., Wang, Z., et al. (2019). Formation of authigenic carbonates at a methane seep site in the middle Okinawa Trough, East China Sea. *J. Asian Earth Sci.* 185, 104028. doi: 10.1016/j.jseaes.2019.104028

Warren, J. (2000). Dolomite: occurrence, evolution and economically important associations. *Earth Sci. Rev.* 52, 1–81. doi: 10.1016/S0012-8252(00)00022-2

Wefer, G., Berger, W. H., Richter, C.Shipboard Scientific Party. (1998). *Proceedings of the Ocean Drilling Program, Initial Reports*. (College Station, TX: Ocean Drilling Program), 175, 487–504.

Wehrmann, L. M., Risgaard-Petersen, N., Schrum, H. N., Walsh, E. A., Huh, Y., Ikehara, M., et al. (2011). Coupled organic and inorganic carbon cycling in the deep subseafloor sediment of the northeastern Bering Sea Slope (IODP Exp.323). *Chem. Geol.* 284, 251–261. doi: 10.1016/j.chemgeo.2011.03.002

Wei, J., Liang, J., Lu, J., Zhang, W., and He, Y. (2019). Characteristics and dynamics of gas hydrate systems in the northwestern South China Sea - Results of the fifth gas hydrate drilling expedition. *Mar. Pet. Geol.* 110, 287–298. doi: 10.1016/j.marpetgeo.2019.07.028

Wei, J., Wu, T., Deng, X., Haider, S. W., Kahkashan, S., and Yang, S. (2021). Seafloor methane emission on the Makran continental margin. *Sci. Total Environ.* 801, 149772. doi: 10.1016/j.scitotenv.2021.149772

Wei, J., Wu, T., Zhang, W., Deng, Y., Xie, R., Feng, J., et al. (2020). Deeply buried authigenic carbonates in the qiongdongnan basin, South China sea: Implications for ancient cold seep activities. *Minerals* 10, 1–19. doi: 10.3390/min10121135

Winde, V., Böttcher, M. E., Escher, P., Böning, P., Beck, M., Liebezeit, G., et al. (2014). Tidal and spatial variations of $DI^{13}C$ and aquatic chemistry in a temperate tidal basin during winter time. *J. Mar. Syst.* 129, 396–404. doi: 10.1016/j.jmarsys.2013.08.005

Wu, T., Deng, X., Yao, H., Liu, B., Ma, J., Haider, S. W., et al. (2021). Distribution and development of submarine mud volcanoes on the Makran Continental Margin, offshore Pakistan. *J. Asian Earth Sci.* 207, 104653. doi: 10.1016/j.jseaes.2020.104653

Wu, L., Yang, S., Liang, J., Su, X., Fu, S., Sha, Z., et al. (2013). Variations of pore water sulfate gradients in sediments as indicator for underlying gas hydrate in Shenhu Area, the South China Sea. *Sci. China-Earth Sci.* 56, 530–540. doi: 10.1007/s11430-012-4545-6

Wu, Z., Zhou, H., Ren, D., Gao, H., and Li, J. (2016). Quantifying the sources of dissolved inorganic carbon within the sulfate-methane transition zone in nearshore sediments of Qi'ao Island, Pearl River Estuary, Southern China. *Sci. China-Earth Sci.* 59, 1959–1970. doi: 10.1007/s11430-016-0057-0

Xu, S., Liu, B., Wu, Z., Kowalski, N., and Böttcher, M. E. (2023). The role of anaerobic methane oxidation on the carbonate authigenesis in sediments of the subtropical Beibu Gulf, South China Sea: A reactive–transport modelling approach. *Chem. Geol.* 619, 121319. doi: 10.1016/j.chemgeo.2023.121319

Zha, R., Yang, T., Shi, X., Su, P., and Fang, Y. (2022). Quantitative assessment of dissolved inorganic carbon cycling in marine sediments from gas hydrate-bearing areas

in the South China Sea. *Mar. Petrol. Geol.* 145, 105881. doi: 10.1016/j.marpetgeo.2022.105881

Zhang, S., and DePaolo, D. J. (2020). Equilibrium calcite-fluid Sr/Ca partition coefficient from marine sediment and pore fluids. *Geochim. Cosmochi. Acta* 289, 33–46. doi: 10.1016/j.gca.2020.08.017

Zhang, X., Gong, J., Sun, Z., Liao, J., Zhai, B., Wang, L., et al. (2021b). Pore-water geochemistry in methane-seep sediments of the Makran accretionary wedge off Pakistan: Possible link to subsurface methane hydrate. *Acta Oceanol. Sin.* 40, 23–32. doi: 10.1007/s13131-021-1899-7

Zhang, Z., He, G., Yao, H.-q., Deng, X., Yu, M., Huang, W., et al. (2020). Diapir structure and its constraint on gas hydrate accumulation in the Makran accretionary prism, offshore Pakistan. *China Geol.* 3, 611–622. doi: 10.31035/cg2020049

Zhang, W., Liang, J., Liang, Q., Wei, J., Wan, Z., Feng, J., et al. (2021a). Gas hydrate accumulation and occurrence associated with cold seep systems in the northern south China sea: an overview. *Geofluids* 2021, 1–24. doi: 10.1155/2021/5571150

Zhao, Y., Liu, J., Uthaipan, K., Song, X., Xu, Y., He, B., et al. (2020). Dynamics of inorganic carbon and pH in a large subtropical continental shelf system: Interaction between eutrophication, hypoxia, and ocean acidification. *Limnol. Oceanogr.* 65, 1359–1379. doi: 10.1002/lno.11393

frontiers | Frontiers in Marine Science

TYPE Original Research
PUBLISHED 11 January 2024
DOI 10.3389/fmars.2023.1320655

Check for updates

OPEN ACCESS

EDITED BY
Glen T. Snyder,
The University of Tokyo, Japan

REVIEWED BY
Natascha Riedinger,
Oklahoma State University, United States
Satoko Owari,
Tokyo University of Marine Science and Technology, Japan

*CORRESPONDENCE
Desiree L. Roerdink
desiree.roerdink@uib.no

RECEIVED 12 October 2023
ACCEPTED 26 December 2023
PUBLISHED 11 January 2024

CITATION
Roerdink DL, Vulcano F, Landro J-K, Moltubakk KE, Babel HR, Jørgensen SL, Baumberger T, Økland IE, Reeves EP, Thorseth IH, Reigstad LJ, Strauss H and Steen IH (2024) Hydrothermal activity fuels microbial sulfate reduction in deep and distal marine settings along the Arctic Mid Ocean Ridges.
Front. Mar. Sci. 10:1320655.
doi: 10.3389/fmars.2023.1320655

COPYRIGHT
© 2024 Roerdink, Vulcano, Landro, Moltubakk, Babel, Jørgensen, Baumberger, Økland, Reeves, Thorseth, Reigstad, Strauss and Steen. This is an open-access article distributed under the terms of the Creative Commons Attribution License (CC BY). The use, distribution or reproduction in other forums is permitted, provided the original author(s) and the copyright owner(s) are credited and that the original publication in this journal is cited, in accordance with accepted academic practice. No use, distribution or reproduction is permitted which does not comply with these terms.

Hydrothermal activity fuels microbial sulfate reduction in deep and distal marine settings along the Arctic Mid Ocean Ridges

Desiree L. Roerdink[1]*, Francesca Vulcano[2], Jan-Kristoffer Landro[1], Karen E. Moltubakk[1], Hannah R. Babel[2], Steffen Leth Jørgensen[1,2], Tamara Baumberger[1,3], Ingeborg E. Økland[1], Eoghan P. Reeves[1], Ingunn H. Thorseth[1], Laila J. Reigstad[2], Harald Strauss[4] and Ida H. Steen[2]

[1]Department of Earth Science and Centre for Deep Sea Research, University of Bergen, Bergen, Norway, [2]Department of Biological Sciences and Centre for Deep Sea Research, University of Bergen, Bergen, Norway, [3]Pacific Marine Environmental Laboratory, National Oceanographic and Atmospheric Administration & Cooperative Institute for Marine Ecosystem and Resources Studies, Oregon State University, Newport, OR, United States, [4]Institute for Geology and Paleontology, Westfälische Wilhelms-Universität Münster, Münster, Germany

Microbial sulfate reduction is generally limited in the deep sea compared to shallower marine environments, but cold seeps and hydrothermal systems are considered an exception. Here, we report sulfate reduction rates and geochemical data from marine sediments and hydrothermal vent fields along the Arctic Mid Ocean Ridges (AMOR), to assess the significance of basalt-hosted hydrothermal activity on sulfate reduction in a distal deep marine setting. We find that cored marine sediments do not display evidence for sulfate reduction, apart from low rates in sediments from the Knipovich Ridge. This likely reflects the overall limited availability of reactive organic matter and low sedimentation rates along the AMOR, except for areas in the vicinity of Svalbard and Bear Island. In contrast, hydrothermal samples from the Seven Sisters, Jan Mayen and Loki's Castle vent fields all demonstrate active microbial sulfate reduction. Rates increase from a few 10s to 100s of pmol SO_4^{2-} cm^{-3} d^{-1} in active high-temperature hydrothermal chimneys, to 10s of nmol SO_4^{2-} cm^{-3} d^{-1} in low-temperature barite chimneys and up to 110 nmol cm^{-3} d^{-1} in diffuse venting hydrothermal sediments in the Barite field at Loki's Castle. Pore fluid and sediment geochemical data suggest that these high rates are sustained by organic compounds from microbial mats and vent fauna as well as methane supplied by high-temperature hydrothermal fluids. However, significant variation was observed between replicate hydrothermal samples and observation of high rates in seemingly inactive barite chimneys suggests that other electron donors may be important as well. Sediment sulfur isotope signatures concur with measured rates in the Barite field and indicate that microbial sulfate reduction has occurred in the hydrothermal sediments since the recent geological past.

Our findings indicate that basalt-hosted vent fields provide sufficient electron donors to support microbial sulfate reduction in high- and low-temperature hydrothermal areas in settings that otherwise show very low sulfate reduction rates.

KEYWORDS

microbial sulfate reduction, hydrothermal chimneys, hydrothermal sediment, marine sediment, spreading ridges, rift valley, radiotracer rates, sulfur isotopes

1 Introduction

Sulfate reduction is a widespread microbial metabolism in marine sediments (e.g. Goldhaber and Kaplan, 1975; Jørgensen, 1982; Canfield, 1991; Jørgensen et al., 2019). Dissimilatory sulfate-reducing bacteria and archaea obtain energy from the reduction of sulfate (SO_4^{2-}) linked to the oxidation of electron donors such as molecular hydrogen, methane or organic acids such as acetate, lactate and pyruvate that are produced by biological degradation of organic matter (Jørgensen and Kasten, 2006). This metabolic coupling with carbon implies that microbial sulfate reduction plays an important role in the global carbon cycle, and estimates suggest that the annual global reduction of 11.3 teramoles of sulfate is responsible for the oxidation of 11-29% of the organic carbon flux to the seafloor (Bowles et al., 2014). The highest activities of sulfate reducers (up to several 100s of nmol SO_4^{2-} cm^{-3} d^{-1}) are typically observed in near-shore shallow marine environments (e.g. Howarth and Jørgensen, 1984; Moeslundi et al., 1994; Thamdrup et al., 1994), where an optimum balance between high sedimentation rates and high primary productivity enables the preservation of organic matter after consumption by oxic respiration (Berner, 1978; Canfield, 1991). In contrast, sediments on the continental rise (2000-3500 m depth) and abyssal plains (>3500 m depth) are typically poor in organic matter, and calculated depth-integrated sulfate reduction rates are one to four orders of magnitude lower than for organic-rich shelf environments (Bowles et al., 2014).

Sedimented hydrothermal vent fields on oceanic spreading ridges have been shown to represent an exception to low microbial sulfate reduction rates found in deep sea settings. Organic-rich hydrothermal sediments in the Guaymas Basin (2000 m depth, Gulf of California) exhibit very high sulfate reduction rates of up to 1560 nmol SO_4^{2-} cm^{-3} d^{-1} (Jørgensen et al., 1990; Elsgaard et al., 1994; Kallmeyer and Boetius, 2004), and rates in the hydrothermal sediments of Middle Valley (2430 m depth, Juan de Fuca Ridge) range up to 100 nmol SO_4^{2-} cm^{-3} d^{-1} (Wankel et al., 2012). In addition, high sulfate reduction rates of up to 1000s of nmol SO_4^{2-} cm^{-3} d^{-1} were measured in actively venting sulfide deposits at Middle Valley (Frank et al., 2013) and a hydrothermal flange at the sediment-influenced Main Endeavour vent field on the Juan de Fuca Ridge (2220 m depth) (Frank et al., 2015). The importance of sulfate reducers in these sedimented hydrothermal systems has been explained by the abundance of sulfate and electron donors resulting from the mixing of reduced hydrothermal fluids and oxidized seawater, as well as the chemosynthetic production of organic carbon (Jannasch and Mottl, 1985; Jørgensen et al., 1990; McCollom and Shock, 1997; Frank et al., 2013). However, the majority of hydrothermal vent fields worldwide occurs on bare volcanic rocks with no or minimal sediment cover (Beaulieu and Szafranski, 2020), and are characterized by high-temperature fluids with lower pH, CH_4 and H_2 concentrations than sediment-associated systems (Baumberger et al., 2016b). In addition, non-hydrothermal sediments surrounding deep sea vent fields typically show very low sulfate reduction rates (cf. Bowles et al., 2014), in contrast to the Guaymas Basin where organic-rich sediments yield rates of up to 11.8 nmol SO_4^{2-} cm^{-3} d^{-1} (Elsgaard et al., 1994). Therefore, to better evaluate the importance of microbial sulfate reduction in hydrothermal systems on global oceanic spreading ridges, additional data is required from geological settings with bare-rock hydrothermal vent sites.

Here, we investigate the significance of hydrothermal activity on microbial sulfate reduction along the Arctic Mid Ocean Ridges (AMOR) in the Norwegian-Greenland Sea. The large variation in water depth, sedimentation rates and hydrothermal geochemistry enables us to compare sulfate reduction rates from marine sediments obtained from rift valleys with hydrothermal systems that cover a range of environmental conditions. We explore high- and low-temperature hydrothermal chimneys as well as hydrothermal sediments from basalt-hosted venting areas at Seven Sisters, Jan Mayen and sediment-influenced Loki's Castle, and evaluate ridge segment-scale variations in microbial sulfate reduction rates in background marine sediments. Our results reinforce those of previous studies showing elevated sulfate reduction rates in hydrothermal settings, and expand this to basalt-hosted systems without significant sediment cover.

2 Geological setting

The AMOR are a system of ultra-slow spreading ridges (full spreading rate 6-20 mm/year) that extends from the northern shelf of Iceland to the Siberian shelf in the Laptev Sea (Pedersen et al.,

2010b). Unlike volcanically active faster spreading ridges, the morphology of ultra-slow spreading ridges is characterized by broad axial rift valleys that are dominated by tectonics (Dick et al., 2003; Snow and Edmonds, 2007). The presence and exposure of ultramafic mantle rocks in these geological settings can generate methane and hydrogen through serpentinization reactions (Seyfried, 1987; Horita and Berndt, 1999; Cannat et al., 2010), resulting in hydrothermal vent sites with highly variable fluid compositions (Kelley et al., 2001; Edmonds et al., 2003; Baker et al., 2004; Pedersen et al., 2010a; Tao et al., 2012; Kinsey and German, 2013). Compared to faster spreading ridges, these hydrothermal systems may be active for longer periods of time and support distinct microbial communities (Nakamura and Takai, 2014; Ding et al., 2017; Lecoeuvre et al., 2021).

We focus on the part of the AMOR in the Norwegian-Greenland Sea that consists of the three segments Kolbeinsey Ridge (66.5 to 71.7°N), Mohns Ridge (70.9 to 73.6°N) and Knipovich Ridge (73.6 to 78.0°N) (Figure 1). Along this section, the rift valley floor is deepening towards the north from 1000 m at the hotspot-influenced Kolbeinsey Ridge to a maximum of 3500 m at the Knipovich Ridge. A sedimentation rate of 2-7 cm per 1000 years results in the accumulation of sediment within the rift valleys (Stein, 1990; Stubseid et al., 2023), in particular along the northernmost segments where the ridge is close to the Svalbard continental margin (Fiedler and Faleide, 1996). Glacigenic sediments from the Bear Island Fan reach the spreading ridge at the Mohns-Knipovich bend (Bruvoll et al., 2009).

Several high-temperature hydrothermal vent fields are located on the AMOR (Pedersen et al., 2010b; Pedersen and Bjerkgård, 2016), of which we focus on three in this study: Seven Sisters, Jan Mayen and Loki's Castle (Table 1). Seven Sisters is a shallow hydrothermal vent field (120 m depth) that occurs in mafic volcaniclastic rocks on top of a flat-topped volcano on the Kolbeinsey Ridge (Marques et al., 2020). Fluids of up to 200°C vent from barite and anhydrite-rich structures and are low in metals, CH_4 and H_2 (Marques et al., 2020) (Table 1). The Jan Mayen vent fields are situated on the southern Mohns Ridge at a depth of 550-700 meters (Pedersen et al., 2005), and consist of the Troll Wall, Soria Moria and Perle & Bruse venting areas. This study concentrates on the basalt-hosted Perle & Bruse field, which is located at 580 m depth at the flank of a large volcano that is undergoing rifting (Pedersen and Bjerkgård, 2016). Sulfide-rich chimneys vent fluids of up to 270°C with higher CH_4 concentrations than at Seven Sisters (Dahle et al., 2018) (Table 1). Loki's Castle vent field occurs at 2300 m depth on the northernmost section of the Mohns Ridge at the Mohns-Knipovich bend (Pedersen et al., 2010a). High-temperature (up to 315°C) fluids with high concentrations of NH_4^+, H_2 and CH_4 at Loki's Castle indicate a sedimentary influence to the basalt-hosted hydrothermal system (Baumberger et al., 2016a; Baumberger et al., 2016b). Adjacent to the high-temperature venting site is a circa 50 by 50 m area (Barite field) with low-temperature (20°C) barite chimneys and diffuse venting from sediments that are covered with microbial mats (Pedersen et al., 2010a; Steen et al., 2016). Previous work has suggested an important role for microbial sulfate reduction in and below the Barite field based on sulfur isotope signatures and sequencing data (Eickmann et al., 2014; Steen et al., 2016).

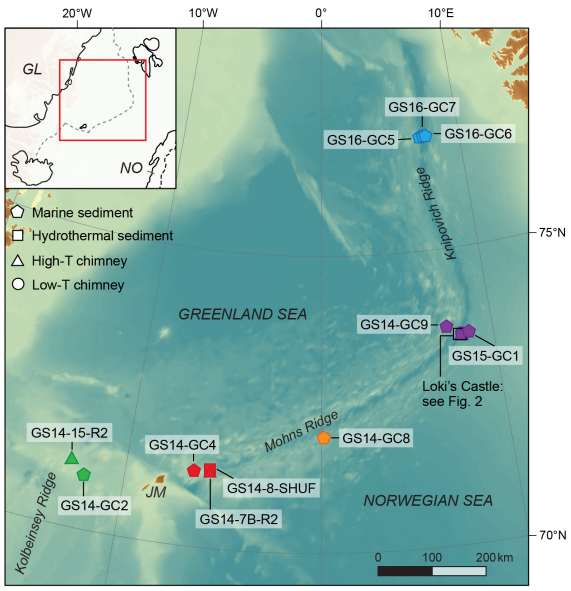

FIGURE 1
The Arctic Mid Ocean Ridge system (AMOR) and the island of Jan Mayen (JM) with locations of sampled marine sediments (diamonds), hydrothermal sediments (squares), high-temperature chimneys (triangles) and low-temperature chimneys (circles). Inset shows the location of the AMOR (dashed grey line) relative to Greenland (GL) and Norway (NO), and the location of the map (red box). Map created with ArcGIS using Ocean Basemap.

3 Materials and methods

3.1 Samples

Samples were collected during five research cruises with R/V G.O. Sars, using gravity coring equipment for marine sediments and ROV Ægir 6000 for hydrothermal chimneys, deposits and sediments (Table 2).

3.1.1 Kolbeinsey Ridge

One anhydrite-sulfide rich hydrothermal chimney sample was collected from the actively venting Lily mound at Seven Sisters vent field (GS14-15-R02). In addition, a 2.2 m long gravity core (GS14-GC2) was collected from the nearest sedimented basin to the ridge, approximately 40 km southeast of the Seven Sisters vent field (Figure 1). No hydrothermal sediments were obtained from this location.

3.1.2 Mohns Ridge

Four sediment cores were collected from rift flanks along the Mohns Ridge (Figure 1). One core (GS14-GC4) was sampled on the southern end of the Mohns Ridge, circa 30 km west of the Jan Mayen vent field on the western rift flank. Another core was collected along the central part of the Mohns Ridge (GS14-GC8)

TABLE 1 Hydrothermal vent fields investigated in this study.

Vent field	Ridge	Host rock	Depth (m)	T (°C)[1]	pH[2]	CH_4 (μM)
Seven Sisters	Kolbeinsey	Basalt	120	200	5.0	30
Jan Mayen	S Mohns	Basalt	580	270	4.7	5400
Loki's Castle	N Mohns	Basalt, sediment[3]	2361	315	5.6	14300

[1]Maximum measured in situ temperature. [2]Determined at 25°C. [3]Interaction with sediments at depth as inferred from fluid geochemistry. Data from Marques et al. (2020) for Lily mound, Seven Sisters; Dahle et al. (2018) for Bruse chimney, Jan Mayen; and Pedersen et al. (2010a); Baumberger et al. (2016b) for Camel chimney, Loki's Castle.

on the eastern flank. Sediment cores were also obtained from both rift flanks at the northern section of the Mohns Ridge near Loki's Castle hydrothermal vent field, with one core (GC14-GC9) taken in a sedimented basin on the Schulz Massif oceanic core complex and one core (GC15-GC1) in distal Bear Island Fan sediments, 5 km east of the rift valley.

Hydrothermal samples were collected from the Jan Mayen and Loki's Castle vent fields on the southern and northern end of the Mohns Ridge, respectively. One anhydrite-sulfide rich sample was obtained from the active Bruse chimney in the basalt-hosted Jan Mayen hydrothermal vent field (GS14-7B-R2), and hydrothermal sediments were collected from the nearby Perle chimney using a shuffle box with a shovel front (GS14-8-SHUF). A temperature of 70°C was measured in the hydrothermal sediments at circa 0.5 m depth. At Loki's Castle, five barite chimneys with different appearances were collected from the low-temperature (20°C) Barite field (Figure 2). Chimneys GS18-28-R6 and GS18-28-R8 are covered with white microbial mats and showed diffuse fluid venting, while chimney GS18-28-R3 is white and yellow-colored with no visible microbial mat, chimney GS15-9-R1 is yellow-colored and GS18-28-R5 is orange-colored (Supplementary Figure 1). Sediments from the Barite field were sampled in three different ways: a push core from the surface sediment layer (~10 cm) in between barite chimneys (GS15-9-PC2), a blade core (~20 cm) from active diffuse venting sediments below a microbial mat (GS18-28-BC3), and a gravity core (207 cm) that was deployed with a transponder to ensure correct positioning within the Barite field (GS14-GC14). One blade core was collected on the outer perimeter of the Barite field (GS18-28-BC4). In addition, one anhydrite-sulfide rich piece from the Camel chimney (GS18-22-R2) was obtained from the western high-temperature hydrothermal mound at Loki's Castle.

3.1.3 Knipovich Ridge

Three gravity cores were collected along an east-west transect on the central Knipovich Ridge (Figure 1), one on the western rift flank (GS16-GC5), one on the eastern rift flank (GS16-GC6) and one within the rift valley (GS16-GC7).

3.2 Methodology

3.2.1 Sulfate reduction rates

3.2.1.1 Marine sediments

Immediately after splitting of the retrieved sediment cores, duplicate subsamples (4 cm^3) were collected at regular depth intervals using sterile plastic syringes without tips (Røy et al., 2014). Sediment samples were subsequently incubated in the on-board laboratory with 10 μL (185 kBq) of $^{35}SO_4^{2-}$ tracer (PerkinElmer) using a Hamilton syringe, sealed off with a butyl rubber stopper and placed in a N_2-filled sealable plastic bag. Based on measured bottom seawater temperatures of ~1°C, samples were incubated in the refrigerator at 4°C for 0.5 to 35 days depending on the expected range of sulfate reduction rates. Re-oxidation of sulfide was avoided by maintaining an anoxic atmosphere during the incubations, and 1 cm^3 of sediment was collected from each horizon and frozen to determine sediment porosity from the weight loss during drying for 3 days at 105°C. At the end of the incubation time, sediment samples were quantitatively transferred into 50 ml Falcon tubes with 5 ml 20% zinc acetate and frozen at -20°C to stop microbial activity. To assess background ^{35}S levels, duplicate sediment samples were transferred directly into 20% zinc acetate solutions without the addition of radiotracer. In addition, controls to determine distillation blanks were collected by adding $^{35}SO_4^{2-}$ and immediately transferring the radiolabeled sediments to 20% zinc acetate solutions.

3.2.1.2 Hydrothermal sediments

Hydrothermal sediments and control samples were collected in a similar way to marine sediments using sterile plastic syringes, but a higher incubation temperature (20°C) was used for the samples collected from the Loki's Castle Barite field based on measured *in situ* sediment temperatures. Incubation times ranged from 0.8 to 3.1 days and control samples were collected to measure background ^{35}S and distillation blanks.

3.2.1.3 Hydrothermal chimneys

High- and low-temperature hydrothermal chimneys were sampled promptly after recovery on board. Chimney fragments were quickly crushed into a slurry using a flame-sterilized steel mortar and pestle and immediately transferred to an anaerobic glove bag filled with N_2. A volume of 2.5 ml of slurry was added to an Exetainer vial, and 1.0 ml of fluid (sampled bottom seawater or artificial seawater) was added to represent *in situ* sulfate concentrations in the chimney, following the method by Frank et al. (2013). Samples were subsequently incubated with 10 μL (185 kBq) of $^{35}SO_4^{2-}$ tracer and Exetainers were flushed with N_2 gas to ensure anoxic conditions during incubation. Incubation was performed at 20°C for chimneys from the Loki's Castle Barite field, reflecting measured temperatures in the barite chimneys. High-temperature chimneys from the Seven Sisters and Jan Mayen vent fields were also incubated at 20°C during initial

10.3389/fmars.2023.1320655

TABLE 2 Overview of samples analyzed for microbial sulfate reduction rates, in order of increasing latitude.

Sample name	Latitude	Longitude	Depth (m)	Description
Kolbeinsey Ridge				
GS14-GC2	70°54.955'N	12°02.202'W	1036	Marine sediment core (2.2 m)
GS14-15-R2	71°08.848'N	12°47.482'W	130	Hydrothermal chimney (200°C)
Mohns Ridge				
GS14-GC4	71°17.082'N	06°33.696'W	1050	Marine sediment core (2.4 m)
GS14-7B-R2	71°17.897'N	05°41.644'W	594	Hydrothermal chimney (270°C)
GS14-8-SHUF	71°17.904'N	05°42.257'W	567	Hydrothermal sediment
GS14-GC8	71°57.953'N	00°06.142'E	2476	Marine sediment core (3.4 m)
GS18-28-R5	73°33.978'N	08°09.726'E	2361	Hydrothermal barite chimney (20°C)
GS18-28-R8	73°33.978'N	08°09.720'E	2361	Hydrothermal barite chimney (20°C)
GS15-9-PC2	73°33.981'N	08°09.740'E	2363	Hydrothermal sediment
GS15-9-R1	73°33.981'N	08°09.764'E	2336	Hydrothermal barite chimney (20°C)
GS18-28-BC3	73°33.984'N	08°09.714'E	2361	Hydrothermal sediment
GS18-28-R3	73°33.984'N	08°09.744'E	2361	Hydrothermal barite chimney (20°C)
GS18-28-R6	73°33.984'N	08°09.726'E	2361	Hydrothermal barite chimney (20°C)
GS14-GC14	73°33.994'N	08°09.686'E	2330	Hydrothermal sediment
GS18-22-R2	73°34.002'N	08°09.402'E	2310	Hydrothermal chimney (315°C)
GS18-28-BC4	73°34.008'N	08°09.738'E	2361	Hydrothermal sediment
GS15-GC1	73°34.533'N	08°30.527'E	2562	Marine sediment core (3.9 m)
GS14-GC9	73°42.032'N	07°20.659'E	2653	Marine sediment core (2.1 m)
Knipovich Ridge				
GS16-GC5	76°54.766'N	07°07.491'E	3007	Marine sediment core (3.6 m)
GS16-GC7	76°55.212'N	07°23.371'E	3493	Marine sediment core (3.5 m)
GS16-GC6	76°55.253'N	07°34.522'E	2994	Marine sediment core (0.9 m)

Sample names include the year in which the sample was collected (GS13 to GS18) and the type of sampling equipment used, GC, gravity corer; PC, push corer; SHUF, shuffle box; BC, blade corer. For ROV-dives, the dive number is listed after AGR or ROV.

experiments due to a lack of suitable incubators on board, versus 80°C for the high-temperature chimney from Loki's Castle that was processed during a different cruise. After incubation, samples were quantitatively transferred into 50 ml Falcon tubes with 5 ml 20% zinc acetate and frozen at -20°C until further processing. Because of the heterogeneous nature of hydrothermal chimneys, each sample was measured at least in triplicate. Control slurries were treated in the same way as the sediments to obtain background ^{35}S values and distillation blanks.

3.2.1.4 Radioactivity measurements

Thawed samples were centrifuged to separate supernatant with the remaining $^{35}SO_4^{2-}$ and solids with precipitated $Zn^{35}S$. A 100 µL aliquot was sampled from the supernatant and mixed with 5 ml 5% zinc acetate and 15 ml Ecoscint XR (National Diagnostics) scintillation fluid. Reduced sulfide was extracted from the sediments and crushed chimneys by cold chromium distillation (Canfield et al., 1986; Fossing and Jørgensen, 1989; Kallmeyer et al., 2004), collected in 5 ml 5% zinc acetate and mixed with 15 ml scintillation fluid. The activity of ^{35}S in the supernatant and reduced sulfide was subsequently counted for two times 20 minutes per sample using a PerkinElmer Tri-Carb 2900TR Liquid Scintillation Analyzer at the Department of Biological Sciences, University of Bergen, with an average detection limit of 34 counts per minute. No background ^{35}S was measured in any of the control samples and the carryover of ^{35}S from sulfate during distillation was negligible for marine sediments. Hydrothermal samples generally yielded a small but non-zero distillation blank of up to 58 counts per minute, and measured blank values were used to calculate blank-corrected activities.

3.2.1.5 Sulfate reduction rate calculations

Sulfate reduction rates (in pmol cm^{-3} d^{-1}) were calculated for the marine and hydrothermal sediments using the following equation:

$$SRR = [SO_4^{2-}]_{pf} \cdot \varphi_{sed} \cdot (a_{TRIS}/a_{TOTAL}) \cdot (1/t) \cdot 1.06 \cdot 10^6 \quad (1)$$

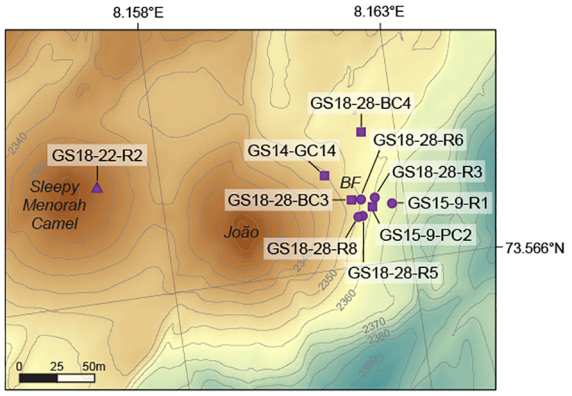

FIGURE 2
Detailed bathymetric map of the Loki's Castle vent field with all sample locations indicated (location of map area is shown in Figure 1). Sleepy, Menorah, Camel and Joao are high-temperature hydrothermal vents located on two hydrothermal mounds. The Barite field (BF) is located to the northeast of the eastern mound. Depth contours are given in meters. Symbols correspond to those used in Figure 1. Map created using ArcGIS.

where $[SO_4^{2-}]_{pf}$ is the measured sulfate concentration (mM) in pore waters at corresponding sediment depths (Section 3.2), φ_{sed} is the measured sediment porosity, a_{TRIS} is the blank-corrected radioactivity in the total reducible inorganic sulfur (TRIS), a_{TOTAL} the total blank-corrected radioactivity in the sample, and t the incubation time in days. No pore fluid sulfate profiles could be obtained for the blade cores, so that $[SO_4^{2-}]_{pf}$ was based on single measurements and assumed to be 23 mM for GS18-ROV28-BC3 and 28 mM for GS18-ROV28-BC4 for all horizons.

For the hydrothermal chimneys, sulfate reduction rates were calculated per volume of dry chimney material using a modified version of Equation 1. Firstly, the volume of chimney material in each sample (V_{dry}) was calculated using Equation 2:

$$V_{dry} = V_{slurry} \cdot (1 - \varphi_{slurry}) \quad (2)$$

where V_{slurry} is the volume of the slurry (2.5 ml) and φ_{slurry} is the porosity of the slurry. The total amount of sulfate present in each sample (in µmol) was calculated Equation 3:

$$SO_4^{2-}{}_{total} = ([SO_4^{2-}]_{slurry} \cdot \varphi_{slurry} \cdot V_{slurry} + [SO_4^{2-}]_{fluid} \cdot V_{fluid}) \quad (3)$$

where $[SO_4^{2-}]_{slurry}$ is the sulfate concentration of fluids naturally present in the slurry, here assumed to be similar to seawater (28 mM) due to flushing during transport from the seafloor, $[SO_4^{2-}]_{fluid}$ is the sulfate concentration in the added incubation fluids, and V_{fluid} is the volume of incubation fluid added (1 ml). Sulfate reduction rates were subsequently calculated (in pmol cm^{-3} d^{-1}) using Equation 4:

$$SRR = SO_4^{2-}{}_{total} \cdot (a_{TRIS}/a_{TOTAL}) \cdot (1/t) \cdot (1/V_{dry}) \cdot 1.06 \cdot 10^6 \quad (4)$$

The average detection limit for sulfate reduction rates is circa 5 pmol cm^{-3} d^{-1}.

3.2.2 Pore fluid and sediment geochemistry

Pore fluids were sampled from sediment cores by vacuum extraction using 0.2 µm Rhizon filters and analyzed promptly for pH and alkalinity (Metrohm Titrando) on board. Ammonium, nitrate/nitrite, dissolved inorganic carbon, sulfide and phosphate were measured on board by a Quaatro continuous flow analyzer (Seal Analytical). Sulfate concentrations were determined on shore by ion chromatography (Metrohm) with a relative standard deviation of <4% on repeated analyses of a multi-element standard, and cations were analyzed in aliquots acidified to 2% HNO_3 by inductively coupled plasma atomic emission spectroscopy (Thermo Scientific iCap 7600 ICP-AES) with Sc as internal standard and repeated measurement of SPS-SW-2 (Spectrapure) for quality control (<5% relative standard deviation). In addition, sediment subsamples (2-5 cm^3) were mixed on board with artificial seawater and He for headspace extraction of dissolved CH_4 and analysis by gas chromatography using a TCD-FID detector (3-5% standard error).

Total organic carbon (TOC) contents and C/N ratios were determined in oven-dried (3 days at 105°C) and finely crushed sediment samples (30-50 mg). GS15 samples were analyzed by elemental analyzer with TIC module (Analytik Jena Multi EA 4000), where TOC was calculated from the difference between total carbon and total inorganic carbon contents. All other samples were reacted with 1 ml phosphoric acid to remove inorganic carbon and subsequently analyzed for TOC and C/N ratios by a Thermo Scientific Flash 1120 EA coupled to a Thermo Scientific Delta V+ mass spectrometer. Precision on total C and N contents was better than 5% based on repeated analyses of a urea standard.

3.2.3 Stable sulfur isotopes

Stable sulfur isotope ratios were measured in hydrothermal sediments from the Barite field at Loki's Castle to identify past microbial activity. A few grams of sediment were collected at different depths from blade core GS18-28-BC3 and gravity core GS14-GC14 and dried at room temperature. Sulfide was subsequently extracted from ca. 20 mg of dried sediment using the hot chromium distillation method (Canfield et al., 1986), and precipitated as silver sulfide (Ag_2S). The fraction of sulfide represents chromium-reducible sulfide (CRS) as no significant amount of acid-volatile sulfide (AVS) was detected during the first acidification step. Ag_2S was converted at the University of Münster into sulfur hexafluoride (SF_6) and subsequently purified by cryogenic and chromatographic methods (Farquhar et al., 2000), after which SF_6 was introduced into a ThermoScientific MAT 253 mass spectrometer via a dual-inlet system. Sulfur isotope data are reported relative to the Vienna Canyon Diablo Troilite (V-CDT) and calculated assuming vales of $\delta^{34}S$ = -0.300‰ and $\delta^{33}S$ = -0.055‰ for the IAEA-S1 standard, using Equations 5, 6 below:

$$\delta^{34}S = 1000\,[(^{34}S/^{32}S_{sample})/(34S/^{32}S_{V-CDT}) - 1] \quad (5)$$

$$\Delta^{33}S = \delta^{33}S - 1000\,[(1 + \delta^{34}S/1000)^{0.515} - 1] \quad (6)$$

The accuracy was monitored using reference standard IAEA-S1, yielding a precision (2s) of 0.09‰ for $\delta^{34}S$ and 0.017‰ for $\Delta^{33}S$.

4 Results

4.1 Kolbeinsey Ridge

Microbial sulfate reduction was not detected in marine sediments sampled at the Kolbeinsey Ridge (Figure 3A, Supplementary Table S1A). These sediments are characterized by low TOC values of 0.2-0.6 wt.%, an average C/N ratio of 2.58 (Supplementary Table S3), and pore fluid sulfate concentrations that are close to seawater values (28.5 mM; Baumberger et al., 2016b) with no significant downcore variation (Figure 4A, Supplementary Table S2A). Ammonium (NH_4^+) and methane (CH_4) are absent from pore waters, and alkalinity increases from 2.7 mM to slightly higher values (3-4 mM) at 200 cm depth. A hydrothermal chimney sample collected from the anhydrite-sulfide rich Lily mound in the Seven Sisters vent field yielded a sulfate reduction rate of 69 ± 34 pmol SO_4^{2-} cm^{-3} d^{-1} (Figure 3C).

4.2 Mohns Ridge

Similar to the Kolbeinsey Ridge, no evidence was found for microbial sulfate reduction in marine sediments from the southern and central Mohns Ridge (Figure 3A) Total organic carbon contents and C/N ratios are comparably low, and range from 0.2-0.6 wt.% TOC and C/N = 3.13 at the southern Mohns Ridge, to 0.2-1.0 wt.% TOC and C/N = 4.80 at the central Mohns Ridge (Figures 4B, C). None of the sediment cores display pore water sulfate concentrations that are distinctly different from seawater values. Ammonium is absent in marine sediments from the southern Mohns Ridge (GS14-GC4), although this core displays the strongest increase in alkalinity from the seawater value (2.3 mM) at the top to 6.5 mM at 237 cm depth (Figure 4B). At the central Mohns Ridge, NH_4^+ appears at a depth of ~200 cm and increases to a value of 35 µM at 3.5 meters below the seafloor (GS14-GC8) with a corresponding change in alkalinity from 2.7 to 3.5 mM. No CH_4 was detected in the pore fluids. In contrast to the marine sediments, hydrothermal sediments (Figure 3B) and the high-temperature hydrothermal chimney Bruse (Figure 3C) from the Perle & Bruse venting area on the southern Mohns Ridge yield measurable sulfate reduction rates of 112 and 541 ± 116 pmol cm^{-3} d^{-1}, respectively (Supplementary Table S1B, S1C).

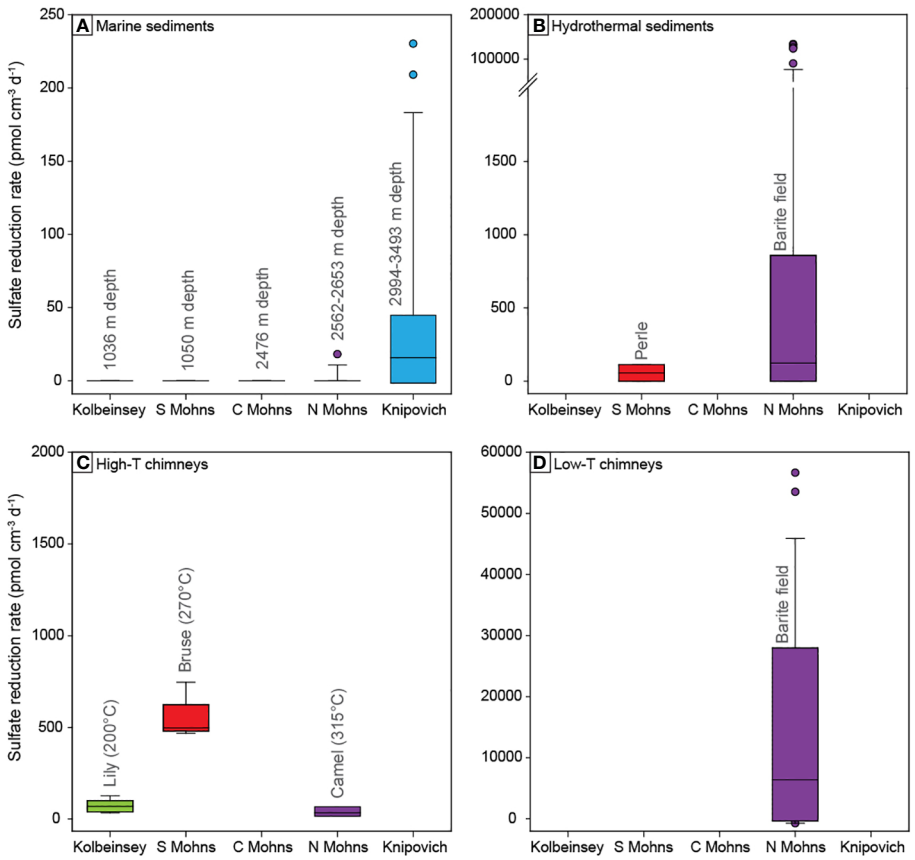

FIGURE 3
Box plots displaying sulfate reduction rates measured along the five segments of the AMOR. Panels reflect **(A)** marine sediments, **(B)** hydrothermal sediments, **(C)** high-temperature hydrothermal chimneys, **(D)** low-temperature hydrothermal chimneys. Note different scales for the y-axes. The highest sulfate reduction rates along the AMOR were measured in hydrothermal sediments from the Barite field.

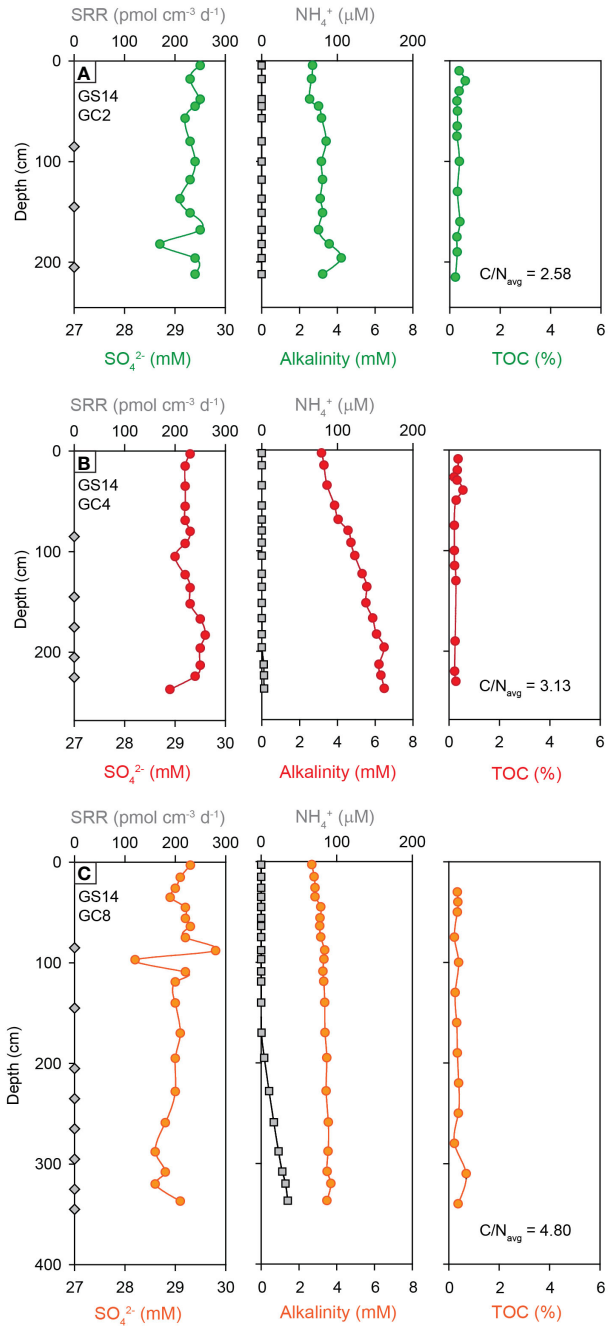

FIGURE 4
Depth profiles of sulfate reduction rates, pore fluid geochemistry (SO_4^{2-}, NH_4^+, alkalinity), total organic carbon (TOC) and average C/N ratios in marine sediment cores from the southern sections of the AMOR, with **(A)** Kolbeinsey Ridge, **(B)** Southern Mohns Ridge, **(C)** Central Mohns Ridge. Note that all sulfate reduction rates were below the detection limit in sediments from the southern AMOR.

Marine sediments from the northern Mohns Ridge (Figure 3A) show a similar absence of detectable microbial sulfate reduction as the southern sections of the Arctic Mid Ocean Ridge system, except for one horizon (380 cm) in sediments from the Bear Island Fan (GS15-GC1) where a rate of 18 pmol SO_4^{2-} cm^{-3} d^{-1} was measured (Figure 5). This core also shows a downcore decrease in SO_4^{2-} concentration, paired with an increase in NH_4^+ and alkalinity, as well as high TOC values of 5-8 wt.% in the bottom of the core (Figure 5). Methane was not detected.

The highest sulfate reduction rates in this study were measured in hydrothermal sediments (Figure 3B) and barite chimneys (Figure 3D) from the low-temperature Barite field at Loki's Castle, northern Mohns Ridge (Supplementary Tables S1B, S1C). Barite chimneys with visible venting and white microbial mats yield a maximum rate of 14633 pmol SO_4^{2-} cm^{-3} d^{-1}, but the variation in rates is significant between duplicate samples as well as the two different chimneys (average 3805 ± 5228 pmol cm^{-3} d^{-1}). Yellow-colored barite chimneys display higher rates than the white mat-covered chimneys, with an average of 31267 ± 17209 pmol cm^{-3} d^{-1} (Figure 6). In contrast, the chimneys that are orange-colored yield a low rate of 205 ± 143 pmol cm^{-3} d^{-1}, versus 929 ± 92 pmol cm^{-3} d^{-1} for white-colored chimneys with microbial mats (Figure 6). A rate of 39 ± 29 pmol cm^{-3} d^{-1} was obtained from the high-temperature sulfide chimney of Camel at Loki's Castle (Figure 3C).

A rate of 110478 pmol cm^{-3} d^{-1} was measured in a surface sediment layer between barite chimneys (GS15-9-PC2), and rates of 14828 to 93064 pmol cm^{-3} d^{-1} were found in sediments at 1-15 cm depth below a microbial mat (GS18-28-BC3) (Figure 7). These surface sediments are characterized by high TOC (6.6 wt.%), and pore water with high alkalinity (5.0 mM), CH_4 (185 nM), H_2S (2555 μM) and NH_4^+ (1255 μM) (Supplementary Table S2B). Sulfur isotopic compositions of sulfide from sample GS18-28-BC3 range from $\delta^{34}S$ = 6.10 to 11.60‰, with positive $\Delta^{33}S$ values of 0.029 to 0.044‰ (Supplementary Table S4). The sulfate concentration in this horizon (21.5 mM) is significantly lower than seawater. In contrast, sediments from the gravity core (GS14-GC14) show much lower sulfate reduction rates, ranging from 3 to 93 pmol cm^{-3} d^{-1} in the upper 120 cm (Figure 7). No sulfate reduction rates were detected from 120 cm to 200 cm depth in the core, and sulfate concentrations are close to seawater (27.9-28.5 mM). Sulfide and methane are detected in pore fluids at concentrations of 7.3-32.4 μM H_2S and 1.3-13.1 μM CH_4. Sulfide sulfur isotope ratios range from $\delta^{34}S$ = -3.74 to -21.68‰ with positive $\Delta^{33}S$ values of 0.021 to 0.138‰ (Supplementary Table S4).

4.3 Knipovich Ridge

Marine sediments from the Knipovich Ridge yield measurable sulfate reduction rates (Figure 8). The highest rates (up to 230 pmol cm^{-3} d^{-1}) were detected in sediments within the rift valley (GS16-GC7), and lower rates of 13-89 pmol cm^{-3} d^{-1} were found in sediments on the eastern and western rift flanks. The Knipovich Ridge sediments are also geochemically distinct from the southern sections of the AMOR, with relatively high TOC values of 0.2-2.2 wt.% and an average C/N ratio of 5.74 ± 1.94, with the highest TOC and C/N measured in the rift valley (1.3 wt.% and 6.88 ± 0.30, respectively). The Knipovich sediments are also characterized by the presence of NH_4^+ just below the sediment-water interface (Figure 8), and alkalinity profiles show an increase from seawater alkalinity to values of 3.1-4.5 mM at depth at these locations. Methane was only detected in marine sediments at the Knipovich Ridge and ranges from 10 to 105 nM.

10.3389/fmars.2023.1320655

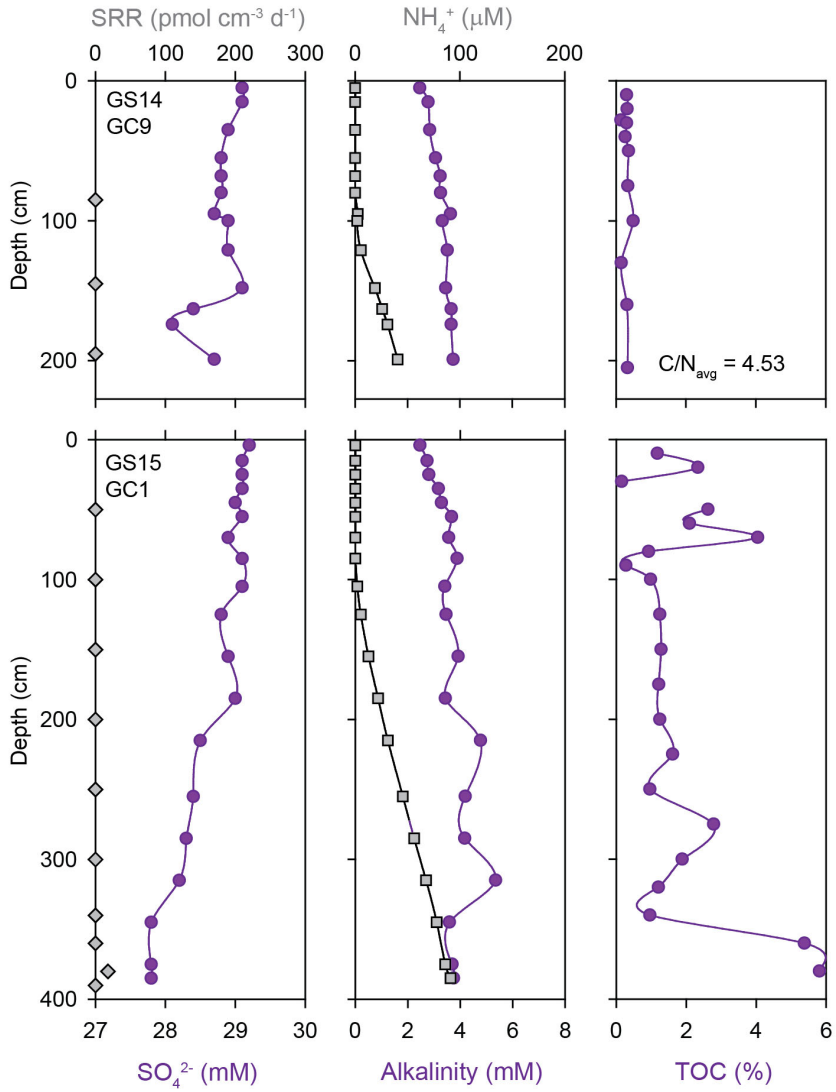

FIGURE 5
Depth profiles of sulfate reduction rates, pore fluid geochemistry (SO_4^{2-}, NH_4^+, alkalinity), total organic carbon (TOC) and average C/N ratios in marine sediment cores from the Northern Mohns Ridge. Note that only one sub-sample had a measurable sulfate reduction rate.

5 Discussion

5.1 Limited microbial sulfate reduction in deep marine sediments

Data presented in this paper expand the record of microbial sulfate reduction rates in the Arctic and confirm the relative insignificance of this metabolic pathway in the uppermost sediments of the deep marine realm in this region (cf. Bowles et al., 2014; Egger et al., 2018). Except for one horizon in core GS15-GC1, none of the marine sediment cores from the Kolbeinsey and Mohns Ridges yielded measurable gross sulfate reduction rates (Figure 3A) or showed significant changes in alkalinity coupled to decreasing sulfate concentrations in pore fluids (Figures 4, 5), indicating an absence of organoclastic sulfate reduction (OSR) and sulfate reduction coupled to anaerobic oxidation of methane (SR-AOM) in the upper 2-3 m of sediment (cf. Fossing et al., 2000; Gieskes et al., 2005; Jørgensen and Parkes, 2010; Wurgaft et al., 2019). This finding is not surprising given the low organic matter contents of the sediments (0.2-0.6 wt.% TOC) due to the relatively low sedimentation rates in the area (2-7 cm/1000 years) (Stein, 1990), and the degraded nature of this organic carbon as indicated by measured C/N ratios below that of marine plankton in Arctic regions (C/N ~ 6) (Martiny et al., 2013) (Figure 4, Figure 5). Such low-reactivity organic carbon has been shown to suppress sulfate reduction rates (Toth and Lerman, 1977; Goldhaber and Kaplan, 1975; Westrich and Berner, 1984), and as a result mineralization of organic carbon by sulfate reducers is not expressed in the studied sediments. Instead, increasing total alkalinity in core GS14-GC4 can be explained by the production of HCO_3^- during higher energy-yielding microbial metabolisms in oxic and suboxic zones, including aerobic degradation of organic matter and microbial oxidation of generated ammonium (NH_4^+) by nitrification (Zhao et al., 2021). Similarly, the NH_4^+ profiles in cores GS14-GC8, GS14-

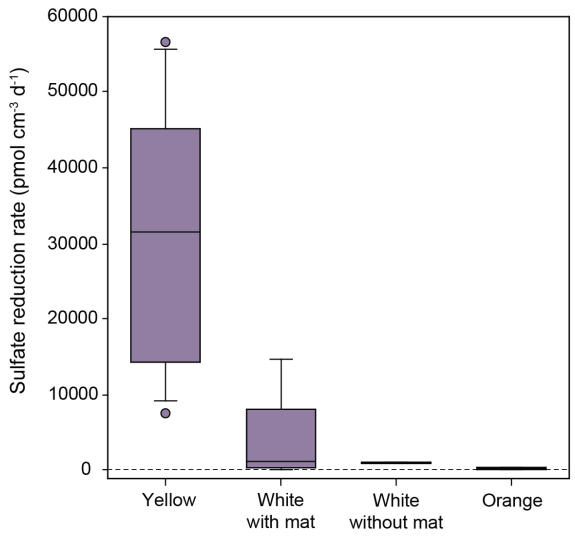

FIGURE 6
Box plots displaying sulfate reduction rates measured in low-temperature barite chimneys in the Loki's Castle Barite field on the Northern Mohns Ridge. Actively venting chimneys with a microbial mat show lower sulfate reduction rates than yellow chimneys without observable venting.

GC9 and GS15-GC1 are indicative of turnover of organic carbon, potentially related to iron and manganese reduction. The only non-zero sulfate reduction rate measured at 380 cm depth in GS15-GC1 may be related to the anomalously high TOC values of 6-8 wt.% at the base of this core (Figure 5), possibly reflecting variations in sedimentary sources during deposition of the glacigenic Bear Island Fan (Laberg and Vorren, 1996).

In contrast to the southern segments of the AMOR, sulfate reduction was detected in marine sediments from the Knipovich Ridge (Figure 3A). The low rates (13-230 pmol cm^{-3} d^{-1}) lead to only minor changes in pore fluid sulfate concentrations and alkalinity with depth (Figure 8) and highlight the importance of radiotracer measurements to detect sulfate reduction in these sediments. We hypothesize that the occurrence of microbial sulfate reduction in the upper sediment layers of the Knipovich Ridge is best explained by a higher abundance of reactive organic matter. Although the Knipovich Ridge is the deepest section of the AMOR in this study (2994-3493 m), sediments have relatively high organic carbon contents of up to 2.2 wt.% TOC compared to a global average of 0.3 wt.% for deep marine settings (Rullkötter, 2006). In addition, measured C/N ratios of up to 6.88 (Figure 8) indicate that this organic matter is less degraded than on the Kolbeinsey and Mohns Ridges, and higher values on the eastern ridge flank (C/N = 3.7-13.6) than the western flank (C/N = 2.1-8.8) suggest that this is related to a supply of organic matter from coastal areas around Svalbard, located ca. 150 km east of the spreading ridge. Higher labile organic matter contents lead to shallower suboxic and anoxic zones, as shown by pore fluid ammonium profiles which demonstrate that oxygen penetrates less deeply into the sediments from the Knipovich Ridge than elsewhere along the AMOR (cf. Zhao et al., 2020). As a result, organoclastic sulfate reduction can be detected in the uppermost studied Knipovich

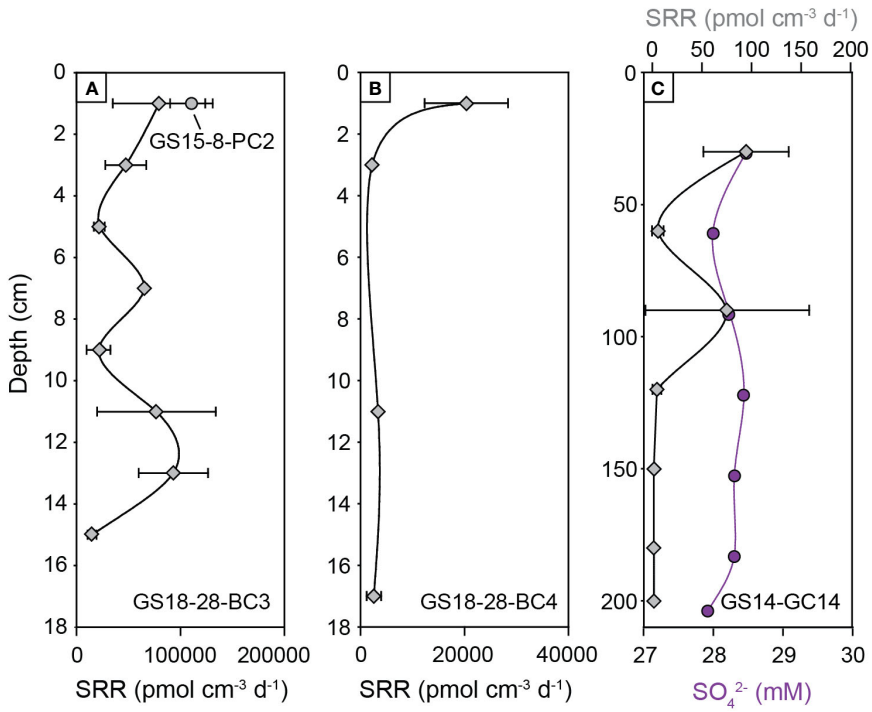

FIGURE 7
Depth profiles of sulfate reduction rates in hydrothermal sediments from the Loki's Castle Barite field, with **(A)** push core GS15-8-PC2 and blade core GS18-28-BC3 from actively venting sediments; **(B)** blade core GS18-28-BC4 from the perimeter of the Barite field; **(C)** gravity core GS14-GC14 from inside the Barite field, with pore fluid sulfate concentrations. Note the different scales for sulfate reduction rates.

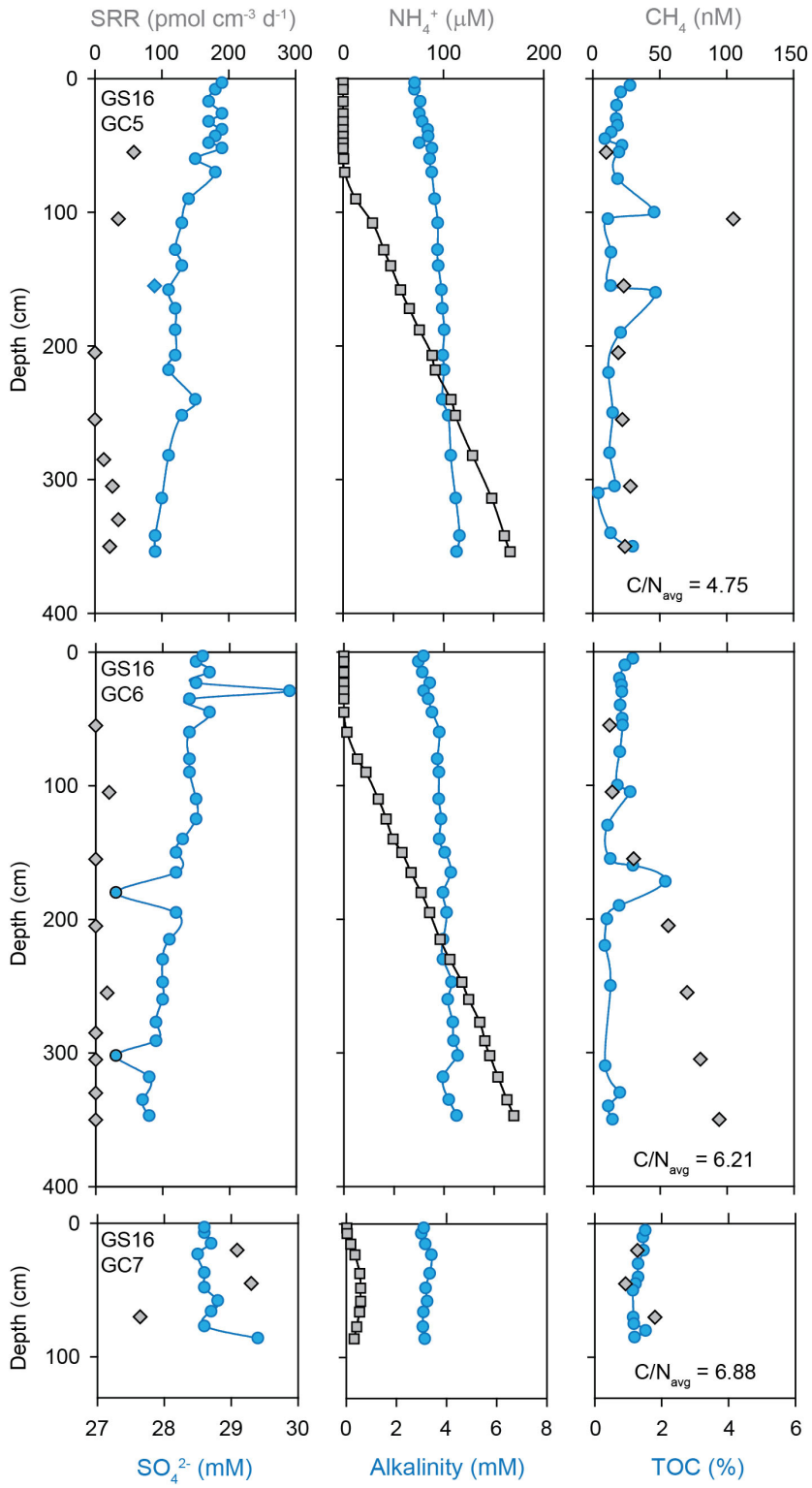

FIGURE 8
Depth profiles of sulfate reduction rates, pore fluid geochemistry (SO_4^{2-}, NH_4^+, alkalinity, CH_4), total organic carbon (TOC) and average C/N ratios in marine sediment cores from the Knipovich Ridge. In contrast to the southern AMOR segments, low but measurable sulfate reduction rates were obtained from all three sediment cores.

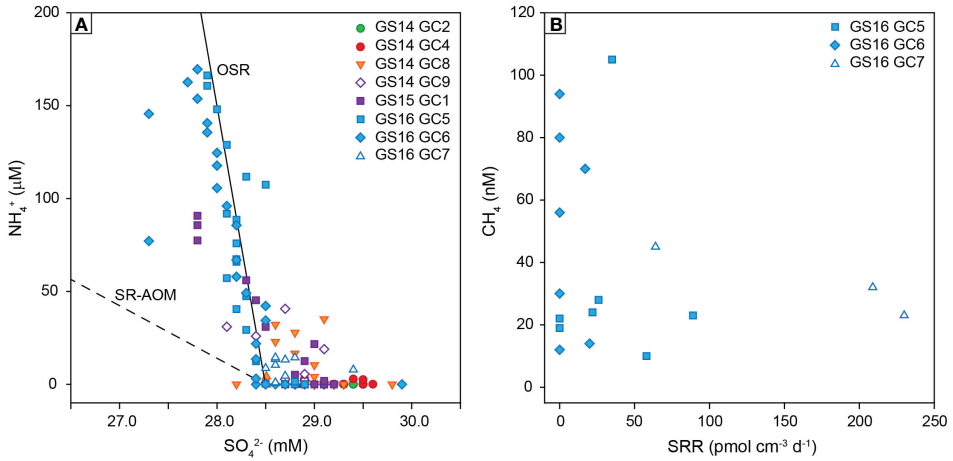

FIGURE 9
Trends in pore fluid geochemistry in marine sediments along the AMOR. **(A)** Pore fluid NH_4^+ versus SO_4^{2-}, with the dashed line displaying the trend associated with sulfate reduction coupled to anaerobic methane oxidation, and the solid line indicating organoclastic sulfate reduction (OSR) (Redfield et al., 1963; Greinert et al., 2002). Sediment cores from the Knipovich Ridge match with the trend predicted for OSR. **(B)** Pore fluid CH_4 versus sulfate reduction rates for sediment cores on the Knipovich Ridge, showing no correlation between methane and sulfate consumption.

Ridge sediments despite the large water depth (Figure 9A). Low levels of methane were also detected in pore fluids (Figure 8), but methane does not appear to be an electron donor for sulfate reducers in the studied Knipovich Ridge sediments, as evidenced by relatively high pore fluid NH_4^+ concentrations compared to SO_4^{2-} (Figure 9A) and a lack of correlation between CH_4 and sulfate reduction rates (Figure 9B).

Our results thus demonstrate that microbial sulfate reduction is near-absent in the uppermost marine sediments investigated along the AMOR, most likely due to a limited availability of reactive organic matter in the distal parts of the ridge system that results in an extension of the oxic and suboxic zones beyond sampled sediment depths. The anoxic sulfate reduction zone was only detected in upper sediment layers from the Knipovich Ridge, where sedimentary influence from nearby Svalbard presumably results in higher electron donor availability and a more condensed redox zonation. However, rates are several orders of magnitude lower than measured in the shallow fjords on the west coast of Svalbard range (1 to 240 nmol SO_4^{2-} cm^{-3} d^{-1}) (Sagemann et al., 1998; Ravenschlag et al., 2000; Arnosti and Jørgensen, 2006; Michaud et al., 2020). Next, we compare these findings from background marine sediments with microbial sulfate reduction rates in three different hydrothermal settings on the AMOR.

5.2 Microbial sulfate reduction in basalt-hosted hydrothermal vent fields

We find evidence for microbial sulfate reduction in all high-temperature iron sulfide-rich hydrothermal chimneys from the basalt-hosted Seven Sisters, Jan Mayen and Loki's Castle vent fields, albeit at different rates (Figure 3C). The maximum measured rate in the Bruse chimney is about six times higher than for the Lily mound despite comparable experimental conditions such as incubation time and temperature (20°C), and more than one order of magnitude higher than the highest rate observed at Camel (incubated at 80°C). Frank et al. (2013) observed similar rate differences between venting deposits at Middle Valley and suggested that these variations are due to distinct biomass and microbial community composition, resulting from differences in substrate availability and physicochemical conditions. Distinct environments also provide a plausible explanation for the different rates at Lily and Bruse as the Seven Sisters vent field occurs at a shallower depth, has lower fluid CH_4 concentrations (Table 1), and hosts an ecosystem with abundant anemones, unlike the Bruse vent (Olsen et al., 2016). In contrast, the rates obtained for the Camel chimney at Loki's Castle more likely reflect the activity of archaeal and thermophilic sulfate reducers at 80°C, instead of mesophilic bacterial sulfate reduction targeted at Lily and Bruse with an incubation temperature of 20°C. The low rates are consistent with the absence of sulfate-reducing archaea *Archaeoglobus* and low relative abundance (<0.1%) of thermophilic sulfate reducers (*Thermodesulfobacteriaceae* and *Desulfohalobiaceae*) in our samples from Camel (Babel, 2019), but contradict with data from other chimneys at Loki's Castle that indicate relatively abundant (10-35%) sulfate-reducing micro-organisms in chimney walls (Vulcano et al., 2022). The low measured sulfate reduction rates at Camel thus most likely result from the sampling of chimney material where the temperature was not optimal for thermophilic sulfate reduction. For example, strong differences in the abundance of thermophilic sulfate reducers were reported between interior and exterior chimney walls (Jaeschke et al., 2012), implying that measured rates are highly dependent on the relative amount of chimney interior in the incubated slurries. This could also explain why we observe significant variations between replicates from individual chimneys (Figure 3C) (cf. Frank et al., 2013; Frank et al., 2015), and underscores the caution that should be exerted when extrapolating sulfate reduction rate data to other chimneys in a vent field.

Regardless of the microbial communities targeted in our incubation experiments, our results provide clear evidence for

microbial sulfate reduction in the basalt-hosted high-temperature venting areas on the AMOR. All high-temperature chimney sulfate reduction rates are higher than the zero background values measured in nearby marine sediment cores (Figure 3A). The inferred importance of the hydrothermal vent systems for microbial sulfate reduction is consistent with the general abundance of electron donors in these settings, including CH_4 and H_2 derived from vent fluids and organic compounds produced by chemoautotrophs and vent fauna (Jannasch and Mottl, 1985; Blake and Hilbig, 1990; McCollom and Shock, 1997; Alain et al., 2002; Sievert and Vetriani, 2012). For the investigated vent fields, energy landscape modeling predicts that organic carbon from primary production is the main electron donor for sulfate reducers (Dahle et al., 2015; Dahle et al., 2018), which is consistent with the detection of organotrophic sulfate reduction from our rate measurements that were performed for all samples in this study without the addition of CH_4 or H_2.

Interestingly, sulfate reduction rates from the AMOR high-temperature (200-315°C) hydrothermal chimneys are several orders of magnitude lower than rates reported from chimneys in other hydrothermal vent fields. Frank et al. (2013) measured rates of 355 to 6675 nmol cm^{-3} d^{-1} at 90°C (converted using a density of 2.5 g cm^{-3}) in high-temperature (123-261°C) chimneys from the sediment-hosted Middle Valley vent field on the Juan de Fuca Ridge, and similar average rates of 41 to 675 nmol cm^{-3} d^{-1} were obtained at 4 and 50°C from a hydrothermal flange (215°C) on the nearby sediment-influenced Main Endeavour Vent (Frank et al., 2015). Although the lower rates could be partly due to sampling of heterogeneous material as outlined above, we find consistently low sulfate reduction rates in chimneys from all three AMOR hydrothermal vent fields. Different experimental conditions, for example no addition of dissolved organic carbon or incubation below (20°C) or above (80°C) optimum temperatures, may also result in measured sulfate reduction rates that are lower than *in situ* rates. However, this is unlikely to explain the five orders of magnitude lower rates in our study, as previous experimental work suggests a much less strong dependency of rates on variables such as temperature (Frank et al., 2015). Relatively low metal concentrations in the Arctic vent fluids (Baumberger et al., 2016b; Marques et al., 2020) also argue against suppression of microbial sulfate reduction by toxic effects of dissolved metals (Frank et al., 2015). Instead, we hypothesize that the difference in sulfate reduction rates between chimneys on the AMOR and the Juan de Fuca Ridge may be related to the nature of the hydrothermal vent fields. Sedimented hydrothermal systems such as Middle Valley are characterized by fluids with higher CH_4 concentrations than basalt-hosted vent fields such as Seven Sisters and Jan Mayen, which would fuel sulfate reduction coupled to the anaerobic oxidation of methane as well as methanotrophy producing organic carbon for organoheterotrophic sulfate reducers in anaerobic niches (Nakamura and Takai, 2014). In contrast, chemosynthetic primary production in hydrothermal vent fields on sediment-free spreading ridges is dominated by aerobic sulfur and hydrogen oxidation in and on chimney walls (McCollom and Shock, 1997; Nakamura and Takai, 2014; Meier et al., 2017). However, further work on a more extensive sample set from the AMOR, in particular the sediment-influenced Loki's Castle vent field, is required to confirm this hypothesis.

5.3 High sulfate reduction rates in low-temperature hydrothermal areas

The highest sulfate reduction rates along the AMOR were measured in low-temperature barite chimneys and hydrothermal sediments from the Barite field at Loki's Castle (Figure 3). Rates of up to 55 nmol SO_4^{2-} cm^{-3} d^{-1} in barite chimneys and 110 nmol SO_4^{2-} cm^{-3} d^{-1} in the diffuse venting sediments at 2300 m depth (Figure 3D) are similar to sulfate reduction rates measured in coastal sediments around Svalbard at shallow water depths of 50-300 m (1-240 nmol SO_4^{2-} cm^{-3} d^{-1}) (Sagemann et al., 1998; Ravenschlag et al., 2000; Arnosti and Jørgensen, 2006; Michaud et al., 2020), and are exceptionally high for deep marine settings (cf. Bowles et al., 2014 and this study). However, our results agree well with sulfate reduction rates reported from hydrothermal sediments on the Juan de Fuca Ridge, with rates of 30 to 1563 nmol SO_4^{2-} cm^{-3} d^{-1} measured in organic-rich hydrothermal sediments at Guaymas Basin (Jørgensen et al., 1990; Elsgaard et al., 1994) and 100 nmol SO_4^{2-} cm^{-3} d^{-1} in metalliferous sediments at the Middle Valley hydrothermal vent field (Wankel et al., 2012). Observation of high sulfate reduction rates in the Barite field is also consistent with previous geochemical and microbiological studies that identified an important role for sulfate reducers in this low-temperature hydrothermal area (Eickmann et al., 2014; Jaeschke et al., 2014; Steen et al., 2016; Eickmann et al., 2020).

Possible substrates for sulfate reducers in the Barite field include organic compounds derived from microbial mats and vent fauna as well as methane supplied by low-temperature hydrothermal fluids. High sulfate reduction rates in sediments directly below a microbial mat with chemolithoautotrophic sulfur oxidizers (GS18-28-BC3; Vulcano et al., 2022) suggest an important role for organic matter production at the sediment-water interface. Similarly, supply of organic carbon from siboglinid tubeworms living at the sediment surface (Kongsrud and Rapp, 2012) explains high sulfate reduction rates in hydrothermal surface sediments with a total organic carbon content of 6.6 wt.% (GS15-8-PC2), as well as the sharp decrease in sulfate reduction rates with depth in sediments collected from the periphery of the Barite field (GS18-28-BC4) (Figure 7B). Organoclastic sulfate reduction was also inferred by Eickmann et al. (2020) to be the main pathway of sulfate reduction in the Barite field, based on pore fluid NH_4^+/SO_4^{2-} and carbon isotope ratios in two gravity cores. However, recent work has additionally identified an abundant population of methane-oxidizing ANME-1 archaea with sulfate reducers as partners in the hydrothermal sediments (Steen et al., 2016; Vulcano et al., 2022), and our pore fluid data provide tentative evidence for methane as an another important electron donor for sulfate reducers in the Barite field. The diffuse venting fluids in the Barite field are thought to represent mixing of Mg-free high-temperature hydrothermal fluids and seawater with 51.8 mM Mg (Baumberger et al., 2016b), producing sediment pore fluids with Mg concentrations below that of seawater (Eickmann et al., 2014). Assuming conservative mixing for

magnesium (Tivey, 2007), we calculate contributions of high-temperature fluids of 5-18% and use this to predict 0.5-2 mM CH_4 in the diffuse vent fluids, based on an average CH_4 concentration of 13.8 mM in the hydrothermal end-member (Baumberger et al., 2016b). Predicted values are significantly higher than CH_4 concentrations of 0.2 to 13 µM measured in the pore fluids and suggest a loss of methane in the subsurface (Figure 10). Since the largest relative depletion in CH_4 is associated with the highest sulfate reduction rate (GS15-8-PC2) and is concomitant with relative enrichment in pore fluid H_2S and deficit in SO_4^{2-}, these findings are best explained by microbial sulfate reduction coupled to anaerobic methane oxidation. Depletions in CH_4 observed below the active sulfate reduction zone in GS14-GC14 most likely reflect the operation of these metabolic processes in the subsurface (cf. Eickmann et al., 2014).

Despite the general abundance of electron donors, sulfate reduction rates are highly heterogeneous in the Barite field. Rates measured in the gravity core (Figure 7C) are nearly three orders of magnitude lower than those measured in the hydrothermal surface sediments (Figure 7A), and yellow-colored barite chimneys show higher rates than white or orange ones (Figure 6). Similar heterogeneity was found in hydrothermal sediments at Guaymas Basin (Jørgensen et al., 1990; Elsgaard et al., 1994) and Middle Valley (Wankel et al., 2012) and is likely inherent to diffuse venting hydrothermal systems, where fluid flow is controlled by subsurface variations in permeability that result in variable physiochemical conditions and biological habitats (Scheirer et al., 2006; Lowell et al., 2015). Likewise, the observed heterogeneity in sulfate reducing activity in the different barite chimneys may be explained by the distinct microbial communities reported for yellow-colored chimneys, which have a higher biomass density and abundance of sulfate reducers than barite chimneys with white microbial mats (Jaeschke et al., 2014; Steen et al., 2016). It should be noted that previous work classified the yellow-colored barite chimneys as inactive and chimneys with white mats as active (Jaeschke et al., 2014; Steen et al., 2016), but our findings suggest that a revision of this terminology is required. Observation of the highest sulfate reduction rates in the yellow barite chimneys (Figure 6) suggests that electron donors are abundant, despite the lack of visible fluid venting. We speculate that these chimneys are not inactive but exhibit very slow diffuse venting that is difficult to observe, and that their yellow appearance may be the result of a different type of microbial mat than the sulfide-oxidizers present in the white mats on visibly venting chimneys (Steen et al., 2016). It remains to be seen what the electron donors are in the different types of barite chimneys, and if they are limited or absent in the orange and white barite chimneys with no microbial mats and low sulfate reduction rates (Figure 6).

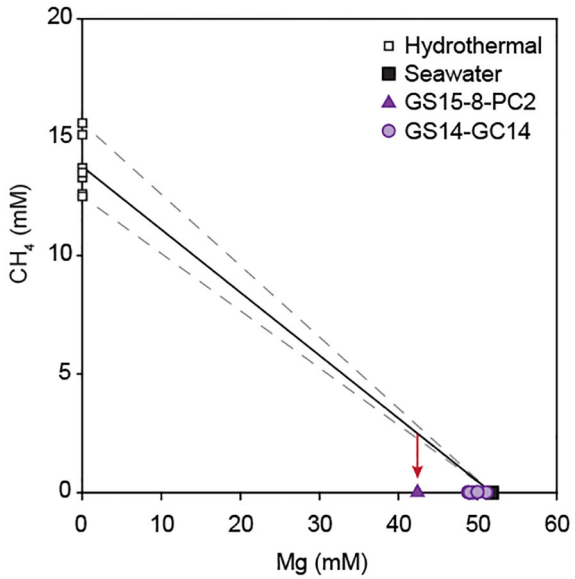

FIGURE 10
Concentration of CH_4 versus Mg in pore fluids from hydrothermal sediments in the Loki's Castle Barite field. The solid line indicates mixing between seawater and the average of end member hydrothermal fluids at Loki's Castle (Baumberger et al., 2016b), dashed lines are mixing lines with the highest and lowest values. The red arrow indicates that methane concentrations in the push core (GS15-8-PC2) and gravity core (GS14-GC14) are lower than expected based on mixing.

In addition to present-day microbial sulfate reduction inferred from our radiotracer incubations, multiple sulfur isotope data provide evidence that this metabolism has been active in the Barite field since the recent geological past. Sulfide minerals in the hydrothermal sediments show $\delta^{34}S$-values lower than ambient seawater ($\delta^{34}S$ = 21.2‰; Eickmann et al., 2014) and mostly fall onto mass relationships between $^{33}S/^{32}S$ and $^{34}S/^{32}S$ (defined as $^{33}\Lambda = \ln^{33}\alpha/\ln^{34}\alpha$) from 0.510 to 0.513 (Figure 11). These findings are consistent with major and minor sulfur isotope effects expected for microbial sulfate reduction (Harrison and Thode, 1958; Habicht and Canfield, 1997; Canfield, 2001; Detmers et al., 2001; Farquhar et al., 2003; Johnston et al., 2005; Johnston et al., 2007), and observation of the least ^{34}S-depleted signatures in sediments with the highest sulfate reduction rates (GS18-28-BC3) agrees well with the predicted inverse correlation between magnitudes of isotope fractionation and sulfate reduction rates (Chambers et al., 1975; Jørgensen, 1979; Davidson et al., 2009; Leavitt et al., 2013). However, we also observe large shifts (25-40‰) in $\delta^{34}S$ relative to seawater in sediment horizons of the gravity core where no active microbial sulfate reduction was detected (156-200 cm; Figure 11). The isotopic composition of sulfides at 167 cm depth can be explained by the presence of Cu-Zn rich sulfide minerals that formed under high-temperature hydrothermal conditions, as suggested by its $^{33}\Lambda$-value of 0.515 that is indicative of a non-biological origin and a $\delta^{34}S$-value close to mantle-sulfur (~0‰) (Figure 11). In contrast, sulfur isotope ratios in sediments at 156 cm and 200 cm depth fall onto the mass relationship of $^{33}\Lambda \sim 0.513$ (Figure 11), which points to a microbial origin of sulfur isotope fractionation (cf. Farquhar et al., 2003; Johnston et al., 2007). The lack of measurable sulfate reduction rates at 156 and 200 cm (Figure 7C) indicates that these biogenic isotope effects are unrelated to current microbial activity, and must instead reflect microbial sulfate reduction before the present day. As such, the slightly lower pore fluid SO_4^{2-} concentration at 200 cm depth (27.9

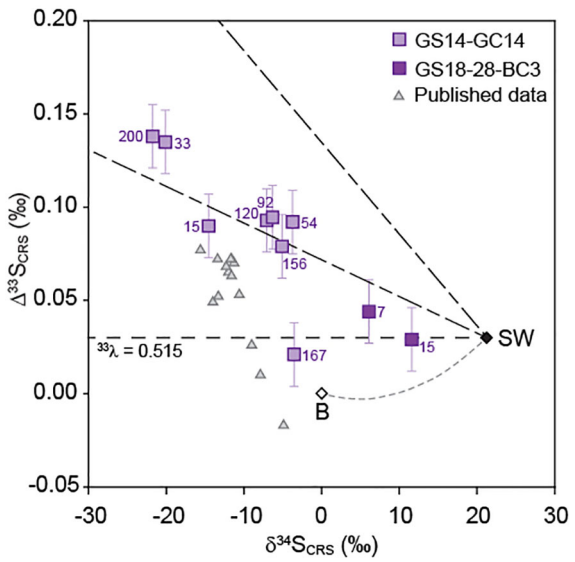

FIGURE 11
Multiple sulfur isotopic compositions of chromium-reducible sulfide (CRS) in blade core sediments (GS18-28-BC3) and gravity core sediments (GS14-GC14) from the Loki's Castle Barite field. Numbers next to symbols indicate core depths. Published data represent gravity cores from Eickmann et al. (2020). Dashed lines reflect isotope fractionation relative to seawater (SW) for different mass-relationships ($^{33}\Lambda$), with 0.510-0.513 reflecting microbial sulfate reduction (Farquhar et al., 2003; Johnston et al., 2007) and 0.515 high-temperature hydrothermal processes. Mixing between seawater (SW) and basalt (B) is also shown for reference. All $\Delta^{33}S$ values are calculated according to the definition in Equation 6 and error bars are 2σ.

mM) compared to seawater (Figure 7C) is more likely related to an increased contribution of sulfate-poor hydrothermal fluid rather than microbial consumption.

6 Conclusion

In this study, we demonstrate that hydrothermal activity can fuel microbial sulfate reduction in deep and distal marine settings on the AMOR that are otherwise characterized by insignificant sulfate reduction rates. Our findings confirm previous conclusions from sedimented and sediment-influenced hydrothermal systems on the Juan de Fuca Ridge that sulfate reduction is an important sulfur metabolism in hydrothermal settings in addition to sulfide oxidation (Jørgensen et al., 1990; Elsgaard et al., 1994; Kallmeyer and Boetius, 2004; Wankel et al., 2012; Frank et al., 2013; Frank et al., 2015), and further expand this to basalt-hosted hydrothermal vent fields. Microbial sulfate reduction is likely supported by an increased supply of electron donors, including organic compounds from primary producers in and on hydrothermal chimneys and vent fauna, as well as methane provided by high-temperature fluids. This is most clearly expressed in hydrothermal sediments and low-temperature barite chimneys from the Barite field at Loki's Castle, where high rates of up to 110 nmol cm^{-3} d^{-1} were measured and a relative depletion in pore fluid methane was observed. Although these results have limited implications for global sulfate reduction rates as the total surface area of hydrothermal vent fields is small compared to the entire ocean floor, our work indicates that the impact of microbial sulfate reduction on the local geochemistry of hydrothermal systems may be significant, in particular for sulfur and carbon cycling. For example, based on our highest measured sulfate reduction rate in hydrothermal sediments, contributions from sulfate reducers to diffuse venting fluids of the Barite field could be up to 10s of moles of sulfide per day. Further quantification of the impact of sulfate reducers on hydrothermal geochemistry requires improved estimates of vent fluxes, but importantly must consider the heterogeneity observed in sulfate reduction rates in the hydrothermal samples in our study.

Data availability statement

The original contributions presented in the study are included in the article/Supplementary Material. Further inquiries can be directed to the corresponding author.

Author contributions

DR: Conceptualization, Investigation, Methodology, Writing – original draft. FV: Investigation, Writing – review & editing. J-KL: Investigation, Writing – review & editing. KM: Investigation, Writing – review & editing. HB: Investigation, Writing – review & editing. SJ: Investigation, Writing – review & editing. TB: Investigation, Writing – review & editing. IØ: Investigation, Writing – review & editing. ER: Investigation, Writing – review & editing. IT: Funding acquisition, Investigation, Writing – review & editing. LR: Methodology, Writing – review & editing. HS: Investigation, Writing – review & editing. IS: Funding acquisition, Investigation, Supervision, Writing – review & editing.

Funding

The author(s) declare financial support was received for the research, authorship, and/or publication of this article. This study was funded by the Research Council of Norway through the Centre for Geobiology, the K.G. Jebsen Foundation, the Trond Mohn Foundation and University of Bergen through the Centre for Deep Sea Research (grant no. TMS2020TMT13).

Acknowledgments

We thank the captain and crew of R/V G.O. Sars, the pilots of ROV Ægir 6000 and cruise leader Rolf Birger Pedersen for their assistance in sample collection. Thibaut Barreyre is thanked for providing bathymetry data from Loki's Castle. Hildegunn Almelid, Pål Tore Mørkved, Anita-Elin Fedøy and Evy Foss Skjoldal are thanked for their technical assistance and geochemical analyses. We thank Dave Butterfield and two reviewers for their constructive comments that helped to improve this manuscript. This study was

funded by the Research Council of Norway through the Centre for Geobiology, the K.G. Jebsen Foundation, the Trond Mohn Foundation and University of Bergen through the Centre for Deep Sea Research (grant no. TMS2020TMT13). This is PMEL contribution 5556.

Conflict of interest

The authors declare that the research was conducted in the absence of any commercial or financial relationships that could be construed as a potential conflict of interest.

Publisher's note

All claims expressed in this article are solely those of the authors and do not necessarily represent those of their affiliated organizations, or those of the publisher, the editors and the reviewers. Any product that may be evaluated in this article, or claim that may be made by its manufacturer, is not guaranteed or endorsed by the publisher.

Supplementary material

The Supplementary Material for this article can be found online at: https://www.frontiersin.org/articles/10.3389/fmars.2023.1320655/full#supplementary-material

References

Alain, K., Olagnon, M., Desbruyères, D., Pagé, A., Barbier, G., Juniper, S. K., et al. (2002). Phylogenetic characterization of the bacterial assemblage associated with mucous secretions of the hydrothermal vent polychaete Paralvinella palmiformis. *FEMS Microbiol. Ecol.* 42, 463–476. doi: 10.1111/j.1574-6941.2002.tb01035.x

Arnosti, C., and Jørgensen, B. B. (2006). Organic carbon degradation in arctic marine sediments, svalbard: a comparison of initial and terminal steps. *Geomicrobiology J.* 23, 551–563. doi: 10.1080/01490450600897336

Babel, H. R. (2019). *Metabolic properties of the hyperthermophilic sulfate reducing archaea of the genus Archaeoglobus in deep-sea hydrothermal vent systems, Department of Biological Sciences* (Norway: University of Bergen).

Baker, E. T., Edmonds, H. N., Michael, P. J., Bach, W., Dick, H. J., Snow, J. E., et al. (2004). Hydrothermal venting in magma deserts: The ultraslow-spreading Gakkel and Southwest Indian Ridges. *Geochemistry Geophysics Geosystems* 5. doi: 10.1029/2004GC000712

Baumberger, T., Früh-Green, G. L., Dini, A., Boschi, C., van Zuilen, K., Thorseth, I. H., et al. (2016a). Constraints on the sedimentary input into the Loki's Castle hydrothermal system (AMOR) from B isotope data. *Chem. Geology* 443, 111–120. doi: 10.1016/j.chemgeo.2016.09.026

Baumberger, T., Früh-Green, G. L., Thorseth, I. H., Lilley, M. D., Hamelin, C., Bernasconi, S. M., et al. (2016b). Fluid composition of the sediment-influenced Loki's castle vent field at the ultra-slow spreading Arctic Mid-Ocean ridge. *Geochimica Cosmochimica Acta* 187, 156–178. doi: 10.1016/j.gca.2016.05.017

Beaulieu, S. E., and Szafranski, K. (2020) *InterRidge global database of active submarine hydrothermal vent fields, version 3.4*. Available at: http://vents-data.interridge.org.

Berner, R. A. (1978). Sulfate reduction and the rate of deposition of marine sediments. *Earth Planetary Sci. Lett.* 37 (3), 492–498. doi: 10.1016/0012-821X(78)90065-1

Blake, J. A., and Hilbig, B. (1990). Polychaeta from the vicinity of deep-sea hydrothermal vents in the eastern Pacific. II. New species and records from the Juan de Fuca and Explorer Ridge systems. *Pac. Sci.* 44v (3), 219–253.

Bowles, M. W., Mogollón, J. M., Kasten, S., Zabel, M., and Hinrichs, K.-U. (2014). Global rates of marine sulfate reduction and implications for sub–sea-floor metabolic activities. *Science* 344, 889–891. doi: 10.1126/science.1249213

Bruvoll, V., Breivik, A. J., Mjelde, R., and Pedersen, R. B. (2009). Burial of the Mohn-Knipovich seafloor spreading ridge by the Bear Island Fan: Time constraints on tectonic evolution from seismic stratigraphy. *Tectonics* 28. doi: 10.1029/2008TC002396

Canfield, D. E. (1991). Sulfate reduction in deep-sea sediments. *Am. J. Sci.* 291, 177–188. doi: 10.2475/ajs.291.2.177

Canfield, D. E. (2001). Isotope fractionation by natural populations of sulfate-reducing bacteria. *Geochimica Cosmochimica Acta* 65, 1117–1124. doi: 10.1016/S0016-7037(00)00584-6

Canfield, D. E., Raiswell, R., Westrich, J. T., Reaves, C. M., and Berner, R. A. (1986). The use of chromium reduction in the analysis of reduced inorganic sulfur in sediments and shales. *Chem. Geology* 54, 149–155. doi: 10.1016/0009-2541(86)90078-1

Cannat, M., Fontaine, F., and Escartin, J. (2010). "Serpentinization and associated hydrogen and methane fluxes at slow spreading ridges," in *Diversity of hydrothermal systems on slow spreading ocean ridges*. Eds. P. A. Rona, C. W. Devey, J. Dyment and B. J. Murton (Washington, DC: AGU), 241–264.

Chambers, L. A., Trudinger, P. A., Smith, J. W., and Burns, M. S. (1975). Fractionation of sulfur isotopes by continuous cultures of Desulfovibrio desulfuricans. *Can. J. Microbiol.* 21, 1602–1607. doi: 10.1139/m75-234

Dahle, H., Le Moine Bauer, S., Baumberger, T., Stokke, R., Pedersen, R. B., Thorseth, I. H., et al. (2018). Energy landscapes in hydrothermal chimneys shape distributions of primary producers. *Front. Microbiol.* 9, 1570. doi: 10.3389/fmicb.2018.01570

Dahle, H., Økland, I., Thorseth, I. H., Pederesen, R. B., and Steen, I. H. (2015). Energy landscapes shape microbial communities in hydrothermal systems on the Arctic Mid-Ocean Ridge. *ISME J.* 9, 1593–1606. doi: 10.1038/ismej.2014.247

Davidson, M. M., Bisher, M., Pratt, L. M., Fong, J., Southam, G., Pfiffner, S. M., et al. (2009). Sulfur isotope enrichment during maintenance metabolism in the thermophilic sulfate-reducing bacterium Desulfotomaculum putei. *Appl. Environ. Microbiol.* 75, 5621–5630. doi: 10.1128/AEM.02948-08

Detmers, J., Bruchert, V., Habicht, K. S., and Kuever, J. (2001). Diversity of sulfur isotope fractionations by sulfate-reducing prokaryotes. *Appl. Environ. Microbiol.* 67, 888–894. doi: 10.1128/AEM.67.2.888-894.2001

Dick, H. J., Lin, J., and Schouten, H. (2003). An ultraslow-spreading class of ocean ridge. *Nature* 426, 405–412. doi: 10.1038/nature02128

Ding, J., Zhang, Y., Wang, H., Jian, H., Leng, H., and Xiao, X. (2017). Microbial community structure of deep-sea hydrothermal vents on the ultraslow spreading Southwest Indian Ridge. *Front. Microbiol.* 8, 1012. doi: 10.3389/fmicb.2017.01012

Edmonds, H., Michael, P., Baker, E., Connelly, D., Snow, J., Langmuir, C., et al. (2003). Discovery of abundant hydrothermal venting on the ultraslow-spreading Gakkel ridge in the Arctic Ocean. *Nature* 421, 252–256. doi: 10.1038/nature01351

Egger, M., Riedinger, N., Mogollón, J. M., and Jørgensen, B. B. (2018). Global diffusive fluxes of methane in marine sediments. *Nat. Geosci.* 11, 421–425. doi: 10.1038/s41561-018-0122-8

Eickmann, B., Baumberger, T., Thorseth, I. H., Strauss, H., Früh-Green, G. L., Pedersen, R. B., et al. (2020). Sub-seafloor sulfur cycling in a low-temperature barite field: A multi-proxy study from the Arctic Loki's Castle vent field. *Chem. Geology* 539, 119495. doi: 10.1016/j.chemgeo.2020.119495

Eickmann, B., Thorseth, I., Peters, M., Strauss, H., Bröcker, M., and Pedersen, R. (2014). Barite in hydrothermal environments as a recorder of subseafloor processes: a multiple-isotope study from the Loki's Castle vent field. *Geobiology* 12, 308–321. doi: 10.1111/gbi.12086

Elsgaard, L., Isaksen, M. F., Jørgensen, B. B., Alayse, A.-M., and Jannasch, H. W. (1994). Microbial sulfate reduction in deep-sea sediments at the Guaymas Basin hydrothermal vent area: influence of temperature and substrates. *Geochimica Cosmochimica Acta* 58, 3335–3343. doi: 10.1016/0016-7037(94)90089-2

Farquhar, J., Bao, H., and Thiemens, M. (2000). Atmospheric influence of earth's earliest sulfur cycle. *Science* 289, 756–758. doi: 10.1126/science.289.5480.756

Farquhar, J., Johnston, D. T., Wing, B. A., Habicht, K. S., Canfield, D. E., Airieau, S., et al. (2003). Multiple sulphur isotopic interpretations of biosynthetic pathways: implications for biological signatures in the sulphur isotope record. *Geobiology* 1, 27–36. doi: 10.1046/j.1472-4669.2003.00007.x

Fiedler, A., and Faleide, J. I. (1996). Cenozoic sedimentation along the southwestern Barents Sea margin in relation to uplift and erosion of the shelf. *Global Planet. Change* 12, 75–93. doi: 10.1016/0921-8181(95)00013-5

Fossing, H., Ferdelman, T. G., and Berg, P. (2000). Sulfate reduction and methane oxidation in continental margin sediments influenced by irrigation (South-East Atlantic off Namibia). *Geochimica Cosmochimica Acta* 64, 897–910. doi: 10.1016/S0016-7037(99)00349-X

Fossing, H., and Jørgensen, B. B. (1989). Measurement of bacterial sulfate reduction in sediments: evaluation of a single-step chromium reduction method. *Biogeochemistry* 8, 205–222. doi: 10.1007/BF00002889

Frank, K. L., Rogers, D. R., Olins, H. C., Vidoudez, C., and Girguis, P. R. (2013). Characterizing the distribution and rates of microbial sulfate reduction at Middle Valley hydrothermal vents. *ISME J.* 7, 1391–1401. doi: 10.1038/ismej.2013.17

Frank, K. L., Rogers, K. L., Rogers, D. R., Johnston, D. T., and Girguis, P. R. (2015). Key factors influencing rates of heterotrophic sulfate reduction in active seafloor hydrothermal massive sulfide deposits. *Front. Microbiol.* 6, 1449. doi: 10.3389/fmicb.2015.01449

Gieskes, J., Mahn, C., Day, S., Martin, J. B., Greinert, J., Rathburn, T., et al. (2005). A study of the chemistry of pore fluids and authigenic carbonates in methane seep environments: Kodiak Trench, Hydrate Ridge, Monterey Bay, and Eel River Basin. *Chem. Geology* 220, 329–345. doi: 10.1016/j.chemgeo.2005.04.002

Goldhaber, M. B., and Kaplan, I. R. (1975). Controls and consequences of sulfate reduction rates in recent marine sediments. *Soil Sci.* 119 (1), 42–55. doi: 10.1097/00010694-197501000-00008

Greinert, J., Bollwerk, S. M., Derkachev, A., Bohrmann, G., and Suess, E. (2002). Massive barite deposits and carbonate mineralization in the Derugin Basin, Sea of Okhotsk: precipitation processes at cold seep sites. *Earth Planetary Sci. Lett.* 203, 165–180. doi: 10.1016/S0012-821X(02)00830-0

Habicht, K. S., and Canfield, D. E. (1997). Sulfur isotope fractionation during bacterial sulfate reduction in organic-rich sediments. *Geochimica Cosmochimica Acta* 61, 5351–5361. doi: 10.1016/S0016-7037(97)00311-6

Harrison, A. G., and Thode, H. G. (1958). Mechanism of the bacterial reduction of sulphate from isotope fractionation studies. *Trans. Faraday Soc.* 53, 84–92. doi: 10.1039/tf9585400084

Horita, J., and Berndt, M. E. (1999). Abiogenic methane formation and isotopic fractionation under hydrothermal conditions. *Science* 285, 1055–1057. doi: 10.1126/science.285.5430.1055

Howarth, R. W., and Jørgensen, B. B. (1984). Formation of 35S-labelled elemental sulfur and pyrite in coastal marine sediments (Limfjorden and Kysing Fjord, Denmark) during short-term 35SO42– reduction measurements. *Geochimica cosmochimica Acta* 48, 1807–1818. doi: 10.1016/0016-7037(84)90034-6

Jaeschke, A., Eickmann, B., Lang, S. Q., Bernasconi, S. M., Strauss, H., and Früh-Green, G. L. (2014). Biosignatures in chimney structures and sediment from the Loki's Castle low-temperature hydrothermal vent field at the Arctic Mid-Ocean Ridge. *Extremophiles* 18, 545–560. doi: 10.1007/s00792-014-0640-2

Jaeschke, A., Jørgensen, S. L., Bernasconi, S. M., Pedersen, R. B., Thorseth, I. H., and Früh-Green, G. L. (2012). Microbial diversity of Loki's Castle black smokers at the Arctic Mid-Ocean Ridge. *Geobiology* 10, 548–561. doi: 10.1111/gbi.12009

Jannasch, H. W., and Mottl, M. J. (1985). Geomicrobiology of deep-sea hydrothermal vents. *Science* 229, 717–725. doi: 10.1126/science.229.4715.717

Johnston, D. T., Farquhar, J., and Canfield, D. E. (2007). Sulfur isotope insights into microbial sulfate reduction: When microbes meet models. *Geochimica Cosmochimica Acta* 71, 3929–3947. doi: 10.1016/j.gca.2007.05.008

Johnston, D. T., Farquhar, J., Wing, B. A., Kaufman, A. J., Canfield, D. E., and Habicht, K. S. (2005). Multiple sulfur isotope fractionations in biological systems: A case study with sulfate reducers and sulfur disproportionators. *Am. J. Sci.* 305, 645–660. doi: 10.2475/ajs.305.6-8.645

Jørgensen, B. B. (1979). A theoretical model of the stable sulfur isotope distribution in marine sediments. *Geochimica Cosmochimica Acta* 43, 363–374. doi: 10.1016/0016-7037(79)90201-1

Jørgensen, B. B. (1982). Mineralization of organic matter in the sea bed—the role of sulphate reduction. *Nature* 296 (5858), 643–645. doi: 10.1038/296643a0

Jørgensen, B. B., Findlay, A. J., and Pellerin, A. (2019). The biogeochemical sulfur cycle of marine sediments. *Front. Microbiol.* 10, 849. doi: 10.3389/fmicb.2019.00849

Jørgensen, B. B., and Kasten, S. (2006). "Sulfur cycling and methane oxidation," in *Marine geochemistry*. Eds. H. D. Schulz and M. Zabel (Berlin: Springer), 271–309.

Jørgensen, B. B., and Parkes, R. J. (2010). Role of sulfate reduction and methane production by organic carbon degradation in eutrophic fjord sediments (Limfjorden, Denmark). *Limnol. Oceanogr.* 55, 1338–1352. doi: 10.4319/lo.2010.55.3.1338

Jørgensen, B. B., Zawacki, L. X., and Jannasch, H. W. (1990). Thermophilic bacterial sulfate reduction in deep-sea sediments at the Guaymas Basin hydrothermal vent site (Gulf of California). *Deep Sea Res. Part A. Oceanographic Res. Papers* 37, 695–710. doi: 10.1016/0198-0149(90)90099-H

Kallmeyer, J., and Boetius, A. (2004). Effects of temperature and pressure on sulfate reduction and anaerobic oxidation of methane in hydrothermal sediments of Guaymas Basin. *Appl. Environ. Microbiol.* 70, 1231–1233. doi: 10.1128/AEM.70.2.1231-1233.2004

Kallmeyer, J., Ferdelman, T. G., Weber, A., Fossing, H., and Jørgensen, B. B. (2004). A cold chromium distillation procedure for radiolabeled sulfide applied to sulfate reduction measurements. *Limnology Oceanography: Methods* 2, 171–180. doi: 10.4319/lom.2004.2.171

Kelley, D. S., Karson, J. A., Blackman, D. K., FruÈh-Green, G. L., Butterfield, D. A., Lilley, M. D., et al. (2001). An off-axis hydrothermal vent field near the Mid-Atlantic Ridge at 30 N. *Nature* 412, 145–149. doi: 10.1038/35084000

Kinsey, J. C., and German, C. R. (2013). Sustained volcanically-hosted venting at ultraslow ridges: Piccard hydrothermal field, Mid-Cayman Rise. *Earth Planetary Sci. Lett.* 380, 162–168. doi: 10.1016/j.epsl.2013.08.001

Kongsrud, J. A., and Rapp, H. T. (2012). Nicomache (Loxochona) lokii sp. nov. (Annelida: Polychaeta: Maldanidae) from the Loki's Castle vent field: an important structure builder in an Arctic vent system. *Polar Biol.* 35, 161–170. doi: 10.1007/s00300-011-1048-4

Laberg, J. S., and Vorren, T. O. (1996). The middle and late pleistocene evolution and the bear island trough mouth fan. *Global Planet. Change* 12, 309–330. doi: 10.1016/0921-8181(95)00026-7

Leavitt, W. D., Halevy, I., Bradley, A. S., and Johnston, D. T. (2013). Influence of sulfate reduction rates on the Phanerozoic sulfur isotope record. *Proc. Natl. Acad. Sci.* 110, 11244–11249. doi: 10.1073/pnas.1218874110

Lecoeuvre, A., Ménez, B., Cannat, M., Chavagnac, V., and Gérard, E. (2021). Microbial ecology of the newly discovered serpentinite-hosted Old City hydrothermal field (southwest Indian ridge). *ISME J.* 15, 818–832. doi: 10.1038/s41396-020-00816-7

Lowell, R. P., Houghton, J. L., Farough, A., Craft, K. L., Larson, B. I., and Meile, C. D. (2015). Mathematical modeling of diffuse flow in seafloor hydrothermal systems: The potential extent of the subsurface biosphere at mid-ocean ridges. *Earth Planetary Sci. Lett.* 425, 145–153. doi: 10.1016/j.epsl.2015.05.047

Marques, A. F., Roerdink, D. L., Baumberger, T., de Ronde, C. E. J., Ditchburn, R. G., Denny, A., et al. (2020). The seven sisters hydrothermal system: first record of shallow hybrid mineralization hosted in mafic volcaniclasts on the arctic mid-ocean ridge. *Minerals* 10, 439. doi: 10.3390/min10050439

Martiny, A. C., Pham, C. T. A., Primeau, F. W., Vrugt, J. A., Moore, J. K., Levin, S. A., et al. (2013). Strong latitudinal patterns in the elemental ratios of marine plankton and organic matter. *Nat. Geosci.* 6, 279–283. doi: 10.1038/ngeo1757

McCollom, T. M., and Shock, E. L. (1997). Geochemical constraints on chemolithoautotrophic metabolism by microorganisms in seafloor hydrothermal systems. *Geochimica cosmochimica Acta* 61, 4375–4391. doi: 10.1016/S0016-7037(97)00241-X

Meier, D. V., Pjevac, P., Bach, W., Hourdez, S., Girguis, P. R., Vidoudez, C., et al. (2017). Niche partitioning of diverse sulfur-oxidizing bacteria at hydrothermal vents. *ISME J.* 11, 1545–1558. doi: 10.1038/ismej.2017.37

Michaud, A. B., Laufer, K., Findlay, A., Pellerin, A., Antler, G., Turchyn, A. V., et al. (2020). Glacial influence on the iron and sulfur cycles in Arctic fjord sediments (Svalbard). *Geochimica Cosmochimica Acta* 280, 423–440. doi: 10.1016/j.gca.2019.12.033

Moeslundi, L., Thamdrup, B., and Jørgensen, B. B. (1994). Sulfur and iron cycling in a coastal sediment: radiotracer studies and seasonal dynamics. *Biogeochemistry* 27, 129–152. doi: 10.1007/BF00002815

Nakamura, K., and Takai, K. (2014). Theoretical constraints of physical and chemical properties of hydrothermal fluids on variations in chemolithotrophic microbial communities in seafloor hydrothermal systems. *Prog. Earth Planetary Sci.* 1, 1–24. doi: 10.1186/2197-4284-1-5

Olsen, B. R., Økland, I. E., Thorseth, I. H., Pedersen, R. B., and Rapp, H. T. (2016). *Environmental challenges related to offshore mining and gas hydrate extraction* (Norway: Norwegian Environment Agency).

Pedersen, R. B., and Bjerkgård, T. (2016). Seafloor massive sulphides in Arctic waters. *Mineral Resour. In Arctic* 1, 209–216.

Pedersen, R. B., Rapp, H. T., Thorseth, I. H., Lilley, M. D., Barriga, F. J. A. S., Baumberger, T., et al. (2010a). Discovery of a black smoker vent field and vent fauna at the Arctic Mid-Ocean Ridge. *Nat. Commun.* 1, 126. doi: 10.1038/ncomms1124

Pedersen, R. B., Thorseth, I. H., Hellevang, B., Schultz, A., Taylor, P., Knudsen, H. P., et al. (2005). Two vent fields discovered at the ultraslow spreading Arctic Ridge System. *Eos Trans. AGU Fall Meet. Suppl.* 86. Abstract OS21C-01.

Pedersen, R. B., Thorseth, I. H., Nygård, T. E., Lilley, M. D., and Kelley, D. S. (2010b). "Hydrothermal activity at the Arctic mid-ocean ridges," in *Diversity of hydrothermal systems on slow spreading ocean ridges*. Eds. P. A. Rona, C. W. Devey, J. Dyment and B. J. Murton (Washington, DC: AGU), 67–89.

Ravenschlag, K., Sahm, K., Knoblauch, C., Jørgensen, B. B., and Amann, R. (2000). Community structure, cellular rRNA content, and activity of sulfate-reducing bacteria in marine arctic sediments. *Appl. Environ. Microbiol.* 66, 3592–3602. doi: 10.1128/AEM.66.8.3592-3602.2000

Redfield, A. C., Ketchum, B. H., and Richards, F. A. (1963). The Influence of Organisms on the Composition of the Sea Water. *The Sea* (New York: Interscience Publishers) 2, 26–77.

Røy, H., Weber, H. S., Tarpgaard, I. H., Ferdelman, T. G., and Jørgensen, B. B. (2014). Determination of dissimilatory sulfate reduction rates in marine sediment via radioactive 35S tracer. *Limnology Oceanography: Methods* 12, 196–211. doi: 10.4319/lom.2014.12.196

Rullkötter, J. (2006). "Organic matter: the driving force for early diagenesis," in *Marine geochemistry*, Eds. H. D. Schulz and M. Zabel (Berlin: Springer),125–168.

Sagemann, J., Jørgensen, B. B., and Greeff, O. (1998). Temperature dependence and rates of sulfate reduction in cold sediments of svalbard, arctic ocean. *Geomicrobiology J.* 15, 85–100. doi: 10.1080/01490459809378067

Scheirer, D. S., Shank, T. M., and Fornari, D. J. (2006). Temperature variations at diffuse and focused flow hydrothermal vent sites along the northern East Pacific Rise. *Geochemistry Geophysics Geosystems* 7. doi: 10.1029/2005GC001094

Seyfried, W. E. (1987). Experimental and theoretical constraints on hydrothermal alteration processes at mid-ocean ridges. *Annu. Rev. Earth Planetary Sci.* 15, 317–335. doi: 10.1146/annurev.ea.15.050187.001533

Sievert, S. M., and Vetriani, C. (2012). Chemoautotrophy at deep-sea vents: past, present, and future. *Oceanography* 25, 218–233. doi: 10.5670/oceanog.2012.21

Snow, J. E., and Edmonds, H. N. (2007). Ultraslow-spreading ridges rapid paradigm changes. *Oceanography* 20, 90–101. doi: 10.5670/oceanog.2007.83

Steen, I. H., Dahle, H., Stokke, R., Roalkvam, I., Daae, F.-L., Rapp, H. T., et al. (2016). Novel barite chimneys at the Loki's castle vent field shed light on key factors shaping microbial communities and functions in hydrothermal systems. *Front. Microbiol.* 6, 1510. doi: 10.3389/fmicb.2015.01510

Stein, R. (1990). Organic carbon content/sedimentation rate relationship and its paleoenvironmental significance for marine sediments. *Geo-Mar. Lett.* 10, 37–44. doi: 10.1007/BF02431020

Stubseid, H. H., Bjerga, A., Haflidason, H., Pedersen, L. E. R., and Pedersen, R. B. (2023). Volcanic evolution of an ultraslow-spreading ridge. *Nat. Commun.* 14, 4134. doi: 10.1038/s41467-023-39925-0

Tao, C., Lin, J., Guo, S., Chen, Y. J., Wu, G., Han, X., et al. (2012). First active hydrothermal vents on an ultraslow-spreading center: Southwest Indian Ridge. *Geology* 40, 47–50. doi: 10.1130/G32389.1

Thamdrup, B., Fossing, H., and Jørgensen, B. B. (1994). Manganese, iron and sulfur cycling in a coastal marine sediment, Aarhus Bay, Denmark. *Geochimica Cosmochimica Acta* 58, 5115–5129. doi: 10.1016/0016-7037(94)90298-4

Tivey, M. K. (2007). Generation of seafloor hydrothermal vent fluids and associated mineral deposits. *Oceanography* 20, 50–65. doi: 10.5670/oceanog.2007.80

Toth, D. J., and Lerman, A. (1977). Organic matter reactivity and sedimentation rates in the ocean. *Am. J. Sci.* 277, 465. doi: 10.2475/ajs.277.4.465

Vulcano, F., Hahn, C. J., Roerdink, D., Dahle, H., Reeves, E. P., Wegener, G., et al. (2022). Phylogenetic and functional diverse ANME-1 thrive in Arctic hydrothermal vents. *FEMS Microbiol. Ecol.* 98. doi: 10.1093/femsec/fiac117

Wankel, S. D., Adams, M. M., Johnston, D. T., Hansel, C. M., Joye, S. B., and Girguis, P. R. (2012). Anaerobic methane oxidation in metalliferous hydrothermal sediments: influence on carbon flux and decoupling from sulfate reduction. *Environ. Microbiol.* 14, 2726–2740. doi: 10.1111/j.1462-2920.2012.02825.x

Westrich, J. T., and Berner, R. A. (1984). The role of sedimentary organic matter in bacterial sulfate reduction: The G model tested. *Limnol. Oceanogr.* 29, 236–249. doi: 10.4319/lo.1984.29.2.0236

Wurgaft, E., Findlay, A. J., Vigderovich, H., Herut, B., and Sivan, O. (2019). Sulfate reduction rates in the sediments of the Mediterranean continental shelf inferred from combined dissolved inorganic carbon and total alkalinity profiles. *Mar. Chem.* 211, 64–74. doi: 10.1016/j.marchem.2019.03.004

Zhao, R., Mogollón, J. M., Abby, S. S., Schleper, C., Biddle, J. F., Roerdink, D. L., et al. (2020). Geochemical transition zone powering microbial growth in subsurface sediments. *Proc. Natl. Acad. Sci.* 117, 32617–32626. doi: 10.1073/pnas.2005917117

Zhao, R., Mogollón, J. M., Roerdink, D. L., Thorseth, I. H., Økland, I., and Jørgensen, S. L. (2021). Ammonia-oxidizing archaea have similar power requirements in diverse marine oxic sediments. *ISME J.* 15, 3657–3667. doi: 10.1038/s41396-021-01041-6

frontiers | Frontiers in Marine Science

TYPE Original Research
PUBLISHED 12 January 2024
DOI 10.3389/fmars.2023.1269411

Check for updates

OPEN ACCESS

EDITED BY
Andrew R Thurber,
Oregon State University, United States

REVIEWED BY
Guoyong Yan,
Hong Kong University of Science and Technology, China
Taewoo Ryu,
Okinawa Institute of Science and Technology Graduate University, Japan

*CORRESPONDENCE
Yuefeng Cai
yuefengcai@jou.edu.cn
Xin Shen
shenthin@163.com

†These authors have contributed equally to this work and share first authorship

RECEIVED 30 July 2023
ACCEPTED 28 December 2023
PUBLISHED 12 January 2024

CITATION
Mao N, Shao W, Cai Y, Kong X, Ji N and Shen X (2024) Comparative omics analysis of a deep-sea barnacle species (Cirripedia, Scalpellomorpha) and shallow-water barnacle species provides insights into deep-sea adaptation.
Front. Mar. Sci. 10:1269411.
doi: 10.3389/fmars.2023.1269411

COPYRIGHT
© 2024 Mao, Shao, Cai, Kong, Ji and Shen. This is an open-access article distributed under the terms of the Creative Commons Attribution License (CC BY). The use, distribution or reproduction in other forums is permitted, provided the original author(s) and the copyright owner(s) are credited and that the original publication in this journal is cited, in accordance with accepted academic practice. No use, distribution or reproduction is permitted which does not comply with these terms.

Comparative omics analysis of a deep-sea barnacle species (Cirripedia, Scalpellomorpha) and shallow-water barnacle species provides insights into deep-sea adaptation

Ning Mao[1,2†], Wentai Shao[1,2†], Yuefeng Cai[1,2*], Xue Kong[1,2], Nanjing Ji[1,2] and Xin Shen[1,2*]

[1]Jiangsu Key Laboratory of Marine Bioresources and Environment, Jiangsu Key Laboratory of Marine Biotechnology, Jiangsu Ocean University, Lianyungang, China, [2]Co-Innovation Center of Jiangsu Marine Bio-Industry Technology, Jiangsu Ocean University, Lianyungang, China

Barnacles have demonstrated adaptability to a range of habitats, spanning from shallow water to the deep sea. Given the harsh conditions present in hydrothermal vents, hydrothermal vent barnacles serve as the model organism for investigating the interplay between evolution and adaptability. In order to gain insights into barnacle adaptive characteristics, particularly within hydrothermal vents, we conducted a comprehensive analysis of the mitogenomes and transcriptome in a deep-sea barnacle (*Neolepas marisindica*), in comparison to its shallow-water related species. The mitogenomes with the same genetic skews and the non-synonymous/synonymous mutation ratios (K_a/K_s) of the mitogenomes indicate that the protein-coding genes (*COIII*, *ND2*, and *ND6*) of *N. marisindica* are under positive selection. Meanwhile, the functional annotation shows that distinctly positive selected orthologs in *N. marisindica* are predominately related to neural signal transduction, immunity, antiapoptotic, and energy metabolism. These results indicate that the mitogenomes and key genes found in transcriptomic analysis are under high-temperature and high-pressure conditions, and which may contribute *N. marisindica* to have evolved to adapt to the extreme hydrothermal vent environments. The findings shed light on the mitogenome and transcriptome of *N. marisindica*, which lays a foundation for the in-depth understanding of the adaptation mechanism of sessile invertebrates to the deep-sea environment.

KEYWORDS

barnacle, *Neolepas marisindica*, deep-sea adaptation, mitogenome, transcriptome

1 Introduction

The general characteristics of the deep-sea environment are high pressure, darkness, and a lack of oxygen. Moreover, the temperature is low and the food source is limited (Danovaro et al., 2014; Lyu et al., 2023). Despite the harsh deep-sea ecosystem, there are still many crustaceans living here, including *Glyptelasma gigas* (Annandale) (Gan et al., 2020b), *Alvinocaris longirostris* (Kikuchi & Ohta) (Hui et al., 2018a; Xin et al., 2021), and *Hirondellea gigas* (Birstein & Vinagradov) (Lan et al., 2017). Additionally, the hereditary characteristics and adaptive evolution of marine organisms may be influenced by these adverse factors. Consequently, a number of reserachers have explored the adaptive evolutionary traits of marine organisms within a specific ecological setting, elucidating the mechanisms by which these organisms adapt to their environment. For instance, the population genetic structure of *Capitulum mitella* (Linnaeus) was explored through single DNA fragments, such as mitochondrial DNA control regions, and a large amount of gene flow was found, indicating that populations living in different regions have significant genetic differentiation due to the differences in their genetic adaptability (Song and Yoon, 2013; Yoon et al., 2013).

In addition, the deep-sea hydrothermal region is the most anoxic and highly toxic marine ecosystem on earth, which plays an important role in mitochondrial division and biological function (Ki et al., 2009). Previous phylogenetic analysis based on fossil and mitochondrial genomes has shown that bathymodiolins (*Bathymodiolus*) gradually evolved characteristics that were adapted to their environment in the process of their origin and evolution (Lorion et al., 2013; Thubaut et al., 2013). However, how bathymodiolin mussels have adapted to deep-sea chemosynthetic environments over the long term, and the genetic bases for these adaptations are still unclear (Zheng et al., 2017). Moreover, there is a lack of molecular data, such as single genes or single proteins, that can be used to deduce the adaptive mechanisms of deep-sea marine organisms. Therefore, it is imperative to conduct an analysis of the crucial mitochondrial functional genes within the immunity metabolic pathway, as this would elucidate the underlying mechanism behind their adaptability to the hydrothermal vent environment.

It is universally acknowledged that the transcriptome can be used to determine the expression of genes at the level of messenger RNA (mRNA) and non-coding RNA transcription and explore the functional genes that are related to environmental adaptation or physiological functions (Wilhelm and Landry, 2009). Consequently, a transcriptomic analysis may also illustrate the adaptive mechanisms of deep-sea organisms in diverse environments. Transcriptome sequencing technology can be used to understand the response of various species to marine ecosystems at the mRNA level, and it has been widely used in researching deep-sea environmental adaptation mechanisms (Zhou et al., 2021; Sun et al., 2022; Yan et al., 2022). For instance, a transcriptomic analysis was conducted on *A. longirostris* from the Iheya North hydrothermal vents and a methane seep in the South China Sea, which found that various genes including *cytochrome P450s* and *Rhodopsin* were related to sulfur metabolism and detoxification, showing their different adaptability between the two extreme conditions (Hui et al., 2018a). Recently, researchers have made significant findings by conducting comparative genomic analysis on deep-sea anemone species. This investigation has led to the identification of multiple genes that exert influence on osmotic metabolism, membrane function, protein translation, and cytoskeleton functions, and which were adapted to the deep-sea environment (Feng et al., 2021). Furthermore, the deep-sea mussel *Gigantidas platifrons* (Hashimoto & Okutani) lived in vent and seep habitats with abundant toxic chemical substances, particularly hydrogen sulfide (H_2S). To adapt to the harsh H_2S-rich environments, its genes control oxidative phosphorylation and the mitochondrial sulfide oxidization pathway, playing important roles in the sulfide tolerance of the mussel (Sun et al., 2022).

Barnacles exhibit a wide widely distribution within the intertidal zone and attaching to marine organisms. Furthermore, certain barnacle have undergone evolutionary adaptations in diverse deep-sea habitats (Sha and Ren, 2015; Chan et al., 2021). Due to their extended attachment to the bottom and confinement to relatively narrow deep zones, deep-sea barnacle adults served as suitable model organisms for conducting research on evolutionary and ecological processes (Gan et al., 2020a). Notably, members of the Scalpellomorpha order have been discovered in hydrothermal vents and cold seeps, suggesting the presence of distinctive adaptive mechanisms enabling their survival in deep-sea chemosynthetic habitats (Gan et al., 2022). However, the difficulty associated with the collection of deep-sea Cirripedia have limited the current research on the barnacle transcriptome to mere transcriptome assembly and the mechanism of barnacle attachment (Al-Aqeel et al., 2016; Ryu et al., 2019; Yan et al., 2020). While studies on other organisms inhabiting extreme deep-sea environments have identified several potential mechanisms, the transcriptome of them remains unexplored. Moreover, few studies have investigated the molecular adaptive characteristics that assist with barnacles' survival in deep-sea harsh chemosynthetic habitats. Due to the limited prior investigations concerning the transcriptome of barnacles, particularly with regard to the deepsea adaptation, our study attempted to address this research gap.

In this study, we collected the deep-sea and shallow-water barnacle individuals at Longqi hydrothermal field on the Southwest Indian Ridge and Guangxi Beibu Gulf, respectively. In order to investigate the adaptability of barnacles to the deep-sea environment, the analysis of positive selection pressure was conducted using the comparative transcriptome of these two individuals, as well as the 13 protein coding genes (PCGs) of mitogenomes from 11 barnacles. This research endeavor aimed to not only provide valuable genomic resources for deep-sea barnacles but also establish a foundation for comprehending their genetic strategies and adaptation mechanisms in the deep-sea habitat.

2 Materials and methods

2.1 Sample collection, DNA and RNA extraction, and sequencing

Samples of the deep-sea barnacles from a hydrothermal vent Longqi hydrothermal field on the Southwest Indian Ridge (49°64'E, 37°17'S) at a depth of 2,759 m in the Southwest Indian Ocean collected on board of "Explorer 1" scientific research ship of

Institute of Deep-sea Science and Engineering (Chinese Academy of Sciences) by using "Deep-sea Warrior" manned submersible during the winter of 2018, we thank the crew for their help during the cruise. Samples of the shallow-water barnacles were obtained from the Guangxi Beibu Gulf (109° 12 ' E, 21° 04 ' N), depth of about 300 m. In contrast to deep-sea species, the depth of 300m can be considered relatively shallow. Therefore, we provisionally identified the two barnacle species as the deep water species *Vulcanolepas fijiensis* (Lee et al., 2019) and the shallow water *Scalpellum stearnsi* (Chan et al., 2010). As a result of the Chen et al. Commentary Paper (Chan et al., 2024) we became aware that our initial identification of *V. fijiensis* was incorrect. We have confirmed that the barnacle is actually *Neolepas marisindica* and have revised this paper to include the correct species indentation. After collection, they were immediately stored at -80°C.

According to the manufacturer's directions, the TIANamp Marine Animal DNA Kit (TIANGEN Biotech, China) was used to extract DNA from the abdominal muscle. Then, 1% gel electrophoresis and ultraviolet spectroscopy (Eppendorf BioPhotometer D30, Eppendorf, Germany) were used to estimate and quantify the genomic DNA. Then, the DNA was randomly cut into 350 bp fragments, which were repaired at the end and amplified by a polymerase chain reaction to construct the sequencing library. Next, Sanger dideoxy sequencing (*N. marisindica*) was conducted on an ABI-3730XL (Thermo Fisher Scientific, USA), and high-throughput sequencing (*S. stearnsi*) was conducted on Illumina NovaSeq 6000 platform (TSINGKE Biotechnology Co, Ltd, China).

For each species of barnacle (*N. marisindica* and *S. stearnsi*), a random selection of three individuals was made, and all RNA was extracted using TRIzol reagent (Invitrogen, USA). The quality of the RNA was assessed through 1% agarose gel electrophoresis. The purity and concentration of the RNA were determined using a NanoPhotometer spectrophotometer (IMPLEN, Germany) and Qubit 2.0 Fluorimeter (Life Technologies, USA), respectively. The integrity of the RNA was evaluated using the RNA Nano 6000 Assay Kit of the Agilent Bioanalyzer 2100 system (Agilent Technologies, USA). The sequencing library was established according to the manufacturer's instructions of the NEBNext Ultra RNA Library Prep Kit (NEB, USA). The mRNA was enriched using poly-T oligo-attached magnetic beads, and an Agilent Bioanalyzer 2100 system (Agilent Technologies) was used to evaluate the synthesis of the complementary DNA (cDNA), the construction of a pair-end library, and the quality of the library. Finally, the two different kinds of species' cDNA libraries were clustered and sequenced using the Illumina HiSeq 2500 platform by NovoGene (Beijing, China).

2.2 Mitogenome assembly, annotation, and analysis

The initial dataset of the mitochondrial genome consisted of 150 base pairs at the paired ends. Reads containing an adapter, reads with a mass score below 20 ($Q< 20$), and duplicated sequences were removed. A reference genome (*Lepas anserifera*) was used to retrieve the reads belonging to the mitochondrial genome for assembly. Then, *de novo* assembly was performed using SPAdes 3.13.0 (Bankevich et al., 2012), and the assembly results were corrected for mutual alignment to confirm the accuracy of the assembled genome sequence. The assembled mitochondrial genomes were subjected to analysis using the online MITOS software (http://mitos.bioinf.unileipzig.de) with default parameters. This software was utilized to predict the PCGs, transfer RNA (tRNA) genes, and ribosomal RNA (*rRNA*) genes. Manual corrections to the genes for the start/stop codons were performed in Sequin 15.10 (http://www.ncbi.nlm.nih.gov/Sequin/index.html) by referencing the mitochondrial genome. On this basis, BLAST (https://blast.ncbi.nlm.nih.gov/Blast.cgi) technology was used to compare the existing research data including the PCGs and *rRNA* to verify and correct the accuracy of the analysis results. The circular mitochondrial genome map was drawn using OGDRAW 1.3.1 (Greiner et al., 2019), and the complete mitogenomes of *N. marisindica* and *S. stearnsi* have been registered as MZ772032 and OP345466 on GenBank.

The biases for the codon usage of the mitogenome can regulate genes and reflect the evolutionary relationship between different species (Wei et al., 2014). Consequently, the usage of codons was analyzed for the PCGs and *rRNA*. Using the following formula, the inclination related to the nucleotide bases was calculated:

$$\text{adenine (A) and thymine (T) skew} = (A - T) \div (A + T)$$

$$\text{guanine (G) and cytosine (C) skew} = (G - C) \div (G + C).$$

2.3 Transcriptome assembly and annotation

The low-quality reads and reads containing adaptors were removed from the raw reads using the internal software (ng_qc) with custom script of NovoGene, and the transcriptome clean reads were obtained. The *de novo* transcriptome assembly was performed using Trinity v2.5.1, with the minimum k-mer parameter coverage of 2, while default parameters were employed for other sections (Grabherr et al., 2011). The longest transcript of each transcription group was regarded as a unigene for the subsequent analysis. Next, BUSCO v1.22 was used to verify the quality of the assembly that was performed using the arthropoda_odb9 database (Simão et al., 2015). Additionally, all the unigenes were annotated by blasting the common databases, such as the National Center for Biotechnology Information non-redundant protein (Nr), Swiss-Prot, and euKaryotic Ortholog Group using DIAMOND v0.8.22 (Buchfink et al., 2015), and the NCBI nucleotide database using BLAST v2.2.28+ (Altschul et al., 1990). The Kyoto Encyclopedia of Genes and Genomes (KEGG) classification was performed using the KEGG Automatic Annotation Server (Moriya et al., 2007). The protein family (Pfam) alignments were put into practice using HMMER v3.0 (http://hmmer.org/) and were based on the results of Nr and Pfam, and Blast2GO v2.5 was used to classify the Gene Ontology (GO) (Götz et al., 2008). The Nr database was searched for unigenes with

BLASTx, and then SOLAR was used to compare the link fragments (Rota-Stabelli et al., 2010), so all the open reading frames (ORF) of the unigenes were obtained and converted into amino acid sequences.

2.4 Identification of the positively selected genes

The target sequences for this analysis consisted of the 13 PCGs from *N. marisindica* and 10 other barnacle species, aligning using clustalW (codons) in MEGA v7.0. Manual removal of gap and stop codons was performed to ensure accurate alignment (Kumar et al., 2016). The resulting sequence alignment file was then utilized for the analysis of positive selection. A molecular phylogenetic tree was constructed using the maximum likelihood method in MEGA v7.0 to assess selective pressure. Subsequently, the reconstructed tree was subjected to EasyCodeML in the PAML software (Gao et al., 2019) to identify natural selection characteristics within the 13 PCGs. Among them, the 13 PCGs from *N. marisindica* were treated as the foreground branch, while PCGs from other barnacle species served as the background branch. Site models were employed to identify the individual sites of PCGs. Changes in the different sites of the 13 PCGs were explored by calculating the ω values ($\omega = K_a/K_s$ or dN/dS). For the positive selection sites ($\omega > 1$), the Bayes Empirical Bayes (BEB) method was used to estimate the Bayesian posterior probabilities (Biswas and Akey, 2006). The likelihood Ratio Test (LRT) was applied to compare the hypothetical models with the corresponding original hypotheses, and the LRT *P*-value was determined using the Chi-square method. The sites of the PCGs with an LRT *P*-value< 0.05 or BEB > 95% were considered to be under evolution and positive selection pressure. The ProtParam program (http://www.expasy.ch/tools/protparam.html) software was utilized to compute the relative molecular weight and isoelectric points of the sequence, and SignalIP 4.1 (http://www.cbs.dtu.dk/services/SignalP/) was employed to predict the signal peptides. Additionally, the SMART program (http://smart.embl-heidelberg.de/) was utilized to predict the conserved functional domains of proteins (Letunic and Bork, 2021). On this basis, we matched the sites to the three-dimensional (3D) conformation of the PCGs to observe their role under positive selection more clearly. The 3D structure of the target proteins was simulated using the SWISS-MODEL (Waterhouse et al., 2018) server, which visualized the positive selection sites in the proteins.

Transcriptome sequence set from the two species (*N. marisindica* and *S. stearnsi*), internal reference (*Amphibalanus Amphitrite*) and external reference species (*Eurytemora affinis*) were utilized for the analysis of the orthologous genes and nonsynonymous (dN)/synonymous (dS) substitution rates. Subsequently, adaptive evolution was assessed by comparing the ω value (dN/dS). BLAST was employed to pair the orthologs with the best hit probabilities. Following this, sequence alignment was conducted using MUSCLE, and all gaps were eliminated. The ω numerical calculation for each ortholog was performed using PAML v4.48a. Genes with ω values exceeding 1 were considered as positively selected genes (PSGs). The PSGs were further subjected to GO and KEGG enrichment analysis using Omicshare CloudTools (http://www.omicshare.com/tools/), with a significance threshold set at a *q*-value less than 0.05.

3 Results

3.1 Mitogenome organization and composition

The complete mitogenomes of *N. marisindica* and *S. stearnsi* are 16,960 bp and 15,462 bp in length, respectively. They each contain the general 13 PCGs (*COI*, *COII*, *COIII*, *ATP8*, *ATP6*, *ND1*, *ND2*, *ND3*, *ND4*, *ND4L*, *ND5*, *ND6* and *COB*), 2 *rRNA* genes (16S and 12S *rRNA*), 22 tRNA genes, and a *D*-loop. With the exception of the nicotinamide adenine dinucleotide hydride (NADH) genes (*ND5*, *ND4*, *ND4L*, *ND1*) and eight tRNA genes (*trnF*, *trnQ*, *trnH*, *trnP*,

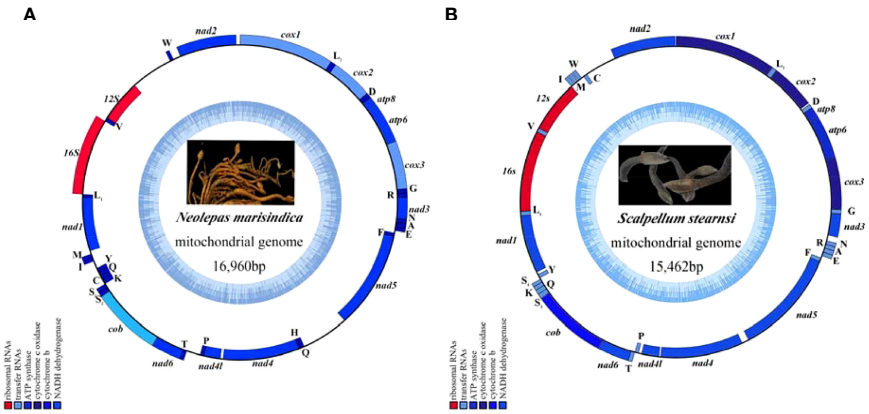

FIGURE 1
The mitochondrial genome map of deep-sea barnacle Neolepas marisindica **(A)** and shallow barnacle Scalpellum stearnsi **(B)** collected for this study, and photographs in the genome map are from preserved samples that were collected for this study, which were collected by Professor Haibin Zhang and kept in Institute of Deep-sea Science and Engineering (Chinese Academy of Sciences). The heavy strand is represented by the outer circle, while the light strand is represented by the inner circle; The tRNA and PCGs are denoted by the blue genes, whereas the 12S *rRNA* and 16S *rRNA* are indicated by the red genes.

10.3389/fmars.2023.1269411

TABLE 1 Summary of the mitogenome features of *Neolepas marisindica* and *Scalpellum stearnsi*.

Gene	Strand	Size (bp)	Codon		GC percent (%)	Anti-codon	Intergenic nucleotide (bp)
			Inferred start codon	Inferred stop codon			
COI	H	1 549/1 536	ATA/ACG	T-/TAA	34.3-36.1		0/4
trnL$_2$	H	88/66				TAA	0
COII	H	684	ATG	TAA	28.0-33.9		0/20
trnD	H	88/63				GTC	0
ATP8	H	159	ATC/ATA	TAA	23.2-26.5		-7
ATP6	H	666	ATG	TAA	26.9-31.4		-1
COIII	H	789/788	ATG	TAA/TA-	33.9-37.7		0/-1
trnG	H	72/64				TCC	0
trnR	H	69/62				TCG	0
ND3	H	348/354	ATT/ATA	TAA	25.3-33.6		0/84
trnN	H	74/62				GTT	0
trnA	H	76/68				TGC	0
trnE	H	68/64				TTC	37/33
trnF	L	63/64				GAA	0
ND5	L	1 695/1 701	ATT	TAA	28.7-29.6		817/0
trnQ	L	65/68				TTG	0
trnH	L	64				GTG	0
ND4	L	1 329/1 330	ATT/ATG	TAA/T-	28.8-29.6		41/23
ND4L	L	285/282	ATG/ATA	TAA	27.7-29.5		0/47
trnP	L	73/61				TGG	233/0
trnT	H	67/62				TGT	0
ND6	H	492/483	ATT	TAA	23.6-26.2		2/-1
COB	H	1 143/1 140	ATG	TAA	32.2-35.8		0/2
trnS$_2$	H	70				TGA	0
trnS$_1$	H	75/54				TCT	0/19
trnK	L/H	84/61				TTT	0
trnC	L	78/63				GCA	0
trnY	L	66/65				GTA	122/40
trnI	H	68/64				GAT	0/6
trnM	H	66/64				CAT	54/10
ND1	L	924/930	ATA/ATT	TAA	28.6-31.9		0
trnL$_1$	L	58/68				TAG	0
lrRNA	L	1 324/1 301			24.5-27.2		0
trnV	L	67/66				TAC	0
srRNA	L	731/839			26.3-31.6		0
trnW	H	65				TCA	126/36
ND2	H	987/984	ATA/ATT	TAA	25.0-29.8		61/9
D-loop	H	736/507					0

trnC, *trnY*, *trnL*, *trnV*), the majority of genes are encoded by the heavy strand (H-strand). Furthermore, apart from a few gene overlaps, the majority of nucleotide gaps are observed between the tRNA. In addition, 16S and 12S are located between $trnL_1$ (TAG), *trnV* (TAC) and *trnW* (TCA) respectively (Figure 1; Table 1).

3.2 Nucleotide composition and bias

The nucleotide compositions (PCGs and *rRNA*) of *N. marisindica* and *S. stearnsi* are 20.9~39.8% A, 5.3~24.1% C, 32.9~48.3% T, and 3.1~24.2% G, with an AT content ranging from 62.4% to 76.8% (Supplementary Tables 1, 2). Their majority of the PCGs have a negative AT skew, except for *ND1*, *ND4*, *ND4L*, and *ND5*, which display a positive GC skew (Figure 2).

3.3 Protein-coding genes and codon usage

Except for *COI*, which is encoded by the ACG codon, the start codons of the PCGs predominantly follow canonical sequences (ATT/ATA/ATG). Additionally, within barnacle mitogenomes, three distinct types of stop codons are identified (T-, TA-, and TAA), with TAA being the most prevalent. Moreover, the T- and TA- stop codons only occur in *COI*, *COIII*, and *ND4* of *N. marisindica* and *S. stearnsi* (Table 1).

The findings show that except for leucine and serine have six to eight codons, the other amino acids of the two examined species have two to four changeable codons (Figure 3). The codon usage analysis demonstrates that the following codon sequences appear with higher frequency: phenylalanine (UUU), isoleucine (AUU), and leucine (UUA). The codons with U or C in the third position occur more frequently than those with A or G. Different from the shallow-sea barnacle, the main amino acids in *N. marisindica* are asparagine and lysine (Figure 3).

3.4 Transcriptome assembly and annotation

A total of 47,593,764 and 47,752,536 raw reads are generated from *S. stearnsi* and *N. marisindica*, respectively. BUSCO assessment of assembly quality are showed in Supplementary Figures 1, 2. The complete single-copy and complete duplicated of the two organisms are over 80%. Through the transcriptome assemblies, there are 98,686 unigenes identified with an N50 length of 916 bp for *S. stearnsi*, and 53,562 unigenes with an N50 length of 1,721 bp for *N. marisindica*.

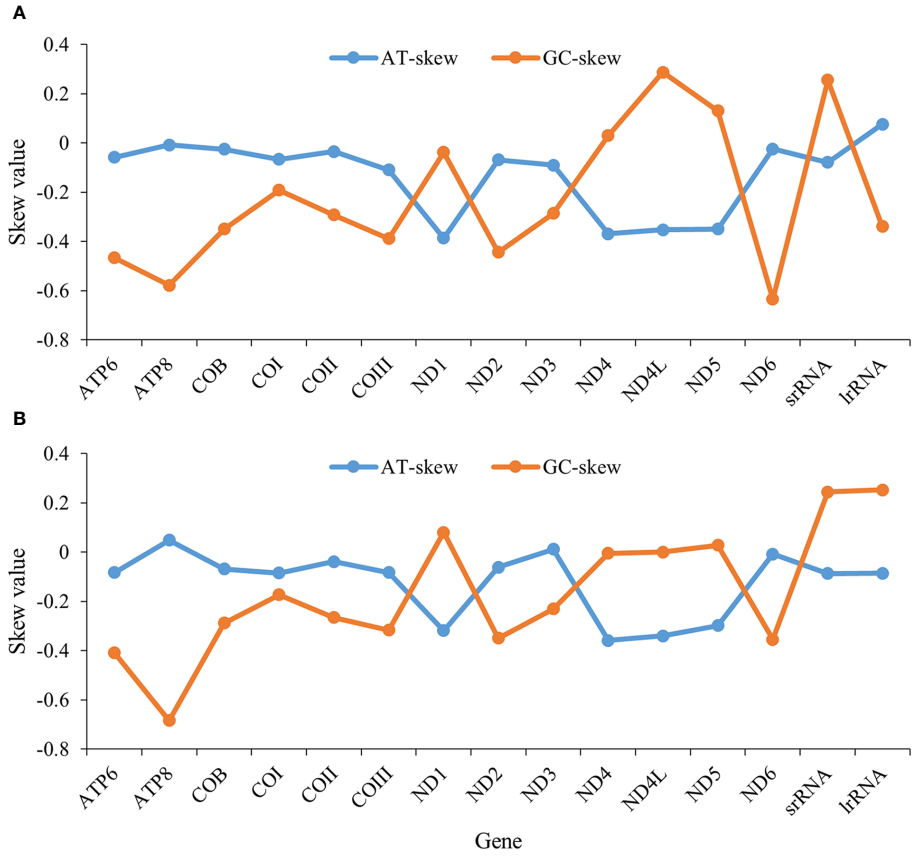

FIGURE 2
AT and GC skews in protein-coding genes of the mitochondrial genomes in deep-sea barnacle *Neolepas marisindica* **(A)** and shallow barnacle Scalpellum stearnsi **(B)**. The horizontal and vertical coordinates represent gene name and skew value, respectively; The blue line represents the AT skew and the orange line represents the GC skew.

10.3389/fmars.2023.1269411

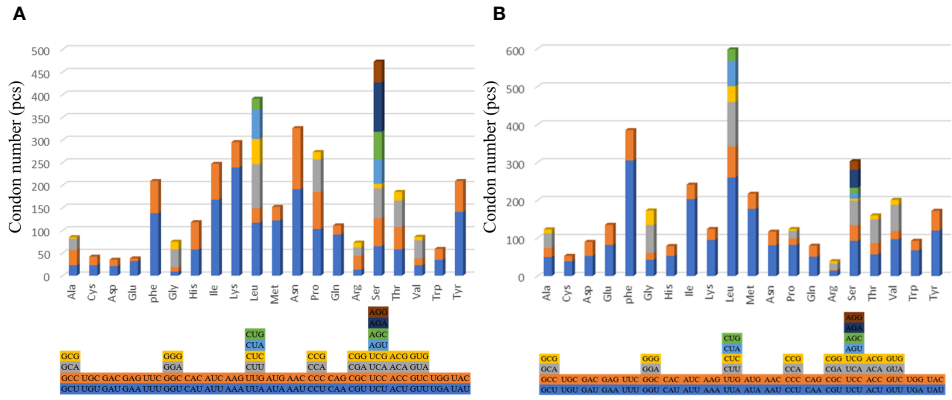

FIGURE 3
The codon usage of the protein-coding genes of the mitochondrial genomes of deep- sea barnacle *Neolepas marisindica* **(A)** and shallow barnacle *Scalpellum stearnsi* **(B)**. The different colors represent different kinds of codons, and the different columns represent different amino acids.

Among these unigenes, 38,666 (39.18%) and 20,628 (38.51%) are successfully annotated in *S. stearnsi* and *N. marisindica*, respectively (Table 2).

The Gene Ontology functional cluster analysis indicates that 26,718 and 16,746 unigenes are successfully clustered in the three functional categories of GO (48 functional items). The major biological processes are the cellular, metabolic, and single-organism processes, with *N. marisindica* lacking the biological phase item and *S. stearnsi* lacking the rhythmic process item.

TABLE 2 Transcriptome library basic information of *Scalpellum stearnsi* and *Neolepas marisindica*.

Class	Item	*Neolepas marisindica*	*Scalpellum stearnsi*
Assembly	Transcript number (bar)	54,446	99,622
	Unigene number (bar)	53,562	98,686
	Total length of Unigenes (bp)	49,774,143	61,491,550
	N50 length of Unigenes (bp)	1,721	916
	Mean length of Unigenes (bp)	929	623
Annotation	Nr	13,679 (25.53%)	26,304 (26.65%)
	Nt	5,150 (9.61%)	8,036 (8.14%)
	Swiss-Prot	12,019 (22.43%)	19,772 (20.03%)
	KEGG Orthology	6,845 (12.77%)	12,042 (12.2%)
	PFAM	16,685 (31.15%)	26,406 (26.75%)
	GO	16,746 (31.26%)	26,718 (27.07%)
	KOG	7,129 (13.3%)	10,959 (11.1%)
	All Databases	2,422 (4.52%)	2,786 (2.82%)
	At least one database	20,628 (38.51%)	38,666 (39.18%)

Within the cellular components, the cell and cell part items are identified. The major molecular functions are binding and catalytic activity (Figure 4). In addition, The KEGG functional cluster analysis shows that 6,845 and 12,042 unigenes in *N. marisindica* and *S. stearnsi* are clustered into five functional groups, respectively, and more genes are annotated in the endocrine system, translation, and signal transduction pathways (Figure 5).

3.5 Positively selected genes analysis

From the complete mitochondrial genome of the 11 barnacle species, namely *N. marisindica*, *Conchoderma hunteri* (Owen), *Lepas anserifera* Linnaeus, *L. australis* Darwin, *L. anatifera* Linnaeus (Lepadidae), *S. stearnsi*, *Arcoscalpellum epeeum* Chan (Scalpellidae), *Altiverruca navicula* Hoek (Verrucidae), *Capitulum mitella* Linnaeus (Pollicipedidae), *Glyptelasma annandalei* Pilsbry (Poecilasmatidae), and *Ibla cumingi* Darwin (Iblidae) (Table 3), 13 PCGs were extracted for positive selection pressure analysis. The positive selection analysis yielded results indicating that the *COIII* and *ND2* genes ($\omega > 1.0$, $P<0.05$) of deep-sea species experience positive selection pressure. The three-dimensional structure model was utilized to identify and highlight specific sites within the genes that are under positive selection pressure, such as 22I, 29T, and 41E in the *COIII* gene, as well as 73F, 75S, and 76L in the *ND2* gene (Table 4; Figure 6).

Genes that are subjected to positive selection tend to respond to natural selection. We identified 148 pairwise orthologs within *N. marisindica*, *S. stearnsi* and two reference species in one-to-one correspondence to confirm the PSGs (Supplementary Table 3, Supplementary Figure 3) and performed an adaptive evolutionary analysis on them. The findings reveal the presence of five orthologs, namely chromosome 3 open reading frame 10 (*C3ORF10*), E74-like factor (*ELF*), ubiquitin-like protein ATG12 (*ATG12*), uracil phosphoribosyltransferase (*UPRT*), and small subunit ribosomal protein S21e (*RPS21*), all exhibiting ω values greater than 1.0. Notably, only *RPS21* did not fall below the significance threshold of 0.05 (Table 5; Supplementary Figure 3). These PSGs are mainly enriched in the RIG-I-like receptor signaling, regulation of autophagy, apoptosis-fly, regulation of the actin cytoskeleton,

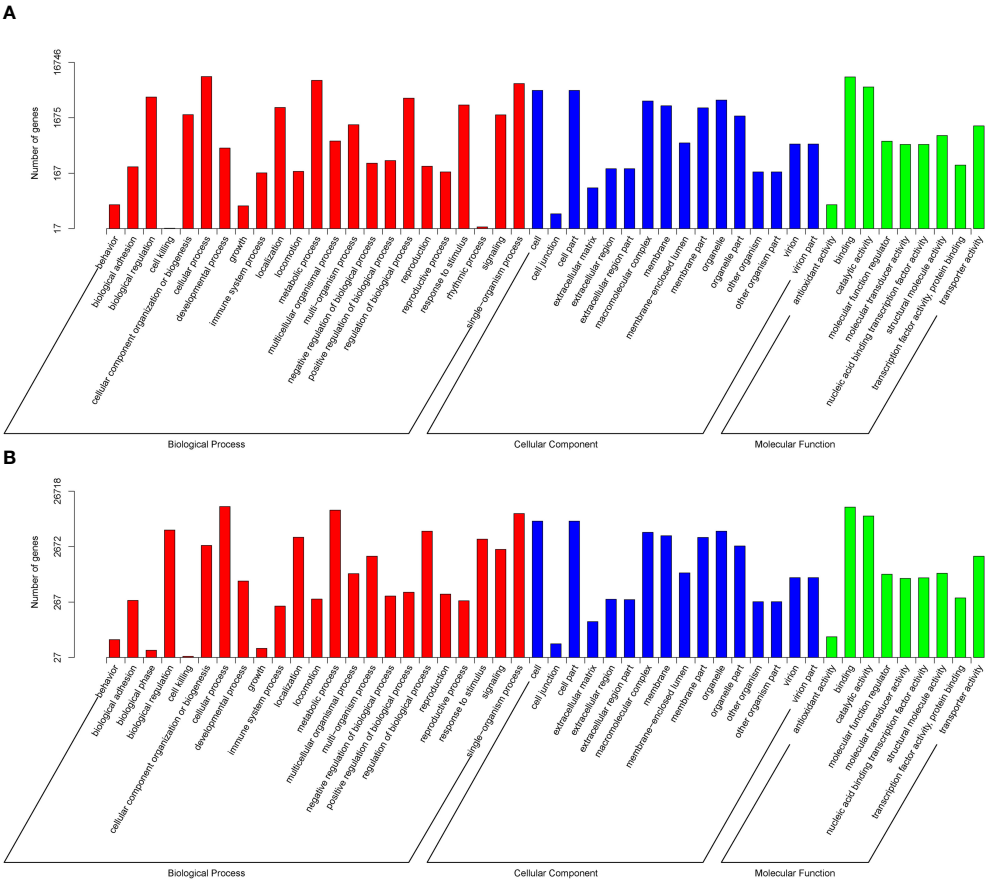

FIGURE 4
Gene Ontology function annotation of the transcriptomes of deep-sea barnacle *Neolepas marisindica* **(A)** and shallow barnacle *Scalpellum stearnsi* **(B)**. The red terms represent Biological Process, the blue terms represent Cellular Composition, and the green terms represent Molecular Function.

pyrimidine metabolism, foxO signaling, and ribosome pathways (Figure 7; Table 5). It is predicted that the ORFs of the five genes under positive selection pressure are all complete. Except for *C3ORF10*, the amino acid domain positions of the other genes are predicted, there is no signal peptide, and the molecular weight range from 9.21 to 27.23 kDa. Additionally, the isoelectric point is relatively similar, ranging from 6.05 to 9.88 (Supplementary Table 4).

4 Discussion

4.1 Mitogenome adaptive evolution

Previous research has identified that certain barnacles exhibit similar arrangement structures within their mitogenomes (Shen et al., 2015). We also find similar genetic structures in the mitogenomes of the deep-sea and shallow barnacles. The AT content in the complete mitogenomes of both organisms, exceeded the GC content, aligning with the base composition observed in the majority of invertebrates (Liu et al., 2018; Wang et al., 2021; Sato et al., 2023). More negative AT skews are observed in *ND1*, *ND4*, *ND4L*, and *ND5* genes of the two barnacles (Figure 2). This phenomenon might be attributed to the deep-sea habitat of these organisms, where DNA replication and transcription processes are subject to the mutations and the natural selection resulting in a bias towards specific nucleotides (Sahyoun et al., 2014; Yu et al., 2019). It is speculated that the different genetic structures of these four genes might be closely related to the pressure of natural selection in the extreme habitats. However, how nucleotide bias affects the initiation and orientation of gene replication and what selective pressures induced nucleotide skews need further study. Furthermore, the amino acid usage patterns observed in *N. marisindica* are similar to those of the shallow barnacle *S. stearnsi* (Figure 3), which provides more evidence for the barnacle nucleotide composition and gene skew results. Generally, more than 95% of energy comes from the oxidative phosphorylation of mitochondria (Auger et al., 2021). In the abyssal zone, the dark and absence of autotrophic primary producers pose constraints on the availability of sustenance (Gattuso et al., 2006). The observed nucleotide compositional biases between *N. marisindica* and *S. stearnsi* indicated that, in their mitogenomes, comparable alterations occurred during the evolutionary progression which might be a means of adapting to the extreme conditions and nutritional scarcity of the deep-sea environment.

Mitochondria serve as a vital pathway for aerobic respiration within cells. To cope with the extreme environment, selection

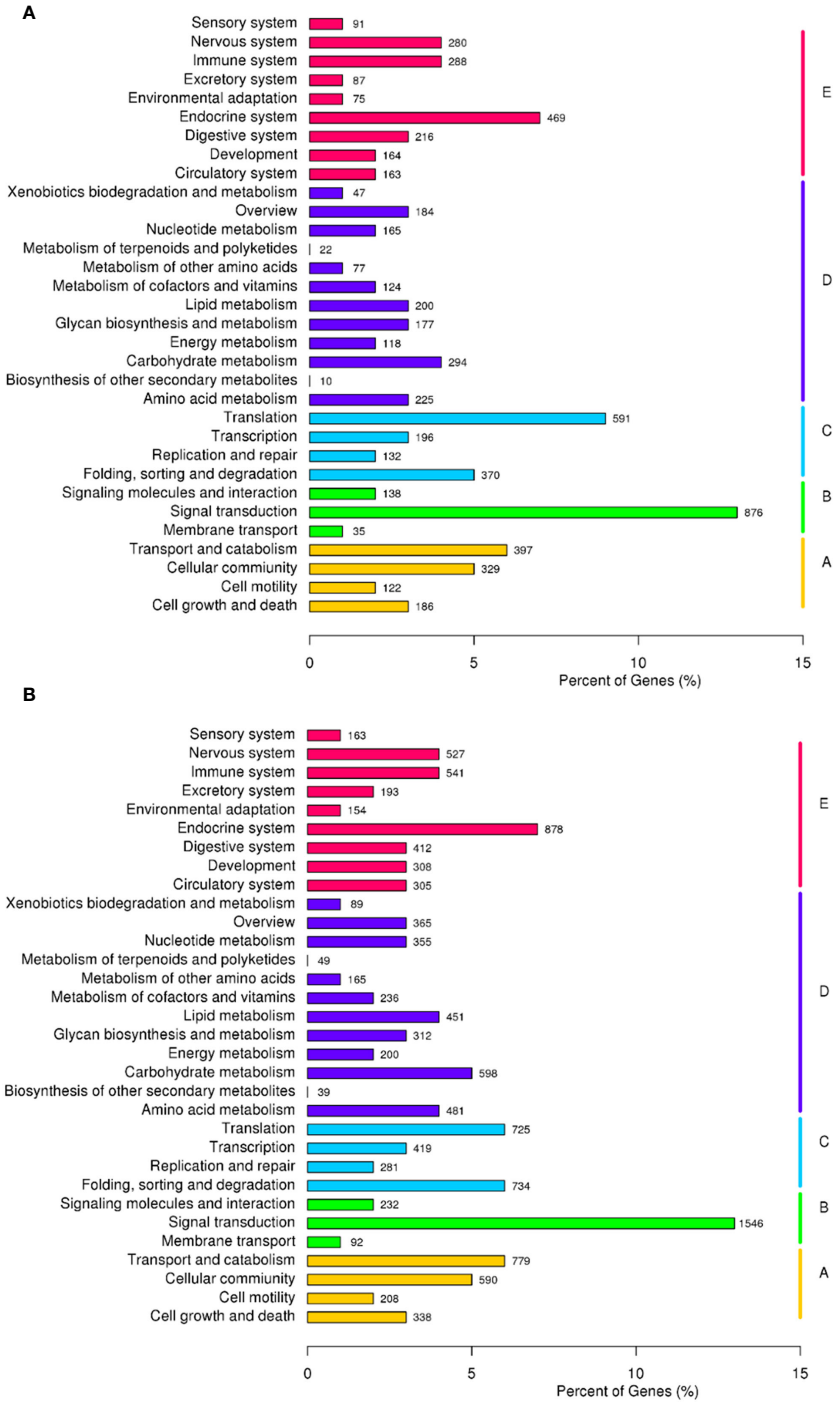

FIGURE 5
Classification of the Kyoto Encyclopedia of Genes and Genomes metabolic pathway of the transcriptomes of deep-sea barnacle *Neolepas marisindica* **(A)** and shallow barnacle *Scalpellum stearnsi* **(B)**. Vertical lines represent five main pathways: red terms denote cellular processes, purple terms denote environmental information processing, blue terms denote genetic information processing, green terms denote metabolism, and yellow terms denote organismal systems.

pressure would have been put on the mitogenome, and non-synonymous mutations are regarded as an adaptive substitution to meet the needs of a new environment (Srivastava et al., 2020). The results of our study indicate that the mitogenomes in *N. marisindica* experienced significant selective pressure, particularly the *COIII* and *ND2* genes, which have specific functional protein sites (Table 4; Figure 6). There is a prevalent belief that functional proteins contain positive selection sites, which serve as a foundation for adaptive responses to alterations in the environment (Rausher and Huang, 2016). *COIII* is one of the core members of cytochrome

TABLE 3 Collection and mitogenome information of the specimens that were used for the positive selection analysis.

Species	Mitochondrial genome size	GenBank accession numbers
Neolepasmarisindica	16,960 bp	MZ772032
Conchoderma hunteri	15,202 bp	OL606642
Scalpellum stearnsi	15,462 bp	OP345466
Lepas anserifera	15,653 bp	OP377772
Lepas australis	15,502 bp	NC025295
Lepas anatifera	15,708 bp	NC062431
Capitulum mitella	14,916 bp	AB167462
Arcoscalpellum epeeum	15,593 bp	MH791047
Altiverruca navicula	15,976 bp	NC037244
Glyptelasma annandalei	16,107 bp	NC043898
Ibla cumingi	15,053 bp	NC066682

C oxidase, a key rate-limiting enzyme at the end of the mitochondrial respiratory chain, which produces ATP and changes oxygen into water for cell metabolism (Timón-Gómez et al., 2018). At the level of mitochondrial transcription and translation, during the respiratory chain embedding in the inner mitochondria, the respiratory supercomplex factor protein family acts in response to biological hypoxia by binding to *COIII* to adapt to environmental and metabolic changes (Lobo-Jarne and Ugalde, 2018). Through bioinformatics analysis, several adaptive residues potentially presented in *COIII* and *ND2* of alvinocaridid shrimp (Alvinocarididae) inhabiting the deep-sea hydrothermal vent environment also have been identified by researchers. These proteins played an important role in regulating mitogenome intracellular energy metabolism and contributed to the adaptation of organisms to the hydrothermal vent environment (Hui et al., 2018b). Consequently, we speculate that the PCGs help *N. marisindica* to resist multiple pressures when adapting to the deep-sea environment.

TABLE 4 Results of the selective pressure acting on the protein-coding genes of *Neolepas marisindica*.

Gene	Model compared	*P*-value	Positive sites
	M1 vs M2/M7 vs M8		
ATP6	$\omega = 1.000/\omega = 1.000$	1.000/0.999	
ATP8	$\omega = 1.000/\omega = 1.000$	0.005/0.999	
COI	$\omega = 26.392/\omega = 1.000$	1.000/0.042	
COII	$\omega = 117.282/\omega = 1.000$	0.999/0.000	
COIII	$\omega = 3.804/\omega = 3.626$	0.000/0.000	22I, 29T etc
COB	$\omega = 34.321/\omega = 1.000$	1.000/0.000	
ND1	$\omega = 1.000/\omega = 1.000$	1.000/0.000	
ND2	$\omega = 26.634/\omega = 1.368$	0.001/0.000	73F, 75S etc
ND3	$\omega = 38.788/\omega = 1.000$	0.999/0.019	
ND4	$\omega = 1.000/\omega = 1.000$	1.000/0.191	
ND4l	$\omega = 1.000/\omega = 1.000$	0.999/0.923	
ND5	$\omega = 976.933/\omega = 15.264$	0.999/0.597	
ND6	$\omega = 40.205/\omega = 1.000$	0.00/0.999	

The NADH dehydrogenases are the largest enzyme complex in the mitochondrial electron transport chain; thus, mutations in these subunits may disturb the efficiency of the electron transport process (Da Fonseca et al., 2008). The NADH dehydrogenase genes of deep-sea anemones exhibited novel genetic structures, which were evidence of adaptation to the deep-sea environment (Zhang et al., 2017). Likewise, the hydrothermal vent environment may potentially exert potential selection pressure on NADH dehydrogenase genes from mitogenomes in *N. marisindica*. This pressure may influence the modulation of mitochondrial complexes and electron transport efficiency and hence, adapting to cold and hypoxic conditions (Luo et al., 2012). Given the crucial role of mitochondria in aerobic respiration and their indispensability for metabolism and energy production, they likely aid the deep-water barnacle in surmounting the constraints imposed by hypoxia, cold and food availability. Additionally, hydrothermal vents are also associated with hydrogen sulfide (H_2S), and the primary cytotoxic effect of H_2S is to interrupt the mitochondrial respiratory chain by directly inhibiting cytochrome *C* oxidase (Cooper and Brown, 2008). Therefore, we infer that the mitogenomes of *N. marisindica* are subjected to multiple selection pressures which led to adaptation to the hydrothermal vent environment under extreme deep-sea conditions.

4.2 Key genes implicated in deep-sea adaptation

Since they cannot swim in the ocean, barnacles are constrained to inhabit a comparatively restricted narrow region, rendering the process of acclimating to the deep-sea milieu arduous. The Southwest Indian Ridge (SWIR) is a typical ultraslow-spreading oceanic ridge, and the Longqi hydrothermal field is the first confirmed active field on the SWIR. Due to the general lack of deep-sea sediments in this hydrothermal zone, which can provide good channels for hydrothermal circulation and spillage, there are a large number of sulfides (Liang et al., 2023). The extreme environment impacts on population vicariance and dispersal, both significant biological processes. However, few researches have focused on the biodiversity of this region (Zhou et al., 2018). Therefore, our research endeavors to fill this gap by examining the effects of *N. marisindica* and *S. stearnsi* in the marine habitat, thereby enhancing our understanding of the adaptations in the harsh deep-sea environment.

ATG12, a core autophagy protein. The interaction between *ATG12* and its active complex can form autophagosome. Autophagy is an evolutionarily conserved catabolic process that generally promotes cell survival by eliminating intracellular pathogens and removing damaged organelles, playing a pivotal

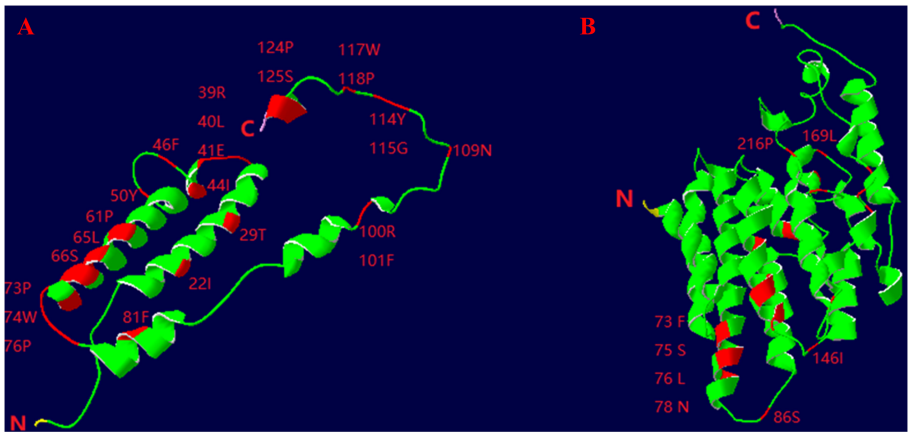

FIGURE 6
Three-dimensional structural models of the COIII **(A)** and ND2 **(B)** genes of deep- sea barnacle Neolepas marisindica. The red represents positive selection site; N represents amino terminus and **(C)** represents carboxy terminus.

TABLE 5 Genes that were subject to positive selection pressure in *Neolepas marisindica* and *Scalpellum stearnsi*.

Gene	Term	orthologs	dN/dS value	*q*-value
chromosome 3 open reading frame 10, *C3ORF10*	Regulation of actin cytoskeleton	OG14862	3.68	0.04
E74-like factor, *ELF*	Apoptosis - fly	OG15174	11.42	0.04
ubiquitin-like protein ATG12, *ATG12*	RIG-I-like receptor signaling pathway	OG15260	4.30	0.01
ubiquitin-like protein ATG12, *ATG12*	Regulation of autophagy	OG15260	4.30	0.01
ubiquitin-like protein ATG12, *ATG12*	FoxO signaling pathway	OG15260	4.30	0.04
uracil phosphoribosyltransferase, *UPRT*	Pyrimidine metabolism	OG15292	7.84	0.04
small subunit ribosomal protein S21e, *RPS21*	Ribosome	OG14951	20.76	0.12

role in cellular homeostasis and adaptation to adverse environments (Chen et al., 2014). During autophagy, *ATG12* binds the E2 ubiquitin conjugating enzyme to form sulfolipid intermediate, which further mediate the binding of phosphatidylethanolamine to LC3 to promote autophagy formation (Yuan et al., 2022). Although the regulation of this process remains incompletely understood, it has been found to induce the formation of the autophagosome membrane and type I interferons (*IFNs*). The process have been shown to play a crucial role in the antiviral immunity of *Larimichthys crocea* (Richardson) (Wei et al., 2021), *Epinephelus coioides* (Hamilton) (Li et al., 2019), and *Ctenopharyngodon idella* (Valenciennes in Cuvier and Valenciennes) (Chu et al., 2019), shedding light on the potential involvement of *ATG12* in antiviral immunity by stimulating both autophagy and type I interferon response. Consequently, it is hypothesized that *ATG12* may eliminate intracellular pathogens and damaged celles within *N. marisindica* by regulating autophagy homeostasis, which have contributed to its adaptation of harsh deep-sea environments. Furthermore, previous studies have demonstrated the involvement of *ATG12* in various cell biological processes such as viability, apoptosis, and autophagy (Wei et al., 2019). Meanwhile, *ATG12* has been found to directly modulate the mitochondrial apoptotic pathway by binding and inactivating prosurvival Bcl-2 family members (Rubinstein et al., 2011). In contrast to barnacles residing in shallow waters, the survival of *N. marisindica* exposed to diverse toxic substances, including H_2S. This exposure may have potentially facilitated the evolution of more effective immune responses and antiapoptotic metabolism (Cooper and Brown, 2008; Liang et al., 2023).

In Addition, the *ELF* (OG15174) and *UPRT* (OG15292) genes are also positively selected from the enriched pathways of apoptosis-fly and pyrimidine metabolism in *N. marisindica*, and they are both involved in adaptive immune responses. *ELF*, a pleiotropic transcription factor that modulates disease susceptibility and mediates several biotic and abiotic stress processes, playing a significant role in the host innate immune defense system (Suico et al., 2017). pH, temperature, and salinity can affect the immune response of crustaceans. *ELF* was involved in regulatory processes in organisms through synergistic or retrograde interactions, maintaining osmotic pressure homeostasis (Zhang et al., 2019). Previous researches has demonstrated that *ELF* was significantly expressed in the hepatopancreas and gill tissue of

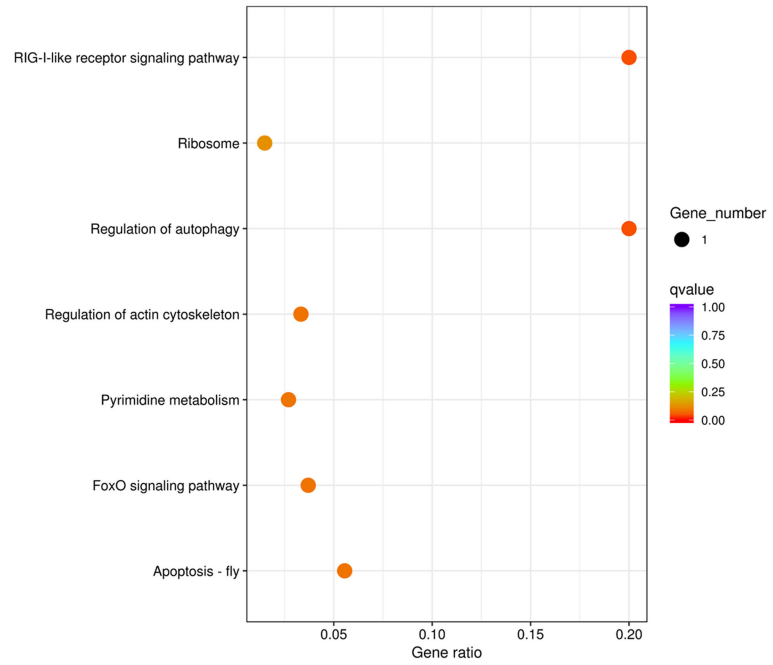

FIGURE 7
Enrichment of the Kyoto Encyclopedia of Genes and Genomes metabolic pathway of the positive selection genes in deep-sea barnacle *Vulcanolepas fijiensis* compared with shallow barnacle *Scalpellum stearnsi*. The circle size represents the number of genes, and the color from cool to warm represents the smaller *q* value.

Penaeus monodon Fabricius under salt stress, showing that *ELF* was involved in the immune stress process of organisms by regulating immune responses and the development of immune-related cells (Si et al., 2022). Simultaneously, *UPRT* maintains the immunocompetent and regulates the sensitivity of organisms to harmful cells (Koyama et al., 2000; Hasegawa et al., 2013). *UPRT* is a pyrimidine salvage enzyme. It can convert 5-flurouracil to a toxic compound, which kills the deleterious cells but subsequent conversion to other metabolites enhances its anti-apoptotic effect, by irreversibly inhibiting thymidylate synthase, DNA synthesis and the processing of rRNA and mRNA (Gopinath and Ghosh, 2008). Thus, it is plausible that these PSGs can potentially contribute to maintaining the immune system of *N. marisindica*, enabling it to withstand the adverse conditions of the deep sea, including low temperatures and toxic substances. Furthermore, high hydrostatic pressure and low temperatures have caused the inhibition of ligand binding and ion channel function which in turn affected signal transduction (Shinozaki and Yamaguchi-Shinozaki, 2000; Siebenaller, 2000). *C3ORF10* has been proposed to regulate actin dynamics, and its expression played a role in regulating actin dynamics during the process of neurite outgrowth (Stradal and Scita, 2006). *C3ORF10* is a member of the SCAR/WAVE complex, which is the effector of Rac1 to regulate actin dynamics, regulating Arp2/3-dependent actin polymerization and the number of axonal collaterals and dendrites (Wang et al., 2013). Consequently, the genes that have undergone positive selection and involved energy utilization, immune response, and signal transduction metabolism, might enhance the ability of *N. marisindica* to effectively employ various diverse adaptive strategies within the extreme conditions of the deep-sea environment. *N. marisindica* also exhibits enrichment of several significant pathways involving genes subject to positive selection, including the apoptosis-fly, regulation of actin cytoskeleton, pyrimidine metabolism, and ribosome pathways. Functionally, the ribosome pathway (K02971) influences almost every aspect of cell and organismal biology including maintaining cell homeostasis in response to changing environmental conditions and acute stress (Ni and Buszczak, 2023). Moreover, impairment of translation can result in the activation of the ribotoxic stress response, implying that ribosomes serve as a signal for the metabolic regulation of stress response (Snieckute et al., 2022), and the inhibition of ribosomal activity hinders the progression of the cell cycle, thereby regulating the adaptive stress response (Stoneley et al., 2022). Consequently, the presence of genes enriched in the ribosomal pathway indicates that the organisms have experienced environmental stress in their habitat.

5 Conclusions

This study is the first to sequence the transcriptome of a deep-sea barnacle *N. marisindica* and compared it with a shallow-water related species. The presence of positive selection in the mitogenome of *N. marisindica* suggested that this species probably evolved efficient adaption to cope with the challenges posed by the extreme deep-sea conditions, including limited oxygen and food availability, as well as a high concentration of H_2S in the hydrothermal vent environment.

Moreover, the identified PSGs from the enriched KEGG pathways are involved in crucial biological processes such as neural signal transduction, immunity, and antiapoptotic metabolism. Nevertheless, it should be noted that the findings presented in this study are preliminary, and additional research is needed to fully understand the evolutionary and adaptive processes of PSGs in the hydrothermal vent environment. Nonetheless, this study provided valuable genomic resources and insighted into the mechanisms of *N. marisindica* and *S. stearnsi*, serving as a foundation for further investigations into the evolution and adaptation of invertebrates within deep-sea ecosystems.

Data availability statement

The Neolepas marisindica and Scalpellum stearnsi datasets generated during the current study are available in the National Center for Biotechnology Information (NCBI) databases in GenBank repository at the following links: https://www.ncbi.nlm.nih.gov/nuccore/MZ772032 and https://www.ncbi.nlm.nih.gov/nuccore/OP345466.

Author contributions

NM: Data curation, Formal analysis, Methodology, Software, Writing – original draft. WS: Data curation, Formal analysis, Methodology, Software, Writing – original draft. YC: Conceptualization, Funding acquisition, Project administration, Resources, Writing – review & editing. XK: Methodology, Project administration, Writing – review & editing. NJ: Methodology, Project administration, Writing – review & editing. XS: Conceptualization, Funding acquisition, Project administration, Resources, Writing – review & editing.

Funding

The author(s) declare financial support was received for the research, authorship, and/or publication of this article. This work was supported by the Natural Science Foundation of China (#42376139), the Jiangsu Provincial Basic Research Program (Natural Science Foundation) Distinguished Youth Fund Project (BK20190048), Postgraduate Research & Practice Innovation Program of Jiangsu Ocean University (KYCX2023-69), Jiangsu Agriculture Science and Technology Innovation Fund (JASTIF) [CX (22) 2032], and the Project Funded by the Priority Academic Program Development of Jiangsu Higher Education Institutions (PAPD).

Acknowledgments

We would like to thank the reviewers and Chan et al. for their detailed comments about misidentification. We agree with the commentary paper of Chan et al. and have changed all reference to Vulcanolepas fijiensis to Neolepas marisindica in our corrected paper. We would also like to thank Professor Haibin Zhang from Institute of Deep-sea Science and Engineering (Chinese Academy of Sciences) for providing the samples and pictures of the deepsea barnacle.

Conflict of interest

The authors declare that the research was conducted in the absence of any commercial or financial relationships that could be construed as a potential conflict of interest.

Publisher's note

All claims expressed in this article are solely those of the authors and do not necessarily represent those of their affiliated organizations, or those of the publisher, the editors and the reviewers. Any product that may be evaluated in this article, or claim that may be made by its manufacturer, is not guaranteed or endorsed by the publisher.

Supplementary material

The Supplementary Material for this article can be found online at: https://www.frontiersin.org/articles/10.3389/fmars.2023.1269411/full#supplementary-material

References

Al-Aqeel, S., Ryu, T., Zhang, H. M., Chandramouli, K. H., and Ravasi, T. (2016). Transcriptome and proteome studies reveal candidate attachment genes during the development of the barnacle *Amphibalanus amphitrite*. *Front. Mar. Sci.* 3. doi: 10.3389/fmars.2016.00171

Altschul, S. F., Gish, W., Miller, W., Myers, E. W., and Lipman, D. J. (1990). Basic local alignment search tool. *J. Mol. Biol.* 215, 403–410. doi: 10.1016/S0022-2836(05)80360-2

Auger, C., Vinaik, R., Appanna, V. D., and Jeschke, M. G. (2021). Beyond mitochondria: Alternative energy-producing pathways from all strata of life. *Metabolism* 118. doi: 10.3389/fmars.2016.00171

Bankevich, A., Nurk, S., Antipov, D., Gurevich, A. A., Dvorkin, M., Kulikov, A. S., et al. (2012). SPAdes: a new genome assembly algorithm and its applications to single-cell sequencing. *J. Comput. Biol.* 19, 455–477. doi: 10.1089/cmb.2012.0021

Biswas, S., and Akey, J. M. (2006). Genomic insights into positive selection. *Trends. Genet.* 22, 437–446. doi: 10.1016/j.tig.2006.06.005

Buchfink, B., Xie, C., and Huson, D. H. (2015). Fast and sensitive protein alignment using DIAMOND. *Nat. Methods* 12, 59–60. doi: 10.1038/nmeth.3176

Chan, B. K., Prabowo, R. E., and Lee, K. S. (2010). North West Pacific deep-sea barnacles (Cirripedia, Thoracica) collected by the Taiwan expeditions, with descriptions of two new species. *Zootaxa* 2405, 1–47. doi: 10.11646/zootaxa.2405.1.1

Chan, B. K., Dreyer, N., Gale, A. S., Glenner, H., Ewers-Saucedo, C., Pérez-Losada, M., et al. (2021). The evolutionary diversity of barnacles, with an updated classification of fossil and living forms. *Zool. J. Linn Soc* 193, 789–846. doi: 10.1093/zoolinnean/zlaa160

Chan, B. K., Watanabe, H. K., and Chen, C. (2024). Commentary: Comparative omics analysis of a new deep-sea barnacle species (Cirripedia, Scalpellomorpha) and

shallow-water barnacle species provides insights into deep-sea adaptation.. *Front. Mar. Sci* 11, 1374419. doi: 10.3389/fmars.2024.1374419

Chen, Z. H., Cao, J. F., Zhou, J. S., Liu, H., Che, L. Q., Mizumura, K., et al. (2014). Interaction of caveolin-1 with ATG12-ATG5 system suppresses autophagy in lung epithelial cells. *Am. J. Physiol. Lung Cell Mol. Physiol.* 306, L1016–L1025. doi: 10.1152/ajplung.00268.2013

Chu, P. F., He, L. B., Yang, C., Zeng, W. C., Huang, R., Liao, L. J., et al. (2019). Grass carp ATG5 and ATG12 promote autophagy but down-regulate the transcriptional expression levels of IFN-I signaling pathway. *Fish. Shellfish. Immunol.* 92, 600–611. doi: 10.1016/j.fsi.2019.06.014

Cooper, C. E., and Brown, G. C. (2008). The inhibition of mitochondrial cytochrome oxidase by the gases carbon monoxide, nitric oxide, hydrogen cyanide and hydrogen sulfide: chemical mechanism and physiological significance. *J. Bioenerg. Biomembr.* 40, 533–539. doi: 10.1007/s10863-008-9166-6

Da Fonseca, R. R., Johnson, W. E., O'brien, S. J., Ramos, M. J., and Antunes, A. (2008). The adaptive evolution of the mammalian mitochondrial genome. *BMC. Genomics* 9, 119. doi: 10.1186/1471-2164-9-119

Danovaro, R., Snelgrove, P. V., and Tyler, P. (2014). Challenging the paradigms of deep-sea ecology. *Trends. Ecol. Evol.* 29, 465–475. doi: 10.1016/j.tree.2014.06.002

Feng, C. G., Liu, R. Y., Xu, W. J., Zhou, Y., Zhu, C. L., Liu, J., et al. (2021). The genome of a new anemone species (Actiniaria: Hormathiidae) provides insights into deep-sea adaptation. *Deep. Sea. Res. 1. Oceanogr. Res. Pap.* 170, 103492. doi: 10.1016/j.dsr.2021.103492

Gan, Z. B., Jones, D. S., Liu, X. M., Sui, J. X., Dong, D., and Li, X. Z. (2022). Phylogeny and adaptative evolution to chemosynthetic habitat in barnacle (Cirripedia: Thoracica) revealed by mitogenomes. *Front. Mar. Sci.* 9. doi: 10.3389/fmars.2022.964114

Gan, Z. B., Xu, P., Li, X. Z., and Wang, C. S. (2020a). Integrative taxonomy reveals two new species of stalked barnacle (Cirripedia, thoracica) from seamounts of the western pacific with a review of barnacles distributed in seamounts worldwide. *Front. Mar. Sci.* 7. doi: 10.3389/fmars.2020.582225

Gan, Z. B., Yuan, J. B., Liu, X. M., Dong, D., Li, F. H., and Li, X. Z. (2020b). Comparative transcriptomic analysis of deep-and shallow-water barnacle species (Cirripedia, Poecilasmatidae) provides insights into deep-sea adaptation of sessile crustaceans. *BMC. Genomics* 21, 1–13. doi: 10.1186/s12864-020-6642-9

Gao, F. L., Chen, C. J., Arab, D. A., Du, Z. G., He, Y. H., and Ho, S. Y. (2019). EasyCodeML: A visual tool for analysis of selection using CodeML. *Ecol. Evol.* 9, 3891–3898. doi: 10.1002/ece3.5015

Gattuso, J. P., Gentili, B., Duarte, C. M., Kleypas, J., Middelburg, J. J., and Antoine, D. (2006). Light availability in the coastal ocean: impact on the distribution of benthic photosynthetic organisms and their contribution to primary production. *Biogeosciences* 3, 489–513. doi: 10.5194/bg-3-489-2006

Gopinath, P., and Ghosh, S. S. (2008). Implication of functional activity for determining therapeutic efficacy of suicide genes *in vitro*. *Biotechnol. Lett.* 30, 1913–1921. doi: 10.1007/s10529-008-9787-1

Götz, S., García-Gómez, J. M., Terol, J., Williams, T. D., Nagaraj, S. H., Nueda, M. J., et al. (2008). High-throughput functional annotation and data mining with the Blast2GO suite. *Nucleic. Acids Res.* 36, 3420–3435. doi: 10.1093/nar/gkn176

Grabherr, M. G., Haas, B. J., Yassour, M., Levin, J. Z., Thompson, D. A., Amit, I., et al. (2011). Full-length transcriptome assembly from RNA-Seq data without a reference genome. *Nat. Biotechnol.* 29, 644–652. doi: 10.1038/nbt.1883

Greiner, S., Lehwark, P., and Bock, R. (2019). OrganellarGenomeDRAW (OGDRAW) version 1.3. 1: expanded toolkit for the graphical visualization of organellar genomes. *Nucleic. Acids Res.* 47, W59–W64. doi: 10.1101/545509

Hasegawa, N., Abei, M., Yokoyama, K. K., Fukuda, K., Seo, E., Kawashima, R., et al. (2013). Cyclophosphamide enhances antitumor efficacy of oncolytic adenovirus expressing uracil phosphoribosyltransferase (UPRT) in immunocompetent Syrian hamsters. *Int. J. Cancer.* 133, 1479–1488. doi: 10.1002/ijc.28132

Hui, M., Cheng, J., and Sha, Z. L. (2018a). Adaptation to the deep-sea hydrothermal vents and cold seeps: insights from the transcriptomes of *Alvinocaris longirostris* in both environments. *Deep. Sea. Res. 1. Oceanogr. Res. Pap.* 135, 23–33. doi: 10.1016/j.dsr.2018.03.014

Hui, M., Wang, M. X., and Sha, Z. L. (2018b). The complete mitochondrial genome of the alvinocaridid shrimp *Shinkaicaris leurokolos* (Decapoda, Caridea): Insight into the mitochondrial genetic basis of deep-sea hydrothermal vent adaptation in the shrimp. *Comp. Biochem. Physiol. Part. D. Genomics Proteomics.* 25, 42–52. doi: 10.1016/j.cbd.2017.11.002

Ki, J. S., Dahms, H. U., Hwang, J. S., and Lee, J. S. (2009). The complete mitogenome of the hydrothermal vent crab *Xenograpsus testudinatus* (Decapoda, Brachyura) and comparison with brachyuran crabs. *Comp. Biochem. Physiol. Part. D. Genomics Proteomics.* 4, 290–299. doi: 10.1016/j.cbd.2009.07.002

Koyama, F., Sawada, H., Fujii, H., Hamada, H., Hirao, T., Ueno, M., et al. (2000). Adenoviral-mediated transfer of Escherichia coli uracil phosphoribosyltransferase (UPRT) gene to modulate the sensitivity of the human colon cancer cells to 5-fluorouracil. *Eur. J. Cancer.* 36, 2403–2410. doi: 10.1016/S0959-8049(00)00338-5

Kumar, S., Stecher, G., and Tamura, K. (2016). MEGA7: molecular evolutionary genetics analysis version 7.0 for bigger datasets. *Mol. Biol. Evol.* 33, 1870–1874. doi: 10.1093/molbev/msw054

Lan, Y., Sun, J., Tian, R., Bartlett, D. H., Li, R. S., Wong, Y. H., et al. (2017). Molecular adaptation in the world's deepest-living animal: Insights from transcriptome sequencing of the hadal amphipod *Hirondellea gigas*. *Mol. Ecol.* 26, 3732–3743. doi: 10.1111/mec.14149

Lee, W. K., Mi Kang, H., Chan, B. K., Ju, S. J., and Kim, S. J. (2019). Complete mitochondrial genome of the hydrothermal vent stalked barnacle *Vulcanolepas fijiensis* (Cirripedia, Scalpelliforms, Eolepadidae). *Mitochondrial DNA B* 4(2), 2725–2726. doi: 10.1080/23802359.2019.1644564

Letunic, L., and Bork, P. (2021). Interactive Tree Of Life (iTOL) v5: an online tool for phylogenetic tree display and annotation. *Nucleic. Acids Res.* 49, W293–W296. doi: 10.1093/nar/gkab301

Li, C., Yu, Y. P., Zhang, X., Wei, J. G., and Qin, Q. W. (2019). Grouper Atg12 negatively regulates the antiviral immune response against Singapore grouper iridovirus (SGIV) infection. *Fish. Shellfish. Immunol.* 93, 702–710. doi: 10.1016/j.fsi.2019.08.037

Liang, J., Tao, C. H., Zheng, Y., Zhang, G. Y., Su, C., Yang, W. F., et al. (2023). Geology context, vent morphology, and sulfide paragenesis of the Longqi-1 modern seafloor hydrothermal system on the ultraslow-spreading Southwest Indian ridge. *Deep. Sea. Res. 1. Oceanogr. Res. Pap.* 194, 103962. doi: 10.1016/j.dsr.2023.103962

Liu, J., Liu, H. L., and Zhang, H. B. (2018). Phylogeny and evolutionary radiation of the marine mussels (Bivalvia: Mytilidae) based on mitochondrial and nuclear genes. *Mol. Phylogenet. Evol.* 126, 233–240. doi: 10.1016/j.ympev.2018.04.019

Lobo-Jarne, T., and Ugalde, C. (2018). Respiratory chain supercomplexes: structures, function and biogenesis. *Semin. Cell. Dev. Biol.* 76, 179–190. doi: 10.1016/j.semcdb.2017.07.021

Lorion, J., Kiel, S., Faure, B., Kawato, M., Ho, S. Y., Marshall, B., et al. (2013). Adaptive radiation of chemosymbiotic deep-sea mussels. *Proc. R. Soc Lond. B. Biol. Sci.* 280, 20131243. doi: 10.1098/rspb.2013.1243

Luo, Y., Chen, Y., Liu, F., and Gao, Y. (2012). Mitochondrial genome of Tibetan wild ass (*Equus kiang*) reveals substitutions in NADH which may reflect evolutionary adaptation to cold and hypoxic conditions. *Asia. Life. Sci.* 21, 1–11.

Lyu, L., Fang, K., Zhu, Z., Li, J., Chen, Y., Wang, L., et al. (2023). Bioaccumulation of emerging persistent organic pollutants in the deep-sea cold seep ecosystems: Evidence from chlorinated paraffin. *J. Hazard. Mater.* 445, 130472. doi: 10.1016/j.jhazmat.2022.130472

Moriya, Y., Itoh, M., Okuda, S., Yoshizawa, A. C., and Kanehisa, M. (2007). KAAS: an automatic genome annotation and pathway reconstruction server. *Nucleic. Acids Res.* 35, W182–W185. doi: 10.1093/nar/gkm321

Ni, C., and Buszczak, M. (2023). The homeostatic regulation of ribosome biogenesis. *Cell. Dev. Biol.* 136, 13–26. doi: 10.1016/j.semcdb.2022.03.043

Rausher, M. D., and Huang, J. (2016). Prolonged adaptive evolution of a defensive gene in the solanaceae. *Mol. Biol. Evol.* 33, 143–151. doi: 10.1093/molbev/msv205

Rota-Stabelli, O., Kayal, E., Gleeson, D., Daub, J., Boore, J. L., Telford, M. J., et al. (2010). Ecdysozoan mitogenomics: evidence for a common origin of the legged invertebrates, the Panarthropoda. *Genome. Biol. Evol.* 2, 425–440. doi: 10.1093/gbe/evq030

Rubinstein, A. D., Eisenstein, M., Ber, Y., Bialik, S., and Kimchi, A. (2011). The autophagy protein Atg12 associates with antiapoptotic Bcl-2 family members to promote mitochondrial apoptosis. *Mol. Cell.* 44, 698–709. doi: 10.1016/j.molcel.2011.10.014

Ryu, T., Woo, S., and Lee, N. (2019). The first reference transcriptome assembly of the stalked barnacle, *Neolepas marisindica*, from the Onnuri Vent Field on the Central Indian Ridge. *Mar. Genomics* 48, 100679. doi: 10.1016/j.margen.2019.04.004

Sahyoun, A. H., Bernt, M., Stadler, P. F., and Tout, K. (2014). GC skew and mitochondrial origins of replication. *Mitochondrion* 17, 56–66. doi: 10.1016/j.mito.2014.05.009

Sato, C., Nendai, N., Nagata, N., Okuzaki, Y., Ikeda, H., Minamiya, Y., et al. (2023). Origin and diversification of pheretimoid megascolecid earthworms in the Japanese Archipelago as revealed by mitogenomic phylogenetics. *Mol. Phylogenet. Evol.* 182, 107735. doi: 10.1016/j.ympev.2023.107735

Sha, Z. L., and Ren, X. Q. (2015). A new species of the genus Arcoscalpellum (Cirripedia, Thoracica, Scalpellidae) from deep waters in the South China Sea. *Chin. J. Oceanol. Limnol.* 33, 732–734. doi: 10.1007/s00343-015-4164-0

Shen, X., Tsang, L. M., Chu, K. H., Achituv, Y., and Chan, B. K. K. (2015). Mitochondrial genome of the intertidal acorn barnacle Tetraclita serrata Darwin 1854 (Crustacea: Sessilia): gene order comparison and phylogenetic consideration within Sessilia. *Mar. Genomics* 22, 63–69. doi: 10.1016/j.margen.2015.04.004

Shinozaki, K., and Yamaguchi-Shinozaki, K. (2000). Molecular responses to dehydration and low temperature: differences and cross-talk between two stress signaling pathways. *Curr. Opin. Plant Biol.* 3, 217–223. doi: 10.1016/S1369-5266(00)80068-0

Si, M. R., Li, Y. D., Jiang, S. G., Yang, Q. B., Jiang, S., Yang, L. S., et al. (2022). Identification of multifunctionality of the PmE74 gene and development of SNPs associated with low salt tolerance in Penaeus monodon. *Fish. Shellfish. Immunol.* 128, 7–18. doi: 10.1016/j.fsi.2022.07.010

Siebenaller, J. (2000). The effects of hydrostatic pressure on signal transduction in brain membranes of deep-sea fishes of the genus Coryphaenoides. *Fish. Physiol. Biochem.* 23, 99–106. doi: 10.1023/A:1007830722804

Simão, F. A., Waterhouse, R. M., Ioannidis, P., Kriventseva, E. V., and Zdobnov, E. M. (2015). BUSCO: assessing genome assembly and annotation completeness with single-copy orthologs. *Bioinformatics* 31, 3210–3212. doi: 10.1093/bioinformatics/btv351

Snieckute, G., Genzor, A. V., Vind, A. C., Ryder, L., Stoneley, M., Chamois, S., et al. (2022). Ribosome stalling is a signal for metabolic regulation by the ribotoxic stress response. *Cell. Metab.* 34, 2036–2046. doi: 10.1016/j.cmet.2022.10.011

Song, Y. J., and Yoon, J. M. (2013). Genetic differences of three *Pollicipes mitella* populations identified by PCR analysis. *Dev. Reprod.* 17, 199. doi: 10.12717/DR.2013.17.3.199

Srivastava, A., Barth, E., Ermolaeva, M. A., Guenther, M., Frahm, C., Marz, M., et al. (2020). Tissue-specific gene expression changes are associated with aging in mice. *Genomics Proteomics. Bioinf.* 18, 430–442. doi: 10.1016/j.gpb.2020.12.001

Stoneley, M., Harvey, R. F., Mulroney, T. E., Mordue, R., Jukes-Jones, R., Cain, K., et al. (2022). Unresolved stalled ribosome complexes restrict cell-cycle progression after genotoxic stress. *Mol. Cell.* 82, 1557–1572. doi: 10.1016/j.molcel.2022.01.019

Stradal, T. E., and Scita, G. (2006). Protein complexes regulating Arp2/3-mediated actin assembly. *Curr. Opin. Cell. Biol.* 18, 4–10. doi: 10.1016/j.ceb.2005.12.003

Suico, M. A., Shuto, T., and Kai, H. (2017). Roles and regulations of the ETS transcription factor ELF4/MEF. *J. Mol. Cell Biol.* 9, 168–177. doi: 10.1093/jmcb/mjw051

Sun, Y., Wang, M. X., Zhong, Z. S., Chen, H., Wang, H., Zhou, L., et al. (2022). Adaption to hydrogen sulfide-rich environments: Strategies for active detoxification in deep-sea symbiotic mussels, *Gigantidas platifrons*. Sci. *Total. Environ.* 804, 150054. doi: 10.1016/j.scitotenv.2021.150054

Thubaut, J., Puillandre, N., Faure, B., Cruaud, C., and Samadi, S. (2013). The contrasted evolutionary fates of deep-sea chemosynthetic mussels (Bivalvia, Bathymodiolinae). *Ecol. Evol.* 3, 4748–4766. doi: 10.1002/ece3.749

Timón-Gómez, A., Nývltová, E., Abriata, L. A., Vila, A. J., Hosler, J., and Barrientos, A. (2018). Mitochondrial cytochrome c oxidase biogenesis: Recent developments. *Semin. Cell. Dev. Biol.* 76, 163–178. doi: 10.1016/j.semcdb.2017.08.055

Wang, P. P., Mao, Y., Su, Y. Q., and Wang, J. (2021). Comparative analysis of transcriptomic data shows the effects of multiple evolutionary selection processes on codon usage in *Marsupenaeus japonicus* and *Marsupenaeus pulchricaudatus*. BMC. *Genomics* 22, 1–14. doi: 10.1186/s12864-021-08106-y

Wang, J. L., Tong, C. W., Chang, W. T., and Huang, A. M. (2013). Novel genes FAM134C, C3orf10 and ENOX1 are regulated by NRF-1 and differentially regulate neurite outgrowth in neuroblastoma cells and hippocampal neurons. *Gene* 529, 7–15. doi: 10.1016/j.gene.2013.08.006

Waterhouse, A., Bertoni, M., Bienert, S., Studer, G., Tauriello, G., Gumienny, R., et al. (2018). SWISS-MODEL: homology modelling of protein structures and complexes. *Nucleic. Acids Res.* 46, W296–W303. doi: 10.1093/nar/gky427

Wei, L., He, J., Jia, X., Qi, Q., Liang, Z. S., Zheng, H., et al. (2014). Analysis of codon usage bias of mitochondrial genome in Bombyx mori and its relation to evolution. *BMC. Evol. Biol.* 14, 262. doi: 10.1186/s12862-014-0262-4

Wei, H. M., Hu, J., Pu, J., Tang, Q. L., Li, W. C., Ma, R. H., et al. (2019). Long noncoding RNA HAGLROS promotes cell proliferation, inhibits apoptosis and enhances autophagy via regulating miR-5095/ATG12 axis in hepatocellular carcinoma cells. *Int. Immunopharmacol.* 73, 72–80. doi: 10.1016/j.intimp.2019.04.049

Wei, Z. Y., Wen, Q., Li, W. R., Yuan, X. Q., Fu, Q. L., Cui, Z. W., et al. (2021). ATG12 is involved in the antiviral immune response in large yellow croaker (*Larimichthys crocea*). *Fish. Shellfish. Immunol.* 119, 262–271. doi: 10.1016/j.fsi.2021.10.015

Wilhelm, B. T., and Landry, J. R. (2009). RNA-Seq—quantitative measurement of expression through massively parallel RNA-sequencing. *Methods* 48, 249–257. doi: 10.1016/j.ymeth.2009.03.016

Xin, Q., Hui, M., Li, C. L., and Sha, Z. L. (2021). Eyes of differing colors in *Alvinocaris longirostris* from deep-sea chemosynthetic ecosystems: genetic and molecular evidence of its formation mechanism. *J. Oceanol. Limnol.* 39, 282–296. doi: 10.1007/s00343-020-9312-5

Yan, G. Y., Lan, Y., Sun, J., Xu, T., Wei, T., and Qian, P. Y. (2022). Comparative transcriptomic analysis of in *situ* and onboard fixed deep-sea limpets reveals sample preparation-related differences. *iScience* 25, 104092. doi: 10.1016/j.isci.2022.104092

Yan, G. Y., Sun, J., Wang, Z. S., Qian, P. Y., and He, L. S. (2020). Insights into the synthesis, secretion and curing of barnacle cyprid adhesive via transcriptomic and proteomic analyses of the cement gland. *Mar. Drugs* 18, 186. doi: 10.3390/md18040186

Yoon, M., Jung, J. Y., and Kim, D. S. (2013). Genetic diversity and gene flow patterns in *Pollicipes mitella* in Korea inferred from mitochondrial DNA sequence analysis. *Fish. Aquatic. Sci.* 16, 243–251. doi: 10.5657/FAS.2013.0243

Yu, P., Zhou, L., Zhou, X. Y., Yang, W. T., Zhang, J., Zhang, X. J., et al. (2019). Unusual AT-skew of *Sinorhodeus microlepis* mitogenome provides new insights into mitogenome features and phylogenetic implications of bitterling fishes. *Int. J. Biol. Macromol.* 129, 339–350. doi: 10.1016/j.ijbiomac.2019.01.200

Yuan, Y., Huang, Y., Jian, J., Cai, S., and Yang, S. (2022). Autophagy genes of ATG5-ATG12 complex in response to exogenous stimulations in *Litopenaeus vannamei*. *Isr. J. Aquacult-Bamid.* 74, 17. doi: 10.46989/001c.55792

Zhang, C., Zhang, Q., Pang, Y., Song, X., Zhou, N., and Wang, J. (2019). The protective effects of melatonin on oxidative damage and the immune system of the Chinese mitten crab (*Eriocheir sinensis*) exposed to deltamethrin. *Sci. Total Environ.* 653, 1426–1434. doi: 10.1016/j.scitotenv.2018.11.063

Zhang, B., Zhang, Y. H., Wang, X., Zhang, H. X., and Lin, Q. (2017). The mitochondrial genome of a sea anemone Bolocera sp. exhibits novel genetic structures potentially involved in adaptation to the deep-sea environment. *Ecol. Evol.* 7, 4951–4962. doi: 10.1002/ece3.3067

Zheng, P., Wang, M. X., Li, C. L., Sun, X. Q., Wang, X. C., Sun, Y., et al. (2017). Insights into deep-sea adaptations and host–symbiont interactions: A comparative transcriptome study on Bathymodiolus mussels and their coastal relatives. *Mol. Ecol.* 26, 5133–5148. doi: 10.1111/mec.14160

Zhou, L., Li, M. N., Zhong, Z. S., Chen, H., Wang, X. C., Wang, M. X., et al. (2021). Biochemical and metabolic responses of the deep-sea mussel Bathymodiolus platifrons to cadmium and copper exposure. *Aquat. Toxicol.* 236, 105845. doi: 10.1016/j.aquatox.2021.105845

Zhou, Y. D., Zhang, D. S., Zhang, R. Y., Liu, Z. S., Tao, C. H., Lu, B., et al. (2018). Characterization of vent fauna at three hydrothermal vent fields on the Southwest Indian Ridge: implications for biogeography and interannual dynamics on ultraslow-spreading ridges. *Deep. Sea. Res. 1. Oceanogr. Res. Pap.* 137, 1–12. doi: 10.1016/j.dsr.2018.05.001

frontiers | Frontiers in Marine Science

TYPE Correction
PUBLISHED 19 August 2024
DOI 10.3389/fmars.2024.1452112

Check for updates

OPEN ACCESS

EDITED AND REVIEWED BY
Glen T. Snyder,
The University of Tokyo, Japan

*CORRESPONDENCE
Yuefeng Cai
yuefengcai@jou.edu.cn
Xin Shen
shenthin@163.com

†These authors have contributed equally to this work and share first authorship

RECEIVED 04 July 2024
ACCEPTED 18 July 2024
PUBLISHED 19 August 2024

CITATION
Mao N, Shao W, Cai Y, Kong X, Ji N and Shen X (2024) Corrigendum: Comparative omics analysis of a deep-sea barnacle species (Cirripedia, Scalpellomorpha) and shallow-water barnacle species provides insights into deep-sea adaptation.
Front. Mar. Sci. 11:1452112.
doi: 10.3389/fmars.2024.1452112

COPYRIGHT
© 2024 Mao, Shao, Cai, Kong, Ji and Shen. This is an open-access article distributed under the terms of the Creative Commons Attribution License (CC BY). The use, distribution or reproduction in other forums is permitted, provided the original author(s) and the copyright owner(s) are credited and that the original publication in this journal is cited, in accordance with accepted academic practice. No use, distribution or reproduction is permitted which does not comply with these terms.

Corrigendum: Comparative omics analysis of a deep-sea barnacle species (Cirripedia, Scalpellomorpha) and shallow-water barnacle species provides insights into deep-sea adaptation

Ning Mao[1,2†], Wentai Shao[1,2†], Yuefeng Cai[1,2*], Xue Kong[1,2], Nanjing Ji[1,2] and Xin Shen[1,2*]

[1]Jiangsu Key Laboratory of Marine Bioresources and Environment, Jiangsu Key Laboratory of Marine Biotechnology, Jiangsu Ocean University, Lianyungang, China, [2]Co-Innovation Center of Jiangsu Marine Bio-Industry Technology, Jiangsu Ocean University, Lianyungang, China

KEYWORDS

barnacle, *Neolepas marisindica*, deep-sea adaptation, mitogenome, transcriptome

A Corrigendum on

Comparative omics analysis of a deep-sea barnacle species (Cirripedia, Scalpellomorpha) and shallow-water barnacle species provides insights into deep-sea adaptation

By Mao N, Shao W, Cai Y, Kong X, Ji N and Shen X (2024). *Front. Mar. Sci.* 10:1269411. doi: 10.3389/fmars.2023.1269411

Error in the Article Title

In the published article, there was an error in the article title. Instead of "*Comparative omics analysis of a new deep-sea barnacle species (Cirripedia, Scalpellomorpha) and shallow-water barnacle species provides insights into deep-sea adaptation*", it should be "*Comparative omics analysis of a deep-sea barnacle species (Cirripedia, Scalpellomorpha) and shallow-water barnacle species provides insights into deep-sea adaptation*".

Text Correction

In the published article, there was an error. We provisionally identified the deep-water species *Vulcanolepas fijiensis*. As a result of the Chan et al. Commentary Paper (2024), we became aware that our initial identification of *Vulcanolepas fijiensis* was incorrect. We have confirmed that the barnacle is actually *Neolepas marisindica* and have revised this paper to include the correct species indentation.

The change to *"Neolepas marisindica"* or "*N. marisindica"* applies to all instances of the words "*Vulcanolepas fijiensis*" and "*V. fijiensis*" respectively, which appear in the

Keywords, **Abstract, Introduction**, **Materials and methods, Results, Discussion,** and **Conclusions.**

A correction has been made to **Introduction**. This sentence previously stated:

"While studies on other organisms inhabiting extreme deep-sea environments have identified several potential mechanisms, the transcriptome of *Vulcanolepas fijiensis* (Chan) and *Scalpellum stearnsi* (Pilsbry) remains unexplored. Moreover, few studies have investigated the molecular adaptive characteristics that assist with barnacles' survival in deep-sea harsh chemosynthetic habitats. Due to the limited prior investigations concerning the transcriptome of barnacles, particularly with regard to the deep-sea adaptation of *V. fijiensis*, our study attempted to address this research gap.

In this study, we collected deep-sea (*V. fijiensis*) and shallow-water (*S. stearnsi*) individuals at Longqi hydrothermal field on the Southwest Indian Ridge and Guangxi Beibu Gulf, respectively. In order to investigate the adaptability of barnacles to the deep-sea environment, the analysis of positive selection pressure was conducted using the comparative transcriptome of these two individuals, as well as the 13 protein-coding genes (PCGs) of mitogenomes from 11 barnacles, including *V. fijiensis*. This research endeavor aimed to not only provide valuable genomic resources for deep-sea barnacles but also establish a foundation for comprehending their genetic strategies and adaptation mechanisms in the deep-sea habitat."

The corrected sentence appears below:

"While studies on other organisms inhabiting extreme deep-sea environments have identified several potential mechanisms, the transcriptome of them remains unexplored. Moreover, few studies have investigated the molecular adaptive characteristics that assist with barnacles' survival in deep-sea harsh chemosynthetic habitats. Due to the limited prior investigations concerning the transcriptome of barnacles, particularly with regard to the deep-sea adaptation, our study attempted to address this research gap.

In this study, we collected the deep-sea and shallow-water barnacle individuals at Longqi hydrothermal field on the Southwest Indian Ridge and Guangxi Beibu Gulf, respectively. In order to investigate the adaptability of barnacles to the deep-sea environment, the analysis of positive selection pressure was conducted using the comparative transcriptome of these two individuals, as well as the 13 protein-coding genes (PCGs) of mitogenomes from 11 barnacles. This research endeavor aimed to not only provide valuable genomic resources for deep-sea barnacles but also establish a foundation for comprehending their genetic strategies and adaptation mechanisms in the deep-sea habitat."

A correction has been made to **Materials and methods**, *2.1 Sample collection, DNA and RNA extraction, and sequencing*, paragraph one. This sentence previously stated:

"A variety of manned submarines were used to obtain *V. fijiensis* from a hydrothermal vent Longqi hydrothermal field on the Southwest Indian Ridge (49°64'E, 37°17'S) at a depth of 2,759 m in the Southwest Indian Ocean. *S. stearnsi* were obtained from the Guangxi Beibu Gulf (109°12'E, 21°04'N), depth of about 300 m. In contrast to deep-sea species, the depth of 300m can be considered relatively shallow. Therefore, we provisionally classified *S. stearnsi* as a shallow species. After collection, they were immediately stored at -80°C."

The corrected sentence appears below:

"Samples of the deep-sea barnacles from a hydrothermal vent Longqi hydrothermal field on the Southwest Indian Ridge (49°64'E, 37°17'S) at a depth of 2,759 m in the Southwest Indian Ocean collected on board of "Explorer 1" scientific research ship of Institute of Deep-sea Science and Engineering (Chinese Academy of Sciences) by using "Deep-sea Warrior" manned submersible during the winter of 2018, we thank the crew for their help during the cruise. Samples of the shallow-water barnacles were obtained from the Guangxi Beibu Gulf (109° 12 ' E, 21° 04 ' N), depth of about 300 m. In contrast to deep-sea species, the depth of 300m can be considered relatively shallow. Therefore, we provisionally identified the two barnacle species as the deep water species *Vulcanolepas fijiensis* (Lee et al., 2019) and the shallow water *Scalpellum stearnsi* (Chan et al., 2010). As a result of the Chen et al. Commentary Paper (Chan et al., 2024) we became aware that our initial identification of *V. fijiensis* was incorrect. We have confirmed that the barnacle is actually *Neolepas marisindica* and have revised this paper to include the correct species indentation. After collection, they were immediately stored at -80°C."

The references for "Lee et al., 2019", "Chan et al., 2010", and "Chan et al., 2024" should be:

"Chan, B. K., Prabowo, R. E., Lee, K. S. (2010). North West Pacific deep-sea barnacles (Cirripedia, Thoracica) collected by the Taiwan expeditions, with descriptions of two new species. *Zootaxa* 2405, 1-47. doi: 10.11646/zootaxa.2405.1.1

Chan, B. K., Watanabe, H. K., Chen, C. (2024) Commentary: Comparative omics analysis of a new deep-sea barnacle species (Cirripedia, Scalpellomorpha) and shallow-water barnacle species provides insights into deep-sea adaptation. *Front. Mar. Sci.* 11, 1374419. doi: 10.3389/fmars.2024.1374419

Lee, W .K., Mi Kang, H., Chan, B. K., Ju, S. J., Kim, S. J. (2019). Complete mitochondrial genome of the hydrothermal vent stalked barnacle *Vulcanolepas fijiensis* (Cirripedia, Scalpelliforms, Eolepadidae). *Mitochondrial DNA B.* 4 (2), 2725-2726. doi: 10.1080/23802359.2019.1644564"

In the published article, there was an error in the **Data availability statement**. Our initial identification of *Vulcanolepas fijiensis* was incorrect. We have confirmed that the barnacle mentioned in the name of our deep-sea barnacle species is actually *Neolepas marisindica*. Therefore, the *Neolepas marisindica* and *Scalpellum stearns*i datasets generated during the current study have been deposited and the statement "The original contributions presented in the study are publicly available. This data can be found here: https://www.ncbi.nlm.nih.gov/, BioProject: PRJNA935972." has been updated. The correct Data Availability statement appears below.

"The *Neolepas marisindica* and *Scalpellum stearns*i datasets generated during the current study are available in the National Center for Biotechnology Information (NCBI) databases in GenBank repository at the following links: https://www.ncbi.nlm.nih.gov/nuccore/MZ772032 and https://www.ncbi.nlm.nih.gov/nuccore/OP345466."

In the published article, there was no **Acknowledgments** section. The correct Acknowledgments section appears below.

"We would like to thank the reviewers and Chan et al. for their detailed comments about misidentification. We agree with the commentary paper of Chan et al. and have changed all reference to *Vulcanolepas fijiensis* to *Neolepas marisindica* in our corrected paper. We would also like to thank Professor Haibin Zhang from Institute of Deep-sea Science and Engineering (Chinese Academy of Sciences) for providing the samples and pictures of the deep-sea barnacle."

Error in Figure

In the published article, there was an error in Figure 1 as published. The use of photos from the database in Figure 1 has raised copyright issues. We apologize for the error and have corrected them to photos taken at the time of collection to eliminate copyright and plagiarism issues.

Furthermore, there was an error in the legend for Figure 1. Our initial identification of *Vulcanolepas fijiensis* was incorrect. We have confirmed that the barnacle mentioned in the caption of Figure 1 is actually *Neolepas marisindica*. Therefore, instead of "The mitochondrial genome map of deep-sea barnacle *Vulcanolepas fijiensis* **(A)** and shallow barnacle *Scalpellum stearnsi* **(B)**", the legend should read: "The mitochondrial genome map of deep-sea barnacle *Neolepas marisindica* (A) and shallow barnacle *Scalpellum stearnsi* (B) collected for this study, and photographs in the genome map are from preserved samples that were collected for this study, which were collected by Professor Haibin Zhang and kept in Institute of Deep-sea Science and Engineering (Chinese Academy of Sciences)". The corrected Figure 1 and its updated caption appear below.

The authors apologize for this error and state that this does not change the scientific conclusions of the article in any way. The original article has been updated.

Error in Tables

In the published article, there was an error in Table 2 as published. Our initial identification of "*Vulcanolepas fijiensis*" in the third column of Table 2 was incorrect and should be "*Neolepas marisindica*" instead. Furthermore, the barnacle mentioned in the legends for Table 2 is actually "*Neolepas marisindica*", not "*Vulcanolepas fijiensis*". The corrected Table 2 and its updated caption appear below.

In the published article, there was an error in Table 3 as published. Our initial identification of "*Vulcanolepas fijiensis*" in the first column of Table 3 was incorrect and should be "*Neolepas marisindica*" instead. The corrected Table 3 and its caption appear below.

The authors apologize for this error and state that this does not change the scientific conclusions of the article in any way. The original article has been updated.

Error in Figure/Table Legend

In the published article, there was an error in the legends for Figures 2 – 7 and in the legends for Tables 1, 4, and 5 as published. Our initial identification of *Vulcanolepas fijiensis* was incorrect. We have confirmed that the barnacle mentioned in the legends for Figures 2 – 7 and in the legends for Tables 1, 4, and 5 should be "*Neolepas marisindica*". The corrected legends appear below.

[TABLE 1 Summary of the mitogenome features of *Neolepas marisindica* and *Scalpellum stearnsi*.]

[FIGURE 2 AT and GC skews in protein-coding genes of the mitochondrial genomes in deep-sea barnacle *Neolepas marisindica* (A) and shallow barnacle *Scalpellum stearnsi* (B). The horizontal and vertical coordinates represent gene name and skew value, respectively; The blue line represents the AT skew and the orange line represents the GC skew.]

[FIGURE 3 The codon usage of the protein-coding genes of the mitochondrial genomes of deep- sea barnacle *Neolepas marisindica* (A) and shallow barnacle *Scalpellum stearnsi* (B). The different colors represent different kinds of codons, and the different columns represent different amino acids.]

[FIGURE 4 Gene Ontology function annotation of the transcriptomes of deep-sea barnacle *Neolepas marisindica* (A) and shallow barnacle *Scalpellum stearnsi* (B). The red terms represent Biological Process, the blue terms represent Cellular Composition, and the green terms represent Molecular Function.]

[FIGURE 5 Classification of the Kyoto Encyclopedia of Genes and Genomes metabolic pathway of the transcriptomes of deep-sea barnacle *Neolepas marisindica* (A) and shallow barnacle *Scalpellum stearnsi* (B). Vertical lines represent five main pathways: red terms denote cellular processes, purple terms denote environmental information processing, blue terms denote genetic information processing, green terms denote metabolism, and yellow terms denote organismal systems.]

[TABLE 4 Results of the selective pressure acting on the protein-coding genes of *Neolepas marisindica*.]

[FIGURE 6 Three-dimensional structural models of the COIII (A) and ND2 (B) genes of deep- sea barnacle *Neolepas marisindica*. The red represents positive selection site; N represents amino terminus and (C) represents carboxy terminus.]

[TABLE 5 Genes that were subject to positive selection pressure in *Neolepas marisindica* and *Scalpellum stearnsi*.]

[FIGURE 7 Enrichment of the Kyoto Encyclopedia of Genes and Genomes metabolic pathway of the positive selection genes in deep-sea barnacle *Vulcanolepas fijiensis* compared with shallow barnacle *Scalpellum stearnsi*. The circle size represents the number of genes, and the color from cool to warm represents the smaller q value.]

The authors apologize for this error and state that this does not change the scientific conclusions of the article in any way. The original article has been updated.

Publisher's note

All claims expressed in this article are solely those of the authors and do not necessarily represent those of their affiliated organizations, or those of the publisher, the editors and the reviewers. Any product that may be evaluated in this article, or claim that may be made by its manufacturer, is not guaranteed or endorsed by the publisher.

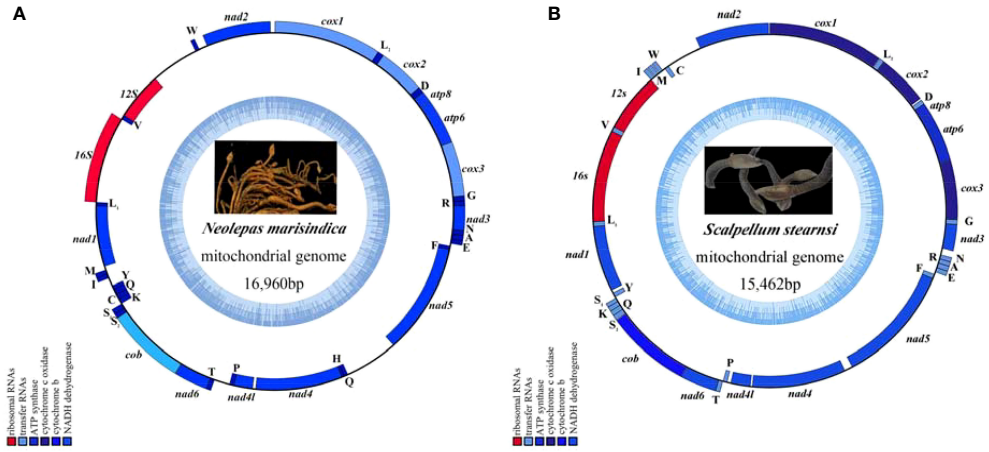

FIGURE 1
The mitochondrial genome map of deep-sea barnacle *Neolepas marisindica* **(A)** and shallow barnacle *Scalpellum stearnsi* **(B)** collected for this study, and photographs in the genome map are from preserved samples that were collected for this study, which were collected by Professor Haibin Zhang and kept in Institute of Deep-sea Science and Engineering (Chinese Academy of Sciences). The heavy strand is represented by the outer circle, while the light strand is represented by the inner circle; The tRNA and PCGs are denoted by the blue genes, whereas the 12S *rRNA* and 16S *rRNA* are indicated by the red genes.

TABLE 2 Transcriptome library basic information of *Scalpellum stearnsi* and *Neolepas marisindica*.

Class	Item	*Neolepas marisindica*	*Scalpellum stearnsi*
Assembly	Transcript number (bar)	54,446	99,622
	Unigene number (bar)	53,562	98,686
	Total length of Unigenes (bp)	49,774,143	61,491,550
	N50 length of Unigenes (bp)	1,721	916
	Mean length of Unigenes (bp)	929	623
Annotation	Nr	13,679 (25.53%)	26,304 (26.65%)
	Nt	5,150 (9.61%)	8,036 (8.14%)
	Swiss-Prot	12,019 (22.43%)	19,772 (20.03%)
	KEGG Orthology	6,845 (12.77%)	12,042 (12.2%)
	PFAM	16,685 (31.15%)	26,406 (26.75%)
	GO	16,746 (31.26%)	26,718 (27.07%)
	KOG	7,129 (13.3%)	10,959 (11.1%)
	All Databases	2,422 (4.52%)	2,786 (2.82%)
	At least one database	20,628 (38.51%)	38,666 (39.18%)

TABLE 3 Collection and mitogenome information of the specimens that were used for the positive selection analysis.

Species	Mitochondrial genome size	GenBank accession numbers
Neolepas marisindica	16,960 bp	MZ772032
Conchoderma hunteri	15,202 bp	OL606642
Scalpellum stearnsi	15,462 bp	OP345466
Lepas anserifera	15,653 bp	OP377772
Lepas australis	15,502 bp	NC025295
Lepas anatifera	15,708 bp	NC062431
Capitulum mitella	14,916 bp	AB167462
Arcoscalpellum epeeum	15,593 bp	MH791047
Altiverruca navicula	15,976 bp	NC037244
Glyptelasma annandalei	16,107 bp	NC043898
Ibla cumingi	15,053 bp	NC066682

frontiers | Frontiers in Marine Science

TYPE General Commentary
PUBLISHED 28 May 2024
DOI 10.3389/fmars.2024.1374419

Check for updates

OPEN ACCESS

EDITED BY
Andrew R. Thurber,
Oregon State University, United States

REVIEWED BY
Wong Yue Him,
Shenzhen University, China
Ryota Hayashi,
Nippon Koei Co., Ltd., Japan

*CORRESPONDENCE
Chong Chen
cchen@jamstec.go.jp

RECEIVED 22 January 2024
ACCEPTED 26 April 2024
PUBLISHED 28 May 2024

CITATION
Chan BKK, Watanabe HK and Chen C (2024) Commentary: Comparative omics analysis of a new deep-sea barnacle species (Cirripedia, Scalpellomorpha) and shallow-water barnacle species provides insights into deep-sea adaptation.
Front. Mar. Sci. 11:1374419.
doi: 10.3389/fmars.2024.1374419

COPYRIGHT
© 2024 Chan, Watanabe and Chen. This is an open-access article distributed under the terms of the Creative Commons Attribution License (CC BY). The use, distribution or reproduction in other forums is permitted, provided the original author(s) and the copyright owner(s) are credited and that the original publication in this journal is cited, in accordance with accepted academic practice. No use, distribution or reproduction is permitted which does not comply with these terms.

Commentary: Comparative omics analysis of a new deep-sea barnacle species (Cirripedia, Scalpellomorpha) and shallow-water barnacle species provides insights into deep-sea adaptation

Benny K. K. Chan [1], Hiromi Kayama Watanabe [2] and Chong Chen [2*]

[1]Biodiversity Research Center, Academia Sinica, Taipei, Taiwan, [2]X-STAR, Japan Agency for Marine-Earth Science and Technology (JAMSTEC), Yokosuka, Kanagawa, Japan

KEYWORDS

chemosynthetic ecosystem, integrative taxonomy, Neolepadidae, phylogeny, species identification, systematics

A Commentary on:

Comparative omics analysis of a new deep-sea barnacle species (Cirripedia, Scalpellomorpha) and shallow-water barnacle species provides insights into deep-sea adaptation

by Mao N, Shao W, Cai Y, Kong X, Ji N and Shen X (2024). *Front. Mar. Sci.* 10:1269411. doi: 10.3389/fmars.2023.1269411

Mao et al. (2024) recently published an article comparing the mitochondrial genome and transcriptome of the deep-sea hydrothermal vent barnacle *Vulcanolepas fijiensis* and the relatively shallower barnacle *Scalpellum stearnsi* (contradictory to the title, no new species was described). This paper concluded that the mitogenomes and key genes found in the transcriptomic analysis were subjected to positive selection related to high-temperature and high-pressure conditions, allowing *V. fijiensis* to adapt to the deep-sea environment. However, the neolepadid hydrothermal vent barnacle used in their study was misidentified and actually represents a different species, *Neolepas marisindica*. We present our evidence and reasoning for this below. Although the main conclusions presented by Mao et al. (2024) still stand because *N. marisindica* is also a deep-sea vent species, their misidentification has connotations on the context, interpretation, and of course future use of their data.

The deep-sea hydrothermal vent barnacle specimen referred to as *V. fijiensis* in Mao et al. (2024) was collected at Longqi hydrothermal vent field on the Southwest Indian Ridge at a depth of 2759 m in the Indian Ocean. *Vulcanolepas fijiensis* was originally described from the North Fiji Basin in the Southwest Pacific (Chan et al., 2019) and had never been reported in the Indian Ocean. Watanabe et al. (2018) were the first to explore the diversity of neolepadid hydrothermal vent barnacles in the Indian Ocean and found only one species, *Neolepas marisindica*, from

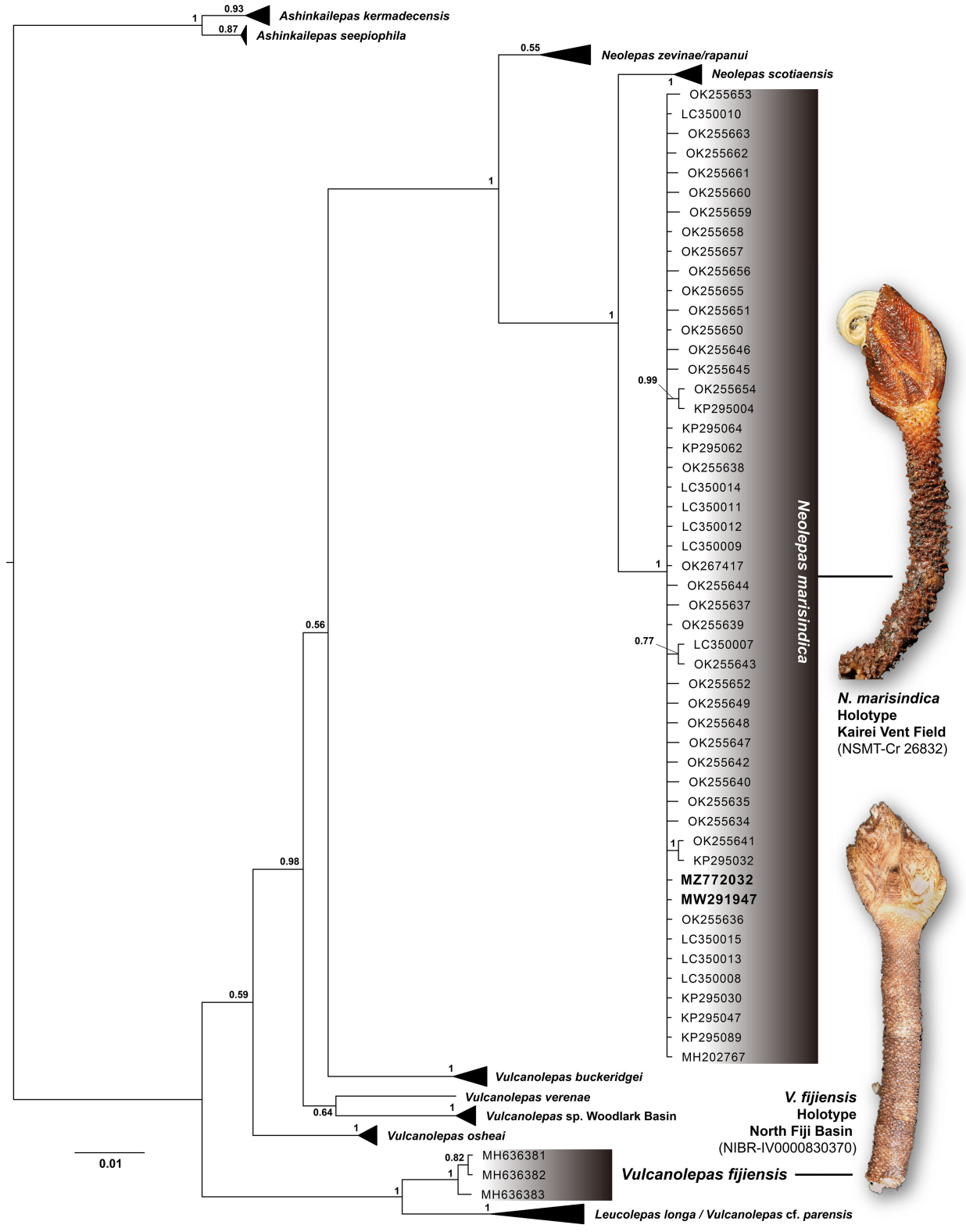

FIGURE 1
Phylogenetic tree of neolepadid stalked barnacles reconstructed by Bayesian inference with the GTR+I+G model, following published methods in Watanabe et al. (2023). For simplicity, taxa other than *Vulcanolepas fijiensis* and *Neolepas marisinidica* have been collapsed. Accession numbers in bold refer to sequences referred to as *V. fijiensis* in Mao et al. (2024). Node values indicate Bayesian posterior probability. The 528 bp alignment used contained all 202 COI barcoding sequences openly available on GenBank, accession numbers as follows: JX036420-JX036464, KF739820-KF739838, KP295001, KP295004-KP295005, KP295007-KP295009, KP295013-KP295014, KP295018-KP295019, KP295022, KP295026-KP295028, KP295030-KP295037, KP295039-KP295042, KP295045-KP295053, KP295055-KP295058, KP295060-KP295064, KP295067-KP295069, KP295073, KP295076, KP295078, KP295080, KP295082-KP295085, KP295089-KP295091, KP295094, KP295097-KP295098, KY502196-KY502197, LC350007-LC350015, MH202767, MH636381-MH636383, MN722546-MN722548, MN722550-MN722551, MT662001, MW291947, MW602536-MW602540, MW602548-MW602549, MW602552-MW602566, MZ772032, OK255634-OK255663, OK267417. Holotype of *V. fijiensis* (NIBR-IV0000830370; Korea National Institute for Biological Resources, Incheon, Korea) as well as *N. marisindica* (NSMT-Cr 26832; National Museum of Nature and Science, Tsukuba, Japan) shown in inset, photographs were taken by Benny K. K. Chan.

several vent fields including the Longqi vent field. Though *N. marisindica* exhibits two morphotypes, these have been shown to be the same species using molecular data (Watanabe et al., 2018).

Using the mitochondrial genome of *V. fijiensis* supplied by Mao et al. (2024) in GenBank (MZ772032), we show in a phylogenetic tree that the mitochondrial COI (cytochrome *c* oxidase subunit I) barcode sequence of *V. fijiensis* in Mao et al. (2023) is nested into a well-supported clade with other available sequences of *N. marisindica* and not with *V. fijiensis* sequences from the original description by Chan et al. (2019) that includes barcodes of the holotype (Figure 1). This sequence from Mao et al. (2024) was identical to published sequences of *N. marisindica* from both Kairei (type locality; LC350008, LC350015) and Solitaire (LC350013) vent fields on the Central Indian Ridge (CIR). Searching on GenBank revealed another mitogenome listed as *V. fijiensis* (MW291947) linked to the Mao et al. (2024) paper, but this too was nested within *N. marisindica* (Figure 1). Furthermore, a mitogenome of the real *V. fijiensis* from the North Fiji Basin had already been published (Lee et al., 2019; MN061491) using one of the original specimens sequenced in the description paper, and a BLAST comparison with the mitogenome (MZ772032) presented by Mao et al. (2024) revealed a percentage identity of only 88.84% between these two mitogenomes. Altogether, these evidences show that the species identification in Mao et al. (2024) was incorrect, and their hydrothermal vent barnacle was actually *N. marisindica*.

We also note that another layer of confusion came from an inset specimen photo used in Figure 1A of Mao et al. (2024), which shows a photo of the real *V. fijiensis* directly taken from figure 3F of Chan et al. (2019) (original authors were not consulted about this use prior to publication). This photograph is of the holotype of *V. fijiensis* housed in the collection of the Korea National Institute for Biological Resources (Incheon, Korea; NIBR-IV0000830370) where it still resides. As such, the photo of *V. fijiensis* presented in Mao et al. (2024) is misleadingly not linked to the actual specimen used in their study.

Hydrothermal vent field stalked barnacles in the family Neolepadidae often exhibit morphological variations in the capitular shells and peduncular scales (Watanabe et al., 2021), which may have contributed to the misidentification in Mao et al. (2024). A more reliable identification for deep-sea hydrothermal vent barnacles should be based on an integrative approach, a combination of morphological and barcoding sequence matching with reference sequences available in GenBank. With the misidentification in Mao et al. (2024) corrected, *Neolepas marisindica* remains the only neolepadid species known from the Indian Ocean so far (Watanabe et al., 2018; Kim et al., 2020; 2021, Zhou et al., 2018; 2022), known from nine vent fields across four ridges (SWIR, CIR, Southeast Indian Ridge, and Carlsberg Ridge). At present, the hydrothermal vent stalked barnacle species identified in the Pacific include *V. fijiensis, V. osheai*, *V. buckeridgei, V. verenae*, *Leucolepas longa*, *Neolepas rapanuii*, and *N. zevinae* (see Watanabe et al., 2021); an undescribed species is also known from Woodlark Basin (Boulart et al., 2022). Such a contrasting diversity pattern between the Pacific and Indian Ocean vent fields supports the Dispersal Corridor Hypothesis, where the ancestors of the Indian Ocean neolepadid barnacles originated from the Pacific Ocean and entered the Indian Ocean via the Southern Ocean (see Watanabe et al., 2018).

Correct species identification is of utmost importance to ensure the correct interpretation and usage of molecular and distribution data. The data in Mao et al. (2024) presents the first assembled and published mitogenome sequence for *N. marisinidica*, a valuable piece of new data that will be useful in the future for understanding the evolutionary history of this species and vent barnacles as a whole. Although previously another transcriptome for this species was published using specimens from Onnuri vent field on the CIR (Ryu et al., 2019), this means the Longqi transcriptome data from Mao et al. (2024) provides an opportunity to make an interesting comparison with Onnuri to reveal potential differences between conspecific barnacles in two different vents across two ridge systems. We hope this case serves as an example for biologists working on difficult-to-identify deep-sea species to embrace integrative taxonomy and to ensure the species identification and taxonomy is correct prior to publication.

Author contributions

BC: Funding acquisition, Writing – original draft, Validation, Investigation, Conceptualization. HW: Writing – original draft, Visualization, Software, Resources, Methodology, Investigation, Formal analysis, Data curation, Conceptualization. CC: Writing – original draft, Visualization, Validation, Methodology, Investigation, Data curation, Conceptualization.

Funding

The author(s) declare financial support was received for the research, authorship, and/or publication of this article. BKKC acknowledges intramural research funding from the Biodiversity Research Center, Academia Sinica, Taiwan.

Conflict of interest

The authors declare that the research was conducted in the absence of any commercial or financial relationships that could be construed as a potential conflict of interest.

The author(s) declared that they were an editorial board member of Frontiers at the time of submission. This had no impact on the peer review process and the final decision.

Publisher's note

All claims expressed in this article are solely those of the authors and do not necessarily represent those of their affiliated organizations, or those of the publisher, the editors and the reviewers. Any product that may be evaluated in this article, or claim that may be made by its manufacturer, is not guaranteed or endorsed by the publisher.

References

Boulart, C., Rouxel, O., Scalabrin, C., Le Meur, P., Pelleter, E., Poitrimol., C., et al. (2022). Active hydrothermal vents in the Woodlark Basin may act as dispersing centres for hydrothermal fauna. *Commun. Earth Env.* 3, 64. doi: 10.1038/s43247–022-00387–9

Chan, B. K. K., Ju, S., and Kim, S. J. (2019). A new species of hydrothermal vent stalked barnacle *Vulcanolepas* (Scalpelliforms: Eolepadidae) from the North Fiji Basin, Southwestern Pacific Ocean. *Zootaxa* 4563, 135–148. doi: 10.11646/ZOOTAXA.4563.1.7

Kim, J., Son, S.-K., Kim, D., Pak, S.-J., Yu, O. H., Walker, S. L., et al. (2020). Discovery of active hydrothermal vent fields along the Central Indian Ridge, 8–12°S. *Geochemistry Geophysics Geosystems* 21, e2020GC009058. doi: 10.1029/2020GC009058

Lee, W.-K., Kang, H. M., Chan, B. K. K., Ju, S.-J., and Kim, S.-J. (2019). Complete mitochondrial genome of the hydrothermal vent stalked barnacle *Vulcanolepas Fijiensis* (Cirripedia, Scalpelliforms, Eolepadidae). *Mitochondrial DNA Part B* 4, 2725–2726. doi: 10.1080/23802359.2019.1644564

Mao, N., Shao, W., Cai, Y., Kong, X., Ji, N., and Shen, X. (2024). Comparative omics analysis of a new deep-sea barnacle species (Cirripedia, Scalpellomorpha) and shallow-water barnacle species provides insights into deep-sea adaptation. *Front. Mar. Sci.* 10, 1269411. doi: 10.3389/fmars.2023.1269411

Ryu, T., Woo, S., and Lee, N. (2019). The first reference transcriptome assembly of the stalked barnacle, *Neolepas marisindica*, from the Onnuri Vent Field on the Central Indian Ridge. *Mar. Genomics* 48, 100679. doi: 10.1016/j.margen.2019.04.004

Watanabe, H. K., Chen, C., and Chan, B. K. K. (2021). A new deep-sea hot vent stalked barnacle from the Mariana Trough with notes on the feeding ecology of *Vulcanolepas*. *Mar. Biodiversity* 51, 9. doi: 10.1007/s12526-020-01144-x

Watanabe, H. K., Chen, C., Marie, D. P., Takai, K., Fujikura, K., and Chan, B. K. K. (2018). Phylogeography of hydrothermal vent stalked barnacles: a new species fills a gap in the Indian Ocean 'dispersal corridor' hypothesis. *R. Soc Open Sci.* 5, 172408. doi: 10.1098/rsos.172408

Watanabe, H. K., Uyeno, D., Yamamori, L., Jimi, N., and Chen, C. (2023). From commensalism to parasitism within a genus-level clade of barnacles. *Biol. Lett.* 19, 20220550. doi: 10.1098/rsbl.2022.0550

Zhou, Y., Chen, C., Zhang, D., Wang, Y., Watanabe, H. K., Sun, J., et al. (2022). Delineating biogeographic regions in Indian Ocean deep-sea vents and implications for conservation. *Diversity Distributions* 28, 2858–2870. doi: 10.1111/ddi.13535

Zhou, Y., Zhang, D., Zhang, R., Liu, Z., Tao, C., Lu, B., et al. (2018). Characterization of vent fauna at three hydrothermal vent fields on the Southwest Indian Ridge: Implications for biogeography and interannual dynamics on ultraslow-spreading ridges. *Deep Sea Res. Part I: Oceanographic Res. Papers* 137, 1–12. doi: 10.1016/j.dsr.2018.05.001

frontiers | Frontiers in Marine Science

TYPE Original Research
PUBLISHED 17 January 2024
DOI 10.3389/fmars.2023.1156918

Check for updates

OPEN ACCESS

EDITED BY
Stéphanie Dupré,
Institut Français de Recherche pour l'Exploitation de la Mer, France

REVIEWED BY
Hailin Yang,
Peking University, China
Thomas Pape,
University of Bremen, Germany

*CORRESPONDENCE
Ji-Hoon Kim
save@kigam.re.kr

†These authors have contributed equally to this work and share first authorship

RECEIVED 02 February 2023
ACCEPTED 26 December 2023
PUBLISHED 17 January 2024

CITATION
Kim J-H, Park M-H, Ryu J-S, Jang K, Choi J, Park S, Song Y, Yi B-Y, Joo YJ, Kim T-H and Hur J (2024) Exploring the pore fluid origin and methane-derived authigenic carbonate properties in response to changes in the methane flux at the southern Ulleung Basin, South Korea. *Front. Mar. Sci.* 10:1156918. doi: 10.3389/fmars.2023.1156918

COPYRIGHT
© 2024 Kim, Park, Ryu, Jang, Choi, Park, Song, Yi, Joo, Kim and Hur. This is an open-access article distributed under the terms of the Creative Commons Attribution License (CC BY). The use, distribution or reproduction in other forums is permitted, provided the original author(s) and the copyright owner(s) are credited and that the original publication in this journal is cited, in accordance with accepted academic practice. No use, distribution or reproduction is permitted which does not comply with these terms.

Exploring the pore fluid origin and methane-derived authigenic carbonate properties in response to changes in the methane flux at the southern Ulleung Basin, South Korea

Ji-Hoon Kim[1*†], Myong-Ho Park[2†], Jong-Sik Ryu[3], Kwangchul Jang[4,5], Jiyoung Choi[1], Sanghee Park[6], Yungoo Song[5], Bo-Yeon Yi[1], Young Ji Joo[3], Tae-Hoon Kim[7] and Jin Hur[8]

[1]Marine Geology & Energy Division, Korea Institute of Geoscience and Mineral Resources, Daejeon, Republic of Korea, [2]Carbon Capture & Storage (CCS) Research Center, Kongju National University, Gongju, Republic of Korea, [3]Department of Earth and Environmental Sciences, Pukyong National University, Busan, Republic of Korea, [4]Division of Glacier Environment Research, Korea Polar Research Institute, Incheon, Republic of Korea, [5]Department of Earth System Sciences, Yonsei University, Seoul, Republic of Korea, [6]Division of Earth and Environment Sciences, Korea Basic Science Institute, Cheongju, Republic of Korea, [7]Geology & Space Division, Korea Institute of Geoscience and Mineral Resources, Daejeon, Republic of Korea, [8]Department of Environment & Energy, Sejong University, Seoul, Republic of Korea

We investigated the geochemistry of gas, pore fluid, and methane-derived authigenic carbonate (MDAC) from four sites in the southern Ulleung Basin, South Korea. In contrast to Sites 16GH-P1 and 16GH-P5, Sites 16GH-P3, and 16GH-P4 are characterized by acoustic chimney structures associated with gas flux. The composition of gas and isotopic signatures of methane (CH_4) (C_1/C_{2+} > 300, $\delta^{13}C_{CH4}$ < -60‰, δD_{CH4} ≤ -190‰) indicate microbial source CH_4 at all sites. The upward migration of CH_4 can affect the chemical and isotopic properties of pore fluid and gas-related byproducts (e.g., gas hydrate (GH) and MDAC) within the shallow sediments including the current sulfate-methane transition (SMT) (< 5 meters below seafloor). Although no GH was found, elevated Cl^- concentrations (maximum = 609 mM) with low δD and $\delta^{18}O$ values in Site 16GH-P4 pore fluids delineate the influence of massive GH formation in deeper sediment. In contrast, relatively constant Cl^-, δD, and $\delta^{18}O$ values in fluids from Sites 16GH-P1, 16GH-P3, and 16GH-P5 indicate a predominant origin from seawater. Pore fluids also exhibit higher concentrations of H_4SiO_4, B, Mg^{2+}, and K^+, along with increasing alkalinity compared to seawater. These observations suggest that marine silicate weathering alters fluid chemistry within the sediment, affecting element and carbon cycles. High alkalinity (up to 60 mM) and Mg^{2+}/Ca^{2+} ratios (> 6) alongside decreasing Ca^{2+} and Sr^{2+} concentrations imply carbonate precipitation. MDACs with diverse morphologies, mainly composed of aragonite and magnesian calcite, and characterized by low carbon isotopic values ($\delta^{13}C_{MDAC}$ < -31.3‰), were found at Sites 16GH-P3 and 16GH-P4. Interestingly, $\delta^{13}C_{MDAC}$ values at Site 16GH-P3 are clearly differentiated above and below the current SMT. High $\delta^{13}C_{MDAC}$ values

above the SMT (> -34.3‰) suggest the combined influence of seawater and CH_4 migrating upward on MDAC precipitation, whereas low $\delta^{13}C_{MDAC}$ values below it (< -41.6‰) indicate a predominant impact of CH_4 on MDAC formation. Additionally, the vertical variation of $\delta^{18}O_{MDAC}$ values at Site 16GH-P4, compared to the theoretical values, reflects an association with GH dissociation and formation. Our findings improve the understanding of fluid, gas, and MDAC geochemistry in continental margin cold seeps, providing insights into global carbon and element cycles.

KEYWORDS

microbial CO_2 reduction, marine silicate weathering, chimney structure, MDACs, gas hydrate, Ulleung Basin

1 Introduction

Cold seep systems that are characterized by the seepage of fluids enriched in methane (CH_4)-dominated hydrocarbons from deep-seated sediments to the seafloor under low temperatures, widely occur in many regions along the continental margin (e.g., Campbell, 2006; Judd and Hovland, 2007; Suess, 2014; Himmler et al., 2015; Mazzini et al., 2016). These systems play an important role in global climate change, element cycles, ocean chemistry, and biology (Dillon et al., 2001; Römer et al., 2014; Koch et al., 2015; Ruppel and Kessler, 2017). They also cause various changes in seafloor morphologies, for example, carbonate pavements, mounds, pockmarks, and mud volcanoes (Bahr et al., 2007; Buerk et al., 2010; Himmler et al., 2011; Römer et al., 2014; Koch et al., 2015). Geophysical investigations, for example, sub-bottom profiles, side scan sonar, and high-resolution seismic data, have been used to identify cold seep systems on the seafloor (e.g., Colbo et al., 2014; Stott et al., 2019; Böttner et al., 2020).

More than 80% of the CH_4 migrating upward below sulfate-methane transition (SMT) in sediments can be consumed via anaerobic oxidation of methane (AOM; Equation 1) mainly coupled with particulate organic carbon sulfate reduction (POCSR; Equation 2) in the SMT (Boetius et al., 2000; Peckmann and Thiel, 2004; Torres et al., 2020).

$$\mathrm{AOM}: CH_4 + SO_4^{2-} \rightarrow HCO_3^- + HS^- + H_2O \quad (1)$$

$$\mathrm{POCSR}: 2(CH_2O)_x(NH_3)_y(H_3PO_4)_z + xSO_4^{2-} \rightarrow xH_2S + 2xHCO_3^- + 2yNH_3 + 2zH_3PO_4 \quad (2)$$

where x, y, and z are derived from C:N:P ratios (Redfield ratios) of the organic matter.

These biogeochemical reactions provide energy for diverse chemosynthetic communities that colonize in the near-surface sediments of cold seeps (Sibuet and Olu, 1998). In addition, high HCO_3^- in pore fluid produced by the reactions provides favorable conditions for the precipitation of methane-derived authigenic carbonates (MDACs; Equation 3) in the sediment and/or water column, which is characterized by the low carbon isotopic value inherited from CH_4 (Peckmann et al., 2001; Luff et al., 2004; Torres et al., 2020). Gas hydrates (GHs) have also been found at cold seeps located in the Arctic regions, Cascadia Margin, and South China Sea (e.g., Han et al., 2008; Malinverno et al., 2008; Wang et al., 2014; Hong et al., 2017; Kim et al., 2020; Kim et al., 2022).

$$\mathrm{MDAC}: 2HCO_3^- + xCa^{2+} + (1-x)Mg^{2+} \rightarrow (Ca_x, Mg_{(1-x)})CO_3 + CO_2 + H_2O \quad (3)$$

where $x = Ca^{2+}/(Ca^{2+} + Mg^{2+})$.

Multichannel seismic investigations have been performed to find GHs in the Ulleung Basin, South Korea, since 2000. The prominent "chimney structures" (e.g., Figures 1B, D) frequently occur in this basin, which are characterized by seismic amplitude reduction resulting from velocity pull-up. These structures are associated with numerous fractures resembling hydrofractures and/or faults, terminating at different stratigraphic levels and, in some cases, extending to the seafloor (e.g., Lee et al., 2005; Haacke et al., 2009; Horozal et al., 2009; Ryu et al., 2009; Kim et al., 2012). Indeed, massive GHs have been found near the seafloor in the Ulleung Basin (e.g., Ryu et al., 2009; Kim et al., 2012; Choi et al., 2013; Kim et al., 2013), where a significant amount of free gas migrates upward from the deep-seated sediment via chimney structures forming GHs. Hence, these seismic structures potentially serve as pathways for the free gas migration feeding massive GH accumulations near the seafloor, which are unique seismic characteristics compared to other regions (e.g., Haacke et al., 2009; Horozal et al., 2009; Ryu et al., 2009; Kim et al., 2012; Choi et al., 2013; Kim et al., 2013; Hong et al., 2014). Many datasets (e.g., seismic survey, pore fluid chemistry, gas chemistry, and sedimentology) have been documented in the Ulleung Basin (e.g., Park et al., 2006; Park et al., 2007; Haacke et al., 2009; Kim et al., 2011; Kim et al., 2012; Choi et al., 2013; Kim et al., 2013), but

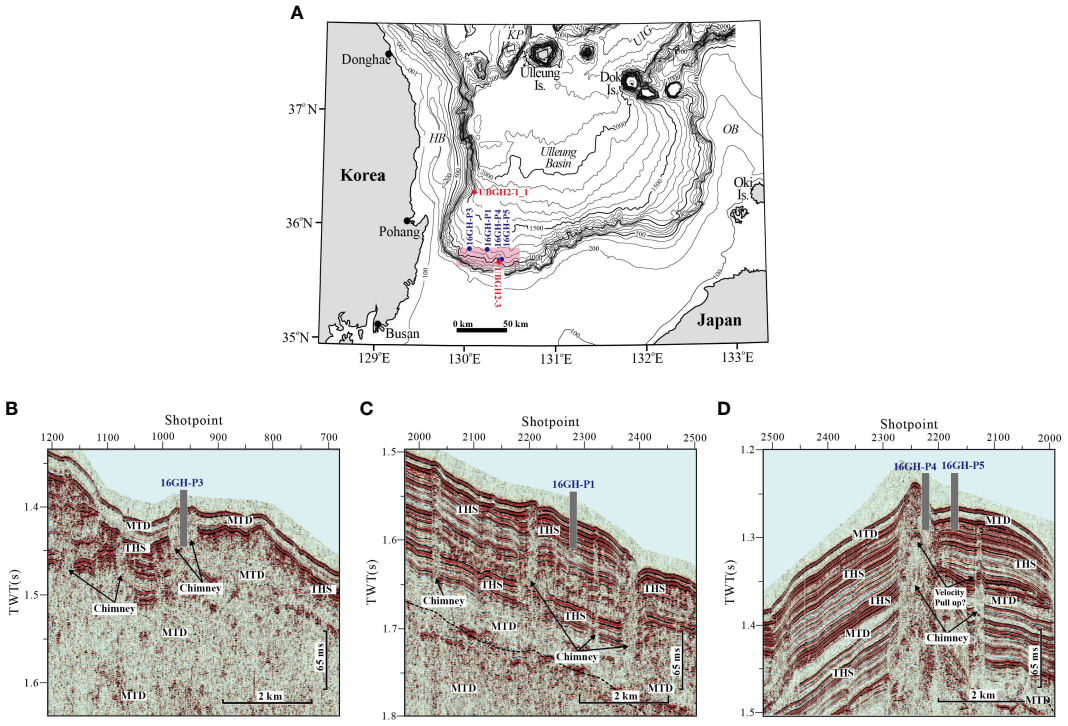

FIGURE 1
(A) Major physiographic features and locations of the study area (contour lines show the bathymetry in meters). KP, Korea Plateau; UIG, Ulleung Interplain Gap; HB, Hupo Bank, and OB, Oki Bank. Seismic profiles of **(B)** Site 16GH-P3 (chimney structure), **(C)** Site 16GH-P1 (non-chimney structure), and **(D)** Sites 16GH-P4 (chimney structure) and 16GH-P5 (non-chimney structure). The core depth at each site has no scale. MTD, mass-transport deposits and THS, turbidite-hemipelagic sediments.

studies for understanding the chemical interactions among gases, pore fluids, and sediments (including MDAC) are still rare in this basin.

In the present article, we investigated 1) how the upward migration of CH_4 from deep-seated sediments via chimney structures impacts the chemical properties of gases and fluids, as well as the characteristics of the shallow sedimentary deposits within the southern Ulleung Basin, and 2) how the petrological and morphological features of MDACs vary within the sediment column. To achieve our goals, we collected and conducted geochemical analysis for gases, pore fluids, and MDAC samples from two MDAC-bearing sites (16GH-P3 and 16GH-P4) and two non-MDAC-bearing sites (16GH-P1 and 16GH-P5).

2 Regional setting

The East Sea is the marginal sea in the northwestern Pacific Ocean and consists of three main basins (East Sea, Yamato, and Ulleung) and four straits (Korea, Tsugaru, Soya, and Tartar). The Ulleung Basin is bounded by the continental slope of the Korean Peninsula to the west and the Korea Plateau to the north and has a relatively steep gradient (up to 10°), while it is bordered by a rather gentle slope (1° ~ 2°) and a broad shelf (30 m ~ 50 km wide) of the Japanese Arc and the Oki Bank (Figure 1). This basin was formed during the late Oligocene to early Miocene by crustal extension (Tamaki et al., 1992; Jolivet et al., 1995).

The uppermost sedimentary sequence (30 m ~ 70 m thick) in the Ulleung Basin mainly consists of various mass-flow deposits along the entire margin of the basin overlain by Holocene hemipelagic mud (1 m ~ 2 m thick) (Chough et al., 2000; Lee et al., 2005). The average sedimentation rates of late Quaternary sediments in the basin range from 9 cm/ka to 20 cm/ka (Park et al., 2006; Park et al., 2007; Kim et al., 2011).

Sediment cores were collected at four sites on the slope of the southwestern part of the Ulleung Basin, ranging in water depth from 902 m to 1,187 m (Figure 1; Table 1). This region is characterized by prominent seafloor gullies due to numerous erosional slump events. The sedimentary deposits within the top 150 meters below seafloor (mbsf) consist mainly of turbidite and hemipelagic sequences that are parallel to the seafloor. Deeper layers are predominantly composed of mass transport deposits, with only a few coherent seismic reflection events discernible (Figures 1B–D). Among the sites, both Sites 16GH-P3 and 16GH-P4 display chimney structures with widths of approximately 600 m and 800 m, respectively, which show structural deformations within the sedimentary layers. However, a conspicuous bottom simulating reflector is not observed at the seismic section of these sites. In contrast, Sites 16GH-P1 and 16GH-P5 show non-chimney structures, which are well represented by the successive acoustic surfaces below the seafloor (Figure 1; Table 1) (KIGAM, 2016).

TABLE 1 Summaries of site information from the 2016 Expedition.

Site	Core	Latitude (°N)	Longitude (°E)	Water Depth (m)	Total Core Length (m)	SMT Depth (mbsf)	Seismic Characteristic	Remark
16GH-P3	16GH-P3*W	35.7681	130.0339	1,054	7.67	1.9	Chimney	***MDAC found
	16GH-P3*A	35.7683	130.0339	1,050	7.70	**——		
16GH-P4	16GH-P4W	35.6908	130.3433	916	6.95	2.5		MDAC not found
	16GH-P4A	35.6909	130.3403	902	7.70	——		MDAC found
16GH-P1	16GH-P1W	35.7992	130.2361	1,187	7.75	4.3	Non-chimney	MDAC not found
	16GH-P1A	35.7993	130.2361	1,187	7.48	——		
16GH-P5	16GH-P5W	35.6915	130.3503	926	7.10	2.7		
	16GH-P5A	35.6909	130.3498	925	7.47	——		

*W: core for geochemical study, A: core for sedimentological study.
**——: no data.
*** MDAC: methane-derived authigenic carbonate.

3 Materials and methods

3.1 Fluid sampling and analyses

Piston cores (PCs) were collected from four sites during the *R/V Tamhae II* cruise of the Korea Institute of Geoscience and Mineral Resources (KIGAM) in 2016. Two parallel PCs were sampled at each site for geochemical and sedimentological studies. These cores were designated as "W" and "A", corresponding to 16GH-P1W and 16GH-P1A, respectively (Table 1). Pore fluid was extracted by Rhizons throughout the whole round core of PC for geochemical analyses at approximately 40 cm ~ 85 cm intervals under 4°C. Extracted fluid was collected in an acid-prewashed syringe equipped with an in-line 0.20 µm disposable polytetrafluoroethylene filter. Fluid aliquots for cations and $^{87}Sr/^{86}Sr$ ratios were transferred into acid-prewashed high-density polyethylene (HDPE) bottles (~2 ml - 4 ml) and acidified with 20 µl ultrapure-grade HNO_3. Fluid subsamples for shipboard and anions analyses were collected in acid-prewashed HDPE bottles without acidification. Subsamples for stable isotopic compositions of water (δD and $\delta^{18}O$) and dissolved inorganic carbon ($\delta^{13}C_{DIC}$) were collected in 2 ml septum screw-lid glass vials. Fluid samples for $\delta^{13}C_{DIC}$ analysis were preserved with 30 µl $HgCl_2$. All fluid samples were stored at ~4°C in the refrigerator until the analyses.

Chlorinity (Cl^-) and alkalinity were analyzed onboard by titration with 0.1 M $AgNO_3$ and with 0.02 M HCl, respectively. The reproducibility of Cl^- and alkalinity was determined to be < 2% and < 0.5%, respectively, by repeated analysis of the International Association of Physical Sciences of the Oceans (IAPSO) standard seawater. Sulfate (SO_4^{2-}) was determined by Dionex ion chromatography (ICS-1100, Thermo Scientific) at the Korea Basic Science Institute (KBSI). IAPSO standard seawater was repeatedly measured to verify the analytical quality of the instruments, and analytical reproducibility was better than ±3%.

Major and minor cations (Na^+, K^+, Mg^{2+}, Ca^{2+}, Ba^{2+}, B, Sr^{2+}, and Si) were analyzed by PerkinElmer inductively coupled plasma-optical emission spectroscopy (Optima 8300 ICP-OES) at the KBSI. The reproducibility estimated from repeated analyses of reference materials (SLRS-5 and NASS-5) was < 5%.

Stable isotopic compositions of water (δD and $\delta^{18}O$) were analyzed by a VG Prism stable isotope ratio mass spectrometer (SIRMS) at the KBSI. The analytical reproducibility was ±1‰ for δD and ±0.1‰ for $\delta^{18}O$. $\delta^{13}C_{DIC}$ was determined with a Finnigan DELTA-Plus stable isotope ratio mass spectrometer using a Gas-Bench II automated sampler at the Oregon State University. The reproducibility was better than 0.07‰, based on the multiple standard measurements. Isotopic values are reported in the conventional δ-notation relative to Vienna Standard Mean Ocean Water (V-SMOW) for hydrogen and oxygen and Vienna Peedee Belemnite (V-PDB) for carbon.

Strontium (Sr) in the fluid was separated for $^{87}Sr/^{86}Sr$ analysis using Sr-Spec columns (Eichrom-Sr resin). The $^{87}Sr/^{86}Sr$ ratio was measured using a Neptune multi-collector inductively coupled plasma mass spectrometer (MC-ICP-MS, Thermo Finnigan) at the KBSI. The measured $^{87}Sr/^{86}Sr$ ratios were normalized to $^{86}Sr/^{88}Sr = 0.1194$, and repeated NBS 987 measurements yielded a value of 0.71025 ± 0.00002 ($2\sigma_{mean}$, $n = 24$).

3.2 Headspace gas sampling and analyses

Bulk sediments (3 ml) were sampled from the core to analyze the chemical compositions and isotopic ratios of headspace gas at approximately 40 cm ~ 82 cm intervals using a 5 ml cutoff plastic

syringe. The sediments were extruded into 20 ml serum glass vials, and 2 ml of saturated NaCl solution was added to them. The vials were immediately capped with rubber septa and sealed with aluminum crimp caps. Headspace gas was extracted by heating the sediment samples at 60°C for 30 minutes at the KIGAM, following the procedure described by Pimmel and Claypool (2001). Aliquot of the headspace gas sample was injected into an Agilent Technologies 7890A gas chromatography with both a flame ionization detector and a thermal conductivity detector to determine the hydrocarbon composition (C_1-C_6) and CO_2. The reproducibility was less than 3% based on repeated standard analyses.

The carbon and hydrogen stable isotopic compositions ($\delta^{13}C_{CH4}$, $\delta^{13}C_{CO2}$, and δD_{CH4}) in headspace gas samples were analyzed by a compound-specific isotope ratio-monitoring gas chromatography/mass spectrometer at Isotech Laboratories Inc. (Champaign, IL, USA). The carbon and hydrogen isotopic values are reported in the conventional δ-notation in permil (‰) relative to V-PDB and V-SMOW, respectively. The reproducibility of the analyses was ±0.1‰ for carbon and ±2‰ for hydrogen.

3.3 MDAC sampling and analyses

The cores for the sedimentological study were cut in the laboratory at KIGAM. One half of each core was preserved as an archived core and the other half was further processed as a working core. MDACs were hand-picked from the split cores of Sites16GH-P3 and 16GH-P4 at the KIGAM (Figure 2; Table 1). These samples were stored at approximately 4°C in the refrigerator until the analyses (< 3 months). Before analysis, the MDAC was washed repeatedly with Milli-Q water (resistivity of 18.2 MΩ·cm), and sonicated for a few minutes to eliminate adhered materials. It was washed again with Milli-Q water and dried at 60°C in an oven for 12 hours.

The thin sections of selected MDACs were observed using a polarization microscope (Nikon LV100N POL) at Yonsei University. The microstructure of the MDACs was examined on freshly fractured surfaces using a scanning electron microscope (SEM; JEOL JSM-5410) at Yonsei University.

For the analyses of bulk mineralogy and isotopic compositions ($\delta^{13}C$ and $\delta^{18}O$) of MDACs, the selected MDAC samples (> 20 g) were finely ground using a mortar and pestle and then thoroughly mixed for homogenization, following the method by Tong et al. (2019). In addition, the surface of the MDAC cutting prepared for the thin section shows little variation in texture and structure within each sample. As a result, the measured mineralogy and isotopic compositions represent the average of each MDAC sample. The bulk mineralogy and the relative abundance of carbonate minerals were determined through X-ray diffraction (XRD) using a Miniflex II XRD (RIGAKU) at Yonsei University. The ground MDAC

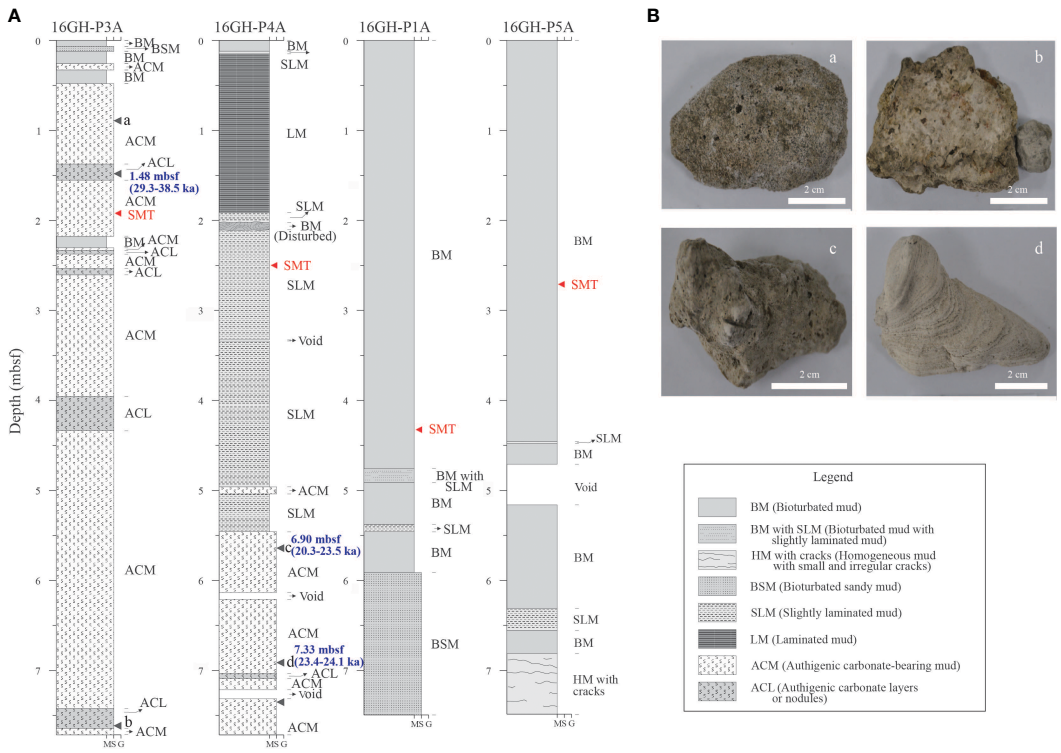

FIGURE 2
(A) Lithology of core sediment from Sites 16GH-P1, 16GH-P3, 16GH-P4, and 16GH-P5 in the southwestern part of the Ulleung Basin (mbsf: meters below seafloor). **(B)** Photographs of methane-derived authigenic carbonates (MDACs) from (a) 0.90 mbsf at Site 16GH-P3 (massive-porous type), (b) 7.69 mbsf at Site 16GH-P3 (semi-/un-consolidated type), (c) 5.70 mbsf at Site 16GH-P4 (massive-porous type), and (d) 6.90 mbsf at Site 16GH-P4 (massive-laminated type). The black closed arrows at Site 16GH-P3 and Site 16GH-P4 are core depths and ages of MDACs determined by U-Th dating, and the red closed arrow indicates the current SMT depth. The lithology description was used in the cores for sedimentological study at Sites 16GH-P1A, 16GH-P3A, 16GH-P4A, and 16GH-P5A. The M, S, and G in the X-axis of **(A)** are mud, sand, and gravel, respectively.

sample was thoroughly mixed homogeneously with corundum (Al_2O_3) powder in a 1:1 weight ratio. The XRD analysis was conducted on the powder samples under Cu-Kα radiation, utilizing a step-scan mode with 0.02° step, 1 sec/step scanning time, and 2° – 55° 2θ range. The analysis was performed using a 6-sample holder. Semi-quantitative analysis of mineral composition was conducted with the Reference Intensity Ratio (RIR) method (Hubbard et al., 1976; Hubbard and Snyder, 1988; Park et al., 2018). The ratio of peak intensities between corundum and major minerals was determined from the results of X-ray diffraction analysis. The quantitative values were then calculated based on the theoretical RIR values.

An aliquot of the bulk MDAC sample (~5 mg) from 0.90 mbsf to 7.69 mbsf at Site 16GH-P3 and from 5.70 mbsf to 7.33 mbsf at Site 16GH-P4 was reacted with 100% H_3PO_4 at 90°C for 5 minutes, and the evolved CO_2 gas was automatically injected into a VG Prism SIRMS in the KBSI for $\delta^{13}C$ and $\delta^{18}O$ analyses. The analytical reproducibility for $\delta^{13}C$ and $\delta^{18}O$ was < ± 0.1‰. Isotopic values are reported in the conventional δ-notation relative to V-PDB for carbon and oxygen.

Uranium (U)-thorium (Th) dating was performed at the NERC Isotope Geosciences Laboratory, British Geological Survey. Sample powders (1.6 mg ~ 8.9 mg) were drilled from 3 MDACs, which were from 3.30 mbsf at Site 16GH-P3, and 6.90 mbsf and 7.33 mbsf at Site 16GH-P4, using a hand-held microdrill. U and Th were separated, concentrated, and measured as described in Crémiere et al. (2016). These samples were dissolved in 8 M HNO_3 and then centrifuged to separate the soluble carbonate fraction from the insoluble detritus. The detritus was digested using a mixture of $HClO_4$:HF:HNO_3 (1:2:8 vol.), dried, and redissolved in 1 M HCl. U and Th were preconcentrated via iron co-precipitation and separated via column ion chromatography (Edwards et al., 1987). Isotope ratios were measured with an MC-ICP-MS (Thermo Finnigan). U-Th age calculations were carried out by the approach of Cheng et al. (2013), and a detrital correction was applied based on average measured $^{232}Th/^{238}U$, $^{230}Th/^{238}U$, and $^{234}U/^{238}U$ activity ratios of carbonate-free detritus samples from the Ulleung Basin.

4 Results

4.1 Sedimentary facies

Sediments in the cores are classified into eight sedimentary facies, mainly based on grain size, sedimentary structures, and distribution pattern of MDACs (Figure 2A). Among them, muddy sediments can be divided into six types: bioturbated mud (BM), bioturbated mud with slightly laminated mud (BM with SLM), homogeneous mud with small and irregular cracks (HM with cracks), bioturbated sandy mud (BSM), slightly laminated mud (SLM), and laminated mud (LM). Laminae are mostly less than a few mm thick and usually consist of coarser and finer (silt-clay) couplets in the LM interval, whereas they are not sharp and distinctly differentiated into coarse-fine couplets in the SLM interval. The BM facies is the most common mud facies in the upper part of the core from Sites 16GH-P1 and 16GH-P5 (non-chimney sites) and is characterized by various burrow structures, such as circular, oval, tubular, or irregular shapes. In contrast, the sediment from Sites 16GH-P3 and 16GH-P4 (chimney sites) is characterized by abundant MDACs in the mud facies (Figure 2A). These sedimentary facies with MDACs can be divided largely into two types: authigenic carbonate-bearing mud (ACM: mud with randomly scattered authigenic carbonate nodules) and authigenic carbonate layers or nodules (ACL) (Figure 2A).

4.2 Geochemical properties of pore fluids

The chemical properties of the pore fluids are shown in Figure 3 and Supplementary Table 1. The Cl^- concentration at all sites can be divided into two groups. The first group, found at Sites 16GH-P3 and 16GHP-P4 (chimney sites), shows a constant Cl^- concentration from the seafloor to 1.50 mbsf (~533 mM) and 0.78 mbsf (~552 mM), respectively. Below 1.50 mbsf at Site 16GH-P3, Cl^- concentration significantly increases and remains constant (~552 mM). Similarly, at Site 16GH-P4, Cl^- concentration gradually increases and maintains a constant value (~571 mM) from 1.28 mbsf to 4.55 mbsf. It reaches a maximum value (609 mM) at approximately 5.58 mbsf ~ 6.05 mbsf at Site 16GH-P4 (Figure 3A; Supplementary Table 1). In contrast, the second group, observed at Sites 16GH-P1 and 16GH-P5 (non-chimney sites), exhibits a constant Cl^- concentration (~533 mM) without significant variation with depth. The downcore profile of Na^+ concentrations at each site generally follows a trend similar to that of Cl^- (Figure 3A).

The SO_4^{2-} concentration at all sites decreases from the seawater value (~30 mM; UBGH2 Scientists, 2010) to ~0 mM (Figure 3A; Supplementary Table 1). The current SMT (hereafter SMT) depth is determined by extrapolating the depth where the SO_4^{2-} concentration reaches 0 mM. The estimated SMT depth of Sites 16GH-P3 and 16GH-P4 (chimney sites) is located at 1.9 mbsf and 2.5 mbsf, respectively, whereas it reaches 4.3 mbsf and 2.7 mbsf at Sites 16GH-P1 and 16GH-P5 (non-chimney sites), respectively. (Table 1). The maximum Ba^{2+} concentration in each site is observed around the SMT and Site 16GH-P3 has the lowest maximum Ba^{2+} concentration among the study sites (Figure 3A).

The alkalinity ranging from 8.9 mM to 60.8 mM increases from the seafloor to the SMT and then shows relatively constant concentration at Site 16GH-P3 or a slightly increasing trend at Sites 16GH-P1, 16GH-P4, and 16GH-P5 (Figure 3A; Supplementary Table 1). In contrast, the downcore profiles of Ca^{2+} and Sr^{2+} concentrations have decreasing trends at all sites. The Mg^{2+} concentration is constant at Sites 16GH-P1 and 16GH-P3 but shows an increasing trend with depth at Sites 16GH-P4 and 16GH-P5. At all sites, the K^+, H_4SiO_4, and B concentrations are generally higher than those in seawater (Figure 3A; Supplementary Table 1). The δD and $\delta^{18}O$ values in pore fluids at all sites vary in narrow ranges from -2.8‰ to 0.2‰ and from -0.2‰ to 0.3‰, respectively. The downcore profile of $\delta^{18}O$ at Site 16GH-P4 shows a slightly decreasing trend compared to other sites. The $\delta^{13}C_{DIC}$ value in pore fluid varies from -28.2‰ to 5.3‰.

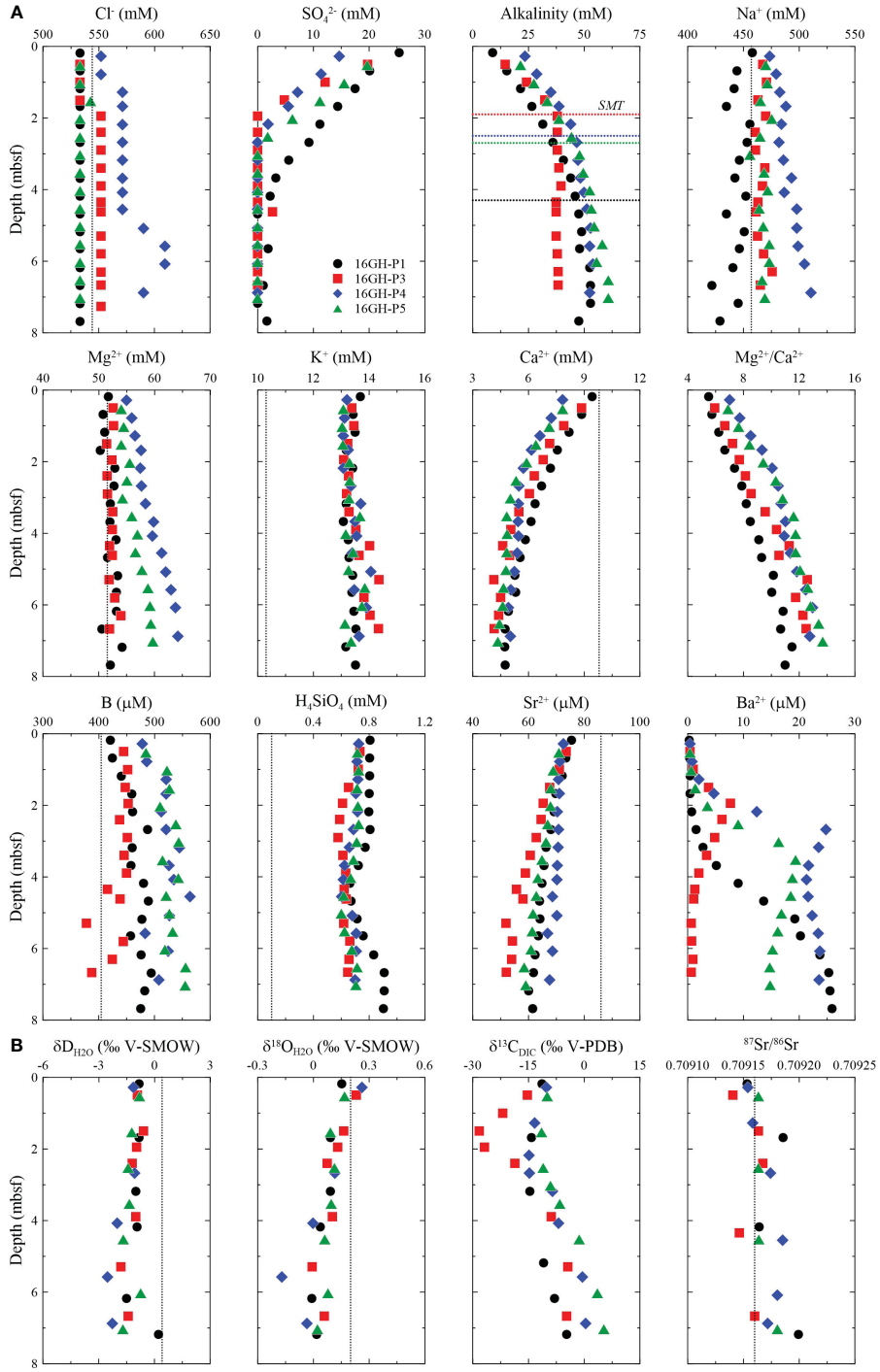

FIGURE 3
Downcore profiles of **(A)** Cl^-, SO_4^{2-}, alkalinity, Na^+, Mg^{2+}, K^+, Ca^{2+}, Mg^{2+}/Ca^{2+}, B, H_4SiO_4, Sr^{2+}, and Ba^{2+}, and **(B)** δD_{H2O}, $\delta^{18}O_{H2O}$, $\delta^{13}C_{DIC}$, and $^{87}Sr/^{86}Sr$ in pore fluids from Sites 16GH-P1, 16GH-P3, 16GH-P4, and 16GH-P5. The horizontal black, red, blue, and green lines in the downcore profile of alkalinity represent the current SMT depth at Sites 16GH-P1, 16GH-P3, 16GH-P4, and 16GH-P5, respectively. The vertical black dashed lines represent the chemical concentration and isotopic ratios of seawater from the Ulleung Basin (UBGH2 Scientists, 2010; Kim et al., 2013).

The minimum $\delta^{13}C_{DIC}$ value in each site is observed around the SMT, ~3.18 mbsf (-14.7‰) at Site 16GH-P1, ~1.50 mbsf (-28.2‰) at Site 16GH-P3, ~2.18 mbsf (-14.9‰) at Site 16GH-P4, and ~1.53 mbsf (-11.5‰) at Site 16GH-P5 (Figure 3B; Supplementary Table 1). The maximum $\delta^{13}C_{DIC}$ value is observed at 7.03 mbsf of Site 16GH-P5 (5.3‰). The $^{87}Sr/^{86}Sr$ ratios are relatively constant (0.70917 ± 0.00001, n = 19) (Figure 3B; Supplementary Table 1), which is similar to that of the open seawater (~0.70917; Paytan et al., 1993) and seawater from the Ulleung Basin (~0.70917; Kim et al., 2013).

10.3389/fmars.2023.1156918

4.3 Geochemical properties of headspace gas

The CH_4 is the primary hydrocarbon component in headspace gas samples at all sites, while C_{2+} is the trace composition. The CH_4 concentration is the lowest near the seafloor (< 300 ppm vol.) and increases sharply below the SMT (> 2,900 ppm vol.) (Figure 4A; Supplementary Table 2), irrespective of the seismic structures. The C_1/C_{2+} ratios at Sites 16GH-P3, 16GH-P4, and 16GH-P5 generally exceed 300, whereas they cannot be calculated at Site 16GH-P1 because the concentration of C_{2+} is below the detection limit. The CO_2 concentration does not show a distinct trend with depth, but its concentration varies from 1.0% vol. to 4.0% vol. at all sites (Figure 4A; Supplementary Table 2). As the measured CO_2 concentrations in headspace gas samples are at least 25 times higher than that in the atmosphere (~420 ppm vol., https://www.climate.gov/news-features/understanding-climate/climate-change-atmospheric-carbon-dioxide), the influence of atmospheric CO_2 in headspace gas is negligible.

The values of $\delta^{13}C_{CH4}$, δD_{CH4}, and $\delta^{13}C_{CO2}$ range from -85.9‰ to -67.2‰, from -204‰ to -190‰, and from -24.8‰ to -16.1‰, respectively. The minimum values for $\delta^{13}C_{CH4}$ and $\delta^{13}C_{CO2}$ generally occur near the SMT and increase with depth below the SMT (Figure 4B; Supplementary Table 2).

4.4 Petrography, mineralogy, isotopic compositions, and age of MDACs

MDACs can be roughly subdivided into three types based on their morphology: 1) massive-porous type, 2) massive-laminated type, and 3) semi-/un-consolidated type (Figure 2B). Massive-porous MDACs (a and c in Figure 2B) are mainly composed of microcrystalline magnesian calcite (Mg-calcite), fibrous aragonite, bioclasts, and detrital fragments (Figures 5B–D). Bioclasts, planktonic foraminifers, diatoms, and radiolarians are the dominant biogenic components of this type; framboidal pyrite is often found within the inner walls of shells. Massive-laminated MDACs (d in Figure 2B) have a massive and slightly wavy-laminated structure with a small number of bioclasts. The average thickness of the lamination varies from 1 mm to 2 mm, and planktonic foraminifers are randomly dispersed in the matrix (Figure 5A). Detrital fragments are also found as a form of anhedral and/or subhedral crystals (Figure 5E). Semi-/un-consolidated MDACs (b in Figure 2B) mainly consist of a microcrystalline matrix with many irregular-shaped pores. In the matrix, diatomaceous fragments with many shapes and sizes are found (Figure 5F).

The content of carbonate minerals in MDACs ranges from 25.6 wt.% of bulk MDAC to 87.8 wt.% of bulk MDAC (Supplementary

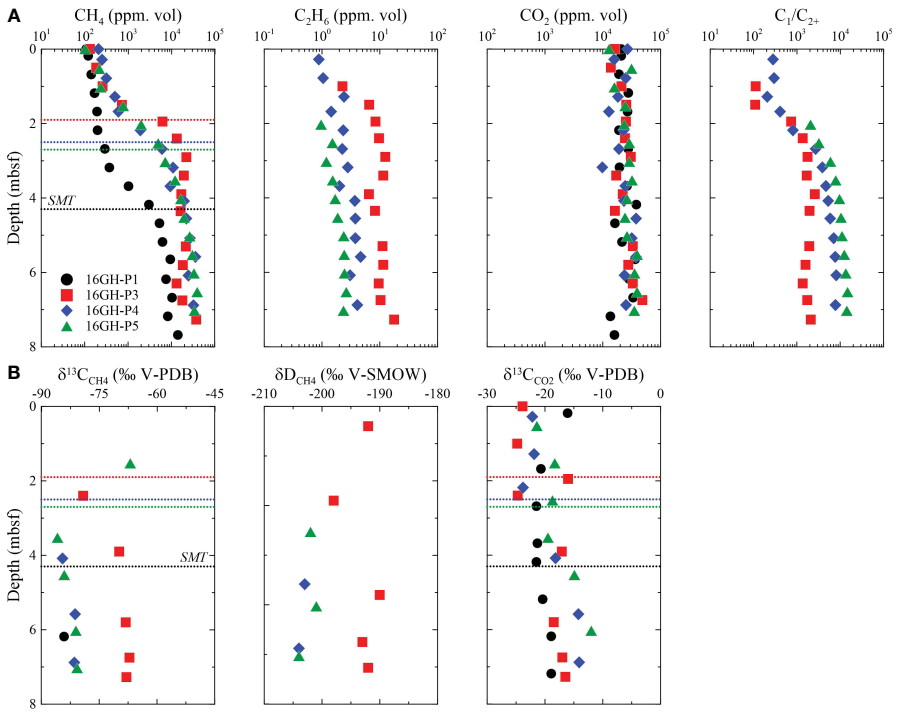

FIGURE 4
Downcore profiles of **(A)** CH_4, C_2H_6, CO_2, and C_1/C_{2+}, and **(B)** $\delta^{13}C_{CH4}$, δD_{CH4}, and $\delta^{13}C_{CO2}$ of headspace gas samples from Sites 16GH-P1, 16GH-P3, 16GH-P4, and 16GH-P5. The dashed line represents the current SMT in each site (black: Site 16GH-P1, red: Site 16GH-P3, blue:16GH-P4, green: Site 16GH-P5).

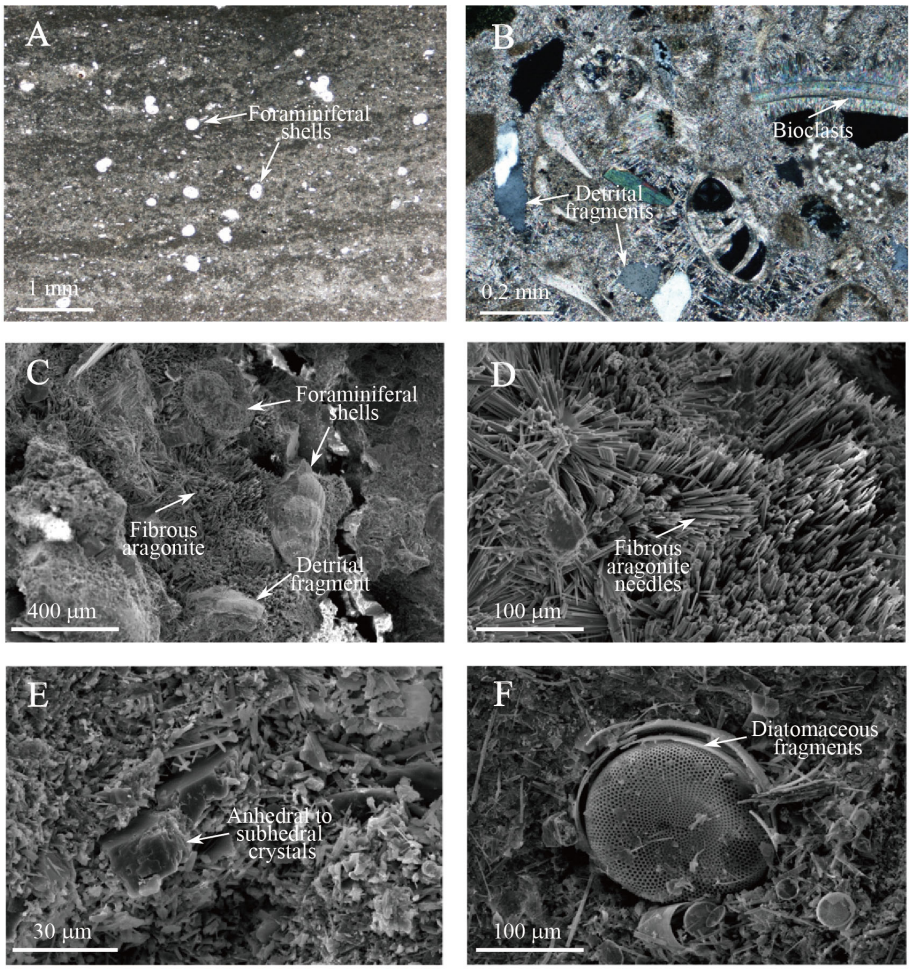

FIGURE 5
Photomicrographs and scanning electron micrographs of MDACs. **(A)** Authigenic carbonate of the massive-laminate type from 6.90 mbsf at Site 16GH-P4. White spots indicate planktonic foraminiferal shells. **(B)** Bioclasts are abundant, and aragonite is present as acicular cement and microcrystalline matrix from 1.48 mbsf at Site 16GH-P3. **(C-D)** Bioclasts and detrital fragments are cemented by fibrous aragonite crystals from 1.48 mbsf of Site 16GH-P3. **(E)** Matrix of microcrystalline magnesian calcite with anhedral and/or subhedral crystals with a few µm in size at 6.90 mbsf of Site 16GH-P4. **(F)** Diatomaceous fragments are found in many shapes and sizes at 7.69 mbsf of Site 16GH-P3.

Table 3). Calcite, aragonite, and Mg-calcite are the dominant carbonate minerals of MDACs, and dolomite is minor (< 1 wt.% of bulk MDAC). MDACs from 7.69 mbsf at Site 16GH-P3 and from 6.63 mbsf, 6.90 mbsf, and 7.33 mbsf at Site 16GH-P4 have a high aragonite content (> 49.5 wt.% of bulk MDAC), whereas MDACs from 3.30 mbsf at Site 16GH-P3 and 5.70 mbsf at Site 16GH-P4 contain abundant Mg-calcite (> 50 wt.% of bulk MDAC). The non-carbonate minerals in MDACs mainly consist of silicates (plagioclase, K-feldspar, quartz, illite, and chlorite) as detrital components (Figure 6A; Supplementary Table 3).

The $\delta^{13}C_{MDAC}$ and $\delta^{18}O_{MDAC}$ values vary from -43.0‰ to -31.3‰ and from 3.9‰ to 5.8‰ at Site 16GH-P3, and from -44.9‰ to -41.7‰ and from 4.1‰ to 5.7‰ at Site 16GH-P4, respectively. MDACs above a depth of 1.50 mbsf at Site 16GH-P3 exhibit higher $\delta^{13}C$ (> -34.3‰) and lower $\delta^{18}O$ (< 4.1‰) values compared to those found below this depth ($\delta^{13}C$ = -43.1‰ ~ -41.6‰; $\delta^{18}O$ = 5.5‰ ~ 5.8‰) (Figure 6B; Supplementary Table 3). Except for these two MDACs, the $\delta^{13}C_{MDAC}$ values are constant (-44.9‰ ~ -41.6‰) at Sites 16GH-P3 and 16GH-P4, irrespective of the morphology. In contrast, the $\delta^{18}O_{MDAC}$ value is the lowest (4.1‰) in the massive-laminated MDAC from Site 16GH-P4 (Supplementary Table 3).

U-Th ages of MDACs are presented in Figure 2A and Supplementary Table 3, although they have large errors. The corrected U-Th ages of the MDAC at 1.48 mbsf of Site 16GH-P3 range from 29.3 ± 15.7 ka BP to 38.5 ± 12.4 ka BP (n = 3). The age at 6.90 mbsf and 7.33 mbsf of Site 16GH-P4 varies from 20.3 ± 8.0 ka BP to 23.5 ± 12.2 ka BP (n = 3) and from 23.4 ± 4.3 ka BP to 24.1± 4.7 ka BP (n = 2), respectively (Figure 2A; Supplementary Table 3). The MDAC from Site 16GH-P3 has an older age than those from Site 16GH-P4.

5 Discussion

5.1 Sedimentary facies distribution and depositional environment

The BM facies was mainly observed from the seafloor to 5.90 mbsf and 6.39 mbsf at Sites 16GH-P1 and 16GH-P5 (non-chimney

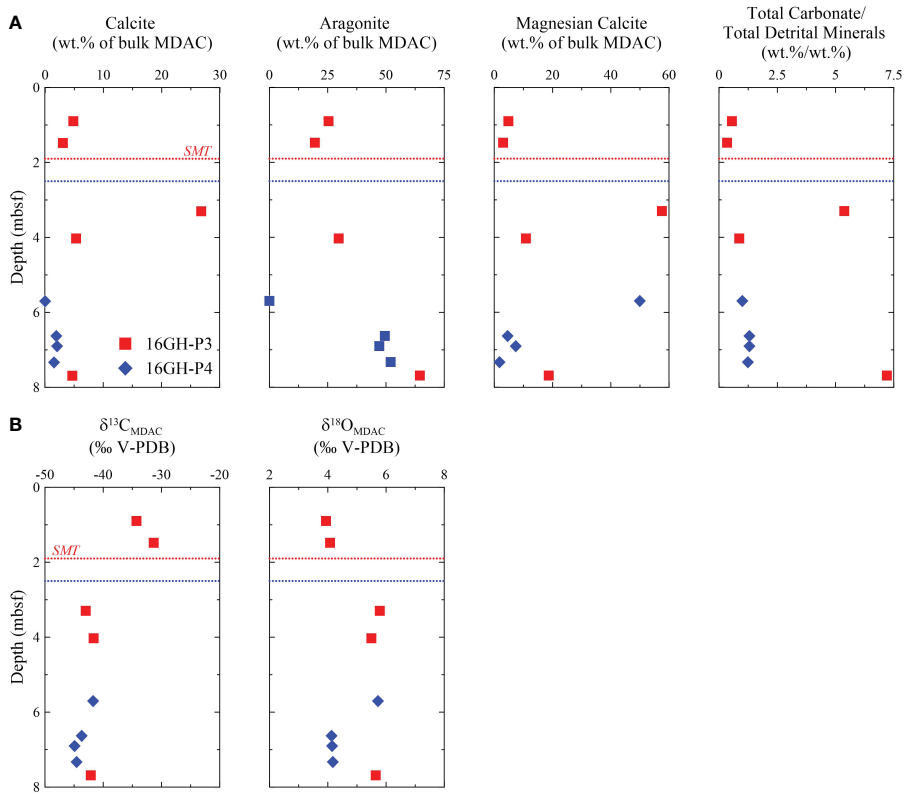

FIGURE 6
Downcore profiles of **(A)** calcite, aragonite, and magnesian calcite content, and total carbonate/total detrital minerals by XRD analysis, and **(B)** $\delta^{13}C$ and $\delta^{18}O$ in MDACs from Sites 16GH-P3 and 16GH-P4. The horizontal red and blue dashed lines represent the current SMT depth at Sites 16GH-P3 and 16GH-P4, respectively.

sites), respectively, while the relatively thin SLM, BSM, and HM appeared below these depths (Figure 2A). The BM interval represents hemipelagic sediment deposition under well-oxygenated conditions (Tada et al., 1999; Gorbarenko and Southon, 2000) during the high sea-level period of marine isotope stage (MIS) 1 (Park et al., 2006; KIGAM, 2016). In the lower part of 16GH-P1, the BM facies changes into BSM facies (Figure 2A). This facies was formed by the increase in coarser sediments, such as sandy particles, which were probably derived from the neighboring continental shelf during the sea invasion period after the Last Glacial Maximum (KIGAM, 2016). The period of sedimentary deposition at Sites 16GH-P1 and 16GH-P5 was estimated to cover the early post-glacial of Late Pleistocene to Holocene high sea-level period.

Sites 16GH-P3 and 16GH-P4 (chimney sites) contain abundant MDACs as randomly scattered nodules or layers form (ACM and ACL facies in Figure 2A). In particular, this distribution pattern of MDACs is well developed in the sediments throughout the core at Site 16GH-P3. At Site 16GH-P4, the LM and SLM facies are thick at the top of the core (0.1 mbsf to ~5.4 mbsf). According to the previous studies (e.g., KIGAM, 2016), it was interpreted that the GH chimney mound underwent a sequential process involving formation, uplift to the sea floor, and erosion. Subsequently, LM and SLM facies at Site 16GHP-P4 were formed during the deglacial phase at the top of the core. The U-Th dating of MDACs also indicates that the top interval of ~5.4 mbsf at Site 16GH-P4 was deposited during a younger period than that of Site 16GH-P3 (Figure 2A).

The matrix of porous MDACs primarily comprises microcrystalline Mg-calcite, and their cavities are mostly filled with aragonite in the form of acicular needles or sometimes botryoidal cement. Fibrous cements and micritic laminated fabrics are also observed in this type of MDAC (Figure 5; Supplementary Table 3). These observations provide evidence for the mixing of methane-rich fluids with seawater and/or the presence of methane and sulfide (e.g., Peckmann et al., 2001; Magalhães et al., 2012).

5.2 Source of pore fluid and CH_4 gas

Cl^- concentrations and isotopic values of water (δD and $\delta^{18}O$) in pore fluids at Sites 16GH-P1 and 16GH-P5 vary in narrow ranges throughout the entire cores (Cl^- = 533 mM ~ 543 mM, δD = -1.7‰ ~ 0.2‰, $\delta^{18}O$ = 0.0‰ ~ 0.2‰) (Figures 3, 7; Supplementary Table 1), and are close to the values of the present-day bottom seawater (Cl^- = 544 mM, $\delta^{18}O$ = 0.2‰, δD = 0.4‰) from the Ulleung Basin (UBGH2 Scientists, 2010; Kim et al., 2013). Hence, the source of pore fluids at these sites mainly originates from ambient seawater. At Site 16GH-P4, Cl^- concentrations are higher

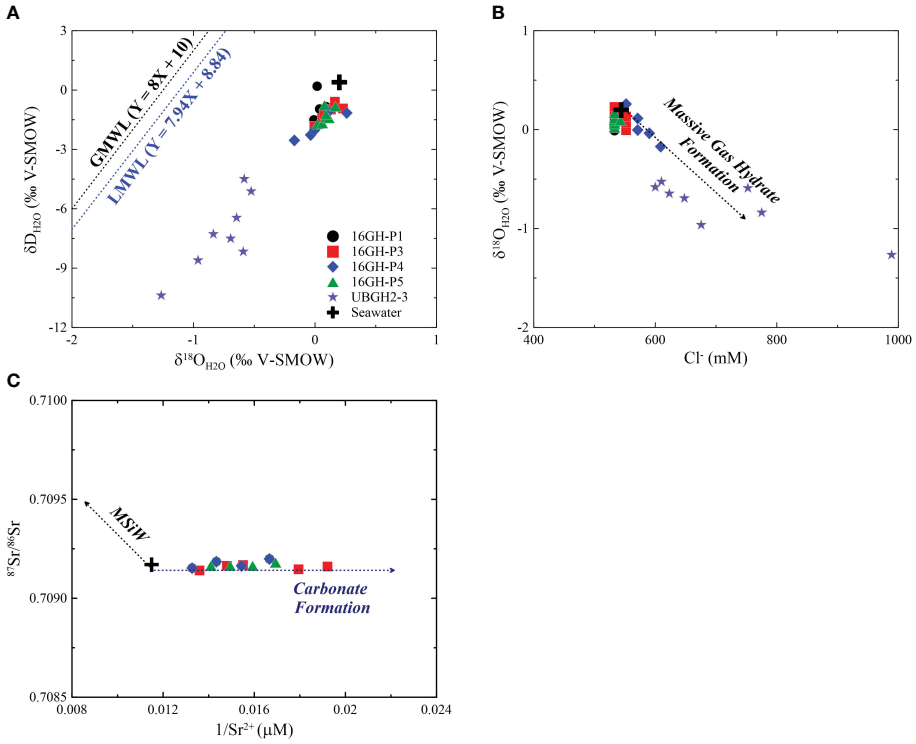

FIGURE 7
Scatter plots of **(A)** δD_{H2O} versus $\delta^{18}O_{H2O}$, **(B)** $\delta^{18}O_{H2O}$ versus Cl^-, and **(C)** $^{87}Sr/^{86}Sr$ versus $1/Sr^{2+}$ in bottom seawater from Site UBGH2-3 and pore fluids from Sites 16GH-P1, 16GH-P3, 16GH-P4, 16GH-P5, and UBGH2-3 (UBGH2 Scientists, 2010; Kim et al., 2013). The δD and $\delta^{18}O$ data of seawater and pore fluid from Site UBGH2-3 are from Kim et al. (2013). The GMWL is the global meteoric water line (Craig, 1961) and the LMWL is the local meteoric water line (Lee et al., 1999). The trend of massive gas hydrate formation in Figure 7B is modified from Tomaru et al. (2006) and the trends of carbonate formation and MSiW in Figure 7C are adapted from Kim et al. (2016). MSiW is marine silicate weathering.

than that of seawater and vary from 591 mM to 609 mM below 5.08 mbsf (Figure 3A; Supplementary Table 1). However, the water stable isotopes (δD and $\delta^{18}O$) at this site generally have lower values (δD = -2.5‰ ~ -1.1‰, $\delta^{18}O$ = -0.2‰ ~ 0.3‰) than those at the other studied sites (δD = -1.8‰ ~ 0.2‰, $\delta^{18}O$ = 0.0‰ ~ 0.2‰), and there is a linear correlation between them (r^2 = 0.85) (Figure 7A; Supplementary Table 1). Furthermore, $\delta^{18}O$ and Cl^- exhibit a negative correlation (r^2 = 0.72) (Figure 7B). During the MIS 2 in the Ulleung Basin, seawater had a low $\delta^{18}O$ value by the freshening of surface water associated with the isolation from the Pacific Ocean (Kim et al., 2000; Lee, 2007; Wu et al., 2020), which is a plausible source for the low $\delta^{18}O$ values of pore fluids. However, this fluid cannot account for the observed high Cl^- concentration in pore fluid at this site. Such characteristics have usually been reported in the bottom water and/or pore fluid in Arctic regions (Alexeev and Alexeeva, 2003; Charkin et al., 2017; Kim et al., 2022) as a result of the formation of submarine ice and/or permafrost within the sediments. Since the water and sediment columns in the southern Ulleung Basin have not been frozen annually, these mechanisms are not attributed to high Cl^- concentration with low δD and $\delta^{18}O$ values in pore fluid observed at Site 16GH-P4. Instead, this can be attributed to the formation of massive GH near the seafloor within fine-grained sediment layers, such as mud, characterized by low permeability (Torres et al., 2004; Riedel et al., 2006; Tomaru et al., 2006; Collett et al., 2008; Hong et al., 2017). In general, when massive GHs form near the seafloor sediment in this layer associated with high upward gas flux, pore fluids exhibit higher Cl^- concentrations and lower δD and $\delta^{18}O$ values in comparison to fluids from the non-GH bearing intervals. Conversely, heavy water isotopes (δD and $\delta^{18}O$) tend to be preferentially incorporated into the clathrate structure. These occur because the fluid released during GH formation does not equilibrate with the pore fluid in the surrounding sediment layers due to low permeability. In contrast, during the formation of the disseminated GH in the sand layer, the pore fluids in the GH-bearing intervals equilibrate with the surrounding sediment fluids due to their high permeability. Consequently, this leads to similar Cl^- concentrations as well as δD and $\delta^{18}O$ values in pore fluids from both GH-bearing and non-GH bearing intervals. Although massive and/or disseminated GHs were not found in the cores investigated, Site 16GH-P4 is located ~0.1 km from Site UBGH2-3, where high Cl^- concentrations (maximum Cl^- = ~1440 mM) and low δD and $\delta^{18}O$ values (minimum δD = ~-14.7‰; minimum $\delta^{18}O$ = ~-1.6‰) have been reported in fluids collected from massive GHs-bearing intervals below 6 mbsf during the UBGH2 Expedition (Kim et al., 2013; Hong et al., 2014). Hence, it is postulated that the similar trends in Cl^- concentrations and δD and $\delta^{18}O$ values in pore fluids at Site 16GH-P4 are impacted by massive GH formation occurring below the depth of retrieved core.

The Cl^- concentrations below 1.95 mbsf (~552 mM) at Site 16GH-P3 are slightly higher than those above this depth (~533

mM), and there is no significant change in δD and $\delta^{18}O$ values throughout the entire sampling depth (Figures 3, 7; Supplementary Table 1). The pore fluid would be potentially influenced by the water-rock interactions or the fluids migrated from the deep sediment; however, the exact mechanism cannot be identified given the dataset.

High C_1/C_{2+} ratios (commonly > 300) in headspace gas samples from Sites 16GH-P1, 16GH-P3, 16GH-P4, and 16GH-P5 (Figures 4A, 8; Supplementary Table 2) indicate that CH_4 predominantly originates from microbial source rather than thermogenic source (Bernard et al., 1978; Whiticar, 1999; Pape et al., 2010; Kim et al., 2011; Kim et al., 2012; Choi et al., 2013; Milkov and Etiope, 2018). The $\delta^{13}C_{CH4}$, δD_{CH4}, and $\delta^{13}C_{CO2}$ values consistently support this interpretation. All headspace gas samples plotted in the region of microbial CH_4 origin via the CO_2 reduction in the diagram, displaying the relationship between $\delta^{13}C_{CH4}$ and C_1/C_{2+} (Figure 8A; Supplementary Table 2). Furthermore, the diagrams depicting the relationships of $\delta^{13}C_{CH4}$ versus δD_{CH4} and $\delta^{13}C_{CH4}$ versus $\delta^{13}C_{CO2}$ provide additional evidence for the microbial CH_4 origin via the CO_2 reduction pathway (Figures 8B, C). This observation aligns with the outcomes of numerous prior investigations conducted in the Ulleung Basin (Kim et al., 2011; Kim et al., 2012; Choi et al., 2013; Kim et al., 2013).

5.3 Occurrence of ongoing marine silicate weathering (MSiW)

Alkalinity in pore fluids above and within the SMT is usually produced by organic matter degradation via POCSR and AOM that consumes SO_4^{2-} as the main electron acceptor. Assuming SO_4^{2-} is mainly derived from the overlying seawater for these reactions (~30 mM; UBGH2 Scientists, 2010), alkalinity can be maximized up to ~60 mM by POCSR and ~30 mM by AOM with the complete consumption of SO_4^{2-}. Hong et al. (2014) have revealed that AOM is a dominant reaction for both carbon and sulfur cycles around the SMT, accounting for at least 85% of these cycles within the chimney structures of the Ulleung Basin in comparison with POCSR. As Sites 16GH-P3 and 16GH-P4 show chimney structures in the subsurface (Figure 1; see Section 2 "Regional Setting"), we can estimate the maximum alkalinity around the SMT of these sites as < ~35 mM by the simple mixing model of two end-members given that the POCSR:AOM is 0.15:0.85. The alkalinity should be lower than this value because of the ongoing carbonate precipitation within the sediment column at both sites as inferred from the decreasing downcore profile of Ca^{2+} and Sr^{2+} concentrations in pore fluids and the existence of MDACs (Figures 2, 3A). However, the measured alkalinity concentrations in the pore fluid around the SMT of Sites

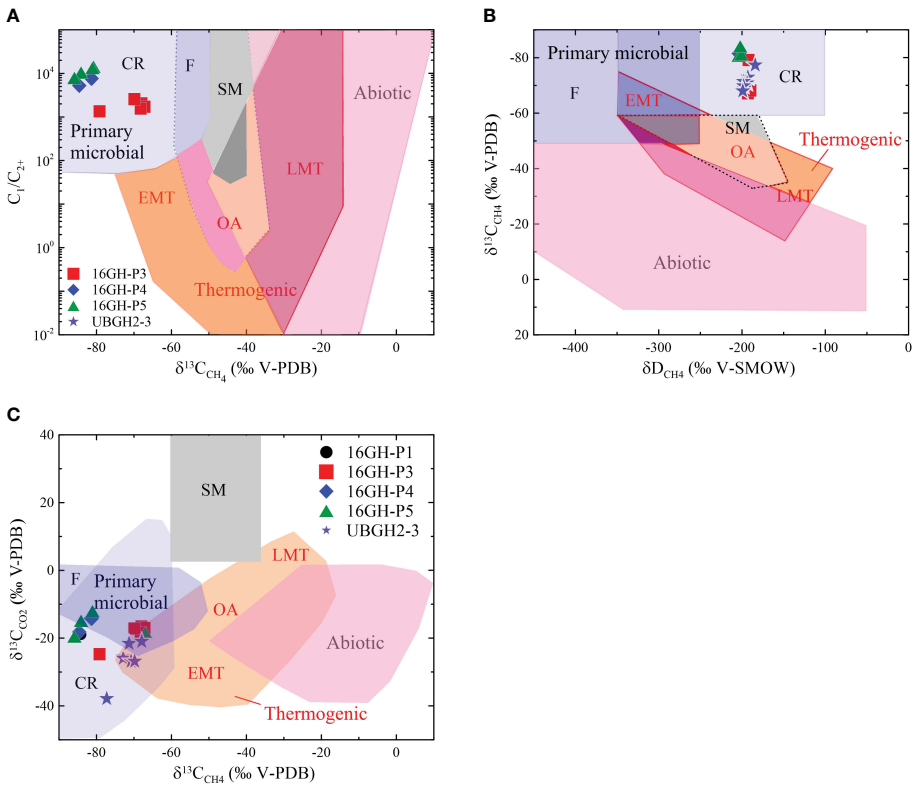

FIGURE 8
(A) Genetic diagram of C_1/C_{2+} versus $\delta^{13}C_{CH4}$ (after Milkov and Etiope, 2018) of headspace gas samples from Sites 16GH-P3, 16GH-P4, 16GH-P5, and UBGH2-3. **(B)** $\delta^{13}C_{CH4}$ versus δD_{CH4} diagram of headspace gas samples from Sites 16GH-P3, 16GH-P4, 16GH-P5, and UBGH2-3 (after Milkov and Etiope, 2018). **(C)** Genetic diagram of $\delta^{13}C_{CH4}$ versus $\delta^{13}C_{CO2}$ (after Milkov and Etiope, 2018) of headspace gas samples from Sites 16GH-P1, 16GH-P3, 16GH-P4, 16GH-P5, and UBGH2-3. The gas compositions and isotopic values of headspace gas samples are from Site UBGH2-3 (KIGAM, 2011). CR, CO_2 reduction; F, methyl-type fermentation; SM, secondary microbial; EMT, early mature thermogenic gas; OA, oil-associated thermogenic gas; LMT, late mature thermogenic gas.

16GH-P3 and 16GH-P4 are ~38 mM and ~45 mM (Figure 3A; Supplementary Table 1), respectively, which (slightly) exceed the estimated concentration. In addition, the downcore alkalinity profile has an increasing trend below the SMT at Sites 16GH-P1, 16GH-P4, and 16GH-P5 (Figure 3A; Supplementary Table 1). These trends are not common and suggest that additional reactions should occur to account for the excess alkalinity in the fluid. The dissolved K^+, B, and H_4SiO_4 in most pore fluid samples from all sites show higher concentrations than those of bottom seawater (K^+ = 10.3 mM, B = 404 μM, H_4SiO_4 = 0.4 mM) (UBGH2 Scientists, 2010; Kim et al., 2013) as alkalinity increases. Additionally, the Mg^{2+} concentration of fluids from Sites 16GH-P4 and 16GH-P5, which mostly range from 54 mM to 64 mM, displays higher concentration than the bottom seawater (~51 mM; UBGH2 Scientists, 2010; Kim et al., 2013), with an increasing downcore profile (Figure 3A; Supplementary Table 1). Kim et al. (2016) have shown a similar result from the pore fluid at Site UBGH2-1_1 (Figure 1A) collected during the UBGH2 Expedition and this result was attributed to marine silicate weathering (MSiW) that converts CO_2 into alkalinity and releases dissolved cations in an anoxic marine system. Our fluid data also point to the occurrence of MSiW in the Ulleung Basin, which significantly impacts the geochemical properties of the pore fluids.

5.4 Influence of CH_4 and seawater on MDAC precipitation

The decreasing downcore profile of Ca^{2+} and Sr^{2+} concentrations at all cores investigated in this study generally shows a similar trend to that of SO_4^{2-} (Figure 3A). These results indicate that continuous carbonate precipitation takes place within the sediments, leading to the consumption of Ca^{2+} and Sr^{2+} in pore fluids (see Equation 3). The relationship between $^{87}Sr/^{86}Sr$ and $1/Sr^{2+}$ (Figure 7C) also supports this interpretation (Kim et al., 2016). Indeed, massive authigenic carbonates were found at Sites 16GH-P3 and 16GH-P4 (Figure 2). The measured $\delta^{13}C_{MDAC}$ values (-44.9‰ to -31.3‰) (Figure 6B; Supplementary Table 3) are lower than those of the organic matter reported in the Ulleung Basin (-24‰ to -21‰) (Choi et al., 2013; Kim et al., 2014) and the measured minimum $\delta^{13}C_{DIC}$ (-28.3‰ and -14.7‰ at Sites 16GH-P3 and 16GH-P4, respectively) in pore fluids (Figure 3; Supplementary Table 1). Hence, the $\delta^{13}C_{MDAC}$ value indicates the presence of an additional DIC source with a lower carbon isotopic value compared to that of pore fluids and organic matter within this basin when MDAC forms. We postulate that the migrating upward fluid, which contains ^{13}C-depleted CH_4 from the deep-seated sediment, is a reasonable source, as this fluid is involved in AOM around the SMT. This process leads to an increase in alkalinity via the production of bicarbonate (HCO_3^-) and subsequent MDAC precipitation (Paull et al., 1992; Aloisi et al., 2000; Peckmann et al., 2001; Aloisi et al., 2002; Naehr et al., 2007; Pierre et al., 2014; Crémière et al., 2016). Consequently, the carbon isotopic property of CH_4 migrating upward significantly inherits that of MDACs produced around the SMT. In general, the $\delta^{13}C_{MDAC}$ values associated with thermogenic CH_4 typically range from ~-40‰ to -20‰, while the values are less than -40‰ via AOM using microbial CH_4 (Naehr et al., 2007; Crémière et al., 2016; Crémière et al., 2018). $\delta^{13}C_{MDAC}$ values of all MDACs from Site 16GH-P4 that show massive-porous and -laminated morphologies are < -41.7‰ (Figure 6B; Supplementary Table 3), thus, AOM that mainly uses microbial CH_4 is incorporated to form MDACs. This finding is consistent with the CH_4 source in headspace gas samples near and below the SMT at this site (-88.0‰ < $\delta^{13}C_{CH4}$ < -81.5‰) (Figure 4; Supplementary Table 2). On the other hand, the wide range of $\delta^{13}C_{MDAC}$ values at Site 16GH-P3 implies that gas sources involved in the MDAC formation rely on the sampling depth (Figure 6B; Supplementary Table 3); 1) massive-porous MDACs above the SMT are related to thermogenic CH_4 ($\delta^{13}C_{MDAC}$ > -35.0‰), and 2) MDACs with semi-consolidated and massive-porous and -laminated morphologies below the SMT are associated with microbial CH_4 ($\delta^{13}C_{MDAC}$ = ~-42‰). $\delta^{13}C_{CH4}$ values (< -67.2‰) in all headspace gas samples below the SMT from Site 16GH-P3 (Figure 4; Supplementary Table 2) indicate that CH_4 has a predominantly microbial origin. In addition, to date, studies have revealed that the CH_4 from the seafloor to 250 mbsf in the Ulleung Basin is microbial origin via CO_2 reduction (Figure 8) based on geochemical features of headspace gas samples from the UBGH2 Expedition as well as other expeditions (Kim et al., 2012; Choi et al., 2013). Hence, thermogenic CH_4 does not involve AOM reaction and MDAC formation in the Ulleung Basin. Rather, the ^{13}C-enriched MDACs are likely affected by HCO_3^- from ambient seawater at this site because these MDACs have often been found in the sediment above the SMT (Peckmann and Thiel, 2004; Crémière et al., 2016; Pierre et al., 2017). The XRD results of MDACs, which display that aragonite and Mg-calcite are the predominant mineral compositions (Figure 6A; Supplementary Table 3), also support our interpretation. Theoretically, aragonite precipitation is kinetically favored in seawater-ventilated environments with high SO_4^{2-} concentration and it has generally low Mg^{2+}/Ca^{2+} ratios compared to high-Mg calcite (Burton, 1993; Mazzini et al., 2006). Indeed, MDACs are found at shallow sediment depth (< 8 mbsf) (Figure 2; Supplementary Table 3) where ambient seawater can influence sediments, and the Mg^{2+}/Ca^{2+} (5.9 to 12.8) in all pore fluids from Sites 16GH-P3 and 16GH-P4 have higher ratios compared to that of seawater (5.5) (Figure 3A; Supplementary Table 1). Thus, these results imply that sufficient conditions for the precipitation of aragonite and low-Mg calcite are provided at both Sites 16GH-P3 and 16GH-P4 rather than high-Mg calcite. Although MDAC morphology is not well matched with $\delta^{13}C_{MDAC}$, microscopic observations have revealed that massive-porous MDACs above the SMT contain abundant bioclasts, planktonic foraminifers, diatoms, radiolarians, and detrital fragments, as compared to MDACs below the SMT at Site 16GH-P3 (Figure 5B). The cavities in this type of MDAC (a and c in Figure 2B) can also act as conduit for CH_4-rich fluid and/or seawater migration due to their high porosity and permeability. Overall, the chemical properties of microbial CH_4 migrating upward are significantly inherited by MDACs at both Sites 16GH-P3 and 16GH-P4 whereas the properties of seawater prominently imprint MDACs found above the SMT at Site 16GH-P3.

5.5 Fluid source of MDAC

Carbonate minerals in MDACs from Sites 16GH-P3 and 16GH-P4 primarily consist of calcite, aragonite, and Mg-calcite, with minor amounts of dolomite. The proportions of calcite, aragonite, and Mg-calcite in the total carbonate minerals (sum of calcite, aragonite, dolomite, and Mg-calcite contents) at both sites range from 0% to 32%, from 3% to 100%, and from 0% to 94%, respectively (Supplementary Table 3). In general, the $\delta^{18}O_{MDAC}$ values are useful to reveal the fluid source during carbonate precipitation (e.g., Greinert et al., 2001; Naehr et al., 2007). Given that the $\delta^{18}O$ values of aragonite and calcite precipitated at isotopic equilibrium with temperature and $\delta^{18}O$ value of the bottom seawater in the Ulleung Basin, the theoretical $\delta^{18}O_{aragonite}$ and $\delta^{18}O_{calcite}$ values can be calculated using Equations 4 and 5, respectively (Kim and O'Neil, 1997; Kim et al., 2007).

$$\mathbf{1000ln\alpha_{aragonite-seawater}} = \mathbf{17.88} \times \frac{\mathbf{10^3}}{\mathbf{T}}\mathbf{(Kelvin)} - \mathbf{31.14} \quad (4)$$

$$\mathbf{1000ln\alpha_{calcite-seawater}} = \mathbf{18.03} \times \frac{\mathbf{10^3}}{\mathbf{T}}\mathbf{(Kelvin)} - \mathbf{32.42} \quad (5)$$

Assuming that the temperature and $\delta^{18}O$ value of the bottom seawater from Ulleung Basin at the present time are 0.5°C and 0.2‰ (V-SMOW) (UBGH2 Scientists, 2010; Kim et al., 2013), respectively, the theoretical $\delta^{18}O$ values of aragonite and calcite calculated by Equations 4 and 5 would be ~4.0‰ (V-PDB) and ~3.3‰ (V-PDB), respectively. The measured $\delta^{18}O_{MDAC}$ values above the SMT at Site 16GH-P3 are similar to the calculated $\delta^{18}O_{MDAC}$ value of aragonite (Supplementary Table 3), suggesting that pore fluid with a similar $\delta^{18}O$ value to that of present-day bottom seawater was involved during MDAC precipitation. For Site 16GH-P3, it is likely that the enrichment in ^{13}C for MDACs from above the SMT (> -34.3‰) compared to those from below the SMT (< -40%) is caused by incorporation of ^{13}C-rich HCO_3^- (~0‰) from seawater during carbonate precipitation (see Section 5.4). In contrast, the $\delta^{18}O_{MDAC}$ values (> ~5.5‰) below the SMT at Site 16GH-P3 and at 5.70 mbsf of Site 16GH-P4 are significantly higher than the calculated theoretical $\delta^{18}O$ values of both aragonite and calcite, implying that MDAC precipitation occurs in association with pore fluid characterized by higher $\delta^{18}O$ value and/or in marine environments with lower temperatures compared to the present seawater conditions. In order to align with the analyzed $\delta^{18}O_{MDAC}$ value (> ~5.5‰) calculated using Equation 5, the temperature has to be lower than -6°C. However, such temperatures are not reasonable, as they would result in the freezing of seawater and sediment. Therefore, we exclude the possibility of lower temperatures for the high $\delta^{18}O_{MDAC}$ values observed in the MDACs. A plausible explanation for these observed $\delta^{18}O_{MDAC}$ values is a fluid source with a high $\delta^{18}O$value. The typical characteristics of clay dehydration and opal diagenesis, such as relatively high $\delta^{18}O$ values with low Cl^- concentrations and relatively low $^{87}Sr/^{86}Sr$ values in pore fluid (Kastner et al., 1991; Kim et al., 2013; Kim et al., 2021; Kim et al., 2022), are not exhibited in fluids from Site 16GH-P3 (Figures 3, 7; Supplementary Table 1). Therefore, we rule out both reactions as sources for the fluid with a high $\delta^{18}O$ value that forms MDACs. Instead, it is reasonable that the fluid source for the formation of ^{18}O-rich MDACs shown below the SMT at Site 16GH-P3 and at 5.70 mbsf of Site 16GH-P4 is derived from GH dissociation. This interpretation is supported by the presence of numerous shallow GHs found in the Ulleung Basin (Kim et al., 2011; Kim et al., 2012; Choi et al., 2013; Kim et al., 2013).

MDACs were collected from 5.70 mbsf to 7.33 mbsf at Site 16GH-P4 (Figure 2; Supplementary Table 3) thus, we anticipated that $\delta^{18}O$ values of MDACs are similar at all sampling intervals within this site. However, these values below 6.63 mbsf are significantly lower than that of 5.70 mbsf at Site 16GH-P4 (up to ~1.5‰), but slightly higher than those above 1.48 mbsf at Site 16GH-P3 (Figure 6B; Supplementary Table 3). The findings suggest that the fluid source contributing to MDACs precipitation underwent significant changes within a 2 m interval of the sediment column (Figure 6B, Supplementary Table 3). The MDAC from 5.70 mbsf appears to inherit its properties from the fluid with a higher $\delta^{18}O$ value, while the other MDACs have primarily originated from fluid with $\delta^{18}O$ values similar to that of the present ambient seawater. However, this interpretation of the rapid change in the fluid source for MDACs is not reasonable in the natural marine system. Thus, this observation remains unexplained.

Kim et al. (2013) revealed that pore fluids with high Cl^- concentration at Site UBGH2-3 have relatively low $\delta^{18}O$ values (< -0.5‰) due to the formation of massive GHs (Figure 7B). In addition, pore fluid from Site 16GH-P4 is characterized by increasing Cl^- concentration and decreasing $\delta^{18}O$ value as fluid sampling depth increases, in comparison to other sites (Figure 3B). It is postulated that massive GHs were probably present below the sampling depth of the retrieved core at Site 16GH-P4 and may have influenced the isotopic composition of the pore fluid, as indicated by the observed low $\delta^{18}O$ value (-0.5‰) at this site. This fluid may contribute to the precipitation of MDACs under the same temperature conditions as the bottom seawater. Under these circumstances, the theoretical $\delta^{18}O$ values of aragonite and calcite calculated by Equations 4 and 5 are ~3.3‰ (V-PDB) and ~2.6‰ (V-PDB), respectively. These values are lower than the measured $\delta^{18}O_{MDAC}$ below 6.63 mbsf at Site 16GH-P4 (Figure 6; Supplementary Table 3). In comparison to the $\delta^{18}O_{MDAC}$ value above 6.63 mbsf at Site 16GH-P4, we postulated that the lower $^{18}O_{MDAC}$ values in this interval can be attributed to residual fluid derived from the massive GH formation.

5.6 Significance of MSiW and MDAC precipitation

Both MSiW and carbonate precipitation play an important role in carbon sinks in the global carbon cycle. Large amounts of dissolved cations and alkalinity released into fluids by MSiW are involved in authigenic carbonate formation (Wallmann et al., 2008; Scholz et al., 2013; Solomon et al., 2014; Torres et al., 2020). Recently, the rate of carbon fixation by carbonate precipitation associated with MSiW has been estimated to be on the order of 10^{12}

mole C yr^{-1} (Torres et al., 2020). It has also been revealed that the maximum alkalinity of pore fluid on the Krishna-Godavari Basin, Indian Margin, in association with ongoing MSiW is less than 45 mM (Solomon et al., 2014) because authigenic carbonate formation consumes the excess alkalinity released by this reaction. Indeed, many MDACs have been documented at this margin (e.g., Teichert et al., 2014). Therefore, both MSiW and MDAC significantly impact on pore fluid geochemistry in the Krishna-Godavari Basin and the Ulleung Basin.

Many MDACs were found at Sites 16GH-P3 and 16GH-P4 (Figure 2; Supplementary Table 3). Compared to the Krishna-Godavari Basin, the maximum alkalinity in pore fluids sampled from the MDAC-bearing interval has a similar concentration at Site 16GH-P3 (< 40 mM), whereas it has a higher concentration at Site 16GH-P4 (up to 54 mM). Additionally, this concentration at Site 16GH-P4 is similar to or slightly lower than those at non-MDAC-bearing sites (Sites 16GH-P1 and 16GH-P5) in this study and many previous investigations in the basin (e.g., UBGH2-1_1; Kim et al., 2013; Kim et al., 2016). Considering that the ACM and ACL facies were observed throughout the retrieved core length of Site 16GH-P3 whereas they were exclusively found below 5.4 mbsf at Site 16GH-P4. MDAC precipitation is likely to be more pronounced at the former site. Pore fluid chemistry in the southern Ulleung Basin from this study also clearly points out the occurrence of MSiW. Since Kim et al. (2016) have documented that the MSiW occurs without MDAC observations in the Ulleung Basin, MDAC and pore chemistry results from this study provide the first evidence for the ongoing occurrence of both reactions in the basin. Moreover, the higher alkalinity (> 45 mM) at Site 16GH-P4 implies that the alkalinity produced by MSiW is much greater in the Ulleung Basin than in the Indian Margin, although it is masked by authigenic carbonate precipitation as a carbon sink. The high alkalinity in pore fluid from the Ulleung Basin is a unique characteristic and plays an important role in the linkage with the carbon cycle in this basin. The cations released by MSiW, such as dissolved Ca^{2+}, Mg^{2+}, B, and H_4SiO_4, also play a pivotal role in impacting the diagenesis and element cycles in this basin, as well as globally. Future geochemical modeling studies are necessary to elucidate the significance of MSiW and MDAC precipitation in the regional and global marine systems.

6 Summary and implications

All four study sites in the southern Ulleung Basin show a shallow SMT depth (< 5 mbsf) and a microbial CH_4 source, regardless of seismic characteristics (chimney structures at Sites 16GH-P3 and 16GH-P4; non-chimney structures at Sites 16GH-P1 and 16GH-P5), which is consistent with many previous investigations in this basin (e.g., Kim et al, 2011; Kim et al., 2012; Choi et al., 2013; Kim et al., 2013). However, pore fluid and sediment characteristics, including MDACs, have similar and/or different aspects at each study site. The highest Cl^- concentration in pore fluids is observed at Site 16GH-P4, which is greater than that of seawater. In addition, δD and $\delta^{18}O$ values are slightly lower at this site compared to the other sites and have a negative correlation with Cl^-. Such characteristics are typical when the fluid related to massive GH formation in the fine sediment layer impacts the fluid chemistry. In contrast, the fluids at other sites predominantly originate from seawater in the Ulleung Basin. We observe 1) high alkalinity around the SMT (> 35 mM), 2) continuous increase in alkalinity with depth, and 3) higher concentrations of K^+, B, Mg^{2+}, and H_4SiO_4 in pore fluids compared to seawater, which is evidence for the ongoing occurrence of MSiW under anoxic conditions at all sites.

The decreasing downcore profile of Ca^{2+} and Sr^{2+} concentrations with relatively high Mg^{2+}/Ca^{2+} ratios (> 6) as alkalinity increases in pore fluids indicates carbonate precipitation within the sediment column at all sites. However, massive MDACs, mainly composed of aragonite and Mg-calcite, have been found at Sites 16GH-P3 and 16GH-P4 (chimney sites) with diverse morphologies and very low $\delta^{13}C_{MDAC}$ values (< -31.3‰). The ongoing occurrence of MSiW and MDAC precipitation in the Ulleung Basin is first documented in this study. Interestingly, $\delta^{13}C_{MDAC}$ values are clearly separated into two groups based on the SMT at Site 16GH-P3; they are lower than -41.6‰ below the SMT while they are higher than -35.0‰ above the SMT. These results mean that HCO_3^- of seawater with a high $\delta^{13}C$ value (~0‰) impacts MDAC precipitation above the SMT, although the chemical properties of microbial CH_4 are critically inherited into MDACs found at both sites. The measured $\delta^{18}O_{MDAC}$ values above the SMT are close to the present-day theoretical equilibrium value of aragonite (~4‰ V-PDB) in this basin, which also supports the influence of seawater on $\delta^{13}C_{MDAC}$ during the MDAC precipitation. However, compared to the calculated theoretical $\delta^{18}O$ value of aragonite, the observed variation of $\delta^{18}O_{MDAC}$ values at Site 16GH-P4 measured below the SMT implies the involvement of other sources. We postulated that the higher $\delta^{18}O_{MDAC}$ value (~5.7‰) above 6.63 mbsf at this site is related to the fluid derived from GH dissociation, whereas the similar $\delta^{18}O_{MDAC}$ value below 6.63 mbsf is associated with fluid from massive GH formation based on our and previous results of pore fluid chemistry in this basin. Future work will need to generalize the correlation between GH behaviors and $\delta^{18}O_{MDAC}$.

The ACM and ACL facies with an abundance of MDACs have been observed at the chimney sites. The LM, BM, and SLM facies, which are the predominant sediment facies of the non-chimney sites, have also been deposited thickly above the ACM and ACL facies at Site 16GH-P4. The U-Th age dating of MDACs reported first in the Ulleung Basin indicates that the upper facies at Site 16GH-P4 was deposited during a younger period (< 20 ka BP) than the facies at Site 16GH-P3 after mound structure formation by the high upward gas flux. Hence, the depositional environment of the ACM and ACL facies probably contains dynamic conditions associated with sediment erosion or collapse in response to gas flux. The chemical properties of pore fluids and MDACs (i.e., higher concentrations of alkalinity, K^+, Mg^{2+}, B, and H_4SiO_4, and lower $\delta^{13}C_{MDAC}$ values than those of seawater) in the southern Ulleung Basin have very unique characteristics compared to other cold seep regions in the continental margin. These properties reflect the complex chemical interactions between fluids and MDACs in response to gas fluxes and the related elements and carbon cycles. Our study provides some important perspectives for the chemical

reactions and elemental cycles in association with the gas flux of this type of cold seep system. Nevertheless, future investigations into both chimney and non-chimney sites within this basin are necessary to better decipher the chemical properties of pore fluids, gases, and MDACs as well as interactions among them and elemental cycles on regional and global scales in response to climate changes throughout geological history.

Data availability statement

The original contributions presented in the study are included in the article/Supplementary Material. Further inquiries can be directed to the corresponding author.

Author contributions

J-HK and M-HP designed and coordinated the study, analyzed the samples, interpreted the data, and led the writing of the manuscript. J-SR, JC, SP, YS, and T-HK analyzed the samples, wrote, and reviewed the manuscript. KJ, B-YY, YJ, and JH wrote and reviewed the draft. All authors contributed to the article and approved the submitted version.

Funding

The author(s) declare financial support was received for the research, authorship, and/or publication of this article. This study was funded by Korea Ministry of Science and ICT (GP2020-006 and GP2021-009), the Korea Ministry of Oceans and Fisheries (20210632), the Korea Ministry of Trade, Industry and Energy (Project No. 20212010200010), and the National Research Foundation of Korea grant supported by the Korea Ministry of Science and ICT (No. NRF-2019R1A2C2085973).

Acknowledgments

We would like to thank the captain and crew of the *R/V Tamhae II* for their help at sea.

Conflict of interest

The authors declare that the research was conducted in the absence of any commercial or financial relationships that could be construed as a potential conflict of interest.

Publisher's note

All claims expressed in this article are solely those of the authors and do not necessarily represent those of their affiliated organizations, or those of the publisher, the editors and the reviewers. Any product that may be evaluated in this article, or claim that may be made by its manufacturer, is not guaranteed or endorsed by the publisher.

Supplementary material

The Supplementary Material for this article can be found online at: https://www.frontiersin.org/articles/10.3389/fmars.2023.1156918/full#supplementary-material

References

Alexeev, S. V., and Alexeeva, L. P. (2003). Hydrogeochemistry of the permafrost zone in the central part of the Yakutian diamond-bearing province, Russia. *Hydrogeol. J.* 11, 574–581. doi: 10.1007/s10040-003-0270-8

Aloisi, G., Bouloubassi, I., Heijs, S. K., Pancost, R. D., Pierre, C., Sinninghe Damsté, J. S., et al. (2002). CH_4-consuming microorganisms and the formation of carbonate crusts at cold seeps. *Earth Planet. Sci. Lett.* 203, 195–203. doi: 10.1016/S0012-821X(02)00878-6

Aloisi, G., Pierre, C., Rouchy, J.-M., Foucher, J.-P., and Woodside, J. (2000). Methane-related authigenic carbonates of eastern Mediterranean Sea mud volcanoes and their possible relation to gas hydrate destabilisation. *Earth Planet. Sci. Lett.* 184, 321–338. doi: 10.1016/S0012-821X(00)00322-8

Bahr, A., Pape, T., Bohrmann, G., Mazzini, A., Haeckel, M., Reitz, A., et al. (2007). Authigenic carbonate precipitates from the NE Black Sea: a mineralogical, geochemical, and lipid biomarker study. *Int. J. Earth Sci.* 98, 677–695. doi: 10.1007/s00531-007-0264-1

Bernard, B. B., Brooks, J. M., and Sackett, W. M. (1978). Light hydrocarbons in recent Texas continental shelf and slope sediments. *J. Geophys. Res.* 83, 4053–4061. doi: 10.1029/JC083iC08p04053

Boetius, A., Ravenschlag, K., Schubert, C. J., Rickert, D., Widdel, F., Gieseke, A., et al. (2000). A marine microbial consortium apparently mediating anaerobic oxidation of methane. *Nature* 407, 623–626. doi: 10.1038/35036572

Böttner, C., Haeckel, M., Schmidt, M., Berndt, C., Vielstädte, L., Kutsch, J. A., et al. (2020). Greenhouse gas emissions from marine decommissioned hydrocarbon wells: leakage detection, monitoring and mitigation strategies. *Int. J. Greenhouse Gas Control.* 100, 103119. doi: 10.1016/j.ijggc.2020.103119

Buerk, D., Klaucke, I., Sahling, H., and Weinrebe, W. (2010). Morpho-acoustic variability of cold seeps on the continental slope offshore Nicaragua: Results of fluid flow interaction with sedimentary processes. *Mar. Geol.* 275, 53–65. doi: 10.1016/j.margeo.2010.04.007

Burton, E. A. (1993). Controls on marine carbonate cement mineralogy: review and reassessment. *Chem. Geo.* 105, 163–179. doi: 10.1016/0009-2541(93)90124-2

Campbell, K. A. (2006). Hydrocarbon seep and hydrothermal vent paleoenvironments and paleontology: Past developments and future research directions. *Palaeogeogr. Palaeoclimatol. Palaeoecol.* 232, 362–407. doi: 10.1016/j.palaeo.2005.06.018

Charkin, A. N., Rutgers van der Loeff, M., Shakhova, N. E., Gustafsson, Ö., Dudarev, O. V., Cherepnev, M. S., et al. (2017). Discovery and characterization of submarine groundwater discharge in the Siberian Arctic seas: a case study in the Buor-Khaya Gulf, Laptev Sea. *Cryosphere* 11, 2305–2327. doi: 10.5194/tc-11-2305-2017

Cheng, H., Edwards, R. L., Shen, C.-C., Polyak, V. J., Asmerom, Y., Woodhead, J., et al. (2013). Improvements in ^{230}Th dating, ^{230}Th and ^{234}U half-life values, and U-Th isotopic measurements by multi-collector inductively coupled plasma mass spectrometry. *Earth Planet. Sci. Lett.* 371-372, 82–91. doi: 10.1016/j.epsl.2013.04.006

Choi, J., Kim, J.-H., Torres, M. E., Hong, W.-L., Lee, J.-W., Yi, B.-Y., et al. (2013). Gas origin and migration in the Ulleung Basin, East Sea; Results from the second Ulleung Basin gas hydrate drilling expedition (UBGH2). *Mar. Pet. Geol.* 47, 113–124. doi: 10.1016/j.marpetgeo.2013.05.022

Chough, S. K., Lee, H. J., and Yoon, S. H. (2000). *Marine geology of korean seas. 2nd ed* (Amsterdam: Elsevier).

Colbo, K., Ross, T., Brown, C., and Weber, T. (2014). A review of oceanographic applications of water column data from multibeam echosounders. *Estuar. Coast. Shelf Sci.* 145, 41–56. doi: 10.1016/j.ecss.2014.04.002

Collett, T. S., Riedel, M., Cochran, J. R., Boswell, R., Presley, J., Kumar, P., et al. (2008). *National gas hydrate program (NGHP) expedition 01 initial reports* (New Delhi: Directorate General of Hydrocarbons).

Craig, H. (1961). Isotopic variation in meteoric waters. *Science* 133, 1702–1703. doi: 10.1126/science.133.3465.1702

Crémière, A., Chand, S., Sahy, D., Thorsnes, T., Martma, T., Noble, S. R., et al. (2018). Structural controls on seepage of thermogenic and microbial methane since the last glacial maximum in the Harstad Basin, southwest Barents Sea. *Mar. Petrol. Geol.* 98, 569–581. doi: 10.1016/j.marpetgeo.2018.07.010

Crémière, A., Lepland, A., Chand, S., Sahy, D., Kirsimäe, K., Bau, M., et al. (2016). Fluid source and methane-related diagenetic processes recorded in cold seep carbonates from the Alvheim channel, central North Sea. *Chem. Geol.* 432, 16–33. doi: 10.1016/j.chemgeo.2016.03.019

Dillon, W. P., Nealon, J. W., Taylor, M. H., Lee, M. W., Drury, R. M., and Anton, C. H. (2001). "Seafloor collapse and methane venting associated with gas hydrate on the blake ridge: causes and implications to seafloor stability and methane release," in *Natural gas hydrates: occurrence, distribution, and detection*. Eds. C. K. Paull and W. P. Dillon (Washington, D.C: American Geophysical Union), 211–233. doi: 10.1029/GM124p0211

Edwards, R. L., Chen, J. H., and Wasserburg, G. J. (1987). ^{238}U-^{234}U-^{230}Th-^{232}Th systematics and the precise measurement of time over the past 500,000 years. *Earth Planet. Sci. Lett.* 81, 175–192. doi: 10.1016/0012-821X(87)90154-3

Gorbarenko, S. A., and Southon, J. R. (2000). Detailed Japan Sea paleoceanography during the last 25 kyr: constraints from AMS dating and δ^{18}O of planktonic foraminifera. *Paleogeogr. Paleoclimatol. Paleoecol.* 156, 177–193. doi: 10.1016/S0031-0182(99)00137-6

Greinert, J., Bohrmann, G., and Suess, E. (2001). "Gas hydrate-associated carbonates and methane-venting at Hydrate Ridge: classification, distribution, and origin of authigenic lithologies," in *Natural gas hydrates: occurrence, distribution, and detection*. Eds. C. K. Paull and W. P. Dillon (Washington, D.C: American Geophysical Union), 99–113.

Haacke, R. R., Hyndman, R. D., Park, K.-P., Yoo, D. G., Stoian, I., and Schmidt, U. (2009). Migration and venting of deep gases into the ocean through hydrate-choked chimneys offshore Korea. *Geology* 37, 531–534. doi: 10.1130/G25681A.1

Han, X. Q., Suess, E., Huang, Y. Y., Wu, N. Y., Bohrmann, G., Su, X., et al. (2008). Jiulong methane reef: microbial mediation of seep carbonates in the South China Sea. *Mar. Geol.* 249, 243–256. doi: 10.1016/j.margeo.2007.11.012

Himmler, T., Birgel, D., Bayon, G., Pape, T., Ge, L., Bohrmann, G., et al. (2015). Formation of seep carbonates along the Makran convergent margin, northern Arabian Sea and a molecular and isotopic approach to constrain the carbon isotopic composition of parent methane. *Chem. Geol.* 415, 102–117. doi: 10.1016/j.chemgeo.2015.09.016

Himmler, T., Brinkmann, F., Bohrmann, G., and Peckmann, J. (2011). Corrosion patterns of seep-carbonates from the eastern Mediterranean Sea. *Terra Nova* 23, 206–212. doi: 10.1111/j.1365-3121.2011.01000.x

Hong, W.-L., Torres, M. E., Carroll, J., Crémière, A., Panieri, G., Yao, H., et al. (2017). Seepage from an Arctic shallow marine gas hydrate reservoir is insensitive to momentary ocean warming. *Nat. Commun.* 8, 5745. doi: 10.1038/ncomms15745

Hong, W.-L., Torres, M. E., Kim, J.-H., Choi, J., and Bahk, J.-J. (2014). Towards quantifying the reaction network around the sulfate-methane transition-zone in the Ulleung Basin, East Sea, with a kinetic modeling approach. *Geochim. Cosmochim. Acta* 140, 127–141. doi: 10.1016/j.gca.2014.05.032

Horozal, S., Lee, G. H., Yi, B. Y., Yoo, D. G., Park, K. P., Lee, H. Y., et al. (2009). Seismic indicators of gas hydrate and associated gas in the Ulleung Basin, East Sea (Japan Sea) and implications of heat flows derived from depths of the bottom-simulating reflector. *Mar. Geol.* 258, 126–138. doi: 10.1016/j.margeo.2008.12.004

Hubbard, C. R., Evans, E. H., and Smith, D. K. (1976). The reference intensity ratio, *I/Ic*, for computer simulated powder patterns. *J. Appl. Crystallogr.* 9, 169–174. doi: 10.1107/S0021889876010807

Hubbard, C. R., and Snyder, R. L. (1988). RIR - measurement and use in quantitative XRD. *Powder Diffr.* 3, 74–77. doi: 10.1017/S0885715600013257

Jolivet, L., Shibuya, H., and Fournier, M. (1995). "Paleomagnetic rotations and the Japan Sea opening," in *Active margins and marginal basins of the western pacific*. Eds. B. Taylor and J. Natland (Washington, D.C: American Geophysical Union), 355–369. doi: 10.1029/GM088p0355

Judd, A., and Hovland, M. (2007). *Seabed fluid flow: the impact on geology, biology and the marine environment* (Cambridge: Cambridge University Press). doi: 10.1017/CBO9780511535918

Kastner, M., Elderfield, H., and Martin, J. B. (1991). Fluids in convergent margins - what do we know about their composition, origin, role in diagenesis and importance for oceanic chemical fluxes. *Philos. Trans. R. Soc A.* 335, 243–259. doi: 10.1098/rsta.1991.0045

KIGAM. (2011). *Studies on gas hydrate geology, geochemistry* (Daejeon: KIGAM).

KIGAM. (2016). *Studies on gas hydrate resource assessment and characterization of chimney structures in the Ulleung Basin* (Daejeon: KIGAM).

Kim, J.-H., Hachikubo, A., Kida, M., Minami, H., Lee, D.-H., Jin, Y. K., et al. (2020). Upwarding gas source and postgenetic processes in the shallow sediments from the ARAON Mounds, Chukchi Sea. *J. Nat. Gas Sci. Eng.* 76, 103223. doi: 10.1016/j.jngse.2020.103223

Kim, J.-H., Hong, W.-L., Torres, M. E., Ryu, J.-S., Kang, M.-H., Han, D., et al. (2021). A pulse of meteoric subsurface fluid discharging into the Chukchi Sea during the Early Holocene Thermal Maximum (EHTM). *Geochem. Geophy. Geosy.* 22, e2021GC009750. doi: 10.1029/2021GC009750

Kim, J.-H., Kong, G. S., Ryu, J.-S., and Park, M.-H. (2014). Revisiting the origin of organic matter and depositional environment of sediment in the central Ulleung Basin, East Sea since the late Quaternary. *Quat. Int.* 344, 181–191. doi: 10.1016/j.quaint.2014.07.022

Kim, J.-H., Park, M.-H., Chun, J.-H., and Lee, J. Y. (2011). Molecular and isotopic signatures in sediments and gas hydrate of the central/southwestern Ulleung Basin: high alkalinity escape fuelled by biogenically sourced methane. *Geo-Mar. Lett.* 31, 37–49. doi: 10.1007/s00367010-0214-y

Kim, J.-H., Park, M.-H., Lee, D.-H., Minami, H., Jin, Y.-K., Hachikubo, A., et al. (2022). Impact of high methane flux on the properties of pore fluid and methane-derived authigenic carbonate in the ARAON Mounds, Chukchi Sea. *Front. Mar. Sci.* 9. doi: 10.3389/fmars.2022.944841

Kim, J.-H., Torres, M. E., Choi, J., Bahk, J.-J., Park, M.-H., and Hong, W.-L. (2012). Inferences on gas transport based on molecular and isotopic signatures of gases at acoustic chimneys and background sites in the Ulleung Basin. *Org. Geochem.* 43, 26–38. doi: 10.1016/j.orggeochem.2011.11.004

Kim, J.-H., Torres, M. E., Haley, B. A., Ryu, J.-S., Park, M.-H., Hong, W.-L., et al. (2016). Marine silicate weathering in the anoxic sediment of the Ulleung Basin: Evidence and consequences. *Geochem. Geophy. Geosy.* 17, 3437–3453. doi: 10.1002/2016GC006356

Kim, J.-H., Torres, M. E., Hong, W.-L., Choi, J., Riedel, M., Bahk, J.-J., et al. (2013). Pore fluid chemistry from the second gas hydrate drilling expedition in the Ulleung Basin (UBGH2): source, mechanisms and consequences of fluid freshening in the central part of the Ulleung Basin, East Sea. *Mar. Petrol. Geol.* 47, 99–112. doi: 10.1016/j.marpetgeo.2012.12.011

Kim, J.-M., Kennett, J. P., Park, B.-K., Kim, D. C., Kim, G. Y., and Roark, E. B. (2000). Paleoceanographic change during the last deglaciation, East Sea of Korea. *Paleoceanography* 15, 254–266. doi: 10.1029/1999PA000393

Kim, S.-T., and O'Neil, J. R. (1997). Equilibrium and nonequilibrium oxygen isotope effects in synthetic carbonates. *Geochim. Cosmochim. Acta* 61, 3461–3475. doi: 10.1016/S0016-7037(97)00169-5

Kim, S.-T., O'Neil, J. R., Hillaire-Marcel, C., and Mucci, A. (2007). Oxygen isotope fractionation between synthetic aragonite and water: influence of temperature and Mg^{2+} concentration. *Geochem. Cosmochim. Acta* 71, 4704–4715. doi: 10.1016/j.gca.2007.04.019

Koch, S., Berndt, C., Bialas, J., Haeckel, M., Crutchley, G., Papenberg, C., et al. (2015). Gas-controlled seafloor doming. *Geology* 43, 571–574. doi: 10.1130/G36596.1

Lee, J. H., Baek, Y. S., Ryu, B. J., Riedel, M., and Hyndman, R. D. (2005). A seismic survey to detect natural gas hydrate in the East Sea of Korea. *Mar. Geophys. Res.* 26, 51–59. doi: 10.1007/s11001-005-6975-4

Lee, K. E. (2007). Surface water changes recorded in Late Quaternary marine sediments of the Ulleung Basin, East Sea (Japan Sea). *Palaeogeogr. Palaeoclimatol. Palaeoecol.* 247, 18–31. doi: 10.1016/j.palaeo.2006.11.019

Lee, K. S., Wenner, D. B., and Lee, I. (1999). Using H- and O-isotopic data for estimating the relative contributions of rainy and dry season precipitation to groundwater: example for Cheju Island, Korea. *J. Hydrol.* 222, 65–74. doi: 10.1016/S0022-1694(99)00099-2

Luff, R., Wallmann, K., and Aloisi, G. (2004). Numerical modeling of carbonate crust formation at cold vent sites: significance for fluid and methane budgets and chemosynthetic biological communities. *Earth Planet. Sci. Lett.* 221, 337–353. doi: 10.1016/S0012-821X(04)00107-4

Magalhães, V. H., Pinheiro, L. M., Ivanov, M. K., Kozlova, E., Blinova, V., Kolganova, J., et al. (2012). Formation processes of methane-derived authigenic carbonates from the Gulf of Cadiz. *Sediment. Geol.* 243-244, 155–168. doi: 10.1016/j.sedgeo.2011.10.013

Malinverno, A., Kastner, M., Torres, M. E., and Wortmann, U. G. (2008). Gas hydrate occurrence in a transect across the Cascadia margin from pore water chlorinity and downhill geophysical logs (IODP 311). *J. Geophys. Res.* 113, B08103. doi: 10.1029/2008JB005702

Mazzini, A., Svensen, H., Hovland, M., and Planke, S. (2006). Comparison and implications from strikingly different authigenic carbonates in a Nyegga complex pockmark, G11, Norwegian Sea. *Mar. Geol.* 231, 443–467. doi: 10.1016/j.margeo.2006.05.012

Mazzini, A., Svensen, H. H., Planke, S., Forsberg, C. F., and Tjelta, T. I. (2016). Pockmarks and methanogenic carbonates above the giant Troll gas field in the Norwegian North Sea. *Mar. Geol.* 373, 26–38. doi: 10.1016/j.margeo.2015.12.012

Milkov, A. V., and Etiope, G. (2018). Revised genetic diagrams for natural gases based on a global dataset of >20,000 samples. *Org. Geochem.* 125, 109–120. doi: 10.1016/j.orggeochem.2018.09.002

Naehr, T. H., Eichhubl, P., Orphan, V. J., Hovland, M., Paull, C. K., Ussler, W. III, et al. (2007). Authigenic carbonate formation at hydrocarbon seeps in continental

margin sediments: a comparative study. *Deep-Sea Res. II: Top. Stud. Oceanogr.* 54, 1268–1291. doi: 10.1016/j.dsr2.2007.04.010

Pape, T., Bahr, A., Rethemeyer, J., Kessler, J. D., Sahling, H., Hinrichs, K.-U., et al. (2010). Molecular and isotopic partitioning of low molecular-weight hydrocarbons during migration and gas hydrate precipitation in deposits of a high-flux seepage site. *Chem. Geol.* 269, 350–363. doi: 10.1016/j.chemgeo.2009.10.009

Park, C., Kim, H., and Song, Y. (2018). Mineralogical, micro-textural, and geochemical characteristics for the carbonate rocks of the lower Makgol Formation in Seokgaejae section. *Econ. Environ. Geol.* 51, 323–343. doi: 10.9719/EEG.2018.51.4.323

Park, M.-H., Kim, J.-H., and Kil, Y.-W. (2007). Identification of the late Quaternary tephra layers in the Ulleung Basin of the East Sea (Sea of Japan) using geochemical and statistical methods. *Mar. Geol.* 244, 196–208. doi: 10.1016/j.margeo.2007.06.006

Park, M. H., Kim, J. H., Ryu, B. J., Kim, I. S., and Chang, H. W. (2006). AMS radiocarbon dating of the marine late Pleistocene-Holocene sediment cores from the Ulleung Basin, East/Japan Sea. *Nucl. Instrum. Methods Phy. Res. B* 243, 211–215. doi: 10.1016/j.nimb.2005.08.120

Paull, C. K., Chanton, J. P., Neumann, A. C., Coston, J. A., Martens, C. S., and Showers, W. (1992). Indicators of methane-derived carbonates and chemosynthetic organic carbon deposits; examples from the Florida Escarpment. *Palaios* 7, 361–375. doi: 10.2307/3514822

Paytan, A., Kastner, M., Martin, E. E., Macdougall, J. D., and Herbert, T. (1993). Marine barite as a monitor of seawater strontium isotope composition. *Nature* 366, 445–449. doi: 10.1038/366445a0

Peckmann, J., Reimer, A., Luth, U., Luth, C., Hansen, B., Heinicke, C., et al. (2001). Methane-derived carbonates and authigenic pyrite from the northwestern Black Sea. *Mar. Geol.* 177, 129–150. doi: 10.1016/S0025-3227(01)00128-1

Peckmann, J., and Thiel, V. (2004). Carbon cycling at ancient methane-seeps. *Chem. Geol.* 205, 443–467. doi: 10.1016/j.chemgeo.2003.12.025

Pierre, C., Bayon, G., Blanc-Valleron, M. M., Mascle, J., and Dupré, S. (2014). Authigenic carbonates related to active seepage of methane-rich hot brines at the Cheops mud volcano, Menes caldera (Nile deep-sea fan, eastern Mediterranean Sea). *Geo-Mar. Lett.* 34, 253–267. doi: 10.1007/s00367-014-0362-6

Pierre, C., Demange, J., Blanc-Valleron, M.-M., and Dupréc, S. (2017). Authigenic carbonate mounds from active methane seeps on the southern Aquitaine Shelf (Bay of Biscay, France): Evidence for anaerobic oxidation of biogenic methane and submarine groundwater discharge during formation. *Cont. Shelf Res.* 133, 13–25. doi: 10.1016/j.csr.2016.12.003

Pimmel, A., and Claypool, G. (2001). *Introduction to shipboard organic geochemistry on the JOIDES Resolution. ODP Tech. Note, 30* (College Station, T.X: Ocean Drilling Program).

Riedel, M., Collett, T. S., Malone, M. J.the Expedition 311 Scientists (2006). *Proceedings of the integrated ocean drilling program, vol. 311* (Washington, D.C: Integrated Ocean Drilling Program Management International).

Römer, M., Sahling, H., Pape, T., Ferreira, C. D., Wenzhöfer, F., Boetius, A., et al. (2014). Methane fluxes and carbonate deposits at a cold seep area of the Central Nile Deep Sea Fan, Eastern Mediterranean Sea. *Mar. Geol.* 347, 27–42. doi: 10.1016/j.margeo.2013.10.011

Ruppel, C. D., and Kessler, J. D. (2017). The interaction of climate change and methane hydrates. *Rev. Geophys.* 55, 126–168. doi: 10.1002/2016RG000534

Ryu, B.-J., Riedel, M., Kim, J.-H., Hyndman, R. D., Lee, Y.-J., Chung, B.-H., et al. (2009). Gas hydrates in the western deep-water Ulleung Basin, East Sea of Korea. *Mar. Petrol. Geol.* 26, 1483–1498. doi: 10.1016/j.marpetgeo.2009.02.004

Scholz, F., Hensen, C., Schmidt, M., and Geersen, J. (2013). Submarine weathering of silicate minerals and the extent of pore water freshening at active continental margins. *Geochim. Cosmochim. Acta* 100, 200–216. doi: 10.1016/j.gca.2012.09.043

Sibuet, M., and Olu, K. (1998). Biogeography, biodiversity and fluid dependence of deep-sea cold-seep communities at active and passive margins. *Deep-Sea Res. II: Top. Stud. Oceanogr.* 45, 517–567. doi: 10.1016/S0967-0645(97)00074-X

Solomon, E. A., Spivack, A. J., Kastner, M., Torres, M. E., and Robertson, G. (2014). Gas hydrate distribution and carbon sequestration through coupled microbial methanogenesis and silicate weathering in the Krishna-Godavari Basin, offshore India. *Mar. Petrol. Geol.* 58, 233–253. doi: 10.1016/j.marpetgeo.2014.08.020

Stott, L., Davy, B., Shao, J., Coffin, R., Pecher, I., Neil, H., et al. (2019). CO_2 release from pockmarks on the Chatham rise-bounty trough at the glacial termination. *Paleoceanogr. Paleoclimatol.* 34, 1726–1743. doi: 10.1029/2019pa003674

Suess, E. (2014). Marine cold seeps and their manifestations: geological control, biogeochemical criteria and environmental conditions. *Int. J. Earth Sci.* 103, 1889–1916. doi: 10.1007/s00531-014-1010-0

Tada, R., Irino, T., and Koizumi, I. (1999). Land-ocean linkages over orbital and millennial timescales recorded in late Quaternary sediments of the Japan Sea. *Paleoceanography* 14, 236–247. doi: 10.1029/1998PA900016

Tamaki, K., Suyehiro, K., Allan, J., Ingle, J. C. Jr., and Pisciotto, K. A. (1992). "Tectonic synthesis and implications of Japan Sea," in *Proceedings of the ocean drilling program scientific results*, vol. 127/ 128 . Eds. K. Tamaki, K. Suyehiro, J. Allan and M. McWilliams (College Station, TX: Ocean Drilling Program).

Teichert, B. M. A., Johnson, J. E., Solomon, E. A., Giosan, L., Rose, K., Kocherla, M., et al. (2014). Composition and origin of authigenic carbonates in the Krishna-Godavari and Mahanadi Basins, eastern continental margin of India. *Mar. Petrol. Geol.* 58, 436–460. doi: 10.1016/j.marpetgeo.2014.08.023

Tomaru, H., Torres, M. E., Matsumoto, R., and Borowski, W. (2006). Effect of massive gas hydrate formation on the water isotopic fractionation of the gas hydrate system at Hydrate Ridge, Cascadia margin offshore OR. *Geochem. Geophy. Geosys.* 7, Q10001. doi: 10.1029/2005GC001207

Tong, H., Feng, D., Peckmann, J., Roberts, H. H., Chen, L., Bian, Y., et al. (2019). Environments favoring dolomite formation at cold seeps: A case study from the Gulf of Mexico. *Chem. Geol.* 518, 9–18. doi: 10.1016/j.chemgeo.2019.04.016

Torres, M. E., Hong, W.-L., Solomon, E. A., Milliken, K., Kim, J.-H., Sample, J. C., et al. (2020). Silicate weathering in anoxic marine sediment as a requirement for authigenic carbonate burial. *Earth-Sci. Rev.* 200, 102960. doi: 10.1016/j.earscirev.2019.102960

Torres, M. E., Wallmann, K., Tréhu, A. M., Bohrmann, G., Borowski, W. S., and Tomaru, H. (2004). Gas hydrate growth, methane transport, and chloride enrichment at the southern summit of Hydrate Ridge, Cascadia margin off Oregon. *Earth Planet. Sci. Lett.* 226, 225–241. doi: 10.1016/j.epsl.2004.07.029

UBGH2 Scientists. (2010). *Ulleung basin gas hydrate drilling expedition 2. Preliminary report* (Daejeon: KIGAM).

Wallmann, K., Aloisi, G., Haeckel, M., Tishchenko, P., Pavlova, G., Greinert, J., et al. (2008). Silicate weathering in anoxic marine sediments. *Geochim. Cosmochim. Acta* 72, 2895–2918. doi: 10.1016/j.gca.2008.03.026

Wang, S., Yan, W., Chen, Z., Zhang, N., and Han, C. (2014). Rare earth elements in cold seep carbonates from the southwestern Dongsha area, northern South China Sea. *Mar. Petrol. Geol.* 57, 482–493. doi: 10.1016/j.marpetgeo.2014.06.017

Whiticar, M. J. (1999). Carbon and hydrogen isotope systematics of bacterial formation and oxidation of methane. *Chem. Geol.* 161, 291–314. doi: 10.1016/S0009-2541(99)00092-3

Wu, Q., Hong, J., and Ruan, Z. (2020). Diurnal variations in tropical cyclone intensification. *Geophys. Res. Lett.* 47, e2020GL090397. doi: 10.1029/2020GL0903

frontiers | Frontiers in Earth Science

TYPE Original Research
PUBLISHED 02 April 2024
DOI 10.3389/feart.2024.1304993

Check for updates

OPEN ACCESS

EDITED BY
Glen T. Snyder,
The University of Tokyo, Japan

REVIEWED BY
Jun-ichiro Ishibashi,
Kobe University, Japan
John William Jamieson,
Memorial University of Newfoundland, Canada
Jonguk Kim,
Korea Institute of Ocean Science and Technology (KIOST), Republic of Korea

*CORRESPONDENCE
Ewan-Loiz Pelleter,
ewan.pelleter@ifremer.fr

RECEIVED 30 September 2023
ACCEPTED 19 January 2024
PUBLISHED 02 April 2024

CITATION
Pelleter E-L, Principaud M, Alix A-S, Boissier A, Cheron S, Besson F, Altorffer V, Guérin C, Gaillot A, Pierre D, Rospabé M, Giunta T, Grenet L, Cathalot C, Cambon M-A and Fouquet Y (2024), Diversity, spatial distribution and evolution of inactive and weakly active hydrothermal deposits in the TAG hydrothermal field.
Front. Earth Sci. 12:1304993.
doi: 10.3389/feart.2024.1304993

COPYRIGHT
© 2024 Pelleter, Principaud, Alix, Boissier, Cheron, Besson, Altorffer, Guérin, Gaillot, Pierre, Rospabé, Giunta, Grenet, Cathalot, Cambon and Fouquet. This is an open-access article distributed under the terms of the Creative Commons Attribution License (CC BY). The use, distribution or reproduction in other forums is permitted, provided the original author(s) and the copyright owner(s) are credited and that the original publication in this journal is cited, in accordance with accepted academic practice. No use, distribution or reproduction is permitted which does not comply with these terms.

Diversity, spatial distribution and evolution of inactive and weakly active hydrothermal deposits in the TAG hydrothermal field

Ewan-Loiz Pelleter[1]*, Mélanie Principaud[1], Anne-Sophie Alix[1], Audrey Boissier[1], Sandrine Cheron[1], Florian Besson[1], Vincent Altorffer[1], Charline Guérin[1], Arnaud Gaillot[1], Delphine Pierre[1], Mathieu Rospabé[1], Thomas Giunta[1], Léa Grenet[1], Cecile Cathalot[1], Marie-Anne Cambon[2] and Yves Fouquet[1]

[1]Geo-Ocean, University Brest, CNRS, Ifremer, UMR6538, Plouzane, France, [2]University Brest, Ifremer, CNRS, BEEP, Plouzané, France

Introduction: Although, there is an increasing focus on inactive or extinct seafloor massive sulfide (SMS) deposits driven by the possibility of marine mining, only few studies have been devoted to them so far. The Trans-Atlantic Geotraverse (TAG) hydrothermal field is probably one of the best-studied hydrothermal systems even if the relict SMS deposits known since the mid-1980s have not been thoroughly explored.

Objectives: The main objective of this study was to describe the characteristics of these so-called inactive sites.

Methods: During four different expeditions, we acquired high-resolution acoustic data and performed numerous human occupied vehicle (HOV) dive operations including extensive rock sampling and *in-situ* temperature measurements.

Results and Discussion: We discovered thirteen new hydrothermal mounds including six large (i.e. > 5,000 m^2) deposits making the TAG hydrothermal field one of the largest accumulation of hydrothermal materials (21.1 Mt) known on the seafloor. However, copper and zinc grades of the largest SMS deposits remain low (i.e. < 1.4 wt%) even compared to on-land volcanogenic massive sulfide deposits. Additionally, eight areas of diffuse hydrothermal fluid flow were identified challenging the presumed inactivity of these SMS deposits and, for the first time, emphasizing the importance of low temperature (LT) hydrothermal activity in whole the TAG field. Inactive and weakly active SMS deposits exhibit a large diversity of surface mineralization (e.g. sulfides, Fe-Mn mineralization, jasper) illustrating complexity of hydrothermal activities but also different ageing history. Several mounds no longer have visible sulfide chimneys and are covered by a widespread layer of manganese and iron oxyhydroxides attesting the longevity of diffuse fluid flow at specific locations even long after last high-temperature (HT) hydrothermal activity has ceased. This contrasts with SMS deposits that are devoid of extensive LT precipitates but characterized by standing or topped sulfide chimney indicating a relatively abrupt cessation of HT hydrothermal activity.

Conclusion: Together these results allow us to propose evolution models to explain the diversity of active, weakly active and inactive SMS deposits in the TAG hydrothermal field.

KEYWORDS

seafloor massive sulfides, inactive deposits, TAG hydrothermal field, Mid-Atlantic Ridge (MAR), diffuse venting

1 Introduction

Seafloor massive sulfide (SMS) deposits are now seen as a possible future resource for base (Zn and Cu), precious (Au and Ag), and rare metals (Se, In, and Ge) (Cathles, 2011; Petersen et al., 2016). However, considered as analogous to land-based volcanogenic massive sulfide (VMS) deposits, SMS deposits are still poorly characterized regarding their distribution, size, and accurate metal tenors. The cumulative tonnage of the 62 best-documented SMS deposits is estimated to be 50 Mt and less than 42 Mt if only large (>5,000 m^2) deposits are considered (Hannington et al., 2010; Hannington et al., 2011). Copper and zinc median grades of SMS (Cu + Zn = 14.9 wt%; n = 62) are higher than those reported for VMS deposits; however, calculations are generally made on the basis of surface sampling, which are not representative of the whole, tridimensional deposits (Hannington et al., 2010; 2011; Lehrmann et al., 2018). Hence, the short-term economic potential of SMS deposits remains highly hypothetical, especially as most of the known SMS deposits are currently active and should be preserved from any exploitation (Van Dover et al., 2018). Research efforts have to be carried out on finding and characterizing inactive and extinct SMS deposits that received little attention from geologists and biologists since the discovery of the first hydrothermal vent and related ecosystems in 1977.

The TAG hydrothermal field on the Mid-Atlantic Ridge is the most extensively studied hydrothermal field in the context of a slow-spreading ridge and is one of those with a higher occurrence of the so-called inactive deposit in the present-day oceans. The spatial distribution of SMS deposits is intriguing and raises fundamental questions about the spatial and temporal evolution of hydrothermal systems associated with detachment faults (Humphris et al., 2015; Graber et al., 2020). Although TAG has been the focus of recent scientific expeditions that have discovered new SMS deposits (Gehrmann et al., 2019; Graber et al., 2020), some of which are being described as extinct (Lehrmann et al., 2018; Murton et al., 2019), few submersible dives and related sampling operations have been carried out on these relict zones since 1994 (Rona et al., 1993a; Humphris and Cann, 2000). As a result, there are still many knowledge gaps about the precise nature of the so-called inactive SMS deposits in the TAG hydrothermal field, including their extent, mineralogy, and geochemistry. Additionally, no detailed exploration aimed at identifying and characterizing areas of hydrothermal fluid flows (e.g., diffuse venting) has been performed, even though this is one of the most important parameters for defining an SMS as active or inactive (Jamieson and Gartman, 2020). Here, we present the results of four cruise expeditions combining high-resolution mapping, dive observations, comprehensive sampling, and temperature measurements that provide new insights into the diversity, spatial distribution, and evolution of inactive and weakly active SMS deposits at slow-spreading ridges.

2 Geological setting

The TAG hydrothermal field is located on a 40-km-long ridge segment with an hourglass morphology, narrowing and shallowing toward the center (Purdy et al., 1990; Sempéré et al., 1990; Smith and Cann, 1990) and bounded to the north and south by non-transform discontinuities. The segment is characterized by a morphological asymmetry between the western and eastern flanks. The western rift valley wall consists of fault escarpments and sedimented terraces (Kleinrock and Humphris, 1996a; Kleinrock and Humphris, 1996b; Humphris and Kleinrock et al., 1996), and volcanic activity in the axial valley is expressed by the juxtaposition of individual volcanoes (Rona et al., 1993b; White et al., 1998). The eastern wall is characterized by a higher, steeper, but smoother morphology than the western flank, and it exposes lower crustal rocks (Zonenshain et al., 1989). Together with the acquisition of magnetic and seismic data, this led authors to identify a detachment fault most likely active since the last 1.35 Myr (Tivey et al., 2003; Canales et al., 2007; deMartin et al., 2007; Zhao et al., 2012). It is now widely accepted that detachment faulting somehow controls the hydrothermal circulation beneath the TAG hydrothermal field, although some debates exist about the location of the heat source (deMartin et al., 2007; Guo et al., 2023; Zhao et al., 2012).

The TAG hydrothermal field is located on the hanging wall of the detachment fault. The whole field spans over an area of 45 km^2, though it has been roughly divided into two main hydrothermal areas distanced by 2 km (Figure 1). The low-temperature zone (LTZ) discovered in 1972–1973 (Scott et al., 1974; Rona et al., 1975) lies at a water depth between 3,000 and 2,500 m and spreads over an area of 12 km^2. Temperature anomalies recorded during HOV Alvin dives were suggestive of probable low-temperature hydrothermal venting at least at one site (Rona et al., 1984). Mineralization mainly consists of low-temperature (LT) Fe–Mn–Si deposits that were formed between 125 and 4 kyr (Lalou et al., 1986). The high-temperature zone (HTZ; Figure 1) lies at a water depth between 3,700 and 3,400 m and was first discovered in 1985 with the TAG active mound (Rona et al., 1986). The TAG active mound is a 200-m-diameter and 50-m-high SMS deposit and the only one in the TAG hydrothermal field to exhibit high-temperature (up to 366°C) hydrothermal activity. The deposit is located at the intersection of axis-parallel faults and axis-oblique faults and close to a large and highly faulted volcanic center (Karson and Rona, 1990; Kleinrock and Humphris, 1996; Bohnenstiehl and Kleinrock, 2000; Graber et al., 2020). It is composed of two stacked circular platforms linked to different

hydrothermal events, anhydrite dissolution, and related collapse of the mound (Humphris et al., 1995; Humphris et al., 1996). The upper platform is topped to the north by the black smoker complex (BSC), a 10–15-m-tall cone-shaped structure, the locus of the high-temperature activity. No venting was observed at the lower platform since the late 1990s, confirming the extinction of Kremlin white smokers (Edmonds et al., 1996). Surface mineralization of the deposits is dominated by sulfides associated with anhydrite. Ocherous Fe oxides were also observed from the steep outer talus slopes on the western, northern, and eastern parts of the deposit (Tivey et al., 1995). A study of the ocher indicates oxidation of primary sulfide assemblages by an LT fluid concomitant with direct precipitation of Fe oxide and silica from this fluid (Tivey et al., 1995). The HTZ also contains several relict SMS deposits (Rona et al., 1993). In this relatively restricted area (approximately 15 km^2), at least 14 hydrothermal deposits are present (for an equivalent mass of 22.1 Mt; Graber et al., 2020) including the active mound (360°C; Rona et al., 1986), the so-called inactive deposits of the Alvin zone, the MIR zone characterized by high heat flow (Rona et al., 1996), and the LT shimmering mound (22.5°C). Recent investigations including drilling operations provide a new model for inactive SMS deposits, highlighting a strong silicification process occurring at the closing stages of hydrothermal episodes (Murton et al., 2019). Sulfide mineralization was formed between 102 kyr and the present, and the dating of two manganese crusts provides an estimated age of 140 and 74 kyrs (Lalou et al., 1990; Lalou et al., 1993; Lalou et al., 1995).

3 Materials and methods

3.1 Acoustic data

Acoustic data were acquired during the Cambon (2014) (https://doi.org/10.17600/14000100) cruise. Regional acoustic surveys were acquired between 8 and 10 knots using the hull-mounted Reson SeaBat 7150 MBES. High-resolution (HR) seafloor mapping was performed using the ROV Victor-mounted Reson SeaBat 7125 MBES (400 kHz). The surveys were made at 0.3 knots at a near-constant altitude of 50 m above seafloor. Horizontal resolutions of 1 m and 0.5 m were obtained for bathymetric maps and acoustic backscatter maps, respectively. Post-processing of raw data files was carried out with SonarScope and GLOBE software (©Ifremer).

3.2 Dive observations, measurements, and sampling

Thirteen dives with sampling and temperature measurements (HOV T-probe) using the HOV Nautile and ROV Victor were made during the Cambon (2014), Fouquet et al. (2017) (https://doi.org/10.17600/17000200), and Pelleter and Cathalot (2022) (https://doi.org/10.17600/18001851) cruises.

To avoid strong sampling bias (e.g., focusing on chimney samples), we favored systematic sampling across SMS deposits (Supplementary Figure S1). When achievable, we focused on massive blocks outcropping from the scarp fault. This strategy is thought to provide a representative view of surface and subsurface mineralization (first 5 m) and, if strongly oxidized samples are excluded, relatively good information of the SMS deposit grades in the upper zones.

3.3 Mineralogy and geochemistry

Sixty-six sulfide-rich rocks and 55 Fe–Mn oxides and silica-rich mineralization were analyzed (Supplementary Tables S1, S2). Mineral identification was done using X-ray diffraction (XRD) analyses conducted with a Bruker AXS D8 Advance diffractometer. Sample powder was top loaded into circular cavity holders, and all analyses were run between 5° and 70°2θ, with 0.01°2θ step at 1s/step (Cu–Kα radiation, 40 kV, 30 mA). Mineral identification was done using DIFFRAC.SUITE EVA software, and semi-quantitative estimation was performed using TOPAS software.

Major and trace element analyses were conducted with a wavelength-dispersive X-ray fluorescence spectrometer (WD-XRF; Bruker AXS S8 TIGER) on fusion beads or compressed pellets, respectively. After data acquisition, measured net peak intensities corrected from inter-element effects were converted into concentrations using relevant calibration curves generated from the analysis of certified reference materials. For gold analyses, samples were digested in aqua regia. Au was adsorbed on a membrane filter, and WD-XRF analysis was performed directly on the filter (Etoubleau et al., 1996).

3.4 Outlines of SMS deposits and volume/tonnage calculations

The geological limits of the SMS deposits are based on integration of dive observations, sample analyses, and bathymetry and backscatter data interpretation. Some outlines (and related volume calculation) must be taken with caution, particularly when no or low coverage of HR acoustic data was available and/or only limited length of the dive track passed through the SMS deposits.

Volume estimations were performed in ArcGIS software. Most of the volume calculations were done using a 2-m resolution digital terrain model (DTM). A lower-resolution DTM (i.e., 20 m) was used for some deposits that were not covered by HR acoustic data surveys. The first step is to use the outlines of SMS deposits for clipping the bathymetric data. In the second step, we generate a reference surface using interpolation methods. The reference surface will represent the expected topography before the formation of SMS deposits (Graber et al., 2020; Sanchez-Mora et al., 2022). Two interpolation methods were tested using the ArcGIS spatial analyst toolbox: (i) inverse distance weighted interpolation and (ii) "Topo to Raster" interpolation tool (see Supplementary Material for details). After interpolation is done, we calculate the volume between the reference surface and the initial DTM. Tonnage is calculated with an average density value of 3.5 t/m^3 (see Supplementary Material for details).

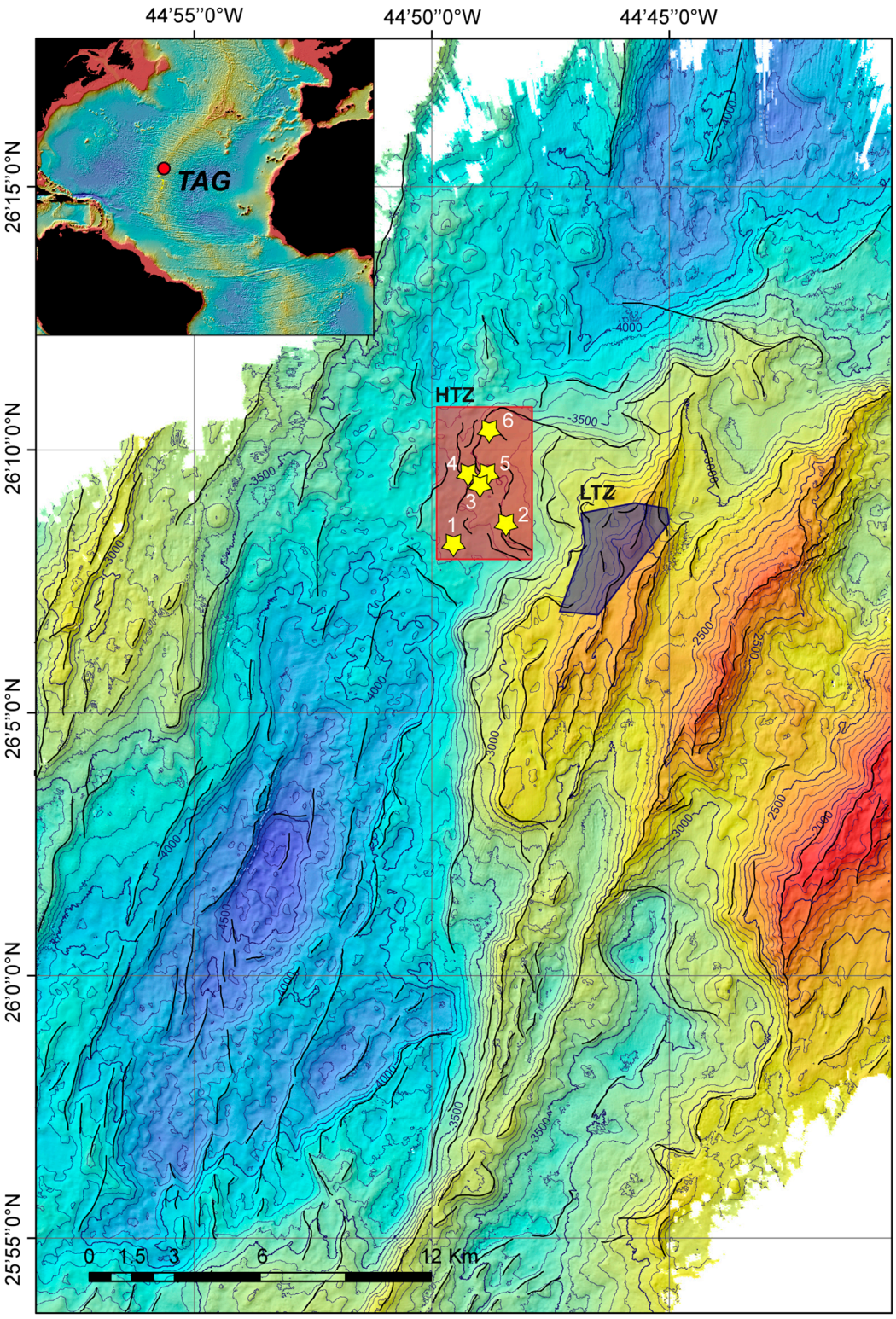

FIGURE 1
Bathymetric map (with 100 m contours) of the TAG region. The HTZ corresponds to the high-temperature zone, and yellow stars correspond to major SMS deposits: 1, TAG active mound; 2, MIR mound; 3, Southern mound; 4, Shinkai mound; 5, Double mound; 6, Shimmering mound. See Figure 2 for detailed information on SMS deposits in the HTZ. The LTZ corresponds to the low-temperature zone enclosing several Fe–Mn–Si deposits and potential diffuse flow.

4 Results

4.1 Hydrothermal zones in the HTZ and characteristics of hydrothermal deposits

According to the spatial distribution of hydrothermal deposits, type of mineralization, and morphology of the mounds, we propose to distinguish four hydrothermal zones (Figure 2): (1) MIR zone, (2) Nautile zone, (3) Alvin zone, and (4) shimmering zone. Note that the Alvin zone defined here corresponds to the Alvin relict zone described by Tivey et al. (1995) and to the southern part of the Alvin relict zone (also called North relict hydrothermal zone) defined by Rona et al. (1986); Rona et al. (1993a). Similarly, the Nautile hydrothermal zone hosts the Abyss mound (discovered by Graber et al., 2020) and most likely includes the northern part of the historical MIR zone defined by Rona et al. (1993a).

There are also two scattered deposits to the southwest (mound #11 and chimney cluster; Figure 2). Mound #11 is a deposit discovered 750 m northwest of the active mound by Graber et al. (2020) and is the most western deposit of the TAG district. Surface mineralization is mainly composed of the Mn±Fe±Si hydrothermal crust covered by pelagic sediment. The summit exhibits a relatively flat, hill-shaped morphology with no visible chimney structure. The small cluster (10–20 m length) of chimneys is located 1.2 km northeast of the active mound. Chimneys lie on pelagic sediments and are distributed along a NNE–SSW fault (axis-parallel faults) and close to an axis-oblique fault.

4.1.1 MIR zone

The MIR zone (Rona et al., 1986; Rona et al., 1993a; Rona et al., 1993b) is a hydrothermal area of 0.5 km^2 located 2 km east of the active mound (Figure 2). Recent studies (Murton et al., 2019; Graber et al., 2020) point out the presence of a major structural feature in this area: a N–S-trending, west-facing fault that extends more than 1 km to the north. At least seven hydrothermal deposits are identified in the MIR zone, and all but one (MIR #2) are located east of the N–S fault on an elevated block (Figure 2). The main mineralized area (MIR) is an oval-shaped 500-m-long and 300-m-wide zone with different morphologies and mineralized structures from the east to the west (Figures 3A, 4A–F). The western part of the MIR zone can be subdivided into two subzones: subzones A and B (Figure 3A), both being separated by an E–W-trending gully composed of metalliferous sediments covered by Mn±Fe±Si hydrothermal crust and/or pelagic sediment. On HR bathymetric maps, subzones A and B are characterized by areas of rough texture which correspond to boulders of massive to semi-massive sulfides, ocherous Fe oxides, jasper, and toppled and standing sulfide chimneys (Figure 4A). The major N–S-trending fault bounds the western border of subzone A and exposes the interior of the mound (Figure 4C). Most of the steep slope consists of broken rock fragments of basalts, together with strongly altered (±mineralized) basalts and sulfides (Figure 4B). Around 5 m under the toppled chimneys, a sharp and narrow transition between altered and mineralized basalts, massive sulfides, and sulfide chimneys (Figure 4C) indicates that deposits in the western part of subzone A are relatively thin (less than 10 m thick). The presence of basalt scree under LT hydrothermal crusts on the plateau between the western limit of subzone A and subzone B confirms that massive sulfide layers do not exceed several meters of thickness in the southwest of the MIR. The thickness of the SMS deposits is greater further east or in subzone B, but most likely does not exceed 25–30 m. Subzone C is situated in the southeastern part of the MIR and has a "crescent-moon" shape. The top of this subzone (approximately 5,000 m^2) exhibits a rough texture on bathymetric map data, similar to those observed for subzones A and B (Figure 3A). However, it does not correspond to chimneys and/or massive sulfide boulders but to metric to up to 6–7-m-tall Mn–Fe–Si mounds (Figure 4D). A widespread surface of these mounds exhibits an ongoing low-temperature activity (maximum T°C up to 29°C; Figure 4E). The associated pale orange and black precipitates are composed of Fe oxides, silica, bacterial mats, and Mn oxides. The northwestern part of subzone C and its flanks show a smooth texture on HR bathymetric map data related to Mn±Fe±Si hydrothermal crusts commonly covered by thin pelagic sediments (Figure 4F). Two holes were drilled on this smooth part of subzone C during the JC138 cruise (Lehrmann et al., 2018; 073RD and 076RD drill holes), which intersect massive sulfides at 3.6 mbsf under the Mn±Fe±Si hydrothermal crust and a jasper layer. The thickness of the mineralization in subzone C can be estimated to be up to 30 m on the basis of the topographic expression and dive observations made on the south and east flanks (see Supplementary Figure S2). Slopes at the MIR are relatively gentle (i.e., mean slope: 23.3°; Table 1), with the steep–slope talus (>40°) being restricted to southeastern and eastern parts of the site.

The other hydrothermal mounds observed in the MIR zone (i.e., MIR #2 to #7) are relatively small, between 30 m and 70 m in diameter. They are separated into two groups based on surface mineralization (i.e., oxide-dominated or sulfide-dominated). The first group is composed of hydrothermal mounds covered by widespread Mn±Fe±Si hydrothermal crusts (MIR #2, #3, #6, and #7; Figure 3A) and pelagic sediments. The top of these deposits is relatively flat, and no standing sulfide chimneys were observed attesting to a long-ceased HT hydrothermal activity. The mean slopes are over 30.5° for MIR #2 and #3 and less than 23.5° for MIR #6 and #7 (Table 1). MIR #2 is made of two coalescent mounds controlled by an N–S-trending lineament. In the northern part of MIR #2, LT hydrothermal activity is inferred from the presence of iron oxide, silica, and bacterial mats that formed along cracks inside an Mn-rich crust. MIR #3 is bounded on its western part by the N–S-trending, west-facing fault. Though Mn±Fe±Si hydrothermal crusts dominate surface mineralization at MIR #3, dredge operation (HER2-DR16) performed on the west cliff provided a large diversity of mineralization including strongly silicified sulfide-bearing rocks and jaspers. MIR #6 and #7, located east of MIR, also show some evidence of the presence of an old high-temperature sulfide mineralization under the Mn±Fe±Si hydrothermal crusts (i.e., sample HER-PL20-06, MIR #6; massive sulfide rocks outcropping at MIR #7).

The second group of mounds (MIR #4 and MIR #5) corresponds to small and thin SMS deposits mainly composed of old broken and fallen chimneys and/or meter-sized (semi-)massive sulfide blocks. A few centimeter-thick, pelagic sediment layers cover the mineralization. The mean slopes are gentle (16.8°–18°; Table 1) because these deposits correspond to scattered sulfide blocks spread on a relatively flat area (<15°).

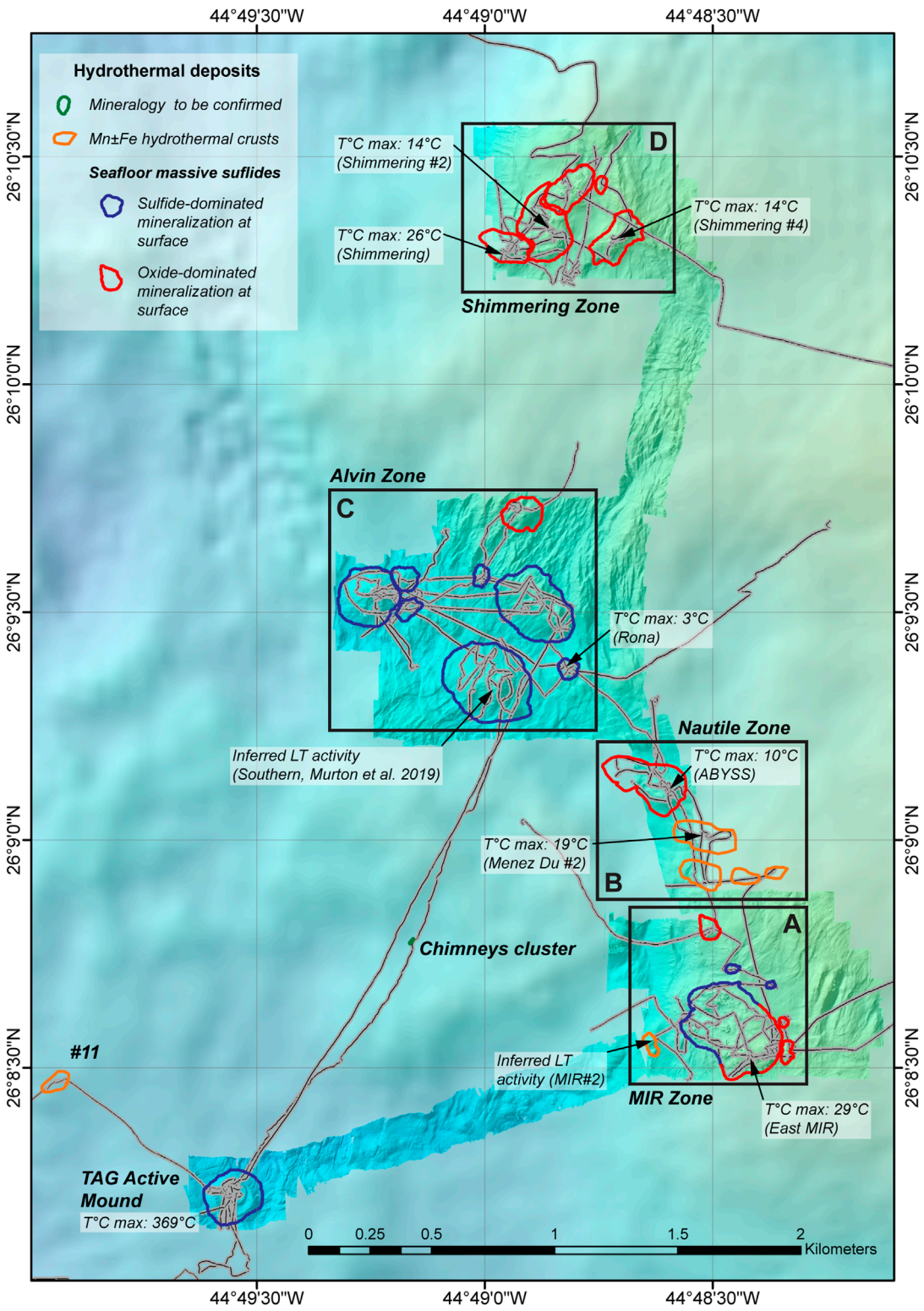

FIGURE 2
Spatial distribution of the 28 SMS deposits in the HTZ of the TAG hydrothermal field. Blue contours: SMS deposits where surface mineralization is dominated by sulfide-rich rocks. Red contours: SMS deposits where surface mineralization is dominated by oxyhydroxide-rich rocks. The maximum temperatures measured for hydrothermal venting are reported. "Inferred LT activity" corresponds to an area where orange/pale yellow precipitates were observed during submersible dives. Black lines with gray halos correspond to submersible dives (HOV Nautile and ROV Victor). High-resolution bathymetric map (1 m grid resolution) acquired during Cambon (2014) (Reson SeaBat 7125 MBES; ROV Victor).

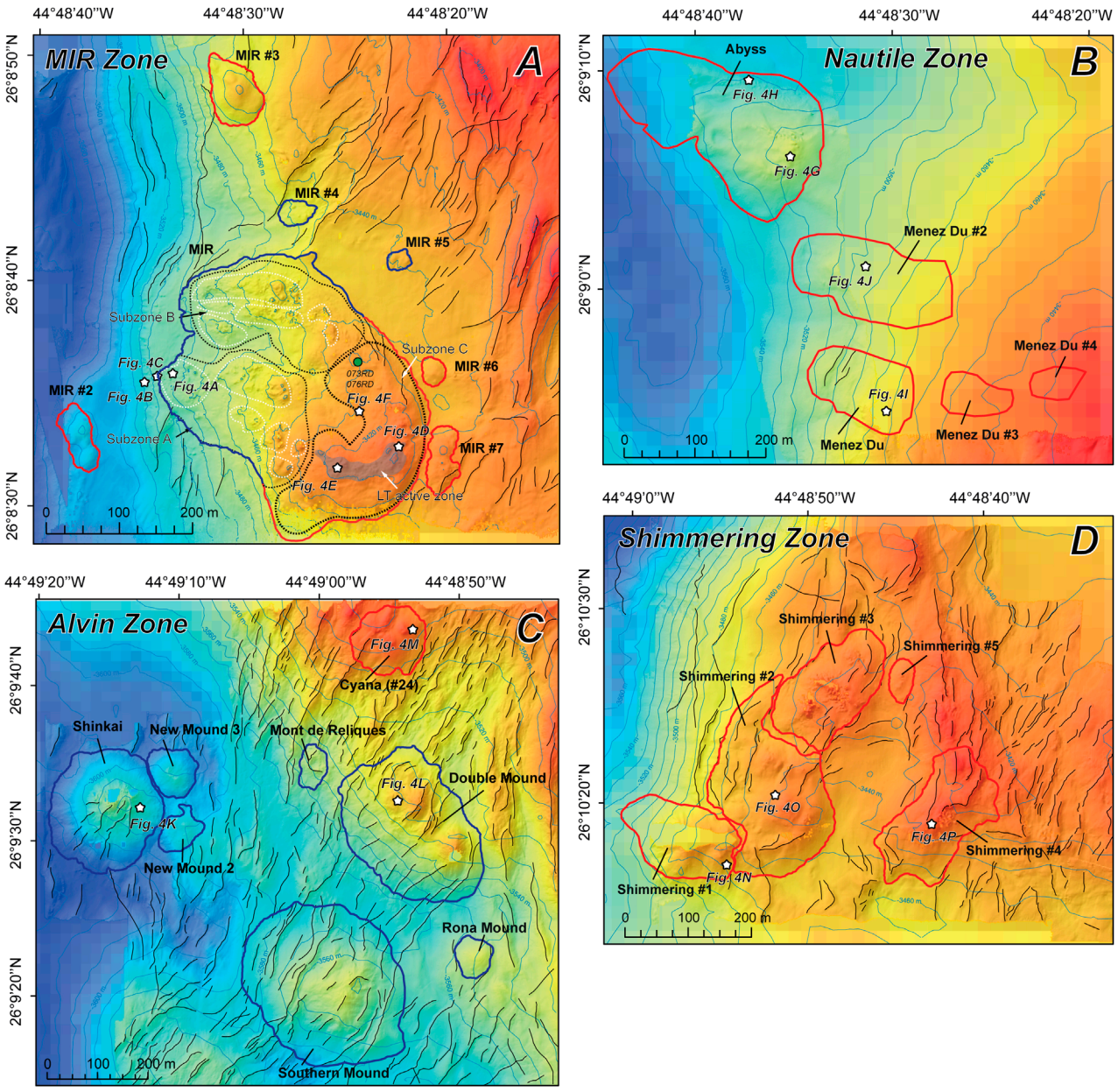

FIGURE 3
Bathymetric maps of the main hydrothermal zones of the TAG hydrothermal field. **(A)** MIR Zone. **(B)** Nautile Zone. **(C)** Alvin Zone. **(D)** Shimmering Zone. Red lines correspond to the proposed limits of the SMS mounds. White stars indicate the location of the photographs presented in Figures 4, 5. Black solid lines are lineaments (e.g., faults) interpreted from the HR bathymetric map.

4.1.2 Nautile zone

The Nautile zone is adjacent to the MIR zone and is composed of at least five deposits in a hydrothermal area of 0.4 km^2, with the southernmost deposit located just 130 m north of MIR #3 (Figure 2). The Abyss mound is located in the northwestern part of the Nautile zone (Figure 3B) and constitutes the largest hydrothermal deposit of the area (325 m × 200 m). It has a WNW–ESE elongated shape attributed to the coalescence of two distinct semi-circular mounds characterized by gentle downslope (18°–25°) from the east to the west. Eastward, the mound is made up of two platforms, with the upper platform (60 m in diameter) superposed rather symmetrically on the lower platform (200 m in diameter). The upper platform shows semi-circular depressions (3–4 m deep, up to 40 m in diameter) and is topped to the east by LT concretions, where weak hydrothermal activity (max: 10°C) is observed (Figure 4G). The talus on the steep slopes is composed of highly oxidized massive sulfides (Figure 4H). Westward, the deposit is composed of one platform (approximately 120 m in diameter) with a central depression attributed to a major collapse of the structure. The proportion of the pelagic sediment cover is relatively high, particularly in the upper part of the platforms where depressions, relatively flat areas, or gentle slopes dominate. Surface samples collected on the Abyss mound are mainly composed of iron oxyhydroxides. Pyrite is restricted to a few relict micrometric minerals in strongly oxidized breccia.

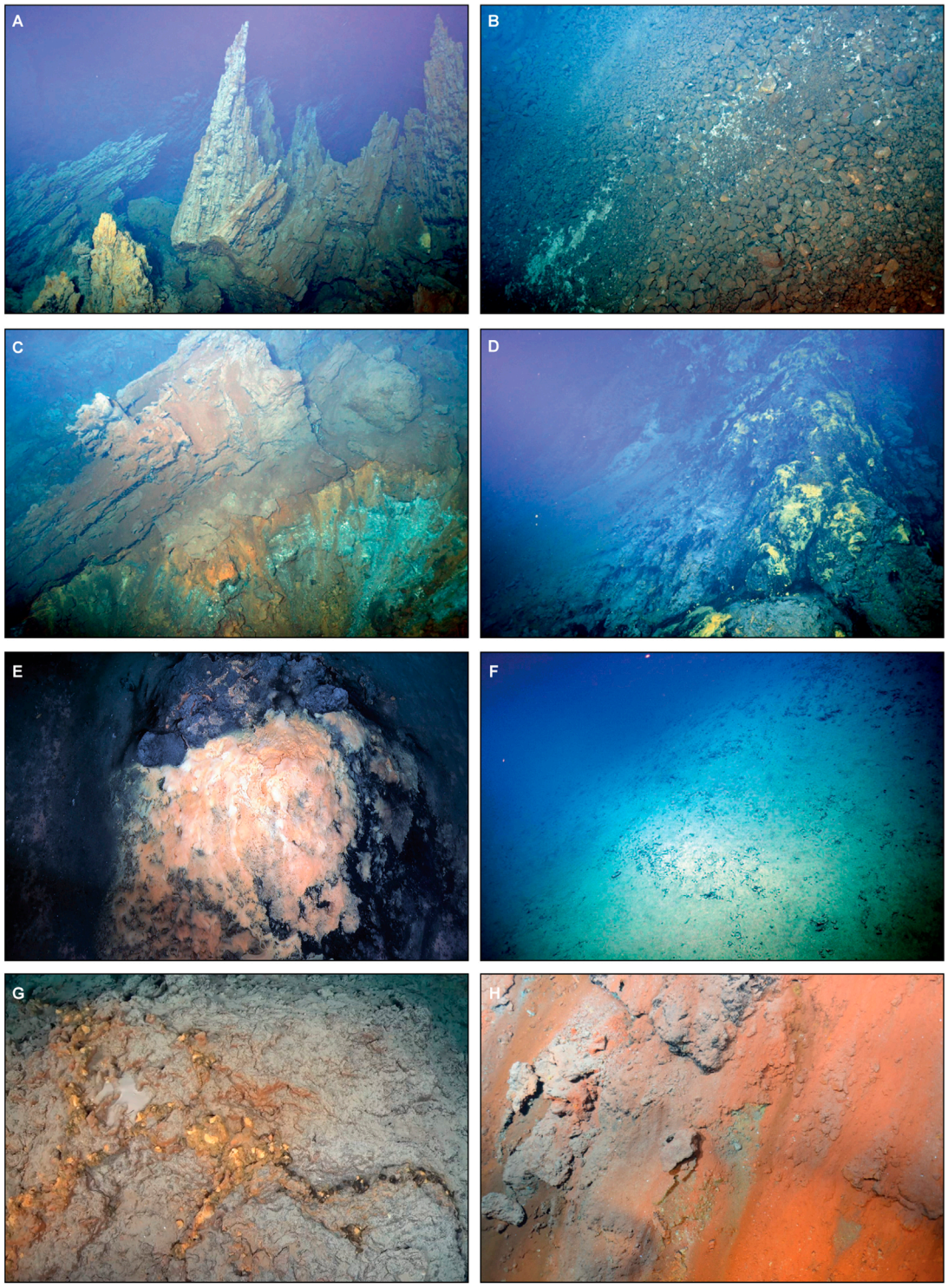

FIGURE 4
(Continued).

The four mounds have been named Menez Du ("black mound" in Breton), #2, #3, and #4 (Figure 3B) because of the presence of massive Mn concretions and crusts outcropping that form pelagic sediments (Figure 4I). These mounds have flat morphologies with gentle slopes (<25°). The top of Menez Du #2 is composed of hill-shaped oxide structures with few plurimetric oxide-dominated blocks at the top. Low-temperature diffusive venting with pale orange precipitates develops along cracks onto Mn±Fe±Si crusts (17.7°C) or between plurimetric-scale oxide blocks (19°C; Figure 4J). At Menez Du, #3 and #4, mineralization is barely

10.3389/feart.2024.1304993

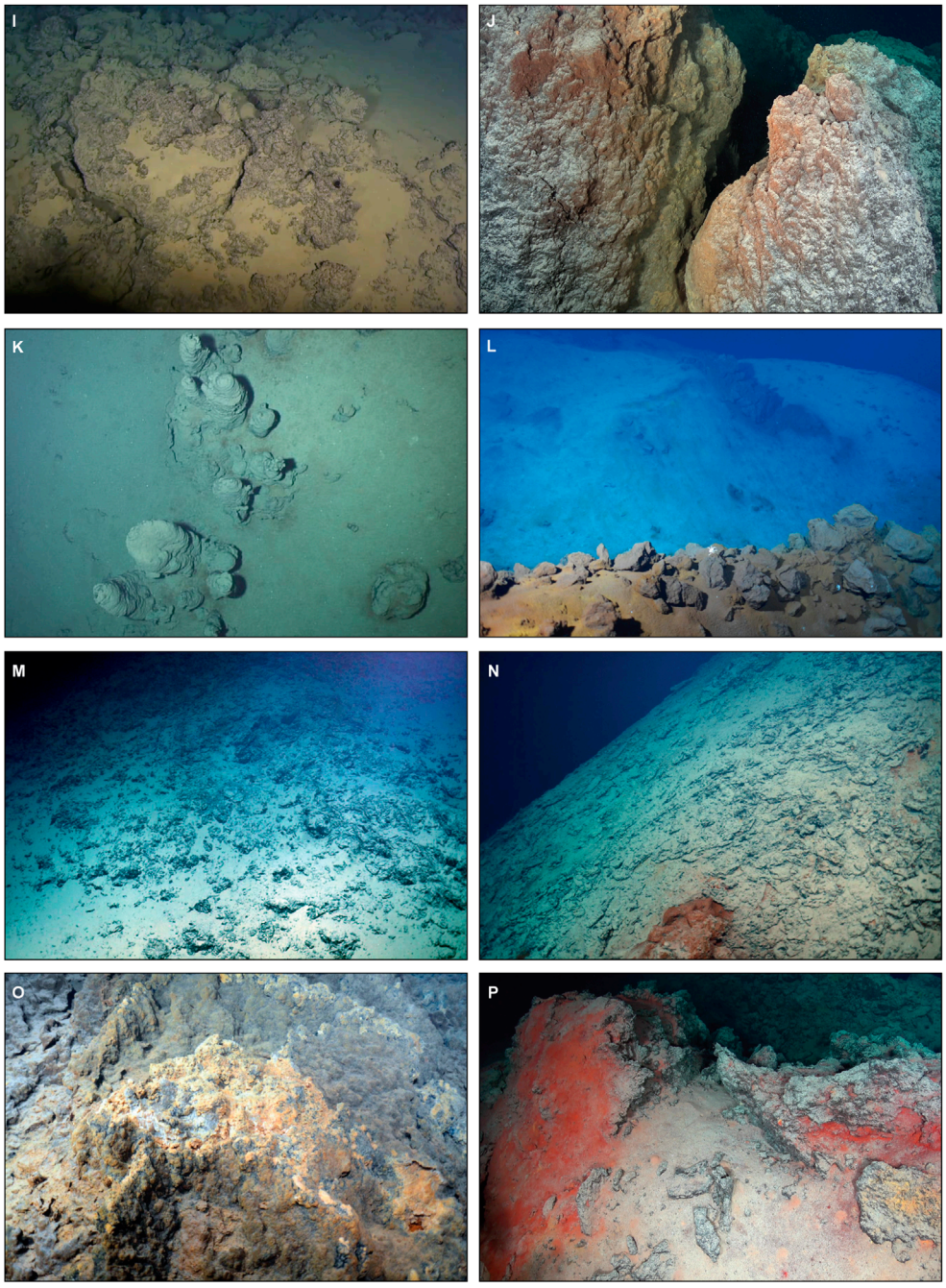

FIGURE 4
(Continued). Photographs of surface mineralization in the TAG hydrothermal field. **(A)** Toppled sulfide chimneys (approximately 5–7 m tall) observed in the western part of the MIR mound (Subzone A). **(B)** Talus with polygenic rock blocks composed of basalt, altered basalts (white), and massive sulfides (west of subzone A; MIR). **(C)** Transition between altered basalt (white zone), massive sulfides (brown zone), and toppled chimney at the western edge of subzone A (MIR). **(D)** Iron–silica–manganese hydrothermal mounds (up to 7 m tall) with diffuse fluids (yellow areas) outcropping in the LT hydrothermal zone southeast of the MIR mound (subzone C). **(E)** Close-up of orange and pale yellow iron–silica precipitates surrounded by black manganese oxyhydroxides (MIR; subzone C). The measured temperature reaches 29°C. **(F)** Manganese crust with pelagic sediment cover (MIR). **(G)** Yellow–orange iron–silica precipitating in fractures inside the Mn–Fe–Si crust (ABYSS). The measured temperature reaches 10°C. **(H)** Nearly fully oxidized massive sulfides (note the bright red color) observed on the northern flank of the Abyss mound. **(I)** Thick manganese crust with pelagic sediment cover observed at the summit of Menez Du. **(J)** Metric oxide-rich blocks at the summit of Menez Du #2. Orange and red colors represent the ongoing precipitation of iron oxides from diffuse venting between the two blocks. The measured temperature reaches 19°C. **(K)** Standing inactive chimneys (approximately 1–2 m tall) observed approximately 50 m east of the summit of the Shinkai mound. **(L)** Massive sulfides scree observed at the fault scarp at the Double mound. A very low pelagic sediment cover indicates that fault movement was recent. In the background, massive sulfides are draped in the veil of the pelagic sediment. **(M)** Widespread manganese crust with pelagic sediment covering massive sulfides at the Cyana mound. **(N)** Manganese crust covering the southeast flank of the Shimmering mound. The brown–red block most likely corresponds to a part of a relict chimney with oxidation at the surface. **(O)** LT fluid (14°C) diffusing through Fe–Si precipitates near the summit of Shimmering zone #2. **(P)** Metric blocks composed of iron–silica-rich rocks (jasper) observed at the summit of Shimmering zone #4.

visible under the pelagic sediment cover. Iron oxyhydroxide patches are observed along fault scraps, and massive Mn crusts and mounds outcrop at the top of the mounds. Outlines of Menez Du #3 and #4 are unclear and must be taken with caution since 1) no HR acoustic data are available, 2) observations were done during one sole dive, and 3) pelagic sediments cover a large surface of the mounds.

4.1.3 Alvin zone

The Alvin zone is a hydrothermal zone of ca. 1 km^2 located just northwest of the Nautile zone (Figure 2). Eight SMS deposits including three of the largest (i.e., > 40,000 m^2) SMS deposits of the TAG hydrothermal field are identified (Figure 3C; Table 1). All but one (Cyana) are dominated by sulfide-rich mineralization at the surface. Shinkai, new mounds #2 and #3, and Mont de reliques are topped by inactive chimneys (Figure 4K), attesting to a relatively recently ceased HT hydrothermal activity. These mounds have generally steep slopes (>30°; e.g., Shinkai; Table 1) and are unaffected by axis-parallel faults. The Shinkai mound is a 200-m-diameter SMS deposit characterized by a regular conical morphology only disrupted by some collapse structures just south and southwest of the summit. Surface mineralization is dominated by chimneys and semi-massive and highly silicified massive sulfides. Metalliferous sediments with scarce meter-scale sulfide blocks (massive sulfides and chimneys) are also present, particularly on the north and northwestern flank of the mound. The southern part of the Shinkai mound is characterized by the presence of meter-sized massive sulfide blocks due to mass wasting. New mound #3 is smaller than Shinkai but possesses similar morphology and surface mineralization. New mound #2 and Mont de reliques differ slightly by exhibiting an irregular central crater. Southern mound, Double mound, Cyana mound, and Rona mound are devoid of standing relict chimneys and generally display a flat surface covered by pelagic sediments at their summits. This indicates a relatively long-ceased HT hydrothermal activity. Southern mound and Double mound are strongly affected by NNW to NW faults (i.e., axis-parallel faults) that expose 1) decimeter- to meter-sized massive sulfide boulders (Figure 4L) embedded in sulfide–sulfate–oxide-rich sediments, 2) indurated sulfide- and/or oxide-rich sediments (with rare aragonite), and 3) chimney-derived materials. Meter-sized massive sulfide boulders related to mass wasting are common on the steepest slopes (e.g., southwestern flanks of the Double mound and Southern mound). Most samples collected in the fault correspond to semi-massive to massive sulfide blocks only oxidized at the surface. On the eastern edge of the Southern mound, a fault scarp shows iron-rich metalliferous sediments up to 7 m in thickness and with only few sulfide rubbles. At the Double mound, a large zone (40 m in diameter) of a thick metalliferous sediment layer (including blocks of the hydrothermal crust) is present in the northern part of the deposit. The Rona mound is a 60-m-diameter deposit lying on the top of a circular volcanic edifice. Gentle slopes (<25°) expose decimeter-sized sulfide-rich blocks embedded in pelagic sediments. Rare meter-sized sulfide boulders were observed on the northern and southern flanks where slopes are steeper (ca. 30°). Small patches of Si–Fe precipitates associated with microbial mats occur ca. 20–30 m from the summit to the north and west. No visible diffuse venting was observed, but a slight temperature anomaly was measured (i.e., 3°C). Similar patches observed at the Southern mound near the summit during dive HER-PL-17 might correspond to microbial mats identified by Murton et al. (2019). The Cyana mound is a 150-m-diameter SMS deposit formed by at least three flat hill-shaped edifices. Gentle slopes characterize the deposit, although it is dissected by a NE–SW axis-parallel fault. A striking feature of this mound compared to other SMS deposits in the Alvin zone is the extent of the LT Mn-rich hydrothermal crust (Figure 4M) that almost entirely covers the sulfide material and can reach a thickness of up to 10 cm. Sulfide rocks were only observed on a slump scarp located south of the NE–SW fault.

4.1.4 Shimmering zone

The shimmering zone is located 1 km north of the northern border of the Alvin zone (Figure 2) in the "smooth northern block" defined by Graber et al. (2020). This hydrothermal area of ca. 0.3 km^2 is located on a bathymetric high bounded by a major west-facing N–S fault (Figure 2). It comprises at least five hydrothermal deposits including four large mounds (>10,000 m^2) and one small mound (<5,000 m^2) (Table 1). Shimmering, Shimmering #2, Shimmering #4, and Shimmering #5 coalesce into a large complex (up to 600 m long and 200 m wide) with a sigmoid-like shape (Figure 3D). Shimmering and Shimmering #2 are bounded to the west by the major N–S fault interpreted as a detachment surface (Szitkar et al., 2019). Shimmering #3 and #5 are located 150 m west of a detachment surface identified by Graber et al. (2020) at the southern edge of an N–S volcanic ridge. Shimmering #4 is separated from the other deposits by a small basin covered by mixed pelagic–hydrothermal sediments. Shimmering #4 lies at the intersection of an N–S volcanic ridge and an axis-perpendicular fault. The Shimmering zone surface mineralization is mainly composed of oxide-rich rocks including Mn crusts (Figure 4N), Fe ± Mn ± Si LT precipitates (Figure 4O), metalliferous sediments, and iron–silica-rich rocks (Figure 4P). Semi-massive sulfide mineralization outcropping is observed at the Shimmering mound where steep slopes (>30°) offer the opportunity to observe subsurface mineralization located under the LT Fe ± Mn ± Si hydrothermal crusts. Several metric-wide LT patches with fluid flow venting at temperatures up to 26°C were observed on the hydrothermal crust near the summit of the Shimmering mound. Widespread LT hydrothermal crusts cover the sub-circular Shimmering #2 mound. The base of the deposit is a 200-m-diameter platform with a steep SE flank (up to 30°) and a gentler NW flank (<25°). The platform is crosscut by N–S to NE–SW faults and topped by at least three smaller cone-shaped structures. These latter structures, less than 50 m in diameter and 15 m in height, appear unaffected by the faults and host several small LT patches (T° up to 14°C; Figure 4O). Shimmering #3 is a (200 m × 100 m) NE–SW-elongated mound with gentle slopes (mean slope 23°). Pelagic sediments cover most of the mineralization except at the summit where metric- to decametric-sized boulders outcrop (rough texture on the HR bathymetric map; Figure 3D). Surprisingly, these large boulders coated by a millimeter-thick hydrogenetic Fe–Mn layer are friable due to a high proportion of oxides and oxyhydroxides with a variable amount of silica. Shimmering #4 is a large (200 m x 100 m) NE–SW-elongated deposit characterized by gentle slopes (mean slope 17.2°). Pelagic sediments cover the base of the southern flank embedding widespread Mn ± Fe ± Si hydrothermal crusts. Metric to decametric boulders outcrop at the summit where an E–W fault and a NNE–SSW fault intersect. It

TABLE 1 Characteristics and volume and tonnage estimates for hydrothermal deposits in the TAG hydrothermal field.

Mound	Hydrothermal area	Mean slope	Mean slope along-axis	Mean slope cross-axis	Area (m^2)[1]	Area (m^2)[2]	Volume (m^3)[1]	Volume (m^3)[2]	Tonnage (Mt)[1]	Tonnage (Mt)[2]	Surface mineralization[3]	Hydrothermal activity–max T°
TAG active mound	West TAG active mound	28.7	26.9–**31.6**	**24.4**–29.1	37,399	39,693	6,13,926	6,47,330	2.15	2.27	Sulfide	Active HT–365°C
#11	West TAG active mound				5,343	11,979	30,497	62,000	0.11	0.22	Oxide	
Total					**42,742**		**6,44,422**		**2.26**	**2.49**		
MIR	MIR zone	23.3	19.4–23.4	**17.5–23.7**	90,914	1,06,128	9,72,467	15,59,520	3.40	5.46	Sulfide and oxide	Active LT–29°C
MIR #2	MIR zone	31.7			3,124		10,194		0.04		Oxide	Inferred activity
MIR #3 (#29)	MIR zone	30.7	**23.6**–28.4	29.9–**31.8**	5,218	8,584	34,717	66,950	0.12	0.23	Oxide	
MIR #4	MIR zone	18.0			1,340		894		0.003		Sulfide	
MIR #5	MIR zone	16.8			711		595		0.002		Sulfide	
MIR #6	MIR zone	23.3			1,018		2,562		0.01		Oxide	
MIR #7	MIR zone	21.8			3,168		7,878		0.03		Oxide	
Total					**1,05,494**		**8,80,527**		**3.08**	**5.69**		
Abyss	NAUTILE zone	25.5	**18.6**–24.6	28.0–**30.3**	42,517	36,160	3,59,033	4,63,840	1.26	1.62	Oxide	Active LT–10°C
Menez Du	NAUTILE zone	21.8			12,886		61,148		0.21		Oxide	
Menez Du 2	NAUTILE zone	23.9			21,479		72,849		0.25		Oxide	Active LT–19°C
Menez Du 3	NAUTILE zone				4,645		9,463		0.03		Oxide	
Menez Du 4	NAUTILE zone				2,722		8,398		0.03		Oxide	
Total					**84,250**		**5,10,890**		**1.79**	**1.62**		
Rona mound	ALVIN zone	29.3	**19.4–29.7**	23.8–23.4	4,639	16,501	25,896	1,09,650	0.09	0.38	Sulfide	Weakly active–3°C
Double mound	ALVIN zone	27.1	28.3–31.8	**20.3–34.3**	61,448	44,126	8,08,767	5,86,310	2.83	2.05	Sulfide	
Southern mound	ALVIN zone	25.0	**22.0**–27.0	28.1–**28.7**	81,896	78,867	12,57,954	12,21,350	4.40	4.27	Sulfide	Inferred activity[4]
Shinkai	ALVIN zone	33.2	32.3–**37.7**	**26.1**–31.0	42,698	48,938	8,58,830	9,45,040	3.01	3.31	Sulfide	
New mound 2	ALVIN zone	31.0			5,061	4,580	26,756	27,440	0.09	0.10	Sulfide	
New mound 3	ALVIN zone	36.2			7,552	7,838	72,070	76,000	0.25	0.27	Sulfide	

(Continued on the following page)

TABLE 1 (*Continued*) Characteristics and volume and tonnage estimates for hydrothermal deposits in the TAG hydrothermal field.

Mound	Hydrothermal area	Mean slope	Mean slope along-axis	Mean slope cross-axis	Area (m^2)[1]	Area (m^2)[2]	Volume (m^3)[1]	Volume (m^3)[2]	Tonnage (Mt)[1]	Tonnage (Mt)[2]	Surface mineralization[3]	Hydrothermal activity–max T°
Mont de Reliques	ALVIN zone	26.4			3,806	2,667	8,088	8,900	0.03	0.03	Sulfide	
Cyana (#24)	ALVIN zone	25.5	**24.6–30.9**	26.1–30.1	15,921	7,405	1,06,641	40,200	0.37	0.14	Oxide	
Total					**2,23,019**		**31,65,001**		**11.08**	**10.55**		
Shimmering #1[a]	Shimmering zone	33.0			17,404	40,792	2,99,401	5,02,520	1.05	1.76	Oxide	Active LT–26°C
Shimmering #2	Shimmering zone	23.0	24.2–**29.9**	**22.4**–22.4	36,851		2,73,463		0.96		Oxide	Active LT–14°C
Shimmering #3	Shimmering zone	23.0	**22.4–28.9**	24.9–27.4	20,433		1,09,824		0.38		Oxide	
Shimmering #4	Shimmering zone	17.2	**16.9**–22.4	25.3–**26.8**	23,380		1,55,328		0.54		Oxide	Active LT–14°C
Shimmering #5	Shimmering zone	25.1			2,144		3,477		0.01		Oxide	
Total					**1,00,212**		**8,41,494**		**2.95**	**1.76**		
Total TAG field					**5,55,717**		**60,42,334**		**21.15**	**22.11**		

[1]This study; [2]Graber et al. (2020); [3]Nature of the dominant surface mineralization; [4]Murton et al. (2019).
Area calculated in [1] and [2] is plain area (m^2).
[a]Shimmering mound defined by Graber et al. (2020) correspond to Shimmering#1 and part of Shimmering#2.

corresponds to iron–silica mineralization (Figure 4P), most likely uplifted during tectonic dissection of the mound. Low-temperature fluids (up to 14°C) diffuse through cracks, and LT precipitates develop on the Fe–Si blocks. Shimmering #5 is a small mound where outcrop LT hydrothermal crusts are covered by pelagic sediments.

4.2 Mineralogy and geochemistry

4.2.1 Sulfide-rich mineralization

Sulfide-rich rocks were sampled in the MIR zone (n = 23), Alvin zone (n = 41), and Shimmering zone (n = 2). In the MIR zone, samples are mainly composed of fragments of chimneys and few semi-massive sulfides. Most of the semi-massive sulfides and strongly silicified sulfide rocks (Figures 5D, E) were recovered at MIR# 3. The mineralogy of the MIR zone is dominated by iron sulfides (pyrite and marcasite; 42 wt%) associated with a significant amount of chalcopyrite (21 wt%) and silica (e.g., quartz and opal; 23 wt%) (Figure 6). Minor minerals include secondary copper minerals (covellite and atacamite) and goethite. MIR #3 samples are commonly silica-rich, which indicates the presence of a strongly silicified zone beneath the Fe–Mn oxyhydroxide crusts. Surface samples at the MIR exhibit a large amount of chalcopyrite (27 wt%) and a lower proportion of silica (3 wt%). Sphalerite is generally scarce, except in chimneys where its proportions can reach up to 56 wt%. The mean copper concentration in the MIR zone is high (ca. 10 wt%), whereas the zinc content is generally lower than 3 wt% (Supplementary Table S1). Average Cu + Zn concentrations reach 13.6 wt% (±9.7; n = 15) and 10.5 wt% (±9.1; n = 7) for MIR and MIR #3, respectively (Figure 7A). High Cu + Zn concentrations (16.8 wt% ±9.8; n = 13) are recorded in chimney samples (Figure 7A). Semi-massive sulfides have very low Zn concentrations (<0.2 wt%) but exhibit relatively high copper contents (up to 13.5 wt%) compared to the Alvin zone (Figure 7A). Gold concentrations vary from less than 0.1 ppm to up to 18.3 ppm (mean Au: 5.8 ppm ±6.2; n = 14). High Au contents are correlated with high Zn, Cd, Ga, and Ag concentrations. However, four samples from MIR #3 are relatively gold-rich (>3 ppm) without significant Zn enrichment (i.e., Zn < 0.7 wt%). These samples are characterized by high silica concentrations (26.67 wt% to 70.92 wt% SiO_2).

Surface and subsurface samples collected in the Alvin zone mainly comprise semi-massive to massive sulfides and rare chimneys (Figures 5A–C). Iron sulfides (pyrite and marcasite; 79 wt%) are dominant, and silica (10 wt%), sphalerite (3 wt%), and chalcopyrite (2 wt%) are only present in minor amounts (Figure 6). The Double mound and Southern mound are predominantly composed of pyrite (81 wt% and 84 wt%, respectively) and minor marcasite (5 wt% and 1 wt%, respectively). Chalcopyrite and sphalerite amounts are low in the two deposits. The higher sphalerite amount for the Double mound (Figure 6) is only due to one Zn-rich sample. The Shinkai mound is characterized by a high proportion of silica minerals (opal, cristobalite, and quartz; 28 wt%) either in the chimney or massive sulfides. High silica content is also recorded in two samples collected at New Mound 2 and New Mound 3 (HER-PL-15-13 and HER-PL-14-03). Marcasite contents are higher in the Shinkai mound samples than in those from the Double mound and Southern mound (Figure 6). The two samples from Mont des reliques are dominated by iron sulfides and show a significant amount of aragonite. Two sulfide-rich rocks were sampled on an NNE–SSW fault that crosscuts the Cyana mound. Pyrite and marcasite are dominant sulfides, but a significant amount of amorphous silica is also detected.

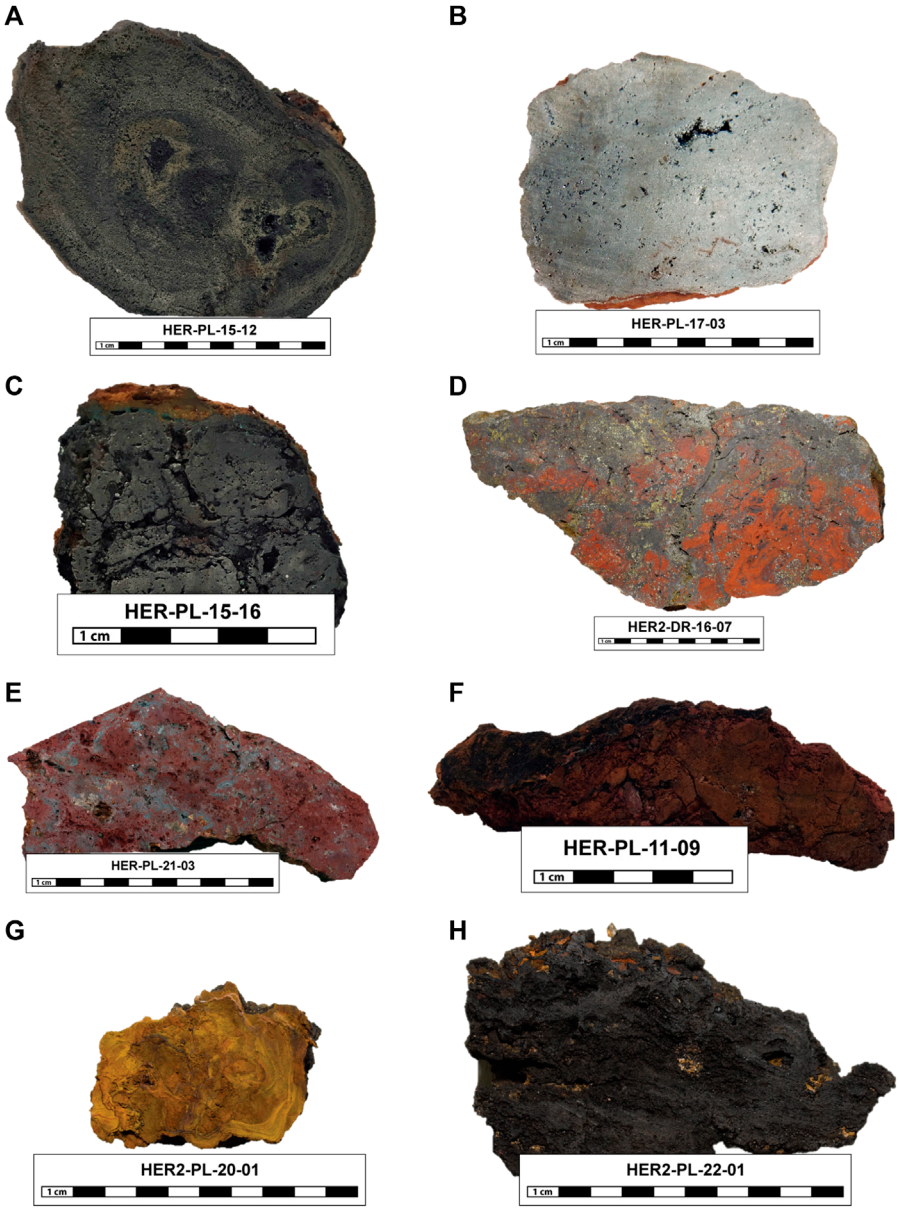

FIGURE 5
Photomicrographs representative of surface mineralization collected in the TAG hydrothermal field. **(A)** Chimney fragment (HER-PL-15-12; New mound #2) with two fluid conduits. The sample is mainly composed of pyrite, marcasite, and chalcopyrite. **(B)** Massive sulfides composed of recrystallized pyrite (HER-PL-17-03; Southern mound). **(C)** Massive sulfides with a brecciated structure (HER-PL-15-16; Double mound) mainly composed of pyrite. The thin lining of chalcopyrite at the boundary of pyrite clasts and cavities indicates late HT pulses (associated with anhydrite dissolution). **(D)** Jasper breccia (bright red) partially replaced by grayish pyritic hydrothermal chert indicating a reaction with reduced, hot (<150°C) fluids (HER-PL-16-07; MIR #3). **(E)** Jasper breccia material with a vuggy texture (HER-PL-21-03; MIR mound). **(F)** Fully oxidized sulfide breccia (HER-PL-11-09; Abyss mound). **(G)** Low-temperature Fe–Si precipitate (HER2-PL-20-01; Shimmering #3). **(H)**. Cu and Zn-rich manganese hydrothermal crust (HER2-PL-22-01; Menez Du #3).

Low average Cu and Zn concentrations characterize SMS deposits of the Alvin zone (Figure 7B). All but two samples exhibit zinc concentrations lower than 2 wt%, and only five samples have copper values greater than 3 wt%. All samples (including chimneys) from the Southern mound and Shinkai mound have zinc contents lower than 1 wt%, and all semi-massive sulfides are rather copper-poor (i.e., < 3 wt%). These two mounds have average copper and zinc concentrations even lower than those of Krasnov and TAG (ODP samples) deposits (Figure 7B). Higher average zinc and copper values and lower Cu/Zn ratio recorded for the Double mound (Figure 7B) are due to a single sample with very high Zn (42.85 wt%) and Cu (13.44 wt%) concentrations. Disregarding this sample, average Zn and Cu contents and Cu/Zn ratio are similar to those recorded for the Shinkai mound. Gold concentrations are low in most sulfide samples from the Alvin zone. No sample from the Southern mound has Au content greater than 1 ppm, and

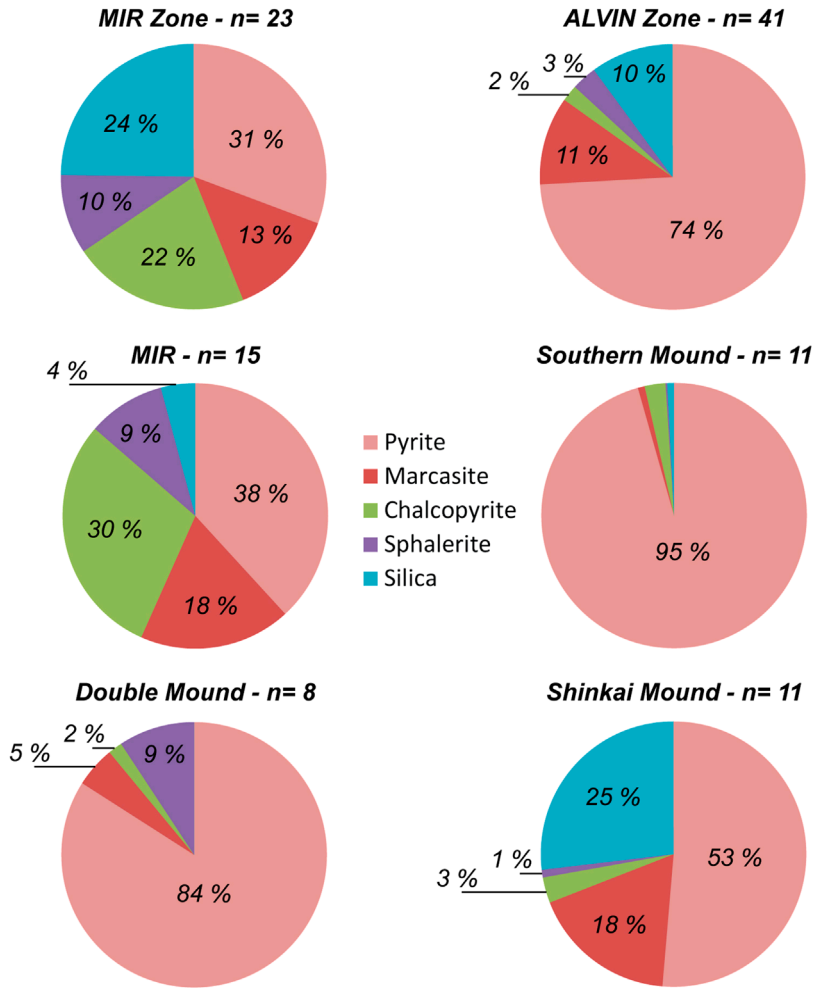

FIGURE 6
Abundance of major minerals estimated by X-Ray diffraction in sulfide-rich rocks sampled in the ALVIN and MIR zones.

only two samples at the Double mound exhibit Au concentrations greater than 1 ppm (i.e., 1.9 ppm). Five samples display relatively high gold contents (i.e., > 3 ppm; up to 31.3 ppm), and all but one have SiO_2 concentrations greater than 33 wt%. Sample HER-PL-14-02 (chimney; New Mound 2) shows an Au concentration of 8.4 ppm correlated with high Zn (10.72 wt%), Ag (470 ppm), and Ga (616 ppm) concentrations. Samples from the Southern mound show high cobalt concentrations (up to 1,669 ppm, average at 598 ppm; *n* = 11) compared to other sulfide mineralization of the Alvin zone.

Two samples of the seventeen collected in the Shimmering zone correspond to sulfide mineralization. They were sampled on the southern flank of the Shimmering mound where steep slopes provide access to deeper parts of the deposit. Pyrite is the major phase, but a significant amount of chalcopyrite is detected (13 wt% and 14 wt%). Zinc concentrations are low (<0.3 wt%), and copper values reach 4.08 wt% (HER-PL-18-01).

4.2.2 Oxyhydroxide-rich and silica-rich mineralization

This group of mineralized rocks comprises LT Fe-rich precipitates (Figure 5G), LT Mn-rich precipitates (Figure 5H), mixed LT Fe–Si–Mn precipitates, metalliferous sediments, strongly to fully oxidized sulfide rocks (Figure 5F), and silica–iron-rich rocks (Figures 5D, E).

At mound #11, two samples from the widespread Mn ± Fe ± Si crust were sampled. The main minerals identified are birnessite, todorokite, goethite, and nontronite. X-ray amorphous FeOOH and silica are also expected. Even though the HER-PL-13-02 sample exhibits a slight copper enrichment (i.e., 0.3 wt%), the precipitates are characterized by low metal contents in accordance with the LT hydrothermal precipitation (Figure 8).

LT mineralization in the MIR zone (*n* = 8) encompasses Mn-rich hydrothermal crusts (*n* = 5) and Fe ± Si-rich deposits (*n* = 3) including currently forming Fe–Si precipitate (sample HER2-PL-22-PBT01). Mn-rich crusts were only sampled at MIR #3, whereas Fe ± Si-rich precipitates were sampled at MIR, MIR #3, and MIR #7. Todorokite and birnessite are the major components of Mn-rich mineralization, except for one sample (HER2-DR-16-10) mainly composed of X-ray amorphous Mn oxyhydroxides. Quartz was also detected as a trace mineral. Two Fe ± Si-rich precipitates are composed of X-ray amorphous FeOOH (e.g., lepidocrocite) and amorphous silica, and one sample from an old

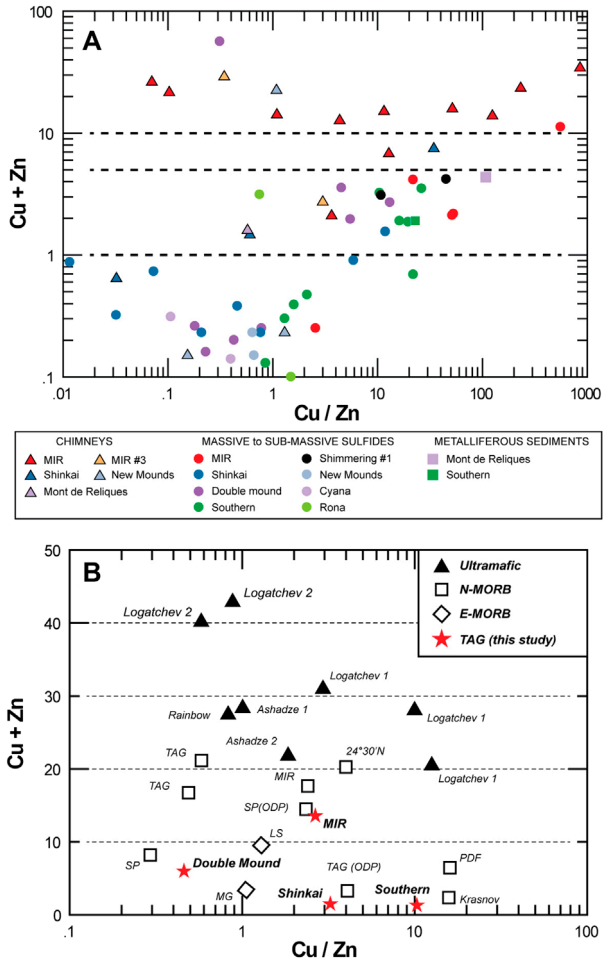

FIGURE 7
(A) Copper and zinc concentrations vs. the Cu/Zn ratio for sulfide chimney (triangles), massive and semi-massive sulfides (circles), and metalliferous sediments (square) sampled in the MIR (black symbols), ALVIN (white symbols), and Shimmering (gray symbols) zones. **(B)** Average copper and zinc concentrations vs. the Cu/Zn ratio for SMS from the Mid-Atlantic Ridge. Red stars: large SMS deposits in the TAG hydrothermal zone (this study).

hydrothermal crust at MIR (HER-PL-21-06) shows the presence of goethite and hematite. Trace elements in LT precipitates are highly variable. Five samples exhibit relatively low metal concentrations in accordance with hydrothermal ferromanganese rocks (e.g., Cu < 0.27 wt%; Zn < 0.42 wt%). Conversely, three Mn hydrothermal crusts have unusually high copper concentrations (3.7–10.7 wt%) for hydrothermal deposits (Figure 8). They also display relatively high Ba values (>0.3 wt%), and Zn contents vary from 0.25 to 0.6 wt%. Molybdenum content is high (i.e., > 1,000 ppm) in all Mn-rich crusts regardless of the copper concentration. Silica–iron mineralization is mainly composed of quartz with minor oxides and/or oxyhydroxides and sulfides. Copper and zinc concentrations vary from 0.16 to 0.59 wt% and <0.01 to 0.4 wt%, respectively.

Samples collected in the Nautile zone can be separated in LT Fe-rich (±Si ± Mn) precipitates (n = 7), Mn-rich hydrothermal crusts (n = 3), metalliferous sediments (n = 1), and strongly oxidized sulfide breccia (n = 1). Samples from the Abyss mound are all iron-rich mineralization and are dominated by iron oxides and/or oxyhydroxides. The main minerals identified are goethite and hematite. Quartz and nontronite were also detected. Mn-rich hydrothermal crusts were sampled at Menez Du and Menez Du #3. They are predominantly composed of birnessite and X-ray amorphous oxyhydroxides with minor calcite (i.e., pelagic sediment in cavities). Menez Du #2 samples include 1) an LT Fe-rich precipitate composed of X-ray amorphous FeOOH and 2) an Fe–Mn–Si hydrothermal crust composed of goethite, X-ray amorphous FeOOH, and X-ray amorphous Mn oxyhydroxides. Low-temperature Fe-rich mineralization in the Nautile zone has low metal concentrations characteristic of hydrothermal deposits (Figure 8). Four samples exhibit manganese concentrations over 10 wt%. Two of these precipitates (HER2-PL-16-04 and HER2-PL-22-01; Menez Du #3) have high copper and zinc concentrations of up to 3.6 wt% and 1 wt%, respectively. Mn-rich crusts sampled at Menez Du have low metal concentrations in agreement with a hydrothermal origin. All Mn-rich samples are characterized by relatively high Mo values, whereas Ni concentrations over 1,000 ppm were only recorded for one Cu-poor (<0.1 wt%) and one Cu-rich (3.6 wt%) Mn crust. Metalliferous sediments (HER-PL-11-10) and strongly oxidized sulfide breccia (HER-PL-11-09) from the Abyss mound display variable but relatively high copper values (0.5 wt% and 2.45 wt%).

Fe ± Si ± Mn mineralization in the Alvin zone comprises metalliferous sediments (n = 9), silica–iron-rich rocks (n = 2), and LT Fe-rich or Mn-rich hydrothermal crusts (n = 2). Goethite is the main phase present in metalliferous sediments (except HER-PL-11-06a). Carbonates are present in three samples, and nontronite was identified in one sample where X-ray amorphous FeOOH is also expected. The HER-PL-11-06a sample shows a high amount of todorokite and birnessite associated with goethite. The LT Fe-rich crust (HER-PL15-17; Double mound) is composed of goethite associated with nontronite. Birnessite is the main mineral detected in sample HER-PL11-01 (Cyana mound), though the presence of X-ray amorphous Mn oxyhydroxides is likely. XRD analyses of silica–iron-rich mineralization detected goethite, jarosite, and sulfides. However, X-ray amorphous FeOOH and amorphous silica are probably the main components of the two samples. Metalliferous sediments exhibit variable but generally high zinc (up to 0.52 wt%) and/or copper (up to 3.9 wt%) concentrations. One exception is the HER-PL-14-07 sample where very low trace element contents and high silica values are recorded. The two LT hydrothermal crust samples (HER-PL-15-17 and HER-PL-11-01) show contrasted geochemical signatures. The LT Fe-rich crust from the Double mound has low metal concentrations, whereas the Mn-rich crust from the Cyana mound exhibits copper and zinc values over 3 wt% and 0.9 wt%, respectively. Silica–iron-rich mineralization (Shinkai mound) displays low Cu concentrations (i.e., < 0.06 wt%) and zinc values between 0.15 and 0.5 wt%. Two samples have gold contents over 1 ppm (i.e., 1.4 and 1.6 ppm).

In the Shimmering zone, LT Fe ± Si ± Mn precipitates, silica–iron-rich mineralization, and metalliferous sediments are mainly composed of X-ray amorphous FeOOH, goethite, hematite, quartz, and X-ray amorphous silica. Calcite is present in one sample (HER-PL-18-07), and pyrite was only detected in an Si–Fe-rich mineralization (HER-PL-20-08a). All but one

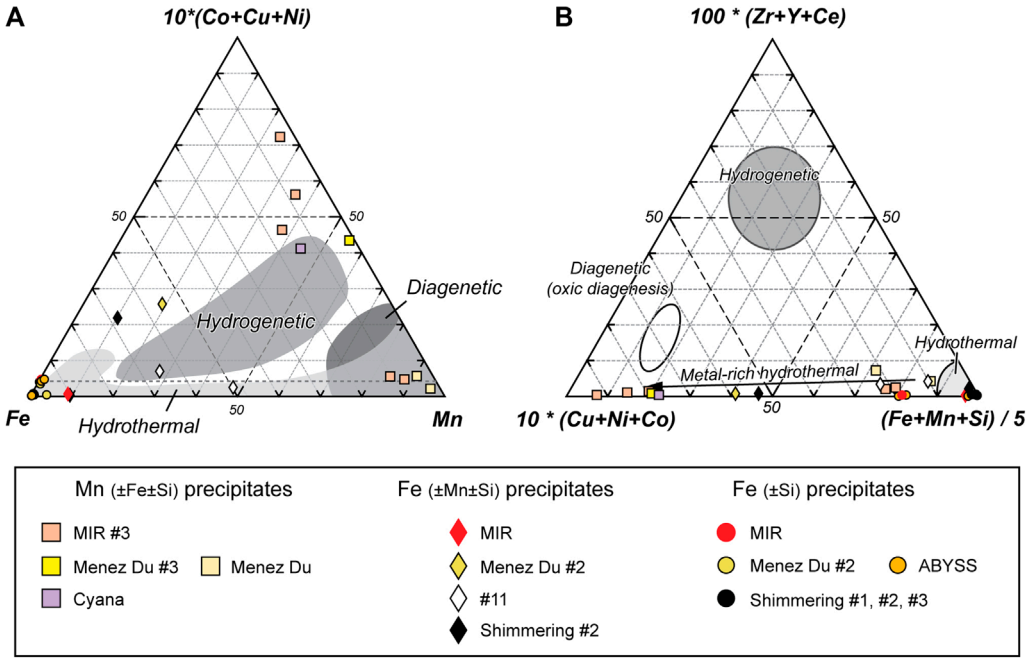

FIGURE 8
Ternary discriminative diagrams of the LT precipitates from the TAG hydrothermal field [**(A)** from Bonatti et al. (1972) and **(B)** modified from Josso et al. (2017)].

sample have copper values lower than 0.21 wt%. The highest Cu concentration (i.e., 1 wt%) is recorded for an LT Fe ± Si ± Mn hydrothermal crust collected at the top of Shimmering mound #2, where active diffuse fluids (13.7°C) were observed. Zinc concentrations vary between <0.01 and 0.64 wt%, with no specific enrichment associated with a type of mineralization (i.e., LT precipitates, metalliferous sediment, and Si–Fe mineralization). Higher zinc concentrations are recorded for an LT Fe ± Si crust (HER-PL-18-05) and an Si–Fe-rich mineralization with relicts of sulfides (HER2-PL-20-08a). Other trace elements are generally low, with the exception of two samples from Shimmering mound #2, which display relatively high Pb concentrations (0.18 wt%).

4.3 Volume and tonnage estimations of hydrothermal deposits

Volume and tonnage estimations are summarized in Table 1. The cumulative tonnage of the TAG hydrothermal field is 21.1 Mt for sulfides deposited onto the seafloor. The Alvin zone represents more than half of this tonnage with three mounds (i.e., Shinkai, Southern, and Double mounds) containing 10.2 Mt of sulfides altogether. The largest SMS deposits are the Southern mound (4.4 Mt), Shinkai mound (3.3 Mt), MIR mound (3.4 Mt), and Double mound (2.8 Mt). At the MIR zone, all but the MIR mound are small SMS deposits with a tonnage less than 0.12 Mt. The Shimmering zone contains four mounds with a tonnage over 0.38 Mt and two hydrothermal deposits with a tonnage approximately 1 Mt. The cumulative tonnage of the Shimmering zone is equivalent to the tonnage of the MIR zone. The Nautile zone has a cumulative tonnage for the five mounds of 1.8 Mt, with most of the tonnage contained in the Abyss deposit (ca. 1.3 Mt). The calculated tonnage for Menez Du and Menez Du #2 is approximately 0.2 Mt. However, calculated tonnages at the Nautile zone must be taken with caution since calculations were based on the lower-resolution digital terrain model (DTM), i.e., 20 m. Indeed, the volumes calculated on the basis of 2 m-resolution DTM are greater by a factor of 1.5–1.8 than the volumes calculated on the basis of 20 m-resolution DTM (Supplementary Table S3).

5 Discussion

5.1 Size, nature, and resource potential of hydrothermal deposits

Extensive exploration of the TAG hydrothermal field led to the discovery of thirteen new hydrothermal deposits. Six newly discovered deposits have dimensions over 5,000 m^2 and can be seen as "significant SMS deposits" (Hannington et al., 2010). The total tonnage of approximately 21.1 Mt of the hydrothermal material deposited on the seafloor is similar, though slightly lower than recent estimation (22.1 Mt; Graber et al., 2020). The lower surface area we defined from extensive dive explorations explains most of the discrepancy between our tonnage estimations and those of Graber et al. (2020). However, we believe that the calculation method used to estimate the mound mass may also lead to an overestimation of tonnages. This is particularly true for MIR deposits, where the IDW interpolation generates an unlikely topography for the reference surface (Supplementary Figure S2),

leading to an increase of more than 50% of the tonnage. Thus, caution must be paid when interpolating a reference surface, especially when deposits lie on a complex topography. At TAG, according to Murton et al. (2019) and Graber et al. (2020), total sulfide mass including subseafloor mineralization might be as high as 26 or 29 Mt. A similar tonnage of 27 Mt can be estimated from our results considering that subseafloor mineralization represents 30% of the surface tonnage (Hannington et al., 1998; Graber et al., 2020). These recent estimations indicate that the TAG hydrothermal field hosts one of the largest accumulations of sulfide materials known in the ocean and remains remarkable even in comparison with that in other large districts, such as Middle Valley (10–15 Mt; Hannington et al., 2011) or Semenov hydrothermal fields (9 Mt; Monecke et al., 2016; 13.95 Mt; Cherkashev et al., 2010; or 40 Mt; Cherkashev et al., 2013).

In the Shimmering zone and Nautile zone, surface mineralization mainly comprises LT hydrothermal precipitates (e.g., Mn–Fe–Si ± Cu crusts), metalliferous sediments, Si–Fe mineralization (e.g., jasper and silicified sulfide breccia), and rare fully weathered sulfide breccias. The average concentrations of economic metals (e.g., Cu, Zn, and Au) are low in many, but not all, samples, indicating that the shallow part of the deposits can be seen as nearly barren. No sulfide-rich rocks were sampled in the Nautile zone, and only two pyrite-rich massive sulfides were recovered at the Shimmering mound, making any interpretation of the economic potential of these deposits not possible. Metalliferous sediments with variable thickness may cover the massive sulfides in the Alvin zone, and a silica cap was identified at the summit of Southern and Rona mounds from drilling operations (Lehrmann et al., 2018; Murton et al., 2019). However, sulfide-rich rocks (i.e., massive to semi-massive sulfides and sulfide chimneys) dominate surface and subsurface mineralization sampled in the Alvin zone. Massive sulfides are mainly composed of pyrite and marcasite with only less amounts of sphalerite and chalcopyrite (Figure 6), and the average copper and zinc concentration is remarkably low (Figure 7B). It is particularly true for Southern and Shinkai mounds where the average copper and zinc contents (Cu + Zn < 1.4 wt%) are lower than that calculated for the TAG active mound (Cu + Zn: 3.2 wt%; Hannington et al., 1998). Such low Zn coupled with rather low Cu is unusual for surface and subsurface massive sulfides as the refining process is thought to trigger Zn remobilization (and to a lesser extent Cu) and its subsequent enrichment in the upper part of an SMS deposit (Hannington et al., 1998; Lehrmann et al., 2018). The presence of Co ± Cu ± Se enrichment (i.e., HT elements; Fouquet et al., 2010) in some sulfides might indicate a preferential sampling of the deepest Cu-rich and Zn-poor parts of the mound (>5 m). However, many samples record relatively high concentrations in Zn-associated LT elements (i.e., Ag: mean approximately 150 ppm; Pb: up to 543 ppm) supporting sampling of the upper 5 m of the sulfide mounds (Hannington et al., 1998). Moreover, drilling results obtained by Murton et al. (2019) for the Southern mound show that Zn concentration is systematically lower than 0.3 wt%. Although the reasons for such zinc depletion (e.g., "over-refining" processes and supergene remobilization of Zn; Lehrmann et al., 2018) are beyond the scope of this study, our results indicate that the Zn (±Cu)-poor upper orebody is distinctive of large SMS deposits hosted in the Alvin zone. On the contrary, smaller mounds such as the Rona mound and Mont de reliques (immature SMS deposits) seem to have higher Zn ± Cu grades (Murton et al., 2019). This questions the economic interest of large mafic-hosted SMS deposits, especially when compared to volcanogenic massive sulfides characterized by mean Cu + Zn greater than 2.66 wt% (Franklin et al., 2005). The gold content is generally low (<1 ppm), except for the strongly silicified sulfides that may enclose secondary gold related to reworking processes (Firstova et al., 2019).

The surface and subsurface mineralization in the MIR zone is composite in nature, divided into 1) Fe ± Mn ± Si mineralization (e.g., east of MIR, MIR #2, #3, #6, and #7) and 2) sulfide chimneys and massive sulfides (e.g., West of MIR, MIR #4, and #5). Several LT Mn-rich crusts exhibit high copper and zinc concentrations that are atypical for this type of hydrothermal mineralization (see Section 5.4). Sulfide mineralization processes in the MIR zone have distinct mineralogical and chemical signatures compared to those collected in other TAG hydrothermal zones. Significant amounts of chalcopyrite and to a lesser extent sphalerite were identified (Figure 6), and high copper (±zinc) concentrations are recorded (Figure 7). Our observations confirm that the MIR deposit is actually a large area of coalesced mounds (Rona et al., 1993a; 1993b) with limited thickness (<30 m). These mounds are most likely immature compared to large SMS deposits of the Alvin zone (i.e., Southern mound, Double mound, and Shinkai mound), where HT hydrothermal fluid flow appears more focused through time. This may explain why copper in the upper orebody at MIR and MIR #3 is highly (6–9-fold) enriched compared to Southern and Shinkai upper orebodies. Though our sampling at the MIR is principally restricted to the west area (subzones A and B) and mostly corresponds to chimneys, drilling conducted on the western border of subzone C confirms the presence of a Cu-rich zone at 4 mbsf (Murton et al., 2019). Gold concentrations over 1 ppm are recorded for more than half of MIR zone samples (Zn-rich chimneys, MIR; silicified sulfides, MIR #3). With all the uncertainties associated with these results, it seems that the MIR hydrothermal zone has the highest SMS resource potential in the TAG field.

5.2 Distribution of hydrothermal deposits

More than two-thirds (20/28) of hydrothermal deposits belong to the contiguous MIR, Nautile, and Alvin hydrothermal zones and span over a narrow (ca. 500 m) curved surface extending 2.5 km from south to north (Figure 2). In the south, i. e., MIR and Nautile zones, the distribution of hydrothermal mounds shows a general N–S trend, whereas SMS deposits in the Alvin zone are roughly aligned along a NW–SE direction. The general distribution of the deposits appears controlled by two major structures: 1) the N–S west-facing fault in the south and 2) the NW–SE trough interpreted by Graber et al. (2020) as an old transfer fault connecting the southern and the northern domains. Considering the distribution and density of hydrothermal deposits, these two major structures have probably maintained a high permeability in a restricted zone through time. At the MIR mound, local modification of permeability and subsequent migration of vent activity to the west is expected according to the composite nature of mineralization from the east (LT crusts) to the west (standing sulfide chimneys) (see also Section 5.5).

The Shimmering zone is formed by a dense cluster of five mounds apparently spatially disconnected from the other contiguous hydrothermal zones located to the south (Figure 2). Deposits are within the "smooth northern block" (Graber et al., 2020) in an area where oblique and axis-perpendicular faults intersect axis-parallel faults. Moreover, a major N–S-trending, west-facing fault scarp bounds the western part of the hydrothermal zone and is interpreted as a detachment surface related to the initiation of a new detachment fault (Szitkar et al., 2019). A consequence would be that the Shimmering zone is structurally distinct from the southern hydrothermal zones (Szitkar et al., 2019; Graber et al., 2020). The "chaotic zone" between the Alvin and Shimmering zones remains poorly explored, so we cannot rule out the presence of small (<< 5,000 m^2) inactive or weakly active deposits. However, with exception to the Cyana mound, no large mounds are inferred from Graber et al. (2020) HR bathymetric maps in this "chaotic zone." This apparent absence of large SMS and thus long-duration HT hydrothermal activity between the Alvin zone and Shimmering zone should be investigated in future work to ascertain if the shimmering zone and the southern hydrothermal zones are connected or not, i.e., if hydrothermal fluids are linked to a single convection cell or different ones (Humphris et al., 2015).

The sparse distribution of the three last deposits (TAG active mound, mound #11, and chimney cluster; Figure 2) compared to that of the other hydrothermal zones, as well as the diverse size, activity, morphology, and mineralization type, is intriguing. Additional exploration of the hydrothermal mounds hosted in the "extensional area" defined by Graber et al. (2020) is necessary to understand the tectonic controls and/or hydrothermal history in this area.

5.3 Current low-temperature activity

The extensive dive observations and measurements performed so far have provided the most comprehensive present-day distribution of hydrothermal activity in the TAG field. A significant result is the presence of low-temperature diffuse flow (<30°C) in nearly all of the investigated hydrothermal zones. Beyond questioning the inactive nature of some old hydrothermal deposits of the TAG hydrothermal field (section 5.6), this brings insights on the current upflow zones. The maximum temperatures measured vary in range, from slightly over the seawater temperature (3°C; Rona mound) to up to 29°C (east of the MIR). The contiguous MIR, Nautile, and Alvin hydrothermal zones show a gradual decrease in maximum temperature from south to north (Figure 2). Furthermore, morphologies of currently forming LT precipitates vary from 7-m-tall hills at the MIR mound to scarce centimeter-scale orange patches at the Rona mound supporting the progressive weakening of the LT activity toward the Alvin zone. Further north, the shimmering zone hosts three areas with significant LT hydrothermal activities (with the maximum temperature ranging from 14°C to 26°C). Presently forming LT precipitates are distributed along cracks in Mn–Fe–Si crusts and span over a surface of tens of meters. At Shimmering zones #2 and #4, the distribution of diffuse fluids and precipitates as well as the intensity of venting are similar to those of Menez Du #2. The relatively intense LT activity (up to 26°C) recorded in the Shimmering zone contrasts with the inactive or very weakly active nature of the Alvin hydrothermal zone yet closest to the HT active mound and MIR and Nautile diffusive zones. If the spatial distribution of venting is representative of the current upflow zones in the subsurface, a lack of visible diffuse venting at the Alvin zone (contrary to all other hydrothermal zones) may provide constraints on subsurface circulation patterns in the hanging wall. Considering a single convection model (i.e., fluids from the same upwelling flow supply all hydrothermal zones), inactivity or very weak activity of the Alvin zone deposits could be seen as reflecting a strong decrease of permeability in the hanging wall below this area. According to the mass of sulfides deposited in the Alvin zone (i.e., half of the total tonnage of the TAG field) and occurrence of standing chimneys, evidence of long-lived upflow zones in the area, the decrease of permeability would have to be recent (<5,000 years). LT hydrothermal activity recorded at the MIR, Nautile, and Shimmering zones (2 km WNW and 4 km NNE of Active mound) might be linked to the presence of major N–S-trending faults that would act as preferential pathways for fluids and thus sustain diffuse venting. However, the apparent spatial disconnection of the Shimmering zone and the absence of visible diffuse venting at the Alvin zone might also be the expression of different circulation cells (Humphris et al., 2015). Additional exploration in the vicinity of the Shimmering zone as well as the east of the MIR (faulted upper terrain described by Graber et al., 2020), i.e., toward the LTZ, together with investigation of fluid geochemistry, is crucial to decipher between a single or multiple convection cell model.

5.4 Past low-temperature activity: insights from hydrothermal Mn–Fe–Si crusts

Several but not all SMS deposits lacking upright chimneys are sealed by widespread Mn–Fe–Si hydrothermal crusts attesting to the longevity of diffuse flow at specific locations even long after ceasing of the last HT hydrothermal activity. The LT hydrothermal crust covers all deposits in the Shimmering zone and Nautile zone. Only Cyana and mound #11 deposits in the Alvin and southwest hydrothermal zones, respectively, display widespread LT hydrothermal crusts at the surface. In the MIR zone, the LT hydrothermal crust entirely covers MIR #2, #3, and the eastern part of the MIR. Hydrothermal mounds covered by LT hydrothermal crusts are characterized by a relatively flat top morphology with rare visible fault scarps indicating that low-temperature activity still occurs after the dissection and collapse of the sulfide mounds. A significant renewal of HT activity after sustained diffuse flow was only seen at the MIR mound (between subzones A/B and subzone C) where small sulfide chimneys developed on Mn–Fe–Si crusts. In the Alvin zone, a decrease in the hydrothermal activity is evident from major silicification of sulfide-rich rocks at the Shinkai mound and the presence of jasper formation at the summit of the Southern mound and Rona mound (Murton et al., 2019). However, large SMS deposits in the Alvin zone are mostly devoid of widespread LT crusts, suggesting no sustained LT diffuse venting in the area since the last HT hydrothermal activity. The spatial distribution of LT hydrothermal crusts is intriguing and points to longevity of the LT discharge zones in the Shimmering, Nautile, and MIR zones

(confirmed by current LT activity). On the contrary, SMS deposits of the Alvin zone located in the heavily tectonized area seem affected by radical changes of upflow zones after HT activity ceased.

LT hydrothermal crusts exhibit a wide variety of Mn, Fe, and Si concentrations and a large range of Fe/Mn that support a hydrothermal origin and different precipitation temperatures. Very high copper and zinc concentrations (up to 10 wt%) recorded make these crusts atypical for low-temperature precipitates and could give misleading information on the origin of this mineralization (Figure 8A), apart from using recent discrimination diagrams based on immobile elements (e.g., Zr, Y, and Ce; Figure 8B; Josso et al., 2017). In the TAG hydrothermal field, five deposits (MIR #3, Menez Du #2 and #3, Cyana, and Shimmering #2) host a hydrothermal crust with copper and zinc concentrations higher than 1 wt%. Mn oxyhydroxides are thought to be the main Cu–Zn-bearing phase since the highest copper and zinc contents (up to 10 wt% Cu and 1 wt% Zn) are recorded for Mn-rich crusts. Metal enrichments (e.g., Ni, Co, Cu, and Zn) in hydrothermal Mn ± Fe ± Si mineralization have already been reported in previous studies (e.g., Hein et al., 2008; Hein et al., 1996; Hein et al., 1992; Hein et al., 1990; Conly et al., 2011; González et al., 2016; Pelleter et al., 2017). Several hypotheses may account for the metal enrichment of hydrothermal Mn mineralization, such as the leaching of magmatic or ultramafic rocks, sulfide mineralization, or biogenic sediments (Hein et al., 2008). Sulfides were sampled under the Mn–Fe–Si crusts at MIR #3 and Cyana mounds and thus are most likely the source of the Cu and Zn recorded in Mn-rich hydrothermal precipitates. Sustained LT hydrothermal activity attested by the presence of widespread Mn–Fe–Si crusts could thus fundamentally alter the pristine surface and subsurface sulfide mineralization and release metals. Though Mn oxyhydroxides appear as potential sinks for copper and to a lesser extent zinc, the ultimate fate of metals during LT hydrothermal activity needs investigations of diffuse fluid and associated LT precipitate chemistry.

5.5 Relative age of the hydrothermal mounds and/or last HT hydrothermal activity

Several geological parameters can help define the relative age/chronology of the hydrothermal processes and age(s) of deposits (e.g., size, morphology, surface, and subsurface geology, including faults).

A first-order criterion is the presence of standing or toppled sulfide chimneys (Figure 4A, C, K) for identifying deposits characterized by a recent cessation of HT activity. Standing and/or toppled chimneys are present in the Alvin zone (Shinkai, New Mound #2 and #3, and Mont de reliques), MIR zone (MIR subzones A and B), and the southwest hydrothermal zone (chimney cluster). No relict chimney was observed at the top of large mounds in the Shimmering zone nor Nautile zone, attesting to long-ceased HT activity. At the MIR, the dating of several standing and toppled chimneys provided ages spanning between 3,000 and 500 years (Lalou et al., 1995). Based on these results, we assume that last HT activity at Shinkai, New mounds, Mont de reliques, and chimney cluster most likely belongs to this period of time (3,000 to approximately 500 years). The TAG active mound is thought to be inactive during this period of time until the recent reactivation of HT activity 60 years ago (Lalou et al., 1995). Therefore, we assume that last HT activity (3,000–500 years) was focused in the western part of the Alvin zone and in a restricted area west of the MIR. Chimney clusters discovered between the Alvin zone and active mound indicate a very short-lived hydrothermal activity (transitional?) in the extensional area.

Other criteria that can be used for deciphering a relative chronology of hydrothermal processes include indirect geological factors such as morphology, pelagic sediment cover, weathering of sulfides, or tectonic dissection (e.g., Murton et al., 2019). The size of the deposit may help localize areas of long-duration HT activity. In the TAG hydrothermal field, thirteen deposits consist of very large deposits (>10,000 m^2), with sulfide accumulation of over 1 Mt and up to 4.4 Mt. The Shimmering zone and Alvin zone have four very large SMS deposits. The Nautile zone hosts three large deposits, and the last two are the MIR mound and Active mound. Dating studies have shown that the active mound has accumulated 2 Mt of sulfides over 50 kyrs, including several episodes of activity (2%–20% of this time) and inactivity (Lalou et al., 1995; Humphris and Cann, 2000). Shinkai, Southern, and Double mounds exhibit circular, conical, to sub-conical shapes suggesting a sustained (yet probably episodic), focused upflow of HT fluids in the Alvin zone. Relatively steep slopes and surface mineralization dominated by sulfides (only oxidized in outer rims) imply that these three SMS deposits are not significantly older than the Active mound. It is in agreement with ages of approximately 50 kyrs, obtained on sulfide samples attributed to the Double mound (Lalou et al., 1995). Based on the morphology, sediment cover, and absence of tectonic dissection, several authors proposed that the age of the Shinkai mound might be less than 40 kyrs (Murton et al., 2019; Graber et al., 2020). Actually, these geological features mostly suggest that the Shinkai mound has experienced a sustained HT hydrothermal episode more recently than Southern and Double mounds, which is different than being intrinsically younger, and a way to illustrate this is to consider the Active mound as an analog. The Active mound is not dissected by axis-oblique or axis-parallel faults, and it has relatively steep mean slopes (28.7°; Table 1) and a thin pelagic sediment cover. However, the maximum age recorded, i.e., the potential first HT hydrothermal activity, is around 50 kyrs (Lalou et al., 1993). Considering the large sulfide volume and assuming episodic HT hydrothermal episodes, the Shinkai mound may be as old as the Active, Double, and Southern mounds. New geochronological studies are needed to determine precisely the maximum age for the Shinkai mound and the age of the last HT event at Southern and Double mounds (i.e., before the spreading-parallel extensional faulting). The morphology and surface geology of the Cyana mound are unique in the Alvin hydrothermal zone with a gentle slope, flat surface, and a widespread layer of the hydrothermal manganese crust. Contrary to the observation by Graber et al. (2020), Cyana is affected by axis-parallel faults and should not be considered certainly younger than the Double mound. Actually, the widespread Mn crust and lack of relict chimneys indicate that last HT activity at the Cyana mound is probably as old as, or older, than that at the Double mound. Interestingly, Lalou et al. (1995) reported one age of 74 kyrs for the Mn crust in the Alvin zone. Though the precise location of the dated sample is unknown, several lines of evidence support an old HT event (>74 kyrs) in

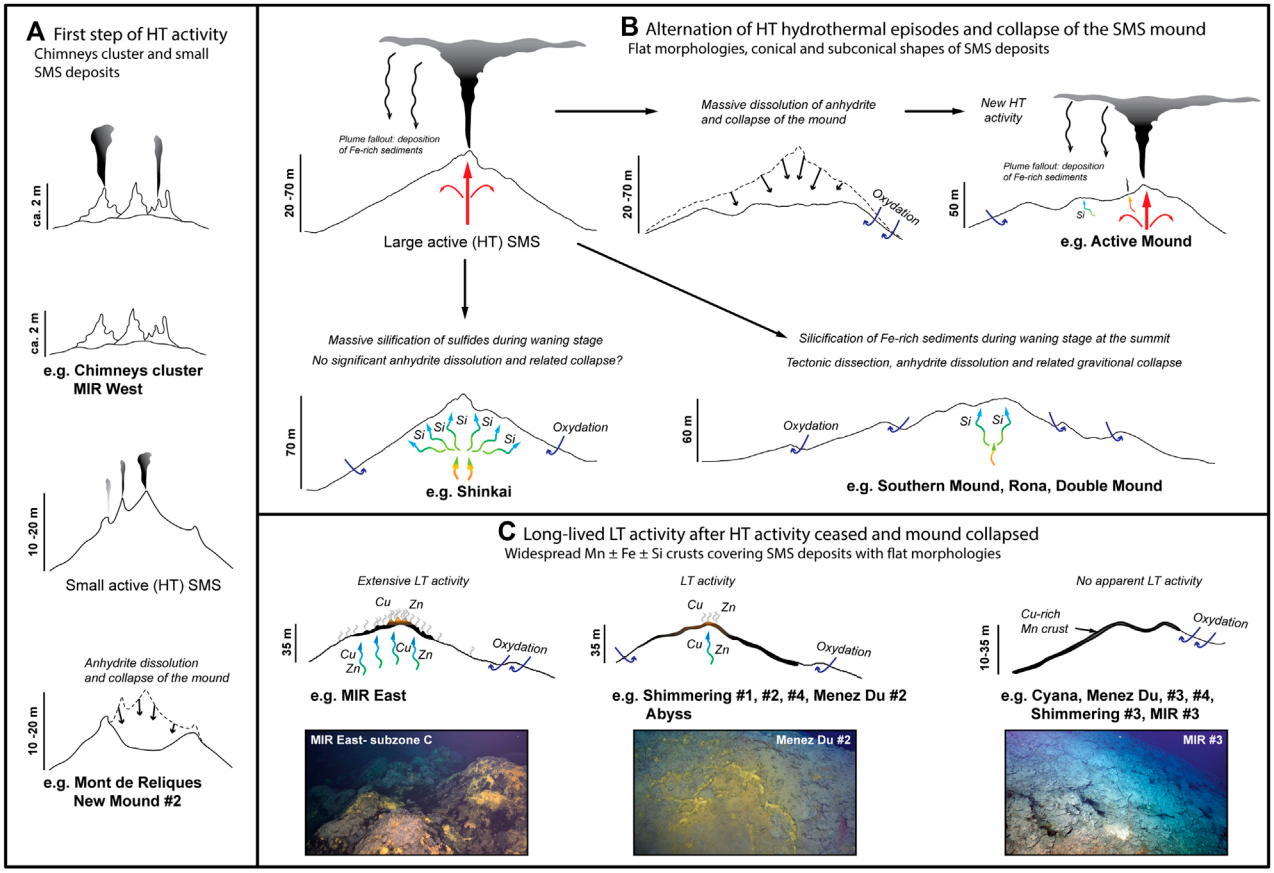

FIGURE 9
Evolution model proposed to explain the diversity of active, weakly active, and inactive SMS deposits in the TAG hydrothermal field. **(A)** Early cycles of HT hydrothermal activity lead to the formation of sulfide chimney clusters and small SMS mounds. Massive anhydrite dissolution (and related collapse of the mound) may follow if strong seawater entrainment into the mound occurred during the HT activity. **(B)** Successive cycles of HT activity and inactivity will eventually lead to the development of large SMS mounds. Massive anhydrite dissolution would explain platform-like shape of some deposits (e.g., TAG active mound, Shimmering #2, and Abyss). Limited anhydrite dissolution and related mass wasting of sulfides combined with tectonic dissection explain morphologies of some SMS deposits (e.g., Southern mound and Double mound). Waning of HT activity associated with the closing stage of the hydrothermal cycles may result in silicification. **(C)** Successive cycles of LT activity long after the mound has collapsed and HT activity has ceased. Massive precipitation of Fe–Si–Mn small mounds and crusts will eventually cover the SMS mound. LT activity may remobilize copper and zinc from massive sulfides. Copper ± zinc may be adsorbed into Mn oxyhydroxides or lost in the water column.

the Alvin zone, which might be attributed to the formation of the Cyana mound.

Gentle slopes and relatively flat morphologies sometimes barely visible on the HR bathymetric map characterize hydrothermal mounds in the Nautile and Shimmering zones. Together with the locally thick sediment cover and presence of oxide-dominated boulders, this supports a very long-ceased HT activity and relatively increased ages for sulfide mineralization (i.e., > 50 kyrs). No absolute ages are presently ascribed for these deposits. However, re-examination of data from the historical MIR zone described by Rona et al. (1993a); Rona et al. (1993b) in regards with new observations suggests that samples collected for dating during Alvin 2188 and 2195 dives do not belong to the MIR mound. This is in agreement with the observation of recent studies highlighting that the MIR mound appears smaller than previously thought (Murton et al., 2019; Graber et al., 2020). Alvin 2188 and 2195 dives most likely occurred several hundreds of meters north to the actual MIR mound, i.e., a zone between MIR #3 and Menez Du #2. High conductive heat flows measured during Alvin 2188 and 2195 dives at 3463, 3483, and 3484 mbsl (Rona et al., 1993b) are also in good accordance with diffuse venting discovered in the southern part of the Nautile zone (up to 19°C measured at Menez Du #2). Two samples collected in this area (i.e., Alvin 2188 3-1 and Alvin 2195 1-1) provided radiometric ages of 102 and 50 kyrs, respectively (Lalou et al., 1995). If our assumptions on localization of historical sample stations and interpretations of geological features are correct, hydrothermal mounds located in the Nautile zone and/or the northern edge of the MIR zone are the oldest deposits in the TAG hydrothermal field. Shimmering zone deposits share common geological features with Nautile zone deposits and the Cyana mound (morphologies, surface mineralization, and sediments cover). Though radiometric dates are needed, deposits hosted in the Shimmering zone appear older than those in Alvin zone mounds (with exception of Cyana) and were probably first active before 74 kyrs (i.e., higher age reported for LT activity in the Alvin zone).

The MIR mound is a complex mineralized area with relatively thin and immature sites with standing and toppled chimneys to the

west (subzones A and B) and larger site(s) with the LT Mn–Fe–Si crust to the east (subzone C). Samples collected in the western part (subzones A and B) during dive MIR 3.76 are no older than 20 kyrs (Lalou et al., 1995), attesting to the relatively recent hydrothermal activity to the west. Though no age is available for the eastern part of the mound, we assume higher ages (>20 kyrs) based on geological characteristics (size, morphology, and surface mineralization). Additional sampling of the eastern zone and geochronological studies would help deciphering the polyphase history of the MIR mound.

Within the limitation of indirect geological characteristics and previous dating studies, the HT hydrothermal history of the TAG hydrothermal field may be summarized as follows:

1) The HT hydrothermal activity that began at least 105–75 kyrs ago was mainly focused in the Nautile zone and most likely in the Shimmering zone. Some SMS mounds might be synchronous in the north of the MIR zone (e.g., MIR #3) and in the Alvin zone (i.e., Cyana).
2) An HT event began at least as early as 50–40 kyrs in the Alvin zone (e.g., Southern and Double mounds) and at the Active mound. It may indicate a southward and/or westward migration of the HT hydrothermal activity. One age south to the Nautile zone or north to the MIR zone corresponds to this period, but no subsequent HT event is recorded in this area after that episode.
3) From 20–10 kyrs, new HT events occurred west of the MIR mound and at the Active mound. It is very likely that episodic activity during this period also took place in the Alvin zone (e.g., Shinkai mound).
4) At around 5 kyrs, a HT activity was recorded at the Active mound (Lalou et al., 1990) which associated with the formation of the upper platform (Humphris and Kleinrock, 1996).
5) toppled A new HT hydrothermal episode attested by the presence of standing andchimneys occurred between 3,000 and 500 years in the Alvin zone (Shinkai, New mounds, Mont de Reliques) and west of the MIR mound.
6) Current HT activity began around 60 years ago and is only present at the Active mound (Lalou et al., 1995).

Possible older HT hydrothermal events (>125 kyrs) may have occurred in the TAG hydrothermal field. Our observations indicate that SMS deposits can be concealed by LT hydrothermal crusts and pelagic sediments. Hence, this may lead to misinterpretation on the nature of the deposit (i.e., SMS deposit *versus* LT deposit only) without extensive exploration and sampling operations. The LTZ localized on the upper eastern flank of the TAG massif (Figure 1) hosts several Mn–Fe deposits (Rona et al., 1975; Rona et al., 1984; Thompson et al., 1985). Even though Mn–Fe–Si crusts in the LTZ (see Plate I of Thomson et al., 1985) are very similar to those covering sulfide mineralization in the HTZ (Figures 4F, M, N) including copper enrichments (Mills et al., 2001), no sulfide mineralization is presently known. Yet, over the last decades, studies have shown that black smoker-type deposits can develop several kilometers off-axis in association with detachment faults (Petersen et al., 2009; Fouquet et al., 2010). The analogy between the Mn–Fe–Si crusts studied here and those described by Thompson et al. (1985) in the LTZ encourages further exploration to the east to find potential old SMS deposits and thus constrain the spatial and temporal extent of the TAG HT hydrothermal field.

5.6 Evolution and genetic models of SMS deposits at the TAG field

The first step of hydrothermal activity led to the formation of chimney clusters and, if HT activity persists, to small SMS mounds (Figure 9A). For the Active mound, formation of the deposit is complex and is linked to cycles of anhydrite precipitation and dissolution, which is responsible for flat tops and platform-like morphology (Humphris and Kleinrock, 1996; Petersen et al., 2000). Anhydrite dissolution and subsequent collapse of the structure may explain the formation of the circular depression observed at Mont de reliques and New mounds #2 (Figure 9A). Nevertheless, the morphology of the Active mound characterized by stacked flat platforms is rather uncommon inside the TAG hydrothermal field. Only Shimmering #2 and Abyss mounds exhibit a similar morphology (i.e., platform(s) shape with a flat top or depression) that may be related to massive anhydrite dissolution and related collapse of the mound. Conversely, large SMS deposits hosted in the Alvin zone display rather conical to sub-conical shapes (e.g., Shinkai, Double, and Southern mounds; Supplementary Figure S3) without significant depression or large flat-top excluding massive anhydrite dissolution. Even though anhydrite dissolution cannot be ruled out from the presence of brecciated sulfides (Murton et al., 2019), the collapse of these mounds is most likely controlled by tectonic dissection and/or mass wasting. Additionally, high silica recorded in massive sulfides at Shinkai may stabilize sulfide structures (Delaney et al., 1992) and, together with filling of some collapse structures by the last ceased HT activity, may explain the striking conical shape of this mound (Figure 9B). A silica cap at depth has also been reported near the summit of the Southern mound and Rona mound and is attributed to a waning phase occurring at the closing stage of the hydrothermal activity (Murton et al., 2019) (Figure 9B).

A second major step of hydrothermal activity in the TAG hydrothermal field is the development of a long-lived, possibly episodic, LT hydrothermal activity. Widespread Mn ± Fe ± Si crusts cover mounds with gentle slopes and relatively flat morphologies with no more standing sulfide chimneys (Figure 9C; Supplementary Figure S3). Together with the presence of active LT venting in the Shimmering zone, Nautile zone, and MIR zone, these observations indicate that LT activity is a major event in the TAG hydrothermal field. This is in good agreement with the large time span (i.e., 140–4 kyrs) recorded for Mn crusts (Lalou et al., 1986; Lalou et al., 1995). LT hydrothermal events are most likely concomitant with oxidation of sulfide minerals in seawater (e.g., Abyss mound), eventually leading to oxide-dominant surface and subsurface mineralization. Oxidation of pristine hydrothermal sulfides by LT hydrothermal fluids and/or seawater may release metals (e.g., Cu, Zn; Dekov et al., 2011) that would either be trapped into secondary minerals (e.g., Fe oxyhydroxides, Mn oxyhydroxydes, and atacamite) or discharged into seawater. Sulfide oxidation and related leaching of metals should be more efficient during the LT hydrothermal activity

than at seawater temperature (e.g., Chandra and Gerson, 2010; Fallon et al., 2017). Then, if the long-lived LT activity identified in the TAG hydrothermal field reveals to be a common process in other hydrothermal fields hosting old SMS deposits, this process should be considered in future studies on biogeochemical cycles of metals in the deep ocean. In addition, such sustained LT activity (10°C–30°C) in a sulfide-rich environment (i.e., SMS) may support diverse mesophilic microbial populations for long durations (Zeng et al., 2021).

5.7 Defining active, inactive, and extinct SMS deposits: insight from the TAG hydrothermal field

With increasing interest in polymetallic sulfides, part of the scientific community working on hydrothermal systems calls for the protection of active hydrothermal sites (Van Dover et al., 2018). As a consequence, potential mining activity would be focused on so-called inactive/extinct sites, though only few studies have been carried out on these deposits. Some authors recently advocated for research efforts to propose a classification of inactive and extinct deposits/vent fields that could help for mining regulations (Jamieson and Gartman, 2020; Van Dover et al., 2020). To our knowledge, the International Seabed Authority (ISA) has only proposed a definition for inactivity and extinction at vent-scale with distinction based on potential hydrothermal rejuvenation from mining activity (ISBA/25/LTC/6 Rev.2, 2022). Jamieson and Gartman (2020) argued that the term "extinct" should be only used for deposits hosted in an inactive vent field for which the probability of hydrothermal rejuvenation is low (but not certain). Considering that TAG hydrothermal mounds are all linked to the same heat source and a common detachment fault system that controls the hydrothermal circulation, Jamieson and Gartman (2020) classified the TAG field as hydrothermally active. This recommendation is relevant, particularly now knowing that all hydrothermal zones in the TAG field exhibit temperature anomalies. However, defining the extent of a single hydrothermal vent field (i.e., cluster(s) of deposits related to a common heat source and/or subseafloor permeability) may be challenging. That is true for TAG, where the location of the heat source and by extension the pattern of hydrothermal circulation is now disputed (e.g., McCaig et al., 2010; Guo et al., 2023). Moreover, the question of geological continuity may arise if inactive sulfide deposits are discovered toward the LTZ at depths shallower than the detachment fault termination (approximately 3,300 m, Graber et al., 2020). As a consequence, considering knowledge gaps and based on a precautionary approach, all known and to-be-discovered deposits belonging to the TAG area (including HTZ and LTZ, i.e., approximately 45 km^2) should be grouped within a single field or district classified as hydrothermally active.

For an inactive field, Jamieson and Gartman (2020) proposed a set of indicators such as the absence of an upright chimney, relatively flat mound, lack of fluid venting, and absence of a vent biological community that may be important to distinguish extinct sites from inactive sites. These criteria are most likely diagnostic for prolonged HT hydrothermal inactivity. The discovery of a long-lived low-temperature hydrothermal activity in the TAG area indicates that deposits with flat morphologies, no more standing chimneys, and a thick Fe–Mn hydrothermal crust may still host hydrothermal activity. Since the episodicity of low-temperature activity is not known, documentation and dating of LT precipitates should be considered to improve the definition of inactivity and extinction. New data arising from active and inactive hydrothermal field exploration programs are essential to fill gaps in scientific knowledge regarding the geology and ecology of inactive/extinct SMS deposits.

6 Conclusion

Extensive dive exploration, sampling, and measurements coupled with high-resolution acoustic data provide new insights on the nature of mafic-hosted SMS deposits as well as their spatial and temporal distribution and evolution in the TAG hydrothermal field. Our conclusions can be summarized as follows:

1) Thirteen new hydrothermal deposits were discovered including six large (>5,000 m^2) deposits. The TAG hydrothermal field currently hosts 28 hydrothermal mounds accumulating 21.1 Mt of hydrothermal materials deposited above the seafloor.
2) Large and mature SMS deposits are mostly characterized by low copper and zinc concentrations compared to mafic-hosted volcanogenic massive sulfides. This questions the economic potential of large mafic-hosted SMS deposits in slow-spreading ridge settings.
3) LT activity (3°C–29°C) is identified in eight different areas including five newly discovered zones of diffuse venting. The spatial distribution of present sites of venting questions the geometry of sub-surface circulation patterns within the hanging wall and should be considered in future 3D flow modeling.
4) Shimme The distribution, morphology, mineralogy, and geochemistry of the hydrothermal deposits can be used to propose a new chronologic framework of the sulfide formation. HT activity was mainly focused in the ring zone and the Nautile zone until 50 kyrs ago. A migration of HT activity to the Alvin zone, MIR zone (e.g., MIR mound), and active mound is likely since 50 kyrs, including different periods of activity (50–40 kyrs, 20–10 kyrs, 5 kyrs, 3,000–500 yrs, and 60 yrs) and inactivity. Excluding the recent rejuvenation of the Active mound at 60 yrs, last HT hydrothermal activity of the TAG field was focused in the western part of the MIR mound and at Shinkai mound, New Mound #2 and #3, and Mont de reliques.
5) Widespread LT crusts covering old flattened SMS mounds indicate that LT hydrothermal events can occur long after ceasing of the last HT hydrothermal activity. This finding indicates that old SMS deposits might be discovered to the east toward the LTZ. Long-lived LT hydrothermal activity (>140 kyrs to present) is a major process in the evolution and aging of SMS mounds in the TAG hydrothermal field, and its consequences on the fate of metals and microbial processes should be investigated in the future.
6) As already mentioned by Jamieson and Gartman (2020), none of the hydrothermal deposits belonging to the TAG area should

be considered extinct. Without additional constrains on the sub-surface fluid flow pathways, all deposits should be grouped in a single hydrothermal field (including the HTZ and LTZ) classified as "active."

Further exploration to the north of the Shimmering zone and east of the Alvin, Nautile, and MIR zones is needed to fully understand the extension of the TAG SMS district. New radiometric dating of sulfides, Mn oxides, and aragonite of well-localized samples is also of prime importance to better constrain the temporal evolution of the TAG hydrothermal field. Knowing the spatial and temporal distribution of active, weakly active, and inactive SMS deposits would help constrain the present and past upflow zones and hence evolution of convection cell(s) associated with the development of detachment fault systems.

Data availability statement

The datasets presented in this study can be found in online repositories. The names of the repository/repositories and accession number(s) can be found in the article/Supplementary Material.

Author contributions

E-LP: conceptualization, investigation, writing–original draft, and writing–review and editing. MP: writing–review and editing. A-SA: data curation, methodology, and writing–review and editing. AB: formal analysis, validation, and writing–review and editing. SC: formal analysis and writing–review and editing. FB: formal analysis and writing–review and editing. VA: formal analysis and writing–review and editing. CG: data curation, formal analysis, and writing–review and editing. AG: formal analysis and writing–review and editing. DP: formal analysis and writing–review and editing. MR: formal analysis and writing–review and editing. TG: writing–review and editing. LG: formal analysis and writing–review and editing. CC: writing–review and editing. M-AC: writing–review and editing. YF: supervision and writing–review and editing.

Funding

The author(s) declare financial support was received for the research, authorship, and/or publication of this article. The HERMINE2 expedition (2022) was carried out thanks to the France 2030 government funding for the "deep sea"—"Projet Mission DMA et CCZ"—ANR-22-MAFM-001."

Acknowledgments

The authors thank the crews of R/V Pourquoi pas? and Nautile HOV and all participants of the BICOSE, HERMINE, and HERMINE2 cruises for their assistance at sea. We thank reviewers J-II, JK and JJ for their thoughtful comments and suggestions, which significantly improved the quality of this paper.

Conflict of interest

The authors declare that the research was conducted in the absence of any commercial or financial relationships that could be construed as a potential conflict of interest.

Publisher's note

All claims expressed in this article are solely those of the authors and do not necessarily represent those of their affiliated organizations, or those of the publisher, the editors, and the reviewers. Any product that may be evaluated in this article, or claim that may be made by its manufacturer, is not guaranteed or endorsed by the publisher.

Supplementary material

The Supplementary Material for this article can be found online at: https://www.frontiersin.org/articles/10.3389/feart.2024.1304993/full#supplementary-material

References

Bohnenstiehl, D. R., and Kleinrock, M. C. (2000). Fissuring near the TAG active hydrothermal mound, 26°N on the Mid-Atlantic Ridge. *J. Volcanol. Geotherm. Res.* 98, 33–48. doi:10.1016/S0377-0273(99)00192-4

Bonatti, E., Kraemer, T., and Rydell, H. (1972). Classification and genesis of submarine iron-manganese deposits, in. *Ferromanganese Deposits of the Ocean Floor*. Editor D. R. Horn (Washington D.C., United States: Seabed Assessment Program, IDOE, NSF), 149–166.

Cambon, M. -A. (2014). BICOSE cruise. *RV Pourquoi pas?* doi:10.17600/14000100

Canales, J. P., Sohn, R. A., and deMartin, B. J. (2007). Crustal structure of the Trans-Atlantic Geotraverse (TAG) segment (Mid-Atlantic Ridge, 26°10′N): implications for the nature of hydrothermal circulation and detachment faulting at slow spreading ridges. *Geochem. Geophys. Geosyst.* 8, Q08004. doi:10.1029/2007GC001629

Cathles, L. M. (2011). What processes at mid-ocean ridges tell us about volcanogenic massive sulfide deposits. *Min. Deposita* 46, 639–657. doi:10.1007/s00126-010-0292-9

Chandra, A. P., and Gerson, A. R. (2010). The mechanisms of pyrite oxidation and leaching: a fundamental perspective. *Surf. Sci. Rep.* 65, 293–315. doi:10.1016/j.surfrep.2010.08.003

Cherkashev, G. A., Ivanov, V. N., Bel'tenev, V. I., Lazareva, L. I., Rozhdestvenskaya, I. I., Samovarov, M. L., et al. (2013). Massive sulfide ores of the northern equatorial Mid-Atlantic Ridge. *Oceanology* 53, 607–619. doi:10.1134/S0001437013050032

Cherkashov, G., Poroshina, I., Stepanova, T., Ivanov, V., Bel'tenev, V., Lazareva, L., et al. (2010). Seafloor massive sulfides from the northern equatorial Mid-Atlantic Ridge: new discoveries and perspectives. *Mar. Georesources Geotechnol.* 28, 222–239. doi:10.1080/1064119X.2010.483308

Conly, A. G., Scott, S. D., and Bellon, H. (2011). Metalliferous manganese oxide mineralization associated with the boléo Cu-Co-Zn district, Mexico. *Econ. Geol.* 106, 1173–1196. doi:10.2113/econgeo.106.7.1173

Dekov, V., Boycheva, T., Hålenius, U., Petersen, S., Billström, K., Stummeyer, J., et al. (2011). Atacamite and paratacamite from the ultramafic-hosted Logatchev seafloor vent field (14°45′N, Mid-Atlantic Ridge). *Chem. Geol.* 286, 169–184. doi:10.1016/j.chemgeo.2011.05.002

Delaney, J. R., Robigou, V., McDuff, R. E., and Tivey, M. K. (1992). Geology of a vigorous hydrothermal system on the Endeavour segment, Juan de Fuca Ridge. *J. Geophys. Res.* 97, 19663–19682. doi:10.1029/92jb00174

deMartin, B. J., Sohn, R. A., Canales, J. P., and Humphris, S. E. (2007). Kinematics and geometry of active detachment faulting beneath the Trans-Atlantic Geotraverse (TAG) hydrothermal field on the Mid-Atlantic Ridge. *Geology* 35, 711–714. doi:10.1130/G23718A.1

Edmonds, H. N., German, C. R., Green, D. R. H., Huh, Y., Gamo, T., and Edmond, J. M. (1996). Continuation of the hydrothermal fluid chemistry time series at TAG, and the effects of ODP drilling. *Geophys. Res. Lett.* 23, 3487–3489. doi:10.1029/96GL01597

Etoubleau, J., Cambon, P., Fouquet, Y., Henry, K., and Moal, S. (1996). Séparation des métaux nobles (Pt, Au) d'une matrice géologique par chromatographie d'échange d'ions et détermination par spectrométrie de fluorescence X. *Le J. de Physique IV* 06, C4-C843–C4-852. doi:10.1051/jp4:1996481

Fallon, E. K., Petersen, S., Brooker, R. A., and Scott, T. B. (2017). Oxidative dissolution of hydrothermal mixed-sulphide ore: an assessment of current knowledge in relation to seafloor massive sulphide mining. *Ore Geol. Rev.* 86, 309–337. doi:10.1016/j.oregeorev.2017.02.028

Firstova, A., Stepanova, T., Sukhanova, A., Cherkashov, G., and Poroshina, I. (2019). Au and Te minerals in seafloor massive sulphides from semyenov-2 hydrothermal field, Mid-Atlantic Ridge. *Minerals* 9, 294. doi:10.3390/min9050294

Fouquet, Y., Cambon, P., Etoubleau, J., Charlou, J. L., OndréAs, H., Barriga, F. J. A. S., et al. (2010). "Geodiversity of hydrothermal processes along the mid-atlantic Ridge and ultramafic-hosted mineralization: a new type of oceanic Cu-Zn-Co-Au volcanogenic massive sulfide deposit," in *Diversity of hydrothermal systems on slow spreading ocean ridges*. Editors P. A. Rona, C. W. Devey, J. Dyment, and B. J. Murton (United States: American Geophysical Union), 321–367.

Fouquet, Y., Pelleter, E., and Cathalot, C. (2017). HERMINE cruise. *RV Pourquoi pas?* doi:10.17600/17000200

Franklin, J. M., Gibson, H. L., Jonasson, I. R., and Galley, A. G. (2005). "Volcanogenic massive sulfide deposits," in *One hundredth anniversary volume*. Editors J. W. Hedenquist, J. F. H. Thompson, R. J. Goldfarb, and J. P. Richards (USA: Society of Economic Geologists), 0. doi:10.5382/AV100.17

Gehrmann, R. a. S., North, L. J., Graber, S., Szitkar, F., Petersen, S., Minshull, T. A., et al. (2019). Marine mineral exploration with controlled source electromagnetics at the TAG hydrothermal field, 26°N mid-Atlantic Ridge. *Geophys. Res. Lett.* 46, 5808–5816. doi:10.1029/2019GL082928

González, F. J., Somoza, L., Hein, J. R., Medialdea, T., León, R., Urgorri, V., et al. (2016). Phosphorites, Co-rich Mn nodules, and Fe-Mn crusts from galicia bank, NE atlantic: reflections of cenozoic tectonics and paleoceanography. *Geochem. Geophys. Geosyst.* 17, 346–374. doi:10.1002/2015GC005861

Graber, S., Petersen, S., Yeo, I., Szitkar, F., Klischies, M., Jamieson, J., et al. (2020). Structural control, evolution, and accumulation rates of massive sulfides in the TAG hydrothermal field. *Geochem. Geophys. Geosystems* 21, e2020GC009185. doi:10.1029/2020GC009185

Guo, Z., Rüpke, L., Petersen, S., German, C. R., Ildefonse, B., Hasenclever, J., et al. (2023). Detachment-parallel recharge can explain high discharge fluxes at the TAG hydrothermal field. *Earth Planet. Sci. Lett.* 617, 118245. doi:10.1016/j.epsl.2023.118245

Hannington, M., Galley, A., Herzig, P. M., and Petersen, S. (1998). "28. Comparison of the tag mound and stockwork complex with Cyprus-type massive sulfide deposits," in *Proceedings of the ocean drilling program* (Scientific Results).

Hannington, M., Jamieson, J., Monecke, T., and Petersen, S. (2010). "Modern Sea-floor massive sulfides and base metal ResourcesToward an estimate of global sea-floor massive sulfide potential," in *The challenge of finding new mineral Resources Global metallogeny, innovative exploration, and new discoveries* (USA: Society of Economic Geologists). doi:10.5382/SP.15.2.001

Hannington, M., Jamieson, J., Monecke, T., Petersen, S., and Beaulieu, S. (2011). The abundance of seafloor massive sulfide deposits. *Geology* 39, 1155–1158. doi:10.1130/G32468.1

Hein, J. R., Ahn, J.-H., Wong, J. C., Kang, J.-K., Smith, V. K., Yoon, S.-H., et al. (1992). *Geology, geophysics, geochemistry, and deep-sea mineral deposits, Federated States OF Micronesia; KORDI-USGS R.V. Farnella cruise F11-90-CP (USGS numbered series No. 92–218), open-file report*. USA: U.S. Geological Survey.

Hein, J. R., Gibbs, A. E., Clague, D. A., and Torresan, M. (1996). Hydrothermal mineralization along submarine rift zones, Hawaii. *Mar. georesources Geotechnol.* 14, 177–203. doi:10.1080/10641199609388310

Hein, J. R., Schulz, M. S., Dunham, R. E., Stern, R. J., and Bloomer, S. H. (2008). Diffuse flow hydrothermal manganese mineralization along the active Mariana and southern Izu-Bonin arc system, western Pacific. *J. Geophys. Res. Solid Earth* 113. doi:10.1029/2007JB005432

Hein, J. R., Schulz, M. S., and Kang, J.-K. (1990). Insular and submarine ferromanganese mineralization of the Tonga-lau region. *Mar. Min.* 9, 305–354.

Humphris, S. E., and Cann, J. R. (2000). Constraints on the energy and chemical balances of the modern TAG and ancient Cyprus seafloor sulfide deposits. *J. Geophys. Res.* 105, 28477–28488. doi:10.1029/2000JB900289

Humphris, S. E., Herzig, P. M., Miller, D. J., Alt, A. C., Becker, K., Brown, D., et al. (1995). The internal structure of an active sea-floor massive sulphide deposit. *Nature* 377, 713–716. doi:10.1038/377713a0

Humphris, S. E., and Kleinrock, M. C. (1996). Detailed morphology of the TAG active hydrothermal mound: insights into its formation and growth. *Geophys. Res. Lett.* 23, 3443–3446. doi:10.1029/96GL03079

Humphris, S. E., Tivey, M. K., and Tivey, M. A. (2015). The Trans-Atlantic Geotraverse hydrothermal field: a hydrothermal system on an active detachment fault. *Rona* 121, 8–16. doi:10.1016/j.dsr2.2015.02.015

ISBA/25/LTC/6 (2022). Recommendations for the guidance of contractors for the assessment of the possible environmental impacts arising from exploration for marine minerals in the Area. Available at: https://www.isa.org.jm/wp-content/uploads/2023/05/ISBA_25_LTC_6_Rev.2-2211076E.pdf.

Jamieson, J. W., and Gartman, A. (2020). Defining active, inactive, and extinct seafloor massive sulfide deposits. *Mar. Policy* 117, 103926. doi:10.1016/j.marpol.2020.103926

Josso, P., Pelleter, E., Pourret, O., Fouquet, Y., Etoubleau, J., Cheron, S., et al. (2017). A new discrimination scheme for oceanic ferromanganese deposits using high field strength and rare earth elements. *Ore Geol. Rev. SI:Marine mineral deposits New Resour. base, precious, Crit. metals* 87, 3–15. doi:10.1016/j.oregeorev.2016.09.003

Karson, J. A., and Rona, P. A. (1990). Block-tilting, transfer faults, and structural control of magmatic and hydrothermal processesin the TAG area, Mid-Atlantic Ridge 26°N. *Geol. Soc. Am. Bull.* 102, 1635–1645. doi:10.1130/0016-7606(1990)102<1635:BTTFAS>2.3.CO;2

Kleinrock, M. C., and Humphris, S. E. (1996a). Structural control on sea-floor hydrothermal activity at the TAG active mound. *Nature* 382, 149–153. doi:10.1038/382149a0

Kleinrock, M. C., and Humphris, S. E. (1996b). Structural asymmetry of the TAG Rift Valley: evidence from a near-bottom survey for episodic spreading. *Geophys. Res. Lett.* 23, 3439–3442. doi:10.1029/96GL03073

Lalou, C., Reyss, J.-L., Brichet, E., Arnold, M., Thompson, G., Fouquet, Y., et al. (1993). New age data for Mid-Atlantic Ridge hydrothermal sites: TAG and Snakepit chronology revisited. *J. Geophys. Res.* 98, 9705–9713. doi:10.1029/92JB01898

Lalou, C., Reyss, J.-L., Brichet, E., Rona, P. A., and Thompson, G. (1995). Hydrothermal activity on a 10^5-year scale at a slow-spreading ridge, TAG hydrothermal field, Mid-Atlantic Ridge 26°N. *J. Geophys. Res.* 100, 17855–17862. doi:10.1029/95JB01858

Lalou, C., Thompson, G., Arnold, M., Brichet, E., Druffel, E., and Rona, P. A. (1990). Geochronology of TAG and Snakepit hydrothermal fields, Mid-Atlantic Ridge: witness to a long and complex hydrothermal history. *Earth Planet. Sci. Lett.* 97, 113–128. doi:10.1016/0012-821X(90)90103-5

Lalou, C., Thompson, G., Rona, P. A., Brichet, E., and Jehanno, C. (1986). Chronology of selected hydrothermal Mn oxide deposits from the transatlantic geotraverse "TAG" area, Mid-Atlantic Ridge 26°N. *Geochimica Cosmochimica Acta* 50, 1737–1743. doi:10.1016/0016-7037(86)90135-3

Lehrmann, B., Stobbs, I. J., Lusty, P. A. J., and Murton, B. J. (2018). Insights into extinct seafloor massive sulfide mounds at the TAG, Mid-Atlantic Ridge. *Minerals* 8, 302. doi:10.3390/min8070302

Mccaig, A. M., Delacour, A., Fallick, A. E., Castelain, T., and FrüH-Green, G. L. (2010). "Detachment Fault control on hydrothermal circulation systems: interpreting the subsurface beneath the tag hydrothermal field using the isotopic and geological evolution of oceanic core complexes in the atlantic," in *Diversity of hydrothermal systems on slow spreading ocean ridges* (United States: American Geophysical Union), 207–239. doi:10.1029/2008GM000729

Mills, R. A., Wells, D. M., and Roberts, S. (2001). Genesis of ferromanganese crusts from the TAG hydrothermal field. *Chem. Geol.* 176, 283–293. doi:10.1016/s0009-2541(00)00404-6

Monecke, T., Petersen, S., Hannington, M. D., Grant, H., and Samson, I. M. (2016). "The minor element endowment of modern sea-floor massive sulfides and comparison with deposits hosted in ancient volcanic successions," in *Rare Earth and critical elements in ore deposits*. Editors P. L. Verplanck, and M. W. Hitzman (USA: Society of Economic Geologists), 0. doi:10.5382/Rev.18.11

Murton, B. J., Lehrmann, B., Dutrieux, A. M., Martins, S., de la Iglesia, A. G., Stobbs, I. J., et al. (2019). Geological fate of seafloor massive sulphides at the TAG hydrothermal field (Mid-Atlantic Ridge). *Ore Geol. Rev.* 107, 903–925. doi:10.1016/j.oregeorev.2019.03.005

Pelleter, E., and Cathalot, C. (2022). HERMINE2 cruise. *RV Pourquoi pas?* doi:10.17600/18001851

Pelleter, E., Fouquet, Y., Etoubleau, J., Cheron, S., Labanieh, S., Josso, P., et al. (2017). Ni-Cu-Co-rich hydrothermal manganese mineralization in the Wallis and Futuna back-arc environment (SW Pacific). *Ore Geol. Rev. SI:Marine mineral deposits New Resour. base, precious, Crit. metals* 87, 126–146. doi:10.1016/j.oregeorev.2016.09.014

Petersen, S., Herzig, P. M., and Hannington, M. D. (2000). Third dimension of a presently forming VMS deposit: TAG hydrothermal mound, Mid-Atlantic Ridge, 26°N. *Mineral. Deposita* 35, 233–259. doi:10.1007/s001260050018

Petersen, S., Krätschell, A., Augustin, N., Jamieson, J., Hein, J. R., and Hannington, M. D. (2016). News from the seabed – geological characteristics and resource potential of deep-sea mineral resources. *Mar. Policy* 70, 175–187. doi:10.1016/j.marpol.2016.03.012

Petersen, S., Kuhn, K., Kuhn, T., Augustin, N., Hékinian, R., Franz, L., et al. (2009). The geological setting of the ultramafic-hosted Logatchev hydrothermal field (14°45′N, Mid-Atlantic Ridge) and its influence on massive sulfide formation. *Lithos, Recent Dev. seafloor petrology Tect.* 112, 40–56. doi:10.1016/j.lithos.2009.02.008

Purdy, G. M., Sempere, J.-C., Schouten, H., Dubois, D. L., and Goldsmith, R. (1990). Bathymetry of the mid-atlantic ridge, 24°-31°N: a map series. *Mar. Geophys Res.* 12, 247–252. doi:10.1007/BF02428196

Rona, P. A., Bogdanov, Y. A., Gurvich, E. G., Rimski-Korsakov, N. A., Sagalevitch, A. M., Hannington, M. D., et al. (1993a). Relict hydrothermal zones in the TAG hydrothermal field, mid-Atlantic Ridge 26°N, 45°W. *J. Geophys. Res.* 98, 9715–9730. doi:10.1029/93JB00552

Rona, P. A., Hannington, M. D., Raman, C. V., Thompson, G., Tivey, M. K., Humphris, S. E., et al. (1993b). Active and relict sea-floor hydrothermal mineralization at the TAG hydrothermal field, Mid-Atlantic Ridge. *Econ. Geol.* 88, 1989–2017. doi:10.2113/gsecongeo.88.8.1989

Rona, P. A., Klinkhammer, G., Nelsen, T. A., Trefry, J. H., and Elderfield, H. (1986). Black smokers, massive sulphides and vent biota at the Mid-Atlantic Ridge. *Nature* 321, 33–37. doi:10.1038/321033a0

Rona, P. A., McGregor, B. A., Betzer, P. R., Bolger, G. W., and Krause, D. C. (1975). Anomalous water temperatures over Mid-Atlantic Ridge crest at 26° North latitude. *Deep Sea Res. Oceanogr. Abstr.* 22, 611–618. doi:10.1016/0011-7471(75)90048-0

Rona, P. A., Petersen, S., Becker, K., Von Herzen, R. P., Hannington, M. D., Herzig, P. M., et al. (1996). Heat flow and mineralogy of TAG relict high-temperature hydrothermal zones: mid-Atlantic Ridge 26°N, 45°W. *Geophys. Res. Lett.* 23, 3507–3510. doi:10.1029/96GL03257

Rona, P. A., Thompson, G., Mottl, M. J., Karson, J. A., Jenkins, W. J., Graham, D., et al. (1984). Hydrothermal activity at the trans-atlantic geotraverse hydrothermal field, mid-Atlantic Ridge crest at 26°N. *J. Geophys. Res.* 89, 11365–11377. doi:10.1029/JB089iB13p11365

Sánchez-Mora, D., Jamieson, J., Cannat, M., Escartín, J., and Barreyre, T. (2022). Age and rate of accumulation of metal-rich hydrothermal deposits on the seafloor: the lucky strike vent field, Mid-Atlantic Ridge. *J. Geophys. Res. Solid Earth* 127, e2022JB024031. doi:10.1029/2022JB024031

Scott, R. B., Rona, P. A., Mcgregor, B. A., and Scott, M. R. (1974). The TAG hydrothermal field. *Nature* 251, 301–302. doi:10.1038/251301a0

Sempéré, J.-C., Purdy, G. M., and Schouten, H. (1990). Segmentation of the Mid-Atlantic Ridge between 24° N and 30°40' N. *Nature* 344, 427–431. doi:10.1038/344427a0

Smith, D. K., and Cann, J. R. (1990). Hundreds of small volcanoes on the median valley floor of the Mid-Atlantic Ridge at 24–30° N. *Nature* 348, 152–155. doi:10.1038/348152a0

Szitkar, F., Dyment, J., Petersen, S., Bialas, J., Klischies, M., Graber, S., et al. (2019). Detachment tectonics at Mid-Atlantic Ridge 26°N. *Sci. Rep.* 9, 11830–11838. doi:10.1038/s41598-019-47974-z

Thompson, G., Mottl, M. J., and Rona, P. A. (1985). Morphology, mineralogy and chemistry of hydrothermal deposits from the TAG area, 26°N Mid-Atlantic Ridge. *Chem. Geol.* 49, 243–257. doi:10.1016/0009-2541(85)90159-7

Tivey, M. A., Schouten, H., and Kleinrock, M. C. (2003). A near-bottom magnetic survey of the Mid-Atlantic Ridge axis at 26°N: implications for the tectonic evolution of the TAG segment. *J. Geophys. Res. Solid Earth* 108. doi:10.1029/2002JB001967

Tivey, M. K., Humphris, S. E., Thompson, G., Hannington, M. D., and Rona, P. A. (1995). Deducing patterns of fluid flow and mixing within the TAG active hydrothermal mound using mineralogical and geochemical data. *J. Geophys. Res.* 100, 12527–12555. doi:10.1029/95JB00610

Van Dover, C. L., Arnaud-Haond, S., Gianni, M., Helmreich, S., Huber, J. A., Jaeckel, A. L., et al. (2018). Scientific rationale and international obligations for protection of active hydrothermal vent ecosystems from deep-sea mining. *Mar. Policy* 90, 20–28. doi:10.1016/j.marpol.2018.01.020

Van Dover, C. L., Colaço, A., Collins, P. C., Croot, P., Metaxas, A., Murton, B. J., et al. (2020). Research is needed to inform environmental management of hydrothermally inactive and extinct polymetallic sulfide (PMS) deposits. *Mar. Policy* 121, 104183. doi:10.1016/j.marpol.2020.104183

White, S. N., Humphris, S. E., and Kleinrock, M. C. (1998). New observations on the distribution of past and present hydrothermal activity in the TAG area of the Mid-Atlantic Ridge (26°08′ N). *Mar. Geophys. Res.* 20, 41–56. doi:10.1023/A:1004376229719

Zeng, X., Alain, K., and Shao, Z. (2021). Microorganisms from deep-sea hydrothermal vents. *Mar. Life Sci. Technol.* 3, 204–230. doi:10.1007/s42995-020-00086-4

Zhao, M., Canales, J. P., and Sohn, R. A. (2012). Three-dimensional seismic structure of a Mid-Atlantic Ridge segment characterized by active detachment faulting (Trans-Atlantic Geotraverse, 25°55′N-26°20′N). *Geochem. Geophys. Geosyst.* 13, Q0AG13. doi:10.1029/2012GC004454

Zonenshain, L. P., Kuzmin, M. I., Lisitsin, A. P., Bogdanov, Yu. A., Baranov, B. V. (1989). Tectonics of the mid-Atlantic rift valley between the TAG and MARK areas (26–24°N): evidence for vertical tectonism. *Tectonophysics* 159, 1–23. doi:10.1016/0040-1951(89)90167-4

frontiers | Frontiers in Earth Science

TYPE Original Research
PUBLISHED 04 April 2024
DOI 10.3389/feart.2024.1354388

Check for updates

OPEN ACCESS

EDITED BY
Glen T. Snyder,
The University of Tokyo, Japan

REVIEWED BY
Hitoshi Tomaru,
Chiba University, Japan
Shinsuke Aoki,
Kagawa University, Japan
Jamshid Gharib,
Fugro, United States

*CORRESPONDENCE
Cliff S. Law,
cliff.law@niwa.co.nz

†PRESENT ADDRESS
Julie C. S. Brown,
Department of Earth Sciences, University College London, London, United Kingdom

RECEIVED 12 December 2023
ACCEPTED 18 March 2024
PUBLISHED 04 April 2024

CITATION
Law CS, Collins C, Marriner A, Bury SJ, Brown JCS and Rickard G (2024), Dispersion and fate of methane emissions from cold seeps on Hikurangi Margin, New Zealand. *Front. Earth Sci.* 12:1354388. doi: 10.3389/feart.2024.1354388

COPYRIGHT
© 2024 Law, Collins, Marriner, Bury, Brown and Rickard. This is an open-access article distributed under the terms of the Creative Commons Attribution License (CC BY). The use, distribution or reproduction in other forums is permitted, provided the original author(s) and the copyright owner(s) are credited and that the original publication in this journal is cited, in accordance with accepted academic practice. No use, distribution or reproduction is permitted which does not comply with these terms.

Dispersion and fate of methane emissions from cold seeps on Hikurangi Margin, New Zealand

Cliff S. Law[1,2]*, Charine Collins[1], A. Marriner[1], Sarah J. Bury[1], Julie C. S. Brown[1†] and Graham Rickard[1]

[1]National Institute of Water and Atmospheric Research, Wellington, New Zealand, [2]Department of Marine Science, University of Otago, Dunedin, New Zealand

The influence of cold seep methane on the surrounding benthos is well-documented but the fate of dissolved methane and its impact on water column biogeochemistry remains less understood. To address this, the distribution of dissolved methane was determined around three seeps on the south-east Hikurangi Margin, south-east of New Zealand, by combining data from discrete water column sampling and a towed methane sensor. Integrating this with bottom water current flow data in a dynamic Gerris model determined an annual methane flux of 3 x 10^5 kg at the main seep. This source was then applied in a Regional Ocean Modelling System (ROMS) simulation to visualize lateral transport of the dissolved methane plume, which dispersed over ~100 km in bottom water within 1 year. Extrapolation of this approach to four other regional seeps identified a combined plume volume of 3,500 km^3 and annual methane emission of 0.4–3.2 x 10^6 kg CH_4 y^{-1}. This suggests a regional methane flux of 1.1–10.9 x 10^7 kg CH_4 y^{-1} for the entire Hikurangi Margin, which is lower than previous hydroacoustic estimates. Carbon stable isotope values in dissolved methane indicated that lateral mixing was the primary determinant of methane in bottom water, with potential methane oxidation rates orders of magnitude lower than the dilution rate. Calculations indicate that oxidation of the annual total methane emitted from the five seeps would not significantly alter bottom water dissolved carbon dioxide, oxygen or pH; however, superimposition of methane plumes from different seeps, which was evident in the ROMS simulation, may have localized impacts. These findings highlight the value of characterizing methane release from multiple seeps within a hydrodynamic model framework to determine the biogeochemical impact, climate feedbacks and connectivity of cold seeps on continental shelf margins.

KEYWORDS

methane, hydrates, hydrodynamic model, methane oxidation, continental shelf, New Zealand, mixing, climate change

1 Introduction

Although the ocean only accounts for 1%–3% of global methane (CH_4) emissions (9–22 Tg CH_4 y^{-1}, Saunois et al., 2020) marine methane is attracting increasing attention, in part due to its sensitivity to climate change. Marine methane sources are dominated by cold seeps on continental shelf margins and coasts (Weber et al., 2019), which primarily originate from underlying gas hydrates. The latter form in the Gas Hydrate Stability Zone (GHSZ),

at low temperature and high pressure, hence their subsurface presence on continental shelves and margins (Hester and Brewer, 2009). Estimates vary widely and indicate that 450–75,000 Pg CH_4 may be stored globally in these reservoirs (Klauda and Sandler, 2005; Wallmann et al., 2012), with annual global seafloor seepage potentially reaching 65 Tg (US EPA: Office of Atmospheric Programs, 2010). However, their contribution to atmospheric emissions is negligible (Saunois et al., 2020), due to a combination of physical, geological and biological barriers that minimize methane transfer to the ocean surface. Methane flux from subsurface hydrates is primarily suppressed by anaerobic methanotrophy in the overlying sediment, which significantly reduces methane release into bottom water to ~0.02 Gt C y^{-1} (Boetius and Wenzhöfer, 2013). However, gaseous methane can evade this benthic filter (Sommer et al., 2006), with bubble ebullition and subsequent diffusion elevating dissolved methane in bottom waters (McGinnis et al., 2006). Dispersion and dilution by bottom currents (Kessler et al., 2011; Steinle et al., 2015), and oxidation via the pelagic filter of aerobic methanotrophs (Reeburgh, 2007) then further reduce dissolved methane concentration (de Angelis et al., 1993; Mau et al., 2013; Leonte et al., 2017). The dominance of lateral flow relative to vertical exchange in bottom and intermediate waters, combined with stratification in the main pycnocline, effectively caps the transfer of dissolved methane to surface waters and the atmosphere, with retention in deeper water ultimately resulting in aerobic oxidation to carbon dioxide (CO_2) (Valentine et al., 2001; Reeburgh, 2007).

Methane release at cold seeps has a significant influence on local benthic biology, as it supports microbial communities and associated biogeochemical pathways that sustain unique infauna and macrofauna assemblages via chemosynthesis (Boetius and Wenzhöfer, 2013; Bowden et al., 2013). There is also evidence around seep sites of trophic transfer of carbon derived from methane in food webs that include commercially important fisheries species (Niemann et al., 2013; Seabrook et al., 2019). The potential sensitivity of hydrates to tectonic activity (Crutchley et al., 2023; Rudebusch et al., 2023) and ocean warming (Ruppel and Kessler, 2017), and also interest in methane hydrates as a potential fuel source (Moridis et al., 2011), has focused attention on the fate of methane in bottom water. Warming of deep water may destabilize hydrates at the upper edge of the GHSZ, as indicated in the paleorecord by significant methane release from subsurface reservoirs coincident with periods of ocean warming (Maslin et al., 2010), and there is increasing contemporary evidence for this (Phrampus and Hornbach, 2012; Trivedi et al., 2022). The resulting increase in methane in deep waters could enhance CO_2 production and consumption of oxygen (O_2) via aerobic oxidation, so accelerating acidification and deoxygenation (Biastoch et al., 2011; Ruppel, 2011; Boudreau et al., 2015). However, the impact of seep methane on water column biogeochemistry has received less attention (Levin et al., 2016), in part due to the challenge of tracking dissolved methane in bottom water.

Fluid seepage and cold seeps are well-characterized along the Hikurangi Margin, east of New Zealand (Lewis and Marshall, 1996; Barnes et al., 2010; Watson et al., 2020), with subsurface hydrates evident as bottom-simulating reflectors in seismic data (Henrys et al., 2003; Klaucke et al., 2010; Crutchley et al., 2021; Crutchley et al., 2023). Regional analysis indicates seepage occurring predominantly along the deforming backstop of the margin, with fluid release from both the subducting plate and the accretionary wedge (Watson et al., 2020). Fluid migration is facilitated by folding, fractures and faults arising from tectonic activity and strata of elevated permeability and porosity. Cold seep location is further evidenced by the presence of gas flares or bubble plumes in hydroacoustic backscatter data (Turco et al., 2022), that may extend up to 1 km above the seafloor (Faure et al., 2010; Law et al., 2010). To determine the fate of methane released from cold seeps, dissolved methane concentrations and related biogeochemical parameters including dissolved O_2 and carbonate system parameters were measured in the water column at three seep sites on the south-east Hikurangi Margin. As tracking of dissolved methane in bottom waters is confounded by tidal currents and dispersal in three dimensions, the dissolved methane source and distribution at the main seep site was simulated at local scales in a hydrodynamic framework using a dynamic Gerris model, with dispersal along the margin then determined using the Regional Ocean Modelling System (ROMS). This was extended to four other regional seeps (Turco et al., 2022) to assess the combined dispersal of seep methane and influence on bottom water biogeochemistry. Methane loss was assessed by potential oxidation rate measurements, with oxidation also examined indirectly using carbon stable isotope values in dissolved methane (δ^{13}C-CH_4), to establish the relative influence of dispersion and oxidation on seep methane in bottom waters along the Hikurangi Margin.

2 Methods

2.1 Regional setting

Sampling was carried out during July 2019 onboard *R/V Tangaroa*, as part of the New Zealand HYDEE (Gas Hydrates: Economic Opportunities and Environmental Implications) programme. The study area lies at the southern end of the Hikurangi subduction margin (Figure 1) where the Pacific Plate subducts obliquely beneath the Australian Plate. Measurements were focused on three seeps - Maungaroa, Glendhu Ridge and Uruti Ridge - with data from two additional seep sites–Pahaua Bank and Uruti Ridge West - also considered in the analysis (Turco et al., 2022; see Table 1). Dispersal modelling focused on the main seep site at Maungaroa, where a subsurface layer of gas of >200 m height below the GHSZ has generated doming, fracturing and formation of a conduit that facilitates gas transfer to the seafloor (Crutchley et al., 2021).

2.2 Bottom water hydrography and properties

A seafloor mooring was deployed in the vicinity of each of the three seeps consecutively to record bottom water physical and biogeochemical properties. The mooring frame was attached to a 460 kg ballast weight and supported a 600 kHz Acoustic Doppler Current Profiler (ADCP) for measuring current direction and velocity. A SBE 37 ODO MicroCAT with conductivity, temperature and optical dissolved O_2 sensors was also deployed on the mooring at ~15 m above the seafloor. The mooring was deployed for periods

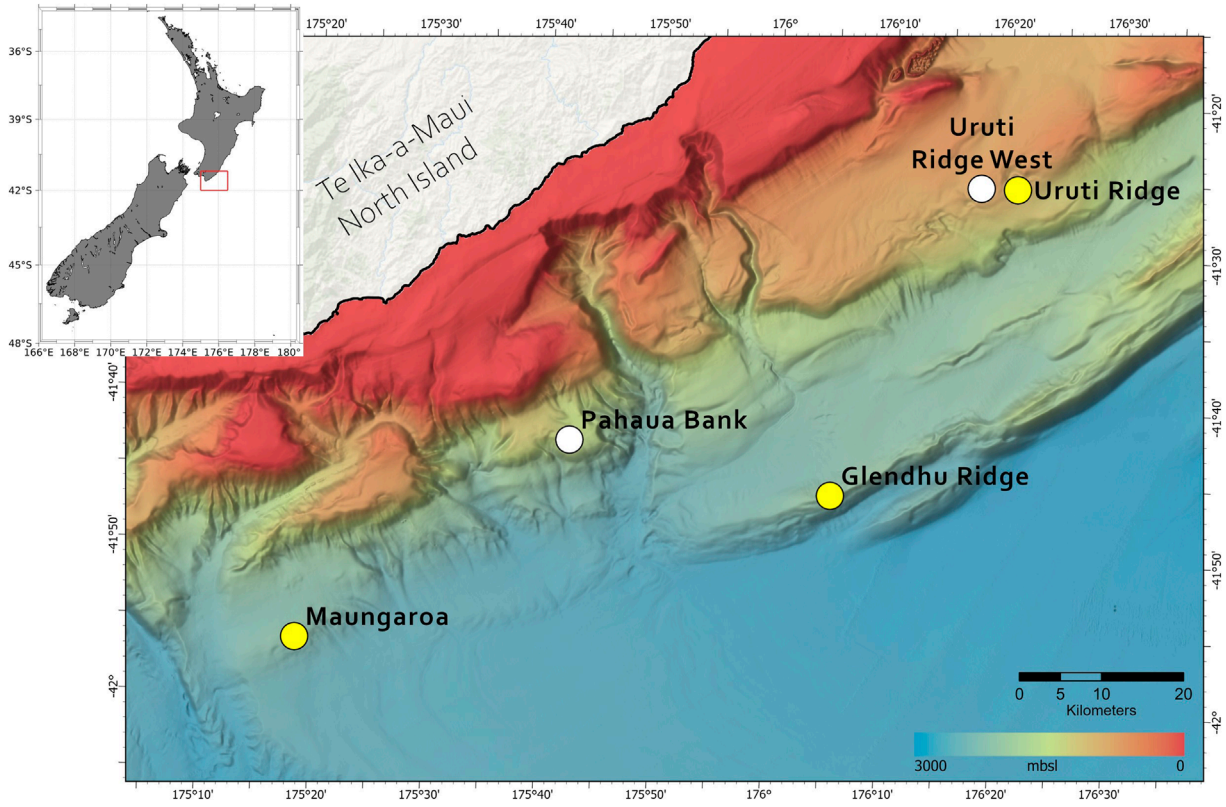

FIGURE 1
Location of the five seep sites on the south-east Hikurangi Margin plotted against bathymetric depth (m), as shown in the colour bar. The three seep sites surveyed in this study (Maungaroa, Uruti Ridge and Glendhu Ridge) are indicated by yellow circles, and the two additional sites (Uruti Ridge West and Pahaua Bank, (Turco et al., 2022) by white circles. The *x*-axis shows longitude (ºEast) and *y*-axis latitude (ºSouth).

TABLE 1 Seep locations and dimensions on the south-east Hikurangi Margin (all data from Turco et al., 2022, except for ∗ Crutchley et al., 2021), with the sites sampled in this study indicated by †.

Seep	Latitude (ºE)	Longitude (ºS)	Depth (m)	Seafloor acoustic anomaly area (km^2)	Bubble plume height (m)	Gas flux from bubble plume (10^6 kg y^{-1})
Maungaroa†	175.310	41.940	2081	0.2 ∗	1,400	2.52–7.18
Pahaua Bank	175.705	41.716	1,500	0.21	810	1.47–5.58
Glendhu Ridge†	176.089	41.768	1950	0.17	1,200	1.57–4.34
Uruti Ridge West	176.294	41.426	1,110	0.45	470	1.82–6.54
Uruti Ridge†	176.347	41.426	1,240	0.45	500–600	1.28–3.55

of 3–5 days at each site, which either preceded or followed other sampling activities to ensure the mooring and sensors were not compromised. On recovery, the mooring frame was decoupled from the ballast by remote activation of an acoustic release device whilst the ballast remained on the seafloor. The ADCP data was processed and quality controlled to generate a filtered data set with records at 120 s intervals over the lifetime of each respective deployment.

2.3 Water column sampling and characterisation

Dissolved methane concentrations were determined by four different approaches: discrete water sample collection in Niskin bottles on a CTD (Conductivity, Temperature and Depth) rosette in either a) standard vertical profiling mode or b) lateral towed mode, with methane concentration also measured by a methane

sensor deployed on c) the CTD or d) a Deep Towed Imaging System (DTIS, Bowden et al., 2013). As the dissolved methane plume was largely retained in near-bottom waters, the CTD and DTIS lateral tows focused on the bottom 10 m of water overlying the seafloor, with each sensor tow orientated relative to the seep by reference to a predetermined location and information from preceding tows. Each sensor tow started ~1 km from the seep and crossed this at the transect mid-point before completion at a similar distance of 1 km. During the CTD sensor tow, Niskin bottle water samples were obtained with increased sampling frequency close to the seep, with the remaining bottles fired in the bottom 200–500 m during retrieval. At least one vertical CTD cast was carried out at a distance of >1 km from the seep at all three sites to characterize background conditions. Bottom waters at Maungaroa received the most intense sampling, with six DTIS tows and 12 CTDs. Stratification was determined using buoyancy frequency squared (N^2), which was calculated as:

$$N^2 = g/\rho_0 . \delta\rho/\rho z$$

where g is gravitational acceleration, ρ_0 is a reference density, and $\delta\rho/\rho z$ is the vertical density gradient (Stevens et al., 2012).

2.4 Dissolved methane measurements

2.4.1 Analysis of discrete water samples

Seawater from the 10-L Niskin bottles was sub-sampled into 240 mL glass serum bottles, which were overflowed by at least 100% to exclude bubbles and then sealed with butyl rubber septa. The samples warmed passively to ambient temperature, with analysis within 4–5 h of collection. A 40 mL headspace of O_2-free nitrogen (N_2) was injected into the bottle whilst 40 mL of seawater was expelled, with the two phases subsequently equilibrated at room temperature for 30 min. The equilibrated headspace was displaced through a drying tube containing magnesium perchlorate and then a 2.9 mL sample loop, the contents of which were injected onto a 1/8" molecular sieve chromatographic column with methane detection by a Flame Ionisation Detector (Law et al., 2010). Calibration was carried out using prepared gas standards certified by comparison in an international calibration exercise (Wilson et al., 2018), with peak area variation of <0.35% over a 12-h analysis period. Dissolved methane concentration (nmol L^{-1}) was calculated from the measured partial pressure of methane in the headspace, following correction for water vapour and using the equilibration temperature and salinity with the solubility coefficients of Weisenburg and Guinasso (1979). Precision of duplicate sample analysis was 2.5% (1 standard deviation), consistent with the reproducibility reported in an international intercomparison (Wilson et al., 2018). Methane saturation from atmospheric equilibrium was calculated using the mean atmospheric methane mixing ratio of 1740 ppb recorded at the nearby National Institute of Water and Atmospheric Research (NIWA) Baring Head Global Atmosphere Watch Programme station (World Data Centre for Greenhouse Gases; kishou.go.jp), with dissolved methane concentration expressed as a percentage of expected saturation. An example of the vertical profile data for dissolved methane and associated parameters is available in Supplementary Table S1 (Supplementary Material), with the data for all profiles available at the associated website.

2.4.2 Continuous dissolved methane measurement

The dissolved methane dataset was extended to greater temporal and spatial resolution by deployment of a METS Sensor (Franatech, Oslo, Norway). This sensor was used in two modes: i) attached to the CTD, which enabled comparison with discrete sample data so enabling sensor calibration at *in situ* temperature and pressure; and ii) mounted on the DTIS (Bowden et al., 2013), which generated detailed transects across the seep region in bottom waters between 2 and 8 m above the seafloor. Each CTD lateral tow was at slightly shallower depths (5–15 m above the seabed), with the CTD initially held for 5–10 min to allow equilibration of the METS sensor before towing commenced. The METS relies upon methane diffusion across a permeable membrane, with diffusion assisted by a pump head, and detection by semi-conductor technology. Methane adsorption results in a change in conductivity which is converted to voltage as an output signal, with temperature sensitivity accounted for by a separate voltage (Krabbenhoefft et al., 2010). As diffusion across the membrane is rate-limiting this results in a lag in METS response, which was corrected for by comparison with *in situ* discrete sample data. The METS working temperature minimum of +2°C and methane concentration sensitivity of ~1 nmol L^{-1} were well suited to measurements in bottom waters along the Hikurangi Margin.

2.5 Dissolved inorganic carbon and total alkalinity

Bottom water collected in the Niskin bottles was subsampled into 1-L and 2-L glass bottles on selected CTD tows and profiles at seep and background stations for analysis of dissolved inorganic carbon (DIC) and total alkalinity (TA), respectively. The bottles were overflowed by 100%, with samples preserved by saturated mercuric chloride addition, sealed with parafilm and stored in the dark, with subsequent analysis in the laboratory. DIC concentration was determined coulometrically (Dickson et al., 2007) with an estimated accuracy and precision of ±1 μmol kg^{-1} based on repeat analysis of Dickson Certified Reference Materials. TA was determined by closed-cell potentiometric titration (Dickson et al., 2007), using a curve-fitting optimization with least squares analysis of the titration curve, with an estimated accuracy and precision ±2 μmol kg^{-1} also based on repeat analysis of Dickson Certified Reference Materials measurements. The DIC and TA data were used to calculate *in situ* pH on the total scale using *in situ* temperature, salinity and pressure and Mehrbach dissociation constants (Mehrbach et al., 1973), as refitted by Dickson and Millero (1987).

2.6 Dissolved methane carbon isotope analysis

Stable C isotope ratios of CO_2 were measured using a GasBench II and GC-PAL autosampler coupled to a DELTA V Plus isotope ratio mass spectrometer (IRMS) (all Thermo Fisher Scientific, Bremen, Germany). Daily checks confirmed that IRMS linearity was <0.06‰ $volt^{-1}$ for a known m/z 44 voltage span, and the standard deviation of $\delta^{13}C$ values from 10 peaks of working standard CO_2 was

always <0.06‰. Values of sample $\delta^{13}C$ were derived relative to the CO_2 working standard gas introduced directly into the IRMS and corrected for ^{17}O (Santrock et al., 1985) by Isodat software (version 3.0.94.17; Thermo Fisher Scientific, Bremen, Germany). Isotopic values were reported in δ-notation relative to the Vienna Pee Dee Belemnite scale. This approach was used for both dissolved methane (Section 2.6.1), and also for DIC in the potential oxidation rate measurement (Section 2.7).

2.6.1 Sample preparation for methane carbon isotope analysis

Seawater samples for dissolved $\delta^{13}C\text{-}CH_4$ analysis were subsampled from the Niskin bottles into 285 mL glass serum bottles, poisoned with mercuric chloride and sealed with butyl rubber septa. Sample temperature was slowly raised to ambient temperature with a hypodermic needle inserted through the septa to allow water to expel during volume change. In the laboratory, a 15 mL headspace of ultra-high purity helium was introduced while withdrawing an equivalent volume of seawater to obtain a seawater:headspace volume ratio of 18, with the two phases equilibrated on a shaker for 30 min. Using a GasBench II and GC PAL autosampler (Thermo Fisher Scientific, Bremen, Germany) the headspace gas was purged at 20 mL min^{-1} in a helium carrier flow and directed through a series of in-line traps to remove water, carbon monoxide and CO_2. A PreCon cold trap immersed in liquid N_2 removed nitrous oxide before sample methane was trapped on a second PreCon automated cold trap comprised of 100 cm of coiled GS-Q capillary column (divinylbenzene (DVB), wide-bore 0.32 mm D; Agilent Technologies, United States) also held in liquid N_2 (Yarnes, 2013). On removal of the second trap from the liquid N_2 the methane was transferred into the helium carrier flow and combusted by passing through the PreCon combustion reactor (99.8% alumina, 1.6 mm outer diameter, 0.8 mm bore, 327 mm length; McDanel Ceramics, United States) at 1,000°C. After drying, the CO_2 produced by methane combustion was cryo-focused in the GasBench II cold trap held in liquid N_2, and then separated from residual gases by a chromatographic column (CP-PoraPLOT Q) at 70°C. C stable isotope analysis was as described above, with $\delta^{13}C\text{-}CH_4$ from clean air from the Baring Head station used to correct sample $\delta^{13}C\text{-}CH_4$ values (Paul et al., 2007).

2.7 Methane oxidation rate

Potential methane oxidation rate was measured in selected bottom water samples using $^{13}C\text{-}CH_4$ addition, following the method of Leonte et al. (2017). Seawater was transferred from the Niskin bottle into 6 x 240 mL serum bottles for each depth sample, sealed with butyl rubber septa and aluminium seals, and placed in the dark at ambient bottom water temperature (2–2.5°C). Within three-five hours, four of the six serum bottles were injected with 50 µL $^{13}C\text{-}CH_4$ mixed with 50 µL ambient air from a gas-tight syringe, during which the serum bottle was inverted and the rubber seal perforated by a separate needle to maintain atmospheric pressure in the bottle. The remaining two serum bottles were not amended and provided a time zero for the rate measurement. All bottles were gently agitated for 20 min on a wrist-action shaker, after which the four amended samples were incubated in the dark at ambient bottom water temperature for three-five days. The incubation was terminated at time zero, Day 2 and Day 4 by removal of 2 mL of water; this was injected into a 12 mL gas-tight glass vial sealed with a rubber septum previously flushed with high purity helium and containing 100 µL of phosphoric acid. In the laboratory, acidified samples were equilibrated overnight at 24°C, during which the CO_2 released by acidification of DIC had equilibrated with the headspace. C stable isotope analysis was as described above in Section 2.6. Reference materials IAEA NBS-18 and IAEA-603 were used to normalize all $\delta^{13}C_{gas}$ values (Paul et al., 2007). Values of $\delta^{13}C$-DIC were calculated from $\delta^{13}C_{gas}$ values by accounting for the C stable isotope fractionation associated with the CO_2 gas-aqueous partition (Assayag et al., 2006). Potential methane oxidation rate was determined by the transfer of ^{13}C from the methane gas to DIC. Background *in situ* DIC concentrations were determined using the individual sample CO_2 peak values generated by the GasBench II, calibrated against a subset of samples analysed by coulometry, as detailed in Section 2.5. Rates (nmol l^{-1} d^{-1}, hereafter identified as nM d^{-1}) were derived using the approach of Leonte et al. (2017), and are regarded as "potential" oxidation, reflecting the large $^{13}C\text{-}CH_4$ addition relative to the background dissolved methane concentration.

2.8 Modelling

2.8.1 Near-field dispersion of dissolved methane in bottom water

A dynamic model of nearfield dispersion of dissolved methane around the Maungaroa seep was developed using Gerris, a semi-structured adaptive grid model for the solution of the non-hydrostatic Navier–Stokes equations (S. Popinet, http://gfs.sf.net; Rickard, 2020). The primary aim of the Gerris modelling was to estimate the source input of methane into the water column by assessing advection and diffusion of the methane tracer via fitting to the spatial and temporal transect observations. Dissolved methane was treated as a passive tracer and so was advected and diffused with the imposed flow. As Gerris is applicable to small scales it was appropriate for modelling dispersion of dissolved methane within a 1 km radius of the seep where most of the water sampling took place. The three-dimensional model domain spanned 2.25 km in each horizontal direction and 250 m in the vertical plane, with grid spacing over most of the domain of 7.8 m. The model incorporated advection associated with M2 tidal currents, as measured by the ADCP, with the seep methane assumed to be entrained within 50 m above the seafloor (see Results). The model was spun up for a number of M2 tidal cycles, thereby allowing the methane tracer to advect and diffuse across the domain, with two to four M2 tidal cycles producing tracer patterns that best fitted the observations. Using these best fits an "optimal" ratio of the observed maximum methane concentration to the Gerris model maximum was determined for each transect and profile, with the average ratio subsequently used to calculate methane emission.

2.8.2 Far-field dispersion of dissolved methane

The ROMS (Haidvogel et al., 2008) was used to simulate the advection of passive 'dye' tracers released at each of the five seep sites (Table 1) along the southern Hikurangi Margin over a period of

1 year. The model domain spans the continental shelf of the eastern North Island of New Zealand, from Cook Strait in the south to East Cape in the North, with a horizontal resolution of 2 km and 30 terrain-following vertical coordinates. The model bathymetry was constructed from various sources including the NIWA gridded bathymetry database, land elevation data, regional coastline data, and the General Bathymetric Chart of the Oceans (GEBCO) gridded ocean bathymetry. The model was initialized on 1 January 2013 with initial and boundary conditions derived from a global ocean reanalysis based on the Hybrid Coordinate Ocean Model (HYCOM; Chassignet et al., 2009). The global HYCOM product used provides daily snapshots of the 3-dimensional state of the global ocean on a 1/12° grid. Tidal currents were added to the HYCOM boundary conditions using amplitude and phase data for 13 tidal constituents derived from the New Zealand tidal model described by Walters et al. (2001). The ROMS simulation was forced at the surface with wind stress calculated from 3-hourly winds obtained from the 12 km New Zealand Limited Area Model (NZLAM; Lane et al., 2009). Heat and freshwater fluxes were obtained from six-hourly NCEP/NCAR reanalysis data with a horizonal resolution of 2.5° (Kalnay et al., 1996).

The passive tracer computational capabilities of ROMS were used to determine the dispersal of methane via a conservative dye tracer released in the bottom three grid cells (150–200 m above the bottom) at each of the five seep sites. The passive tracers were advected from the release locations following the same governing equations as temperature and salinity. The passive tracer has a unit concentration and was initialized from each location with a value of 100. To simulate a continuous release, the passive tracers were nudged back to a value of 100 at the release locations on a daily basis using a nudging coefficient of 0.05 $days^{-1}$.

The calculated methane source function generated by the Gerris model was applied to the ROMS dye tracer to determine dispersion from the Maungaroa seep in bottom waters along the Hikurangi Margin. The ratio of the Gerris source function to an independent estimate of methane emission from hydroacoustic backscatter (Turco et al., 2022) was generated for Maungaroa, and then applied to the estimated methane emission from hydroacoustic backscatter for the other four sites (Turco et al., 2022) to re-evaluate the total emission from the five seeps.

3 Results

3.1 Dissolved methane distribution

Analysis of the integrated discrete water sample and high-resolution sensor data determined that most of the dissolved methane was retained in bottom waters up to 200 m above the seafloor, although this was biased by the large number of sensor measurements obtained within 5 m of the seafloor. Dissolved methane concentration varied over four orders of magnitude, with maximum concentrations exceeding 2 μmol L^{-1} (supersaturation of 60,000 relative to atmospheric methane) at the Maungaroa and Uruti Ridge sites (Figure 2, Supplementary Table S1). The lower dissolved methane maximum at Glendhu Ridge may reflect that this site is characterized by a number of smaller dispersed seeps (Turco et al., 2022). All three sites showed methane undersaturation, indicative of methane oxidation, in the mid-water column at depths of 750–1,000 m for the shallower Uruti Ridge site and 1,000–1,500 m for the two deeper sites (Figure 2; Supplementary Table S1). Mid-water column methane concentrations were similar at the background and seep stations at Maungaroa, although elevated methane concentration of ~20 nmol L^{-1} was evident at 1,600–1800 m at the background sites. All three sites exhibited a mean methane concentration of ~4.5 nmol L^{-1} between 500 m and the surface, with a maximum of ~12.5 nmol L^{-1} at a background site near Maungaroa. The near-surface methane supersaturation of <150% was consistent with previous regional surveys (Law et al., 2010), confirming low regional methane flux to the atmosphere. Although there was no evidence of seep methane reaching the surface, emissions from shallower seeps along the Hikurangi Margin may occur (Higgs et al., 2019). Alternatively, the low methane supersaturation in surface waters may be produced by methane phosphonate or methylotrophic pathways (Karl et al., 2008; Weller et al., 2013).

3.1.1 High resolution dissolved methane in bottom waters

Comparison of discrete sample and sensor data on three CTD tows at the Maungaroa seep (Figure 3) indicated that the sensor generally overestimated background dissolved methane concentration and underestimated high values. This was not surprising as diffusion limits the sensor response with equilibrium taking longer than exposure to the methane maximum during towing. This also resulted in a "memory" effect, with temporal smearing generating lower broad dissolved methane concentrations relative to the sharper and higher concentrations in the discrete bottle data (see Figure 3). Corrected *in situ* dissolved methane concentrations ($CH_{4\ insitu}$) were generated from the sensor data by applying the equation $CH_{4\ insitu} = (CH4_{sens} - 2)^{1.15}$, which was derived from *in situ* calibration of the sensor relative to discrete bottom water samples. The limiting step of diffusion also caused a sensor response lag of ~5–6 min, as confirmed by comparison of sensor and discrete sample data, and so the dissolved $CH_{4\ insitu}$ was also corrected for this delay (Figure 3). However, the *in situ* temporal lag was shorter than in pre-voyage laboratory tests, potentially reflecting increased diffusion at the elevated *in situ* pressure in bottom water. Although the sensor "memory" could not be explicitly determined, the combined concentration and temporal corrections showed good agreement between the calculated $CH_{4\ insitu}$ and the bottle data (Figures 3A, B), with some indication of smearing following the methane maxima.

The lateral distribution of dissolved methane at Maungaroa was determined by a series of transects carried out with reference to the seep location and also elevated backscatter, which indicated the presence of authigenic carbonates formed by precipitation that is characteristic of seeps along the Hikurangi Margin (Figure 4C; Bowden et al., 2013; Crutchley et al., 2021). In two of the CTD transects dissolved methane associated with the bubble plume reached a water column depth of ~1,600 m with lateral transport to the north-east (towards 4 in Figure 4B). Retention in bottom waters occurred, with over 50% of total dissolved methane within 50 m of the seafloor and 75% in the bottom 200 m. This largely reflects rapid diffusion of methane out of the bubbles (McGinnis et al., 2006),

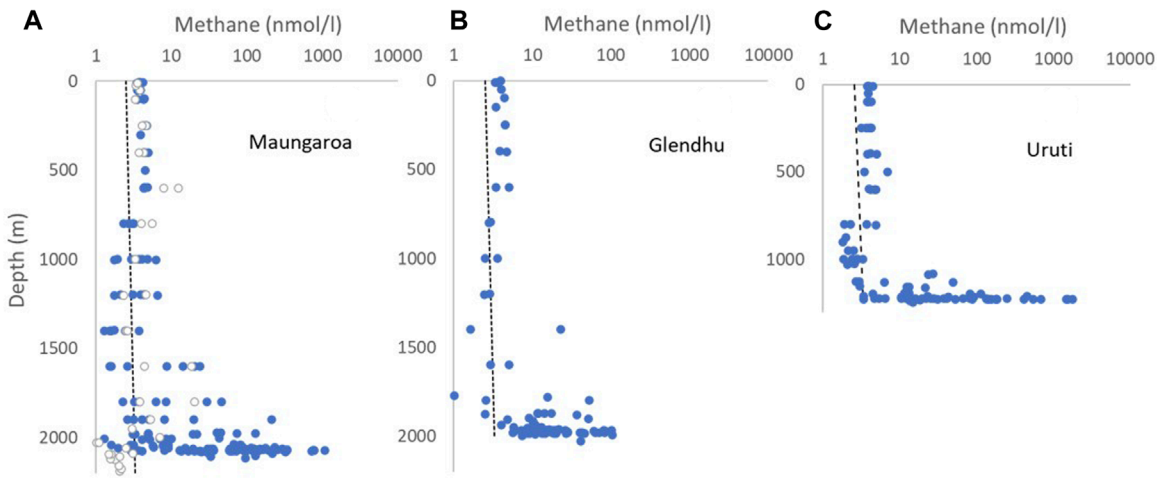

FIGURE 2
Vertical profiles of dissolved methane concentration (nmol/l) at the three seep sites: **(A)** Maungaroa, **(B)** Glendhu Ridge and **(C)** Uruti Ridge, with consistent depth and concentration scales used for comparison. The dashed line indicates the dissolved methane concentration expected from equilibrium with atmospheric methane. In **(A)** samples within 1 km of the Maungaroa seep are shown by blue circles, and those from background sites >1 km from the seep by open circles.

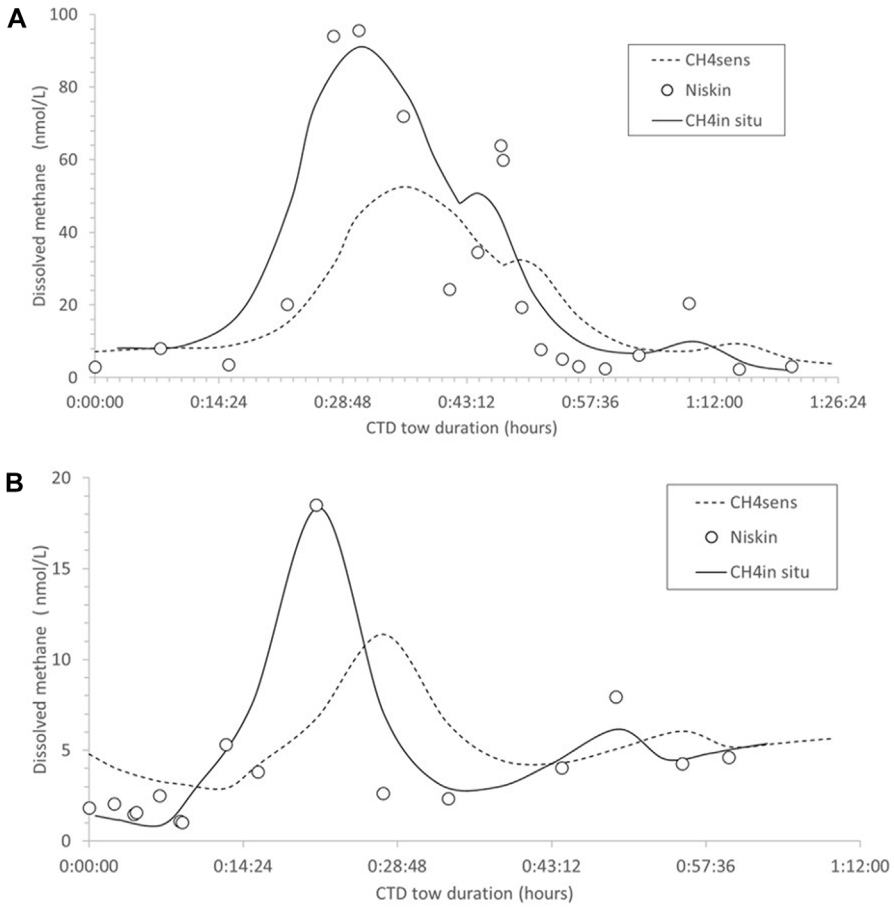

FIGURE 3
(A,B) CTD-sensor transects in bottom waters 5 m above the seafloor at Maungaroa, showing dissolved methane concentration (nmol/L) as determined by the sensor ($CH_{4\ sens}$, dashed line), and discrete Niskin samples (open circles), overlain by the corrected sensor data ($CH_{4\ insitu}$, black lines). The *y*-axis indicates the duration of the sensor tow in hours.

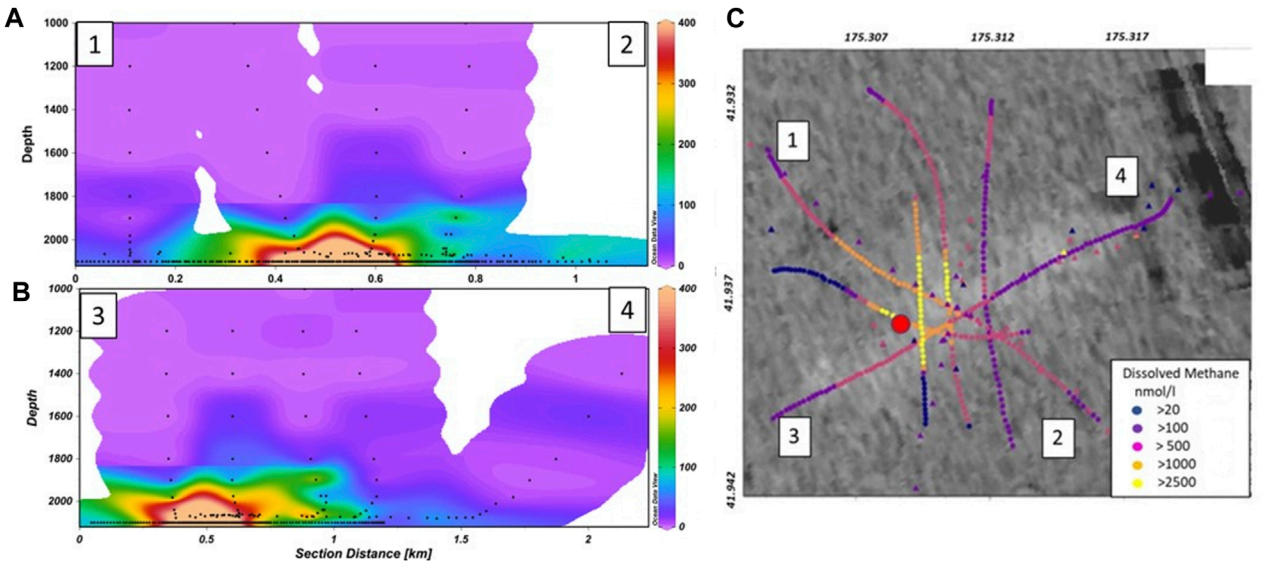

FIGURE 4
Contour plots showing the vertical distribution of dissolved methane concentration (nmol L^{-1}, see colour bar) below 1,000 m water depth along: **(A)** a NW–SE transect (1–2), and **(B)** a SW-NE transect (3–4) across the Maungaroa seep, with sample depths indicated by the black dots. **(C)** shows the spatial distribution of dissolved methane (nmol/l, see key), from discrete bottle samples (triangles) and sensor measurements (circles), overlain on subsurface backscatter around the Maungaroa seep, with transects 1–2 and 3–4 and mooring location (red dot) identified. The elevated backscatter in the upper right of **(C)** is an artefact related to swell or outer beam noise. **(A,B)** were created using Ocean Data View (Schlitzer, 2021), and the spatial plot **(C)** using ArcGIS.

which is then transferred laterally in dissolved form by bottom currents. This may be supplemented by dissolved methane in fluid release at the seafloor (Krabbenhoeff et al., 2010), although these two sources are indistinguishable with the techniques employed in the current study.

3.2 Bottom water currents and properties

Regional circulation in the water column overlying the Maungaroa Seep is influenced by eddies and mixing between the northward-flowing Southland Current and the D'Urville Current which flows through the Cook Strait. This generates the Wairarapa Coastal Current (WCC), a relatively cool northward flow along the outer shelf and upper slope (Figure 5D), inshore of the southward-flowing East Cape Current (ECC, Chiswell, 2003). The observed salinity variation between 200 m and 400 m (Figure 5C) likely reflects variability in the relative contributions of the Southland Current, ECC and D'Urville Current between sampling profiles. Below this the Antarctic Intermediate Water (AAIW) is evident as a salinity minimum around 1,000 m depth, with salinity increasing to the seafloor in Pacific Deep Water (PDW).

The mean Buoyancy Frequency squared (N^2) profile showed strongest vertical stratification between 250 m and 400 m depth at the base of the WCC (Figure 5B), and then decreased to the core of the AAIW at 1,000 m depth. N^2 subsequently increased to ~1,250 m depth, at the interface between the AAIW and PDW, before decreasing again to the seafloor. Comparison with the dissolved methane profile at Maungaroa (Figure 5A; also Figures 4A, B) suggests that water column structure and stability have a limited influence on vertical dissolved methane distribution. The bubble plume extended to a water column depth of ~1,000 m, shallower than the mid-water column stratification maximum at 1,250 m (compare Figures 5B, E), whereas dissolved methane was largely retained below 1,500 m where there was no corresponding N^2 maximum (compare Figures 5A, B). The absence of near-seafloor stratification (Figure 5B) is in contrast to Opouawe Bank nearby, where dissolved methane from a shallower seep (depth of ~1,080 m) was constrained by elevated N^2 just above the seafloor (Law et al., 2010).

The mooring at Maungaroa was located less than 100 m from the seep centre, with sensor measurements at 15 m above the seafloor. The ADCP recorded relatively low currents (<0.15 m s^{-1}), with north-easterly flow dominating and tidal currents running along the shelf parallel to the coast (Supplementary Figure S1). Fitting of M2 tides confirmed that tidal forcing was the dominant factor, despite an apparent anomaly in flow direction on Day 2. The tidal influence was also apparent in bottom water temperature and salinity, which showed an inverse relationship and variability of <0.2°C and 0.02 ppt, respectively, over the 5-day period. Dissolved O_2 concentration showed minor variation of <2 µmol L^{-1} relative to a bottom water mean of 152.5–155 µmol L^{-1} (44.8%–45.5% saturation with respect to the atmosphere). This variability primarily reflected temperature-related variation in solubility and there was no temperature or dissolved O_2 signal associated with the seep plume (Supplementary Figure S1), as reported in a previous regional study (Krabbenhoefft et al., 2010).

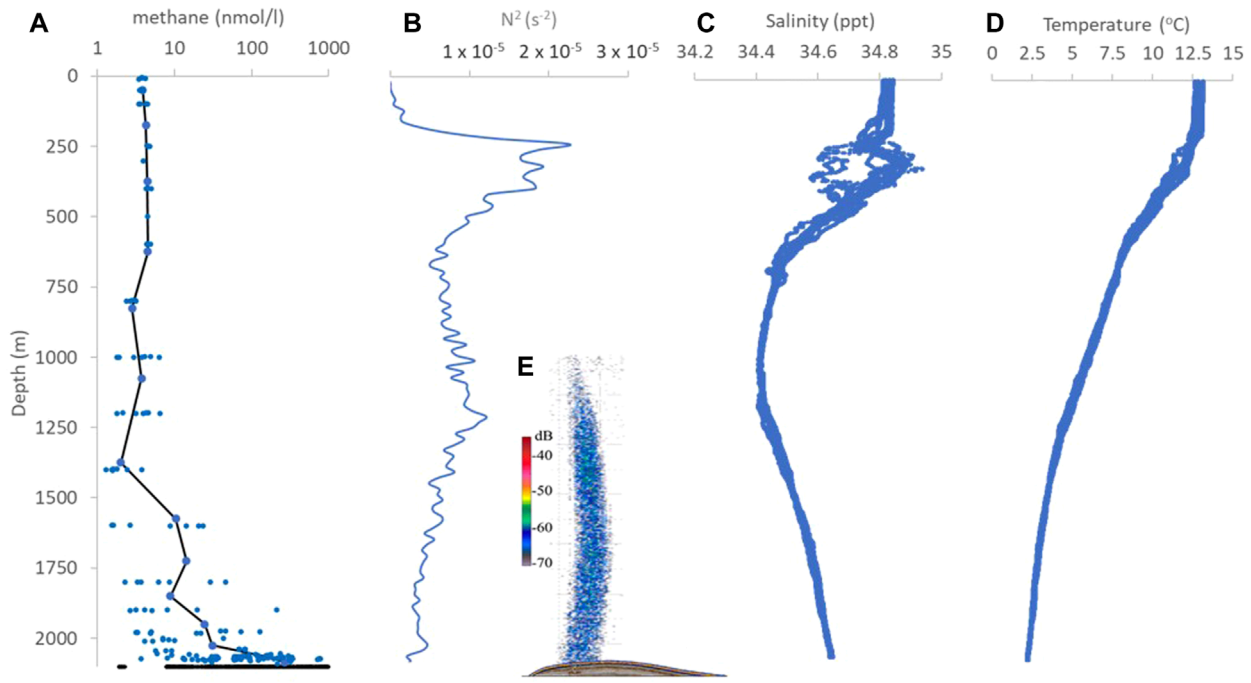

FIGURE 5
Water column profiles at Maungaroa showing: **(A)** methane concentration (nmol/l), from discrete samples (blue symbols), and corrected sensor data ($CH_{4\ insitu}$, black points between 2070 and 2080 m depth), with bin average methane concentration (black line), **(B)** buoyancy frequency squared N^2 (20 m bin average), **(C)** salinity and **(D)** temperature at 1 m resolution from 12 separate vertical profiles. The inset **(E)** shows the bubble plume at the Maungaroa seep, as imaged by the 38 kHz channel in the multibeam data (reproduced with permission from Turco et al., 2022). All profiles and inset are scaled to the same vertical depth range.

3.3 Modelled near-field methane distribution

The modelled methane was scaled by reference to the observed dissolved methane concentration in bottom waters within a 1 km radius around the seep using the Gerris model to estimate the methane source function, which was then converted to a flux by applying this to a source volume. Figures 6A, B show two sensor tows that crossed the Maungaroa seep, with the modelled distribution at the corresponding tidal state shown in Figures 6C, D. Overlaying the transects in Figures 6C, D highlights the overriding influence of the tidal cycle on the spatial distribution of seep-derived methane in bottom waters; despite both transects passing within 50 m of the seep, the modelled methane concentrations and distribution differ markedly due to the tidal state, as shown in the corresponding model simulations.

The footprint of the seep was assessed using different approaches. Previous measurement of water column backscatter indicated a seep footprint of ~200 m^2 at Maungaroa (Crutchley et al., 2021), although this is likely an overestimate as the bubble plume will be dispersed over a broader area by bottom currents and advection relative to the actual seafloor release area. An alternative approach to estimating seep spatial extent utilized the decline in meiobenthos abundance from the seep centre to background (D. Leduc, pers. comm.) which provided a horizontal length scale of ~50 m. As the latter estimate is consistent with the length scale reported for active fluid release at seeps along the Hikurangi Margin (Klaucke et al., 2010), a footprint of 50 m x 50 m was applied with the Gerris simulation, to generate a source function of 4.7 x 10^{-6} mol m^{-3} s^{-1} methane, and so an annual methane emission of 3 x 10^5 kg at the Maungaroa seep.

3.3.1 Modelled far-field dispersion of dissolved methane

ROMS-simulated bottom water currents were comparable with the ADCP currents in strength (<0.15 m s^{-1}) and direction, with north-easterly and south-easterly flow combining with tides to generate a net north-easterly advection (Figure 7A). Dye tracer released at the Maungaroa seep site in the ROMS simulation advected along the 2000 m isobath a maximum distance of ~87 km north-east of the seep location over 1 year. Scaling the ROMS tracer concentration to the Gerris-derived source function showed that modelled methane concentration was highest in a plume extending north-east of the seep centre (Figure 7B), but this declined sharply, falling below 500 and 200 nmol L^{-1} within 10 and 20 km of the seep location, respectively, with a total plume surface area of 4,000 km^2 after 1 year (see Supplementary Table S2).

The ROMS model was subsequently applied across the south-east Hikurangi Margin to assess plume dispersion for the four other cold seeps, characterized by Turco et al. (2022); see Table 1). Although the tracer was advected primarily to the north-east

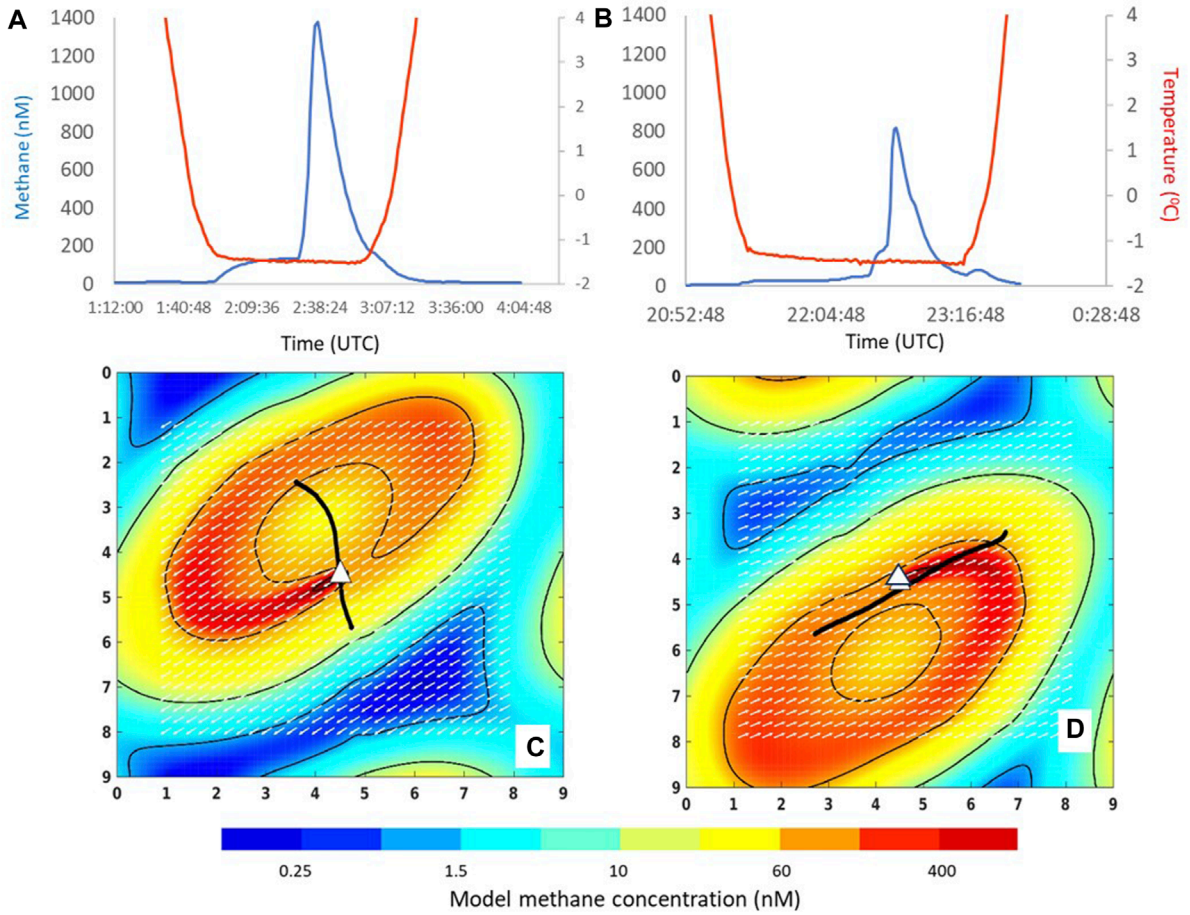

FIGURE 6
(A,B) Bottom water methane concentration (nM, blue line) and temperature (°C, red line) during two sensor transects across the Maungaroa seep, shown against time (UTC) on the *x*-axis. **(C,D)** show the corresponding dissolved methane distribution in bottom water, based on data obtained in A and B, respectively, as generated by the Gerris model at 2.5 and 3.0 tidal cycles. The seep location is indicated by the white triangle, the sensor transects by the continuous black line, and the modelled dissolved methane concentration by colour corresponding to the underlying colour bar. The white arrows show the tidal flow vectors at the time of the concentration contour snapshot in each frame, to indicate how flow influences dispersal. The total domain is 2.25 km x 2.25 km, with the numbers on the x- and *y*-axis corresponding to increments of 250 m.

at Maungaroa (Figures 7, 8), individual snapshots of tracer concentration over the simulation period showed that some seep plumes advected south-west on occasions (Figure 9). Lateral plume dispersion varied between seeps, with the tracer released at Pahaua Bank advecting a maximum distance of 104 km between the 1,000 m and 2000 m isobaths, in contrast to the shallower Uruti Ridge site, where dispersal was only 50 km within a year. At all sites elevated dye concentration (>0.25%) was generally constrained within 10 km of the release location, although elevated tracer plumes occasionally extended 50 km from the release site (Figure 9).

The extent of the dye tracer footprint for each seep plume was estimated based on a polygon enclosed by the contour associated with a dye concentration of 0.005. After 1 year the surface area of the individual dye tracer plumes ranged from 2,370 to 4,000 km^2 (Supplementary Table S2). The modelled vertical plume dispersal extended 1,000 m above the seafloor, resulting in a combined plume volume for the five seeps of 3,500 km^3 (Supplementary Table S3). The combination of reversing tidal currents, the relative proximity of seeps and their co-location primarily at similar depths resulted in overlap of the tracer plumes from individual seeps. This is evident as extended plumes of elevated tracer concentration (>0.25%) beyond 20 km from the seep location on occasions, such as for Maungaroa and Glendhu Ridge in September 2013 (Figure 9C). The ratio of the Gerris model flux estimate to the hydroacoustic flux estimate for Maungaroa (Turco et al., 2022) was then applied to the other seeps in Table 1 to generate a total methane flux for the five seeps of 0.4–3.2 x 10^6 kg CH_4 y^{-1}. Extrapolating this estimate using the approach of Turco et al. (2022) to all seeps across the Hikurangi Margin (Watson et al., 2020) results in a total methane emission of 1.1–10.9 x 10^7 kg CH_4 y^{-1}.

3.4 Potential methane oxidation rate

Measurements in 15 bottom water samples obtained within 1 km of the three seep sites (Maungaroa, Uruti Ridge and Glendhu Ridge)

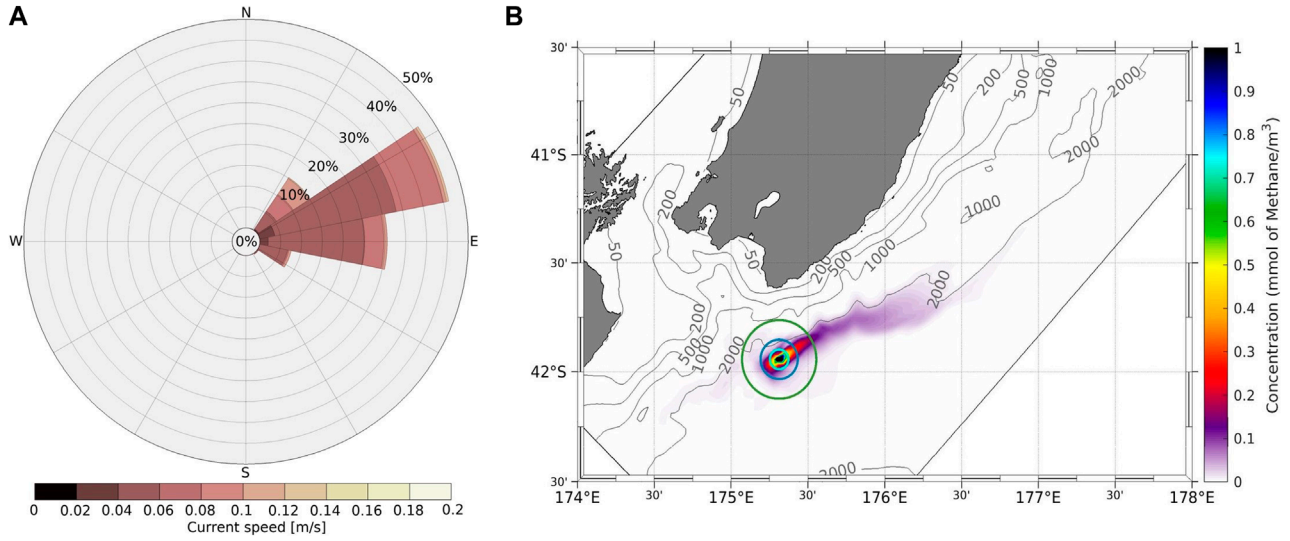

FIGURE 7
(A) Rose of current speed (m/s) averaged over a polygon spanning the methane seep locations. **(B)** Time-averaged dissolved methane concentration (mmol m^{-3}) for Maungaroa for the simulation period 1 January 2013–16 December 2013, with the turquoise, blue and green concentric circles indicating radii of 5 km, 10 km and 20 km from the release point, respectively. The modelled dissolved methane concentration is shown on the colour bar, with isobaths indicated by the grey contours.

generated potential methane oxidation rates of 1.79 ± 0.64 nM d^{-1} (Supplementary Figure S2). Rates were relatively insensitive to bottom water DIC concentration (mean 2058.1 μ mol kg^{-1}), and also showed no trend with distance from seep location or between the three seeps. In addition, there was no relationship between potential oxidation rate and *in situ* methane concentration, despite three orders of magnitude variation in the latter (Supplementary Figure S2).

3.5 Dissolved δ^{13}C-CH_4

Hydrates release methane with a characteristic low stable isotope (δ^{13}C-CH_4) value that results from fractionation during bacterial methanogenesis (Reeburgh, 2007), and consequently elevated methane concentrations in bottom water overlying the Hikurangi Margin seeps were associated with low δ^{13}C-CH_4. The three seep sites showed a similar relationship between dissolved methane concentration and δ^{13}C-CH_4 in waters between 1,000 m depth and the seafloor (Figure 10A), suggesting that there was no significant differences in either the source or processing of methane in bottom waters at the three sites. However, the more extensive dataset obtained at Maungaroa showed greater variability than the other two sites. Analysis of data from this site for the bottom 200 m of water, where most seep methane was retained (Figures 4, 5), showed a linear relationship between methane concentration and δ^{13}C-CH_4 (Figure 10B), as would be expected for lateral mixing of seep-derived methane with background water. However, variability precluded identification of end-member values, and indicated the influence of other factors.

4 Discussion

4.1 Methane emissions

Integration of *in situ* measurements in the Gerris model and ROMS simulation provided a new approach to estimating methane seep emissions on the Hikurangi Margin. The resulting methane flux for the Maungaroa seep of 3 x 10^5 kg CH_4 y^{-1} is 4%–12% of a previous estimate of 2.5–7.2 × 10^6 kg CH_4 y^{-1} derived from hydroacoustic data (Turco et al., 2022). These different estimates reflect methodological assumptions and uncertainties, as described in Turco et al. (2022) and other studies (Mitchell, et al., 2022). The hydroacoustic calculation likely overestimates the flux, as diffusive loss of methane during bubble rise (McGinnis et al., 2006) was not accounted for, whereas the Gerris model included uncertainty regarding the spatial dimensions of the methane source (see Section 3.3). The dissolved methane measurements in this study may also have included fluid input, although previous regional studies indicate that fluid release is relatively minor in relation to free gas (Luo et al., 2016). Although emissions from seeps are generally consistent in terms of location and magnitude on the Hikurangi Margin (Law et al., 2010), temporal variation in emissions has been reported (Naudts et al., 2010). Consequently, the emission estimates in this study and that of Turco et al. (2022) provide boundaries on annual methane emissions at Maungaroa of 0.3–7.2 x 10^6 kg CH_4 y^{-1}. This estimate is high relative to other seeps on Hikurangi Margin, for which annual emissions range from 10^2 to 10^4 kg CH_4 y^{-1} (Naudts et al., 2010; Luo et al., 2016), but is consistent with a first order estimate derived from hydroacoustic data and residence time for the Opouawe Bank seep located at a shallower depth

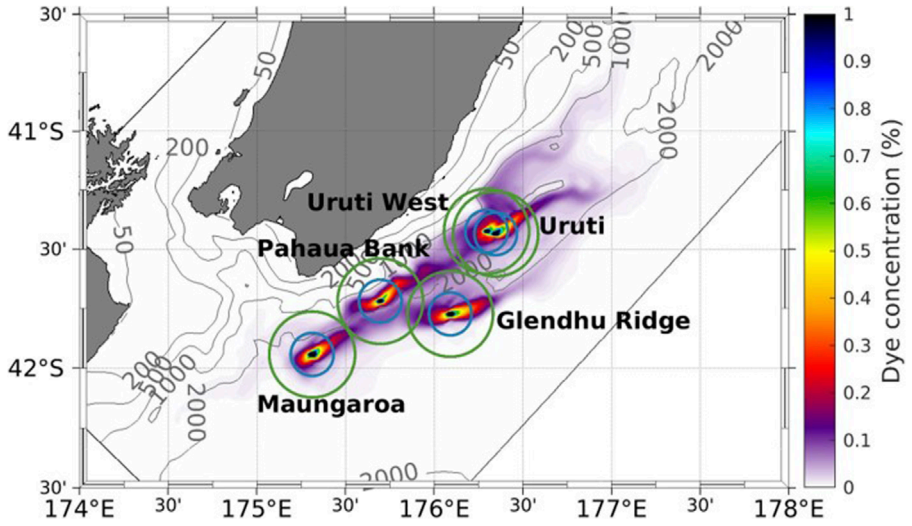

FIGURE 8
Time-averaged concentration of dye tracer at the five seep locations on the south-east Hikurangi Margin for the period 1 January 2013–16 December 2013. The blue and green circles show radii of 10 and 20 km, respectively, from the release point at each seep. Dye tracer is shown as a percentage relative to 1.0 at the source location, as indicated in the colour bar, with isobaths indicated by the grey contours.

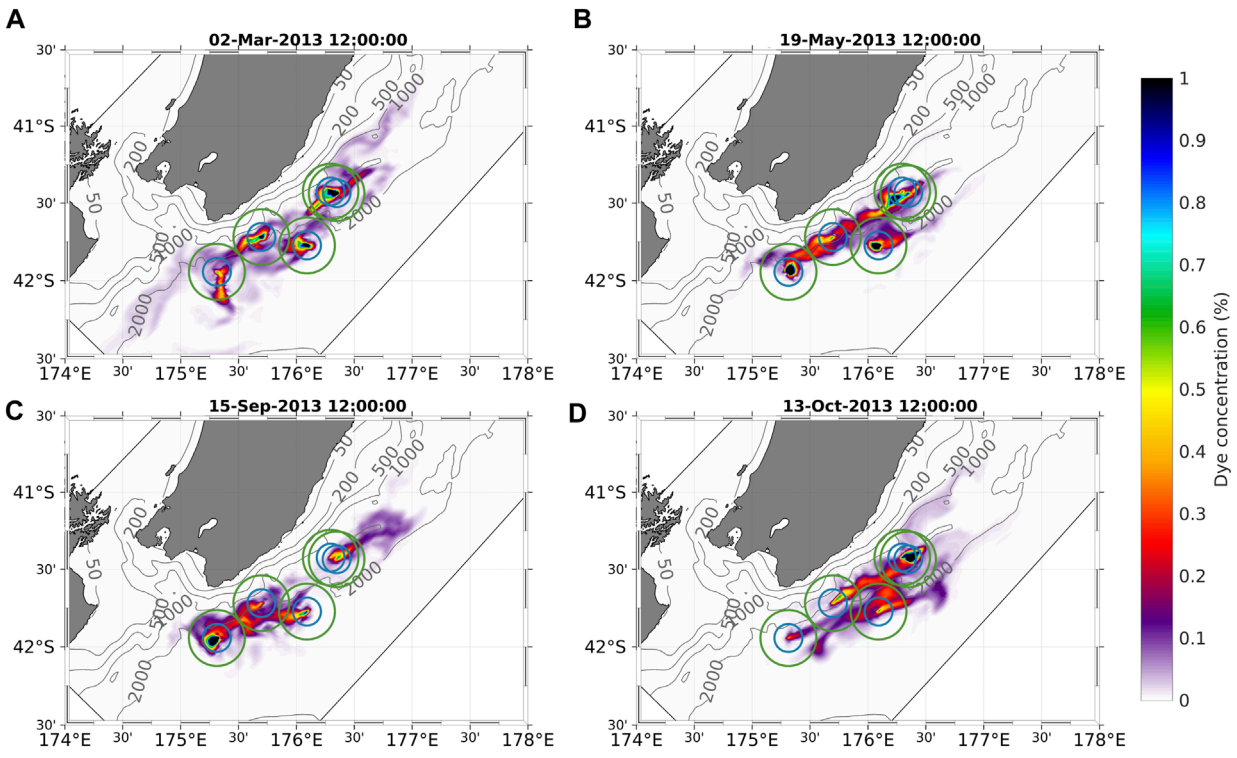

FIGURE 9
(A–D) Daily snapshots of dye tracer concentration on the south-east Hikurangi Margin at four different timepoints between 1 January 2013 and 16 December 2013. The blue and green circles indicate radii of 10 and 20 km, respectively, from the release point at each location. Dye tracer is shown as a percentage relative to 1.0 at the source location, as indicated in the colour bar, with isobaths indicated by the grey contours.

close to Maungaroa (4.9–9.8 x 10^5 kg CH_4 y^{-1}, Law et al., 2010). The revised methane emission for the entire Hikurangi Margin, of 1.1–10.9 x 10^7 kg CH_4 y^{-1}, is equivalent to 0.8%–7.9% of New Zealand terrestrial emissions (Ministry for Environment, 2022), and of similar magnitude to the calculated air-sea methane flux for the entire New Zealand Exclusive Economic Zone (4.1 x 10^7 kg y^{-1}, based upon 130% surface supersaturation; Law et al., 2010). This highlights the critical role of horizontal dilution and the pelagic

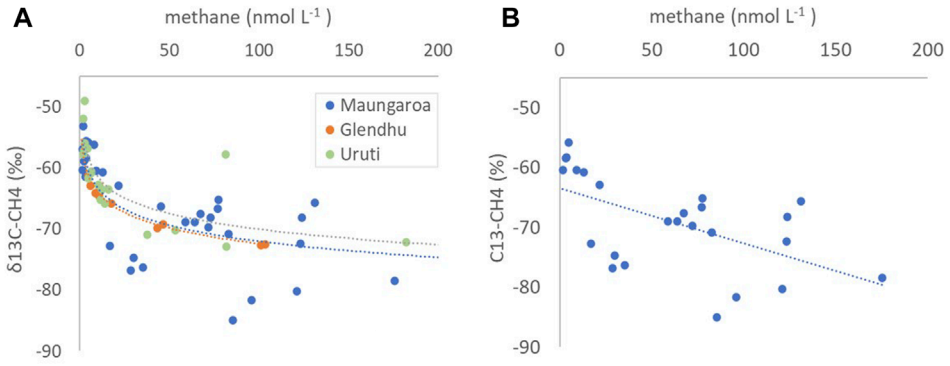

FIGURE 10
(A) The relationship between dissolved methane concentration (nmol L^{-1}) and $\delta^{13}C\text{-}CH_4$ values (‰) at depths >1,000 m for the three main seep sites, with the fits indicated by dotted lines and corresponding color for each seep (see key) **(B)** Dissolved methane concentration - $\delta^{13}C\text{-}CH_4$ relationship for Maungaroa in bottom water up to 200 m above the seafloor, with the dashed line indicating the mean linear fit.

methane filter in minimizing transfer of seep-derived methane to the atmosphere.

4.2 The relative roles of methane oxidation and dispersion

A primary aim of this study was to distinguish the relative contributions of dilution and methanotrophy in determining the distribution and concentration of methane in bottom waters along the Hikurangi Margin. The observed decrease in methane concentration in the vicinity of the seep, and corresponding diffusion and advection in the Gerris model, indicate dilution of two orders of magnitude. The equivalent dilution rate of ~1 mol m^{-3} d^{-1} is considerably larger than the measured potential oxidation rate of ~2 x 10^{-6} mol m^{-3} d^{-1} and, consequently, advection and dilution are the dominant determinants of methane concentration for the volume of interest and timescales of days in this study.

However, methanotrophy is an important sink for dissolved methane that not only reduces methane concentrations in the deep ocean but also flux to the atmosphere (Mao et al., 2022). The potential contribution of methanotrophy in this study was examined by two independent techniques: measurement of potential oxidation rate in isotope tracer incubations and interpretation of the dissolved $\delta^{13}C\text{-}CH_4$ values in bottom waters. The potential oxidation rates were relatively invariant, despite being sampled from within the seep plume through to background locations at all three seep sites (Supplementary Figure S2). This uniformity could reflect tidal retention in bottom waters along the shelf (Figure 9), resulting in a homogenised methanotroph community with uniform oxidation capacity. Although the potential oxidation rate technique relies upon addition of isotopic tracer at concentrations in excess of *in situ* methane concentrations (Leonte et al., 2018), the observed range and low variability are similar to rates reported at other seeps (5.6 ± 2.3 nM d^{-1}; Leonte et al., 2017; 0–3 nM d^{-1}; Graves et al., 2015; 0–2.5 nM d^{-1}; Weinstein et al., 2016), and marine systems (0–2.5 nM d^{-1}, Steinle et al., 2015; Osudar et al., 2015; 1–10 nM d^{-1}; Mau et al., 2013; 0.01–7.5 nM d^{-1}; Mao et al., 2022). This consistency is surprising, considering the range of environments and ambient methane concentrations, and also the different techniques used to measure methane oxidation. However, it should be noted that rate measurements in this and other studies were predominately carried out at atmospheric pressure, which may alter microbial metabolism and so methane oxidation, relative to that at *in situ* pressure in the deep ocean (Fortunato et al., 2021).

The absence of a relationship between potential oxidation rate and *in situ* methane concentration, despite three orders of magnitude variation in the latter (Supplementary Figure S2), has been reported in other studies. However, a first-order relationship has also been reported for some hydrate seeps (Valentine et al., 2001), and hydrothermal plumes (de Angelis et al., 1993), with strong evidence from the Deep Water Horizon wellhead blowout in the Gulf of Mexico after which rates rose by four orders of magnitude (Crespo-Medina et al., 2014). Methanotrophic response is slow (Valentine et al., 2001), with rates increasing ~1–2 months after methane addition and reaching a maximum after 3–4 months, as confirmed by modelling, oxidation rate and *in situ* O_2 measurements in the Gulf of Mexico (Kessler et al., 2011; Du and Kessler, 2012; Crespo-Medina et al., 2014). This may reflect slow adjustment of methanotroph metabolism or alternatively adaptation at the community level to elevated methane, which may account for the absence of a relationship between oxidation rate and *in situ* dissolved methane concentration (Supplementary Figure S2). Alternatively, this lag may reflect other controls of methane oxidation (Steinle et al., 2016), as suggested by shorter response times to methane addition at near-seep sites relative to sites at distance (Chan et al., 2019). As dilution was excluded in the Chan et al. study, the results suggest that near-seep methanotrophs were primed by prior exposure to elevated methane, or alternatively availability of a limiting factor such as trace metals or macronutrients (De Angelis et al., 1993; Beal et al., 2009).

The relatively constant potential oxidation rate across three orders of magnitude in dissolved methane concentration in this

study resulted in a range in turnover time of 6–1,000 days, consistent with other systems (7–560 days, De Angelis et al., 1993; 3–1,000 days; Osudar et al., 2015; 500 days to decades; Valentine et al., 2001). However, shorter turnover times have been recorded at seeps where mixing and circulation is constrained (0.3–3.7 days, Leonte et al., 2017; 1.3–24.0 days; Weinstein et al., 2016). Indeed, residence time is an important determinant of methane oxidation rate, with regional geomorphology, seasonal and water mass variation influencing methanotroph distribution, abundance and activity via dilution and current flow (Steinle et al., 2016; Gründger et al., 2021). The Maungaroa seep is located on a relatively flat ridge on the Hikurangi Margin (Turco et al., 2022), without canyons or seafloor morphology that might enhance regional retention and entrainment of bottom water, and so accumulation of dissolved methane, and thus methane oxidation, might be expected to be low. Although this is supported by the linear relationship between methane concentration and $\delta^{13}C\text{-}CH_4$ in bottom waters, other influences are also apparent (Figure 10B). This may reflect tidal circulation and entrainment of methane in the vicinity of the seep, as visualized in the Gerris and ROMS model simulations (Figures 6 and 9), with fresh seep methane of lower $\delta^{13}C\text{-}CH_4$ mixing with recirculated "older" methane with higher $\delta^{13}C\text{-}CH_4$ values due to oxidation. Despite potential methane oxidation rates being low (Supplementary Figure S2) relative to mixing, local retention could enhance methanotroph adaptation to elevated methane, resulting in higher $\delta^{13}C\text{-}CH_4$ values. Conversely, the variability at Maungaroa in Figure 10B may arise due to methane input from other regional seeps, as illustrated in the ROMS simulation in Figure 9. Methane release from hydrates will not have a uniform regional isotopic value but will vary between sites. In addition, thermogenic methane input has been reported for the Hikurangi Margin (Henrys et al., 2009), which could be a source of methane with higher $\delta^{13}C\text{-}CH_4$. Although tidal circulation of bottom waters may increase methane oxidation and mixing with methane from other sources this also confounds determination of their relative contribution to local methane dynamics.

4.3 Potential influence of methane emissions on water column biogeochemistry

Methane oxidation provides a source of energy and C for methanotroph growth (Hanson and Hanson, 1996), and ultimately produces CO_2 whilst consuming O_2. This is reflected in the elevated O_2 consumption in seafloor seep communities relative to non-seep benthos (Boetius and Wenzhöfer, 2013), that arises directly from methanotrophy and indirectly from chemosynthetically-supported benthic communities. However, there was no evidence of the Hikurangi Margin seeps influencing bottom water O_2 concentrations in either the mooring data (Supplementary Figure S1) or CTD profiles (data not shown), and the measured potential methane oxidation rates would have negligible effect on bottom water O_2. If the total methane release by the five seeps was completely oxidized within the modeled plume volume (90% of dye tracer, ~1,000 km^3) within 1 year, the decrease in dissolved O_2 concentration would be <0.3%. This assumes utilization of 2 mol of O_2 during methanotrophy and so conversion of all methane-fueled biomass to CO_2 (Chan et al., 2019), with resulting CO_2 production of <0.2 μmol L^{-1} and a corresponding decrease in pH of <0.002 relative to a background of 7.87. This minor influence is consistent with observations at the Hudson Canyon seeps, where aerobic methane oxidation accounted for only 0.3% of observed changes in DIC (Garcia-Tigreros and Kessler, 2018). A previous estimate based upon all Hikurangi Margin seeps suggested a greater impact of methane oxidation on dissolved O_2 and the carbonate system (Turco et al., 2022), but this was derived using a higher seep methane flux and also did not consider dilution and dispersion. Although the current assessment indicates negligible impact of seep methane on bottom water biogeochemistry it does not account for superimposition of plumes from different seeps along the Hikurangi Margin, as shown in Figure 9, which may result in localized impacts. For example, oxidation of seep methane in overlapping plumes could generate localized decreases of 0.53% in dissolved O_2 concentration and 0.005 in pH. These localized methanotrophy-driven decreases would compound the current low dissolved O_2 saturation in deep water along the Hikurangi Margin, and contribute to ongoing deoxygenation and carbonate saturation horizon shoaling (Feely et al., 2012; Oschlies et al., 2018).

4.4 Characterizing seep dispersal using hydrodynamic models

This study highlights the value of assessing the influence of methane seeps on bottom waters by integrating observations within a hydrodynamic framework. Although bottom water currents confound characterization of dissolved methane distribution around a seep, as illustrated in Figure 6, tidal dispersion and dilution was accounted for in a Gerris model. The ROMS model subsequently simulated methane concentration and distribution using the source function and location generated by the Gerris model but did not include loss to methane oxidation. Although rate measurements indicate that this process is insignificant relative to dispersion, further model development should incorporate methane oxidation, informed by measurements along the Hikurangi Margin to investigate the apparent uniformity in rate and also establish the relative contribution of oxidation to bottom water methane dynamics. The superimposition of multiple seeps could be further examined by applying the ROMS framework to the full suite of seeps along the Hikurangi Margin (Watson et al., 2020). As with many global studies, methane release from seeps is not apparent in surface waters along the Hikurangi Margin, except for some shallow seeps (Higgs et al., 2019); however, there is the potential for transfer via vertical mixing associated with geomorphological features and eddies. Application of the ROMS model framework to the broader shelf region could determine whether this represents a "shortcut" for seep methane transfer to surface waters and flux to the atmosphere along the Hikurangi Margin. The ROMS simulation also suggests that tidal retention and superimposition of plumes may facilitate connectivity between seeps, which should be examined with respect to larval dispersion and connectivity between seep populations (Levin et al., 2016) along the broader Hikurangi Margin. In addition, integration of regional hydrodynamic models with Earth System Models

(Rickard et al., 2023) could examine future climate-driven changes in bottom water and the associated biogeochemical impacts along the Hikurangi Margin.

5 Conclusion

Integration of methane data in a ROMS simulation established the methane source strength of five cold seeps on the south-eastern slope of the Hikurangi Margin. Although the combined methane plumes dispersed over a volume of 3,500 km^3 and depth of 1,000 m over a year, elevated concentrations were largely restricted to bottom waters 20 km downstream of the seep location. Potential methane oxidation rates were low and invariant in bottom waters, regardless of dissolved methane concentration, indicating slow turnover of dissolved methane. Despite dilution being orders of magnitude greater than aerobic oxidation, $\delta^{13}C\text{-}CH_4$ values showed some variability in bottom waters, reflecting a potential contribution of methane oxidation or other sources. The total methane release was revised to 0.4–3.2 x 10^6 kg CH_4 y^{-1} for the five seeps, and 1.1–10.9 x 10^7 kg CH_4 y^{-1} for the entire Hikurangi Margin, equivalent to the estimated air-sea flux for the entire Exclusive Economic Zone but less than 8% of New Zealand terrestrial emissions. Oxidation of total annual emissions from the five seeps would not significantly affect bottom water O_2, CO_2 and pH; however, superimposition of plumes from different seeps could support localised maxima in methane and methanotrophy in bottom waters. Integration of methane concentration within a hydrodynamic framework provides insight into the relative roles of dilution and oxidation in determining dissolved methane concentration in bottom waters, and also an approach for assessing the contribution to and sensitivity of cold seeps to climate change.

Data availability statement

The datasets presented in this study can be found in online repositories. The names of the repository/repositories and accession number(s) can be found below: Data and animations of the seep dispersal are available at https://zenodo.org/records/10373095.

Author contributions

CL: Conceptualization, Data curation, Formal Analysis, Funding acquisition, Investigation, Methodology, Project administration, Resources, Writing–original draft, Writing–review and editing. CC: Data curation, Investigation, Methodology, Software, Visualization, Writing–review and editing. AM: Data curation, Investigation, Methodology, Resources, Writing–review and editing. SB: Methodology, Resources, Writing–review and editing. JB: Formal Analysis, Investigation, Methodology, Resources, Writing–review and editing. GR: Data curation, Formal Analysis, Investigation, Methodology, Software, Validation, Visualization, Writing–review and editing.

Funding

The author(s) declare that financial support was received for the research, authorship, and/or publication of this article. Funding for this work was provided by the New Zealand Hīkina Whakatutuki MBIE Endeavor Fund Programme Gas Hydrates: Economic Opportunities and Environmental Impact (HYDEE; contract CO5X1708), with support from Strategic Scientific Investment Funds to the NIWA Ocean Centre.

Acknowledgments

We thank the Officers and Crew of the R/V Tangaroa, Ashley Rowden for voyage leadership; Brett Grant, Fiona Elliot and Chris Ray for mooring design and construction; Sarah Searson for mooring deployment and recovery; Josette Delgado for stable isotope analysis; Kim Currie and Judith Murdoch for carbonate system analysis; Steve George and Sarah Searson for CTD operations; Dave Bowden for DTIS location data; Susi Woelz for the site map, Arne Pallentin for ArcGIS data manipulation, and Sarah Seabrook for constructive comments.

Conflict of interest

The authors declare that the research was conducted in the absence of any commercial or financial relationships that could be construed as a potential conflict of interest.

Publisher's note

All claims expressed in this article are solely those of the authors and do not necessarily represent those of their affiliated organizations, or those of the publisher, the editors and the reviewers. Any product that may be evaluated in this article, or claim that may be made by its manufacturer, is not guaranteed or endorsed by the publisher.

Supplementary material

The Supplementary Material for this article can be found online at: https://www.frontiersin.org/articles/10.3389/feart.2024.1354388/full#supplementary-material

References

Assayag, N., Rivé, K., Ader, M., Jézéquel, D., and Agrinier, P. (2006). Improved method for isotopic and quantitative analysis of dissolved inorganic carbon in natural water samples. *Rapid Commun. Mass Spectrom.* 20, 2243–2251. doi:10.1002/rcm.2585

Barnes, P. M., Lamarche, G., Bialas, J., Henrys, S., Pecher, I., Netzeband, G. L., et al. (2010). Tectonic and geological framework for gas hydrates and cold seeps on the Hikurangi subduction margin, New Zealand. *Mar. Geol.* 272 (1-4), 26–48. doi:10.1016/j.margeo.2009.03.012

Beal, E. J., House, C. H., and Orphan, V. J. (2009). Manganese-and iron-dependent marine methane oxidation. *Science* 325 (5937), 184–187. doi:10.1126/science.1169984

Biastoch, A., Treude, T., Rüpke, L. H., Riebesell, U., Roth, C., Burwicz, E. B., et al. (2011). Rising Arctic Ocean temperatures cause gas hydrate destabilization and ocean acidification. *Geophys. Res. Lett.* 38 (8). doi:10.1029/2011gl047222

Boetius, A., and Wenzhöfer, F. (2013). Seafloor oxygen consumption fuelled by methane from cold seeps. *Nat. Geosci.* 6 (9), 725–734. doi:10.1038/ngeo1926

Boudreau, B. P., Luo, Y., Meysman, F. J., Middelburg, J. J., and Dickens, G. R. (2015). Gas hydrate dissociation prolongs acidification of the Anthropocene oceans. *Geophys. Res. Lett.* 42 (21), 9337–9344. doi:10.1002/2015gl065779

Bowden, D. A., Rowden, A. A., Thurber, A. R., Baco, A. R., Levin, L. A., and Smith, C. R. (2013). Cold seep epifaunal communities on the Hikurangi margin, New Zealand: composition, succession, and vulnerability to human activities. *PLoS ONE* 8 (10), e76869. doi:10.1371/journal.pone.0076869

Chan, E. W., Shiller, A. M., Joung, D. J., Arrington, E. C., Valentine, D. L., Redmond, M. C., et al. (2019). Investigations of aerobic methane oxidation in two marine seep environments: Part 1—chemical kinetics. *J. Geophys. Res. Oceans* 124 (12), 8852–8868. doi:10.1029/2019jc015594

Chassignet, E. P., Hurlburt, H. E., Metzger, E. J., Smedstad, O. M., Cummings, J. A., Halliwell, G. R., et al. (2009). US GODAE: global ocean prediction with the Hybrid Coordinate Ocean Model (HYCOM). *Oceanography* 22 (2), 64–75. doi:10.5670/oceanog.2009.39

Chiswell, S. M. (2003). Circulation within the Wairarapa eddy, New Zealand. *N. Z. J. Mar. Freshw. Res.* 37 (4), 691–704. doi:10.1080/00288330.2003.9517199

Crespo-Medina, M., Meile, C. D., Hunter, K. S., Diercks, A. R., Asper, V. L., Orphan, V. J., et al. (2014). The rise and fall of methanotrophy following a deepwater oil-well blowout. *Nat. Geosci.* 7 (6), 423–427. doi:10.1038/ngeo2156

Crutchley, G. J., Hillman, J. I., Kroeger, K. F., Watson, S. J., Turco, F., Mountjoy, J. J., et al. (2023). Both longitudinal and transverse extension controlling gas migration through submarine anticlinal ridges, New Zealand's southern Hikurangi margin. *J. Geophys. Res. Solid Earth* 128 (6), e2022JB026279. doi:10.1029/2022jb026279

Crutchley, G. J., Mountjoy, J. J., Hillman, J. I. T., Turco, F., Watson, S., Flemings, P. B., et al. (2021). Upward doming zones of gas hydrate and free gas at the bases of gas chimneys, New Zealand's Hikurangi margin. *J. Geophys. Res. Solid Earth* 126, e2020JB021489. doi:10.1029/2020jb021489

De Angelis, M. A., Lilley, M. D., and Baross, J. A. (1993). Methane oxidation in deep-sea hydrothermal plumes of the endeavour segment of the juan de Fuca ridge. *Deep Sea Res. Part I Oceanogr. Res. Pap.* 40 (6), 1169–1186. doi:10.1016/0967-0637(93)90132-m

Dickson, A., and Millero, F. (1987). A comparison of the equilibrium constants for the dissociation of carbonic acid in seawater media. *Deep Sea Res.* 34, 1733–1743. doi:10.1016/0198-0149(87)90021-5

Dickson, A., Sabine, C., and Christian, J. (2007). "*Guide to best Practices for ocean CO_2 measurements*," in *PICES special publication 3 IOCCP report* (Sidney, BC: North Pacific Marine Science Organization).

Du, M., and Kessler, J. D. (2012). Assessment of the spatial and temporal variability of bulk hydrocarbon respiration following the Deepwater Horizon oil spill. *Environ. Sci. Technol.* 46 (19), 10499–10507. doi:10.1021/es301363k

Faure, K., Greinert, J., von Deimling, J. S., McGinnis, D. F., Kipfer, R., and Linke, P. (2010). Methane seepage along the Hikurangi Margin of New Zealand: geochemical and physical data from the water column, sea surface and atmosphere. *Mar. Geol.* 272 (1-4), 170–188. doi:10.1016/j.margeo.2010.01.001

Feely, R. A., Sabine, C. L., Byrne, R. H., Millero, F. J., Dickson, A. G., Wanninkhof, R., et al. (2012). Decadal changes in the aragonite and calcite saturation state of the Pacific Ocean. *Glob. Biogeochem. Cycles* 26 (3), 4157. doi:10.1029/2011gb004157

Fortunato, C. S., Butterfield, D. A., Larson, B., Lawrence-Slavas, N., Algar, C. K., Zeigler Allen, L., et al. (2021). Seafloor incubation experiment with deep-sea hydrothermal vent fluid reveals effect of pressure and lag time on autotrophic microbial communities. *Appl. Environ. Microbiol.* 87 (9), 000788–e121. doi:10.1128/aem.00078-21

Garcia-Tigreros, F., and Kessler, J. D. (2018). Limited acute influence of aerobic methane oxidation on ocean carbon dioxide and pH in Hudson canyon, northern U.S. Atlantic margin. *J. Geophys. Res. Biogeosciences* 123, 2135–2144. doi:10.1029/2018jg004384

Graves, C. A., Steinle, L., Rehder, G., Niemann, H., Connelly, D. P., Lowry, D., et al. (2015). Fluxes and fate of dissolved methane released at the seafloor at the landward limit of the gas hydrate stability zone offshore western Svalbard. *J. Geophys. Res. Oceans* 120, 6185–6201. doi:10.1002/2015jc011084

Gründger, F., Probandt, D., Knittel, K., Carrier, V., Kalenitchenko, D., Silyakova, A., et al. (2021). Seasonal shifts of microbial methane oxidation in Arctic shelf waters above gas seeps. *Limnol. Oceanogr.* 66 (5), 1896–1914. doi:10.1002/lno.11731

Haidvogel, D. B., Arango, H., Budgell, W. P., Cornuelle, B. D., Curchitser, E., Di Lorenzo, E., et al. (2008). Ocean forecasting in terrain-following coordinates: formulation and skill assessment of the regional Ocean modeling system. *J. Comput. Phys.* 227, 3595–3624. doi:10.1016/j.jcp.2007.06.016

Hanson, R. S., and Hanson, T. E. (1996). Methanotrophic bacteria. *Microbiol. Rev.* 60, 439–471. doi:10.1128/mr.60.2.439-471.1996

Henrys, S. A., Ellis, S., and Uruski, C. (2003). Conductive heat flow variations from bottom-simulating reflectors on the Hikurangi margin, New Zealand. *Geophys. Res. Lett.* 30 (2). doi:10.1029/2002gl015772

Henrys, S. A., Woodward, D. J., and Pecher, I. A. (2009). "Variation of bottom-simulating-reflection strength in a high-flux methane province, Hikurangi margin, New Zealand," in *Natural gas hydrates - energy resource potential and associated geologic hazards*. Editors T. Collett, A. Johnson, C. Knapp, and R. Boswell (AAPG Memoir), 481–489.

Hester, K. C., and Brewer, P. G. (2009). Clathrate hydrates in nature. *Annu. Rev. Mar. Sci.* 1, 303–327. doi:10.1146/annurev.marine.010908.163824

Higgs, B., Mountjoy, J. J., Crutchley, G. J., Townend, J., Ladroit, Y., Greinert, J., et al. (2019). Seep-bubble characteristics and gas flow rates from a shallow-water, high-density seep field on the shelf-to-slope transition of the Hikurangi subduction margin. *Mar. Geol.* 417, 105985. doi:10.1016/j.margeo.2019.105985

Kalnay, E., Kanimitsu, M., Kistler, R., Collins, W., Deaven, D., Gandin, L., et al. (1996). The NCEP/NCAR 40-year reanalysis Project. *Bull. Am. Meteorological Soc.* 77 (3), 437–471. doi:10.1175/1520-0477(1996)077<0437:tnyrp>2.0.co;2

Karl, D. M., Beversdorf, L., Björkman, K. M., Church, M. J., Martinez, A., and Delong, E. F. (2008). Aerobic production of methane in the sea. *Nat. Geosci.* 1 (7), 473–478. doi:10.1038/ngeo234

Kessler, J. D., Valentine, D. L., Redmond, M. C., Du, M., Chan, E. W., Mendes, S. D., et al. (2011). A persistent oxygen anomaly reveals the fate of spilled methane in the deep Gulf of Mexico. *Science* 331 (6015), 312–315. doi:10.1126/science.1199697

Klaucke, I., Weinrebe, W., Petersen, C. J., and Bowden, D. (2010). Temporal variability of gas seeps offshore New Zealand: multi-frequency geoacoustic imaging of the Wairarapa area, Hikurangi margin. *Mar. Geol.* 272 (1-4), 49–58. doi:10.1016/j.margeo.2009.02.009

Klauda, J. B., and Sandler, S. I. (2005). Global distribution of methane hydrate in ocean sediment. *Energy Fuels.* 19, 459–470. doi:10.1021/ef049798o

Krabbenhöft, A., Netzeband, G. L., Bialas, J., and Papenberg, C. (2010). Episodic methane concentrations at seep sites on the upper slope Opouawe Bank, southern Hikurangi Margin, New Zealand. *Mar. Geol.* 272 (1-4), 71–78. doi:10.1016/j.margeo.2009.08.001

Lane, E. M., Walters, R. A., Gillibrand, P., and Uddstrom, M. (2009). Operational forecasting of sea level height using an unstructured grid ocean model. *Ocean. Model.* 28, 88–96. doi:10.1016/j.ocemod.2008.11.004

Law, C. S., Nodder, S. D., Mountjoy, J., Marriner, A., Orpin, A., Pilditch, C. A., et al. (2010). Geological, hydrodynamic and biogeochemical variability of a New Zealand deep-water methane cold seep during an integrated three year time-series study. *Mar. Geol.* 272, 189–208. doi:10.1016/j.margeo.2009.06.018

Leonte, M., Kessler, J. D., Kellermann, M. Y., Arrington, E. C., Valentine, D. L., and Sylva, S. P. (2017). Rapid rates of aerobic methane oxidation at the feather edge of gas hydrate stability in the waters of Hudson Canyon, US Atlantic Margin. *Geochimica Cosmochimica Acta* 204, 375–387. doi:10.1016/j.gca.2017.01.009

Leonte, M., Wang, B., Socolofsky, S. A., Mau, S., Breier, J. A., and Kessler, J. D. (2018). Using carbon isotope fractionation to constrain the extent of methane dissolution into the water column surrounding a natural hydrocarbon gas seep in the northern Gulf of Mexico. *Geochem. Geophys. Geosystems* 19, 4459–4475. doi:10.1029/2018gc007705

Levin, L. A., Baco, A. R., Bowden, D. A., Colaco, A., Cordes, E. E., Cunha, M. R., et al. (2016). Hydrothermal vents and methane seeps: rethinking the sphere of influence. *Front. Mar. Sci.* 3, 3–72. doi:10.3389/fmars.2016.00072

Lewis, K. B., and Marshall, B. A. (1996). Seep faunas and other indicators of methane-rich dewatering on New Zealand convergent margins. *N. Z. J. Geol. Geophys.* 39 (2), 181–200. doi:10.1080/00288306.1996.9514704

Luo, M., Dale, A. W., Haffert, L., Haeckel, M., Koch, S., Crutchley, G., et al. (2016). A quantitative assessment of methane cycling in Hikurangi Margin sediments (New Zealand) using geophysical imaging and biogeochemical modeling. *Geochem. Geophys. Geosyst.* 17, 4817–4835. doi:10.1002/2016gc006643

Mao, S. H., Zhang, H. H., Zhuang, G. C., Li, X. J., Liu, Q., Zhou, Z., et al. (2022). Aerobic oxidation of methane significantly reduces global diffusive methane emissions from shallow marine waters. *Nat. Commun.* 13 (1), 7309. doi:10.1038/s41467-022-35082-y

Maslin, M., Owen, M., Betts, R., Day, S., Dunkley Jones, T., and Ridgwell, A. (2010). Gas hydrates: past and future geohazard? *Philosophical Trans. R. Soc. A Math. Phys. Eng. Sci.* 368 (1919), 2369–2393. doi:10.1098/rsta.2010.0065

Mau, S., Blees, J., Helmke, E., Niemann, H., and Damm, E. (2013). Vertical distribution of methane oxidation and methanotrophic response to elevated methane

concentrations in stratified waters of the Arctic fjord Storfjorden (Svalbard, Norway). *Biogeosciences* 10 (10), 6267–6278. doi:10.5194/bg-10-6267-2013

McGinnis, D. F., Greinert, J., Artemov, Y., Beaubien, S. E., and Wüest, A. N. D. A. (2006). Fate of rising methane bubbles in stratified waters: how much methane reaches the atmosphere? *J. Geophys. Res. Oceans* 111 (C9), 3183. doi:10.1029/2005jc003183

Mehrbach, C., Culberson, C. H., Hawley, J. E., and Pytkowicz, R. M. (1973). Measurement of the apparent dissociation constants of carbonic acid in seawater at atmospheric pressure. *Limnol. Oceanogr.* 19, 897–907. doi:10.4319/lo.1973.18.6.0897

Ministry for the Environment (2022). *New Zealand's Greenhouse gas inventory 1990–2020*. Wellington: Ministry for the Environment.

Mitchell, G. A., Mayer, L. A., and Gharib, J. J. (2022). Bubble vent localization for marine hydrocarbon seep surveys. *Interpretation* 10 (1), SB107–SB128. doi:10.1190/int-2021-0084.1

Moridis, G. J., Collett, T. S., Pooladi-Darvish, M., Hancock, S., Santamarina, C., Boswell, R., et al. (2011). Challenges, uncertainties, and issues facing gas production from gas-hydrate deposits. *SPE Reserv. Eval. Eng.* 14 (01), 76–112. doi:10.2118/131792-pa

Naudts, L., Greinert, J., Poort, J., Belza, J., Vangampelaere, E., Boone, D., et al. (2010). Active venting sites on the gas-hydrate-bearing Hikurangi Margin, off New Zealand: diffusive-versus bubble-released methane. *Mar. Geol.* 272 (1-4), 233–250. doi:10.1016/j.margeo.2009.08.002

Niemann, H., Linke, P., Knittel, K., MacPherson, E., Boetius, A., Brueckmann, W., et al. (2013). Methane-carbon flow into the benthic food web at cold seeps–a case study from the Costa Rica subduction zone. *PLoS One* 8 (10), e74894. doi:10.1371/journal.pone.0074894

Oschlies, A., Brandt, P., Stramma, L., and Schmidtko, S. (2018). Drivers and mechanisms of ocean deoxygenation. *Nat. Geosci.* 11 (7), 467–473. doi:10.1038/s41561-018-0152-2

Osudar, R., Matoušů, A., Alawi, M., Wagner, D., and Bussmann, I. (2015). Environmental factors affecting methane distribution and bacterial methane oxidation in the German Bight (North Sea). *Estuar. Coast. Shelf Sci.* 160, 10–21. doi:10.1016/j.ecss.2015.03.028

Paul, D., Skrzypek, G., and Forizs, I. (2007). Normalization of measured stable isotopic compositions to isotope reference scales - a review. *Rapid Commun. Mass Spectrom.* 21 (18), 3006–3014. doi:10.1002/rcm.3185

Phrampus, B. J., and Hornbach, M. J. (2012). Recent changes to the Gulf Stream causing widespread gas hydrate destabilization. *Nature* 490 (7421), 527–530. doi:10.1038/nature11528

Reeburgh, W. S. (2007). Oceanic methane biogeochemistry. *Chem. Rev.* 107 (2), 486–513. doi:10.1021/cr050362v

Rickard, G. (2020). Three-dimensional hydrodynamic modelling of tidal flows interacting with aquaculture fish cages. *J. Fluids Struct.* 93, 102871. doi:10.1016/j.jfluidstructs.2020.102871

Rickard, G. J., Behrens, E., Chiswell, S., Law, C. S., and Pinkerton, M. H. (2023). Biogeochemical and physical assessment of CMIP5 and CMIP6 ocean components for the southwest pacific ocean JGR *biogeosciences*. *JGR. Biogeosciences* 128, e2022JG007123. doi:10.1029/2022jg007123

Rudebusch, J. A., Prouty, N. G., Conrad, J. E., Watt, J. T., Kluesner, J., Hill, J. C., et al. (2023). Diving deeper into seep distribution along the Cascadia convergent margin, United States. *Front. Earth Sci.* 11, 1205211. doi:10.3389/feart.2023.1205211

Ruppel, C. D. (2011). Methane hydrates and contemporary climate change. *Nat. Educ. Knowl.* 2 (12), 12.

Ruppel, C. D., and Kessler, J. D. (2017). The interaction of climate change and methane hydrates. *Rev. Geophys.* 55 (1), 126–168. doi:10.1002/2016rg000534

Santrock, J., Studley, S. A., and Hayes, J. M. (1985). Isotopic analyses based on the mass spectra of carbon dioxide. *Anal. Chem.* 57, 1444–1448. doi:10.1021/ac00284a060

Saunois, M., Stavert, A. R., Poulter, B., Bousquet, P., Canadell, J. G., Jackson, R. B., et al. (2020). The global methane budget 2000–2017. *Earth Syst. Sci. data* 12 (3), 1561–1623. doi:10.5194/essd-12-1561-2020

Schlitzer, R. (2021). Ocean data View. Avaliable At: https://odv.awi.de.

Seabrook, S., De Leo, F. C., and Thurber, A. R. (2019). Flipping for food: the use of a methane seep by tanner crabs (Chionoecetes tanneri). *Front. Mar. Sci.* 6, 43. doi:10.3389/fmars.2019.00043

Sommer, S., Pfannkuche, O., Linke, P., Luff, R., Greinert, J., Drews, M., et al. (2006). Efficiency of the benthic filter: biological control of the emission of dissolved methane from sediments containing shallow gas hydrates at Hydrate Ridge. *Glob. Biogeochem. Cycles* 20, GB2019. doi:10.1029/2004gb002389

Steinle, L., Graves, C. A., Treude, T., Ferré, B., Biastoch, A., Bussmann, I., et al. (2015). Water column methanotrophy controlled by a rapid oceanographic switch. *Nat. Geosci.* 8 (5), 378–382. doi:10.1038/ngeo2420

Steinle, L., Schmidt, M., Bryant, L., Haeckel, M., Linke, P., Sommer, S., et al. (2016). Linked sediment and water-column methanotrophy at a man-made gas blowout in the North Sea: implications for methane budgeting in seasonally stratified shallow seas. *Limnol. Oceanogr.* 61 (S1), S367–S386. doi:10.1002/lno.10388

Stevens, C. L., Sutton, P. J., and Law, C. S. (2012). Internal waves downstream of Norfolk Ridge, western Pacific, and their biophysical implications. *Limnol. Oceanogr.* 57 (4), 897–911. doi:10.4319/lo.2012.57.4.0897

Trivedi, A., Sarkar, S., Marin-Moreno, H., Minshull, T. A., Whitehouse, P. L., and Singh, U. (2022). Reassessment of hydrate destabilization mechanisms offshore west Svalbard confirms link to recent ocean warming. *J. Geophys. Res. Solid Earth* 127 (11), e2022JB025231. doi:10.1029/2022jb025231

Turco, F., Ladroit, Y., Watson, S. J., Seabrook, S., Law, C. S., Crutchley, G. J., et al. (2022). Estimates of methane release from gas seeps at the southern Hikurangi margin, New Zealand. *Front. Earth Sci.* 10, 834047. doi:10.3389/feart.2022.834047

USEPA: Office of Atmospheric Programs (6207J) (2010). *Methane and nitrous oxide emissions from natural sources*. Washington, DC: U.S. Environmental Protection Agency. Available at: http://nepis.epa.gov/.

Valentine, D. L., Blanton, D. C., Reeburgh, W. S., and Kastner, M. (2001). Water column methane oxidation adjacent to an area of active hydrate dissociation, Eel River Basin. *Geochimica Cosmochimica Acta* 65 (16), 2633–2640. doi:10.1016/s0016-7037(01)00625-1

Wallmann, K., Pinero, E., Burwicz, E., Haeckel, M., Hensen, C., Dale, A., et al. (2012). The global inventory of methane hydrate in marine sediments: a theoretical approach. *Energies* 5, 2449–2498. doi:10.3390/en5072449

Walters, R. A., Goring, D. G., and Bell, R. G. (2001). Ocean tides around New Zealand. *N. Z. J. Mar. Freshw. Res.* 35, 567–579. doi:10.1080/00288330.2001.9517023

Watson, S. J., Mountjoy, J. J., Barnes, P. M., Crutchley, G. J., Lamarche, G., Higgs, B., et al. (2020). Focused fluid seepage related to variations in accretionary wedge structure, Hikurangi margin, New Zealand. *Geology* 48 (1), 56–61. doi:10.1130/g46666.1

Weber, T., Wiseman, N. A., and Kock, A. (2019). Global ocean methane emissions dominated by shallow coastal waters. *Nat. Commun.* 10, 4584–4610. doi:10.1038/s41467-019-12541-7

Weinstein, A., Navarrete, L., Ruppel, C., Weber, T. C., Leonte, M., Kellermann, M. Y., et al. (2016). Determining the flux of methane into Hudson Canyon at the edge of methane clathrate hydrate stability. *Geochem. Geophys. Geosystems* 17 (10), 3882–3892. doi:10.1002/2016gc006421

Weisenburg, D. A., and Guinasso, N. L. (1979). Equilibrium solubilities of methane, carbon monoxide and hydrogen in water and seawater. *J. Chem. Eng. Data* 24, 354–360. doi:10.1021/je60083a006

Weller, D. I., Law, C. S., Maas, E. W., Marriner, A., Nodder, S., Chang, H., et al. (2013). Temporal variation of dissolved methane in a subtropical mesoscale eddy during a phytoplankton bloom in the southwest Pacific Ocean. *Prog. Oceanogr.* 116, 193–206. doi:10.1016/j.pocean.2013.07.008

Wilson, S. T., Bange, H. W., Arévalo-Martínez, D. L., Barnes, J., Borges, A. V., Brown, I., et al. (2018). An intercomparison of oceanic methane and nitrous oxide measurements. *Biogeosciences* 15, 5891–5907. doi:10.5194/bg-15-5891-2018

Yarnes, C. (2013). δ13C and δ2H measurement of methane from ecological and geological sources by gas chromatography/combustion/pyrolysis isotope-ratio mass spectrometry. *Rapid Commun. Mass Spectrom.* 27, 1036–1044. doi:10.1002/rcm.6549

Frontiers in Earth Science

Investigates the processes operating within the major spheres of our planet

Advances our understanding across the earth sciences, providing a theoretical background for better use of our planet's resources and equipping us to face major environmental challenges.

Discover the latest Research Topics

See more →



Frontiers

Avenue du Tribunal-Fédéral 34
1005 Lausanne, Switzerland
frontiersin.org

Contact us

+41 (0)21 510 17 00
frontiersin.org/about/contact